Handbook on the Physics and Chemistry of Rare Earths, volume 24

Elsevier, 1997

Edited by: Karl A. Gschneidner, Jr. and LeRoy Eyring
ISBN: 978-0-444-82607-7

Handbook on the Physics and Chemistry of Rare Earths
Vol. 24
edited by K.A. Gschneidner, Jr. and L. Eyring

PREFACE

Karl A. GSCHNEIDNER, Jr., and LeRoy EYRING

These elements perplex us in our rearches [sic], *baffle us in our speculations, and haunt us in our very dreams. They stretch like an unknown sea before us – mocking, mystifying, and murmuring strange revelations and possibilities.*

Sir William Crookes (February 16, 1887)

This volume contains a potpourri of topics concerning the physics and materials science of mostly metallic rare earth materials. Topics deal with the formation of amorphous, microcrystalline and quasicrystalline phases by mechanical alloying (ch. 160), rapid solidification and even normal casting operations (ch. 161). As is often the case with these 4f elements, magnetism is a dominant topic: included in this volume are surface magnetism (ch. 159), electron-spin resonance (ch. 162), exchange coupling in lanthanide–transition metal phases (ch. 163), and the magnetic behavior of ternary rare-earth stannides, plus their crystal structures (ch. 164).

As described in the first chapter (159), by Dowben, McIlroy and Li, the surface magnetism of the lanthanide metals is significantly different from the bulk magnetic properties, which in part is due to enhanced magnetization at the surface, imperfect ferromagnetic alignment of the surface with the bulk, and a magnetic coupling at the surface which is significantly different from that in the bulk. One of the unusual features is that the Curie temperature of the surface is significantly enhanced (5 to 10% higher) from that of the bulk material.

The use of mechanical alloying as a processing technique to prepare amorphous, nanocrystalline and metastable phases is discussed by McCormick in ch. 160. Many times these states of matter are used as intermediates for forming equilibrium materials by additional processing steps. These include the rare-earth permanent-magnet materials $SmCo_5$, Nd_2Fe14_B and $Sm_2Fe_{17}N$. Also as described, this technique can be used to refine metals and compounds, and induce other chemical reactions at or near room temperature.

Metastable metallic systems were discovered about 35 years ago and interest has grown by leaps and bounds ever since then. However, extensive research on rare-earth-containing materials did not begin until about 10 years ago. In this decade many novel materials have been prepared, as pointed out by Inoue (ch. 161). These include the strongest Al-based alloys ever prepared, and some unique Mg-based and Al-based quasicrystalline

materials. The former, interestingly enough, is an amorphous aluminum–transition metal–rare-earth metal alloy. Although most of these amorphous alloys are obtained as thin strips by rapid solidification techniques, bulk amorphous alloys have been prepared by casting and, amazingly enough, the rare-earth element is the major component of these materials.

Electron-spin resonance (ESR) is an extremely useful tool for probing the localized magnetic moment in a variety of materials. The chapter (162) by Elschner and Loidl focuses on metallic lanthanide systems, reviewing both the classical ESR behaviors and the role of ESR in newly developed branches of solid-state physics. The former includes the determination of the site symmetry of the ESR probe and measurement of the crystal field (CF) and how it (CF) differs in metallic systems from that in insulators. The latter deals with Van Vleck systems, spin glasses, Kondo systems, heavy-fermion and intermediate-valence compounds, and high-temperature superconductors.

In the next chapter (163) Duc examines the exchange interactions and magnetocrystalline anisotropies in lanthanide–transition metal intermetallic compounds. The three interactions are: between the 4f metals, between the 4f metal and the transition metal, and between transition metals. The last interaction is primarily responsible for strong magnetic properties and high magnetic ordering temperatures. The first two give rise to large magnetic anisotropies, and the combination of all three accounts for some of the most important commercial applications of rare-earth materials – permanent magnets, magneto-optic recording and magnetostrictive devices.

The final chapter (164) by Skolozdra reviews the phase relationships, crystallography and crystal chemistry of binary and ternary rare-earth–tin materials. The third component is mostly a late transition metal from the first series (i.e., Mn, Fe, Co, Ni and Cu) but also includes information on the second series (Ru, Rh, Pd and Ag) and the third series (Os, Ir, Pt and Au). The last quarter of his review examines the physical property behaviors of these ternary compounds and summarizes the known magnetic, electrical resistivity, thermoelectric and superconducting properties. Some of the more interesting stannides included are the RRh_xSn_y or ROs_uSn_v phases which exhibit both a superconducting and a ferromagnetic transition. In general the material has a ferromagnetic ground state, which becomes a superconductor upon heating, and finally a normal metal.

CONTENTS

CONTENTS OF VOLUMES 1–23

VOLUME 4: Non-metallic compounds – II

1979, 1st repr. 1984; ISBN 0-444-85216-6

VOLUME 5

1982, 1st repr. 1984; ISBN 0-444-86375-3

VOLUME 6

1984; ISBN 0-444-86592-6

VOLUME 7

1984; ISBN 0-444-86851-8

VOLUME 8

1986; ISBN 0-444-86971-9

VOLUME 9

1987; ISBN 0-444-87045-8

VOLUME 10: High energy spectroscopy

1988; ISBN 0-444-87063-6

VOLUME 11: Two-hundred-year impact of rare earths on science

1988; ISBN 0-444-87080-6

VOLUME 12

1989; ISBN 0-444-87105-5

VOLUME 13

1990; ISBN 0-444-88547-1

VOLUME 14

1991; ISBN 0-444-88743-1

VOLUME 15

1991; ISBN 0-444-88966-3

MASTER INDEX, Vols. 1–15
1993; ISBN 0-444-89965-0

VOLUME 16
1993; ISBN 0-444-89782-8

VOLUME 17: Lanthanides/Actinides: Physics – I
1993; ISBN 0-444-81502-3

VOLUME 18: Lanthanides/Actinides: Chemistry
1994; ISBN 0-444-81724-7

VOLUME 19: Lanthanides/Actinides: Physics – II

1994; ISBN 0-444-82015-9

VOLUME 20

1995; ISBN 0-444-82014-0

VOLUME 21

1995; ISBN 0-444-82178-3

VOLUME 22

1996; ISBN 0-444-82288-7

VOLUME 23

1996; ISBN 0-444-82507-X

Handbook on the Physics and Chemistry of Rare Earths
Vol. 24
edited by K.A. Gschneidner, Jr. and L. Eyring

Chapter 159

SURFACE MAGNETISM OF THE LANTHANIDES

P.A. Dowben and D.N. McIlroy
Department of Physics and the Center for Materials Research and Analysis, Behlen Laboratory of Physics, University of Nebraska, Lincoln, NB 68588-0111, USA

Dongqi Li
Materials Science Division, Argonne National Laboratory, Argonne, IL 60439, USA

Contents

List of symbols

a	lattice constant
C_{6v}	six-fold rotation group of the (0001) hexagonal close packed surface
d	film thickness
E_s	surface energy density
E_F	Fermi level
ΔE_{ex}	exchange splitting
$\Delta E_{ex,local}$	local exchange splitting
J_{sc}	critical magnetic coupling strength
J_b	magnetic coupling strength with the bulk
J_s	magnetic coupling strength within the surface layer
$\boldsymbol{k}$	wave vector of the band electron
$\boldsymbol{k}_{\parallel}$	wave vector of the band electron parallel to the surface
$\boldsymbol{k}_{\perp}$	wave vector of the band electron normal to the surface
k_B	Boltzmann constant
K_s	surface anisotropy constant
l	electron phase coherence length
M	magnetization
M_R	remanent magnetization
ps	picosecond
T	temperature
t	reduced temperature $(T-T_C)/T_C$
T_C	Curie temperature
T_C(surface)	surface Curie temperature
T_C(bulk)	bulk Curie temperature
T_N	Néel temperature
T_N(bulk)	bulk Néel temperature
U	Coulomb repulsion energy or correlation energy
w	band width
β	critical exponent for magnetization

γ	critical exponent for static susceptibility	θ	angle between the surface and the bulk
$\bar{\Gamma},\Gamma,A,\bar{M},M,$ $H,L,\bar{K},K$	high symmetry points of the bulk and surface Brillouin zone as indicated in fig. 3	μ_B	Bohr magneton
		ν	critical exponent for finite size scaling
		χ	static susceptibility
$\Delta_1,\Delta_2,$ Δ_5,Δ_6	group representation elements in the six-fold rotation group corresponding to the representation elements A_1, A_2, E_1, and E_2, respectively		

1. Introduction

At first glance, it would seem that the lanthanide metals should be amongst the most simple of magnetic systems. The magnetic moments are dominated by the highly localized 4f orbitals. These metals should be excellent examples of local moment ferromagnets, and the local spin density approximation should be valid. As with many aspects of magnetism, there are, in fact, a number of complications that are observed upon closer inspection. The complications include enhanced magnetization at the surface, imperfect ferromagnetic alignment of the surface with the bulk, and vastly different magnetic coupling at the surface, as opposed to that within the bulk. Unfortunately, these complications are not reflected in many simple models of magnetism. Local density approximations are among the methods that often fail to provide an accurate description of these localized moment systems. Thus, the magnetic properties of the lanthanides, particularly at the surface, are often understood in terms of the experimental results and not theoretical predictions.

Much of our own work has been motivated by the apparent simplicity of the rare-earth metals. The lanthanides are elemental ferromagnets with large moments as a result of the 4f electrons. The metals (primarily gadolinium and terbium) show magnetic behavior in the very thinnest of films (less than ten atoms thick), that surprisingly, agrees well with simple mean-field models of ferromagnetism (Dowben et al. 1991, 1993, LaGraffe et al. 1990a,b, Miller and Dowben 1993, Taborelli et al. 1986). While it is satisfying and even seductive, to have experimental agreement with easily expressed theoretical models, the agreement between experiment and theory cannot hide the complex interplay between electronic structure and the magnetic properties of the rare-earth systems.

Pure rare-earth thin film metals and surfaces are far too reactive (see chs. 41 and 43, vol. 5 and ch. 136, vol. 20 of this Handbook series) to have directly practical industrial applications such as in the area of magnetic recording media. Nonetheless, an understanding of the pure materials provides insight into the rare-earth alloys and rare earth–transition metal multilayers that are far more likely to have many immediate and long term applications (Parker 1990). Examples include materials like $SmCo_5$ and $Nd_2Fe_{14}B$ that are strong permanent magnet materials, and rare-earth alloys and lanthanide–transition-metal multilayers often possess perpendicular magnetic anisotropy, which is important for magnetic recording media (Parker 1990, Sellmyer 1992, 1994, Shan and Sellmyer 1996). Developing an accurate picture of the relationship between the

electronic structure and magnetic properties in the lanthanide metals is invaluable to the understanding of these more complex systems.

To understand the surface magnetism of the lanthanides, one needs to understand the electronic structure. The conduction electrons are the medium of exchange interaction between adjacent 4f moments, so that electron itinerancy plays a strong role in lanthanide magnetism. Both the surface magnetic properties and the surface electronic structure of the lanthanide metals differ from that of the bulk. This review will, therefore, often include descriptions of the bulk magnetic and electronic structure so that comparisons between the bulk and the surface can be made more readily.

The prosaic experimental difficulties that are encountered when working with surfaces of the rare-earth metals have proven to be formidable barriers to the study of their magnetic properties. These impediments have sometimes led otherwise careful experimentalists astray. These difficulties include such basic problems as preparing a clean rare-earth surface, growing a clean and well-ordered thin film, rapid alloying or interdiffusion with some substrates, and preserving a clean surface during the acquisition of data (Barrett 1992, Netzer and Matthew 1986). These problems are so intractable that the study of lanthanide surface magnetic properties has been largely restricted to polycrystalline materials or the (0001) basal plane surfaces of gadolinium and terbium crystals and thin films. In spite of these hurdles, the picture that emerges of the surface magnetic properties is fascinating and provides insight into the problems associated with understanding surface magnetism in general. The study of the lanthanide surfaces has been, and will continue to be, an integral part of the overall investigation of surface magnetism.

2. The enhanced Curie temperature of the surface

Due to the reduced dimensionality of surfaces, it is now quite clear that the surface may exhibit different magnetic properties from the bulk (Binder 1985, Diehl 1986, Freeman and Fu 1986, Freeman and Wu 1991, Kaneyoshi 1991b, Mills 1970). Perhaps the most remarkable example of the unique magnetic properties possible at surfaces is the condition of magnetically ordered surfaces at temperatures where the bulk material is paramagnetic. This is well documented for the lanthanides. An enhanced magnetization has been proposed for chromium surfaces (Freeman and Wu 1991, Ferguson 1978). Another example of this behavior is seen in the face-centered iron phase formed by iron deposition on Cu(100) (Dongqi Li et al. 1994b, Thomasson et al. 1992). This property of lanthanide surfaces is a dramatic example of the different magnetic properties that exist at surfaces and it is where we begin this review.

The lanthanide surfaces have an enhanced Curie temperature: a surface Curie temperature higher for the surface than for the bulk. This phenomenon was first observed for gadolinium, as indicated in fig. 1. Using spin-polarized electron capture techniques, the surface Curie temperature, T_C(surface), was found to be about 17 K higher than the bulk Curie temperature where T_C(bulk) = 293 K. Values for the surface Curie temperature

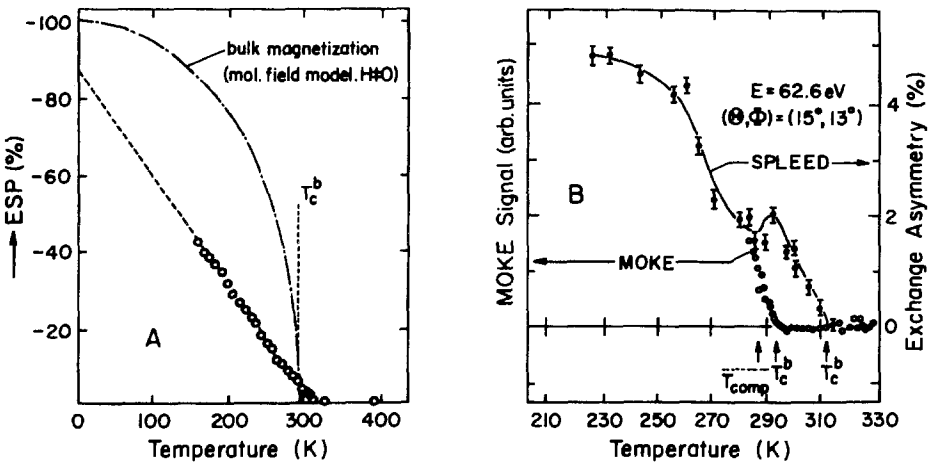

Fig. 1. The surface magnetization of gadolinium as a function of temperature: (A) electron spin polarization, taken from Rau and Eichner (1981) and Rau (1982); (B) the surface Curie temperature measured from SPLEED compared with the bulk Curie temperature derived from MOKE, as taken from Weller et al. (1985a).

of 310 K (Rau and Eichner 1986), and 311 K (Rau and Eichner 1981, Rau 1982) have been reported. By combining spin-polarized low-energy electron diffraction (SPLEED) to measure the surface magnetic ordering with magneto-optic Kerr effect (MOKE) techniques (as indicated in fig. 1), the enhanced surface Curie temperature T_C(surface) of Gd(0001) was found to be about 315 K, or 22 K higher than the bulk value (Weller and Alvarado 1985b, Weller et al. 1985a,b). These results have been supported by recent spin-polarized photoemission and spin secondary electron spectroscopy measurements which have also demonstrated that the surface Curie temperature, T_C(surface), of gadolinium is higher than observed for the bulk (Dongqi Li et al. 1993b, 1995, 1996, Tang et al. 1993a,b, Vescovo et al. 1993b). A surface Curie temperature, T_C(surface), some 60±2 K higher than T_C(bulk) has now been observed for Gd(0001) (Tang et al. 1993a,b), as indicated by the two distinct transitions in fig. 2. Some results suggest that the difference between the two Curie temperatures may be even higher (Vescovo et al. 1993b).

The general increase in T_C(surface) over T_C(bulk) with time can be attributed to the improving gadolinium film quality. Even though these studies have been carried out on evaporated films, the art of growing flat, well ordered films of great purity has taken some time to develop.

In addition to gadolinium, terbium also has a higher surface Curie temperature, T_C(surface), relative to the bulk. Surface Curie temperatures of 248 K (Rau and Waters 1988, Rau et al. 1988, 1989a) to 250 K (Rau and Jin 1988, Rau 1989, Rau et al. 1989b) have been observed, ranging from 20 to 22 K higher than the bulk Néel temperature T_N(bulk) = 228 K, and 28 to 30 K higher than the bulk Curie temperature T_C(bulk) = 220 K.

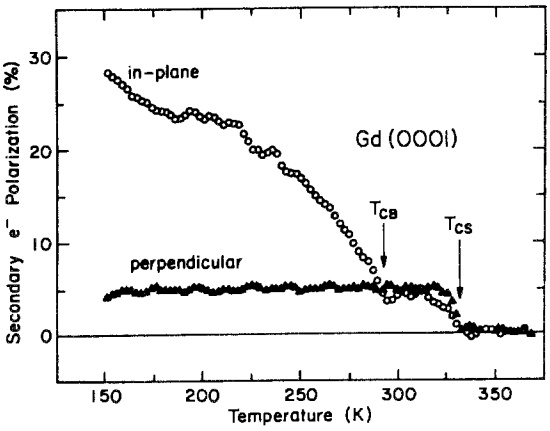

Fig. 2. The spin polarization of the 2 eV secondary electrons from a 400 Å thick film oriented along Gd(0001). The bulk and surface Curie temperatures are indicated. (Data from Tang et al. 1993a,b.)

The higher surface Curie temperature implies that there is enhanced magnetic order at the surface relative to the bulk. The higher surface Curie temperature has been extensively studied with various statistical models (Binder 1985, Diehl 1986, Mills 1970). The models investigated semi-infinite systems with varying magnetic coupling strength within the surface (J_s), with respect to the coupling strength within the bulk (J_b). These calculations indicate that the surface Curie temperature, T_C(surface), equals the bulk Curie temperature, T_C(bulk), for small J_s. For sufficiently enhanced coupling in the surface layer ($J_s > J_{sc}$), then T_C(surface) > T_C(bulk), where J_{sc} is the critical coupling strength. For a semi-infinite Ising system, J_{sc}/J_b is estimated as 1.5 based on Monte Carlo simulations (Binder 1985, Diehl 1986, Mills 1970). For $J_s < J_b$, the surface becomes magnetically soft to spin-wave excitations and this will result in suppressed surface magnetic order at finite temperatures. The question is: how does the coupling become enhanced at the surfaces of gadolinium and terbium? Since the coupling of the 4f moments is indirect through the conduction electrons, the answer should lie in the altered surface electronic structure. In other words, for enhanced surface magnetic order to occur, there must exist a distinctly different electronic structure at the surface compared to the bulk. It is this issue we address next.

3. The electronic structure of the surface

The two fundamental elements of magnetism – magnetic moment and exchange coupling – are both determined by the electronic structure of the system. In describing the origin of the magnetic properties of the surface, we must also characterize the surface electronic structure. Our emphasis will be on the valence and conduction band electronic structure. As indicated in our introductory remarks, the valence electrons determine the exchange coupling and provide the additional contribution to the magnetic moment besides the 4f contribution. Thus, the bands generated by the 5d and 6s electrons constitute

the area of the electronic structure of the lanthanides that is of greatest interest to the discussion of magnetism.

The occupied 4f levels form "shallow" core levels that can be observed in the valence band region of the lanthanides. In photoemission, the 4f levels dominate the spectrum at high energies (photon energies above 70 eV), while the 5d/6s bands only dominate the spectrum at lower photon energies (below 50 eV). The 4f levels are effectively isolated from the conduction electrons by a strong centrifugal barrier, although there is some mixing between the 4f and conduction electron states. While the bandwidths, both measured and expected, for the 4f states are quite small (of the order of 100 meV or less), the 4f levels can have a rich structure in photoemission. This is primarily a consequence of the multiplet structure that forms as a consequence of the photoemission final states (Baer and Schneider 1987, Cox 1975, Cox et al. 1973, 1981, Liu 1978, Thole et al. 1993). For gadolinium, the 4f levels are exactly half filled, i.e. ($4f^7 5d^1 6s^2$), and are 100% spin polarized in the ground state. The 4f levels provide a large moment of $7\mu_B$, which dominates the gadolinium magnetic moment. It is gadolinium, the only lanthanide that exhibits ferromagnetism at room temperature, that in fact has the most simple photoemission valence-band spectra among the lanthanides. This is due to the simple multiplet structure of the 4f levels (Baer and Schneider 1987, Cox 1975, Cox et al. 1973, 1981, Liu 1978, Thole et al. 1993). The gadolinium 5d/6s bands are between the Fermi energy E_F and 3 eV below E_F (Barrett 1992, Dongqi Li et al. 1991a, 1992a,b, 1993a,b, 1994a, Vescovo et al. 1993a), while the 4f levels are about 8.5 eV below E_F (Barrett 1992, Lang et al. 1981, Ortega et al. 1994).

A great deal of the experimental work related to the electronic structure has concerned core level (inner shell) spectroscopy as can be seen from the literature in table 1. Much of that work has looked at final-state effects (Baer and Schneider 1987, Campagna and Hillebrecht 1987, Herbst et al. 1972, B. Johansson 1974, B. Johansson and Rosengren 1975) such as multiplets (Baer and Schneider 1987, Cox 1975, Cox et al. 1973, 1981, Gerken 1983, Liu 1978, Thole et al. 1993) and other effects such as the surface to bulk core-level shift (Aldén et al. 1995, Flodström et al. 1992, Gerken et al. 1985, B. Johansson 1979, B. Johansson and Mårtensson 1983, Erbudak et al. 1983, Rosengren and Johansson 1982, Wertheim and Crecelius 1978). Core-level spectroscopies, particularly for spin-integrated electron spectroscopies, do not generally provide great insight into the magnetic properties or the band structure (Ahuja et al. 1994, Begley et al. 1990, Fedorov et al. 1993, Kaindl et al. 1995, Navas et al. 1993). Spin-polarized measurements of the shallow 4f levels, however, can provide valuable information on the magnetic ordering at the surface, as will be discussed later.

As can be seen from table 1, most of the band structure calculations are for the bulk (for reviews of the bulk electronic structure see Barrett 1992 and Liu 1978). Often these calculations are along the Γ-A direction of the bulk Brillouin zone (as indicated in the diagram of the surface and bulk Brillouin zone in fig. 3). There are a few calculations that do consider the electronic structure of the surface. Of particular interest are surface states: states that occur in a gap of the bulk band structure when projected on to the surface Brillouin zone. Surface resonances, i.e. states where there is considerable weight

Table 1
Summary of the studies of electronic structure and the band structure of the rare-earth metals

R	Theory	References	Experiment	References
Sc	APW	Fleming and Loucks 1968, Rath and Freeman 1975	dHvA	Schirber et al. 1983
	KKR	Matsumoto et al. 1991	IPE/BIS	Lamouri et al. 1995, Speier et al. 1984
	LDOS	Feibelman and Hamann 1979	XPS/UPS	Eastman 1969
	LAPW	Blaha et al. 1988	ARUPS	Barrett 1992, Blyth et al. 1992, Patchett et al. 1993, 1994
	LMTO	Lamouri et al. 1995		
	LCAO	Das 1976		
	cellular method	Altmann and Bradley 1967		
Y	APW	Gupta and Loucks 1968, Loucks 1966	positron annihilation	Williams et al. 1966, Williams and Mackintosh 1968
	LAPW	Blaha et al. 1988	ARUPS	Barrett and Jordan 1987, Barrett et al. 1987, 1989a–c, 1991a,b, Barrett 1992, Blyth et al. 1991a,c,d, 1992, Jordan et al. 1990
	KKR	Matsumoto et al. 1991	IPES/BIS	Barrett 1992, Blyth et al. 1991c,d, Speier et al. 1984
	cellular method	Altmann and Bradley 1967	XPS/UPS	Eastman 1969, L.I. Johansson et al. 1980, Stenborg et al. 1989a
			dHvA	Young et al. 1974
La	RAPW	Fleming and Loucks 1968, Fleming et al. 1968, Myron and Liu 1970	ARUPS	Barrett and Jordan 1987, Barrett et al. 1987, Fedorov et al. 1994b, Weschke et al. 1994
	LMTO	Aldén et al. 1995, McMahan et al. 1981, Min et al. 1986d	IPE/BIS	Duò et al. 1993, Fedorov et al. 1993, J.K. Lang et al. 1978, 1981, Liefeld et al. 1974, Riehl 1978, Weschke et al. 1994
	SC-LAPW	Singh 1991a	EELS	Matthew et al. 1983, Moser et al. 1984, Netzer et al. 1983a, Netzer et al. 1985, Strasser et al. 1984, 1985
	RHF	Herbst 1992	XPS/UPS	Baer and Busch 1973, Crecelius et al. 1978, Kowalczyk et al. 1974, J.K. Lang et al. 1981, McFeely et al. 1974, Moser et al. 1984, Nilsson et al. 1985, Platau et al. 1981, Wertheim and Campagna 1978, Wieliczka et al. 1984a
			positron annihilation	Szuszkiewicz 1973

continued on next page

Table 1, *continued*

R	Theory	References	Experiment	References
Ce	APW	Hill and Kmetko 1975, Kmetko and Hill 1976	ARUPS	Jensen and Wieliczka 1984, Rosina et al. 1985, 1986a
	LMTO	Aldén et al. 1995, Glötzel 1978, Glötzel 1981, Min et al. 1986b,d,e, Podloucky and Glötzel 1983	XPS/UPS	Allen et al. 1981, Allen and Martin 1982, Baer and Busch 1973, 1974, Baer et al. 1981, Crecelius et al. 1978, Fujimori and Weaver 1985, Gerken et al. 1982a,b, Gu et al. 1991, Helms and Spicer 1972, Herbst et al. 1972, Hüfner and Steiner 1982, L.I. Johansson et al. 1978, Kierren et al. 1996, Kowalczyk et al. 1974, J.K. Lang et al. 1981, Lawrence et al. 1982, Liu and Ho 1982, Liu and Ho 1983, Mårtensson et al. 1982, McFeely et al. 1974, Matthew et al. 1982, 1983, Patthey et al. 1985, Platau and Karlsson 1978, Platau et al. 1981, Vescovo and Carbone 1996, Weaver et al. 1985, Weschke et al. 1991, Weschke et al. 1994, Wieliczka et al. 1982, 1984a,b, Wolff et al. 1976, Wuilloud et al. 1983
	LAPW	Min et al. 1986b, Pickett et al. 1981	IPE/BIS	Baer et al. 1981, Chamberlain et al. 1974, Gudat et al. 1982, J.K. Lang et al. 1978, 1981, Wuilloud et al. 1983
	RHF	Herbst and Wilkins 1984	EELS	Netzer et al. 1985, Rosina et al. 1986b, Strasser and Netzer 1984, Strasser et al. 1985
	LDA	Mukhopadhyay and Majumdar 1969, Schlüter and Varma 1983	positron annihilation	Gempel et al. 1972, Gustafson et al. 1969, Szuszkiewicz 1973
			MCD	Hüfner et al. 1984
			CIS	Johansson et al. 1978, Lawrence et al. 1982
Pr	RAPW	Dakshinamoorthy et al. 1984, Fleming and Loucks 1968, Fleming et al. 1968, 1969, Myron and Liu 1970	dHvA	Irvine et al. 1978, Wulff et al. 1988
	LMTO	Aldén et al. 1995, Dhesi et al. 1992, Min et al. 1986d, Skriver 1981	ARUPS	Barrett 1992, Blyth et al. 1992, Dhesi et al. 1992

continued on next page

Table 1, *continued*

R	Theory	References	Experiment	References
	LDA	Jepsen and Andersen 1971, Lehman and Taut 1972, Temmerman et al. 1993	XPS/UPS	Baer and Busch 1973, 1974, Crecelius et al. 1978, Gerken et al. 1985, J.K. Lang et al. 1978, 1981, McFeely et al. 1974, Platau et al. 1981, Wieliczka et al. 1984a,b
	LAPW	De et al. 1985, De and Chatterjee 1987	IPE/BIS	J.K. Lang et al. 1978, J.K. Lang et al. 1981
	SC-LSDA	Szotek et al. 1993	EELS	Della Valle and Modesti 1989, Netzer et al. 1985
			positron annihilation	Szuszkiewicz 1973
Nd	RAPW	Fleming et al. 1968, 1969	XPS/UPS	Baer and Busch 1973, 1974, Gerken et al. 1985, Hedén et al. 1971, J.K. Lang et al. 1978, 1981, McFeely et al. 1974, Nix and Lambert 1989, Nix et al. 1989, Platau et al. 1981
	LMTO	Aldén et al. 1995, Min et al. 1986d	IPE/BIS	J.K. Lang et al. 1978, 1981
			EELS	Della Valle and Modesti 1989, Netzer et al. 1985
			positron annihilation	Szuszkiewicz 1973
Pm	LMTO	Aldén et al. 1995, Min et al. 1986d	positron annihilation	Szuszkiewicz 1973
Sm	LMTO	Aldén et al. 1995, Min et al. 1986d	positron annihilation	Szuszkiewicz 1973
	RHF	Herbst and Wilkins 1984	IPE/BIS	J.K. Lang et al. 1978, 1981, Lang and Baer 1979
			XPS/UPS	Allen et al. 1978, 1980, Baer and Busch 1974, Bertel et al. 1982a, Brodén 1972, denBoer et al. 1988, Fäldt and Myers 1983, 1984a,b, 1985, Fäldt et al. 1988, Gerken et al. 1982a,b, 1985, Gudat et al. 1981, Hedén et al. 1971, B. Johansson 1979, B. Johansson and Mårtensson 1983, Jørgensen et al. 1991, Kowalczyk et al. 1974, J.K. Lang et al. 1978, 1981, Lang and Baer 1979, McFeely et al. 1974, Sairanen and Aksela 1992, Stenborg et al. 1989b, Wertheim and Campagna 1977, Wertheim and Crecelius et al. 1978, Wertheim et al. 1978

continued on next page

Table 1, *continued*

R	Theory	References	Experiment	References
Sm (*cont'd*)			EELS	Bertel et al. 1982a, Della Valle and Modesti 1989, Modesti et al. 1985, Netzer et al. 1985, Stenborg and Bauer 1987, 1988
Eu	LMTO	Aldén et al. 1995, Min et al. 1986d	ARUPS	Kaindl et al. 1995
	RHF	Herbst and Wilkins 1987	IPE/BIS	Duò et al. 1993, Hofmann and Netzer 1991, Hofmann et al. 1991, J.K. Lang et al. 1978, 1981
	APW	Freeman and Dimmock 1966	XPS/UPS	Barth et al. 1983, Berg et al. 1992, Bertran et al. 1991, 1992, Brodén 1972, Brodén et al. 1973, Gerken et al. 1985, Hedén et al. 1972, Kaindl et al. 1983, Kammerer et al. 1982, Kowalczyk et al. 1974, J.K. Lang et al. 1978, 1981, McFeely et al. 1974, Netzer et al. 1981
	RAPW	Andersen and Loucks 1968	EELS	Bauer and Kolaczkiewicz 1985, Netzer et al. 1983b, Netzer et al. 1985
	LDA	Min et al. 1986a	positron annihilation	Szuszkiewicz 1973
			MCD	Arenholz et al. 1995b
Gd	APW	Cornwell 1966, Dimmock and Freeman 1964, Dimmock et al. 1965, Harmon and Freeman 1974a,b, Keeton and Loucks 1968, Knyazev and Noskov 1970, Leung et al. 1988, Lindgård et al. 1975, Singh 1991b, Liu et al. 1971	ARUPS	Barrett 1992, Blyth et al. 1992, Fedorov et al. 1994a, Himpsel and Reihl 1983, Hübinger et al. 1995, Dongqi Li et al. 1991a,b, Dongqi Li et al. 1992b,c, Dongqi Li et al. 1993c, Dongqi Li et al. 1994a, H. Li et al. 1992, Kim et al. 1992, Ortega et al. 1994, Vescovo et al. 1993a, Weschke et al. 1996
	LMTO	Ahuja et al. 1994, Aldén et al. 1995, Heineman and Temmerman 1994, Temmerman and Sterne 1990	positron annihilation	Hohenemser et al. 1968, Szuszkiewicz 1973, Williams et al. 1966, Williams and Mackintosh 1968
	LSDA	Antropov et al. 1995, Arenholz et al. 1995a,b, Bylander and Kleinman 1994, Eriksson et al. 1995, Harmon et al. 1995, Heineman and Temmerman 1994, Kim et al. 1992, Nolting et al. 1995, Singh 1991b, Temmerman and Sterne 1990	XPS/UPS	Baer and Busch 1974, Blodgett et al. 1966, Dowben et al. 1989, Eastman 1969, Gerken et al. 1985, Jordan 1986, LaGraffe et al. 1989a,b,c, J.K. Lang et al. 1978, 1981, Dongqi Li et al. 1992a, Kammerer et al. 1982, Kowalczyk et al. 1974, McFeely et al. 1973, 1974, Miller and Dowben 1993, Murgai et al. 1988, Reihl and Himpsel 1982, Scarfe et al. 1992, Thole et al. 1993, Wandelt and Brundle 1985, Weller and Alvarado 1985b, Weller et al. 1985a,b

continued on next page

Table 1, *continued*

R	Theory	References	Experiment	References
	ASW	Borgiel et al. 1986, Krutzen and Springelkamp 1989, Nolting et al. 1993, 1994, Sticht and Kübler 1985	S-ARUPS	Busch et al. 1969, Carbone and Kisker 1987, Dongqi Li et al. 1993a,b, Dongqi Li et al. 1995, Dongqi Li et al. 1996, McIlroy et al. 1996, Mauri and Landolt 1981, Mulhollan et al. 1992, Tang et al. 1993a,b, Vescovo et al. 1993b, Weller et al. 1985a
	SC-LSD	Harmon 1979, Leung et al. 1988	IPE/BIS	Fauster and Himpsel 1984, Fedorov et al. 1993, 1994a,c, Hofmann and Netzer 1991, Hofmann et al. 1991, Hübinger et al. 1995, J.K. Lang et al. 1978, 1981, Dongqi Li et al. 1994a, Ortega et al. 1994, Donath et al. 1996, Weschke et al. 1996
	SCF-LMTO	Ahuja et al. 1994, Aldén et al. 1995, Brooks et al. 1992, Min et al. 1986d, Temmerman and Sterne 1990	MCD	Arenholz et al. 1995a,b, Fedorov et al. 1994a, Hüfner et al. 1984, Schutz et al. 1988, Starke et al. 1993, Weschke et al. 1994, Krisch et al. 1996
	LCAO	Evenson and Liu 1968, 1969, Harmon and Freeman 1974b, Liu 1962, Richter and Eschrig 1989	EELS	Bauer and Kolaczkiewicz 1985, Lehman and Taut 1972, Matthew et al. 1983, 1991, Modesti et al. 1985, Netzer et al. 1985, Weller and Alvarado 1985a, Della Valle and Modesti 1989
	FLAPW	Freeman and Wu 1991, Novák and Kuriplach 1992, Ruquian Wu and Freeman 1991, Ruquian Wu et al. 1991	CIS	Dowben et al. 1989, 1995, LaGraffe et al. 1989a,c, Murgai et al. 1988
	RASW	Krutzen and Springelkamp 1989	dHvA	Mattocks and Young 1977a,b, Roeland et al. 1975, Schirber et al. 1976, Sondhelm and Young 1985, Young et al. 1973, 1976, Young and Hulbert 1974, Young 1979
	RAPW	Keeton and Loucks 1968		
Tb	RAPW	Fleming and Liu 1970, Jackson 1969, Keeton and Loucks 1968, Mackintosh 1968	positron annihilation	Szuszkiewicz 1973, Williams et al. 1966, Williams and Mackintosh 1968
	LMTO	Ahuja et al. 1994, Aldén et al. 1995, Begley et al. 1990, Min et al. 1986d, S.C. Wu et al. 1990, S.C. Wu et al. 1991a	ARUPS	Barrett 1992, Begley et al. 1990, Blyth et al. 1991b, Hübinger et al. 1995, H. Li et al. 1992, Navas et al. 1993, S.C. Wu et al. 1990, 1991a,b, 1992

continued on next page

Table 1, *continued*

R	Theory	References	Experiment	References
Tb (*cont'd*)	FLAPW	Novák and Kuriplach 1992	XPS/UPS	Baer and Busch 1973, 1974, Dowben et al. 1990, 1991, 1993, Gerken et al. 1985, LaGraffe et al. 1990a,b, J.K. Lang et al. 1978, 1981, Dongqi Li et al. 1992a, McFeely et al. 1974, Miller and Dowben 1993, Padalia et al. 1977, Thole et al. 1993
	LCAO	Liu 1962	IPE/BIS	Hübinger et al. 1995, J.K. Lang et al. 1978, 1981
			MCD	Arenholz et al. 1995a, Schutz et al. 1988
			EELS	Bauer and Kolaczkiewicz 1985, Colliex et al. 1976, Della Valle and Modesti 1989, Netzer et al. 1985
			CIS	Dowben et al. 1990
			dHvA	Mattocks and Young 1977b
Dy	RAPW	Keeton and Loucks 1968	positron annihilation	Szuszkiewicz 1973, Williams et al. 1966, Williams and Mackintosh 1968
	LMTO	Aldén et al. 1995, Min et al. 1986d	ARUPS	Kaindl et al. 1995, H. Li et al. 1992
	LCAO	Evenson and Liu 1968, 1969, Harmon and Freeman 1974b	XPS/UPS	Baer and Busch 1973, 1974, Dowben et al. 1990, Gerken et al. 1982a,b, 1985, Gudat et al. 1981, Hedén et al. 1971, J.K. Lang et al. 1978, 1981, Lapeyre 1969, McFeely et al. 1974, Padalia et al. 1977
			IPE/BIS	J.K. Lang et al. 1978, 1981
			MCD	Arenholz et al. 1995a, Sacchi et al. 1991
			EELS	Della Valle and Modesti 1989, Modesti et al. 1985, Netzer et al. 1985
			CIS	Dowben et al. 1990
Ho	LMTO	Aldén et al. 1995, Blyth et al. 1991a, Min et al. 1986d	ARUPS	Barrett et al. 1991b, Barrett 1992, Blyth et al. 1991a,c, Kaindl et al. 1995, Weschke et al. 1994
			positron annihilation	Szuszkiewicz 1973, Williams et al. 1966, Williams and Mackintosh 1968
			XPS/UPS	Blyth et al. 1991e, Dowben et al. 1992, Gerken et al. 1985, J.K. Lang et al. 1978, 1981, McFeely et al. 1974, Padalia et al. 1977

continued on next page

Table 1, *continued*

R	Theory	References	Experiment	References
			IPE/BIS	J.K. Lang et al. 1978, 1981
			EELS	Della Valle and Modesti 1989, Netzer et al. 1985
Er	RAPW	Keeton and Loucks 1968	ARUPS	Barrett et al. 1991b, Barrett 1992, Blyth et al. 1991c, H. Li et al. 1992
	LMTO	Aldén et al. 1995, Min et al. 1986d	positron annihilation	Szuszkiewicz 1973, Williams et al. 1966, Williams and Mackintosh 1968
	RHF	Herbst and Wilkins 1984	XPS/UPS	Baer and Busch 1973, 1974, Brodén 1972, Gerken et al. 1985, Hedén et al. 1971, J.K. Lang et al. 1978, 1981, Netzer et al. 1981, Padalia et al. 1976, 1977
	LCAO	Evenson and Liu 1968, 1969	IPE/BIS	J.K. Lang et al. 1978, 1981
			EELS	Bertel et al. 1981, 1982a, Della Valle and Modesti 1989, Netzer et al. 1985
Tm	APW	Freeman et al. 1966, Watson et al. 1968	ARUPS	Bodenbach et al. 1994
	LMTO	Aldén et al. 1995, Bodenbach et al. 1994, Min et al. 1986d	XPS/UPS	Baer and Busch 1973, 1974, Domke et al. 1986, Egelhoff et al. 1981, Gerken et al. 1985, J.K. Lang et al. 1978, 1981, Padalia et al. 1977, Weschke et al. 1994
	RHF	Herbst and Wilkins 1984	IPE/BIS	J.K. Lang et al. 1978, 1981
			EELS	Netzer et al. 1985
			positron annihilation	Szuszkiewicz 1973
Yb	LMTO	Aldén et al. 1995, Bodenbach et al. 1994, Min et al. 1986d	ARUPS	Bodenbach et al. 1994, Takakuwa et al. 1984
	RAPW	Jepsen and Andersen 1971, Johanssen and Mackintosh 1970, Koelling and Harmon 1972	XPS/UPS	Alvarado et al. 1980, Baer and Busch 1973, 1974, Beaurepaire et al. 1989, Brodén et al. 1970, 1973, Chorkendorff et al. 1985a,b, Gerken et al. 1982a,b, 1985, B. Johansson and Mårtensson 1980, Kaindl et al. 1983, Kowalczyk et al. 1974, W.C. Lang et al. 1974, J.K. Lang et al. 1978, 1981, Mårtensson et al. 1988, McFeely et al. 1974, Nilsson et al. 1985, 1988, Padalia et al. 1976, 1977, Schneider et al. 1983, Takakuwa et al. 1982, Weschke et al. 1994

continued on next page

Table 1, *continued*

R	Theory	References	Experiment	References
Yb (*cont'd*)	RHF	Herbst and Wilkins 1984	dHvA	Datar and Tanuma 1968, Tanuma et al. 1967, 1970
	LDA	Min et al. 1986a	EELS	Bertel et al. 1982b, Della Valle and Modesti 1989, Netzer et al. 1985, Onsgaard et al. 1984, Onsgaard and Chorkendorff 1986, Stenborg and Bauer 1987, 1988, Strasser et al. 1985
			IPE/BIS	J.K. Lang et al. 1981
			positron annihilation	Szuszkiewicz 1973
			CIS	L.I. Johansson et al. 1980
Lu	RAPW	Keeton and Loucks 1966, 1968	dHvA	Hoekstra and Phillips 1971, W.R. Johansson et al. 1982
	LMTO	Aldén et al. 1995, Min et al. 1986c,d	ARUPS	Kaindl et al. 1995
	LCAO	Evenson and Liu 1968, 1969, Nemoshkalenko et al. 1978	XPS/UPS	Baer and Busch 1974, Gerken et al. 1985, Kowalczyk et al. 1974, W.C. Lang et al. 1974, J.K. Lang et al. 1978, 1981, McFeely et al. 1974, Padalia et al. 1977
			IPE/BIS	J.K. Lang et al. 1978, 1981
			EELS	Netzer et al. 1985

The calculations are assigned categories in a somewhat arbitrary manner.
The abbreviations refer to measurements and calculations as indicated:
APW, augmented plane wave
ARUPS, angle resolved photoemission
ASW atomic sphere approximation
CIS, constant initial state spectroscopy
FLAPW, full potential linearized augmented plane wave
EELS, electron energy loss
LAPW, linear augmented plane wave
dHvA, de Haas-van Alphen
LCAO, linear combination of atomic orbitals
IPE/BIS, inverse photoemission or Bremsstrahlung isochromat spectroscopy
LDA, local density approximation
LDOS, layer density of states
MCD, magnetic circular dichroism
LMTO, linear muffin tin orbital
S-ARUPS, spin polarized angle resolved photoemission
LSDA, local spin density approximation
XPS/UPS, X-ray photoemission or angle integrated photoemission
KKR, Korringa–Kohn–Rostocker
RAPW, relativistic augmented plane wave
RHF, relativistic Hartree–Fock
SC-LSD, self-consistent LSDA
SCF-LMTO, self-consistent field LMTO

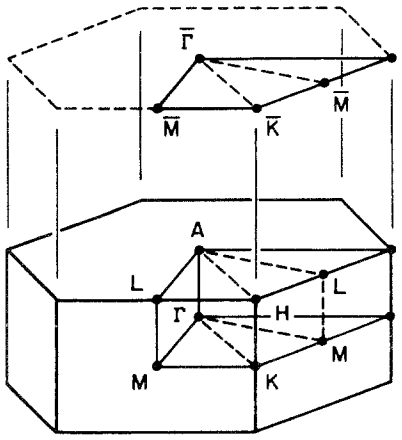

Fig. 3. The surface and bulk Brillouin zone of bulk hexagonal close packed crystals. The surface Brillouin zone is shown for the (0001) basal face.

at the surface but overlap with the bulk band structure, are also of interest. Both the surface and bulk 5d/6s occupied bands are typically within 3 eV of the Fermi energy for all the rare earths, as observed using photoemission. In the six-fold point group symmetry of the surface, these bands generally are seen to have Δ_1 or Δ_2 symmetry (representation elements A_1 and A_2 in C_{6v}) at the surface Brillouin zone center ($\bar{\Gamma}$). This means that the contributing rectangular representations to these bands are of 6s and $5d_{3z^2-r^2}$ character.

Feibelman and Hamann (1979) found several unoccupied surface states near E_F in theoretical LDOS calculations for Sc(0001). Their surface state near the surface Brillouin zone center ($\bar{\Gamma}$) was largely $d_{3z^2-r^2}$ in character. Similar results were found in the LMTO calculation of Lamouri and coworkers (1995). The FLAPW calculations of Gd(0001) (Ruquian Wu and Freeman 1991, Ruquian Wu et al. 1991) also indicate the existence of a surface state. An occupied magnetic surface state was predicted near $\bar{\Gamma}$, just below E_F. This occurs for a surface with moments either ferromagnetically or antiferromagnetically oriented with respect to the bulk moments, as shown in fig. 4. This highly localized (little dispersion with $\boldsymbol{k}_{\|}$) surface state in the vicinity of the center of the surface Brillouin zone ($\bar{\Gamma}$) was calculated to be highly spin polarized with symmetry similar to that of the Sc(0001) surface state ($d_{3z^2-r^2}$ character) (Ruquian Wu and Freeman 1991, Ruquian Wu et al. 1991).

The calculations on the existence of this highly localized magnetic surface state for Gd(0001) (Ruquian Wu and Freeman 1991, Ruquian Wu et al. 1991) are in good agreement with the experimental discovery (Dongqi Li et al. 1991a,b) of this same occupied surface state. The surface state in the vicinity of the center of the surface Brillouin zone ($\bar{\Gamma}$) was first identified for ordered crystalline Gd(0001) films (Dongqi Li et al. 1991a,b). This surface state conserved two-dimensionality of state; meaning that this state exhibited a binding energy that did not vary with photon energy, or $\boldsymbol{k}_{\perp}$ (wave vector along the surface normal) (Dongqi Li et al. 1991a) as indicated in fig. 5. This demonstrates that in contrast with previous studies of the bulk bands (Barrett 1992, Himpsel and Reihl 1983, Dongqi Li et al. 1994a), this state is localized to the surface. The state is in

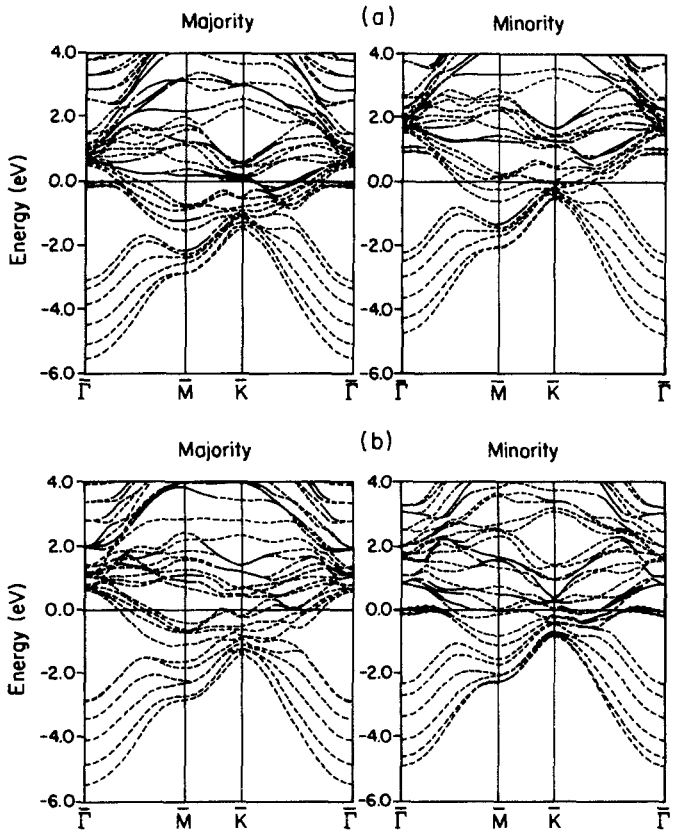

Fig. 4. Energy bands along the high-symmetry directions of Gd(0001) from FLAPW calculation for (a) ferromagnetic alignment between the surface layer and the bulk and (b) antiferromagnetic alignment between the surface and the bulk. The solid lines represent states with more than 50% weight in the surface muffin-tin sphere. Solid lines with circles show the surface states with more than 70% projection in the surface region. (From Ruquian Wu et al. 1991.)

the gap of the bulk band structure projected onto the surface and exhibits considerable surface sensitivity (as will be noted later). This state is thus a true surface state. This surface state crosses the bulk band about half way across the surface Brillouin zone, as indicated in fig. 6 by the increasing photoemission halfwidth (Dongqi Li et al. 1991a). Qualitatively, the experimental surface band structure (shown in fig. 7) agrees with theory. The symmetry of the state was found to be of $d_{3z^2-r^2}$ character (Dongqi Li et al. 1991a), also consistent with theory (Ruquian Wu and Freeman 1991, Ruquian Wu et al. 1991). This surface state was subsequently identified by spin-integrated photoemission from a Gd(0001) single crystal (Kim et al. 1992).

Similar surface states near the Fermi energy at the center of the surface Brillouin zone ($\bar{\Gamma}$), have now been identified for the surfaces of Tb(0001) (H. Li et al. 1992, Hübinger et

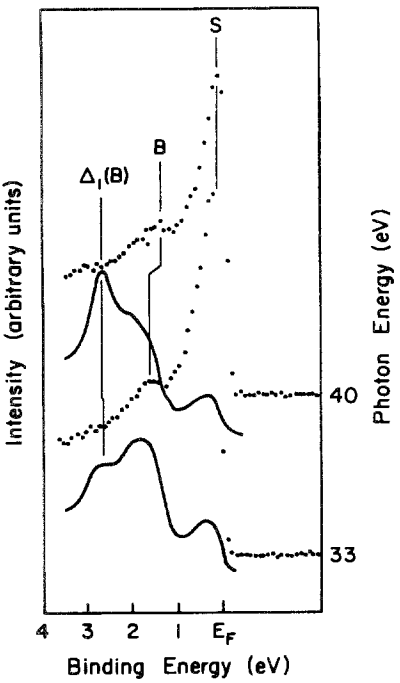

Fig. 5. Photoemission spectra of an ordered Gd(0001) film deposited on W(110) showing the Gd 5d surface state (S) and bulk bands (B). The spectra were taken along the Γ-A direction of the bulk band structure. Data taken from Dongqi Li et al. (1991a). The solid lines indicate the energy distribution curves taken for bulk gadolinium, adapted from Himpsel and Reihl (1983).

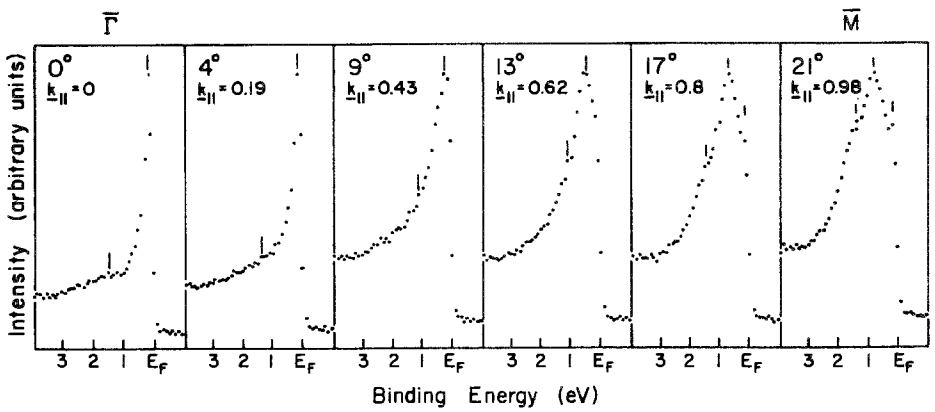

Fig. 6. The energy distribution curves for an ordered Gd(0001) film deposited on W(110) as a function of emission angle (changing $k_{\parallel}$). The spectra were taken along the $\bar{\Sigma}$ line ($\bar{\Gamma}$-$\bar{M}$ of the surface Brillouin zone). (From Dongqi Li et al. 1991a.)

al. 1995, Navas et al. 1993, S.C. Wu et al. 1991b), Tm(0001) and Yb(111) (Bodenbach et al. 1994), La(0001) (Fedorov et al. 1994a–c, Weschke et al. 1994), Eu(110) (Kaindl et al.1995), Dy(0001) (Kaindl et al. 1995, H. Li et al. 1992), Ho(0001) (Blyth et al. 1991a, Kaindl et al. 1995, Weschke et al. 1994), Er(0001) (Kaindl et al. 1995, H. Li et

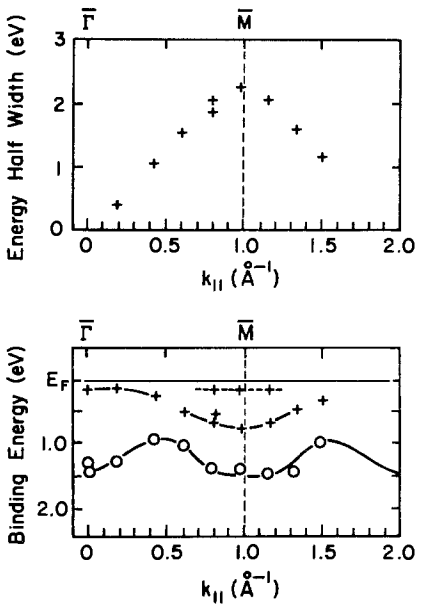

Fig. 7. The experimental surface band structure of an ordered Gd(0001) film on W(110) from $\bar{\Gamma}$-$\bar{M}$ of the surface Brillouin zone. The data were reduced from fig. 6 and taken from Dongqi Li et al. (1991a). The increasing density of bulk band states near $\bar{M}$ is evident from the width of the d-band states near the Fermi energy as a function of $k_{||}$, as plotted in the top panel.

al. 1992), Pr(0001) (Dhesi et al. 1992) and Lu(0001) (Kaindl et al. 1995). This suggests that the existence of a 5d surface state is a general phenomenon for the lanthanides, although it only contributes to surface magnetism for the magnetic metals. This should not be surprising given the similarities (Barrett 1992, Liu 1978) between the experimental 5d bulk band structures of Gd(0001) (Barrett 1992, Himpsel and Reihl 1983, Kim et al. 1992), Tb(0001) (Barrett 1992, S.C. Wu et al. 1990, 1992), Ho(0001) (Barrett 1992, Weschke et al. 1994), Pr(0001) (Barrett 1992, Dhesi et al. 1992), Er(0001) (Barrett 1992), and La(0001) (Weschke et al. 1994) as well as the 4d bands of Y(0001) (Barrett 1992, Barrett and Jordan 1987, Barrett et al. 1987). (For further experimental lanthanide metal bulk band structure references, see table 1.)

Spin-polarized photoemission has shown (fig. 8) that the surface state of Gd(0001) is highly spin polarized (Dongqi Li et al. 1993a,b, 1995, 1996, Mulhollan et al. 1992) and hence a magnetic surface state, consistent with theoretical expectations (Ruquian Wu and Freeman 1991, Ruquian Wu et al. 1991). This surface state has majority spin character as indicated by the corresponding spin character of the bulk bands (Dongqi Li et al. 1995, 1996) and the 4f levels (Dongqi Li et al. 1993a,b, Mulhollan et al. 1992). Experimentally, the surface state of Gd(0001) near the Fermi energy is highly localized, as is indicated by the rather small dispersion (Dongqi Li et al. 1991a), as seen in fig. 7. Such localization of this magnetic surface state is related to the enhanced surface magnetic order and is also consistent with calculations (Ruquian Wu and Freeman 1991, Ruquian Wu et al. 1991).

As a prototypical localized magnetic system, the magnetic coupling between the magnetic moments of the gadolinium atoms is indirect (de Gennes 1958, Ruderman and Kittel 1954). The large local moment from the Gd 4f electrons ($7\mu_B$) has no wave-function

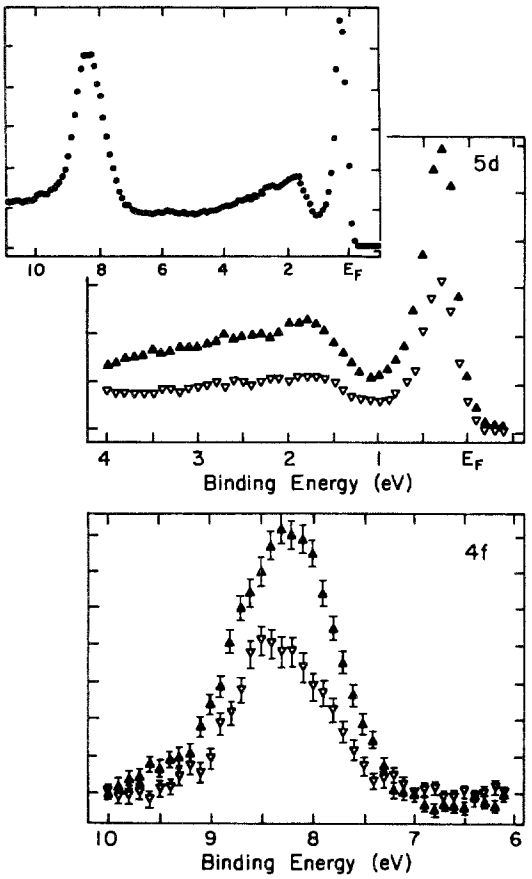

Fig. 8. The spin-polarized photoemission spectra of an ordered Gd(0001) film on W(110). The spin-majority signal (solid triangles) and spin minority signal (open triangles) were measured in the plane of the film. The photoelectrons were collected normal to the surface so that the surface state (200 meV binding energy) can be distinguished from the bulk Gd(0001) bands (1–4 eV binding energy). The insert shows the spin-integrated spectrum. (From Dongqi Li et al. 1993a.)

overlap with the 4f electrons on adjacent atoms, as demonstrated by fig. 9. Instead, the 4f electrons have an exchange interaction with the valence and/or conduction band electrons. This partly polarizes the valence and/or conduction electrons, as is indicated by the majority spin polarization of the surface state and the exchange splitting of the bulk 5d/6s bands (fig. 8) (Dongqi Li et al. 1995, 1996, Mulhollan et al. 1992). This polarization of the 5d and 6s electrons contributes (Ahuja et al. 1994, Brooks et al. 1992, 1993, Eriksson et al. 1995, Freeman and Wu 1991, Harmon 1979, Leung et al. 1988, Min et al. 1986d, Sticht and Kübler 1985, Temmerman and Sterne 1990, Watson et al. 1968, Ruquian Wu and Freeman 1991, Ruquian Wu et al. 1991) an additional $0.63\mu_B$ to the bulk moment of gadolinium (Roeland et al. 1975, Moon et al. 1972), and an even larger moment for the surface. It is these delocalized valence and/or conduction electrons, especially the 5d electrons in the case of gadolinium (Brooks et al. 1993, Dimmock and Freeman 1964, Harmon 1979, Harmon and Freeman 1974a,b, Leung et al. 1988, Nolting et al. 1994, Singh 1991b), that magnetically couple the 4f moments of nearby atoms. As

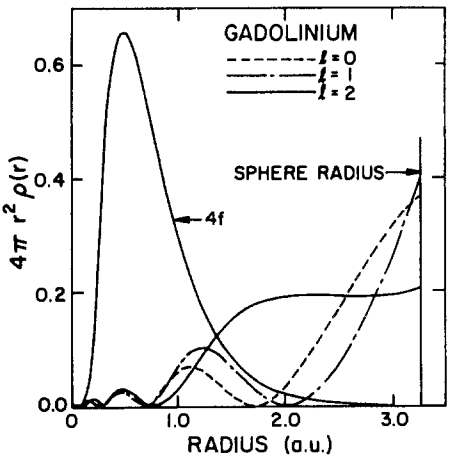

Fig. 9. The calculated radial charge densities of the 4f, 5d and 6s electrons in the Wigner–Seitz sphere of gadolinium metal, taken from Harmon and Freeman (1974a,b).

is clear from fig. 9, the 4f–5d overlap, and therefore the exchange interaction between the 5d and 4f electrons, increases with increasing localization of the 5d electrons. The fact that there is a localized 5d surface state and more dispersive 5d bulk states for Gd(0001) suggests that intra-atomic magnetic 4f and 5d coupling is enhanced at the surface relative to the bulk. In general, the Curie temperature is expected to scale with the 4f to 5d exchange interaction for all of the lanthanides (Brooks et al. 1992).

As indicated in the previous section, an enhanced exchange coupling in the surface is crucial for the existence of the enhanced surface magnetic ordering. Theoretical studies of semi-infinite (Binder and Hohenberg 1976, Binder and Landau 1984, 1985, Kaneyoshi 1991b) suggest that the magnetic coupling in the surface layer (J_s) is the main factor affecting surface magnetic order. As indicated in the previous section, enhanced surface magnetic order can only occur when $J_s > J_{sc}$ (Binder and Hohenberg 1976, Binder and Landau 1984, 1985). For this kind of indirect coupling in the lanthanide metals, the net magnetic moment of the conduction electrons can be estimated as proportional to the density of states at E_F (Watson et al. 1968), or perhaps more accurately, inversely proportional to the Bloch bandwidth (Nolting et al. 1994). From the photoemission results (Dongqi Li et al. 1991a), it is clear that the surface state bandwidth is far smaller than is the case for the bulk. Calculations (Freeman and Wu 1991, Eriksson et al. 1995, Ruquian Wu et al. 1991) for a Gd(0001) surface ferromagnetically aligned with the bulk provide a surface 5d moment ($0.58\mu_B$), significantly higher than the bulk value of $0.47\mu_B$. This issue shall prove to be important in the next section where we will deal with the 5d exchange splitting.

The spin-minority counterpart of the occupied 5d surface state for Gd(0001) is predicted to be an unoccupied state (Ruquian Wu and Freeman 1991, Ruquian Wu et al. 1991). Surface states and surface resonances of Gd(0001) (Arenholz et al. 1995b, Fedorov et al. 1994c, Dongqi Li et al. 1994a, Ortega et al. 1994), Tb(0001) (Hübinger et al. 1995) and Y(0001) (Barrett 1992, Blyth et al. 1991c,d) have also been identified

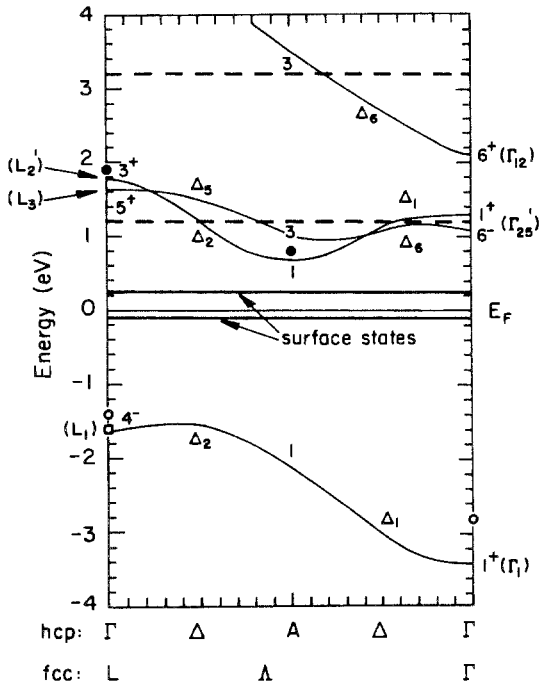

Fig. 10. The experimentally derived surface states (thick lines) and/or surface resonances (dashed lines) and bulk band critical points (solid dots from Dongqi Li et al. 1994a; open squares from Kim et al. 1992; open circles from Himpsel and Reihl 1983). The band structure for paramagnetic bulk gadolinium is shown with the hcp symmetry labels. Some fcc symmetry labels are given in brackets for comparison. (Adapted from Dongqi Li et al. 1994a.)

in the unoccupied band structure. The actual identification of these unoccupied states plays a significant role in our discussion of the gadolinium 5d exchange splitting and the temperature dependence of the band structure (which we discuss in the next section). An unoccupied gadolinium surface state just above E_F, for Gd(0001) at room temperature, is perhaps the most prominent of these surface sensitive states (Fedorov et al. 1994c, Hübinger et al. 1995, Dongqi Li et al. 1994a). Both the surface state just above E_F (Fedorov et al. 1994c, Hübinger et al. 1995, Weschke et al. 1996, Donath et al. 1996) and a surface resonance at 1.2 eV above E_F (Dongqi Li et al. 1994a) have been postulated to be the spin-minority counterpart to the occupied gadolinium surface state just below E_f (discussed above). On the basis of the surface exchange splitting (Dowben et al. 1989, Dowben et al. 1995, LaGraffe et al. 1989c, Dongqi Li et al. 1994a, 1995, Ruquian Wu et al. 1991) and the calculated band structure (Ruquian Wu and Freeman 1991, Ruquian Wu et al. 1991), the former assignment provides a more cogent picture. It now appears that the state just above E_F is the spin-minority counterpart (Donath et al. 1996, Weschke et al. 1996). The surface sensitive state at about 3.1 eV above E_F has been assigned (Fedorov et al. 1994a, Dongqi Li et al. 1994a) to an image state.

The combination of photoemission and inverse photoemission provides a general picture of the 5d/6s gadolinium band structure along the Γ-A direction of bulk Brillouin zone, as is summarized in fig. 10. As previously pointed out, fig. 10 makes clear that the surface states fall into a gap of the projected bulk band structure. Note that while the

occupied bulk band structure is dominated by states of Δ_1 or Δ_2 symmetry (representation elements A_1 and A_2 in C_{6v}), the unoccupied gadolinium bands contain states of not only Δ_1 and Δ_2 symmetry, but also Δ_5 or Δ_6 symmetry (representation elements E_1 and E_2 in C_{6v}). This means that the contributions to these unoccupied bands are atomic wave functions of $6p_{x,y}$ (Δ_5), $5d_{x^2-y^2}$ (Δ_6), $5d_{xz,yz}$ (Δ_5) and $5d_{xy}$ (Δ_6) character. Greater attention must be paid to the symmetry as well as spin of the magnetic states. Both the exchange-split majority and minority spin pair of bands, formed as a result of a magnetic moment, must share the same symmetry.

4. Enhanced exchange splitting and finite-temperature magnetism

The magnetic moments, necessary for ferromagnetism (or antiferromagnetism) in solids, can originate from either itinerant or localized electrons (Nolting et al. 1994). Stoner's model (Stoner 1936) provided the first practical description of itinerant electron magnetism. The model defines an exchange splitting ΔE_{ex} as the energy difference between the majority and minority spin bands. In this model, the exchange splitting is used as a characteristic parameter in conjunction with the macroscopic magnetization. This concept of the exchange splitting is relatively well-developed for the ground state, i.e. at absolute zero, and can be modeled using spin-resolved band structure calculations. A similar level of understanding for finite temperatures does not, as yet, exist, though in practice the investigation of the magnetic moments is the study of the finite temperature behavior of a ferromagnetic system. The picture presented by Stoner's model has a decrease in both the exchange splitting ΔE_{ex} and the magnetic moment with increasing temperature, where both quantities vanish to zero at the Curie temperature.

Such a model is not realized for transition-metal ferromagnets. For the transition metals, "local band theory" (Borgiel and Nolting 1990, Capellmann 1979, Korenman et al. 1977a,b, Nolting et al. 1989, 1991) and the "disordered local moment" model (Hasegawa 1979, Pindor et al. 1983) have been introduced to explain the loss of magnetization at T_C. Instead of a collapse of the exchange splitting, by considering transverse fluctuations of the local moment near T_C, the energy-split states remain more or less fixed with a "local exchange splitting" $\Delta E_{ex,local}$. This energy splitting of each state, $\Delta E_{ex,local}$, reflects the existence of a local moment and/or short-range order, but with a net spin polarization that changes with temperature due to spin mixing. With spin mixing, as the temperature increases, the spin polarization of each band becomes less polarized, but the binding energy of each band remains more or less fixed. In other terms, one can imagine this model as resulting in not two but four subbands: a spin majority and spin minority pair of bands at two different binding energies, where each pair approaches equal weight at the Curie temperature. The temperature dependence of the band structure is a way to probe the exchange splitting and hence the moment, as well as gain insight into the coupling.

The temperature dependence of the Gd(0001) band structure near T_C has been studied with spin-integrated photoemission (Kim et al. 1992, Dongqi Li et al. 1992b,c). The results demonstrated a "Stoner-like" behavior of the Gd bulk 5d/6s bands (Kim et al. 1992,

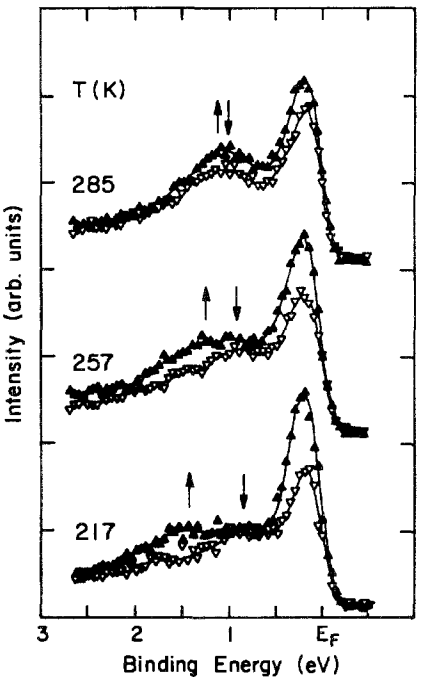

Fig. 11. Spin-polarized photoemission spectra at different temperatures at normal emission (center of the surface Brillouin zone). The majority and minority components are shown with solid (up) and open (down) triangles, respectively. The majority and minority bulk bands are marked with up and down arrows. (From Dongqi Li et al. 1995.)

Dongqi Li et al. 1992b,c), but suggest that the Gd 5d surface state behaves differently (Hübinger et al. 1995, Dongqi Li et al. 1992c, 1995, 1996). These results were supported by calculations that took into account the temperature dependence of the band structure (Borgiel et al. 1986, Nolting 1985, Nolting et al. 1994, 1995). Because of the importance of the 4f–5d hybridization, Sandratskii and Kübler (1993) suggested that the conduction 5d/6s electrons would always retain a local moment from the local 4f moment, though the spin polarization and magnetization of the conduction band would be lost at an elevated temperature due to global spin-hybridization effects. This possible controversy was laid to rest with temperature-dependent spin-polarized photoemission measurements of the valence band (Dongqi Li et al. 1995). As seen in fig. 11, the bulk 5d/6s bands at 1–2 eV binding energy show two features with majority and minority spin character. With increasing temperature, the spin polarization of the two bulk bands is retained, while ΔE_{ex} decreases and approaches zero at T_C. This implies that the temperature dependence of the exchange splitting for the gadolinium 5d bulk bands is well defined, even at finite temperature, and has Stoner-like behavior (Dongqi Li et al. 1995, 1996). An empirical relationship was suggested between exchange splitting ΔE_{ex} and magnetic moment for 3d itinerant electrons (1 eV of ΔE_{ex} corresponds to about $1\mu_B$ in magnetic moment) (Himpsel 1991). The change in the bulk 5d moment also decreases with increasing temperature and approaches zero at T_C: i.e. Stoner-like behavior (Nolting et al. 1994), which may indicate a decrease of local moment.

In spite of the suggestion that the exchange splitting of the bulk bands is constant throughout the Brillouin zone at finite temperature, based upon experimental fits of the $\boldsymbol{k}$-dependent exchange splitting with a ground state (zero degree) calculation (Kim et al. 1992), this is not the case. Both experiment (Dongqi Li et al. 1992b,c) and theory (Nolting et al. 1994) provide evidence that there is some $\boldsymbol{k}$ dependence of the bulk 5d exchange splitting at finite temperature. It should be realized that the bulk 5d/6s gadolinium bands do not behave like a 'perfect' Stoner ferromagnet. Some of the bands, in particular the unoccupied bands, are predicted to have a 'local-moment' induced, but unpolarized, splitting in the paramagnetic phase (Nolting et al. 1994). The large local moment (resulting from the 4f levels), local ferromagnetic order, and local 4f polarization may persist even when long-range ferromagnetic order is extinct. Close to T_C, it is likely that the failures of the Stoner model will become even more apparent.

As was clear from the discussion in the previous section, the occupied Gd(0001) surface state near E_F is a magnetic surface state with spin polarization. The polarization of this state is in the same direction as that of the 4f levels (fig. 8) and the bulk band spin majority feature (fig. 11). Thus, the surface state has spin majority character, an issue that will be discussed further in the next section. While the spin polarization of the surface state decreases with increasing temperature, the binding energy of spin-majority and spin-minority components of this state appear to remain fixed in temperature near T_C(surface) (Dongqi Li et al. 1995). The intensity of this surface state also remains fixed above and below T_C (Dongqi Li et al. 1992c, 1995), while the width of this surface state changes linearly with temperature (Dongqi Li et al. 1992c). All of this indicates that the dramatic change in the surface polarization does not originate from the collapse of the exchange splitting, but instead follows spin-mixing behavior expected for an itinerant electron system with transversely fluctuating local moments (Borgiel and Nolting 1990, Capellmann 1979, Hasegawa 1979, Korenman et al. 1977a,b, Dongqi Li et al. 1992c, Nolting et al. 1989, 1991, Pindor et al. 1983). Others (Donath et al. 1996, Weschke et al. 1996) argue for a Stoner-like behavior for the surface.

The occupied bulk 5d/6s bands exhibits Stoner-like exchange splitting while the surface exhibits some spin-mixing behavior. The exchange splitting ΔE_{ex}(surface) of the surface state becomes ill defined at elevated temperature due to the different spin components gradually becoming hybridized as a consequence of the loss of long-range order. Such behavior is similar to that of the disordered local-moment model (Borgiel and Nolting 1990, Capellmann 1979, Korenman et al. 1977a,b, Nolting et al. 1989, 1991) or local band theory (Hasegawa 1979, Pindor et al. 1983), as developed for transition metals. In the case of the Gd(0001) surface, a local magnetic moment and "local" exchange splitting $\Delta E_{ex,local}$ exist and $\Delta E_{ex,local}$ remains more or less fixed in energy with temperature. This is due to a finite local 5d moment and/or the short-range order of the itinerant electrons. For the surface state of Gd(0001), this $\Delta E_{ex,local}$ does not go to zero at the surface Curie temperature (Hübinger et al. 1995, Dongqi Li et al. 1995). This suggests a finite local 5d moment at the surface even above the surface Curie temperature. In spite of the suggestion, based upon inverse-photoemission results, that the Gd(0001) surface state exhibits Stoner-like collapse of exchange splitting (Fedorov et al. 1994c,

Donath et al. 1996, Weschke et al. 1996), both the Gd(0001) 5d surface states (Dongqi Li et al. 1995, Donath et al. 1996) and the unoccupied bulk 5d/6s states (Nolting et al. 1994) fail to follow Stoner-like exchange-splitting behavior. It is now also clear from inverse-photoemission studies that the temperature dependence of the unoccupied surface states near the Fermi energy of both Gd(0001) and Tb(0001) fail to support ideal Stoner-like behavior (Hübinger et al. 1995, Donath et al. 1996).

The difference between the surface state and the bulk 5d/6s band behavior of gadolinium can be qualitatively understood from the fact that while both surface and bulk Gd atoms are polarized by the 4f moments, the surface is relatively localized when compared with the bulk bands. The localization of the surface state, as noted in the previous section, helps the Gd 5d electrons remain locally polarized by the 4f moment on the same atom, even after the 4f moments lose their long-range order at the surface Curie temperature. The more itinerant bulk 5d band electrons experience the collective polarization from the 4f moments of more than one atom, as a mean-field effect, and therefore the bulk 5d moment and exchange splitting vary with temperature. We believe that the photoemission results and the quasiparticle calculations of Nolting and coworkers (Nolting 1985, Nolting et al. 1987) strongly argue for a relationship between itinerancy and the temperature dependence of the electronic structure. The work of Nolting and colleagues (Nolting 1985, Nolting et al. 1987, 1994), in the narrow-bandwidth limit (i.e. the atomic limit), leads to four distinct quasiparticle bands with a temperature-dependent spin distribution that changes the relative occupancy of these levels. This can be considered as a spin-mixing in the language we have used here. With a finite bandwidth (a non-zero itinerancy), the quasiparticle bands change shape and shift in binding energy with temperature. This reflects the transition between spin mixing and exchange splitting collapse as a result of changing bandwidth (i.e. itinerancy) (Dongqi Li et al. 1992c).

As a result of these differences between the surface and the bulk, the electrons in the surface state remain phase coherent on a length scale less than the magnetic correlation length, while the opposite is true of the bulk bands (Dongqi Li et al. 1995). From the band dispersion of the bulk bands and the surface state, the electron phase coherence length, l, has been estimated (Dongqi Li et al. 1995) using $l \approx (w/k_b T_C)^{1/2} a$ (where w is the bandwidth, a is the lattice constant and k_b is the Boltzmann constant) (Capellmann and Vieira 1982). Given the in-plane Gd(0001) lattice parameter $a = 3.64$ Å and estimating the bandwidth of the bulk bands of interest to be about 1.5 eV (Dongqi Li et al. 1991a, 1992c, Ruquian Wu and Freeman 1991, Ruquian Wu et al. 1991), l is approximately 28 Å for the bulk band and much shorter for the surface state. This also implies that an upper limit of the extent of short-range order in the bulk is also 28 Å (Dongqi Li et al. 1995). The spin-lattice relaxation time, the characteristic time needed for establishing thermal equilibrium between the spin ordering and the lattice for bulk gadolinium has been measured (Vaterlaus et al. 1992). This value of 100 ± 80 ps for ferromagnetic gadolinium does suggest there is some phonon–magnon coupling. It is clear from neutron scattering that some magnetic disorder persists in bulk gadolinium well below T_C (Child 1978).

There exists indirect evidence that the surface Gd 5d exchange splitting, and thus the moment, is enhanced over the bulk (Dowben et al. 1989, 1995, LaGraffe et al.

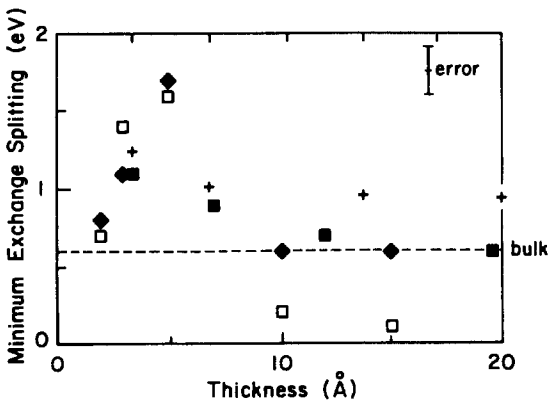

Fig. 12. The minimum 5d Gd exchange splitting, taken from Dowben et al. (1995). Solid diamonds: Gd/W(110) at 210 K; open squares: Gd/W(110) at 295 K; solid squares: Gd/Cu(100) at 230 K. The calculated exchange splittings for ferromagnetic surface layers (from Ruquian Wu et al. 1991) are indicated with crosses for comparison.

1989a,c). For thin films of only a monolayer or a few atoms thickness, symmetry-selective resonant photoemission involving excitations from the occupied 5p states to the unoccupied 5d levels suggests a lower bound to the exchange splitting of the Gd $d_{3z^2-r^2}$ surface state (Dowben et al. 1995) greatly enhanced over the accepted bulk value of 0.6–0.7 eV (Besnosov et al. 1984, Schutz et al. 1988). This is reassuring since the magnetic moment of the surface is calculated (Freeman and Wu 1991, Ruquian Wu et al. 1991) to be larger than the bulk. These minimum values for the thin-film surface 5d exchange splitting are consistent with calculations (Ruquian Wu et al. 1991), as seen in fig. 12. The inferred enhanced local exchange splitting of these thin films, nonetheless, does appear to exhibit the characteristics of a spin-mixing model of ferromagnetism with a $\Delta E_{ex,local}$ that persists near T_C. There is the assumption that the 5d exchange splitting of ultrathin films is akin to the 5d exchange splitting of the surface of a much thicker film (an assumption that is quite likely to fail), nonetheless, the results are consistent with the photoemission results just discussed (Dowben et al. 1995).

A more direct measure of the surface 5d exchange splitting is still needed, but requires better resolution of the spin-resolved unoccupied surface sensitive states. A Stoner-like exchange splitting at the surface would require a complete collapse of the surface state exchange splitting near the Fermi energy as the temperature approaches T_C(surface). Spin-mixing behavior suggests that there should be a persistent surface state or resonance surface exchange splitting, and with a very different temperature dependence. If the surface follows pure spin-mixing behavior, and the spin-minority component to the occupied surface state is just above the Fermi energy, as proposed for both Tb(0001) and Gd(0001) (Hübinger et al. 1995, Donath et al. 1996, Weschke et al. 1996), then the calculated (Ruquian Wu et al. 1991) surface 5d exchange splitting is in error.

5. Ferromagnetic or antiferromagnetic alignment of the surface with the bulk?

Local density full potential linearized augmented plane wave (FLAPW) calculations (Ruquian Wu et al. 1991) and a local spin density approximation (LSDA) calculation

(Heineman and Temmerman 1994) indicated that the surface of Gd(0001) is antiferromagnetically coupled with the bulk magnetic moment. This calculated antiferromagnetic alignment of the surface and bulk appeared to support early spin-polarized photoemission experiments (Weller et al. 1985a).

For ordered Gd(0001) thin films, the magnetization is largely in plane (Arenholz et al. 1995a,b, Berger et al. 1995, Donath et al. 1996, Dowben et al. 1991, 1993, Fedorov et al. 1994a, LaGraffe et al. 1990b, Dongqi Li et al. 1993a,b, 1995, 1996, McIlroy et al. 1996, Miller and Dowben 1993, Mulhollan et al. 1992, Pang et al. 1994, Starke et al. 1993, Taborelli et al. 1986, Tang et al. 1993a,b, Vescovo et al. 1993b, Weschke et al. 1994, Weller and Alvarado 1985a,b, Weller et al. 1985a), and this antiferromagnetic alignment would be in the plane of the Gd(0001) film. The surface and the bulk have a different environment resulting in a surface to bulk core-level shift for gadolinium (Barrett 1992, Fedorov et al. 1994a, Kammerer et al. 1982, LaGraffe et al. 1989b, Dongqi Li et al. 1993a,b, McIlroy et al. 1996, Mulhollan et al. 1992, Ortega et al. 1994, Starke et al. 1993, Vescovo et al. 1993b, Weller and Alvarado 1985b, Weller et al. 1985a,b, Weschke et al. 1994). Using the slight binding-energy differences for the Gd 4f states at the surface relative to the bulk and the variation in spin polarization, spin-polarized measurements of the 4f levels (Weller and Alvarado 1985b, Weller et al. 1985a) seemed to suggest antiferromagnetic alignment.

Subsequent results from spin-polarized electron spectroscopies (Dongqi Li et al. 1993a,b, 1995, 1996, McIlroy et al. 1996, Mulhollan et al. 1992, Tang et al. 1993a,b) and magnetic circular dichroism (Arenholz et al. 1995a,b, Fedorov et al. 1994a, Starke et al. 1993, Weschke et al. 1994) indicated largely in-plane ferromagnetic alignment of the surface and the bulk for Gd(0001), as well as for ferromagnetic Tb(0001) (Arenholz et al. 1995a). A clear comparison of the bulk and surface ferromagnetic orientation has been made in these experiments by comparing an electronic state characteristic of the surface, such as the Gd(0001) surface state, with an electronic state characteristic of the bulk. Since the Gd 5d electron ($5d^1$) is polarized by the 4f moment, its polarization direction is always indicative of the magnetic moment direction of the atom. As seen in fig. 8, the Gd(0001) surface state (Dongqi Li et al. 1993a, Mulhollan et al. 1992) has a spin polarization of majority character with respect to the bulk 4f spin polarization. The bulk 5d/6s bands also indicate a similar alignment of the spin polarization with respect to the surface state (Dongqi Li et al. 1993a, 1995, 1996, Mulhollan et al. 1992) as seen in fig. 11. Spin-polarized photoemission experiments (Dongqi Li et al. 1993a, McIlroy et al. 1996, Tang et al. 1993a,b) and magnetic circular dichroism (Arenholz et al. 1995a,b, Fedorov et al. 1994a, Starke et al. 1993, Weschke et al. 1994) from the 4f levels also unambiguously show that the surface component of the 4f levels has the spin-polarization direction of the bulk 4f levels and that the surface and the bulk are, therefore, ferromagnetically aligned.

By adding a Coulomb repulsion energy or correlation energy U to the LSDA calculation, Antropov, Harmon and coworkers (Harmon et al. 1995) were able to obtain a ferromagnetic ground state for gadolinium instead of an antiferromagnetic ground state (Heineman and Temmerman 1994), as seen in fig. 13. This tends to suggest that the failure

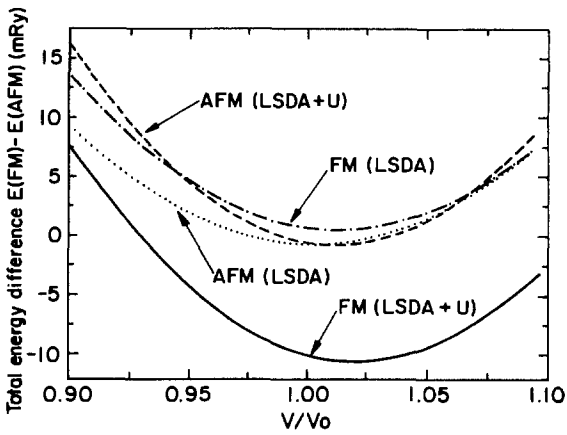

Fig. 13. Total energy of ferromagnetically and antiferromagnetically ordered states of gadolinium with gradient correction approximations in the local spin density approximation (LSDA) and in LSDA + U. (From Harmon et al. 1995.)

of theory to accurately predict the magnetic alignment of the surface and the bulk is a direct result of the need to include correlation energies into the theory. Slightly different corrections to LSDA (Bylander and Kleinman 1994, Eriksson et al. 1995) both yield good agreement with the experiments that indicate ferromagnetic alignment of the surface and bulk moments.

In fact, the surface moments are not perfectly aligned with the bulk. By measuring the in-plane, as well as the perpendicular components of the secondary electron polarization from Gd(0001), it was shown that there is significant polarization normal to the surface (Tang et al. 1993a,b), as is indicated by fig. 2. The polarization along the surface normal persists well above the bulk Curie temperature and indicates that this out-of-plane component of the magnetization is a result of a strong surface contribution (Tang et al. 1993a,b).

The canting of the surface magnetization out of plane was confirmed by a re-examination of the surface and bulk spin-polarized photoemission signals from the Gd(0001) 4f levels (Dongqi Li et al. 1993a,b, McIlroy et al. 1996). While these spin-polarized photoemission signals measured only the in-plane polarization, there was a difference in the polarization from the surface and bulk components as seen in fig. 14. This result was also attributed to an "imperfect" alignment of the surface and bulk magnetization directions (Dongqi Li et al. 1993a,b, McIlroy et al. 1996). In other words, an out-of-plane component to the surface magnetization probably exists (Dongqi Li et al. 1993b). This view is supported by the expectation that the surface component of the 4f levels should exhibit an enhanced polarization (Arenholz et al. 1995a) as the temperature approaches the Curie temperature. It may be that the earlier measurements by Weller (Weller et al. 1985a), that appeared to suggest antiferromagnetic alignment, of the surface and the bulk, were strongly affected by the imperfect alignment of the surface and the bulk.

Since the surface is influenced by the magnetic field of the substrate (Mills 1991), the canting of the surface magnetization might increase when the bulk becomes paramagnetic

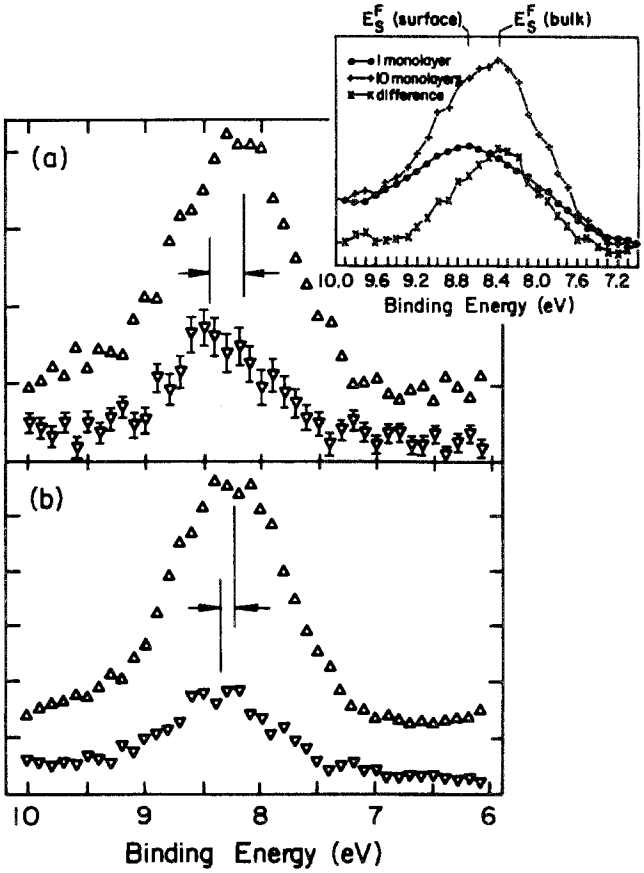

Fig. 14. The in-plane spin-polarized photoemission spectra for Gd(0001) films on W(110) at 100 K across the Gd 4f level, taken from Dongqi Li et al. (1993a). (a) the spectra of a freshly deposited film and (b) following exposure to a small amount of contamination. Spin-majority (up triangles) and spin-minority (down triangles) are indicated. The inset shows the different 4f photoemission spectra for one monolayer and ten monolayers of gadolinium (and the difference spectrum) on Cu(100) (LaGraffe et al. 1989b), illuminating the different surface and bulk contributions to the Gd 4f feature.

(i.e. above the bulk Curie temperature, but while the surface is still ferromagnetic; Tang et al. 1993a,b). Depending upon the relative contributions of the surface and the bulk to the in-plane component of the magnetization (Vescovo et al. 1993b), this phenomenon may be reflected by the combination of the results in fig. 2 (Tang et al. 1993a,b) and recent spin-polarized photoemission studies (Vescovo et al. 1993b).

Other complications may also exist in relating the surface magnetization direction with the bulk. Such complications may include misalignment of the in-plane components of the surface and bulk magnetization, the domain structures and the existence of out-of-plane magnetization components for both the surface and bulk. Such complications cannot be

completely excluded with currently available data. So far there is no theoretical model that deals with the surface anisotropy of the lanthanide metals. In addition, recent studies of the magnetic reorientation of thicker ($\geqslant$40 nm) gadolinium films on W(110) revealed the complicated temperature dependence of the bulk anisotropy which leads to canting of the bulk moments at higher temperature (Berger et al. 1995). What makes this picture even more complicated is the possible role played by surface contamination.

6. Suppression of the surface magnetization

The idea of magnetically "dead" layers or surfaces was introduced by Liebermann (Liebermann et al. 1969, 1970) in order to explain his results obtained for transition-metal films. For a surface of a ferromagnet, a completely "dead" surface in terms of the magnetic ordering is not possible in the context of Maxwell's equations (Dowben et al. 1991, Miller and Dowben 1993), since a paramagnetic overlayer on top of a ferromagnet will, at least, exhibit some induced moment. Nonetheless, the surface magnetization can be suppressed. This is most easily achieved for the lanthanide surfaces through disorder or contamination. Surface adsorbates can suppress the surface magnetization.

One of the most traditional methods for changing the surface magnetization is through the adsorption of hydrogen. Cerri, Mauri and Landolt (1983) found that a submonolayer of adsorbed hydrogen reduced the observed spin polarization of the surface at 20 K (well below T_C) from 70% for the clean surface to 30–45% for the surface with adsorbed hydrogen. They postulated that hydrogen chemisorption introduced some disorder in the 4f spin structure at the Gd surface. An experimental band mapping of the Gd(0001) surface (Dongqi Li et al. 1993c) showed that hydrogen chemisorption not only destroys the Gd(0001) surface state (as seen in fig. 15), but also results in the formation of filled bands far more itinerant than the surface state band away from E_f.

These highly dispersive hydrogen adsorption induced bands (Dongqi Li et al. 1993c) result in the delocalization of the Gd 5d/6s electrons and in a decrease in the density of states at E_F. As has been alluded to previously, in the discussion of the origin of the enhanced magnetization of the surface relative to the bulk, this decrease in localization of the conduction electrons is also believed to be accompanied by a decrease in the intra-atomic overlap of the 5d states with the 4f electrons. This can lead to a decrease in the induced 5d/6s moment and the exchange coupling in the surface layer (Dongqi Li et al. 1993c).

Other adsorbates, including oxygen (Ortega et al. 1994, Vescovo et al. 1993a, Zhang et al. 1995) and nitrogen (Waldfried et al. 1995), also destroy the Gd(0001) surface state upon chemisorption. Dissociative chemisorption of oxygen at a fraction of a monolayer is seen to suppress the overall spin polarization of gadolinium (Dongqi Li et al. 1996, McIlroy et al. 1996), as seen in fig. 16. We do not consider the evidence to be either compelling or convincing, but small amounts of contaminants (Dongqi Li et al. 1993a, McIlroy et al. 1996) may accompany changes in magnitude and direction of the surface magnetization with respect to the bulk magnetization, as indicated in fig. 14. The role of

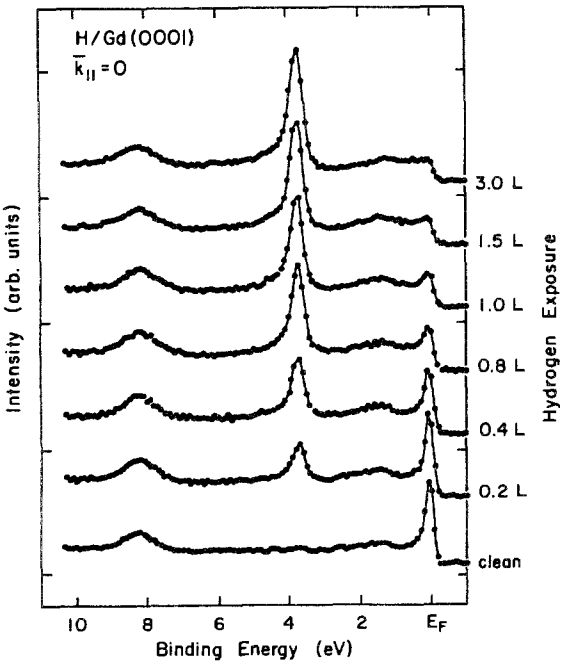

Fig. 15. Typical photoemission spectra of the chemisorption of hydrogen on Gd(0001). (From Dongqi Li et al. 1993c.)

adsorbates upon the surface magnetization is clearly an important issue that needs to be addressed.

7. Critical phenomena and finite-size scaling

Phase transitions in low dimensions have always been one of the main driving forces behind the research efforts on surfaces and ultrathin films (Binder and Landau 1985, Freeman and Fu 1986, Freeman and Wu 1991, Kaneyoshi 1991b, Mills 1970). Statistical mechanics predicts different critical phenomena for these systems' different dimensions (Binder and Hohenberg 1976, Binder and Landau 1984, 1985, Kaneyoshi 1991a,b, Mills 1970). The lanthanide metals provide an ideal testing ground for statistical-mechanics models (Kaneyoshi 1991a). These metals have large localized moments, as is assumed in statistical models, and exhibit unusual surface magnetic order as discussed earlier. Before discussing the critical exponents of the magnetic phase transitions, which we shall address for both the surface and the bulk, finite-size scaling should be addressed. These are the effects of film thickness on the phase transition. In practice, this is important since, after all, we study finite systems, not infinite ones. The problem of spontaneous magnetization in films has been a subject that has attracted considerable thought and the study of surfaces often requires that one studies thin films.

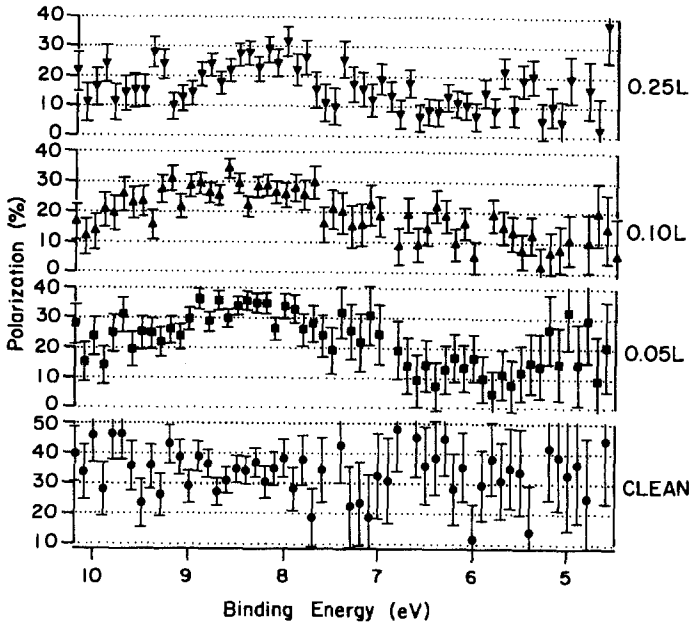

Fig. 16. The spin polarization in the region of the gadolinium 4f levels of an 80 Å thick film as a function of oxygen dosing. With increasing amounts of chemisorbed oxygen the overall net polarization is seen to decrease. (Adapted from McIlroy et al. 1996.)

Statistical mechanics predicts the phase transition temperature to scale with the size of the system. When the magnetic system approaches two dimensions from three dimensions (toward thin films from thicker films), the Curie temperature for a ferromagnetic film is strongly dependent upon the film thickness. This film-thickness dependence can provide some insight into the ferromagnetic coupling that exists within the film, as well as what model can be applied. Typically to measure the Curie temperature, T_C [and for most experiments related to the lanthanides, this means $T_C(d)$ of the bulk of the film], the remanent magnetization (M_R) is plotted against the temperature ideally for zero applied field. T_C is defined by $M_R(T=T_C)=0$, though many quantities can be used to measure T_C. The Curie temperature T_C depends on the film thickness d as a power law (Allen 1974, Fischer and Ferdinand 1967):

$$\frac{\Delta T_C}{T_C(\text{bulk})} = \frac{T_C(\text{bulk}) - T_C(d)}{T_C(\text{bulk})} = C_0 d^{1/\nu}.$$

For the Ising model (Binder 1974, Fischer and Ferdinand 1967), the critical exponent ν, generally, is found to be $\nu=0.63$. For the Ising model calculated using a mean-field formalism (Binder and Hohenberg 1972) $\nu=0.5$ was derived. The Heisenberg model results in a value $\nu=0.59$ (Corcioveei 1960, Valenta 1962).

This power law dependence is fairly close to what is observed experimentally. For gadolinium films on niobium (Paschen et al. 1993) a value of $\nu=0.625$ was reported,

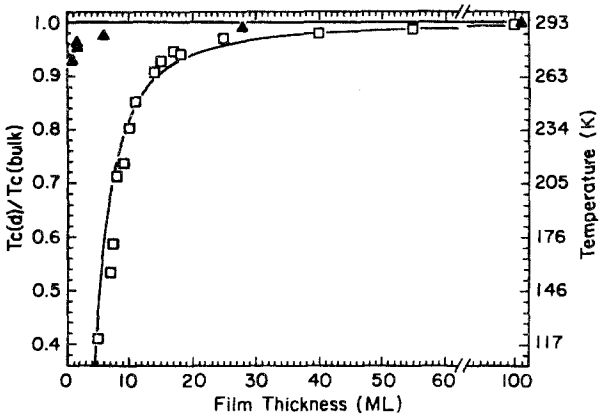

Fig. 17. The reduced Curie temperature as a function of the Gd(0001) film thickness. The open squares show data for the optimally prepared films while the solid triangles show data from rougher films. The line is drawn using a power-law dependence with $\nu = 0.63$. (From Farle et al. 1993.)

while for Gd(0001) grown on W(110) (Farle et al. 1993) a value of $\nu = 0.63$ was obtained. Failure to follow layer-by-layer growth of the film was postulated to cause the deviations from a power-law dependence, where ν has a value of approximately 0.5–0.65 (Farle et al. 1993, Stetter et al. 1992), as seen in fig. 17, but in general the experimental results are fairly close to what is expected.

These scaling relations of statistical mechanics fail in the very small size limit (of the order of a few angstroms). Clusters of gadolinium atoms (Douglass et al. 1992, 1993) exhibit moments per atom that are relatively constant for all cluster sizes below Gd_{30} except for Gd_{17}, Gd_{18}, Gd_{28} and Gd_{29}. Furthermore, the moments "lock" with respect to the cluster lattice at low temperatures (Douglass et al. 1992, 1993). Even more importantly, the Curie temperature of these small clusters does not follow the finite-size scaling relationships. The Curie temperature of these small clusters is, in fact, greater than that of bulk gadolinium (Douglass et al. 1992, 1993).

This effect of the finite thickness of the film has its fundamental origin in the finite size of the sample which limits the correlation length from approaching infinity at T_C. On the other hand, this effect is also a simple expression of the phenomenon that the ultra thin films should exhibit behavior characteristic of two dimensionality while the thick films should exhibit behavior characteristic of a three dimensional system (Mills 1991). Thus, the scaling with film thickness is accompanied by a dimensionality cross-over. Using electron spin resonance (Baberschke et al. 1987, Farle and Baberschke 1987) and ac susceptibility (Aspelmeier et al. 1994, Farle et al. 1993) to measure the critical exponents of the gadolinium film ferromagnetism, a cross-over from two dimensional Ising-like behavior to a three dimensional Ising-like behavior has been indeed observed. This occurs with a gadolinium film thickness of about 15 layers (Aspelmeier et al. 1994).

Farle and Baberschke (1987) demonstrated that for $T \to T_C$, the static susceptibility of Gd follows a power law, $\chi \approx t^{-\gamma}$ (where $t = (T - T_C)/T_C$) with $\gamma = 1.8$ for a monolayer and $\gamma = 1.25$ for an 80 Å film. This is in good agreement with the theoretical γ of 2D and 3D Ising systems, namely, 7/4 or 1.24 (Kaneyoshi 1991b, Stanley 1971) (as well as the thickness dependence of the Curie temperature noted above). It should be noted,

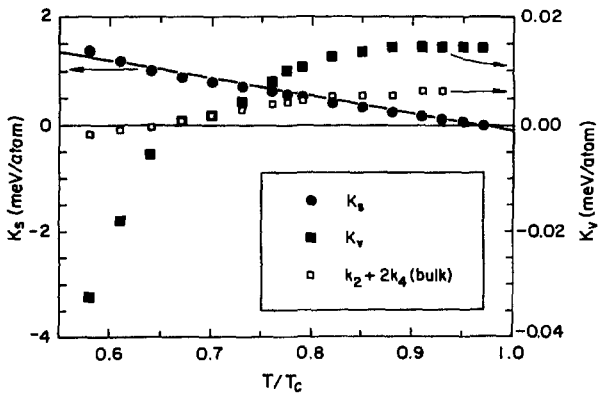

Fig. 18. The variation of the volume and surface/interface uniaxial anisotropy energy with temperature. Data are derived from films of several different thicknesses. The magnetocrystalline anisotropy K_2+2K_4 of bulk gadolinium has been plotted for comparison. (From André et al. 1995.)

however, that the monolayer in this work was grown at elevated temperature, which may yield island growth instead of the ideal 2-dimensional 'flat' monolayer.

The magnetic moments at the surface experience a lower symmetry than is the case for the bulk and this can produce an anisotropy term that is different from the case for the bulk. Phenomenologically treated by Néel (1954), the surface anisotropy can be related to a surface energy density, E_S, by $E_S = K_S \cos^2 \theta$, where K_S is the surface anisotropy constant and θ is the angle between the magnetization direction and the surface normal (Kaneyoshi 1991a,b). In addition, an in-plane shape anisotropy occurs with a thin film due to the demagnetization field. This major anisotropy in gadolinium thin films keeps the easy axis always in-plane. Bulk Gd has a relatively weak anisotropy because of the isotropic half-filled 4f shell. For thin films and monolayers, however, anisotropy becomes important. There has been some discussion of the anisotropy in gadolinium films (André et al. 1995, Berger et al. 1994, Berghaus et al. 1990). A recent study, utilizing ferromagnetic resonance, has measured the uniaxial anisotropy of Gd(0001) films grown on W(110) (André et al. 1995). This work separated the thickness-independent volume anisotropy from the surface/interface part of the anisotropy which is proportional to $1/d$. There is a significant Néel-type anisotropy (André et al. 1995), as seen in fig. 18. The thin film magnetic orientation is observed to be both temperature dependent (Berger et al. 1994, 1995, Pang et al. 1994) and thickness dependent (Berger et al. 1994, 1995), complicating the simple pictures of finite size scaling. This is another aspect of reduced dimensionality that must be considered.

Surfaces can be viewed in terms of semi-infinite systems that are different from either 2-dimensional (2D) or 3-dimensional (3D) systems (Kaneyoshi 1991b, Berger et al. 1994, Berghaus et al. 1990, Mills 1991). For a normal surface, i.e., T_C(surface) = T_C(bulk), the critical exponent β is predicted as 0.84 (Diehl and Nusser 1986) and 0.78 (Binder and Landau 1984, 1985, Diehl and Eisenriegler 1982) for Heisenberg and Ising systems, respectively, where β is defined by $M \approx t^{-\beta}$, where M is the magnetization. These values are significantly higher than the critical exponents for either strictly 3-dimensional or 2-dimensional systems, regardless of the model (Kaneyoshi 1991b). There are

experimentally measured surface critical exponents for Ni ($\beta = 0.8$, Dauth et al. 1987) and EuS ($\beta = 0.72$, Alvarado et al. 1982a,b). For Tb(0001) surface, however, the critical exponent β was measured with electron capture spectroscopy where a value of 0.35 was obtained (Rau et al. 1989b), lower than the values normally expected for surfaces, yet higher than that of a 2-dimensional Ising system ($\beta = 0.125$).

This could be related to the exchange interaction J (Binder 1985, Kaneyoshi 1991a,b, Mills 1970). Binder and Landau (1984, 1985) pointed out that for J_s/J_b above some critical value, say 1.5, not only the surface T_C, but also surface critical exponents should vary with the J_s/J_b ratio. For $J_s/J_b > 1$, β decreases, while for $J_s/J_b < 1$, the critical exponent is the same as for the Ising surface behavior (the critical exponent $\beta = 0.78$). The deviation of β from that of other surfaces like Ni and EuS is therefore the reflection of the strong coupling in the surface of lanthanide metals. However, it is predicted (Binder and Landau 1984, 1985) that the β of any extraordinary surface, where $J_s > J_{sc}$ (the critical value for the surface J) and $T_C(\text{surface}) > T_C(\text{bulk})$, should be smaller than that of the 2-dimensional case, i.e. $\beta = 0.125$. The cause of this disagreement with experiment is unclear.

8. The future

There are many unresolved issues related to the surface magnetism of the lanthanides. The lanthanide metals are not only the prototypical local-moment magnetic systems but also demonstrate the extremes in surface magnetic phenomena, namely, the enhanced surface magnetic ordering of Gd and Tb. So far, surface magnetism studies have concentrated mainly on Gd and Tb. The 4f levels of Gd are half-filled with no orbital moment, which suggests weaker anisotropy and simple magnetic structures (Coqblin 1977). It is well-known that the other magnetic lanthanides show complicated spiral-like magnetic structures in the bulk (Elliot 1972). It would be interesting to investigate systems with additional anisotropy and complicated exchange interactions which should affect the surface magnetic ordering.

The anisotropy will also affect the spin waves (Mills 1991). Measurements of spin wave relaxation along the lines of the work by Vaterlaus, Beutler and Meier (1992) are indicated. There is also a need for mapping the spin wave dispersion, as has been undertaken for Tm (McEwan et al. 1995), but for thin films. We would expect that the lanthanide metals will exhibit spin waves at temperatures above the Curie temperature, much in the same way as has already been observed for Ni (Lynn and Mook 1981, Mook et al. 1973, Mook and Paul 1985, 1988, Mook and Lynn 1986, Steinsvoll et al. 1983, Uemura et al. 1983). Plasmon and other collective electron effects, as well as magnon dispersion, also need to be investigated and such studies are currently only at a preliminary stage for surfaces.

Although it is relatively straightforward to calculate the magnetic moments and predict enhanced moments at surfaces (particularly at finite temperatures), it remains a challenge to calculate the exchange coupling, a quantity even more important in understanding the

surface magnetic ordering. Other unsettled theoretical issues include finite-temperature magnetism, short-range order, etc. Many of the complications that are important to magnetism still need to be included in most current band-structure models. These include spin–orbit interactions, correlation energies, and finite-temperature effects. In addition, sophisticated band-structure calculations that include surface effects are still limited in number (and exist only for a few of the lanthanide metals).

There is a need for proper identification of the unoccupied surface states. Without this, it is difficult to more directly measure the surface exchange splitting with temperature. With well-defined surface states this should provide a means to study the surface magnetization separately from the bulk.

We need to study the surface magnetism of the lanthanides on surfaces other than the basal plane (0001). Studies of prism faces are limited, and none exist of the surface magnetization. This is, as indicated in the introduction, a result of experimental complications, but these experimental difficulties can be overcome. It is now known that the unusual surface magnetic order is determined by the surface electronic structure, namely, 5d surface states. Since the electronic structure at different surfaces should be different, so should the surface magnetic order. It would be interesting to systematically investigate how the T_C(surface) and surface anisotropy change for different high-symmetry planes.

While finite-size effects and the physics of small clusters are currently being explored for lanthanide thin films, there is a need to account for the surface in the context of finite-size scaling. As is clear from the work thus far for the lanthanides, the surface magnetic properties differ substantially from the bulk. For the thinnest of films (films of only a few monolayers or atoms thick) this may strongly perturb the magnetic properties. This will be even more complicated if the other interfaces (other than the surface) have large interfacial energies and consequently different magnetic properties as well. Such results may provide important insight not only into the pure rare-earth metals, but also on the properties of lanthanide multilayers.

The future is exciting for both experiment and theory. There should be many exciting results to emerge from the study of lanthanide surface magnetism.

Acknowledgments

This work was supported by the NSF, through grants number DMR-92-21655 and DMR-94-96131, and by the DOE, for work done at Argonne National Labs through BES-MS #W-31-109-ENG-38. The authors would like to thank their many colleagues, in particular Sam Bader, Karl Garrison, Franz Himpsel, Peter Johnson, Dave LaGraffe, Martin Landolt, Allen Miller, Marshall Onellion, David Sellmyer, Carlo Waldfried, and Jiandi Zhang, who contributed to making this work possible. The authors would also like to thank Sam Bader (Argonne), Markus Donath (Garching), M. Farle (Berlin) and K. Baberschke (Berlin) for their comments.

References

Ahuja, R., S. Auluck, B. Johansson and M.S.S. Brooks, 1994, Phys. Rev. B **50**, 5147.

Aldén, M., B. Johansson and H.L. Skriver, 1995, Phys. Rev. B **51**, 5386.

Allen, G.A.T., 1974, Phys. Rev. B **1**, 352.

Allen, J.W., and R.M. Martin, 1982, Phys. Rev. Lett. **49**, 1106.

Allen, J.W., L.I. Johansson, R.S. Bauer, I. Lindau and S.B.M. Hagström, 1978, Phys. Rev. Lett. **41**, 1499.

Allen, J.W., L.I. Johansson, I. Lindau and S.B.M. Hagström, 1980, Phys. Rev. B **21**, 1335.

Allen, J.W., S.-J. Oh, I. Lindau, J.M. Lawrence, L.I. Johansson and S.B. Hagström, 1981, Phys. Rev. Lett. **46**, 1100.

Altmann, S.L., and J.C. Bradley, 1967, Proc. Phys. Soc. London **92**, 764.

Alvarado, S.F., M. Campagna and W. Gudat, 1980, J. Electron Spectrosc. Relat. Phenom. **18**, 43.

Alvarado, S.F., M. Campagna and H. Hopster, 1982a, Phys. Rev. Lett. **48**, 51.

Alvarado, S.F., M. Campagna, F. Ciccacci and H. Hopster, 1982b, J. Appl. Phys. **53**, 7920.

Andersen, O.K., and T.L. Loucks, 1968, Phys. Rev. **167**, 551.

André, G., A. Aspelmeier, B. Schulz, M. Farle and K. Baberschke, 1995, Surf. Sci. **326**, 275.

Antropov, V.P., A.I. Liechtenstein and B.N. Harmon, 1995, J. Magn. & Magn. Mater. **140–144**, 1161.

Arenholz, E., E. Navas, K. Starke, L. Baumgarten and G. Kaindl, 1995a, Phys. Rev. B **51**, 8211.

Arenholz, E., K. Starke and G. Kaindl, 1995b, J. Electron Spectrosc. Relat. Phenom. **76**, 183.

Aspelmeier, A., F. Gerhardter and K. Baberschke, 1994, J. Magn. & Magn. Mater. **132**, 22.

Baberschke, K., M. Farle and M. Zomack, 1987, Appl. Phys. A **144**, 13.

Baer, Y., and G. Busch, 1973, Phys. Rev. Lett. **31**, 35.

Baer, Y., and G. Busch, 1974, J. Electron Spectrosc. Relat. Phenom. **5**, 611.

Baer, Y., and W.-D. Schneider, 1987, in: Handbook on the Physics and Chemistry of Rare Earths, Vol. 10, eds K.A. Gschneidner Jr, L. Eyring and S. Hüfner (North-Holland, Amsterdam) ch. 62, p. 1.

Baer, Y., H. Rott, J.C. Fuggle and L.E. DeLong, 1981, Phys. Rev. B **24**, 5384.

Barrett, S.D., 1992, Surf. Sci. Rep. **14**, 271.

Barrett, S.D., and R.G. Jordan, 1987, Z. Phys. B **66**, 375.

Barrett, S.D., R.G. Jordan and A.M. Begley, 1987, J. Phys. **17**, L145.

Barrett, S.D., A.M. Begley, P.J. Durham, R.G. Jordan and W.M. Temmerman, 1989a, J. Phys.: Condens. Matter **1**, SB243.

Barrett, S.D., R.G. Jordan, A.M. Begley and R.I.R. Blyth, 1989b, Z. Phys. Condens. Matter **76**, 137.

Barrett, S.D., A.M. Begley, P.J. Durham and R.G. Jordan, 1989c, Solid State Commun. **71**, 111.

Barrett, S.D., R.I.R. Blyth, S.S. Dhesi and K. Newstead, 1991a, J. Phys.: Condens. Matter **3**, 1953.

Barrett, S.D., R.I.R. Blyth, A.M. Begley, S.S. Dhesi and R.G. Jordan, 1991b, Phys. Rev. B **43**, 4573.

Barth, J., F. Gerken, J. Schmidt-May, A. Flodström and L.I. Johansson, 1983, Chem. Phys. Lett. **96**, 532.

Bauer, E., and J. Kolaczkiewicz, 1985, Phys. Status Solidi B **131**, 699.

Beaurepaire, E., B. Carrière, P. Légaré, G. Krill, C. Brouder, D. Chandesris and J. Lecante, 1989, Surf. Sci. **211/212**, 448.

Begley, A.M., R.G. Jordan, W.M. Temmerman and P.J. Durham, 1990, Phys. Rev. B **41**, 11780.

Berg, C., S. Raaen and M.W. Ruckman, 1992, J. Phys.: Condens. Matter **4**, 4213.

Berger, A., A.W. Pang and H. Hopster, 1994, J. Magn. & Magn. Mater. **137**, L1.

Berger, A., A.W. Pang and H. Hopster, 1995, Phys. Rev. B **52**, 1078.

Berghaus, A., M. Farle, Y. Li and K. Baberschke, 1990, in: Magnetic Properties of Low Dimensional Systems II, eds L.M. Falicov, F. Mejia-Lira and J.L. Morán-López (Springer, Berlin) p. 61.

Bertel, E., F.P. Netzer and J.A.D. Matthew, 1981, Surf. Sci. **103**, 1.

Bertel, E., G. Strasser, F.P. Netzer and J.A.D. Matthew, 1982a, Phys. Rev. B **25**, 3374.

Bertel, E., G. Strasser, F.P. Netzer and J.A.D. Matthew, 1982b, Surf. Sci. **118**, 387.

Bertran, F., T. Gouriex, G. Krill, M. Alnot, J.J. Ehrhardt and W. Felsch, 1991, Surf. Sci. **245**, L163.

Bertran, F., T. Gouriex, G. Krill, M. Alnot, J.J. Ehrhardt and W. Felsch, 1992, Phys. Rev. B **46**, 7829.

Besnosov, A.B., V.V. Eremendo and V.P. Gnezdilov, 1984, J. Magn. & Magn. Mater. **43**, 243.

Binder, K., 1974, Thin Solid Films, **20**, 367.

Binder, K., 1985, in: Phase Transitions and Critical Phenomena, Vol. 8, eds C. Domb and J.L. Lebowitz (Academic Press, New York) p. 1.

Binder, K., and P.C. Hohenberg, 1972, Phys. Rev. B **6**, 3461.

Binder, K., and P.C. Hohenberg, 1976, Phys. Rev. B **9**, 2194.

Binder, K., and D.P. Landau, 1984, Phys. Rev. Lett. **52**, 318.

Binder, K., and D.P. Landau, 1985, Surf. Sci. **151**, 409.

Blaha, P., K. Schwarz and P.H. Dedrichs, 1988, Phys. Rev. B **38**, 9368.

Blodgett, A.J., W.E. Spicer and A.Y.-C. Yu, 1966, in: Optical Properties and Electronic Structure of Metals and Alloys, Proc. Int. Colloquium, ed. F. Abelès (North-Holland, Amsterdam) p. 246.

Blyth, R.I.R., S.D. Barrett, S.S. Dhesi, R. Cosso, N. Heritage, A.M. Begley and R.G. Jordan, 1991a, Phys. Rev. B **44**, 5423.

Blyth, R.I.R., S.S. Dhesi, A.J. Patchett, T. Mitrelias, N.P. Prince and S.D. Barrett, 1991b, J. Phys.: Condens. Matter **3**, 6165.

Blyth, R.I.R., R. Cosso, S.S. Dhesi, K. Newstead, A.M. Begley, R.G. Jordan and S.D. Barrett, 1991c, Surf. Sci. **251/252**, 722.

Blyth, R.I.R., P.T. Andrews and S.D. Barrett, 1991d, J. Phys.: Condens. Matt. **3**, 2827.

Blyth, R.I.R., A.J. Patchett, S.S. Dhesi, R. Cosso and S.D. Barrett, 1991e, J. Phys.: Condens. Matter **3**, S287.

Blyth, R.I.R., S.S. Dhesi, P.A. Gravil, K. Newstead, R. Cosso, R.J. Cole, A.J. Patchett, T. Mitrelias, N.P. Prince and S.D. Barrett, 1992, J. Alloys & Compounds, **180**, 259.

Bodenbach, M., A. Höhr, C. Laubschat, G. Kaindl and M. Methfessel, 1994, Phys. Rev. B **50**, 14446.

Borgiel, W., and W. Nolting, 1990, Z. Phys. B **78**, 241.

Borgiel, W., G. Borstel and W. Nolting, 1986, Solid State Commun. **60**, 313.

Brodén, G., 1972, Phys. Kondens. Mater. **15**, 171.

Brodén, G., S.B.M. Hagström and C. Norris, 1970, Phys. Rev. Lett. **24**, 1173.

Brodén, G., S.B.M. Hagström and C. Norris, 1973, Phys. Kondens. Mater. **15**, 327.

Brooks, M.S.S., S. Auluck, T. Gasche, L. Trygg, L. Nordström, L. Severin and B. Johansson, 1992, J. Magn. & Magn. Mater. **104–107**, 1496.

Brooks, M.S.S., O. Eriksson, L. Severin and B. Johansson, 1993, Physica B **192**, 39.

Busch, G., M. Campagna, C. Cotti and H.C. Siegman, 1969, Phys. Rev. Lett., **22**, 597.

Bylander, D.M., and L. Kleinman, 1994, Phys. Rev. B **50**, 4996.

Campagna, M., and F.U. Hillebrecht, 1987, in: Handbook on the Physics and Chemistry of the Rare Earths, Vol. 10, eds K.A. Gschneidner Jr, L. Eyring and S. Hüfner (North-Holland, Amsterdam) ch. 63, p. 75.

Capellmann, H., 1979, Z. Phys. B **34**, 29.

Capellmann, H., and V. Vieira, 1982, Solid State Commun. **43**, 747.

Carbone, C., and E. Kisker, 1987, Phys. Rev. B **36**, 1280.

Cerri, A., D. Mauri and M. Landolt, 1983, Phys. Rev. B **27**, 6526.

Chamberlain, M.B., A.F. Burr and R.J. Liefeld, 1974, Phys. Rev. A **9**, 663.

Child, H.R., 1978, Phys. Rev. B **18**, 1247.

Chorkendorff, I., J. Kofoed and J. Onsgaard, 1985a, Surf. Sci. **152/153**, 749.

Chorkendorff, I., J. Onsgaard, J. Schmidt-May and R. Nyholm, 1985b, Surf. Sci. **160**, 587.

Colliex, C., M. Gasgnier and P. Trebbia, 1976, J. Phys. **37**, 397.

Coqblin, B., 1977, The Electronic Structure of the Rare Earth Metals and Alloys. The magnetic heavy rare earths (Academic Press, New York).

Corcioveei, A., 1960, Czech. J. Phys. B **10**, 568.

Cornwell, J.F., 1966, Phys. Kondens. Mater. **4**, 327.

Cox, P.A., 1975, Structure and Bonding, Springer Tracts in Physics, Vol. 24 (Springer, Berlin) p. 59.

Cox, P.A., Y. Baer and C.K. Jørgensen, 1973, Chem. Phys. Lett. **22**, 433.

Cox, P.A., J.K. Lang and Y. Baer, 1981, J. Phys. F **11**, 113.

Crecelius, G., G.K. Wertheim and D.N.E. Buchanan, 1978, Phys. Rev. B **18**, 6519.

Dakshinamoorthy, M., K. Iyakutti, S. Sankar and R. Asokamani, 1984, Z. Phys. B **55**, 299.

Das, S.G., 1976, Phys. Rev. B **13**, 3978.

Datar, W.R., and S. Tanuma, 1968, Phys. Lett. A **27**, 182.

Dauth, B.H., S.F. Alvarado and M. Campagna, 1987, Phys. Rev. Lett. **58**, 2118.

De, S., I. Bose and S. Chatterjee, 1985, Phys. Status Solidi B **127**, 605.

De, S.K., and S. Chatterjee, 1987, J. Phys. F. **17**, 2057.

de Gennes, P.G., 1958, Compt. Rend. **247**, 1836.

Della Valle, F., and S. Modesti, 1989, Phys. Rev. B **40**, 933.

denBoer, M.L., C.L. Chang, S. Horn and V. Murgai, 1988, Phys. Rev. B **37**, 6605.

Dhesi, S.S., R.J.R. Blyth, R.J. Cole, P.A. Gravil and S.D. Barrett, 1992, J. Phys.: Condens. Matter **4**, 9811.

Diehl, H.W., 1986, Phase Transitions and Critical Phenomena, Vol. 10, eds C. Domb and J.L. Lebowitz (Academic Press, New York).

Diehl, H.W., and E. Eisenriegler, 1982, Phys. Rev. Lett. **48**, 1767.

Diehl, H.W., and A. Nusser, 1986, Phys. Rev. Lett. **56**, 2834.

Dimmock, J.O., and A.J. Freeman, 1964, Phys. Rev. Lett. **13**, 750.

Dimmock, J.O., A.J. Freeman and R.E. Watson, 1965, J. Appl. Phys. **36**, 1142.

Domke, M., C. Laubschat, M. Prietsch, T. Mandel, G. Kaindl and W.-D. Schneider, 1986, Phys. Rev. Lett. **56**, 1287.

Donath, M., B. Gubanka and F. Passek, 1996, Phys. Rev. Lett. **77**, 5138.

Douglass, D.C., J.P. Bucher and L.A. Bloomfield, 1992, Phys. Rev. Lett. **68**, 1774.

Douglass, D.C., A.J. Cox, J.P. Bucher and L.A. Bloomfield, 1993, Phys. Rev. B **47**, 12874.

Dowben, P.A., D. LaGraffe and M. Onellion, 1989, J. Phys.: Condens. Matter **1**, 6571.

Dowben, P.A., D. LaGraffe, Dongqi Li, L. Dottl, C. Hwang, Y. Ufuktepe and M. Onellion, 1990, J. Phys.: Condens. Matter **2**, 8801.

Dowben, P.A., D. LaGraffe, Dongqi Li, A. Miller, Ling Zhang, L. Dottl and M. Onellion, 1991, Phys. Rev. B **43**, 3171.

Dowben, P.A., Dongqi Li and M. Onellion, 1992, J. Phys.: Condens. Matter **4**, 7021.

Dowben, P.A., W. Hürsch and M. Landolt, 1993, J. Magn. & Magn. Mater. **125**, 120.

Dowben, P.A., Dongqi Li, Jiandi Zhang and M. Onellion, 1995, J. Vac. Sci. & Technol. A **13**, 1549.

Duò, L., M. Finazzi and L. Braicovich, 1993, Phys. Rev. B **48**, 10728.

Eastman, D.E., 1969, Solid State Commun. **7**, 1697.

Egelhoff, W.F., G.G. Tibbetts, M.H. Hecht and I. Lindau, 1981, Phys. Rev. Lett. **46**, 1071.

Elliot, R.J., 1972, Magnetic Properties of the Rare Earths Metals (Plenum Press, New York).

Erbudak, M., P. Kalt, L. Schlapbach and K. Bennemann, 1983, Surf. Sci. **126**, 101.

Eriksson, O., R. Ahuja, A. Ormeci, J. Trygg, O. Hjortstam, P. Söderlind, B. Johansson and J.M. Wills, 1995, Phys. Rev. B **52**, 4420.

Evenson, W.E., and S.H. Liu, 1968, Phys. Rev. Lett. **21**, 432.

Evenson, W.E., and S.H. Liu, 1969, Phys. Rev. **178**, 783.

Fäldt, Å., and H.P. Myers, 1983, Solid State Commun. **48**, 253.

Fäldt, Å., and H.P. Myers, 1984a, Phys. Rev. Lett. **52**, 1315.

Fäldt, Å., and H.P. Myers, 1984b, Phys. Rev. B **30**, 5481.

Fäldt, Å., and H.P. Myers, 1985, J. Magn. & Magn. Mater. **47/48**, 255.

Fäldt, Å., D.K. Kristensson and H.P. Myers, 1988, Phys. Rev. B **37**, 2682.

Farle, M., and K. Baberschke, 1987, Phys. Rev. Lett. **58**, 511.

Farle, M., K. Baberschke, U. Stetter, A. Aspelmeier and F. Gerhardter, 1993, Phys. Rev. B **47**, 11571.

Fauster, Th., and F.J. Himpsel, 1984, Phys. Rev. B **30**, 1874.

Fedorov, A.V., C. Laubschat, K. Starke, E. Weschke, K.-U. Barholz and G. Kaindl, 1993, Phys. Rev. Lett. **70**, 1719.

Fedorov, A.V., E. Arenholz, K. Starke, E. Navas, L. Baumgarten, C. Laubschat and G. Kaindl, 1994a, Phys. Rev. Lett. **73**, 601.

Fedorov, A.V., A. Höhr, E. Weschke, K. Starke, V.K. Adamchuk and G. Kaindl, 1994b, Phys. Rev. B **49**, 5117.

Fedorov, A.V., K. Starke and G. Kaindl, 1994c, Phys. Rev. B **50**, 2739.

Feibelman, P.J., and D.R. Hamann, 1979, Solid State Commun. **31**, 413.

Ferguson, P.E., 1978, J. Appl. Phys. **49**, 2203.

Fischer, M.E., and A.E. Ferdinand, 1967, Phys. Rev. Lett. **19**, 169.

Fleming, G.S., and S.H. Liu, 1970, Phys. Rev. B **2**, 164.

Fleming, G.S., and T.L. Loucks, 1968, Phys. Rev. **173**, 685.

Fleming, G.S., S.H. Liu and T.L. Loucks, 1968, Phys. Rev. Lett. **21**, 1524.

Fleming, G.S., S.H. Liu and T.L. Loucks, 1969, J. Appl. Phys. **40**, 1285.

Flodström, A., R. Nyholm and B. Johansson, 1992, in: Advances in Surface and Interface Science, Vol. 1, ed. R.Z. Bachrach (Plenum Press, New York).

Freeman, A.J., and J.O. Dimmock, 1966, Bull. Am. Phys. Soc. **11**, 216.

Freeman, A.J., and C.L. Fu, 1986, in: Magnetic Properties of Low Dimensional Systems, Springer Proceedings in Physics, Vol. 14, eds L.M. Falicov and J.L. Morán-López (Springer, Berlin) p. 16.

Freeman, A.J., and Ruquian Wu, 1991, J. Magn. & Magn. Mater. **100**, 497.

Freeman, A.J., J.O. Dimmock and R.E. Watson, 1966, Phys. Rev. Lett. **16**, 94.

Fujimori, A., and J.H. Weaver, 1985, Phys. Rev. B **32**, 3422.

Gempel, R.F., D.R. Gustafson and J.D. Willenberg, 1972, Phys. Rev. B **5**, 2082.

Gerken, F., 1983, J. Phys. F **13**, 703.

Gerken, F., J. Barth, R. Kammerer, L.I. Johansson and A. Flodström, 1982a, Surf. Sci. **117**, 468.

Gerken, F., J. Barth and C. Kunz, 1982b, AIP Conf. Proc. **94**, 602.

Gerken, F., A.S. Flodström, J. Barth, L.I. Johansson and C. Kunz, 1985, Phys. Scripta **32**, 43.

Glötzel, D., 1978, J. Phys. F **8**, L163.

Glötzel, D., 1981, in: Physics of Solids Under High Pressure, eds J.S. Schilling and R.N. Shelton (North-Holland, Amsterdam) p. 263.

Gu, C., X. Wu, C.G. Olson and D.W. Lynch, 1991, Phys. Rev. Lett. **67**, 1622.

Gudat, W., M. Campagna, R. Rosei, J.H. Weaver, W. Eberhardt, F. Hulliger and E. Kaldis, 1981, J. Appl. Phys. **52**, 2123.

Gudat, W., R. Rosei, J.H. Weaver, E. Kaldis and F. Hulliger, 1982, Solid State Commun. **41**, 37.

Gupta, R.P., and T.L. Loucks, 1968, Phys. Rev. **176**, 848.

Gustafson, D.R., J.D. McNutt and L.C. Roelling, 1969, Phys. Rev. **183**, 435.

Harmon, B.N., 1979, J. Phys. (Paris) Colloq. **40**, C5-65.

Harmon, B.N., and A.J. Freeman, 1974a, Phys. Rev. B **10**, 1979.

Harmon, B.N., and A.J. Freeman, 1974b, Phys. Rev. B **10**, 4849.

Harmon, B.N., V.P. Antropov, A.I. Liechtenstein, I.V. Solovyev and V.I. Anisimov, 1995, J. Phys. & Chem. Solids **56**, 1521.

Hasegawa, H., 1979, J. Phys. Soc. Jpn. **46**, 1504.

Hedén, P.O., H. Löfgren and S.B.M. Hagström, 1971, Phys. Rev. Lett. **26**, 432.

Hedén, P.O., H. Löfgren and S.B.M. Hagström, 1972, Phys. Status Solidi B **49**, 721.

Heineman, M., and W.M. Temmerman, 1994, Surf. Sci. **307–309**, 1121.

Helms, C.R., and W.E. Spicer, 1972, Appl. Phys. Lett. **21**, 237.

Herbst, J.F., 1992, Phys. Rev. B **46**, 6665.

Herbst, J.F., and J.W. Wilkins, 1984, Phys. Rev. B **29**, 5992.

Herbst, J.F., and J.W. Wilkins, 1987, Phys. Rev. B **36**, 2557.

Herbst, J.F., D.N. Lowy and R.E. Watson, 1972, Phys. Rev. B **6**, 1913.

Hill, H.H., and E.A. Kmetko, 1975, J. Phys. F **5**, 1119.

Himpsel, F.J., 1991, J. Magn. & Magn. Mater. **102**, 261.

Himpsel, F.J., and B. Reihl, 1983, Phys. Rev. B **28**, 574.

Hoekstra, J.A., and R.A. Phillips, 1971, Phys. Rev. B **4**, 4184.

Hofmann, R., and F.P. Netzer, 1991, Phys. Rev. B **43**, 9720.

Hofmann, R., W.A. Henle and F.P. Netzer, 1991, Phys. Rev. B **44**, 3133.

Hohenemser, C., J.M. Weingart and S. Berko, 1968, Phys. Rev. Lett. A **28**, 41.

Hübinger, F., C. Schüßler-Langheine, A.V. Fedorov, K. Starke, E. Weschke, A. Höhr, S. Vandré and G. Kaindl, 1995, J. Electron Spectrosc. Relat. Phenom. **76**, 535.

Hüfner, S., and P. Steiner, 1982, Z. Phys. B **46**, 37.

Hüfner, S., G.L. Bona, F. Meier and D. Pescia, 1984, Solid State Commun. **51**, 163.

Irvine, S.J.C., R.C. Young, D. Fort and D.W. Jones, 1978, J. Phys. F **8**, L269.

Jackson, C., 1969, Phys. Rev. **178**, 949.

Jensen, E., and D.M. Wieliczka, 1984, Phys. Rev. B **30**, 7340.

Jepsen, O., and O.K. Andersen, 1971, Solid State Commun. **9**, 1763.

Johanssen, G., and A.R. Mackintosh, 1970, Solid State Commun. **8**, 121.

Johansson, B., 1974, J. Phys. F **4**, L169.

Johansson, B., 1979, Phys. Rev. B **19**, 6615.

Johansson, B., and N. Mårtensson, 1980, Phys. Rev. B **21**, 4427.

Johansson, B., and N. Mårtensson, 1983, Helv. Phys. Acta **56**, 405.

Johansson, B., and A. Rosengren, 1975, Phys. Rev. B **11**, 1367.

Johansson, L.I., J.W. Allen, T. Gustafsson, I. Lindau and S.B. Hagström, 1978, Solid State Commun. **28**, 53.

Johansson, L.I., J.W. Allen, I. Lindau, M.M. Hecht and S.B.M. Hagström, 1980, Phys. Rev. B **21**, 1408.

Johansson, W.R., G.W. Crabtree and F.A. Schmidt, 1982, J. Appl. Phys. **53**, 2041.

Jordan, R.G., 1986, Phys. Scripta T **13**, 22.

Jordan, R.G., A.M. Begley, S.D. Barrett, P.J. Durham and W.M. Temmerman, 1990, Solid State Commun. **76**, 579.

Jørgensen, B., M. Christiansen and J. Onsgaard, 1991, Surf. Sci. **251/252**, 519.

Kaindl, G., W.D. Schneider, C. Laubschat, B. Reihl and N. Mårtensson, 1983, Surf. Sci. **126**, 105.

Kaindl, G., A. Höhr, E. Weschke, S. Vandré, C. Schüßler-Langeheine and C. Laubschat, 1995, Phys. Rev. B **51**, 7920.

Kammerer, R., J. Barth, F. Gerken, A. Flodström and L.I. Johansson, 1982, Solid State Commun. **41**, 435.

Kaneyoshi, T., 1991a, J. Phys.: Condens. Matter **3**, 4497.

Kaneyoshi, T., 1991b, Introduction to Surface Magnetism (CRC Press, Boca Raton, FL).

Keeton, S.C., and T.L. Loucks, 1966, Phys. Rev. **146**, 429.

Keeton, S.C., and T.L. Loucks, 1968, Phys. Rev. **168**, 672.

Kierren, B., F. Bertran, T. Gourieux, D. Malterre and G. Krill, 1996, Europhys. Lett. **33**, 35.

Kim, Bongsoo, A.B. Andrews, J.L. Erskine, K.J. Kim and B.N. Harmon, 1992, Phys. Rev. Lett. **68**, 1931.

Kmetko, D.D., and H.H. Hill, 1976, J. Phys. F **6**, 1025.

Knyazev, Yu.V., and M.M. Noskov, 1970, Fiz. Met. Metalloved **30**, 214 [Phys. Met. Metallogr. **31**, 230].

Koelling, D.D., and B.N. Harmon, 1972, Bull. Am. Phys. Soc. **17**, 94.

Korenman, V., J.L. Murray and R.E. Prenge, 1977a, Phys. Rev. B **16**, 4032.

Korenman, V., J.L. Murray and R.E. Prenge, 1977b, Phys. Rev. B **16**, 4048.

Kowalczyk, S.P., N. Edelstein, F.R. McFeely, L. Ley and D.A. Shirley, 1974, Chem. Phys. Lett. **29**, 491.

Krisch, M.H., F. Sette, U. Bergmann, C. Masciovecchio, R. Verbeni, J. Goulon, W. Caliebe and C.C. Kao, 1996, Phys. Rev. B **54**, R12673.

Krutzen, B.C.H., and F. Springelkamp, 1989, J. Phys.: Condens. Matter **1**, 8369.

LaGraffe, D., P.A. Dowben and M. Onellion, 1989a, Phys. Rev. B **40**, 970.

LaGraffe, D., P.A. Dowben and M. Onellion, 1989b, Phys. Rev. B **40**, 3348.

LaGraffe, D., P.A. Dowben and M. Onellion, 1989c, in: Growth, Characterization and Properties of Ultrathin Magnetic Films and Multilayers, eds B.T. Jonker, J.P. Heremans and E.E. Marino, Mater. Res. Soc. Symp. Proc. **151**, 71.

LaGraffe, D., P.A. Dowben and M. Onellion, 1990a, Phys. Lett. A **147**, 240.

LaGraffe, D., A. Miller, P.A. Dowben and M. Onellion, 1990b, in: Thin Film Structures and Phase Stability, eds B.M. Clemens and W.I. Johnson, Mater. Res. Soc. Symp. Proc. **187**, 225.

Lamouri, A., I.L. Krainsky, A.G. Petukhov, W.R.L. Lambrecht and B. Segall, 1995, Phys. Rev. B **51**, 1803.

Lang, J.K., and Y. Baer, 1979, Solid State Commun. **31**, 945.

Lang, J.K., Y. Baer and P.A. Cox, 1978, Phys. Rev. Lett. **42**, 74.

Lang, J.K., Y. Baer and P.A. Cox, 1981, J. Phys. F **11**, 121.

Lang, W.C., B.D. Padalia, D.J. Fabian and L.M. Watson, 1974, J. Electron. Spectrosc. Relat. Phenom. **5**, 207.

Lapeyre, G.J., 1969, Phys. Rev. **179**, 623.

Lawrence, J.M., J.W. Allen, S.-J. Oh and I. Lindau, 1982, Phys. Rev. B **26**, 2362.

Lehman, G., and M. Taut, 1972, Phys. Status Solidi B **54**, 469.

Leung, T.C., X.W. Wang and B.N. Harmon, 1988, Physica B **149**, 131.

Li, Dongqi, C.W. Hutchings, P.A. Dowben, C. Hwang, Rong-Tzong Wu, M. Onellion, A.B. Andrews and J.L. Erskine, 1991a, J. Magn. & Magn. Mater. **99**, 85.

Li, Dongqi, C.W. Hutchings, P.A. Dowben, Rong-Tzong Wu, C. Hwang, M. Onellion, A.B. Andrews and J.L. Erskine, 1991b, J. Appl. Phys. **70**, 6565.

Li, Dongqi, P.A. Dowben and M. Onellion, 1992a, in: Magnetic Thin Films, Surfaces and Multilayers, eds S.S.P. Parkin, H. Hopster, J.-P. Renard, T. Shinjo and W. Zinn, Mater. Res. Soc. Symp. Proc. **231**, 107.

Li, Dongqi, Jiandi Zhang, P.A. Dowben, R.-T. Wu and M. Onellion, 1992b, J. Phys.: Condens. Matter **4**, 3929.

Li, Dongqi, Jiandi Zhang, P.A. Dowben and M. Onellion, 1992c, Phys. Rev. B **45**, 7272.

Li, Dongqi, Jiandi Zhang, P.A. Dowben and K. Garrison, 1993a, J. Phys.: Condens. Matter **5**, L73.

Li, Dongqi, Jiandi Zhang, P.A. Dowben, K. Garrison, P.D. Johnson, H. Tang, T.G. Walker, H. Hopster, J.C. Scott, D. Weller and D.P. Pappas, 1993b, Mater. Res. Soc. Symp. Proc. **313**, 451.

Li, Dongqi, Jiandi Zhang, P.A. Dowben and M. Onellion, 1993c, Phys. Rev. B **48**, 5612.

Li, Dongqi, P.A. Dowben, J.E. Ortega and F.J. Himpsel, 1994a, Phys. Rev. B **49**, 7734.

Li, Dongqi, M. Freitag, J. Pearson, Z.Q. Qiu and S.D. Bader, 1994b, Phys. Rev. Lett. **72**, 3112.

Li, Dongqi, J. Pearson, S.D. Bader, D.N. McIlroy, C. Walfried and P.A. Dowben, 1995, Phys. Rev. B **51**, 13895.

Li, Dongqi, J. Pearson, S.D. Bader, D.N. McIlroy, C. Walfried and P.A. Dowben, 1996, J. Appl. Phys. 79, 5838.

Li, H., D. Tian, J. Quinn, Y.S. Li, S.C. Wu and F. Jona, 1992, Phys. Rev. B **45**, 3853.

Liebermann, L.N., D.P. Fredkin and H.B. Shore, 1969, Phys. Rev. Lett. **22**, 539.

Liebermann, L.N., J. Clinton, D.M. Edwards and J. Mathon, 1970, Phys. Rev. Lett. **25**, 4.

Liefeld, R.J., A.F. Burr and M.B. Chamberlain, 1974, Phys. Rev. A **9**, 316.

Lindgård, P.A., B.N. Harmon and A.J. Freeman, 1975, Phys. Rev. Lett. **35**, 383.

Liu, S.H., 1962, Phys. Rev. **127**, 1889.

Liu, S.H., 1978, Electronic structure of the rare earth metals, in: Handbook on the Physics and Chemistry of the Rare Earths, Vol. 1, eds K.A. Gschneidner Jr and L. Eyring (North-Holland, Amsterdam) ch. 3, p. 233.

Liu, S.H., and K.M. Ho, 1982, Phys. Rev. B **26**, 7052.

Liu, S.H., and K.M. Ho, 1983, Phys. Rev. B **28**, 4220.

Liu, S.H., R.P. Gupta and S.K. Sinha, 1971, Phys. Rev. B **4**, 1100.

Loucks, T.L., 1966, Phys. Rev. **144**, 504.

Lynn, J.W., and H.A. Mook, 1981, Phys. Rev. B **23**, 198.

Mackintosh, A.R., 1968, Phys. Lett. A **28**, 217.

Mårtensson, N., B. Reihl and R.D. Parks, 1982, Solid State Commun. **41**, 573.

Mårtensson, N., A. Stenborg, O. Björneholm, A. Nilsson and J.N. Andersen, 1988, Phys. Rev. Lett. **60**, 1731.

Matsumoto, M., J.B. Staunton and P. Strange, 1991, J. Phys.: Condens. Matter **3**, 1453.

Matthew, J.A.D., G. Strasser and F.P. Netzer, 1982, J. Phys. C **15**, L1019.

Matthew, J.A.D., G. Strasser and F.P. Netzer, 1983, Phys. Rev. B **27**, 5839.

Matthew, J.A.D., W.A. Henle, M.G. Ramsey and F.P. Netzer, 1991, Phys. Rev. B **43**, 4897.

Mattocks, P.G., and R.C. Young, 1977a, J. Phys. F **7**, 1219.

Mattocks, P.G., and R.C. Young, 1977b, J. Phys. F **7**, L19.

Mauri, D., and M. Landolt, 1981, Phys. Rev. Lett. **47**, 1322.

McEwan, K.A., U. Steigenberger, L. Weiss, T. Zeiske and J. Jensen, 1995, J. Magn. & Magn. Mater. **140–144**, 767.

McFeely, F.R., S.P. Kowalczyk, L. Ley and D.A. Shirley, 1973, Phys. Lett. A **45**, 227.

McFeely, F.R., S.P. Kowalczyk, L. Ley and D.A. Shirley, 1974, Phys. Lett. A **49**, 301.

McIlroy, D.N., C. Waldfried, Dongqi Li, J. Pearson, S. Bader, D.-J. Huang, P.D. Johnson, R.F. Sabirianov, S.S. Jaswal and P.A. Dowben, 1996, Phys. Rev. Lett. **76**, 2802.

McMahan, A.K., H.L. Skriver and B. Johansson, 1981, in: Physics of Solids Under High Pressure, eds J.S. Schilling and R.N. Shelton (North-Holland, Amsterdam) p. 169.

Miller, A., and P.A. Dowben, 1993, J. Phys.: Condens. Matter **5**, 5459.

Mills, D.L., 1970, J. Phys. (Paris) Colloq. **31**, C1-33.

Mills, D.L., 1991, J. Magn. & Magn. Mater. **100**, 515.

Min, B.I., H.J.F. Jansen, T. Oguchi and A.J. Freeman, 1986a, J. Magn. & Magn. Mater. **59**, 277.

Min, B.I., H.J.F. Jansen, T. Oguchi and A.J. Freeman, 1986b, Phys. Rev. B **34**, 369.

Min, B.I., T. Oguchi, H.F.J. Jansen and A.J. Freeman, 1986c, Phys. Rev. B **34**, 654.

Min, B.I., H.J.F. Jansen, T. Oguchi and A.J. Freeman, 1986d, J. Magn. & Magn. Mater. **61**, 139.

Min, B.I., T. Oguchi, H.F.J. Jansen and A.J. Freeman, 1986e, Phys. Rev. B **33**, 8005.

Modesti, S., G. Paolucci and E. Tosatti, 1985, Phys. Rev. Lett. **55**, 2995.

Mook, H.A., and J.W. Lynn, 1986, Phys. Rev. Lett., **57**, 150.

Mook, H.A., and D.McK. Paul, 1985, Phys. Rev. Lett. **54**, 227.

Mook, H.A., and D.Mck. Paul, 1988, Phys. Rev. B **38**, 12058.

Mook, H.A., J.W. Lynn and R.M. Nicklow, 1973, Phys. Rev. Lett. **30**, 556.

Moon, R.M., W.C. Koehler, J.W. Cable and H.R. Child, 1972, Phys. Rev. B **5**, 997.

Moser, H.R., B. Delley, W.-D. Schneider and Y. Baer, 1984, Phys. Rev. B **29**, 2947.

Mukhopadhyay, G., and C.K. Majumdar, 1969, J. Phys. C **2**, 924.

Mulhollan, G.A., K. Garrison and J.L. Erskine, 1992, Phys. Rev. Lett., **69**, 3240.

Murgai, V., Y.-S. Huang, M.L. denBoer and S. Horn, 1988, Solid State Commun. **66**, 329.

Myron, H.W., and S.H. Liu, 1970, Phys. Rev. B **1**, 2414.

Navas, E., K. Starke, C. Laubschat, E. Weschke and G. Kaindl, 1993, Phys. Rev. B **48**, 14753.

Néel, L., 1954, J. Phys. Radium **15**, 225.

Nemoshkalenko, V.V., V.C. Antonov, V.N. Antonov, P. Ziesche and H. Wonn, 1978, Phys. Status Solidi B **88**, K83.

Netzer, F.P., and J.A.D. Matthew, 1986, Rep. Prog. Phys. **49**, 621.

Netzer, F.P., R.A. Wille and M. Grunze, 1981, Surf. Sci. **102**, 75.

Netzer, F.P., G. Strasser and J.A.D. Matthew, 1983a, Phys. Rev. Lett. **51**, 211.

Netzer, F.P., G. Strasser and J.A.D. Matthew, 1983b, Solid State Commun. **45**, 171.

Netzer, F.P., G. Strasser, G. Rosina and J.A.D. Matthew, 1985, Surf. Sci. **152/153**, 757.

Nilsson, A., N. Mårtensson, J. Hedman, B. Eriksson, R. Bergman and U. Gelius, 1985, Surf. Sci. **162**, 51.

Nilsson, A., B. Eriksson, N. Mårtensson, J.N. Andersen and J. Onsgaard, 1988, Phys. Rev. B **38**, 10357.

Nix, R.M., and R.M. Lambert, 1989, Surf. Sci. **220**, L657.

Nix, R.M., R.W. Judd and R.M. Lambert, 1989, Surf. Sci. **215**, L316.

Nolting, W., 1985, Phys. Rev. B **32**, 403.

Nolting, W., W. Borgiel and G. Borstel, 1987, Phys. Rev. B **35**, 7025.

Nolting, W., W. Borgiel, V. Dose and Th. Fauster, 1989, Phys. Rev. B **40**, 5015.

Nolting, W., S. Bei de Kellen and G. Borstel, 1991, Phys. Rev. B **43**, 1117.

Nolting, W., T. Dambeck and G. Borstel, 1993, Z. Phys. B **90**, 413.

Nolting, W., T. Dambeck and G. Borstel, 1994, Z. Phys. B **94**, 409.

Nolting, W., G. Borstel, T. Dambeck, T. Fauster and A. Vega, 1995, J. Magn. & Magn. Mater. **140–144**, 55.

Novák, P., and J. Kuriplach, 1992, J. Magn. & Magn. Mater. **104–107**, 1499.

Onsgaard, J., and I. Chorkendorff, 1986, Phys. Rev. B **33**, 3503.

Onsgaard, J., I. Chorkendorff, O. Ellegaard and O. Sörensen, 1984, Surf. Sci. **138**, 148.

Ortega, J.E., F.J. Himpsel, Dongqi Li and P.A. Dowben, 1994, Solid State Commun. **91**, 807.

Padalia, B.D., J.K. Gimzewski, S. Affrossman, W.C. Lang, L.M. Watson and D.J. Fabian, 1976, Surf. Sci. **61**, 468.

Padalia, B.D., W.C. Lang, P.R. Norris, L.M. Watson and D.J. Fabian, 1977, Proc. R. Soc. London A **354**, 269.

Pang, A.W., A. Berger and H. Hopster, 1994, Phys. Rev. B **50**, 6457.

Parker, R.J., 1990, Advances in Permanent Magnetism (Wiley, New York).

Paschen, U., C. Sürgers and H. v. Löhneysen, 1993, Z. Phys. B **90**, 289.

Patchett, A.J., S.S. Dhesi, R.I.R. Blyth and S.D. Barrett, 1993, Surf. Sci. **291**, 402.

Patchett, A.J., S.S. Dhesi, R.I.R. Blyth and S.D. Barrett, 1994, Surf. Rev. Lett. **1**, 649.

Patthey, F., B. Delley, W.-D. Schneider and Y. Baer, 1985, Phys. Rev. Lett. **55**, 1518.

Pickett, W.E., A.J. Freeman and D.D. Koelling, 1981, Phys. Rev. B **23**, 1266.

Pindor, A.J., J. Staunton, G.M. Stocks and H. Winter, 1983, J. Phys. F **13**, 979.

Platau, A., and S.-E. Karlsson, 1978, Phys. Rev. B **18**, 3820.

Platau, A., A. Callenås and S.-E. Karlsson, 1981, Solid State Commun. **37**, 829.

Podloucky, R., and D. Glötzel, 1983, Phys. Rev. B **27**, 3390.

Rath, J., and A.J. Freeman, 1975, Phys. Rev. B **11**, 2109.

Rau, C., 1982, J. Magn. & Magn. Mater. **30**, 141.

Rau, C., 1989, Appl. Phys. A **49**, 579.

Rau, C., and S. Eichner, 1981, in: Inelastic Particle–Surface Collisions, Proc. Third Int. Workshop on Inelastic Ion Surface Collisions, eds E. Taglauer and W. Heiland (Springer, Berlin) p. 138.

Rau, C., and S. Eichner, 1986, Phys. Rev. B **34**, 6347.

Rau, C., and C. Jin, 1988, J. Phys. (Paris) Colloque **C8**, 1627.

Rau, C., and K. Waters, 1988, Nucl. Instrum. Methods Phys. Res. B **33**, 378.

Rau, C., C. Jin and M. Robert, 1988, J. Appl. Phys. **63**, 3667.

Rau, C., C. Jin and C. Liu, 1989a, Vacuum **39**, 129.

Rau, C., C. Jin and M. Robert, 1989b, Phys. Lett. A **138**, 334.

Reihl, B., and F.J. Himpsel, 1982, Solid State Commun. **44**, 1131.

Richter, M., and H. Eschrig, 1989, Solid State Commun. **72**, 263.

Riehl, F., 1978, Jpn. J. Appl. Phys. **17**, Suppl. 17-2, 314.

Roeland, L.W., G.J. Cock, F.A. Muller, C.A. Moleman, K.A.M. McEwan, R.C. Jordan and D.W. Jones, 1975, J. Phys. F **5**, L233.

Rosengren, A., and B. Johansson, 1982, Phys. Rev. B **26**, 3068.

Rosina, G., E. Bertel and F.P. Netzer, 1985, J. Less-Common Met. **111**, 285.

Rosina, G., E. Bertel, F.P. Netzer and J. Redinger, 1986a, Phys. Rev. B **33**, 2364.

Rosina, G., E. Bertel and F.P. Netzer, 1986b, Phys. Rev. B **34**, 5746.

Ruderman, M.A., and C. Kittel, 1954, Phys. Rev. **96**, 99.

Sacchi, M., O. Sakho, F. Sirotti, X. Jin and G. Rossi, 1991, Surf. Sci. **251/252**, 346.

Sairanen, O.-P., and S. Aksela, 1992, J. Phys.: Condens. Matter, **4**, 9213.

Sandratskii, L.M., and J. Kübler, 1993, Europhys. Lett. **23**, 661.

Scarfe, J.A., A.R. Law, H.P. Hughes, J.A.C. Bland, G.M. Roe and A.P. Walker, 1992, Phys. Status Solidi B **171**, 377.

Schirber, J.E., F.A. Schmidt, B.N. Harmon and D.D. Koelling, 1976, Phys. Rev. Lett. **36**, 448.

Schirber, J.E., A.C. Switendick and F.A. Schmidt, 1983, Phys. Rev. B **27**, 6475.

Schlüter, M., and C.M. Varma, 1983, Helv. Phys. Acta, **56**, 147.

Schneider, W.D., C. Laubschat and B. Reihl, 1983, Phys. Rev. B **27**, 6538.

Schutz, G., M. Knulle, R. Wienke, W. Wilhelm, W. Wagner, P. Kienle and R. Frahm, 1988, Z. Phys. B **73**, 67.

Sellmyer, D.J., 1992, J. Alloys & Compounds **181**, 397.

Sellmyer, D.J., 1994, in: Nanophase Materials, eds G.C. Hadjipanaysis and R.W. Siegel (Kluwer Academic Publishers, Dordrecht) p. 537.

Shan, Z.S., and D.J. Sellmyer, 1996, Nanoscale rare earth–transition metal multilayers: magnetic structure and properties, in: Handbook on the Physics and Chemistry of Rare Earths, Vol. 22, eds K.A. Gschneidner Jr and L. Eyring (North-Holland, Amsterdam) ch. 148, p. 81.

Singh, D.J., 1991a, Phys. Rev. B **43**, 6388.

Singh, D.J., 1991b, Phys. Rev. B **44**, 7451.

Skriver, H.L., 1981, in: Physics of Solids Under High Pressure, eds J.S. Schilling and R.N. Shelton (North-Holland, Amsterdam) p. 270.

Sondhelm, S.A., and R.C. Young, 1985, J. Phys. F **15**, L261.

Speier, W., J.C. Fuggle, R. Zeller, B. Ackerman, K. Szot, F.U. Hillebrecht and M. Campagna, 1984, Phys. Rev. B **30**, 6921.

Stanley, H.E., 1971, Introduction to Phase Transitions and Critical Phenomena (Clarendon Press, Oxford).

Starke, K., E. Navas, L. Baumgarten and G. Kaindl, 1993, Phys. Rev. B **48**, 1329.

Steinsvoll, O., C.F. Majkrzak, G. Shirane and J. Wicksted, 1983, Phys. Rev. Lett. **51**, 300.

Stenborg, A., and E. Bauer, 1987, Surf. Sci. **185**, 394.

Stenborg, A., and E. Bauer, 1988, Solid State Commun. **66**, 561.

Stenborg, A., O. Björneholm, A. Nilsson, N. Mårtensson, J.N. Andersen and C. Wigren, 1989a, Surf. Sci. **211/212**, 470.

Stenborg, A., O. Björneholm, A. Nilsson, N. Mårtensson, J.N. Andersen and C. Wigren, 1989b, Phys. Rev. B **40**, 5916.

Stetter, U., M. Farle, K. Baberschke and W.G. Clark, 1992, Phys. Rev. B **45**, 503.

Sticht, J., and J. Kübler, 1985, Solid State Commun. **53**, 529.

Stoner, E.C., 1936, Proc. R. Soc. London A **154**, 656.

Strasser, G., and F.P. Netzer, 1984, J. Vac. Sci. & Technol. A **2**, 826.

Strasser, G., F.P. Netzer and J.A.D. Matthew, 1984, Solid State Commun. **49**, 817.

Strasser, G., G. Rosina, E. Bertel and F.P. Netzer, 1985, Surf. Sci. **152/153**, 765.

Szotek, Z., W.M. Temmerman and H. Winter, 1993, Phys. Rev. B **47**, 1124.

Szuszkiewicz, S., 1973, Acta Phys. Pol. A **44**, 691.

Taborelli, M., R. Allenspach, G. Boffa and M. Landolt, 1986, Phys. Rev. Lett. **56**, 2869.

Takakuwa, Y., S. Takahashi, S. Suzuki, S. Kono, T. Yokutsuka, T. Takahashi and T. Sagawa, 1982, J. Phys. Soc. Jpn. **51**, 2045.

Takakuwa, Y., S. Suzuki, T. Yokotsuta and T. Sagawa, 1984, J. Phys. Soc. Jpn. **53**, 687.

Tang, H., D. Weller, T.G. Walker, J.C. Scott, C. Chappert, H. Hopster, A.W. Pang, D.S. Dessau and D.P. Pappas, 1993a, Phys. Rev. Lett. **71**, 444.

Tang, H., T.G. Walker, H. Hopster, A.W. Pang, D. Weller, J.C. Scott, C. Chappert, D.P. Pappas and D.S. Dessau, 1993b, J. Appl. Phys. **73**, 6770.

Tanuma, S., Y. Ishizawa, H. Nagasawa and T. Sugawara, 1967, Phys. Lett. A **25**, 669.

Tanuma, S., W.R. Datar, H. Doi and A. Dunsworth, 1970, Solid State Commun. **8**, 1107.

Temmerman, W.M., and P.A. Sterne, 1990, J. Phys.: Condens. Matter **2**, 5529.

Temmerman, W.M., Z. Szotek and H. Winter, 1993, Phys. Rev. B **47**, 1184.

Thole, B.T., X.D. Wang, B.N. Harmon, Dongqi Li and P.A. Dowben, 1993, Phys. Rev. B **47**, 9098.

Thomasson, J., F. May, B. Feldman, M. Wuttig and H. Ibach, 1992, Phys. Rev. Lett. **69**, 3831.

Uemura, Y.J., G. Shirane, O. Steinvoll and J. Wicksted, 1983, Phys. Rev. Lett. **51**, 2322.

Valenta, L., 1962, Phys. Status Solidi **2**, 112.

Vaterlaus, A., T. Beutler and F. Meier, 1992, J. Magn. & Magn. Mater. **104–107**, 1693.

Vescovo, E., and C. Carbone, 1996, Phys. Rev. B **53**, 4142.

Vescovo, E., O. Rader, T. Kachel, U. Alkemper and C. Carbone, 1993a, Phys. Rev. B **47**, 13899.

Vescovo, E., C. Carbone and O. Rader, 1993b, Phys. Rev. B **48**, 7731.

Waldfried, C., D.N. McIlroy, Dongqi Li, J. Pearson, S. Bader and P.A. Dowben, 1995, Surf. Sci. **341**, L1072.

Wandelt, K., and C.R. Brundle, 1985, Surf. Sci. **157**, 162.

Watson, R.E., A.J. Freeman and J.P. Dimmock, 1968, Phys. Rev. **167**, 497.

Weaver, J.H., M. Grioni, J.J. Joyce and M. del Giudice, 1985, Phys. Rev. B **31**, 5290.

Weller, D., and S.F. Alvarado, 1985a, Z. Phys. B **58**, 261.

Weller, D., and S.F. Alvarado, 1985b, Physica B **130**, 72.

Weller, D., S.F. Alvarado, W. Gudat, K. Schröder and M. Campagna, 1985a, Phys. Rev. Lett. **54**, 1555.

Weller, D., S.F. Alvarado, M. Campagna, W. Gudat and D.D. Sarma, 1985b, J. Less-Common Met. **111**, 277.

Wertheim, G.K., and M. Campagna, 1977, Chem. Phys. Lett. **47**, 182.

Wertheim, G.K., and M. Campagna, 1978, Solid State Commun. **26**, 553.

Wertheim, G.K., and G. Crecelius, 1978, Phys. Rev. Lett. **40**, 813.

Wertheim, G.K., J.H. Wernick and G. Crecelius, 1978, Phys. Rev. B **18**, 875.

Weschke, E., C. Laubschat, T. Simmons, M. Domke, O. Strebel and G. Kaindl, 1991, Phys. Rev. B **44**, 8304.

Weschke, E., C. Laubschat, A. Höhr, K. Starke, E. Navas, L. Baumgarten, A.V. Fedorov and G. Kaindl, 1994, J. Electron Spectrosc. Relat. Phenom. **68**, 515.

Weschke, E., C. Schüssler-Langeheine, R. Meier, A.V. Fedorov, K. Starke, F. Hübinger and G. Kaindl, 1996, Phys. Rev. Lett. **77**, 3415.

Wieliczka, D.M., J.H. Weaver, D.W. Lynch and C.G. Olson, 1982, Phys. Rev. B **26**, 7056.

Wieliczka, D.M., C.G. Olson and D.W. Lynch, 1984a, Phys. Rev. Lett. **52**, 2180.

Wieliczka, D.M., C.G. Olson and D.W. Lynch, 1984b, Phys. Rev. B **29**, 3028.

Williams, R.W., and A.R. Mackintosh, 1968, Phys. Rev. **168**, 679.

Williams, R.W., T.L. Loucks and A.R. Mackintosh, 1966, Phys. Rev. Lett. **16**, 168.

Wolff, H.W., R. Bruhn, K. Radler and B. Sonntag, 1976, Phys. Lett. A **59**, 67.

Wu, Ruquian, and A.J. Freeman, 1991, J. Magn. & Magn. Mater. **99**, 81.

Wu, Ruquian, Chun Li, A.J. Freeman and C.L. Fu, 1991, Phys. Rev. B **44**, 9400.

Wu, S.C., H. Li, D. Tian, J. Quinn, Y.S. Li, F. Jona, J. Sokolov and N.E. Christensen, 1990, Phys. Rev. B **41**, 11912.

Wu, S.C., H. Li, D. Tian, J. Quinn, Y.S. Li, F. Jona, J. Sokolov and N.E. Christensen, 1991a, Phys. Rev. B **43**, 12060.

Wu, S.C., H. Li, Y.S. Li, D. Tian, J. Quinn, F. Jona and D. Fort, 1991b, Phys. Rev. B **44**, 13720.

Wu, S.C., H. Li, Y.S. Li, D. Tian, J. Quinn, F. Jona, D. Fort and N.E. Christensen, 1992, Phys. Rev. B **45**, 8867.

Wuilloud, E., H.R. Moser, W.D. Schneider and Y. Baer, 1983, Phys. Rev. B **28**, 7354.

Wulff, M., G.G. Lonzarich, D. Fort and H.L. Skriver, 1988, Europhys. Lett. **7**, 629.

Young, R.C., 1979, J. Phys. (Paris) Colloq. **40**, C5-71.

Young, R.C., and J.K. Hulbert, 1974, Phys. Lett. A **47**, 367.

Young, R.C., R.G. Jordan and D.W. Jones, 1973, Phys. Rev. Lett. **31**, 1473.

Young, R.C., R.G. Jordan and D.W. Jones, 1974, J. Phys. F **4**, L84.

Young, R.C., R.G. Jordan and D.W. Jones, 1976, J. Phys. F **6**, L37.

Zhang, Jiandi, P.A. Dowben, Dongqi Li and M. Onellion, 1995, Surf. Sci. **329**, 177.

Handbook on the Physics and Chemistry of Rare Earths
Vol. 24
edited by K.A. Gschneidner, Jr. and L. Eyring

Chapter 160

MECHANICAL ALLOYING AND MECHANICALLY INDUCED CHEMICAL REACTIONS

P.G. McCORMICK
Special Research Centre for Advanced Mineral and Materials Processing, University of Western Australia, Nedlands, W.A. 6907, Australia

Contents

List of symbols

t_{ig}	ignition time	M_r	remanent magnetization
T_c	collision temperature	H_c	coercivity
T_{ig}	ignition temperature	$(BH)_{max}$	maximum energy product
M_{rev}	reversible magnetization	f_α	fraction of α-Fe phase
M_s	saturation magnetization		

1. Introduction

Mechanical alloying and mechanochemical processing refer to the use of mechanical energy to activate chemical reactions and structural changes. The use of mechanically activated processes dates back to the early history of mankind. The first and today still the most common use of mechanical activation is the use of flints to initiate fires. The term "mechanochemical" was coined by Ostwald in 1911 (Ostwald 1919),

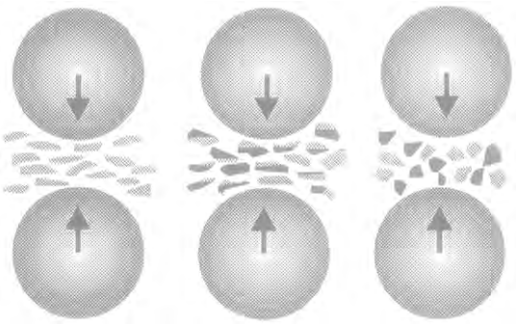

Fig. 1. Schematic representation of ball/powder collision event.

to refer to the effect of mechanical energy on chemical reactions. The general field of mechanochemistry and tribochemistry has had a rich history, particularly in Europe (Thiessen et al. 1996, Heinicke 1984), culminating in the 1990s with the development of mechanical processes for the synthesis of advanced materials exhibiting a wide range of new and different properties. The synthesis of metastable phases by mechanical processing has been extensively studied in recent years, and of wide interest has been the formation of amorphous and nanocrystalline phases of intermetallic compounds.

Mechanochemical processes are most commonly carried out using ball mills and driven by repeated collisions between balls and powder. As shown schematically in fig. 1, the collision events cause the powder particles to be deformed and work-hardened. Cold-welding of overlapping particles occurs between atomistically clean surfaces formed by prior fracture. The competing processes of deformation, fracture and welding continue during milling, and can result in composition changes and microstructural refinement. As will be discussed in sect. 2, a variety of different ball mills have been used to activate mechanochemical reactions, each characterized by a unique milling environment. Of particular importance in determining the evolution of microstructure and chemical change during milling are the local conditions of temperature, pressure, etc., which are developed during ball/powder collision events.

In this review three different types of mechanochemical processes are distinguished: mechanical milling, mechanical alloying, and reaction milling. Mechanical alloying, which evolved from the more general field of mechanochemical processing, refers specifically to the formation of alloys from elemental precursors during mechanical processing. The use of mechanical alloying as a technique for producing alloy powders dates back only some 20–25 years to the work of Benjamin (1970, 1976). Benjamin (1976) showed, using magnetic measurements, that the mechanical alloying of Fe and Cr powders resulted in true alloying on an atomic level. The studies of Benjamin resulted in the development of a process for the manufacture of oxide-dispersion strengthened (ODS) superalloys (Schaffer and McCormick 1992a), which remains as the only commercial mechanical alloying based process for the production of alloys.

Mechanical alloying has been shown to cause significant microstructural changes, including the formation of a nanocrystalline grain structure, extended solid solubility, disordering, formation of metastable phases, amorphization and disproportionation of pre-

existing phases. The discovery by Koch et al. (1983) that mechanical alloying can result in the formation of amorphous structures was a significant breakthrough, and a significant research effort has been devoted to studies of mechanically induced amorphization reactions over the past ten years (Koch 1989, Weeber and Bakker 1988).

As will be discussed in sects. 3–5, studies of mechanical alloying and mechanically induced reactions in rare-earth materials have been primarily focused on the synthesis of hard magnetic rare-earth–transition-metal compounds such as $SmCo_5$ and $Nd_2Fe_{14}B$. The nanocrystalline grain structures developed in mechanically alloyed and heat treated powders result in high coercivities in single-phase materials and significant exchange coupling in materials containing mixtures of hard and soft magnetic phases.

Mechanical milling refers to the milling of a pure metal or compound which is in a state of thermodynamic equilibrium at the start of milling. Mechanical milling can also cause disordering, amorphization and composition changes, including disproportionation. The structures generated by the two processes are similar. Structural and chemical changes accompanying mechanical milling of rare-earth metals and compounds are discussed in sect. 3.

Reaction milling uses mechanical processing to induce chemical reactions. As well as providing a means for solid-state alloying, it has been shown that mechanical activation can also substantially increase the kinetics of solid-state chemical reactions, such as oxidation–reduction reactions (Schaffer and McCormick 1989a). The repeated welding and fracture of particles during ball–powder collision events dynamically maintain the reacting surfaces during milling. As a consequence, reactions which are normally sustained only at high temperatures, due to separation of the reacting phases by the product phases, occur at low temperatures in a ball mill without any need for external heating. As would be expected, the kinetics of such reactions depend on both the thermodynamic properties of the reaction, the mechanical properties of the reactants, and milling parameters such as the collision energy and frequency. The application of reaction milling to the synthesis of rare-earth–transition-metal permanent magnet alloys is discussed in sect. 4.

It has also been shown that self-propagating combustion reactions can be ignited by ball–powder collisions if the reaction enthalpy change is sufficiently large (Schaffer and McCormick 1989b). Such mechanochemical combustion reactions require a critical time of milling (ignition time) for combustion to occur. As will be discussed in sect. 2, measurements of the ignition time provide a useful means of characterizing structural and chemical changes during milling.

2. Overview of mechanical processing

2.1. *Introduction*

The mechanical milling of powders is an inherently complex process which depends on the interdependence of the internal mechanics of the specific mill being used and the

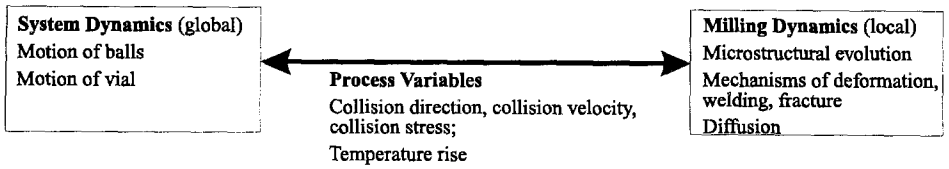

Fig. 2. Interrelation of local and global dynamics of mechanical milling processes.

properties of the materials being processed. Microstructural development during milling is a strong function of the dynamic state of the mill as determined by the combination of system and milling dynamics. System dynamics is defined as the global dynamics involved in a particular milling process such as the macroscopic motion of the balls and container. Milling dynamics refers to the local dynamics involved in individual ball/powder collision events, such as particle deformation, coalescence and fracture events. The relationship between local and global dynamics is illustrated in fig. 2.

2.2. *Ball mills*

A variety of different types of ball mills have been used for the mechanical processing of powders, including vibratory mills, attritors, planetary mills and tumbling ball mills. The most common ball mills used for experimental studies are vibratory mills, such as the SPEX 8000 mixer/mill (Davis et al. 1988). In the SPEX mill a cylindrical vial of ~0.1 liter capacity undergoes vibratory motion in a figure-eight trajectory. The vial typically contains 5–10 g of powder and 50–100 g of grinding balls, and vibrates at a frequency and amplitude of approximately 20 Hz and 100 mm, respectively. Numerical modelling of the system dynamics of a SPEX mill and image analyses of ball motion have been carried out by Davis et al. (1988). It was estimated that the average impact velocity of the balls is ~6 m/s. It was also shown that only a small fraction (0.4%) of all ball collisions are head-on collisions, with the majority being glancing collisions of relatively low impact energy. While the SPEX mill is convenient for laboratory experiments, it has not been scaled up to a larger size.

Relatively few studies have been carried out using conventional horizontal-axis tumbling ball mills which are widely used for mineral processing applications. Such mills can require very long processing times (weeks) for mechanical alloying, and the collision energies are limited by the diameter of the container. Commercial production of mechanically alloyed oxide-dispersion strengthened (ODS) nickel alloys utilises tumbling mills (Schaffer and McCormick 1992a).

With planetary mills the container is rotated about two separate parallel axes, similar to the rotation of the earth about the sun. The kinematics of planetary and tumbling mills are similar, however, the speed, and hence milling time, of a planetary mill is not limited by centrifugal forces. A number of studies have analysed ball motion and collision energies in planetary mills (Burgio et al. 1991, Dallimore et al. 1994). It has been shown that ball/container slip can have an important effect on ball trajectories, limiting collision

energies and milling performance (Dallimore et al. 1994). In general, planetary mills exhibit high collision energies, but are difficult to scale up.

Attritor mills are widely used for the ultrafine grinding of ceramics and industrial minerals. Milling occurs in a stationary container filled with grinding balls which are stirred by impellers attached to a vertical drive shaft. Ball/powder collisions tend to be of the shear or glancing type associated with the differential velocity of the balls. A major problem experienced using vertical-axis attritor mills for dry grinding is gravity-driven segregation of the powder to the bottom of the mill, which may be largely eliminated through using a horizontal stirring axis.

2.3. *Mechanisms of mechanical alloying*

During mechanical alloying mechanically induced reactions occur between and within the powder constituents, resulting in changes to composition and microstructure. This is in contrast to the use of ball milling as a comminution process where the particle size is reduced but particle chemistry and structure are not changed. Mechanical alloying may be distinguished from other ball-milling processes by the fact that, in addition to particle fracture, inter-particle welding and particle deformation processes determine the nature of the resulting powder. If mechanical alloying is carried out in an inert atmosphere, surfaces created by fracture events remain unoxidized and are welded together on subsequent collisions. Diffusion and chemical reactions occur across these interfaces at a rate determined by the interfacial area and local diffusion coefficients.

All solid state reactions, whether alloying or oxidation/reduction reactions, involve the formation of one or more product phases between the reactants. Without mechanical alloying, the reactant phases become separated and the reaction rate is determined by the contact area and the diffusion path length through the product phases. Diffusion through the product phases is invariably the rate-controlling process, and consequently high temperatures are required for the reaction to occur at a measurable rate.

Mechanical alloying is able to overcome the diffusion limitation which prevents most solid-state reactions from occurring at low temperatures. The reaction area, while dependent on the initial surface area of the reactants, increases during milling as particle and grain sizes decrease, resulting in an increase in chemical reactivity. In addition the reaction area is dynamically maintained during milling as fracture and welding events continually occur. As well as maintaining reaction areas, diffusion distances are decreased during milling as particle and grain sizes decrease. An additional factor that influences reactivity is the generation of defects, such as vacancies, by plastic deformation which accelerate diffusion rates at low temperatures.

Studies of reaction kinetics are currently an active area of research. However, relatively few studies have aimed at delineating the factors controlling reaction rates. While dynamic models can be constructed to evaluate collision frequencies, impact energies and other quantities, the characterization of different types of mills and process optimization requires accurate assessment of the effect of various milling parameters on reaction kinetics. For such studies it is necessary to quantitatively measure the progress of a

particular reaction during milling under a certain set of conditions. Displacement reactions which involve a single ferromagnetic phase provide a simple and direct method of monitoring the progress of a reaction during milling, enabling direct comparison between different milling conditions (Dallimore et al. 1994). Initial measurements have shown that reaction kinetics are a function of both the collision frequency, the collision energy and the nature of the collision.

2.3.1. *Microstructural evolution*

The changes in microstructure that occur during mechanical alloying depend on the mechanical properties of the constituent powders. Koch (1989) has classified starting powders into three groups: ductile–ductile, ductile–brittle and brittle–brittle. When the precursor powders are all ductile, plastic deformation and welding of the particles results in the development of a composite layered structure in the early stages of milling. The ball/powder collision event can be thought of as a micro forging, flattening the particles into plates which fracture on reaching sufficiently high strains. According to Maurice and Courtney (1994), welding and coalescence characteristics should depend on the relative hardness of the reacting powders. With further milling the composite layered structure is progressively refined by repeated fracture, welding and deformation, as well as by defect enhanced diffusion through the layers, until it is impossible to detect any chemical inhomogeneity within the powder.

The mechanical alloying of mixtures of ductile and brittle components results in the brittle particles being trapped at the layered welded interfaces of the ductile component (Benjamin 1970, Maurice and Courtney 1994). Continued milling results in fracture of the brittle particles and the development of a uniform distribution of particles of the brittle phase within the matrix of the ductile phase. This is in contrast to the distribution in conventional powder systems where the dispersoid particles are confined to the prior particle boundaries. Mechanically alloyed ODS alloys are an important practical example of a ductile/brittle system. If the volume fraction of the brittle phase is of the order of 0.5, the characteristic layered structure does not form. Rather, the microstructure consists of a uniformly distributed nanocrystalline mixture of the two phases (Schaffer and McCormick 1990a).

Ductility of one of the constituent powders is not a requirement for mechanical alloying to occur. A number of brittle/brittle systems have been shown to form solid solutions of intermetallic compounds during milling (Davis et al. 1988, Davis and Koch 1987). In contrast to the layered morphology exhibited by ductile systems, brittle/brittle systems develop a granular morphology. While the alloying mechanism is not well understood with brittle systems it is evident that material transfer between the components plays an important role (Davis et al. 1988).

While microstructural evolution during milling depends on the mechanical properties of the component powders being milled, a nanoscale microstructure is generally developed provided mechanical alloying has been carried out to completion. Mechanical alloying has become an important method for synthesizing crystallite sizes as small as 2 nm. However,

few studies have been carried out to delineate the factors which control the scale of the as-milled microstructure.

2.3.2. *Non-equilibrium structures and amorphization*

The structures formed during mechanical alloying or mechanical milling are determined by a dynamic balance between mechanically induced disorder and diffusion-controlled recovery. If the diffusion rates are sufficiently high, any mechanically induced disorder will be recovered between collisions and amorphization will not occur. On the other hand, if the rate of recovery of the disorder is slow relative to the rate of disordering, then it is possible for the disorder and defect structure introduced by milling to lead to amorphization. It has been shown that amorphization occurs least readily in phases with high atomic diffusivities or phases which have relatively small, simple unit cells where only a small number of atom jumps are required to re-establish order. It has also been established that milling under conditions which generate high temperatures, i.e., high collision energies, tends to form nanocrystalline structures, while lower milling energies tend to favor the formation of amorphous structures, provided the milling energy is not too low (Koch 1989, Eckert et al. 1991, Gerasimov et al. 1991).

Both mechanical alloying and mechanical milling can result in the formation of amorphous phases. As summarized by Weeber and Bakker (1988), there appear to be at least three different ways by which an amorphous phase can form, all driven by mechanically induced disorder and microstructural refinement. The most direct amorphization process involves the reduction of the grain size of the milled powders to a critical value. Amorphization has been shown to occur when the crystallite size reaches ~2 nm. Jang and Koch (1990) have argued that with a ~2 nm crystallite size the grain-boundary energy is sufficient to provide the energy necessary to induce a crystalline to amorphous transition. Alternatively amorphization may be induced by disorder and defects introduced during milling, in a manner similar to amorphization caused by irradiation (Koch and Kim 1987). In either case, X-ray patterns show a continual broadening of the diffraction peaks with increasing milling time, associated with the decrease in crystallite size, into a broad peak characteristic of the amorphous alloy. In a review Koch (1989) has summarized data which indicate that a combination of grain-boundary energy and anti-site disordering energy may be required to cause amorphization reaction.

Alternatively, amorphization during mechanical alloying can occur by a solid-state amorphization reaction between adjacent layers welded together during collisions, similar to the amorphization reaction occurring between thin films of two different metals (Schwarz and Johnson 1983). The driving force for the solid-state amorphization reaction is a large negative free energy of mixing of the components. In addition to a sufficiently large free-energy change, a kinetic constraint to the formation of the equilibrium crystalline intermetallic phase must also exist. Schwarz and Johnson (1983) have proposed that such constraint is provided by a large difference in the diffusion coefficients of the two components. The occurrence of a solid-state amorphization reaction is evidenced by

a broad amorphous peak on the diffraction curve at an early stage of milling, in addition to the peaks corresponding to the crystalline phases. During milling the amorphous peak increases as the crystal reflections broaden and lose intensity.

Amorphization has also been found to occur by a two-stage reaction during mechanical alloying (Koch 1995). The first stage involves the formation of a crystalline intermetallic phase from the starting metals. A crystalline to amorphous transition then occurs at longer milling times. When amorphization reactions accompany the mechanical milling of intermetallics, the defect-induced disorder caused by milling must provide the free-energy change required for the crystalline to amorphous transition to occur.

2.4. *Reaction milling*

While the classical use of mechanical alloying has been for the synthesis of alloys from elemental metal precursors, the ball mill may be used to initiate a wide range of chemical reactions. Thus the ball mill may be considered to be a chemical reactor in which reactions are mechanically initiated. It has been shown that a wide variety of oxidation–reduction reactions can be activated during mechanical milling of an oxide and a suitable reductant. For example, the milling of CuO with a reductant such as Ca results in the reduction of the cupric oxide to Cu metal (Schaffer and McCormick 1989a). Co-reduction processes to directly form alloys, such as the formation of brass from CuO and ZnO by milling with Ca, have also been reported. Examples of potentially important refining reactions include the reduction of $TiCl_4$ with Mg (McCormick et al. 1991a), and the formation of rare-earth alloys by reduction reactions with Ca and Na (see sect. 4).

Mechanically activated reactions have been shown to exhibit sigmoidal reaction curves. Quantitative studies using X-ray diffraction and magnetization measurements have shown that the reaction rate initially increases with milling time consistent with the effect of particle size and microstructural refinement on reaction kinetics. A maximum reaction rate is observed at intermediate milling times and the reaction rate decreases as the reaction progresses to completion. Compounds which exhibit multiple valencies are generally observed to exhibit multistage reduction reactions. For example, the reduction of CuO by carbon during milling was found to proceed by a two-stage $CuO \rightarrow Cu_2O \rightarrow Cu$ reaction (H. Yang et al. 1994). Similarly, the reduction of $TiCl_4$ by Mg proceeds via the intermediate $TiCl_3$ and $TiCl_2$ compounds (McCormick et al. 1991a). The $TiCl_4$/Mg reaction is also of interest because $TiCl_4$ is a liquid at room temperature and thus is an example of the mechanical activation of a liquid–solid reaction. It has been shown that decreasing the milling temperature to below the melting temperature of $TiCl_4$ increases the reaction kinetics by a factor of six, demonstrating the importance of solid–solid interactions at welded interfaces during milling (McCormick et al. 1991a).

Most solid-state mechanochemical reactions have been displacement reactions, with two or more product phases being formed. The microstructure of the as-milled powders consists of a nanocomposite mixture of the product phases, with 5–20 nm crystallites of the reduced metallic phase being uniformly intermixed with an amorphous or nanocrystalline oxidized by-product phase. The separation or removal of unwanted

reaction by-product phases can be difficult due to the high reactivity of the metallic phase associated with its nanocrystalline grain size, inter-mixing of the phases induced by the mechanical milling process, or limited solubility of the by-product phase. The use of carbon as the reductant obviates the need to remove the reaction by-products, since gaseous CO_2 is formed by the reaction (H. Yang et al. 1994). Alternatively, by appropriate selection of the reaction chemistry it may be possible to form by-product phases, such as chlorides, which are soluble in inert liquids or may be removed by vacuum distillation (Richmond et al. 1997).

2.5. *Mechanochemical combustion reactions*

The efficacy of the mechanical alloying process is such that for many oxidation–reduction reactions self-sustaining combustion reactions are initiated on milling for a critical time, defined as the ignition time, t_{ig} (Schaffer and McCormick 1989b). Such reactions exhibit large enthalpy changes and, as a consequence, also undergo a thermal combustion reaction if heated to above a critical ignition temperature, T_{ig}.

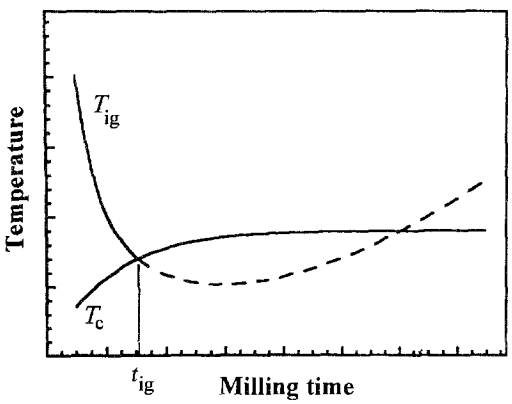

Fig. 3. Variation of T_{ig} and T_c during milling.

It has been postulated (Schaffer and McCormick 1991) that the ignition time is determined by the milling time required for the ignition temperature to decrease to the collision temperature, i.e. the temperature of the powder T_c, during ball/powder collision events. The variation of T_{ig} and T_c during milling is illustrated schematically in fig. 3. The ignition temperature is a function of the reaction enthalpy and microstructural parameters, such as particle and crystallite sizes, and other factors which influence reaction kinetics. The ignition temperature decreases with milling time, with the refinement of microstructure during milling being the major factor causing this decrease. The collision temperature increases with milling time due to the slow increase in the background temperature resulting from energy dissipation in the mill, until a steady-state value is reached.

By assuming that combustion occurs during milling when T_{ig} decreases to the value of the collision temperature, values of T_c can be estimated by extrapolating the values of T_{ig},

obtained from DTA measurements in samples milled for times less than t_{ig}, to the ignition time. Values of T_c obtained in this manner using a SPEX 8000 mixer mill and 12 mm diameter balls have been found to be in the range of 400–640 K, consistent with values calculated from modelling studies (Maurice and Courtney 1990). However, recent measurements of combustion during the milling of Mg with V_2O_5 indicated that the initiation of combustion in this system could not be associated with a reduction of the ignition temperature during milling (H. Yang and McCormick 1994).

From fig. 3 it is evident that combustion should only occur if T_c exceeds the minimum value of T_{ig}. The value of T_c is dependent on a number of factors, including the collision energy and the work dissipated during the collision event. The collision energy can be controlled by varying milling parameters such as collision frequency, ball size and the type of mill, or by choosing reductants which minimise the enthalpy change. With the CuO/Fe oxidation–reduction reaction it has been shown that combustion requires a ball size of 12 mm or greater (Schaffer and McCormick 1992b). With smaller ball sizes the measurements of T_{ig} were found to decrease to a minimum and then increase with further milling as the reaction occurs in a steady-state manner.

Combustion can also be avoided through the use of diluents and through the use of process lubricants which inhibit interparticle welding. For example, Schaffer and McCormick (1989b) found that the milling of CuO and Ca in a SPEX mill resulted in a combustion reaction ($CuO + Ca \rightarrow Cu + CaO$) within 7 min. On adding anhydrous toluene as a process control agent the reaction occurred in a continuous manner, reaching completion after milling for ~100 min.

The examination of powders immediately after combustion has revealed a rich variety of structures which reflect the high temperatures reached during the combustion event (Schaffer and McCormick 1989b, 1990a,b, H. Yang and McCormick 1994). Estimates of adiabatic temperature rises are in the range of 3000–5000 K, and structures consistent with melting and vaporization of the constituents are observed. In general the as-combusted powders consist of heterogeneous mixtures of varying size, from nodules as large as 1–5 mm down to particles less than 100 nm in diameter. TEM examination of fine as-combusted powders has revealed spherical and hexagonal single-crystalline particles, as well as unusual filamentary particles (H. Yang and McCormick 1994). Such particle morphologies are similar to ultrafine metal and oxide smoke particles formed by gas-phase condensation, and thus indicate the occurrence of vaporization during combustion. It is thus clear that temperatures approaching adiabatic reaction temperatures are reached during mechanically activated combustion.

3. Mechanical alloying and mechanical milling of rare-earth materials

The application of mechanical alloying to the synthesis of rare-earth alloys has been extensively studied in recent years. Changes in structure and properties accompanying the mechanical milling of rare-earth compounds have also been widely studied. Tables 1 and 2 summarize the systems studied and the range of structures that have been observed

Table 1
Summary of mechanically alloyed systems

System	Equilibrium phase	As-milled structure	Reference
Gd–Co	$Gd_{50}Co_{50}$	amorphous	1
Yb + Ce	Yb + Ce (immiscible)	$Yb_{50}Ce_{50}$ – fcc	2
Sm–Fe	Sm_2Fe_{17}	α-Fe + amorphous Sm–Fe	3–8
Sm–Fe–V	$Sm_2(Fe, V)_{12}$	α-Fe + amorphous phase	9
Sm–Fe–Ti	$Sm_2(Fe, Ti)_{12}$	α-Fe + amorphous phase	9
Sm–Fe–Zr	$Sm_2(Fe, Zr)_{12}$	α-Fe + amorphous phase	9
Ce–Fe–Zr	$(Fe, Ce)_{0.7}Zr_{0.3}$	amorphous	6
Dy–Fe–Zr	$(Fe, Dy)_{0.7}Zr_{0.3}$	amorphous	6
Er–Fe–Zr	$(Fe, Er)_{0.7}Zr_{0.3}$	amorphous	10
Gd–Co	Gd_xCo_{1-x}, $x = 0.10$–0.25	amorphous + Gd + Gd_2Co_{17}	11
Dy–Fe	$DyFe_2$	$DyFe_2$	11
Sm–Co	Sm_2Co_{17}	Co + amorphous	13
Sm–Co	$SmCo_5$	amorphous	13
Sm–Co	$SmCo_5/Sm_2Co_{17}$	amorphous	14
Nd–Fe–B	$Nd_2Fe_{14}B$	α-Fe + amorphous	15,16
Sm–Co–Fe	$Sm_{13}(Co_{1-x}Fe_x)_{87}$	amorphous ($x < 0.2$)	17
Sm–Co–Fe	$Sm_{13}(Co_{1-x}Fe_x)_{87}$	α-Fe + amorphous ($x > 0.2$)	17
Sm–Co–Fe	$Sm_2(Co, Fe)_{17}$	α-Fe + amorphous	18
Nd–Fe–Ti	$Nd_3(Fe, Ti)_{29}$	α-Fe + amorphous	19
Sm–Fe–Ti	$Sm_3(Fe, Ti)_{29}$	α-Fe + amorphous	19
Nd_2O_3–Fe_3O_4	$NdFeO_3$	crystalline	20
Sm–Fe	$SmFe_2$	α-Fe + amorphous	21
FeB		amorphous	22

References

(1) Girardin and Maurer (1989)
(2) Ivanov et al. (1993a,b)
(3) Schnitzke et al. (1990a)
(4) Ding et al. (1992a,b)
(5) Lue et al. (1992a,b)
(6) Takeuchi et al. (1995)
(7) Smith and McCormick (1992)
(8) Kuhrt et al. (1992b)
(9) Schultz et al. (1991)
(10) Ding et al. (1993c)
(11) Ruuskanen et al. (1994)
(12) Milham (1993)
(13) Wecker et al. (1991)
(14) Ding et al. (1993a,b)
(15) Schultz et al. (1987)
(16) Gong and Hadjipanayis (1994)
(17) Ding et al. (1994a)
(18) Smith et al. (1996)
(19) Ding et al. (1995)
(20) Alonso et al. (1992b)
(21) Milham (1994)
(22) Balough et al. (1995)

in as-milled powders. The materials studied to date have generally been found to exhibit amorphous phases or nanoscale amorphous–crystalline phase mixtures, with the formation of metastable crystalline phases being reported in relatively few systems. Reports of the formation of equilibrium crystalline phases during mechanical alloying or milling are virtually non-existent. An exception is the formation of the orthoferrite phase $NdFeO_3$ by mechanically alloying the respective oxides Nd_2O_3 and Fe_3O4 (Alonso et al. 1992b).

Table 2
Summary of mechanically milled rare-earth systems

System	Equilibrium phase	As-milled structure	Reference
La–Al–Ni	$La_{11}Al_5Ni_4$	amorphous	1
Y–Co	YCo_3, Y_2Co_7, YCo_5, Y_2Co_{17}	amorphous	2
Gd–Co	$GdCo_3$, Gd_2Co_7	amorphous + crystalline	3
La–Au	$LaAu + La_2Au_3$	amorphous	4
Dy_2S_3	α-phase (orthorhombic)	γ-phase (cubic, Th_3P_4 type)	5
Y_2S_3	δ-phase (monoclinic)	γ-phase (cubic)	5
Sm	rhombohedral	rhombohedral	6
Sm–Fe	Sm_2Fe_{17}	α-Fe + amorphous	7–9
Sm–Fe–C	$Sm_2Fe_{17}C$	α-Fe + amorphous	8
Sm–Fe–C	$Sm_2Fe_{17}C_2$	amorphous	8
Nd–Fe–B	$Nd_2Fe_{14}B$	α-Fe + amorphous	6,10,11
Sm–Fe–Ga–C	$Sm_2Fe_{17-x}Ga_xC_2$ ($x=2,3$)	amorphous	12
LaNi	$LaNi_5$	crystalline	13

References
(1) Matsuki et al. (1992)
(2) Ermakov et al. (1981)
(3) Ermakov et al. (1982)
(4) Loeff and Bakker (1988)
(5) Han et al. (1991)
(6) Alonso et al. (1992a)
(7) Smith and McCormick (1992)
(8) Majima et al. (1993)
(9) Wang et al. (1993)
(10) Miao et al. (1996)
(11) Jurczyk et al. (1995)
(12) Ding et al. (1994d)
(13) Zaluski et al. (1995)

3.1. *Non-equilibrium crystalline phases*

Han et al. (1991, 1992, 1994) have reported the formation of metastable phases during the mechanical milling of rare-earth sesquisulfide phases. The mechanical milling of α-Dy_2S_3 (orthorhombic) for one hour resulted in the formation of the cubic high-temperature γ-phase, normally stable at temperatures in excess of 1463 K. A similar transformation was observed in milled Cu-doped η-Dy_2S_3 (U_2S_3-type) samples, $Cu_x(Dy_2S_3)_{1-x}$, with $x=0$–0.15. Hot pressing at 1373 K caused transformation back to the equilibrium phase, with the exception of samples having the composition $Cu_{0.025}(Dy_2S_3)_{0.075}$, where the Gd_2S_3-type orthorhombic α-phase formed instead (Han et al. 1994). Mechanical milling of monoclinic δ-Y_2S_3, δ-Er_2S_3 and δ-Tm_2S_3 caused the formation of their respective cubic high-pressure γ polymorphs. With rhombohedral ε-Yb_2S_3 and ε-Lu_2S_3, milling for up to 40 h resulted in only a partial transformation to their respective high-pressure γ polymorphs. Hot pressing of mechanically milled η-Y_2S_3 caused the structure to revert back to the equilibrium δ-phase.

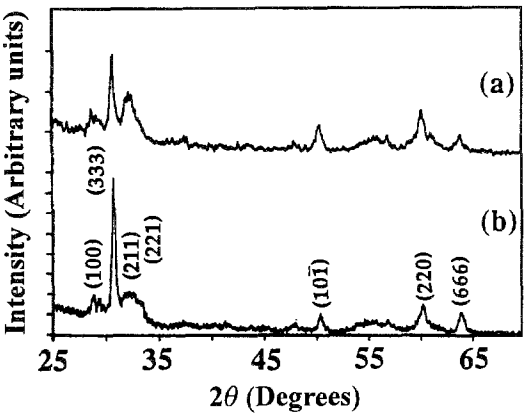

Fig. 4. Effect of milling on X-ray diffraction curves for Sm: (a) milled 24 h; (b) as-received (Alonso et al. 1992a).

The formation of metastable phases during mechanical alloying of Ce–Yb alloys has been reported by Ivanov et al. (1993a,b). Cerium and ytterbium are immiscible in each other. Mechanical alloying of mixtures with the compositions CeYb and $Ce_{75}Yb_{25}$, respectively, resulted in a decrease in the lattice parameter of the Ce and the formation of a new fcc phase with smaller lattice constant. It was suggested that the decrease in lattice parameter was associated with a change in the valence state of Yb from divalent to trivalent during mechanical alloying (Ivanov et al. 1993a).

The rare earths are well known to exhibit polymorphic transitions at high hydrostatic pressures (Jayaraman 1969, Johansson and Rosengren 1971). The crystal structures differ by the stacking sequence of the close packed planes, becoming more cubic, i.e. hcp → rhombohedral (Sm type) → dhcp → fcc, with increasing pressure and decreasing atomic number. In view of the formation of metastable phases in rare-earth compounds discussed above, it could be expected that metastable phases in certain of the rare-earth metals may form during mechanical milling. However, attempts to form high-pressure phases in rare-earth metals by mechanical milling have not been successful. Alonso et al. (1991) reported the presence of high-pressure fcc phases in several rare-earth metals after mechanical milling. However, as will be discussed in sect. 3.3, these phases have been subsequently shown to be NaCl-type rare-earth oxynitride phases resulting from reaction with oxygen and nitrogen in a poorly sealed container (Alonso et al. 1992a). The effect of mechanical milling in a well-sealed container on the structure of Sm powder is shown in fig. 4 (Alonso et al. 1992a). Milling for 24 hours resulted in line broadening associated with the formation of a nanocrystalline grain structure, however, no change in crystal structure occurred.

3.2. *Formation of amorphous phases*

As shown in Tables 1 and 2, a number of rare-earth alloys have been amorphized by mechanical alloying or mechanical milling treatments. Although the first report of amorphization of an intermetallic compound by a mechanical milling process was carried

out on Y–Co intermetallics (Ermakov et al. 1981), relatively few studies have been carried out on the effect of mechanical milling on the structure and properties of rare-earth metals and compounds. Ermakov et al. (1981), using X-ray and Mössbauer measurements, showed that the compounds YCo_3, Y_2Co_7, YCo_5 and Y_2Co_{17} undergo a crystalline to amorphous transition during mechanical milling.

With several rare-earth alloys the structures generated by milling have been shown to be a function of the alloy composition, the type of mill used and other milling parameters. Wecker et al. (1991) reported that an amorphous structure was formed in $SmCo_5$ after mechanical alloying, and a two-phase amorphous–crystalline mixture in mechanically alloyed Sm_2Co_{17}. A planetary mill was used in the studies of Wecker et al. (1991). Ding et al. (1993a,b) reported the formation of amorphous phases in mechanically alloyed Sm–Co alloys covering the range from Sm_2Co_{17} to $SmCo_5$ in studies using a SPEX vibratory mill.

In Gd–Co intermetallics, fully amorphous structures have been reported for the composition $Gd_{50}Co_{50}$ (Girardin and Maurer 1989), while with other compositions amorphous–nanocrystalline mixtures have been obtained (Ruuskanen et al. 1994). Girardin and Maurer (1989) reported that the amorphization of $Gd_{50}Co_{50}$ during mechanical milling occurred in two stages. In the first stage an unidentified fcc phase with a lattice parameter of 5.3 Å formed from the starting structure, which consisted of a mixture of $GdCo_2$ and Gd_4Co_3. In the second stage the fcc structure decomposed to the amorphous phase. Cyclohexane was used as a process control agent, and as will be discussed in sect. 3.3, it is possible that the formation of the fcc phase may have been associated with its reaction with Gd.

3.3. *Contamination effects*

Rare-earth elements are well known to react strongly with O, N and H (Spedding and Beaudry 1971). This high reactivity combined with the small particle size and large surface areas generated by mechanical processing requires considerable care and attention during powder handling and milling to avoid contamination of the materials being processed. Several studies have shown that the structures formed during the mechanical processing can be influenced by the inadvertent reaction with oxygen and nitrogen during milling. The formation of NaCl-type rare-earth oxynitride phases during the mechanical milling of several lanthanide metals, including Nd, Sm, Gd and Dy, in a poorly sealed container has been reported by Alonso et al. (1991). Chemical analyses showed that the samples contained oxygen and nitrogen in a ratio of approximately 2:3.

Loeff et al. (1989) reported the decomposition of La–Ag, La–Ni and La–Co into two-phase mixtures of fcc β-La and Ag, Ni or Co, respectively, during mechanical milling. The β-La phase has been subsequently identified as LaN (NaCl structure) formed by reaction with nitrogen during milling in a glovebox. Fu et al. (1991) showed that the mechanical milling of Fe_2Er in a leaking container resulted in the formation of α-Fe and an fcc phase identified as ErN. These investigators suggested that the formation of the nitride phase required the presence of a catalyst such as Fe to enable the dissociation of N_2. However,

Table 3
Impurity levels in mechanically milled Sm and mechanically alloyed + annealed Sm_2Fe_{17} (Alonso et al. 1992a)

Sample	Condition	O (at.%)	N (at.%)	H (at.%)
Sm	as-received	2.34	0.15	6.07
Sm	as-milled	3.45	0.32	7.14
Sm_2Fe_{14}	as-milled	2.99	0.57	1.47
Sm_2Fe_{14}	annealed	3.15	0.59	1.20

samples of Ti milled in air, using both steel and tungsten carbide containers and grinding media, have shown that the resulting composition and structure are not dependent on the presence of iron (H. Yang and McCormick 1993).

Provided sufficient attention is paid to sealing and powder handling procedures, rare-earth compounds can be prepared by mechanical alloying with minimal pickup of impurities during milling and subsequent heat treatment. Table 3 shows measurements of the oxygen, nitrogen and hydrogen levels present in the starting materials and at various stages of preparation of Sm_2Fe_{17} by mechanical alloying (Alonso et al. 1992a). It is seen that only a relatively small increase in impurity levels accompanied milling and heat treatment. It should be noted that the starting materials had fairly high impurity concentrations to begin with, and it is not known if this small increase in the contamination levels would be the case if one started out with high-purity materials with one tenth to one one-hundredth amounts of H, N and O (Beaudry and Gschneidner 1978).

3.4. *Crystalline–amorphous phase mixtures*

The structure of mechanically alloyed rare-earth–transition-metal systems, particularly those known to exhibit interesting magnetic properties, are frequently found to consist of a mixture of amorphous and nanocrystalline phases. Schultz et al. (1987) attempted to synthesize the hard magnetic phase $Nd_2Fe_{14}B$ by mechanically alloying the elemental precursors. The $Nd_2Fe_{14}B$ phase was not found to form during mechanical alloying. Instead a nanoscale two-phase mixture of α-Fe and an amorphous phase, initially taken to be Nd (Schultz et al. 1987), was formed. Subsequent annealing at 700°C was required to form the $Nd_2Fe_{14}B$ phase.

Similar two-phase mixtures of amorphous and crystalline phases have been reported in Sm_2Fe_{17} (Schnitzke et al. 1990a, Ding et al. 1992a,b, 1993c, Lue et al. 1992a,b, Smith and McCormick 1992, Murillo et al. 1993) and $Sm(Fe,X)_{12}$ (X = V, Zr, Ti) (Schultz et al. 1991). Figure 5 shows an X-ray diffraction pattern of as-milled mechanically alloyed Sm_2Fe_{17} powder (Smith and McCormick 1992). Only the main diffraction peaks of α-Fe are present in the curve. The Sm_2Fe_{17} phase formed during heat treatment above 850 K. Mössbauer measurements on as-milled Sm_2Fe_{17} powder showed that the composition of the amorphous phase was approximately $Sm_{23}Fe_{77}$ (McCormick 1995).

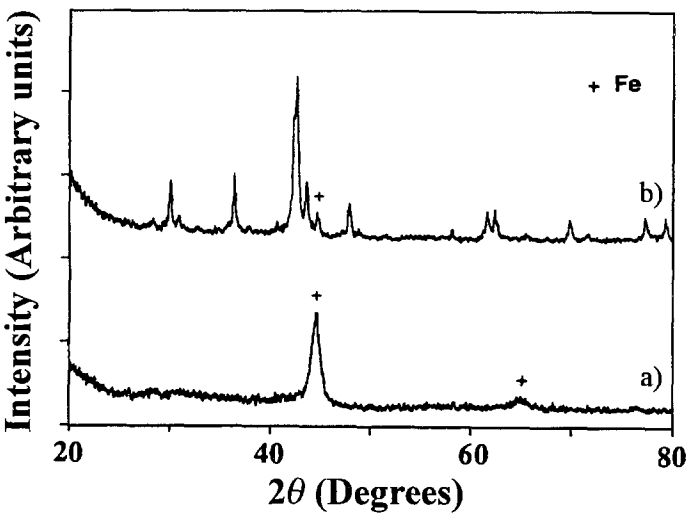

Fig. 5. X-ray diffraction patterns for (a) as-milled and (b) annealed Sm_2Fe_{17} (Smith and McCormick 1992).

As discussed previously, it appears that the as-milled structure in Sm–Co alloys is dependent on the milling conditions. Ding et al. (1994a) and Smith et al. (1996) found that the addition of sufficient Fe to Sm–Co alloys causes the as-milled structure to change from amorphous to a two-phase amorphous–crystalline mixture.

Schultz et al. (1987) pointed out that the formation of the two-phase amorphous–crystalline mixture in NdFeB reflected an apparent lack of mixing of the components during mechanical alloying, and that this behaviour is a consequence of the relatively small value of the free energy of mixing of the $Nd_2Fe_{14}B$ intermetallic. If the free energy of the intermetallic phase is not significantly less than that of the starting mixture, the free energy of the amorphous phase will be higher than that of the unmixed constituents, and if diffusional recovery occurs during milling, relaxation can occur to either the unmixed state or the intermetallic, depending on the respective rate constants. The factors influencing the formation of fully amorphous or amorphous–nanocrystalline phase mixtures will be discussed further in sect. 3.5.

It is noted that, because non-equilibrium structures are generated, it is possible to form more than two phases in a binary alloy during milling. Ruuskanen et al. (1994) reported the formation of a three-phase mixture consisting of an amorphous phase, Gd and Gd_2Co_{17}, in mechanically alloyed $Gd_xCo_{(1-x)}$, with $x = 0.1$, 0.15, 0.2 and 0.25.

3.5. *Disproportionation during mechanical milling*

The mechanical milling of certain rare-earth compounds has been found to result in decomposition. Ermakov et al. (1982) found that $GdCo_3$ decomposed to a mixture of crystalline and amorphous phases during the early stages of mechanical milling. A single

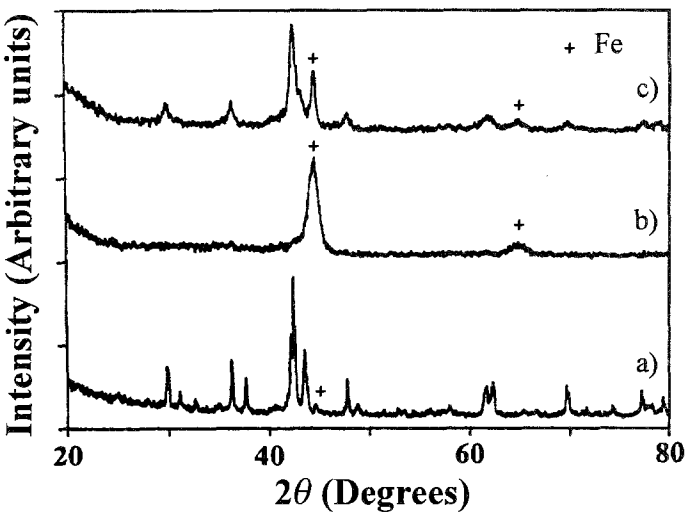

Fig. 6. X-ray diffraction patterns for Sm_2Fe_{17}: (a) as-received; (b) after mechanical milling for 24 h; (c) after milling and heat treatment at 973 K (Smith and McCormick 1992).

amorphous phase was found to develop from the two-phase mixture after further milling. Similar results were obtained with Gd_2Co_7.

Recent studies have shown that both $Nd_2Fe_{14}B$ and Sm_2Fe_{17} intermetallic compounds decompose during mechanical milling. Alonso et al. (1992c) reported that milling melt-quenched $Nd_2Fe_{14}B$ magnet powder in a sealed SPEX mill resulted in decomposition to a two-phase mixture of α-Fe and an amorphous phase. Similar results have been reported in Sm_2Fe_{17} (Smith and McCormick 1992). X-ray diffraction patterns for Sm_2Fe_{17} before and after milling for 24 hours in a SPEX mill are shown in fig. 6. The diffraction peaks of the starting material correspond to the Sm_2Fe_{17} (Th_2Zn_{17}) structure. Following milling, the pattern showed only peaks associated with α-Fe. No Sm_2Fe_{17} diffraction peaks were present. Heat treatment of the milled powder at temperatures above 973 K resulted in crystallization of the Sm_2Fe_{17} phase as shown in fig. 6.

The similar structures obtained in mechanically alloyed and mechanically milled $Nd_2Fe_{14}B$ and Sm_2Fe_{17} clearly indicate that the phase structures formed during milling, while not equilibrium structures, are essentially independent of the starting structure, provided the same milling conditions are employed. Intermetallic compounds which do not form during mechanical alloying, decompose during mechanical milling. Two-phase mixtures can form during mechanical milling of an intermetallic compound if the free energy of the disordered state initially formed during milling is higher than the mixture of elements. The processes of disordering and amorphization increase the free energy regardless of whether the starting material is the intermetallic compound or a mixture of the elements. The final structure is determined by the rates of mechanically induced disordering and diffusion controlled recovery.

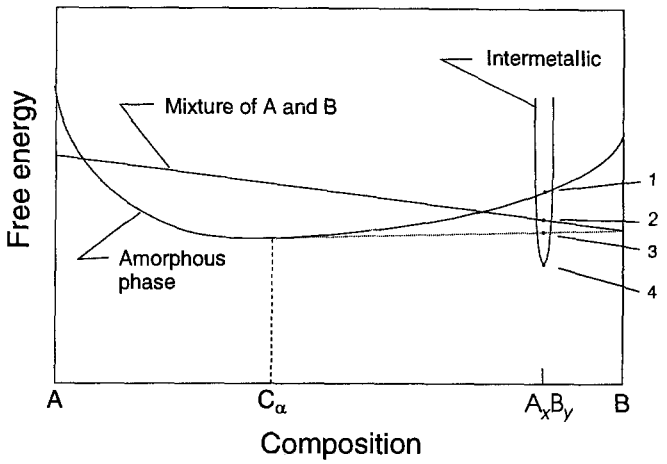

Fig. 7. Schematic free energy diagram (Smith and McCormick 1992).

In fig. 7 the free energies of the amorphous and intermetallic phases are plotted schematically as a function of composition (Smith and McCormick 1992). With mechanical alloying the starting point corresponds to point (4) in the figure, while with mechanical milling the starting point is at (2). In either case milling increases the free energy toward that of the amorphous phase (1) and relaxation can occur to: a mixture of the crystalline components (2), a mixture of a crystalline component and an amorphous phase (3), or to the crystalline intermetallic (4), since all have lower free energies than the amorphous state. The structure which forms will be determined by the rate constants associated with the formation of the respective phases. Gerasimov et al. (1991) have shown that phase separation is favored by milling conditions which generate high temperatures, while amorphization is favored by conditions which generate low temperatures. It is also noted that fig. 7 predicts a central amorphous composition range surrounded on each side by two-phase amorphous–crystalline regions, as observed in a number of alloy systems (Weeber and Bakker 1988).

Miao et al. (1996) have recently carried out a comparative study of the structure and properties of $Nd_{10}Fe_{84}B_6$ prepared by mechanical milling and mechanical alloying. Both processing methods resulted in as-milled two-phase structures, consisting of α-Fe and an amorphous phase. However, the fraction of α-Fe and Fe content of the amorphous phase were found to depend on the method of processing. Mössbauer measurements showed that in the mechanically alloyed powders, 85% of the iron atoms were located in the α-Fe phase as compared to only 50% for the mechanically milled powders. The corresponding compositions of the amorphous phase were 44 at.% Fe and 72 at.% Fe for the mechanically alloyed and mechanically milled powders, respectively. After annealing to crystallize the $Fe_2Nd_{14}B$ phase, the mechanically alloyed powders showed a somewhat coarser, non-uniform grain structure in comparison with the annealed mechanically milled powders.

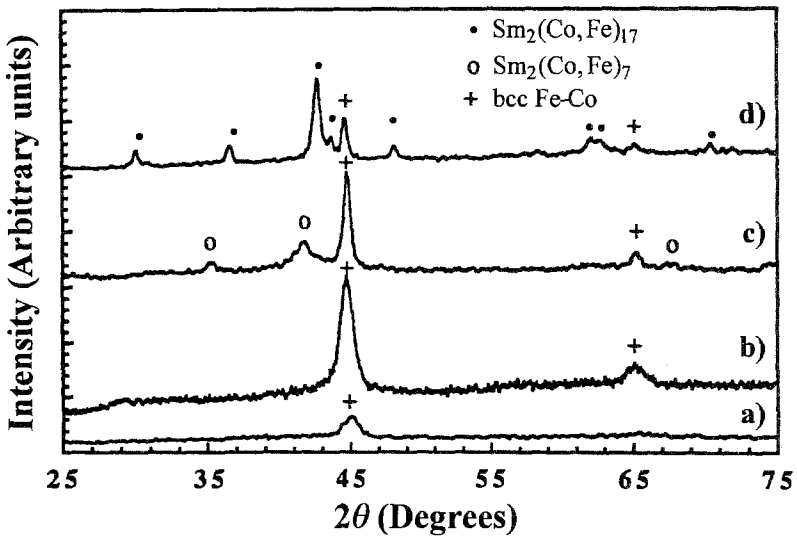

Fig. 8. Phases present in as-milled and heat-treated $Sm_{10.5}Co_{49.5}Fe_{40}$: (a) as-milled; (b) annealed 120 min at 623 K; (c) annealed 10 min at 873 K; (d) annealed 10 min at 973 K (Smith et al. 1996).

3.6. *Effect of heat treatment*

The effect of heat treatment on the structure of as-milled powders has been extensively studied. Heat treatment of as-milled amorphous structures generally results in crystallization on reaching a critical temperature. Crystallization may involve the formation of the equilibrium phase, or alternatively, one or more non-equilibrium phases may crystallize, which then transform to the equilibrium phase at higher temperatures. For example, Ding et al. (1993a) showed that the as-milled amorphous $Sm_{13}Co_{87}$ initially crystallized as a $TbCu_7$ type phase (disordered Th_2Zn_{17} structure) on heating above 773 K. The equilibrium Sm_2Co_{17} phase formed on heating to temperatures above 973 K.

In as-milled two-phase SmFe and SmCoFe alloys the α-Fe crystallites have been shown to recrystallize during heating to a temperature below the crystallization temperature of the amorphous phase. X-ray diffraction patterns of as-milled and heat-treated $Sm_{10.5}Co_{49.5}Fe_{40}$ samples are shown in fig. 8 (Smith et al. 1996). The as-milled powder showed only a single broad peak associated with the α-(Fe,Co) phase. Heat treatment at 350°C resulted in significant sharpening of the α-phase peaks, indicative of recrystallization and grain growth, without any crystallization of the amorphous phase. Heat treatment at higher temperatures resulted in the formation of the $Sm_2(Co,Fe)_7$ phase at 600°C and the $Sm_2(Co,Fe)_{17}$ phase at 700°C (fig. 8). DSC measurements exhibited an exothermic peak at ~300°C which was associated with recrystallization of the bcc (FeCo) phase, and a second exothermic peak at ~500°C accompanying crystallization of the amorphous phase to $Sm_2(Co,Fe)_7$.

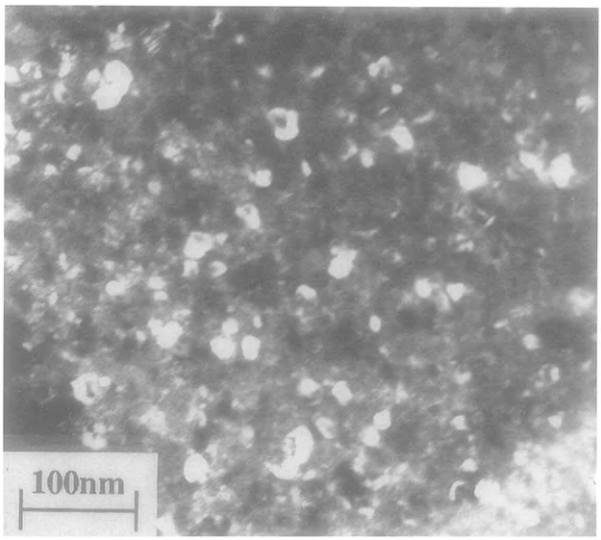

Fig. 9. Nanocrystalline structure of $Sm_{10.5}Co_{49.5}Fe_{40}$ after heat treatment at 873 K (Smith et al. 1996).

In most studies the crystallization temperatures of mechanically alloyed or mechanically milled structures are sufficiently low, i.e. less than 1000 K, so that little or no grain growth accompanies crystallization. As a consequence the crystallite sizes are of nanometer dimensions, i.e. 5–50 nm. Figure 9 shows a nanophase mixture of α-(Fe,Co) and $Sm_2(Co,Fe)_7$ present in a $Sm_{10.5}Co_{49.5}Fe_{40}$ sample heat-treated at 873 K (Smith et al. 1995). In alloys containing a mixture of two phases, such as Sm_2Fe_{17}–α-Fe mixtures, grain growth is generally observed to occur at different rates in the two phases.

With intermetallic phases containing interstitials, e.g. rare-earth–transition-metal nitrides, the high stability of rare-earth interstitial phases may necessitate a two-stage heat treatment. For example, to synthesize $Sm_2Fe_{17}N_x$ it is necessary to first crystallize the mechanically alloyed Sm and Fe at temperatures of ~900 K to form Sm_2Fe_{17}. The nitride phase is subsequently formed by nitriding at ~650–700 K. This procedure is necessary because $Sm_2Fe_{17}N_x$ decomposes to SmN and α-Fe at temperatures above ~700 K.

It is clear from the results of studies carried out to date that a wide variety of non-equilibrium structures can be synthesized in rare-earth–transition-metal alloys by mechanical alloying and subsequent heat treatment. As an illustration, the phases observed to be present in $Sm_{13}(Co_{1-x}Fe_x)_{87}$ alloys are shown in fig. 10 as a function of Fe content and heat-treatment temperatures (Ding et al. 1994a). In general, it is found that crystallization of the amorphous phase initially occurs in a manner which minimises the amount of diffusion required. As a consequence, metastable intermetallic phases tend to form which have compositions similar to that of the amorphous phase. In systems which disproportionate during milling, higher temperatures are required to form the equilibrium

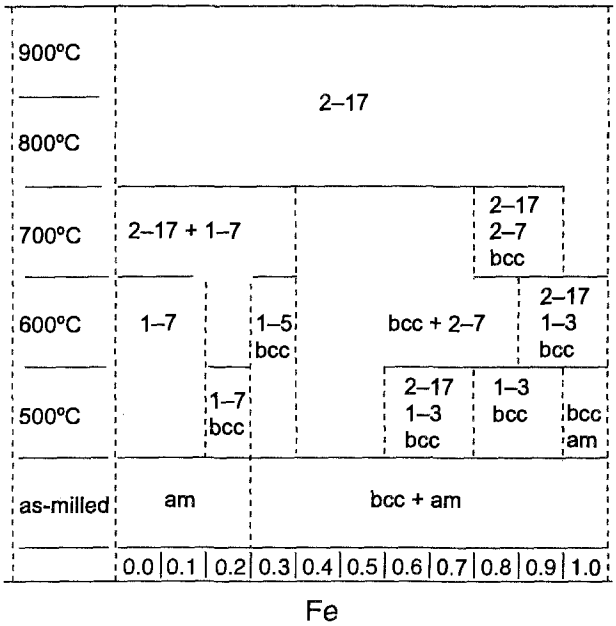

Fig. 10. Effect of Fe content and annealing temperature on phases present in mechanically alloyed $Sm_{13}(Co_{1-x}Fe_x)_{87}$ alloys (Ding et al. 1994a).

structure as long-range diffusion between the two phases is required for the necessary composition changes to occur.

4. Mechanochemical reactions involving rare-earth materials

4.1. *Refining of metals*

The rare earths are amongst the most difficult materials to refine. These metals are conventionally refined by calciothermic reduction at temperatures exceeding 1300 K, with the exception of Sm, Eu and Yb which require the use of La or mischmetal as the reductant due to the high stability of their respective divalent chlorides (Beaudry and Gschneidner 1978).

The refining of rare-earth metals by solid-state reduction of their chlorides during mechanical alloying with a reductant has been reported (McCormick et al. 1991b, Alonso et al. 1993). The reduction of $ErCl_3$ and $GdCl_3$ by Ca during mechanical alloying has been shown to occur after milling for 24 hours in a SPEX mill (McCormick et al. 1991b). X-ray diffraction patterns of as-milled $ErCl_3$/Ca and $GdCl_3$/Ca mixtures are shown in fig. 11. The as-milled structures consisted of fine mixtures of metal crystallites in an amorphous $CaCl_2$ matrix. Crystallite sizes of 14 nm for Er and 9 nm for Gd were estimated from X-ray diffraction measurements. The as-milled particle size was approximately 2.5 μm

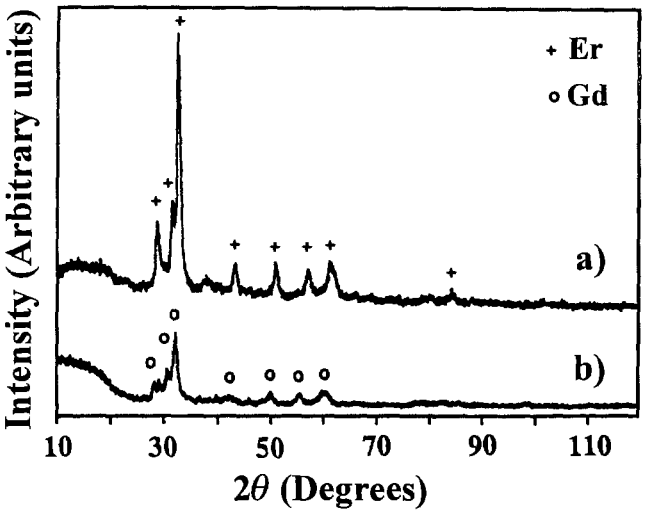

Fig. 11. X-ray diffraction patterns of (a) Er and (b) Gd refined by mechanochemical reactions of their respective chlorides with Ca (McCormick et al. 1991b).

and the as-milled powders were extremely reactive, making it necessary to use special handling procedures to avoid contamination. As discussed in sect. 3.3, the reaction of rare-earth metals with oxygen and nitrogen during milling can result in the formation of NaCl-type phases.

As indicated above, to chemically refine $SmCl_3$ it is necessary to use a highly electronegative reductant, such as La or mischmetal, due to the low free energy of the $SmCl_2$ phase. Examination of free-energy data indicates that it should be possible to refine $SmCl_3$ at low temperatures, using Na as the reductant. Values of the free-energy change associated with the formation of $SmCl_2$ and Sm, respectively, are plotted as a function of temperature in fig. 12. The curves cross at approximately 400 K, with the $SmCl_3 + 3Na \rightarrow Sm + 3NaCl$ reaction being favoured at lower temperatures.

The reduction of $SmCl_3$ by Na during milling has been reported by Alonso et al. (1993). X-ray diffraction patterns of a sample milled for 16 hours in a SPEX mill (fig. 13) show the presence of a two-phase mixture of Sm and NaCl. To test the thermal stability of the Sm, samples of the as-milled powder were vacuum-annealed at 575 and 823 K, respectively. As shown in fig. 13, annealing at 575 K resulted in growth of the Sm crystals, however, no formation of $SmCl_2$ occurred as would be expected from free-energy data. Annealing at 823 K resulted in the formation of $SmCl_2$. Although there may be some uncertainty as to the exact value of the temperature below which Sm is stable, the formation of Sm by mechanical alloying is an important confirmation of the low-temperature nature of the process. While it is not possible to directly measure particle temperatures reached during collision events, values of maximum collision temperatures inferred by combustion experiments and calculations (see sect. 2.5) are estimated to be of the order of 450 K. However, it is unlikely that temperatures exceeding ~400 K would

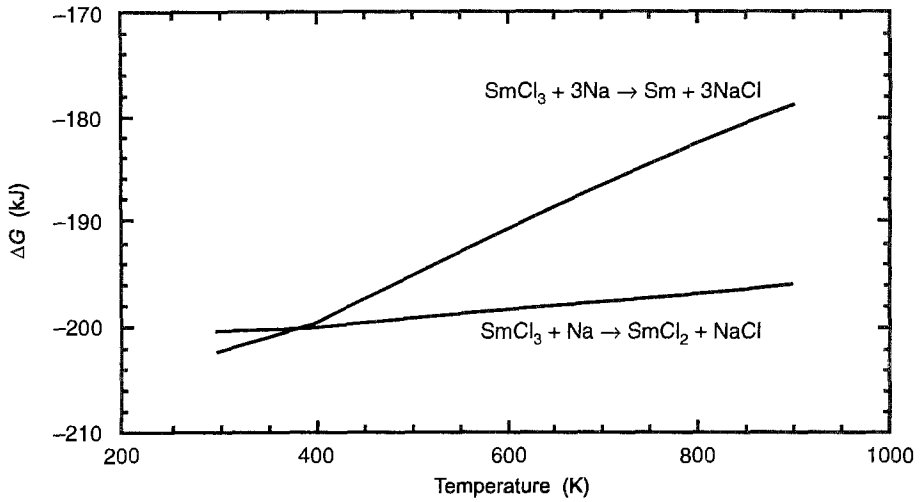

Fig. 12. Effect of temperature on the free energy changes associated with the reduction of $SmCl_3$ with Na to form Sm and $SmCl_2$ (Alonso et al. 1993).

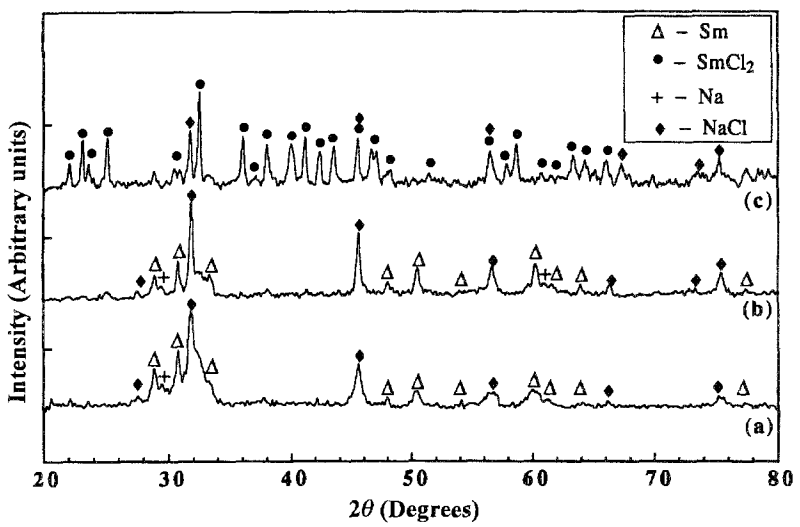

Fig. 13. X-ray diffraction patterns for $SmCl_3 + Na$ reaction: (a) as-milled; (b) after heat treatment at 573 K; (c) after heat treatment at 823 K (Alonso et al. 1993).

have been reached due to local melting of Na on reaching 371 K. The discovery of other low-temperature reactions that can be uniquely induced by mechanical alloying, which for thermodynamic or other reasons will not occur at elevated temperatures, is an exciting prospect.

4.2. *Refining of alloys*

The synthesis of rare-earth permanent magnet alloys directly from rare-earth oxides or halides by milling with a suitable reductant has also been investigated. The reactions that have been studied are given in table 4. Most work to date has been carried out on the synthesis of $SmCo_5$ or Sm_2Co_{17} by milling Co with Sm_2O_3, $SmCl_3$ or SmF_3 precursors using Ca or Na as reductants.

Table 4
Rare earth alloy reduction reactions

Reaction	As-milled structure	Reference
$Sm_2O_3 + 3Ca + 10Co \rightarrow 2SmCo_5 + 3CaO$	amorphous + CaO	1
$2SmF_3 + 3Ca + 10Co \rightarrow 2SmCo_5 + 3CaF_2$	crystalline + CaF_2	2
$2SmCl_3 + 3Ca + 10Co \rightarrow 2SmCo_5 + 3CaCl_2$	amorphous	3
$SmCl_3 + 3Na + 5Co \rightarrow SmCo_5 + 3NaCl$	crystalline, Sm, Co, NaCl	3
$Sm_2O_3 + 3Ca + 17Co \rightarrow Sm_2Co_{17} + 3CaO$	amorphous + CaO	4
$Sm_2O_3 + 3Ca + 17Fe \rightarrow Sm_2Fe_{17} + 3CaO$	amorphous + CaO	4
$Nd_2O_3 + 3Ca + 14Fe + B \rightarrow Nd_2Fe_{14}B + 3CaO$	amorphous + CaO	4
$Dy_2O_3 + 3Ca + 4Fe \rightarrow 2DyFe_2 + 3CaO$	crystalline + CaO	5

References
(1) Liu et al. (1992a)
(2) Liu et al. (1992b)
(3) Richmond et al. (1997)
(4) Liu et al. (1994c)
(5) Milham (1993)

4.2.1. *As-milled structures*

Comparison of tables 1 and 4 shows that the as-milled structures are generally similar to that obtained by the mechanical alloying of the rare-earth metals, except for the presence of the reaction by-products. CaO, CaF_2 and NaCl by-products all form as equilibrium nanocrystalline structures during milling, while $CaCl_2$ forms an amorphous phase. For example, an X-ray pattern showing the as-milled structure formed by mechanochemical reaction of Fe, B, Nd_2O_3 and Ca is shown in fig. 14 (Liu et al. 1994c). The phases present after milling are α-Fe, CaO and an amorphous Nd-rich phase.

With the synthesis of $SmCo_5$, an amorphous as-milled SmCo structure has been obtained using Sm_2O_3 and $SmCl_3$ precursors with Ca (Richmond et al. 1997, Liu et al. 1992a), in agreement with the structure obtained by mechanically alloying Sm with Co. In fact, using $SmCl_3$ and Ca the as-milled structure is entirely amorphous (Richmond et al. 1997). On the other hand, the synthesis of $SmCo_5$ from SmF_3 using Ca as the reductant resulted in the formation of crystalline $SmCo_5$ (Liu et al. 1992b). X-ray and TEM examination showed that the as-milled particles contained a uniform mixture of $SmCo_5$ and CaF_2 crystallites of less than 10 nm size. Attempts to synthesize $SmCo_5$ from $SmCl_3$ and Co using Na as the reductant have been found to result in a nanocrystalline

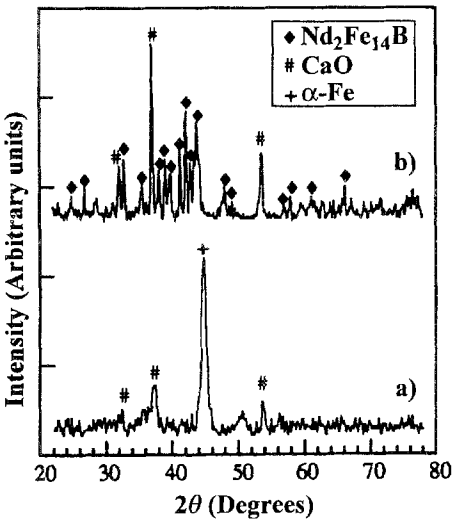

Fig. 14. X-ray diffraction patterns for $Nd_2Fe_{14}B$ prepared by mechanochemical reaction of Fe, B, Nd_2O_3 and Ca: (a) as-milled, (b) after heat treatment at 975 K (Liu et al. 1994c).

mixture of Sm, Co and NaCl (Richmond et al. 1997). Surprisingly, the reduction of $SmCl_3$ resulted in the formation of Sm rather than $SmCo_5$ or an amorphous phase.

4.2.2. *Heat treatment*

Heat treatment of the as-milled powders has generally been shown to result in the formation of equilibrium phases. For example, with $Nd_2Fe_{14}B$ formed from the reaction of Nd_2O_3 with Ca, heat treatment at temperatures above 873 K is required to form the $Nd_2Fe_{14}B$ phase (Liu et al. 1994c). However, some differences have been observed in the structures synthesized via different reactions. In particular, the stability of the $SmCo_5$ phase appears to depend on the reductant and on whether an oxide or a halide is being reduced (Richmond et al. 1997).

4.2.3. *Removal of reaction by-products*

The ability of mechanochemical processing to combine refining, alloying and powder manufacture into a single, low-temperature process provides significant potential for reducing processing costs. The reactions shown in table 4 are all applicable to the synthesis of hard magnets, however, removal of the reaction by-product is required to obtain useful properties.

With the exception of CaF_2, the reaction by-products shown in table 4 are soluble in a variety of solvents. Recent studies have shown that $CaCl_2$ may be removed from heat-treated Sm–Co powder by washing in a suitable solvent (Richmond et al. 1997). Changes in the chemical composition during processing are given in table 5. It is seen that some loss of $CaCl_2$ and excess Ca occurred during heat treatment and that the washing procedure was effective in removing the $CaCl_2$ to a low level without increasing the

Table 5
Changes in chemical composition during processing of Sm–Co (Richmond et al. 1997)

Condition	Composition (wt.%)					
	Sm	Co	Ca	Cl	O	N
As-received	24.2	45.1	12.6	17.0	0.4	<0.1
As-milled	24.3	45.7	11.8	15.3	0.7	<0.1
Annealed for 1 h at 973 K	24.5	46.1	10.7	9.6	0.8	<0.1
Washed	32.1	63.2	1.3	0.4	0.8	<0.1

oxygen content. It is also evident that only a minor pick-up of oxygen occurred during milling and annealing.

5. Applications of mechanically alloyed compounds

5.1. *Permanent magnets*

The application of mechanical alloying to the synthesis of rare-earth permanent magnets was first demonstrated by the work of Schultz and co-workers (Schultz et al. 1987). Subsequently, the magnetic properties of a number of rare-earth–transition-metal compounds synthesized by the mechanical alloying of elemental powders, mechanical milling of intermetallic compounds, or by mechanochemical reaction, using oxide and halide precursors, have been studied.

The structures obtained in these materials after milling and heat treatment have been discussed in sect. 3. The amorphous structures generated by mechanical alloying and mechanical milling exhibit soft magnetic behaviour, and to obtain useful magnetic properties, it is necessary to crystallize the as-milled material. As discussed in sect. 3.6, crystallization of a particular alloy can result in one or more intermediate metastable phases prior to formation of the equilibrium intermetallic phase. Characterization of the metastable phases formed during the heat treatment of milled rare-earth–transition-metal alloys and their respective magnetic properties is currently an active area of research.

The magnetic properties of mechanically alloyed and heat-treated alloys are shown in table 6. Remarkably high values of coercivity, H_c, have been reported, particularly in $SmCo_5$, where samples synthesized from SmF_3 have exhibited values of H_c in excess of 75 kOe (Liu et al. 1992b). The high values of coercivity exhibited by these alloys are associated with the nanocrystalline grain structure developed by mechanical alloying and heat treatment, which results in strong domain-wall pinning at grain boundaries. In addition, the presence of non-metallic phases at grain boundaries reduces exchange interactions between adjacent grains. Measurements of the effect of heat-treatment temperature on coercivity have shown that there is an optimum heat-treatment temperature, above which H_c decreases due to the increase in crystallite size with increasing temperature.

Table 6
Magnetic properties of mechanically alloyed rare earth permanent magnet alloys

Alloy	$4\pi M_r$ (kG)	H_c (kOe)	$(BH)_{max}$ (MGOe)	Reference
$Nd_2Fe_{14}B$	8.0	13	12.8	1
$Nd_2Fe_{14}B$[a]	13.2	9.8	41.3	2
$Nd_2Fe_{14}B$	5.7	13.1	13.7	3
$Nd(Fe,Mo)_{12}N_x$	–	9.0	6.6	4
$Pr(Fe,Mo)_{12}N_x$	–	6.0	4.5	4
$SmCo_5$	5.2	30	–	5
$SmCo_5$	4.0	57.1	–	6
$SmCo_5$	5.4	65	–	7
Sm_2Co_{17}	6.8	6.28	–	2
$Sm_2Fe_{17}C_2$	6.1	23.2	7.4	8
$Sm_2Fe_{17}N_{2.5}$	–	29.5	12.8	9
$Sm_2Fe_{17}N_x$	7.5	30	10.9	10
$Sm_2Fe_{17}N_x$	7.0	31.3	10.5	11
$Sm_2Fe_{17}N_x$	8.0	44	13.7	12
$Sm_2Fe_{17}N_x$	8.0	44	14.3	13
$Sm_2Fe_{17}N_x$	7.2	32.2	11.0	14
$Sm_2Fe_{17}C_x$	6.1	23.2	7.0	14
$Sm_2Fe_{17}N_x$[b]	4.0	43.6	–	14
$Sm_2Fe_{17}N_x$	4.0	43.6	–	15
$Sm(Fe,V)_{12}$	5.0	10	–	16
$Sm_{12}Fe_{73}V_{15}$	4.9	10.6	5.2	17
$Sm_2Fe_{14}Ga_3C_2$	4.2	12.7	–	18
$Sm(Fe,Ti)_{12}$	2.5	64.5	–	16
$Sm_{20}Fe_{70}Ti_{10}$	3.0	50.3	2.2	19
$Sm_8Fe_{80}Mo_{12}$	10.0	–	3.8	20
$Pr(Mo,Fe)_{12}N_x$	7.5	6.0	–	21
$Sm_{10}Fe_{70}Co_{10}Mo_{10}$	5.2	5.0	4.9	22
$Sm_{26}Fe_{65}Ti_9$	2.7	65.2	1.9	23
$Sm_{11}Fe_{84}Ti_{15}N_x$	8.0	20	–	24

[a] Anisotropic.

[b] Zinc bonded.

References

(1) Schultz et al. (1987)
(2) Wecker et al. (1994)
(3) Liu et al. (1994c)
(4) Y.C. Yang et al. (1994)
(5) Wecker et al. (1991)
(6) Ding et al. (1993b)
(7) Liu et al. (1992b)
(8) Kuhrt et al. (1992b)
(9) Ding et al. (1992b, 1993c)
(10) Schnitzke et al. (1990b)
(11) Wang et al. (1993)
(12) Liu et al. (1994a)
(13) Liu et al. (1994b)
(14) Kuhrt et al. (1993)
(15) Kuhrt et al. (1992a)
(16) Schultz et al. (1991)
(17) Schultz et al. (1990)
(18) Ding et al. (1994d)
(19) Schnitzke et al. (1990c)
(20) Schultz and Wecker (1988)
(21) Pan et al. (1994)
(22) Schultz et al. (1989)
(23) J. Yang et al. (1994)
(24) Ding et al. (1995)

The grain structures formed by mechanical alloying and heat treatment do not exhibit any crystallographic texture. As a consequence, the magnetic properties are isotropic and the remanent magnetization, M_r, and maximum energy product, $(BH)_{max}$, are limited to 0.5 and 0.25, respectively, of the values achievable with full crystallographic alignment of

single-domain grains. Schultz and co-workers (Schultz et al. 1989, Wecker et al. 1994), have demonstrated that the use of high-temperature die upsetting, following mechanical alloying and heat treatment, can be used to develop texture. Values of maximum energy product, $(BH)_{max}$, equal to 41.3 MGOe have been reported in mechanically alloyed and die-upset $Nd_2Fe_{14}B$. Such values approach that obtained in fully aligned $Nd_2Fe_{14}B$ magnets manufactured by the conventional powder metallurgy route. High-temperature forming methods cannot be used to consolidate or develop texture in $Sm_2Fe_{17}N_x$ because the temperatures required ($T > 900$ K) result in decomposition of the alloy to α-Fe and samarium nitride.

5.2. *Nanocomposite magnets*

As discussed previously, isotropic magnetic behaviour limits the properties of mechanically alloyed rare-earth magnets, which are not processed further to develop a crystallographic texture. Recent studies (Ding et al. 1993a–c, 1994b,c, O'Donnell et al. 1994a,b, Gong and Hadjipanayis 1994, Smith et al. 1994–1996) have demonstrated that mechanically alloyed two-phase rare-earth permanent magnet materials exhibit the phenomena of remanence enhancement, whereby the remanent magnetization, M_r, exceeds one half of the saturation magnetization, M_s, in isotropic materials. Remanence enhancement is associated with exchange coupling at interfaces between nanocrystalline hard and soft magnetic phases (McCormick et al. 1996). The exchange coupling causes the magnetization vector of the soft phase to be rotated toward that of the hard phase, increasing the remanent magnetization in the direction of initial magnetization. As a consequence, the material, although crystallographically isotropic, can exhibit remanence values approaching that achieved in fully aligned materials without the necessity of crystallographic alignment.

The nanocrystalline microstructures inherently developed by the mechanical alloying process appear to be ideally suited to remanence-enhanced magnetic materials. Ideally the soft phase should have the highest possible value of M_s. A number of soft magnetic phases exhibit significantly higher values of M_s than the rare-earth–transition-metal phases and are much less costly. For example, the value of M_s for α-Fe is 2.1 T as compared with 1.6 T for $Nd_2Fe_{14}B$.

Ding et al. (1993c, 1994b) first reported remanence enhancement in mechanically alloyed two-phase α-Fe/$Sm_2Fe_{17}N_{2.6}$ alloys containing 5–11 at% Sm. The as-milled structures consisted of two-phase mixtures of α-Fe and an amorphous phase. Crystallization at temperatures above 773 K resulted in two-phase α-Fe/Sm_2Fe_{17} mixtures which were subsequently nitrided at 673 K to form $Sm_2Fe_{17}N_{2.6}$. The crystallite size was ~15–20 nm in samples crystallized at 873 K.

The magnetization behaviour of a typical remanence-enhanced magnet is shown in fig. 15 (Smith et al. 1996). Remanence enhancement is evidenced by the high value of M_r relative to the saturation magnetization at high values of applied field. Values of M_r/M_s exceeding 0.75 have been reported in several two-phase systems (table 7). Such values of

Table 7
Properties of remanence enhanced magnet alloys

Alloy	Structure	M_r/M_s	H_c (kOe)	Reference
$Sm_{13}Co_{87}$	$SmCo_5 + Sm_2Co_{17}$	0.7–0.8	8.3	1
$Sm_7Fe_{93}N_{2.6}$	$Sm_2Fe_{17}N_{2.6} + Fe$	0.75	8.0	2
$Sm_7Fe_{93}N_3$	$Sm_2Fe_{17}N_3 + Fe$	0.82	4.0	3
NdFeB	$Nd_2Fe_{14}B + Fe$	0.60	6.0	4
NdFeCoB	$Nd_2Fe_{14}B + FeCo$	0.62	4.4	4
NdTbFeNb	$(NdTb)_2Fe_{14}B + FeNb$	0.68	6.0	4
$Sm_{13}Co_{61}Fe_{26}$	$Sm(Co, Fe)_7 + FeCo$	0.8	4.7	5
$Sm_{14.4}Co_{65.6}Fe_{20}$	$Sm(Co, Fe)_7 + FeCo$	0.74	9.1	6
$Sm_{10.5}Co_{49.5}Fe_{40}$	$Sm2(Co, Fe)_7 + FeCo$	0.79	4.0	7
SmFeGaC	$Sm_2Fe_{14}Ga_3C_2 + Fe$	0.65	5.0	8

References
(1) Ding et al. (1993a,b)
(2) Ding et al. (1993c, 1994b)
(3) O'Donnell et al. (1994a,b)
(4) Gong and Hadjipanayis (1994)
(5) Ding et al. (1994c)
(6) Smith et al. (1994)
(7) Smith et al. (1995, 1996)
(8) McCormick et al. (1996)

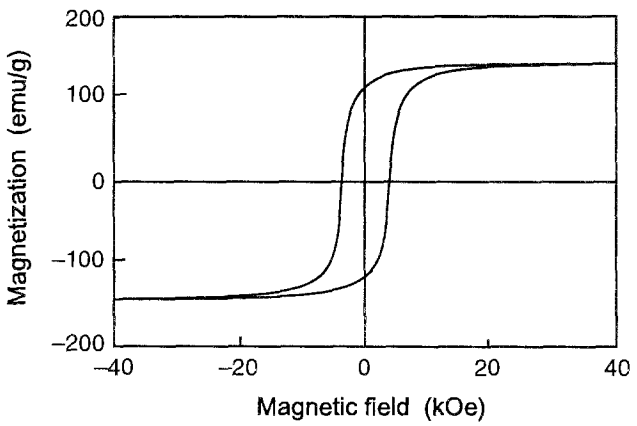

Fig. 15. Magnetization curve for remanence enhanced α-Fe+$Sm_2(CoFe)_{17}$ (Smith et al. 1996).

M_s/M_r generally require crystallite sizes less than 20 nm. Microstructures of remanence-enhanced alloys are similar to that shown in fig. 9.

The crystallite size and fraction of soft phase are key parameters influencing the degree of remanence enhancement and coercivity. In fig. 16 the effect of annealing temperature on the coercivity, H_c, and remanence of two-phase α-Fe/$Sm_2Fe_{17}N_{2.6}$ is shown. Both H_c and M_r decrease with increasing temperature above ~873 K due to the increase in crystallite size, and two-phase magnetic behaviour is observed in samples

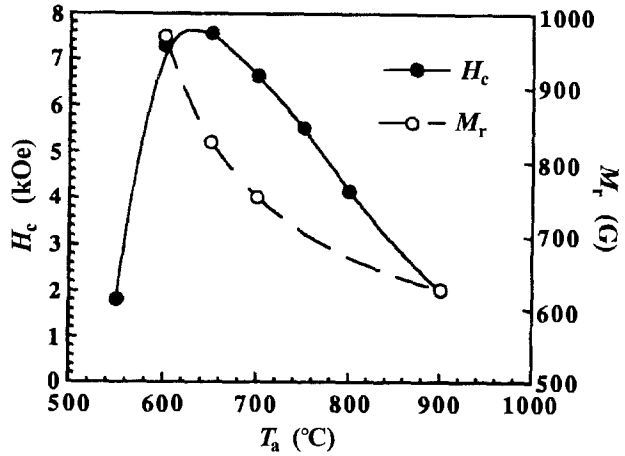

Fig. 16. Effect of annealing temperature on coercivity and remanent magnetization for α-Fe+$Sm_2Fe_{17}N_{2.6}$ (Ding et al. 1994b).

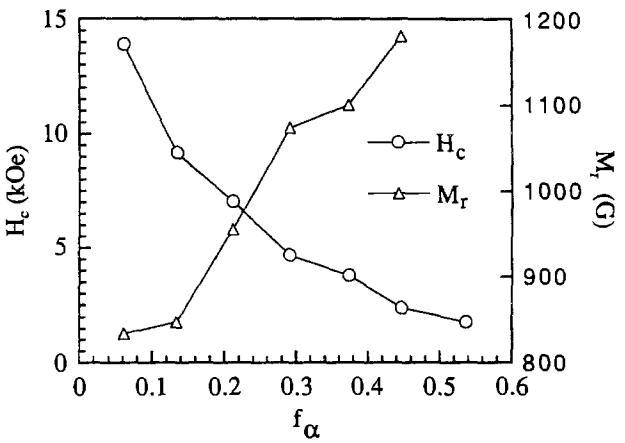

Fig. 17. Effect of f_α on the coercivity and remanent magnetization for α-Fe+$Sm_2Fe_{17}N_{2.6}$ (Ding et al. 1994b).

annealed above a critical temperature (Ding et al. 1993c). The effect of the volume fraction, f_α, of the α-Fe phase on the measurements of M_r and H_c are shown in fig. 17 for two-phase α-Fe/$Sm_2Fe_{17}N_{2.6}$. As expected, M_r increases and H_c decreases with increasing f_α. For intermediate values of f_α promising combinations of $(BH)_{max}$ and H_c are obtained, e.g. $H_c = 8$–10 kOe and $(BH)_{max} = 20$–22 MGOe.

In addition to the increased values of M_r, exchange-coupled two-phase magnets exhibit lower values of coercivity and higher values of reversible magnetization relative to single-phase magnets. In fig. 18 measurements of the ratio of reversible magnetization, M_{rev}, to saturation magnetization are plotted as a function of the applied field for single-phase $Sm_2Fe_{14}Ga_3C_2$ and two-phase exchange-coupled α-Fe+$Sm_2Fe_{14}Ga_3C_2$ samples

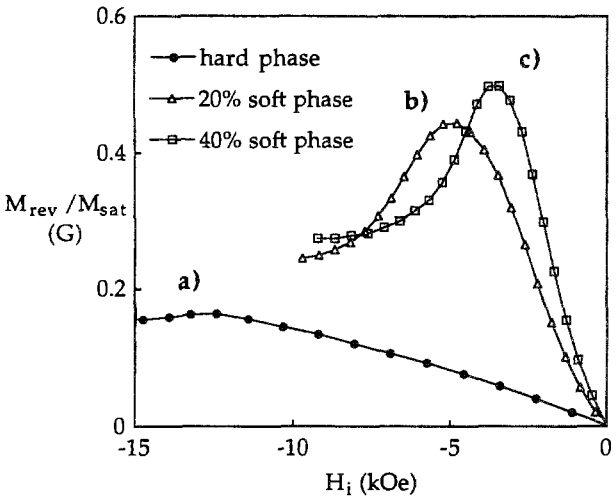

Fig. 18. Effect of the fraction of soft phase on the ratio of reversible to saturation magnetization in α-Fe+ $Sm_2Fe_{14}Ga_3C_2$ (McCormick et al. 1996).

containing 20 and 40 vol% soft phase (McCormick et al. 1996). The high value of M_{rev} in the two-phase samples at applied fields significantly greater than the coercive field of α-Fe is indicative of exchange coupling of the hard and soft phases.

5.3. *Hydrogen storage alloys*

The hydrogen absorption characteristics of mechanically milled $LaNi_5$ powders have been studied by Zaluski et al. (1995). Nanocrystalline powders were prepared from arc-melted $LaNi_5$ by milling in a SPEX mill under an argon atmosphere. As-milled samples exposed to hydrogen at 50 bar at room temperature required an incubation time of 7 min and a half reaction time, $t_{1/2}$, of 25 min. The addition of ~1% Pd to the powder during milling resulted in a significant improvement in the hydrogenation kinetics, with the incubation time being reduced to zero and $t_{1/2}$ to 22 s. The improvement in hydrogenation kinetics was attributed to the effect of Pd in catalysing the hydrogen disassociation reaction on the surface of the $LaNi_5$ particles.

6. Summary

Studies of mechanical alloying and mechanochemical processing of the rare earths and their alloys have shown that a wide variety of structures, ranging from metastable nanocrystalline to amorphous phases, can be synthesized. The ability to alloy and form phases at low temperatures, without melting or high-temperature processing, is a unique feature of mechanically activated processing. The low-temperature nature of the process enables disordering and amorphization to occur, with the resulting structures

being determined by kinetic rather than thermodynamic considerations. Low-temperature heat treatment of mechanically alloyed structures can also result in the formation of new non-equilibrium phases due to the kinetic constraints of diffusion.

The application of mechanical alloying to chemical refining also enables the direct synthesis of metals and alloys, without the need for heating. While in principle mechano-chemical processing allows three processes, refining, alloying and powder manufacture, to be carried out in a single low-temperature process, attention must be given to the handling, further processing of highly reactive as-milled powders, and the removal of reaction by-products.

Mechanical alloying provides significant advantages in the processing of rare-earth permanent magnets. The production of alloy powder by low-temperature processing in a sealed, inert environment minimises the sources of oxidation inherent in conventional processes. The structures obtained by mechanical alloying and heat treatment are characterized by excellent hard magnetic properties. In particular, the nanocrystalline microstructures inherently developed by the mechanical alloying process, appear to be ideally suited to the synthesis of remanence-enhanced magnetic materials. Since with remanence enhancement there is no need for an alignment process, significant potential exists for achieving cost savings and simplification of the manufacturing process.

As shown by the studies on rare-earth permanent magnets, the non-equilibrium structures developed by mechanical alloying, with or without subsequent heat treatment, exhibit unique properties. There is thus much potential for the development of new mechanically alloyed materials for applications such as catalysts, electrodes, hydrogen-storage containers and other applications, where property improvements are associated with the amorphous and nanocrystalline structures developed by mechanical alloying.

References

Alonso, T., Y. Liu, T.C. Parks and P.G. McCormick, 1991, Scripta Metall. Mater. **25**, 1607.

Alonso, T., Y. Liu, T.C. Parks and P.G. McCormick, 1992a, Scripta Metall. Mater. **26**, 1931.

Alonso, T., Y. Liu and P.G. McCormick, 1992b, Mater. Sci. Lett. **11**, 164.

Alonso, T., H. Yang, Y. Liu and P.G. McCormick, 1992c, Appl. Phys. Lett. **60**, 833.

Alonso, T., Y. Liu, M.P. Dallimore and P.G. McCormick, 1993, Scripta Metall. Mater. **29**, 55.

Balough, J., T. Kemeny, I. Vincze, L. Bujdoso, L. Toth and G. Vincze, 1995, J. Appl. Phys. **77**, 4997.

Beaudry, B.J., and K.A. Gschneidner Jr, 1978, in: Handbook on the Physics and Chemistry of Rare Earths, Vol. 1, eds K.A. Gschneidner Jr and L. Eyring (North-Holland, Amsterdam) ch. 2 (in particular see p. 183, table 2.5).

Benjamin, J.S., 1970, Metall. Trans. **1**, 2954.

Benjamin, J.S., 1976, Sci. Am. **234**, 40.

Burgio, N., A. Iasonna, M. Magini, S. Martelli and F. Padella, 1991, Nuovo Cimento D **13**, 459.

Dallimore, M., H. Huang, J. Ding, J. Pan and P.G. McCormick, 1994, in: Proc. 2nd. Int. Conf. on Structural Applications of Mechanical Alloying, ed. R. Schwartz (ASM Int., Materials Park), p. 45.

Davis, R.M., and C.C. Koch, 1987, Scripta Metall. **21**, 305.

Davis, R.M., B. McDermott and C.C. Koch, 1988, Metall. Trans. A **19**, 2867.

Ding, J., P.G. McCormick and R. Street, 1992a, Appl. Phys. Lett. **61**, 2721.

Ding, J., P.G. McCormick and R. Street, 1992b, J. Alloys & Compounds **189**, 83.

Ding, J., Y. Liu, P.G. McCormick and R. Street, 1993a, J. Magn. & Magn. Mater. **123**, L239.

Ding, J., P.G. McCormick and R. Street, 1993b, J. Alloys & Compounds **191**, 197.

Ding, J., P.G. McCormick and R. Street, 1993c, J. Magn. & Magn. Mater. **124**, 1.

Ding, J., P.G. McCormick and R. Street, 1994a, J. Magn. & Magn. Mater. **135**, 201.

Ding, J., Y. Liu, R. Street and P.G. McCormick, 1994b, J. Appl. Phys. **75**, 1032.

Ding, J., P.G. McCormick and R. Street, 1994c, in: Proc. 13th Int. Workshop on Rare Earth Magnets and their Applications, University of Birmingham, Publ. 851.

Ding, J., Bao-gen Shen, P.G. McCormick, R. Street and Fang-wei Wang, 1994d, J. Alloys & Compounds **209**, 221.

Ding, J., P.G. McCormick and R. Street, 1995, J. Alloys & Compounds **217**, 108.

Eckert, J., L. Schultz and K. Urban, 1991, J. Mater. Sci. **26**, 441.

Ermakov, A.E., E.E. Yurchikov and V.A. Barinov, 1981, Fiz. Met. Metalloved. **52**, 1184.

Ermakov, A.E., V.A. Barinov and E.E. Yurchikov, 1982, Fiz. Met. Metalloved. **54**, 935.

Fu, Z., H.J. Fecht and W.L. Johnson, 1991, MRS Symp. Proc. **186**, 169.

Gerasimov, K.B., A.A. Gusev, E.Y. Ivanov and V.V. Boldyrev, 1991, J. Mater. Sci. **26**, 2495.

Girardin, D., and M. Maurer, 1989, in: New Materials by Mechanical Alloying Techniques, eds E. Artz and L. Schultz (DGM, Oberursel) p. 91.

Gong, W., and G.C. Hadjipanayis, 1994, J. Appl. Phys. **75**, 6649.

Han, S.H., K.A. Gschneidner Jr and B.J. Beaudry, 1991, Scripta Metall. Mater. **24**, 295.

Han, S.H., K.A. Gschneidner Jr and B.J. Beaudry, 1992, J. Alloys & Compounds **181**, 463.

Han, S.H., K.A. Gschneidner Jr and B.A. Cook, 1994, J. Appl. Phys. **76**, 7899.

Heinicke, G., 1984, Tribochemistry (Akademie-Verlag, Berlin).

Ivanov, E., K. Sumiyama, H. Yamauchi, K. Yanai and K. Suzuki, 1993a, J. Alloys & Compounds **198**, 105.

Ivanov, E., K. Sumiyama, H. Yamauchi and K. Suzuki, 1993b, J. Alloys & Compounds **192**, 251.

Jang, J.S.C., and C.C. Koch, 1990, J. Mater. Res. **5**, 498.

Jayaraman, A., 1969, Phys. Rev. A **139**, 609.

Johansson, B., and A. Rosengren, 1971, Phys. Rev. B **11**, 2836.

Jurczyk, M., J.S. Cook and S.J. Collocott, 1995, J. Alloys & Compounds **217**, 65.

Koch, C.C., 1989, Annu. Rev. Mater. Sci. **19**, 121.

Koch, C.C., 1995, Mater. Trans. JIM **36**, 85.

Koch, C.C., and M.S. Kim, 1987, J. Appl. Phys. **62**, 3450.

Koch, C.C., O.B. Calvin, C.G. McKamey and C.G. Scarbrough, 1983, Appl. Phys Lett. **43**, 1017.

Kuhrt, C., K. O'Donnell, M. Katter, J. Wecker, K. Schnitzke and L. Schultz, 1992a, Appl. Phys. Lett. **60**, 3316.

Kuhrt, C., M. Katter, J. Wecker, K. Schnitzke and L. Schultz, 1992b, Appl. Phys. Lett. **60**, 2029.

Kuhrt, C., K. Schnitzke and L. Schultz, 1993, J. Appl. Phys. **73**, 6026.

Liu, W., Q. Wang, X.K. Sun, X. Zhao, Z. Zhang, Q. Xiao, T. Zhao and Y.C. Chuang, 1994a, J. Alloys & Compounds **215**, 257.

Liu, W., Q. Wang, X.K. Sun, X. Zhao, T. Zhao, Z. Zhang and Y.C. Chuang, 1994b, J. Magn. & Magn. Mater. **131**, 413.

Liu, Y., M.P. Dallimore, P.G. McCormick and T. Alonso, 1992a, Appl. Phys. Lett. **60**, 3186.

Liu, Y., M.P. Dallimore, P.G. McCormick and T. Alonso, 1992b, J. Magn. & Magn. Mater. **116**, L320.

Liu, Y., T. Alonso, M.P. Dallimore and P.G. McCormick, 1994c, Trans. Mater. Res. Soc. Jpn. **14**, 961.

Loeff, P.I., and H. Bakker, 1988, Scripta Metall. **22**, 401.

Loeff, P.I., H. Bakker and F.R. de Boer, 1989, in: New Materials by Mechanical Alloying, eds E. Artz and L. Schultz (DGM) p. 119.

Lue, M.Q., K.Y. Wang, M.F. Miao, Q.H. Sun, W.E. Wei and L.B. Wang, 1992a, J. Appl. Phys. **71**, 6146.

Lue, M.Q., M.F. Miao, Q. Song, Q.H. Sun, K.Y. Wang, W.E. Wei and L.B. Wang, 1992b, J. Alloys & Compounds **185**, 73.

Majima, K., N. Niimi, S. Katsuyama, H. Hagai and H. Tomizawa, 1993, J. Alloys & Compounds **193**, 268.

Matsuki, K., F. Abe, A. Inoue and T. Maumoto, 1992, Mater. Sci. Forum **88–90**, 313.

Maurice, D., and T.H. Courtney, 1990, Metall. Trans. A **21**, 289.

Maurice, D., and T.H. Courtney, 1994, Metall. Trans. A **25**, 147.

McCormick, P.G., 1995, Mater. Trans. JIM **36**, 161.

McCormick, P.G., V.N. Wharton, M.M. Reyhani and G.B. Schaffer, 1991a, in: Microcomposites and Nanophase Materials, eds D.C. Van Aken, G.S. Was and A.K. Ghosh (The Metallurgical Society, Warrendale, PA) p. 65.

McCormick, P.G., T. Alonso, Y. Liu, F.J. Lincoln, T.C. Parks and G.B. Schaffer, 1991b, in: Rare Earths – Resources, Science, Technology and Applications, eds R.G. Bautista and N. Jackson (The Metallurgical Society, Warrendale, PA) p. 247.

McCormick, P.G., J. Ding, E.H. Feutrill and R. Street, 1996, J. Magn. & Magn. Mater. **157–158**, 7.

Miao, W.F., J. Ding, R. Street and P.G. McCormick, 1996, J. Appl. Phys. **79**, 2079.

Milham, C.D., 1993, in: Proc. Int. Conf. on Processing Materials for Properties, eds I.E. Anderson and K. Morinaga (The Metallurgical Society, Warrendale, PA) p. 449.

Milham, C.D., 1994, J. Appl. Phys. **75**, 5659.

Murillo, N., J. Gonzalez, F. Cebollada, V.E. Martin and J.M. Gonzalez, 1993, IEEE Trans. Magn. **29**, 2857.

O'Donnell, K., C. Kuhrt and J.M.D. Coey, 1994a, J. Appl. Phys. **76**, 7068.

O'Donnell, K., C. Kuhrt and J.M.D. Coey, 1994b, in: Proc. 13th Int. Workshop on Rare Earth Magnets and their Applications, University of Birmingham, Publ. 851.

Ostwald, W., 1919, Handbuch der allgemeine Chemie, Vol. I (Leipzig) p. 70.

Pan, Q., X. Zhang, B. Cheng and Y. Yang, 1994, J. Appl. Phys. **75**, 5441.

Richmond, W., W.F. Miao and P.G. McCormick, 1997, in: Proc. Int. Symp. on Reactive Metals (The Metallurgical Society, Warrendale, PA) in press.

Ruuskanen, P.R., R.B. Schwarz and J.D. Thompson, 1994, Phil. Mag. B **69**, 47.

Schaffer, G.B., and P.G. McCormick, 1989a, Appl. Phys. Lett. **55**, 45.

Schaffer, G.B., and P.G. McCormick, 1989b, Scripta Metall. **23**, 835.

Schaffer, G.B., and P.G. McCormick, 1990a, Metall. Trans. A **21**, 2789.

Schaffer, G.B., and P.G. McCormick, 1990b, J. Mater. Sci. Lett. **9**, 1014.

Schaffer, G.B., and P.G. McCormick, 1991, Metall. Trans. A **22**, 3019.

Schaffer, G.B., and P.G. McCormick, 1992a, Mater. Forum **16**, 91.

Schaffer, G.B., and P.G. McCormick, 1992b, Metall. Trans. A **23**, 1285.

Schnitzke, K., L. Schultz, J. Wecker and M. Katter, 1990a, Appl. Phys Lett. **57**, 2853.

Schnitzke, K., L. Schultz, J. Wecker and M. Katter, 1990b, Appl. Phys. Lett. **57**, 2853.

Schnitzke, K., L. Schultz, J. Wecker and M. Katter, 1990c, Appl. Phys. Lett. **56**, 587.

Schultz, L., and J. Wecker, 1988, J. Appl. Phys. **64**, 5711.

Schultz, L., K. Schnitzke and J. Wecker, 1987, J. Appl. Phys. **63**, 3583.

Schultz, L., K. Schnitzke and J. Wecker, 1989, J. Magn. & Magn. Mater. **80**, 115.

Schultz, L., K. Schnitzke and J. Wecker, 1990, Appl. Phys. Lett. **56**, 868.

Schultz, L., K. Schnitzke, J. Wecker and M. Katter, 1991, Mater. Sci. Eng. A **133**, 143.

Schwarz, R.B., and W.L. Johnson, 1983, Phys. Rev. Lett. **51**, 415.

Smith, P.A.I., and P.G. McCormick, 1992, Scripta Metall. Mater. **26**, 485.

Smith, P.A.I., P.G. McCormick and R. Street, 1994, in: Proc. 13th Int. Workshop on Rare Earth Magnets and their Applications, University of Birmingham, Publ. 851.

Smith, P.A.I., P.G. McCormick and R. Street, 1995, Mater. Sci. Forum **179–181**, 527–532.

Smith, P.A.I., J. Ding, R. Street and P.G. McCormick, 1996, Scripta Metall. Mater., p. 61.

Spedding, F.H., and B.J. Beaudry, 1971, J. Less-Common Met. **25**, 61.

Takeuchi, J., H. Katsube, I. Hirositsu and T. Ito, 1995, J. Magn. & Magn. Mater. **140–144**, 303.

Thiessen, P.A., K. Meyer and G. Heinicke, 1996, Grundlagen der Tribochemie, Abh. dtsch Akad. Wiss., Kl. Chem. u. Biol., Nr. 1.

Wang, K.Y., Y.Z. Wang, L. Yin, L. Song, X.L. Rao, G.C. Liu and B.P. Hu, 1993, Solid State Commun. **88**, 521.

Wecker, J., M. Katter and L. Schultz, 1991, J. Appl. Phys. **69**, 6058.

Wecker, J., H. Cerva, C. Kuhrt, K. Schnitzke and L. Schultz, 1994, J. Appl. Phys. **76**, 6238.

Weeber, A.W., and H. Bakker, 1988, Physica B **153**, 93.

Yang, H., and P.G. McCormick, 1993, J. Mater. Sci. **28**, 5663.

Yang, H., and P.G. McCormick, 1994, J. Solid State Chem. **110**, 136.

Yang, H., G. Nguyen and P.G. McCormick, 1994, Scripta Metall. Mater. **32**, 681.

Yang, J., Q. Wang, X.K. Sun, G. Zeng, M. Chen, W. Liu, X. Zhao, T. Zhao and Z. Zhang, 1994, J. Magn. & Magn. Mater. **132**, 197.

Yang, Y.C., Q. Pan, B.P. Cheng, X.D. Zhang, Z.X. Liu and Y.X. Sun, 1994, J. Appl. Phys. **76**, 6725.

Zaluski, L., A. Zaluska, P. Tessier, J.O. Ström-Olsen and R. Schulz, 1995, J. Alloys & Compounds **217**, 295.

Handbook on the Physics and Chemistry of Rare Earths
Vol. 24
edited by K.A. Gschneidner, Jr. and L. Eyring

Chapter 161

AMORPHOUS, QUASICRYSTALLINE AND NANOCRYSTALLINE ALLOYS IN AL- AND MG-BASED SYSTEMS

Akihisa INOUE
Institute for Materials Research, Tohoku University, Sendai 980-77, Japan

Contents

List of symbols

a_T	shift factor
C_b	solute concentration
C_b^{min}	minimum solute concentration necessary for amorphous formation
C_p	specific heat
$C_{p,a}$	specific heat of annealed sample
$C_{p,e}$	specific heat of supercooled liquid
$C_{p,q}$	specific heat of as-quenched sample
$C_{p,s}$	specific heat of the sample heated up to glass transition temperature
$C_{p,v}$	vibrational specific heat
ΔC_p	difference in specific heat
$\Delta C_{p,endo}$	difference in specific heat between $C_{p,a}$ and $C_{p,s}$
$\Delta C_{p,max}$	the largest value of the difference between $C_{p,a}$ and $C_{p,s}$
$\Delta C_{p,s\to l}$	difference in specific heat between amorphous solid and supercooled liquid
d_c	critical diameter for amorphous formation
d_r	minimum strain rate for reductilization
E	Young's modulus
E'	storage modulus
E''	loss modulus
E_a	activation energy
e/a	valence electrons per atom
EM	early (group IV–VI) transition metal
H	relaxation spectrum
H_{c2}	superconducting critical magnetic field
ΔH_{endo}	enthalpy of reversible structural relaxation
ΔH_{exo}	heat of irreversible structural relaxation
ΔH_x	heat of crystallization
H_v	Vickers hardness
ΔI	difference of scattering intensity
k_B	Boltzman constant
K_p	wave vector of diffraction peak
LM	late (group VII and VIII) transition metal
m	strain rate sensitivity exponent
N	atomic density
n_e	number of electrons per atom
$N(E_f)$	electronic bare density of states at the Fermi level
$N^*(E_f)$	electronic dressed density of states at the Fermi level
Q	interference function
r	correlation length
R	rare earth metal
R_c	critical cooling rate for amorphous formation
RDF	radial distribution function
R_e	electrical resistance
R_H	Hall coefficient
T_a	annealing temperature
$\tan\delta$	loss tangent
T_c	superconducting transition temperature
TCR	temperature coefficient of resistivity
T_d	deformation temperature
T_e	extrusion temperature
T_g	glass transition temperature
T_g/T_m	reduced glass transition temperature
T_H	heating temperature
T_m	melting temperature
T_r	onset temperature of structural relaxation
T_x	crystallization temperature

ΔT_x	$(= T_x - T_g)$, temperature interval of supercooled liquid region before crystallization	ρ	specific density
		ρ_n	electrical resistivity at normal state
ΔV	volume mismatch of constituent atoms	$\sigma_{0.2}$	tensile yield strength at 0.2% elongation
α	coefficient of thermal expansion	$\sigma_{0.2}/\rho$	specific yield strength at 0.2% elongation
$\varepsilon_{b,f}$	bending fracture strain	σ_B	ultimate tensile strength
$\varepsilon_{c,y}$	compressive yield strain	$\sigma_{c,f}$	compressive fracture strength
ε_p	plastic elongation	σ_f	tensile fracture strength
$\varepsilon_{t,f}$	tensile fracture elongation	σ_f/ρ	specific tensile fracture strength
η	viscosity	σ_H	flow stress at heating temperature
λ	electron–phonon coupling constant	σ_{RT}	electrical resistivity at room temperature
λ_o	critical size factor for amorphous formation	τ	relaxation time
		ϕ	Gaussian distribution
λ_s	atomic size factor	ω	frequency

1. Introduction

Amorphous alloys in the Au–Si system were first synthesized by liquid quenching in 1960, Klement et al. (1960). Since then a great number of amorphous alloys have been prepared in the order of noble-metal-, transition-metal-, refractory-metal- and rare-earth-metal-based systems. Thus, amorphization has been achieved in engineeringly important alloy systems containing Fe, Co, Ni, Cu or Ti as a main component and these alloys have been used commercially because of their good mechanical, physical and chemical properties. In addition to the above-described alloy systems, the search of Al- and Mg-based amorphous alloys has been actively pursued aiming at high-strength materials with low density. The first successful data on the formation of their amorphous alloys exhibiting good ductility and high strength were presented in 1987 for the Al-based alloys and in 1988 for the Mg-based alloys, Inoue et al. (1987a). In the development of new amorphous alloys in the Al- and Mg-based systems, the dissolution of rare earth (R) elements is recognized to play a dominant role in the formation of the amorphous phase as well as in the appearance of interesting properties of the amorphous alloys. This review is intended to summarize the recent progress made on amorphous and quasicrystalline alloys in Al- and Mg-based systems containing R elements, which was achieved mainly by the present author and his co-workers.

2. Al-based amorphous alloys

2.1. *History of aluminum-based amorphous alloys*

The formation of Al-based amorphous alloys by liquid quenching was first tried in binary systems of Al–metalloid and Al–transition-metal (M) alloys. As a result, it was found in

Al–Si (Predecki et al. 1965), Al–Ge (Ramachandrarao et al. 1972) and Al–M (M = Cu) (Davies and Hull 1972), Ni (Chattopadyay et al. 1976), Cr (Furrer and Warlimont 1977) or Pd (Sastry et al. 1978) alloys that a coexistent structure of amorphous and crystalline phases is formed only near the holes in their thin foils prepared by the gun quenching technique in which the cooling rate is higher than that for the melt spinning method. However, no amorphous phase without crystallinity was prepared by the melt spinning method nor by the gun– and piston–anvil methods. The first formation of an amorphous single phase in Al-based alloys containing more than 50 at% Al was found in 1981 for Al–Fe–B and Al–Co–B ternary alloys (Inoue et al. 1981). However, these amorphous alloys are extremely brittle and hence have not attracted strong attention. Subsequently, an amorphous phase was found in melt-spun Al–Fe–Si, Al–Fe–Ge and Al–Mn–Si alloys, but they were also brittle, similar to the Al–(Fe or Co)–B amorphous alloys. It was believed from these data that the brittleness might be an inherent property of Al-based amorphous alloys. However, in 1987, an amorphous phase with good bending ductility was discovered by Inoue et al. (1987a) being formed at compositions above about 80 at% Al in Al–Ni–Si and Al–Ni–Ge systems. Since the discovery, ductile Al-based amorphous alloys have successively been found in a number of ternary alloys consisting of Al–early transition metal–late transition metal (Al–EM–LM) (Tsai et al. 1988a,b), which are exemplified for Al–Zr–Cu, Al–Zr–Ni and Al–Nb–Ni. These were followed by Al–rare earth metal–late transition metal (Al–R–LM) ternary alloys (Inoue et al. 1988a,b) in which the EM is substituted by R, and then Al–R binary alloys without M elements (Inoue et al. 1988c,d, 1989a). A review on the formation, structure and properties of Al-based amorphous alloys will be described in the order of the metal–metalloid type system of Al–M–(Si or Ge) alloys and the metal–metal type system of Al–EM–LM, Al–R and Al–R–LM alloys.

2.2. *Metal–metalloid amorphous alloys*

2.2.1. *Formation ranges (Inoue et al. 1987a, 1988e)*

A mostly single amorphous phase defined by no trace of crystallinity in the X-ray diffraction pattern was formed in Al–Si–M (M = Cr, Mo, Mn, Fe, Co or Ni) and Al–Ge–M (M = V, Cr, Mo, Mn, Fe, Co or Ni) systems. No amorphous phase was formed in Al–Si–M systems with M = Ti, Zr, Hf, V, Nb, Ta, W or Cu and Al–Ge–M systems with M = Ti,Zr, Hf, Nb, Ta, W or Cu. Figure 1 shows the compositional ranges of Al–Si–M and Al–Ge–M amorphous alloys. Their amorphous phases are formed in the range 12 to 42 at% Si and 8 to 23 at% M for Al–Si–M alloys and 12 to 53 at% Ge and 8 to 23 at% M for Al–Ge–M alloys. The formation range of the Al–Si–M amorphous alloys is the widest for Al–Si–Co, followed by Al–Si–Fe, Al–Si–Mn, Al–Si–Ni and Al–Si–Cr, and that for the Al–Ge–M amorphous alloys is the widest for Al–Ge–Fe and becomes narrower in the order of Al–Ge–Co, Al–Ge–Cr, Al–Ge–V and Al–Ge–Mn. The amorphous phase is also formed in the Al–Si–V system, but it is always coexistent with a crystalline phase. Although the compositional ranges of the amorphous phase are almost the same between Al–Si–M and Al–Ge–M systems, one can notice a difference in that the metalloid concentration ranges

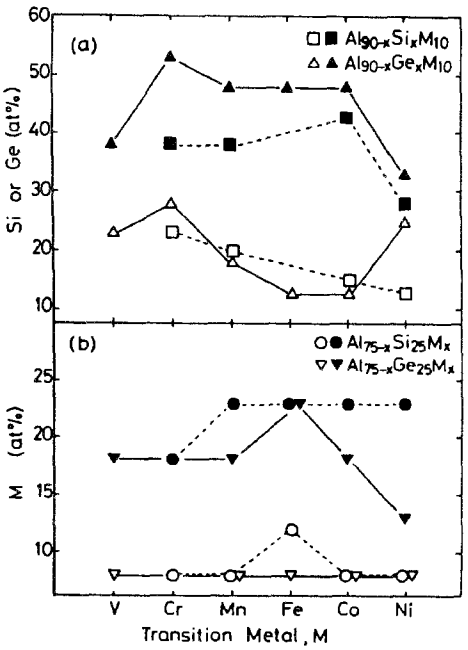

Fig. 1. Composition ranges for formation of an amorphous phase in melt-spun (a) Al_{90-x}(Si or Ge)$_xM_{10}$ and (b) Al_{75-x}(Si or Ge)$_{25}M_x$ (M = V, Cr, Mn, Fe, Co or Ni) alloys. The open and solid symbols represent the minimum and maximum concentrations, respectively, of M to form the amorphous phase.

are considerably wider for Al–Ge–M than for Al–Si–M and the M concentration range is wider for Al–Si–M.

It is generally known, see e.g. Davies (1983), that the formation of an amorphous alloy is easier at an eutectic composition with a lower melting temperature. No equilibrium phase diagrams of Al–Si–M and Al–Ge–M alloys are available over the present wide composition ranges. The eutectic compositions of Al–Si and Al–Ge binary alloys are 11.3 at% Si and 30.3 at% Ge, respectively, (Massalski 1986), which is significantly different. The metalloid concentration at which the amorphous phase is formed lies in the range 12–3 at% Ge and 12–2 at% Si. This indicates that the formation range extends over both sides of the eutectic composition of Al–Ge for the Al–Ge–M system and only on the hypereutectic side of Al–Si for the Al–Si–M system. Thus, lowering of the melting temperature (T_m) at a eutectic point is not thought to be a dominant factor for the amorphization of Al–Si–M and Al–Ge–M alloys. On the other hand, the M content for glass formation is in the range 8 to 23 at%, where various kinds of intermetallic compounds are formed in Al–M binary alloys, and T_m is in the range 1533 to 1921 K, Massalski (1986). The limitation of the M content is probably due to the increase of T_m on the upper side and the decrease of the attractive bonding nature of Al and M atoms for glass formation on the lower side. In any case, the new information that an amorphous single phase is formed over wide composition ranges in Al–Si–M and Al–Ge–M alloys containing a large amount of Si or Ge without an attractive interaction with Al is different from the general concept, Davies (1983), for the glass formation of metal–metalloid type

alloys. The abnormality is expected to result in the appearance of significantly different structure and properties.

2.2.2. *Amorphous structure (Inoue et al. 1987a,b)*

Figure 2 shows a bright-field electron micrograph (a) and a selected-area diffraction pattern (b) taken from an electrolytically thinned $Al_{50}Ge_{40}Mn_{10}$ amorphous alloy, along with the X-ray diffraction pattern of the same alloy not subjected to the thinning treatment. The lack of contrast characteristic of a crystalline phase in the bright-field image (a), and the broad diffuse haloes in the electron and X-ray diffraction patterns (b) and (c) clearly indicate the formation of an amorphous structure with no trace of crystallinity. The magnitude of the scattering vector defined by $k = 4\pi \sin\theta/\lambda$ at the two peaks of the X-ray diffractograms, K_p, was measured to be 23.58 and 31.48 nm^{-1}. From the K_p values and the atomic scattering amplitude of each constituent element – Al, Ge and Mn – the two K_p values of the Al–Ge–Mn alloy are analyzed to originate from the Al–Ge interaction for the low-angle halo and from the Ge–Ge, Al–Mn, and Mn–Mn interactions for the high-angle halo. The two split haloes in the X-ray and electron diffraction patterns were observed for all amorphous alloys in the Al–Si–M and Al–Ge–M (M = V, Cr, Mo, Mn, Fe, Co or Ni) systems.

Figure 3 shows a bright-field electron micrograph and a selected-area diffraction pattern of an $Al_{50}Ge_{40}Mn_{10}$ amorphous alloy annealed for 10 min at 520 K with an internal energy lower by about 1.8 kJ/mol as compared with the as-quenched amorphous phase.

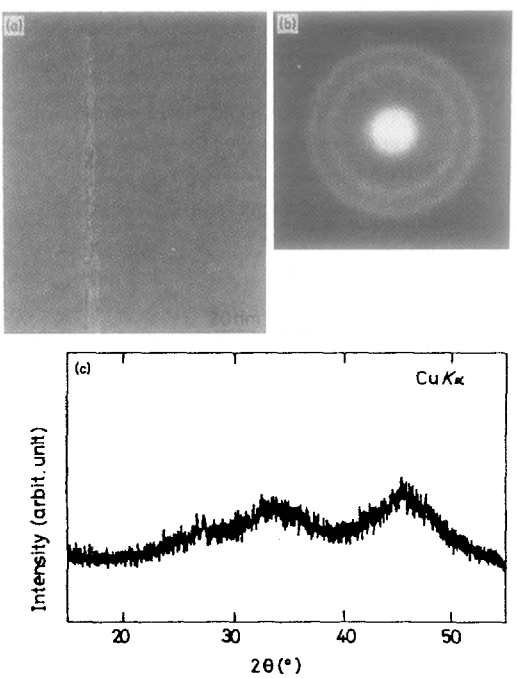

Fig. 2. (a) Bright-field electron micrograph, (b) selected-area electron diffraction pattern and (c) X-ray diffraction pattern of melt-spun $Al_{50}Ge_{40}Mn_{10}$ alloy.

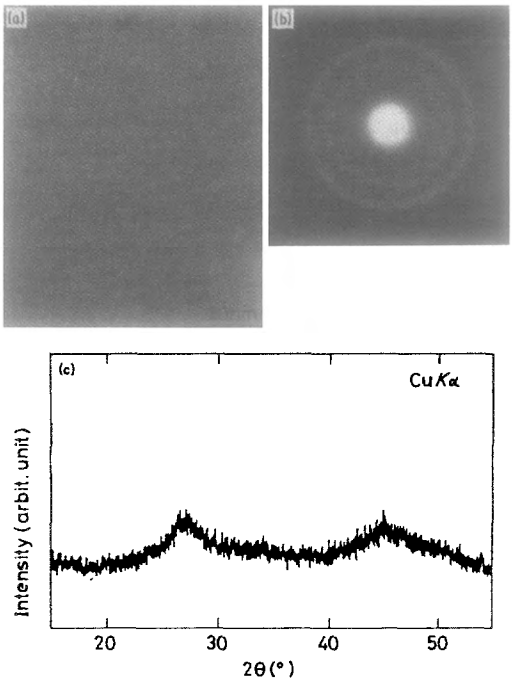

Fig. 3. (a) Bright-field electron micrograph, (b) selected-area electron diffraction pattern and (c) X-ray diffraction pattern of amorphous $Al_{50}Ge_{40}Mn_{10}$ alloy annealed for 600 s at 520 K.

No change in the contrast revealing the precipitation of a crystalline phase is seen in the bright-field micrograph (a) even after annealing for 10 min at 520 K, while significant changes can be seen in the electron and X-ray diffraction patterns (b) and (c). The changes are summarized as follows: (1) the broad peak at the low diffraction angle corresponding to $K_p = 23.58\,nm^{-1}$ decreases significantly and the high-angle diffraction peak at $K_p = 31.48\,nm^{-1}$ becomes broad; (2) a new broad peak appears at a low diffraction angle corresponding to $K_p = 18.77\,nm^{-1}$.

Considering the significant decrease in the low-angle peak at $K_p = 23.58\,nm^{-1}$ resulting from the Al–Ge interaction and the broadening of the high-angle peak resulting from the Ge–Ge and Al–Mn interactions, the structural relaxation upon heating at 520 K for 10 min appears to occur through a decrease in the number of Al–Ge pairs with a weak bonding nature and an increase in the number of Ge–Ge and Al–Mn pairs with a strong bonding nature. The development of the compositional short-range ordering of a Ge–Ge pair is also supported from the results obtained from anomalous X-ray scattering profiles at the Ni and Ge K-edges of the amorphous $Al_{60}Ge_{30}Ni_{10}$ alloy. The weak bonding nature of Al–Ge atoms and the strong bonding nature of Ge–Ge and Al–Mn atoms are presumed from the equilibrium phase diagrams of Al–Ge with a wholly insoluble type of solid, and Al–Mn with many intermetallic compounds, Massalski (1986), and a covalent-type bonding of the Ge semiconductor. Furthermore, the new appearance of a small-angle peak at $K_p = 18.77\,nm^{-1}$ suggests that the compositional short-range ordering consisting of Ge–Ge pairs with the strongest bonding force among the three constituent atoms

developed on the scale of 0.3 to 0.4 nm. It has been shown by Inoue et al. (1987b) that the irreversible structural change is accompanied by an exothermic heat of 1.8 kJ/mol upon continuous heating up to 570 K. Accordingly, the relaxation is presumably due to the local rearrangement of the constituent atoms leading to the development of compositional short-range ordering consisting of Ge–Ge and Al–Mn pairs with a weak bonding nature, in addition to the annihilation of various kinds of quenched-in "defects". As is demonstrated above, by using an Al-based alloy with an appropriate composition, it is possible, even by conventional X-ray diffractometry, to examine the annealing-induced change in the fraction of each pair of Al–M, Al–metalloid and metalloid–metalloid and the degree of compositional short-range ordering.

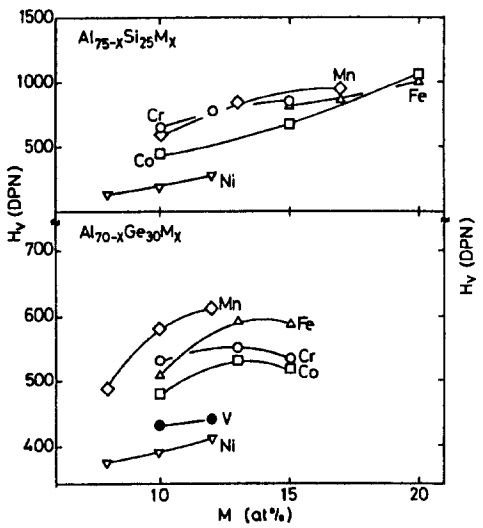

Fig. 4. Change in Vickers hardness (H_v) of Al–Si–M and Al–Ge–M (M = Cr, Mn, Fe, Co or Ni) amorphous alloys with M content.

2.2.3. *Hardness (Inoue et al. 1987a, 1988e)*

Figure 4 shows the change of Vickers hardness, H_v, as a function of M content for Al–Si–M (M = Cr, Mn, Fe, Co or Ni) and Al–Ge–M (M = Cr, Fe or Co) amorphous alloys with 25% Si and 30% Ge. H_v has a distinct M concentration dependence and increases with increasing M content from 365 to 600 at 10% M to 730 to 1120 at 20% M. The compositional dependence of H_v is similar in the Al–Si–M and Al–Ge–M alloys. Figure 4 also shows that the H_v values of Al–Si–M and Al–Ge–M alloys are higher for the alloys with M = Cr, Mn or Fe than for the alloys with M = Ni or V and there is no appreciable difference in H_v between the alloys with M = Cr, Mn or Fe. The H_v values at 20% M may be as high as 700 to 1100 even for Al-based alloys, comparable to the high H_v values of Dubois et al. (1985) for M–metalloid type amorphous alloys. Figure 5 shows the change of H_v as a function of Si content for Al–Si–M amorphous alloys with a constant M content

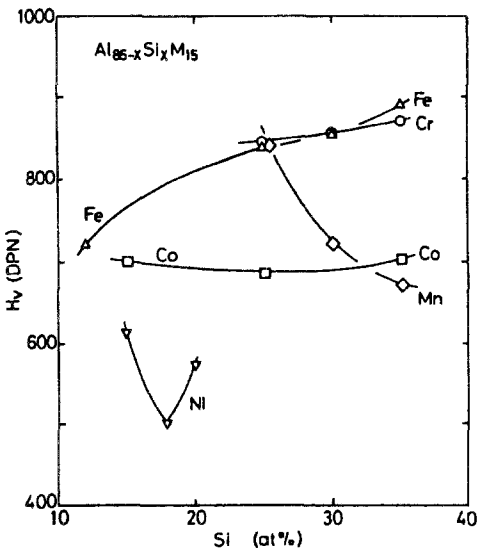

Fig. 5. Change in H_v of Al–Si–M (M = Cr, Mn, Fe, Co or Ni) amorphous alloys with Si content.

of 15%. No distinct metalloid compositional dependence was observed for the Al–Ge–M alloys. Thus, the replacement of Al by M gives rise to a significant increase in H_v for all the alloy systems, whereas the increase in H_v by the replacement of Al by Si or Ge is less significant except for Al–Si–M with M = Mn and Fe. The bonding nature of the constituent atoms in Al–Si(or Ge)–M alloys increases in the order M–(Si or Ge) > Al–M > Al–(Si or Ge) as can be seen from the fact that T_m (Massalski 1986) and H_v (Voisin and Pasturel 1987) are larger for M–(Si or Ge) compounds than for Al–M compounds and no compound is formed in Al–(Si or Ge) alloys (Massalski 1986). Accordingly, an increase in M content is presumed to bring about an increase in H_v of the amorphous alloys, consistent with the results shown in figs. 4 and 5.

2.2.4. *Crystallization temperature (T_x)*

T_x also shows a similar compositional dependence as that for H_v. As shown in fig. 6, as the M content increases from 8 to 20%, T_x increases from 498 to 715 K for Al–Si–(Cr, Mn, Fe or Co) alloys and from 370 to 575 K for Al–Si–Ni alloys. On the other hand, the increase in T_x of Al–Ge–M alloys with increasing M content is considerably smaller than that of Al–Si–M alloys, and the increase of T_x with increasing M content from 8 to 15% is as small as about 50 K. Furthermore, T_x is higher by 50 to 150 K for Al–Si–M alloys than for Al–Ge–M alloys. This difference is probably because the eutectic temperature of the Al–Si alloy is higher by 153 K than that of the Al–Ge alloy, Massalski (1986). The T_x values of Al–Si–M alloys are considerably higher for Al–Si–(Cr, Mn, Fe or Co) alloys than for Al–Si–Ni and the Al–Si–M (M = Cr, Mn, Fe or Co) alloys have nearly the same T_x values. No distinct change in T_x with Si and Ge content is observed as shown in fig. 7. Thus, the H_v and T_x of Al–Si–M and Al–Ge–M amorphous

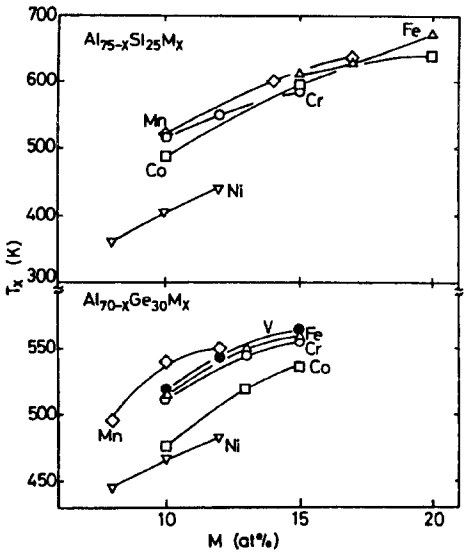

Fig. 6. Change in crystallization temperature (T_x) of Al–Si–M and Al–Ge–M (M = Cr, Mn, Fe, Co or Ni) amorphous alloys with M content.

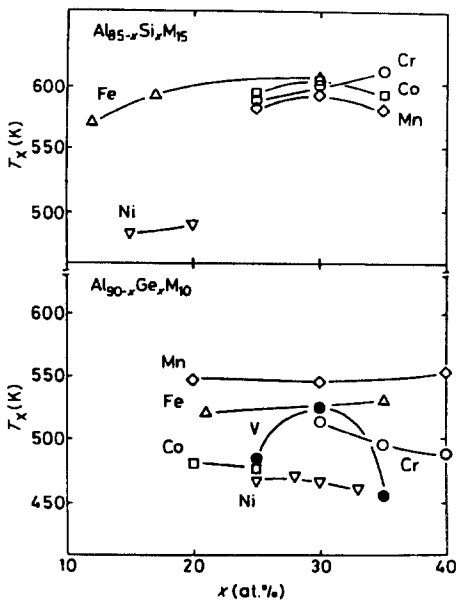

Fig. 7. Change in T_x of Al–Si–M and Al–Ge–M (M = Cr, Mn, Fe, Co or Ni) amorphous alloys with Si or Ge content.

alloys increase significantly with the increase in the amount of Al replaced by M, while they do not change as a function of Si or Ge content. Such compositional dependences probably occur because an increasing M content results in an increase in the number of M–(Si or Ge) bonds with strongly attractive interaction and a decrease in the number of Al–(Si or Ge) bonds with repulsive interaction. On the other hand, an increase in Si or Ge content does not cause a change in the number of M–(Si or Ge) bonds. Such a change as a function of metalloid content is significantly different from the general tendency (Dubois et al. 1985) that H_v and T_x of M–metalloid amorphous alloys increase with increasing metalloid content. This significant difference is interpreted as due to the difference of the bonding nature between M–(Si or Ge) atoms with strongly attractive interaction and Al–(Si or Ge) with repulsive interaction. Thus, it is said that the interaction of the constituent atoms for Al-based amorphous alloys is significantly different from that for M–metalloid type amorphous alloys reported previously, though the alloy compositions belong to the same category of metal–metalloid types.

2.2.5. *Ductility and tensile strength (Inoue et al. 1987a, 1988e)*

The Al–Si–Ni and Al–Ge–Ni amorphous alloys containing less than about 15% Ni were found to exhibit a good ductility which is shown by a 180° bending without fracture. No ductile amorphous samples were obtained at the other alloy compositions in Al–(Si or Ge)–Ni systems and in the other alloy systems. Thus, the ductility is significantly

Table 1
Mechanical properties, thermal stability and electrical properties for Al–Si–Ni and Al–Ge–Ni amorphous alloys

Alloy (at%)	Ductility	σ_f (MPa)	ε_f (%)	H_v (DPN)	T_a (K)	ΔH^* (kJ mol^{-1})	ρ_{293} ($\mu\Omega$ cm)	TCR at 293 K (K^{-1})
$Al_{75}Si_{15}Ni_{10}$	Ductile	440	1.4	370	465	2.80	150	–
$Al_{70}Si_{20}Ni_{10}$	Ductile	375	1.2	295	400	2.95	170	-2.65×10^{-4}
$Al_{65}Si_{25}Ni_{10}$	Ductile	–	–	265	405	3.60	300	-3.58×10^{-4}
$Al_{70}Si_{15}Ni_{15}$	Brittle	–	–	610	510	2.90	230	–
$Al_{68}Si_{17}Ni_{15}$	Brittle	–	–	485	500	3.25	410	–
$Al_{65}Si_{20}Ni_{15}$	Brittle	–	–	570	505	3.20	660	–
$Al_{68}Si_{20}Ni_{12}$	Ductile	–	–	435	440	2.90	340	–
$Al_{65}Ge_{25}Ni_{10}$	Ductile	–	–	385	460	1.80	440	-1.10×10^{-3}
$Al_{60}Ge_{30}Ni_{10}$	Brittle	–	–	390	470	1.70	1030	-2.06×10^{-3}

dependent on the kind and concentration of M elements. The reason for such a good ductility only for Al–Si–Ni and Al–Ge–Ni amorphous alloys is presumably because the bonding nature of Ni–Al, Ni–Si or Ni–Ge pairs is the weakest among the bonds of M (M = Cr, Mn, Fe, Co or Ni) and Al, Si or Ge atoms. The results and discussion above are also consistent with the present presumption that the attractive bondings of M–Al, M–Si or M–Ge pairs play a dominant part in the glass formation.

Table 1 summarizes the bending ductility, tensile fracture strength (σ_f), tensile fracture elongation (ε_f), H_v, T_x, heat of crystallization (ΔH_x), electrical resistivity at 293 K (ρ_{293}) and temperature coefficient of resistivity (TCR) of the Al–Si–Ni and Al–Ge–Ni amorphous alloys. The terms ductile and brittle distinguish the success and failure in bending through 180°. Although σ_f and ΔH_x are of the same order as those of conventional amorphous alloys (Voisin and Pasturel 1987), σ_f, H_v and T_x are rather low, presumably because of the weak bonding nature among the constituent atoms in Al-rich alloys and the low values of T_m, strength and hardness of Al itself. Furthermore, it is seen in table 1 that ρ_{293} and the magnitude of TCR increase with decreasing Al content.

2.2.6. *Electrical resistivity (Inoue et al. 1987a, 1988e)*

Figures 8 and 9 show the change of electrical resistivity at room temperature (RT), ρ_{RT}, for Al–Si–M amorphous alloys with M and Si content. The ρ_{RT} increases significantly with increasing M and Si content and the increase is more remarkable for the increase in M. The ρ_{RT} values lie in the range 220 to 1760 $\mu\Omega$ cm which are two to six times higher than those (100 to 300 $\mu\Omega$ cm, Rao 1983) for M-based amorphous alloys. A similar metalloid composition dependence of ρ_{RT} has also been recognized in $Al_{90-x}Ge_xM_{10}$ amorphous alloys by Inoue et al. (1988e). The ρ_{RT} increases significantly from 500 to 850 $\mu\Omega$ cm at 20% Ge to 860 to 1940 $\mu\Omega$ cm at 40% Ge. Although the increase in ρ_{RT} with increasing Si or Ge content can be interpreted by taking the semiconducting nature of Si and Ge into

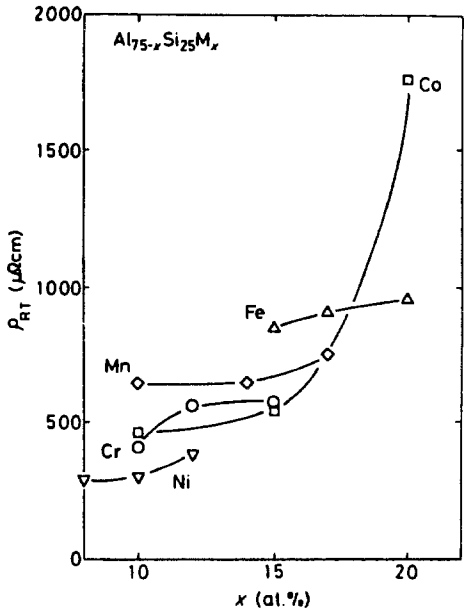

Fig. 8. Change in electrical resistivity at room temperature (ρ_{RT}) of $Al_{75-x}Si_{25}M_x$ (M = Cr, Mn, Fe, Co or Ni) amorphous alloys with M content.

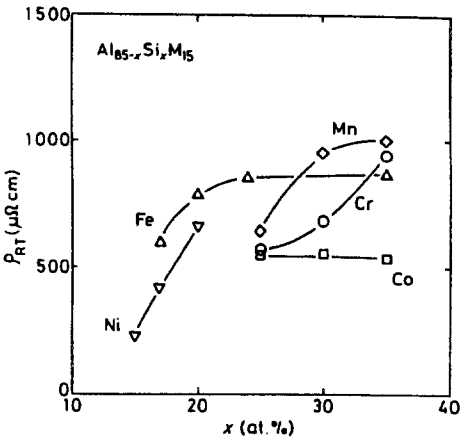

Fig. 9. Change in ρ_{RT} of $Al_{85-x}Si_xM_{15}$ (M = Cr, Mn, Fe, Co or Ni) amorphous alloys with Si content.

consideration, the increase in ρ_{RT} with increasing M and Si or Ge content is also thought to be related to the anomalous structure of the Al-based amorphous alloys. That is, as exemplified in figs. 2 and 3, the X-ray and electron diffraction patterns of the Al–Si–M and Al–Ge–M amorphous alloys show split first halo peaks, this split is thought to be due to the phase separation into Al-rich and Si- or Ge-rich phases over a short range (Inoue et al. 1987a,b), i.e., the sites of Al and Si or Ge atoms in the amorphous structure are not random but are distributed at distinguishable sites on a scale of about 1 nm. It has been clarified by Inoue et al. (1987b) that the splitting phenomenon becomes significant with increasing M content. The split structure on a scale of about 1 nm is presumed to result in a much higher ρ_{RT} than that of amorphous alloys with a homogeneously single structure.

Finally, the effect of M elements on the T_x, H_v and ρ_{RT} values of Al–Si–M and Al–Ge–M amorphous alloys is summarized in figs. 10 and 11. T_x and H_v show a similar change; both values are the highest for alloys containing Cr, Mn and Fe and tend to decrease with decreasing group number in the periodic table. The systematic change as a function of the group number is interpreted as due to the bonding nature of M–Al, M–Si and M–Ge atomic pairs being stronger for the group VI and VII elements. Additionally, the compositional effect of ρ_{RT} is thought to reflect that the number of conductive free electrons in the outer d-shell which do not contribute to the covalent bonding of M–Al, M–Si and M–Ge pairs is smaller for M = Cr and Mn and the hybridization between the d-band of the transition metal M and the s- and p-bands of Al is stronger for M = Cr and Mn (Voisin and Pasturel 1987).

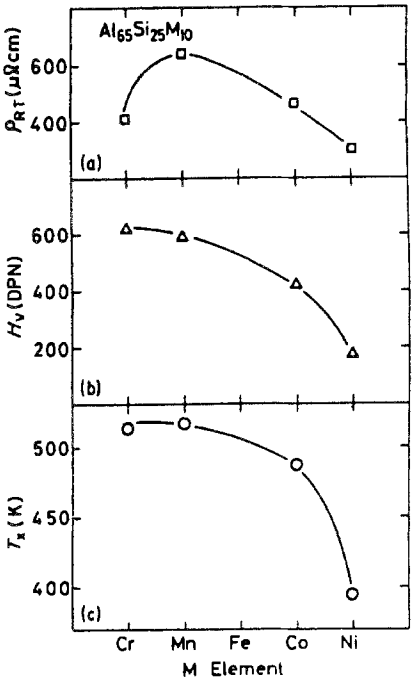

Fig. 10. Changes in ρ_{RT}, H_v and T_x of Al–Si–M amorphous alloys with the period group number of the M metals.

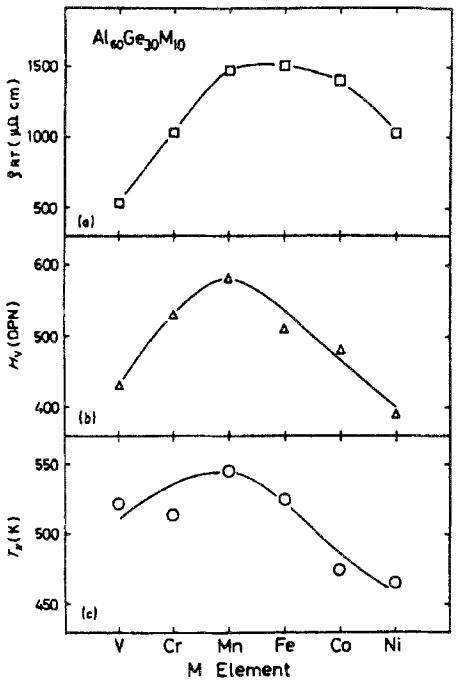

Fig. 11. Changes in ρ_{RT}, H_v and T_x of Al–Ge–M amorphous alloys with the period group number of the M metals.

2.3. *Al–EM–LM amorphous alloys*

2.3.1. *Amorphous alloy systems (Tsai et al. 1988a,b)*

Figure 12 shows the effect of EM (EM = Ti, Zr, Hf, V, Nb, Ta, Cr, Mo or W) elements on the glass formation of $Al_{70}Fe_{20}M_{10}$, $Al_{70}Co_{20}M_{10}$, $Al_{70}Ni_{20}M_{10}$ and $Al_{70}Cu_{20}M_{10}$ alloys by melt spinning. The effectiveness of the M elements to form an amorphous phase is greatest for Zr and Hf and decreases in the order of Ti > V > Mo > Nb > Cr > Ta. No amorphous phase was observed in the Al-based alloys containing W. Thus, alloys are composed of the LM of Fe, Co, Ni and Cu, and the EM of Ti, Zr, Hf etc., and Al can form metal–metal type Al-based amorphous structures. It is also noteworthy that the

M	Ti	Zr	Hf	V	Nb	Ta	Cr	Mo	W
$Al_{70}Fe_{20}M_{10}$	●	○	○	●	●	●	●	●	●
$Al_{70}Co_{20}M_{10}$	○	○	○	●	●	●	●	●	●
$Al_{70}Ni_{20}M_{10}$	○	○	○	○	○	◑	◑	○	●
$Al_{70}Cu_{20}M_{10}$	◑	○	○	○	●	●	◑	○	●

○ Amorphous ◑ Amorphous + crystalline ● Crystalline

Fig. 12. Effect of the early transition M metals on the glass formation of $Al_{70}Fe_{20}M_{10}$, $Al_{70}Co_{20}M_{10}$, $Al_{70}Ni_{20}M_{10}$ and $Al_{70}Cu_{20}M_{10}$ (M = Ti, Zr, Hf, V, Nb, Ta, Cr, Mo or W) alloys by melt spinning.

formation of the amorphous alloys extends over rather wide compositional ranges around the $Al_7(LM)_2(EM)_1$ compositions. For instance, the formation range extends from 5 to 35% Cu and 5 to 15% V for the Al–Cu–V system (Tsai et al. 1988c) and from 10 to 30% Ni and 5 to 20% Zr for the Al–Ni–Zr systems (Tsai et al. 1988b).

The reason for the glass formation of the metal–metal type Al-based alloys is briefly discussed. The amorphous alloys are composed of Al, LM and EM. Furthermore, most of the binary alloys consisting of LM and EM except Al can be amorphized by melt spinning as exemplified for Fe–(Zr or Hf), Co–(Ti, Zr or Hf), Ni–(Ti, Zr or Hf) and Cu–(Zr or Hf), e.g., see Davies (1983). It is generally known (Davies, 1983) that the amorphization of alloys is closely related to the ratio T_g/T_m and the larger the ratio the higher is the glass-forming tendency. Although the T_m of Al–Cu alloys decreases with increasing Cu content in the range below 17.3%, the T_m of the other Al–M binary alloys rises rapidly with increasing M content (Massalski 1986). However, in the presence of LM and EM, the rise in T_m of Al-based ternary alloys is thought to be significantly depressed because many eutectic points exist in the binary alloys of LM and EM (Massalski 1986). In addition, a number of intermetallic compounds are formed in Al–M alloys as well as in EM–LM alloys (Massalski 1986). It is therefore presumed that the attractive interaction among the constituent elements is significantly enhanced by adding EM to Al–LM binary alloys, leading to an increase of the viscosity of the supercooled liquid and its temperature dependence which causes the enhancement of glass formation. The decrease of T_m and the increase of the attractive interaction among the constituent elements caused by the coexistence of Al, LM and EM appear to be dominant factors for the amorphization of the present metal–metal type amorphous alloys. On the other hand, the reason why no amorphization was observed in alloy systems such as Al–(Fe, Co, Ni or Cu)–W and Al–(Fe or Co)–(V, Nb, Ta, Cr, Mo or W) etc. is probably due to the weak attractive interaction between LM and EM, as is evidenced from the existence of a wide solid solubility range in the binary alloys of LM and EM (Massalski 1986).

2.3.2. *Thermal stability and hardness*

Figures 13 and 14 show the changes in T_x, ΔH_x and H_v of the amorphous $Al_{70}Fe_{20}M_{10}$, $Al_{70}Co_{20}M_{10}$, $Al_{70}Ni_{20}M_{10}$ and $Al_{70}Cu_{20}M_{10}$ (M = Ti, Zr, Hf, V, Nb or Mo) alloys with M elements. Considering the $Al_{70}Ni_{20}M_{10}$ alloys where amorphization is achieved for various kinds of M elements, the values of T_x, ΔH_x and H_v in the same group tend to increase with increasing atomic number while no systematic change in these values with group number is observed. Additionally, T_x and H_v decrease in the order of Fe > Co > Ni > Cu in $Al_{70}Fe_{20}M_{10}$, $Al_{70}Co_{20}M_{10}$, $Al_{70}Ni_{20}M_{10}$ and $Al_{70}Cu_{20}M_{10}$ amorphous alloys, suggesting that the bonding nature between Fe, Co, Ni or Cu and the other constituent elements decreases in the same order. This order agrees with the result (Massalski 1986) that the T_m of Al-rich Al–EM and Al–LM compounds and EM–LM compounds decrease in the order of Fe > Co > Ni > Cu. The highest values of T_x and H_v reach 825 K and 900, respectively, for $Al_{70}Fe_{20}Hf_{10}$, which is comparable to those reported by Inoue et al. (1988f) for Fe-, Co- and Ni-based amorphous alloys.

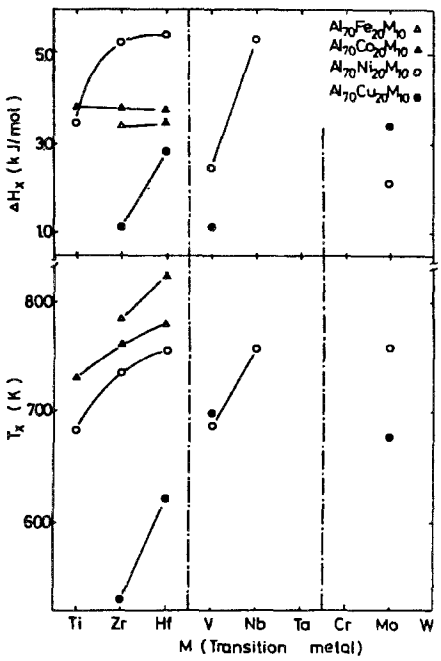

Fig. 13. Changes in T_x and heat of crystallization (ΔH_x) of $Al_{70}Fe_{20}M_{10}$, $Al_{70}Co_{20}M_{10}$, $Al_{70}Ni_{20}M_{10}$ and $Al_{70}Cu_{20}M_{10}$ amorphous alloys with early transition M metals.

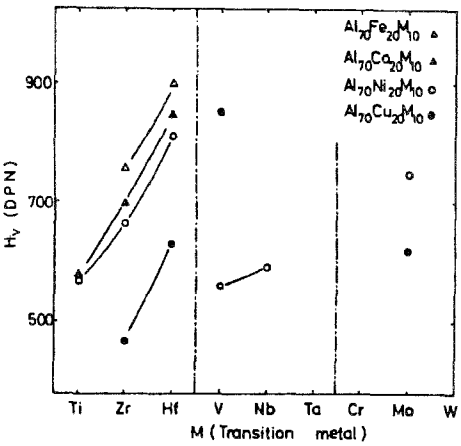

Fig. 14. Change in H_v of $Al_{70}Fe_{20}M_{10}$, $Al_{70}Co_{20}M_{10}$, $Al_{70}Ni_{20}M_{10}$ and $Al_{70}Cu_{20}M_{10}$ amorphous alloys with early transition M metals.

2.3.3. *Tensile strength*

Amongst Al–EM–LM amorphous alloys, the Al–Ni–Zr and Al–Ni–Hf alloys are alloy systems with high glass-forming capacity and their easy amorphization enabled us to examine the compositional dependence of σ_f and Young's modulus (E). As an example, fig. 15 shows the compositional range in which the amorphous Al–Ni–Zr phase is formed by melt spinning, along with the data of T_x and the bending ductility of the amorphous alloys. Glass formation occurs in the range of 8 to 32% Ni and 3 to 18% Zr. The amorphous alloys containing more than about 80% Al can be completely bent through 180° without fracture and no appreciable cracking is observed even at the severely deformed area. The ductility of Al–Ni–Zr amorphous alloys is strongly dependent on the alloy composition and there is a clear tendency that the higher the Al content the higher is the ductility. On the other hand, T_x increases with decreasing Al content and shows the highest value (790 K) at 30% Ni and 10% Zr.

The σ_f, E, H_v and T_x of Al–Ni–Zr and Al–Ni–Hf amorphous alloys are summarized in table 2. The data of tensile fracture strain ($\varepsilon_f = \sigma_f/E$) and compressive yield strain ($\varepsilon_y \equiv 9.8H_v/3E$) are based on the fact that amorphous alloys exhibit little work-hardening and thus the compressive yield strength is related by $\sigma_y \equiv 9.8H_v/3$ Chen et al. (1975). It can be seen in the table that the decrease in Al content gives rise to an increase from 580 to 800 MPa for σ_f, 50 to 80 GPa for E, 2740 to 3330 MPa for H_v and 452 to 515 K for T_x, indicating a similar compositional dependence in σ_f, E, H_v and T_x. Additionally, fig. 16 shows the correlation between E and the properties T_x, σ_f and H_v

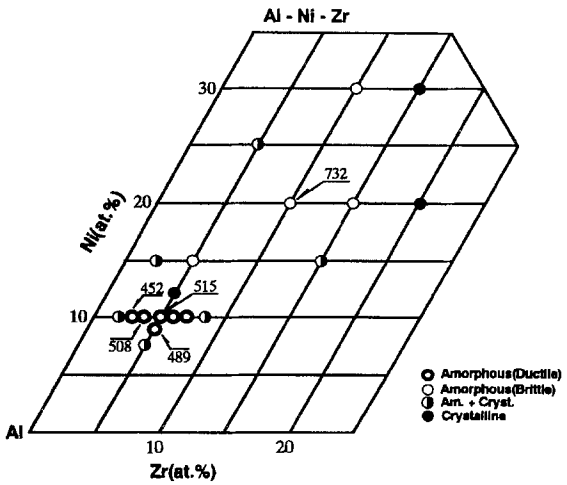

Fig. 15. Composition range and T_x in melt-spun Al–Ni–Zr alloys.

Table 2
Mechanical properties, thermal stability and electrical resistivity of Al–Ni–Zr, Al–Ni–Hf and Al–Ni–Nb amorphous alloys

Alloy (at%)	T_x (K)	σ_f (MPa)	E (MPa)	H_v (DPN)	$\rho_{R.T.}$ ($\mu\Omega$ cm)	$1/\rho_{R.T.}$ ($d\rho/dT$) (K^{-1})
$Al_{87}Zr_3Ni_{10}$	452	580	50000	280	–	–
$Al_{86}Zr_4Ni_{10}$	508	680	65700	330	340	5.23×10^{-5}
$Al_{86}Zr_5Ni_9$	489	750	72500	300	200	0.74×10^{-5}
$Al_{85}Zr_5Ni_{10}$	515	800	80400	340	460	0.97×10^{-5}
$Al_{85}Hf_5Ni_{10}$	560	730	75800	350	380	3.25×10^{-5}
$Al_{85}Nb_5Ni_{10}$	460	–	–	280	280	0.43×10^{-5}

for Al–Ni–Zr amorphous alloys. The three properties T_x, σ_f and H_v tend to increase with increasing E: the correlation between E and σ_f or H_v can be empirically expressed by the following approximate equations: $\varepsilon_f = \sigma_f/E \equiv 0.011$ and $\varepsilon_y \equiv 9.8H_v/3E \equiv 0.015$. The fracture behavior for Al–Ni–Zr amorphous alloys is the same as that reported previously (Masumoto and Maddin 1971) for other ductile amorphous alloys.

2.3.4. *Electronic properties*

The electrical resistivity of ductile Al–Ni–Zr and Al–Ni–Hf amorphous alloys falls in the range 200 to 460 $\mu\Omega$ cm at room temperature and decreases almost linearly only by about 0.5 to 3.5% with decreasing temperature to 4.2 K. A further decrease in temperature gives rise to the appearance of superconductivity at 2.05 K for the $Al_{87}Ni_{10}Zr_3$ alloy. The temperature gradient of the upper critical magnetic field H_{c2} near T_c is 0.20 T/K.

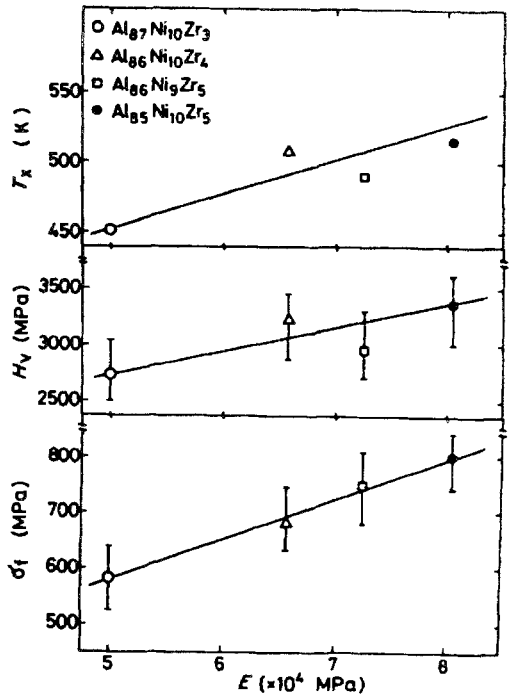

Fig. 16. Correlation between Young's modulus (E) and T_x, tensile fracture strength (σ_f) or H_v for Al–Ni–Zr amorphous alloys.

The gradient value is about one-tenth as large as that (about 2.0 T/K) (Johnson 1978 and Inoue et al. 1981) for amorphous superconductors in Zr-, Nb- and Mo-based alloys. This significant difference is thought to reflect the difference in electrons contributing to superconductivity, i.e., heavy d-electrons for the M-based amorphous alloys and s- and p-electrons for the Al-based amorphous alloys.

2.4. *Al–rare earth metal (Al–R) amorphous alloys*

2.4.1. *Formation ranges (Inoue et al. 1988c,d, 1989a)*

Figure 17 shows the compositional dependence of the as-quenched phase in the Al–R (R = Y, La, Ce, Pr, Nd, Sm, Gd, Tb, Dy, Ho, Er or Yb) binary systems. The amorphous phase is formed in the compositional ranges 9 to 13% Y, 7 to 11% La or Ce, 10% Pr, 8 to 12% Nd or Gd, 8 to 16% Sm, 9 to 14% Tb and 9 to 12% of Dy, Ho, Er or Yb. Thus, the glass formation range is the widest for Al–Sm, followed by Al–Tb, Al–(Y, Nd or Gd), Al–(La, Ce, Dy, Ho, Er or Yb) and then Al–Pr. Furthermore, a supersaturated fcc solid solution is formed in the concentration ranges below the glass formation ranges instead of an equilibrium mixture of fcc Al and intermetallic Al–Ln compounds. In the concentration range about 1 at% higher than the glass formation range, the quenching-induced phases are amorphous plus unidentified x-phases in almost all the Al–R systems. A further

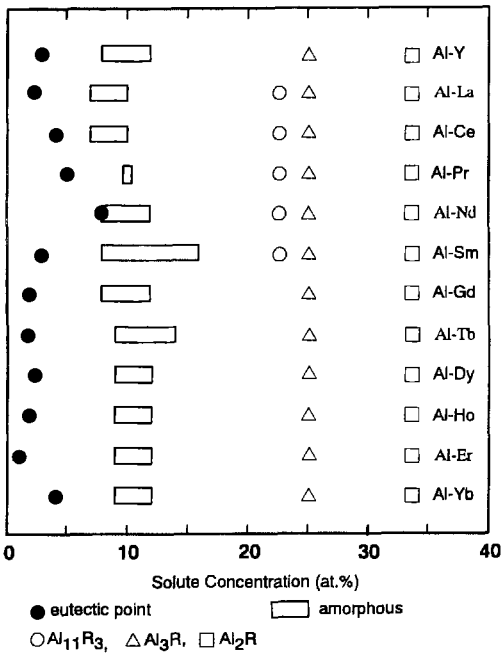

Fig. 17. Compositional dependence of structure in melt-spun Al–R (R = Y, La, Ce, Pr, Nd, Sm, Gd, Tb, Dy, Ho, Er or Yb) binary alloys.

increase of the solute concentration gives rise to the formation of equilibrium phases of either Al plus $Al_{11}R_3$ or Al plus Al_3R.

Figure 18 shows the relation between the glass formation range and the equilibrium phase diagram (Massalski 1986) for Al–R binary alloys. Except for the Al–Nd system the glass formation ranges lie in the composition range between a eutectic point and $Al_{11}R_3$ (R = La, Ce, Pr, Nd or Sm) or Al_3R (R = Y, Gd, Tb, Dy, Ho, Er or Yb) compounds. Furthermore, the solidus temperature and the temperature difference between the liquidus and solidus points in their glass formation ranges are in the range of 625 to 655 K and 305 to 627 K, respectively. The melt-quenched phase at the eutectic composition with the lowest melting temperature is composed only of the fcc solid solution in all the alloys systems. This result is in disagreement with the previous tendency that the solute-poor amorphous alloys in metal–metal systems such as (Fe, Co or Ni)–Zr (Nose and Masumoto 1980) and (Fe, Co or Ni)–Hf (Inoue et al. 1980), lie in the composition range including their eutectic points. The reason why the fcc single phase forms in place of an amorphous phase in spite of its trough of T_m near the eutectic composition is presumably because their eutectic compositions are too low to construct an amorphous structure.

2.4.2. *Glass-forming ability*

We discuss the reason for the formation of binary Al–R (R = Y, La, Ce, Pr, Nd, Sm, Gd, Tb, Dy, Ho, Er or Yb) amorphous alloys on the basis of previous empirical factors for the glass formation of binary alloys by liquid quenching; namely, (1) the atomic

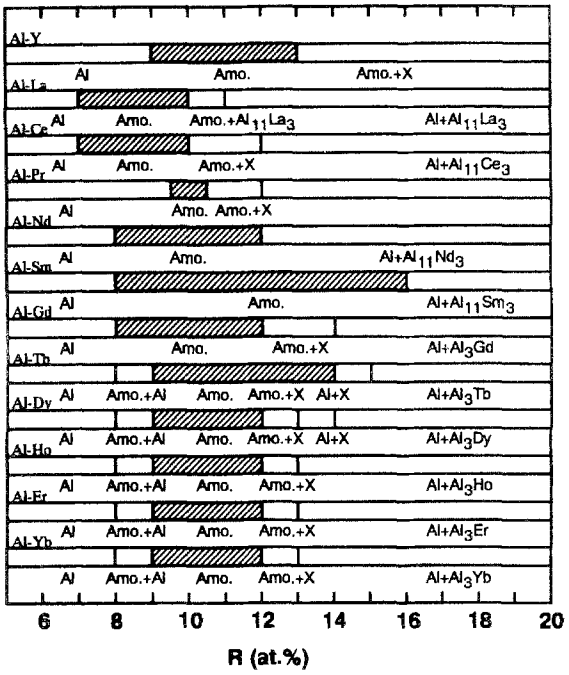

Fig. 18. Composition ranges for the formation of an amorphous phase in melt-spun Al–R (R = Y, La, Ce, Pr, Nd, Sm, Gd, Tb, Dy, Ho, Er or Yb) binary alloys. Their binary phase diagrams were adopted from Massalski (1986). The symbols of Amo. and X represent amorphous and unidentified crystalline phases, respectively.

size ratio of the constituent atoms is below ~0.8, and (2) the interaction between the constituent atoms is attractive and the mixing enthalpy is relatively large. Egami and Waseda (1984) proposed the concept that the change from a crystalline solid solution to an amorphous phase in rapidly solidified alloys takes place when a volume mismatch due to the difference in atomic size exceeds a critical size factor (λ_o). Furthermore, it has empirically been shown that the λ_o value is nearly equal to 0.1 for binary amorphous alloys. Here, λ_o is given by the product of the minimum solute concentration (C_b^{min}) for the glass formation in a binary alloy system by liquid quenching and the volume mismatch of the constituent atoms (ΔV). The λ_o values calculated at the minimum concentration for Al–R alloys are summarized in table 3 together with the data of C_b^{min}. As shown in table 3, the λ_o values except that of Al–Yb tend to decrease from 0.098 to 0.072 with increasing atomic number of the R metals because of the decrease in atomic size. The λ_o values for the Al-based alloys containing R metals with atomic number below 60 are in the range of 0.08 to 0.10, which is roughly consistent with the empirical λ_o value of 0.1 for the glass formation. However, the λ_o values for the Al–R alloys containing the heavier lanthanide metals, except Yb, are less than 0.08. Al–Yb has a high value of 0.135, which deviates largely from the critical λ_o value ($\equiv 0.10$), inconsistent with the empirical rule. Furthermore, although the atomic size ratios of the Al–R alloys are in the range of 0.73 to 0.80 for Y, La, Ce, Pr, Nd, Sm, or Gd, the ratios for the other R metals are larger than the empirical critical size ratio of 0.80 for the glass formation by liquid quenching. The inconsistency of λ_o and atomic size ratio for the Al–R (R = Tb, Dy, Ho, Er or Yb) alloys

Table 3
The minimum solute concentration (C_b^{min}) for glass formation in Al–R (R = Y, La, Ce, Pr, Nd, Sm, Gd, Tb, Dy, Ho, Er or Yb) binary alloys by liquid quenching, the volume mismatch between Al and R atoms (ΔV) and the critical size factor (λ_o) obtained by the product of C_b^{min} and ΔV

Ln metal	r (nm)	C_b^{min}	ΔV	λ_o
Y	0.182	0.09	1.062	0.096
La	0.188	0.07	1.272	0.087
Ce	0.183	0.07	1.096	0.077
Pr	0.183	0.09	1.096	0.098
Nd	0.182	0.08	1.062	0.084
Sm	0.179	0.08	0.961	0.077
Gd	0.178	0.08	0.929	0.083
Tb	0.176	0.09	0.864	0.078
Dy	0.175	0.09	0.833	0.075
Ho	0.175	0.09	0.833	0.075
Er	0.174	0.09	0.802	0.072
Yb	0.194	0.09	1.497	0.135

indicates that amorphization of the present binary alloys cannot be explained only by the empirical concept of the volume mismatch caused by the difference in atomic size.

It is pointed out in sect. 2.4 that the attractive interaction between Al and M should be taken into consideration in the glass formation of Al–EM–LM alloys such as Al–Ni–Zr, AL–Ni–Nb and Al–Ni–Hf etc., because the empirical critical size ratio of 0.8 is not satisfied in many Al-rich amorphous alloys belonging to the Al–EM–LM system. It is reasonable to consider that the concept of attractive interaction can be also applied to the interpretation of the glass formation of the present Al–R alloys. Although there are no measurement data of the mixing energies between Al and R metals, the enthalpy of mixing for Al–Y and Al–La alloys has theoretically been predicted by Miedema et al. (1977) to be −131 and −109 kJ/gat, respectively. In addition, the equilibrium phase diagrams (Massalski 1986) of the Al–R binary alloys indicate that intermetallic compounds with high melting temperature exist at Al-rich compositions and the solute concentrations and melting temperature, which reflect the magnitude of the attractive interaction (mixing energy) between Al and R metals, are in the range of 21.4 to 25 at% and 1253 and 1723 K, respectively. The minimum solute concentrations (21.4 to 25 at%) for the formation of Al-rich compounds are equal to or lower than that of Al–M binary alloys, and the melting temperatures of $Al_{11}R_3$ and Al_3R compounds are higher than those (973 to 1217 K) of Al-rich compounds (Al_4Co and Al_9Co_2) with solute concentrations below 25 at%. These data allow us to conclude that the magnitude of attractive interaction between Al and R metals is larger for R metals than for other solute metals. Accordingly, it may be concluded that the glass formation in Al–R binary alloys by liquid quenching results mainly from a strong attractive interaction of the constituent elements rather than from

the volume mismatch by the difference in the atomic size ratio. The enhancement of the glass-forming capacity by the increase of the attractive interaction of the constituent atoms is probably because diffusion of the constituent atoms in the supercooled liquid region becomes difficult and the temperature dependence of viscosity becomes steep for the supercooled liquid.

2.4.3. *Amorphous structure*

The structure of an $Al_{90}Y_{10}$ amorphous alloy was examined by Matsubara et al. (1989) by anomalous X-ray scattering (AXS) at the Y and Ni K-edges using synchrotron radiation at the Photon Factory of the National Laboratory for High Energy Physics, Tsukuba Japan. Details of the experimental setting and analysis are explained in Matsubara et al. (1988a). Figure 19 shows the scattering intensities measured at 17.0126 and 16.7380 keV below the Y K-edge in the binary $Al_{90}Y_{10}$ alloy. The fundamental features of both profiles are typical for noncrystallinity. A distinct feature observed in these profiles is a pronounced prepeak at $Q = 13\ nm^{-1}$, which is indicated with an arrow in the figure. In general, the prepeak is qualitatively interpreted as indicating compound formation, and the partial structure factor of unlike-atom pairs in this type of disordered alloys is found to show a sharp first peak with a prepeak, e.g. see Steeb and Hezel (1963) and Buhner and Steeb (1969). It may be noted that similar profiles were observed in other amorphous Al-based alloys, such as Al–Si–Mn and Al–Mn (Chen et al. 1987a, Matsubara et al. 1988b). The differential intensity profile at the Y K-edge, calculated by taking the difference between the two intensity profiles, is shown at the top of fig. 19. The prepeak is still observed in the differential profile, which again implies the presence of a certain local ordering formed by the Y and Al atoms. The Fourier transform of this differential profile gave the environmental radial distribution function (RDF) around Y, which is shown at the top of fig. 20. The ordinary RDF, which is given at the bottom of fig. 20, was also computed from the intensity measured at 17.0126 keV.

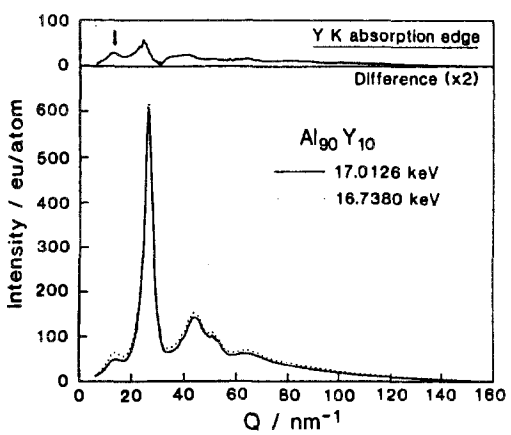

Fig. 19. (top) Differential intensity profile of amorphous $Al_{90}Y_{10}$ alloy determined from the intensity profiles (bottom) measured at incident energies of 17.0126 and 16.7380 keV, which correspond to energies of 25 and 300 eV below the Y K-absorption edge. The arrow indicates the prepeak.

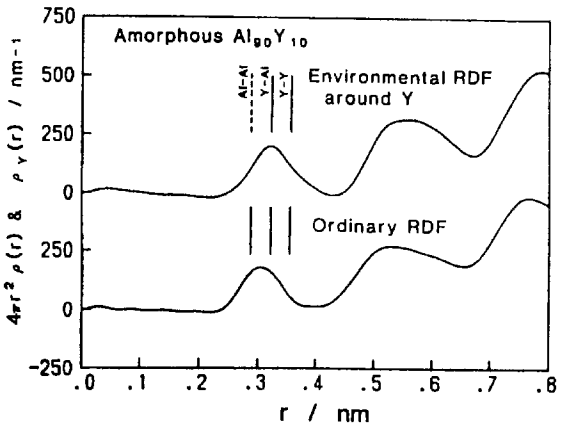

Fig. 20. Environmental radial distribution fucntion (RDF) of amorphous $Al_{90}Y_{10}$ alloy (density = 2.87 g/cm^3).

Both RDFs indicate an almost completely resolved first peak and rather prominent oscillations over a wide range of r, compared with the RDF of a typical amorphous alloy. This type of atomic configuration in disordered systems corresponds to distinct local near-neighbor correlations as seen in semiconducting liquids and oxide glasses, accompanying a complete loss of correlation between such local units at larger distances (Waseda 1980). Thus, certain short-range clusters, which are different from those normally obtained in a random mixture of constituents, are present in the amorphous $Al_{90}Y_{10}$ alloy.

The distances of atomic pairs Al–Al, Al–Y and Y–Y computed from the tabulated metallic bonding distances (Kittel 1976) are indicated in the figure. In $Al_{90}Y_{10}$, the ordinary RDF is the sum of three partial RDFs of Al–Al, Al–Y and Y–Y pairs, and the environmental RDF around Y contains only two partial RDFs of Al–Y and Y–Y pairs. With this fact in mind, the first peak of the ordinary RDF is considered to be due to Al–Al, Al–Y and Y–Y pairs, whereas the first peak of the environmental RDF around Y is likely expressed by a correlation of Al–Y and Y–Y pairs. This is clearly supported by the observation that the peak caused by the correlation of Al–Al pairs disappears in the environmental RDF, and by the rather broad first peak of the ordinary RDF formed mainly by Al–Al and Al–Y pairs with a small contribution from the Y–Y pairs. In the environmental RDF, the maximum of the first peak and a tail extending to longer r are found to correspond to the computed distances of Al–Y and Y–Y pairs, respectively. Thus, it is expected that Y atoms are mainly surrounded by Al atoms instead of Y atoms. Coordination numbers and distances for these pairs are estimated by fitting this first peak with Gaussians at approximate bonding distances. The coordination numbers of Al and Y around Y determined from the environmental RDF are 14.1 and 1.1, respectively. The large coordination number of Al around Y may be explained by considering that the size of a Y atom is about 20% larger than that of an Al atom. Using the values determined in the environmental RDF around Y, the coordination number and atomic distance for Al–Al pairs are determined from the first peak of the ordinary RDF. The results are summarized in table 4. From this table it is found that more than 92% of the near-neighbor atoms of

Table 4
Coordination numbers, N, and interatomic distance, r, for amorphous $Al_{90}Y_{10}$ alloy experimentally determined from the first peaks of the ordinary RDF and the environmental RDF around Y

Pairs	Ordinary RDF		Environmental RDF around Y	
	r (nm)	N	r (nm)	N
Al–Al	0.288	10.7±0.8		
Al–Y	0.320	1.6±0.2		
Y–Al	0.320	14.2±1.3	0.320	14.1±1.5
Y–Y	0.362	1.2±0.9	0.362	1.1±0.4

Y are Al atoms, which indicates that the Y atoms are almost completely surrounded by Al atoms since the atomic fraction of Al is 0.9.

There is an empirical relation between the correlation length, r, in real space and the peak position, Q, in the intensity profile, i.e., $Q_r = 2.5$ in molten transition metal and metalloid alloys (Waseda 1980). It is plausible that this relation is also valid in the amorphous state. Thus, the correlation length causing the prepeak at 13 nm^{-1} is estimated to be 0.60 nm, which agrees well with the distance between neighboring Y atoms bonded through an Al atom. Consequently, these experimental results prove the presence of Y atoms surrounded by Al atoms in the binary $Al_{90}Y_{10}$ alloy.

2.4.4. *Thermal stability (Inoue et al. 1989a)*

Figure 21 shows the onset temperature of the first exothermic peak (T_x) as a function of R content for the Al–R amorphous alloys. With increasing R content from 7 to 12 at%, T_x increases significantly from 434 to 534 K and no further increase of T_x is seen in the R concentration range of 12 to 16 at%. Thus, the compositional effect of T_x is almost independent of the atomic number of the Ln elements, though the Al–Er and Al–Yb alloys exhibit lower T_x values. In order to clarify the reason for the significant increase of T_x for the Al–R amorphous alloys with increasing R content from 7 to 12 at%, the crystallization behavior was examined for some Al–R amorphous alloys. As an example, fig. 22 shows differential scanning calorimetric curves of amorphous $Al_{100-x}Tb_x$ and $Al_{100-x}Dy_x$ ($x = 9$, 10, 11 and 12 at%) alloys. Two or three exothermic peaks are seen on the DSC curves, indicating that the crystallization takes place through two or three stages. From the X-ray diffraction analyses, it was confirmed that the broad exothermic peak at the low-temperature side for $Al_{91}Tb_9$, $Al_{90}Tb_{10}$ and $Al_{91}Dy_9$ alloys is due to the precipitation of fcc Al and the second exothermic peak is due to the precipitation of Al, x and Al_3Tb or Al_3Dy phases from the remaining amorphous phase. The increase of T_x at the disappearance of the Al phase is also seen for the other Al–R (R = Y, La, Ce, Nd or Sm) amorphous alloys. Accordingly, the strong compositional dependence of T_x shown in fig. 21 is due to the disappearance of the fcc Al phase resulting from the change of

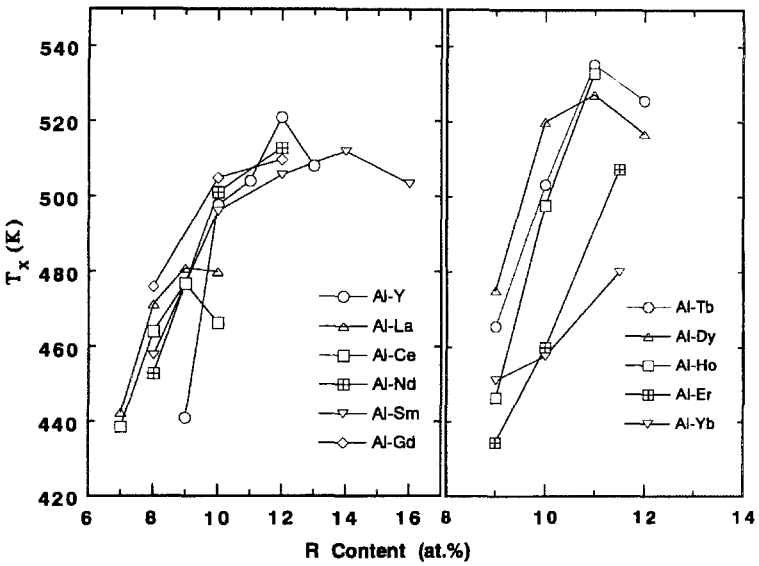

Fig. 21. Crystallization temperature (T_x) of amorphous Al–R (R = Y, La, Ce, Nd, Sm, Gd, Tb, Dy, Ho, Er or Yb) alloys as a function of R content.

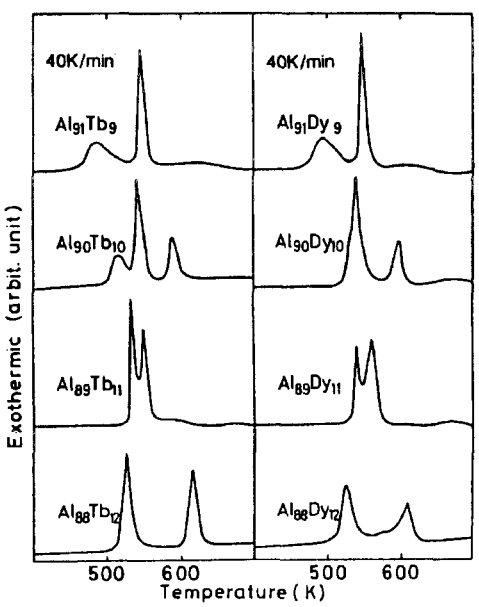

Fig. 22. Differential scanning calorimetric curves of amorphous $Al_{100-x}Tb_x$ and $Al_{100-x}Dy_x$ (x = 9, 10, 11 and 12 at%) alloys.

the crystallization process of Am → Am + Al → Al + Al_3R to Am → Al + x + Al_3R → Al + Al_3R or Am → Al + Al_3R.

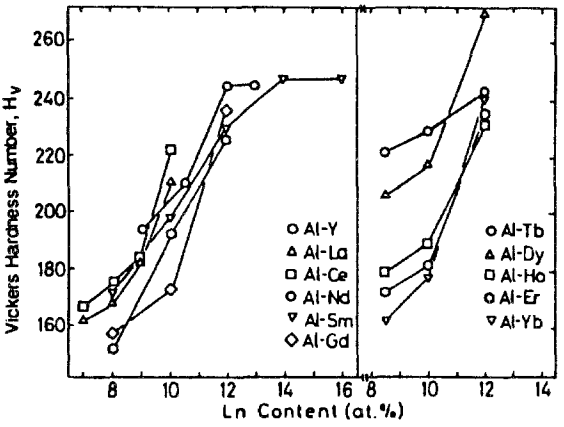

Fig. 23. Vickers hardness (H_v) of amorphous Al–R (R = Y, La, Ce, Nd, Sm, Gd, Tb, Dy, Ho, Er or Yb) alloys as a function of R content.

2.4.5. *Mechanical properties (Inoue et al. 1989a)*

Figure 23 shows the change of H_v as a function of R content for the Al–R amorphous alloys. The H_v shows an almost linear dependence over the entire composition range and increases significantly from 150 to 270 for the Al–R alloys. Although the Al–Sm, Al–Dy and Al–Tb amorphous alloys exhibit higher H_v values, no systematic change in H_v with the atomic number of the R elements is seen for the Al–R amorphous alloys. All the amorphous alloys in the Al–R binary system have a good ductility which is shown by a 180° bending without fracture. Figure 24 shows the change of σ_f as a function of R content for the Al–R amorphous alloys. σ_f increases significantly from 360 to 870 MPa

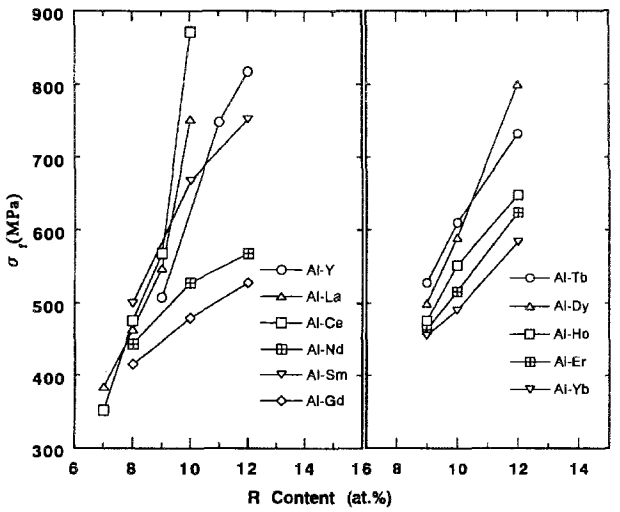

Fig. 24. Tensile fracture strength (σ_f) of amorphous Al–R (R = Y, La, Ce, Nd, Sm, Gd, Tb, Dy, Ho, Er or Yb) alloys as a function of R content.

with increasing R content. It should be noted that all the amorphous alloys in the Al–R systems exhibit tensile strengths which exceed the highest value (530 MPa) obtained in optimal age-hardened Al-based alloys. The fracture surface appearance was also examined for Al–R amorphous ribbons fractured by the uniaxial tensile test and the fracture behavior was confirmed to be just the same as that for conventional ductile amorphous alloys.

It was described in sect. 2.4.2 that the attractive bonding nature between Al and R metals plays an important role in the glass formation of Al–R binary alloys. Furthermore, the structural data described in sect. 2.4.3 indicate that the coordination number of Al atoms around Y atoms is about 1.4 times as large as the average value expected from the atomic concentration of the alloy and hence the short-range ordering of Al–Y pairs develops homogeneously in the Al–Y amorphous phase. The formation of the short-range ordered structure is presumably due to the strongly attractive interaction between Al and Y atoms. It is therefore reasonable to consider that the number of attractive Al–Y pairs in the Al–Y amorphous alloys increases linearly with increasing Y content, leading to a linear increase of the mechanical strength. This presumption is consistent with the result in which the σ_f and H_v values of Al–R amorphous alloys increase almost linearly with increasing Ln content and are independent of the atomic number of the R metals. In other words, the high strength of the Al–R binary amorphous alloys seems to result from the Al–R bonding with strongly attractive interaction and the remarkable increase of σ_f and H_v is due to the increase of the number of the Al–R bonds. Furthermore, the attractive bonding nature between Al and R metals is presumably due to a high hybridization tendency between s–p electrons in Al and s–d electrons in R metals.

It has been shown that all the properties of T_x, H_v, σ_f and electrical resistivity at room temperature (ρ_{RT}) for the Al–R amorphous alloys were essentially independent of the atomic number of the R metals. The atomic size of the R metals varies systematically with the atomic number and hence the atomic size factor also seems to have little effect on the above-mentioned properties. On the other hand, it is generally known that the inherent chemical nature of the lanthanide metals results from 4f-electrons which lie at the inner side in their atoms. Although the number of 4f-electrons varies systematically with the atomic number, the electrons are screened by $5s^2$- and $5p^6$-electrons which lie at the outer side of the atoms, resulting in a similarity in chemical properties of the lanthanide metals. Accordingly, it may reasonably be assumed that the independence of the properties of the Al–R amorphous alloys as a function of atomic number is due to the unique electronic structure in which the 4f-electrons are screened by 5s- and 5p-electrons.

Similarly, the disappearance of the primary Al phase with increasing R content in the crystallization process of the Al–R amorphous alloys is explained on the basis of the decrease of the number of Al atoms which do not bond with R metals. The suppression of the primary Al phase gave rise to a rapid increase of T_x. However, the increase of the number of Al–R pairs seems to bring about the easy precipitation of Al–R compounds, resulting in almost saturated T_x values at high R concentrations in the Al–R amorphous alloys as is shown in fig. 21.

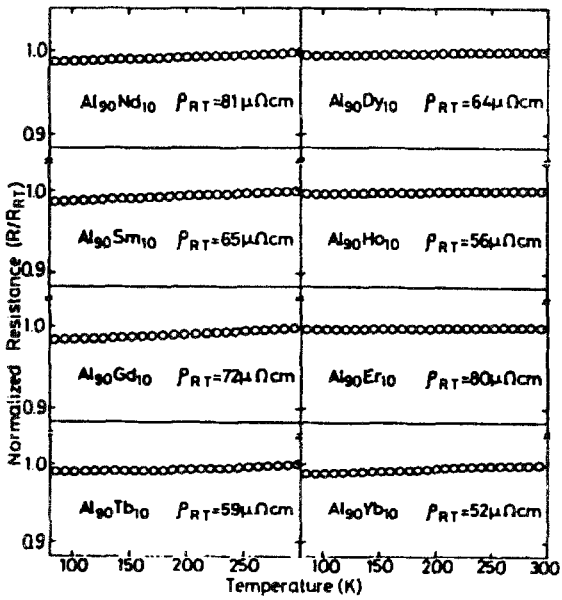

Fig. 25. Electrical resistivity of amorphous Al–R (R = Nd, Sm, Gd, Tb, Dy, Ho, Er or Yb) alloys as a function of temperature.

2.4.6. *Electrical resistivity (Inoue et al. 1988c, 1989a)*

Figure 25 shows the temperature dependence of the electrical resistivity in the range of 77 K to room temperature for amorphous $Al_{90}R_{10}$ (R = Nd, Sm, Gd, Tb, Dy, Ho, Er or Yb) alloys. It can be seen for all the amorphous alloys that the resistivity change is positive in the entire temperature range and almost linear at temperatures above 150 K. As the R content increased from 8 to 12 at%, the resistivity at room temperature was found to increase from 48–65 to 76–109 μΩ cm. Furthermore, the temperature coefficient of resistivity defined by $1/\rho_{RT}\,(d\rho/dT)$ for $Al_{90}R_{10}$ is in the range of 0.134×10^{-4} to $6.29\times10^{-4}\,K^{-1}$. Thus, the resistivity behavior is also independent of the atomic number of the R elements.

As described above, the electrical resistivity at room temperature for the Al–R amorphous alloys increases significantly from 48 to 109 μΩ cm with increasing R content from 8 to 12 at%. Furthermore, it has previously been reported by Pont et al. (1989) that the Hall coefficient (R_H) at room temperature for the Al–Y amorphous alloys is negative and its magnitude increases from 22×10^{-12} to 32×10^{-12} m^3/A s with increasing Y content. From the increase in the magnitude of the negative R_H, it is interpreted that the number of free electrons contributing to electrical conductivity decreases with increasing Y content, if one assumes the relation of $R_H = -1/Nne$, which can be derived from the nearly free-electron model, holds. Here, N is the atomic density and n is the number of electrons per atom. The strongly attractive interaction between Al and R atoms suggests that the s- and p-electrons in Al hybridize with s- and d-electrons in R, leading to a decrease of the free electrons which are attributed to electrical conductivity. As a result, the increase of the number of Al–R pairs in Al–R amorphous alloys with increasing

R content gives the significant increase in electrical resistivity and in the magnitude of the negative R_H.

As described in this section, the glass formation of Al–R binary alloys and the compositional dependences of σ_f, H_v, ρ_{RT} and R_H are explained by the common concept that Al–R pairs with an attractive bonding nature are formed preferentially in Al–R amorphous alloys and the s- and p-electrons in Al hybridize tightly with the s- and 5d-electrons in the R metals.

2.5. *Al–rare earth metal–transition metal (Al–R–M) amorphous alloys*

2.5.1. *Formation ranges (Inoue et al. 1988a,b)*

Figure 26 shows the compositional ranges in which amorphous Al–Y–M, Al–La–M and Al–Ce–M (M = Fe, Co, Ni or Cu) phases are formed by melt spinning. The formation ranges of Al–Y–M and Al–Ce–M amorphous alloys are the widest for the Al–Y–Ni and Al–Ce–Ni systems. No distinct difference is seen among the other three alloys in the Al–Y–M and Al–Ce–M systems, while those for the Al–La–M amorphous alloys are the narrowest for the Al–La–Cu system and much wider for the other Al–La–(Fe, Co or Ni) systems. Accordingly, the effectiveness of M elements on the compositional range for formation of the Al-based amorphous alloys is the greatest for Ni, followed by Fe, Co and then Cu. These amorphous alloys containing more than about 80% Al can be completely bent by 180° without fracture, and no appreciable crack is observed even in the severely deformed area. The ductility of the Al–R–M amorphous alloys is strongly dependent on

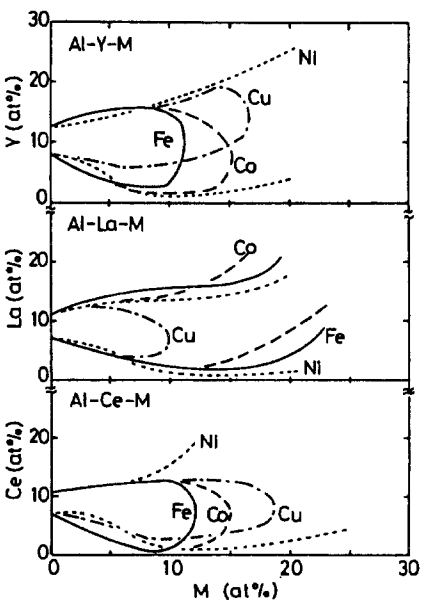

Fig. 26. Compositional ranges for formation of an amorphous phase in Al–Y–M, Al–La–M and Al–Ce–M (M = Fe, Co, Ni or Cu) systems.

alloy composition and there is a clear tendency for the ductility to increase with increasing Al content.

2.5.2. *Amorphous structure (Matsubara et al. 1989)*

Intensity profiles measured at the Y K-edge for two incident energies in the amorphous $Al_{87}Y_8Ni_5$ alloy and their difference are shown in fig. 27. These intensity profiles are similar to those (fig. 19) observed in the binary $Al_{90}Y_{10}$ alloy. They also include the prepeak at about 13 nm^{-1}. Thus, the structural features of the ternary alloy seem to be similar to those of the binary alloy. For this ternary alloy, the environmental RDF around Y as well as the ordinary RDF shown in fig. 28 were estimated. As drawn in the RDFs of fig. 28, the nearest-neighbor distances of pairs calculated from the metallic bonding distances of Al, Y and Ni are indicated in the figure. The ordinary RDFs of $Al_{90}Y_{10}$ and $Al_{87}Y_8Ni_5$ are compared at the bottom of fig. 28. The solid and dotted curves correspond to the RDFs of the ternary and binary alloys, respectively. It is found that the first peak of the ternary alloy extends to a lower r than that of the binary alloy. By comparing the peak position with the calculated bonding distances of the pairs, it is found that this tail at the lower r side corresponds to Ni–Ni and Ni–Al pairs which are not included in the binary Al–Y alloy. The environmental RDF around Y contains three partial RDFs of Y–Ni, Y–Al and Y–Y. This is clearly seen in the profiles of the peaks of the RDFs in fig. 28. The atomic positions of pairs without Y disappear in the environmental RDF around Y. A tail at lower r of the first peak in the environmental RDF around Y of the Al–Y–Ni alloys, which is not observed in the environmental RDF around Y of the Al–Y alloy, appears to be due to the correlation of Y–Ni pairs. Gaussian fitting of the first peak of the environmental RDF in fig. 28 gave the coordination numbers and atomic distances of the Y–Ni, Y–Al and Y–Y pairs. Considering the coordination number and its error for Y–Y, the number of Y–Y pairs are again insignificant in this ternary alloy. These results are summarized in table 5. From these results, about 16% of the atoms surrounding a Y atom are found to be Ni, which is much more than the value expected from the Ni

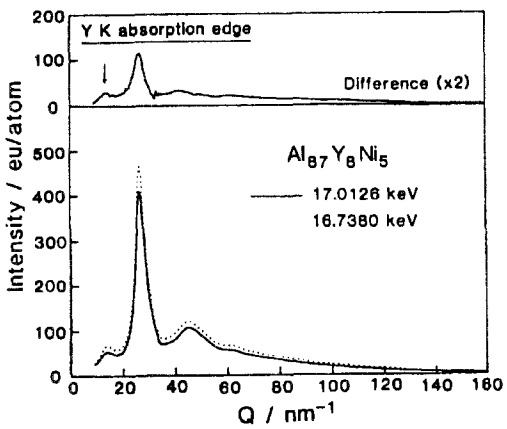

Fig. 27. Differential intensity profile of amorphous $Al_{87}Y_8Ni_5$ alloy (top) determined from the intensity profiles (bottom) measured at incidence energies of 17.0126 and 16.7380 keV, which correspond to energies of 25 and 300 eV below the Y K-absorption edge. The arrow indicates the prepeak.

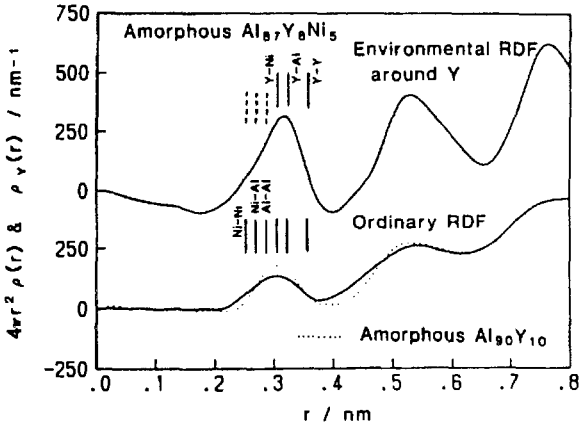

Fig. 28. Environmental RDF around Y (top) and ordinary RDF (bottom) of amorphous $Al_{87}Y_8Ni_5$ alloy (density = 3.09 g/cm^3). Also shown as a dotted line in the ordinary RDF for the binary amorphous alloy $Al_{90}Y_{10}$.

Table 5
Coordination numbers, N, and interatomic distances, r, for amorphous $Al_{87}Y_8Ni_5$ alloy experimentally determined from the first peaks of the ordinary RDF and the environmetal RDF around Y

Pairs	Ordinary RDF		Environmental RDF around Y	
	r (nm)	N	r (nm)	N
Al–Ni	0.268	6.5±0.2		
Ni–Al	0.268	0.4±0.1		
Al–Al	0.286	7.2±0.8		
Ni–Y	0.303	3.5±2.6		
Y–Ni	0.303	2.2±1.7	0.297	2.7±0.7
Al–Y	0.320	1.2±0.2		
Y–Al	0.320	13.5±2.7	0.320	14.3±1.9
Y–Y	0.356	0.8±0.6	0.356	0.4±0.4

concentration. It suggests that the local ordering structure formed in the ternary alloy included Ni as well as Al and Y.

In $Al_{87}Y_8Ni_5$, anomalous X-ray scattering (AXS) measurements were also carried out around the Ni K-edge. The scattering profile of the ternary alloy measured at 8.3067 and 8.0316 keV, which are the energies of 25 and 300 eV below the Ni K-edge, respectively, and their difference are shown in fig. 29. In the intensity difference plot a prepeak, which is indicated with an arrow in the figure, is still observed at about 13 nm^{-1}. A similar prepeak was observed in the intensity difference plot at the Y K-edge in fig. 27. These prepeaks in the differential intensity profiles at the Ni and Y K-edges support the results of the environmental RDF around Y discussed above, i.e., the presence of clusters consisting of the three constituent elements. The environmental RDF around Ni obtained from the Fourier transform of the differential intensity profile is inserted in the figure. As shown in

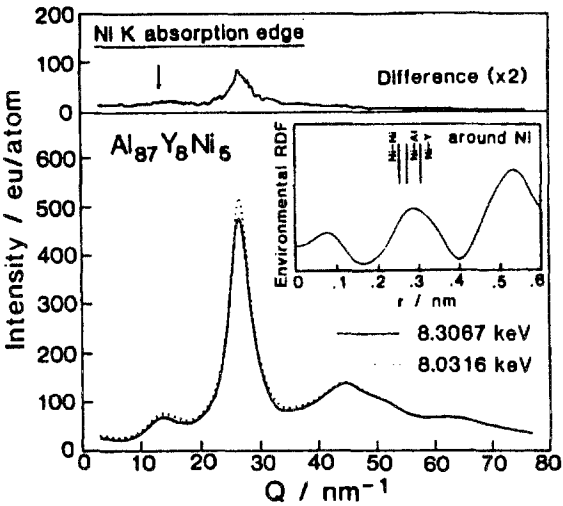

Fig. 29. Differential intensity profile of amorphous $Al_{87}Y_8Ni_5$ alloy (top) determined from the intensity profiles (bottom) measured at incidence energies of 8.3067 and 8.0316 keV, which correspond to energies of 25 and 300 eV below the Ni K-absorption edge. The arrow indicates the prepeak. The environmental RDF around Ni is inserted in the figure.

fig. 29, the AXS data of the Ni K-edge are restricted to a wavevector Q range up to about 76 nm^{-1}, arising from the relatively low energy absorption edge (8.333 keV) of Ni. This prevents us from obtaining an accurate environmental RDF around Ni due to the finite termination in the Fourier transformation, compared with the AXS data of the Y K-edge. Therefore, the information of the Ni environment is less quantitative than that for the Y environment. A careful interpretation is required for the environmental RDF around Ni, which is the sum of the three partial RDFs of Ni–Ni, Ni–Al and Ni–Y. The near-neighbor distances of the Ni–Ni, Ni–Al and Ni–Y pairs computed from the bonding distances are indicated in the figure. The first peak of the environmental RDF around Ni seems to be mainly due to Ni–Al and Ni–Y pairs, the contribution of Ni–Ni pairs to the first peak being small. Thus, the tail at lower r of the first peak in the ordinary RDF was only fitted with Ni–Al pairs. Based on these results of the environmental RDFs around Ni and Y, the first peak of the ordinary RDF was fitted with Ni–Al, Al–Al, Ni–Y, Al–Y and Y–Y pairs. The resultant coordination numbers and atomic distances are summarized in table 5.

Fractions of occupancy for the constituent elements around Al in the near-neighbor region are estimated. The values for Al, Y and Ni are about 82, 14 and 4%, respectively. The value for Al is smaller than its concentration while the value of Y is larger than its concentration. This suggests that there is a strong interaction between Al and Y. On the other hand, it is noteworthy that the value of Ni is almost equal to its concentration. Similarly, fractions around Y were computed. Ni atoms occupy about 14% in the near-neighbor region around Y, and the rest is mostly occupied by Al. The value for Ni is much higher than the number expected from the Ni concentration. This indicates a strong interaction between Y and Ni. From these results, it is concluded that Al atoms surrounding Y in the binary Al–Y alloy are preferably replaced by Ni atoms in the ternary Al–Y–Ni alloy and a local ordering is formed by the three elements. This is consistent with the result concluded from the environmental RDF around Y. It is inferred from

the prepeak of the environmental RDF around Y in the binary alloy that the prepeak at about 13 nm^{-1} in both the environmental RDFs of the ternary alloys represents the atomic correlation between Y and Al or Ni.

The Al–Y and Al–Ni systems have a very shallow eutectic point in the Al-rich region. Then, it is rather surprising that the Al–Y–Ni alloy can be amorphized by melt quenching. The formation of local ordering structures observed in the present study would facilitate the glass formation in these alloys. As described later, the fracture strength of amorphous alloys is much higher than that of crystalline metals and approaches the theoretical strength, and yet their ductility is high. Thus, most of the attractive mechanical properties of high fracture strength and ductility in the ternary amorphous Al–Y–Ni alloys may be attributed to the particular structural features of the amorphous phase. As-spun Al–Ge–Ni alloys, which form an amorphous phase over a wide range of concentrations (Inoue et al. 1987a, 1988e), do not show good mechanical properties. The structural analysis of an amorphous $Al_{60}Ge_{30}Ni_{10}$ alloy by ordinary X-ray diffraction and AXS technique (Matsubara et al. 1988c) disclosed that its structure is a mixture of Ni-rich highly ordered crystal-like regions and Ge-rich regions. This contrasts to the present Al–Y–Ni alloy structure. Therefore, the homogeneity of the amorphous phase seems to be another factor to improve its mechanical properties.

2.5.3. *Electrical resistivity (ρ_{RT}) and Hall coefficient (R_H) (Pont et al. 1989)*

Figure 30 shows the ρ_{RT} of $Al_{90-x}Fe_xR_{10}$ (R = Y or La) as a function of Fe content. It is observed that the ρ_{RT} increases rapidly with Fe content. The increase in the Al–Fe–La system is not as pronounced as in the Al–Fe–Y system. Therefore, a marked difference which depends on the two R species is observed. The effect of substituting Co for Al on the ρ_{RT} and R_H for $Al_{90-x}Co_x(Y\text{ or }La)_{10}$ are shown in figs. 31a and 31b, respectively. The ρ_{RT} increases with the concentration of M as we have already seen in fig. 30, but in

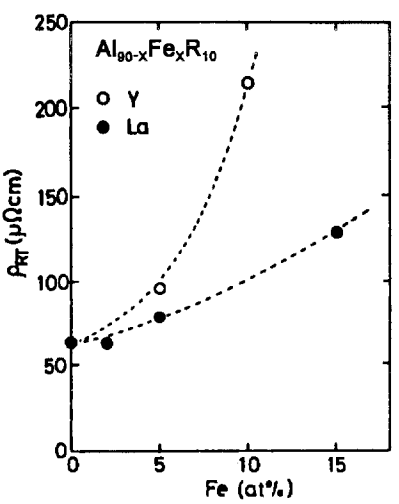

Fig. 30. Fe concentration dependence of σ_{RT} for amorphous $Al_{90-x}Fe_xR_{10}$ alloys.

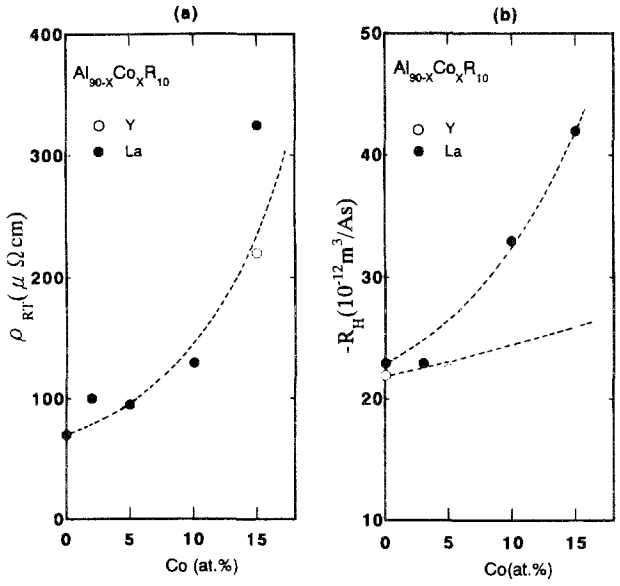

Fig. 31. Co concentration dependence of (a) ρ_{RT} and (b) R_H for amorphous $Al_{90-x}Co_xR_{10}$ alloys.

this case it is independent of the nature of the R element. In contrast to the similarity in the resistivity behavior, the R_H, which is found to be negative for all the alloys studied here, is found to depend on the R element. However, the general feature is that as the solute content increases the magnitude of the R_H also increases. Figures 32a,b show the concentration dependence of ρ_{RT} and R_H for amorphous Al–Ni–R alloys with 10% R (R = Y or La), respectively. The observed dependences on Ni concentration are quite similar to those on Co substitution except that in the present alloys both R_H and ρ_{RT} do not seem to depend on Y or La.

Figures 33a,b show the ρ_{RT} and R_H of $Al_{90-x}Co_{10}(Y\text{ or }La)_x$ as a function of R content. It is observed that the ρ_{RT} increases rapidly from about 90 to 220 μΩcm with 13% substitution of R, varies almost parabolically with R content, but is independent of the R elements. The magnitude of the R_H is also seen to increase rapidly with the content of R, independent of whether Y or La is substituted. In addition, figs. 34a,b show the ρ_{RT} data for $Al_{90-x}M_xY_{10}$ (M = Fe, Co, Ni or Cu). Similar data were obtained for the Al–M–La alloys. It is easily seen from fig. 34a that the ρ_{RT} increases with M content, in a manner already noted before. This increase is more pronounced in the alloys containing Fe and Co (in that order), while for Ni and Cu substitution the ρ_{RT} is almost constant. The increase in the magnitude of the R_H does not appear to depend on the nature of the M element.

The electronic properties of simple metal amorphous alloys are expected to behave according to the free-electron model since the spatial isotropy that should exist in homogeneous amorphous alloys would lead to a spherical Fermi surface. However, substitution of Al by R and/or M species raises the fundamental question as to how

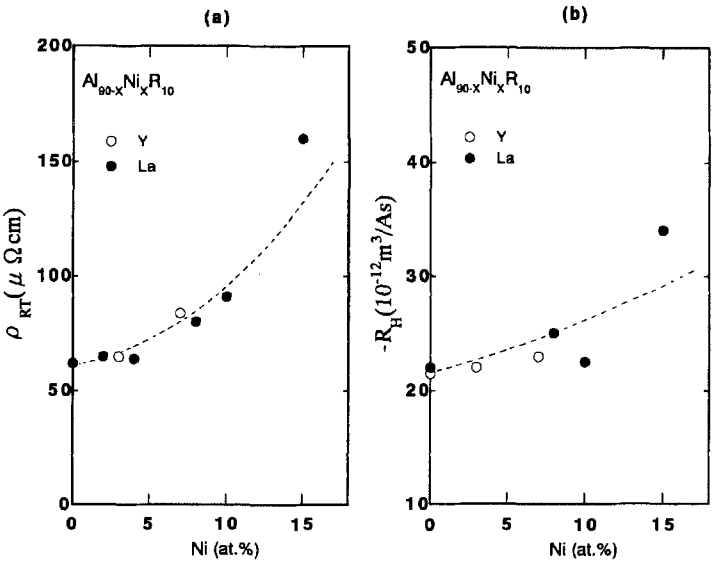

Fig. 32. Ni concentration dependence of (a) ρ_{RT} and (b) R_H for amorphous $Al_{90-x}Ni_xR_{10}$ alloys.

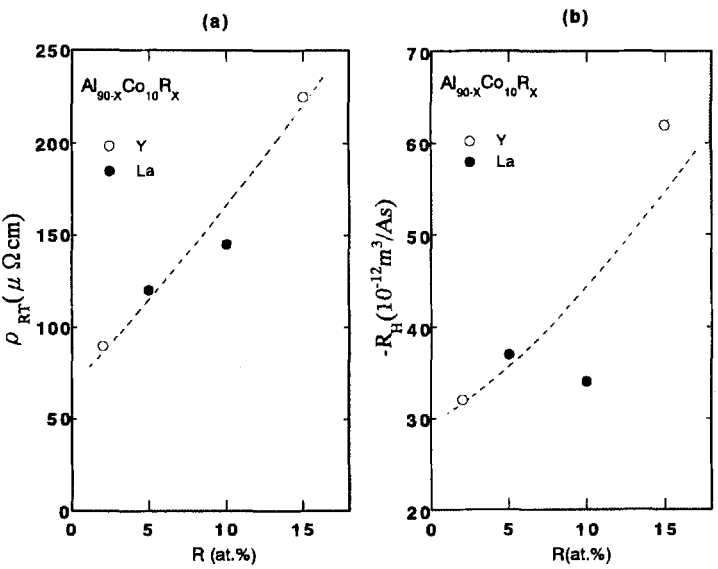

Fig. 33. R concentration dependence of (a) ρ_{RT} and (b) R_H for amorphous $Al_{90-x}Co_{10}R_x$ alloys with R = Y or La.

the free-electron-like behavior expected for Al will be altered by the presence of other atoms with a very different electronic structure and atomic size. The two R species examined in this work, Y and La, have a similar atomic radius and the same outer

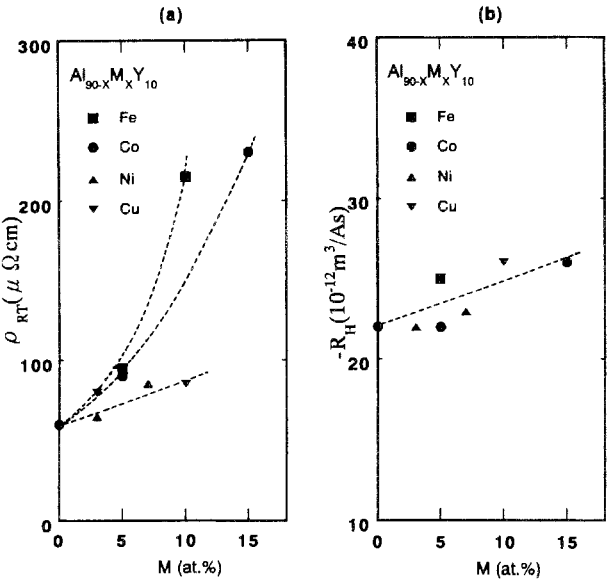

Fig. 34. (a) ρ_{RT} and (b) R_H for amorphous $Al_{90-x}M_xY_{10}$ alloys with M = Fe, Co, Ni or Cu.

namely (d^1s^2), thus substitution of 10 at% of Al by any R element should essentially produce similar changes in the electronic properties. Indeed this is what we observe experimentally: For example, within the limits of experimental error both $Al_{90}La_{10}$ and $Al_{90}Y_{10}$ present an electrical resistivity of 66 μΩcm and an ordinary R_H, -22.5×10^{-12} m^3/As. In a free-electron model it will be expected that the R_H of these two alloys shows an almost free-electron value, given by $R_H = -1/(Nne)$. Assuming three conduction electrons per Al and Y (or La) atoms, the equation gives a R_H of -38×10^{-12} m^3/As. This is almost twice the experimental value. On the other hand, it has been shown that La-based amorphous alloys have positive R_H (Delgado et al. 1986) and for liquid La the value of $R_H = +61.5\times10^{-12}$ m^3/As has been reported by Bush and Güntherodt (1974).

We now discuss the effects of M elements on partial substitution of Al. The Hall-effect data (fig. 34b) indicate that there is a decrease in the carrier density when increasing the M content probably because of the formation of additional Al–M bonds in addition to the existence of Al–R bonds. Thus, while the progressive formation of local Al–M covalent bonds seems to result in a decrease in the effective free-electron concentration irrespective of the nature of the M, the ρ_{RT} strongly suggests that s–d scattering contribution decreases with Fe, Co and Ni, in that order, as expected from the d-state occupation in these elements. The Cu atom has its 3d band filled and thus no (s,p)–d scattering is expected to contribute to the ρ_{RT} which will be determined by (s,p) electrons. On the other hand, the Fe and Co atoms with an incomplete 3d band offer a more complex situation. In this case both the formation of covalent bonds and a larger probability for the conduction electrons of Al to be scattered into d states of the M atoms contribute to an increase

to the ρ_{RT}. An X-ray photoemission spectroscopy study of LM dissolved in Al (Steiner et al. 1980) indicates that there is an hybridization of the 3d electrons of the M with the conduction electrons (s,p) of Al which lead to a density of states in the Fermi level characterized by (s,p) electrons and the 3d band of the M atoms lying well below the Fermi level. The hybridization will enhance (s,p)–d scattering, in agreement with the present measurements. This would explain, in part, the additional contribution and different rates of increase of the ρ_{RT} as being due to s–d scattering from Fe, Co, Ni and Cu. However, it is necessary to point out that the total change in the magnitude of the ρ_{RT} from about 65 μΩcm to as high as 250 μΩcm or more in the amorphous state for a change in concentration of the additional elements by about 15 at% is unusual. Such large changes in ρ_{RT} are not observed with compositional changes of the order of 20 at% in d-band amorphous materials rich in M components (Cote and Meisel 1981).

Despite the negative values observed for the R_H in all the alloys studied, and the increase in magnitude when Al is substituted by M and R indicating a decrease in the density of carriers, we have shown that a free-electron model is not quantitatively applicable even though the high concentration of Al might indicate the possibility of the free-electron model. This fact suggests that s–d scattering which is assumed to contribute to the ρ_{RT} is also important in order to understand quantitatively the R_H for these alloys.

2.5.4. *Superconducting properties (Inoue et al. 1989b)*

Figure 35 shows the normalized electrical resistance $R/R_{4.2}$ for amorphous $Al_{85}La_{7.5}M_{7.5}$ (M = Zr, Nb, Mo or Ni) alloys. The transition into a superconducting state occurs sharply with a temperature width of less than 0.3 K. The transition temperature (T_c) defined by 50% of $R_{4.2}$ increases from 2.56 to 4.02 K in the order of Ni < Zr < Mo < Nb and no superconductivity at temperatures above 1.5 K was detected for the corresponding alloys containing Co or Fe. There is a tendency for T_c to be higher for the alloys containing M elements of the fifth period of the periodic table as compared to the fourth period elements and T_c decreases significantly by the dissolution of magnetic elements. The T_c

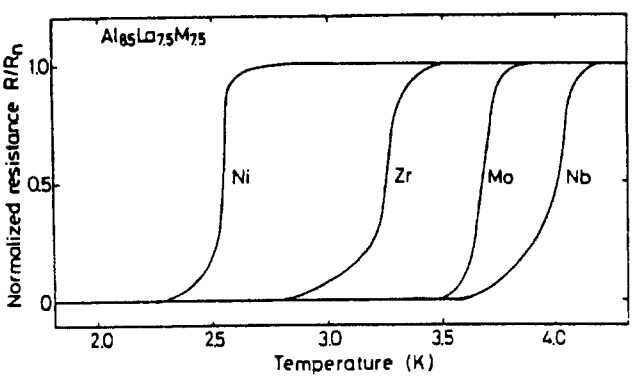

Fig. 35. Normalized electrical resistance, R/R_n, as a function of temperature for $Al_{85}La_{7.5}M_{7.5}$ (M = Zr, Nb, Mo or Ni) amorphous alloys.

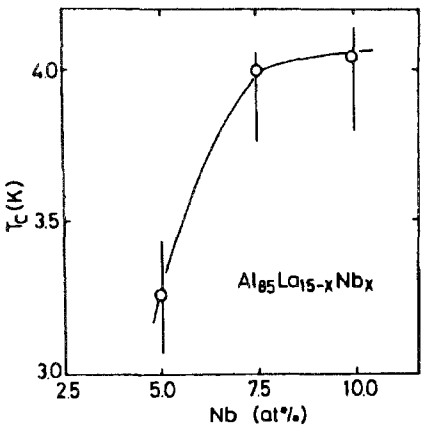

Fig. 36. Change in T_c for $Al_{85}La_{15-x}Nb_x$ amorphous alloys with Nb content.

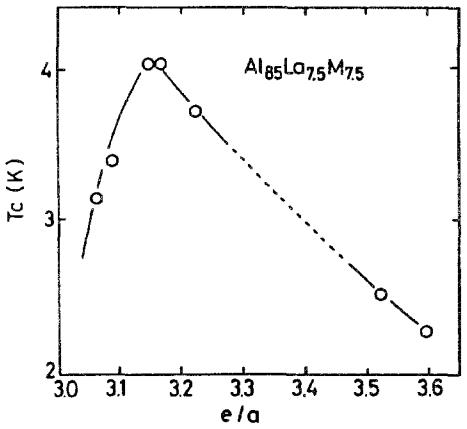

Fig. 37. Change in T_c for $Al_{85}La_{7.5}M_{7.5}$ (M = Zr, Nb, Mo, Ni or Cu) amorphous alloys with e/a.

values of the Al-based amorphous alloys are much higher than that (0.9 K) (Blackford 1976) of pure Al. From the expectation of a high T_c in the amorphous Al–La–Nb system, the compositional change of T_c was examined for the $Al_{85}La_{15-x}Nb_x$ alloys. As shown in fig. 36, T_c increases from 3.25 to 4.07 K with an increase of Nb content from 5 to 7.5% and then becomes nearly constant.

It is known that the compositional dependence of T_c for amorphous alloy superconductors containing M of the fourth and fifth periods as major elements is closely related to the change in the average number of outer electrons per atom (e/a). The strong correlation between T_c and e/a has been named as the Collver–Hammond rule, e.g. see Collver and Hammond (1973), for amorphous superconductors and T_c shows a maximum value at e/a = 6.4 for the 4d transition metals and alloys. The T_c values as a function of e/a for the $Al_{85}La_{7.5}M_{7.5}$ alloys are shown in fig. 37. One notices a maximum value of T_c at e/a = 3.15, being significantly different from the Collver–Hammond rule. Furthermore, the previous empirical rule suggests that T_c is higher for $Al_{85}La_{7.5}Mo_{7.5}$ than for $Al_{85}La_{7.5}Nb_{7.5}$, but the suggestion is inconsistent with the present result. This inconsistency suggests that the contribution of Al must be taken into consideration for the interpretation of the presence of superconductivity.

Figure 38 shows the temperature dependence of H_{c2} for the $Al_{85}La_{7.5}M_{7.5}$ amorphous alloys. Here, H_{c2} is defined to be the applied magnetic field at which the resistance of the samples reaches one half of its normal value. H_{c2} increases linearly when lowering the temperature in the range above $t = T/T_c = 0.58$–0.72, but it shows a negative deviation from linearity at low temperatures. The temperature gradient of H_{c2} near T_c, $-(dH_{c2}/dT)T_c$, increases in the range of 0.221 to 0.308 T/K in the order of Ni < Zr < Nb < Mo. The gradients are about one tenth of the values (1.5 to 3.0 T/K) (Johnson 1978, Inoue and Masumoto 1981) for amorphous alloy superconductors in M-based systems. The H_{c2} value at 1.8 K is in the range 0.40 to 0.57 T which is much lower than that for other

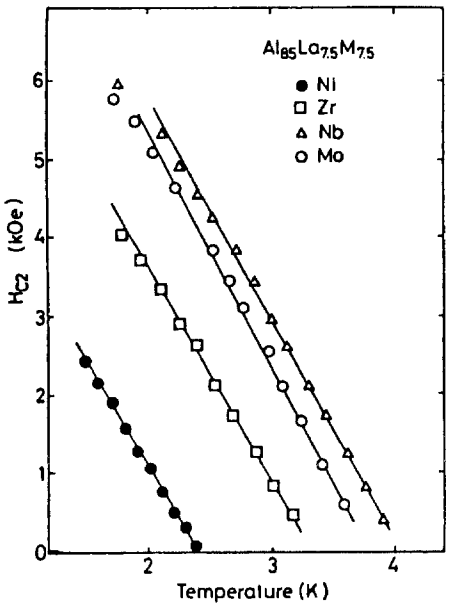

Fig. 38. The upper critical magnetic field H_{c2} at various temperatures for $Al_{85}La_{7.5}M_{7.5}$ (M = Zr, Nb, Mo or Ni) amorphous alloys. The solid lines represent a linear extrapolation at T_c.

amorphous superconductors because of the much lower $(dH_{c2}/dT)T_c$ values. The strong correlation between T_c and e/a for the Al-based amorphous superconductors shown in fig. 37 is thought to be attributed to the change in $N(E_f)$ with e/a. The electronic dressed density of states at the Fermi level, $N^*(E_f) = N(E_f)(1+\lambda)$, was estimated from the measured values of the H_{c2} gradient near T_c, $-(dH_{c2}/dT)T_c$, and the normal electrical resistivity at 4.2 K, $\rho_{4.2}$, by using the following formula which is derived from the Ginzburg–Landau–Abrikosov–Gorkov (GLAG) theory (e.g., Orlando et al. 1979) and is applicable for the dirty-type superconductors of the Al–La–M amorphous alloys:

$$N(E_f)(1+\lambda) = -\pi/[8k_B\rho_n(dH_{c2}/dT)T_c]. \quad (1)$$

As shown in table 6, the values of $N(E_f)(1+\lambda)$ thus obtained tend to increase from 0.24×10^{47} to 0.66×10^{47} in the order of Ni < Zr < Nb ≡ Mo as does T_c, suggesting that T_c is dominated by $N(E_f)$ and/or λ. The problem which parameter, $N(E_f)$ or λ, dominates the change in T_c with M elements remains unsolved within the present study and an investigation of the low-temperature specific heat is necessary to determine the most dominant factor.

It was shown in fig. 38 that the gradient of H_{c2} in the vicinity of T_c for Al–La–M amorphous alloys is about 10% of that (Johnson 1978, Inoue and Masumoto 1981) of amorphous alloy superconductors in M-based systems. Equation (1) indicates that the gradient is dependent on ρ_n, $N(E_f)$ and λ. One of the reasons for the extremely low gradient values is probably the low electrical resistivities which are about 50% of those (200 to 300 μΩ cm) (Rao 1983, Mizutani et al. 1989) for M-based amorphous

Table 6
Thermal stability and electrical and superconducting properties of $Al_{85}La_{7.5}M_{7.5}$ (M = Zr, Nb, Mo, Ni or Cu) amorphous alloys

Alloy	T_x (K)	$\rho_{4.2}$ ($\mu\Omega$ cm)	T_c (K)	ΔT_c (K)	H_{c2} (kOe/K)	$-(dH_{c2}/dT)_{T_c}$ (kOe/K)	$N^*(E_f)$
$Al_{85}La_{7.5}Zr_{7.5}$	430	142	3.26	0.30	4.01	2.70	0.33
$Al_{85}La_{7.5}Nb_{7.5}$	488	86	4.02	0.24	5.54	2.91	0.61
$Al_{85}La_{7.5}Mo_{7.5}$	511	96	3.71	0.19	5.70	3.08	0.66
$Al_{85}La_{7.5}Ni_{7.5}$	559	185	2.56	0.11	1.60	2.45	0.24
$Al_{85}La_{7.5}Cu_{7.5}$	496	30	2.04	–	–	–	–

superconductors. Furthermore, it is known that Al metal with T_c at 0.9 K has 3s- and 3p-electrons in the outer shell, which are different from the 3d- and 4d-electrons for the M-based alloys, and in a weak coupling superconductor with a low λ value ($\equiv 0.38$) (McMillan 1968). The different type of outer electrons and the low λ value appear to be another reason for the small temperature gradient of H_{c2} for Al–La–M amorphous alloys.

2.5.5. *Thermal stability (Inoue et al. 1988a,b,g)*

In order to clarify the compositional dependence of the thermal stability for the Al–Y–M, Al–La–M and Al–Ce–M amorphous alloys, T_x values are plotted as a function of M content (M = Fe, Co, Ni or Cu) in fig. 39 and as a function of R content (R = Y, La or Ce) in fig. 40. T_x values of the Al-based alloys without Cu have a distinct compositional

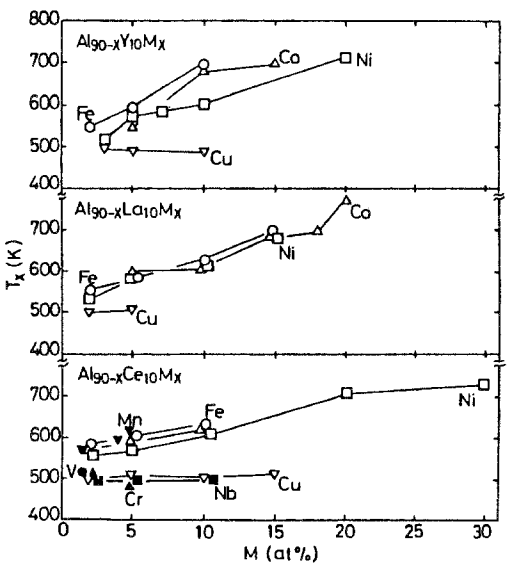

Fig. 39. Change in T_x as a function of M (M = Fe, Co, Ni or Cu) concentration for $Al_{90-x}Y_{10}M_x$, $Al_{90-x}La_{10}M_x$ and $Al_{90-x}Ce_{10}M_x$ amorphous alloys.

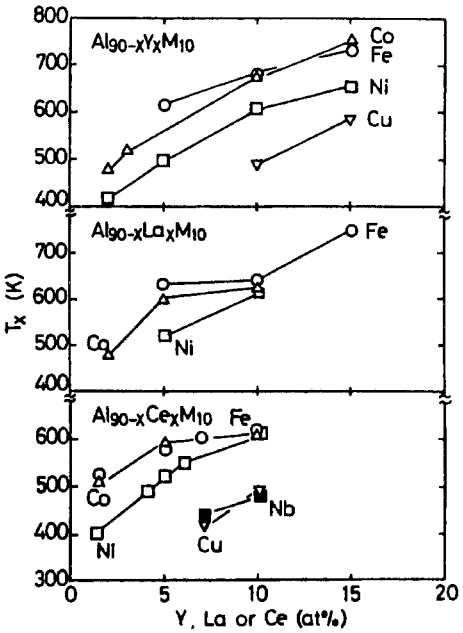

Fig. 40. Change in T_x as a function of Y, La or Ce concentration for $Al_{90-x}Y_xM_{10}$, $Al_{90-x}La_xM_{10}$ and $Al_{90-x}Ce_xM_{10}$ (M = Fe, Co, Ni or Cu) amorphous alloys.

dependence and increase significantly with increasing Fe, Co, Ni, Y, La or Ce content, i.e., from 528 to 724 K for $Al_{90-x}Y_{10}M_x$, 544 to 793 K for $Al_{90-x}La_{10}M_x$, 500 to 730 K for $Al_{90-x}Ce_{10}M_x$, 414 to 750 K for $Al_{90-x}Y_xM_{10}$, 486 to 740 K for $Al_{90-x}La_xM_{10}$ and 402 to 620 K for $Al_{90-x}Ce_xM_{10}$. There is no distinguishable difference in the compositional dependence of T_x among the Al–Y–M, Al–La–M and Al–Ce–M alloys. The effect of M elements on the increase of T_x tends to decrease in the order of Fe > Co > Ni and no distinct change in T_x with Cu is seen for either the Al–Y–Cu or Al–La–Cu alloy.

The structural skeleton in the Al-based amorphous alloys is thought to consist mainly of Al–M and Al–R bonds with attractive interaction. The equilibrium phase diagrams (Massalski 1986) of Al–M and Al–R alloys indicate the existence of a number of intermetallic compounds in their binary alloy systems. When the formation tendency and T_m of intermetallic compounds in Al-rich composition ranges corresponding to the glass formation ranges in the Al–R–M systems are compared with those in Al–R alloys, one notices that the minimum solute concentration for the formation of Al-rich compounds is 25% Y (Al_3Y), 20% La (Al_4La) and 20% Ce (Al_4Ce) and the T_m of these compounds is considerably higher for Al_4(La or Ce) than for Al_3Y (Massalski 1986). These differences suggest that the attractive interaction between Al and R atoms is considerably stronger for Al–La and Al–Ce atoms than for Al–Y atoms. This is presumably because the T_x values are higher for Al–La–M and Al–Ce–M amorphous alloys. On the basis of a similar concept that the degree of attractive interaction between the constituent atoms exerts a significant effect on T_x, one can explain the result that T_x decreases in the order of Al–Fe–R > Al–Co–R > Al–Ni–R ≪ Al–Cu–R, because the T_m of Al-rich Al_3Fe, Al_9Co_2,

Al_3Ni and Al_2Ce compounds decreases in the order of Fe > Co > Ni > Cu (Massalski 1986). The good coincidence between T_x of the amorphous alloys and T_m of the Al-rich intermetallic compounds appears to support the appropriateness of the concept that the attractive interaction among the constituent elements contributes significantly to the glass formation of the metal–metal type amorphous alloys.

2.5.6. *Mechanical properties and corrosion resistance (Inoue et al. 1988g, 1989c)*
The σ_f, E and H_v of the Al–Y–Ni, Al–La–Ni and Al–Ce–Ni amorphous alloys are summarized in table 7, where the data of $\varepsilon_{t,f} = \sigma_f/E$, $\varepsilon_{c,y} \equiv 9.8H_v/3E$ and $\sigma_{c,y} \equiv 9.8H_v/3$ are also shown for reference. The approximation of $\varepsilon_{c,y} \equiv 9.8H_v/3E$ is based on the fact that an amorphous alloy exhibits little work-hardening and thus the compressive yield strength is related by $\sigma_{c,y} \equiv 9.8H_v/3$ (Chen et al. 1975). As seen in the table, σ_f lies in the range of 920 to 1140 MPa for the Al–Y–Ni alloys, 1010 to 1080 MPa for the Al–La–Ni alloys, and 810 to 935 MPa for the Al–Ce–Ni alloys and is considerably higher for the Al–Y–Ni and Al–La–Ni alloys than for the Al–Ce–Ni alloys. No distinct compositional dependence of σ_f is seen for the three alloy systems, while E, H_v, and $\sigma_{c,y}$ increase with decreasing Al content; from 52.4 to 84.2 GPa, 300 to 380 and 980 to 1240 MPa, respectively, for the Al–Y–Ni alloys; from 64.7 to 88.9 GPa, 260 to 320 and 850 to 1080 MPa, respectively, for the Al–La–Ni alloys; and from 53.2 to 60.3 GPa, 215 to 335 and 555 to 935 MPa, respectively, for the Al–Ce–Ni alloys. Thus, the properties except σ_f have a similar compositional dependence. The nonexistence of a compositional dependence for σ_f is presumably because σ_f is highly sensitive to the structure and smoothness of the sample surface. $Al_{87}Y_8Ni_5$ and $Al_{87}La_8Ni_5$ amorphous alloys exhibit high static strengths of 1080–1140 MPa for σ_f and 260–300 for H_v which greatly exceed the highest values of 550 MPa and 180 (Metals Databook 1983), respectively, for conventional Al-based crystalline alloys subjected to an optimum age-hardening treatment. The specific strength defined by the ratio of σ_f to density (ρ) is estimated to reach 38 for the $Al_{87}Y_8Ni_5$ alloy and 34 for the $Al_{87}La_8Ni_5$ alloy, which is higher than that (33) reported by Inoue et al. (1987d) for Ni–Si–B–Al amorphous wires with σ_f of about 2750 MPa. However, these values for σ_f/ρ are slightly lower than those (40–56) for Fe–Si–B (Hagiwara et al. 1982a) and Co–Si–B (Hagiwara et al. 1982b) amorphous wires with a high σ_f which ranges from 3000 to 3900 MPa.

Table 7
Mechanical properties of Al–Y–Ni, Al–La–Ni and Al–Ce–Ni amorphous alloys

Alloy (at%)	σ_f (MPa)	E (GPa)	H_v	$\varepsilon_{t,f} = \sigma_f/E$	$\varepsilon_{c,y} \approx 9.8H_v/3E$
$Al_{88}Y_2Ni_{10}$	920	71.0	340	0.013	0.016
$Al_{87}Y_8Ni_5$	1140	71.2	300	0.016	0.014
$Al_{87}La_8Ni_5$	1080	88.9	260	0.012	0.010
$Al_{84}La_6Ni_{10}$	1010	83.6	280	0.012	0.010
$Al_{86}Ce_4Ni_{10}$	810	54.6	300	0.015	0.018
$Al_{85}Ce_5Ni_{10}$	935	59.4	320	0.016	0.018

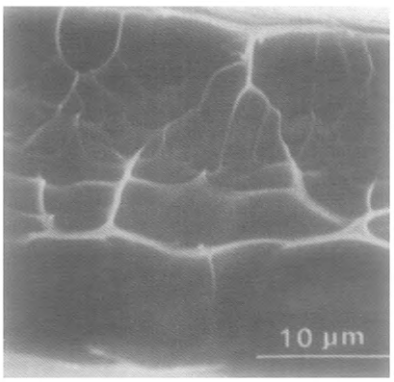

Fig. 41. Scanning electron micrograph showing the tensile fracture appearance of $Al_{87}Y_8Ni_5$ amorphous ribbon.

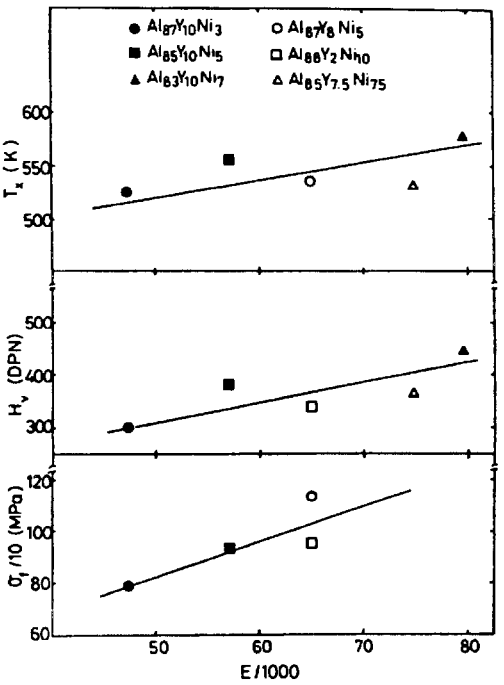

Fig. 42. Correlation between E and σ_f, H_v or T_x for Al–Y–Ni amorphous alloys.

Figure 41 shows the fracture surface appearance of an $Al_{87}Y_8Ni_5$ amorphous ribbon fractured by uniaxial tensile test. The fracture surface consists of a smooth region caused by shear sliding and a vein region caused by final catastrophic fracture after shear sliding. It has been reported by Masumoto and Maddin (1971) that the fracture accompanying the shear sliding takes place along the shear plane declined by 45° to 55° to the direction of the tensile load. A similar feature of the fracture surface appearance was also observed for Al–La–Ni and Al–Ce–Ni amorphous ribbons. These features in the fracture behavior are similar to those reported previously (Li 1993) for the other ductile amorphous alloys produced by liquid quenching. The similarity allows us to infer that the Al-based amorphous alloys have good ductility comparable to conventional ductile amorphous alloys.

Figure 42 shows the correlation between E and σ_f, H_v or T_x for the Al–Y–Ni amorphous alloys. The three properties σ_f, H_v and T_x tend to increase with increasing E. As shown in table 7 and fig. 42, the correlation between E and σ_f or H_v can be empirically expressed by the following approximate equations: $\varepsilon_{t,f} = \sigma_f/E \equiv 0.015$ and $\varepsilon_{c,y} \equiv 9.8H_v/3E \equiv 0.017$. The $\varepsilon_{t,f}$ and $\varepsilon_{c,y}$ values are nearly equal to the respective values of 0.018 and 0.014 (Inoue et al. 1988f) for the Fe-, Co-, Ni-, Pd-, Pt- and Cu-based amorphous alloy wires.

In addition, the Al–Y–Ni and Al–La–Ni amorphous alloys with high tensile strength, i.e., above 1000 MPa, were found to exhibit high corrosion resistance in HCl and NaOH

Table 8
Corrosion losses of $Al_{85}Y_{10}Ni_5$ amorphous alloy in 1N HCl and 0.25N NaOH solutions. The data of conventional Al-based crystalline alloys are also shown for comparison

Alloy	Corrosion loss (mm/year)	
	In 0.25N NaOH at 293 K (mm/year)	In 1N HCl at 293 K
$Al_{85}Y_{10}Ni_5$	2.5	0.055
Al(99.99%)	18.6	0.72
Al–Cu–Mg (2024)	170.0	13.0

solutions which greatly exceed that of conventional Al-based crystalline alloys. As shown in table 8, the corrosion losses of the Al–Y–Ni amorphous alloy in 1 N HCl and 0.25 N NaOH solutions at 293 K are 68 and 240 times as small as those for the high-strength Al–Cu–Mg alloy subjected to an optimal heat treatment. It is particularly notable that the Al-based amorphous alloys have high corrosion resistance even in alkaline solution. This is in contrast to the fact that the solution has generally been used as a reagent for dissolving Al-based crystalline alloys. The discovery of the Al–Y–Ni and Al–La–Ni amorphous alloys exhibiting high specific strength combined with good ductility and high corrosion resistance allows us to expect that the high-strength Al-based amorphous alloys will be valuable for applications in areas where these properties are required simultaneously.

2.5.7. *Glass transition behavior (Inoue et al. 1988h)*

Figure 43 shows the compositional dependences of the glass transition temperature (T_g) and T_x for amorphous Al–Y–Ni and Al–Ce–Ni alloys measured at a scanning rate of 0.67 K/s. In the figure, T_g is represented by an asterisk. It is seen that the glass transition phenomenon was observed prior to crystallization in the vicinity of 10% Y for the Al–Y–Ni system and 6% Ce for the Al–Ce–Ni system, indicating that the separation of glass transition from crystallization is mainly dominated by the R metals of Y and Ce and is independent of Ni content. T_g and T_x increase significantly with increasing solute concentration from 490 to 582 K and 518 to 604 K, respectively, for the Al–Y–Ni alloys and from 500 to 573 K and 517 to 600 K, respectively, for the Al–Ce–Ni alloys. In addition, fig. 43 shows a general tendency that the amorphous alloys exhibiting a glass transition have a good bending ductility.

As an example, fig. 44 shows the thermograms of an amorphous $Al_{84}Ce_6Ni_{10}$ alloy. The C_p value of the as-quenched phase is 22.8 J/mol K near room temperature. As the temperature rises, the C_p value gradually increases initially and then begins to decrease at about 365 K, indicating an irreversible structural relaxation at about 365 K. With a further increase in temperature, the C_p value shows a minimum at about 500 K, then increases rapidly in the region of glass transition at about 515 K and reaches 32.4 J/mol K for the supercooled liquid around 535 K. With a further increase of the temperature, the

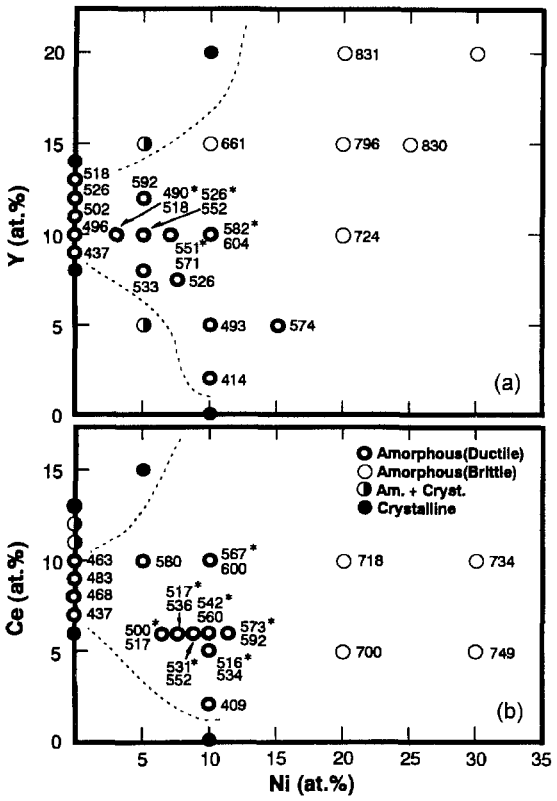

Fig. 43. Composition ranges for the formation of the amorphous phase, and the changes of T_g and T_x in (a) Al–Y–Ni and (b) Al–Ce–Ni systems. Double open circle, amorphous (ductile); open circle, amorphous (brittle); semi-open circle, amorphous plus crystalline; solid circle, crystalline. The asterisk represents T_g.

supercooled liquid begins to crystallize at 540 K. Figure 44 also shows that the amorphous alloys have a large difference in specific heat, $\Delta C_{p,s\to l}$, between the amorphous solid and supercooled liquid reaching 9.2 J/mol K. The difference in $C_p(T)$ between the as-quenched and the reheated states, $[\Delta C_p(T)]$, manifests the irreversible structural relaxation which is presumed to arise from the annihilation of various kinds of quenched-in "defects" and the enhancement of the topological and chemical short-range ordering through the atomic rearrangement. The T_g and $\Delta C_{p,s\to l}$ as a function of Ni or Ce concentration for the Al–Y–Ni and Al–Ce–Ni amorphous alloys are plotted in fig. 45. The T_g increases almost linearly with increasing solute concentration, while the $\Delta C_{p,s\to l}$ values are the largest near the center of the compositional range where the amorphous alloys with a glass transition are obtained. Considering the general tendency (see Chen 1986) that the larger the $\Delta C_{p,s\to l}$ values the easier is the formation of an amorphous phase, it is expected that an amorphous phase with high structural stability is obtained in the vicinity of $Al_{83}Y_{10}Ni_7$ and $Al_{84}Ce_6Ni_{10}$. Thus, the Al content of stable amorphous alloys with the largest $\Delta C_{p,s\to l}$ is nearly equal in the two alloys, but the ratios of Y or Ce to Ni are significantly different.

Figure 46 shows an elongation curve of an amorphous $Al_{85}Y_{10}Ni_5$ alloy measured under an initial tensile stress of 0.98 MPa at a heating rate of 0.17 K/s. The length of the

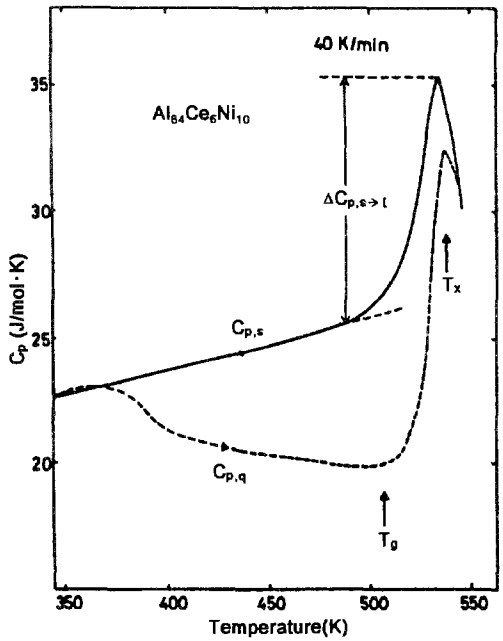

Fig. 44. The thermogram $C_{p,q}(T)$ of an amorphous $Al_{84}Ce_6Ni_{10}$ alloy in the as-quenched state. The solid line represents the thermogram $C_{p,s}(T)$ of the sample heated to 520 K.

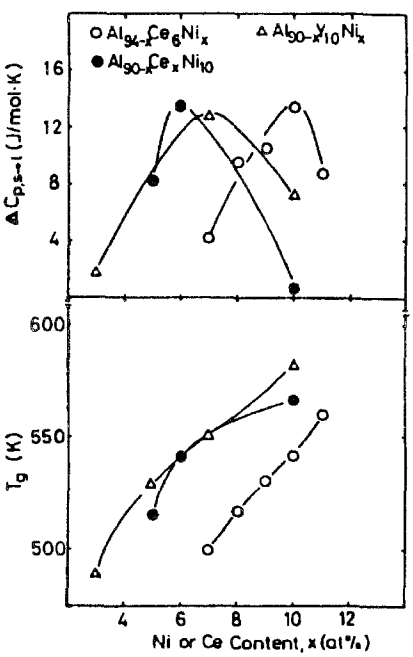

Fig. 45. Changes in T_g and the difference of the specific heat between amorphous solid and supercooled liquid ($\Delta C_{p,sdl}$) as a function of Ni or Ce concentration for Al–Y–Ni and Al–Ce–Ni amorphous alloys.

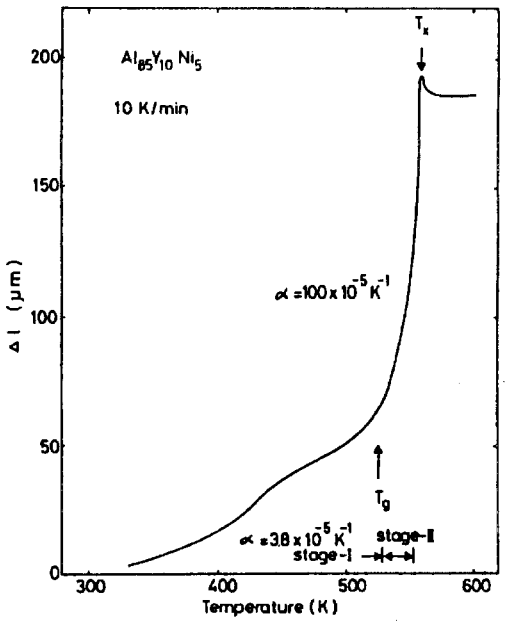

Fig. 46. Change in length (Δl) of amorphous $Al_{85}Y_{10}Ni_5$ alloy with heating. The value of the coefficient of thermal expansion (α) is also shown for reference.

specimen begins to increase at about 320 K and increases gradually up to about 520 K and then rapidly in the range from 530 to 560 K. With a further increase in temperature, the increase in the length stops suddenly due to crystallization. The elongation curve before crystallization can be divided into two stages corresponding to an amorphous solid and a supercooled liquid as shown in fig. 46 and each coefficient of thermal expansion (α) is estimated to be $3.8 \times 10^{-5}\,K^{-1}$ for the amorphous solid in the range of 320 to 520 K (stage-I) and $100 \times 10^{-5}\,K^{-1}$ for the supercooled liquid in the range of 530 to 560 K (stage-II). The extraordinarily high α value for the supercooled liquid is due to a much lower viscosity.

Based on the data shown in fig. 46, the viscosities (η) as a function of temperature were evaluated for amorphous $Al_{85}Y_{10}Ni_5$ and $Al_{84}Ce_6Ni_{10}$ alloys. Figure 47 plots the η values as a function of reciprocal temperature. The η values of the Al-based alloys decrease significantly from 2×10^{14} Pa s (2×10^{15} poise) at 488 K to 3×10^{12} Pa s at 521 K, and no distinct difference in $\eta(T)$ is seen for the two amorphous alloys. The η value (3×10^{12} Pa s) at 521 K is nearly equal to 10^{12} Pa s which has been reported (Chen 1986) to be the viscosity value for a supercooled liquid near T_g. This indicates that the amorphous solid heated at 521 K changes to a nearly equilibrium supercooled liquid state.

It is generally known that the glass transition gives rise to significant changes of E, σ_f and in deformation behavior, in addition to the above-described changes in specific heat and viscosity. It is of importance for the present Al-based amorphous alloys to clarify the changes in E, σ_f, elongation and fracture behavior by the transition from amorphous solid to supercooled liquid. Figure 48 shows the temperature dependence of σ_f, ε_f and

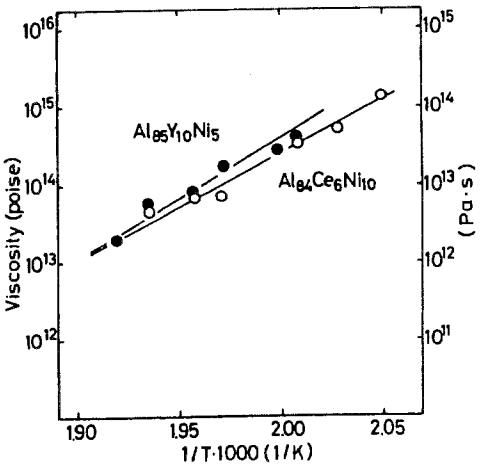

Fig. 47. Change in viscosity of amorphous $Al_{85}Y_{10}Ni_5$ and $Al_{84}Ce_6Ni_{10}$ alloys as a function of reciprocal temperature.

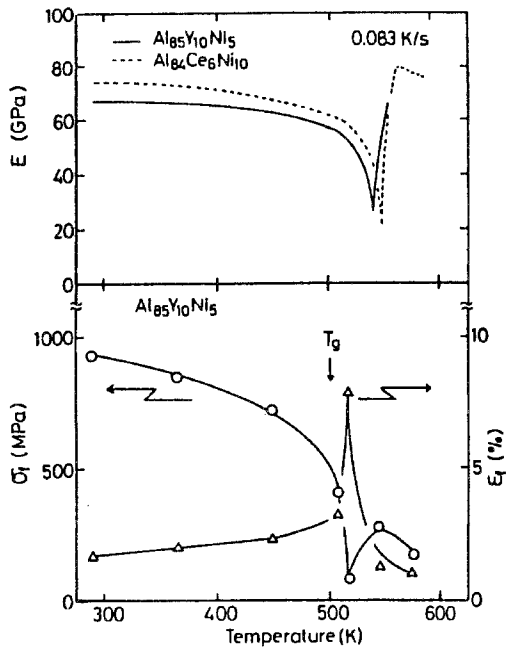

Fig. 48. Changes in E, σ_f and tensile fracture strain (ε_f) of amorphous $Al_{85}Y_{10}Ni_5$ and $Al_{84}Ce_6Ni_{10}$ alloys as a function of testing temperature.

E for the $Al_{85}Y_{10}Ni_5$ and $Al_{84}Ce_6Ni_{10}$ amorphous alloys. With increasing temperature, the σ_f and E values gradually decrease from 920 to 700 MPa and 72.6 to 55.0 GPa, respectively, in the amorphous solid and rapidly to 100 MPa and 21.6 GPa, respectively, in the supercooled liquid and then increase steeply upon crystallization. On the other hand, ε_f steeply increases to 8% in the vicinity of glass transition, followed by a significant decrease of ε_f by crystallization. Figure 49 shows the fracture surface appearance of the

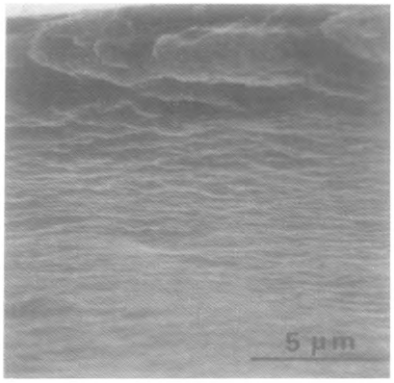

Fig. 49. Scanning electron micrograph showing the tensile fracture surface appearance of amorphous $Al_{85}Y_{10}Ni_5$ alloy tested at 508 K.

amorphous $Al_{85}Y_{10}Ni_5$ alloy tested at 508 K near the glass transition. The specimen is subjected to a severe homogeneous necking which appears to have taken place through a viscous flow mechanism. The features of deformation and fracture behavior shown in figs. 48 and 49 agree with that for Pd-based amorphous alloys exhibiting the glass transition phenomenon (Masumoto and Maddin 1971).

2.5.8. *Amorphous alloy powders and their consolidation into an amorphous bulk (Inoue et al. 1989d)*

The production of Al–Ni–Y amorphous powders was tried by high-pressure helium atomization. Figure 50 shows the shape and morphology of an $Al_{85}Ni_5Y_{10}$ powder with a particle size fraction below 25 μm (< 25 μm). The powder has a spherical shape. The surface is very smooth and no grain boundary is seen. The X-ray diffraction pattern of the < 25 μm powder consisted of broad diffraction peaks, indicating the formation of an almost single amorphous phase. With further increasing powder diameter, the structure is composed of amorphous and crystalline phases for the 25–37 μm fraction and a crystalline phase for the powder with a size fraction above 37 μm. In addition, the size fraction of the amorphous Al–Ni–Y powder was measured by the microtrac analysis method. The fraction is 41% for the powder below 10 μm in size, followed by 24% for the powder between 10 and 15 μm in size, 25% for the 15–21 μm powder and 11% for the powder >21 μm in size. It is thus notable that the powder below 15 μm in size was prepared with a high yield fraction of 65%. Furthermore, the DSC curve obtained from the $Al_{85}Ni_5Y_{10}$ amorphous powder was confirmed to be the same as that for the melt-spun amorphous ribbon, and no appreciable difference in T_g and T_x values was seen by Inoue et al. (1988i). It is therefore concluded that the amorphous powder produced by high-pressure helium atomization can be used as a raw material to produce an amorphous bulk by consolidation at temperatures near T_g.

The extrusion of the $Al_{85}Ni_5Y_{10}$ amorphous powder into an amorphous bulk at extrusion ratios of four and seven was tried by changing the extrusion temperature. The extruded bulk was obtained at temperatures above 543 K and the relative density was measured to be 0.969 at 543 K, 0.980 at 573 K, 0.987 at 603 K and 0.996 at 673 K. The

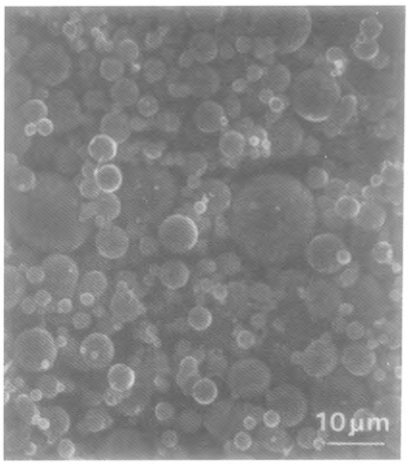

Fig. 50. Scanning electron micrograph showing $Al_{85}Y_{10}Ni_5$ amorphous powder with a size fraction below 25 μm produced by high-pressure helium atomization.

structure of the extruded bulk consists of an almost amorphous phase at 543 K, coexisting amorphous + Al phases at 573 K, coexisting amorphous + Al + unidentified compound at 603 K and Al + unidentified compound at 673 K.

Figure 51 shows the compressive stress–strain curves of $Al_{85}Ni_5Y_{10}$ bulk samples with high densities, >98%, extruded at 603 and 673 K, along with the data of a conventional high-strength Al-based crystalline alloy (2017). The bulk consisting of amorphous and Al phases exhibits a high compressive fracture strength ($\sigma_{c,f}$) reaching 1470 MPa and an E of 145 GPa, although no appreciable plastic elongation is seen. The increase of the extruded temperature to 673 K results in a decrease of the yield (0.2% proof) stress to

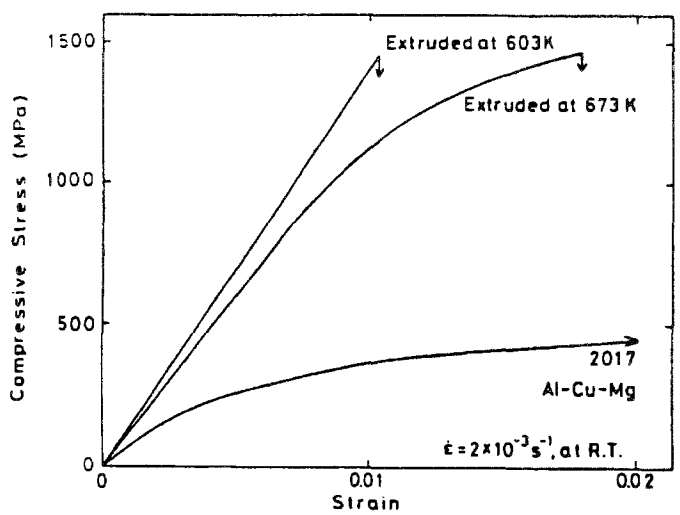

Fig. 51. Compressive stress–strain curves of $Al_{85}Y_{10}Ni_5$ amorphous bulk material produced by extrusion of amorphous alloy powders at 603 and 673 K.

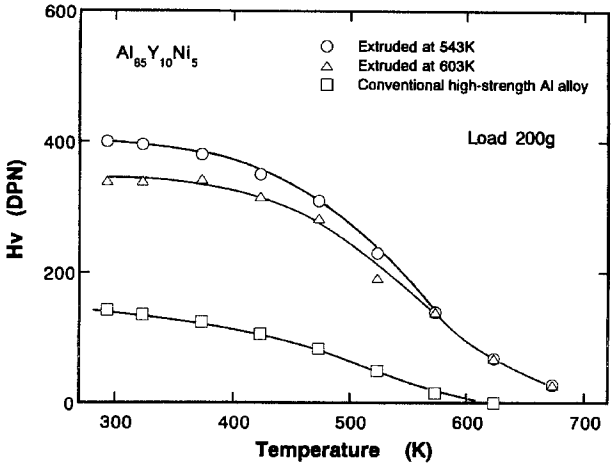

Fig. 52. Change in H_v of extruded $Al_{85}Y_{10}Ni_5$ bulks as a function of testing temperature.

1220 MPa and E to 120 GPa, and an increase of plastic elongation to 0.6%, though the $\sigma_{c,y}$ remains unchanged. It is seen that $\sigma_{c,f}$ and E for the bulk material with a mixed structure of amorphous and fcc phases are about 2 to 3 times as large as those (450 MPa and 71 GPa) for the optimally aged 2017 alloy. The extremely high $\sigma_{c,f}$ which exceeds the tensile fracture strength ($\sigma_{t,f} \equiv 1140$ MPa) of the $Al_{85}Ni_5Y_{10}$ amorphous ribbon is presumably due to a dispersion hardening resulting from a homogeneous dispersion of the spherical Al phase with a size of about 30 nm in an amorphous matrix.

The high-temperature hardness of the high-strength $Al_{85}Ni_5Y_{10}$ bulk samples consisting of an almost amorphous phase or coexisting amorphous + Al phases was measured as a function of the testing temperature. The heating rate to each testing temperature was 10 K/min and the sample was kept for 10 min at each testing temperature. As shown in fig. 52, H_v at room temperature is 340 for the amorphous bulk extruded at 543 K and 405 for the amorphous + Al bulk extruded at 603 K, being about three times as high as that (145) for the 2017 alloy. Furthermore, the high hardness of 150 at 573 K is obtained for the bulk sample extruded at 603 K. It is thus concluded that the extruded bulk materials have high heat-resistant hardness as well as high $\sigma_{c,f}$ and E values. The good mechanical strengths allow us to expect that the extruded bulk samples may be used as a high-strength material with low density under compressive stress conditions.

2.6. *Al-based nanocrystalline alloys by extrusion of amorphous powders*

Amorphous alloy powders in Al–Y–Ni and Al–Ce–Ni systems have been produced by Inoue et al. (1988i) by gas atomization with an applied pressure of 4–10 MPa. Although the formation of their amorphous powders is limited to a particle size fraction below 25 μm, the weight ratio is as high as 85%. Thus, it is concluded that Al-based amorphous powders can be obtained at high production ratios.

Warm extrusion of Al-based amorphous powders was carried out over a wide temperature (T_e) range of 500–783 K (Inoue et al. 1989d, Inoue and Masumoto 1991). For instance, the warm extrusion of an $Al_{85}Y_{10}Ni_5$ amorphous powder was possible at temperatures above 540 K. The packing density was 97% at $T_e = 543$ K. With increasing T_e, the density increases and reaches about 100% at T_e above 673 K. The structure of the extruded alloy consists of an amorphous single phase at 543 and 573 K, a duplex structure of amorphous and Al phases at 603 K and mixed phases of $Al + Al_3Y + Al_3Ni$ above 673 K. $\sigma_{c,f}$ and E of the extruded alloy consisting of amorphous and Al phases are 1470 MPa and 145 GPa, respectively, which is two to three times higher than those ($\sigma_{c,y} = 450$ MPa, $E = 71$ GPa, Vasudevan and Doherty 1989) of the conventional 2017 aluminum alloy. As T_e rises to 673 K, $\sigma_{c,f}$ and E decrease to 1220 MPa and 121 GPa, accompanying the appearance of plastic elongation of 0.5–1.0%. The $\sigma_{c,f}$ value of the extruded alloy is higher than that ($\sigma_f = 1140$ MPa) of a melt-spun $Al_{85}Y_{10}Ni_5$ amorphous ribbon. The increase in $\sigma_{c,f}$ is thought to originate from the dispersion strengthening caused by the homogeneous dispersion of nanoscale Al particles with a size of about 30 nm in the amorphous matrix.

As described above, although the compressive strength of the $Al_{85}Y_{10}Ni_5$ alloy consolidated at temperatures below 673 K is high, the tensile fracture strength (σ_f) shows lower values ranging from 500 to 700 MPa. Consolidation at temperatures above 703 K was carried out with the aim of increasing σ_f. The $Al_{85}Y_{7.5}Ni_{7.5}$ alloy extruded at 783 K has a mixed structure consisting of dispersed Al_3Y and Al_3Ni compounds with a size of about 50 nm in the Al matrix with a grain size of about 0.1 μm. Judging from the previous result noted by Inoue et al. (1990a) that the grain size of a metastable Al-based solid solution in a rapidly solidified $Al_{95}Ce_3Fe_2$ alloy is about 2 μm, it is concluded that the present process consisting of warm extrusion of the amorphous powders is useful for the formation of an ultrafine mixed structure consisting of fine Al_3Ni and Al_3Y particles embedded in the Al matrix. Figure 53 shows the temperature dependence of σ_f, E, $\varepsilon_{t,p}$ and H_v of the $Al_{85}Y_{7.5}Ni_{7.5}$ and $Al_{91}Y_{4.8}Ni_3Co_{1.2}$ alloys along with the data of Vasudevan and Doherty (1989) for the commercial 2014-T6 and 7075-T6 alloys. The σ_f, E, $\varepsilon_{t,p}$ and H_v values at room temperature are 940 MPa, 115 GPa, 2.0% and 265, respectively, for the former alloy and 800 MPa, 84 GPa, 3.5% and 220, respectively, for the latter alloy. Although these values decrease with increasing temperature, the high strength level of $\sigma_f = 380$ MPa, $E = 85$ GPa and $H_v = 105$ is kept at 573 K. It is interesting that these values are about twice as high as those for commercial Al-based alloys. On the other hand, the $\varepsilon_{t,p}$ increases with increasing temperature and is about 10% at 573 K.

The stability of the high σ_f values against annealing is also shown for the bulk $Al_{88.5}Ni_8Mm_{3.5}$ alloy (where Mm = mischmetal) extruded at 633 K in fig. 54 (Ohtera et al. 1992a,b), in comparison with the data of Vasudevan and Doherty (1989) for the A7075 alloy. The open and closed circles in the figure represent the data after annealing at each temperature for 1 and 100 h, respectively. σ_f in the case of 1 h annealing for the extruded Al–Ni–Mm bulk is as high as 940 MPa at room temperature which is much higher than that (700 MPa) for the A7075 alloy. Although σ_f decreases monotonously with increasing temperature, it keeps rather high values of 700 MPa at 423 K and 520 MPa at 473 K. No

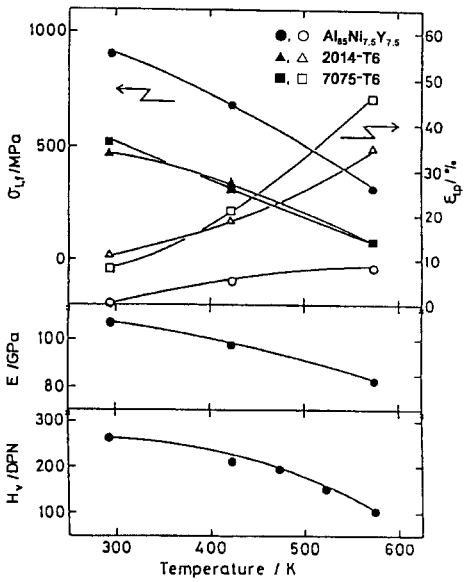

Fig. 53. Changes in mechanical properties with temperature for an $Al_{85}Ni_{7.5}Y_{7.5}$ bulk produced by extrusion at 783 K and an extrusion ratio of 12.

appreciable decrease in σ_f is seen even after annealing for 100 h, although σ_f of the A7075 alloy decreases by 5% at 423 K and by 45% at 473 K. Consequently, in addition to the high tensile strength, the Al–Ni–Mm alloy also has a good heat resistance of the tensile strength. The Young's modulus of the extruded Al–Ni–Mm alloy was also as high as 91 GPa. The achievement of the extremely high tensile strength has been attributed to the formation of a mixed structure consisting of homogeneously dispersed Al_3Ni and $Al_{11}(La,Ce)_3$ compounds with a size of 50 nm in an Al matrix with a grain size of 100–200 nm, as shown in fig. 55. Furthermore, the high σ_f has been roughly evaluated by Ohtera et al. (1992a) from the sum of the dispersion strengthening and the strengthening

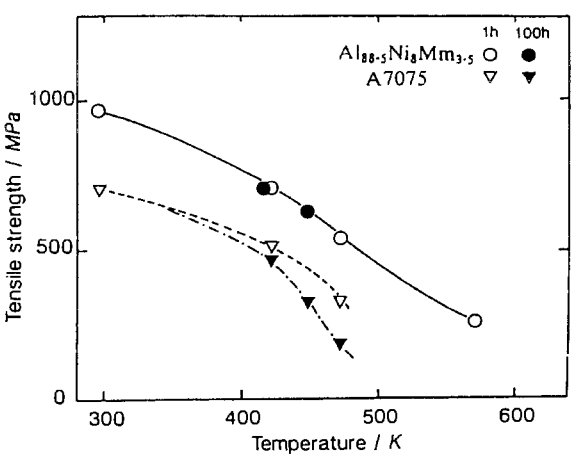

Fig. 54. Temperature dependence of tensile strength for as-extruded bulk $Al_{88.5}Ni_8Mm_{3.5}$ annealed for 1 h and 100 h at each testing temperature. The data for the A7075 alloy are also shown for comparison.

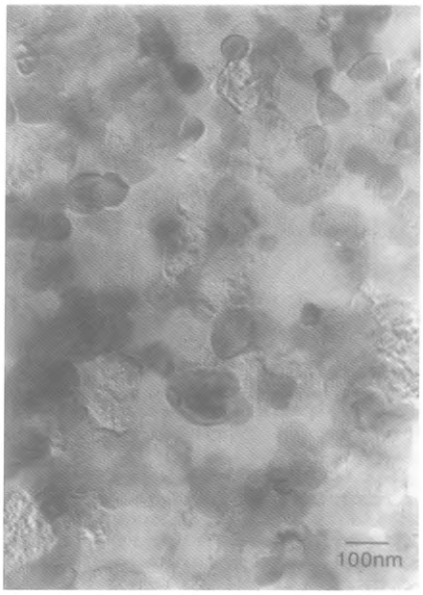

Fig. 55. Bright-field electron micrograph of an as-extruded $Al_{88.5}Ni_8Mm_{3.5}$ alloy.

due to grain size refinement, as shown in fig. 56. Such a finely mixed structure cannot be obtained by conventional thermomechanical treatments. The good heat resistance of σ_f for the present alloy is presumably because the strength mechanism is due to the dispersion hardening by the intermetallic compounds, which is different from the result (Vasudevan and Doherty 1989) that the strengthening mechanism for the A7075 alloy is due to the age-hardening mechanism.

The fatigue limit after cycles of 10^7 for the extruded Al–Ni–Mm alloy was measured to be 330 MPa at 293 K and 196 MPa at 473 K. In order to compare the present fatigue limit with the data for other Al-based alloys, the fatigue limit is plotted against the

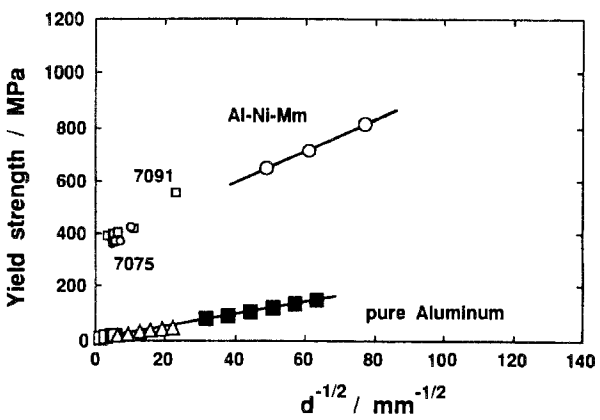

Fig. 56. Hall–Petch relation of the yield strength ($\sigma_{0.2}$) at room temperature for as-extruded $Al_{88.5}Ni_8Mm_{3.5}$ alloys.

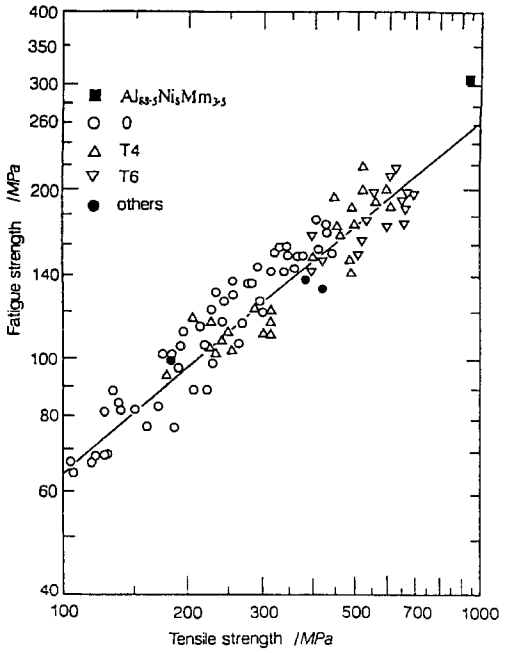

Fig. 57. Relation between fatigue limit after the cycles of 10^7 and tensile fracture strength for an as-extruded $Al_{88.5}Ni_8Mm_{3.5}$ alloy. The data for conventional Al-based alloys are also shown for comparison. The symbols O, T4 and T6 represent the samples that were subjected to annealing, natural aging after solid solutioning and artificial aging after solid solutioning, respectively.

tensile strength for Al-based alloys in fig. 57. It can be seen that the fatigue limit is about 1.3 times as high as the highest fatigue limit (260 MPa) reported by Vasudevan and Doherty (1989) for newly developed Al-based alloys made from rapidly solidified powders. It is therefore concluded that both the tensile strength and the fatigue limit for the extruded Al–Ni–Mm alloy are much superior to those for the newly commercialized Al-based alloys developed by using the powder metallurgy technique as well as the conventional Al-based alloys.

It is also expected that a low coefficient of thermal expansion and a high wear resistance are also obtained for the Al–Ni–Mm alloy because of the precipitation of a large amount of Al_3Ni and $Al_{11}(La,Ce)_3$ compounds. The coefficient of thermal expansion (α) in the temperature range of 423–473 K and the relative wear resistance against S45C were examined in comparison with the data of Vasudevan and Doherty (1989) for the A6061 and A5056 alloys. The α value is about 20% smaller than that for the conventional Al-based alloys. The wear loss is also about 25% smaller than that for the Al–Si–Mg and Al–Mg base alloys. It is thus concluded that the Al–Ni–Mm alloy has a high wear resistance as well as a low coefficient of thermal expansion.

In addition to the good mechanical properties resulting from the finely mixed structure, the bulk alloys have been reported by Higashi et al. (1992, 1993) to exhibit marked superplasticity in a high strain rate range of $0.1–10\,s^{-1}$, as shown in fig. 58 in which the strain rate sensitivity exponent (m value) is above 0.5 and the maximum elongation reaches as large as 550% at a strain rate of about $1.0\,s^{-1}$.

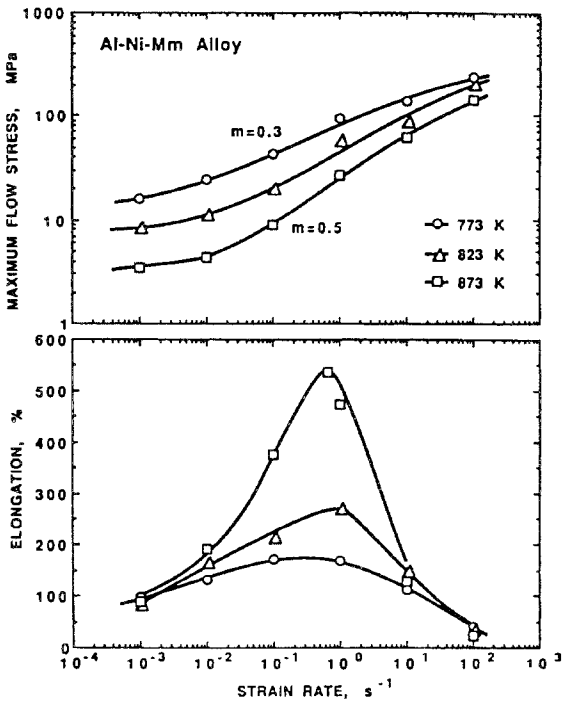

Fig. 58. Variation of (top) flow stress and (bottom) elongation for as-extruded $Al_{88.5}Ni_8Mm_{3.5}$ alloys as a function of strain rate at temperatures between 773 and 873 K.

By utilizing the good superplasticity, the present mixed phase alloys have been deformed into machinery parts with various complicated morphologies. The bulk Al–Ni–Mm alloys produced through the process of extrusion, forging and mechanical polishing have been used by Ohtera et al. (1991) as machine parts that are required to have simultaneously high σ_f, high fatigue limit and low coefficient of thermal expansion, as exemplified in fig. 59. In addition to such machine parts, the new Al-based alloys produced by extrusion of amorphous powders are expected to be used in various application

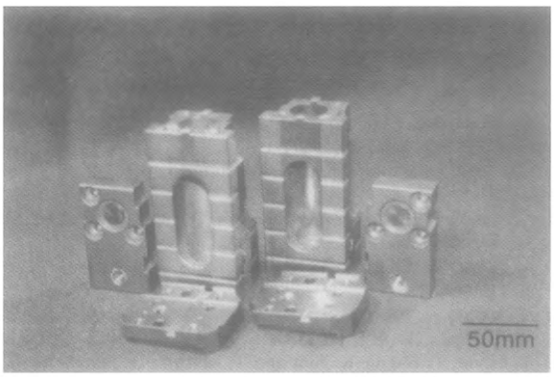

Fig. 59. Machinery parts made from $Al_{88.5}Ni_8Mm_{3.5}$ powders were produced by extrusion, forging and mechanical polishing.

fields where the simultaneous achievement of high strength with light weight, high heat resistance of strength, high fatigue strength, low coefficient of thermal expansion and wear resistance is required.

2.7. *Al-based amorphous alloys containing nanoscale Al particles (Y.H. Kim et al. 1990, 1991a,b, Inoue et al. 1992a,b)*

With the aim of fabricating Al-based alloys with much higher tensile strength, we investigated the strengthening mechanism of metallic materials. It is well known that a metallic whisker with perfect crystalline structure has a much higher tensile strength as compared with an amorphous alloy (Inoue 1995a). Therefore, we thought that the further decrease in particle size of the crystalline phase causes the absence of internal defects. If we could produce a finely mixed phase alloy consisting of amorphous and nanoscale crystalline particles, the resulting mixed phase alloys are expected to exhibit a tensile strength exceeding largely the σ_f values of amorphous single phase alloys. Inoue et al. (1988h) noticed that Al-rich amorphous alloys prepared by a two-stage crystallization process consisting of Am $\rightarrow$ fcc-Al + Am′ $\rightarrow$ Al + intermetallic compounds have a two-stage continuous cooling transformation behavior where an Al phase field is located at the lower temperature side, as illustrated in fig. 60. The control of the cooling rate for this type of Al-based alloys is expected to result in the fabrication of a finely mixed structure consisting of nanoscale Al particles and an amorphous phase. As the rotation speed of the wheel (cooling rate) decreases, the structure of an $Al_{88}Ni_9Y_2Fe_1$ alloy changes from an amorphous single phase to mixed phases consisting of nanoscale Al particles embedded in an amorphous matrix. The particle size of the Al phase is as small as 3–5 nm. The volume fraction (V_f) of the Al phase can be estimated to be in the range from about 4 to 40% by measuring the change in the exothermic energy due to the precipitation of the Al phase. The homogeneous dispersion of the nanoscale Al particles was found to cause a significant increase in σ_f from 900 to 1100 MPa to 1560 MPa at $V_f \equiv 20\%$, depending on the alloy components. This is also accompanied

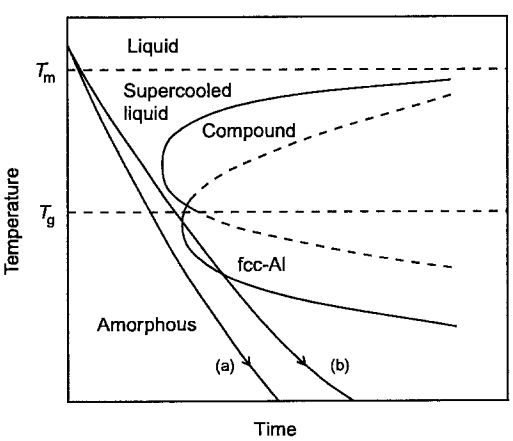

Fig. 60. Schematic illustration of a two-stage continuous cooling transformation (C.C.T.) behavior for Al-rich amorphous alloys and two kinds of cooling curves.

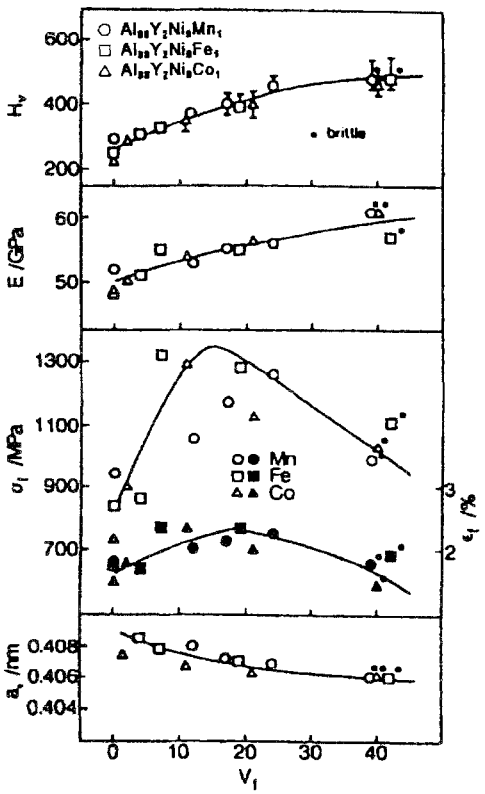

Fig. 61. Changes in σ_f, E, H_v, ε_f and a_0 as a function of V_f for rapidly solidified $Al_{88}Ni_9Y_2M_1$ (M = Mn, Fe or Co) alloys.

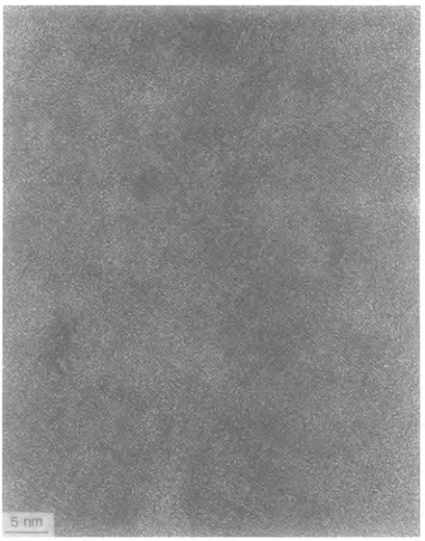

Fig. 62. High-resolution TEM image of a rapidly solidified $Al_{88}Ni_9Y_2Fe_1$ alloy prepared at a rotation speed of 33 m/s.

by a slight increase in ε_f, E and H_v, as shown in fig. 61. The lattice parameter (a_0) also shows a continuous decrease with increasing V_f. The continuous decrease in a_0 has been interpreted to result from the gradual decrease in Ce content in the Al phase. When the conventional mixing rule is used in the interpretation of the reason for the achievement of the high tensile strength for the mixed phase alloy, the nanoscale Al phase is estimated to have an extremely high σ_f of 4500 MPa which is about 65% as high as the theoretical strength of Al-based alloys.

In order to clarify the reason why the nanoscale Al particles have such a high tensile strength, the internal structure of the mixed phases was examined by the high-resolution TEM technique. Figure 62 shows the high-resolution TEM image of the mixed phases in the rapidly solidified $Al_{88}Ni_9Y_2Fe_1$ alloy. No appreciable contrast revealing the existence of internal defects is seen in the nanoscale Al particles. The absence of internal defects is presumably because the annihilation of the internal defects along the phase boundary between fcc-Al and amorphous phases causes the decrease in internal energy. That is, the nanoscale Al particles are too small to contain internal defects. The interface between Al and amorphous phases does not have any faceted planes and appears to have a highly dense atomic configuration presumably because of the wetting effect resulting from an

amorphous (liquid-like) structure and a very low interfacial energy between amorphous (liquid) and Al phases. This interface structure seems to be appropriate for the increase in σ_f by utilizing the Al particles with high strength through the good transmittance state of the applied load between amorphous and fcc-Al phases and the suppression of the failure at the interface. Furthermore, each Al particle has independent orientations in spite of the nanoscale interparticle spacings because of homogeneous precipitation from the amorphous phase. Based on these results, it is presumed that ultrahigh mechanical strength achieved is due to the combination of the following three effects (Inoue and Masumoto 1993a): (1) perfect crystal effect resulting from the annihilation of defects along the interface between Al and amorphous phases, the isostatic internal stress field caused by structural and compositional homogeneity, and the ease of stress (strain) relaxation of the amorphous matrix; (2) interface effect resulting from a good adhesive bonding state caused by the liquid-like amorphous structure and continuous changes in the alloy components and structure, resulting from an indistinct interfacial structure; and (3) nanoscale particle size effect resulting from a particle size smaller than the thickness of the inhomogeneous shear deformation region in an amorphous matrix. According to Masumoto and Maddin (1971) amorphous alloys are deformed along the maximum shear plane with a thickness of 10 to 20 nm which is declined by about 45° from the tensile direction. Therefore, only when the particle size is comparable to or smaller than the thickness of the shear deformation band, the particles can act as an effective barrier against the subsequent shear deformation of the amorphous matrix.

A similar finely mixed structure consisting of nanoscale Al particles and an amorphous matrix was also obtained by annealing Al-based amorphous alloys containing Cu, Ag or Ga (Inoue et al. 1994a) which is soluble in the Al phase at elevated temperatures. The particle size of the Al precipitates is as small as 3 to 5 nm for the Cu- or Ag-containing alloys. The homogeneous precipitation causes a significant increase in σ_f to about 1500 MPa which is about 1.4 times as high as that for the amorphous single phase, as exemplified for the $Al_{87}Ni_7Cu_3Nd_3$ alloy in fig. 63 (Inoue et al. 1994b).

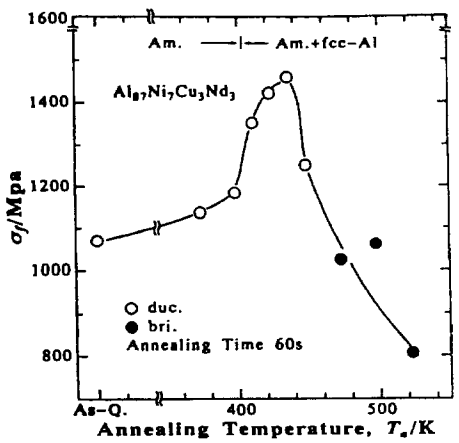

Fig. 63. Change in σ_f of an amorphous $Al_{87}Ni_7Cu_3Nd_3$ alloy with annealing temperature. The data of structural change are also shown for reference.

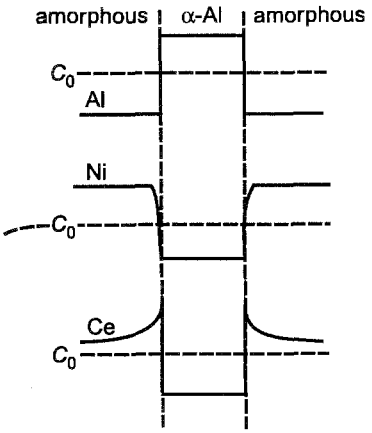

Fig. 64. Schematic illustration of the concentration profiles of Al, Ni and Co elements across the interface between fcc–Al and amorphous phases for an amorphous $Al_{87}Ni_{10}Ce_3$ alloy annealed for 180 s at 553 K.

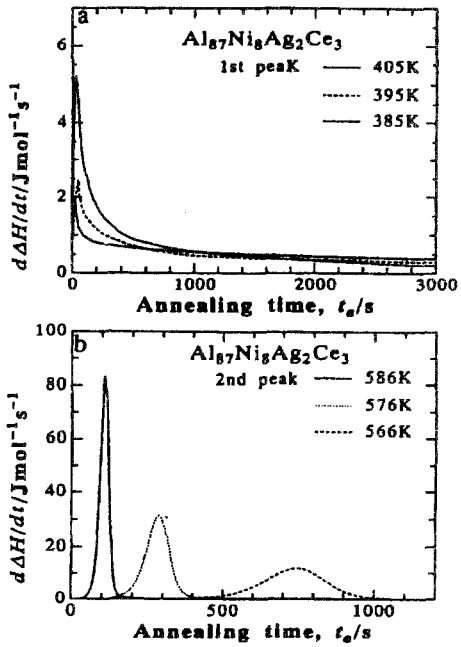

Fig. 65. Change in the exothermic energy with annealing time for an $Al_{87}Ni_8Ag_2Ce_3$ alloy subjected to isothermal annealing at various temperatures. (a) The first-stage exothermic peak due to the precipitation of fcc–Al particles, (b) the second-stage exothermic peak due to the precipitation of mixed fcc–Al and compound phases.

We have investigated why Al particles can keep the nanoscale in the as-quenched and annealed states by the atom probe field ion microscopy technique (Hono et al. 1995). The concentration profiles of each constituent element in an $Al_{87}Ni_{10}Ce_3$ amorphous alloy with a mixed structure of Al and amorphous phases annealed for 180 s at 553 K are illustrated in fig. 64. Only Ce is significantly enriched in the amorphous phase field just near the interface between Al and amorphous phases because of the low atomic diffusivity of Ce which has the largest atomic size of the three components at the low annealing temperature. The significant enrichment of Ce in the amorphous phase near the interface seems to be the origin for the maintenance of the nanoscale particle size for the Al phase. This result also indicates that the elimination of Ce from the Al phase to the remaining amorphous phase is very sluggish, which is consistent with the gradual decrease in a_0 of the Al phase with increasing annealing temperature and annealing time.

Inoue et al. (1994c) also investigated the precipitation behavior of nanoscale Al particles during low-temperature annealing, with the aim of understanding the feature of the precipitation of the nanoscale Al particles during continuous cooling from liquid. The $Al_{87}Ni_8Ag_2Ce_3$ sample subjected to isothermal annealing at various temperatures well below T_x shows a continuous decrease in the exothermic energy as shown in fig. 65. It is therefore thought that the precipitation of the nanoscale Al phase takes place in a

continuous growth mode (Chen and Spaepen 1988) of the pre-existing Al nuclei. This precipitation behavior is in contrast to the conventional nucleation and growth mode for the precipitation of mixed Al and intermetallic compounds at the second stage. The distinct change in the exothermic reaction with temperature and time during isothermal annealing indicates the possibility of controlling the nucleation and growth reactions for the precipitation of the Al phase. It is therefore expected that a further precise control of the nucleation and growth mode causes the formation of a mixed phase alloy containing smaller Al particles of 1 to 3 nm which enables the further increase in σ_f.

2.8. *Al-based nanoquasicrystalline alloys (Inoue et al. 1992c, 1994d, 1995a, Watanabe et al. 1993)*

Although the quasicrystalline alloys reported up to date can be divided into icosahedral, decagonal, dodecagonal and octagonal phases, the quasicrystals which are composed of a single phase are limited to icosahedral and decagonal phases. It is known that the icosahedral phase is formed in a number of Al–TM alloy systems containing Mn, Cr, V, Fe, Cu or Pd etc. as TM elements. The icosahedral phase in the Al–TM base system has been reported by Elser and Henley (1985) to be composed of Mackay icosahedral clusters containing 55 atoms which are arranged through glue atoms to the three-dimensional quasiperiodic lattice. Consequently, from the large unit volume and the number of constituent atoms in the icosahedral structure, it is expected that subnanoscale control of the icosahedral structure enables the improvement of ductility and toughness and the achievement of high magnetization at room temperature. In this section, we present the data of high σ_f and good ductility for the icosahedral base alloys in the Al-based system.

In order to fabricate such a new material with the novel properties, it is necessary to understand the deformation and fracture behavior of the icosahedral phase itself. It is generally known, e.g. see Voisin and Pasturel (1987), that the icosahedral alloy can contain dislocations. However, the movement of the dislocations is difficult at room temperature and elevated temperatures because the movement of the dislocations destroys the quasiperiodic lattice (Takeuchi 1992). This fact indicates that the increase in the deformability of the icosahedral alloy must be accomplished by another mechanism. More recently, we have succeeded (Inoue et al. 1994e) in preparing a large single $Al_{70}Pd_{20}Mn_{10}$ quasicrystal with an icosahedral structure by the Czochralski technique which is 12 mm in diameter and 140 mm in length. In the nominal compressive stress–strain curves for the single quasicrystal subjected to testing at various temperatures, no appreciable plastic elongation is seen in the temperature range below 1000 K, but an increase in the testing temperature causes the appearance of a significant elongation. The flow stress of about 650 MPa at 1073 K is considerably higher than that of a heat-resistant Ni_3Al compound. Furthermore, the Young's modulus at room temperature is as high as 200 GPa which is about 3 times higher than that for conventional Al-based alloys. The plastic deformation of the $Al_{70}Pd_{20}Mn_{10}$ single quasicrystal in the temperature range above 1000 K takes place preferentially along the severely limited deformation bands (Yokoyama et al. 1993).

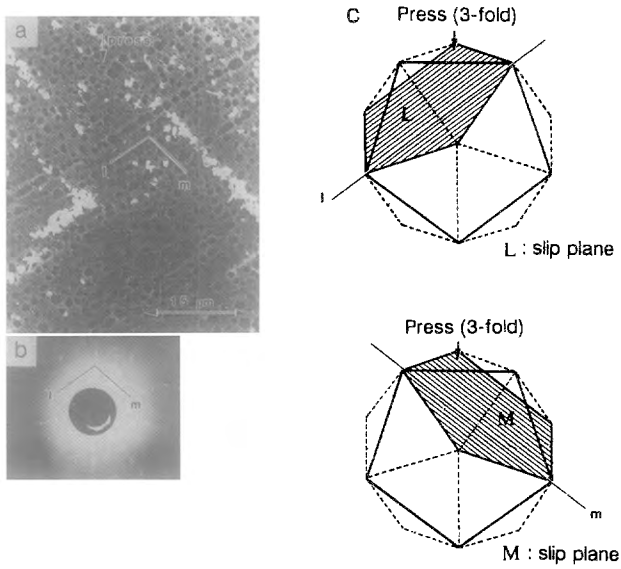

Fig. 66. (a) Scanning electron micrograph and (b) X-ray Laue pattern taken from the lateral surface in the $Al_{70}Pd_{20}Mn_{10}$ single quasicrystal deformed up to 20% elongation at 1073 K and (c) the analytical result in which the L and M planes lie along the fivefold planes.

Furthermore, the Al concentration at the deformation bands increases distinctly and a deformation-induced deviation of the alloy components has been detected. As exemplified in fig. 66, the deformation bands lie along the close-packed fivefold planes. Furthermore, one can see the contrast of pentagonal shaped precipitates, which have been confirmed by Inoue et al. (1994e) to have an approximate crystalline structure by TEM analyses. From these experimental results, we have proposed (Inoue et al. 1994e) that plastic deformation takes place through the following process; the generation of strain by the application of load introduces a linear phason accompanying the deviation of the alloy components, leading to the formation of approximate crystalline phases with a periodic atomic configuration. It is therefore presumed that the plastic deformation takes place preferentially at the interface between icosahedral and approximate crystalline phases. One can notice that the anomalous deformation mode comes from a unique transformation behavior. That is, it is known (Bak 1985) that the mismatch of tiling in the construction of a penrose tiling pattern causes the formation of small regions with periodic atomic configurations through the introduction of phason defects. Furthermore, by the deviation of two-dimensional quasiperiodic lattice points, we can obtain one-dimensional approximate crystalline phases accompanying the formation of the phason defects (Levine et al. 1985). Thus, the transformation of the icosahedral phase to approximate crystalline phases can take place on a subnanoscale according to Ishii (1989). By utilizing the anomalous deformation mode resulting from the unique transformation behavior, we can expect to fabricate a quasicrystal which can be deformed at room temperature. That is, by

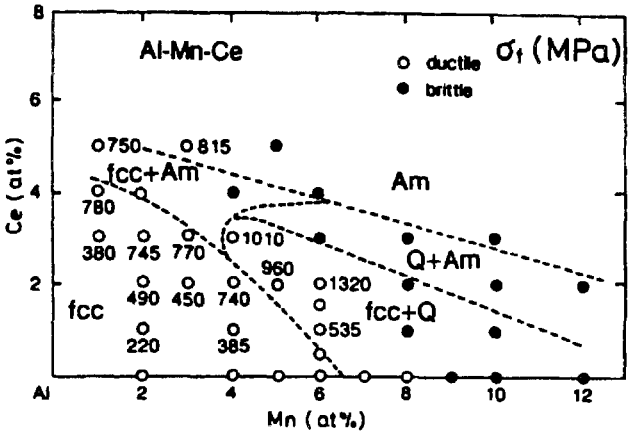

Fig. 67. Compositional dependence of as-quenched structure and mechanical properties for rapidly solidified Al–Mn–Ce alloys. Am, amorphous; Q, icosahedral quasicrystalline phases.

refinement to a nanoscale size and the deviation of the alloy components to the Al-rich range, we can introduce a high density of phason defects into the nanoscale Al-rich icosahedral phase, leading to the formation of coexistent icosahedral and approximate crystalline phases at Al-rich compositions.

The above-described nanoscale structure control was examined for rapidly solidified Al–Mn–R by Inoue et al. (1992c) and Watanabe et al. (1993) and for Al–Cr–R by Inoue et al. (1994d). These alloy systems were chosen because Al–Mn (Shechtman et al. 1984) and Al–Cr (Inoue et al. 1987c) alloys are well-known icosahedral-forming alloy systems and R is the most effective element to increase the quenching effect for Al–TM alloys. Figure 67 shows the compositional dependence of structure and mechanical properties of rapidly solidified Al–Mn–Ce alloys (Inoue et al. 1992c). The mixed fcc-Al and icosahedral phases are formed in the high Al concentration range above 92 at% Al and the mixed phase alloys exhibit good bending ductility and high tensile strength reaching 1320 MPa. Figure 68 shows the bright-field electron micrograph and the selected-area electron diffraction pattern of the rapidly solidified $Al_{92}Mn_6Ce_2$ alloy with the highest σ_f value. The structure consists of spherical icosahedral particles with a particle size of 30 to 50 nm surrounded by a thin fcc-Al phase with a thickness of about 10 nm. The nanoscale icosahedral particles disperse in an isolated state at the nanoscale interparticle spacing. The reflection rings come from the icosahedral particles, indicating that these icosahedral particles have random orientations because of the solidification mode of the primary precipitates of the icosahedral phase, followed by solidification of the fcc-Al phase from the remaining liquid. Furthermore, one can see a significant scattering of the reflection rings, suggesting that the icosahedral particles contain a high density of phason defects and approximate crystalline phase fields. The volume fraction of the icosahedral phase is as high as about 70%.

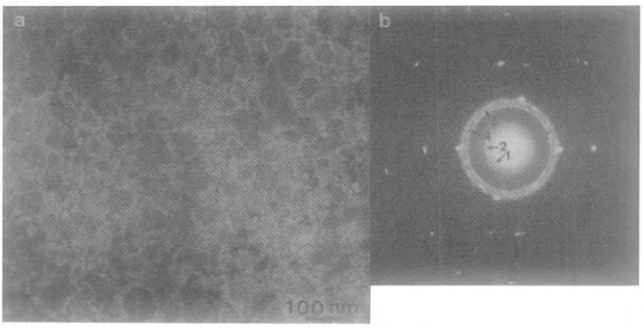

Fig. 68. (a) Bright-field electron micrograph and (b) selected-area electron diffraction pattern of a rapidly solidified $Al_{92}Mn_6Ce_2$ alloy. The numbers 1, 2, 3 and 4 in (b) represent the (111000), (111100), (211111) and (221001) reflection rings, respectively, of the icosahedral phase.

A similar finely mixed structure has also been obtained for Al–Cr base alloys, Inoue et al. (1994d, 1995a). As an example, fig. 69 shows the bright- and dark-field images and the selected-area electron diffraction pattern of a rapidly solidified $Al_{94.5}Cr_3Ce_1Co_{1.5}$ alloy with a high tensile strength of 1340 MPa. The dark-field image was taken from a part of the $(211111)_i$ and $(221001)_i$ reflection rings resulting from the icosahedral phase. It is seen that icosahedral particles with a size of 10 to 30 nm distribute very homogeneously and the surrounding Al phase does not contain any appreciable high-angle grain boundaries. These structural features are thought to result from the unique solidification mode which consists of precipitation of the primary icosahedral phase, followed by the solidification of the Al phase from the remaining liquid (Inoue 1994a). Furthermore, the appearance of distinct reflection rings similar to halo rings suggests that the nanoscale icosahedral particles have a highly disordered icosahedral structure. A similar high tensile strength exceeding 1000 MPa is also obtained for rapidly solidified $Al_{93.5}Cr_3Co_{1.5}Ce_1M_1$ (M = Ti, Mn, Fe, Co, Ni, Cu, Zr or Mo) alloys and the highest σ_f reaches as high as 1350 MPa for $Al_{93.5}Cr_3Co_{1.5}Ce_1Ti_1$. The achievement of high σ_f values exceeding 1000 MPa is independent of the kind of transition elements.

To clarify why these icosahedral base alloys exhibit high tensile strength and good bending ductility, the internal structure of the icosahedral phase was examined by Inoue et al. (1995b) using high-resolution TEM. The high-resolution TEM image shown in fig. 70 was taken from the icosahedral phase field in rapidly solidified $Al_{94.5}Cr_3Ce_1Co_{1.5}$. No contrast revealing a fivefold atomic configuration is seen over the whole image. One can see a modulated contrast typical for an amorphous phase over almost all the areas, though there are small regions with fringe contrast corresponding to the fcc-Al phase. The nanobeam electron diffraction pattern taken from the small region (B) with a diameter of 1 nm in the modulated contrast region consists only of halo rings. The structural features in which the modulated contrast is observed in the high-resolution TEM image and the halo rings appear in the nanobeam diffraction pattern are confirmed to be always observed in other icosahedral phase fields. However, in the nanobeam diffraction pattern taken from the region with a diameter of 3 nm, reflection spots with fivefold

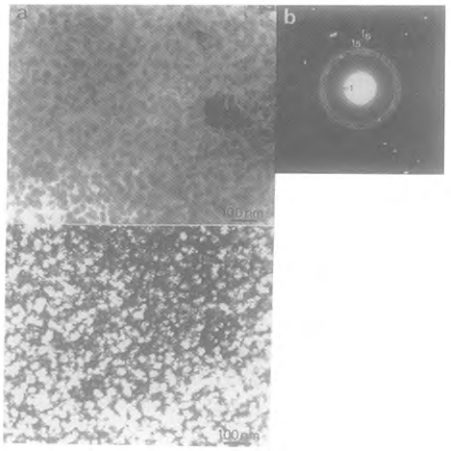

Fig. 69. (a) TEM bright-field micrograph, (b) selected-area diffraction pattern and (c) dark-field micrograph of a rapidly solidified $Al_{94.5}Cr_3Ce_1Co_{1.5}$ alloy. The dark-field image was taken from a part of $(211111)_i$ and $(221001)_i$ reflection rings of the icosahedral phase. The numbers 1, 3, 4, 5 and 6 in (b) represent the (111100), (211111), (221001), (322101) and (332002) reflection rings, respectively, of the icosahedral phase.

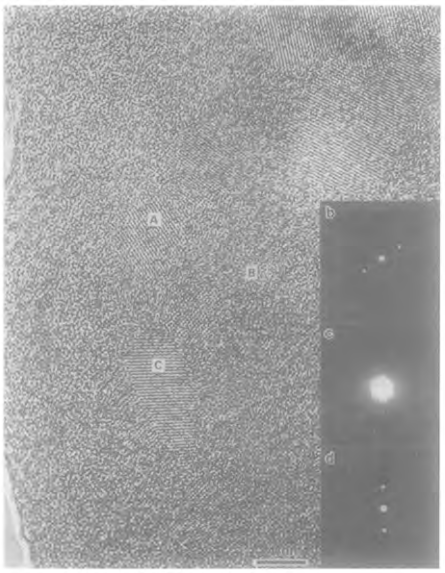

Fig. 70. (a) High-resolution TEM image and (b–d) nanobeam diffraction patterns taken from the icosahedral phase field in a rapidly solidified $Al_{94.5}Cr_3Ce_1Co_{1.5}$ alloy. Patterns (b), (c) and (d) were taken from the regions A, B and C, respectively, with a diameter of 1 nm.

symmetry have scarcely been observed in the superimposed state with halo rings. These data indicate that the nanoscale icosahedral particles with a size of 10 to 30 nm have a disordered atomic configuration on the short-range scale less than about 1 nm and an icosahedral atomic configuration on the long-range scale above 3 nm. The short-range disorder and long-range icosahedral structure seems to be a new type of nonequilibrium structure which is different from amorphous, quasicrystalline and crystalline structures. The new nonequilibrium structure can be said to have the following features: (1) existence of attractive bonding between major (Al) and minor atoms; (2) absence of slip planes; (3) existence of voids which enable the local movement of the constituent atoms; (4) unfixed atomic configurations leading to structural relaxation; and (5) existence of Al–Al bonding pairs because of the Al-rich concentrations. These features are nearly the same as those for metallic amorphous alloys with high tensile strength and good ductility. It is therefore presumed that this similarity is the origin for the achievement of high tensile strength and good ductility in icosahedral base alloys.

Inoue et al. (1995b) have confirmed that the icosahedral base structure caused by rapid solidification can be kept up to an annealing treatment for 3.6 ks at 823 K. The high thermal stability of the icosahedral base structure enables the production of bulk icosahedral base alloys by extrusion of atomized icosahedral base powders in the

temperature range of 573 to 673 K well below the decomposition temperature of the icosahedral phase (Inoue 1994b). Figure 71 shows the correlation between σ_f and tensile elongation for the bulk icosahedral base alloys in Al–Mn–Ce–Co and Al–Cr–Ce–Co systems, along with the data of commercial Al-based alloys and bulk nanogranular Al alloys obtained by extrusion of atomized amorphous powders at temperatures above T_x. It is seen that the bulk icosahedral base alloys exhibit high σ_f combined with large elongation. The elongation is about 2 to 3 times as large as that for conventional high-strength type Al alloys. The bulk icosahedral alloys also exhibit a high elevated-temperature strength above 200 MPa at 573 K which is about 5 to 10 times higher than that for conventional age-hardening type Al alloys. Furthermore, the Young's modulus of

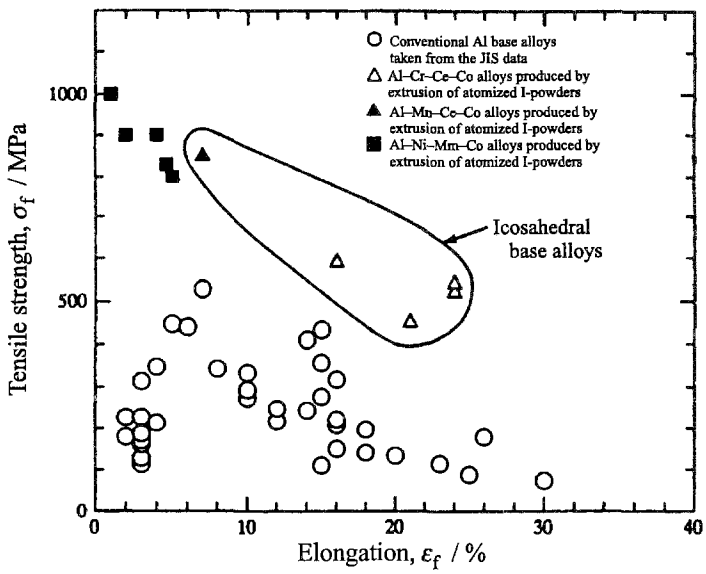

Fig. 71. Relation between σ_f and ε_f for bulk icosahedral base Al–Mn–Ce–Co and Al–Cr–Ce–Co alloys produced by extrusion of atomized icosahedral base powders in the temperature range of 573 to 673 K. The data of conventional Al-based alloys and nanogranular crystalline Al-based bulk alloys prepared by extrusion of atomized amorphous powders are also shown for comparison.

the bulk icosahedral base alloys at room temperature is as high as 97 to 102 GPa which is about 1.5 times higher than that for conventional Al alloys. In summary, bulk icosahedral base alloys have the following features: (1) new nanostructure with short-range disorder and long-range quasiperiodicity; (2) new strengthening mechanism; (3) high specific strength; (4) high specific modulus; (5) high ductility leading to cold formability; and (6) high elevated-temperature strength. These features allow us to expect that the present icosahedral base alloys will be developed as a new type of high-strength Al alloys.

3. Mg–R base amorphous alloys

3.1. *History of Mg-based amorphous alloys*

We have investigated the effect of solute elements on the glass-forming tendency, mechanical strength and thermal stability of Al-rich amorphous alloys in the systems Al–M–Si (M = transition metal) (Inoue et al. 1987a), Al–M–Ge (Inoue et al. 1988e) and Al–EM–LM (EM = group IV to VI transition metal, LM = group VII and VIII transition metal) (Tsai et al. 1988a). We have derived two empirical rules for the formation of the Al-based amorphous phase, namely, (1) large negative heats of mixing among Al and solute elements, and (2) significantly different atomic size ratios between Al and solute elements.

Based on these empirical factors, we have searched for the formation of an amorphous phase in the Al–R systems (Massalski 1990). First, we have succeeded in producing amorphous alloys with high tensile strength in Al–R (Inoue et al. 1988c,j, 1989a) and Al–R–M (Inoue et al. 1988a,b) systems. Subsequently, by taking into consideration the similarity of the bonding nature between Al–R and Mg–R atomic pairs, we have also succeeded in synthesizing Mg-based amorphous alloys in Mg–R–M (Inoue et al. 1988k, 1989e) and Mg–R (S.G. Kim et al. 1989) systems by melt spinning. In particular the Mg–R–M amorphous alloys have high tensile strength, good ductility, a wide supercooled liquid region before crystallization and large glass-forming ability. Before the discovery of the new Mg-based amorphous alloys in Mg–R and Mg–R–M systems in 1988, the glass formation of Mg-based alloys had been limited to the Mg–Zn and Mg–Cu binary systems (e.g. see respectively, Calka et al. 1977, Sommer et al. 1980). However, the Zn and Cu concentrations leading to the formation of an amorphous single phase in these alloy systems are as high as 25 to 35% Zn and 20 to 40% Cu and the resulting amorphous alloys are brittle, i.e., the melt-spun ribbons fracture during bending deformation through 180°. No Mg-based amorphous alloys with high mechanical strength and good ductility had been obtained. Since the discovery of Mg-based amorphous alloys with high tensile strength in Mg–R (S.G. Kim et al. 1989) and Mg–R–M (Inoue et al. 1988k, 1989e), the extension of the mechanism for the glass formation has enabled the synthesis of a number of Mg-based amorphous alloys in Mg–Ni (Sommer et al. 1980) and Mg–Ca (Shibata et al. 1993) binary and Mg–Y–R (S.G. Kim et al. 1990), Mg–Y–Al (S.G. Kim et al. 1990), Mg–Ca–Al (Kato et al. 1995), Mg–Zn–Al (Niikura et al. 1994b) and Mg–Al–Ga (Shibata et al. 1994) ternary systems.

In this section, we report our recent results on the synthesis of Mg-based amorphous alloys in ribbon, bulk and powder forms by various preparation techniques such as melt spinning, metallic mold casting, high-pressure die casting and high-pressure gas atomization, and on their thermal, mechanical and chemical properties. This review also deals with the microstructure and mechanical properties of Mg-based alloys produced by warm consolidation of the atomized powders.

Table 9
Mg-based amorphous alloys produced by melt spinning

Alloy component	Metal–metal system[a]	Metal–metalloid system
Binary	Mg–Ca, Mg–Ni, Mg–Cu, Mg–Zn, Mg–Y	
Ternary	Mg–Ca–Al, Mg–Ca–Li, Mg–Ca–M, Mg–Sr–M, Mg–Al–R, Mg–Al–Zn, Mg–Ni–R, Mg–Cu–R, Mg–Zn–R	Mg–Ca–Si, Mg–Ca–Ge, Mg–Ni–Si, Mg–Ni–Ge, Mg–Cu–Si, Mg–Cu–Ge, Mg–Zn–Si, Mg–Zn–Ge

[a] R, rare earth; M, transition metal (Ni, Cu, Zn).

3.2. *Amorphous alloy systems*

Table 9 summarizes the glass formation in Mg-based alloys containing more than 50 at% Mg by melt spinning in an argon atmosphere (Inoue and Masumoto 1993a). The alloy systems can be divided into two types: metal–metal and metal–metalloid. Although glass formation in Mg–R binary systems is limited to Mg–Y, it has been extended to a number of alloy systems by the addition of M elements. In these alloy systems, the Mg–R–M system is the most important because of the achievement of the highest tensile fracture strength. As examples, the composition ranges in which an amorphous phase is formed in Mg–Ni–R and Mg–Cu–R systems are shown in fig. 72. An amorphous phase is formed in almost all the composition ranges with solute concentrations above 12 at% in both alloy series. However, glass formation in Mg–R binary systems is limited to Mg–Y and no amorphous phase is formed in melt-spun Mg–R (R = La, Ce or Nd) binary alloys. Here, it is important to understand why the glass formation range is limited to the Mg–Y system. The equilibrium phase diagrams of Mg–R binary alloys (Massalski 1990) show that the eutectic composition at the Mg-rich composition side is about 8.9 at% Y, 2.3 at% La, 4.5 at% Ce and 6.5 at% Nd. Therefore, it is presumed that except for Y the eutectic concentration for R elements is too low to construct a disordered structure.

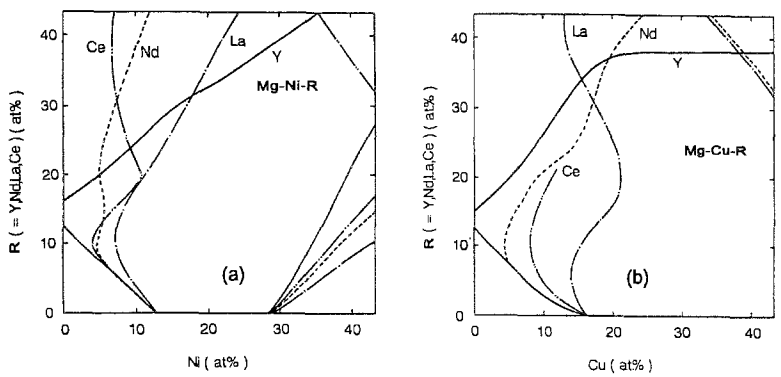

Fig. 72. Composition ranges in which an amorphous phase is formed in (a) Mg–Ni–R and (b) Mg–Cu–R (R = Y, La, Ce or Nd) systems by melt spinning.

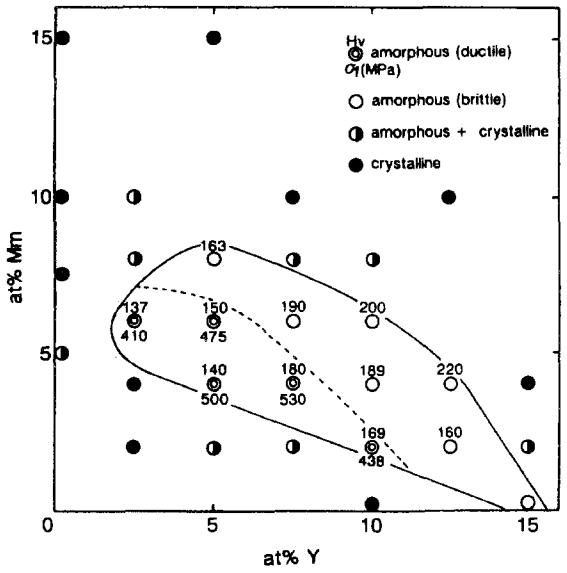

Fig. 73. Composition range in which an amorphous phase is formed in Mg–Y–Mm (Mm = mischmetal) system by melt spinning.

Furthermore, one can see in fig. 72 that the glass formation in the Mg-rich composition range above 80 at% Mg is wider in the order of Y > Nd > Ce > La, regardless of the kind of M element. This order agrees with that of the eutectic concentrations (Y > Nd > Ce > La). These data allow us to presume that glass formation requires an attractive bonding of the solute elements toward Mg, and they must be present above a critical concentration (≡ 12 at%). Moreover, alloys containing the critical solute concentration have a lower melting temperature which results from an eutectic reaction.

In addition to the Mg–R–M system, the Mg–Ca–Al, Mg–Y–Al and Mg–Y–R systems are also attractive for the attainment of high corrosion resistance. As an example, fig. 73 shows the composition range in which an amorphous phase in the Mg–Y–Mm (Mm = mischmetal) system is formed by melt spinning (Horikiri et al. 1994). The term "ductile" implies that the sample can be bent through 180° without fracture, while the word "brittle" means that the sample fractures during bending deformation. The amorphous single phase is formed in the composition range of 2.5 to 15 at% Y and 0 to 7.5 at% Mm. The amorphous phase is formed at a Mg-rich composition of 5 at% Y and 4 at% Mm. Glass formation at a Mg-rich composition above 90 at% Mg is very important for the development of a high-strength material with low weight by utilizing the crystallization of an amorphous phase. We have also reported the formation of Mg–Ca–Al (Kato et al. 1995) and Mg–Ca–Li (Niikura et al. 1994a) amorphous alloys with high tensile strength and low weight. Considering that the formation of an amorphous phase was limited to Mg–Zn (Calka et al. 1977) and Mg–Cu (Sommer et al. 1980) alloys before 1988, the subsequent findings of these Mg-based amorphous alloys allow us to expect that new amorphous alloys will be found in other Mg-based alloy systems and the engineering importance of Mg-based amorphous alloys will increase hereafter.

Table 10
Mechanical properties of melt-spun Mg-based amorphous alloys

Alloy (at%)	σ_f (MPa)	E (GPa)	H_v	σ_f/ρ (10^5 Nm kg^{-1})	$\varepsilon_{t,f} = \sigma_f/E$	$\varepsilon_{c,y} \approx 9.8H_v/3E$
$Mg_{70}Ca_{10}Al_{20}$	670	35	199	3.7	0.019	0.019
$Mg_{90}Ca_{2.5}Ni_{7.5}$	670	40	182	3.4	0.017	0.015
$Mg_{87.5}Ca_5Ni_{7.5}$	720	47	176	3.7	0.015	0.012
$Mg_{84}Sr_1Ni_{15}$	680	40	215	3.0	0.017	0.018
$Mg_{80}Y_5Ni_{15}$	830	46	224	2.5	0.018	0.016
$Mg_{85}Y_{10}Cu_5$	800	44	205	2.3	0.018	0.015
$Mg_{80}Y_{10}Cu_{10}$	820	46	218	2.5	0.018	0.016
$Mg_{91}Y_5Mm_4$	550	30	140	2.3	0.018	0.015

3.3. *Mechanical properties*

Most of the Mg-based amorphous alloys containing more than about 80 at% Mg in a ribbon form have good bending ductility and can be bent through 180° without fracture. Young's modulus E, tensile fracture strength σ_f and Vickers hardness H_v for Mg-based amorphous alloys with good bending ductility are summarized in table 10 (Inoue and Masumoto 1993a), together with the data for σ_f/E, $\sigma_f/9.8H_v$ and specific strength σ_f/ρ. As shown in the table, Mg-based amorphous alloys belonging to the Mg–R–M system exhibit higher σ_f values as compared with other amorphous alloys. The highest σ_f value reaches 830 MPa which is about twice as high as that for conventional Mg-based crystalline alloys. E and H_v for the alloy exhibiting the highest σ_f value are 46 GPa and 224, respectively. Contrarily, although σ_f values of Mg–Ca–Al amorphous alloys are considerably lower than those for the Mg–R–M alloys, no distinct reduction in the specific strength of the Mg–Ca–Al alloys is seen because of their low densities. The contribution of R and M elements to the increase of the values of the mechanical properties was examined for the Mg–R–M amorphous alloys. As exemplified for H_v of Mg–Cu–Y in fig. 74, the H_v values increase almost linearly with increasing Cu and Y content and there is no appreciable difference in the degree of the increase in H_v between Cu and Y. The distinct increase in H_v is interpreted to originate from the increase in the number of Mg–Cu, Mg–Y and Cu–Y atomic pairs with a much stronger bonding nature as compared with a Mg–Mg atomic pair.

The tensile fracture surface consists of a smooth region due to shear sliding and a vein region due to final fracture after the shear sliding. This feature is just the same as that (Chen 1980) for other conventional amorphous alloys with good ductility. Most of the present Mg-based amorphous alloys have a good ductile nature in the as-quenched state even at high solute concentrations of about 40 at%. However, the amorphous alloys containing less than 80 at% Mg become brittle during room temperature aging and the degree of embrittlement becomes significant with decreasing Mg content. The increase

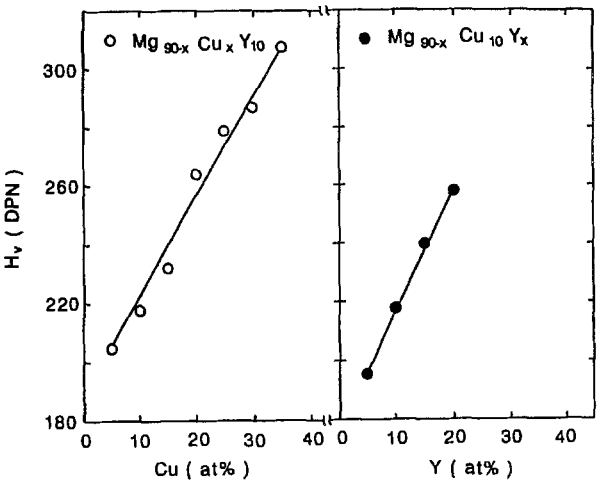

Fig. 74. Compositional dependence of H_v for melt-spun Mg–Cu–Y amorphous alloys.

in embrittlement tendency is presumably due to the development of short-range ordering between Mg and solute atoms.

It is shown in sect. 3.1 that Mg-based amorphous alloys are obtained in Mg–Ni–R and Mg–Cu–R and that glass formation is independent of the kind of R element. It is important to know the influence of the atomic size of R on the Vickers hardness (H_v) of Mg–R–M amorphous alloys. Figure 75 shows the change in H_v of the amorphous $Mg_{65}Cu_{25}R_{10}$ alloys with the kind of R element, together with the data of their atomic radii (S.G. Kim 1992). Although exceptional H_v values are observed only for Eu and Yb, which also have significantly different atomic sizes, there is a tendency for H_v to increase from about 180 for R = La to about 310 for the R element with the smallest atomic radius.

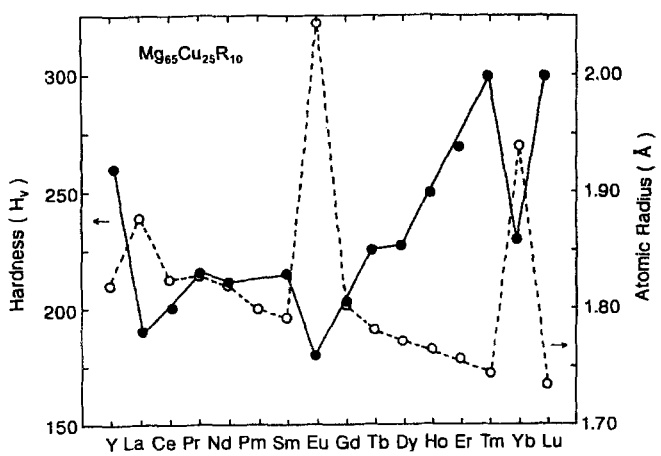

Fig. 75. H_v of melt-spun $Mg_{65}Cu_{25}R_{10}$ amorphous alloys (solid circles) and atomic radius of R elements (open circles).

Considering that the melting temperatures of Mg_2R and Cu_2R compounds also increase with decreasing atomic radius (Massalski 1990), the increase in H_v with increasing atomic number of the R elements is due to the increase in the bonding nature of Mg–R and Cu–R atomic pairs with decreasing atomic radius of the R elements. Furthermore, the anomalous increase in atomic radius for Eu and Yb causes the decrease in H_v as compared with the general trend. This exceptional result also supports the idea that the bonding nature of the constituent elements becomes stronger with decreasing atomic size.

Now we compare the mechanical strengths of Al- and Mg-based amorphous alloys, based on the data summarized in tables 7 and 10. Although the solute concentrations are nearly the same for both alloy series, the σ_f and E values are always lower for the Mg-based alloys than for the Al-based alloys and the strength level for the Mg-based alloys is about 80% as high as that for the Al-based alloys. Considering that the melting temperatures (or decomposition temperatures) of Mg-rich Mg–R and Mg–M compounds are about 70% of those of Al-rich Al–R and Al–M compounds, the lower mechanical strengths of Mg-based amorphous alloys are due to the weaker bonding nature between Mg and other constituent elements as compared with that between Al and solute elements. The σ_f and E values of conventional Al- and Mg-based crystalline alloys are also compared. The σ_f values of the amorphous alloys are about twice as high as those for the crystalline alloys, regardless of the difference in Al and Mg elements, while the E values of the Al- and Mg-based alloys are nearly the same for amorphous and crystalline alloys. These tendencies in σ_f and E are consistent with the previous data (Chen 1980) for other amorphous alloys with good bending ductility. The high σ_f values of amorphous alloys are due to the difficulty of a massive movement of the constituent atoms in the disordered atomic configuration and the strong bonding nature among the constituent elements. Contrarily, the lower E values are due to the ease of atomic rearrangement on a short-range scale because of the high density of voids and/or vacancies in the disordered structure.

3.4. *Glass transition and supercooled liquid*

The crystallization temperature of Mg–R–M amorphous alloys is in the range from 440 to 600 K and there is a tendency for T_x to increase with increasing solute content. The increase in T_x is greater for R than for M, though the change in T_x is almost independent of the kind of R elements. Amorphous alloys in the Mg–R–M system exhibit a distinct glass transition, followed by the appearance of a wide supercooled liquid region and then crystallization (Massalski 1990, Inoue et al. 1988k). Figure 76 shows typical differential scanning calorimetry (DSC) curves for Mg–Ni–Y and Mg–Cu–Y amorphous alloys. One can see the appearance of the glass transition and the supercooled liquid region. The temperature interval $\Delta T_x (= T_x - T_g)$ of the supercooled liquid region reaches as large as 69 K for $Mg_{65}Cu_{25}Y_{10}$. Figure 76 also shows that the amorphous alloys with their wide supercooled liquid region crystallize through one sharp exothermic peak. That is, crystallization from the supercooled liquid occurs through simultaneous precipitation of more than two phases. Figure 77 shows the compositional dependence of ΔT_x for amorphous Mg–Cu–Y alloys. The glass transition phenomenon is observed in a wide

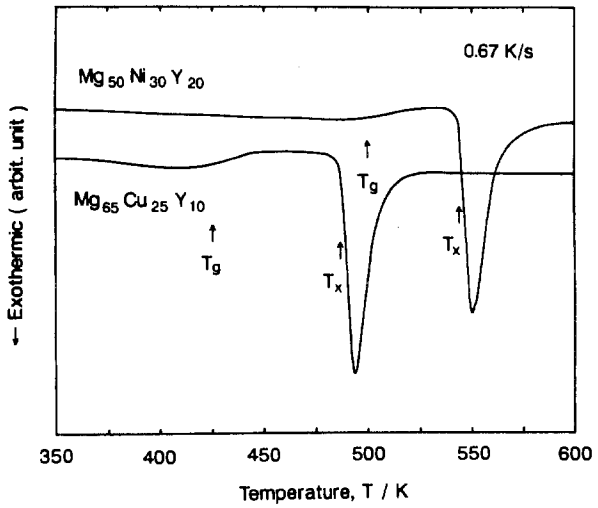

Fig. 76. DSC curves of amorphous $Mg_{50}Ni_{30}Y_{20}$ and $Mg_{65}Cu_{25}Y_{10}$ alloys.

composition range from 3 to 5 at% Y and 5 to 55 at% Cu. The wide supercooled liquid region, which exists 50 K above the crystallization temperature, is obtained for Mg–Cu–Y alloys ranging from 8 to 18% Y and 20 to 37 at% Cu. This distinct compositional dependence indicates that the largest thermal stability of the supercooled liquid is obtained for an optimal amorphous structure, i.e., a topologically dense and chemically ordered atomic configuration. It has further been confirmed S.G. Kim et al. (1989) that the $Mg_{65}Cu_{25}Y_{10}$ alloy has the lowest T_m in the ternary system. Although the T_g value also tends to increase with increasing Y and Cu content, the increase in T_g is much greater for Y than for Cu. This tendency is similar to that for T_x.

We also examined the changes in T_x, T_g and ΔT_x of the Mg–R–M amorphous alloys with the kind of R element, i.e., with the atomic number of R. As plotted for $Mg_{65}Cu_{25}R_{10}$ in fig. 78, ΔT_x increases significantly with decreasing atomic radius, shows a maximum

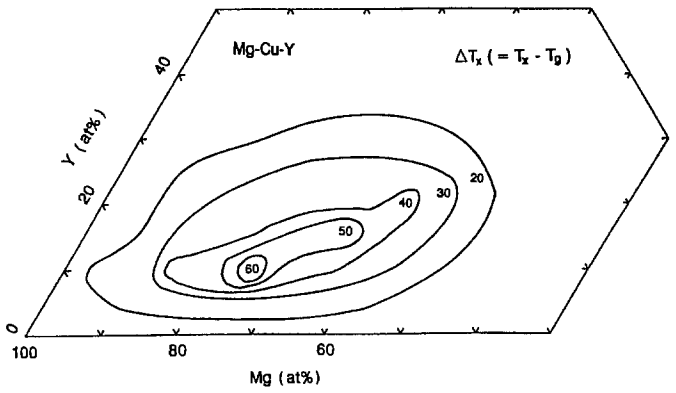

Fig. 77. Compositional dependence of $\Delta T_x (= T_x - T_g)$ for amorphous Mg–Cu–Y alloys.

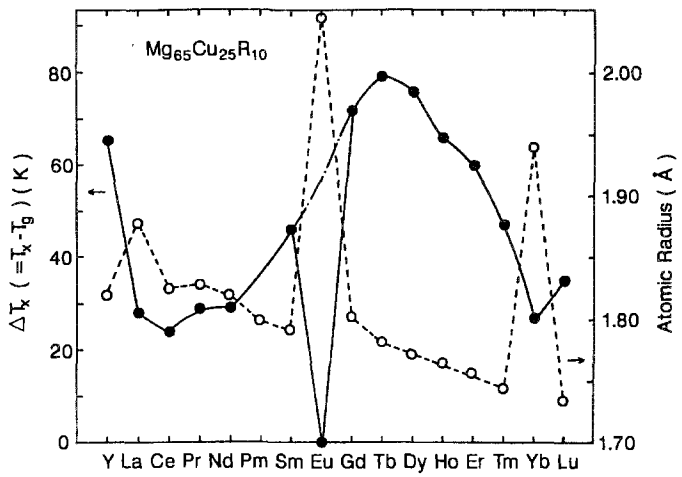

Fig. 78. ΔT_x of amorphous $Mg_{65}Cu_{25}R_{10}$ alloys (solid circles) and atomic radius of the R elements (open circles).

value of 78 K for R = Tb and then decreases with further increasing atomic radius. The systematic change in ΔT_x with the atomic radius of the R element indicates that the ΔT_x value is strongly dependent on the atomic sizes of the constituent elements. The importance of the atomic size is also supported by the result that the anomalous increase in atomic size for R = Eu and Yb causes the significant decrease in ΔT_x and no glass transition phenomenon is observed in the $Mg_{65}Cu_{25}Eu_{10}$ amorphous alloy. The atomic size ratio among the constituent elements is 1.10 for Tb/Mg, 1.25 for Mg/Cu and 1.38 for Tb/Cu. The significant contribution of the atomic size ratio of the constituent elements for the appearance of a wide supercooled liquid region has also been recognized for R–Al–M (Inoue et al. 1989f, 1990b), Zr–Al–M (Inoue et al. 1990c) and Hf–Al–M (Zhang et al. 1993) ternary amorphous alloys. The reason for the contribution is discussed later.

3.5. *Crystallization behavior*

As shown in fig. 76, the amorphous alloy $Mg_{65}Cu_{25}Y_{10}$ with its large ΔT_x value crystallizes through a single stage corresponding to the simultaneous precipitation of more than two kinds of crystalline phases. This consistency was also examined for the alloy series $Mg_{65}Cu_{25}R_{10}$. As shown in fig. 79, the crystallization from the supercooled liquid takes place through a single stage for R = Y and Tb, two stages for R = Sm and Nd and three stages for R = Yb. More crystallization stages cause a significant decrease in ΔT_x, indicating clearly that ΔT_x is strongly dependent on the crystallization process. The crystallization processes are

$$Am \rightarrow Mg_2Cu + Mg + MgTb \quad \text{for } Mg_{65}Cu_{25}Tb_{10},$$

$$Am \rightarrow Am' + Mg_2Cu + Mg \rightarrow Mg_2Cu + Mg + MgSm \quad \text{for } Mg_{65}Cu_{25}Sm_{10},$$

$$Am \rightarrow Am' + Mg_2Cu \rightarrow Am'' + Mg_2Cu + Mg \rightarrow Mg_2Cu + Mg + Mg_2Yb \quad \text{for } Mg_{65}Cu_{25}Yb_{10}.$$

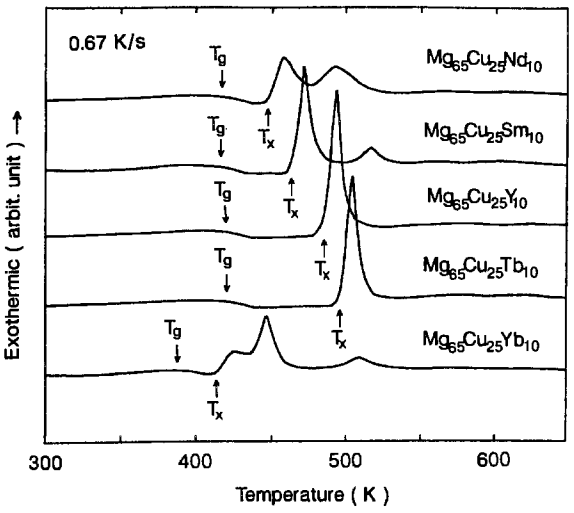

Fig. 79. DSC curves of amorphous $Mg_{65}Cu_{25}R_{10}$ (R = Y, Nd, Sm, Tb or Yb) alloys.

Achieving a large ΔT_x value in the case of simultaneous precipitation of three kinds of crystalline phases indicates that long-range rearrangements of the constituent elements which are essential for the simultaneous growth of more than two kinds of crystalline phases are needed for the formation of a supercooled liquid with high thermal stability.

3.6. *Large glass-forming ability*

It was shown in sect. 3.4 that a wide supercooled liquid region existing 50 K before the crystallization temperature is observed in Mg–R–M amorphous alloys. The appearance of this wide supercooled liquid region indicates that the phase transition into a crystalline phase is difficult even in the supercooled liquid state where the atoms can diffuse rather easily. This result also implies that the supercooled liquid obtained by quenching the melt also has a high resistance against nucleation and growth of a crystalline phase. That is, amorphous alloys with large ΔT_x values are concluded to have a large glass-forming ability.

The evaluation of the glass-forming ability for Mg–R–M alloys was done by the metallic mold casting method where the molten alloy is ejected into copper molds through a quartz nozzle by an applied pressure of 0.1–0.4 MPa (Inoue et al. 1991a). The increase in solute content from 20 to 35 at% for Mg–Cu–Y amorphous alloys caused the increase of the critical sample thickness for the formation of an amorphous phase from 1.5 to 4.0 mm by the copper mold casting process, indicating that the glass-forming ability is strongly dependent on ΔT_x.

Figure 80 shows the relation between ΔT_x and the critical diameter d_c for the formation of an amorphous phase for Mg–Cu–Y alloys obtained by copper mold casting. There is a clear tendency for d_c to increase with increasing ΔT_x. Furthermore, the critical cooling rate (R_c) for the formation of an amorphous phase has been evaluated to be as low as 80–

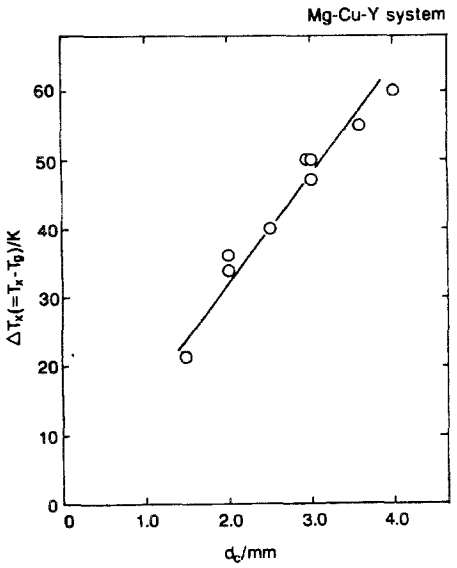

Fig. 80. Relation between ΔT_x and the critical diameter d_c for formation of an amorphous phase for Mg–Cu–Y alloys prepared by copper mold casting.

400 K/s (Inoue et al. 1991a) for Mg–Cu–Y alloys containing 65–80 at% Mg, based on the experimental data as well as the direct finite difference method. It is therefore concluded that Mg-based amorphous alloys have an extremely large glass-forming ability due to the high resistance of the supercooled liquid against crystallization.

Here, we consider why Mg-based amorphous alloys in the Mg–R–M system exhibiting a single-stage crystallization process have a large glass-forming ability. In addition to the large ΔT_x value, it is known that a large glass-forming ability is obtained for alloys with a large reduced glass transition temperature (T_g/T_m). Therefore, T_m and T_g/T_m of the Mg–R–M alloys are also examined systematically. It has been confirmed that T_m is the lowest for $Mg_{65}Cu_{25}Y_{10}$ exhibiting the largest ΔT_x value. The T_g/T_m values for the $Mg_{65}Cu_{25}R_{10}$ amorphous alloys are also shown as a function of the atomic number of the R element in fig. 81. The T_g/T_m value is higher than 0.58 for the Mg–Cu–R alloys with ΔT_x values larger than about 50 K and the largest T_g/T_m is obtained for the Mg–Cu–Tb alloys with the largest ΔT_x value. Thus, there is a clear tendency for the T_g/T_m value to increase with increasing ΔT_x. The large glass-forming ability which is related to large ΔT_x and T_g/T_m values has been thought (Inoue 1995b–d) to originate from the difficult nucleation reaction based on the increase in the liquid/solid interfacial energy which is obtained from the increase in the degree of the dense randomly packed structure for the Mg–R–M alloys consisting of constituent elements with significantly different atomic sizes (R > Mg > M) and large negative heats of mixing ($\Delta H_{mix} < 0$). Furthermore, the difficult atomic rearrangement for the growth of three crystalline phases in a highly dense random packed structure has been thought to be another important factor for the achievement of a large glass-forming ability for the present Mg–R–M alloys. The high resistance has been thought (Inoue and Masumoto 1993b) to originate from the decrease in atomic diffusivity

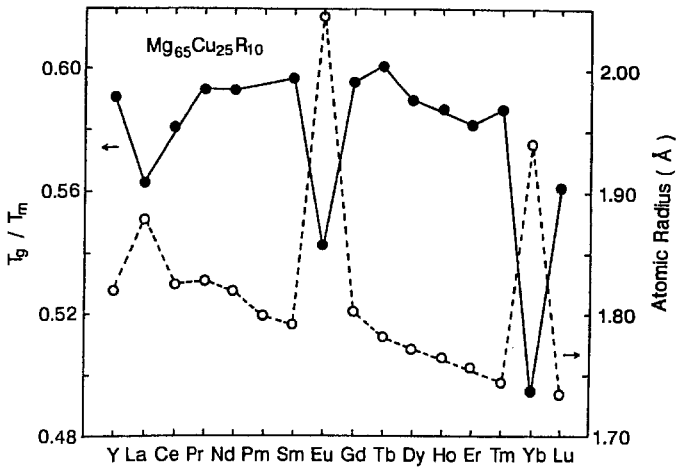

Fig. 81. T_g/T_m of amorphous $Mg_{65}Cu_{25}R_{10}$ alloys (solid circles) and atomic radius of the R elements (open circles).

and the increase in interface energy resulting from the increase in the packing fraction of the constituent atoms for the Mg–R–M alloys consisting of constituent elements with significantly different atomic sizes. In addition to the atomic size effect, the large negative heats of mixing among the three elements as well as the simultaneous (eutectic type) precipitation of more than two kinds of precipitates which requires redistribution of the constituent atoms on a long-range scale has also been thought, e.g. see Inoue and Masumoto (1993a) and Inoue (1995b–d), to be important for the achievement of a large glass-forming ability for the Mg–R–M alloys.

3.7. *Structure analyses*

With the aim of investigating, from a structural point of view, the reason for the achievement of a large glass-forming ability for the Mg–R–M amorphous alloys, the structure was examined for an amorphous $Mg_{50}Ni_{30}La_{20}$ alloy by using the anomalous X-ray scattering (AXS) method (Matsubara et al. 1990). The scattering intensity profiles observed at 8.306 and 8.031 keV below the Ni K-edge in a ternary amorphous alloy are shown in fig. 82. The fundamental features of both profiles are typical for noncrystallinity except for a prepeak at $Q = 14\,nm^{-1}$. The prepeak is indicated with an arrow in fig. 82. A similar prepeak was observed in other amorphous and liquid magnesium alloys by Paasch et al. (1972), and Lukens and Wagner (1976), which is qualitatively interpreted as indicating the presence of a certain strong chemical short-range ordering. It is seen in fig. 82 that the position of the first peak of ΔI_{Ni} shifts to the higher-Q side by taking the difference between the two scattering intensities. This peak shift can also be qualitatively explained by the fact that the atomic size of Ni (0.248 nm) is much smaller than those of the other two constituent elements Mg (0.320 nm) and La (0.374 nm). No prepeak is present in the differential intensity profile at the top of fig. 82.

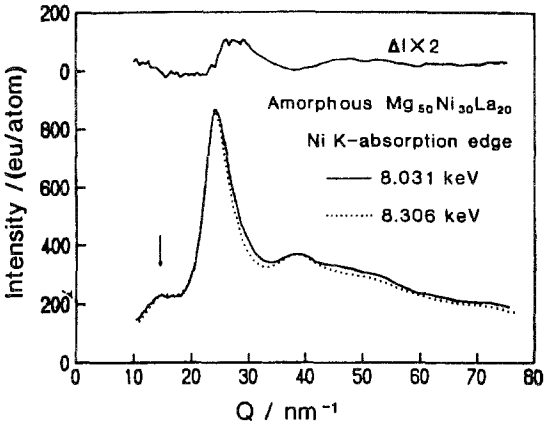

Fig. 82. Differential intensity profile of amorphous $Mg_{50}Ni_{30}La_{20}$ alloy (top) determined from scattering intensities (bottom) measured at 8.031 keV (solid) and 8.306 keV (dotted) which correspond to energies of 300 and 25 eV below the Ni K-absorption edge. The arrow indicates the prepeak.

The environmental radial distribution function (RDF) for Ni is plotted with a solid curve in fig. 83. The ordinary RDF computed from the interference function, Q_i (Q), which is shown in fig. 84, is shown as a dotted curve in fig. 83. Although six partial RDFs are overlapped in the ordinary RDF, the environmental RDF for Ni is only the sum of the three partial RDFs of Ni–Ni, Ni–Mg and Ni–La pairs. In terms of three constituent elements of different sizes, the first peak of the ordinary RDF consists of some broad diffuse peaks. It is almost impossible to determine an atomic distance and a coordination number for each atomic pair in the nearest-neighbor region from the ordinary RDF. On the other hand, the first peak in the environmental RDF for Ni becomes an

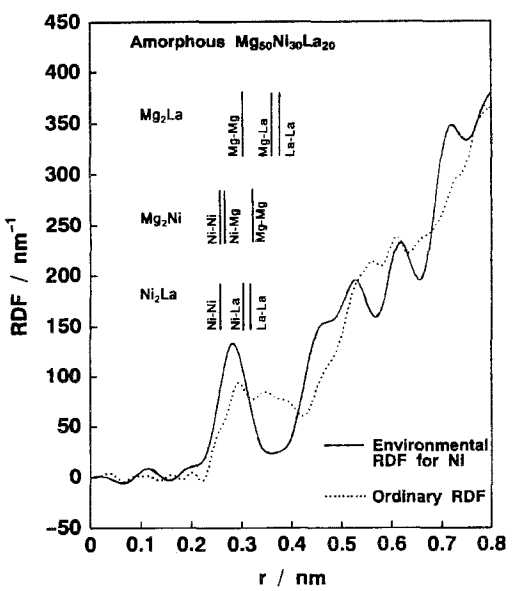

Fig. 83. The environmental radial distribution function (RDF) for Ni (solid) and the ordinary RDF (dotted) of amorphous $Mg_{50}Ni_{30}La_{20}$ alloy.

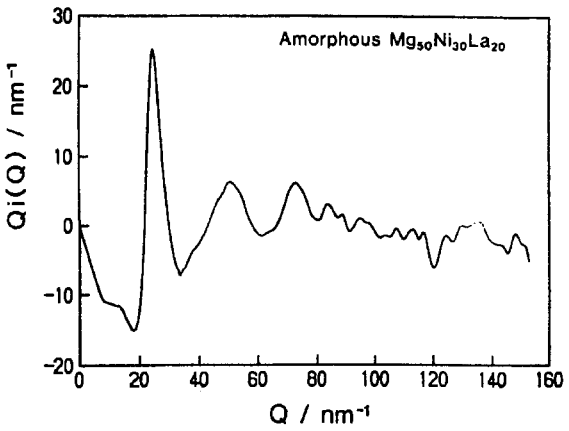

Fig. 84. Interference function of amorphous $Mg_{50}Ni_{30}La_{20}$ alloy.

isolated peak and some diffuse maxima in the first peak of the ordinary RDF completely disappear. However, it should be kept in mind that the absolute values of the ordinary and environmental RDFs provide a different physical meaning, and only then a direct comparison for peak positions is significant.

By comparing the environmental RDF for Ni with the distances of various atomic pairs computed from the crystalline data of Mg_2Ni, Mg_2La and Ni_2La (Pearson 1967) which are indicated in fig. 84, it is found that the first peak region involves the correlations of the Ni–Ni, Ni–Mg and Ni–La pairs and no peak is seen at the positions for the Mg–Mg, La–La and Mg–La pairs. This is a strong evidence that the present AXS measurement was successfully carried out. Since the contribution from each pair of Ni–Ni, Ni–Mg and Ni–La to the first peak cannot be determined separately in the present study, the average coordination number and atomic distance computed from the area and the position of the first peak were estimated to be 9.13 at 0.284 nm. This coordination number agrees well with the total coordination number, 9.12, calculated from the numbers of the Ni–Ni and Ni–Mg pairs in crystalline Mg_2Ni.

The present particular amorphous alloy $Mg_{50}Ni_{30}La_{20}$ involves lanthanum atoms, and therefore the actual coordination number should be slightly different from the value estimated from crystalline Mg_2Ni. However, the author takes the view that the similarity of both values clearly suggests that local ordering clusters are formed by Mg and the other constituent elements in the amorphous $Mg_{50}Ni_{30}La_{20}$ alloy. This conclusion is also supported by the presence of the prepeak in the intensity profile for the reason given in the following paragraph, although a definite comment about the actual local ordering structure has not been drawn from the present result.

An empirical relation between the correlation length, r, in real space and the peak position, Q, in the intensity profile, $Q_r = 2.5\pi$ is known in various noncrystalline systems of liquids and amorphous alloys (Waseda 1980). By applying this empirical relation to the prepeak in the intensity profile, the correlation length causing the prepeak at 14 nm^{-1} was estimated to be 0.561 nm. Since this value is comparable to the distance between the

second neighboring Mg atoms observed in Mg_2Ni and Mg_2La, it may also be concluded that the prepeak is caused by a strong correlation between magnesium atoms in the local ordering clusters in the amorphous $Mg_{50}Ni_{30}La_{20}$ alloy. This assumption is also consistent with the fact that there is no prepeak in the differential intensity profile which includes the Mg–Mg correlation. These characteristic structural features may be part of the origins for the extremely wide supercooled liquid region and large glass-forming ability observed in the new amorphous $Mg_{50}Ni_{30}La_{20}$ alloy.

3.8. *Bulk amorphous alloys produced by casting*

It is shown in sect. 3.5 that the bulk Mg-based amorphous alloys are produced in cylinders with diameters below 4 mm by the use of a metallic mold casting method. This result suggests that application of the high-pressure die-casting technique to the Mg-based alloys would enable the production of bulk amorphous alloys with larger diameters (larger thicknesses) and various shapes. Figure 85 shows a schematic illustration of a newly designed high-pressure die-casting equipment which consists mainly of sleeve and plunger for melting the mother alloy, a plunger to apply high pressure through hydraulic pressure, a casting copper mold with a high squeeze pressure and an evacuation system to eliminate gas in the crucible and mold immediately before casting (Inoue et al. 1992d). The sleeve and plunger were made from heat-resistant tool steel (SKD61). The mother alloy is melted in the sleeve in an argon atmosphere with a high frequency induction coil and cast into the copper mold by moving the plunger through hydraulic pressure.

Figure 86 shows as-cast $Mg_{65}Cu_{25}Y_{10}$ samples in cylinder and sheet forms with diameters of 1–9 mm and thicknesses of 0.5–9 mm. The length of the samples is fixed at 80 mm from the inner shape of the copper mold. As shown in the photograph, neither holes nor cavities are seen on the outer surface of the as-cast samples and their surfaces

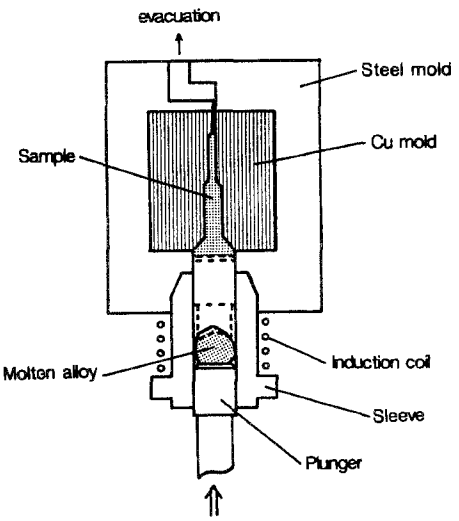

Fig. 85. Schematic illustration of a high-pressure die casting equipment used for the production of Mg-based bulk amorphous alloys.

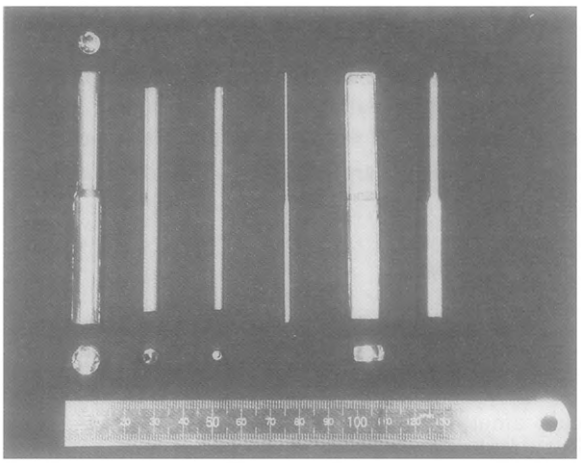

Fig. 86. Surface appearance of amorphous $Mg_{65}Cu_{25}Y_{10}$ alloys in cylindrical and sheet forms produced by high-pressure die casting.

have a good luster. The compositional dependence of the critical diameter for formation of an amorphous phase was examined for the $Mg_{90-x}Cu_xY_{10}$ cylinders produced by the high-pressure die-casting method. The critical diameter d_c is 3 mm for $Mg_{80}Cu_{10}Y_{10}$ and increases significantly with increasing Cu content. The largest d_c value of 7 mm is obtained for $Mg_{65}Cu_{25}Y_{10}$ and a further increase in Cu content causes a decrease in d_c. The significant compositional dependence of d_c reflects the thermal stability of the supercooled liquid which is observed in the temperature range below T_x.

It is generally known that die-cast alloys include a rather large volume fraction of pores resulting from the evolvement of gas. The size and distribution of the pores were examined for the present die-cast alloys. Figure 87 shows an optical micrograph revealing a transverse cross-sectional surface in an unetched state for the as-cast $Mg_{65}Cu_{25}Y_{10}$ cylinder with a diameter of 3 mm. Although no contrast corresponding to the precipitation of any crystalline phases is seen over the entire transverse cross section, a number of

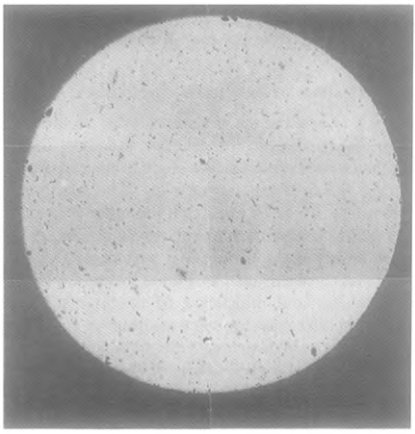

Fig. 87. Transverse cross sectional structure of cylindrical $Mg_{65}Cu_{25}Y_{10}$ amorphous alloy with a diameter of 3 mm produced by high-pressure die casting.

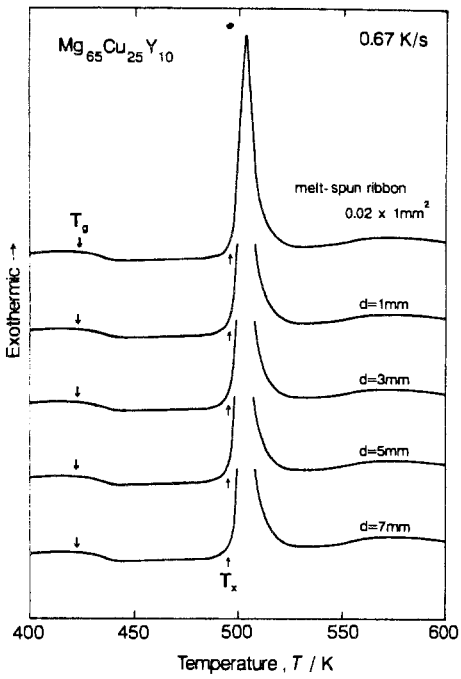

Fig. 88. DSC curves of amorphous $Mg_{65}Cu_{25}Y_{10}$ cylinders with diameters of 1 to 7 mm.

dark spots with sizes of 5 to 40 μm are distributed homogeneously. The dark spots have previously been confirmed to correspond to pores by SEM and hence the porosity for the present Mg–Cu–Y cylinders produced by the high-pressure die-casting method is evaluated to be about 17%. In addition, as shown in fig. 87, the distribution of the pores is uniform and no distinct change in the porosity is seen between the central region and the surface region. The uniform distribution of the small pores indicates that the cylinder was cast at a rather high cooling rate so as to suppress both the coalescence of pores and the annihilation of pores at the surface. The porosity is about 15% for $d = 1$ mm, 17% for $d = 3$ mm and 16% for $d = 7$ mm, being independent of the sample diameter, i.e., the cooling rate of the samples.

The DSC curves of the amorphous $Mg_{65}Cu_{25}Y_{10}$ cylinders with different diameters are shown in fig. 88, together with that of the melt-spun amorphous ribbon. T_g and T_x of the bulk samples are 420 and 490 K, respectively, independent of the diameter of the cylinders. Furthermore, there is no appreciable difference in the T_g and T_x values between the cast and melt-spun samples. The heat of crystallization (ΔH_x) was measured to be 3.63 to 3.47 kJ/mol for the cylinders with diameters of 1 to 7 mm and 3.57 kJ/mol for the ribbon, being nearly the same in the five samples. It is thus concluded that the sequential transition behavior of the glass transition, supercooled liquid and crystallization is independent of the preparation conditions. It is reasonable to consider that the cooling rate of the Mg–Cu–Y alloys is significantly different between the cylinder samples and the

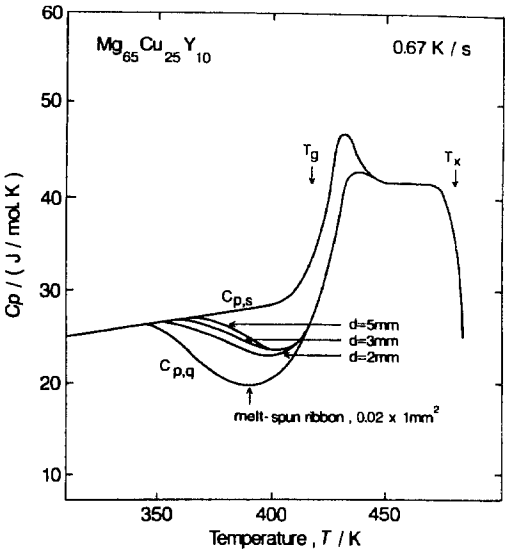

Fig. 89. Thermograms of cylinders of amorphous $Mg_{65}Cu_{25}Y_{10}$ with different diameters of 2 to 5 mm.

melt-spun ribbon and hence these samples have a significantly different disordered state. The difference in the disordered state was examined by measuring the enthalpy released during continuous heating.

Figure 89 shows the thermograms of the amorphous $Mg_{65}Cu_{25}Y_{10}$ cylinders with different diameters of 2 to 5 mm produced by casting, along with those of the melt-spun amorphous ribbon. Similar thermograms are seen in the three samples. As the temperature increases, the C_p value of the amorphous bulk samples increases gradually and then begins to decrease, indicating an irreversible structural relaxation at 355 K (T_r) for the 2 mm cylinder and 365 K for the 5 mm cylinder. With a further increase in the temperature, the C_p value shows its minimum in the temperature range 395–400 K, then increases rapidly in the glass transition range from 405 to 440 K and reaches 42 J/mol K for the supercooled liquid around 440 K. The C_p value of the supercooled liquid decreases slightly to 41 J/mol K with increasing temperature in the range of 440 to 470 K. Above 470 K, the supercooled liquid crystallizes at 480 K, with accompanying ΔH_x of 3.5 kJ/mol as indicated in fig. 88. It is also seen in fig. 89 that the cast samples have a large difference in the specific heat, $\Delta C_{p,s\rightarrow l}$, between the reheated amorphous solid and supercooled liquid reaching 19.5 J/mol K. The difference in $C_p(T)$ between the as-cast and the reheated states, $\Delta C_p(T)$, manifests the irreversible structural relaxation which is presumed to arise from the annihilation of quenched-in "defects" and the enhancement of the topological and chemical short-range ordering through atomic rearrangement. The heat of irreversible structural relaxation, ΔH_r ($\int \Delta C_p \, dT$, $\Delta C_p = C_{p,s} - C_{p,q} > 0$), was evaluated to be 385 J/mol for the 2 mm cylinder and 330 J/mol for the 5 mm cylinder. Comparing the thermograms of the cast samples with that of the melt-spun ribbon, it should be noticed that the former samples have higher values by 10 to 20 K for T_r and

smaller values by 175 to 230 J/mol for ΔH_r and there are no significant differences in T_g, $\Delta C_{p,s\to l}$, T_x and ΔH_x. The smaller ΔH_r values for the cast samples imply that the amorphous phase produced by die casting has a more relaxed atomic configuration as compared with that for the melt-spun amorphous phase because of the lower cooling rate. Furthermore, it is seen in fig. 89 that the 2 mm cylinder has a lower T_r and a larger ΔH_r as compared with those for the 5 mm cylinder, even though no appreciable difference is seen in the T_g and ΔH_x.

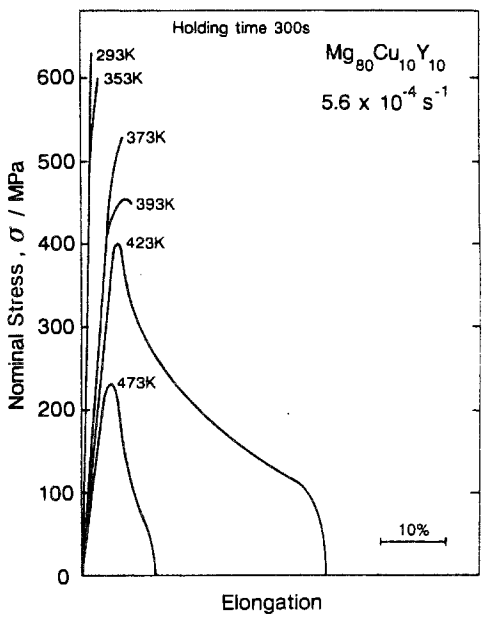

Fig. 90. The temperature dependence of the nominal tensile stress–elongation curves of amorphous $Mg_{80}Cu_{10}Y_{10}$ sheets with a thickness of 0.5 mm and a width of 3 mm.

Figure 90 shows the nominal tensile stress and elongation curves of the $Mg_{80}Cu_{10}Y_{10}$ amorphous sheet tested at different temperatures between 293 and 473 K (Inoue et al. 1992d). The stress–elongation curves can be divided into the following three types: (1) high fracture stress and no appreciable elongation at 293 K; (2) high yield stress and small elongation in the temperature range from 353 to 393 K; (3) a clear yield phenomenon, followed by a significant decrease in nominal flow stress, accompanying large elongation in the range above 423 K. The fracture stress is 630 MPa at 293 K, remains almost unchanged at temperatures up to 353 K and then decreases rapidly with increasing temperature. Thus, the high proof stress exceeding 400 MPa is kept in the temperature range below 373 K. On the contrary, the elongation is below 7% in the temperature range below 393 K, because of inhomogeneous deformation and fracture behavior without distinct work hardenability, and increases rapidly to about 37% in the temperature range above 400 K, because of the significant viscous flow.

3.9. *Upset deformation of bulk amorphous alloys in supercooled liquid region*

As described above, the Mg-based amorphous alloys have a wide supercooled liquid region before crystallization as well as high glass-forming ability, in addition to high mechanical strengths. However, Mg-based amorphous alloys in the Mg–Y–M system with a wide supercooled liquid region lie in the high solute concentration range of 30 to 40 at%. The high solute concentrations cause some disadvantages of an increase in the embrittlement tendency as well as a decrease in specific strength, though plastic deformation and consolidation by utilizing the viscous flow of the supercooled liquid are relatively easy. Although the decrease in the solute content causes the reduction of the embrittlement tendency during aging and an increase in the specific strength, the temperature interval of the supercooled liquid region also decreases significantly with decreasing solute content. It is generally recognized that the change in T_x with heating rate is more significant as compared with that for T_g. That is, the increase in heating rate is expected to cause the extension of the supercooled liquid region. Little is known about the changes in the glass transition and crystallization behavior with heating rate for Mg-based amorphous alloys.

Besides, the possibility of subjecting the significant plastic deformation by utilizing the viscous flow obtained through the extension of the supercooled liquid region was examined for the Mg-rich $Mg_{85}Y_{10}Cu_5$ amorphous alloy by using a specially designed equipment in which rapid heating up to 300 K/s and subsequent rapid cooling with high-pressure water jets were made under an applied load up to 43 kN (Inoue et al. 1994f). Figure 91 shows the schematic illustration of the equipment including the description of the principles for measurement and detection. The maximum punch speed for upset deformation is 50 mm/s. The measurement of sample temperature was made with a chromel–alumel thermocouple which was in direct contact with the bulk sample and the accuracy was evaluated to be within 5 K from the comparison with the temperature obtained with an electronic thermometer. The accuracy of the displacement of the punch is within 0.1 mm.

Figure 92 shows the heating and cooling curves and the structure for the bulk $Mg_{85}Y_{10}Cu_5$ alloy which was heated up to the different temperatures ranging from 468 to 633 K, along with the DSC curve of the as-extruded bulk measured at a heating rate of 0.67 K/s. The bulk alloy keeps an amorphous structure even after rapid heating up to 513 K and changes to mixed amorphous plus crystalline phases upon rapid heating to 523 and 573 K and finally to a crystalline structure upon rapid heating to 633 K. Judging from the result that the onset temperature of crystallization measured at a heating rate of 0.67 K/s is 463 K, rapid heating is very effective for increasing the crystallization temperature. The magnitude of the increase in T_x is 55 K.

The temperature interval of the supercooled liquid for the extruded bulk measured at a heating rate of 0.67 K/s is 28 K. The increase in T_x by 55 K is expected to cause the extension of the supercooled liquid region. As a method of detecting the glass transition temperature (T_g), we utilized the drastic decrease in flow stress in the vicinity of T_g. As shown in fig. 93, a compressive stress of 300 MPa was applied to the sample and

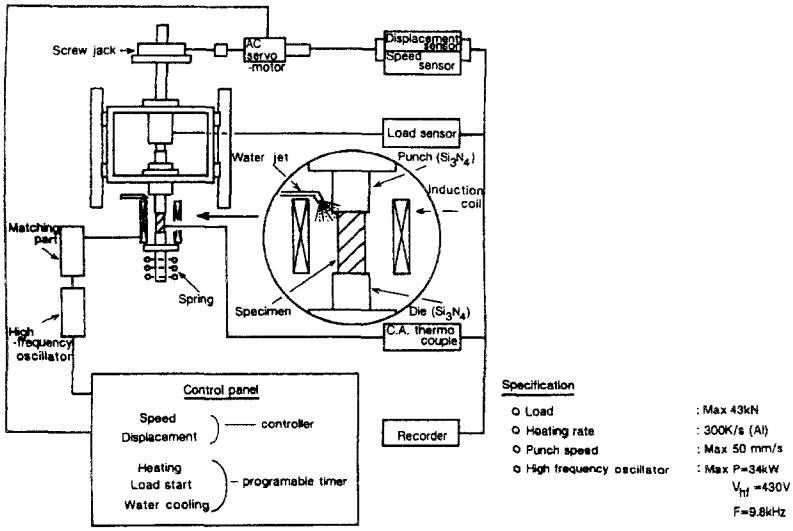

Fig. 91. Schematic illustration of a newly designed equipment which enables the rapid heating at a maximum rate of 300 K/s, followed by quick upset deformation at a rate of 50 mm/s under an applied load of 43 kN and then water cooling.

the change in the compressive stress of the sample by rapid heating was measured as a function of heating temperature. In the figure, T_H and σ_H represent the heating temperature and the flow stress of the bulk sample at T_H, respectively. In addition, the temperature at which the applied pressure begins to decrease is defined as T_g. As shown in

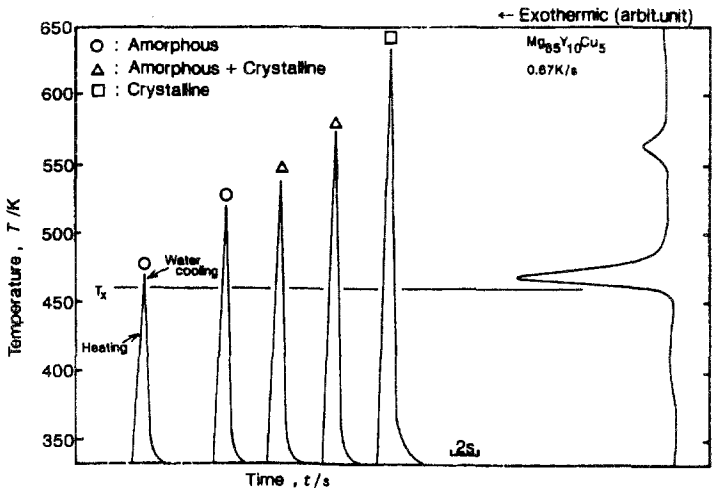

Fig. 92. Heating and cooling curves of a cylindrical $Mg_{85}Y_{10}Cu_5$ alloy obtained by using the present equipment and the structure of the samples subjected to the thermal treatments. The DSC curve is also shown for reference.

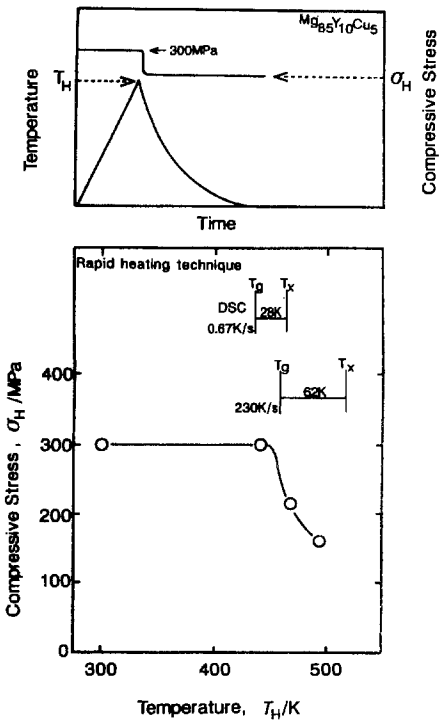

Fig. 93. Change in the compressive stress (σ_H) under an applied load of 300 MPa as a function of heating temperature (T_H) for a cylindrical $Mg_{85}Y_{10}Cu_5$ amorphous alloy heated at a rate of 0.67 and 230 K/s. The definition of σ_H and T_H is also shown for reference in the upper part of the figure.

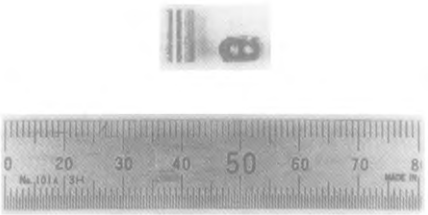

Fig. 94. Change in the cylindrical morphology of an amorphous $Mg_{85}Y_{10}Cu_5$ alloy by the upset deformation for 0.5 s at a punch speed of 10 mm/s at 493 K.

the figure, σ_H remains unchanged up to 443 K and decreases significantly to 212 MPa at 468 K, indicating that T_g lies in the vicinity of 456 K. The resulting temperature interval between T_g and T_x increases to 62 K which is about 2.2 times as large as that at a heating rate of 0.67 K/s. This result indicates clearly that the increase in heating rate is effective for extending the supercooled liquid region. The degree of the extension is estimated to be about 15 K for an increase in the heating rate of 100 K/s, in the assumption that the linear relation between ΔT_x and heating rate is satisfied between 0.67 and 230 K/s.

Figure 94 shows the change in the sample shape of the extruded $Mg_{85}Y_{10}Cu_5$ alloy subjected to rapid heating up to 493 K at a rate of 230 K/s, followed by upset deformation at a punch speed of 10 mm/s for 0.5 s and then water cooling. Within a short time of about 2 s, the extruded amorphous alloy was deformed significantly and the upsetting ratio is evaluated to be about 50%. Although this result is in a preliminary state, the new thermomechanical treatment consisting of rapid heating, upset deformation and water cooling is expected to become important in the enhancement of the needs to utilize the excellent properties inherent to amorphous alloys.

The change in the viscosity of the amorphous alloy by glass transition was examined by measuring the change in the strain rate under various compressive loads during heating at a constant rate (S.G. Kim 1992). As an example, fig. 95 shows the change in the viscosity between the glass transition and crystallization temperature for the

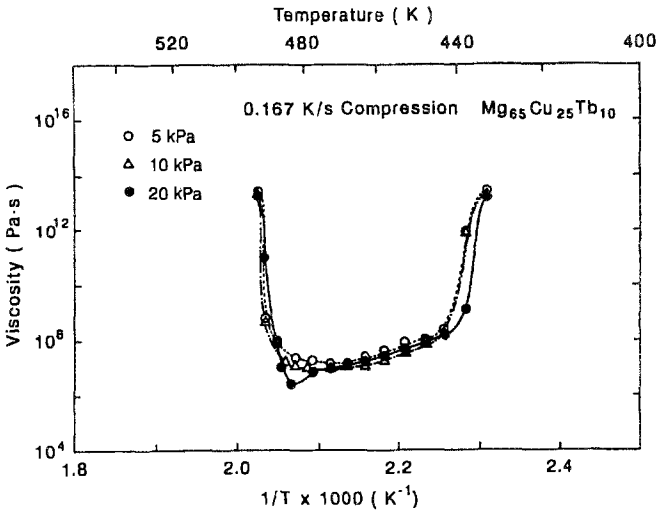

Fig. 95. Temperature dependence of viscosity for an amorphous $Mg_{65}Cu_{25}Tb_{10}$ alloy.

amorphous $Mg_{65}Cu_{25}Tb_{10}$ alloy with the largest ΔT_x value. The viscosity is 10^{13} Pa s for the amorphous solid at 435 K, decreases drastically to 10^8 Pa s in the glass transition temperature range around 440 K and gradually to about 10^6 Pa s in the supercooled liquid in the temperature range 445–490 K and then increases rapidly to about 10^{14} Pa s by crystallization at about 495 K. Thus, the decrease in viscosity in the supercooled liquid region is much smaller as compared with that at the glass transition temperature. The small degree of the decrease in viscosity is presumably due to the easy development of a short-range ordering resulting from the ease of atomic diffusivity in the supercooled liquid.

3.10. *Bulk amorphous alloys produced by atomization and extrusion techniques*

It was shown in sect. 3.7 that Mg-based bulk amorphous alloys with high tensile strength are produced by copper mold casting and high-pressure die casting. The high-strength Mg-based amorphous alloys are in a bulk form with thicknesses less than 7 mm. However, production of Mg-based amorphous alloys with a larger thickness by these techniques is difficult because of the limitation of the glass-forming ability. It is expected that extrusion of atomized amorphous powders in the temperature range well below T_x causes the elimination of the limitation of the amorphous sample shape. The possibility of producing a high-strength bulk amorphous alloy in the Mg-based alloy system by the extrusion technique has been examined for the Mg-rich $Mg_{85}Y_{10}Cu_5$ amorphous alloy. Since Mg-based alloy powders are extremely reactive and are likely to explode, it is essential to control very strictly the oxygen and moisture contents in the atmosphere during atomization. Figure 96 is a schematic illustration of the high-pressure gas atomization and subsequent consolidation equipment which were newly designed for the production

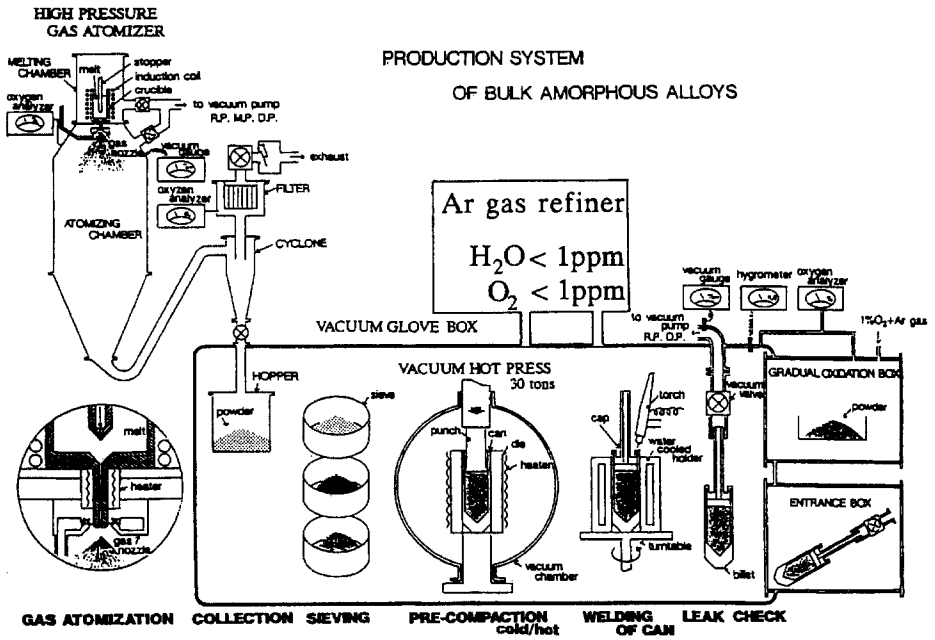

Fig. 96. Schematic illustration showing the sequential closed processing system in which the production of atomized Mg-based amorphous powders and their consolidation into a bulk form can be carried out in a well-controlled atmosphere.

and precompaction of Mg-based amorphous powders (Kato et al. 1994b,c). The sequential processes of melting the Mg-based mother alloys, atomization into Mg-based powders and their collection, sieving and precompaction into an aluminum tube can be carried out in a well-controlled argon atmosphere containing oxygen and moisture levels of less than 1 ppm. The Mg-based powders produced by the atomization equipment have a spherical shape and their average particle size is about 20 μm. Mg-based alloy systems in which we have succeeded in producing nonequilibrium phase powders with an amorphous main phase are Mg–Cu–Y, Mg–Cu–Nd, Mg–Ni–Y, Mg–Ca–Al, Mg–Cu–Y and Mg–Al–Zn etc., e.g. see Inoue and Masumoto (1993a). The critical particle size for the formation of nonequilibrium phase powders consisting of amorphous plus hcp-Mg without compound phase is about 35 μm for the Mg–M–R alloys and <25 μm for the other Mg-based alloys. The difference in the critical particle size seems to reflect the difference in the glass-forming ability of their Mg-based alloys.

By using atomized $Mg_{85}Y_{10}Cu_5$ powders with a particle size fraction less than 25 μm, we tried to produce a bulk alloy with full density which retains the as-quenched structure (Kato et al. 1994a). No appreciable voids are seen in the cross-sectional structure of the extruded Mg–Y–Cu alloy, indicating that the atomized powders are consolidated into the fully dense bulk form even at the low extrusion temperature of 373 K. The good consolidation tendency presumably is a result of the clean surface

state of the atomized powders during preparation and consolidation in a well-controlled atmosphere. Furthermore, considering that no distinct contrast revealing the precipitation of a crystalline phase is seen in the cross-sectional structure, extrusion at 373 K is suitable enough to keep the nonequilibrium phase in the as-quenched state. The absence of a crystalline phase in the extruded bulk alloy has been confirmed by X-ray diffraction and differential scanning calorimetric analyses for the bulk $Mg_{85}Y_{10}Cu_5$ alloy extruded at 373 K.

The extruded $Mg_{85}Y_{10}Cu_5$ alloy fractures with an accompanying elastic elongation of about 1.8% at room temperature, and no appreciable plastic elongation is seen. This feature results from the elastic–plastic deformation mode which is typical for an amorphous alloy without work hardenability, being just the same as that for the melt-spun amorphous ribbon. The Young's modulus and fracture strength were measured to be 46 GPa and 750 MPa, respectively, which are nearly the same as those for the corresponding amorphous ribbon sample. Fracturing of the bulk alloy takes place along the maximum shear plane which is declined by about 45° to the direction of the applied load and the surface consists mainly of a vein pattern which is typical for ductile amorphous alloys. No trace revealing the original boundary between the powders is observed even on the fracture surface, indicating that the amorphous powders have been consolidated in a truly bonding state.

3.11. *Bulk crystalline alloys produced by atomization and extrusion techniques*

In addition to the production of amorphous powders in the Mg–Cu–Y system with a large glass-forming ability, we have produced nonequilibrium phase powders with an amorphous phase in a number of alloy systems such as Mg–Cu–Nd, Mg–Ni–Y, Mg–Ca–Al, Mg–Zn–Y and Mg–Zn–Al etc. (Kato et al. 1994b,c, 1995, Kato 1995). The critical particle size for formation of nonequilibrium phase powders consisting of amorphous plus hcp-Mg without compound phase is about 35 μm for Mg-rich Mg–TM–R alloys containing 80 at% Mg and below 25 μm for the other Mg-rich alloys with the same Mg content. The difference in the critical particle size seems to reflect the difference in the glass-forming ability of their Mg-based alloys.

The extrusion of Mg-rich nonequilibrium phase powders at temperatures above T_x is expected to cause the production of bulk alloys consisting of a finely mixed structure of hcp-Mg and intermetallic compounds exhibiting good mechanical properties. As examples, fig. 97 shows bright-field electron micrographs of bulk $Mg_{95.5}Y_{2.5}Mm_2$ and $Mg_{70}Ca_{10}Al_{20}$ alloys produced by extrusion of atomized powders consisting of amorphous and hcp-Mg phases at an extrusion ratio of 10 and at extrusion temperatures of 598 and 673 K, respectively. The compositions of the extruded alloys are $Mg + Mg_{12}(Ce,Nd) + Mg_{17}La + Mg_4Y_5$ for Mg–Y–Mm and $Mg + Al_2Ca$ for Mg–Ca–Al. The grain size is about 400 nm for the Mg phase and 200 nm for the Mg–R compounds in the former alloy and 100 nm for the Mg phase and 80 nm for Al_2Ca in the latter alloy. No appreciable interface between the original atomized powders is seen in the micrograph and hence the present sequential process is concluded to be useful for the formation of

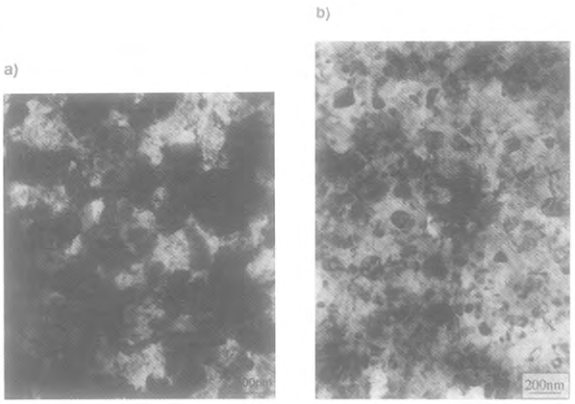

Fig. 97. Bright-field electron micrographs of two extruded Mg alloys: (a) $Mg_{95.5}Y_{2.5}Mm_2$; (b) $Mg_{70}Ca_{10}Al_{20}$.

a finely mixed structure even for the reactive Mg-based alloys. A similar finely mixed structure has also been obtained in a bulk $Mg_{87.5}Cu_5Y_{7.5}$ alloy produced by extrusion at 673 K.

The temperature dependence of the tensile yield strength $\sigma_{0.2}$ for bulk $Mg_{95.5}Y_{2.5}Mm_2$ (Horikiri et al. 1994), $Mg_{87.5}Cu_5Y_{7.5}$ (Kato et al. 1995) and $Mg_{70}Ca_{10}Al_{20}$ (Kato et al. 1995) is shown in fig. 98, together with the data of the heat-resistant WE54-T6 alloy (Unsworth 1989) which has recently been commercialized. $\sigma_{0.2}$ at room temperature is 560 MPa for the Mg–Y–Mm alloy, 740 MPa for the Mg–Cu–Y alloy and 600 MPa for the Mg–Ca–Al alloy. Although the $\sigma_{0.2}$ values decrease with increasing temperature, Mg–Cu–Y and Mg–Ca–Al alloys keep high $\sigma_{0.2}$ values of 650 MPa and 365 MPa respectively at 473 K and 610 MPa and 280 MPa respectively at 523 K. It is thus concluded that Mg-based alloys with a finely mixed structure produced by the present process have much higher

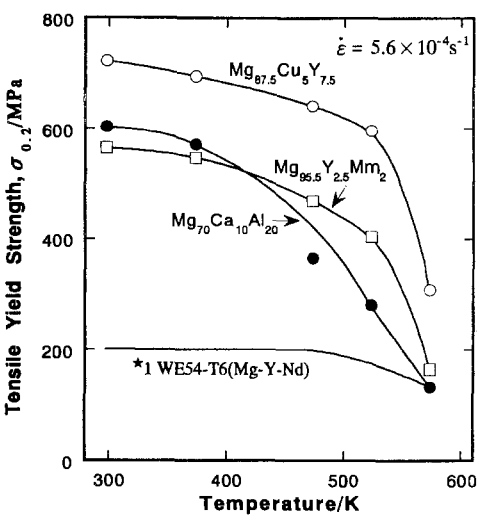

Fig. 98. Temperature dependence of tensile yield strength, $\sigma_{0.2}$, for as-extruded $Mg_{95.5}Y_{2.5}Mm_2$, $Mg_{87.5}Cu_5Y_{7.5}$ and $Mg_{70}Ca_{10}Al_{20}$ alloys. The data for the commercial WE54-T6 (Mg–Y–Nd) alloy taken from Magnesium Committee (1987) and Materials Database Committee (1988) are also shown for comparison.

elevated-temperature strengths as compared with that of the WE54-T6 alloy. The high tensile strength combined with a rather large elongation as well as the high elevated-temperature strength is due to the formation of a mixed structure with a homogeneous dispersion of a large amount of fine compounds. The specific tensile yield strength $\sigma_{0.2}/\rho$ of the present Mg-based alloys is as high as $3.3\times10^5\,\mathrm{Nm\,kg^{-1}}$ which is much higher than that for commercial Mg-based alloys, e.g. see Magnesium Committee (1987), and Materials Database Committee (1988).

Furthermore, Kato et al. (1995) have shown that bulk Mg–Ca–Al alloys have a corrosion resistance superior to that of the AZ91-T6 alloy. It is therefore concluded that bulk Mg–Y–Mm, Mg–Cu–Y and Mg–Ca–Al alloys obtained by extrusion of atomized amorphous powders exhibit high tensile strength at room temperature and elevated temperatures and Mg–Ca–Al alloys a high corrosion resistance as well. These excellent properties allow us to expect that the Mg-based alloys could be used in various application fields where high specific strength and corrosion resistance are required.

3.12. *Mg-based amorphous alloys containing nanoscale Mg particles (S.G. Kim et al. 1991, Inoue et al. 1992e)*

As described above, the highest Mg content at which an amorphous single phase is obtained by melt spinning is about 83 at%. The formation of a Mg-rich amorphous phase with a higher Mg concentration has strongly been desired aiming at the development of Mg-based alloys with a higher specific strength. It was shown in sect. 2.8 that Al-rich alloys with Al compositions (85–90 at% Al) higher than the glass formation range in the Al–R–M ternary system have a rapidly solidified structure consisting of fcc-Al particles embedded in an amorphous matrix. Furthermore, mixed phase alloys have been found to exhibit excellent mechanical strength which is about twice as high as that of amorphous single phase alloys with the same alloy composition. It is expected that a similar mixed structure is formed at Mg-rich compositions in the Mg–R–M alloys and high mechanical strengths exceeding that of the amorphous single phase are obtained in the mixed phase alloys. In a systematic investigation of the formation and mechanical properties of Mg-rich alloys consisting of amorphous and hcp-Mg phases, we have found that the mixed phase alloys exhibiting high mechanical strength and good bending ductility are formed in Mg–Zn–R (R = La or Ce) ternary systems.

Figure 99 shows the X-ray diffraction patterns of as-quenched and annealed (383 K, 20 s) phases of melt-spun $Mg_{85}Zn_{12}Ce_3$. Sharp diffraction peaks due to the precipitation of a crystalline phase are seen, in addition to a broad diffraction peak revealing the formation of an amorphous phase. All the crystalline peaks are identified as hcp-Mg phases and hence the as-quenched and annealed phases are concluded to consist of amorphous and hcp-Mg phases. In addition, it is seen that the amount of precipitated hcp-Mg phase increases significantly by annealing. The lattice parameter of the hcp-Mg phase was $c_0 = 0.5163$ nm in the as-quenched state and $a_0 = 0.3236$ nm and $c_0 = 0.5168$ nm in the annealed state. Comparing the extrapolated values with the actually measured values of the hcp-Mg solid solution in $Mg_{85}Zn_{12}Ce_3$, the hcp-Mg–Zn–Ce phase has a_0 and c_0 values

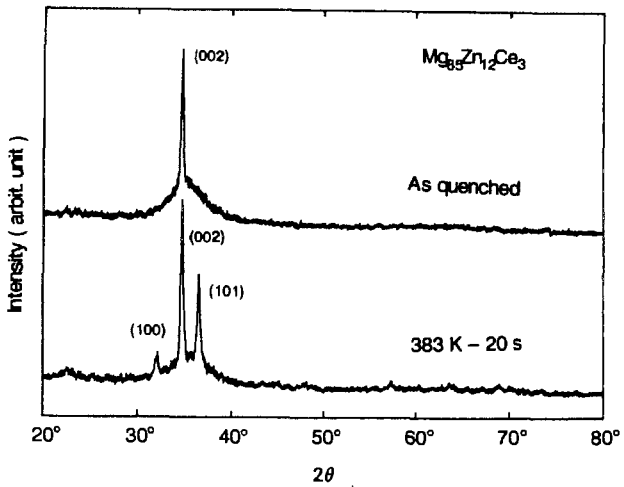

Fig. 99. X-ray diffraction patterns of as-quenched and annealed (383 K, 20 s) phases of the melt-spun $Mg_{85}Zn_{12}Ce_3$ alloy.

much larger than those of the hypothetical Mg–Zn supersaturated solid solution. This significant difference is interpreted to result from the quenching-induced dissolution of Ce, which has the largest atomic size of the three components, into the hcp phase. It is therefore concluded that the hcp particles embedded in the amorphous phase form a supersaturated solid solution with Zn and Ce contents above their equilibrium solubility limits.

The TEM image of the as-quenched $Mg_{85}Zn_{12}Ce_3$ alloy shown in fig. 100 reveals that the alloy consists of a crystalline phase with a particle size of about 3 nm homogeneously dispersed in an amorphous matrix. It is seen from the electron diffraction pattern that the crystalline phase has a hcp structure with lattice parameters $a_0 = 0.324$ nm and $c_0 = 0.517$ nm and hence can be identified to be a Mg-based solid solution. It has further been observed that the volume fraction of the Mg particles increases significantly by annealing for 20 s at 383 K, accompanying an increase of the average particle size from 3 to 20 nm and a decrease of the interparticle spacing from 10 to 5 nm.

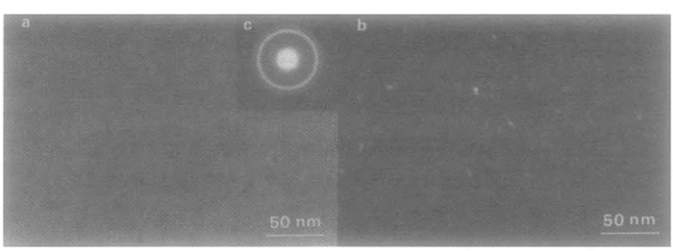

Fig. 100. (a) TEM bright-field image, (b) dark-field image and (c) selected-area electron diffraction pattern of the melt-spun $Mg_{85}Zn_{12}Ce_3$ alloy. The dark-field image was taken from a part of the reflection rings of the hcp phase.

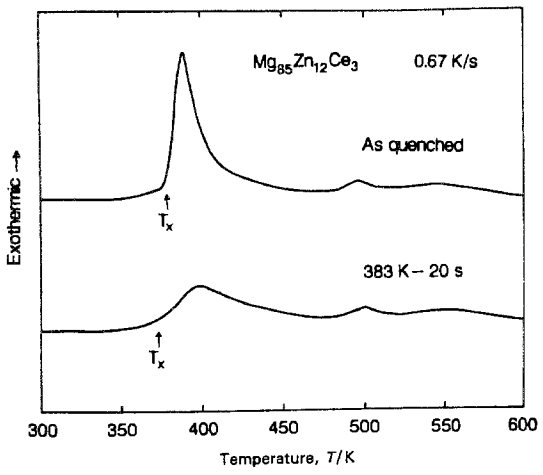

Fig. 101. DSC curves of the melt-spun $Mg_{85}Zn_{12}Ce_3$ alloy in as-quenched and annealed (383 K, 20 s) states.

Figure 101 shows the DSC curves of the as-quenched and annealed $Mg_{85}Zn_{12}Ce_3$ ribbons having a mixed structure. Three exothermic peaks are seen in the temperature ranges 371–415, 484–509 and 529–574 K. It was confirmed from the X-ray diffraction analyses and TEM observation that the three exothermic peaks are due to (1) the precipitation of the hcp-Mg phase from the amorphous matrix, (2) the transformation of the remaining amorphous phase to compound phases, and (3) the recrystallization of crystallization-induced Mg and compound phases. The magnitude of the first exothermic peak decreases significantly by heating for 20 s at 383 K because of the precipitation of Mg during heating, though there is no appreciable change in the magnitude of the second and third peaks upon heating. It is thus said that the amount of precipitated Mg phase can be controlled by subsequent heat treatment and the thermal stability of the remaining amorphous phase increases significantly after precipitation of the Mg phase. The mixed phase ribbons in as-quenched and annealed states exhibit a good bending ductility and can be bent through 180° without fracture. Tensile strength and fracture behavior were examined for these mixed phase ribbons.

Figure 102 shows the nominal tensile stress–strain curves of the $Mg_{85}Zn_{12}Ce_3$ ribbons in as-quenched state and annealed for 20 s at 383 K. The proof strength at 0.2% elongation ($\sigma_{0.2}$), ultimate tensile strength (σ_B) and fracture elongation including elastic elongation (ε_f) are 550 MPa, 655 MPa and 7.0%, respectively, for the as-quenched ribbon. The annealing treatment causes an increase of $\sigma_{0.2}$ and σ_B to 735 MPa and 936 MPa, respectively, and a decrease of ε_f to 2.9%. Thus, $\sigma_{0.2}$ and σ_B increase significantly with increasing amount of precipitation of hcp-Mg phase during heating. The σ_B value for the annealed sample is about 3.2 times as high as the highest σ_B value (Magnesium Committee 1987, Materials Database Committee 1988) for conventional Mg-based crystalline alloys. Furthermore, the appearance of significant plastic elongation is quite different from the previous result (Chen 1980) that a highly ductile amorphous ribbon fractures through inhomogeneous shear sliding without distinct plastic elongation. The

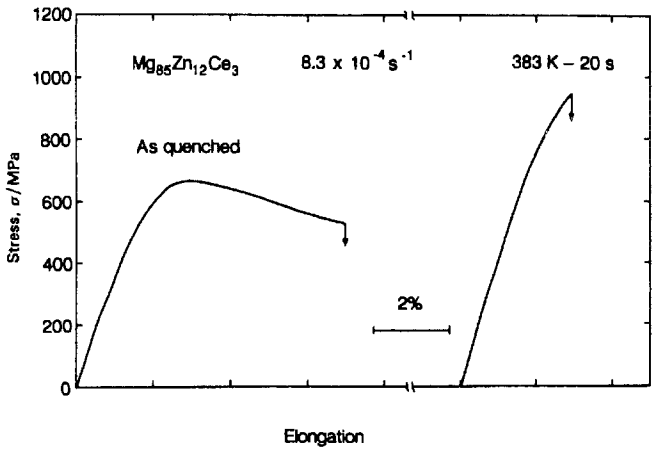

Fig. 102. Tensile stress–elongation curves of the melt-spun $Mg_{85}Zn_{12}Ce_3$ alloys in as-quenched and annealed states.

large plastic elongation indicates that the homogeneous dispersion of ultrafine hcp-Mg particles embedded in the amorphous matrix suppresses the generation of local shear deformation and assists homogeneous plastic deformation.

The tensile fracture surface for the as-quenched $Mg_{85}Zn_{12}Ce_3$ sample consists of smooth and vein pattern regions. Although these features are similar to those for an amorphous single phase with good bending ductility, it has been recognized (Inoue et al. 1992e) that the smooth region occupies about 65% of the fracture surface area and distinctly developed ledges exist on the fracture surface of the mixed phase alloy. This difference suggests that the fine hcp particles act as a resistance to local shear deformation and enhance the degree of local adiabatic heating in the final fracture stage, leading to a more significant viscous flow of the amorphous matrix. In summary, the mixed phase alloy consisting of ultrafine hcp-Mg particles embedded in an amorphous matrix exhibits σ_B and ε_f values much higher than the highest values ($\sigma_B = 650$ MPa, $\varepsilon_f \equiv 2.5\%$) (Kato 1995) for amorphous single phase alloys in the Mg–Zn–Ce system.

4. Mg-based quasicrystals containing R elements

It has been reported that the addition of a small amount of R elements to Al-rich Al–Mn (Inoue et al. 1992c), Al–Cr (Inoue et al. 1994d) and Al–V (Inoue et al. 1995b) alloys is quite effective for the refinement of icosahedral particles to nanoscale sizes below 50 nm, the spheroidization of the particle shape, and the change in the precipitation mode of the icosahedral phase to the primary type in the as-quenched state. These structural modifications have been clarified to be essential to achieve high tensile strength combined with good ductility for the rapidly solidified Al-based alloys (Inoue 1994b). These effects caused by the addition of R elements have been explained (Inoue 1995e) as a combined

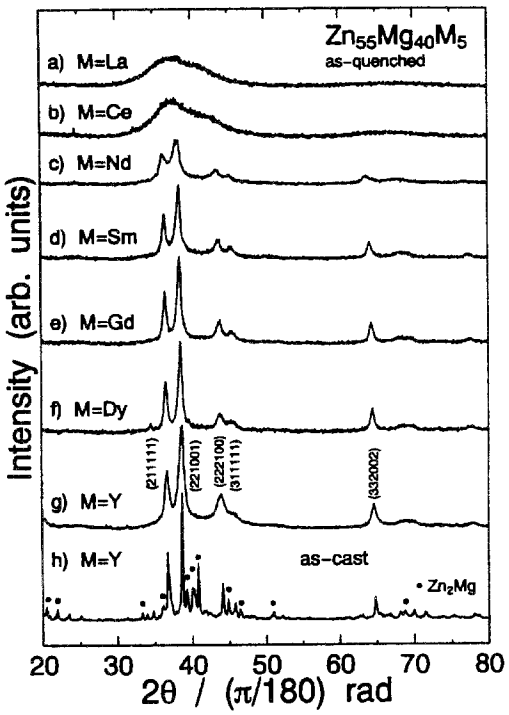

Fig. 103. X-ray diffraction patterns of melt-spun $Zn_{55}Mg_{40}R_5$ (R = La, Ce, Nd, Sm, Gd, Dy or Y) alloys. The data of an icosahedral $Zn_{55}Mg_{40}Y_5$ ingot prepared by conventional solidification are also shown for comparison.

result from (1) the increase in supercooling ability of the molten alloy as is evidenced from the formation of an amorphous phase in Mg–R–M systems, (2) the decrease in atomic diffusivity due to the dissolution of R elements with larger atomic sizes and large negative heats of mixing with other elements, and (3) the introduction of significant internal strains into the icosahedral phase by the reinforced dissolution of R elements. Similar structural effects are also expected for other alloy systems. As shown in sect. 3, an amorphous single phase coexisting with amorphous and hcp-Mg phases is formed in rapidly solidified Mg–Zn–R alloys. The composition range of the amorphous phase lies in the ranges 20–45 at% Zn and 0–10 at% Ln. Nonequilibrium phases including the amorphous phase are formed in the composition range which is adjacent to the amorphous single phase region. In the search for an additional effect of the R elements on the formation of nonequilibrium phases in the Mg–Zn–R system, an icosahedral phase was found to be formed in rapidly solidified $Zn_{55}Mg_{40}R_5$ (R = Sm, Gd and Dy) alloys (Niikura et al. 1994b). This is believed to be the first evidence for the formation of an icosahedral phase in the R-containing alloys. Figure 103 shows the X-ray diffraction patterns of rapidly solidified $Zn_{55}Mg_{40}R_5$ (R = La, Ce, Nd, Sm, Gd, Dy or Y) alloys (Niikura et al. 1994b), along with the data of an as-cast $Zn_{55}Mg_{40}Y_5$ alloy. The as-quenched structure consists of an amorphous phase for R = La and Ce, coexisting amorphous and icosahedral phases for R = Nd and Y, and an icosahedral phase for R = Sm, Gd and Dy. Substitution

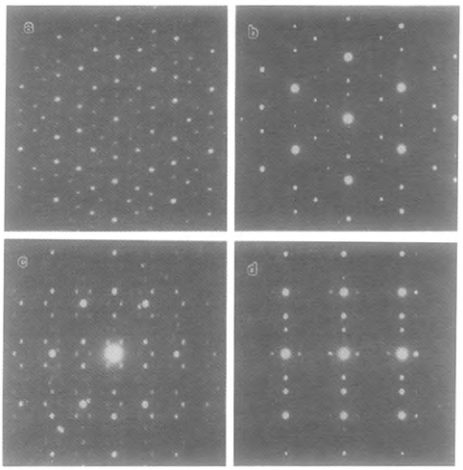

Fig. 104. Selected-area electron diffraction patterns of the icosahedral $Zn_{55}Mg_{40}Y_5$ alloy prepared by melt spinning. Incident beam along (a) fivefold axis, (b) threefold axis, (c) twofold axis, and (d) mirror-zone axes.

of only 5 at% R leads to the change from an amorphous to an icosahedral phase in the rapidly solidified structure. A few split broad peaks were observed in the X-ray diffraction patterns of the amorphous alloys, located at nearly the same peak positions as the icosahedral phase. This implies that the local structure is similar between the amorphous and the icosahedral phase. The (222100) peak of the icosahedral phase is very intense, characteristic of the Frank–Kasper type icosahedral phase (Chen et al. 1987b). The quasilattice parameters of the icosahedral phase were calculated to be 0.527 nm for $Zn_{55}Mg_{40}Nd_5$, 0.525 nm for $Zn_{55}Mg_{40}Sm_5$, 0.524 nm for $Zn_{55}Mg_{40}Gd_5$, 0.520 nm for $Zn_{55}Mg_{40}Dy_5$ and 0.520 nm for $Zn_{55}Mg_{40}Y_5$ from the $(211111)_i$ peak; found to decrease with decreasing atomic diameter of the R metal; and are comparable with those in icosahedral Al–Mg–Zn (0.516 nm) and Al–Li–Cu(0.503 nm) alloys. The diffraction pattern of icosahedral $Zn_{55}Mg_{40}Y_5$ prepared by conventional solidification (as-cast) is also shown for comparison in fig. 103b. Figures 104a–d show the selected-area electron diffraction patterns taken from icosahedral $Zn_{55}Mg_{40}Y_5$ with incident beams along (a) fivefold, (b) threefold, (c) twofold and (d) mirror-zone axes (Niikura et al. 1994b). The distortions in the spots are quite prominent in the fivefold pattern, e.g., the triangular shape of the innermost spots. The distortion of the spots is thought to originate from phason strains (Socoler and Wright 1987). Obviously, the twofold pattern indicates that the present rapidly solidified icosahedral phase has a simple icosahedral lattice.

Figure 105 summarizes the changes in the as-quenched phase and the atomic diameter in the $Zn_{55}Mg_{40}R_5$ alloys with the R elements. We note a systematic change dependent on the atomic size of the R elements. The as-quenched structure exhibits the amorphous phase when it contains La, Ce, Pr or Eu, and the icosahedral phase when it contains Nd, Sm, Gd, Tb, Dy, Ho, Er, Tm, Yb, Lu or Y. It seems that the atomic size of the R element is an important factor for the formation of amorphous and icosahedral phases. The alloys containing an R element with an atomic diameter larger than 0.366 nm, except Yb, form

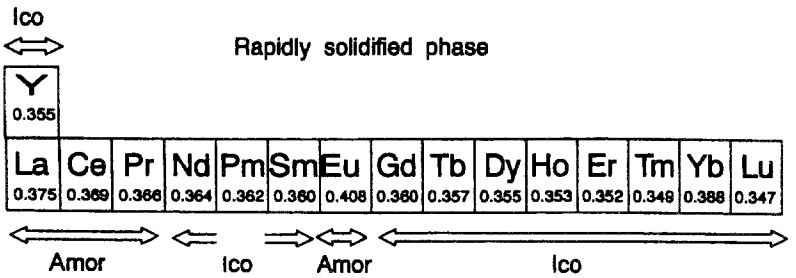

Fig. 105. Change in the as-quenched phase with atomic number of R elements for the melt-spun $Zn_{55}Mg_{40}R_5$ alloys. The values listed below each element are the atomic radii.

the amorphous phase, and those containing an R element with an atomic diameter smaller than 0.364 nm form the icosahedral phase.

In order to examine the atomic level stresses in those alloys, the atomic size factor (λ_s) was estimated (Egami and Waseda 1984) from the atomic volume mismatch ($|(V_b - V_a)/V_a|$) and the solute concentration (C_b) of each nonequilibrium phase by

$$\Delta V_{ab}/V_a = (V_b - V_a)/V_a = (r_b/r_a)^3 - 1, \tag{2}$$

$$\lambda_s = |\Delta V_{ab}/V_a| C_b + |\Delta V_{ac}/V_a| C_c. \tag{3}$$

Here, V_a and r_a are the atomic volume and atomic radius of the matrix and V_b (or V_c) and r_b (or r_c) are those of the solute elements, respectively. The product of the atomic volume mismatch and the minimum solute concentration required to obtain an amorphous phase was empirically shown to be a constant value in glass-forming alloy systems. The λ_s values were estimated to be 0.282 for amorphous $Zn_{55}Mg_{40}La_5$, 0.272 for icosahedral $Zn_{55}Mg_{40}Nd_5$, 0.267 for icosahedral $Zn_{55}Mg_{40}Gd_5$, 0.263 for icosahedral $Zn_{55}Mg_{40}Y_5$ and 0.256 for icosahedral $Zn_{55}Mg_{40}Lu_5$. The amorphous phase has higher λ_s values than those of the icosahedral phases and contains a larger amount of distortion. The increase of the atomic level distortion would induce a structural change from icosahedral to amorphous phase.

In the binary system, rapidly solidified $Zn_{60}Mg_{40}$ consists of amorphous and Zn_2Mg crystalline phases. When only 5 at% Zn in the $Zn_{60}Mg_{40}$ alloy is replaced with R, the rapidly solidified structure of this alloy is changed to the single amorphous or icosahedral phase of $Zn_{55}Mg_{40}La_5$ or $Zn_{55}Mg_{40}Y_5$, respectively. Since the R metals have larger atomic sizes than Mg or Zn, replacement with even a small amount of R metal leads to a structural change, accompanying the generation of the atomic level distortion.

Furthermore, the X-ray diffraction pattern of the as-cast $Zn_{55}Mg_{40}Y_5$ alloy confirms the existence of a stable icosahedral phase. Electron diffraction patterns taken with incident beams parallel to the fivefold, threefold and twofold directions of the icosahedral phase from the as-cast $Zn_{50}Mg_{45}Y_5$ alloy are shown in figs. 104a, b and c, respectively. When the diffraction patterns of the icosahedral $Zn_{50}Mg_{45}Y_5$ alloy are compared with those (Niikura 1995) of the icosahedral Al_5Li_3Cu alloy, it is seen that the patterns of the former

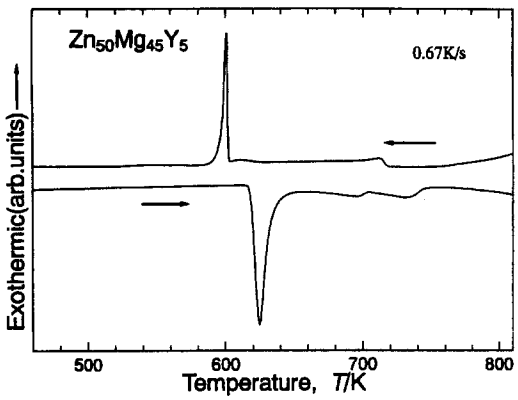

Fig. 106. DSC curve of the as-cast $Zn_{50}Mg_{45}Y_5$ ingot.

reveal sharp reflections and a number of extra fine spots. In addition, reflection spots due to a lattice spacing of 1.6 nm have been recognized in the innermost part of the fivefold pattern. The deviation of the reflections from the ideal icosahedral symmetrical positions due to phason strains and the irregularity of the shapes of the reflections are as small as those (Tsai et al. 1989) in the icosahedral $Al_{65}Cu_{20}Fe_{15}$ alloy. To our knowledge, the present icosahedral phase is the phase with the most highly ordered structure in the Frank–Kasper type quasicrystals.

Figure 106 shows the DSC curve of the as-cast $Zn_{50}Mg_{45}Y_5$ ingot. No exothermic peaks characterized by the transformation from metastable to stable phase are observed, and only endothermic peaks corresponding to melting are seen during heating (lower curve). The cooling curve (upper curve) reproduces well the peritectic reaction. The melting phenomena above 635 K are confirmed by direct observation. Annealing of the alloy for 48 h at 573 K, or heating to melting in the differential scanning calorimeter, does not induce the disappearance of the icosahedral phase, as shown in fig. 103h, proving that the icosahedral phase is thermodynamically stable.

On the basis of the evidence in fig. 106 for the thermodynamic stability of the icosahedral phase, we conclude that it should be possible to obtain large icosahedral grains by slow cooling from the melt. Figure 107 shows the solidification morphology observed

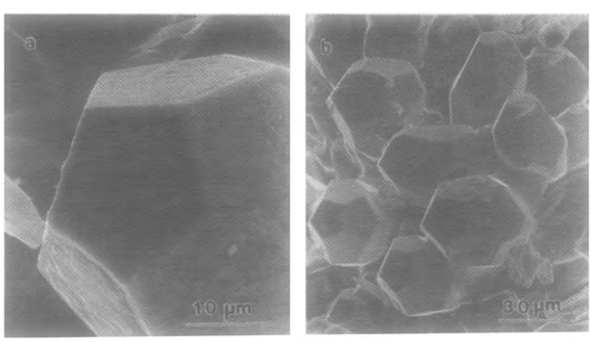

Fig. 107. Surface morphology of the as-cast $Zn_{50}Mg_{45}Y_5$ alloy.

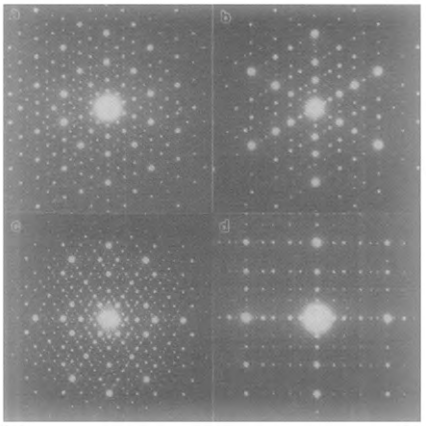

Fig. 108. Selected-area electron diffraction patterns of the cast $Zn_{50}Mg_{42}Dy_8$ alloy.

in a shrinkage cavity at the top surface of the $Zn_{50}Mg_{45}Y_5$ alloy prepared in a boron nitride crucible under an argon atmosphere (Niikura et al. 1994c). The growth morphology of this icosahedral phase is pentagonal dodecahedral; all the angles between edges on the same face were found to be 108° by matching them with edges of an appropriate projection of a regular pentagon. The grain size had an average diameter of about 30 μm. The composition of the icosahedral grains was found by energy-dispersive X-ray spectroscopy to be about $Zn_{54.7}Mg_{42.2}Y_{3.1}$. Similar morphologies have been observed in icosahedral Al–Cu–Fe (Tsai et al. 1989) and Mg–Ga–Zn (Ohashi and Spaepen 1987). It is somewhat surprising that icosahedral $Zn_{50}Mg_{45}Y_5$ and Mg–Ga–Zn alloys have a face-centered icosahedral lattice and a simple icosahedral lattice respectively, whereas they reveal the same pentagonal dodecahedral morphology. Finally, it is important to point out that a stable face-centered icosahedral phase in the Frank–Kasper system is a new structure that needs further structural investigation. Similar stable face-centered icosahedral structures have been also identified in Zn–Mg–Ho, Zn–Mg–Tb, Zn–Mg–Er and Zn–Mg–Dy alloys (Niikura 1995).

The further modification of alloy components caused the formation of a highly ordered and nearly perfect face-centered icosahedral lattice in fully annealed $Zn_{52}Mg_{40}R_8$ alloys (R = Gd, Tb, Dy, Ho or Er) (Tsai et al. 1994), as shown in fig. 108. Figures 108a–d show the selected-area electron diffraction patterns of the as-cast $Zn_{50}Mg_{42}Dy_8$ alloy taken with the incident beams parallel to the fivefold, threefold, twofold and mirror axes, respectively. We have also observed the innermost spots corresponding to long-range correlations of 2.72 nm in the twofold pattern. In addition, the diffraction spots in fig. 108a are located at perfect fivefold symmetrical positions and do not exhibit distortions due to phason strains.

Figure 109 shows the high-resolution TEM image of the cast $Zn_{50}Mg_{42}Dy_8$ alloy taken with the incident beam parallel to the fivefold symmetrical axis (Tsai et al. 1994). Throughout the whole region, the image exhibits a uniform distribution of bright rings lying along the fivefold symmetry directions without a clear shift. It can be noted that

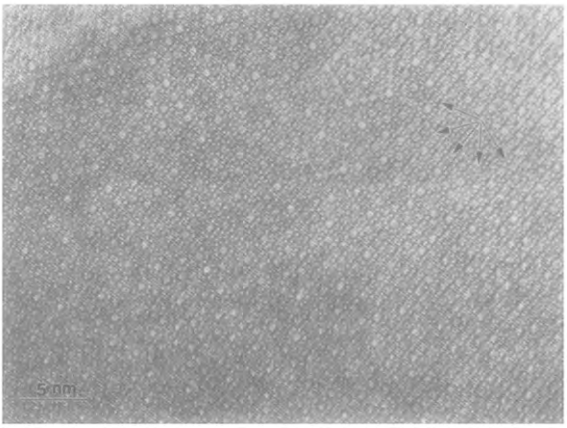

Fig. 109. High-resolution TEM image of the cast $Zn_{50}Mg_{42}Dy_8$ alloy.

the ring contrast forms various sizes of pentagons and they can be inflated easily because of the lack of a shift in the lattice planes.

Such a high-quality icosahedral phase was not only observed in the Zn–Mg–Dy system but also identified in several Zn–Mg–R alloys. Figure 110 shows the X-ray diffraction

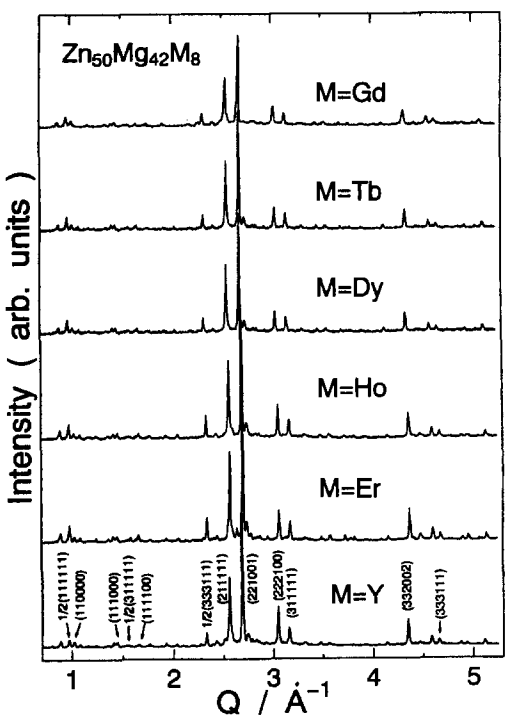

Fig. 110. X-ray diffraction patterns of the cast $Zn_{50}Mg_{42}R_8$ (R = Y, Gd, Tb, Dy, Ho or Er) alloys.

patterns of the as-cast $Zn_{50}Mg_{42}R_8$ (R = Y, Gd, Tb, Dy, Ho or Er) samples (Niikura 1995), indicating the formation of an almost single icosahedral phase, as identified by indexing. Except for the extra superlattice peaks, the overall intensity distribution of the diffraction peaks is quite similar to that of the icosahedral phase in the Al–Li–Cu (Dubost et al. 1986) or Mg–Ga–Zn (Ohashi and Spaepen 1987) alloys. It should be noted that superlattice peaks indexed as 1/2(111111) and 1/2(333111) are more pronounced than 1/2(311111) which are much stronger in icosahedral $Al_{70}Pd_{20}Mn_{10}$ and $Al_{65}Cu_{20}Fe_{15}$ alloys. Thus, the present icosahedral phase is described by the same face-centered icosahedral lattice as icosahedral $Al_{70}Pd_{20}Mn_{10}$ and $Al_{65}Cu_{20}Fe_{15}$ alloys.

5. R-based amorphous alloys

5.1. *History of R-based amorphous alloys*

There are some reports on the formation of an amorphous phase in melt-spun R-based binary alloys. The R-based amorphous phase has been reported to be formed in binary alloy systems containing solute elements such as Ag, Al, Au, Fe, Co, Ni, Cu, Pb, Si or Sn (Mizutani et al. 1986). Although R-based amorphous alloys of more than 80 at% R are obtained for the R–M (M = Ag, Al or Si) systems, other R-based amorphous alloys are located at higher solute concentrations and their formation is also limited to narrow solute concentration ranges. R-based binary amorphous alloys have some disadvantages: easy oxidation in air resulting from the high concentration of reactive R elements, significant progress of structural relaxation during room temperature aging, and low crystallization temperatures. The latter two disadvantages are due to the low melting temperatures of R–M binary alloys because their glass formation ranges are located in the vicinity of a eutectic point. These disadvantages disturb the detailed clarification of structure, thermal stability and fundamental properties of R-based amorphous alloys. In a subsequent study, addition of Al or Ga to R–M alloys was found to be very effective to increase the glass-forming ability and to expand the glass formation range, besides the elimination of the above-described disadvantages for binary R-based amorphous alloys. It is particularly to be noticed that bulk amorphous alloys with diameters of several millimeters are formed in R–Al–M and R–Ga–M systems by the copper mold casting method (Inoue et al. 1992f). Consequently, the subsequent investigation of R-based amorphous alloys is focused on the R–Al–M (M = Co, Ni, Cu) amorphous alloys consisting of more than three constituent elements.

5.2. *Glass formation ranges*

Amorphous single phase alloys with good bending ductility have been reported for R-rich R–Al–M systems (Inoue et al. 1989f, 1990d). As an example, the composition range in which an amorphous single phase is formed in the La–Al–Ni system by melt spinning is shown in fig. 111 (Inoue et al. 1989f), along with the data of the ductility of the amorphous

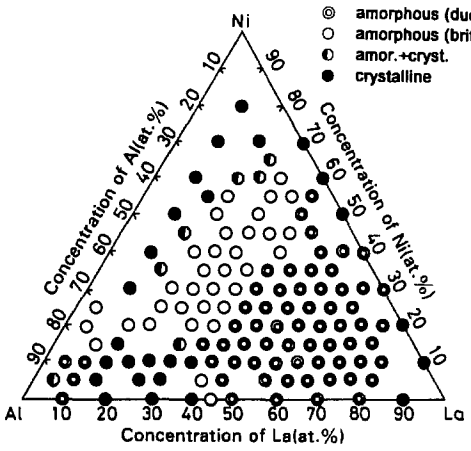

Fig. 111. Composition range in which an amorphous phase is formed in La–Al–Ni system by melt spinning. The double open circles, open circles, semisolid circles and solid circles represent the formation of ductile amorphous phase, brittle amorphous phase, coexistent amorphous plus crystalline phases and crystalline phase, respectively.

alloys. The glass formation range is quite wide and can be divided into two categories of Al-rich and La-rich compositions; 3–18 at% La and 0–15% Ni for the Al-rich alloys and 20–83% La and 0–60% Ni for the La-rich alloys. In addition, it is seen in fig. 111 that binary amorphous alloys are formed in the Al–La and La–Ni systems, and that the La–Al–Ni alloys can be amorphized over a wide composition range which is comparable to 60–70% in area over the entire compositional range of the ternary system. Figure 111 also shows that ductile amorphous alloys, which can be bent through 180° without fracture, are obtained in the Al-rich range of 3–13% La and 0–12% Ni and in the La-rich range of 35–83% La and 0–55% Ni. One can see a tendency that an alloy composition approaching $(Al,Ni)_2La$ brings about the transition from ductile to brittle for La–Al–Ni amorphous alloys. Glass formation over a similar wide composition range has also been observed in the La–Al–Cu (Inoue et al. 1990d) and La–Al–Co (Zhang 1993) systems.

5.3. *Thermal properties*

Figure 112 shows the compositional dependence of the crystallization temperature (T_x) for the La–Al–Ni amorphous alloys (Inoue et al. 1989f). The T_x value is 425–500 K for La-rich alloys containing more than 60% La, increases significantly with increasing Al and Ni content and reaches 750 K for $Al_{50}La_{20}Ni_{30}$. With further increasing Al content, T_x decreases significantly to 542 K for $Al_{85}La_5Ni_{10}$. As is evident from the contour lines of T_x in fig. 112, the T_x values of the La–Al–Ni amorphous alloys except the Al-rich alloys are mainly dominated by Al and Ni contents and there is no distinct difference between the compositional effects of Al and Ni on T_x.

These R-based amorphous alloys exhibit a wide supercooled liquid region in the temperature range below T_x. As examples, fig. 113 shows the DSC curves of the $La_{55}Al_{45-x}Ni_x$ ($x = 15$, 20 and 25 at%) amorphous alloys (Inoue et al. 1989f). The three alloys crystallize through a single stage with an exothermic heat of 4.82 to 5.14 kJ/mol. In addition to the exothermic peak, one can notice an endothermic reaction with a very

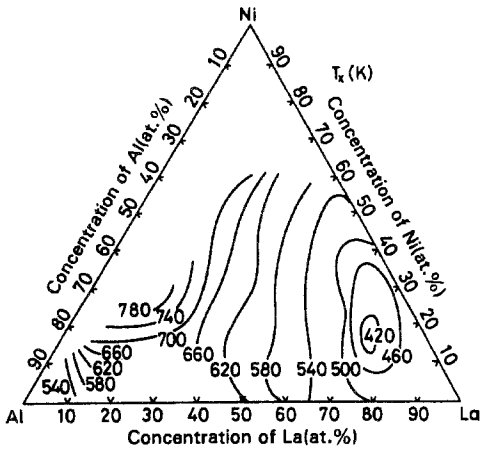

Fig. 112. Compositional dependence of crystallization temperature (T_x) for La–Al–Ni amorphous alloys.

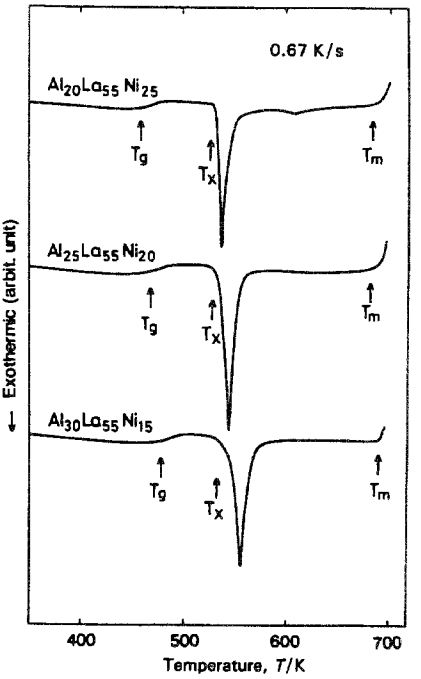

Fig. 113. DSC curves of amorphous $La_{55}Al_{45-x}Ni_x$ ($x = 15$, 20 and 25 at%) alloys.

wide temperature span below T_x. For instance, $La_{55}Al_{25}Ni_{20}$ begins to transform from an amorphous solid to a supercooled liquid at 465 K and maintains the supercooled liquid state over a wide temperature range reaching about 70 K, followed by crystallization at 545 K. The widest temperature spans of the supercooled liquid region for amorphous alloys previously reported are about 60 K for Pt–Ni–P (Chen 1980), 50 K for Pd–Ni–P (Chen 1980) and 58 K for Mg–Ni–La (Inoue et al. 1989g), and thus the $La_{50}Al_{25}Ni_{20}$ alloy has a much larger ΔT_x value as compared with other amorphous alloys.

Figure 114 shows the compositional effect on the ΔT_x value for the La–Al–Ni amorphous alloys. ΔT_x is maximum (69 K) for $La_{55}Al_{25}Ni_{20}$ and decreases with a deviation from the alloy component. However, the ΔT_x value above 50 K is obtained in the range 40–65% La and 13–30% Ni and the glass transition phenomenon is observed over a wide compositional range from 25 to 78% La and 5 to 50% Ni. The ΔT_x value for the La-based amorphous alloys increases for the multicomponent $La_{55}Al_{25}(Co,Ni,Cu)_{20}$ alloys and the largest value reaches 98 K for $La_{55}Al_{25}Co_5Ni_5Cu_{10}$ (Zhang et al. 1992).

The change of the specific heat of the transition from amorphous solid to supercooled liquid as well as the temperature dependence of the specific heat in the amorphous solid and supercooled liquid has been examined for the La–Al–Ni amorphous alloys through detailed differential scanning calorimetric measurements (Inoue et al. 1989f). As an example, fig. 115 shows the thermograms of the amorphous $La_{55}Al_{25}Ni_{20}$ alloy with the widest supercooled liquid region. The C_p value of the as-quenched phase is 24 J/mol K

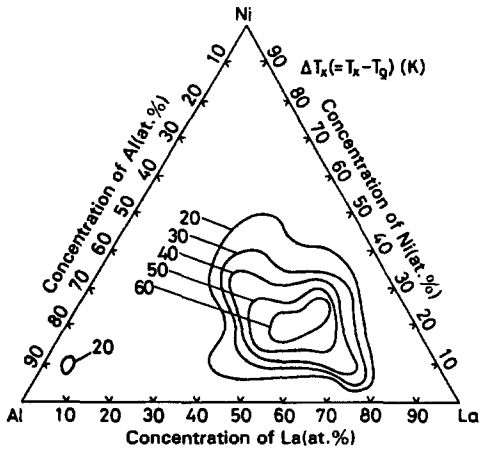

Fig. 114. Compositional dependence of ΔT_x for La–Al–Ni amorphous alloys.

near room temperature. As the temperature increases, the C_p value increases gradually and begins to decrease at about 355 K, indicating an irreversible structural relaxation. With a further increase in temperature, the C_p value increases rapidly in the glass transition range from 465 to 495 K and reaches 38.4 J/mol K for the supercooled liquid around 515 K. With further increasing temperature, the C_p value of the supercooled liquid decreases gradually and then rapidly due to crystallization at 545 K. It is seen in fig. 115 that the transition of the amorphous solid to the supercooled liquid takes place accompanied by a large increase in the specific heat, $\Delta C_{p,s\rightarrow l}$, reaching 14 J/mol K. The difference in $C_p(T)$ between the as-quenched and the reheated states, $\Delta C_p(T)$, manifests the irreversible structural relaxation which is presumed to arise from the annihilation of various kinds of

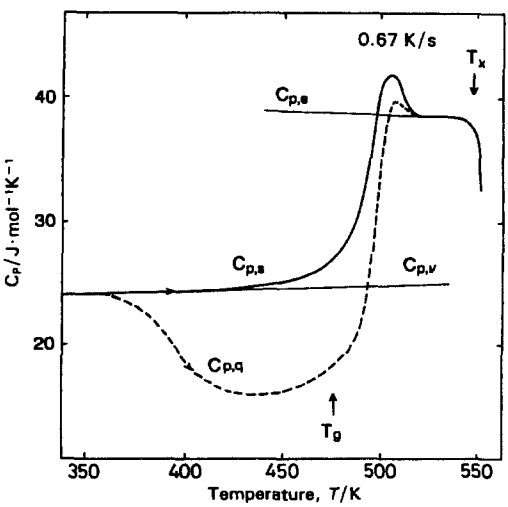

Fig. 115. The thermograms of an amorphous $La_{55}Al_{25}Ni_{20}$ alloy.

quenched-in "defects" and the enhancement of the topological and chemical short-range orderings through atomic rearrangement. The details of the structural relaxation behavior have been described in Inoue et al. (1992g).

The $C_{p,s}$ curve of the reheated (control) sample is unaffected by thermal changes and consists of configurational contributions as well as those arising from purely thermal vibrations. Therefore, the vibrational specific heat, $C_{p,v}$, for the amorphous alloy is extrapolated from the C_p values in the low-temperature region and is a linear function of temperature, viz.,

$$C_{p,v} = 24.2 + 4.65 \times 10^{-4}(T - 360) \quad 360 \leqslant T \leqslant 425. \tag{4}$$

Similarly, the equilibrium specific heat, $C_{p,e}$, of the supercooled liquid, including the vibrational and configurational specific heats, can be expressed by eq. (5) based on the data shown in fig. 115,

$$C_{p,e} = 38.4 + 5.11 \times 10^{-4}(540 - T) \quad 517 \leqslant T \leqslant 545. \tag{5}$$

The $\Delta C_{p,s\to l}$ value for the La–Al–Ni amorphous alloys was examined as a function of composition. It was found that the $\Delta C_{p,s\to l}$ value is about 14 J/mol in the vicinity of $La_{55}Al_{25}Ni_{20}$ and tends to decrease with a deviation from this alloy composition, being similar to the compositional dependence of ΔT_x. That is, there is a tendency for $\Delta C_{p,s\to l}$ to increase with increasing ΔT_x. The $\Delta C_{p,s\to l}$ values are nearly equal to those for Pt–Ni–P (Chen 1980), Pd–Ni–P (Chen 1980) and Mg–Ni–La (Inoue et al. 1989g) amorphous alloys.

It is important to examine the reduced glass transition temperature (T_g/T_m) for La–Al–Ni amorphous alloys with wide supercooled liquid region before crystallization. The onset temperature of fusion can be accurately measured from the DSC curve. Regarding the onset temperature of the endothermic reaction in the temperature range above T_x as melting temperature (T_m), the T_g/T_m values have been evaluated by Inoue et al. (1989f). The T_g/T_m value is about 0.71 in the vicinity of $La_{50}Al_{25}Ni_{25}$ and decreases gradually with a deviation from the composition. There is a clear tendency for T_g/T_m to increase with increasing ΔT_x and $\Delta C_{p,s\to l}$.

5.4. *Mechanical properties*

Vickers hardness (H_v) and tensile fracture strength (σ_f) were measured for the ductile La–Al–Ni amorphous alloys exhibiting large values of ΔT_x, $\Delta C_{p,s\to l}$ and T_g/T_m. Figure 116 shows the compositional dependence of H_v for the La–Al–Ni amorphous alloys (Inoue et al. 1989f). The H_v number is about 180 in the vicinity of $La_{70}Al_{15}Ni_{15}$, increases significantly with increasing Al and Ni content and reaches a maximum value of 520 in the vicinity of $La_{20}Al_{40}Ni_{40}$. The increase of H_v with increasing Al and Ni content is more remarkable for the compositional condition of Al/Ni $\equiv$ 1.0. The feature of the compositional effect on H_v is analogous to those for T_g and T_x.

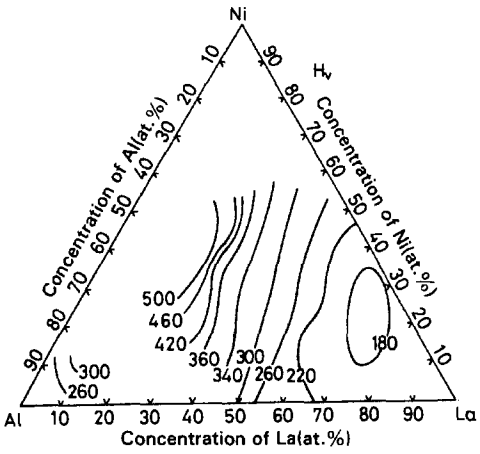

Fig. 116. Compositional dependence of H_v for La–Al–Ni amorphous alloys.

A similar compositional effect was also recognized for the tensile fracture strength (σ_f) and Young's modulus (E). The σ_f and E values increase with increasing Al and Ni content, in the range of 515 to 795 MPa and 33.8 to 52.3 GPa, respectively. The values $\sigma_f > 700$ MPa, $E > 500$ GPa, $\Delta C_{p,s\to l} > 10$ J/mol K and $T_g/T_m > 0.68$ are obtained simultaneously for some amorphous alloys in the La–Al–Ni system.

5.5. *Compositional effect on thermal and mechanical properties*

It was shown in sect. 5.4 that the T_x, H_v, E and σ_f values of the La–Al–Ni amorphous alloys have the same compositional effect and increase with increasing Al and Ni content. The maximum values of T_x, H_v and E are obtained in the vicinity of $La(Al,Ni)_2$, accompanying the ductile to brittle transition, and the increase in T_x, H_v and E is the largest when the concentration ratio of Al to Ni is nearly 1.0. Although the atomic configuration of the La–Al–Ni amorphous alloys is described later, it is interpreted that the simultaneous existence of the solute elements (Al and Ni) in the La base amorphous alloys brings about the increase in T_x, H_v and E. Although there is no equilibrium phase diagram available for the La–Al–Ni ternary alloys, the binary phase diagrams of La–Al (Gschneidner and Calderwood 1986) and La–Ni (Massalski 1990, Klimyenko et al. 1988, Zhang et al. 1991a) alloys indicate that the increase in T_x, H_v and E corresponds well to the significant increase in T_m from 823 to 1678 K for the La–Al system and from 805 to 1623 K for the La–Ni system, accompanying the structural changes of $La_3Al \rightarrow LaAl \rightarrow LaAl_2$ and $La_3Ni \rightarrow LaNi \rightarrow LaNi_{2.286}$. From the similarities of the chemical formula and crystal structure of their compounds in the La–Al and La–Ni systems (Villars and Calvert 1985), it is reasonable to consider that the compounds in the La–Al–Ni ternary system change in the order of $La_3(Al,Ni) \rightarrow La(Al,Ni) \rightarrow La(Al,Ni)_{\sim 2}$ with increasing Al and Ni content, accompanying the significant increase in T_m. The atomic configuration on a short-range scale also varies with the sequence change in the equilibrium compounds. That is, the amorphous structure reflects the $La_3(Al,Ni)$

with the lowest T_m in the La-rich compositional range and the increase in Al and Ni content causes the variation in the amorphous structure which reflects the La(Al,Ni) and La(Al,Ni)$_{\sim 2}$ compounds with higher T_m. Consequently, the monotonous and significant increases in T_x, H_v, E and σ_f with Al and Ni content may be explained by the variation of the short-range atomic configurations which reflect the change of the equilibrium compounds of $La_3(Al,Ni) \rightarrow La(Al,Ni) \rightarrow La(Al,Ni)_{\sim 2}$. The entire replacement between Al and Ni for La_3M, LaM and $LaM_{\sim 2}$ seems to be possible because of the similar types of chemical formula and crystal structure of the three compounds La–Al (Gschneidner and Calderwood 1986) and La–Ni (Massalski 1990, Klimyenko et al. 1988) systems. It is commonly expected for solid solutions that the entire replacement gives rise to the maximum values of T_x and H_v in the compositional range where the concentration ratio of Al to Ni is nearly 1.0. Furthermore, the attractive bonding nature between Al and Ni atoms is thought to play an important role in the increase of T_x, H_v, E and σ_f with increasing Al and Ni content. The attractive bonding is also expected to be the largest in the vicinity of Al/Ni $\equiv$ 1.0, because of the highest T_m value at 83% Ni (Massalski 1990, Zhang et al. 1991a) in the Al–Ni binary system. The compositional effect of the attractive bonding nature between Al and Ni is presumed to bring about the compositional dependence in which T_x and H_v show their maximum values at Al/Ni $\equiv$ 1.0.

A similar concept can be applied to explain the compositional dependence of T_x and H_v in the Al-rich amorphous alloys. The Al-rich binary amorphous phase is formed in the vicinity of $Al_{90}La_{10}$ (Inoue et al. 1988c), while the Al–Ni binary alloys cannot be amorphized (Inoue et al. 1988l). It is therefore thought that the glass formation for the Al-rich Al–La–Ni alloys is mainly dominated by the attractive bonding nature between Al and La atoms. The T_m of Al–La binary alloys decreases significantly from 1678 to 913 K with decreasing La content from 33.3 to 2.5% (Gschneidner and Calderwood 1986). The compositional effect on T_x and H_v for the Al-rich amorphous alloys is similar to that for T_m and hence the decrease of T_x and H_v for the La–Al–Ni amorphous alloys with increasing La content from about 30 to 80 at% seems to result from the short-range atomic configuration which reflects the change of the equilibrium phases leading to the decrease in T_m.

5.6. *Compositional effect on $\Delta T_x (= T_x - T_g)$ and T_g/T_m*

The supercooled liquid region at temperatures below T_x was observed in wide composition ranges of 25 to 78% La and 5 to 50% Ni for the La-rich alloys and 5 to 9% La and 8 to 12% Ni for the Al-rich alloys. The temperature span (ΔT_x) of the supercooled liquid is as large as 69 K in the vicinity of $La_{50}Al_{25}Ni_{25}$. Furthermore, the amorphous alloys with large ΔT_x values have high T_g/T_m values reaching about 0.7. The large values of ΔT_x and T_g/T_m indicate that the supercooled liquid of the La–Al–Ni amorphous alloys has a high stability to nucleation and growth of crystalline phases. The retardation of the transformation to a crystalline phase for the supercooled liquid is thought to bring about high ΔT_x and T_g/T_m values. The reason why the large values of ΔT_x and T_g/T_m are obtained in the vicinity of $La_{50}Al_{25}Ni_{25}$ is discussed in this section. The equilibrium phase

diagrams of La–Al (Gschneidner and Calderwood 1986) and La–Ni (Massalski 1990) binary alloys show the existence of a deep trough in the vicinity of 70% La, indicating a high stability of the liquidus structure at their alloy compositions. The ratios of Al to La and Ni to La at the compositions are nearly equal to those for the $La_{50}Al_{25}Ni_{25}$ alloy with the largest ΔT_x and T_g/T_m values. This agreement suggests that the liquidus structure is more stable in the vicinity of $La_{50}Al_{25}Ni_{25}$. The existence of the deep trough also implies the ease of obtaining a high degree of supercooling probably because of the high stability of the supercooled liquid at that composition. Thus, the equilibrium phase diagrams allow us to presume that the high stability of the supercooled liquid is closely related to easy supercooling of the liquid state. Although a number of eutectic-type alloy systems have an easy supercooling capacity of the liquid state, no amorphous alloys with large ΔT_x have been obtained in most of the eutectic-type alloys, see e.g. Masumoto et al. (1982). The extraordinary high stability of the supercooled liquid in the La–Al–Ni system seems to be attributed to attractive bonding and a high degree of dense randomly packed structure for the La–Al–Ni amorphous alloys consisting of constituent elements with significantly different atomic size ratios and large negative heats of mixing.

5.7. *High glass-forming ability*

As described above, the large ΔT_x values imply that the supercooled liquid can exist over a wide temperature range before crystallization and has a high resistance to nucleation and growth of crystalline phases. The high resistance also implies that the supercooled liquid obtained by melt spinning can also have a high resistance to nucleation and growth of crystalline phases, leading to a high glass-forming capacity, though the origin for the high resistance of the Al–La–Ni alloys remains unknown. It is known that the T_g/T_m value is closely related to the glass-forming capacity and there is a tendency for the glass-forming ability to increase with increasing T_g/T_m. The empirical relation, e.g. see Davies (1983) between T_g/T_m and the minimum cooling rate for formation of an amorphous phase allows us to evaluate that the minimum cooling rate for the $La_{50}Al_{25}Ni_{25}$ alloy is as small as about 10^2 K/s. The cooling rate is almost comparable to that which can be achieved even by water quenching, indicating the possibility of obtaining a bulky amorphous alloy by water quenching. This possibility has been confirmed by the evidence that an amorphous $La_{50}Al_{25}Ni_{25}$ alloy in a cylindrical form with diameters below 4 mm is formed by water quenching (Inoue et al. 1989h).

The high T_g/T_m value also implies that the viscosity of the supercooled liquid can reach about 10^{12} Pa s by a lower degree of supercooling. It is thus said that the temperature dependence of viscosity of the supercooled liquid is very steep. The steep increase of viscosity with decreasing temperature is presumably due to a rapid increase in the difficulty of the diffusivity of the constituent atoms. The difficulty of the diffusivity is thought to take place by the achievement of a tight bonding state of the constituent atoms. Considering that the alloys exhibiting the largest values of ΔT_x and T_g/T_m are located in the vicinity of $La_{50}Al_{25}Ni_{25}$ (La_2AlNi), the short-range atomic configuration which

reflects the stoichiometric $La_2Al_1Ni_1$ compound may be favorable for the suppression of the diffusivity of the constituent atoms.

5.8. *Structure analyses*

The atomic sizes of the constituent elements in the ternary R–Al–M amorphous alloys differ significantly. Therefore, the interpretation of the total radial distribution function (RDf) obtained by the ordinary X-ray diffraction method is complicated, and it is extremely hard to obtain structural parameters for each independent pair of elements. By using the anomalous X-ray scattering (AXS) method with which the structural environment around a particular constituent element can be determined, it is expected that this difference is observed and the structural environment around Ni in the amorphous $La_{55}Al_{25}Ni_{20}$ alloy is estimated in as-quenched, annealed (in the supercooled liquid region) and crystallized states. From these systematic AXS measurements, the structural changes due to crystallization were discussed.

The interference functions, Q_i (Q), estimated from the ordinary X-ray scattering profiles of the annealed samples are compared with the interference function of the as-quenched sample in fig. 117 (Inoue et al. 1991b). The solid and dotted curves at the top of the figure correspond to the interference functions for the as-quenched sample and that annealed for 300 s at 510 K, respectively. The three profiles below them indicate the difference between the interference function for the as-quenched sample and those for samples annealed for 300 s at 510 K, for 1800 s at 488 K, and for 10.8 ks at 418 K, respectively. For the sample annealed for 300 s at 510 K in the supercooled liquid region, the entire profile of Q_i (Q) shifts slightly towards a lower Q value, as is clearly seen around the first

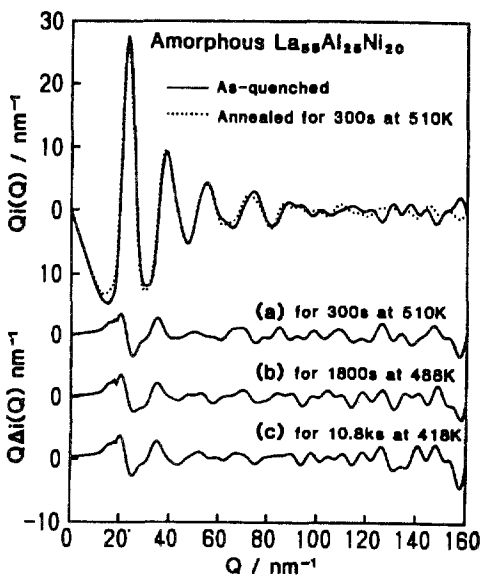

Fig. 117. Interference functions for amorphous $La_{55}Al_{25}Ni_{20}$ samples in as-quenched and annealed (510 K, 300 s) states.

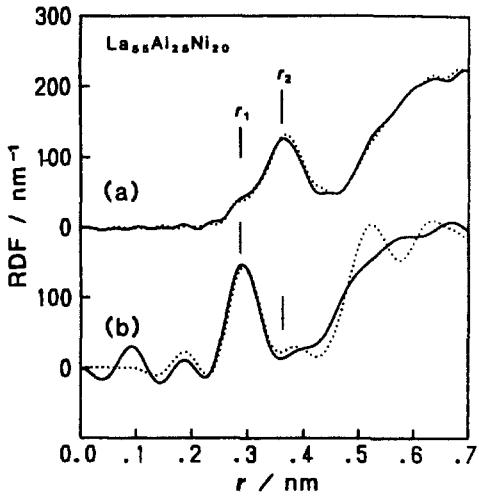

Fig. 118. (a) Ordinary RDF and (b) environmental RDF around Ni atoms for amorphous $La_{55}Al_{25}Ni_{20}$ samples in as-quenched (solid curve) and after annealing for 300 s at 510 K (dotted curve).

two peaks in the difference profile. It is surprising that the differences show an almost identical pattern for every set of annealing conditions. Although the atomic structure after annealing is different from the one obtained from the scattering intensity for the as-quenched sample, the present result in fig. 117 has an important implication. Namely, no significant change in chemical configuration, which is accompanied by diffusion, can occur due to annealing, even in the supercooled liquid region, and there can be no difference between the structural change in the sample annealed above T_g and that resulting from irreversible structural relaxation below T_g.

The ordinary RDF and the environmental RDF around Ni for the amorphous samples are shown in figs. 118a,b (Inoue et al. 1991b) where the solid and dotted curves correspond to the as-quenched sample and that annealed in the supercooled liquid region, respectively. As expected from the interference function in fig. 117, the ordinary RDFs for both of the samples in fig. 118a are almost identical. The first peak at about 0.36 nm in the total RDF has a shoulder at 0.28 nm. For convenience, this shoulder and peak are labeled r_1 and r_2, respectively. The first peak in the environmental RDF around Ni has a single peak at r_1 and there is no peak at r_2.

The ordinary RDF and the environmental RDF around Ni for the fully crystallized $La_{55}Al_{25}Ni_{20}$ alloy are shown in fig. 119. The profile in the near-neighbor region is different from that of the amorphous phase in fig. 118. An additional shoulder appears on the high r side of the first peak in the ordinary RDF and an extra peak is observed on the high r side of the first peak in the Ni environmental RDF. By comparing the RDFs for the crystallized sample in fig. 119 with those for the amorphous samples in fig. 118, it is found that the shoulder on the low r side of the first peak in the ordinary RDF and the first peak in the environmental RDF in fig. 119 are located at r_1 in fig. 118, and the first peak in the ordinary RDF of fig. 119 is located at r_2 in fig. 118. On the other hand, the

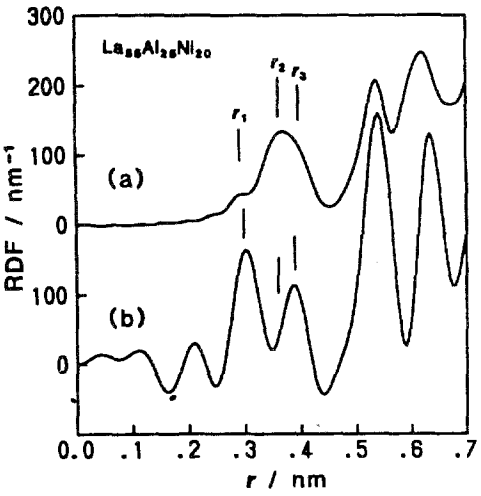

Fig. 119. (a) Ordinary RDF and (b) environmental RDF around Ni for the crystallized $La_{55}Al_{25}Ni_{20}$ alloy prepared by annealing for 360 ks at 510 K.

shoulder on the high r side of the first peak in the ordinary RDF and the second peak in the environmental RDF in fig. 119 are located at almost the same distance labelled r_3.

Taking account of the definition of the environmental RDF around Ni, which represents only the pairs including Ni, the peak at r_1 in fig. 119b is mainly attributed to the atomic correlations between La and Ni atoms. Similarly, the peak at r_2 is attributed to La–La and La–Al pairs. From the present study alone, the contributions of these two pairs cannot be determined independently. However, since the contribution of La–La pairs to the ordinary RDF, estimated from the appropriate partial RDF coefficient, is about four times larger than that for La–Al pairs in the present system, it was assumed that the peak at r_2 is ascribed to La–La pairs. Under this assumption, the coordination numbers and interatomic distances for the corresponding pairs were estimated by fitting the peaks and shoulders in each RDF with Gaussians. The structural parameters obtained are summarized in table 11. The structural parameters for the contribution at r_1, determined from the two RDFs, appear to be in good agreement with each other. This justifies the present AXS analysis.

In fig. 120, the scattering profile of the crystallized sample is compared with the peak positions for several La–Ni and La–Al compounds (Matsubara et al. 1992). All of the compounds except La_3Ni explain the experimental data, although a complete match between the compounds and the data is not obtained. Thus, at the present stage, decisive conclusions about the crystalline phase(s) in the crystallized sample cannot be drawn. However, it is plausible that the atomic structure of the crystallized sample may be close to that of these compounds. From a calculation of interatomic distances in La_7Ni_3 and LaNi, it is predicted that the atomic distance r_3 is estimated by assuming La–Ni pairs. Identical coordination numbers are obtained for both RDFs in fig. 119, although the difference between the atomic distances in the two RDFs for the crystallized sample is much larger than that for the amorphous samples. This may result from an incorrect assumption concerning the crystalline phase(s) present.

Table 11
Coordination numbers, N, and interatomic distances, r, for the as-quenched, annealed and crystallized $La_{55}Al_{25}Ni_{20}$ alloys[a]

State	La–Ni		La–La		La–Al	
	N	r_1 (nm)	N	r_1 (nm)	N	r_1 (nm)
As-quenched	1.5±0.1	0.283±0.002	9.4±0.5	0.358±0.002		
	1.4±0.1	0.287±0.002				
Annealed	1.5±0.1	0.284±0.002	9.8±0.5	0.362±0.002		
	1.4±0.1	0.290±0.002				
Crystallized	1.2±0.1	0.284±0.002	9.8±0.5	0.360±0.002	0.8±0.1	0.402±0.002
	1.2±0.1	0.299±0.002				0.385±0.002

[a]Structural parameters at the top and bottom in the same frame correspond to the values estimated from the ordinary RDF and the environmental RDF around Ni, respectively.

From the coordination numbers for the La–Ni and La–La pairs in the amorphous phase, it is noted that the number of La atoms around La is much larger than the number expected from the La concentration. This implies that the distribution of atoms is not random in the amorphous alloys. No significant change in the structural parameters for the amorphous alloys is observed due to low-temperature annealing. However, on crystallization, the coordination number for Ni atoms around La at the nearest-neighbor distance decreases slightly and a new peak, which may correspond to second-neighbor La–Ni pairs, appears. This indicates that the configurations of La atoms around Ni atoms in the crystallized sample are extremely different from that in the amorphous sample. Therefore, La atoms present at the near-neighborhood of Ni atoms must diffuse during crystallization while dragging the strong chemical bonds with the other atoms.

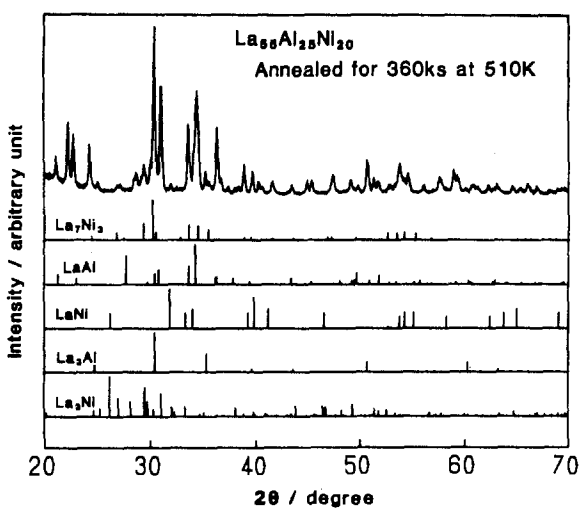

Fig. 120. The scattered intensity profile for the crystallized $La_{55}Al_{25}Ni_{20}$ alloy compared with the peak locations for some crystalline La–Ni and La–Al compounds.

The difficult atomic rearrangement of La atoms is presumed to be the reason for the appearance of the wide supercooled liquid region.

5.9. *Structural relaxation upon annealing*

It is of importance to know the structural relaxation and glass transition behavior for amorphous alloys with a wide supercooled liquid region before crystallization. A large number of studies on structural relaxation have been carried out (Inoue et al. 1992g) for amorphous alloys in the metal–metalloid and metal–metal systems because the structural relaxation causes significant changes in physical, mechanical and chemical properties. Most of the information on structural relaxation has been obtained for amorphous alloys with a supercooled liquid region of $\leqslant$50 K. There is no information on the structural relaxation behavior of metal–metal amorphous alloys with a wide supercooled liquid region (>50 K). Elucidation of the structural relaxation in these amorphous alloys is expected to give useful information on the reason for the appearance of a wide supercooled liquid region in limited alloy systems.

Figure 121 shows the change in the thermograms of a $La_{55}Al_{25}Ni_{20}$ amorphous alloy with annealing temperature, T_a, for an annealing period, t_a, of 6 h. On heating the as-quenched sample, $C_{p,q}$ begins to decrease, indicative of a structural relaxation at about 350 K, and shows a minimum value at about 435 K. With a further increase in temperature, $C_{p,q}$ increases gradually up to about 470 K and then rapidly in the glass transition range from 480 to 500 K, reaching 36.8 J/mol K for the supercooled liquid around 515 K. It then decreases rapidly due to crystallization at 540 K. The heating curve for the annealed

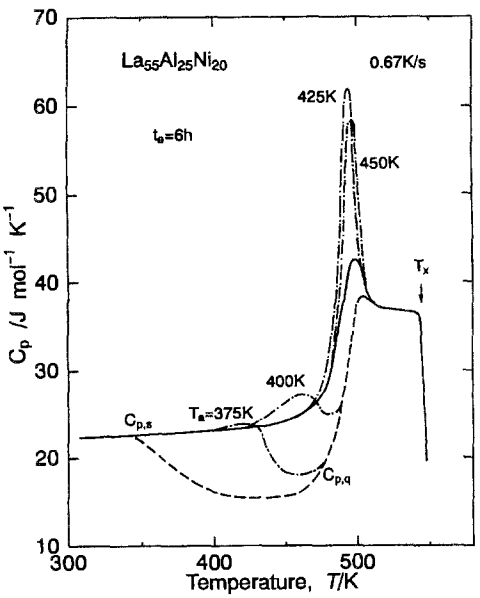

Fig. 121. The thermograms of an amorphous $La_{55}Al_{25}Ni_{20}$ alloy annealed for 12 h at various temperatures.

sample shows a $C_{p,a}(T)$ behavior which closely follows the C_p curve of the reference sample, $C_{p,s}$, up to each T_a and then exhibits an excess endothermic reaction relative to the reference sample before merging with that of the as-quenched sample in the supercooled liquid region above 510 K.

The main features of fig. 121 are summarized as follows. (1) The sample annealed at T_a shows an excess endothermic specific heat beginning at T_a, implying that the C_p value in the temperature range above T_a is dependent on the thermal history and consists of configurational contributions as well as those arising from purely thermal vibrations. (2) The magnitude of the endothermic peak increases rapidly at T_a just below T_g. (3) The excess endothermic peak is recoverable, while the exothermic broad peak is irrecoverable and the $C_{p,a}(T)$ curves for the annealed samples couple the recoverable endothermic and irrecoverable exothermic reaction. The excess endothermic peak has been thought (Zhang et al. 1992) to occur through the rearrangement from a relaxed atomic configuration caused by annealing to an atomic configuration which is more stable at temperatures above T_a. Thus, the excess endothermic reaction reflects the atomic configuration caused by annealing and hence we can obtain information on the structural relaxation during annealing by examining the change in the excess endothermic peak with T_a and t_a.

The temperature dependence of the differences in C_p between the annealed and the reference states, $(\Delta C_{p,\text{endo}} = C_{p,a}(T) - C_{p,s}(T)$, is shown in fig. 122 for $La_{55}Al_{25}Ni_{20}$. With increasing T_a, $\Delta C_{p,\max}$ of the two alloys initially increases gradually, followed by a rapid

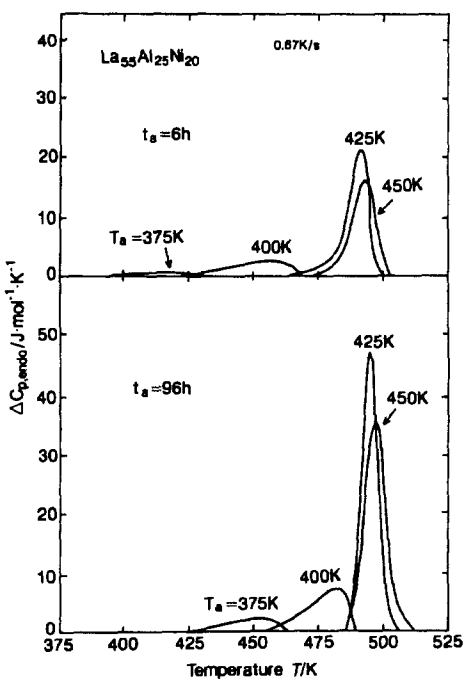

Fig. 122. Temperature dependence of the $\Delta C_{p,\text{enod}}$ $(= C_{p,a}(T) - C_{p,s}(T))$ for an amorphous $La_{55}Al_{25}Ni_{20}$ alloy.

increase at temperatures slightly below T_g. The rapid increase in $\Delta C_{p,max}$ is interpreted as corresponding to glass transition phenomena. Similarly, the rapid decrease in $\Delta C_{p,max}$ above T_g is due to the achievement of internal equilibrium resulting from the very short relaxation times in the supercooled liquid region. Although the change in $\Delta C_{p,max}$ as a function of T_a is similar to that for Zr–Cu and Zr–Ni amorphous alloys (Chen 1983), it is significantly different from the two-stage changes which have been observed (Inoue et al. 1985) for all amorphous alloys in metal–metal–metalloid systems containing more than two types of metallic elements. It has been thought (Inoue et al. 1985) that the appearance of the two-stage relaxation process is due to the difference in the relaxation time between the metal–metal pairs with weaker bonding, and the metal–metalloid pairs with stronger bonding. Since no splitting of $\Delta C_{p,max}$ into two stages is seen as a function of T_a for the present La–Al–Ni amorphous alloy, the relaxation times seem to be nearly the same for the La–Al, Al–Ni and La–Ni pairs, which have large negative enthalpies of mixing. This result suggests that there is no appreciable difference in the attractive bonding between the atomic pairs and that the constituent atoms in these amorphous alloys are in an optimal bonding state. The optimal bonding state prevents easy atomic movement, even in the supercooled liquid, and suppresses the nucleation and growth of a crystalline phase, leading to the appearance of the extremely wide supercooled liquid region.

5.10. *Viscoelasticity*

Figure 123 shows the temperature dependence of storage (Young's) modulus (E'), loss modulus (E'') and loss tangent ($\tan\delta$) of the amorphous $La_{55}Al_{25}Ni_{20}$ alloy (Okumura et al. 1991). E' decreases gradually from 33.5 GPa at room temperature to 28.9 GPa

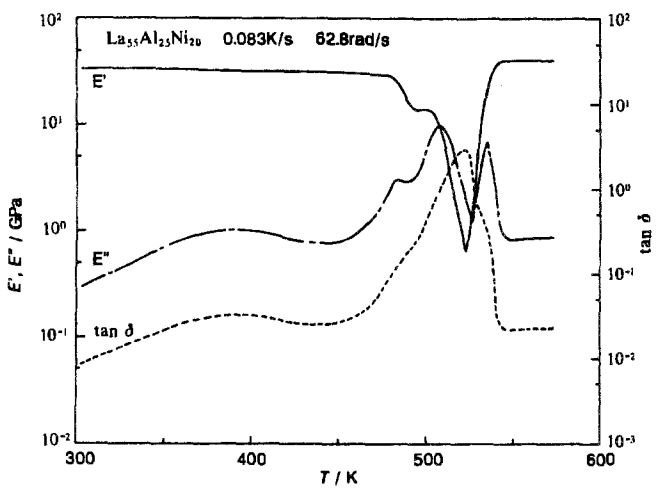

Fig. 123. Temperature dependence of storage (Young's) modulus (E'), loss modulus (E'') and $\tan\delta$ for an amorphous $La_{55}Al_{25}Ni_{20}$ alloy.

at 473 K and rapidly to 13.4 GPa at about 480 K because of the glass transition. The E' shows a plateau at temperatures between 491 and 503 K and then decreases rapidly to 1.79 GPa at 523 K. With further increasing temperature, E' increases significantly by crystallization. E'' corresponding to the heat loss caused by a thermally activated process such as diffusion shows a peak at each temperature of 394, 483, 507 and 535 K. The lowest- and the highest-temperature peaks are associated with structural relaxation and crystallization, respectively. In the temperature range above the offset temperature of crystallization (541 K), no distinct change in E'' is seen because of the formation of a stable crystalline phase. The two peaks at 483 and 507 K in the glass transition region correspond to the two-stage reductions in E'', indicating the existence of two distinguishable relaxation processes. The large decrease of E'' to 8.5 GPa with increasing temperature from 507 to 527 K indicates that the transition to the supercooled liquid is completed, leading to an approach to an internal equilibrium state with short relaxation times. The $\tan\delta$ associated with E'' shows a few peaks and the highest peak of 3.32 appears at 522 K where the E' shows a minimum value. The main peak with each shoulder at both sides corresponds to the second-stage glass transition peak of E'' and the two shoulders result from the first-stage glass transition peak and crystallization peak, respectively.

5.11. *Two-stage glass transitions in mechanical relaxation*

Glass transition is a type of dynamical transition in a substance which is a consequence of changes of diffusivity, viscosity, and relaxation time (Hiwatari et al. 1991). In order to examine the relaxation time for atomic rearrangements, an internal friction measurement has commonly been used. The internal friction shows a peak when the frequency used in the measurement approaches the corresponding relaxation time. A number of studies on the internal friction of amorphous alloys have been carried out and the appearance of a sharp and large internal friction peak has been reported in the glass transition region, e.g. see Chen and Morito (1985), Lanping and Yizen (1988), Sinning and Haessner (1986), and Sinning (1989). The application of dynamic mechanical measurement to the $La_{55}Al_{25}Ni_{20}$ amorphous alloy with a wide supercooled liquid region Okumura et al. (1991) is expected to give detailed information on the dynamical relaxation in the glass transition and supercooled liquid.

Figure 124 shows the storage, E', and loss, E'', moduli for the $La_{55}Al_{25}Ni_{20}$ amorphous alloy measured at a heating rate of 0.083 K/s and at frequencies of 0.628, 6.28 and 62.8 rad/s (Okumura et al. 1992a). At 62.8 rad/s, E' decreases in two regions at 480 and 503 K and then increases in the range above 523 K due to crystallization. E'' shows two peaks at 483 and 507 K, corresponding to the two decreasing regions for E', and a crystallization peak at 523 K. As the frequency decreases, the two peaks shift to a lower temperature and the resolution between them increases i.e., 475 and 499 K at 6.28 rad/s and 466 and 493 K at 0.628 rad/s. This result indicates that there are two relaxation mechanisms in the glass transition region, although no distinction is detected in a differential scanning calorimetric measurement (Okumura et al. 1991). On the other

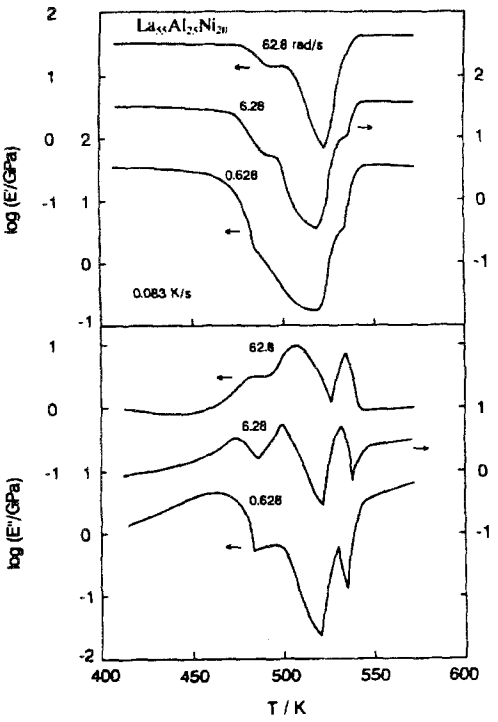

Fig. 124. Temperature dependence of storage (E') and loss (E'') moduli for an amorphous $La_{55}Al_{25}Ni_{20}$ alloy measured at various frequencies.

hand, the third E'' peak caused by crystallization is independent of frequency because the crystallization is not a relaxation process.

The change in $E''(T)$ behavior at 6.28 rad/s with the heating rate is shown in fig. 125. The first peak temperature is at about 472 K and almost independent of the heating rate, while the second peak temperature shifts from 490 to 503 K with increasing heating rate from 0.017 to 0.13 K/s. The third peak temperature also shifts to a higher value with increasing heating rate. Consequently, the first and second peaks tend to be further apart at higher heating rates.

The negligible shift in the first E'' peak temperature with heating rate is somewhat striking. This, seemingly, puzzling behavior is explained in view of the potential phase separation in this $La_{55}Al_{25}Ni_{20}$ amorphous alloy, consistent with the appearance of two E'' relaxation peaks in the glass transition region (Okumura et al. 1992a). Since the as-quenched samples exhibit a high atomic mobility, a considerable phase separation would occur during heating before the appearance of the glass transition. The faster the heating rate, the less the phase separation, thus the first peak corresponds to a faster diffusing separated phase. The E'' peaks observed at different heating rates are attributed to different configurational structures. In fact, the reduced phase separation and faster scanning rate effects completely offset each other and the first peak temperature appears independent of heating rate. On the other hand, the second E'' peak corresponds,

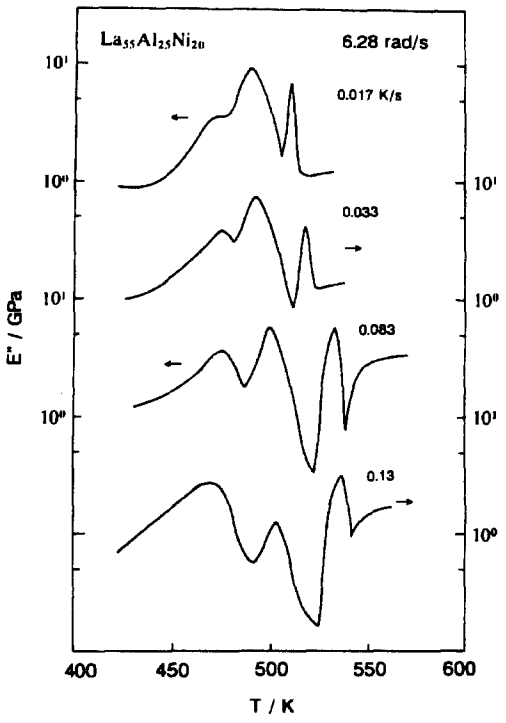

Fig. 125. Change in $E''(T)$ at 6.28 rad/s with the heating rate for an amorphous $La_{55}Al_{25}Ni_{20}$ alloy.

approximately, to the iso-configurational structure and the peak temperature shifts with heating rate for a thermally activated process.

It has been reported from the DSC measurements that T_g for the $La_{55}Al_{25}Ni_{20}$ amorphous alloy is independent of the heating rate and that the apparent activation energy, E_a, evaluated using the Kissinger equation (Kissinger 1957) is 302±19 kJ/mol (Okumura et al. 1992b). Using the Kissinger equation, the value of E_a for the second peak in E'' is 300±20 kJ/mol, in agreement with the value obtained from the DSC measurements. From the shift of the onset temperature of the third peak, we obtain a value for the activation energy of crystallization, $E_a = 180 \pm 20$ kJ/mol, which is in good agreement with the value, 176±10 kJ/mol, obtained from the DSC measurements.

Figure 126 shows the frequency dependence of E'', in which nine points per decade were measured. E'' increases with increasing frequency to a maximum and then decreases rather slowly. All the $E''(\omega)$ data exhibit a kink at a frequency about one and half decades higher than each maximum point, as marked with arrows. The kink at the higher frequency corresponds to the first T_g peak in the $E''(T)$ curve. During the isothermal measurements, the sample has relaxed spontaneously and hence the resolution of the two peaks is decreased. With increasing temperature, the two peaks shift to a higher frequency.

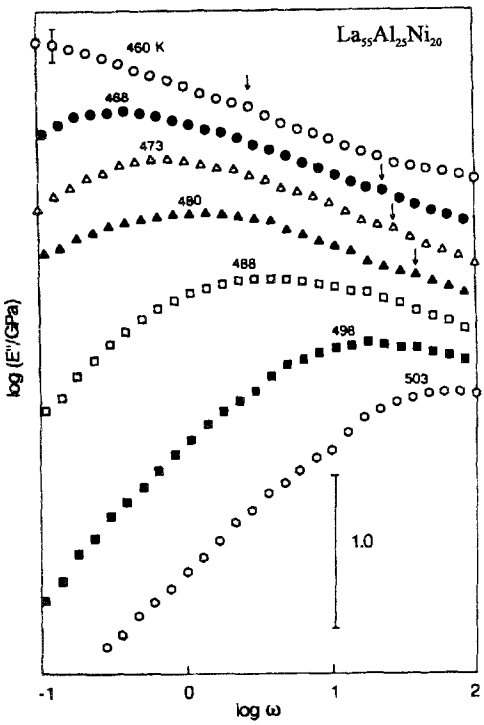

Fig. 126. Frequency dependence of E'' for an amorphous $La_{55}Al_{25}Ni_{20}$ alloy.

Using the time–temperature superposition process (Tobolsky 1956) a master curve for E'' at 480 K is derived and shown in fig. 127. The scale on the right-hand side of the figure indicates the relaxation spectrum, $H(\log\omega)2E''/\pi$ (Nowick and Berry 1972a). The overall $E''(\log\omega)$ spectrum consists of two features with the high frequency as a shoulder, as mentioned above. The main peak at the lower frequency is rather narrow, but it is slightly broader than the Debye peak (Nowick and Berry 1972a) as shown by the dash-dotted line in the figure. The peak is well fitted with a Gaussian distribution, $\phi(z)=\beta^{-1}\pi^{-1/2}\exp[-(z/\beta)^2]$, with $z=\ln(\omega_\tau/\omega_m\tau_m)$ and $\beta=1.25$ (Nowick and Berry 1972b), as shown by the broken line. A nearly single relaxation has also been found in another amorphous alloy (Chen and Morito 1985) and is thought to be an intrinsic characteristic of the glass transition.

Figure 128 shows the temperature dependence of shift factor, a_T, obtained from the time–temperature shift. The data consist of two straight lines connected by a step at about 480 K. The occurrence of two activation processes is in accordance with the temperature and frequency scanning data. From the Arrhenius parts of the curve, the E_a value is evaluated to be 400±20 and 550±20 kJ/mol for the higher and the lower frequency peaks, respectively. If all the data were used to evaluate E_a as a single straight line, E_a would be 290±20 kJ/mol which agrees with the value obtained from the DSC measurement. This

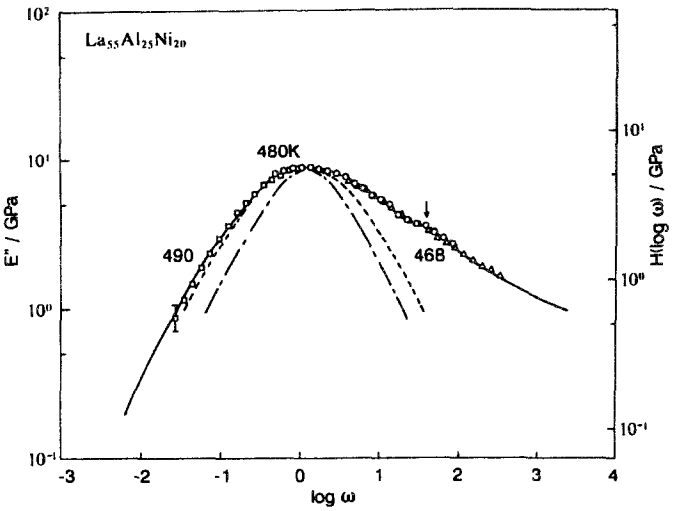

Fig. 127. A master curve for E'' at 480 K for an amorphous $La_{55}Al_{25}Ni_{20}$ alloy.

result allows us to conclude that dynamic mechanical measurements in the glass transition region are more useful than the calorimetric analysis.

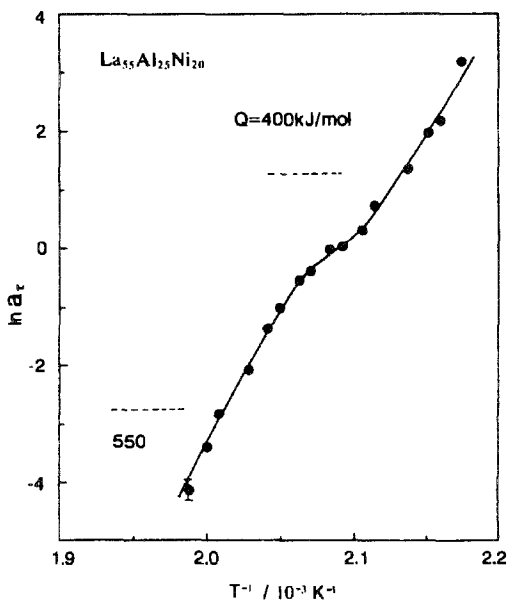

Fig. 128. Temperature dependence of shift factor (a_τ) obtained from the time-temperature shift for an amorphous $La_{55}Al_{25}Ni_{20}$ alloy.

5.12. *Reductilization phenomenon*

5.12.1. *Water quenching from supercooled liquid*

It is generally known, e.g. see Chen (1980) and Greer (1984), that a number of amorphous alloys belonging to Fe- and Co-based alloy systems exhibit a catastrophic loss of ductility upon annealing at temperatures well below T_x, though their amorphous alloys in the as-quenched state possess good bending ductility. The catastrophic loss of ductility causes a severe limitation in practical uses of amorphous alloys at elevated temperatures. Accordingly, a number of studies on the annealing-induced embrittlement phenomenon in an amorphous single state without any appreciable crystalline phases have been carried out, with the aim of clarifying the mechanism for the embrittlement phenomenon (Chen 1980, Greer 1984), as well as of finding a technique to restore the ductile state from the brittle state (Mulder et al. 1988). However, little knowledge has been obtained about the mechanism and technique. It has recently been reported that Fe–Ni–P and Cu–Ti amorphous alloys subjected to the first-stage embrittlement upon annealing at temperatures (T_a) well below T_x can be reductilized by heating for a short time at temperatures above T_a, followed by water quenching (Gerling et al. 1988a), in addition to the reductilization by neutron irradiation (Gerling et al. 1987, 1988b). Furthermore, it has been pointed out from the measurement of relative density that the reductilization obtained by the two techniques is presumably due to the introduction of excess free volume into the embrittled sample in which the excess free volume was lost by annealing. Thus, the reductilization treatments are valid only for the samples which were embrittled at a low T_a range by the loss of quenching-induced excess free volume. There is no report on the reductilization of the sample which was subjected to the second-stage in a high T_a range where cooperative atomic rearrangement as well as the loss of free volume takes place. More recently, we have found that the $La_{55}Al_{25}Ni_{20}$ amorphous alloy exhibiting a distinct supercooled liquid region before crystallization can be reductilized from an annealing-induced embrittled state by water quenching of the sample from the temperature region in a supercooled liquid state, though the heat treatment in the amorphous solid proposed for the Fe–Ni–P and Cu–Ti systems (Gerling et al. 1988a) does not induce a reductilization of the La–Al–Ni amorphous alloy embrittled at the high T_a of $0.95T_g$.

Figure 129 shows the change of the bending fracture strain ($\varepsilon_{b,f}$) as a function of T_a for the amorphous $La_{55}Al_{25}Ni_{20}$ ribbon (Inoue et al. 1991b). Although $\varepsilon_{b,f}$ remains unchanged in the T_a range below 416 K, it decreases drastically from 1.0 to 0.04 in the narrow temperature range between 416 and 434 K and shows a nearly constant value of about 0.03 in the temperature range above 434 K. The change of $\varepsilon_{b,f}$ with T_a clearly indicates that the La–Al–Ni amorphous ribbon becomes brittle at 416 K when annealed for 1.8 ks. The ratios of the onset temperature of the annealing-induced embrittlement to T_g and T_x are 0.87 and 0.76, respectively.

Figure 130 shows the thermograms of the $La_{55}Al_{25}Ni_{20}$ amorphous samples annealed for 1.8 ks at different temperatures ranging from 390 to 450 K including the ductile–brittle transition temperature (Inoue et al. 1991b). Here, $C_{p,q}$ and $C_{p,a}$ denote the specific heat curves of the as-quenched and annealed samples, respectively, and $C_{p,s}$ represents the

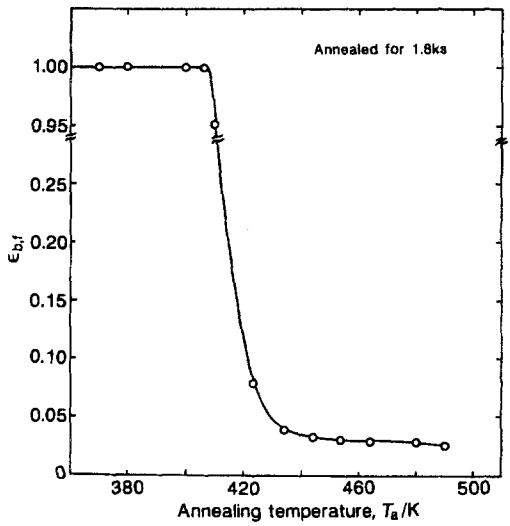

Fig. 129. Change in bending fracture strain ($\varepsilon_{b,f}$) as a function of annealing temperature for an amorphous $La_{55}Al_{25}Ni_{20}$ alloy.

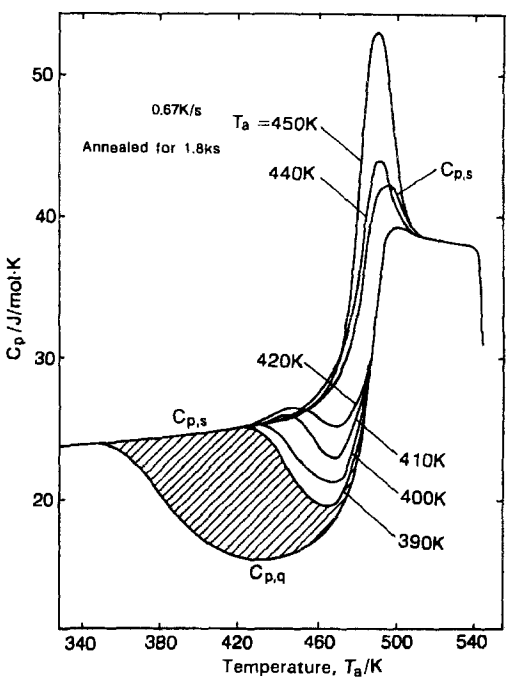

Fig. 130. The temperature dependence of apparent specific heat ($C_{p,a}$) of a melt-spun $La_{55}Al_{25}Ni_{20}$ amorphous alloy annealed for 1.8 ks at different temperatures between 390 and 450 K. The data of the as-quenched ($C_{p,q}$) sample and the sample heated for 60 s at 520 K ($C_{p,s}$) are also shown for comparison.

specific heat curve during reheating of the sample which was heated once to 510 K in the supercooled liquid region. The C_p value of the melt-spun sample is about 22.5 J/mol K near room temperature. On subsequent heating, C_p begins to decrease at about 350 K,

indicative of a structural relaxation, and shows a minimum value at about 434 K. With a further increase in temperature, C_p increases gradually up to about 460 K, then increases rapidly in the glass transition range from 470 to 500 K and reaches 37.0 J/mol K for the supercooled liquid around 515 K. With further increasing temperature, the C_p value of the supercooled liquid decreases gradually and then rapidly due to crystallization at 545 K.

The heating curve of the sample embrittled by annealing at T_a above 416 K, $C_{p,a}$, shows a $C_p(T)$ behavior which closely follows the specific curve of the reference sample, $C_{p,s}$, up to each T_a, and then exhibits an excess endothermic peak relative to the reference sample before merging with that of the melt-spun sample at a temperature below $T_g = 476$ K. The $C_{p,a}$ of the sample without the loss of ductility subjected to annealing for 1.8 ks at 390 K begins to decrease at about 420 K due to the heating-induced irreversible structural relaxation. In other words, the internal energy of the sample decreases by an enthalpy (ΔH_{exo}) of 662 J/mol corresponding to the area marked with the oblique line. The irreversible enthalpy ΔH_{exo} was defined by $\Delta H_{exo} = \int \Delta C_p \, dT$, $\Delta C_p (= C_{p,a} - C_{p,q}) \geqslant 0$. In the relation between ΔH_{exo} and T_a for the La–Al–Ni amorphous samples, the ΔH_{exo} increases gradually with increasing T_a in the temperature range below 430 K and shows a constant value at temperatures above 440 K. This indicates that the irreversible structural relaxation is completed upon annealing for 1.8 ks at temperatures above 430 K. As shown in fig. 129, the annealing-induced embrittlement takes place for the sample in which the ΔH_{exo} is released by about 74%, indicating that there is a rather close correspondence between the embrittlement tendency and the release of ΔH_{exo}.

In addition to ΔH_{exo} corresponding to the difference between $C_{p,a}$ and $C_{p,q}$, only for the samples embrittled upon annealing at T_a above 420 K, one can notice the difference between $C_{p,a}$ and $C_{p,s}$ corresponding to an endothermic reaction which can be evaluated by the equation, $\Delta H_{endo} = \int \Delta C_p (= C_{p,a} - C_{p,q}) \, dT$, $\Delta C_p (= C_{p,a} - C_{p,s}) \geqslant 0$. That is, the ΔH_{endo} reaction is recognized only for the embrittled samples. It has been reported (Inoue et al. 1985) that the endothermic reaction takes place reversibly by the reversion of an annealing-induced relaxed structure into an unrelaxed structure upon heating to a higher temperature above T_a. Accordingly, the development of the structural relaxation leading to the endothermic reaction appears to take place only in the embrittled samples, indicating the possibility that the embrittlement takes place through the development of structural relaxation leading to the endothermic reaction. In other words, the annealing treatment which does not cause the appearance of the endothermic reaction does not have a harmful influence on the good bending ductility which is inherent to the as-quenched amorphous alloy.

The endothermic reaction for the sample annealed at T_a above 420 K is a reversible process (Chen 1981). Accordingly, when the endothermic reaction of the embrittled sample is eliminated by subsequent heat treatment, it is expected that the embrittled sample changes into a ductile state. It is generally known that the structural relaxation caused by annealing can be eliminated by water quenching from the supercooled liquid state between T_g and T_x, accompanying the introduction of disordered atomic configurations leading to an exothermic reaction. Accordingly, the change in ε_f as a function of water quenching temperature was examined for the La–Al–Ni amorphous

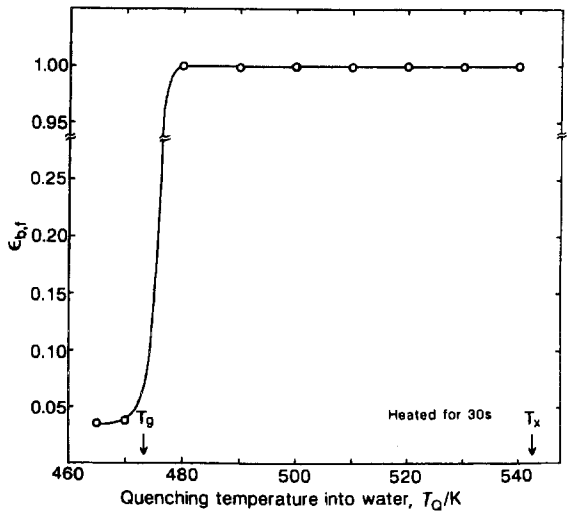

Fig. 131. Change in $\varepsilon_{b,f}$ as a function of water quenching temperature (T_Q) for an amorphous $La_{55}Al_{25}Ni_{20}$ alloy embrittled upon annealing for 1.8 ks at 450 K.

alloy embrittled by annealing for 1.8 ks at a high temperature of 450 K corresponding to $0.95T_g$. As shown in fig. 131, the samples which were quenched from the temperature region between T_g and T_x into water exhibit a fully restored ductility defined by $\varepsilon_{b,f} = 1.0$. In order to confirm the reductilization phenomenon of the embrittled sample, the fracture surface appearance was observed by SEM. Figure 132 shows the tensile fracture surface appearance of the $La_{55}Al_{25}Ni_{20}$ amorphous samples in a melt-spun state, an annealed state for 1.8 ks at 450 K and a water-quenched state from 510 K after the annealing. It is seen that the fracture surface appearance of the three samples corresponds to the ductile, brittle and ductile states, respectively. That is, the ductile samples in the melt-spun and the water-quenched states exhibit the surface appearance consisting of a smooth region caused by shear sliding and a vein region by subsequent catastrophic failure. On the other hand, the embrittled sample shows a shell-like pattern. It should be noticed that the shell-like pattern for the embrittled sample changes to the pattern consisting of smooth and vein regions characteristic of the ductile amorphous sample. It is believed that this is the first evidence of a fracture surface appearance revealing the recovery of the embrittled to reductilized states for amorphous metallic materials.

Figure 133 shows the thermograms of the $La_{55}Al_{25}Ni_{20}$ amorphous samples subjected to water quenching from the temperature range of 480 to 540 K after annealing for 1.8 ks at 450 K. The samples reductilized by water quenching from the temperature above T_g (≡470 K) show only the exothermic reaction due to structural relaxation and one cannot see an endothermic peak which is observed for the embrittled sample. On the other hand, the sample subjected to water quenching from temperatures of 450 and 460 K below T_g remains brittle and shows a similar endothermic reaction as that for the annealed sample. These data allow us to conclude that the structural change in the amorphous phase leading to the disappearance of the endothermic reaction as well as the appearance of the exothermic reaction plays an important role in the achievement of the reductilized state.

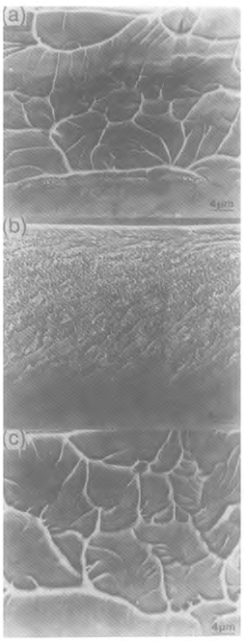

Fig. 132. Tensile fracture surface appearance of an amorphous $La_{55}Al_{25}Ni_{20}$ alloy: (a) melt-spun; (b) annealed for 1.8 ks at 450 K; (c) water-quenched from 510 K after annealing for 1.8 ks at 450 K.

It has been reported (Chen 1983) that the endothermic reaction is due to the annihilation of the relaxed atomic configuration and the exothermic reaction due to the development of structural relaxation from the quenching-induced disordered state. Accordingly, the reductilization caused by water quenching from the temperature region between T_g and T_x is presumed to originate from the annihilation of the annealing-induced relaxed structure and the introduction of quenching-induced disordered structure.

The interference functions of the as-quenched, embrittled and reductilized samples are shown in fig. 134. Some differences are observed in the interference functions of the as-quenched and embrittled samples. For example, a shift towards smaller Q values and an increase in the amplitude of the oscillations. Similar structural variations related to the structural relaxation process due to annealing are commonly obtained in other amorphous alloys, e.g. see Waseda (1980). On the other hand, the interference functions of the embrittled and reductilized samples are almost identical, which implies that the reductilization process is not accompanied by a distinct change in the total atomic structure. Nevertheless, the following observation may be suggested in terms of the near-neighbor atomic distribution described in the reduced RDFs of fig. 135. By comparing the reduced RDF of the as-quenched sample with the embrittled sample, the main peak shows a shift towards larger r, and the first peak maximum becomes more intense and sharper in the embrittled sample. Because of the ternary system, the reduced RDF is the sum of 6 partial reduced RDFs of the 6 different atomic pairs. Thus, the separation of the reduced RDF into partial RDFs is practically impossible in the present measurements alone. However, referring to the Goldschmidt radii of La (0.187 nm), Al (0.143 nm) and

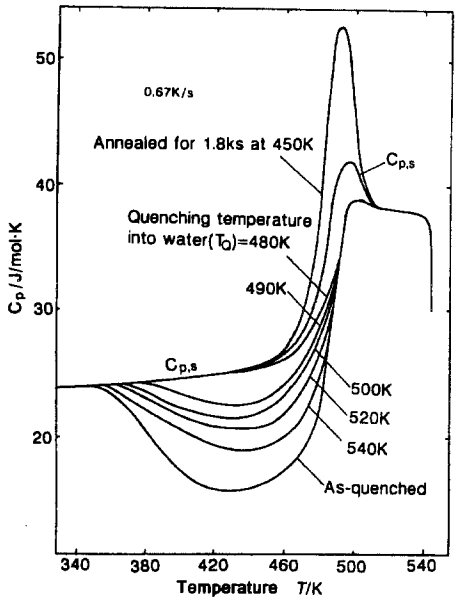

Fig. 133. The temperature dependence of apparent specific heat ($C_{p,a}$) of an amorphous $La_{55}Al_{25}Ni_{20}$ alloy subjected to water quenching from different temperatures between 450 and 540 K after annealing for 1.8 ks at 450 K. The data of $C_{p,q}$ and $C_{p,s}$ are also shown for comparison.

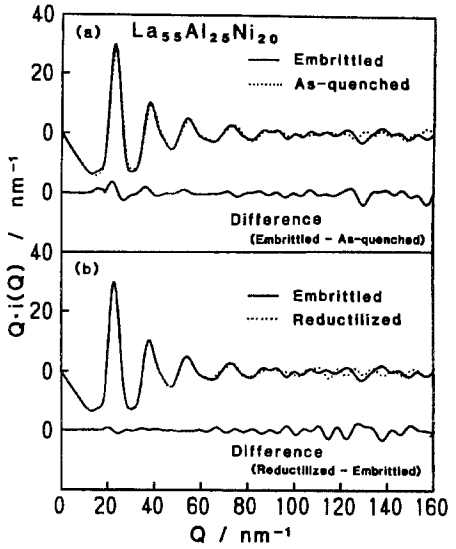

Fig. 134. (a) Interference functions $Q_i(Q)$ for embrittled (full curve) and as-quenched (dotted curve) samples and their difference; (b) same for reductilized (dotted curve) and embrittled (full curve) samples. Densities of the as-quenched, embrittled and reductilized samples are 5.83, 5.91 and 5.95 Mg/m^3, respectively.

Ni (0.124 nm) (Goldschmidt 1954), it is likely that the environmental structure around La is mainly changed in the embrittlement process. On the other hand, the reductilization process produces a slight shift of the first peak maximum towards a smaller r, and the sharpness of the peak is decreased and smoothed out at some details as shown at the bottom of fig. 135. The differences of the reduced RDFs between the embrittled and as-quenched samples, and between the reductilized and embrittled samples in the nearest-neighbor region from 0.2 to 0.45 nm are magnified and shown with the full and dotted curves in the middle of fig. 135. The profiles of the difference show an inverse pattern of $G(r)$. Consequently, it appears that the reductilization process is reversed by the embrittlement process.

Srolovitz et al. (1981) explained the width and height of the peaks of the RDF by atomic-level hydrostatic stress introduced into amorphous solids by rapid quenching and mentioned that the width of the hydrostatic stress distribution provides an indication regarding the degree of the structural relaxation of the amorphous solids. According to their discussion, the features of the RDF observed in the reductilization process are related with a wider stress distribution. Although the relaxed structure in the embrittled sample does not change much by annealing at a temperature above T_g, stress fluctuation

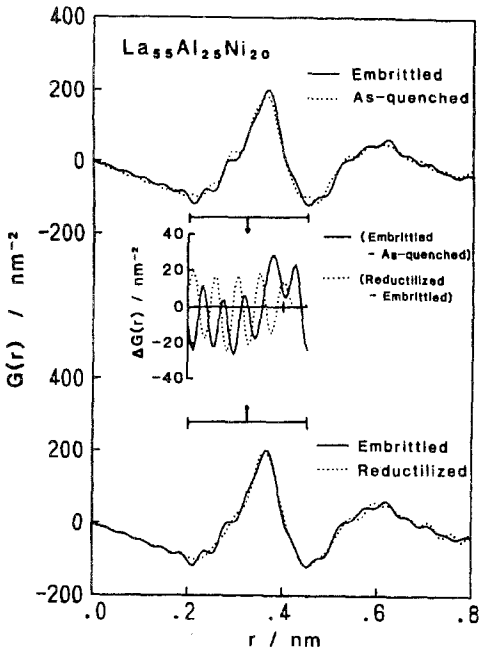

Fig. 135. Comparison of reduced RDF $G(r)$ of embrittled (full curve) and as-quenched (dotted curve) samples in the top panel and those of reductilized (dotted curve) and embrittled (full curve) samples in the bottom panel. The difference in $G(r)$ between the embrittled and as-quenched samples, and between the reductilized and embrittled samples in the nearest-neighboring region from 0.2 nm to 0.45 nm are shown in the middle panel.

is introduced by water quenching from the supercooled liquid region analogous to the sample rapidly quenched from the melt. It appears that this introduced stress fluctuation stabilizes the amorphous alloys with a disordered atomic configuration and recovers the ductility (Egami and Waseda 1984).

5.12.2. *Viscous flow deformation in the supercooled liquid region*

Bulk amorphous alloys of Mg and La systems have been produced with a thickness of about 10 mm (Inoue et al. 1992g) by high-pressure die casting. The water quenching treatment leading to reductilization cannot be applied to these bulk amorphous alloys, because the cooling rate obtained by water quenching is not high enough to introduce the necessary excess free volume into the bulk samples. Here, we introduce another reductilization method which can be applied for bulk amorphous alloys. In this method, the viscous flow deformation in a supercooled liquid region must be subjected at high strain rates exceeding a critical value.

It is shown in fig. 129 that $\varepsilon_{b,f}$ of the amorphous $La_{55}Al_{25}Ni_{20}$ ribbon remains unchanged in the T_a range below 406 K, decreases from 1.0 to 0.04 in the narrow T_a range between 406 and 434 K and shows a nearly constant value of about 0.03 in the T_a range above 434 K. The change in $\varepsilon_{b,f}$ with T_a indicates that the amorphous ribbon becomes brittle at 416 K in the case of an annealing time of 1.8 ks. The exothermic reaction for the as-quenched sample as well as the endothermic reaction for the annealed sample is a reversible process for the La–Al–Ni amorphous alloy with a wide supercooled liquid

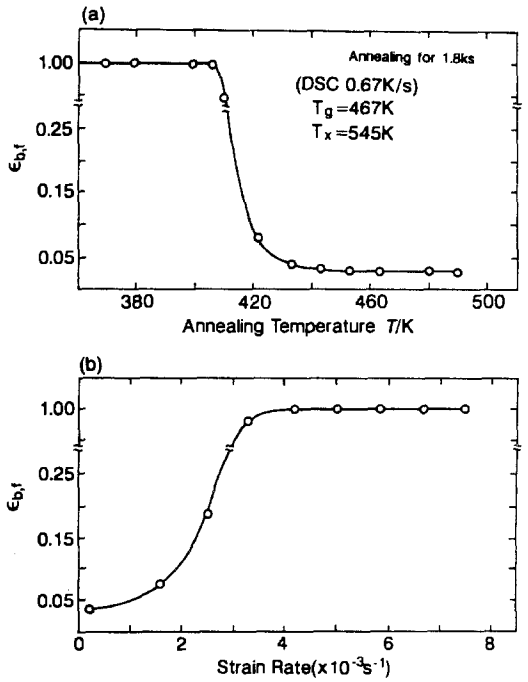

Fig. 136. Change in $\varepsilon_{b,f}$ with strain rate at 500 K for an amorphous $La_{55}Al_{25}Ni_{20}$ alloy subjected to tensile deformation at 500 K after the embrittlement treatment by annealing for 1.8 ks at 450 K.

region before crystallization. Accordingly, when the exothermic reaction is induced into the embrittled sample and the endothermic reaction is eliminated from it, it is expected that the embrittled sample recovers into a ductile state. It is thought that the relaxed atomic configuration caused by annealing is destroyed by severe deformation in the supercooled liquid region between T_g and T_x, accompanying the introduction of excess free volume which leads to the recovery of the exothermic reaction. Accordingly, the change in $\varepsilon_{b,f}$ as a function of strain rate during deformation to 50% elongation at 500 K was examined for the La–Al–Ni amorphous alloy which had been embrittled by annealing for 1.8 ks at 450 K corresponding to $0.95T_g$. As shown in fig. 136, the samples deformed at strain rates above 4×10^{-3} s^{-1} exhibit a fully restored ductility defined by $\varepsilon_{b,f} = 1.0$. The reductilization phenomenon of the embrittled sample was also examined by observation of the fracture surface appearance. The tensile fracture surface was examined for amorphous samples which were annealed for 1.8 ks at 450 K and deformed at a strain rate of 4.0×10^{-3} s^{-1} at 500 K after annealing. These samples correspond to the brittle and ductile states, respectively. It has been confirmed that the embrittled sample shows a shell-like pattern while the ductile sample in the deformed state consists of a smooth region caused by shear sliding and a region with vein-like structures generated by subsequent catastrophic failure. It should be noted that the shell-like pattern for the embrittled sample changes reversibly to the smooth and vein patterns typical for the ductile amorphous sample.

The minimum strain rate leading to reductilization, d_r, for the $La_{55}Al_{25}Ni_{20}$ alloy was examined as a function of deformation temperature, T_d. As T_d increases, d_r increases

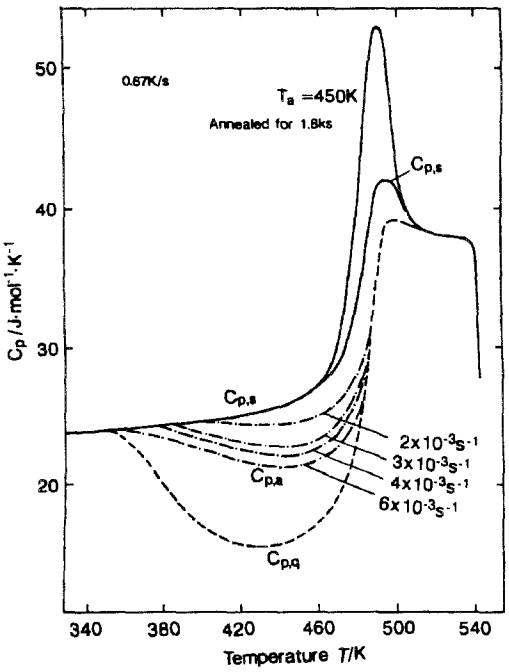

Fig. 137. The thermograms of amorphous $La_{55}Al_{25}Ni_{20}$ samples subjected to deformation up to an elongation of 50% at 500 K at strain rates of 2×10^{-3} to 6×10^{-3} s^{-1}. The data of the as-quenched and annealed (450 K, 1.8 ks) samples are also shown for comparison.

slightly in the range of 470 to 490 K corresponding to T_g and rapidly in the range of 500 to 530 K corresponding to the supercooled liquid region. Thus, there is a clear tendency for R_c to increase with increasing T_d in the supercooled liquid region. This tendency is explained by the fact that the critical strain rate required for the generation of excess free volume increases with an increase in atomic mobility and/or a decrease in relaxation time and viscosity. The annealing-induced relaxed structure disappears easily upon heating in the supercooled liquid region. Accordingly, the strong dependence of d_r on T_d indicates that the introduction of excess free volume by high-speed deformation is a dominant factor for the achievement of reductilization.

Figure 137 shows the thermograms of the $La_{55}Al_{25}Ni_{20}$ amorphous samples subjected to deformation up to an elongation of 50% at 500 K at strain rates ranging from 2×10^{-3} to 6×10^{-3} s^{-1}, along with the data for the as-quenched and annealed (450 K; 1.8 ks) samples (Inoue et al. 1993a). The deformed samples show the exothermic reaction due to structural relaxation, by contrast with the appearance of the endothermic reaction for the sample embrittled by annealing for 1.8 ks at 450 K. Complete reductilization, defined by the recovery to $\varepsilon_{b,f} = 1.0$, is achieved when ΔH_{exo} marked by dashed lines is larger than 246 J/mol and the onset temperature for structural relaxation is below 386 K. Accordingly, we can draw the conclusion that the structural change in the amorphous phase leading to the disappearance of the endothermic reaction plays an important role in the achievement of the reductilized state. It has previously been reported (Egami 1978)

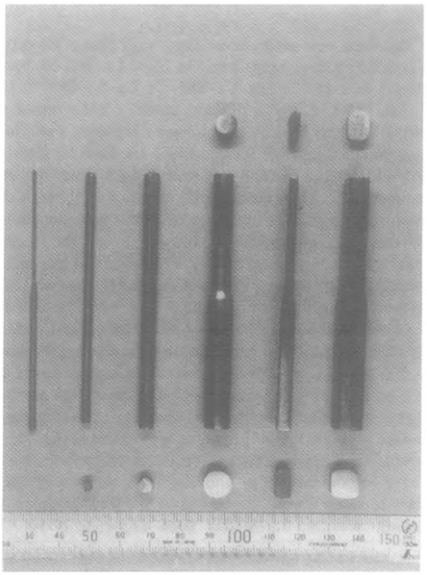

Fig. 138. Outer surface appearance of cylindrical, sheet and tube forms for an amorphous $La_{55}Al_{25}Ni_{20}$ alloy.

that the exothermic reaction is due to the annihilation of excess free volume and the development of topological and chemical short-range ordering.

5.13. *Bulk amorphous alloys by casting*

The appearance of a supercooled liquid region reaching about 92 K in the temperature range below T_x implies that the supercooled liquid obtained by supercooling of the melt which was heated above T_m also has high resistance against crystallization and the R–Al–M alloys have large glass-forming ability. By utilizing the high thermal stability of the supercooled liquid, we have produced bulk amorphous alloys in cylindrical, sheet and tube forms by using various solidification methods of water quenching, copper mold casting and high-pressure die-casting etc. As examples, fig. 138 shows the outer surface appearance of amorphous cylindrical, sheet and tube samples with composition $La_{55}Al_{25}Ni_{20}$ prepared by copper mold casting or high-pressure die casting (Inoue et al. 1993b). As shown in these photographs, neither holes nor cavities are seen on the outer surface of these as-cast samples and the surface has good luster. Considering that the shape and dimension of the as-cast samples are the same as the cavity shapes of the copper molds, the copper mold and high-pressure die-casting methods seem to be useful for the production of R–Al–M bulk amorphous alloys with various shapes and dimensions. No appreciable crystalline peak is seen in the X-ray diffraction patterns taken from the central region in the transverse cross section of the cast samples with diameters up to 3.0 mm for the copper mold casting method and 9.0 mm for the high-pressure die-casting method. The absence of any crystallinity is also confirmed from an optical micrograph taken from the transverse cross-sectional structure of the as-cast $La_{55}Al_{25}Ni_{20}$ samples. Even after

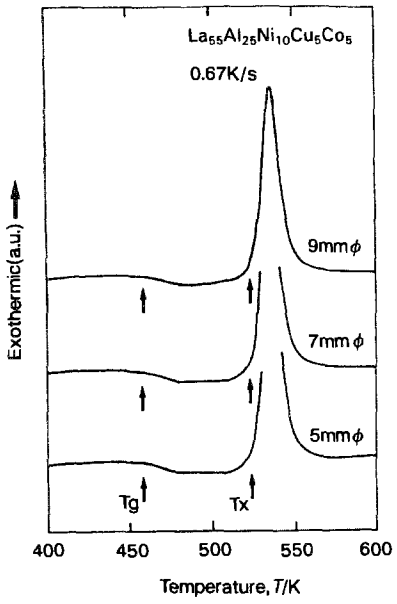

Fig. 139. DSC curves of amorphous $La_{55}Al_{25}Ni_{10}Cu_5Co_5$ cylinders with different diameters.

an etched state, no contrast corresponding to the precipitation of any crystalline phases is seen over the entire transverse cross section. Thus, the cast bulk samples are composed of an amorphous phase which does not include any appreciable crystalline phase.

The DSC curves of the amorphous $La_{55}Al_{25}Ni_{10}Cu_5Co_5$ cylinders are shown in fig. 139 (Inoue 1995b). T_g and T_x of the bulk samples are 460 and 527 K, respectively, independent of the diameter of the cylinders. On the basis of the DSC curves shown in fig. 139, T_g, T_x and the heat of crystallization (ΔH_x) for the La–Al–Ni–Cu–Co cylinders are examined as a function of sample diameter. T_g and T_x are independent of the diameter in the entire range of 1 to 9 mm and ΔH_x also remains almost constant in the diameter range of 1 to 7 mm, though ΔH_x decreases by about 15% for a diameter of 9 mm. We confirmed that the T_g, T_x and ΔH_x values of the cylinder samples with diameters below 7 mm agree with those of the melt-spun ribbon which was prepared by using the as-cast cylinder as a mother alloy. These data on the thermal stability indicate that the cylinder samples in the diameter range below 7 mm have a mostly single amorphous phase and the further increase in diameter causes the precipitation of a crystalline phase of about 15% into the amorphous matrix. The maximum sample thickness for formation of an amorphous single phase by high-pressure die casting increases to about 10 mm for the $La_{50}Al_{25}Cu_{10}Ni_{10}Co_5$ alloys with larger ΔT_x values.

Thus, multiplication of the alloy components from the ternary to the penternary system through the quaternary system causes a distinct increase in maximum diameter, accompanying a significant increase in ΔT_x. However, the T_g/T_m ratio has a high value of $\equiv 0.60$ for all the alloys and no distinct correlation is seen between T_g/T_m and the maximum diameter. This result indicates that the formation of these bulk amorphous

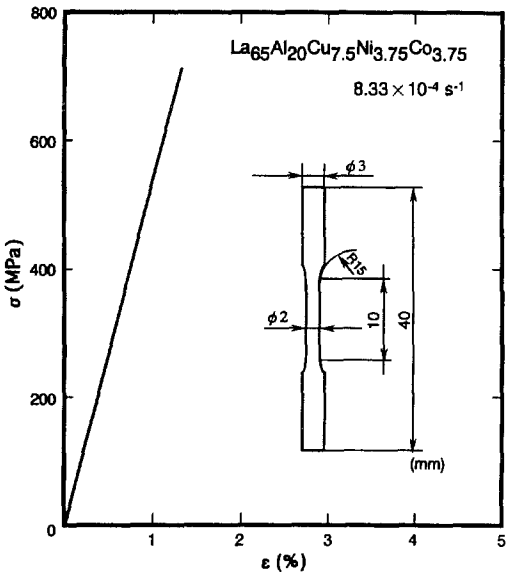

Fig. 140. Tensile stress–elongation curve at room temperature for a 3 mm diameter cylinder of amorphous $La_{65}Al_{20}Cu_{7.5}Ni_{3.75}Co_{3.75}$.

alloys with large diameters is due to the large glass-forming ability resulting from the increase in ΔT_x. It has been presumed (Inoue 1995b) that the increase in ΔT_x originates from the difficulty in the nucleation and growth of a crystalline phase even in a supercooled liquid where the constituent elements have a rather large atomic diffusivity.

The La–Al–Cu–Ni–Co amorphous cylinders prepared by the high-pressure die-casting technique exhibit a high tensile strength which is nearly the same as that for the corresponding melt-spun ribbon. Figure 140 shows the nominal tensile stress–elongation curve at room temperature for the $La_{65}Al_{20}Cu_{7.5}Ni_{3.75}Co_{3.75}$ cylinder with a diameter of 3 mm, along with the shape and dimensions of the sample used for the tensile test. The tensile strength and the fracture elongation including elastic elongation are 700 MPa and 1.5%, respectively, which are about 80% as high as those (880 MPa and 2.0%) (Zhang et al. 1991b) for the melt-spun La–Al–Cu–Ni–Co ribbon with a thickness of about 20 μm. On the tensile fracture surface of the cylinder sample, the vein pattern typical for an amorphous alloy with good bending ductility is observed over the whole fracture surface. However, some pores with sizes of 2 to 25 μm are also seen on the fracture surface and the area fraction occupied by the pores is measured to be about 20% which is nearly the same as the porosity (≡ 20%) evaluated from the optical micrographs of the cross section. Here, it appears important to point out that the true fracture strength evaluated by taking the porosity into consideration is 875 MPa which is nearly the same as that (880 MPa) for the melt-spun amorphous ribbon. The approximate agreement suggests that the La–Al–Cu–Ni–Co amorphous cylinder has a good ductility and the existence of pores does not exert harmful influences on the tensile strength. It is, therefore, said that the elimination of pores gives rise to the achievement of a tensile strength which is just the same as that

for the corresponding melt-spun ribbon sample in spite of the significant increase in the sample thickness.

It is important to know the cooling rate of the molten alloy in the present high-pressure die-casting process. There are no experimental data on the cooling rate for the bulk La–Al–M alloys obtained by high-pressure die casting. However, the compositional dependence of the maximum diameter (or thickness) and the critical cooling rate for formation of an amorphous single phase have been examined for the La–Al–M alloys (Inoue et al. 1993b). It has been confirmed that there is a strong correlation for d_c to increase with a decrease in R_c. That is, the cooling rate changes in the range of 55 to 120 K/s in the sample diameter range of 3 to 9 mm. Thus, the cooling rate of the molten alloy is dependent on the diameter of the cast sample.

6. Conclusions

All of the data on the Al–R–M and Mg–R–M alloys consisting mainly of amorphous, quasicrystalline or nanocrystalline structures, which have been presented here, were obtained in the last eight years after the discovery of ductile Al-based amorphous alloys. These new nonequilibrium phase alloys are concluded to be formed through the dissolution of R elements with larger atomic sizes and large negative heats of mixing against the other constituent elements. By utilizing the peculiarity of the R elements, there is a high possibility of finding other new nonequilibrium phases with useful characteristics for the R-containing alloys in the near future. In any case, the subsequent successes of finding nonequilibrium phases with amorphous, quasicrystalline or nanocrystalline structure in the Al-and Mg-based alloys containing R elements by melt spinning provide the opening of a new research field of light-metal base amorphous, quasicrystalline and nanocrystalline alloys. It is, hereafter, expected that the interest in R-containing alloys will steadily increase also for other alloy systems and novel data, which are important for basic science and promotion of practical uses, will be obtained for the alloys containing R elements.

References

Bak, P., 1985, Phys. Rev. Lett. **54**, 1517.

Blackford, B.L., 1976, J. Low Temp. Phys. **23**, 43.

Buhner, H.F., and S. Steeb, 1969, Z. Naturforsch. **24a**, 428.

Bush, G., and H.J. Güntherodt, 1974, in: Solid State Physics, Vol. 29, eds F. Seitz and D. Turnbull (Academic Press, New York) p. 235.

Calka, A., H. Matyja, D.E. Polk, B.C. Giessen, J.V. Sande and M. Madhava, 1977, Scr. Metall. **11**, 65.

Chattopadyay, K., R. Ramachandrarao, S. Lele and T.R. Anantharaman, 1976, in: Proc. 2nd Int. Conf. on Rapidly Quenched Metals, eds N.J. Grant and B.C. Giessen (MIT Press, Cambridge, MA) p. 157.

Chen, H.S., 1980, Rep. Prog. Phys. **43**, 353.

Chen, H.S., 1981, J. Non-Cryst. Solids **46**, 289.

Chen, H.S., 1983, in: Amorphous Metallic Alloys, ed. F.E. Luborsky (Butterworths, London) p. 169.

Chen, H.S., 1986, in: Glass: Science and Technology, Vol. 3 (Academic Press, New York) p. 181.

Chen, H.S., and N. Morito, 1985, J. Non-Cryst. Solids **72**, 287.

Chen, H.S., J.T. Krause and E. Coleman, 1975, J. Non-Cryst. Solids **78**, 157.

Chen, H.S., D. Koskenmaki and C.H. Chen, 1987a, Phys. Rev. B **35**, 3715.

Chen, H.S., J.C. Phillips, P. Villars, A.R. Kortan and A. Inoue, 1987b, Phys. Rev. B **35**, 9326.

Chen, L.C., and F. Spaepen, 1988, Nature **336**, 366.

Collver, M.M., and R.H. Hammond, 1973, Phys. Rev. Lett. **30**, 92.

Cote, P.J., and L.V. Meisel, 1981, in: Glassy Metals I. Topics in Applied Physics, Vol. 46, eds H.J. Güntherodt and H. Beck (Springer, Berlin) p. 141.

Davies, H.A., 1983, in: Amorphous Metallic Alloys, ed. F.E. Luborsky (Butterworths, London) p. 8.

Davies, H.A., and J.B. Hull, 1972, Scr. Metall. **6**, 241.

Delgado, R., H. Armbruster, D.B. Naugle, C.L. Tsai, W.L. Johnson and A. Williams, 1986, Phys. Rev. B **34**, 8288.

Dubois, J.M., G. Le Caer and K. Dehghan, 1985, in: Rapidly Quenched Metals, eds S. Steeb and H. Warlimont (Elsevier, Amsterdam) p. 197.

Dubost, B., J.M. Lang, H. Tanaka, P. Sainfort and M. Audier, 1986, Nature **330**, 48.

Egami, T., 1978, Mater. Res. Bull. **13**, 557.

Egami, T., and Y. Waseda, 1984, J. Non-Cryst. Solids **64**, 113.

Elser, Y., and C.L. Henley, 1985, Phys. Rev. Lett. **55**, 2883.

Furrer, P., and H. Warlimont, 1977, Mater. Sci. Eng. **28**, 127.

Gerling, R., F.P. Schimansky and R. Wagner, 1987, Acta Metall. **35**, 1001.

Gerling, R., F.P. Schimansky and R. Wagner, 1988a, Scr. Metall. **22**, 1291.

Gerling, R., F.P. Schimansky and R. Wagner, 1988b, Acta Metall. **36**, 575.

Goldschmidt, V.M., 1954, Geochemistry (Oxford, London) p. 118.

Greer, A.L., 1984, J. Non-Cryst. Solids **61&62**, 737.

Gschneidner Jr, K.A., and F.W. Calderwood, 1986, in: Binary Alloy Phase Diagrams, ed. T.B. Massalski (ASM, Ohio) p. 125.

Hagiwara, M., A. Inoue and T. Masumoto, 1982a, Metall. Trans. **13A**, 373.

Hagiwara, M., A. Inoue and T. Masumoto, 1982b, Mater. Sci. Eng. **54**, 197.

Higashi, K., T. Mukai, S. Tanimura, A. Inoue, T. Masumoto, K. Kita, K. Ohtera and J. Nagahora, 1992, Scr. Metall. **26**, 191.

Higashi, K., T. Mukai, S. Tanimura, A. Inoue, T. Masumoto and K. Ohtera, 1993, J. Alloys Comp. **193**, 29.

Hiwatari, Y., H. Miyagawa and T. Odagaki, 1991, Butsuri **46**, 90.

Hono, K., Y. Zhang, A.P. Tsai, A. Inoue and T. Sakurai, 1995, Scr. Metall. Mater. **32**, 191.

Horikiri, H., A. Kato, A. Inoue and T. Masumoto, 1994, Mater. Sci. Eng. **A179/A180**, 702.

Inoue, A., 1994a, Mater. Sci. Eng. **A179/A180**, 57.

Inoue, A., 1994b, J. Jpn. Soc. Powder Powder Metall. **41**, 899.

Inoue, A., 1995a, J. Jpn. Inst. Light Met. **45**, 284.

Inoue, A., 1995b, Mater. Trans. JIM **36**, 866.

Inoue, A., 1995c, Mater. Sci. Forum **179–181**, 691.

Inoue, A., 1995d, in: Nanostructured and Non-Crystalline Materials, eds M. Vazquez and A. Hernando (World Scientific, Singapore) p. 15.

Inoue, A., 1995e, Nanostruct. Mater. **6**, 53.

Inoue, A., and T. Masumoto, 1981, Sci. Rep. Res. Inst. Tohoku Univ. **A-29**, 305.

Inoue, A., and T. Masumoto, 1991, Mater. Sci. Eng. **A133**, 6.

Inoue, A., and T. Masumoto, 1993a, Mater. Sci. Eng. **A173**, 1.

Inoue, A., and T. Masumoto, 1993b, in: Amorphous Alloys, eds Y. Sakurai et al. (Elsevier, Amsterdam) p. 133.

Inoue, A., K. Kobayashi and T. Masumoto, 1980, in: Metallic Glasses, Science and Technology, Vol. 2, eds C. Hargital, I. Bakonyi and T. Kemeny (Centr. Res. Inst. Phys., Budapest) p. 217.

Inoue, A., A. Kitamura and T. Masumoto, 1981, J. Mater. Sci. **16**, 1895.

Inoue, A., T. Masumoto and H.S. Chen, 1985, J. Mater. Sci. **20**, 2417.

Inoue, A., M. Yamamoto, H.M. Kimura and T. Masumoto, 1987a, J. Mater. Sci. Lett. **6**, 194.

Inoue, A., Y. Bizen, H.M. Kimura, M. Yamamoto, A.P. Tsai and T. Masumoto, 1987b, J. Mater. Sci. Lett. **6**, 811.

Inoue, A., H.M. Kimura and T. Masumoto, 1987c, J. Mater. Sci. **22**, 1758.

Inoue, A., S. Furukawa, M. Hagiwara and T. Masumoto, 1987d, Metall. Trans. **18A**, 621.

Inoue, A., K. Ohtera, A.P. Tsai and T. Masumoto, 1988a, Jpn. J. Appl. Phys. **27**, L280.

Inoue, A., K. Ohtera and T. Masumoto, 1988b, Jpn. J. Appl. Phys. **27**, L1796.

Inoue, A., K. Ohtera and T. Masumoto, 1988c, Jpn. J. Appl. Phys. **27**, L736.

Inoue, A., K. Ohtera, T. Zhang and T. Masumoto, 1988d, Jpn. J. Appl. Phys. **27**, L1583.

Inoue, A., Y. Bizen, H.M. Kimura, T. Masumoto and M. Sakamoto, 1988e, J. Mater. Sci. **23**, 3640.

Inoue, A., M. Hagiwara and T. Masumoto, 1988f, Sci. Rep. Res. Inst. Tohoku Univ. **34A**, 48.

Inoue, A., K. Ohtera, A.P. Tsai and T. Masumoto, 1988g, Jpn. J. Appl. Phys. **27**, L479.

Inoue, A., K. Ohtera, A.P. Tsai, H.M. Kimura and T. Masumoto, 1988h, Jpn. J. Appl. Phys. **27**, L1579.

Inoue, A., K. Kita, K. Ohtera and T. Masumoto, 1988i, J. Mater. Sci. Lett. **7**, 1287.

Inoue, A., K. Ohtera, T. Zhang and T. Masumoto, 1988j, Jpn. J. Appl. Phys. **27**, L1583.

Inoue, A., K. Ohtera, K. Kita and T. Masumoto, 1988k, Jpn. J. Appl. Phys. **27**, L2248.

Inoue, A., K. Ohtera, A.P. Tsai and T. Masumoto, 1988l, Jpn. J. Appl. Phys. **27**, L280.

Inoue, A., T. Zhang, K. Kita and T. Masumoto, 1989a, Mater. Trans. JIM **30**, 870.

Inoue, A., A.P. Tsai, K. Ohtera, K. Matsuzaki and T. Masumoto, 1989b, in: Proc. MRS Int. Meeting on Advanced Materials, Vol. 3, eds M. Doyama, S. Sōmiya and R.P.H. Chang (MRS, Pittsburgh) p. 411.

Inoue, A., K. Ohtera, A.P. Tsai and T. Masumoto, 1989c, in: Proc. MRS Int. Meeting on Advanced Materials, Vol. 3, eds M. Doyama, S. Sōmiya and R.P.H. Chang (MRS, Pittsburgh) p. 411.

Inoue, A., K. Ohtera, K. Kita and T. Masumoto, 1989d, in: Proc. 1st Jpn. Int. SAMPE Symposium and Exhibition, eds N. Igata et al. (Nikkan Kogyo Shinbun Ltd., Tokyo) p. 7.

Inoue, A., M. Kohinata, K. Ohtera, A.P. Tsai and T. Masumoto, 1989e, Mater. Trans. JIM **30**, 378.

Inoue, A., T. Zhang and T. Masumoto, 1989f, Mater. Trans. JIM **30**, 965.

Inoue, A., M. Kohinata, K. Ohtera, A.P. Tsai and T. Masumoto, 1989g, Mater. Trans. JIM **30**, 78.

Inoue, A., K. Kita, T. Zhang and T. Masumoto, 1989h, Mater. Trans. JIM **30**, 722.

Inoue, A., H. Yamaguchi, M. Kikuchi and T. Masumoto, 1990a, Sci. Rep. Res. Inst. Tohoku Univ. **A35**, 101.

Inoue, A., H. Yamaguchi, T. Zhang and T. Masumoto, 1990b, Mater. Trans. JIM **31**, 104.

Inoue, A., T. Zhang and T. Masumoto, 1990c, Mater. Trans. JIM **31**, 177.

Inoue, A., H. Yamaguchi, T. Zhang and T. Masumoto, 1990d, Mater. Trans. JIM **31**, 104.

Inoue, A., A. Kato, T. Zhang, S.G. Kim and T. Masumoto, 1991a, Mater. Trans. JIM **32**, 609.

Inoue, A., T. Zhang, E. Matsubara, Y. Waseda and T. Masumoto, 1991b, Mater. Trans. JIM **32**, 201.

Inoue, A., Y.H. Kim and T. Masumoto, 1992a, Mater. Trans. JIM **33**, 487.

Inoue, A., Y. Horio, Y.H. Kim and T. Masumoto, 1992b, Mater. Trans. JIM **33**, 669.

Inoue, A., M. Watanabe, H.M. Kimura, F. Takahashi, A. Nagata and T. Masumoto, 1992c, Mater. Trans. JIM **33**, 723.

Inoue, A., T. Nakamura, N. Nishiyama and T. Masumoto, 1992d, Mater. Trans. JIM **33**, 937.

Inoue, A., N. Nishiyama, S.G. Kim and T. Msumoto, 1992e, Mater. Trans. JIM **33**, 360.

Inoue, A., T. Zhang and T. Masumoto, 1992f, J. Non-Cryst. Solids **150**, 396.

Inoue, A., T. Nakamura, N. Nishiyama and T. Masumoto, 1992g, Mater. Trans. JIM **33**, 937.

Inoue, A., T. Zhang and T. Masumoto, 1993a, J. Non-Cryst. Solids **156–158**, 598.

Inoue, A., T. Nakamura, T. Sugita, T. Zhang and T. Masumoto, 1993b, Mater. Trans. JIM **34**, 351.

Inoue, A., K. Nakazato, Y. Kawamura, A.P. Tsai and T. Masumoto, 1994a, Mater. Trans. JIM **35**, 95.

Inoue, A., T. Ochiai, Y. Horio and T. Masumoto, 1994b, Mater. Sci. Eng. **A179/A180**, 649.

Inoue, A., K. Nakazato, Y. Kawamura and T. Masumoto, 1994c, Mater. Sci. Eng. **A179/A180**, 654.

Inoue, A., H.M. Kimura, K. Sasamori and T. Masumoto, 1994d, Mater. Trans. JIM **35**, 85.

Inoue, A., Y. Yokoyama and T. Masumoto, 1994e, Mater. Sci. Eng. **A181/A182**, 850.

Inoue, A., H. Horikiri, A. Kato and T. Masumoto, 1994f, Mater. Trans. JIM **35**, 79.

Inoue, A., H.M. Kimura, K. Sasamori and T. Masumoto, 1995a, Mater. Trans. JIM **36**, 1219.

Inoue, A., H.M. Kimura, K. Sasamori and T. Masumoto, 1995b, Mater. Trans. JIM **36**, 6.

Ishii, Y., 1989, Phys. Rev. B **39**, 11862.

Johnson, W.L., 1978, Rapidly Quenched Metals III, Vol. 2, ed. B. Cantor (The Metals Society, London) p. 1.

Kato, A., 1995, Doctor Thesis (Tohoku University).

Kato, A., A. Inoue, H. Horikiri and T. Masumoto, 1994a, Mater. Trans. JIM **35**, 125.

Kato, A., T. Suganuma, H. Horikiri, Y. Kawamura, A. Inoue and T. Masumoto, 1994b, Mater. Sci. Eng. **A179/A180**, 112.

Kato, A., H. Horikiri, A. Inoue and T. Masumoto, 1994c, Mater. Sci. Eng. **A179/A180**, 707.

Kato, A., A. Inoue, H. Horikiri and T. Masumoto, 1995, Mater. Trans. JIM **36**, 977.

Kim, S.G., 1992, Doctor Thesis (Tohoku University).

Kim, S.G., A. Inoue and T. Masumoto, 1989, Mater. Trans. JIM **30**, 378.

Kim, S.G., A. Inoue and T. Masumoto, 1990, Mater. Trans. JIM **31**, 929.

Kim, S.G., A. Inoue and T. Masumoto, 1991, Mater. Trans. JIM **32**, 875.

Kim, Y.H., A. Inoue and T. Masumoto, 1990, Mater. Trans. JIM **31**, 747.

Kim, Y.H., A. Inoue and T. Masumoto, 1991a, Mater. Trans. JIM **32**, 599.

Kim, Y.H., A. Inoue and T. Masumoto, 1991b, J. Jpn. Inst. Light Met. **42**, 217.

Kissinger, H.E., 1957, Anal. Chem. **29**, 1702.

Kittel, C., 1976, Introduction to Solid State Physics, 5th Ed. (Wiley, New York) p. 32.

Klement, W., R.H. Wilens and P. Duwez, 1960, Nature **187**, 869.

Klimyenko, A.V., J. Seuntjens, L.L. Miller, B.J. Beaudry, R.A. Jacobson and K.A. Gschneidner Jr, 1988, J. Less-Common Met. **144**, 133.

Lanping, Y., and H. Yizen, 1988, J. Non-Cryst. Solids **105**, 33.

Levine, D., T.C. Lubensky, S. Ostlund, S. Rawaswamy, P.J. Steinhardt and J. Toner, 1985, Phys. Rev. Lett. **54**, 1520.

Li, J.C.M., 1993, in: Rapidly Solidified Alloys, ed. Howard H. Lieberman (Marcel Dekker, New York) p. 379.

Lukens, W.E., and C.N.J. Wagner, 1976, J. Appl. Cryst. **9**, 159.

Magnesium Committee, 1987, Magnesium Manual '87 (Japan Light Metal Association, Tokyo) p. 58.

Massalski, T.B., 1986, Binary Alloy Phase Diagrams (American Society for Metals, Ohio).

Massalski, T.B., 1990, Binary Phase Diagrams, 2nd Ed. (ASM, Materials Park, Ohio).

Masumoto, T., and R. Maddin, 1971, Acta Met. **19**, 725.

Masumoto, T., K. Suzuki, H. Fujimori and K. Hashimoto, 1982, Materials Science of Amorphous Metals, ed. T. Masumoto (Ohm Pub., Tokyo) p. 28.

Materials Database Committee, 1988, Material Database (Nikkan Kogyo Newspaper, Tokyo) p. 1571.

Matsubara, E., K. Harada, Y. Waseda and M. Iwase, 1988a, Z. Naturforsch. **43a**, 181.

Matsubara, E., K. Harada, Y. Waseda, H.S. Chen, A. Inoue and T. Masumoto, 1988b, J. Mater. Sci. **23**, 753.

Matsubara, E., K. Harada, Y. Waseda, A. Inoue, Y. Bizen and T. Masumoto, 1988c, J. Mater. Sci. **23**, 3485.

Matsubara, E., Y. Waseda, A. Inoue, K. Ohtera and T. Masumoto, 1989, Z. Naturforsch. **44a**, 814.

Matsubara, E., T. Tamura, Y. Waseda, A. Inoue, M. Kohinata and T. Masumoto, 1990, Mater. Trans. JIM **31**, 228.

Matsubara, E., T. Tamura, Y. Waseda, T. Zhang, A. Inoue and T. Masumoto, 1992, J. Non-Cryst. Solids **150**, 380.

McMillan, W.L., 1968, Phys. Rev. **167**, 331.

Metals Databook, 1983, ed. Japan Inst. Metals (Maruzen, Tokyo) p. 175.

Miedema, A.R., F.R. de Boer and R. Boom, 1977, CALPHAD, Vol. 1 (Pergamon Press, Great Britain) p. 341.

Mizutani, U., Y. Hoshino and H. Yamada, eds, 1986, Handbook for Formation of Amorphous Alloys (Agne, Tokyo).

Mizutani, U., T. Hasegawa, K. Fukamichi, T. Goto and T. Matsuda, 1989, Mater. Trans. JIM **30**, 951.

Mulder, A.L., S. Zwaag and A. Beukel, 1988, Scr. Metall. **22**, 1291.

Niikura, A., 1995, Doctor Thesis (Tohoku University).

Niikura, A., A.P. Tsai, A. Inoue and T. Masumoto, 1994a, Met. Trans. **25A**, 1323.

Niikura, A., A.P. Tsai, A. Inoue and T. Masumoto, 1994b, Jpn. J. Appl. Phys. **33**, L1538.

Niikura, A., A.P. Tsai, A. Inoue and T. Masumoto, 1994c, Phil. Mag. **69**, 351.

Nose, M., and T. Masumoto, 1980, Sci. Rep. Res. Inst. Tohoku Univ. **A-28**, 222.

Nowick, A.S., and B.S. Berry, 1972a, Anelastic Relaxation in Crystalline Solids (Academic Press, New York) p. 87.

Nowick, A.S., and B.S. Berry, 1972b, Anelastic Relaxation in Crystalline Solids (Academic Press, New York) p. 94.

Ohashi, W., and F. Spaepen, 1987, Nature **330**, 555.

Ohtera, K., T. Terabayashi, H. Nagahama, A. Inoue and T. Masumoto, 1991, J. Jpn. Soc. Powder Powder Metall. **38**, 953.

Ohtera, K., A. Inoue, T. Terabayashi, H. Nagahama and T. Masumoto, 1992a, Mater. Trans. JIM **33**, 775.

Ohtera, K., K. Kita, N. Nagahama, A. Inoue and T. Masumoto, 1992b, Proc. 3rd Int. Conf. on Aluminum Alloys, ed. L. Arnberg et al. (SINTEF, Trondheim, Norway) p. 58.

Okumura, H., A. Inoue and T. Masumoto, 1991, Mater. Trans. JIM **32**, 593.

Okumura, H., H.S. Chen, A. Inoue and T. Masumoto, 1992a, J. Non-Cryst. Solids **142**, 165.

Okumura, H., H.S. Chen, A. Inoue and T. Masumoto, 1992b, J. Non-Cryst. Solids **150**, 401.

Orlando, T.R., E.J. McNiff Jr, S. Foner and M.R. Beasley, 1979, Phys, Rev. B **19**, 4545.

Paasch, G., A. Schwerdtner and P. Terpte, 1972, J. Phys. C **5**, 2991.

Pearson, W.B., 1967, Handbook of Lattice Spacings and Structure of Metals (Pergamon, New York).

Pont, M., J. Gonzalo, K.V. Rao and A. Inoue, 1989, Phys. Rev. B **40**, 1345.

Predecki, P., B.C. Giessen and N.J. Grant, 1965, Trans. Metall. Soc. AIME **233**, 1438.

Ramachandrarao, P., M. Laridjani and R.W. Cahn, 1972, Z. Metallkd. **63**, 43.

Rao, K.V., 1983, Amorphous Metallic Alloys, ed. F.E. Luborsky (Butterworths, London) p. 401.

Sastry, G.V.S., C. Suryanarayana, O.N. Srivastava and H.A. Davies, 1978, Trans. Indian Inst. Met. **31**, 292.

Shechtman, D., L.A. Blech, D. Gratias and J.W. Cahn, 1984, Phys. Rev. Lett. **53**, 1951.

Shibata, T., A. Inoue and T. Masumoto, 1993, J. Mater. Sci. **28**, 379.

Shibata, T., A. Inoue and T. Masumoto, 1994, Mater. Sci. Eng. **A179/A180**, 659.

Sinning, H.R., 1989, J. Non-Cryst. Solids **110**, 195.

Sinning, H.R., and F. Haessner, 1986, Scr. Metall. **20**, 1541.

Socoler, J.E.S., and D.C. Wright, 1987, Phys. Rev. Lett. **59**, 221.

Sommer, F., G. Bucher and B. Fredel, 1980, J. Phys. C **41**, 563.

Srolovitz, D., T. Egami and V. Vitek, 1981, Phys. Rev. B **24**, 6939.

Steeb, S., and R. Hezel, 1963, Z. Metallkd. **57**, 374.

Steiner, P., H. Hochst, W. Steffen and S. Hufner, 1980, Z. Phys. B **38**, 191.

Takeuchi, S., 1992, Tetsu-to-Hagane **78**, 1517.

Tobolsky, A.V., 1956, J. Appl. Phys. **27**, 673.

Tsai, A.P., A. Inoue and T. Masumoto, 1988a, Met. Trans. **19A**, 1369.

Tsai, A.P., A. Inoue and T. Masumoto, 1988b, J. Mater. Sci. Lett. **7**, 805.

Tsai, A.P., A. Inoue and T. Masumoto, 1988c, Met. Trans. **19A**, 391.

Tsai, A.P., A. Inoue and T. Masumoto, 1989, Jpn. J. Appl. Phys. **26**, L1505.

Tsai, A.P., A. Niikura, A. Inoue, T. Masumoto, Y. Nishida, K. Tsuda and M. Tanaka, 1994, Phil. Mag. **70**, 169.

Unsworth, W., 1989, J. Mater. Product Technol. **4**, 359.

Vasudevan, A.K., and R.O. Doherty, 1989, Aluminum Alloys (Academic Press, London).

Villars, P., and L.D. Calvert, 1985, Pearson's Handbook of Crystallographic Data for Intermetallic Phases, Vol. 3 (ASM, Metals Park, Ohio) p. 2628.

Voisin, E., and A. Pasturel, 1987, Phil. Mag. Lett. **55**, 123.

Waseda, Y., 1980, Structure of Non-Crystalline Materials (McGraw-Hill, New York) p. 60.

Watanabe, M., A. Inoue, H.M. Kimura, T. Aiba and T. Masumoto, 1993, Mater. Trans. JIM **34**, 162.

Yokoyama, Y., A. Inoue and T. Masumoto, 1993, Mater. Trans. JIM **34**, 135.

Zhang, D., J. Tang and K.A. Gschneidner Jr, 1991a, J. Less-Common Met. **169**, 45.

Zhang, T., 1993, Doctor Thesis (Tohoku University).

Zhang, T., A. Inoue and T. Masumoto, 1991b, unpublished research.

Zhang, T., A. Inoue and T. Masumoto, 1992, unpublished research.

Zhang, T., A. Inoue and T. Masumoto, 1993, Mater. Lett. **15**, 379.

Handbook on the Physics and Chemistry of Rare Earths
Vol. 24
edited by K.A. Gschneidner, Jr. and L. Eyring

Chapter 162

ELECTRON-SPIN RESONANCE ON LOCALIZED MAGNETIC MOMENTS IN METALS

Bruno ELSCHNER and Alois LOIDL
Institut für Festkörperphysik/Experimentalphysik,
Technische Hochschule Darmstadt, 64289 Darmstadt, Germany

Contents

List of abbreviations

ac	alternating current	KI	Kondo insulator
AFM	antiferromagnetic	KL	Kondo lattice
BCS	Bardeen–Cooper–Schrieffer	LLW	Lea, Leask and Wolf
CF	crystal field	MI	metal-to-insulator
cw	continuous wave	μSR	muon spin rotation
dc	direct current	NMR	nuclear magnetic resonance
DOS	density of states	pc	point charge
FM	ferromagnetic	PM	paramagnetic
ESR	electron-spin resonance	RESR	Reflection Electron-Spin Resonance
HF	heavy fermion	RKKY	Ruderman–Kittel–Kasuya–Yosida
HFBM	heavy-fermion band magnets	SG	spin glass
HFS	heavy-fermion systems	sc	superconducting
INS	inelastic neutron scattering	SC	superconductors
IV	intermediate valence	TESR	Transmission Electron-Spin Resonance
IVC	intermediate-valence compounds		

List of symbols

a	residual linewidth, also denoted ΔH_0	Δg_o	g-shift without bottleneck, i.e. in the extreme isothermal case
A	hyperfine constant in the ESR Hamiltonian	Δg_σ	g-shift due to coupling of ESR probe to conduction electrons
b	$= d(\Delta H)/dT$: Korringa slope	Δg_f	g-shift due to magnetic, RKKY-type interactions
b_4, b_6	CF parameters	G	gauss unit
B_4, B_6	CF parameters	H	external magnetic field
c	$= \delta_{eL}/\delta_{ei}$: bottleneck factor	H_{res}	magnetic field at resonance absorption
C	covalency parameter	ΔH	ESR-linewidth at resonance absorption
D	CF parameter in axial symmetry	ΔH_0	residual linewidth, $\Delta H(T \rightarrow 0\,K)$, sometimes denoted a
g	ESR g-value	ΔH_{if}	Korringa broadening of ESR linewidth
g_e	conduction-electron g-value		
g_{exp}	experimentally observed g-value		
g_i	g-value of ESR probe		
g_{iso}	g-value of an ion in an insulator		
g_N	nuclear g-value		
Δg	$= g_{exp} - g_{iso}$: g-shift		

$\Delta H_{i\sigma}$	linewidth broadening due to RKKY interactions	T_2	spin–spin relaxation time
J	exchange constant	γ	Sommerfeld coefficient of the electronic specific heat; sometimes used for the gyromagnetic ratio
J_{eff}	effective coupling constant		
J_{fs}	exchange between f-electrons and s-band electrons	Γ	magnetic relaxation rate
		Γ_{ESR}	magnetic relaxation rate as determined in ESR experiments
J_{fd}	exchange between f-electrons and d-band electrons	δ	relaxation rate
J_1	exchange constant derived from the g-shift	δ_{ie}	Korringa relaxation rate (relaxation from ion to electrons)
J_2	exchange constant derived from the Korringa slope	δ_{ei}	Overhauser relaxation rate (relaxation from electrons to ion)
k_{B}	Boltzmann constant	δ_{eL}	lattice relaxation rate (relaxation from electrons to the lattice)
K_{if}	coupling constant of the spin of the ESR probe to the f moment	$\delta^{\text{o}}_{\text{eL}}$	intrinsic lattice relaxation rate
$N(E_{\text{F}})$	density of states at the Fermi energy	Δ	energy difference between ground state and first excited state of CF
O^i_j	spin operators		
$\boldsymbol{Q}$	momentum transfer	Θ	Curie–Weiss temperature
R	$=g\mu_{\text{B}}b/\pi k_{\text{B}}(\Delta g_0)^2$: Korringa ratio	λ	molecular field constant
$S(\boldsymbol{Q},\omega,T)$	dynamic structure factor	μ_{B}	Bohr magneton
S_{i}	spin of impurity (ESR probe)	$\sigma(r)$	spin density of conduction electrons
T	temperature	χ	static magnetic susceptibility
T_0	temperature of linewidth maximum in SG systems	χ^*	complex dynamic magnetic susceptibility
T_{K}	Kondo temperature (magnetic impurity)	χ'	real part of the dynamical susceptibility
T^*	Kondo-lattice temperature, characteristic temperature of a lattice-periodic f metal with magnetic moments	χ''	imaginary part of the dynamical susceptibility
		ω	angular frequency
		ω_0	measuring frequency of resonance experiment
T_{c}	sc to normal conducting phase-transition temperature		
T_1	spin–lattice relaxation time		

1. Introduction

The investigation of the dynamic behavior of localized magnetic moments in metallic host lattices by Electron-Spin-Resonance (ESR) techniques is about 50 years old. There are some excellent review articles which cover the first half of this period. The first review written by Peter et al. (1967) gives a survey of the theoretical background and provides information on the "direct" and "indirect" g-shift data known at that time. In a comprehensive review article by Taylor (1975) almost all experimental results reported until 1974 are presented, including a complete list of references. Our review links up with Taylor's work. The situation of the experimental and theoretical state of ESR in metals

until 1973 is examined in an article by Orbach et al. (1974). Finally, S.E. Barnes (1981a) provides a detailed survey about the theory of ESR on localized moments in metals. This article is a great help for the experimental spectroscopist, too, as this review contains numerous short and significant descriptions of the experimental results. In addition, ESR on localized magnetic moments in metals has been subject of invited talks on several conferences, e.g. by Orbach (1975) and Dupraz et al. (1970).

The reader is strongly encouraged to consult these articles for more detailed information on the early ESR work. The present review article deals with the further development of ESR in metals since 1974, focusing especially on the experimental situation. For this reason we give the theoretical background only in a very comprehensive form and refer to the relevant literature, especially to the review by S.E. Barnes (1981a), but also to textbooks like that written by Abragam and Bleaney (1970).

In the review article by Taylor (1975) one finds a diagram which shows the number of relevant papers dealing with ESR of ions in metals published year by year. The diagram shows a maximum of 25 papers for 1973. We did not continue this graphical illustration, but certainly we believe that the number of publications in this field dropped during the last years. An exception may be the late eighties with an incredible amount of publications dealing with high-temperature superconductors. Nevertheless important contributions opened new fields of activities, e.g. ESR on heavy-fermion systems and mixed-valence compounds, ESR on metallic systems under high pressure, ESR on metallic van-Vleck systems and ESR investigations on doped and undoped high-T_c superconductors. The fact that many fundamental features of ESR spectra in metals are now understood and that in the eighties many interesting new branches, which came into the focus of solid state physicists, have been investigated using ESR techniques, confirmed our plan to write this review article.

There have been some important developments on the ESR on localized moments in organic metals and synthetic conductors. In these compounds "radicals" are ESR active and can be detected using standard ESR techniques. The temperature dependence of the ESR linewidths and g-values mostly serve as a characterization of phase transitions and the magnetic state of the compounds. At present there exists a large number of experimental results which is growing month by month and to review the ESR results obtained in this class of synthetic materials must be the content of a separate review article.

This review is organized in the following way: After briefly discussing the theoretical basics – here we mention only crystal-field effects and provide a short description of the so-called bottleneck phenomena, which play an important role in the ESR on localized moments in metals – we focus especially on the experimental results since 1975. Of course, whenever necessary to understand the recent developments, older work will be cited. This experimental survey is the main part of the present review. Sections 3–5 discuss the ESR results in metals and alloys where the ESR probes have been substituted in a dilute limit, usually with concentrations less than 5%. The ESR probes are 3d and 4f impurities. In sect. 6 systems with concentrated ESR probes are discussed. In these compounds 4f moments have been substituted at high concentrations or the ESR

probe is a constituent of the lattice itself. Finally van-Vleck systems are discussed in sect. 7. The metals and alloys discussed in sections 3–7 have been the classical areas of ESR research in metallic alloys. In what follows, we provide an overlook over more recent developments, including spin glasses (sect. 8), Kondo impurities (sect. 9) and superconductors (sect. 11). Special emphasis has been given to the areas of heavy-fermion systems and intermediate valence compounds (sect. 10) as well as to the wide field of high-T_c superconductors (sect. 12). Finally we try to give a short outlook which, according to our understanding, will be the most relevant areas of research in forthcoming ESR investigations on metals.

2. Theoretical background

2.1. *General remarks*

Localized magnetic moments in metallic hosts (e.g. Gd^{3+} in $LaAl_2$) usually show a single ESR absorption line. In many cases the width of this line is unexpectedly small and does not show any crystalline field (CF) effects. The dynamics of the combined system (localized impurity moment plus conduction electrons) is determined by the exchange interaction

$$H_{ex} = -\sum_i 2J\boldsymbol{S}_i\,\boldsymbol{\sigma}(\boldsymbol{r})\,\delta(\boldsymbol{r}). \tag{1}$$

$\boldsymbol{S}_i$ is the spin of the impurity ion (ESR probe) and $\boldsymbol{\sigma}$ denotes the spin density of the conduction electrons. J is a general exchange parameter which can contain positive or negative contributions. It is common practice to consider this exchange interaction as purely isotropic. ESR is perhaps the only method which makes it possible to determine this quantity directly.

The exchange constant J can be expanded according to Watson et al. (1969):

$$J_{\boldsymbol{k}',\boldsymbol{k}} = \sum_{l=0}^{\infty} (2l+1)\,J_l(|\boldsymbol{k}'|,|\boldsymbol{k}|)\,P_l(\cos\Theta_{\boldsymbol{k}',\boldsymbol{k}}) \equiv J(\boldsymbol{q}), \tag{2}$$

with $\boldsymbol{q} = (|\boldsymbol{k}'|,|\boldsymbol{k}|)$. This exchange interaction has two consequences for the ESR signal:

(i) It can be the reason for a g-shift Δg, with $\Delta g = g_{exp} - g_{iso}$. Here g_{exp} is the experimentally observed g-value and g_{iso} corresponds to the g-value of the local moment in an insulator:

$$\Delta g = J(0)\,N(E_F), \tag{3}$$

where $J(0)$ is the exchange interaction at zero wave vector, $J(\boldsymbol{q}=0)$, and $N(E_F)$ is the density of states at the Fermi energy (see e.g. S.E. Barnes 1981a).

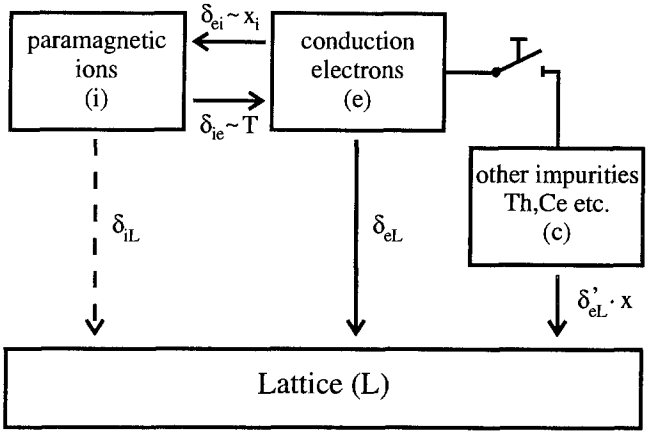

Fig. 1. The flow scheme of magnetization for electron-spin-resonance in a metal. This scheme is the basis for the Hasegawa equations. Taken from Baberschke (1976).

(ii) Fluctuations of the conduction-electron spins give rise to a relaxation rate δ_{ie} (here i denotes the ion and e the conduction electron). For the local moments these fluctuations are the reason for a finite linewidth ΔH of the resonance absorption, given by

$$\Delta H = \hbar\delta_{ie}/g_e\mu_B = 4\pi N^2(E_F)\,\langle J_q\rangle^2\, k_B T/g_e\mu_B \tag{4}$$

Here the average is taken over the Fermi surface (Walstedt and Walker 1975).

Equation (4) corresponds to the "Korringa relaxation", which is well known in nuclear magnetic resonance (NMR) spectroscopy in metals.

Frequently the temperature dependence of ΔH can be expressed in the form

$$\Delta H = a + bT. \tag{5}$$

The constant a is a temperature-independent residual linewidth $\Delta H_0 = \Delta H(T \to 0\,\mathrm{K})$ and b corresponds to the Korringa slope $\mathrm{d}(\Delta H)/\mathrm{d}T$. Whereas eq. (4) expresses the flow of magnetization from the localized moments to the conduction electrons, the inverse process influences the linewidth of the conduction electrons. Both processes are related via a detailed balance condition:

$$\delta_{ei}\chi_e/g_e^2 = \delta_{ie}\chi_i/g_i^2. \tag{6}$$

In eq. (6) the appropriate susceptibilities χ for the conduction electrons and the impurities are the static ($q = 0$) exchange enhanced values. δ_{ei} is the Overhauser rate (Overhauser 1953) which depends on concentration x_i of the paramagnetic impurities with spin S:

$$\delta_{ei} = 8\pi x_i S(S+1)N(E_F)J^2/3\hbar. \tag{7}$$

Yafet (1963) calculated the relaxation of the conduction electrons to the lattice δ_{eL} due to spin–orbit scattering. δ_{eL} can be separated into δ^0_{eL} (intrinsic) and $\delta'_{eL}\cdot x$. Hereby x denotes the concentration of the extrinsic scatterers. Hasegawa (1959) analyzed the situation which is shown in fig. 1 by Bloch-type equations. In this scenario the paramagnetic ions are

strongly coupled to the conduction electrons, but much weaker to the lattice. Hasegawa (1959) derived the following results:

$$\Delta g = \Delta g_0 \frac{\delta_{eL}^2}{(\lambda\gamma\chi_i H)^2 + (\delta_{eL} + \delta_{ei})^2}, \tag{8}$$

$$\Delta H = \Delta H_0 \frac{\left[\delta_{ei}^2 + (\lambda\gamma\chi_i H)^2\right](\delta_{eL}/\delta_{ei}) + \delta_{eL}^2}{(\lambda\gamma\chi_i H)^2 + (\delta_{eL} + \delta_{ei})^2}. \tag{9}$$

Here γ is the gyromagnetic ratio for both local moments and conduction electrons, and λ is the molecular field constant determined by $J(0)$. The term containing the field H is the "dynamic term". A clear experimental proof of this term has been provided in the systems Yb(Eu^{2+}) and Yb/Ca(Eu^{2+}) (Schmidt 1972, Schmidt et al. 1972). In controversial form Davidov and Shaltiel (1968) and Male and Taylor (1975) discussed the possibility to observe dynamic effects in the system $LaNi_5$(Gd).

Usually these dynamic terms can be neglected as they are small compared with the relaxation rates δ_{ei} and δ_{eL}. If this is true, much simpler expressions can be derived from the Hasegawa equations (eqs. 8, 9):

$$\Delta g = \Delta g_0 \frac{c^2}{(1+c)^2}, \qquad \Delta H = \Delta H_0 \frac{c}{(1+c)}. \tag{10,11}$$

Here c denotes the ratio of the relaxation rates, namely $c \equiv \delta_{eL}/\delta_{ei}$. For $c \ll 1$ both linewidth and g-shift are reduced by factors c or c^2, respectively. This behavior is well known in the literature as a resonance "bottleneck". This bottleneck explains, e.g., the unexpected small ESR linewidth in the system Cu(Mn) (see Owen et al. 1957).

The intermetallic compound $Lu_{1-x-y}Th_yGd_xAl_2$ (Rettori et al. 1974) shows both bottleneck and dynamic effects in the relaxation mechanism. By adding nonmagnetic Th ions, the bottleneck is opened and at the same time dynamic effects are suppressed. $LuAl_2$ is a suitable system for such investigations. Due to the larger spin–orbit coupling, δ_{eL} is larger in $LuAl_2$ than in $LaAl_2$ or YAl_2. Therefore, the bottleneck can be opened using relatively high Gd concentrations. The controlling factor $c \gg 1$ warrants the full linewidth ΔH_0 (eq. 11) or the full g-shift Δg_0 (eq. 10).

Without the bottleneck there is only little hope to observe ESR spectra from 3d-ions in metallic hosts at moderate temperatures. But there are some exceptions which will discussed below, e.g. $CePd_3$(Mn) (Schaeffer and Elschner 1985). We will not discuss the bottleneck problem further. The most important and significant contributions on this subject appeared twenty years ago and have been reviewed in full detail by Taylor (1975). A careful investigation of the bottleneck behavior of a variety of systems has been published by S.E. Barnes (1981a). Textbook examples for bottleneck behavior are, e.g. $La_{1-x-y}Th_xGd_yAl_2$ (Baberschke 1976) or $Y_{1-x}Gd_xAl_2$ (Schäfer et al. 1972). A clear description of the resonance spectrum including fine structure and hyperfine structure in the bottleneck limit was given by Orbach (1980).

2.2. *The crystalline electric field*

The 4f electrons of the rare-earth ions are characterized by their total momentum $\boldsymbol{J}$ where J is in general a good quantum number, $\boldsymbol{J}=\boldsymbol{L}+\boldsymbol{S}$. For a cubic crystal field (CF), group theory predicts that manifolds with $J<2$ are not split. The ground state hereby is a Γ_6 doublet for $J=\frac{1}{2}$, a Γ_4 triplet for $J=1$ or a Γ_8 quartet for $J=\frac{3}{2}$. The doublets Γ_6 and Γ_7 ($J>2$) can be described by spin Hamiltonians with $S=\frac{1}{2}$ and have isotropic g-values (Abragam and Bleaney 1970). The Γ_8 quartet can be described by a spin Hamiltonian with $S=\frac{3}{2}$. Its peculiar magnetic properties are described in detail by Abragam and Bleaney (1970).

The theory of CF originates from the early work of Bethe (1929). A number of complete review articles have appeared which describe theoretical models and experimental effects of CF in rare earths (Fulde 1979). For crystal fields of cubic symmetry the spin Hamiltonian with reference to the fourfold axis can be expressed conveniently in the operator-equivalent form (Hutchings 1964, Stevens 1967)

$$H_{\mathrm{CF}} = B_4 O_4 + B_6 O_6, \tag{12}$$

where O_4 and O_6 are the fourth- and sixth-degree cubic operators

$$O_4 = O_4^0 + 5 \cdot O_4^4, \qquad O_6 = O_6^0 - 21 \cdot O_6^4. \tag{13,14}$$

For numerical convenience, Lea, Leask and Wolf (LLW) (1962) wrote the cubic potential as

$$H_{\mathrm{CF}} = B_4 F(4) \cdot \frac{O_4}{F(4)} + B_6 F(6) \cdot \frac{O_6}{F(6)}. \tag{15}$$

Two new constants, W and x, are defined using the relations

$$W \cdot x = B_4 F(4), \qquad B_6 F(6) = W(1 - |x|). \tag{16,17}$$

The Hamiltonian H_{CF} can then be rewritten as

$$H_{\mathrm{CF}} = W \left(x \cdot \frac{O_4}{F(4)} + (1 - |x|) \cdot \frac{O_6}{F(6)} \right). \tag{18}$$

$F(4)$ and $F(6)$ are numerical parameters given by LLW (1962). W is the single energy parameter, which is proportional to the overall splitting. All possible values B_4/B_6 are within the range $-1 \leqslant x \leqslant 1$. B_4 and B_6 are regarded as parameters which have to be determined experimentally. For numerical convenience the modified parameters $b_4 = 60 B_4$ and $b_6 = 1260 B_6$ are often used.

Unfortunately, analogous to the situation in insulators, experimental results for b_4 and b_6 in metals do not reveal significant correlations with theoretical predictions. As

expected, point-charge (pc) models are successful only in special cases probably more or less accidently. The best way to determine b_4 and b_6 from ESR experiments is the observation of the angular dependence of the resonance fields of a single-crystalline sample under conditions that the ESR spectrum is well resolved. Additional investigations of the temperature dependence of the transition intensities often allow the determination of the sign of b_4 or b_6. Unfortunately and as is generally known, fully resolved spectra in metals are the exception. Until 1973 only a few cases of well-resolved spectra in metals were known. Gd in single crystals of palladium (Devine et al. 1972a) is an elucidating example. Normally the spectra of localized moments in metals are almost or fully narrowed due to the strong exchange interaction between the 4f moments of the rare earth ions and conduction electrons.

2.3. *Dynamic magnetic susceptibilities as measured by electron-spin resonance, nuclear-spin resonance and inelastic neutron scattering experiments*

When dynamical processes of spin systems are studied, the behavior may be characterized in terms of relaxation times. In magnetic resonance experiments two such times usually have to be considered. These are the longitudinal (spin-lattice) relaxation time, T_1, and the transverse (spin–spin) relaxation time, T_2. In ESR and NMR experiments the resonance signal contains components which are in phase and out of phase with the incident high-frequency field, so that it is useful to define a complex susceptibility, $\chi^* = \chi' - \mathrm{i}\,\chi''$. The dispersion component χ' is in phase and the absorption component χ'' is out of phase. By introducing the exponential decay constants T_1 and T_2 for the magnetization parallel and perpendicular to the applied magnetic field, Bloch et al. (1946) derived expressions for the magnetization as a function of frequency. If the amplitude of the high-frequency magnetic field is low, the shape of the resonance line reveals a Lorentzian profile whose width only depends on T_2, but is independent of T_1.

In NMR experiments, T_1 and T_2 are determined using pulse methods. Here, a variety of specific pulse sequences has been developed. ESR experiments, especially in metals, are performed by steady-state (continuous wave, cw) methods only. In these experiments the linewidth ΔH of the resonance absorption is determined by the characteristic relaxation time. In metals we can assume $\omega_0 \cdot \tau_c \ll 1$ and hence $T_1 = T_2$. Here ω_0 is the resonance frequency and τ_c is the correlation time of the conduction electrons. An extensive discussion on the comparison of NMR, ESR and Mössbauer techniques has been given by R.G. Barnes (1979).

If a metal with localized magnetic moments is investigated by resonance techniques, the probing spin (nuclear spin or electron spin) can relax via the conduction electrons but also via spin fluctuations which are mediated through the conduction electrons (RKKY-type interactions). Hence the probing spins allow a direct access to the dynamic magnetic susceptibility of the host lattice χ^*_{host}. In the case of ESR the probing spin directly couples to the conduction electrons via an effective coupling constant J_{eff}. In NMR experiments this effective coupling is transferred to the nuclear spin via hyperfine interactions. In both cases, J_{eff} will depend on the site and the distance of all neighboring local moments

of the host. Under the most naive assumptions, if one neglects all dependences on the momentum transfer $\boldsymbol{Q}$ and assumes an isotropic and effective coupling constant only, the linewidth in case of cw ESR experiments and the spin-lattice relaxation rate in case of pulsed NMR experiments is given by

$$\Delta H \approx k_B \cdot T \cdot \frac{\chi''_{host}}{\omega_o}. \tag{19}$$

The spin-lattice relaxation rate in case of pulsed NMR experiments is determined by

$$\frac{1}{T_1} \approx k_B \cdot T \cdot \frac{\chi''_{host}}{\omega_o}. \tag{20}$$

Here ω_o is the measuring frequency of the resonance experiment which is in the MHz range in NMR and in the GHz range in ESR experiments.

In inelastic neutron scattering (INS) experiments, the dynamic structure factor $S(\boldsymbol{Q},\omega,T)$ is related to the dynamic susceptibility weighted with the detailed balance factor

$$S(\boldsymbol{Q}, \omega, T) = \frac{1}{1 - \exp(-\hbar\omega/k_B T)} \chi''(\boldsymbol{Q}, \omega, T). \tag{21}$$

For high temperatures and again neglecting all $\boldsymbol{Q}$-dependences we find

$$S(\omega, T) = k_B \cdot T \cdot \frac{\chi''(\omega, T)}{\omega}. \tag{22}$$

$\chi''(\omega)$ is the imaginary part of the dynamical susceptibility of the material under investigation and corresponds to $\chi''_{host}(\omega)$ of the resonance techniques. In ESR experiments one has to take into account that probing electron-spins (e.g. Gd^{3+} ions) are substituted into the compound and may influence $\chi''_{host}(\omega)$. Eqs. (19), (20) and (22) demonstrate that INS, NMR, and ESR experiments provide direct information on the dynamic magnetic susceptibility of the host material. Of course one has to keep in mind that these experimental techniques operate on vastly different frequency scales. Only in INS experiments χ'' can be fully determined as a function of frequency, while NMR and ESR experiments operate at a given frequency only. In addition, NMR and ESR are local probes and only INS experiments can provide the full information of the $\boldsymbol{Q}$-dependence of the dynamic susceptibility if single crystalline material is used.

3. 3d impurities as ESR probes in metals and alloys

On a first glance one could presume that many 3d ions are well suited as ESR probes in metals. Most of the 3d ions have well-developed stable magnetic moments. And indeed, some of them show ESR spectra even at room temperature, however mostly in

insulating host lattices only. The situation changes drastically if one considers metallic host lattices. Apart from Mn^{2+} ($3d^5$) and Fe^{3+} ($3d^5$) no resonance absorption from diluted 3d-transition ions in metals ever has been observed. Hirst (1972) gave an explanation for the observation or non-observation of resonance absorption for most of the 3d impurities. He related this problem to the appearance of a bottleneck situation. The resonance bottleneck reduces the thermal broadening of the linewidth and brings it into scale with the window of observation set by the sweep range of the external magnetic field. 3d ions suitable for a strong bottleneck are Mn^{2+} ($3d^5$) and Fe^{3+} ($3d^5$), both characterized by a stable S ground state configuration (see, e.g., S.E. Barnes 1981a). Hence, only these ions can serve as 3d-ESR probes in metals.

3.1. *Manganese*

We begin our survey with contributions which appeared in 1975 and later. For previous publications the reader is referred to the review article by Taylor (1975). Alquie et al. (1978) suggested that the dilute $Pd_{1-x}Mn_x$ system ($200\,\text{ppm} \leqslant x \leqslant 5000\,\text{ppm}$) reveals a bottleneck despite of the strong d-character of the host matrix. This result is in clear contradiction to previous suggestions about these systems (see, e.g., Taylor 1975). The experimental evidence for a bottleneck situation in $Pd_{1-x}Mn_x$ are: (i) the temperature dependence of the g-factor which occurs in the bottleneck regime if $g_i \neq g_e$; (ii) the fact that the linewidth is a nonlinear function of temperature; and (iii) the possibility that the bottleneck can be opened, at least partially, by doping with lead (~5% Pb). The Pb ions are highly effective to increase the relaxation rate δ_{eL} via their spin–orbit coupling and to open the bottleneck in this way. It is surprising and unexpected that a transition metal with such a strong d-character as Pd shows bottleneck behavior. One would assume that in such host matrices the relaxation rate δ_{eL} is large enough to prevent a bottleneck. Obviously, the contribution of the molecular field term in the bottleneck eqs. (8) and (9) are large due to the high density of states of the d band of Pd and to the enhanced susceptibility and hence, compensate the δ_{eL} term making the observation of a bottleneck more likely. For Pd the authors find a conduction-electron g-factor, $g_e = 2.25$, which means a large deviation from the free spin value of 2.0. This result indicates a large spin–orbit contribution to g_e. The g-factor as observed for Mn^{2+} in a Pd matrix was reported to amount to $g_i = 2.055$. Together with the extracted values of $\lambda\chi_e$ the authors calculated the "true" Korringa g-factor for Mn^{2+} in Pd, $g_K = 3.1 \pm 0.1$. The corresponding paramagnetic giant moment amounts to $9.15\mu_B$. The authors were not able to observe this Korringa value $g_K \approx 3$ directly. However, for the 500 ppm sample which had been powdered very carefully, they observed $g \approx 2.6$, indicating that the bottleneck can be partially opened by grinding the sample.

Alquie et al. (1976) reported on g-shifts and linewidths of Pd and $Pd_{1-x}H_x$ doped with Mn^{2+} ($x \approx 0.7$). Again a bottleneck seems to occur in the samples loaded with hydrogen, but with a much lower value of Δg. This indicates that the hydrogen ions do not participate in the relaxation of the s electrons towards the lattice. The authors assumed that this observation may have its origin in the interstitial position of H^+ in the host lattice and in

the small spin–orbit scattering of the conduction electrons on the H^+ ions. The effect of hydrogen on the paramagnetic resonance of Mn in Pd were also investigated by Devine et al. (1975). At 1.5 K they observed two distinct ESR lines in the α and β mixed-phase region. The hydrogen-rich phase ($H/Pd \approx 0.75$) showed linewidths of approximately 250 G, while the hydrogen-poor phase ($H/Pd \approx 0$) revealed almost a Korringa behavior. The authors claimed spatially varying exchange interactions as well as a spatially varying electronic densities of states in this mixed-phase samples.

Davidov et al. (1975a) reported on ESR measurements on diluted $Ag_{1-x}Mn_x$ alloys ($50\,\text{ppm} \leqslant x \leqslant 1500\,\text{ppm}$). Some of the samples contained nonmagnetic Sb or Au impurities, in addition. The use of powerful conduction-electron spin-flip scatterers, like Sb or Au, leads to an increase of δ_{eL} and opens the bottleneck. The measurements were performed at X-band frequencies and in the liquid-helium range ($1.4\,\text{K} \leqslant T \leqslant 4.2\,\text{K}$). The values of g-shift and Korringa broadening in the isothermal limit were found to amount to $\Delta g = -0.035 \pm 0.01$ and $d(\Delta H)/dT = 45 \pm 10$ G/K, respectively. The authors used g-shift and thermal broadening to obtain the spin-flip scattering rates for Sb and Au impurities. The scattering rate for Sb is two times larger than that of Au. g-shift and thermal broadening were analysed in terms of a set of partial-wave amplitudes. It was concluded that the d-wave amplitude in $Ag_{1-x}Mn_x$ is negative and smaller in magnitude than for Mn in Cu. The impact of these amplitudes on the change in the hyperfine field upon going from the insulating to the metallic state and on the shape of the ESR lines in the presence of the hyperfine splitting was examined. For the highest Mn concentration used in these experiments, the six hyperfine lines were narrowed into a single line due to the strong exchange interactions.

Transmission electron-spin-resonance (TESR) on single crystals of $Mg_{1-x}Mn_x$ (with $x = 60\,\text{ppm}$) were carried out by Oseroff et al. (1977a) at 9.2 and 35 GHz. The authors observed a single resonance line which exhibited an angular anisotropy and a thermal broadening. From the angular variation of the ESR-line they deduced the second-order axial CF parameter (see, e.g., Abragam and Bleaney 1970), $D = 70 \pm 10$ G. The observed g-value for the Mn ions amounted to $g_{Mn} = 2.18$.

3.2. *Iron*

Except for Mn^{2+}, resonance absorption of 3d transition ions in metallic hosts had not been observed until 1976. Devine (1976) claimed the observation of the paramagnetic resonance of Fe in palladium. The Fe concentrations ranged from $630 \leqslant x \leqslant 5000\,\text{ppm}$. At low temperatures, three of the samples revealed ferromagnetic order. Above the Curie temperature T_c ($T_c \approx 9.5\,\text{K}$ for $x = 500\,\text{ppm}$) the temperature dependences of the linewidths were Korringa-like, with only weak concentration dependent Korringa slopes, $b = d(\Delta H)/dT$. When extrapolated to zero concentration, $b = 31 \pm 3$ G/K. The g-value, again extrapolated to zero concentration was found to be $g_{x=0} = 2.15$. The author calculated the appropriate exchange parameters $J_{s,p,d}$ by a partial wave expansion of the total exchange parameter. Obviously such a procedure contains severe assumptions about the bottleneck, the density of states at the Fermi energy, enhancement factors etc.

Nevertheless the comparison of these Fe-ESR results with those deduced from other experimental techniques are satisfying and agree well with those found for Mn in Pd. In a subsequent paper, Devine (1977) repeated these measurements and extended them to samples doped with hydrogen. He was able to follow the resonance for the hydrogen-free samples up to $4T_c$ and claimed that these experiments clearly are conducted in the paramagnetic regime. But the author pointed out that the observation of a resonance does not enable to deduce whether this resonance originates simply from Fe or from Fe plus a spin-polarized cloud which is responsible for the formation of the well-known giant moment. The hydrogen-charged samples are certainly not in a single phase but contain the α-phase of Pd and $PdH_{0.65}$ (α′-phase). The α-phase practically does not contain any hydrogen at low temperatures ($T \leqslant 20\,K$). Unfortunately, to our knowledge similar investigations on Fe in palladium or in other metallic hosts have not been performed. Only recently, Fe-ESR investigations in high-T_c superconducting materials were published (Sienkiewicz et al. 1990, Shengelaya et al. 1994, Kruschel 1993).

A comprehensive study of TESR in dilute Cu(Fe) alloys (5–10 ppm Fe), was carried out by Ritter and Silsbee (1978) for temperatures $2\,K < T < 40\,K$. These measurements represent the first observation of TESR in a dilute magnetic alloy below its Kondo temperature. The authors analyzed the results in terms of coupled Bloch equations. The effective relaxation rate for the Cu(Fe) samples showed a clear minimum at approximately 2.5 K, with the rate increasing by about 40% to an apparent plateau at the lowest temperatures investigated. The effective g-value of the Cu(Fe) samples does not show any deviation of the observed g-value from that of pure Cu. The results indicate that the Cu(Fe) system is strongly bottlenecked.

4. Lanthanide impurities as ESR probes in pure metals

In metals 4f ions are much better ESR probes than 3d ions due to fact that the exchange parameter J_{ie} is about ten times smaller for the exchange interactions between 4f electrons and the band states. The solubility of the 4f ions in many metallic elements is sufficient to perform ESR experiments and at least at low temperatures, narrow absorption lines can be expected. In most cases line positions and linewidths are determined by CF effects in addition to the well-known Korringa behavior. Again the ions with an S ground state like Gd^{3+} and Eu^{2+} are the preferred probes for ESR investigations. They warrant small crystalline-field influences on the linewidth and on the resonance field. This is the reason that by far most of the publications deal with Gd^{3+}.

4.1. *Gadolinium*

As reported already in previous papers (see, e.g., Devine et al. 1972a), Moret et al. (1975) investigated single crystals of Pd with 300 and 500 ppm Gd in the temperature range from 1.32 to 5.16 K. The single crystals were grown by a recrystallization technique and especially pure and carefully prepared materials were used. The ESR spectra revealed

a fine structure according to a local cubic environment. By extending the formalism of exchange-narrowing introduced by S.E. Barnes (1974) and Zimmermann et al. (1972) to cubic hosts, the authors were able to reproduce the experimentally observed shape of the fine-structure spectrum. The intensity of the $+\frac{1}{2} \leftrightarrow -\frac{1}{2}$ transition is larger than theoretically expected and this effect becomes even more pronounced at higher Gd concentrations. The reason for this extra line originates from a long-range indirect exchange interaction between Gd spins within a volume of about 200 lattice sites. The g-value for the $\pm\frac{1}{2}$ line is 1.788 ± 0.007 for the 300 and 500 ppm samples and corresponds to the center of gravity of the fine-structure line.

Shaltiel et al. (1977) investigated the Gd resonance in Pd single crystals with even lower Gd-concentrations (3000 and 25 ppm) at X- and Q-band frequencies. In the Q-band investigations and at $T = 1.4$ K, only the lowest of the eight Zeeman levels are populated. The spectrum with 25 ppm Gd does not show the extra line at the center of gravity of the fine-structure spectrum, an observation that confirms the assumption of a "cluster" line in samples with higher Gd concentrations. The spectra can be described by a g-value, $g = 1.795\pm0.005$ and by a Korringa slope $b = 8\pm1$ G/K. This thermal broadening is thought to correspond to the "true" value for the isolated ion. The crystal field parameter extracted from these experiments amounts to $b_4 = 29\pm1$ G, which is in good agreement with previous results.

Shaltiel et al. (1964a) noticed that Sm produces a positive g-shift for the Gd resonance in $Pd_{0.96}Gd_{0.02}Sm_{0.02}$, opposite to what is expected from a simple model. They pointed to the fact that the temperature-independent van-Vleck part of the susceptibility should produce an additional positive shift. Malik and Vijayaraghavan (1975) confirmed these results and provided more detailed information. They found that the distance between the $^6H_{5/2}$ ground state and the $^6H_{7/2}$ first excited state of Sm^{3+} is so small that the van-Vleck terms contribute appreciably and as a consequence the z-component of the lanthanide spin changes sign.

Drulis et al. (1977) investigated the system $Pd_{1-y}Gd_yH_x$ for concentrations $y = 0.5\%$ and $0 \leqslant x \leqslant 0.75$. A single resonance line with $g = 1.81$ was found for samples with hydrogen concentrations up to $x \approx 0.11$. The samples with the highest hydrogen concentration ($x = 0.75$) again showed a single line, but with $g = 1.99$. Above 5 K, Korringa behavior was detected with slope b which depends on the x-values ($b = 6.3$ G/K for $x = 0$ and $b = 0.6$ G/K for $x = 0.75$). The authors claim that the single ESR lines for smaller x-values belongs to the α-phase of the alloy and the other line ($g \approx 1.99$) originates from the β-phase. The small Korringa slope for the β-phase agrees with the well-known fact that the hydrogen-rich phase is characterized by an extremely small density of states at the Fermi energy.

Another important host for Gd-ESR investigations is the element platinum (Hardiman et al. 1977, 1980). The ESR spectra were taken at the X- and Q-band on Pt single crystals and polycrystalline samples containing between 1000 and 1500 ppm Gd. The spectra show fully resolved fine structures (fig. 2). The relevant fitting parameters that have been used to describe these experimental results were, in addition to the CF parameters b_4 and b_6, two variables governing the residual linewidths and a parameter which provides a measure of the degree of bottleneck. The authors obtained $b_4 = +86\pm3$ G and $b_6 = -2.6\pm5$ G. These

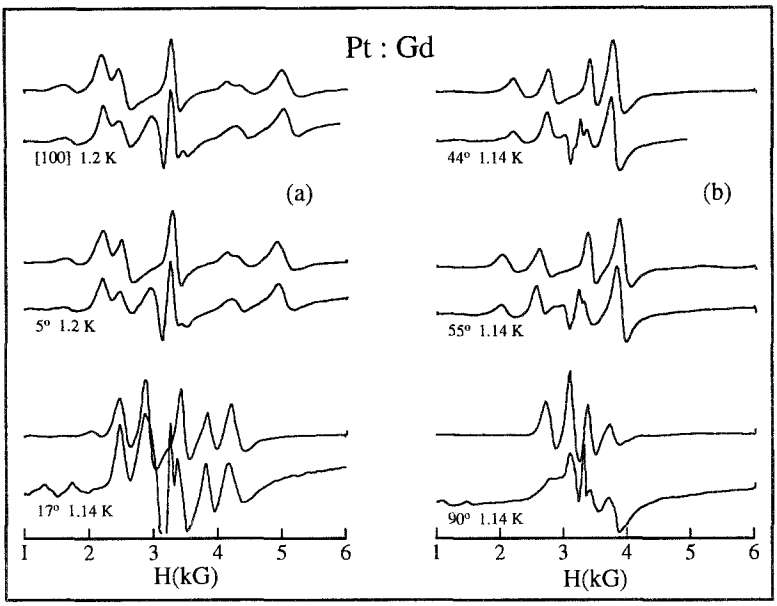

Fig. 2. Angular variation of the fine structure of the Gd^{3+} resonance absorption in a platinum single crystal doped with 1300 ppm Gd, at X-band frequency. At all angles, the upper spectra are calculated, while the lower spectra are experimentally observed (Hardiman et al. 1980).

values are about three times larger than those found in other cubic metals. An additional "cluster" line appears with the same g-value ($g = 1.94$) as for the single-ion fine-structure spectrum. The existence and behavior of the cluster line is qualitatively explained in terms of a cross-relaxation process. The thermal broadening of the absorption lines in the powdered samples appears to be linear, with approximately 2 G/K, and is increasing with decreasing concentration indicating a bottleneck behavior. The electron-lattice relaxation rate δ_{eL} determines the degree of bottleneck. δ_{eL} appears as a parameter in the fitting procedure, yielding $\delta_{eL} = 5 \times 10^{10}\ s^{-1}$. The agreement between the experimental single-ion spectra and those simulated using the Barnes–Plefka motional-narrowing theory (S.E. Barnes 1974, Plefka 1973) is excellent for most directions in the (110) plane. The observed negative exchange parameters (i.e. negative Δg) in Pt:Gd and Pd:Gd are essentially explained in terms of an interatomic covalent mixing. The local 5d-density of states at the impurity site should be an order of magnitude smaller in the case of Pt:Gd in comparison with La:Gd, another d-host metal. As a consequence of this difference, the intra-atomic exchange processes may be strongly reduced in the case of Pt:Gd, while they seem to play an essential role in the case of La:Gd.

The other 5d host, La with Gd or Eu as impurities was investigated by Koopmann et al. (1975, 1977a). In fcc-lanthanum both the Gd resonance and the Eu resonance are bottlenecked. The authors opened the bottleneck by systematic variations of the impurity concentrations. At low concentrations, $La_{1-x}Eu_x$ ($x = 4$ ppm) and $La_{1-x}Gd_x$

($x = 10$ ppm) the isothermic (unbottlenecked) limit is obtained, yielding $\Delta g_{max} = +0.12$ for both $La_{1-x}Eu_x$ and $La_{1-x}Gd_x$. It is important to notice that Δg is positive, in contrast to the 5d hosts Pt or Pd. The fact that the values Δg_{max} are identical, provides experimental evidence that the bottleneck factor is similar for both systems. Pure La is a superconductor with a relatively high superconducting phase-transition temperature $T_c = 6.05$ K. The transition temperature depends linearly on the impurity concentrations ($0 \leqslant x \leqslant 0.01$) (see Abrikosov and Gorkov 1961). The experimental values are $\Delta T_c/\Delta x = 2.1$ K/at% for $La_{1-x}Eu_x$ and 4.0 K/at% for $La_{1-x}Gd_x$. Using the relation $\Delta T_c/\Delta x = 3\hbar\pi\,\Delta\delta_{ei}/16k_B\Delta x$, Koopmann et al. (1975, 1977a) calculated the depression of T_c in the case of Gd and determined a value of 4.1 K/at%, which is in good agreement with the values cited above.

A further example of a comparison of experimental results with the theoretical predictions of the Barnes–Plefka theory is the investigation of scandium single crystals doped with 2400 and 300 ppm Gd at temperatures between 1.4 and 4.2 K by S.E. Barnes et al. (1983) and by Nagel and Baberschke (1976). These experiments were performed using measuring frequencies of 10 and 35 GHz and revealed that Sc(Gd) is a bottleneck system and, similar to the observations in Mg(Gd) (see Zimmermann et al. 1972), the bottlenecked system is strongly exchange narrowed. By adding nonmagnetic Th ions the authors were able to open the bottleneck, yielding strong exchange-narrowing effects without bottleneck. The increased narrowing in the bottlenecked case is caused by processes discussed by S.E. Barnes et al. (1971). At least two reasons were found to be responsible for this narrowing processes, namely the internal fields and ion–ion cross relaxations mediated by the conduction electrons.

A very different behavior of the ESR data has been obtained in the system $Sc_{1-x}Gd_xH_{1.9}$ investigated by Venturini and Morosin (1977). They studied powdered samples at X-band frequencies in the temperature range $76 < T < 300$ K. The linewidths exhibit a Korringa-like linear increase but with a pronounced change of slope from 1.0 G/K below 120 K to 0.4 G/K above 140 K. The g-value is constant $= 1.994 \pm 0.004$, i.e. $\Delta g = 0$ for all temperatures. The question about a bottleneck in $ScH_{1.9}$ remains open. The authors discussed the break in the Korringa slope as an isostructural phase transition. And indeed, measurements of the lattice constants revealed a low-temperature cell with a slightly smaller volume.

The d^1-metal sequence Sc($3d^1$), Y($4d^1$), La($5d^1$) evidently can be expanded by lutetium Lu($4f^{14}\,5d^1$). Baberschke and Nagel (1976) and Nagel and Baberschke (1976) measured the Gd-ESR in Lu single crystals and in polycrystalline material. They used Gd concentrations between 600 and 7800 ppm and observed a single line for all samples investigated. The thermal broadening of the linewidth does not show any concentration dependence. Hence, the conclusion has been drawn that Lu:Gd is unbottlenecked, in contrast to the isostructural Y:Gd and Sc:Gd compounds. g-shifts and Korringa slopes were determined and were found to amount to: $\Delta g = +0.108 \pm 0.010$ and $b = 80 \pm 8$ G/K, respectively. These values are of comparable size as those obtained in Sc and Y. The resonance field and the linewidth are functions of the crystal orientation with respect to the external applied field. A fit of the Barnes–Plefka theory to the angular dependence of the resonance field allowed one to determine, in addition to the g-value, also the axial

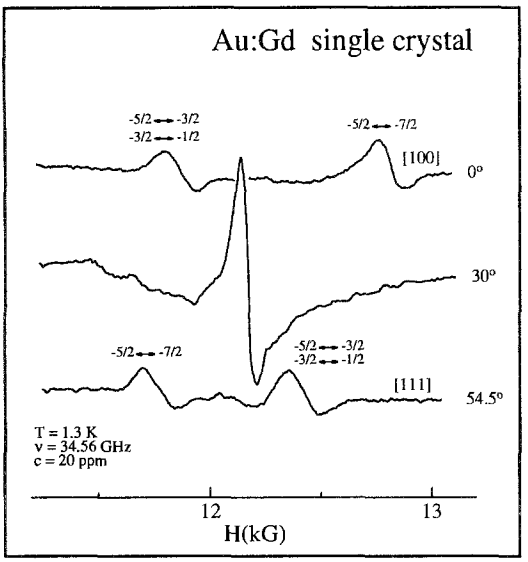

Fig. 3. Gd-ESR in a Au single crystal at Q-band frequency. The Gd concentration used in these experiments was 20 ppm. With respect to the external magnetic field the crystal is rotated in the (101) plane. From the spectrum a positive CF parameter $b_4 = 30$ G can be deduced. From Baberschke and von Spalden (1979).

term in the spin Hamiltonian of the hexagonal Lu host, $D = -63 \pm 6$ G. The authors argue that the reason for the non-bottleneck behavior in the Lu compound has to be attributed to the larger electron-lattice relaxation compared to the other isostructural d^1 hosts. The large residual linewidth (320 G for all Gd concentrations) supports this idea.

The splitting of the energy levels of S-state ions, like Gd^{3+}, in cubic or noncubic metallic hosts can be described by a positive b_4 or b_4^0 value in the spin Hamiltonian. Until 1979 only one "exception" has been documented in the literature, namely the system Au:Gd (Chock et al. 1971), with a negative b_4 value. Baberschke and von Spalden (1979) reinvestigated the system $Au_{1-x}Gd_x$. Single crystals were grown using the Bridgman technique, with Gd concentrations between $20 \leqslant x \leqslant 300$ ppm. The ESR measurements were performed at X- and Q-band frequencies. At $T = 1.3$ K and 35 GHz (Q-band) most of the Zeeman-levels are depopulated and only two transitions, namely the transition $-\frac{7}{2} \leftrightarrow -\frac{5}{2}$ and the exchange-narrowed transitions $-\frac{5}{2} \leftrightarrow -\frac{3}{2}$ and $-\frac{3}{2} \leftrightarrow -\frac{1}{2}$ were observed. The results at Q-band frequencies and at different crystal orientations are shown in fig. 3. Already this low-temperature spectrum determines a positive $b_4 = +30.5 \pm 1$ G. In addition to these transitions characteristic for Gd single ions, a concentration-dependent central line has been observed (Baberschke and von Spalden 1979). This line shows all characteristics of an exchange-narrowed spectrum due to impurity-impurity interactions. At 300 ppm and higher concentrations only this line appears in the spectrum. For the collapsed angle $\Theta = 30°$ (see fig. 3), the linewidth $\Delta H(T)$ follows a Korringa law with a residual linewidth $a = 28$ G and a Korringa slope $b = 98$ G/K. b is independent of the Gd concentration, i.e. no bottleneck effects can be observed. The g-value, $g = 2.041$ has been obtained, yielding a positive g-shift, $\Delta g = +0.05$. From the relative overall intensity of the central line and the single-ion spectrum the authors infer that approximately 50%

of Gd in the 100 ppm sample act as individual spins and the rest of the spin system shows dynamical spin–spin interactions giving rise to the central line.

Oseroff et al. (1975) and Fredkin and Schultz (1975) presented an experimental and theoretical paper on ESR of S-state ions in metals where they compare the spectra obtained by the usual reflection electron-spin-resonance (RESR) with transmission electron-spin resonance (TESR) results at 9.2 and 35 GHz. The spectra were obtained from single-crystalline $Ag_{1-x}Gd_x$ ($17\,\text{ppm} \leqslant x \leqslant 450\,\text{ppm}$). The starting point of this investigation was the fact that the observed g-values, corresponding to RESR and TESR in $Ag_{1-x}Gd_x$ were appreciably different: $g_{RESR} = 2.09$ and $g_{TESR} = 2.00$, with the peculiarity that in the case of RESR and at high concentrations ($x = 500\,\text{ppm}$) both lines were observed (see Davidov et al. 1973b). The ratio of the intensity of the two lines depended on concentration x. For the sample with a Gd concentration $x = 500\,\text{ppm}$, only the lines with $g = 2.00$ can be observed clearly, whereas for $x = 17\,\text{ppm}$, only the line characterized by $g = 2.08$ appears. The TESR for concentrations $x = 17$ and 50 ppm shows only the line at $g = 2.00$. To resolve this paradox the authors suggested the interpretation that the TESR and the RESR signals are associated with the same resonance mode of the homogeneous systems, i.e. they did not consider the possibility of Gd clusters. But rather different signals originate from low wave vectors (lwv) and high wave vectors (hwv) within the same mode. The hwv signal emerges within the skin depth and is too damped to be seen in transmission experiments. The hwv resonance ($g_{RESR} = 2.09$) is completely unbottlenecked, whereas the lwv resonance ($g_{TESR} = 2.00$) shows all signs of a bottleneck. The Korringa slope b is inferred from the thermal broadening of the hwv resonance at low Gd-concentration, $b = 2.5$ G/K. Like in many other cases, the exchange parameter $J(\boldsymbol{k},\boldsymbol{k}')$ for the interaction between conduction-electrons and Gd ions are different, depending how they were determined. If we denote the exchange parameters J as determined via the g-shift J_1, and those determined via the Korringa slope J_2, we find that they differ considerably, $J_1/J_2 = 3.0 \pm 0.6$. Unfortunately, this interesting aspect of ESR in localized magnetic moments in metals did not result in any follow-up papers.

Ce as a host metal is an interesting candidate for two reasons: (i) as a function of temperature cerium reveals different structural and magnetic phases, and (ii) the density of states at the Fermi energy strongly depends on the hybridization of the 4f-electrons with the band states. Rettori et al. (1978) studied powdered samples of $Ce_{1-x}Gd_x$ ($100 \leqslant x \leqslant 30\,000\,\text{ppm}$) in the temperature range $1.4\,\text{K} < T < 20\,\text{K}$. The dilute alloys exhibit a single line. The linewidth follows a Korringa law. The Korringa slope, $b = 2.5$ G/K, is concentration independent at least for $x < 10\,000$ ppm, whereas the residual linewidth a, varies considerably with Gd-concentration ($150 < a < 650$ G). Substituting additional nonmagnetic impurities (e.g. Y) hardly changes the magnetic resonance properties. The absence of a concentration dependence of the g-value ($g = 2.090 \pm 0.015$) and of the Korringa slope, indicates the absence of a bottleneck in the relaxation. A comparison of the ESR data of α-Ce, α-La and α-Th, which all crystallize in the same fcc structure, permits the conclusion that the magnetic resonance properties only reflect the properties of the α-phase of cerium. These results are supported by the recent phase diagram of Ce (Johansson et al. 1995). The results indicate further that the contribution

of the f-electrons to the Korringa broadening and to the g-shift are not important, i.e. that the 4f-density of states at the Fermi level is rather small.

In this context it would be interesting to investigate the Gd resonance in the γ-phase of cerium where the 4f states are localized and carry a magnetic moment, in contrast to the itinerant character of the 4f electrons in the α-phase.

4.2. *Europium*

Semi-metals with two intersecting bands at the Fermi level are good candidates to study metal–insulator (MI) transitions. As driving mechanism for MI transitions, very often pressure can be utilized, which increases the hybridization between the overlapping bands, giving rise to a repulsion between them, thereby eventually opening a gap in the electronic density of states. Previous studies of pressure-induced transitions in divalent metals have mainly been performed using transport measurements (McWhan et al. 1969, Jullien and Jerome 1971). For ytterbium the critical pressure has been determined to be approximately $p_c \approx 13$ kbar.

Continentino et al. (1995) presented the first magnetic-resonance study of a MI transition. They used 0.8% Eu^{2+} dissolved in Yb to serve as an ESR probe and measured the linewidth and g-shift of the Eu resonance in a wide range of temperatures and up to 29 kbar at X-band frequency. As shown in fig. 4a, the observed resonance line

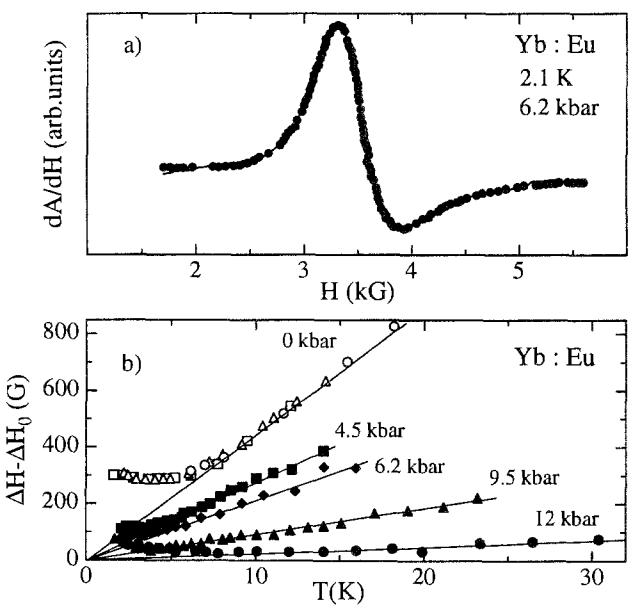

Fig. 4. (a) ESR resonance line in Yb(Eu) at a hydrostatic pressure of 6.2 kbar and at 2.1 K. The dotted line represents a fit to the field derivative of a single Lorentzian absorption line. (b) Temperature dependence of the linewidth ($\Delta H - \Delta H_0$) at different pressures. From Continentino et al. (1995).

can be fitted at all temperatures and pressures by single Lorentzian lineshapes. The pressure-induced shifts in the resonance field are small, $g = 2.04 \pm 0.01$ ($p = 3$ kbar) and $g = 1.95 \pm 0.01$ ($p = 25$ kbar) and the g-values are nearly temperature independent at all pressures. Considering the experimental uncertainties, the g-shifts do not provide as significant information as can be obtained from the linewidth broadening. Already Schmidt (1972) found out that one cannot presume any of the extreme bottleneck cases for relaxation in the system Yb(Eu). Neither the bottleneck-condition $\delta_{eL}/\delta_{ei} \ll 1$ nor the isothermal-condition $\delta_{eL}/\delta_{e} \gg 1$ are fulfilled. The large spin-flip scattering of the Eu impurities in Yb is responsible that the bottleneck regime is not fully achieved.

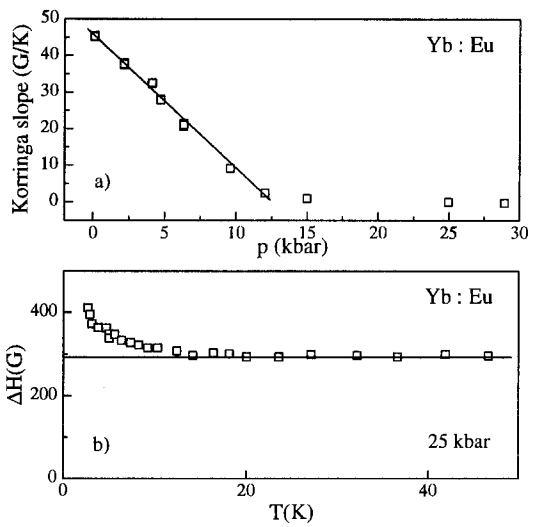

Fig. 5. (a) Korringa slope of the linewidths in Yb(Eu) as a function of pressure. (b) The low-temperature linewidth in Yb(Eu) for a hydrostatic pressure of 25 kbar. The increase of ΔH at low temperatures was associated with the localization of the conduction electrons. From Continentino et al. (1995).

Figure 4b shows the linewidth as a function of temperature for several pressures. For sufficiently high temperatures, ΔH increases linearly with temperature. The slope b decreases linearly with pressure. An extrapolation to zero slope yields a critical pressure $p_c \approx 12.5$ kbar (fig. 5a). The disappearance of a finite Korringa slope b at the critical pressure p_c can be associated with a vanishing density of states at the Fermi level, i.e. with the opening of an energy-gap at E_F. A single Lorentzian line without any fine or hyperfine structure describes the resonance absorption for all pressures and temperatures, below and even above p_c. This implies the existence of electron hopping processes for $p > p_c$, characterized by an appropriate small hopping time τ, so that the narrowing condition is satisfied even in the semiconducting state. That localization and electron hopping, indeed play an essential role in the semiconducting state is documented by the temperature dependence of the linewidth for $p > p_c$ (fig. 5b). The increase of the linewidth at low temperatures was associated with localization processes (Continentino et al. 1995).

4.3. *Erbium*

Erbium ions (Er^{3+} with the electronic configuration $4f^{11}$) are also well-suited ESR probes. In cubic environments commonly a Γ_7 ground state has been detected yielding narrow ESR lines even in experiments using powdered samples. The stable odd erbium isotope ^{167}Er, with a natural abundance of 23%, has a nuclear spin $I=\frac{7}{2}$ and is therefore a good candidate to investigate the hyperfine structure of the ESR signal in metals. Nagel et al. (1980) reported on measurements using an ESR spectrometer at 3 GHz and a $^3He/^4He$ dilution refrigerator. In these experiments only the sample is cooled down into the millikelvin range, but the cavity remains at room temperature. A cold finger, which is attached to the mixing chamber of the $^3He/^4He$ refrigerator, cools the sample. Three quartz glassfingers and an infrared radiation shield cover the sample. The authors measured ESR in $Au_{1-x}Er_x$ ($x=250$ ppm). Above 400 mK the thermal broadening amounts approximately to 2.5 G/K. On cooling, the increase of the linewidth below 200 mK is due to Er–Er interactions. The sample investigated was a gold single crystal. The high quality of the host gave a narrow absorption line with $\Delta H(300\,\text{mK})=3$ G. This value corresponds to the narrowest line ever observed in ESR experiments on metals. The narrow line allows a precise determination of the g-value, $g=6.790\pm0.005$. This value has to be compared with the theoretical g-value for an isolated Γ_7 ground state, $g(\Gamma_7)=6.80$. Hence, no shift of the resonance line can be observed in Au(Er). The resonance absorption was described by a perfect Dysonian line, i.e. crystal-field effects were fully exchange narrowed.

The direct observation of hyperfine resonances of the Γ_7 ground state of isotopically enriched ^{167}Er in a powdered gold matrix was reported by Sjöstrand and Seidel (1975). In weak external fields for $S=\frac{1}{2}$ and $I=\frac{7}{2}$, two hyperfine multiplets, $F=3$ and 4, are expected. The appropriate isotropic spin Hamiltonian is given by

$$H = g\mu_B \boldsymbol{HS} + \boldsymbol{AIS} + g_N\mu_N \boldsymbol{HJ}, \tag{23}$$

where the first and third term characterize the electronic and nuclear Zeeman energies and the second term represents the hyperfine interaction. Transitions between m_F and m_{F+1} are observed. The resonance data were taken in the temperature range $40\,\text{mK} < T < 300\,\text{mK}$ and at frequencies of 230, 250 and 300 MHz. The hyperfine transitions occur in an external magnetic field between 150 and 550 G. The constants A and g_N were determined by fitting eq. (23) to the observed spectra. The values $A=-73.5\pm0.7$ G and $g_N=-29\pm2$, have been obtained. This g_N-value, which is enhanced by a factor 185 when compared to the g_N-value of the free Er atom, can be understood by considering the mixing of the Γ_7 ground doublet with the excited $\Gamma_8^{(1)}$ quartet. The spectra show that the linewidths of the resonance lines vary from line to line and increase with magnetic field. This is also a consequence of the Γ_7–$\Gamma_8^{(1)}$ mixing. The observed A-value is, within experimental errors, the same as that observed in ^{167}Er in nonmetallic hosts with the same local symmetry, e.g. ^{167}Er in ThO_2 with $|A|=73.85$ G (Abraham et al. 1965).

It has been demonstrated that the effects produced in metals by cold-working can be utilized ESR of magnetic impurities (Raizman et al. 1979). The alloy used in

these experiments was Au (purity $5N$) with a nominal Er concentration of 1000 ppm. The samples were cold-worked at room temperature and then investigated by ESR measurements. After a heat treatment of 1 h at 670 K in a vacuum of 10^{-6} Torr the samples were measured again. Detailed investigation of the residual linewidths, the asymmetry parameters A/B, g-factors, hyperfine constant, etc. yielded the following results:

In heated samples drastic changes were observed in the residual linewidth, the A/B ratio and the total intensity. The total intensity of the ESR signal is reduced by a factor 20 after heating the rolled sample. Successively rolled samples recovered in ESR intensity. During heating a thermally activated motion of the dislocations occurs. These displacements are locked at the Er ions which cannot contribute to the ESR signal anymore since they are exposed to a crystalline field of much lower symmetry. Renewed rolling frees the dislocations from the Er sites and in the high-symmetry crystalline environment they again can contribute to the ESR signal. However, repeated rolling increases the residual linewidth by creating internal strain fields.

A novel application of the ESR technique has been demonstrated by Raizman et al. (1981, 1984). They discovered and studied the internal oxidation of Er^{3+} ions in dilute gold–erbium alloys. They used samples of Au doped with 2000 ppm Er in the form of thin foils, which had been produced by rolling. The authors showed that heating a sample in air for 1 h at 670 K produces a near-surface layer of approximately 5000 Å thickness, with properties different from the bulk material. This near-surface layer causes significant changes in the ESR-line of Er^{3+}: ΔH and the total intensity become significantly reduced, whereas the A/B ratio increases. In contrast to this finding, heating of the samples in high vacuum ($\sim 3 \times 10^{-8}$ Torr) causes an increase in the intensity of the resonance line. The authors claim that internal oxidation of Er^{3+} in the near-surface layer is responsible for the decrease in ESR intensity.

The effects of nonmagnetic impurities (M) on the residual ESR linewidth of polycrystalline $Ag_{1-x-y}M_yEr_x$, $\Delta H_0 = \Delta H(T \to 0)$, were studied by Dahlberg et al. (1990). The nonmagnetic impurities M = In, Sn, Sb, Y and Lu were substituted in a concentration range $500 < y < 4600$ ppm. The alloys contained erbium as ESR probe with a concentration $x = 200$ ppm. The residual linewidth was determined by plotting the measured linewidth versus temperature and by a linear extrapolation towards $T \to 0$ K. In fig. 6 the residual linewidth is shown as a function of the concentrations of nonmagnetic impurities M = In, Sb and Y. The residual linewidth broadening was found to amount to 0.2±0.1, 0.49±0.1, 0.51±0.1, 1.4±0.2 and 1.4±0.3 G/(1000 ppm Hz) for In^{3+}, Sn^{4+}, Sb^{5+}, Y^{3+} and Lu^{3+}, respectively. For the first three nonmagnetic impurity ions in this series the charge difference is systematically changed. This fact is reflected, at least to some extent, in the values of the residual linewidth (see fig. 7) The experimental results can be represented by a function of the form

$$\Delta H_0 = h(x) + y\nu k, \tag{24}$$

Here h depends on the Er concentration x, k is proportional to the impurity-induced electric-field-gradient (EFG), y is the dopant concentration of the nonmagnetic impurities and ν the measuring frequency.

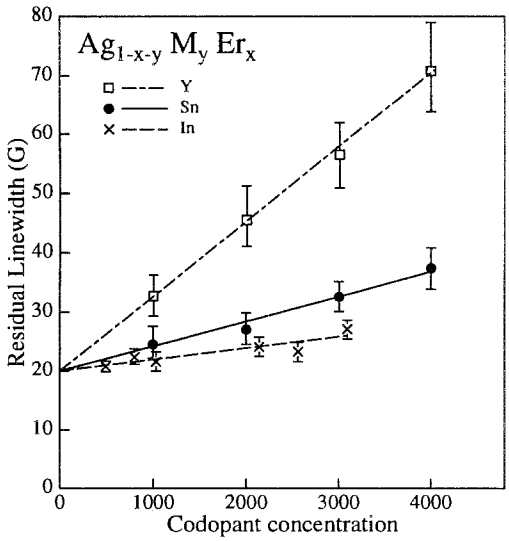

Fig. 6. The residual linewidth for Er-ESR in Ag as a function of the impurity concentrations Y, Sn and In. From Dahlberg et al. (1990).

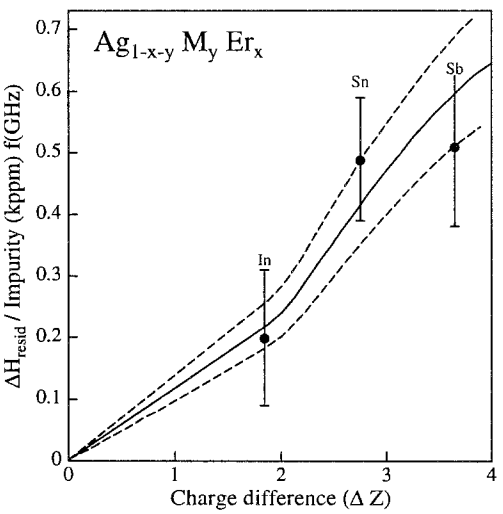

Fig. 7. Increase of the residual linewidth vs the effective charge difference between the substitutional defect M = In, Sn and Sb, and the Ag host (Dahlberg et al. 1990).

The ESR spectrum of Er in Ag arises from an isolated Γ_7 ground-state doublet. The first excited state, $\Gamma_8^{(1)}$, approximately is 35 K above the ground state. The theoretical g-value of the isotropic Γ_7 ground state amounts to $g = 6.8$. A small admixture of the $\Gamma_8^{(1)}$ state into the Γ_7 ground state can change the g-value slightly. This can be the reason for an inhomogeneous broadening of the Er resonance line in a powdered sample. In that case we would observe a linewidth which scales with the measuring frequency. The $\Gamma_7 \leftrightarrow \Gamma_8$ mixing can be due to electric field gradients (EFG) caused by charged impurities in the

host which may be the Er ions themselves (Dahlberg 1977). These charge oscillations around the impurity site can disturb the crystalline field seen by the Er ions and mix the Γ_7 and Γ_8 states. The magnitude of these oscillations in the conduction-electron density, which generate the EFG's, were calculated by Kohn and Vosko (1960). An important ingredient of this model is the quantity ΔZ, the valence difference between the host and the impurity ions. Unfortunately, the validity of this EFG model has not been tested with other lanthanide ions, as the mixing effect should crucially depend on the distance of the ground state and the first excited level of the CF scheme. A comprehensive treatment of the complex problem of the residual linewidth of ESR in metals can be found in an article by S.E. Barnes (1981a).

Silver doped with erbium is a system with two well-separated, albeit coupled, resonances. One of these resonances is due to the conduction electrons ($g_e = 1.983$ for pure Ag; see Schultz et al. 1967) and the other due to the Γ_7 ground state of Er^{3+} in a cubic crystal field ($g(\Gamma_7) = 6.8$; see Griffiths and Coles 1966). Oseroff et al. (1977b) reported on measurements of the magnetic susceptibility $\chi(T)$, reflexion ESR at different frequencies and transmission ESR on single crystals of $Ag_{1-x}Er_x$, with erbium concentrations $0.002 < x < 0.02$. As expected, the resonances are completely unbottlenecked because of the large differences in the g-values. An analysis of the susceptibility and the ESR data revealed an energy separation between the Γ_7 ground state and the Γ_8 first excited state, $\Delta = 30 \pm 5$ K.

Magnetic resonance experiments on thin (< 1 μm) Ag(Er) films, epitaxially grown on cleaved NaCl (001) faces, have been reported by Arbilly et al. (1975). The high quality of the single-crystal films was examined by electron diffraction and electron microscopy. In this paper the authors demonstrate how ESR techniques can be used to probe internal strain fields in thin single-crystalline films and how to determine their overall magnitude, direction and spatial distribution. The nominal Er concentration in these experiments was 10^4 ppm but the authors mentioned that the true concentration may be five times lower. From the measured anisotropy of the g-factor of the central Er line, originating from the even Er isotopes, the magnitude of the orbit–lattice-coupling constant has been calculated. It was the first time that this coupling strength has been determined. The g-values varied between $g_{\parallel} = 6.6346 \pm 0.0046$ and $g_{\perp} = 6.8886 \pm 0.0046$ when the external magnetic field H_0 was rotated in the (100) plane from $\Theta = 0$, i.e. H_0 parallel to the z-axis, to $\Theta = 90°$, i.e. H_0 parallel to the [010] axis. The z-axis was oriented perpendicular to the plane of the film. At the same time the linewidth changes with the angular variation according to $\Delta H = u + v(|3\cos^2\Theta - 1|)$, with $u = 352 \pm 0.65$ G and $v = 4.0 \pm 0.55$ G. The variation of the linewidth allowed one to estimate the magnitude and spatial dependence of the anelastic response.

Similar measurements on Ag(Er) thin films deposited on [111] NaCl faces were repeated by Barberis et al. (1977). Due to the different crystallographic orientation of the deposition plane, which had been used in this study compared to the work of Arbilly et al. (1975), the authors were able to determine the trigonal second-order orbit–lattice coupling. Whereas the tetragonal parameter has positive sign (see Arbilly et al. 1975), a negative sign has been found for the trigonal parameter. It is interesting to note that

none of the films in the paper of Barberis et al. (1977) showed anisotropy, neither in the linewidth ΔH, nor in the lineshape, when H_0 is rotated in a plane perpendicular to the film plane. Therefore the authors conclude that the strain distribution across the film is highly uniform. The anisotropy in the g-values can only be explained when strains in the film are induced by the substrate.

Finally, Dodds and Sanny (1978) observed the Er resonance in polycrystalline films which were deposited at room temperature onto fused-quartz or plexiglass substrates at pressures of approximately 1×10^{-6} Torr. The nominal erbium concentration varied between 0.2 and 2%. The angular variation of the g-value and linewidth was measured for each sample at a fixed temperature in the liquid He range. During cooling, the difference in thermal contraction between film and substrate produced an effective uniaxial strain in the film. The contraction of the substrate forces the film to expand in the direction perpendicular to the substrate, which becomes the preferred axis and the g-value will depend on the orientation of the field with respect to this axis. In this way even in polycrystalline films an anisotropy of the g-value can be observed. The inferred orbit–lattice coefficients were somewhat smaller than those observed in insulators. They were the same for films on quartz or on plexiglass substrates. This fact supports the conclusion that the strain is macroscopically uniform in contrast to the argumentation of Arbilly et al. (1975).

Garifullin et al. (1985) tried to avoid the uncertainties, e.g. due to a poor adhesion of the films on the substrate, by performing ESR studies in bulk metallic samples subjected to a controlled elastic deformation. They used single crystals of the system $Ag_{1-x}Er_x$ ($x \approx 0.03$ at%) or $Cu_{1-x}Er_x$ in a cylindrical form with the cylinder axis along the [110] direction. The tensile stress (up to 0.4 kbar) was applied to the sample in the [110] direction and perpendicular to the plane in which the external field H_0 was rotated. On applying the tensile stress to the sample, the angular dependence of the linewidth was not noticeably changed while the g-factor became strongly anisotropic. The orbital–lattice parameters deduced from this experiment were significantly larger compared with the values obtained on films but they coincide in sign.

In full detail, Zevin et al. (1977a) reexamined the ESR spectrum of Er^{3+} in a cubic symmetry (see also Devine et al. 1972a, Zingg et al. 1974). The first excited state in Pd:Er has been determined to be a Γ_6 state with an energy $\Delta(\Gamma_8 - \Gamma_6) \approx 16$ K above the ground state. The angular dependence of the ESR spectrum of Pd single crystals with 1000 ppm Er and especially the unexpected "fine splitting" of the transitions $1 \leftrightarrow 2$ and $3 \leftrightarrow 4$ of the Γ_8 ground state in the [111] direction can be explained by introducing a trigonal distortion. The axial CF parameter D amounts to $D \approx -33$ G. The authors used the well-known spin Hamiltonian for Γ_8 state with $S = \frac{3}{2}$ (see, e.g. Abragam and Bleaney 1970) and included possible contributions of the excited Γ_6 level, an axial D-term and an appropriate hyperfine term. Using this ansatz, they were able to explain the appearance of the forbidden hyperfine spectrum in the [111] direction and the variation in the intensity of the allowed, as well as of the forbidden hyperfine lines. The addition of an interference term between the magnetic and the quadrupolar parts of the hyperfine Hamiltonian provided an excellent agreement between experiment and model calculations

of the separation of the hyperfine lines. But the origin of the trigonal deformation remains unclear. In crystals grown by zone-melting, the transitions $1 \leftrightarrow 2$ and $3 \leftrightarrow 4$ were not resolved. They were found to be much broader than those observed in crystals grown by recrystallization methods. This splitting of the $1 \leftrightarrow 2$ and $3 \leftrightarrow 4$ transitions in [111] direction of the Γ_8 ground state in Pd (Er) is the subject of a paper by Dixon (1977). He explains the angular variation of the resonance field without introducing static lattice distortions with deviations from cubic symmetry. Alternatively, he discussed the possibility of a dynamic Jahn–Teller coupling between the Γ_8 electronic state and Γ_5 lattice modes. The observed separation of the $1 \leftrightarrow 2$ and $3 \leftrightarrow 4$ transitions along any [111] direction can be obtained by this model. In this paper the intensities and the separations of the hyperfine lines were not considered.

Aluminium has a strong conduction-electron ESR signal which can be detected up to liquid-nitrogen temperatures. Therefore it is a well-suited host metal for transmission electron-spin resonance. Siebert et al. (1974, 1976) investigated the TESR on aluminium containing low concentrations of Er^{3+}, Tm^{3+} and Lu^{3+}. When the impurities are magnetic, the conduction-electron magnetization is dynamically coupled to the local-moment magnetization. In the case of Al(Er), Er^{3+} has a Γ_7 ground state with a g-value of ~6.8, well separated from $g=2$. The ground state of Tm^{3+} is nonmagnetic. The resonances of both alloys are therefore unbottlenecked and the effects of coupling between the local moments and the band states are rather small due to the big difference in g-values. The first-order effect of the exchange coupling between the lanthanide ions and conduction electrons is experimentally evidenced via a temperature and crystal-field dependent shift and broadening of the TESR signal. The authors were able to deduce crystal-field and exchange parameters for each alloy. This information can be gained as long as the impurity ions have low-lying CF levels that are thermally populated in the experimentally accessible temperature range. Within experimental errors, both alloys are characterized by the same exchange ratio, $J(0)^2/\langle|J(q)|^2\rangle_{EF} = 1.5 \pm 0.3$. This is in contrast to similar measurements of lanthanide impurities in Ag (see, e.g., Oseroff et al. 1975) which yield much higher exchange ratios, ranging from 2 to 3.

ESR experiments of Er^{3+} and Dy^{3+} in cerium are reported by Rettori et al. (1978). Both Er^{3+} and Dy^{3+}, have Γ_7 ground states with negative fourth-order CF parameters, $A_4 < 0$. In contrast, a simple point-charge model predicts $A_4 > 0$. The authors suggest that 4f electrons of α-Ce may be responsible for this sign reversal of the A_4 parameter. The analysis of the temperature dependence of the linewidth in terms of a Korringa behavior, $\Delta H = a + b \cdot T$, yield values of the residual linewidths which are concentration dependent: $a = 255\,\text{G} - 258\,\text{G}$ for Ce(Dy) and $a = 120\,\text{G} - 160\,\text{G}$ for Ce(Er). The values characteristic for the thermal broadening were found to be concentration independent, yielding $b = 23 \pm 5$ G/K for Ce(Dy) and 13 ± 3 G/K for Ce(Er). It is interesting to compare the ratios $b(\text{Dy})/b(\text{Gd}) = 0.9 \pm 0.4$ and $b(\text{Er})/b(\text{Gd}) = 0.5 \pm 0.2$. The agreement with the theoretical predictions for these ratios, namely 0.96 and 0.38, respectively, supported the idea that the exchange does not depend on the 4f occupation number.

A number of controversial discussions treated questions concerning the possible differences of the hyperfine constant as observed in insulators and in metals. To answer

these questions Rettori et al. (1974) investigated the ESR spectra of $Th_{1-x}Er_x$ (with an erbium concentration $x = 180$ ppm of enriched ^{167}Er) at temperatures down to 0.7 K. These investigations revealed well-resolved hyperfine spectra with linewidths of the hyperfine components of only ~25 G. This enables the authors to extract a very accurate value of the hyperfine constant by fitting the line positions with the second-order hyperfine-splitting formula

$$H = H_0 - AM_I - A^2 \frac{I(I+1) - M_I^2}{2H_0}. \tag{25}$$

H_0 characterizes the magnetic field of the resonance absorption of the even Er isotopes, $I = \frac{7}{2}$ is the nuclear spin of ^{167}Er, A is the hyperfine constant and M_I the magnetic quantum number of the nuclear spin. From the best fit a hyperfine coupling constant $A = 75 \pm 1$ G has been derived. This value is slightly larger than the value observed in an insulator (e.g., $A(^{167}Er) = 73.8$ G for Er in CaF_2). This difference has been attributed to contributions from the conduction electrons (Hirst 1971). But the simple relation $\Delta A(\boldsymbol{q} = 0) = \Delta g/2A(\boldsymbol{q} = 0)$ should hold only under the condition that the $\boldsymbol{q} = 0$ component dominates. Thus, the exact origin of the enhancement in A remains unclear, due to the possible influence of screening electrons with d-character.

Usually a bottleneck behavior is to be expected only if the two subsystems have almost the same g-value. But it has been shown (see Dupraz et al. 1970) that the bottleneck situation also can occur under the condition $\omega_s - \omega_e \ll \delta_{es} + \delta_{se}$. δ_{es} denotes the Overhauser rate and δ_{se} the Korringa rate. ω_s, ω_e are the resonant frequencies of the localized moments (ω_s) and of the conduction electrons (ω_e). Al'tshuler et al. (1974) reported on the observation of such a bottleneck situation in the system $Cu_{1-x}Er_x$ ($0.01 \leqslant x \leqslant 0.16$) in the temperature range $1.6 \leqslant T \leqslant 4.2$ K. The Er spectrum consists of a central line (^{166}Er, ^{168}Er and ^{170}Er) with a g-value, $g = 6.84 \pm 0.02$, independent of x and six hyperfine lines due to the odd ^{167}Er isotope, with a hyperfine constant $A = 74.8 \pm 1.5$ G, a value that again is slightly enhanced in comparison with those observed in insulators. In the temperature range of this study the linewidth followed a Korringa law with a slope which significantly depends on the concentration x. For $x = 0.01$ the slope is 7.7 G/K and for $x = 0.16$ the Korringa slope amounts to 3.4 G/K. This behavior, namely that $b \sim 1/x$ is typical for a bottleneck situation. Only by taking into account the finite heat capacity of the two subsystems, namely conduction-electrons and localized Er moments, the authors were able to explain the peculiar behavior of the $Cu_{1-x}Er_x$ system.

4.4. *Dysprosium*

Dysprosium (Dy^{3+}) diluted in metallic hosts has been used for a number of ESR investigations. Al'tshuler et al. (1977) observed the ESR of Dy^{3+} in Cu single crystals. The Dy concentration was estimated to be $x \approx 0.05$ at%. The experimental g-value of 7.63 ± 0.02 is reasonably close to the theoretical value, $g = 7.56$, expected for a Γ_7 ground state in a cubic environment. The hyperfine constant (^{163}Dy) was evaluated by the Breit–Rabi formula with $A = 80 \pm 3$ G. In the temperature range $1.6 < T < 4.2$ K the linewidth

again is Korringa-like with a slope $b = 19 \pm 1$ G/K. The residual linewidth is surprisingly small, $\Delta H_0 = 16$ G. Obviously, the excited CF states, Γ_8 and Γ_6, do not influence the ESR signal of $Cu_{1-x}Dy_x$ at these low temperatures.

The linewidth and resonance field of the ^{164}Dy-ESR line in single crystals of silver revealed a pronounced angular variation, at X-band and Q-band frequencies (Oseroff and Calvo 1978, Oseroff et al. 1977a,b). The ground state is a Γ_7 doublet with $g_{exp} = 7.67$. The linewidth anisotropies depend on the magnetic field and are more pronounced at the Q-band frequency. In view of the small CF splitting $(\Gamma_8 - \Gamma_7) \approx 13$ K one has to discuss the modification of the Korringa relaxation due to the Zeeman interaction. But this model gives a contribution to the g-shift which is smaller than that observed experimentally and has the wrong sign. In analogy to Feher (1964), who discussed a random distribution of internal stresses in the host sample, the authors explained their experimental data on Ag(Dy) by this random-stress model. In this model the full cubic local symmetry at the impurity sites is preserved. Davidov et al. (1975b) used a similar model to explain the broadening of the ESR line of Dy in LaSb. The problem of a strain dependence of the ESR line of Dy in Ag and Al thin films has also been investigated by Dodds et al. (1978).

5. Lanthanide impurities as ESR probes in alloys

5.1. *Lanthanide ions as ESR probes in metallic compounds with CsCl, Cu_2Mg and Cu_3Au structure*

This section deals with ESR on localized probes in metallic compounds with CsCl, Cu_2Mg or Cu_3Au structure. A systematic investigation of the ESR spectra in CsCl structures has been performed by Seipler (1975), Seipler and Elschner (1975), Seipler and Plefka (1978) and Seipler et al. (1977). Calculation of the band structures of these intermetallic compounds (Belakhovsky et al. 1972, Kübler 1978) indicates that in these systems a considerable part of the density of states $N(E_F)$ at the Fermi surface has d-character, whereas macroscopic measurements, e.g. specific heat or magnetic susceptibility, yield only the sum of all contributions of the various bands to the electronic density of states, ESR measurements using Gd^{3+} as paramagnetic probes have the potential to provide valuable information about the contributions of each single band. Three quantities were used to analyze these ESR-measurements, namely the g-shift, $\Delta g = (g_{exp} - g_{iso})$, the Korringa slope, $b = d(\Delta H)/dT$ and the "Korringa ratio" R, $R\pi k_B/g\mu_B = b/(\Delta g_0)^2$. The simplest approach for an analysis of the ESR results in these compounds is a so-called "two-band-model" where Δg and b are separated in two parts, e.g. $\Delta g = (J_{fs}N(E_F)_s + J_{fd}N(E_F)_d)$. A more detailed analysis of this model was carried out by Davidov et al. (1973a).

The systematic investigation of AB compounds with CsCl structure (A = Sc, Y and La; B = Ag, Cu, Pd, Rh, Ir and Ru) allowed for a classification into three groups:

Group I: The density of states at E_F consists of large d-contributions from the A site and weaker s, (p)-contributions from both sites (A and B). LaAg, ScAg, ScCu, and

Table 1
ESR data in $A_{1-x}Gd_xB$ compounds with CsCl structure (A = La, Sc or Y; B = Ag, Cu, Pd, Ru, Rh or Ir)[a]

Compound	Δg	$\frac{d\Delta H}{dT}$ (G/K)	R
LaAg	+0.078	29±4	0.21
ScAg	+0.085±0.02	26±2	0.15
ScCu	+0.065±0.01	20±4	0.2
ScPd	+0.053±0.05	15±2	0.23
YCu	+0.058±0.004	21±4	0.27
YAg	+0.067±0.005	20±3	0.19
	+0.075	14	0.11
ScRu	+0.018±0.005	10±2	1.3
YRh	+0.006±0.002	3±1	3.5
ScRh	+0.006±0.002	1.9±0.5	2.3
ScIr	−0.008±0.002	0.6±0.2	0.4

[a] From Seipler and Elschner (1977).

ScPd definitely belong to this group. The Δg-values are positive and relatively large. The Korringa slopes are large. The alloys $Sc_{1-x}Gd_xAg$, $Sc_{1-x}Gd_xCu$ and $Y_{1-x}Gd_xAg$ are even bottlenecked. The R values scatter around ~0.2.

Group II: In addition to the s(p)-contributions from both sites, large d-contributions originate from the B site. ScRu is a representative of this group. The Δg-values are still positive, but clearly smaller than those of group I. The Korringa slopes are somewhat smaller. The resulting R values are large and amount to $R \approx 1.3$.

Group III: The d-contributions which possibly originate from both sites are small; s(p)-contributions preponderate. The Δg-values are positive and small, or are even negative. The b values are more than one order of magnitude smaller than those of the compounds of group I or II. The alloys YRh, ScRh and ScIr belong to this group.

Table 1 gives a survey of the experimental results (Seipler and Elschner 1977) and fig. 8 shows the Korringa slopes in several CsCl structures as a function of the electronic configuration. A comparison of these experimentally observed ESR systematics, with calculated energy bands and density of states by Kübler (1978) revealed a remarkable agreement which is nicely documented in table 2 (after Seipler and Elschner 1977).

Already Shaltiel et al. (1964b) made a systematic investigation of the sign and magnitude of the g-shifts using 1–5% Gd as ESR probes, substituted into AB_2 Laves phases. The authors were able to explain the g-shifts and Korringa slopes. However, new questions arose in the following years. This was predominantly due to the fact, that single crystals of these compounds became available. Baberschke et al. (1978, 1980a,b) reported ESR measurements at X- and Q-band frequencies on single crystals of $La_{1-x}Gd_xAl_2$ and $La_{1-x}Eu_xAl_2$ ($100 \leqslant x \leqslant 1000$ ppm). The Gd spectra yielded a single line only. No angular dependence of the resonance field or of the linewidth could be detected. This can only be explained assuming that the crystal field splitting, characterized by the

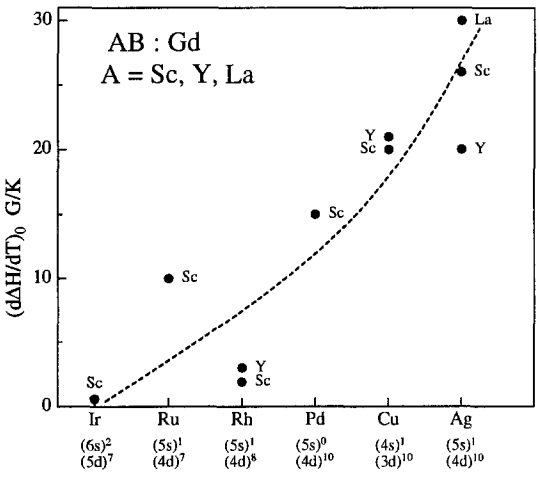

Fig. 8. Isothermal limit of the Korringa slopes for Gd ESR in metallic compounds with CsCl structure. The experimental values were taken from Seipler and Elschner (1977) and Davidov et al. (1973c). The dashed line is a guide to the eye.

Table 2
Experimental and computed local partial densities of states (eV^{-1} $atom^{-1}$ $spin^{-1}$) at the Fermi energy[a,b]

Compound	N^{Sc}_{s+p}	N^{S}_{d}	N^{B}_{s+p}	N^{B}_{d}	N_{tot}	
ScRu	0.34	0	0.34	0.40	1.08±0.17	Experiment
	0.11	0.19	0.14	0.59	1.03	Theory
ScRh	0.11	0.06	0.06	0.06	0.29±0.09	Experiment
	0.04	0.09	0.06	0.09	0.28	Theory
ScPd	0.19	0.33	0.19	0	0.70±0.14	Experiment
	0.10	0.34	0.16	0.11	0.71	Theory
ScAg	0.26	0.51	0.12	0	0.90±0.14	Experiment
	0.11	0.42	0.18	0.04	0.75	Theory

[a] From Seipler and Elschner (1977).
[b] N^{Sc}_{s+p} and N^{B}_{s+p} are the added s and p contributions at the Sc or B sites, respectively. N^{Sc}_{d} and N^{B}_{d} are the d contributions at the Sc or B sites, respectively.

coefficient b_4, is very small. A rough estimate yielded $b_4 \leqslant 10$ G. In contrast to this finding, a fully resolved fine structure was observed for Eu in $LaAl_2$. This experiment represents the first observation of a resolved fine structure in the bottleneck regime (see fig. 9). The different effects of the bottleneck and non-bottleneck case on the ESR fine structure were theoretically predicted by Plefka (1973) and S.E. Barnes (1974). The resonance at the collapsed angle, $\Theta = 30°$, has a thermal broadening of 21 G/K whereas the isothermal Korringa rate $b_K = 31$ G/K. The $-\frac{7}{2} \leftrightarrow -\frac{5}{2}$ transition yielded the thermal broadening of 225 G/K ($225/7 \approx 32$) which is in rough agreement with b_K. A fit to the angular dependence of the resonance fields yielded $b_4 = +112$ G and $b_6 = -8$ G. The exchange constant derived from the g-shift equals $J_1 = 0.04$ eV whereas J_2 derived from the isothermal Korringa slope amounts to 0.024 eV.

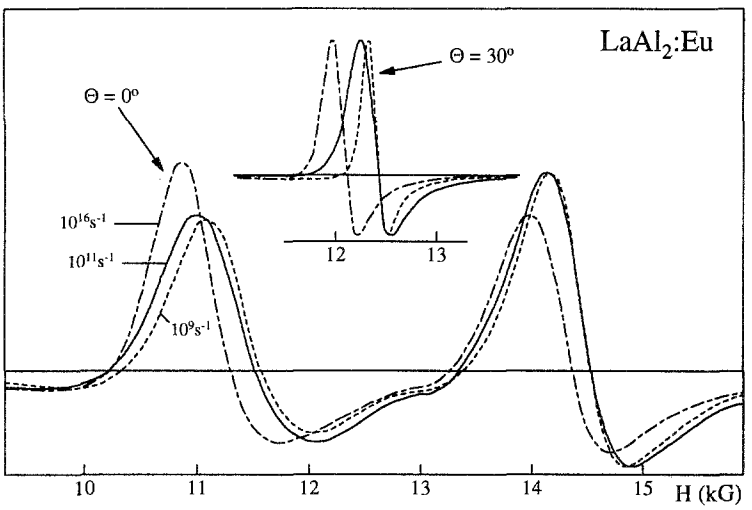

Fig. 9. Calculated and experimentally observed (solid line) ESR spectrum for $LaAl_2$(Eu) for two different angles ($\Theta = 0°$ and $\Theta = 30°$) of the external magnetic field with respect to the crystallographic cube axis. The relaxation rates $\delta_{eL} = 10^{16}\,s^{-1}$ and $\delta_{eL} = 10^{9}\,s^{-1}$ correspond to the isothermal limit and to the extreme bottleneck limit, respectively. $\delta_{eL} = 10^{11}\,s^{-1}$ corresponds to the experimentally observed lineshapes. The effective g-value for the latter case amounts to 2.02 (Baberschke et al. 1980a).

Luft et al. (1981) performed ESR measurements on single crystals of $LaOs_2$ doped with Gd (250 and 2500 ppm) in the temperature range $1.1\,K \leqslant T \leqslant 4.2\,K$, i.e. well below the superconducting (sc) transition temperature ($T_c \approx 6.7\,K$ for $H_0 = 13\,kG$). They observed a clearly resolved fine structure in the superconducting state at $T < 3\,K$ (fig. 10). The cubic crystal field parameter was determined as $b_4 = -18 \pm 2\,G$. The negative sign is in contrast to the sign of the CF parameter for Gd in other metallic hosts. The identification of the different ESR lines as a fine structure of Gd^{3+} allows the statement that the anomalous ESR line shapes in polycrystalline superconductors can be attributed to crystal field effects rather than to field inhomogeneities in the vortex state (Schrittenlacher et al. 1975). From the temperature dependence of the resolved spectrum in the sc state an exponential decay of the Korringa relaxation rate has been derived. The fit yielded a gap parameter $2\Delta = 5 \pm 2 k_B T_c$, i.e. the bulk order parameter is responsible for the relaxation rate δ_{ie} of the local moments in the superconducting state.

$YbAl_2$ has an anomalously large electronic specific heat coefficient $\gamma \approx 17\,mJ/mol\,K^2$. This may indicate an intermediate valence state in $YbAl_2$ at low temperatures. Furthermore all dialuminides show bottleneck behavior in the Gd and Eu ESR experiments and hence allow to determine the relaxation rate δ^0_{eL}. Levin et al. (1982) investigated $YbAl_2$:R (R = Nd, Eu, Gd, Dy, Er) and reported the observation of bottleneck situations for Eu and Gd as ESR probes. They broke the bottleneck by the addition of nonmagnetic thorium ions or by diminution of the Gd and Eu concentration and reached the isothermal limits: $\Delta g_0 = +0.09 \pm 0.01$ and $d\Delta H/dT = 25 \pm 5\,G/K$ for Gd and $\Delta g_0 = +0.06 \pm 0.01$ and

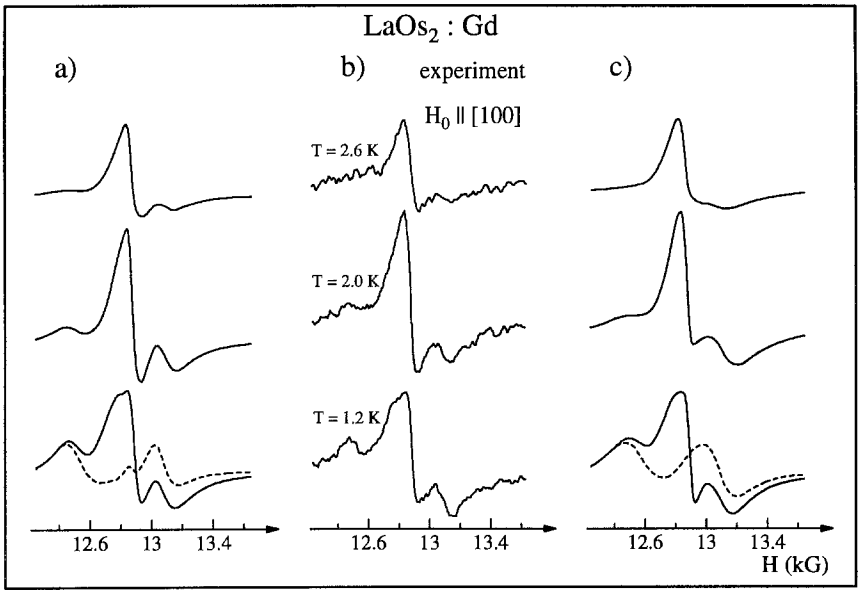

Fig. 10. Crystal-field splitting of the Gd-resonance line in $LaOs_2$ at various temperatures below the superconducting phase transition. The experimental values (b) are compared with simulated spectra using different values of δ_{eL}/T (a and c). From Luft and Baberschke (1981).

$d\Delta H/dT = 28 \pm 5$ G/K for Eu. Taking into account the theoretical expressions for the bottleneck case, the experimental results, e.g. for Δg as a function of the Th-concentration, were fitted with one free parameter, δ^0_{eL}, only. Hence, it was possible to determine the rate for the relaxation from the conduction electrons to lattice, yielding $\delta^0_{eL} = 50 \pm 20 \times 10^{11}\ s^{-1}$ for Gd^{3+} and $\delta^0_{eL} = 35 \pm 15 \times 10^{11}\ s^{-1}$ for Eu^{2+}. A comparison with δ^0_{eL} values of other dialuminides (e.g. $Lu_{1-x}Gd_xAl_2$: $\delta^0_{eL} = 43 \pm 16\ s^{-1}$, Chock et al. 1977) shows that in $YbAl_2$ charge fluctuations are not very important. The remarkable variation of δ^0_{eL} from $ScAl_2$ to $LuAl_2$ can be explained by the difference of the scattering cross-section for conduction-electron spin-flip relaxations on the R ion in RAl_2, only. The exchange parameters have been extracted from the thermal broadening of the ESR lines in the isothermal limit of various $YbAl_2$:R samples (fig. 11). The exchange parameters clearly decrease with increasing 4f occupation number in the first half of the lanthanide series and remain almost constant in the second half. This behavior seems to be quite general (Barberis et al. 1978, 1981a,b, Dokter et al. 1977) and is in agreement with theoretical predictions from Watson et al. (1965).

In a detailed investigation Döbler et al. (1983) reported on ESR in Er-doped YAl_2 single crystals. An almost perfect analysis of X- and Q-band data was achieved when the admixture of the first excited state, $\Gamma_8^{(2)}$, into the ground state, $\Gamma_8^{(3)}$, via the Zeeman interaction was taken into account. Using this analysis the full angular dependence of all observed transitions can be explained. The energy distance between $\Gamma_8^{(2)}$ and $\Gamma_8^{(3)}$ amounts to 17 K and one observes three allowed transition within the ground state quartet

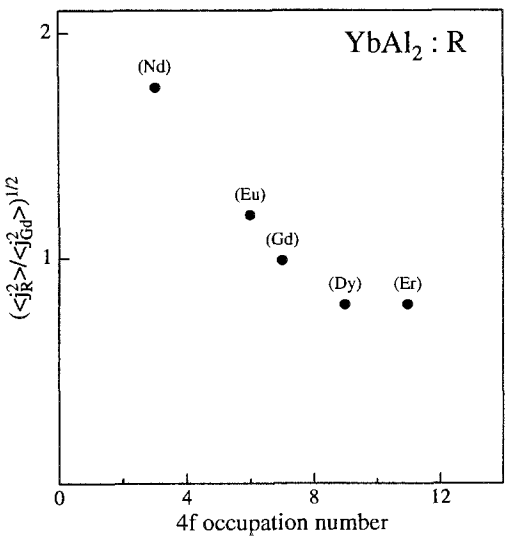

Fig. 11. The exchange parameters for various R ions (normalized with respect to Gd) vs the 4f occupation number as observed by ESR experiments in $YbAl_2$. The exchange parameters were extracted from the Korringa broadening in the isothermal limit (Levin et al. 1982).

($\Gamma_8^{(3)}$). The authors were able to determine the LLW parameters, $x = -0.332 \pm 0.02$ and $W = -0.29 \pm 0.02$ K. It is important to notice that due to a careful single-crystal preparation the residual linewidth for the ESR transitions was quite small (e.g. $\Delta H_0 \approx 1$ G for the $2 \leftrightarrow 3$ transition in the $\Theta \approx 0°$ position).

Barberis et al. (1979a) made a careful and detailed study of the ESR on powdered samples of various intermetallic compounds of AB_2 cubic structure where B = Ir, Pt or Rh and A is a nonmagnetic ion (La, Ce^{4+} or Y). The Gd^{3+} ESR spectra exhibit a single isotropic line with a slightly positive g-shift with respect to the insulator value $g = 1.993$. One exception to this behavior was found in $LaIr_2$(Gd), where a clear negative g-shift, $\Delta g = -0.013 \pm 0.005$, has been observed. The linewidth follows a Korringa law without indication of any bottleneck behavior. The parameter R (see Seipler and Elschner 1975) which gives the ratio of the exchange parameters as extracted from the linewidth and the g-shift, is larger than 10. This indicates that the results cannot be described by a single-band model. A multiband model with different competing mechanisms yielding different signs has to be invoked. It gives a resulting g-shift which is almost zero, but yields a finite thermal broadening. The detailed discussion is based on a preprint by Troper et al. (1979). Unfortunately, due to the numerous free parameters which are not known precisely, a clear separation between the various exchange mechanisms ($J_A^{(d)}$, $J_B^{(d)}$ and $J^{(s)}$) is not possible. The Nd-hyperfine constants in these AB_2 compounds are 5 to 6% smaller compared to the corresponding values for CeO_2. Probably the 6s electrons are responsible for the observed negative contribution to the hyperfine field. The authors were able to relate the observed g-shift to exchange-transfer processes of electrons having d-character from the B site into bonding orbitals at the A site. The larger this charge transfer, the less negative is the g-shift and the larger will be the stability of the compound.

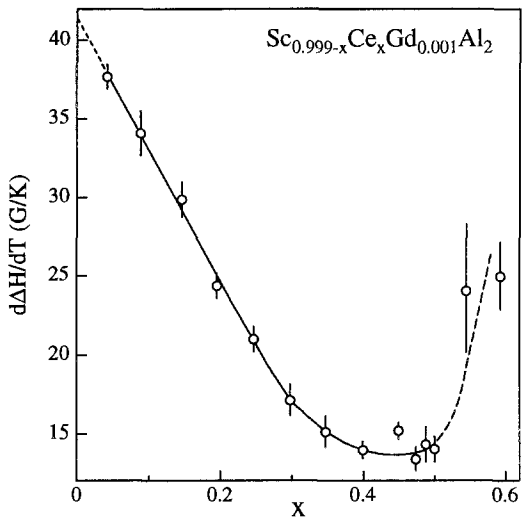

Fig. 12. Korringa slopes for the Gd resonance as observed in $Sc_{1-x}Ce_xAl_2$(Gd) vs the cerium concentration x. In this compound the valency of Ce can be changed continuously by varying the Ce content. Neutron scattering experiments and susceptibility measurements indicate an intermediate valence state of Ce for concentrations $0.05 < 0.4$ (Preusse et al. 1981).

The spin-flip scattering of conduction electrons by Ce ions was measured by Rettori et al. (1975a) via the ESR bottleneck which is active in the compounds $LuAl_2$:Gd and YAl_2:Gd doped with cerium. Similar investigations were reported in a paper by Preusse et al. (1981).

$Sc_{1-x-y}Ce_xGd_yAl_2$ intermetallic compounds reveal bottleneck behavior for $x \leqslant 5\%$. The isothermal values can be extrapolated according to $b = 42 \pm 5$ G/K and $\Delta g_0 = 0.089 \pm 0.006$. With higher Ce-concentrations ($x > 5\%$) the line shape differs systematically from the Lorentzian shape and the authors used a superposition of two lines to fit the experimentally observed resonance lines. The two lines differ substantially in linewidth but they exhibit almost the same resonance field. The narrow line is attributed to the Gd ions at lattice sites with all next-nearest neighbors being Sc ions and no Ce ions. In fig. 12 the Korringa slope of this narrow line is plotted as a function of the Ce concentration x. For $0.05 \leqslant x \leqslant 0.45$ the Korringa slopes decrease with increasing Ce concentration. For these concentrations the residual linewidths slightly decrease. In this regime the Ce ions are assumed to be in an intermediate-valence state, similar to the observations in $CePd_3$. For $x > 0.5$ the linewidth increases rapidly and the Korringa slope starts to increase again, both facts indicating the appearance of Ce^{3+}-ions with stable magnetic moments.

AB_2 intermetallic compounds (A = Y, La, Ce, Lu; B = Ir, Rh) with Gd^{3+} and Nd^{3+} as ESR probes were investigated by Dokter et al. (1977). The measurements were performed on powdered samples in the X-band in the temperature range $1.4 \leqslant T \leqslant 4.1$ K. In all compounds investigated, Nd^{3+} has a Γ_6 crystal-field ground state. The hyperfine satellites due to ^{143}Nd ($I = \frac{7}{2}$) and ^{145}Nd ($I = \frac{7}{2}$) isotopes with natural abundances are clearly resolved. Taking second-order hyperfine splitting into account the data could well be described and the fitting procedure yielded the ^{143}Nd hyperfine constant, $A = 210 \pm 10$ G.

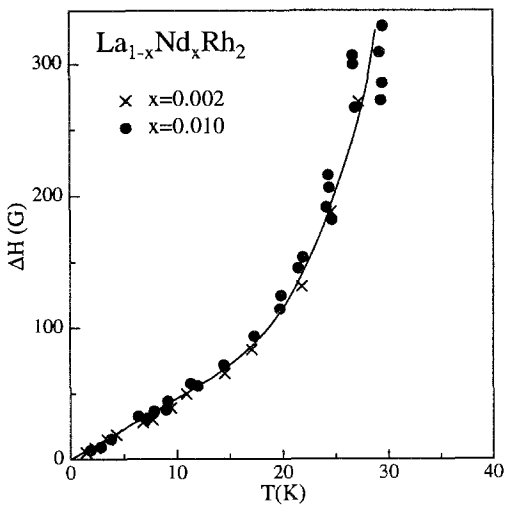

Fig. 13. Temperature dependence of the Nd ESR linewidth in $LaRh_2$ for two concentrations of the ESR probe. The residual linewidths have been subtracted. The solid line is a fit using eq. (26) with the parameters $b = 4.5$ G/K, $c = 140$ G/K and $\Delta = 135$ K. From Dodds et al. (1978).

The Nd^{3+}-lines exhibit a much larger thermal broadening than the Gd^{3+} resonance absorption, e.g. $LuIr_2$ (800 ppm Nd) revealed a Korringa slope $b = 16 \pm 2$ G/K, compared to only 3.5 ± 2 G/K observed in $LuIr_2$ (1000 ppm Gd). Using the standard equations for exchange-induced thermal broadening, one can derive the ratio of the exchange parameters: $\langle J^2 \rangle_{Nd} / \langle J^2 \rangle_{Gd} \approx 5$ for $LuIr_2$. The authors assumed that the large magnitude of J(Nd) might be associated with the large radius of the $Nd^{3+}(4f)^3$ shell leading to a large overlap between the host d-electrons and the Nd(4f) electrons or with a large covalent mixing.

The first ESR observation of Nd^{3+} in a cubic metal ($LaRh_2$) was reported by Dodds et al. (1978). The resonance arises from a Γ_6 ground state ($g_{exp} = 2.63 \pm 0.01$, independent of the Nd concentration). At 1.5 K and low Nd concentrations the hyperfine structure of ^{143}Nd and ^{145}Nd was observed. The resulting spectrum can well be described by the Breit–Rabi formula, yielding $A(^{143}Nd) = 212 \pm 1$ G and $A(^{145}Nd) = 131 \pm 1$ G. These A-values are somewhat larger than those observed in insulating CeO_2. For temperatures $T > 12$ K, the linewidth increases exponentially as a function of temperature due to resonant phonon-relaxation processes (Orbach processes) (fig. 13). The data can conveniently be described by the function

$$\Delta H - \Delta H_0 = b \cdot T + c \cdot \frac{\Delta}{\exp(\Delta/T) - 1}. \tag{26}$$

Here Δ is the energy of the excited state relative to the ground state. The data for $LaRh_2$ are accurately described using $b = 4.5 \pm 0.2$ G/K, $c = 120 \pm 40$ G/K and $\Delta = 125 \pm 10$ K (see the solid line in fig. 13). The observed g-shift relative to $g(\Gamma_6) = 2.67$, is $\Delta g = -0.037 \pm 0.01$ (i.e. -1.4%).

Normally a bottleneck situation in the relaxational behavior can be expected when the impurity and conduction-electron g-values are almost equal. If the g-values are different,

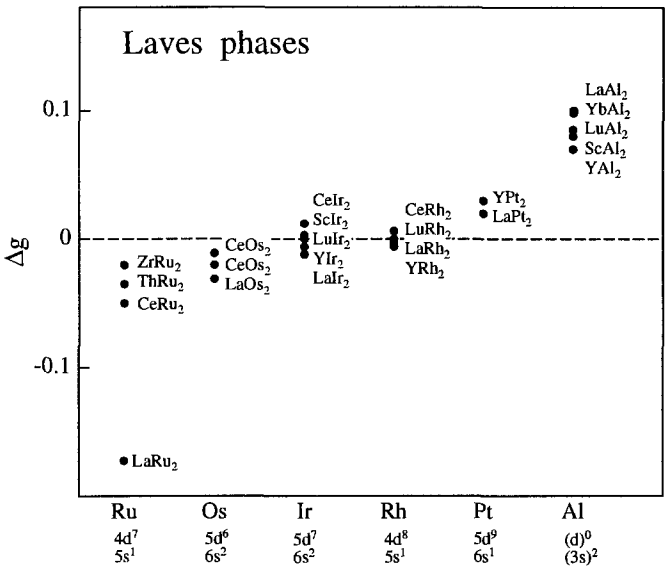

Fig. 14. Experimentally observed g-shift for Gd^{3+} in AB_2 Laves compounds.

as is the case for Nd^{3+} in a metal, it is still possible to estimate the effect of the coupling of the conduction electrons on the impurity resonance (Dodds et al. 1978). Barberis et al. (1981a) demonstrated the existence of the bottleneck effect in the relaxation mechanism of Nd^{3+} in $LuRh_2$, a d-band intermetallic compound. The extracted value of δ_{eL} is smaller than those observed for the analogous s-band compounds. The absence of any deviation from linearity of the linewidth versus temperature strongly supports the idea that the resonance properties are unaffected by the presence of excited CF levels. ESR of gadolinium and neodymium in RCo_2 and RNi_2 (R = Sc, Y, Zr, Lu and Ce) were reported by Donoso et al. (1981). The Gd resonance in RCo_2 compounds exhibits large and negative g-shift ranging from $\Delta g = -0.17 \pm 0.04$ for $CeCo_2$ to $\Delta g = -0.44 \pm 0.1$ in $LuCo_2$. The Gd g-shifts in the RNi_2 compounds are slightly positive and significantly smaller than those observed in the RCo_2 hosts. The thermal broadening of the Gd ESR is larger when compared to the results obtained in RNi_2 compounds. This reflects the much higher density of states and enhancement factors in the Co-series of compounds. The authors suggest a direct 4f–3d coupling to explain the origin of internal molecular field and in this way the substantial negative g-shift. The negative Gd shift should decrease significantly upon d-band filling across the transition metal series. A similar correlation has been demonstrated by Barberis et al. (1979a) in AB_2 compounds which exhibit the Laves structure and where the B atom belongs to an element of the 4d or 5d transition metals. Figure 14 provides a survey of experimentally observed Δg-values for Gd^{3+} resonances in AB_2 Laves phases. It clearly demonstrates that the g-shift becomes increasingly positive with increasing d-band filling.

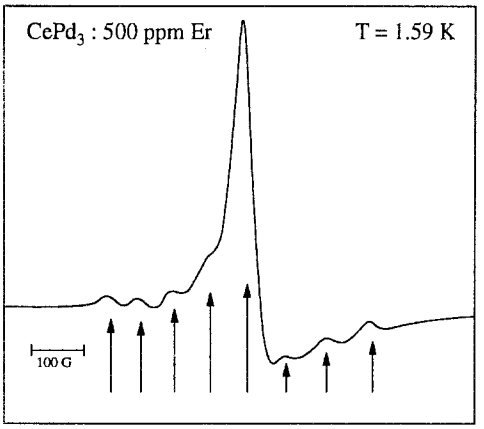

Fig. 15. ESR spectrum of $CePd_3$ (500 ppm Er) at X-band frequency and 1.59 K. The arrows indicate the hyperfine components of ^{167}Er. From Gambke et al. (1983).

A detailed investigation of the ESR in intermetallic compounds with $AuCu_3$ structure was published by Gambke et al. (1983) They report ESR results of Gd^{3+}, Er^{3+} and Yb^{3+} in powdered samples of RPd_3 (R = Sc, Y, La, Ce and Lu) and in $CeRh_3$. X-band measurements were carried out between 0.6 and 40 K. Below $T = 1.6$ K, a continuously working ^3He cryostat has been used. The Gd resonance in $ScPd_3$ and YPd_3 shows a weak bottleneck behavior. In $CePd_3$ the Er resonance originates from a Γ_7 ground state with $g = 6.78$ and a well-resolved hyperfine structure (fig. 15). In $ScPd_3$ and YPd_3 the Er ions have a Γ_6 ground state, possibly affected by an anisotropic Γ_8 quartet and an excited Γ_7 crystal field level. Yb^{3+} resonances were observed in all RPd_3 compounds and in $CeRh_3$ with a Γ_7 ground state. In order to extract the linewidth, a detailed analysis of the Yb^{3+} spectra has been carried out taking into account both isotopes ^{171}Yb and ^{173}Yb. It has been found that third-order corrections are important to determine the hyperfine constant of ^{171}Yb. This contribution is noticeable since the resonance field H_0 of the central line is relatively low. The experimentally observed spectrum of YPd_3:Yb, together with the results of model calculations, is shown in fig. 16. At temperatures above 6 K a pronounced deviation from the linear thermal broadening was observed for all compounds studied. As a representative example in fig. 17 the thermal broadening is shown for $ScPd_3$:Yb for different Yb concentrations. An accurate analysis of the spectra was carried out. The solid line in fig. 17 represents a fit of eq. (26) to the experimental data. The values for b and ΔH_0 were determined independently by measurements in the temperature range $0.8 < T < 4.2$ K. Table 3 shows the values obtained for Δ and c, when eq. (26) is fitted to the experimental results obtained for RPd_3 and $CeRh_3$. In the cases of $Y_{1-x}Er_xPd_3$ and $Sc_{1-x}Er_xPd_3$ ($x = 3000$ ppm) a double resonance line has been obtained (fig. 18), in agreement with earlier findings of Rettori et al. (1981) for the system $Y_{1-x}Er_xPd_3$. The ratio of the intensities of the two components depended on the temperature. The g-value, $g \approx 6.0$, for the component which dominates at the lowest temperature is compatible with a Γ_6 ground state, whereas the g-value, $g \approx 6.7$, for the component which appears at higher temperature indicates an excited Γ_7 state. The resulting R-values amount to $R \approx 0.2$ for

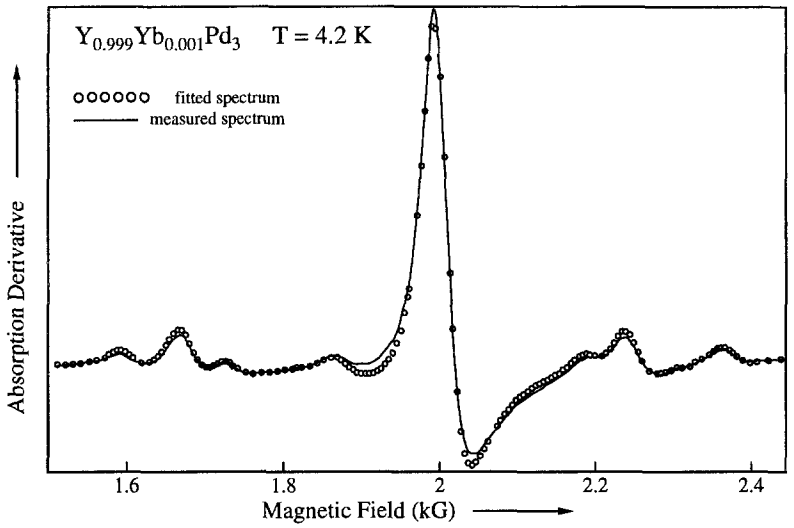

Fig. 16. Yb ESR spectrum of YPd_3 at X-band frequency. The satellites belong to the isotopes of Yb. A model (open symbols) including the third-order hyperfine splitting was used to describe the experimentally observed spectra (solid line). From Gambke et al. (1983).

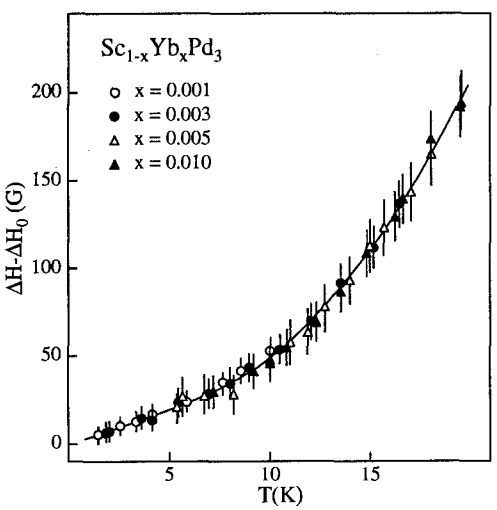

Fig. 17. Temperature dependence of the linewidth of the Yb ESR absorption in $ScPd_3$ for different Yb concentrations. The solid line represents a fit using eq. (26). From Gambke et al. (1983).

all $R_{1-x}Gd_xPd_3$ samples (table 4). This fact demonstrates that the conduction electrons at the Fermi surface have predominantly d-character and originate from Sc, Y, and La sites. A predominant d-contribution from Pd sites would have the consequence of an additional negative contribution to Δg (i.e. larger R values).

Table 3
CF parameter Δ and constant c extracted from a least-squares fit of the experimental values to eq. (26) in a series of compounds with Cu_3Au structure (Gambke et al. 1983)

Compound	Δ (K)[a]	$10^{-3}c$ (G)
$ScPd_3$:Yb	51±10	1.5±0.3
YPd_3:Yb	47±10	1.6±0.3
$LaPd_3$:Yb	74±12	13.4±2.0
$CePd_3$:Yb	57±10	3.5±0.8
$LuPd_3$:Yb	39±10	1.4±0.3
$CeRh_3$:Yb	44±10	0.9±0.2

[a] Δ, the Γ_7–Γ_8 level splitting.

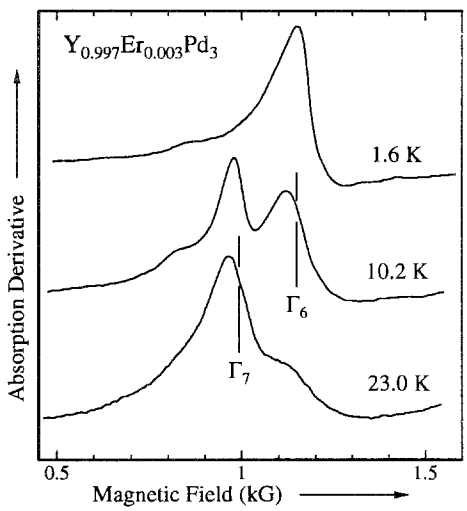

Fig. 18. Er ESR spectrum in YPd_3 at different temperatures. The positions of the crystal field levels, Γ_6 and Γ_7, are indicated. The relatively broad lineshapes prevent the observation of the hyperfine components (Gambke et al. 1983).

In a large number of compounds the exchange parameters for R-conduction electron exchange are systematically larger for Nd^{3+} than that for Gd^{3+} impurities (Barberis et al. 1979a). This was attributed to the larger ionic radius of Nd^{3+} as compared with that of Gd^{3+}. Stein et al. (1981) confirmed this rule giving a further example: $Zr_{1-x}R_xIr_2$ ($R=Nd^{3+}$, Gd^{3+}). The measured g-value for Nd at low concentrations is close to that expected for a Γ_6 doublet ($g=2.667$). The thermal broadening of the linewidths for Nd^{3+} and Gd^{3+} are 90±20 G/K and 7±2 G/K, respectively. Considering the different g_J factors for Nd^{3+} and Gd^{3+} the authors obtain the ratio of the exchange parameter from the ratio of the Korringa slopes:

$$\frac{J^2_{\text{Nd–Ce}}}{J^2_{\text{Gd–Ce}}} = 15\pm4.$$

Table 4
Residual linewidth ΔH_0, Korringa slope b, g-shift, and Korringa ratio R as determined from the linewidth broadening of Gd^{3+} in MPd_3 for temperatures $2\,K \leqslant T \leqslant 50\,K$ (M = Sc, Y, La, Lu, Ce)[a]

Compound	x (%)	ΔH_0 (G)	b (G K^{-1})	Δg	R
$Sc_{1-x}Gd_xPd_3$	0.01	73	5.2±0.3	0.030±0.003	0.25
	0.1	76	4.3±0.6	0.025±0.003	
	1	90	2.2±0.3	0.016±0.003	
$Y_{1-x}Gd_xPd_3$	0.05	43	4.0±0.3	0.028±0.003	0.22
	0.1	37	4.0±0.3	0.026±0.003	
	1	82	3.1±0.3	0.015±0.003	
$La_{1-x}Gd_xPd_3$	0.025	42	2.0±0.1	0.021±0.002	0.19
	0.05	66	2.3±0.3	0.020±0.002	
	0.1	105	1.3±0.5	0.018±0.004	
	1	85	1.6±0.3	0.010±0.003	
$Lu_{1-x}Gd_xPd_3$	0.05	52	4.7±0.3	0.031±0.003	0.21
	0.25	76	4.4±0.3	0.028±0.003	
	1	93	4.0±0.3	0.025±0.003	
	2	208	3.9±0.3	0.029±0.003	
$Ce_{1-x}Gd_xPd_3$	0.1		0.4–2.1	0.032	

[a] From Gambke et al. (1983).

Finally, Kim and Karra (1977) provided experimental evidence of the sensitivity of ESR investigations to characterize sample qualities. These authors investigated the Korringa slope and g-shift of $La_{1-x}Gd_xPd_3$ as a function of the annealing temperature. The different annealing temperatures (1010 and 1110 K) seem to have significant effects on the structural composition of the lattice, yielding significant changes in the ratio δ_{eL}/δ_{ei}. The experimental results indicated that the samples annealed at 1000 K have a higher degree of long-range order and reveal a higher homogeneity than those annealed at 1100 K.

5.2. *Lanthanide ions as ESR probes in monochalcogenides and monopnictides*

The monochalcogenides RB (R = Sc, Y, La, Tm; B = S, Se, Te) and the monopnictides RZ (R = Sc, Y, La; Z = P, As, Sb, Bi) crystallize in the cubic NaCl structure (with the exception of ScTe which is hexagonal). Lanthanide ions (3+) are quite soluble in these materials and most of them are good ESR probes. The monochalcogenides and the heavy monopnictides of the trivalent rare earths are known to be intrinsic metallic conductors (Gambino et al. 1971). Their density of states at the Fermi energy is generally low enough to observe a resolved crystal-field splitting to be fulfilled quite easily. Furthermore, it is not too difficult to get good single crystals from these materials. Hence, the metallic or semimetallic compounds RB and RZ doped with lanthanide ions seem to be good candidates for ESR investigations with the aim to study the ground state symmetry, the exchange interaction between 4f ions and conduction electrons and the details of the

exchange narrowing process. These experimental results can be compared with the well-known theories of S.E. Barnes (1974) and Plefka (1973). Finally, the influence of higher crystal-field levels on the ESR spectra of the ground state can be investigated.

5.2.1. *Monochalcogenides*

Urban et al. (1974a,b) investigated the polycrystalline metallic compounds $Gd_xY_{1-x}S$ and $Gd_xLa_{1-x}S$ covering the complete Gd-concentration regime from $0.001 \leqslant x \leqslant 1$. They provided experimental evidence for the existence of an exchange interaction between conduction electrons and localized 4f moments in these sulphides. The x dependence of the Korringa slopes and of the g-values unambiguously demonstrates the occurrence of a bottleneck situation. In comparison with metallic GdS the linewidth in the insulating EuS shows no temperature dependence in the range $100 < T < 500$ K. Guided by the fact that the bottleneck is so dominant in the two systems, the authors proposed an s–f exchange interaction with an estimated exchange constant $J_{sf} > 0.04$ eV.

A true textbook example demonstrating the effects arising from the interactions between the band states and the 4f electrons has been published by Salomons et al. (1974). The system La_2S_3 is a good insulator. In contrast, isostructural La_3S_4 behaves metallic with one conduction electron per unit cell. As a consequence the Gd^{3+} ESR in La_3S_4 yields a Korringa-type of behavior of the linewidth with a Korringa slope $b = 2.35$ G/K, whereas the Gd linewidth in La_2S_3 is temperature independent (fig. 19). The residual linewidth in both systems is the same and amounts to $\Delta H_0 = 180$ G.

Upon rotating the magnetic field in the (011) plane of a single crystal of LaS doped with 2000 ppm Er, Bloch et al. (1982) found an angular-dependent linewidth. They assumed a Γ_7 ground state of Er^{3+} followed by a $\Gamma_8^{(1)}$ excited state. Internal strains of Γ_3 type are coupled to the lanthanide ions via magnetoelastic effects. The spin Hamiltonian

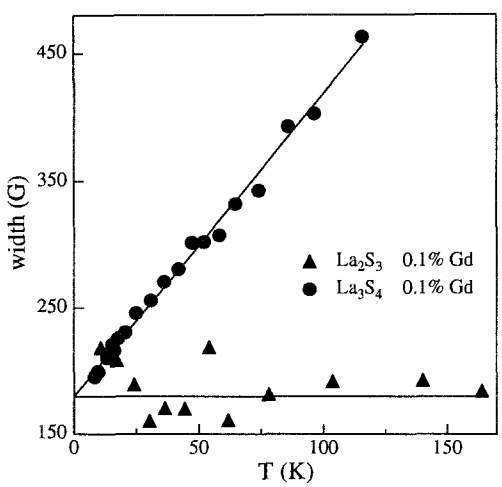

Fig. 19. Temperature dependence of the Gd linewidth in insulating La_2S_3 (0.1% Gd) and in metallic La_3S_4 (0.1% Gd). From Salomons et al. (1974).

contains the Zeeman effect, cubic crystal-field terms and the ion–lattice coupling. The diagonalization yields the energy splitting of the ground-state doublet influenced by the admixture with the $\Gamma_8^{(1)}$ excited state. This admixture is sensitive to the presence of strains and external magnetic fields. From this analysis the following expression for the second moment $\langle\omega^2\rangle$ of the ESR linewidth, as function of the magnetic field can be derived

$$\langle\omega^2\rangle = A(3\cos^2\Theta - 1)^2 + B. \tag{27}$$

For LaS:Er the fit of eq. (27) to the experimental results yielded $A = 350\,\mathrm{G}^2$ and $B = 4225\,\mathrm{G}^2$. The positive value of A indicates that Γ_3 modes are the dominant stress modes in this case.

Early ESR data on LaSb:Dy were reported by Davidov et al. (1975b) and Oseroff and Calvo (1978). The results were interpreted by a random stress model and were evaluated by second-moment calculations. The resulting A-value is much higher compared to that observed on LaS:Er. The ESR line of the Γ_6 ground state of dysprosium shows a broad asymmetrical structure and therefore the second-moment analysis can be a first approximation only.

5.2.2. *Monopnictides*

5.2.2.1. *Ce^{3+}*. Davidov et al. (1974a,b) reported the first observation of a Ce^{3+} resonance in metallic hosts (LaSb:Ce and YSb:Ce). The observed resonance absorption was interpreted as a Γ_7 ground-state doublet. The experimentally observed g-value amounted to 1.43 ± 0.02, close to the theoretical value, $g(\Gamma_7) = 1.43$. Two years later Sugawara and Huang (1976a) published a more detailed investigation of Ce^{3+} in LaX (X = P, As, Sb). Again they found g-values near the theoretical value of a Γ_7 ground state. In addition they followed the temperature dependence of the linewidth and found a sharp increase of the linewidth for $T > 10\,\mathrm{K}$. Following Hirst (1969), they assumed a multilevel system and fitted the experimental data using eq. (26).

The constants b and c which enter into eq. (26) are related to the strength of the s–f-interaction, to the conduction electron density of states and to the appropriate matrix elements (Rettori et al. 1973a). Δ is the energy difference between the ground state and the first excited state. The Δ values, as determined via eq. (26) seem reasonable since similar values for the energy splitting of the CF levels were obtained from correlations of Δ with the lattice constant (see later). This is true despite the fact that Orbach processes have been neglected (Rettori et al. 1973a).

Wienand et al. (1982) worked extensively on cerium-based monopnictides. They combined temperature dependent measurements of the susceptibility, resistivity and ESR on powdered samples of RZ (R = Sc, Y, La; Z = Sb, Bi) and on YAs, containing small amounts of cerium ions. In addition to the already known Ce resonances they found well-defined resonance absorptions in LaBi, YAs and YBi. The absorption lines were characteristic of a Γ_7 ground doublet, with $g(\Gamma_7) = 1.42\pm0.02$. ScSb and ScBi did not show any indications of a cerium resonance. The model of Takegahara et al. (1981), which explains the surprisingly small crystal-field splittings of some monopnictides, inspired

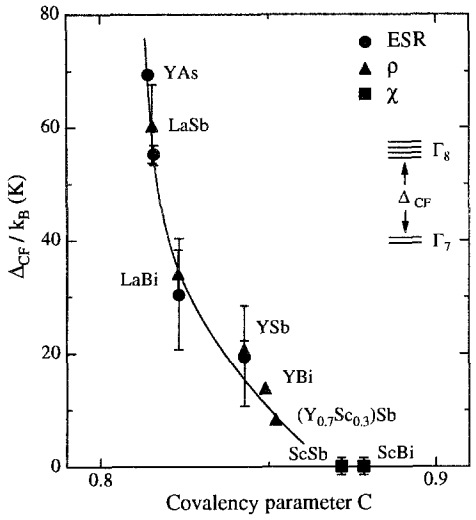

Fig. 20. Crystal-field splitting of the Ce^{3+} ground state multiplet as a function of the "covalency parameter" for various Ce-doped monopnictides. ESR results (circles) are compared with those obtained by resistivity (triangles) and susceptibility (squares) measurements. From Wienand et al. (1982).

Wienand et al. (1982) to propose and to test the correlations between the energy distance $\Delta \equiv E(\Gamma_8) - E(\Gamma_7)$ and the phenomenological "covalency parameter" of the host lattice, as defined by Hannay and Smyth (1946):

$$C = 1 - 0.16(\chi_Z - \chi_R) - 0.035(\chi_Z - \chi_R)^2, \tag{28}$$

where χ_Z and χ_R are tabulated values of the electronegativity for the insulating compounds Z and R. $C \approx 1$ characterizes a bond between Z and R which is exclusively covalent in nature. The covalent bonding of the host ions will influence the crystal field which is experienced by the Ce^{3+} ions. With increasing covalency of the host, the strength of the point charges decreases, yielding smaller CF splittings Δ. Figure 20 shows a significant correlation of the covalency parameter with the CF splitting. The Δ-values range between $\Delta \approx 70\,K$ for YAs:Ce and $\Delta \leqslant 1\,K$ for ScSb:Ce. The small Δ-values for the Sc compounds may be the reason that in these compounds an ESR-signal is not observable. The covalent bonding between Ce and the surrounding ions obviously does not play the dominant role. This can be concluded from the fact that in all compounds the experimentally observed $g(\Gamma_7)$ value for Ce^{3+} coincides with the theoretical value within the estimated experimental uncertainties (± 0.02).

5.2.2.2. *Dy^{3+}*. Davidov et al. (1974a,b) investigated the Dy^{3+} resonance in LaSb and YSb (unoriented chips). A Γ_6 ground-state doublet has been detected with an experimental g-value of 6.70 ± 0.1 for LaSb, and 6.62 ± 0.01 for YSb. Theoretically one expects $g(\Gamma_6) = 6.67$. This observation is consistent with positive values for both $A_4\langle r^4 \rangle$ and $A_6\langle r^6 \rangle$, the fourth-order and sixth-order crystalline field parameters, respectively (Lea et al. 1962). It can be calculated within a simple point-charge model for octahedral symmetry with negative charges on the ligands and no screening effects at the cerium site.

Bloch and Davidov (1982) investigated LaSb:Dy^{3+} single crystals. Their results support the hypothesis that Γ_3 strains (see, e.g., Bloch et al. 1982) play the most important role for the linewidth variation. The authors calculate the free energy as a function of strains and provide strong evidence for a "single ion" Jahn–Teller effect at low temperatures. Combined ESR and magnetization measurements provided detailed information about the coupling constant between the Dy^{3+} ion (Γ_6 ground state) and the Γ_3 strain modes $|V(\Gamma_3)| = 24$ K.

5.2.2.3. *Er^{3+}*. Davidov et al. (1974a,b) report on ESR investigations of Er^{3+} in YSb, LaSb, LuSb, LaBi and LuBi. They used single crystals and microwave frequencies of 20 GHz. The nominal Er concentrations were 2000 and 500 ppm. All samples showed a strong Er resonance with a pronounced angular dependence. The observed line was identified as the $\frac{1}{2} \leftrightarrow -\frac{1}{2}$ transition of the effective spin $S = \frac{3}{2}$ in the $\Gamma_8^{(1)}$ spin Hamiltonian. The fit to the angular dependence of the resonance field yielded positive values for both $A_4\langle r^4\rangle$ and $A_6\langle r^6\rangle$, again in agreement with the simple pc model. The observed hyperfine lines associated with the ^{167}Er isotope ($I = \frac{7}{2}$) provided experimental evidence that the anisotropic line was associated with Er^{3+} at a cubic site.

5.2.2.4. *Yb^{3+}*. Yb^{3+} as an impurity in monopnictides was found to give rise to a single line which is associated with a Γ_6 ground state, with a theoretically predicted g-value, $g(\Gamma_6) = 2.67$ (Davidov et al. 1974a,b, Wienand et al. 1982). The difference between experimental and theoretical g-values is larger than in the case of Ce^{3+},which has been discussed before: $g = 2.45$ in YSb, 2.50 in LaSb and 2.53 in YAs and is always negative. It is likely that the covalency between Yb^{3+} and its neighboring ions is more pronounced as in the case of Ce^{3+}. But again, the covalency parameter C, as defined in eq. (28) is an appropriate variable in considering g-values and Korringa slopes (fig. 21). The thermal broadening of the ESR line is strictly linear in temperature and no second line occurs up

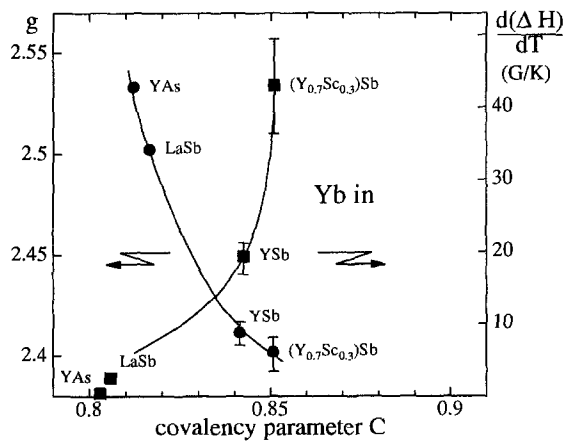

Fig. 21. Korringa slopes (right scale) and g-values (left scale) of the Yb^{3+} resonance absorption Γ_6 vs the "covalency parameter" as observed in YAs and in some yttrium antimonides. From Wienand et al. (1982).

to 20 K. So the next higher crystal-field levels (Γ_8, Γ_7) are at least 100 K above the Γ_6 ground state, in agreement with the resistivity results.

5.2.2.5. *Gd^{3+}*. Gd^{3+} has been the most investigated ESR probe in these compounds. This certainly is connected with the fact that Gd^{3+} is an S-state ion ($L=0$) and that it can easily be substituted for other 3+ ions, like La^{3+}, Sc^{3+}, etc. The phase diagrams reveal complete solubility of Gd in monopnictides (e.g., $0 \leqslant x \leqslant 1$ for $Gd_xR_{1-x}Z$). In the following, we will roughly distinguish between the two limiting cases, namely diluted systems and concentrated systems. In this section we will focus on diluted systems with Gd concentrations $x < 0.05$, only.

Davidov et al. (1974c) reported on Gd ESR on single crystals of LaSb at temperatures between 1.3 and 4.2 K at X-band frequencies. The spectra were almost completely resolved. The thermal broadening of the $\frac{1}{2} \leftrightarrow -\frac{1}{2}$ transition was measured to amount to 1.0±0.5 G/K. No significant exchange narrowing or broadening effects were found in the limited temperature range of this investigation. A fit to the spectra yielded an estimate of the fourth order cubic CF parameter $b_4 = 30 \pm 2$ G and a g-value, $g = 1.987 \pm 0.005$. Almost at the same time, Urban et al. (1974a) reported on ESR investigations of Gd-doped LaBi single crystals (500 and 1000 ppm) at 35 GHz. A representative Gd spectrum as observed in LaBi is shown in fig. 22. The spectrum is well resolved and can be described with a CF parameter $b_4 = 63.7 \pm 3.2$ G. This is one of the largest values observed for Gd^{3+} in a cubic environment. The overall zero-field splitting amounts to $32b_4 = 27$ K. With the high covalency of LaBi this result can qualitatively be understood if one considers the increase of the b_4 values with increasing covalency in insulating crystals (Title 1965).

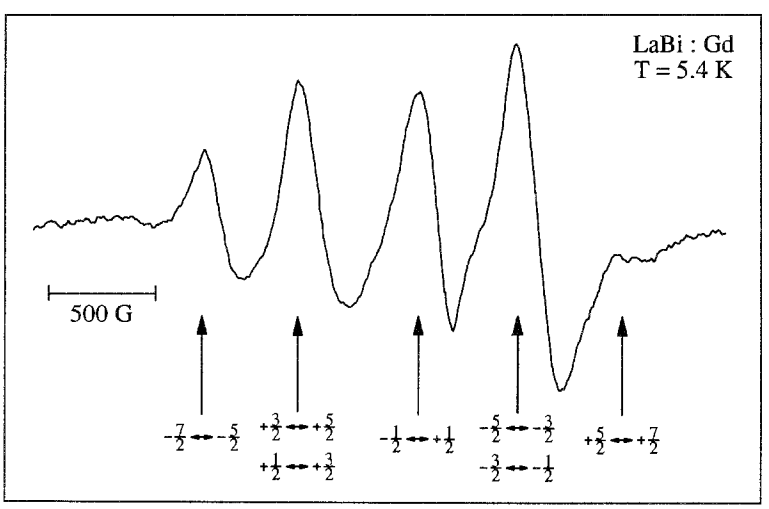

Fig. 22. ESR spectrum of LaBi doped with 1000 ppm Gd^{3+} at a measuring frequency of 34.625 GHz and at $T = 5.4$ K. The external magnetic field is parallel to [111]. The transition $-1/2 \leftrightarrow +1/2$ is superimposed by a signal at $g = 1.992$, the intensity of which strongly depends on sample preparation and aging (Urban et al. 1974a).

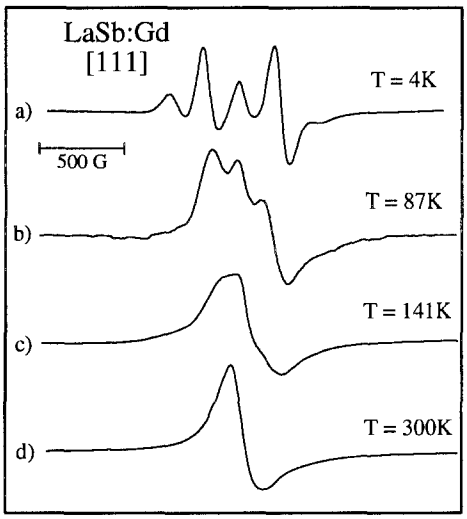

Fig. 23. Gd ESR (2000 ppm) in single crystalline LaSb at Q-band frequency and at various temperatures between liquid helium and room temperature. The spectra were taken with the external magnetic field along the [111] direction. From Urban et al. (1975).

These investigations revealed that the system $Gd_xR_{1-x}Z$ may be a prototype sample to study narrowing effects (Plefka 1973, S.E. Barnes 1974) by performing ESR experiments at higher temperatures. Urban et al. (1975) reported ESR investigations of Gd in LaSb single crystals in a wide temperature range between 1.7 and 300 K at Q-band frequencies. As the temperature is increased, exchange-narrowing effects in the ESR spectra become important. These narrowing effects manifest themselves by a complete collapse of the fine structure into a single anisotropic (Dysonian) line at high temperatures (fig. 23). The theoretical analysis shows that this behavior is in complete agreement with the theoretical predictions for exchange interaction in dilute magnetic alloys (Plefka 1973, S.E. Barnes 1974). LaSb:Gd reveals a relatively low density of states $N(E_F) \approx 0.1$ states/eV spin (Gambino et al. 1971) at the Fermi level, and concomitantly a small Korringa-relaxation rate. The relatively large b_4 value allows the observation of a "single-ion" narrowing effects over a wide temperature range. These observed narrowing effects in the ESR spectra of Gd in metals are true textbook examples. The Korringa-like thermal broadening was measured with the external magnetic field in the (110) plane, at an angle of 30° with respect to the [001] direction. At this particular orientation a single ESR line with the minimum linewidth is observed. The complete angular variation of the resonance absorption lines of Gd^{3+} in LaBi is shown in fig. 24. Here the magic angle at $\Theta = 30°$ can well be identified. At high temperatures, the two samples (with 250 and 2000 ppm Gd) revealed the same Korringa slope $b = 0.19 \pm 0.03$ G/K. The independence of the slope from concentration of the ESR probe indicated the absence of a bottleneck effect in the relaxation mechanism. In addition, the authors measured the thermal broadening of a special fine-structure line $(+\frac{1}{2} \leftrightarrow -\frac{1}{2})$ up to 20 K. This line broadens with a slope $b = 2.0 \pm 0.5$ G/K, again in complete agreement with the theory of S.E. Barnes (1974) and Plefka (1973).

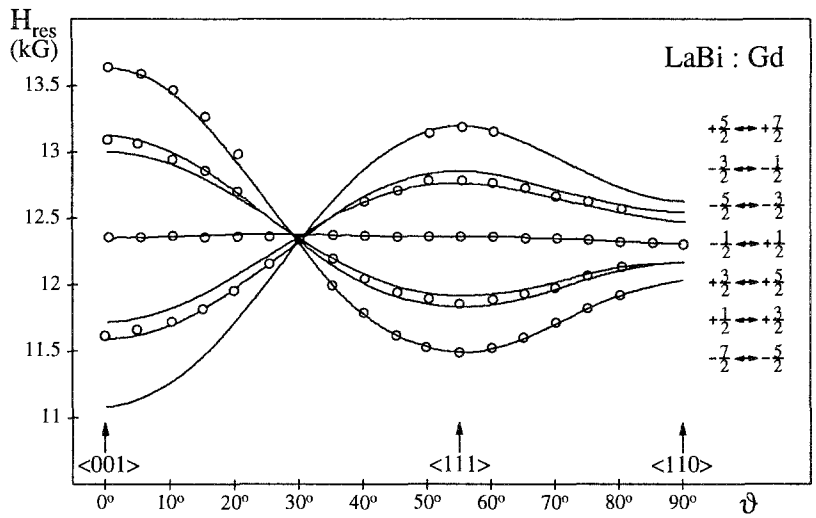

Fig. 24. Angular variation of the Gd resonance fields of the seven $\Delta M = 1$ transitions in LaBi (open circles). The solid lines were calculated using the CF parameter $b_4 = 63.7$ G, the g-value $g = 2.002$, and a frequency $\nu = 34.625$ GHz. From Urban et al. (1974a).

Baberschke and Davidov (1975) discussed the size of the b_4 parameters obtained for YSb, YBi, LaSb and LaBi in terms of a virtual-bound state model. In this model the conduction electrons of 5d character, originating from the Gd atoms, are supposed to act as screening charges and to over-compensate the influence of the ligands. In this way they offer a plausible explanation for the discrepancy of expected b_4 values and lattice parameter a_0. According to a simple point charge model, b_4 should be proportional to $(a_0)^{-5}$ in contrast to the experimental observations.

Urban and Seipler (1977) reported on a method to derive the crystal field parameter b_4 from spectra of polycrystalline samples. Figure 25 shows the CF parameter b_4 versus the lattice parameter a_0 for some oxides and monopnictides, all having NaCl structure. For the oxides the sign of b_4 is negative and decreases with decreasing lattice parameters. For the pnictides b_4 is positive and increases with increasing a_0. No statements could be made for ScSb, ScBi, LuSb and LuBi because the Gd concentrations of 1000 and 2000 ppm, used in these experiments, were too high and narrowing effects were provoked.

Davidov et al. (1974b) reported on a resolved fine-structure splitting of Gd in YSb single crystals at 1.8 K. A fit to the experimental data yielded a fourth-order CF parameter $b_4 = 29 \pm 3$ G. Some transitions appeared as overlapping lines, indicating significant exchange-narrowing effects even at this low temperature. Sugawara and Huang (1975) investigated the Gd ESR in powdered samples of monopnictides RB (R = Y; B = P, As or Sb) up to a Gd concentration $x \approx 10\%$ in a wide temperature range. The absorption lines in both compounds, YAs and YSb, reached the isothermal limit for $x < 0.01$ and they progressively became bottlenecked with increasing Gd concentrations. The maximum

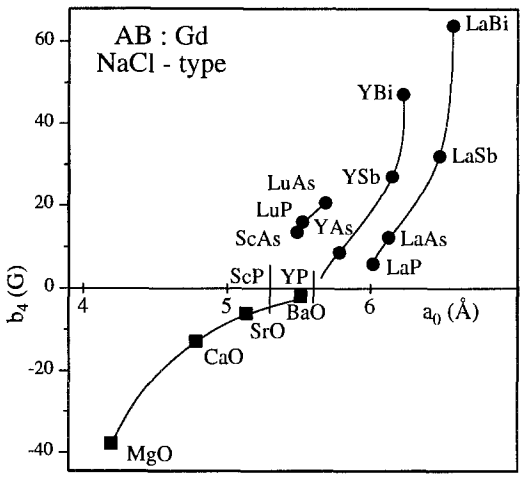

Fig. 25. Crystal-field parameters b_4 vs the lattice spacings a_0 for Gd^{3+} as ESR probe in monopnictides and in some oxides with NaCl structure. From Urban and Seipler (1977).

Korringa slopes $(d\Delta H/dT)_{max}$ reach 0.68 G/K for YSb and 0.15 G/K for YP and they increase with increasing lattice constants.

In a detailed paper, P. Urban et al. (1978) studied the linear increase of the ESR linewidth with temperature for Gd in the metallic monopnictides RB (R = Sc, Y, La, Lu and B = P, As, Sb, Bi) using both single crystals and powdered samples. The single crystals were oriented approximately 30° from the [001] direction in the (110) plane where the seven fine-structure lines almost collapse (see e.g. fig. 24). For $T > 10$ K the linewidths show a linear increase as a function of temperature. For these compounds, a remarkable correlation between lattice constants and the Korringa slopes exists. The dependence of the Korringa slopes on the lattice constants for the whole series of compounds is shown in fig. 26. This figure clearly demonstrates that, within each series and for a given rare-earth ion, the Korringa slopes increase with increasing lattice constant. The value of the Korringa slope is associated either with the variation of J_{eff} or $N(E_F)$, or with the variation of both quantities. Specific heat studies (Gambino et al. 1971, Birgeneau et al. 1973) have indicated that the Sommerfeld coefficient γ of the linear temperature term does not vary considerably across the series of host compounds. Therefore an almost constant conduction-electron density of states at E_F can be assumed. This is the reason the authors argue that J_{eff} might change appreciably across the pnictide series and is considerably dependent on the amount of overlap of the d-electron wave functions originating from the Gd site and the R site. They suggest an effective exchange interaction between the Gd 4f shell and the host d-like electrons at the Gd site.

An ESR investigation of 500 and 5000 ppm Gd in powdered LaP has performed by Bartkowski (1972) for temperatures from 2 to 300 K. Variation of the microwave power and knowledge of the microwave field are required for the saturation experiments which were conducted. The calibration is checked by saturation of DPPH at room temperature in comparison with published values of T_1. The T_1 value for Gd^{3+} in LaP is 5000 times

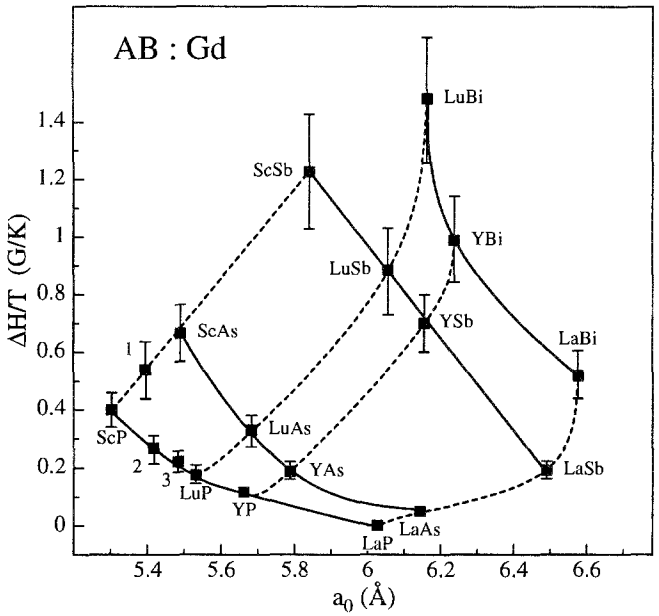

Fig. 26. Korringa slopes characteristic for Gd^{3+} ESR experiments in monopnictides as a function of the lattice parameter. The squares with numbers indicate the results for mixed compounds (Urban et al. 1978).

shorter compared with T_1 measurements of Gd^{3+} in CaF_2. A linear dependence of $(T_1)^{-1}$ over a large temperature range was found and it has been concluded that the conduction electrons are responsible for the relaxation process.

The ESR behavior of 0.1 and 1% Gd^{3+} in powdered samples of thulium monochalcogenides was investigated by Huang and Sugawara (1977). They found that Tm is trivalent, divalent, and mixed-valent in TmS, TmTe and TmSe, respectively. The temperature dependences of the linewidths and of the g-values of all three compounds are plotted in figs. 27a–f. The experimentally observed lineshapes were Lorentzian and their width changed in characteristic signatures as a function of temperature: In the case of TmS the thulium ions are trivalent with a nonmagnetic ground state and a $\Gamma_4^{(3)}$ first excited state ($\Gamma_4^{(3)} - \Gamma_1 \approx 15 \pm 3$ K). The Gd^{3+} linewidth broadens thermally activated and closely follows the thermal population of the excited magnetic states (fig. 27a). Tm in TmTe is divalent with a Γ_6 ground doublet followed by a Γ_7 doublet and a Γ_8 quartet. Using the well-established theory of Moriya and Obata (1958) for an ESR probe in a magnetically fluctuating environment, the linewidth can be approximately given by

$$\Delta H = A \cdot k_B T(\chi_T - \chi_{iso}). \tag{29}$$

The scaling factor A depends on the coupling between Gd^{3+} 4f moment and the fluctuating Tm moments and on the relaxation time τ of the Tm moments. χ_T is the isothermal

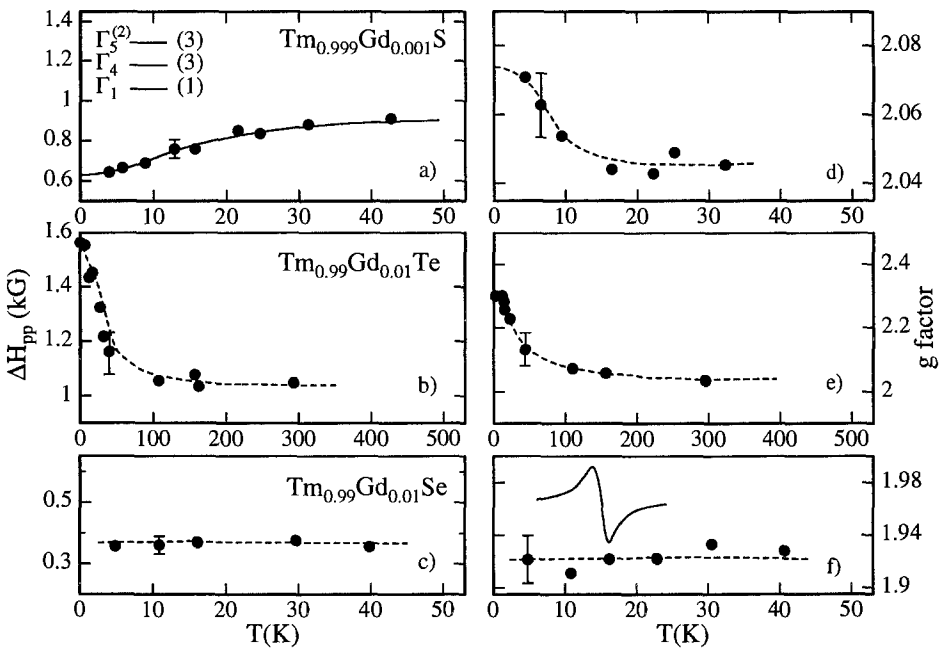

Fig. 27. Gd^{3+} ESR linewidths (peak to peak distance of the absorption derivative; left frames, a–c) and g-values (right frames, d–f) for TmS (a,d), TmTe(b,e) and TmSe(c,f). From Huang and Sugawara (1977).

susceptibility of the host-magnetic ion when the magnetic system remains in thermal equilibrium with the lattice during the measuring period. χ_{iso} is the isolated or adiabatic susceptibility which is measured when the thermal populations of the level do not vary with the static field (i.e., it measures the pure polarization effects). Using eq. (29) one expects a broad Gd^{3+} linewidth which is nearly temperature independent ($\chi_T \sim 1/T$). On the contrary, as shown in fig. 27b, the linewidth decreases drastically from 5 to 40 K. This unexpected temperature dependence is believed to originate from the presence of an "extra" electron, which results from the substitution of the divalent Tm ions of the host lattice by trivalent Gd ions. This is in analogy to the case of SmB_6 (Gd) which is described below. The presence of an "extra" electron contributes directly to the exchange interaction between Gd^{3+} ion and its surrounding Tm^{2+} ligands. At higher temperatures these "extra" electrons are delocalized, resulting in a reduction of the 4f(Gd^{3+})–4f(Tm^{2+}) exchange interaction and, hence, give rise to the narrowing of the Gd^{3+} linewidth. The linewidth (fig. 27c) and the remarkable negative g-shift (fig. 27f) for TmSe (1% Gd) are temperature independent between 5 and 300 K. One observes a single narrow line due to the extreme "motional narrowing" case. The fluctuation rate ($Tm^{2+} \leftrightarrow Tm^{3+}$) is much faster than the separation between two Gd^{3+} resonance lines.

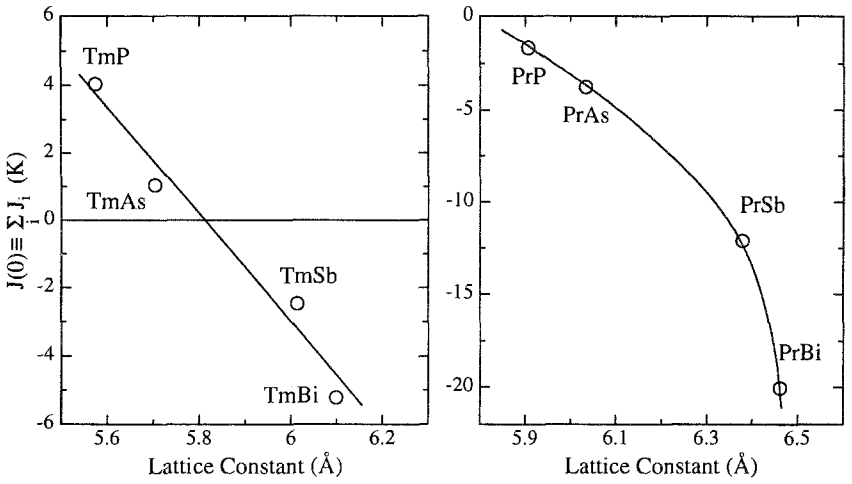

Fig. 28. Exchange interaction between the host 4f moments and the Gd spins, which are substituted as ESR probes, as a function of the lattice constant: (a) Gd–Tm exchange interaction in TmX compounds (X = P, As, Sb and Bi); (b) Gd–Pr exchange in PrX compounds (from Sugawara et al. 1975).

The singlet-ground-state systems TmB and PrB (B = P, As, Sb, Bi) diluted with Gd^{3+} as ESR probe are well suited for investigations of the Gd–Tm or Gd–Pr exchange (Sugawara et al. 1975). An analysis of the temperature-dependent g-values of Gd^{3+} directly allowed the determination of the exchange parameters. The Gd–Tm exchange changes sign with increasing lattice parameter (fig. 28), while the Gd–Pr exchange becomes increasingly negative with increasing lattice parameters. For Gd concentrations $0.1 < x < 10\%$ Gd the temperature dependence of the g-values and the linewidth were independent of Gd concentration.The linewidth of the Gd resonance is influenced by the thermal population of the excited CF states, which is similar to results obtained in the monochalcogenides (Huang and Sugawara 1977). In the case of stable Tm or Pr ions the influence of the excited CF levels yielded a strongly increasing linewidth with increasing temperature, for temperatures small compared to the energy splitting $E(\Gamma_1) - E(\Gamma_4)$. The lack of any dependence of the linewidths and the g-values on the Gd concentration indicated that the Korringa-type contributions to the temperature dependence are rather small.

In two detailed theoretical papers Sugawara (1977a,b) treated the effects of crystal fields on magnetic resonance in metals, particularly in rare-earth monopnictides with Ce^{3+}, Yb^{3+} and with the singlet-ground-state ions Tm^{3+} and Pr^{3+}. The author provided predictions of the temperature dependence of the second moments of Pr^{3+} and Tm^{3+} linewidths and discussed how the low-frequency modes of the magnetic fluctuations effect the relaxation rate of impurity ESR and host NMR. These considerations basically are founded on calculations of the second moments, for both, the combination of CF plus exchange and the magnetic fluctuations of the paramagnetic surroundings.

5.3. *Lanthanide ions as ESR probes in hexaborides*

5.3.1. *LaB_6*

The ESR on single crystals of $La_{1-x}Gd_xB_6$ ($x < 500$ ppm) has been reported by H. Luft et al. (1982). The Gd-ESR spectrum consists of one single resonance line. The linewidth and the resonance position are angular and temperature dependent due to the influence of the fourth-order crystal field. The temperature dependence of the linewidth at the "magic" angle, $\theta = 30°$ (θ denotes the angle between the external magnetic field and the [001] direction), exactly obeys a Korringa law with a Korringa slope $b = 9 \pm 0.5$ G/K and a residual linewidth $\Delta H_0 = 10$ G (200 ppm) and 17 G (433 ppm) in the temperature range $1 < T < 4$ K. Despite the lack of a well-resolved spectrum the authors were able to extract a b_4 value from the angular dependence of the linewidth: $b_4 = +12 \pm 3$ G, a remarkably large value, but positive in sign, in agreement with most of the published b_4 parameters of Gd in metals.

The same authors (Luft et al. 1983) communicated on ESR investigations of $La_{1-x}Er_xB_6$ ($x = 0.001$ and 0.01) single crystals at three different frequencies (4, 9 and 35 GHz). Again, a single resonance line due to the Er isotope with $I = 0$ has been observed. In addition, at 1.3 K the eight hyperfine lines of ^{167}Er ($I = \frac{7}{2}$) appear and allow the determination of the hyperfine constant, $|A| = 75 \pm 1$ G. At S- and X-band frequencies only small angular variations of the resonance field were observed, whereas the Q-band spectrum showed an overall variation of 250 G. The experimentally observed angular dependence of the g-values at different measuring frequencies is shown in fig. 29. The solid lines were calculated with $g_{\text{eff}} = g^0_{\text{eff}} + \nu^2[A + Bp(\theta)]$, where the factors A and B contain transition-matrix elements of magnetic dipole transitions between the Γ_6 ground state and Γ_8 excited state divided by the square of the energy splitting $\Delta = E(\Gamma_8) - E(\Gamma_6) \approx 8.5$ K and the function $p(\Theta) = 1 - 5\sin^2\Theta + 15\sin^4\Theta/4$. This angular dependence is clearly seen in the Q-band results. The observed g-value amounted to 5.875 ± 0.020, close to the

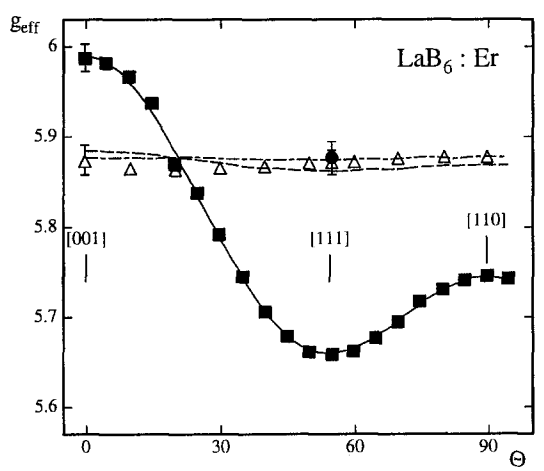

Fig. 29. g-Values as a function of crystal orientation, observed in $La_{1-x}Er_xB_6$ ($x = 0.001$) at different measuring frequencies: 34.652 GHz (squares); 9.367 GHz (triangles) and 4.053 GHz (circles). The lines were fitted to the experimental results using a model as described in the text. All data could be described using the constants $A = -7.1 \times 10^{-5}$ (GHz)$^{-2}$ and $B = +16.6 \times 10^{-5}$ (GHz)$^{-2}$. From Luft et al. (1983).

theoretical value, $g(\Gamma_6)=6$. The small difference between observed and calculated values corresponds to contributions from exchange interactions with conduction electrons and from the chemical shift.

5.3.2. *SmB_6*

The rare-earth compound SmB_6 can be considered as the prototype of a mixed-valence system. It is generally believed and accepted that at low temperatures, SmB_6 is a semiconductor with an extremely small band gap of about 3–4 meV (von Molnar et al. 1982). Recently it has been classified as a Kondo insulator (KI) (Aeppli and Fisk 1992). In a KI a semiconducting gap appears in the density of states due to the hybridization of the 4f electrons with the band states. The nature of this gap has been under controversial dispute for a long time. Kojima et al. (1978) measured g-shifts and ESR linewidths of Gd^{3+} and Eu^{2+} in SmB_6 powders in the temperature range between 1.6 and 20 K. The g-shifts are negative and amount to -0.07 for Gd^{3+} and -0.06 for Eu^{2+}, in contrast to the positive g-shifts of Gd^{3+} and Eu^{2+} in the Sm monochalcogenides (Birgeneau et al. 1972). In the latter compound the Sm ions are in a $4f^6$ configuration with a nonmagnetic $^7F_0$ ground state.

In the mixed-valent compound SmB_6 the exchange interactions between the impurity and the host 4f electrons contribute the main part to the g-shift. The ESR linewidths show a remarkable temperature dependence. As the temperature increases the linewidth of the Gd^{3+}-absorption line remains nearly constant below 4 K, increases rapidly between 4 and 10 K, followed by a more gradual increase above 10 K. This broadening is less developed in the case of Eu^{2+}. This temperature behavior of the linewidths can be explained by a band-structure model of Kasuya (1976), assuming that the localized 4f electrons and the delocalized 5d orbitals are strongly mixed and form a hybridization gap.

Al'tshuler et al. (1984, 1986) followed the linewidth of Gd^{3+}, Eu^{2+} and Er^{3+} over a larger temperature range, $1.7 < T < 150$ K. They used both powder and single-crystal samples of SmB_6. The exponential growth of the linewidth at low temperatures has been explained by the presence of a gap in the density of states. However their calculations in the framework of a f–d-hybridization model with a constant gap does not yield a satisfactory description of the dependence $\Delta H(T)$. From their fitting procedure they infer a gap value, $\Delta(0\,\mathrm{K}) \approx 4.3$ meV. The size of the gap is temperature dependent and disappears approximately at 150 K, in contrast to a temperature independent hybridization gap. Their spectra of the Gd^{3+} and Eu^{2+} ions in powdered samples show a single line with $g = 1.92 \pm 0{,}02$. The Er^{3+} spectra in single crystals consist of a double line due to a Γ_8 quartet with $g = 4.4$. On heating, this line disappears close to 12 K and only a single line due to an excited Γ_8 doublet with $g = 5.83$ has been observed.

In addition, Al'tshuler et al. (1982) investigated the ESR spectra of SmB_6 single crystals containing Eu impurities (0.03%) at X-band frequencies and temperatures $1.7 < T < 4.2$ K. They observed well-resolved fine and hyperfine spectra which could be described with the usual spin Hamiltonian of cubic symmetry by the following parameters: $g = 1.932 \pm 0.005$,

$b_4 = -6.6$ mK, $b_6 = 3.0\,\mu$K, $A(^{151}\mathrm{Eu}) = 4.8$ mK and $A(^{153}\mathrm{Eu}) = 2.1$ mK. Apart from the negative g-shift, these parameters are not unusual for Eu^{2+} ions in a cubic crystal field.

At low temperatures, $1.6 < T < 4.2$ K, the linewidth of powdered samples stayed constant $\Delta H(4\,\mathrm{K}) \approx 14.3$ G (Al'tshuler et al. 1982). At higher temperatures, $10 < T < 150$ K, an exponential increase of the linewidth $\Delta H(T)$ has been detected. Again the broadening can be described by an opening of a gap in the density of states. With a gap of 6.3 meV and a band width of the Sm 4f-structure at a Fermi energy of 14.1 meV the author gets a satisfying fit for the whole temperature range (Al'tshuler et al. 1986). Similar results are described in papers by Kunii et al. (1985) and Kan (1986). They used X, K and Q-band frequencies in the temperature range $2 < T < 10$ K.

H. Sturm et al. (1985) investigated the ESR of Er^{3+} in SmB_6 single crystals at X, K and Q-band frequencies and at low temperatures, $1.3 < T < 4.2$ K. They found a spectrum which is markedly different from those of comparable host systems with integral valence, e.g. LaB_6 or CaB_6. The unusual spectra were analyzed in terms of a dynamic Jahn–Teller (JT) effect within the Γ_8 cubic CF-ground state in the framework of a vibronic model. The fitting procedure provided $\Delta = 5.13$ K for the JT tunnel-split ground state. In contrast to this unusual multiline spectra of Er^{3+} in mixed-valent SmB_6, X-band spectra of Er^{3+} in the isostructural metallic compound LaB_6 (Luft et al. 1983) as well as in the semiconducting compounds BaB_6, YbB_6 and CaB_6 (Sturm and Elschner 1985) show only a single isotropic line, corresponding to a Γ_6 ground states which is not JT active.

In addition, Wiese et al. (1990) observed an anomalous ESR spectrum of Gd ions in SmB_6 below 5 K. The spectrum cannot be explained by the electronic configuration Gd^{3+} ($4f^7$), instead the authors discussed the appearance of the strange multiline spectrum (fig. 30) by a trapped conduction electron, forming a divalent Gd ($4f^7$) ($5d^1$) ground state. The Hamiltonian of the ($4f^7$) ($5d^1$) configuration, including a dynamic Jahn–Teller effect of the 5d electron, described the complicated Gd spectrum reasonably well. Above 6 K the anomalous spectrum vanished and the usual Gd^{3+} Dysonian resonance is observed, with $g = 1.92$ as in conventional metals. The linewidth increased rapidly on heating ($\Delta H = 80$ G at 6 K and 300 G at 10 K). The microscopic origin of this mixed electronic state at the defect site remains to be explained. It has to be mentioned that similar effects were not observed in Eu^{2+}:SmB_6 (Kunii et al. 1985, Al'tshuler et al. 1982, Kan 1986).

Stimulated by these ESR measurements, Weber et al. (1985–1987) and Brandt et al. (1994) published a series of detailed theoretical papers in which they proposed a new Jahn–Teller mechanism for Er^{3+} in mixed valence hosts. In this model the degenerate Er ground state interacts with excitations of the mixed-valent state, whereas the direct erbium–phonon interactions are as small as in conventional host crystals. The electron capture at the impurity site can be explained within this model by formation of a band-gap state in the coupled system.

That a dynamic Jahn–Teller effect indeed may be of importance in SmB_6 has also been suggested in a paper by Uemura et al. (1986a,b). They clearly observe unusual $\Delta M = \pm 2$ and $\Delta M = \pm 3$ transitions in the ESR spectra of Eu^{2+} in SmB_6, although the mixing matrix elements in cubic symmetry should be negligible. Reasons for the appearance of the forbidden transitions could be a dynamical JT-effect and/or fluctuations between

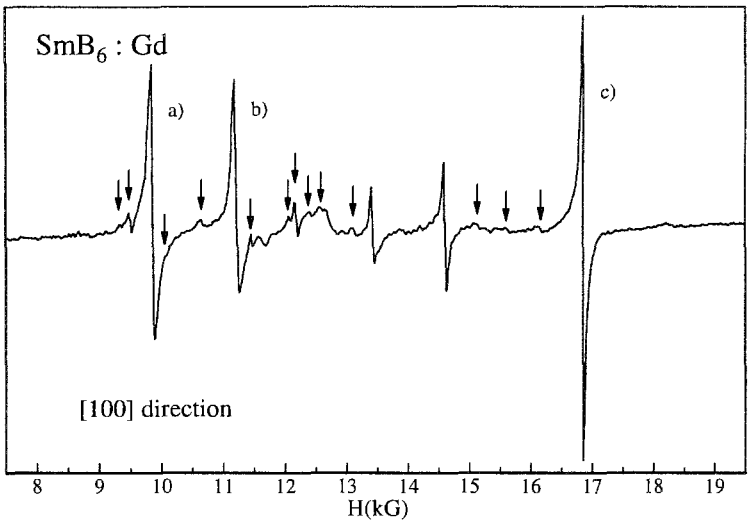

Fig. 30. ESR spectrum of Gd (3000 ppm) in single-crystalline SmB_6 measured at 33.5 GHz and 1.5 K. The external magnetic field is parallel to the [100] axis. The lines labelled a), b) and c) are interchanged on rotation into the [110] direction. The arrows and the labels a), b) and c) indicate absorption lines that have been predicted theoretically. From Wiese et al. (1990).

different valence states. It has been noticed that the hyperfine splitting in the $\Delta M = \pm 2, \pm 3$ resonances is averaged out, i.e. time-dependent modulations which include S_x^2 and S_x^3 terms are highly effective.

6. Concentrated ESR probes in metallic systems

In this section we deal with ESR in metallic systems where the ESR-active probe is substituted at relatively high concentrations (i.e. more than 10%) or where the ESR probe is a constituent of the alloy itself, i.e. Gd metal, GdAgIn or $GdAl_2$. In many of these alloys or compounds one can observe magnetic ordering. In such cases we consider only investigations of the resonance absorption above the Curie or Néel temperature, i.e. we do not include measurements on ferro-, ferri- or antiferromagnetic compounds. The demarcation line to resonance experiments in spin-glass systems in many cases is rather arbitrary.

6.1. *Simple metals and alloys*

ESR in single crystals of undoped gadolinium metal has been investigated near T_c (~293 K) by Burgardt and Seehra (1977). On cooling the ESR linewidth passes through a broad minimum at about 325 K which corresponds $(T-T_c)/T_c = 0.11$. On further decreasing temperatures ΔH increases and reaches a maximum at $T_m > T_c$ ($H_o \perp c$) or

at $T_m \approx T_c$ ($H_o \parallel c$). It is evident that a considerable contribution to the linewidth stems from critical fluctuations. This crossover behavior of the linewidth near T_c, namely an increase in ΔH followed by a decrease as T approaches T_c from above, seems to be characteristic for ferromagnets as long as the resonance field is considerably smaller than the exchange field, e.g. $CrBr_3$ and EuO. For more detailed information see the review article by Seehra and Huber (1975). Similar results for nickel single crystals are reported by Spörel and Biller (1975). In this case the linewidth reveals a maximum $\Delta H \approx 1.6$ kG at the temperature $T_m = 638$ K ($T_c = 630$ K). In both cases, the resonance fields follow the theoretical predictions for ferromagnetic samples, i.e. the resonance fields decrease with decreasing temperature. Measurements in higher fields, i.e. with higher probing frequencies would wipe out the critical effects. This may be the reason, that in Fe only a narrowing of ΔH has been observed as T_c is approached from above (Bhagat and Rothstein 1972).

Burzo and Balanescu (1980) reported on magnetic resonance experiments in $GdNi_x$ alloys with Ni concentrations $x = 3$, 3.5 and 8.5, both below and above the ferrimagnetic ordering temperature T_c. Approaching T_c from above, the linewidths again reveal an increase. $GdNi_5$ has been reinvestigated by Burzo and Ursu (1971) in the temperature range $100 < T < 300$ K (i.e. above the ordering temperature ~30 K). Nickel exhibits no magnetic moment in this compound. A temperature independent g-value of 1.944 and a Korringa slope of 6.4 G/K have been obtained. The experimental Korringa slope is about one order of magnitude less than that calculated from the g-shift. The authors explained this discrepancy by the fact that the interelectronic correlations have been neglected. They did not consider the q-dependence of the exchange parameter.

The magnetic resonance of the Laves-phase compounds RM_2 (M = Fe, Ni, Co or Al and R = Gd or $Gd_{1-x}Y_x$) were investigated by several groups: Burzo and Balanescu (1978) reported on paramagnetic resonance experiments on $Gd(Co_xNi_{1-x})_2$ compounds with Co concentrations $x = 0$, 0.2, 0.4, 0.6 and 0.8 at temperatures $150 < T < 320$ K. For $x = 0$ the authors obtain a linear temperature dependence of the linewidth with a Korringa slope of 2.45 G/K. This small value may indicate a bottleneck behavior of the relaxation channel. For $x > 0$ obviously the bottleneck is opened and the linewidth reveals a strong and nonlinear increase as a function of temperature. The linewidth passes through a minimum at a temperature $T_0 > T_c$, followed by an increase of ΔH as T_c is approached. This increase has been attributed to the appearance of magnetic-ordering processes. The graph $\Delta H(T)$ clearly reveals that the minimum $\Delta H_{min}(x)$ does not coincide with the linear Korringa behavior for $x = 0$ at this temperature. Similar results were reported by Tari and Kuentzler (1986) on the system $(Gd_{1-x}Y_x)Ni_2$ for Y concentrations $0.02 \leqslant x \leqslant 0.8$. Here again a linear increase of $\Delta H(T)$, indicative for a pure Korringa behavior, has been observed. The slope increases monotonically from 2.6 G/K in $GdNi_2$ to 4.9 G/K in $(Gd_{0.02}Y_{0.98})Ni_2$. These experimental observations indicated a shallow bottleneck. The authors claimed that such a bottleneck behavior indicates the dominance of d-electrons over s-states in the conduction band. Again, below the minimum the linewidth increases on approaching T_c.

Zipper et al. (1984) presented ESR measurements on $Gd_xR_{1-x}Al_2$ (R = La, Lu, Y) in the high concentration range $0 < x < 1$. This paper provides interesting insights into the role of s- and d-electron contributions to the bottleneck behavior. The authors observe positive g-shifts and a drastic increase in the Korringa slope for $x \ll 1$. Obviously, in this concentration regime the bottleneck is opened. But for $0.05 \leqslant x \leqslant 1$ the g-shift changes sign and the Korringa slope only depends weakly on concentration. They claim that the sign of the g-shift is determined by $(g_e - g_s) \cdot J$ and not only by the sign of J (see eq. 3). Here g_e and g_s are the g-factors for the conduction electrons and the local moments. $g_s = 1.993$ for Gd^{3+}, but the g-factor for d-band electrons is different from 2 (Zipper 1982). In particular, it is smaller than 2 for d-band electrons in the lanthanide series since they are less than half filled. The authors proposed the following model: The s-band relaxes slowly towards the lattice, $\delta_{eL}^{(s)} \approx 10^{10}\,s^{-1}$ and the system is bottlenecked due to the s electrons ($x \leqslant 0.01$). At higher Gd concentrations only d-electrons are effective in the electron-lattice relaxation, $\delta_{eL}^{(d)} \approx 10^{11}$–$10^{12}\,s^{-1}$ and the system becomes more and more bottlenecked according to the d-band contributions. This analysis shows unambiguously the dominating role played by d-electrons in these systems. If the conduction electrons had only s character it would be impossible to explain the change of sign of the g-shift, Δg, when passing from dilute to concentrated systems. In particular this model gives an explanation of the negative g-shift in concentrated bottlenecked systems under the assumption of a positive exchange coupling between localized spins and band electrons. In a series of experiments on $Gd(Co_xAl_{1-x})_2$ alloys (Kaczmarska et al. 1979, Chiu et al. 1980, Burzo 1981) it has been demonstrated that the g-factor decreases with increasing Co concentration. Within the above-mentioned model, Zipper (1983) explained the experimentally observed (Burzo and Baican 1974) positive g-shifts in the unbottlenecked regime and negative g-shift in the bottleneck region for $(Gd_xY_{1-x})Cu$ ($0 < x \leqslant 1$). Figure 31 shows the temperature dependences of the g-shift and of the thermal broadening in $Gd_xY_{1-x}Cu$ versus the Gd concentration (Burzo and Baican 1974). The solid lines were calculated according to the model proposed by Zipper (1983).

In $Gd(Al_{1-x}Ni_x)_2$ (Kaczmarska et al. 1985) the substitution of Ni does not change the g-factor for all compounds investigated, although a small negative g-shift is observed, i.e. Ni does not open the strong bottleneck. This behavior indicates that Ni is nonmagnetic in these compounds and does not exhibit d-electron character. The Korringa slope changes only slightly with increasing Ni concentrations (2.5 G/K for $x = 0$ and 6 G/K for $x = 0.18$). Near the ferromagnetic Curie temperature a rapid increase in the width can be noticed, similar to the examples described above (Burgardt and Seehra 1977, Spörel and Biller 1975).

Chiu et al. (1979) opened the bottleneck in Gd-ESR experiments in $Gd_{0.5}Dy_yY_{0.5-y}Ir_2$ by adding small amounts of dysprosium ($y \leqslant 0.007$). This demonstrates the significance of the anisotropic interactions between conduction electrons and Dy ions. This interaction leads to a large increase of δ_{eL} at the dysprosium sites. Furthermore it seems that there is a local enhancement of the density of states at the Dy sites which affects neighboring Gd spins. Similar investigations have been performed by Kwapulinska and Kaczmarska

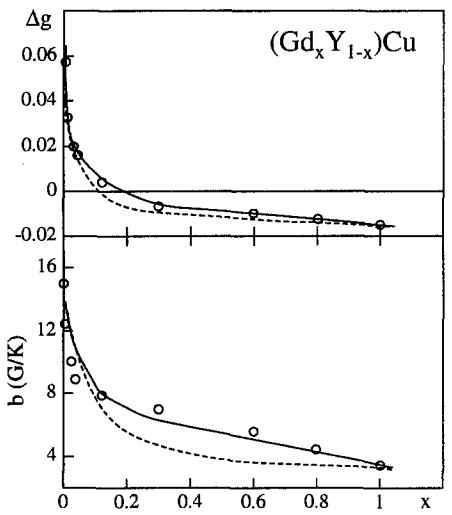

Fig. 31. Concentration dependence of the g-shift Δg, and the Korringa broadening as observed in $(Gd_xY_{1-x})Cu$ as a function of the Gd concentration x (from Burzo and Baican 1974). The dashed and solid lines represent fits from Zipper (1983).

(1990) on the systems $Gd_yLa_{1-y}Cu_6$ $(0.3 \leqslant y \leqslant 1)$ and $Gd_yCe_{1-y}Cu_6$ $(0.7 \leqslant y \leqslant 1)$. Here again a negative g-shift has been observed for all concentrations of La or Ce. $GdCu_6$ is a strongly bottlenecked system. Ce ions open this bottleneck much more efficiently than La ions. But the bottleneck is not opened completely due to the high Gd concentration. In addition, it has to be noticed that Ce impurities broaden the line approximately by a factor of three in comparison with La.

Pelegrini et al. (1982) report on ESR measurements on $Gd_{1-x}Tb_xAl_2$ $(0 < x < 0.05)$ single crystals. The ESR linewidths revealed a broadening which increases proportional to $(T - \Theta)$, right down to the paramagnetic Curie–Weiss temperature Θ, with only a small residual linewidth at $T = \Theta$. Tb ions again act effectively in opening the bottleneck. The authors use a modified Hasegawa theory (see Than-Trong et al. 1981) to interpret their results concerning the resonance bottleneck and the Curie–Weiss behavior of ΔH. The temperature-independent g-shift predicted by this unified theory could not be detected in $Gd_{1-x}Tb_xAl_2$. The reason for a zero g-shift may be due to the fact that J_{Tb-e} and J_{Gd-e} are too similar, i.e. the change in Δg is too small to be detected. However, this temperature-independent but concentration-dependent indirect g-shift in the bottleneck regime has been detected by Than-Trong et al. (1981) in the systems $Gd_{1-x}Dy_xAl_2$ and $Gd_{1-x}Sm_xAl_2$ $(0 \leqslant y \leqslant 0.13)$. Both systems show this unexpected feature of a positive g-shift. The shift should be opposite in sign as Dy and Sm are symmetric with respect to Gd in the periodic table. If one considers an additional ferromagnetic exchange interaction between Gd^{3+} and Sm^{3+} which is much larger than the external field, the Sm^{3+} spins are parallel to those of the Gd^{3+} ions and therefore give rise to a positive indirect shift. Yet in both systems the linewidth ΔH is linear as a function of $(T - \Theta)$, with a small residual linewidth ΔH_0 $(T = \Theta)$.

Larica and Guimareas (1976) investigated the intermetallic compounds $GdAg_{1-x}In_x$ ($0 \leqslant x \leqslant 0.6$). The linewidths show a Korringa behavior above a certain temperature, T_{min}, with a slope b which scarcely depends on x. However, T_{min} depends on x. At T_{min} the linewidth passes through a minimum ($\Delta H_{min} \approx 380$–$750$ G) and rises again towards lower temperatures. The authors analyse their data within a two-band model. In the framework of this model the g-shift, Δg, in GdAg is created by d-electrons only, while the s-contributions are strongly bottlenecked.

The Gd-ESR in $Gd(Co_xIr_{1-x})_2$ ($0 \leqslant x \leqslant 0.55$) has been investigated by Chiu et al. (1979). The Gd bottleneck is gradually opened for $x < 0.4$, indicating a strong conduction-electron spin–orbit scattering by the nonmagnetic Co ions. For the samples with $x > 0.4$ the Co ions form a magnetic moment and provide an additional relaxation channel. For $0 \leqslant x \leqslant 0.55$ the linewidths above the Curie points follow a linear Korringa law with $\Delta H = \Delta H_0 + b(T - \Theta)$, similar to that observed by Than-Trong et al. (1981) in the $GdAl_2$ system. The ΔH_0 values are remarkably high (~1 kG). The observed g-shift always remains negative. This result is expected when only d-electrons contribute to the g-shift.

The formation of a concentration-dependent magnetic moment in an alloy has been investigated by Slebarski et al. (1983) on the system $GdMn_xAl_{2-x}$. The Mn ions are nonmagnetic up to 20% Mn. In this concentration range the strong bottleneck is weakened by the addition of Mn. For higher Mn concentrations the d-electrons become localized and a magnetic moment appears at the site of the Mn ions, which leads to a nonlinear behavior of the resonance linewidth.

In a series of papers Coldea et al. (1980, 1985) studied the ESR of $Gd_2Ni_{17-x}Al_2$ and $Gd_2Co_6Al_{11}$. From the experimental g-shift and the magnetic susceptibility data, exchange constants for the exchange interactions between conduction electrons and the d- and s-electrons of the host metal were inferred. Similar results were reported by Burzo et al. (1982) on the compounds $Gd(Co_xAl_{1-x})_3$. By substituting Co for Al a gradual opening of the s-band relaxation takes place by means of the orbital contribution of the 3d-electrons of cobalt, i.e. the bottleneck is broken. The g-shifts again are negative and it seems that for an interpretation the ideas of Zipper (1982, 1983) can be applied in these cases, too.

Taylor and Coles (1975) give an excellent review on experimental results of ESR in concentrated alloys over the temperature range from 1.5 to 300 K. This survey includes a variety of types of compounds over a broad range of composition revealing both ferromagnetic and antiferromagnetic order. In this article the interested reader finds an almost complete description of all papers which appeared until 1974.

6.2. *Chalcogenides and pnictides*

ESR studies of excited crystal-field states were reviewed by Huang et al. (1976). The observed resonances result from the excited $\Gamma_5^{(2)}$ level of Tm^{3+} in TmP (fig. 32), of the $\Gamma_5^{(2)}$ level of Tb^{3+} in antiferromagnetic TbB (B = P, As, Sb) and of the excited Γ_8 state for the Kramers ion Ce^{3+} in antiferromagnetic CeP (see also Yang et al. 1979). From the g-factors at high temperatures and the temperature dependence of the ESR intensity, the resonance in the latter case has been identified as originating from the excited Γ_8

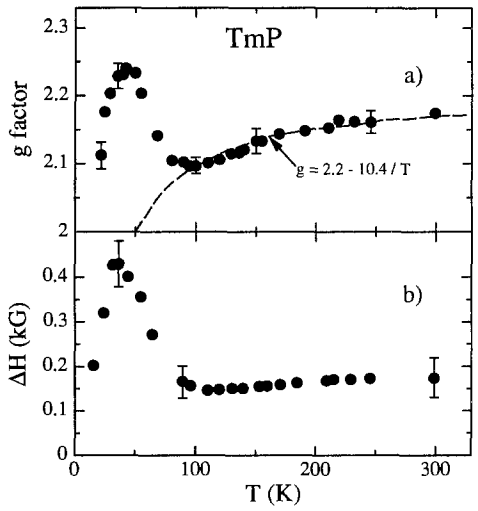

Fig. 32. (a) Temperature dependence of the g-value of the excited $\Gamma_5^{(2)}$ level of Tm^{3+} in TmP. (b) Temperature dependence of the linewidth of excited $\Gamma_5^{(2)}$ level of Tm^{3+} in TmP. From Huang et al. (1976).

quartet which lies about 200 K above the Γ_7 ground state (fig. 33). By observation of the temperature dependence of the g-value one gets the possibility to decide whether the exchange between the magnetic ions is antiferromagnetic (e.g. in TmP) or ferromagnetic (e.g. in TmN). These results are in agreement with neutron scattering results from Heer et al. (1976).

Jansen and Sperlich (1975) investigated the frequency dependence of the high-temperature ($T \approx 290$ K) ESR linewidth of the metallic lanthanide pnictides $Gd_xM_{1-x}P$ (M = Y, Sc) and $Gd_xY_{1-x}As$ in the concentration range $0.2 \leqslant x \leqslant 1$ from 9 up to 71 GHz.

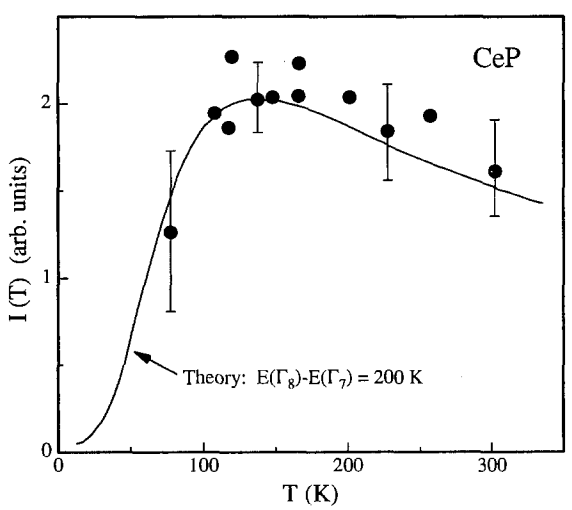

Fig. 33. Temperature dependence of the intensity of the resonance line of Ce^{3+} in polycrystalline CeP. The resonance originates from transitions within the excited Γ_8 quartet. The solid line has been calculated assuming a level separation of 200 K. According to neutron scattering results the Γ_8 levels are approximately 170 K above the Γ_7 ground state (Huang et al. 1976).

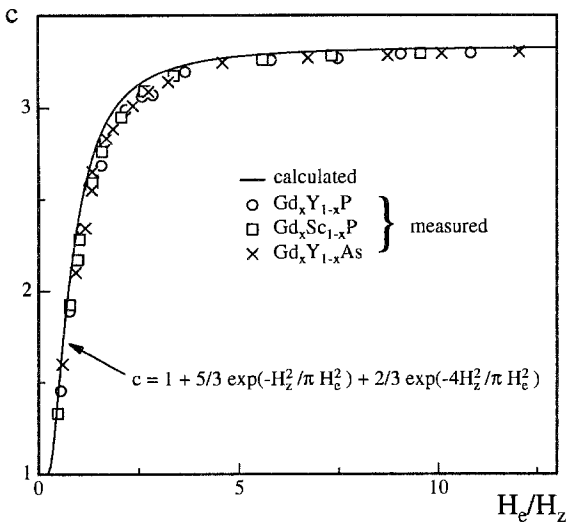

Fig. 34. Comparison of the measured c-values for $Gd_xY_{1-x}P$, $Gd_{1-x}Sc_{1-x}P$ and $Gd_xY_{1-x}As$ $(0.2 < x < 1)$, with those derived from the theory of the linear response as discussed by Kubo and Tomita (1954). Taken from Jansen and Sperlich (1975).

At room temperature the observed linewidth was strongly exchange narrowed. For the analysis of the frequency dependence of this exchange-narrowed linewidth ΔH_{ex}, the authors applied a formalism that has been worked out for exchange-narrowed lines by Gulley et al. (1970):

$$\Delta H_{ex} = \frac{M_2^{3/2}\pi^{1/2}}{\sqrt{2M_4}} \equiv \frac{M_2}{H_e}. \tag{30}$$

Here M_2 and M_4 are the second and the fourth moment of the resonance lineshape. Equation (30) defines the exchange field H_e. In the well-known relation, $\Delta H_{ex} = cH_D^2/H_e$, where H_D defines the dipolar broadening, a factor c emerges. Van Vleck (1948) calculated this factor for the two extreme cases $H_z \gg H_e$ $(c = 1)$ and $H_z \ll H_e$ $(c = 10/3)$. Hence, the ESR linewidth is expected to show a significant frequency dependence when the external field H_z and the exchange field H_{ex} are of comparable size. In the framework of a linear response theory Kubo and Tomita (1954) calculated this factor c. The result is shown in fig. 34 and compared to experimental results of the Gd-resonance experiments in YP, ScP and YAs. Figure (34) clearly demonstrates that almost all data fall onto an universal curve which is discussed in detail by Sperlich and Jansen (1974). For $H_e \ll H_z$ the value of c approaches 1 and for $H_e \gg H_z$, c amounts to 10/3. The numerical calculations yield $H_e = 36.0$ and 40.3 kG for the Gd–Gd exchange in GaP and GdAs, respectively.

Exchange-narrowed resonance lines have also been observed in GdB (B = P, As, Sb and Bi) by Allenson and Taylor (1968) in the temperature range 17–400 K. The Gd–Gd exchange parameter derived from the linewidths has been expressed in terms of the nearest-neighbor superexchange and a further temperature-dependent term. In all the compounds the impurity-level excitation energy is found to amount to 10^{-2} eV.

Similar results were reported by Neukomm and Hauger (1975) on powdered samples of $Gd_xY_{1-x}B$ (B = P, As and Sb) in a wide concentration range $0.01 \leqslant x \leqslant 1$, between the ordering temperature and room temperature. The narrowed line is explained by dipolar and exchange interactions between the Gd ions. The observed line broadening at lower temperatures is an indication for the onset of magnetic order.

The effect of exchange narrowing is proportional to the sum of the absolute values of the exchange parameter. Both exchange constants, J_1 and J_2 are effective for the narrowing process independent of the sign of J_1 or J_2. Sugawara et al. (1977) showed that values for the Néel temperature T_N can be inferred from coincident anomalies in ΔH and g_{eff}. The measurements were carried out on powder samples of GdB (B = As, Sb, Bi, S and Se). The discrepancy between the magnetic ordering temperatures as determined from ESR compared to those inferred from other methods is evident. One possible source for the discrepancy is the finite external magnetic field.

6.3. *Metallic bronzes*

A paper by G. Sperlich et al. (1973) reports on ESR and magnetic susceptibility measurements on the metallic blue bronze $La_{x-y}Gd_yWO_3$. They investigated powder samples with concentrations $x = 0.1$ and 0.15 and Gd concentrations $0.001 \leqslant y \leqslant x$ in the temperature range $4 < T < 300$ K. The system crystallizes in the cubic perovskite structure ABO_3 where the lanthanide ions occupy the A sites randomly. An asymmetric ESR signal occurs at $g = 1.991$ the usual g-value of Gd^{3+} in an insulator. The ideal Dysonian line shape, which normally is expected in metallic powder samples is not observed. Strong additional wings below and above the resonance field appear in the line shape. The linewidth ΔH increases with increasing Gd concentration y. And finally, ΔH is temperature independent, i.e. a Korringa law is not observed. This behavior can only be understood if the $6s^25d^1$ electrons of the Gd atom are transferred to a conduction band of the WO_6 octahedrons in whose formation they do not participate. Therefore, a measurable exchange between the 4f moments and conduction electrons cannot take place. The lanthanide ions in $La_{x-y}Gd_yWO_3$ behave like free ions which are completely surrounded by conduction electrons of the WO_6 cage, but are fully decoupled from them. NMR measurements (Jones et al. 1962) have confirmed this interpretation. Due to this decoupling, the crystal field splitting is not completely narrowed and gives rise to the wings in the lineshape which have been experimentally observed.

6.4. *Hexaborides*

An ESR study of the concentration dependence of the fully narrowed resonance linewidth in the hexaborides $M_xEu_{1-x}B_6$ (M = Sr or La) in a wide concentration range $0 < x < 1$ (Mercurio et al. 1979) showed that the exchange between Eu^{2+}-ions is due to the presence of free carriers (indirect exchange via the RKKY-interaction), although a straightforward application of the RKKY-theory gives only qualitative agreement with the experimentally observed $\Delta H(x)$ curves. In the lanthanum compounds, the concentration dependence of

$\Delta H(x)$ differs significantly from the RKKY predictions, probably due to a loosely bound 5d-electron introduced into the lattice via the substitution of La ions.

7. ESR in van-Vleck systems

Van-Vleck systems are characterized by a nonmagnetic ground-state and excited crystal-field levels which are located about 10–100 K above the ground state. Magnetic ordering can only occur in these compounds provided that the exchange interaction between the magnetic host ions exceeds the crystal-field effects. The magnetic ordering is achieved via the magnetic polarization of the singlet-ground state (e.g. Γ_1 which is nonmagnetic) by admixture of higher crystal-field terms. It is in general accepted to classify the van-Vleck systems, depending on the ratio J/Δ (J is the exchange constant and Δ measures the CF splitting between the ground state and the first excited magnetic state) into three groups:

(a) $J/\Delta \gg 1$: magnetic order will occur at low temperatures,

(b) $J/\Delta \approx 1$: "strongly coupled" van-Vleck compounds, and

(c) $J/\Delta \ll 1$: "weakly coupled" van-Vleck compounds.

For a more detailed discussion the reader is referred to the review papers by Cooper and Vogt (1971) and Birgeneau (1973).

To understand the nature of van-Vleck compounds it is helpful to know details of both the crystal field and the exchange interaction between the lanthanide ions. Pr^{3+} ($4f^2$) and Tm^{3+} ($4f^{12}$) are favorable van-Vleck ions, which very often yield Γ_1 or Γ_2 ground states, depending on the crystal structure of the compound and the symmetry of the 4f site. The ESR on suitable probes doped into van-Vleck host lattices (e.g. Gd^{3+} or Er^{3+} in TmSb) can give valuable information about the electronic dynamics in these peculiar materials, specifically on the fluctuation spectra of singlet-ground-state systems.

The ESR-spectra of Gd^{3+} or other lanthanide ions in van-Vleck hosts all reveal similar features: large g-shifts relative to the undisturbed g-value and thermal broadenings of the linewidths, which are typically nonlinear functions on temperature. These general features sometimes are influenced by additional Korringa processes. In certain cases a bottleneck behavior can be detected. The giant g-shifts are connected with the large susceptibilities, χ_{vv}, of the van-Vleck host ($\chi_{vv} \approx 10^{-1}$ emu/mol) and with the total exchange interaction $J = \sum J_i$. Here J_i represents the exchange constants for the interaction between ESR probe and R ions of the host lattice. The index i characterizes the lattice site of the R ion. In the molecular field approximation the g-shift induced on the ESR probe ion can be calculated (see, e.g. Rettori et al. 1975b or Sugawara et al. 1975) according to

$$\Delta g = g_0 \frac{g_J - 1}{g_J} \frac{g_{J'} - 1}{g_{J'}} \frac{\chi_{vv} J}{\mu_B^2 N_0}, \tag{31}$$

where g_0 is the g-value of the impurity ion in the absence of any exchange, g_J and $g_{J'}$ are the Landé factors for the impurity and the host magnetic ions, respectively, and χ_{vv} is the van-Vleck susceptibility in the presence of host R–R exchange interaction.

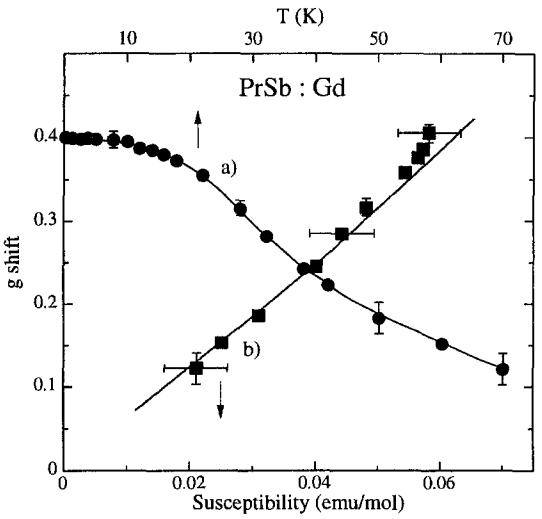

Fig. 35. The Gd g-shift in PrSb doped with 9000 ppm Gd. The g-shift is plotted versus temperature (upper scale) and versus the magnetic susceptibility (lower scale). From Rettori et al. (1975a).

For Gd^{3+} as an impurity ion eq. (31) reduces to

$$\Delta g = \frac{g_J - 1}{g_J} \frac{\chi_{vv} J}{\mu_B^2 N_0}. \tag{32}$$

It is common practice to use eqs. (31) and (32) for the determination of the exchange interactions using the experimentally known values of Δg and χ_{vv}. Figure 35 shows the g-shift Δg of Gd^{3+} in PrSb versus temperature (circles, upper scale) and versus susceptibility (squares, lower scale) (Rettori et al. 1975b).

A detailed investigation of the temperature dependence of the ESR linewidth in weakly coupled van-Vleck paramagnets has been published by Davidov et al. (1977). They have shown that the impurity relaxation sensitively depends on the fluctuation spectra of the host lanthanide ions, due to transitions within the Zeeman levels of the excited states. The host exchange interaction has been extracted by fitting a model function to the experimentally observed thermal broadening.

7.1. *Van-Vleck metals*

Al'tshuler et al. (1981) report on ESR experiments on Er^{3+} and Gd^{3+} in metallic praseodymium. They investigated powdered samples with 1–3% Er or 10% Gd. At 4.2 K they obtain an Er^{3+} signal with $g = 8.7 \pm 0.05$ and $\Delta H = 200 \pm 25$ G. The authors assume that the ESR spectrum in bulk Pr is determined mainly by the Er^{3+} ions that are substituted in a cubic environment (50% of the Er ions). Compared with metallic lanthanum ($g_{La} = 6.8$), a large g-shift ($\Delta g = +1.9$) occurs, which is determined by two contributions: The direct Pr–Gd exchange and an indirect exchange via conduction

Table 5
The exchange parameters J(Gd–M) extracted from the observed g values in various van-Vleck beryllides MBe_{13} (M = Pr, Eu, Tm, U); the host susceptibilities as well as the ground states and the first excited states of the host M ions are also given[a]

Host	Host susceptibility at $T = 1.8$ K (emu mol^{-1})	Ground state host M ions	First excited state	Energy splitting Δ (K)	Gd g value at $T = 1.8$ K	Exchange interaction J(Gd–M) (meV)
$PrBe_{13}$	0.047	Γ_1	Γ_4	73	1.90±0.01	+0.40±0.05
$EuBe_{13}$	0.0064	$J = 0$	$J = 1$	476	2.135±0.016	+0.46±0.05
$TmBe_{13}$	2.59	Γ_2	Γ_5	8	3.80±0.3	+0.15±0.03
UBe_{13}	0.124	?[b]	?[b]	?[b]	2.08±0.01	−0.08±0.02

[a] From Bloch et al. (1976). [b] Unknown at present.

electrons. It is believed that the indirect part of exchange produces the main contribution to the experimentally observed g-shift.

In the case of Gd^{3+} in praseodymium an ESR signal with $g = 2.3 \pm 0.1$ and a linewidth, $\Delta H = 1600$ G has been observed (Al'tshuler et al. 1981). ΔH does not depend on temperature. The authors explain this behavior assuming a bottleneck behavior in this system.

In a second contribution Al'tshuler et al. (1983) investigated the metallic system $La_{1-x-y}Gd_xPr_yAl_2$ with concentrations $x = 0.3\%$ and $y = 0$, 0.2% and 0.3%. The temperature dependence of the linewidth becomes nonlinear for higher Pr concentrations. The authors suggest that the main source for the increase of the linewidth is the exchange interactions between the Gd and Pr moments, which is mediated via the conduction electrons (RKKY-type of interaction). Since the praseodymium ions are situated randomly in the crystal the shift of the resonance has a spatial dispersion. This leads to an inhomogeneous broadening of the Gd^{3+} linewidth.

Bloch et al. (1976) investigated the van-Vleck beryllides MBe_{13} (M = Pr, Eu, Tm and U) using Gd as an ESR probe. They used powdered samples and the measurements at X-band frequencies were performed for temperatures $1.8 < T < 4.2$ K. The main goal of this investigation was to determine the exchange parameters J(Gd–M) as derived from the g-values using eq. (32) and taking the exchange between the Gd ions and the conduction-electrons into account. Table 5 shows the exchange parameters deduced by this procedure (Bloch et al. 1976).

The Gd-ESR in the metallic $PrIn_3$ has been reported by Davidov et al. (1977). The measurements were performed on powdered samples. The g-value, $g = 2.40 \pm 0.01$, is constant in the temperature range $1.4 < T < 4.2$ K. The inferred exchange parameter $J(\text{Gd} \leftrightarrow \text{Pr})$ amounts to -1.6 meV. The linewidth increases linearly for $T \leqslant 10$ K with a Korringa slope of 16±5 G/K. At higher temperatures, ΔH rises nonlinearly, reaching values of 1.6 kG at 30 K. The rapid thermal broadening above 10 K is attributed to fluctuations of the host Pr ions at the Gd-resonance frequency. The frequencies which are

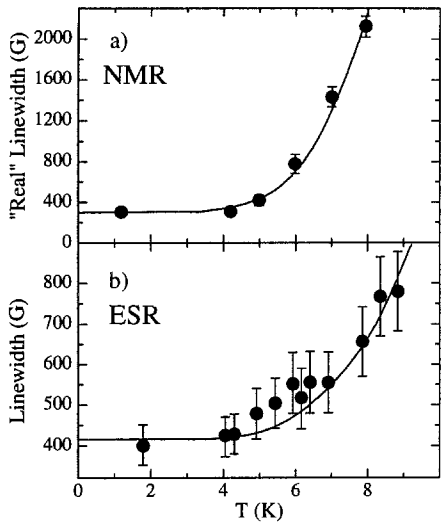

Fig. 36. (a) ^{141}Pr-NMR and (b) Gd^{3+}-ESR linewidth vs. temperature in single-crystalline $PrNi_5$. The solid line in (a) represents the prediction of model calculations with exchange $\left[\sum_k (J^k_{Pr})^2\right]^{1/2} = 20\,\mu eV$ and $\Delta H_0 = 300\,G$. The solid line in (b) represent a fit using the same Pr exchange and in addition $\left[\sum_k (J^k_{Gd})^2\right]^{1/2} = 360\,\mu eV$ and $\Delta H_0 = 400\,G$. From Levin et al. (1979a).

important for this broadening belong to the "low frequency" part of the spectral function and refer to transitions between Zeeman levels in the excited crystal field states of the van-Vleck host ions. These fluctuations are transferred to the Gd ions by the exchange interaction with the host Pr ions.

Giant g-shifts have been observed in the system $PrNi_5$:Gd by Levin et al. (1975). They determined a negative g-shift, $\Delta g = -0.73$ (with respect to $g = 2$ of Gd in an insulating host). This shift again has been interpreted in terms of the exchange between Gd and Pr ions. In a second paper R. Levin et al. (1979a) conducted both NMR and ESR experiments in single crystals of $PrNi_5$(Gd). Again, on heating a dramatic increase of the resonance linewidth occurs in the NMR of ^{141}Pr and in the ESR of Gd^{3+} for temperatures $4 < T < 10\,K$ (fig. 36). The authors analyze the combined NMR and ESR experiments in terms of fluctuations of the Pr ions in the $PrNi_5$ matrix caused by Pr–Pr exchange. They extract the exchange constants $J(Pr–Pr) = 0.02\,meV$ and $J(Gd–Pr) = 0.36\,meV$. Contributions to the linewidth which are associated with the Korringa mechanism or ion–phonon scattering have been neglected, due to the fact that the Korringa rates for Gd in isostructural $LaNi_5$ are relatively small (~3 G/K, see Levin et al. 1979b). These combined NMR and ESR experiments allow direct and valuable reflections about the Pr–Pr exchange in the host lattice on a microscopic scale.

The metallic van-Vleck paramagnets $PrPb_3$ ($AuCu_3$ structure) and TmCd (CsCl structure) have been investigated by Sugawara and Huang (1976b). They used powdered samples with 2 and 3% Gd^{3+}, respectively. The g-values change drastically in the case of $PrPb_3$ from 2.3 ($T = 10\,K$) to 2.05 ($T = 40\,K$), whereas they remain almost constant for TmCd in the same temperature range. Using eq. (32), the exchange constants $J(Pr \leftrightarrow Gd) = -0.43 \pm 0.07\,meV$ for $PrPb_3$ and $J(Tm \leftrightarrow Gd) \approx -7\,\mu eV$ in TmCd have been obtained.

In contrast to the model of Davidov et al. (1977), which is based on the Bloch–Wangsness–Redfield equations (Bloch 1956, Redfield 1955), Sugawara and Huang (1976b) explained the temperature dependence of the linewidth of the Gd-ESR via a temperature dependent population of the crystal-field levels using the theory of Moriya and Obata (1958) and Kubo and Tomita (1954). In these theories the calculation of $\Delta H(T)$ is reduced to the calculation of T_2, i.e. to the calculation of the frequency distribution or time-correlation functions of the paramagnetic spin fluctuations assuming that the degeneracy of the spin levels is completely lifted by the crystalline-electric field. Many experimental results can be interpreted using both models.

7.2. *Van-Vleck chalcogenides*

ESR measurements on $Pr_{1-x}Gd_xM$ (M = S, Se, Te) with Gd^{3+} ($1000 < x < 6000$ ppm) were performed at X-band frequencies at low temperatures Davidov et al. (1976). Again the exchange parameter $J(Pr \leftrightarrow Gd)$ were extracted from the g-shifts using eq. (31). Figure 37 shows a comparison of the exchange parameters $J(Gd \leftrightarrow Pr)$ as a function of the lattice constant for various chalcogenides and pnictides. It is interesting to note that the variation of $J(Gd \leftrightarrow Pr)$ in the pnictide series is much more pronounced in contrast to the moderate variation across the series of the chalcogenides. The authors claim that the dominant mechanism for the Gd–Pr exchange is RKKY-like in the chalcogenides due to the fact that the exchange via conduction electrons is almost independent of the lattice constant. The negative signs of the exchange parameters are consistent with the positive Δg-values as a result of the Landé-factor of Pr^{3+} ($g_J = 0.8$). This fact is responsible for the negative sign of $(g_J - 1)$ in eq. (32).

Sugawara and Huang (1976b) reported on Dy^{3+} and Ce^{3+} ESR in PrS. For Dy^{3+} a Γ_6 ground state doublet with $g_{exp} \approx 6.6$, has been detected. This g-value indicates, that the exchange interactions between Dy^{3+} and Pr^{3+} are completely absent in PrS. In contrast

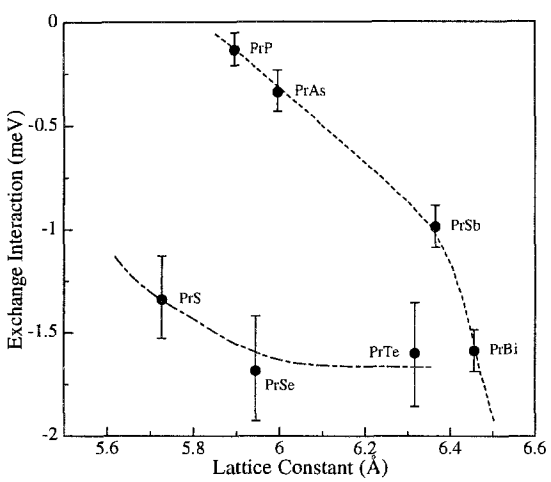

Fig. 37. Exchange interactions between the ESR probe Gd^{3+} and the host Pr ions vs the lattice constant for various pnictides and chalcogenides. Note the large variation in the exchange interaction strength across the pnictides in comparison to the minor changes across the chalcogenides.

to this finding, the system PrS doped with Ce^{3+} (Γ_7 ground state for Ce^{3+}) shows a slight positive g-shift ($\Delta g = 0.05$) and eq. (31) yields a Ce^{3+}–Pr^{3+} exchange of ~1.3 meV. For Ce^{3+} in TmS the g-shift is almost the same and accordingly the sign of the exchange parameter changes, i.e. $J(Ce^{3+}\text{–}Tm^{3+}) \approx -0.17$ meV (Sugawara and Huang 1976b).

Pressure measurements (Guertin et al. 1975) of the magnetic susceptibility χ_m allow an extraction of dJ_{Pr-Pr}/dr. These results can be compared with the ESR-values of dJ_{Gd-Pr}/dr. The strong correlation indicates that both derivatives of the exchange on the distance originate from the same mechanism. ESR studies of the temperature dependence of the linewidth further support the assumption of a dominant RKKY-like mechanism being present in the Pr-chalcogenides. For $La_{1-x}Gd_xS$ a Korringa slope of 12 G/K was observed (Urban et al. 1974b). The same values were obtained for $La_{1-x}Gd_xSe$ and $La_{1-x}Gd_xTe$. In clear contrast to the chalcogenides, the thermal broadening in the pnictide series amounts to 0.2 G/K (see e.g. Urban et al. 1975). The product $J \cdot N(E_F)$ is about one order of magnitude smaller in the pnictides than in the chalcogenides, i.e. the RKKY contribution is expected to be more significant in the chalcogenides.

7.3. *Van-Vleck monopnictides*

Van-Vleck monopnictides like PrX or TmX (X = N, P, As, Sb and Bi) doped with Gd^{3+} or other lanthanide probes were the subjects of detailed ESR investigations. Here again the exchange parameter, e.g. $J(Gd^{3+} \leftrightarrow Pr^{3+})$, were of main interest. A peculiarity of these compounds is the change from semiconducting behavior (e.g. in the nitrides; X = N) to metallic behavior (e.g. X = Sb, Bi). Furthermore, the investigation of the exchange parameters as a function of the lattice spacings remains an interesting problem. Rettori et al. (1975b) reported on direct measurements of the exchange interaction between Gd^{3+} and Tm^{3+} or Pr^{3+} in the metallic van-Vleck compounds, TmSb, TmBi, PrSb and PrBi. Large g-shifts were observed due to the enhanced van-Vleck susceptibility χ_{vv} and due to the Gd–R exchange (see eq. 32). Most of the experiments were performed on single crystals and at liquid helium temperatures. The single crystals with relatively small Gd concentration ($x < 300$ ppm) exhibited resolved Gd fine structures, whereas higher Gd concentrations show a single anisotropic line. This behavior has been interpreted as an exchange-narrowed fine structure of the Gd^{3+} spectrum in a cubic environment, as described by S.E. Barnes (1974) and Plefka (1973). But the main result of this paper was the observation of giant g-shifts with different signs for the Tm ($\Delta g < 0$) and Pr compounds ($\Delta g > 0$), respectively. These different signs were associated with the different signs of $(g_J - 1)$ in eq. (32), i.e. the sign of the exchange parameter $J(Gd \leftrightarrow Tm, Pr)$ remains always negative. The fact that the authors were able to observe resolved fine structures of the Gd line at resonance absorption in connection with giant g-shifts (e.g. $\Delta g = -0.96$ for TmBi) revealed that large polarization exists without relaxation; i.e. the frequencies of the fluctuations in the host system are much higher than the Gd-resonance frequency.

The van-Vleck nitrides (see Davidov et al. 1975b) follow the general trend, that with smaller lattice constant the exchange parameters becomes increasingly positive; they achieve +2.75 meV (PrN:Gd) or +0.8 meV (TmN:Gd). It remains an interesting question

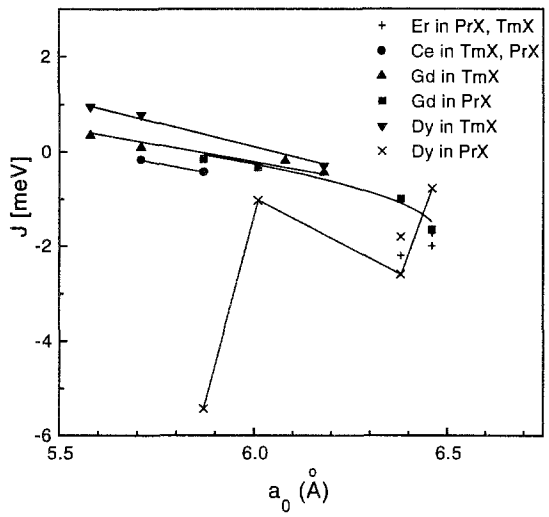

Fig. 38. Exchange parameters for monopnictides (X = P, As, Sb and Bi) as a function of the lattice spacings a_0.

whether the change of the sign of the exchange constant J at approximately $a \approx 6$ Å stems from contributions of the conduction electrons, i.e. via a RKKY-type interaction between Gd^{3+} and Pr^{3+} or Tm^{3+}. This speculation is supported by the fact that the heavy monopnictides have a more pronounced metallic character. Urban et al. (1978) came to the same conclusion guided by ESR studies of Gd in the nonmagnetic hosts LaX (X = P, Sb, Bi).

The linewidths of PrX:Gd (X = P, As, Sb, Bi) have been measured by different groups (see Sugawara et al. 1975 and Davidov et al. 1977). Similar to the other metallic van-Vleck compounds there is a rapid nonlinear thermal broadening in the temperature range above 40–50 K, yet the increase in the linewidth is more moderate in the case of monopnictides compared, e.g. to metallic $PrPb_3$. The paper by Davidov et al. (1977) provides arguments why the Gaussian distribution of fluctuations $\Delta\omega$ is located in between Δ (crystal field splitting) and ω_0 (Gd resonance): $\Delta > \Delta\omega \gg \omega_0$. With this assumption a reasonable agreement between theory and experiment exists, although the fit is better for the light pnictides PrP and PrAs. Sugawara's model, which is based on the theory of Moriya and Obata (1958) yields a satisfactory agreement between theory and experiment. The linewidth analysis after Sugawara et al. (1975) allows one to extract crystal-field splittings $E(\Gamma_4) - E(\Gamma_1)$ which are in excellent agreement with the results of neutron scattering for all Tm- and Pr-monopnictides. Sugawara and Huang (1976a,b) examined non-S-state ions like Dy^{3+} and Ce^{3+} as ESR probes in some Tm- and Pr-monopnictides. Dy^{3+} has a doublet Γ_6 ground state with an isotropic g-value of 6.67. The crystal-field ground-state of Ce^{3+} in monopnictides is Γ_7 ($g = 1.43$). The measured g-value for e.g. Dy^{3+} in TmP is $g_{exp} = 9.3$. Here the small distance between Γ_6 and first excited Γ_8 state is responsible for this large g-shift.

Figure 38 gives a survey of almost all results for the exchange parameters between the ESR probe and the host van-Vleck ions. The general trend of an increasing

negative J value for increasing lattice parameters is well documented. Only the exchange parameters $J(Dy^{3+}\,Pr^{3+})$, measured by Sugawara and Huang (1976b), do not follow this general trend. Unfortunately there are no comparative values for this exception in the literature.

Davidov et al. (1979) presented the first observation of fine-structure relaxation narrowing of Gd ESR in single crystals of PrSb. They followed the lineshape over a large temperature range $4.2 < T < 60\,\mathrm{K}$. At low temperature the spectra are well resolved and show three crystal field components. At higher temperature the evolution of a single line towards $g \approx 2$ can be clearly noticed, totally in the sense of the Barnes–Plefka approach. The relaxation rate δ is expressed as the sum of two contributions, $\delta = \delta_{Pr} + \delta_e$, where δ_e is the well-known Korringa relaxation and δ_{Pr} is the contribution originating with Pr fluctuations at the Gd-resonance frequency (see e.g. Zevin et al. 1977b). The narrowing effect occurs in a much narrower temperature range, compared to the results obtained on LaSb:Gd (Urban et al. 1975), i.e. it cannot be caused only by conduction electrons, even if a much larger Korringa relaxation is assumed for PrSb:Gd. Therefore the main mechanism responsible for the narrowing is associated with Pr fluctuations induced by Pr–Pr exchange. With the well-known CF levels and the value of the exchange constant, $J_{Gd\text{–}Pr}$, the relaxation δ_{Pr} can be calculated with only one unknown parameter, namely the exchange parameter, $J_{Pr\text{–}Pr}$. δ_{Pr} depends on the population of the excited Γ_4 and Γ_5 levels and consequently it is only effective for temperature above ~8 K. For lower temperatures δ_e becomes more and more important. From their analysis the authors determined the g-value, $g = 2.40$ at $T = 4.2\,\mathrm{K}$, and the exchange constant between the Gd and the Pr ion, $J_{Gd\text{–}P} = 0.96\,\mathrm{meV}$.

Relaxation phenomena and host exchange interactions in Tm-based van-Vleck compounds are described in a detailed paper by Zevin et al. (1977b). The ESR lineshape of Gd in metallic TmX (X = P, Sb and Bi) are treated by generalizing the theories of Plefka and Barnes by including three coupled spin systems (i.e. Gd spins, Tm spins and conduction-electron spins). Kinetic equations and density matrix formalisms are used in analogy to the work of Redfield (1955) and Bloch (1956). The fitting procedure yields the result that for TmP and TmBi the distribution of the fluctuation spectra $\Delta\omega$ is larger than the Gd-resonance frequency: $\Delta\omega \geqslant \omega_0$. On the contrary, in the case of TmSb the result $\Delta\omega < \omega_0$ has been obtained. The extracted J(Gd–Tm) parameters are in agreement with those in fig. 38. The J(Tm–Tm) exchange parameters show that the exchange interaction $Tm^{3+} \leftrightarrow Tm^{3+}$ for TmSb is smaller by almost an order of magnitude with respect to those of TmP and TmBi. This result confirms the results of Birgeneau et al. (1972), who explained neutron scattering spectra of TmSb without taking $Tm^{3+} \leftrightarrow Tm^{3+}$ exchange interactions into account.

8. Spin glasses

Spin glasses (SG) are magnetic systems in which the magnetic moments are frozen into a low-temperature state devoid a conventional magnetic order. Long-range FM or AFM

order is suppressed due to structural disorder and "frustrated" magnetic interaction. That is, the RKKY interaction oscillates between positive and negative values as a function of distance. Structural disorder may originate in random dilution, like in the canonical spin glasses Cu:Mn, Au:Fe, etc., but may also be due to noncrystallinity, like in amorphous metals. The interplay of RKKY interactions and site disorder of the localized spins can drive a cooperative freezing transition into a disordered state. The experimental facts and theoretical concepts concerning spin glasses have been reviewed in detail by Binder and Young (1986).

The universal characteristic feature of SG, namely a sharp and frequency dependent cusp in the magnetic susceptibility, has first been reported by Cannella and Mydosh (1972) in the dilute magnetic alloy Cu:Mn and in the concentrated semiconductor $Eu_xSr_{1-x}S$ by Maletta and Felsch (1979). Since then enormous experimental and theoretical progress has been made in the understanding of the physics of spin glasses and in the magnetism of disordered systems. From the early 1970s to the late 1980s SG were in the focus of solid state physicists. During this period a large number of ESR experiments was performed and theoretical concepts for their interpretation have been developed (S.E. Barnes 1981a,b, 1984). However, and this should serve as an introductory comment and warning, the problem of ESR techniques is that the dynamical susceptibility is studied in relatively large magnetic fields. For example, if the frequency dependence of freezing phenomena is studied, one has to increase the magnetic field with increasing frequency, leading to inherent problems with the interpretation of the results.

After the pioneering work of Owen et al. (1956, 1957) on diluted localized moments in metals (Cu:Mn), twenty years later a large amount of experimental ESR work has been devoted to classical spin-glass systems. The experiments can be divided in two groups: one in the SG state at $T \ll T_g$ and one at $T > T_g$, where T_g is the glass transition temperature which depends on the measuring frequency.

In SG-state experiments with $T \ll T_g$, the main interest concerns the position of the resonance signal as a function of field and frequency. The prototype of this class of experiments was performed by Monod and Berthier (1980) who found that the resonance frequency depends linearly on the external field, i.e. $\omega = \gamma(aH + H_c)$ where H is the applied static field and the constant $a \leqslant 1$. For zero-field cooled samples $a \approx 0.5$, while for those cooled in large fields $a \approx 1$. The additional field H_c is a property of the system and represents an anisotropy field. Similar observations have been reported by Schultz et al. (1980) who found in addition a second resonance mode. They proposed a rather unconventional form of the anisotropy energy. Later on Fert and Levy (1980) proposed a three-site Dzyaloshinsky–Moriya mechanism to explain these results, while S.E. Barnes (1981b) pointed out that the observed EPR modes in Cu:Mn alloys can be described using an Edwards–Anderson-type theory for spin glasses including an anisotropy term.

However, the bulk of experiments in spin glasses was concerned with the temperature dependence of the resonance field, $H_{res}(T)$ and the linewidth at resonance absorption, $\Delta H(T)$ for $T > T_g$. A large amount of experimental work that belongs to this second class has been devoted to classical SG systems: Cu:Mn (Salamon and Herman 1978, Salamon 1979), Ag:Mn (Dahlberg et al. 1978, 1979, Mozurkewich et al. 1984, Wu et al. 1985,

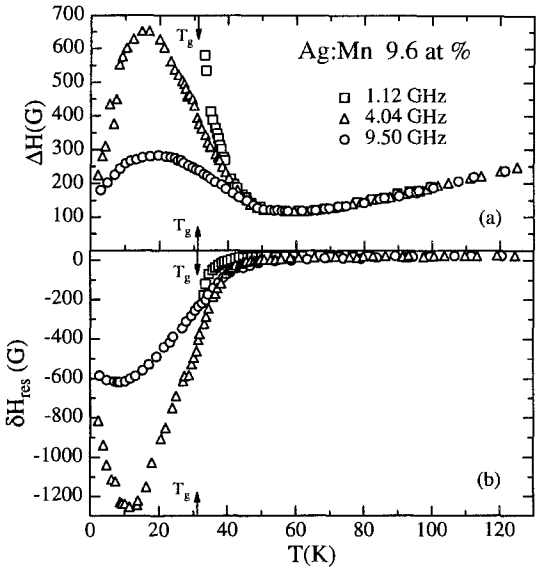

Fig. 39. (a) ESR linewidth ΔH and (b) resonance shift δH_{res} in Ag:Mn as a function of temperature at different measuring frequencies (from Mahdjour et al. 1986).

Mahdjour et al. 1986), Au:Mn (Varknin et al. 1981) and Au:Fe (Coles et al. 1978, Sarkissan 1979, Weissenberger et al. 1986).

The general behavior of the temperature dependence of the linewidth ΔH and the resonance field H_{res} is shown in figs 39a,b (Mahdjour et al. 1986). At high temperatures the ESR linewidth increases almost linearly with temperature. The Korringa slope b for most systems investigated only weakly depends on the concentration of localized spins, i. e. no bottleneck for relaxation is active in these systems. With further decreasing temperatures ΔH passes through a minimum ($T \approx 2T_g$) and increases rapidly towards T_g. Similar to the findings in fig. 39a, in many experiments a maximum in $\Delta H(T)$ is observed close to the glass-transition temperature. This cusp-shaped maximum of the linewidth strongly depends on measuring frequency and spin concentration. The resonance field is close to $g=2$ in the high-temperature limit and deviates significantly towards lower temperature, again revealing a characteristic frequency and concentration dependence, as shown in fig. 39b.

Coles et al. (1978) studied the spin-glass system $Au_{1-x}Fe_x$ close to the critical concentration ($x_c \approx 0.15$), separating the SG and the FM regime in the (x, T)-phase diagram. They found a maximum in $\Delta H(T)$ close to the glass-transition temperature T_g as determined via magnetization data and an increase towards higher temperatures much faster than a normal metallic Korringa behavior. These data were discussed and interpreted in full detail by Sarkissan (1979). He argued that for concentrations above the percolation limit, x_c, the spin of a finite cluster provides a powerful relaxation channel for the infinite cluster through which energy flow to the lattice is possible. The freezing of the finite clusters strongly influences the magnetic relaxation as no equilibrium between the spin

system and the lattice can be achieved. Hence, $\Delta H(T)$ displays a maximum close to T_g. For $T > T_g$ the temperature dependence can be understood in terms of exchange narrowing processes via spin–spin interactions.

Dahlberg et al. (1979) reported ESR experiments on Ag:Mn at 1.6 and 9.1 GHz. The low-temperature increase of ΔH has been explained assuming local field fluctuations. These fluctuations are quenched with increasing external fields (increasing probing frequency) yielding a suppression of the maximum in $\Delta H(T)$ with increasing measuring frequency. In close analogy, the excess linewidth Ag:Mn for $T > T_g$ has been interpreted as being due to critical spin fluctuations (Mahdjour et al. 1986). In the course of this work a scaling function using the nonlinear (spin glass) susceptibility as scaling variable has been worked out.

Measurements in Au:Fe alloys were described by Weissenberger et al. (1986) in the framework of a cluster model in which the average coupling between the finite and the infinite cluster plays on important role. Specifically, these authors explained the maximum in $\Delta H(T)$ as follows: For $T > T_0$ (here T_0 is the temperature of the linewidth maximum), resonant processes of the excited modes in the finite clusters with the infinite cluster yield the increase of the linewidth. For $T < T_0$ the decrease arises from a modulation of the population of states accessible to finite clusters by the spin waves propagating in the infinite cluster.

Finally we would like to mention that results in Cu:Mn (Salamon and Herman 1978) and in Ag:Mn (Wu et al. 1985) were interpreted assuming critical dynamics close to a phase transition. Hence, these data were taken as evidence for a thermodynamic phase transition into a disordered magnet.

In addition to these ESR experiments on canonical spin glasses, also lanthanide spin glasses and amorphous metals, revealing the characteristic relaxation processes of disordered magnets, have been investigated. ESR measurements on lanthanide spin glasses with results similar to those presented in fig. 39 have been reported by Malozemoff and Janet (1977), Janet and Malozemoff (1978), Zomack and Baberschke (1981) and Zomack et al. (1983). The central observation, a Korringa behavior at high temperatures and a strong increase of $\Delta H(T)$ towards the glass-transition temperature has been reported in all experiments.

A careful analysis of the experimental results in the SG $(LaGd)Al_2$ has been performed by Zomack et al. (1983). They found that the residual linewidth $\Delta H_0 = \Delta H(T \rightarrow 0)$, as determined from the Korringa increase depends on the paramagnetic Curie–Weiss temperature, namely $\Delta H_0 = a_0 - b\theta$ (S.E. Barnes 1984). Here a_0 is a constant, b the Korringa slope and θ the Curie–Weiss temperature. The increase of $\Delta H(T)$ below the minimum was described assuming correlated spins yielding a linewidth $\Delta H = (a_0 + bT)\chi^0/\chi$ where χ is the spin-glass susceptibility and χ^0 is the static susceptibility which follows a Curie-type of behavior. According to this formalism the linewidth at low temperatures depends on the inverse susceptibility of the SG.

The temperature dependence of the absorption linewidth in a large number of different disordered magnets has been studied by Bhagat et al. (1981). They proposed an exponential increase of the linewidth for decreasing temperature according to

$\Delta H(T) = \Delta H_0(x,\nu) + \Delta H_1(x) \exp[-T/T_0(x)]$, where ν is the measuring frequency and x the concentration of localized moments. This exponential behavior has been fitted to results in canonical spin glasses, like Cu:Mn and Ag:Mn (Bhagat et al. 1981), in amorphous alloys like $(Fe_xNi_{1-x})_{75}P_{16}B_6Al_3$ (Bhagat et al. 1980) and in semiconducting SG like $Cd_{1-x}Mn_xTe$ (Sayad and Bhagat 1985) and $Zn_{1-x}Mn_xTe$ (Bhagat and Sayadian 1986).

We close this section by purely mentioning that a number of ESR experiments were performed in the insulating spin glass $Eu_xSr_{1-x}S$. The results of the frequency and temperature dependence of linewidth and resonance field essentially reconciled the results in metallic spin glasses, namely a strong increase of ΔH and concomitantly a strong decrease of H_{res} towards the spin-glass temperature (Monod et al. 1986, Deville et al. 1981, Continentino et al. 1988). In contrast to metallic spin glasses, insulating SGs display a constant and temperature independent linewidth at high temperatures, which markedly increases with the spin concentration x (Monod et al. 1986).

9. Kondo impurities

It has been pointed out early that the ESR of local moments could be used to observe the Kondo effect directly by studying the resonance absorption of the Kondo impurity itself. Spencer and Doniach (1967) calculated the g-shift and Walker (1968) the relaxation rate due to the Kondo effect. Both contributions are rather small and experimentally hard to measure. This is partly due to the large residual linewidths typically found in Kondo alloys.

The first observation of the ESR of a Kondo impurity was made by Hirst et al. (1968) in Au:Yb. They found a negative g-shift indicating AFM interactions between the conduction electrons and the Yb impurities. In this system, in a series of papers Baberschke and his Berlin group reported on Kondo anomalies in the g-shift and in the relaxation rate of the Kondo impurity Yb^{3+} (Baberschke and Tsang 1980, Baberschke et al. 1980a,b, Nagel et al. 1980). By means of low-temperature and low-frequency ESR they detected the logarithmic temperature dependence of both the g-shift as well as the linewidth, below 1 K. The experiments were performed at 1.1, 3.4, 4.1 and 9.0 GHz in a ^{3}He–^{4}He dilution refrigerator. The intensity ratio of the two hyperfine lines of the Yb ($I = \frac{1}{2}$) probe guaranteed a precise determination of the measuring temperature. The lowest temperature reached was 90 mK. The ESR lines were extremely narrow and allowed the determination of the resonance field with high accuracy. Figure 40 shows the temperature dependence of the Yb g-value in Au:Yb measured at different frequencies and with different Yb doping levels as indicated in the figure. The experimental results were fitted using

$$\Delta g = 0.418 \frac{d}{\ln(T_K/T)}. \tag{33}$$

Here T_K is the Kondo temperature and d characterizes the degeneracy of the local-moment conduction-electron interaction channels. The solid line in fig. 40 has been calculated using a Kondo temperature $T_K = 4\mu K$ and $d = 3.8$ (Baberschke and Tsang 1980). Later

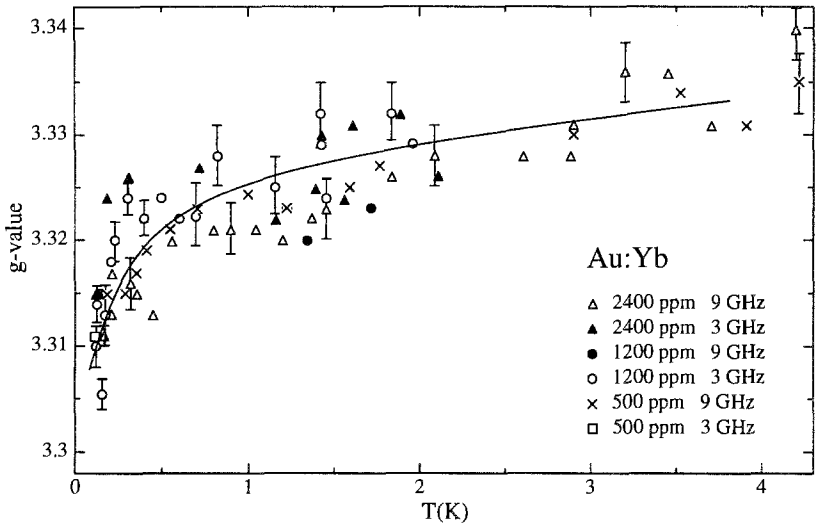

Fig. 40. Temperature dependence of the g-value in Au:Yb, obtained at different Yb doping levels and different measuring frequencies (from Baberschke and Tsang 1980). The solid line has been calculated using a simple model (eq. 33) as described in the text.

on, von Spalden et al. (1983) reanalyzed the data and calculated the longitudinal and the transverse spin susceptibilities following Götze and Wölfle (1971). The only parameters which enter this refined theoretical model to describe the g-shifts and the relaxation rates are the g-value of the ground state and the Kondo temperature T_K. The experimental data were well described, however, vastly different Kondo temperatures were deduced from the g-shift and from the relaxation data.

A number of multi-impurity experiments on Kondo systems were reported in the literature. Most of the early work is cited in the review by S.E. Barnes (1981a). A tutorial discussion on the Kondo effect has been given by Taylor (1975). Of these multi-impurity experiments, here we discuss Gd-ESR experiments obtained in $LaAl_2$ doped with Kondo impurities. Gd-ESR has been utilized to study the effects of a Kondo impurity in the pseudobinary alloy $La_{1-x}Ce_xAl_2$:Gd (Davidov et al. 1972). Similar experiments were performed by Weissenberger (1981) in the intermetallic compound (La, Y, Ce)Al_2:Gd. In this alloy Ce behaves like a Kondo impurity and the Kondo temperature can be varied from 0.4 to 100 K. The most important result of this investigation was the dependence of the residual linewidth ΔH_0 on the state of the Ce impurity, e.g. on the single-ion Kondo temperature.

10. Heavy-fermion systems and intermediate valence compounds

In this section we will review recent ESR studies in heavy-fermion systems (HFS) and in intermediate-valence compounds (IVC). We try to document that ESR results yield

similar insights into the physics of highly correlated electron systems, as nuclear magnetic resonance (NMR) and muon spin-rotation (μSR) techniques. It seems specifically interesting to compare the results of these different local-probe techniques, as they measure the local dynamical susceptibility of spin fluctuations and the electronic density of states at the Fermi energy at different sites. Hence this comparison allows for a detailed analysis of the band character or local character of heavy quasi particles and they provide insight into the strength and the dynamics of spin fluctuations at different lattice sites.

10.1. *Electronic correlations in systems with strongly hybridized local moments*

In dilute Kondo systems, Kondo impurities carrying local spins are embedded in metallic matrices. In these systems the characteristic temperature corresponds to the single-ion Kondo temperature T_K. In HFS and IVC the Kondo ions occupy the sites of a regular lattice (Kondo lattice, KL) and the characteristic temperature is the Kondo-lattice temperature T^*. Typical systems are some Ce-, Sm-, Eu-, Yb- and U- compounds. In these KL the 4f/5f electrons strongly interact with the conduction electrons. This hybridization of the local f moments with the band states is the origin and reason of fascinating and new ground states in metallic systems. They behave like paramagnets with local moments at high temperatures. However, below the characteristic temperature T^* the magnetic moments are compensated by the conduction electrons and these compounds reveal a strongly enhanced temperature-independent Pauli-spin susceptibility and a high Sommerfeld coefficient γ of the metallic specific heat. Concomitantly, for $T \ll T^*$ the resistivity is dominated by electron–electron scattering processes and follows a T^2-dependence. This phenomenology can be explained assuming conduction electrons with effective masses that are enhanced by two to three orders of magnitude.

Heavy-fermion (HF) behavior is observed at intermediate hybridization strengths between the f-electrons and the band states and conceptually it is assumed that the spin degrees of freedom are transferred from the f-electrons into the band states, while the charge resides almost completely at the f site. Coherent, magnetic and superconducting ground states have been found in HFS (Grewe and Steglich 1991). For compounds with strong hybridization even the charge of the 4f/5f electrons is fully or partially transferred to the conduction band. This regime is characteristic for intermediate valence compounds (see e.g. Lawrence et al. 1981).

A classification of compounds into HFS and IVC is rather artificial. As a rule of thumb, if the Sommerfeld coefficient $\gamma > 100\,\mathrm{mJ/(mol\,K^2)}$ the compound belongs to the class of heavy-fermion systems, otherwise they are counted as intermediate valence compounds. In addition, there exists an increasing amount of experimental evidence that Ce and U compounds behave rather different (Steglich et al. 1995). For example, superconductivity and long-range ordered magnetic phases coexist in U compounds, but superconducting (sc) and magnetic ground states compete in Ce alloys. These differences have been related to the differences in spatial extent of the 4f and 5f wave functions. The 5f wave functions are more extended yielding a much stronger 5f-ligand hybridization and hence the 5f states behave more like itinerant, band-like states. Nevertheless, strong Coulomb correlations

cause the low-lying energy scales of the excitations which are characteristic for heavy-fermion compounds (Steglich et al. 1995).

10.2. *Heavy-fermion systems*

Although electronically highly correlated compounds have been in the focus of interest for the last two decades, only a few Kondo and HFS were investigated by ESR techniques. In these experiments, the linewidth ΔH and the g-value provide a measure of the (local) density of electronic states at the Fermi level. Hence, ESR experiments seem to be particularly suited to measure the enhancement of the density of states below T^* (Abrikosov–Suhl resonance) which is the origin of the large effective masses in HFS. At first sight one expects a strongly enhanced Korringa relaxation rate as compared to metals with a normal density of states, characterized by effective masses $m^*/m \approx 1$.

It has been pointed out by Coldea et al. (1987) that in addition to the Korringa contribution to the linewidth, further broadening effects of the resonance absorption due to spin fluctuations have to be taken into account. According to Coldea et al. (1987) the temperature dependence of the linewidth is given by

$$\Delta H(T) = \Delta H_{ie}(T) + \Delta H_{if}, \tag{34}$$

where i denotes the impurity spin, e the conduction electron spin and f the f-electron moment of the host ions. ΔH_{ie} is the usual Korringa-type broadening,

$$\Delta H_{ie} = \pi k_B \cdot J^2 \cdot N^2(E_F) \cdot \frac{T}{g\mu_B}, \tag{35}$$

where J denotes the exchange coupling of the ESR probe to the conduction electrons and $N(E_F)$ is the electronic density of states at the Fermi level at the site of the probe. The second term in eq. (34) describes the contribution to the linewidth broadening due to RKKY-type magnetic interactions:

$$\Delta H_{if} = 2k_B T \chi_f \sum_j \frac{K_{if}^2(r_j)}{g_f^2 g_i \mu_B^3 h \Gamma}. \tag{36}$$

Here χ_f is the static susceptibility of the f-electron system, Γ is the magnetic relaxation rate of the f-state and K_{if}^2 denotes the coupling constant of the spin of the ESR probe to the f moment via the indirect RKKY exchange. A schematic representation of the interactions which are described in eq. (34) and are responsible for the linewidth broadening in HFS is shown in fig. 41.

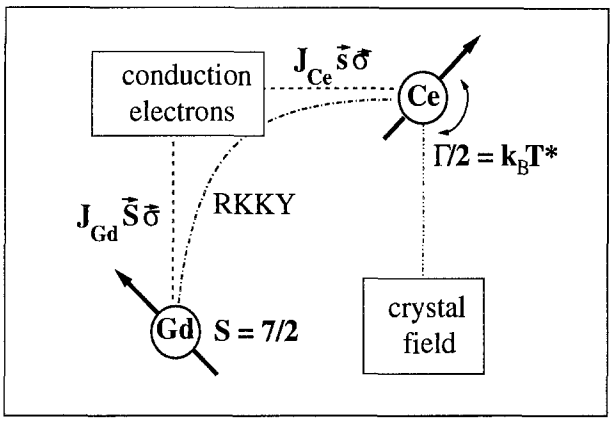

Fig. 41. Schematic representation of the interactions that contribute to the magnetic relaxation in heavy-fermion compounds. Here a Gd ion is taken as ESR probe in a Ce-based heavy-fermion material.

In deriving eq. (36) a purely relaxational ansatz has been used for the dynamical susceptibility, namely

$$\chi''(\omega) = \frac{\omega\chi_f\Gamma}{\omega^2 + \Gamma^2}. \tag{37}$$

This dynamical susceptibility neglects all Q-dependence and strictly represents a local quantity only. A similar expression can be derived for the temperature dependence of the g-value,

$$g(T) = g_{iso} + \Delta g_e + \Delta g_f, \tag{38}$$

where g_{iso} represents the value of the g-factor in an insulating material, e.g. for Gd^{3+} $g_{iso} = 1.992$. Δg_e represents the g-shift due to the coupling of the ESR probe to the conduction electrons:

$$\Delta g_e = JN(E_F) \tag{39}$$

and Δg_f is the g-shift due to magnetic fluctuations which are coupled to the ESR probe via RKKY-type interactions

$$\Delta g_f = \chi_f \sum_j \frac{K(r_j)}{\mu_B^2 g_f}, \tag{40}$$

and, again, has to be estimated in calculating all contributions from neighboring f sites.It is important to note that Δg_f solely depends on the static susceptibility of the f-electron system.

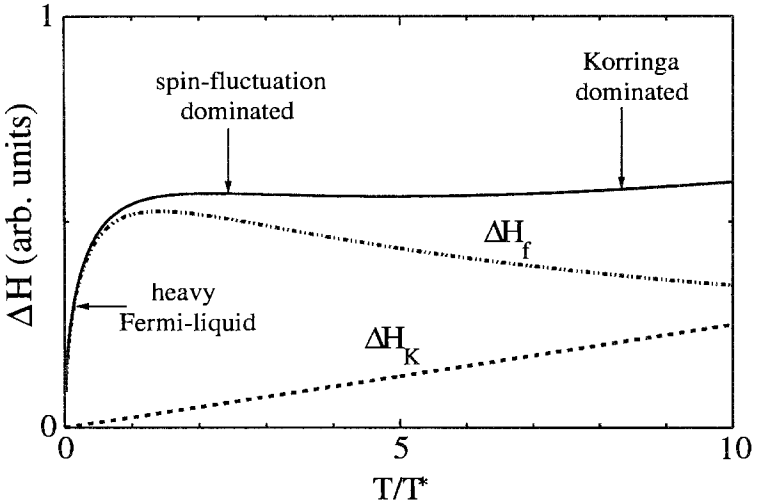

Fig. 42. Schematic temperature dependence of the linewidth in HFS (full line): contributions due to the on-site Korringa relaxation ΔH_K (narrow-dashed line) and inter-site spin fluctuations ΔH_f (long-dashed line) are indicated separately. The parameters that have been used in these calculations are indicated in the text.

A highly schematic temperature dependence of ΔH for a heavy-electron material, following the ideas outlined above, is presented in fig. 42. At high temperatures ($T \gg T^*$), ΔH is dominated by the normal Korringa behavior ΔH_e. With decreasing temperatures contributions due to spin fluctuations (ΔH_f) become important and are responsible for the significant deviations from a Korringa-like increase. Finally, for $T < T^*$ the local moments are fully Kondo-compensated and ΔH reveals a linear Korringa slope which is strongly enhanced compared to normal metals. $\Delta H(T)$ in fig. 43 has been calculated using eqs. (34–36). In these model calculations a square-root dependence of the magnetic relaxation rate and Curie–Weiss-like static susceptibility have been used in the paramagnetic regime. For $T < T^*$ both the static susceptibility and the magnetic relaxation rate were assumed to be temperature independent. In the framework of a microscopic theory, recently the dynamical susceptibilities were calculated by Wright (1995). With this theoretical approach it was possible to calculate the experimentally observed thermal broadening of the resonance absorption in the HFS $CeCu_2Si_2$ and $CeAl_3$ which looks very similar to the results shown in fig. 42.

And indeed, this characteristic temperature dependence of the linewidth of the resonance absorption has been detected in Gd-ESR experiments in the prototypical heavy-electron material $CeCu_2Si_2$ as compared to results in $LaCu_2Si_2$ (fig. 43). Below $T \approx 15\,K$ the increase in the HFS is strongly enhanced compared to the normal metal. For $T > T^*$ spin fluctuations dominate $\Delta H(T)$ yielding a weak temperature dependence only. However, already at first sight it becomes clear that the enhancement of the Korringa slope in $CeCu_2Si_2$ for $T < T^*$ as compared to $LaCu_2Si_2$ is far too small. From the mass enhancement that follows from the heat capacity and susceptibility results one would

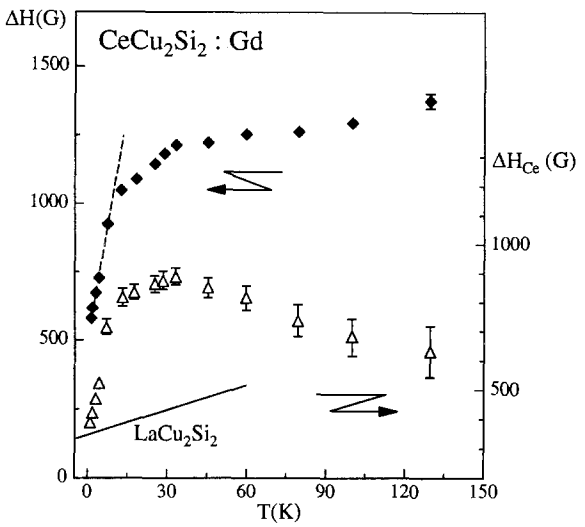

Fig. 43. Temperature dependence of the Gd-ESR linewidth in $CeCu_2Si_2$ (diamonds) and in $LaCu_2Si_2$ (solid line). The dashed line indicates the Korringa relaxation in the heavy Fermi-liquid regime. The points shown as triangles were obtained by subtraction of $\Delta H(T)$ as determined in $LaCu_2Si_2$ from $\Delta H(T)$ of $CeCu_2Si_2$ and are estimates of the pure intersite effects. From Elschner and Schlott (1988).

expect that the Korringa slope is enhanced by at least a factor of 10^6. Experimentally one observes a factor of 10, a fact that reveals the strongly local character of the heavy quasi-particles. In what follows we try to discuss experimental ESR results in Ce and U compounds in full detail.

10.2.1. *Ce compounds*

$Ce_xY_{1-x}Al_2$ was one of the first compounds in which a systematic investigation of the effect of the 4f spin fluctuations on the line broadening was performed. $CeAl_2$ is a Kondo-lattice system with a characteristic temperature $T^* \approx 3.5\,K$ and an AFM phase-transition temperature $T_N \approx 3.9\,K$. On dilution with Y, the magnetic order is suppressed and, concomitantly, the Kondo temperature is steadily increased (Aarts et al. 1981, Schefzyk et al. 1985). For $x < 0.3$ the system reveals the characteristic signatures of IV compounds. A systematic Gd-ESR investigation has been performed by Coldea et al. (1987). The temperature dependence of the linewidth for Ce concentrations $0.08 \leqslant x \leqslant 0.5$ is shown in fig. 44. For the lowest Ce concentrations a constant, Korringa-type, increase was detected with a slope $b \approx 50\,G/K$. This value is close to the isothermal (without bottleneck effects) Korringa slopes as observed in $LaAl_2$ and YAl_2 (Schäfer 1971). With increasing x, the slope $\Delta H/\Delta T$ increases significantly, reaching values of approximately 270 G/K at $x = 0.5$ and $T < 10\,K$. The enhanced slope corresponds to a Korringa relaxation of the Gd spin to a heavy Fermi liquid. For higher temperatures and for Ce concentrations

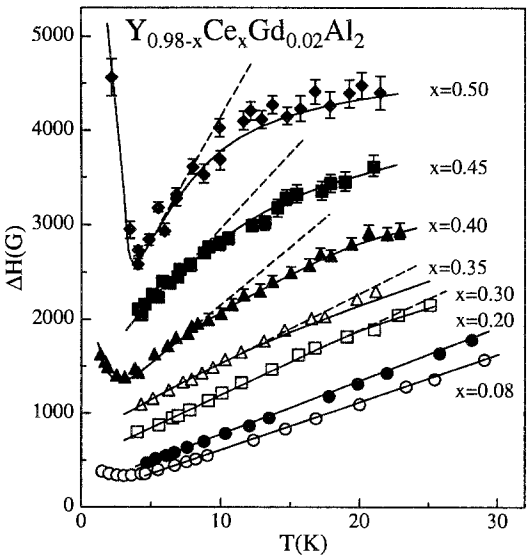

Fig. 44. Temperature dependence of the Gd-ESR linewidth in $Y_{1-x}Ce_xAl_2$:Gd. The solid lines were drawn to guide the eye. The dashed lines are extrapolations of the low-temperature Korringa slopes. From Coldea et al. (1987).

$x \geqslant 0.3$, the deviations from a constant slope indicate the increasing importance of spin fluctuations leading to an overall behavior of $\Delta H(T)$ as indicated schematically in fig. 42.

Gd-ESR experiments on $CeCu_2Si_2$ were performed by Schlott et al. (1988) and by Elschner and Schlott (1988). $CeCu_2Si_2$ is the archetypical HF superconductor with a characteristic temperature $T^* \approx 10\,\mathrm{K}$ and a superconducting phase transition at $T_c \approx 0.5\,\mathrm{K}$ (Grewe and Steglich 1991). It has been demonstrated unambiguously that the superconductivity is carried by the heavy quasiparticles (Steglich et al. 1979). The temperature dependence of the linewidth as observed in Gd-doped single crystals is shown in fig. 43 and compared to the Korringa type of behavior as observed in $LaCu_2Si_2$:Gd (solid line in fig. 43). The Korringa slope in $CeCu_2Si_2$ in the heavy Fermi liquid regime amounts to $b = 47\,\mathrm{G/K}$ as compared to $b = 4.5\,\mathrm{G/K}$ which is the Gd-Korringa slope of the "normal" metallic $LaCu_2Si_2$. The resulting linewidth dependence $\Delta H_{Ce}(T)$ in $CeCu_2Si_2$, after corrections due to ΔH_K as determined in $LaCu_2Si_2$, is shown in fig. 43 using open symbols.

It should be mentioned that the observed Gd-ESR spectra in $CeCu_2Si_2$ are exchange narrowed and were described by a single Lorentzian resonance line. Both the resonance field and the linewidth are strongly anisotropic and depend on the angle Θ between the crystallographic c direction and the external magnetic field. This has been demonstrated by Schlott et al. (1988) and Schlott (1989) in Gd-doped $CeCu_2Si_2$ single crystals. The angular variation of the linewidth and resonance field due to crystalline-electric field effects were well described within the Barnes–Plefka theory (S.E. Barnes 1974, Plefka 1973) for a partially exchange narrowed spectrum with an axial splitting $B_2^0 = 46\,\mathrm{mK}$ (Schlott et al. 1988). It has been shown recently that data of similar quality as in single crystalline material can be obtained from grain-oriented samples (Schütz 1996).

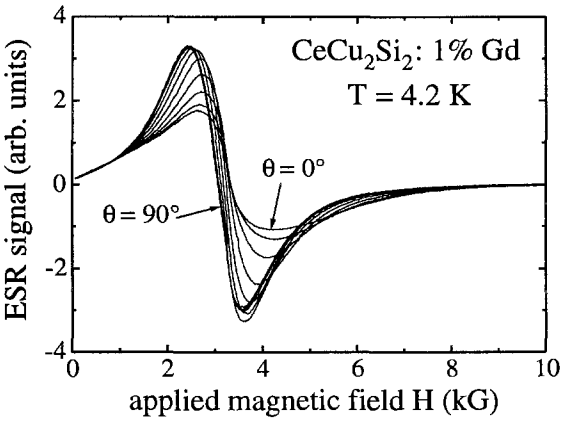

Fig. 45. Angular variation of the Gd-resonance absorption in $CeCu_2Si_2$ at 4.2 K. In these experiments the c-axis of the grain-oriented powder is rotated with respect to the external magnetic field. From Schütz (1996).

A representative result showing the angular dependence of the Gd-resonance absorption in grain-oriented $CeCu_2Si_2$ is shown in fig. 45. In this experiment the c-axis of the oriented grains is rotated with respect to the external magnetic field. The grain-oriented results reproduce those obtained in single crystals by Schlott et al. (1988) in full detail. The temperature dependence of the linewidth in $CeCu_2Si_2$:Gd as observed in grain-oriented samples is documented in fig. 46 (solid squares). These results are compared to single crystal data (open triangles: Schlott et al. 1988).

Similar results were obtained for $CeAl_3$. $CeAl_3$ is a magnetic heavy-fermion compound with $T^* \approx 4\,\mathrm{K}$ and $T_N \approx 1.6\,\mathrm{K}$ (Andres et al. 1975, Grewe and Steglich 1991). Gd-ESR measurements were performed by Schlott et al. (1988) and Elschner and Schlott (1988). Results for the temperature dependence of ΔH and ΔH_{Ce} are shown in fig. 47. Again

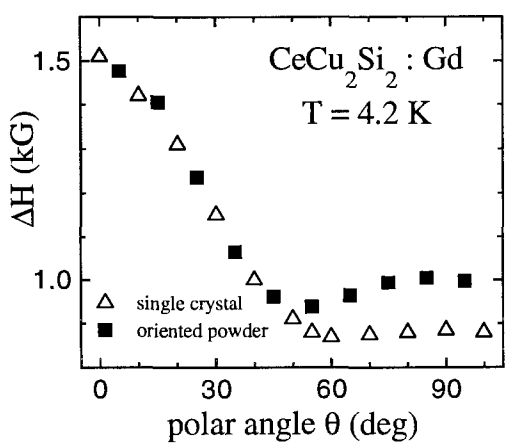

Fig. 46. Angular dependence of the Gd-ESR linewidth in $CeCu_2Si_2$ at 4.2 K as observed in grain-oriented powder (solid squares). From Schütz (1996). The results are compared to single-crystal results from Schlott et al. (1988) (open triangles).

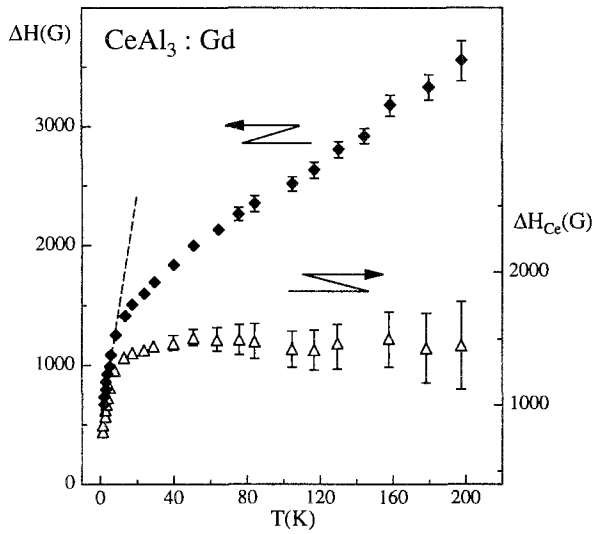

Fig. 47. Temperature dependence of the Gd-ESR linewidth in $CeAl_3$:Gd. The dashed line is an extrapolation of the low-temperature Korringa slope. The open triangles represent the estimated contribution to the linewidth from spin fluctuations only. From Elschner and Schlott (1988).

the prototypical behavior, namely indications of spin fluctuations for $T \geqslant T^*$ and a heavy Fermi liquid for $T < T^*$ were observed. The Korringa slope b amounts to 138 G/K for $T < T^*$ compared to $b = 11$ G/K observed in $LaAl_3$.

The temperature dependence of the g-factor is shown in fig. 48 (Schlott 1989). For temperatures above 20 K, $g(T)$ closely follows the temperature dependence of the bulk susceptibility. At low temperatures the onset of moment compensation is clearly visible leading to an enhanced temperature-independent Pauli-spin susceptibility. Fig. 48 clearly indicates the power and the potential of magnetic resonance experiments: Moment compensation can easily be detected in the local susceptibility of microscopic measurements. It can hardly be detected in bulk measurements due to the contributions from defect states with local moments.

At this point it is interesting to note that Gd-ESR has been investigated in $GdAl_3$ by Coles et al. (1987). $GdAl_3$ exhibits long-range magnetic order below $T_N = 17$ K. For $T < 100$ K and decreasing temperatures the linewidth steadily increases towards T_N, with a sharp increase below T_N. The authors interpreted these results as the possible signature of frustrated magnetic interactions. According to our interpretation these results indicate strong spin fluctuations for $T > T_N$. The rapid increase below T_N signals the onset of an inhomogeneous line broadening due to the onset of antiferromagnetic order and concomitant strong local magnetic fields.

The temperature dependence of the resonance absorption of Gd-doped $CeAl_3$ has been investigated as a function of hydrostatic pressure by Elschner and Schlott (1988). The results for the pressure and temperature dependence of the linewidth are shown

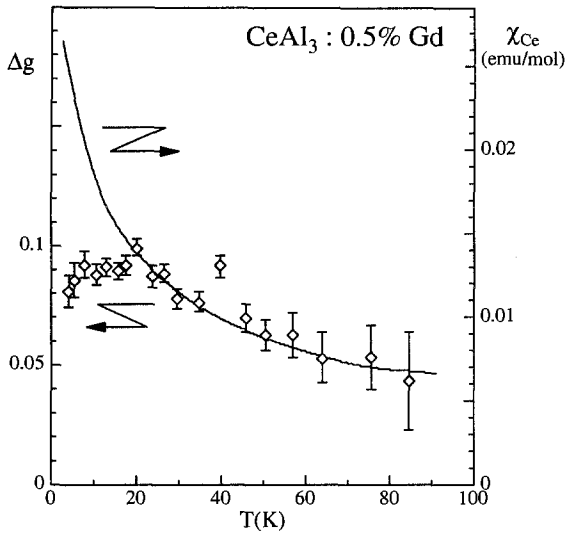

Fig. 48. Temperature dependence of the Gd g-shift in $CeAl_3$:Gd. The solid line represents the static bulk susceptibility of $CeAl_3$. From Schlott (1989).

in fig. 49. Under hydrostatic pressure the Kondo-lattice temperature T^* is increased due to an increased hybridization of the 4f moments with the band states. Utilizing heat capacity experiments under hydrostatic pressure Brodale et al. (1986) found that at pressures of 8 kbar the Sommerfeld coefficient γ is reduced to 550 mJ/(mol K^2) compared to 1200 mJ/(mol K^2) at atmospheric pressure. From the observed pressure dependence of γ it can be concluded that the characteristic temperature has been increased by more than a factor of two ($\gamma \sim 1/T^*$). Accordingly, the Korringa slope b at low temperatures, which is a direct measure of the mass enhancement of the heavy quasiparticles, steadily decreases with increasing pressure. $b = 138$ G/K at atmospheric pressure and is reduced to values of 9 G/K at 17 kbar, which is close to the Korringa slope found in the non-magnetic reference compound $LaAl_3$ ($b = 11$ G/K). Even more important, fig. 49 provides some experimental evidence that for pressures $p > 5$ kbar in the temperature dependence of ΔH a positive curvature develops. This can be interpreted that at low temperatures, at the Gd site the density of states is reduced as compared to the paramagnetic metal. This phenomenon which will be discussed later in full detail, and can be interpreted in the phenomenology of a hybridization gap at the Gd site.

$CeCu_6$ is a HFS with a paramagnetic and normal conducting ground state (Stewart et al. 1984). Gd-ESR experiments in highly concentrated $Gd_xLa_{1-x}Cu_6$ and $Gd_xCe_{1-x}Cu_6$ have been reported by Kwapulinska and Kaczmarska (1990). Only samples with Gd concentrations $x > 0.3$ have been studied and g-values and linewidth broadenings were investigated as a function of temperature. In pure $GdCu_6$ the g-value, $g = 1.99$ and the Korringa slope amounts to $b = 1.75$ G/K. In both compounds the Korringa slopes increase with decreasing Gd concentrations. The increase is much stronger in the Ce compound. The authors conclude that $GdCu_6$ is a strongly bottlenecked system and that Ce opens

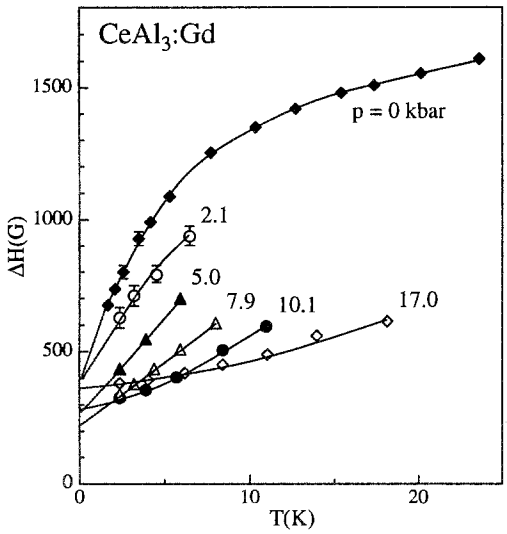

Fig. 49. Temperature dependence of the Gd-ESR linewidth in $CeAl_3$:Gd at different pressures from 0 to 17 kbar. The lines are drawn to guide the eye. From Elschner and Schlott (1988).

the bottleneck much more effectively than La. However, the increase in linewidth with increasing Ce concentration may be partly due to spin fluctuation effects of the Kondo ions.

Recently we have undertaken a systematic Gd-ESR study on CeM_2X_2 compounds with M = Cu, Ag, Au, Ni, Ru and X = Si and Ge. Depending on the hybridization strength, i.e. on the values of T^* and T_N, different relaxation behaviors can be observed, which range from normal metallic behavior with a Korringa-like increase of the linewidth at resonance absorption (e.g. $CeAu_2Ge_2$) to true heavy-fermion behavior like in $CeCu_2Si_2$ (Todt 1993, Schütz 1996). The evolution of the temperature dependence of the linewidth with increasing hybridization strength has been nicely demonstrated in the pseudo-ternary compound $Ce(Cu_{1-x}Ni_x)_2Ge_2$. $CeCu_2Ge_2$ is a heavy-fermion system with a magnetic ground state with a characteristic temperature $T^* \approx 6$ K and a magnetic ordering temperature $T_N = 4.1$ K (Knopp et al. 1988a). On dilution of Cu with Ni, a complex magnetic phase diagram evolves (Loidl et al. 1992), and close to the pure Ni compound the local moments are compensated and T^* increases strongly. $CeNi_2Ge_2$ is a nonmagnetic HFS with $T^* \approx 30$ K (Knopp et al. 1988b). Systematic Gd-ESR experiments were performed by Krug von Nidda et al. (1997) for systems covering the complete concentration range. $\Delta H(T)$ for concentrations $x = 0.5$, 0.6, 0.7, 0.8 and 0.9 is shown in fig. 50. For concentrations $x < 0.8$, the linewidth in the temperature range investigated clearly is dominated by magnetic interactions (see the model calculations shown in fig. 42). The strong increase of $\Delta H(T)$ for $x = 0.5$ and $x = 0.6$ below 4 K is due to an inhomogeneous broadening of the line in the magnetically ordered state. The onset of magnetic order can hardly be detected in the compounds with Ni concentrations $x = 0.65$ and 0.7. Possibly this is due to the fact that the ordered moments in this concentration

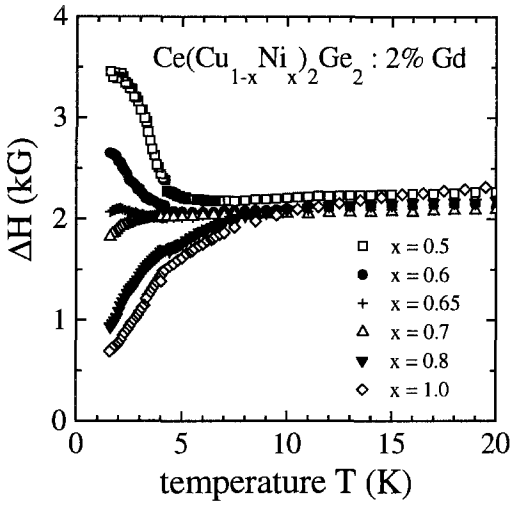

Fig. 50. Temperature dependence of the Gd-ESR linewidth in $Ce(Cu_{1-x}Ni_x)_2Ge_2$ doped with 2% Gd for Ni-concentrations $x = 0.5$, 0.6, 0.65, 0.7, 0.8 and 1.0. From Krug von Nidda et al. (1997).

regime are small (Loidl et al. 1992). For $x \geqslant 0.8$ the moments become fully compensated for $T < 10$ K and a heavy Fermi liquid behavior is responsible for the strong Korringa-like increase of ΔH at the lowest temperatures.

10.2.2. *Uranium compounds*

There have been early attempts to determine the ESR properties of UBe_{13} (Gandra et al. 1985) and UPt_3 (Gandra et al. 1987). Measurements of the local-moment ESR of Er, Dy and Gd were performed in the temperature region where a large variation in the enhanced specific heat has been detected. In clear distinction to what has been expected, the authors found a normal Korringa-type of increase of the linewidths at resonance absorption and no anomaly in the temperature dependences of the g-values. Specifically, in case of the Gd probe the Korringa slopes amounted to values of $b = 21$ G/K for UBe_{13} and $b = 1.1$ G/K for UPt_3. In the reference compound $LaBe_{13}$ a b value of 18 G/K was detected. The absence of any significant enhancement to the thermal broadening and the lack of any anomaly in the g-values lead the authors to conclude that the ESR probes substituting at the U sites are not significantly coupled to the heavy-fermion system. This conclusion was somewhat contrary to the Be NMR data of McLaughlin et al. (1984), who observed a greatly enhanced nuclear relaxation rate and significant deviations from a linear behavior. The findings of Gandra et al. (1985, 1987) that the local-moment relaxation in UBe_{13} and UPt_3 is of the same order as in materials with ordinary effective masses, have led Varma (1985) to propose that the renormalizations in the life time τ^* and the effective masses m^* may cancel each other leaving the local-moment relaxation unaffected.

However, later on Cox (1987) suggested that nuclear resonance is a more effective method to probe the heavy-fermion state than electron-spin resonance, simply because the probe nuclei usually is closer to the heavy-electron sites so that the strong range

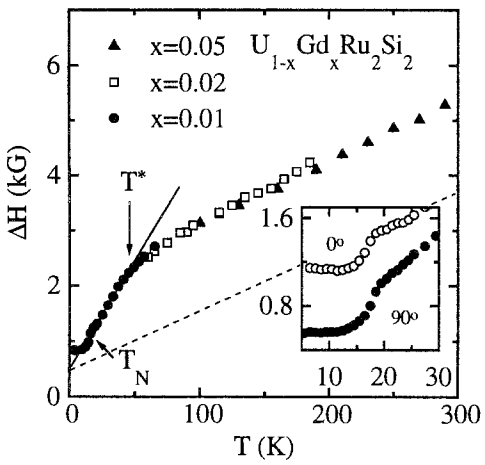

Fig. 51. Temperature dependence of the Gd-ESR linewidth in URu_2Si_2 for different Gd concentrations. The experiments have been performed on grain-oriented samples. The solid line indicates the heavy-Fermi liquid-like Korringa behavior. The inset shows ΔH vs. T in the vicinity of the AFM phase transition for two orientations. From Spitzfaden et al. (1996).

dependence of both dipolar and RKKY interactions favors nuclear relaxation. From the experimental point of view, we suggest that the ESR experiments in UPt_3 and UBe_{13} over a larger temperature range be repeated. In these cases the enhancement of the Korringa slope in the HF state may be small and deviations from a normal Korringa-like behavior may only be observed in systematic investigations.

Er-ESR experiments in the superconducting state of the heavy-fermion system URu_2Si_2 were reported by Taleb et al. (1988). The measurements were performed from 0.5 to 4 K. No anomaly has been detected in the Er^{3+} g-shift. With decreasing temperatures the linewidth decreases linearly with a Korringa slope $b = 4$ G/K and the linewidth increases slightly on passing from the normal to the superconducting state. These observations were explained to be consistent with singlet pairing and strong spin–orbit scattering (Taleb et al. 1988).

A detailed ESR study on the heavy-fermion system URu_2Si_2 was performed by Spitzfaden et al. (1996). URu_2Si_2 undergoes an antiferromagnetic transition at $T_N = 17.5$ K and becomes superconducting below $T_c = 1.2$ K (Palstra et al. 1985, Maple et al. 1986). The ordered moment is extremely small and amounts to $0.03\mu_B$ at the lowest temperatures (Broholm et al. 1986, Mason et al. 1990, Isaacs et al. 1990). The increase of the resistance in passing T_N from above provides some experimental evidence for the opening of a band gap at the Fermi energy due to the formation of a spin-density wave. It is important to note that superconductivity coexists with long-range AFM order. The Gd-ESR experiments were performed on grain-oriented samples. The resonance absorption was found to be strongly exchange narrowed. The g-values were measured with the magnetic field parallel and perpendicular to the c-axis. It has been found that the anisotropy of the g-values mirrors the anisotropy of the bulk susceptibility as observed in single crystals. The temperature dependence of the linewidth is shown in fig. 51 (Spitzfaden et al. 1996). With decreasing temperatures, the linewidth decreases almost linearly. Below the characteristic

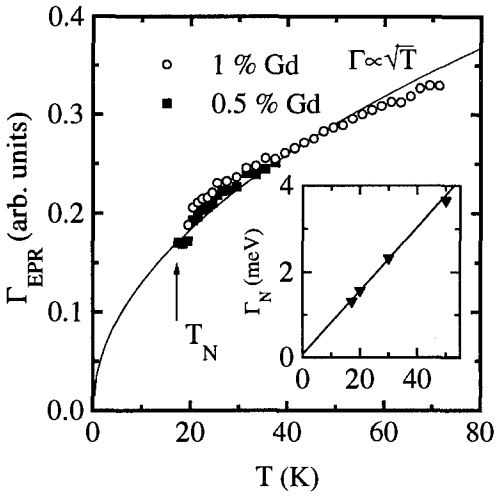

Fig. 52. Magnetic relaxation rate Γ_{ESR} in URu_2Si_2 as calculated from the results shown in fig. 51. The solid line represents a square-root behavior. The inset shows the neutron scattering results $\Gamma_N(T)$ which reveal a linear temperature dependence in a limited temperature range. From Spitzfaden et al. (1996).

temperature $T^* \approx 70\,K$ the enhanced Korringa slope signals the onset of heavy Fermi liquid behavior. For $T < T_N$, ΔH decreases abruptly, indicating a reduced relaxation of the local moments due to the opening of a gap in the electronic density of states. This behavior is clearly documented in the inset of fig. 51.

It is clear that the Fermi liquid regime in which the linewidth decreases with decreasing temperature is characterized by fully compensated moments. And it is important to note that magnetic order develops out of this Fermi liquid. As moment compensation has set in already at 70 K, the results have been interpreted as a band-like magnetism. In heavy-fermion band magnets (HFBM) the spin degrees of freedom have been transferred from the 4f sites to the conduction electrons. The evolution of heavy-fermion magnetism with extremely small moment has been theoretically described by Grewe and Welslau (1988). The extremely reduced Korringa slope at low temperatures (see the inset of fig. 51) compared to the Korringa slope for $T > T_N$ is a clear experimental evidence for the reduction of the electronic density of states.

Finally, $\Delta H(T)$ and the experimentally determined static susceptibilities have been used (Spitzfaden et al. 1996) to calculate the temperature dependence of the magnetic relaxation rates. The result is shown in fig. 52. Here $\Gamma_{ESR}(T)$ is plotted in the paramagnetic regime and compared with the theoretical predictions by Cox et al. (1986) and Bickers et al. (1985). These authors predicted a square-root dependence of the magnetic relaxation rate for temperatures $T > T^*$. The inset of fig. 52. shows the magnetic relaxation rate as determined in inelastic neutron scattering experiments. In these experiments a linear temperature dependence has been observed, but only in a limited temperature range (Holland-Moritz et al. 1987).

A number of uranium-based intermetallic compounds in which spin fluctuations seem to play an important role were investigated by Larica and Coles (1985) using Gd as ESR probe. Negative g-shifts which usually are associated with significant d-electron

contributions to the electronic susceptibility were observed in UCo_2, while positive g-shifts were reported for URh_3. The temperature dependences of the linewidths in both compounds were rather small and amounted to 10 G/K (UCo_2 : 1% Gd) and 2.6 G/K (URh_3 : 1% Gd). No resonance absorption was observed for UAl_2. An experimental fact that has been ascribed to strongly fluctuating 5f spins.

10.3. *Intermediate valence systems*

At first sight, ESR experiments can provide a direct information about the valence state of impurity ions in metals. That is, the observation of an ESR signal in Au:Yb with a g-value of $g = 3.34$ is a direct proof of Yb^{3+} ($4f^{13}$) with a Γ_7 ground state (Hirst et al. 1968, Tao et al. 1971). A Yb signal is not observable in Ag:Yb indicating a transition into a mixed valent state ($4f^{13}$–$4f^{14}$). Nagel et al. (1973) systematically studied the intermetallic compound Au_xAg_{1-x}:Yb for Au concentrations $1 < x < 0.7$. With decreasing x they found a steadily increasing Korringa slope of the linewidths and a steadily increasing negative g-shift, indicating the transition from a stable f configuration into a mixed valence behavior. These experimental results are shown in fig. 53 (Nagel et al. 1973).

In Kondo lattices the resonance absorption of the f ions is usually not observable and the systems have to be studied using a further ESR probe, mostly gadolinium. α-Ce is the most prominent mixed-valence system. However, it has been demonstrated that in this compound the 4f electrons do not contribute significantly to the linewidth and to the g-value of the ESR probe (Rettori et al. 1978). Hence, α-cerium was discussed in detail in sect. 4.1. Valence transitions generally evolve slowly as a function of temperature. Besides the well-defined transition in α-cerium another sharp, temperature-induced valence transition has been detected in $Yb_{0.4}In_{0.6}Cu_2$ (Felner and Nowik 1986).

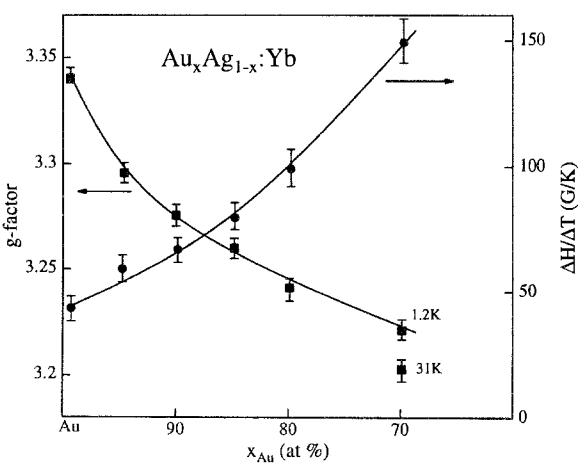

Fig. 53. Concentration dependence of the Korringa slope and the g-shift in the intermetallic compounds Au_xAg_{1-x}:Yb. From Nagel et al. (1973).

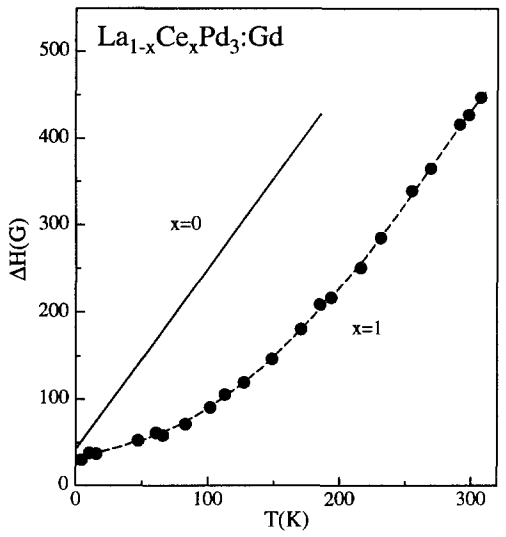

Fig. 54. Temperature dependence of the Gd-ESR linewidth in $CePd_3$ (open squares) and $LaPd_3$ (solid line). The dashed line is drawn to guide the eye.

Later on, it had been shown that this transition appears over a wide range of concentrations in the pseudobinary $Yb_{1-x}In_xCu_2$ compounds (Shimizu et al. 1988). A detailed ESR study of the valence transition in $YbInCu_4$ has been performed by Al'tshuler et al. (1995), using Gd as an ESR probe. The g-shift and the linewidth were studied as a function of temperature. On decreasing temperatures the g-shift increases continuously and exhibits a discontinuity close to 70 K, well above the valence transition temperature which appears at 50 K. This difference in the characteristic temperatures has been ascribed to Gd–Gd interactions, but is not fully understood at present. The linewidth remains constant for temperatures $T > 150$ K, drops significantly towards the valence transition and exhibits a pure Korringa-type of behavior at the lowest temperatures. The Korringa slope is significantly enhanced (15 G/K) reminiscent of the behavior found in HFS. From these results, in close agreement with results from other experimental techniques, it can be concluded that Yb in $YbInCu_2$ is trivalent at high temperatures and reveals a mixed valence state at low temperatures.

In a series of investigations the Darmstadt group investigated the Gd-ESR in a variety of intermediate valence compounds. Guided by the results on HFS one might expect that the charge fluctuations couple to the Gd moment and increase the linewidth when compared to the value observed in isostructural (and often isoelectronic) normal metallic hosts. Surprisingly, Gd^{3+} or other lanthanide ions used as ESR probes in various IV compounds revealed unexpected narrow absorption lines. The ESR linewidth of $CePd_3$:Gd has been measured as a function of temperature at X- and Q-band frequencies (Gambke et al. 1978, Gambke and Elschner 1979, Schaeffer and Elschner 1983). At low temperatures the observed linewidth reveals a Korringa-like relaxation rate with a slope b that is significantly smaller than in the isostructural "normal" metals $LaPd_3$ and YPd_3. For

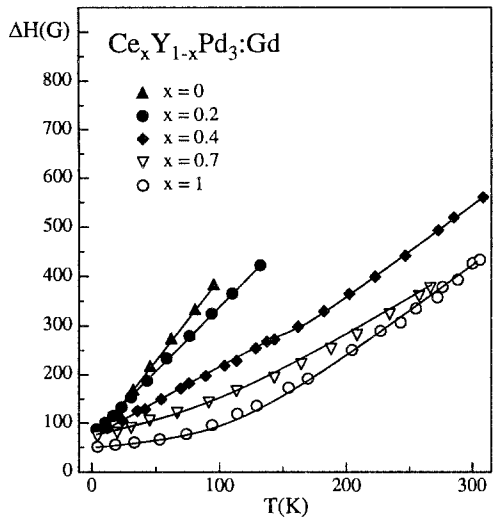

Fig. 55. Temperature dependence of the Gd-ESR linewidth in $Ce_xY_{1-x}Pd_3$ for different yttrium concentrations. The lines are drawn to guide the eye. From Elschner and Schlott (1988).

higher temperatures the Korringa slope increases, reaching the values of the isostructural compounds for $T > 100$ K. A representative result is shown in fig. 54, where $\Delta H(T)$ as observed in polycrystalline $CePd_3$ is compared to results obtained from $LaPd_3$. The continuous increases of the Korringa slope with dilution of Ce by Y is documented in fig. 55 for the system $Ce_xY_{1-x}Pd_3$ (Schaeffer and Elschner 1983, Elschner and Schlott 1988). For YPd_3 the Korringa slope has been determined as $b \approx 4$ G/K. On dilution with Ce the slope remains almost constant as long as the Ce ions are tetravalent. However, when the IV behavior starts, the temperature dependence of ΔH becomes more and more nonlinear. In the limit of $x = 1$ for $CePd_3$, the low-temperature slope $b \approx 0.4$ G/K which points towards a highly reduced density of states at the Fermi level at the Gd site. The experimental ESR results in $CePd_3$ have been explained theoretically using band-structure calculations including hybridization effects by Sticht et al. (1988) and by Ochi and Menezes (1991) within a phenomenological hybridization model.

The situation appears even more complicated in the IV compound $CeOs_2$ doped with lanthanum (Schlott et al. 1986). The temperature dependence of the Gd-ESR linewidth resembles that obtained in $CePd_3$, with an unusually small Korringa slope at low temperatures ($T < 100$ K) and a "normal" metallic slope at high temperatures ($T > 200$ K). On dilution of cerium by lanthanum, ΔH reveals an S-shaped temperature dependence. Characteristic temperature dependences of the Gd-ESR linewidths in $Ce_xLa_{1-x}Os_2$ are shown in fig. 56. These results in $CePd_3$ and $Ce{:}LaOs_2$ have been explained in the framework of the theory of a hybridization gap (Schaeffer and Elschner 1983, Schlott et al. 1986). According to this model, for $T < T^*$ due to coherence effects a pseudo-gap develops in the density of states (DOS). This pseudo-gap develops in the 4f-derived density of states, as well as in the band states. It is believed that no spatial overlap exists between the hybridized 4f states, and hence Gd relaxation occurs via the extended

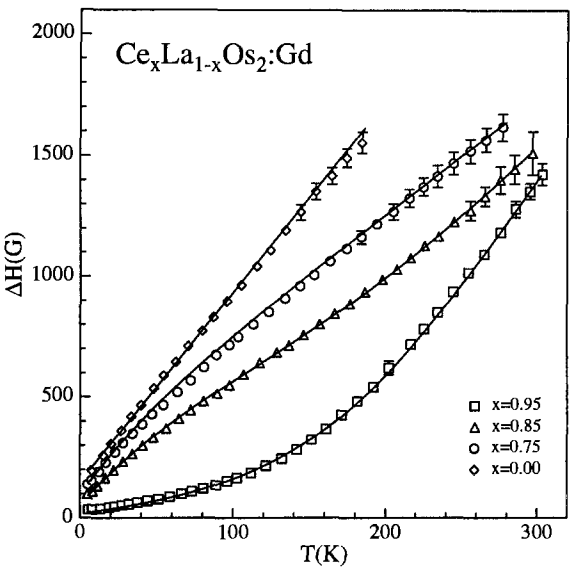

Fig. 56. Temperature dependence of the Gd-ESR linewidth in $Ce_xLa_{1-x}Os_2$. From Schlott (1984).

band states whose DOS is reduced near the Fermi level. This explains the effect that the Gd-ESR relaxation is smaller in the IV compound $CePd_3$ than in the normal metallic $LaPd_3$ (Schlott et al. 1986). The close correlation of the decrease of the Korringa slope with the increase of the valency of the Ce ions has been demonstrated in $Ce_{1-x}Sc_xPd_3$ by Gambke et al. (1980). Figure 57 reveals unambiguously that, as a function of Sc concentration x, the anomalies in the Korringa slope b, in the g-shift and the bulk susceptibility map each other. Similar Gd-ESR experiments have been performed on $Ce(Pd_{1-x}Rh_x)_3$ and $Ce(Pd_{1-x}Ag_x)_3$ (Schaeffer and Elschner 1983, Gambke et al. 1981). All these experiments convincingly demonstrate that a low temperatures gap appears in the electronic density of states at the Gd site. In fact, the conduction electron density of states at the Fermi level must be extremely small, as it was possible to observe a resolved hyperfine structure of a Mn-ESR spectrum in $CePd_3$ (Schaeffer and Elschner 1985). This was the first and, at the time being, the only observation of a resolved Mn hyperfine spectrum in a metallic host. A representative result of this resolved Mn-hyperfine spectrum in $CePd_3$ is shown in fig. 58 and is an important experimental proof of the reduced density of states at the site of the ESR probe. The g-value of the Mn^{2+} resonance in $CePd_3$ is substantially reduced ($g_{Mn} = 1.877 \pm 0.004$ at 1.4 K) and the hyperfine constant amounts to $A(^{55}Mn) = 63.0 \pm 0.5$ G. This value has to be compared with the hyperfine constant of Mn^{2+} ($3d^5\,4s^0$) in CaF_2 (95 G) or that of Mn^0 ($3d^5\,4s^2$) in an argon matrix (26 G). The authors estimated that in $CePd_3$ only a fraction of the 1.2 4s-electrons/Mn are effectively involved in the core polarization process. This reduction of the core polarization by the 3d electrons confirms that the 4s electrons in $CePd_3$ participate in chemical bonds.

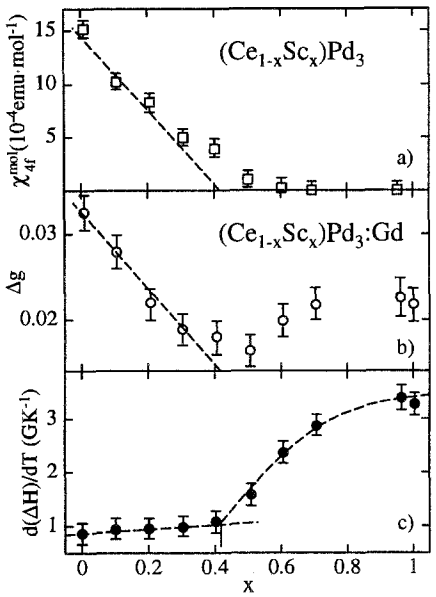

Fig. 57. Magnetic susceptibility, g-shift and Korringa slope as a function of Sc concentration x in $Ce_{1-x}Sc_xPd_3$:Gd: (a) molar susceptibility of the f-electron at 150 K as a function of x; (b, c) g-shift and Korringa rate vs. Sc concentration as determined at Q-band frequencies. From Gambke et al. (1980).

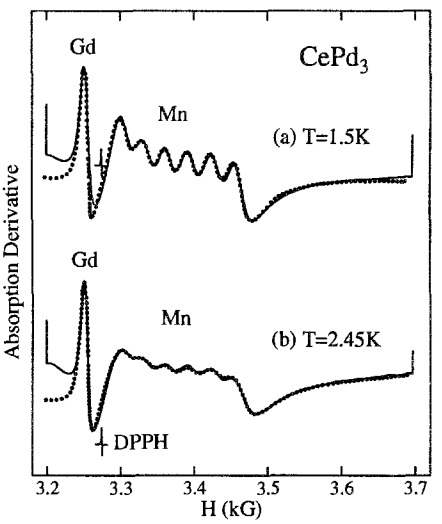

Fig. 58. ESR spectra of 150 ppm Mn and 6 ppm Gd in $CePd_3$ at 1.5 K and 2.45 K. The experimental results have been fitted using a Dysonian line shape. This is the only example of a well-resolved Mn-hyperfine spectrum in a metal. From Schaeffer and Elschner (1985).

That IVC can reveal a different behavior, e.g. an enhanced linewidth as compared to the non-magnetic reference compounds, has been shown by Barberis et al. (1979a,b, 1980). They measured the g-values and the linewidths of Gd and Nd hosts in the IV compounds $CeRh_2$ and $CeIr_2$. These compounds exhibit a significantly enhanced Pauli-spin susceptibility compared to the lanthanum compounds and usually are counted as IV systems. The temperature dependence of the Nd-ESR linewidth has been fitted using a combination of Orbach and Hirst processes with a crystal field splitting of the order of 100 K (Barberis et al. 1979a,b). The Korringa slopes in $CeRh_2$ and $CeIr_2$ were determined as 100 and 85 G/K, respectively, compared to 4.8 and 10 G/K obtained in the La reference compounds. Also the Gd linewidths in both IV compounds were enhanced by a factor of 10 compared to $LaRh_2$ and $LaIr_2$ (Barberis et al. 1979b).

Barberis et al. (1980) investigated the Nd-ESR in the pseudobinary alloys $Ce(Ir_{1-x}Os_x)_2$ and $Ce(Ir_{1-x}Pt_x)_2$. $CePt_2$ exhibits magnetic order at low temperatures and the valence of Ce is close to 3^+. $CeOs_2$ and $CeIr_2$ are IV systems with susceptibilities of the order of 60×10^{-5} emu/mol. The low-temperature Korringa slopes b and the g-values of the alloys are shown in fig. 59. The thermal broadening reveals an anomalous concentration dependence with a maximum at $CeIr_2$ ($b \approx 100$ G/K) and very low values for $CeOs_2$ and

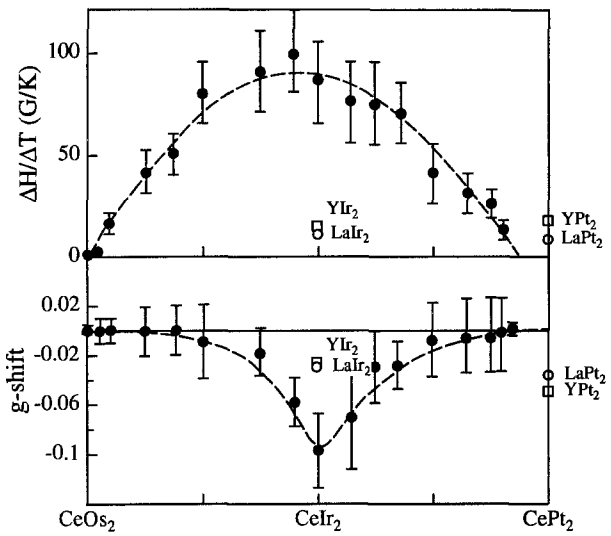

Fig. 59. Low-temperature Korringa slopes and g-shifts for various $Ce(Ir_xOs_{1-x})_2$:Nd and $Ce(Pt_xIr_{1-x})_2$:Nd mixtures. For comparison, the Korringa slopes and g-shifts for the isostructural YX_2 and LaX_2 compounds are also indicated. The dashed lines are drawn to guide the eye. From Barberis et al. (1980).

$CePt_2$. The g-shift is almost zero at the endpoints of the pure Pt and Os compounds and is large and negative for the Ir compound ($\Delta g = -0.1$).

Gd-ESR has been investigated in a number of IV systems, e.g. $CePd_3$, $CeIr_2$, $CeRh_2$ and $CeBe_{13}$, by Heinrich et al. (1982), with special emphasis on a number of lanthanide beryllides (Heinrich and Meyer 1977, Heinrich et al. 1979). The authors arrived at the main conclusion that the g-shift essentially does not vary with respect to the La-reference compounds, the linewidth broadening can be increased, reduced or it can remain unchanged. However, the relaxation rates of the conduction electrons, as calculated from the ESR experiments in the bottleneck regime, are highly enhanced in close agreement with the spin-fluctuation rates obtained by other experimental techniques. Increased thermal broadenings of Er in $CeBe_{13}$ have also been observed by Hoekstra et al. (1982).

Finally, it has to be mentioned that Nd and Er resonances have been studied in $Ce(Rh_xPt_{1-x})_2$ by Stein et al. (1983) and the Er and Yb resonances in the series of uranium-based compounds $U(Pt_{1-x}Pd_x)_3$ by Gandra and Pontes (1988). In the latter compounds Yb behaves like a valence fluctuating ion.

$CeRu_2$ is a mixed-valence system with a valency close to 4. The ESR experiments on this system are reviewed in sect. 12, which deals with local moment spin resonance in conventional superconductors. SmB_6 is an intermediate valence system, but belongs to a new class of small gap semiconductors. These materials exhibit Kondo-lattice behavior at elevated temperatures but evolve into semiconducting materials with small gaps of the order of a few kelvins or a few tens of kelvins as the temperature is lowered (Aeppli and

Fisk 1992). It is reasonable to believe that the hybridization of the f-electrons with the band states accounts for the unusual properties of these materials. ESR experiments on SmB_6 are discussed in detail in sect. 5.3.2. There it was shown that the opening of a gap indeed can be deduced from the temperature dependence of the linewidth. It is clearly apparent that ESR is an extremely useful technique to study the dynamical susceptibilities in Kondo insulators.

11. Superconductors

The first ESR spectroscopy of a local moment in the superconducting state had been reported by Al'tshuler et al. (1972) in La_3In:Gd. Shortly later the temperature dependence of the ESR linewidth and the resonance field were measured in full detail by Rettori et al. (1973a,b) in $LaRu_2$:Gd, by Engel et al. (1973) in $LaRu_2$:Gd and $CeRu_2$:Gd and by Alekseevskii et al. (1973) for La:Er. All these systems revealed characteristic changes in linewidth, g-value and line shape in passing through the superconducting (sc) phase transition temperature T_c.

What is expected theoretically? It has been pointed out by S.E. Barnes (1981a) that the theory of the nuclear relaxation can easily be transferred to the ESR case. In NMR experiments on conventional superconductors (SC) the spin-lattice relaxation rate $(1/T_1)$ reveals an enhancement just below T_c and decreases exponentially towards $T=0\,K$. A leveling-off towards a residual finite value is often ascribed to the presence of magnetic impurities or to the fact that the coherence length becomes comparable to the spin–orbit scattering length. Theoretically it has been shown by Anderson (1959) that in the presence of strong spin–orbit coupling the spin susceptibility is finite at $T=0\,K$, yielding a finite relaxation rate. Neglecting the coupling between the magnetic impurities and the conduction electrons, Maki (1973) has developed a theory for ESR in gapless superconductors, and Orbach (1974) has investigated the relevance of the internal field distribution in the vortex state of type-II SC for g-values and line shapes.

From the experimental side, in order to observe an ESR signal in the superconducting phase, the upper critical field should not lie within the field sweep at a given probing frequency. This has been pointed out in full detail by Davidov et al. (1974b). Favorable conditions at liquid He temperatures are met in the A15 and the C15 compounds, as well as in the Chevrel phases (besides the high-T_c superconductors, which will be discussed in full detail in the next section). As the C15 compounds are easy to prepare, most of the experimental work was devoted to $CeRu_2$, $LaRu_2$ and $LaOs_2$. Early ESR experiments in conventional SC are reviewed by Taylor (1975), Baberschke (1976) and S.E. Barnes (1981a). Hence, we keep this section rather short and describe the experiments on the new class of high-T_c SC in the following section.

The main ESR results in conventional superconductors (C15 compounds) can be summarized as follows:

(i) The line shape changes significantly in passing from the normal to the superconducting state. This behavior is shown in fig. 60 for $CeRu_2$:Gd (Baberschke

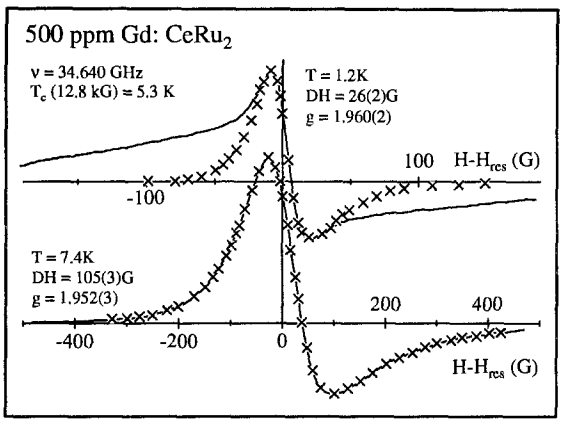

Fig. 60. Line shapes of Gd-ESR experiments in normal and in the superconducting state of $CeRu_2$. Note the strong deviations from a Dysonian lineshape in the sc state. From Baberschke et al. (1974).

et al. 1974). While the absorption in the normal state can well be described by a Dysonian profile, significant deviations appear for $T < T_c$. It has been pointed out later on by Baberschke (1976) that the line shape can not be fully understood by the field distribution of the vortex state.

(ii) The g-shift for $T < T_c$ strongly depends on the measuring frequency (Baberschke et al. 1974). This effect is due to a competition of the internal field distribution of the vortex structure and the reduction of the conduction electron susceptibility (Baberschke 1976).

(iii) Some ESR experiments provide evidence of a "Hebel–Schlichter peak" in the temperature dependence of the linewidth just below T_c. As an example, fig. 61 shows $\Delta H(T)$ in $CeRu_2$:Gd for a series of Gd concentrations (Davidov et al. 1974b) where the coherence peak consistently is detected for all samples. However, in some cases this enhancement could not be detected (Engel et al. 1973) and in certain cases the linewidth passes the sc phase transition temperature with no anomaly at all. For example, in $CeRu_2$:Nd the Korringa slope remains constant for all temperatures, ranging from $T \ll T_c$ to $T > T_c$ (Barberis et al. 1978, 1981b).

Gd-ESR experiments in Chevrel phases have been reported by Odermatt et al. (1979a,b). These authors performed ESR experiments at 35 and 60 GHz on powdered samples of $SnMo_6S_8$ and $PbMo_6S_8$. Both compounds exhibit a sc phase-transition temperature close to 12 K. At the lowest temperatures investigated (4.2 K), the Gd resonance appears unbottlenecked, revealing a fully resolved fine structure from which the crystal field parameters were determined. With increasing temperature the fine structure is rapidly narrowed and has practically disappeared when T_c is reached. From this observation it has been concluded that the impurity-to-conduction electron relaxation rate, which determines the linewidth of the ESR absorption, increases exponentially at low temperatures, yielding a gap value $2\Delta/k_B T = 5$, indicative for strong coupling. Across T_c and within the experimental resolution, no g-shift could be detected. A fact that is not surprising in view of the strong spin–orbit coupling inferred from measurements of the upper critical field.

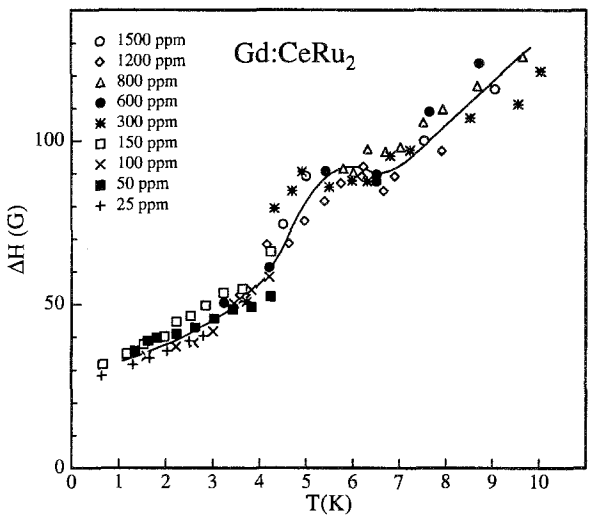

Fig. 61. Temperature dependence of the Gd linewidth in $CeRu_2$ doped with a series of Gd concentrations. The data provide experimental evidence for the appearance of a coherence peak (Hebel–Schlichter peak) just below the sc phase transition. From Davidov et al. (1974b).

12. High-T_c superconductors

The discovery of high-temperature superconductivity by Bednorz and Müller (1986) has stimulated an enormous number of experimental and theoretical studies to clarify physical and chemical properties, as well as the mechanisms of the superconductivity in these ternary copper oxides. One of the characteristic crystallographic features is that they are layered compounds, with CuO_2 layers or bilayers as the essential structural unit carrying the superconducting current. Shortly after bulk superconductivity had been detected in La–Sr–Cu–O ($T_c \approx 40$ K) and Y–Ba–Cu–O ($T_c \approx 90$ K) the question arose whether these materials can be described by standard BCS theory or if other pairing mechanisms establish unconventional superconductivity. Specifically the facts that all these materials are close to a metal-to-insulator transition and, in addition, are close to a magnetic instability have encouraged these speculations. Hence, considerable efforts have been made to understand the low-frequency spin dynamics of the superconducting cuprates and the undoped parent compounds. This activity is stimulated by the widespread belief that many aspects of the high-T_c superconductivity are intimately related to the two-dimensional spin fluctuations.

So far the main experimental information of the Cu spin dynamics comes from neutron scattering (for a review see, e.g., Rossat-Mignod et al. 1992) and from nuclear magnetic resonance (NMR) experiments (for a review see, e.g., Rigamonti et al. 1990, Brinkmann and Mali 1994). In the normal conducting state, in La–Sr–Cu–O (Keimer et al. 1991) as well as in weakly doped metallic Y–Ba–Cu–O (Sternlieb et al. 1993) a universal ω/T scaling of the dynamical susceptibility has been observed. This scaling relation has been

theoretically proposed by Varma et al. (1989). In addition, it has been demonstrated using inelastic neutron scattering (INS) (Sternlieb et al. 1993, Rossat-Mignod et al. 1992, Mason et al. 1992, Matsuda et al. 1994) and NMR techniques (Takigawa et al. 1991) that a spin gap opens in the magnetic excitation spectrum which appears to depend strongly on doping. It has been suggested by Millis and Monien (1993) that although the experimental features in La–Sr–Cu–O and Y–Ba–Cu–O look similar, the opening of the pseudo-gap is due to the ordering of the spin density wave in La–Sr–Cu–O, while it is due to singlet pairing in Y–Ba–Cu–O.

In this section we will report ESR results on high-T_c superconductors. A complete and detailed discussion would be far beyond the aim of the present review. Hence we focus predominantly on results obtained in single crystalline materials and on results which yield information on the spin dynamics in the CuO_2 planes. We subdivide this section into systems in which the ESR signals result from paramagnetic centers in the CuO_2 planes or in which ESR results from local moments of ions (e.g. Mn, Fe, Gd, Eu) doped into the high-T_c materials.

12.1. *"Cu-ESR" in high-T_c superconductors and undoped parent compounds*

12.1.1. *$YBa_2Cu_3O_{6+\delta}$*

Soon after the discovery of high-T_c superconductivity by Bednorz and Müller (1986) the observation of ESR signals due to the presence of Cu^{2+} had been reported in $YBa_2Cu_3O_7$ with a superconducting phase transition $T_c \approx 90$ K. Most of this early work had been performed on powdered ceramic samples, and soon it became clear that the ESR signals were due to impurity phases (see, e.g., Vier et al. 1987, Bowden et al. 1987, Genossar et al. 1989, Deville et al. 1989) or were due to complex paramagnetic defect states (Stankowski et al. 1991). A good survey on the early ESR work in $YBa_2Cu_3O_7$ with a complete list of references has been given by Hoffmann et al. (1990) and by Punnoose and Singh (1995). There have been a number of suggestions why no Cu-ESR signals can be observed in pure $YBa_2Cu_3O_7$. For example, it has been speculated that the Cu valence is unstable and fluctuates between Cu^{2+} and Cu^{3+} configurations, or that the Cu^{2+} ions are strongly antiferromagnetically coupled in pairs with a nonmagnetic ($S=0$) ground state and an excited triplet state ($S=1$) and with a level splitting much larger than the thermal energy (for references see Hoffmann et al. 1990). While it seems clear that the Cu resonance cannot be observed in $YBa_2Cu_3O_{6+\delta}$ for $\delta=1$ (Mehran et al. 1988a), the observation of intrinsic ESR signals has been reported for crystals with $\delta<1$. The first observation of Cu^{2+} paramagnetic center in an as-grown single crystal ($T_c \approx 40$ K) has been reported by Mehran et al. (1988b). They observed a slightly anisotropic g-factor for $T>T_c$ which becomes fully isotropic in the superconducting phase. The most convincing experimental evidence for an intrinsic paramagnetic centers in as-grown crystals has been provided by Shaltiel et al. (1989b). These experiments revealed an anisotropic g-factor of tetragonal symmetry with $g_\perp = 2.0418(5)$ and $g_\parallel = 2.2949(5)$ and were attributed to the existence of Cu^{2+} in an octahedral oxygen coordination. Below 90 K the ESR signal broadened considerably and disappeared rapidly. This unusual temperature dependence

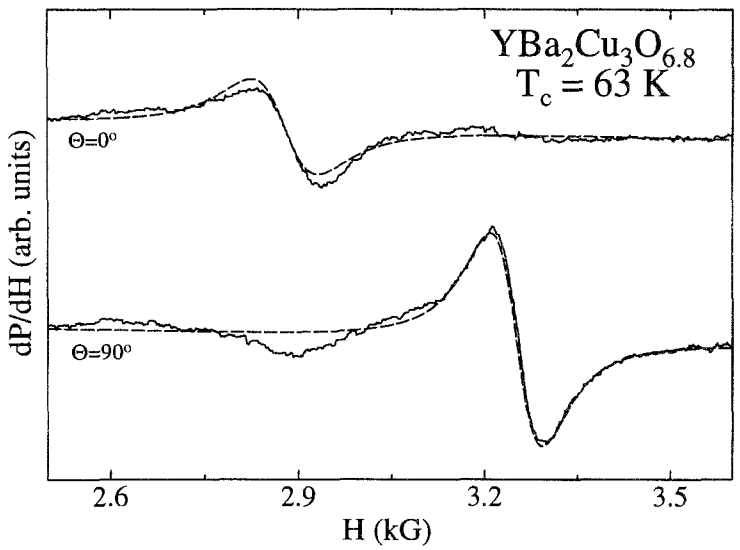

Fig. 62. Absorption derivative vs magnetic field in $YBa_2Cu_3O_{6.8}$ at two different crystal orientations at 105 K. The fits with Lorentzian line shapes are indicated by dashed lines. From Sichelschmidt et al. (1995a).

of the linewidth at resonance absorption has been explained by the onset of local superconductivity (Shaltiel et al. 1989b). Similar results were obtained by Alekseevskii et al. (1989) and Garifullin et al. (1991) in polycrystalline samples and by Kochelaev et al. (1990) in single crystals with $\delta < 1$.

A detailed ESR investigation in $YBa_2Cu_3O_{6+\delta}$ single crystals as a function of oxygen concentration had been performed by Sichelschmidt et al. (1994, 1995a). Well-defined but weak ESR signals were observed in crystals with oxygen concentrations $0.7 \leqslant \delta \leqslant 0.9$ and for temperatures $80 < T < 200$ K. A typical example of an experimentally observed spectrum is shown in fig. 62 for $YBa_2Cu_3O_{6.8}$ ($T_c = 63$ K) at 105 K. (Sichelschmidt et al. 1995a). Upon rotation of the crystallographic c-axis from parallel ($\Theta = 0°$) to perpendicular ($\Theta = 90°$) with respect to the external field, the resonance field is shifted by almost 0.4 kG. When the a/b plane is rotated, the resonance field is constant. For all angles the absorption lines can well be described by Lorentzian line shapes (see dashed lines in fig. 62). The angular dependence of the resonance field could well be described by g factors in an $S = \frac{1}{2}$ system with uniaxial symmetry with $g_\perp = 2.03(1)$ and $g_\parallel = 2.28(1)$ in close agreement with the results from Shaltiel et al. (1989b). Figure 63 shows the integrated intensity of the absorption line versus the oxygen concentration δ together with the δ-dependence of the superconducting phase transition temperature. The strongest signals were detected close to $\delta = 0.8$ while no signals were observed for $\delta < 0.7$ and $\delta > 0.9$ (Sichelschmidt et al. 1994). It has been suggested that these ESR signals result from paramagnetic chain fragments along the b-axis. A similar concentration dependence of paramagnetic chain fragments has been calculated using a modified lattice-

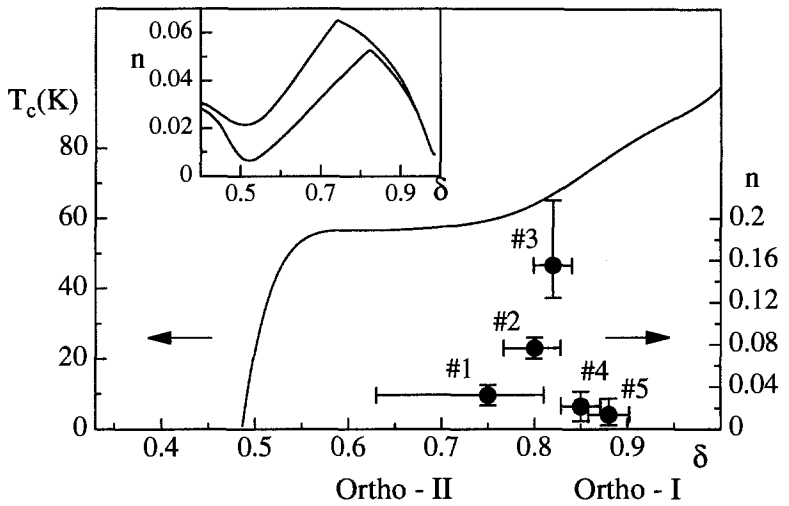

Fig. 63. Oxygen concentration dependence of the fraction of paramagnetic chain fragments as calculated from the integrated intensities of the ESR signals in $YBa_2Cu_3O_{6.8}$ (solid symbols, right scale). The oxygen concentration dependence of the sc phase-transition temperatures T_c is also shown (solid line, left scale). The inset shows the concentration dependence of the paramagnetically active chain fragments for two different "sample preparation" temperatures as calculated using a modified lattice gas model. From Sichelschmidt et al. (1995a).

gas model (Uimin and Rossat-Mignod 1992, Uimin and Stepanov 1993). The temperature dependence of the intensity of the absorption line, the g-factors and the linewidth at resonance absorption, ΔH, is documented in fig. 64 (Sichelschmidt et al. 1995a). Specifically interesting is $\Delta H(T)$ which decreases with decreasing temperatures, passes through a minimum and increases rapidly towards lower temperatures. The resonance line becomes unobservably broad well above the sc phase-transition temperature. The results were interpreted within a model where the paramagnetic chain fragments are strongly coupled (similar to a bottleneck effect) to the spin fluctuations in the CuO_2 planes. In this theory the linewidth ΔH is inversely proportional to the dynamical susceptibility of the planes (Sichelschmidt et al. 1995a). Using a phenomenological ansatz, similar to what has been used by Tranquada et al. (1992) to describe neutron scattering results, $\Delta H(T)$ was consistently explained. Figure 65 shows the temperature dependence of the linewidth ΔH for five samples with different oxygen concentrations. The solid line represent results of a fit using the phenomenological model (Sichelschmidt et al. 1995a). It is important to note that the minimum in $\Delta H(T)$ represents roughly the maximum in the dynamical susceptibility and the large increase towards lower temperatures is due to the opening of a spin gap. A gap energy of approximately 45 meV, independent of oxygen concentration ($0.7 < \Delta < 0.9$), has been determined from these ESR results (Sichelschmidt et al. 1995b). This gap value is significantly larger than the gap energy as determined from neutron scattering and NMR experiments (Rossat-Mignod et al. 1992, Tranquada et al. 1992).

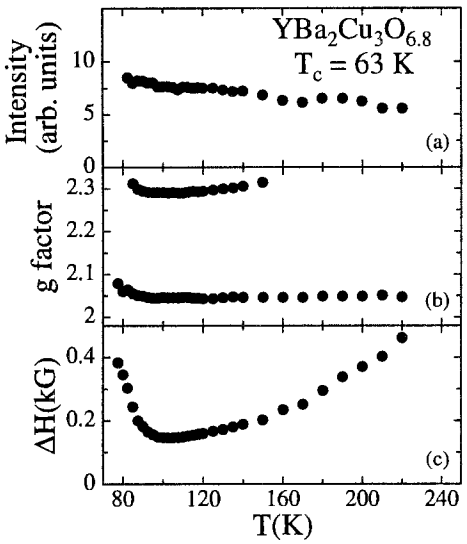

Fig. 64. Temperature dependence of (a) the intensity of the absorption line, (b) the g-values and (c) the linewidth in $YBa_2Cu_3O_{6.8}$. From Sichelschmidt et al. (1995a).

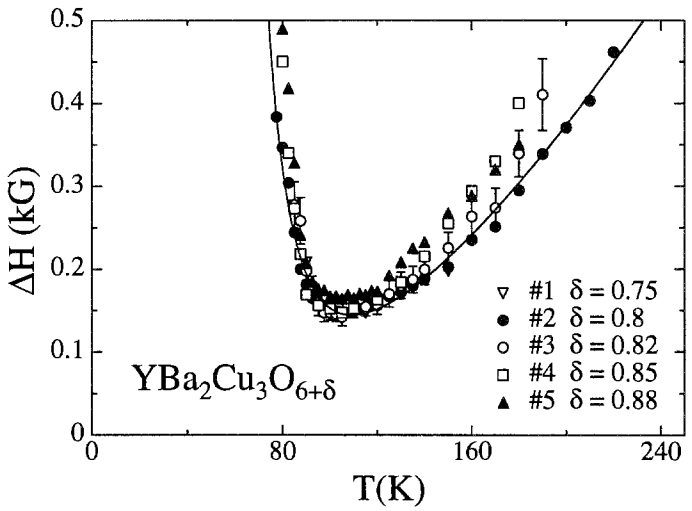

Fig. 65. Temperature dependence of the linewidth ΔH in $YBa_2Cu_3O_{6+\delta}$ for five samples with different oxygen concentrations. The solid lines represent the result of a fit using a model outlined in the text. From Sichelschmidt et al. (1995a).

12.1.2. *Other high-T_c compounds*

12.1.2.1. *La–Sr–Cu–O.* Not many ESR investigations were devoted to this system, although there is only one Cu site per unit cell. It is generally believed that pure La_2CuO_4 is ESR silent and theoretical arguments have been put forward by Chakravarty and Orbach (1990) as well as by Mehran and Anderson (1989) why an intrinsic ESR signal of Cu^{2+}

cannot be observed from the CuO_2 planes of undoped and antiferromagnetic La_2CuO_4. The ESR signal in the insulating state will be severely broadened by the anisotropic Cu–O–Cu exchange making it unlikely that an ESR signal can be detected. Later on, it has been pointed out by Lazuta (1991) that an ESR signal may be observable in pure an stoichiometric La_2CuO_4. For the total spin relaxation rate, values of 2.7 kG at 300 K and 0.6 kG at 400 K have been calculated. And indeed, the observation of a Cu^{2+} signal in $La_{2-x}Sr_xCuO_4$ has been reported (Kruschel 1993). For Sr-concentrations $x > 0.06$ $\Delta H(T)$ reveals a Korringa-like broadening at high temperatures with linewidths between 4 and 9 kG. The slope increases with increasing x and saturates for $x > 0.2$ at a value of approximately 50 G/K. Analogous to what has been found in $YBa_2Cu_3O_{6+\delta}$, the linewidth passes through a minimum and strongly increases towards low temperatures.

12.1.2.2. *Tl–Ba–Ca–Cu–O, Bi–Sr–Ca–Cu–O.* There have been some speculations that the ESR of conduction electrons (holes) has been observed in the Tl–Ba–Ca–Cu–O system (Hayashi et al. 1989). However, it has been demonstrated by Edwards et al. (1990) that the Tl–Ba–Ca–Cu–O, as well as the Bi–Sr–Ca–Cu–O compounds are ESR silent. Also Mehran et al. (1988a) reported about the absence of ESR signals in $Bi_2Sr_2CaCu_2O_x$ for temperatures up to 570 K.

12.2. *ESR experiments on high-temperature superconductors using localized moments as microscopic probes*

A large number of investigations were performed on high-T_c materials or related compounds using 3d (Fe, Mn, ...) or 4f (Gd, Eu, ...) ions with localized moments as ESR probes. It is far outside the scope of this review to give a detailed description and a complete list of references of these investigations and we will focus on some important results only. The reader is kindly referred to the original literature for further information.

12.2.1. *$YBa_2Cu_3O_{6+\delta}$:Gd*

Gd substitutes for Y at all concentrations and does not perturb the superconducting properties. For example, T_c in pure $GdB_2Cu_3O_7$ is close to 90 K and the Gd–Gd interaction is weak, yielding an antiferromagnetic ordering temperature $T_N \approx 2.3$ K. At low Gd doping levels, careful measurements of the angular dependence of the resonance field in the *a–c* plane have been performed by Shaltiel et al. (1989a) at X- and Q-band frequencies at 77 K. The observed ESR spectra in single crystalline Gd:$YBa_2Cu_3O_{6+\delta}$ were essentially identical for insulating ($\delta \approx 0.1$) and superconducting samples ($\delta \approx 0.7$). All ESR spectra provide evidence for exchange narrowing effects and reveal strong deviations from ideal, metallic Dysonian line shapes. From the fact that the exchange narrowing is rather similar for $\delta = 0.1$ and 0.7, the authors concluded that the same interactions are responsible for the observed line shapes in the insulating and in the superconducting sample, and, hence, that the coupling of the Gd spin to the spin fluctuations in the CuO_2 plane can be neglected. At low temperatures the crystal-field spectrum has been fully resolved. The data allowed an unambiguous determination of the

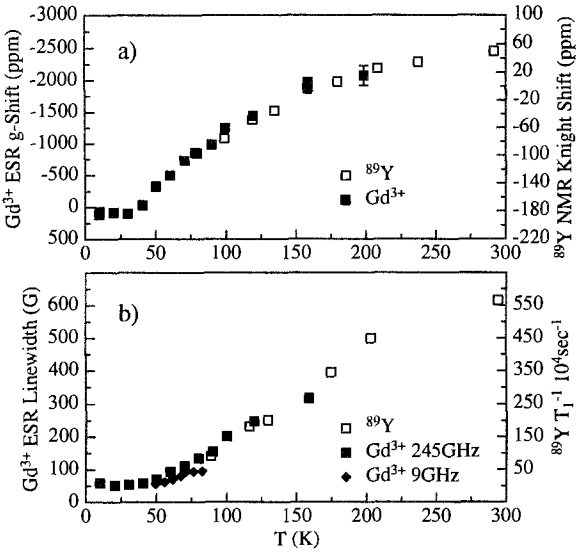

Fig. 66. Temperature dependence (a) of the Gd g-value, measured at 245 GHz in $YBa_2Cu_3O_{6+\delta}$:Gd as compared to the ^{89}Y Knight shift from NMR experiments and (b) of the Gd-ESR linewidth compared to the NMR spin-lattice ralaxation rate. From Janossy et al. (1996).

crystal electric field parameters of the Gd^{3+} probe in $YBa_2Cu_3O_{6+\delta}$. The CF parameters are rather similar for $\delta = 0.1$ and $\delta = 0.7$. Similar results were obtained by Janossy et al. (1990a) in oriented Gd:$YBa_2Cu_3O_{6.02}$ powder. Later on these authors used similar results in a series of oriented powders with different oxygen contents to determine the oxygen order as a function of the oxygen concentration δ via crystal field effects (Janossy et al. 1990b).

Using high-field ESR techniques, Janossy et al. (1996) determined the temperature dependence of the resonance field of Gd in $YBa_2Cu_3O_{6+\delta}$ at 245 GHz. For $\delta = 0.76$ the Gd g-value closely follows the ^{89}Y Knight-shift as determined by NMR techniques (fig. 66). The g-factor decreases with decreasing temperature and, obviously, is dominated by the opening of a gap in the low-lying spin excitations. For $\delta = 1$, the g-value is almost temperature independent for $T > T_c$ and decreases abruptly for $T < T_c$ (Janossy et al. 1996).

12.2.2. *$GdBa_2Cu_3O_{6+\delta}$*

ESR investigations on pure $GdBa_2Cu_3O_{6+\delta}$ ceramics and single crystals were performed by Nakamura et al. (1990a,b) and Deville et al. (1993). Nakamura et al. (1990a,b) investigated in addition $GdBa_2(Cu_{1-x}M_x)_3O_7$ samples with M = Ni, Fe, Co at X-, K- and Q-band frequencies. All these experiments revealed an exchange-narrowed line whose width and g-values are almost temperature independent. The Gd linewidth depends on the probing frequency and on the concentration of the M dopants. It has been concluded

that the broadening of ΔH is partly due to dipolar Gd–Gd interactions and partly due to superexchange interactions between the Gd ions via the CuO_2 planes (Nakamura et al. 1990a).

12.2.3. *$YBa_2(Cu_{1-x}M_x)_3O_{7-\delta}$ ($M = Mn$, Fe)*

A number of ESR experiments were performed using Mn^{2+} as microscopic probes. At present it seems clear that Mn cannot be substituted in $YBa_2Cu_3O_7$ single crystals at any amount. The ESR signal in Mn-doped polycrystalline samples originate from antiferromagnetically interacting Mn ions in phase-separated clusters (Moto et al. 1990). The absence of any intrinsic ESR signal due to divalent Mn has been demonstrated unambiguously several times (Skrzypek et al. 1991, Kaise et al. 1990). ESR measurements on Fe doped oxygen-deficient $YBa_2Cu_3O_{6+\delta}$ ceramics were carried out at X-band frequencies by Romanyukha et al. (1990). ESR signals could only be detected in underdoped samples with relatively small concentrations of Fe^{3+} ions. The values of the linewidth and the g-factor were close to those found in samples without Fe. However, Fe-doping essentially changes the magnetic properties of $YBa_2Cu_3O_{6+\delta}$.

12.2.4. *ESR experiments on $La_{2-x}Sr_xCuO_4$ using Er^{3+}, Mn^{2+}, Fe^{3+} and Gd^{3+} as local probes*

The Darmstadt group performed a systematic ESR study on ceramic La–Sr–Cu–O compounds. Samples with Sr-concentrations $0.15 \leqslant x \leqslant 0.35$ were investigated. For these investigations the samples were doped with 1% Er. The RE doped samples revealed the same electrical properties as the undoped compounds. Er^{3+} ESR spectra were investigated at X-band frequencies as a function of temperature and Sr concentration (Kan et al. 1991). $\Delta H(T)$ and $g(T)$ were determined using an analytical expression for the line shape analysis by Searl et al. (1961). A Lorentzian line shape has been assumed for a single microcrystal. The temperature dependence of the linewidth was described assuming a Korringa relaxation and an Orbach relaxation process. The Korringa slope clearly was correlated with the Sr concentration. This implies that the hole-doping with Sr increases the density of states also at the La site, demonstrating that the Fermi surface has a three-dimensional character. On the other hand, the linewidth stays almost unchanged at the sc phase transition. This result may correspond to the fact that the correlation length in this high-T_c materials perpendicular to the planes is short (Kan et al. 1991).

Similar experiments were performed in $La_{2-x}Sr_xCuO_4$ doped with Mn^{2+}. The Mn ion is substituted for the Cu ion and hence, the Mn ESR allows one to probe the spin fluctuations in the CuO_2 planes (Kochelaev et al. 1994). Ceramic samples with Sr concentrations $0 \leqslant x \leqslant 0.3$ were doped with up to 6% Mn. The samples were characterized by measuring the electrical resistivity and the dc susceptibility, as Mn doping suppresses superconductivity. The Mn-ESR experiments were performed at X-band frequencies for temperatures $4 < T < 300$ K. The powder spectrum revealed a pure Lorentzian profile. $\Delta H(T)$ exhibits a peculiar temperature dependence: with decreasing temperatures, ΔH decreases, passes through a minimum and increases towards low temperatures. It is essentially the same

overall behavior as that found from the ESR experiments in underdoped $YBa_2Cu_3O_{6+\delta}$ (Sichelschmidt et al. 1995a). It has been shown theoretically by Kochelaev et al. (1994) that the localized Mn spins are strongly coupled to the spin fluctuations in the CuO_2 plane (bottleneck effect) and probe the dynamical susceptibility of the spin fluctuations. The observed increase of the linewidth for $T \rightarrow 0\,\mathrm{K}$ has been explained assuming a relaxation due to two-magnon processes which are relevant even in the paramagnetic phase. It has been pointed out that although the general behavior of the EPR linewidth of $La_{2-x}Sr_xCu_3O_{6+\delta}$ is very similar, the interpretation is different. While the broadening of the EPR line follows a T^2 behavior in La–Sr–Cu–O (Kochelaev et al. 1994) the analysis in the Y–Ba–Cu–O system required an exponential function displaying the opening of a gap in the magnetic excitation spectrum (Sichelschmidt et al. 1995a). This interpretation is consistent with the theory by Millis and Monien (1993), who proposed that the decrease of the susceptibility is due to an incipient spin-density wave ordering in the case of $La_{2-x}Sr_yCuO_{4+\delta}$ but is due to the appearance of a spin gap in $YBa_2Cu_3O_{6+\delta}$.

ESR experiments using Fe^{3+} in $La_{2-x}Sr_xCuO_4$ ($0 \ll x \ll 0.25$) have been performed Cieplak et al. (1993) and by Shengelaya et al. (1994). The temperature dependence of the linewidth reveals a Korringa type of broadening for $T \gg 40\,\mathrm{K}$ and a strong increase of $\Delta H(T)$ towards the lowest temperatures. The Korringa slope b decreases linearly with decreasing Sr concentration x and becomes zero close to $x_c = 0.06$ (Shengelaya et al. 1994) which indicates the border line from metallic ($x > x_c$) to insulating behavior ($x < x_c$). It has been suggested that the low-temperature upturn of the ESR linewidth results from the slowing down of spin fluctuations.

Gd-ESR experiments in $La_{2-x}Sr_xCuO_4$ were carried out by Rettori et al. (1993) and by Kataev et al. (1993). Rettori et al. (1993) determined four different Gd sites characteristic for a twinned crystal. The temperature dependence of the splitting of the resonance line yields the magnetic moment of the Cu ions, $\mu_S = 0.6\mu_B$/Cu. Kataev et al. (1993) observed a Korringa relaxation for the Gd absorption and found a linear increase of b with increasing Sr concentration similar to the observations of Shengelaya et al. (1994) for the Fe^{3+} resonance line.

12.2.5. $Nd_{2-x}Ce_xCuO_{4+\delta}$

$Nd_{2-x}Ce_xCuO_{4+\delta}$ is the only electron-doped high-T_c superconductor. In the pure compound the Nd moments order antiferromagnetically below 1.7 K. The Cu ions in the CuO_2 planes reveal three subsequent magnetic phase transitions below room temperature. In single crystalline Nd_2CuO_4 Kontani et al. (1990) observed a Nd resonance below 20 K. A systematic Gd-ESR investigation on ceramic $Nd_{2-x}Ce_xCuO_{4+\delta}$ has been performed by Shimizu (1991). The Gd^{3+} ions are embedded in the Nd magnetic lattice. In the Ce-doped ($x = 0.15$) and in the undoped sample the linewidth of the Gd resonance absorption increases with decreasing temperature with a small anomaly close to 50 K (Shimizu 1991). The increase of the linewidth has been attributed to magnetic fluctuations of the Nd spins in the paramagnetic state. The anomaly at low temperatures was explained to be due to a magnetic phase transition of the Cu spins (Shimizu 1991).

13. Conclusions, outstanding problems and further developments

In contrast to many other experimental techniques, like magnetic susceptibility, heat capacity, electrical resistivity, etc., the ESR on localized magnetic moments in metals is a truly local method. ESR can be directly compared to NMR and μSR techniques. While in the case of NMR, the probing spin is a nucleus of the host material and in μSR experiments the probe is implanted into the metal or alloy, the ESR probe usually has to be chemically substituted into the compound. Of course, in certain cases the ESR ions can influence the magnetic properties of the host and this has to be avoided carefully. On the other hand, the ESR probe is located on a well-defined crystallographic site in the crystal, which is not always true for μSR experiments. However, all magnetic resonance techniques yield valuable information about the electronic density of states and about the local magnetic fields at the site of the probe. A comparison of the results obtained with all three experimental techniques can yield a direct contour map of the local electronic densities in real space. This information is extremely useful in electronically highly correlated systems which are described by heavy-mass quasiparticles. And a lot of work still has to be performed in this direction. A univocal proof of the local character of conduction-electron densities has been provided by the ESR on $CePd_3$(Gd). The host density of states of $CePd_3$, e.g. measured by heat capacity, is large relative to the isostructural compound YPd_3 and on a first glance the Gd-ESR which directly measures the density of states should be highly enhanced. In contrast, the experiments reveal an extremely narrow ESR line indicating a very low density of electronic states at the Gd probe, which is substituted at a Ce site. This immediately shows that in HFS and IV compounds the notation "band state" has to be used with caution.

The main experimental information that usually can be deduced from ESR experiments in metals are the g-shift and the linewidth broadening. Both quantities can be measured as a function of an external parameter, like temperature or pressure. The g-shift corresponds to the Knight-shift in NMR experiments and yields information about the static susceptibility. This review nicely documents how the experimental results on the g-shifts in metals provide direct and detailed information on the band structure. The ESR linewidth in metals is determined by the spin-lattice relaxation time and has to be compared to $1/T_1$ as deduced from NMR results. The linewidth is determined by the density of states, but in addition yields detailed information on the low-frequency spectrum of spin fluctuations. This is of high relevance in the field of high-T_c superconductors and heavy-fermion compounds.

The first part of this review deals with classical ESR results in metals. Here ESR can determine the site symmetry of the probe and measures CF effects in full detail. In this field of research ESR has made notable contributions. Some interesting physics developed from the comparison of the magnitude of the cubic fine structure parameter for metals and for insulators. The systematic differences are probably caused by covalent mixing contributions as a consequence of the conduction-electron hopping on and off the local moment site. In addition, ESR in metals is the only method to determine quantitatively the relaxation rates between the lattice, the band states and the impurities. It has been shown,

that ESR is a valuable tool to study the metal-to-insulator transition. The only existing magnetic resonance study of a pressure-induced MI transition in Yb is an illuminating example and, clearly, much more experimental work should be directed along this lines.

The second half of this review deals with newly developed branches of solid state physics. Here it is evident that ESR made major contributions to the physics of electronically highly correlated systems, like heavy-fermion systems and intermediate-valence compounds. In the latter compounds it still has to be proven that the low density of states, which have been detected experimentally, results from the so-called Kondo whole and is a characteristic feature of IVCs. Certainly a further interesting area of ESR will be the study of Kondo insulators. In KI a hybridization gap, as a consequence of the interaction of the band states with the f-electron system, develops at low temperatures. In KI a non-magnetic impurity will reveal an effective spin $\frac{1}{2}$ and, hence, one expects that non-magnetic impurities become ESR active below a characteristic temperature. So far we are not aware of any ESR experiments of that type in Kondo insulators.

A very interesting branch of ESR in metals remains the investigation of 3d ions, like Mn or Fe, in cuprate superconductors. In these materials the 3d ions are strongly coupled to the antiferromagnetic spin fluctuations in the Cu–O planes and the temperature dependence of the ESR linewidth provides detailed information on the dynamical spin susceptibilities. Hence, utilizing ESR techniques the opening of the spin gap above the superconducting phase-transition temperature can be studied in detail. But this field of research is just at the beginning and is still far from being fully understood.

Acknowledgements

We have benefitted over the years from collaborations and discussions with many colleagues, in particular with the members of the Sonderforschungsbereich (SFB) 252 "Elektronisch hochkorrelierte metallische Materialien", Darmstadt/Frankfurt.a.M/Mainz/Stuttgart.

References

Aarts, J., F.R. de Boer, F. Horn, F. Steglich and D. Meschede, 1981, Demagnetization of Ce in (Ce, Y)Al_2, in: Proc. Int. Conf. on Valence Fluctuations in Solids, eds L.M. Falicov, W. Hanke and M.P. Maple (North-Holland, Amsterdam) pp. 301–304.

Abragam, A., and B. Bleaney, 1970, Electron Paramagnetic Resonance of Transition Ions (Clarendon Press, Oxford).

Abraham, M.M., R.A. Weeks, G.W. Clark and C.B. Finch, 1965, Phys. Rev. A **137**, 138.

Abrikosov, A.A., and L.P. Gorkov, 1961, J. Exp. Theor. Phys. **12**, 1243.

Aeppli, G., and Z. Fisk, 1992, Comments Condens. Mater. Phys. **16**, 155.

Alekseevskii, N.E., I.A. Garifullin, B.I. Kochelaev and E.G. Karakhash'yan, 1973, J. Exp. Theor. Phys. **18**, 323.

Alekseevskii, N.E., A.V. Mitin, V.I. Nizhankovskii, I.A. Garifullin, N.N. Garifyanov, G.G. Khaliullin, E.P. Khylov, B.I. Kochelaev and L.R. Tagirov, 1989, Low Temp. Phys. **77**, 87.

Allenson, M.B., and K.N.R. Taylor, 1968, J. Appl. Phys. **39**, 1094.

Alquie, G., A. Kreisler and J.P. Burger, 1976, J. Less-Common Met. **49**, 97.

Alquie, G., A. Kreisler and J.P. Burger, 1978, Solid State Commun. **26**, 265.

Al'tshuler, T.S., I.A. Garifullin and E.G. Kharakhash'yan, 1972, Phys. Solid State (Russia) **14**, 213.

Al'tshuler, T.S., M.M. Zaripov, E.F. Kukovitskii, E.P. Khaimovich and E.G. Kharakhash'yan, 1974, J. Exp. Theor. Phys. Lett. **20**, 187.

Al'tshuler, T.S., E.G. Kharakhash'yan, E.F. Kukovitskii and M.M. Zaripov, 1977, Phys. Status Solidi B **80**, K109.

Al'tshuler, T.S., V.E. Kafaev and S.L. Tsarevskii, 1981, Phys. Solid State (Russia) **23**, 1550.

Al'tshuler, T.S., V.N. Mirnov and M.M. Zaripov, 1982, J. Phys. C **15**, 3785.

Al'tshuler, T.S., V.E. Kataev and G.G. Khaliullin, 1983, Phys. Solid State (Russia) **25**, 1239.

Al'tshuler, T.S., V.N. Mironov, G.G. Khaliullin and D.I. Khomskii, 1984, J. Exp. Theor. Phys. Lett. **40**, 754.

Al'tshuler, T.S., G.G. Khaliullin and D.I. Khomskii, 1986, Sov. Phys. JETP **63**, 1234.

Al'tshuler, T.S., M.S. Bresler, M. Schlott, B. Elschner and E. Gratz, 1995, Z. Phys. B **99**, 57.

Anderson, P.W., 1959, Phys. Rev. Lett. **3**, 325.

Andres, K., J.E. Graebner and H.R. Ott, 1975, Phys. Rev. Lett. **35**, 1779.

Arbilly, D., G. Deutscher, E. Grunbaum, R. Orbach and J.T. Suss, 1975, Phys. Rev. B **12**, 5068.

Baberschke, K., 1976, Z. Phys. B **24**, 53.

Baberschke, K., and D. Davidov, 1975, On the crystalline field of rare-earth ions in Metallic Pnictides, in: Proc. XIVth Int. Conf. on Low-Temperature Physics (LT14), eds M. Krusius and M. Vuorio (North-Holland, Amsterdam) pp. 484–486.

Baberschke, K., and J. Nagel, 1976, Phys. Rev. B **13**, 2793.

Baberschke, K., and E. Tsang, 1980, Phys. Rev. Lett. **45**, 1512.

Baberschke, K., and Y. von Spalden, 1979, Phys. Rev. B **19**, 5933.

Baberschke, K., U. Engel and S. Hüfner, 1974, Solid State Commun. **15**, 1101.

Baberschke, K., H.J. Jenrich and J. Nagel, 1978, Crystal field parameters and relaxation rates of Gd^{3+} and Eu^{2+} in $LaAl_2$ single crystals, in: Int. Conf. on Rare Earth and Actinides, eds W.D. Conner and B.C. Tanner, Conference Series, Vol. 37 (The Institute of Physics, Bristol) pp. 161–165.

Baberschke, K., B. Bachor and S.E. Barnes, 1980a, Phys. Rev. B **21**, 2666.

Baberschke, K., S.E. Barnes and B. Bachor, 1980b, J. Magn. & Magn. Mater. **15**, 733.

Barberis, G.E., J.F. Suassuna, C. Rettori and C.A. Pela, 1977, Solid State Commun. **23**, 603.

Barberis, G.E., D. Davidov, J.P. Donoso, F.G. Gandra, C. Rettori and J.F. Suassuna, 1978, Solid State Commun. **28**, 427.

Barberis, G.E., D. Davidov, J.P. Donoso, C. Rettori, J.F. Suassuna and H.D. Dokter, 1979a, Phys. Rev. B **19**, 5495.

Barberis, G.E., D. Davidov, J.P. Donoso, C. Rettori, J.F. Suassuna and H.D. Dokter, 1979b, J. Appl. Phys. **5D**, 2318.

Barberis, G.E., D. Davidov, C. Rettori, J.P. Donoso, I. Torriani and F.C.G. Gandra, 1980, Phys. Rev. Lett. **45**, 1966.

Barberis, G.E., D. Davidov, H.D. Dokter and F.R. Hoekstra, 1981a, Solid State Commun. **38**, 67.

Barberis, G.E., D. Davidov, J.P. Donoso, F.C. Gandra and C. Rettori, 1981b, J. Phys. F **11**, 1246.

Barnes, R.G., 1979, NMR, EPR and Mössbauer effect: metals, alloys and compounds, in: Handbook on the Physics and Chemistry of Rare Earths, Vol. 2, eds K.A. Gschneidner Jr. and L.R. Eyring (North-Holland, Amsterdam) pp. 387–505.

Barnes, S.E., 1974, Phys. Rev. B **9**, 4789.

Barnes, S.E., 1981a, Adv. Phys. **30**, 801.

Barnes, S.E., 1981b, Phys. Rev. Lett. **47**, 1613.

Barnes, S.E., 1984, Phys. Rev. B **30**, 3944.

Barnes, S.E., J. Dupraz and R. Orbach, 1971, J. Appl. Phys. **42**, 1569.

Barnes, S.E., K. Baberschke and J. Nagel, 1983, J. Phys. F **13**, 347.

Bartkowski, R.R., 1972, Conduction-electron effects in the ESR of Gd in LaP, in: AIP Conference Proceedings 5: Magnetism and Magnetic Materials, eds C.D. Graham Jr. and J.J. Rhyne (American Institute of Physics, New York) pp. 1174–1178.

Bednorz, J.G., and K.A. Müller, 1986, Z. Physik B: Condens. Matter **64**, 189.

Belakhovsky, M., J. Pierre and D.K. Ray, 1972, Phys. Rev. B **6**, 939.

Bethe, H., 1929, Ann. Physik **3**, 133.

Bhagat, S.M., and M.S. Rothstein, 1972, Solid State Commun. **1**, 1535.

Bhagat, S.M., and H.A. Sayadian, 1986, J. Magn. & Magn. Mater. **61**, 151.

Bhagat, S.M., M.L. Spano, H.S. Chen and K.V. Rao, 1980, Solid State Commun. **33**, 303.

Bhagat, S.M., M.L. Spano and J.N. Lloyd, 1981, Solid State Commun. **38**, 261.

Bickers, N.E., D.L. Cox and J.W. Wilkins, 1985, Phys. Rev. Lett. **54**, 230.

Binder, K., and A.P. Young, 1986, Rev. Mod. Phys. **58**, 801.

Birgeneau, R.J., 1973, Singlet-ground-state dynamics, in: AIP Conference Proceedings 10: Magnetism and Magnetic Materials, eds C.D. Graham jr and J.J. Rhyne (American Institute of Physics, New York) pp. 1664–1688.

Birgeneau, R.J., E. Bucher, L.W. Rupp Jr and W.M. Walsh Jr, 1972, Phys. Rev. B **5**, 3412.

Birgeneau, R.J., E. Bucher, J.P. Maita, L. Passell and K.C. Turberfield, 1973, Phys. Rev. B **8**, 5345.

Bloch, F., 1956, Phys. Rev. **102**, 104.

Bloch, F., W.W. Hansen and M. Packard, 1946, Phys. Rev. **69**, 127.

Bloch, J.M., and D. Davidov, 1982, Phys. Rev. B **26**, 3631.

Bloch, J.M., D. Davidov, J. Felner and D. Shaltiel, 1976, J. Phys. F **6**, 1979.

Bloch, J.M., D. Davidov and C. Rettori, 1982, J. Magn. & Magn. Mater. **25**, 271.

Bowden, G.J., P.R. Elliston, K.T. Wan, S.X. Don, K.E. Easterling, A. Bourdillon, C.C. Sorrell, B.A. Cornell and F. Separovic, 1987, J. Phys. C **20**, L545.

Brandt, O., E. Sigmund and M. Wagner, 1994, Phys. Rev. B **49**, 5508.

Brinkmann, D., and M. Mali, 1994, NMR-NQR studies of high-temperature superconductors, in: NMR Basic Principles and Progress, Vol. 31, eds P. Diehl, E. Fluck, H. Günther, R, Kosfeld and J. Seelig (Springer, Berlin) pp. 171–211.

Brodale, G.E., R.A. Fisher, N.E. Phillips and J. Flouquet, 1986, Phys. Rev. Lett. **56**, 390.

Broholm, C., J.K. Kjems, W.J.L. Buyers, P. Matthews, T.T.M. Palstra, A.A. Menovsky and J.A. Mydosh, 1986, Phys. Rev. Lett. **58**, 1467.

Burgardt, P., and M.S. Seehra, 1977, Phys. Rev. B **16**, 1802.

Burzo, E., 1981, J. Less-Commmon Met. **77**, 251.

Burzo, E., and R. Baican, 1974, EPR study of $Gd_xY_{1-x}Cu$ compounds, in: Magnetic Resonance and Related Phenomena, Proc. XVIII Congress AMPERE, eds P.S. Allen, E.R. Andrew and C.A. Bates (North-Holland/Elsevier, Amsterdam) pp. 151–152.

Burzo, E., and M. Balanescu, 1978, Solid State Commun. **28**, 693.

Burzo, E., and M. Balanescu, 1980, Phys. Status Solidi B **100**, K33.

Burzo, E., and J. Ursu, 1971, Solid State Commun. **9**, 2289.

Burzo, E., D. Seitabla and M. Chipara, 1982, Phys. Status Solidi A **113**, 87.

Cannella, V., and I.A. Mydosh, 1972, Phys. Rev. B **6**, 4220.

Chakravarty, S., and R. Orbach, 1990, Phys. Rev. Lett. **64**, 224.

Chiu, L.B., P.R. Elliston, A.M. Stewart and K.N.R. Taylor, 1979, J. Phys. F **9**, 955.

Chiu, L.B., P.R. Elliston, A.M. Stewart, K.N.R. Taylor and M.M.A. Issa, 1980, J. Phys. F **10**, 2297.

Chock, E.P., R. Chui, D. Davidov, R. Orbach, D. Shaltiel and L.J. Tao, 1971, Phys. Rev. Lett. **27**, 582.

Chock, E.P., R.A.B. Devine, S.A. Dodds, R. Orbach and L. Tippie, 1977, J. Phys. F **7**, 1097.

Cieplak, M.Z., A. Sienkiewicz, F. Mila, S. Quha, G. Xiao, J.Q. Xiao and C.L. Chien, 1993, Phys. Rev. B **48**, 4019.

Coldea, M., N. Dihoiu and J. Pop, 1980, Phys. Status Solidi A **59**, K187.

Coldea, M., J. Pop and V. Crisan, 1985, Physica **130B**, 478.

Coldea, M., H. Schaeffer, V. Weissenberger and B. Elschner, 1987, Z. Physik B **68**, 25.

Coles, B.R., B.V.B. Sarkissian and R.H. Taylor, 1978, Phil. Mag. B **37**, 489.

Coles, B.R., S. Oseroff and Z. Fisk, 1987, J. Phys. F **17**, L169.

Continentino, M., B. Elschner and G. Jakob, 1995, Europhys. Lett. **31**, 485.

Continentino, M.A., E. Skatulla, B. Elschner and H. Maletta, 1988, Z. Physik B **72**, 471.

Cooper, B.R., and O. Vogt, 1971, J. Phys. (Paris) **32**, C1.

Cox, D.L., 1987, Phys. Rev. B **35**, 6504.

Cox, D.L., N.E. Bickers and J.W. Wilkins, 1986, J. Magn. & Magn. Mater. **54–57**, 1986.

Dahlberg, E.D., 1977, Phys. Rev. B **16**, 170.

Dahlberg, E.D., M. Hardiman and J. Souletie, 1978, J. Phys. (Paris) Lett. **39**, L389.

Dahlberg, E.D., M. Hardiman, R. Orbach and J. Souletie, 1979, Phys. Rev. Lett. **42**, 401.

Dahlberg, E.D., J. Souletie, S.A. Dodds, E.P. Chock and R.L. Orbach, 1990, Phys. Rev. B **41**, 10897.

Davidov, D., and D. Shaltiel, 1968, Phys. Rev. Lett. **21**, 1752.

Davidov, D., C. Rettori, E.P. Chock, R. Orbach and M.B. Maple, 1972, Conduction electron spin-flip scattering in $LaAl_2$ doped with Gd, Ce, Th and U impurities, in: Magnetism and Magnetic Materials, AIP Conference Proceedings, Vol. 10, eds C.D. Graham Jr and J.J. Rhyne (American Institute of Physics, New York) pp. 138–142.

Davidov, D., A. Chelkowski, C. Rettori, R. Orbach and M.B. Maple, 1973a, Phys. Rev. B 7, 1029.

Davidov, D., A. Dixon, K. Baberschke, E.P. Chock and R. Orbach, 1973b, Phys. Rev. B **8**, 3563.

Davidov, D., K. Maki, R. Orbach, C. Rettori and E.P. Chock, 1973c, Solid State Commun. **12**, 621.

Davidov, D., E. Bucher, L.W. Rupp Jr, L.D. Longinotti and C. Rettori, 1974a, Phys. Rev. B **9**, 2879.

Davidov, D., C. Rettori and H.M. Kim, 1974b, Phys. Rev. B **9**, 147.

Davidov, D., C. Rettori, G. Ng and E.P. Chock, 1974c, Phys. Lett. **49A**, 320.

Davidov, D., C. Rettori and D. Shaltiel, 1974d, Phys. Lett. **50A**, 392.

Davidov, D., J.M. Bloch, R. Levin, C. Rettori and D. Shaltiel, 1975a, Phys. Lett. **53A**, 290.

Davidov, D., C. Rettori, R. Orbach, A. Dixon and E.P. Chock, 1975b, Phys. Rev. B **11**, 3546.

Davidov, D., C. Rettori and V. Zevin, 1975c, Solid State Commun. **16**, 247.

Davidov, D., V. Zevin, J.M. Bloch and C. Rettori, 1975d, Solid State Commun. **17**, 1279.

Davidov, D., P. Urban and L.D. Longinotti, 1976, Solid State Commun. **19**, 249.

Davidov, D., V. Zevin, R. Levin, D. Shaltiel and K. Baberschke, 1977, Phys. Rev. B **15**, 2771.

Davidov, D., G. Barberis, C. Rettori, J.F. Suassuna and R. Levin, 1979, Solid State Commun. **31**, 867.

Deville, A., C. Arzoumanian, B. Gaillard and C. Blanchard, 1981, J. Phys. (Paris) **42**, 1641.

Deville, A., B. Gaillard, H. Noel, M. Potel, P. Gougeon and J.C. Levet, 1989, J. Phys. (Paris) **50**, 2357.

Deville, A., L. Bejjit, B. Gaillard, J.P. Sorbier, O. Monnereau, H. Noel and M. Potel, 1993, Phys. Rev. B **47**, 2840.

Devine, R.A.B., 1976, Solid State Commun. **19**, 351.

Devine, R.A.B., 1977, J. Phys. F **7**, 461.

Devine, R.A.B., D. Shaltiel, J.N. Moret, J. Ortelli, W. Zingg and M. Peter, 1972a, Solid State Commun. **11**, 525.

Devine, R.A.B., W. Zingg and J.M. Moret, 1972b, Solid State Commun. **11**, 233.

Devine, R.A.B., J.G.H. Chiu and M. Poirier, 1975, J. Phys. F **5**, 2362.

Dixon, J.M., 1977, Crystal fields and dynamic Jahn–Teller effect of an electron quartet to Γ_5 lattice modes in the fine structure of Er^{3+} in Pd–Er, in: Int. Conf. on Crystal Field Effects in Metals and Alloys, ed. A. Furrer (Plenum Press, New York) pp. 89–93.

Döbler, U., K. Baberschke and S.E. Barnes, 1983, Phys. Rev. B **27**, 6593.

Dodds, S.A., and J. Sanny, 1978, Phys. Rev. B **18**, 39.

Dodds, S.A., J. Sanny and R. Orbach, 1978, Phys. Rev. B **18**, 1016.

Dokter, H.D., D. Davidov and D. Shaltiel, 1977, Phys. Lett. **62A**, 371.

Donoso, J.P., C. Rettori, G.E. Barberis and D. Davidov, 1981, Solid State Commun. **39**, 203.

Drulis, H., I.A. Garifullin, E.G. Kharakhashyan, B. Stalinski, N.M. Sulymanov and M.M. Zaripov, 1977, Phys. Status Solidi A **40**, K11.

Dupraz, J., B. Giovannini, R. Orbach, J.D. Riley and J. Zitkova, 1970, Electron spin resonance in dilute magnetic alloys, in: Proc. Int. Symp. on Electron and Nuclear Magnetic Resonance, eds C.K. Coogan, N.S. Ham, S.N. Stuart, J.R. Pilbrown and G.V.H. Wilson (Plenum Press, New York) pp. 197–226.

Edwards, P.P., R. Janes, R.S. Lin, P.T. Wu and C.T. Chang, 1990, Jpn. J. Appl. Phys. **29**, L258.

Elschner, B., and M. Schlott, 1988, J. Magn. & Magn. Mater. **76&77**, 444.

Engel, U., K. Baberschke, G. Koopman and S. Hüfner, 1973, Solid State Commun. **12**, 977.

Feher, E.R., 1964, Phys. Rev. **136**, A145.

Felner, I., and I. Nowik, 1986, Phys. Rev. B **33**, 617.

Fert, A., and P. Levy, 1980, Phys. Rev. Lett. **44**, 1538.

Fredkin, D.R., and S. Schultz, 1975, Phys. Rev. Lett. **35**, 682.

Fulde, P., 1979, Crystal fields, in: Handbook on the Physics and Chemistry of Rare Earths, Vol. 2, eds K.A. Gschneidner Jr and L.R. Eyring (North-Holland, Amsterdam) pp. 295–386.

Gambino, R.J., D.E. Eastman, T.R. McGuire, V.L. Morazzi and W.D. Grobman, 1971, J. Appl. Phys. **42**, 1468.

Gambke, T., and B. Elschner, 1979, J. Phys. (Paris) **40**, C5–331.

Gambke, T., B. Elschner and L.L. Hirst, 1978, Phys. Rev. Lett. **40**, 1290.

Gambke, T., B. Elschner and J. Schaafhausen, 1980, Phys. Lett. **78A**, 413.

Gambke, T., B. Elschner, J. Schaafhausen and H. Schaeffer, 1981, Intermediate valence and

ESR of Gd^{3+} in the intermetallic compounds $Ce_{1-x}M_xPd_3$ (M = Sc, Y, La) and $Ce(Pd_{1-y}N_y)_3$ (N = Rh, Ag), in: Valence Fluctuations in Solids, eds L. Falicov, W. Hanke and M.B. Maple (North-Holland, Amsterdam) pp. 447–450.

Gambke, T., B. Elschner, R. Kremer and M. Schanz, 1983, J. Magn. & Magn. Mater. **36**, 115.

Gandra, F.G., and M.J. Pontes, 1988, J. Magn. Magn, Mater. **76&77**, 481.

Gandra, F.G., S. Schultz, S.B. Oseroff, Z. Fisk and J.L. Smith, 1985, Phys. Rev. Lett. **55**, 2719.

Gandra, F.G., M.J. Pontes, S. Schultz and S.B. Oseroff, 1987, Solid State Commun. **64**, 859.

Garifullin, I.A., T.O. Farzan, G.G. Khaliullin and E.F. Kukovitsky, 1985, J. Phys. F **15**, 979.

Garifullin, I.A., N.N. Garif'yanov, N.E. Alekseevskii and S.F. Kim, 1991, Physica C **179**, 9.

Genossar, J., D. Shaltiel, V. Zevin, A. Grayevsky and B. Fisher, 1989, J. Phys.: Condens. Matter **1**, 9471.

Götze, W., and P. Wölfle, 1971, J. Low Temp. Phys. **5**, 575.

Grewe, N., and F. Steglich, 1991, Heavy fermions, in: Handbook on the Physics and Chemistry of Rare Earths, Vol. 14, eds K.A. Gschneidner Jr and L. Eyring (North-Holland, Amsterdam) pp. 343–474.

Grewe, N., and B. Welslau, 1988, Solid State Commun. **65**, 437.

Griffiths, D., and B.R. Coles, 1966, Phys. Rev. Lett. **16**, 1093.

Guertin, R.P., J.E. Crow, L.D. Longinotti, E. Bucher, L. Kupferberg and S. Fonger, 1975, Phys. Rev. B **12**, 1005.

Gulley, J.E., D. Hone, D.J. Scalapino and B.G. Silbernagel, 1970, Phys. Rev. B **1**, 1020.

Hannay, N.B., and C.F. Smyth, 1946, J. Am. Chem. Soc. **68**, 171.

Hardiman, M., S.E. Barnes and J. Pellisson, 1977, EPR fine structure of S state ions, in: Int. Conf. on Crystal Field Effect in Metals and Alloys, ed. A. Furrer (Plenum Press, New York) pp. 71–75.

Hardiman, M., J. Pellisson, S.E. Barnes, P.E. Bisson and M. Peter, 1980, Phys. Rev. B **22**, 2175.

Hasegawa, H., 1959, Prog. Theor. Phys. (Japan) **21**, 483.

Hayashi, Y., M. Fukui, T. Fujita, H. Shibayama, K. Wahashi and K. Adachi, 1989, Jpn. J. Appl. Phys. **28**, L910.

Heer, H., A. Furrer and W. Hälg, 1976, J. Magn. & Magn. Mater. **3**, 55.

Heinrich, G., and A. Meyer, 1977, Solid State Commun. **24**, 1.

Heinrich, G., J.P. Kappler and A. Meyer, 1979, Phys. Lett. **74A**, 121.

Heinrich, G., J.P. Kappler and A. Meyer, 1982, J. Appl. Phys. **53**, 2155.

Hirst, L.L., 1969, Phys. Rev. **181**, 597.

Hirst, L.L., 1971, Z. Physik **245**, 378.

Hirst, L.L., 1972, Adv. Phys. **21**, 759.

Hirst, L.L., G. Williams and B.R. Coles, 1968, J. Appl. Phys. **39**, 844.

Hoekstra, F.R., D. Davidov, G.J. Nieuwenhuys and I. Felner, 1982, Phys. Lett. **88A**, 420.

Hoffmann, S.K., B. Czyzak and J. Stankowski, 1990, Acta Phys. Pol. A **7**, 621.

Holland-Moritz, E., W. Schlabitz, M. Loewenhaupt, U. Walter and C.K. Loong, 1987, J. Magn. & Magn. Mater. **63&64**, 187.

Huang, C.Y., and K. Sugawara, 1977, J. Low Temp. Phys. **28**, 229.

Huang, C.Y., K. Sugawara and B.R. Cooper, 1976, EPR studies of excited-state exchange and crystal-field effects in rare-earth compounds, in: Int. Conf. on Crystal-Field Effects in Metals and Alloys, ed. A. Furrer (Plenum Press, New York) pp. 5–60.

Hutchings, M.T., 1964, Point charge calculations of energy levels of magnetic ions in crystalline electric fields, in: Solid State Physics, Vol. 16, eds F. Seitz and D. Turnball (Academic Press, New York) pp. 227–273.

Isaacs, E.D., D.B. Mc Whan, R.N. Kleimau, D.J. Bishop, C.P. Ice, P. Zschach, B.D. Gaulin, T.E. Mason, J.D. Garrett and W.J.L. Buyers, 1990, Phys. Rev. Lett. **65**, 3185.

Janet, J.P., and A.P. Malozemoff, 1978, Phys. Rev. B **18**, 75.

Janossy, A., A. Rockenbauer and S. Pekker, 1990a, Physica C **167**, 301.

Janossy, A., A. Rockenbauer, S. Pekker, G. Oszlanyi, G. Faigel and L. Korez, 1990b, Physica C **171**, 457.

Janossy, A., L.-C. Brunel and J.R. Cooper, 1996, Phys. Rev. B **54**, 10186.

Jansen, K., and G. Sperlich, 1975, Solid State Commun. **17**, 1179.

Johansson, J., I.A. Abrikosov, M. Alde'n and H.L. Skriver, 1995, Phys. Rev. Lett. **74**, 2335.

Jones, W.H., E.A. Garbaty and R.G. Barnes, 1962, J. Chem. Phys. **36**, 494.

Jullien, R., and D. Jerome, 1971, J. Phys. Chem. Solids **32**, 257.

Kaczmarska, K., E. Kwapulinska and A. Chelkowski, 1979, Acta Phys. Pol. A **55**, 69.

Kaczmarska, K., E. Kwapulinska, A. Slebarski, E. Zipper and A. Chełkowski, 1985, J. Magn. & Magn. Mater. **50**, 101.

Kaise, M., M. Mizuno, C. Nishihara, H. Nozoye and H. Shindo, 1990, in: Advances in Superconductivity II, eds T. Ishiguro and K. Kajimura (Springer, Tokyo) p. 543.

Kan, L., 1986, Diploma Thesis (TH Darmstadt) unpublished.

Kan, L., S. Elschner and B. Elschner, 1991, Solid State Commun. **79**, 61.

Kasuya, T., 1976, A mechanism for the metal insulator transition and various properties in samarium compounds, in: Proc. Int. Conf. on Metal–Nonmetal Transitions, J. Phys. (Paris) Suppl. Colloq. **4**, pp. 261–265.

Kataev, V., Yu. Greznev, G. Teitel'baum, M. Breuer and N. Knauf, 1993, Phys. Rev. B **48**, 13042.

Keimer, B., R.J. Birgeneau, A. Cassanho, Y. Endoh, R.W. Erwin, M.A. Kastner and G. Shirane, 1991, Phys. Rev. Lett. **67**, 1930.

Kim, J.N., and J.S. Karra, 1977, Phys. Rev. B **15**, 2538.

Knopp, G., A. Loidl, K. Knorr, L. Pawlack, M. Duczmal, R. Caspary, U. Gottwick, H. Spille, F. Steglich and A.P. Murani, 1988a, Z. Phys. B **77**, 341.

Knopp, G., A. Loidl, R. Caspary, U. Gottwick, C.D. Bredl, H. Spille, F. Steglich and A.P. Murani, 1988b, J. Magn. & Magn. Mater. **74**, 341.

Kochelaev, B.I., L.R. Tagirov, J.A. Garifullin, N.N. Garifyanov, G.G. Khaliullin, N.E. Alekseevskii, A.V. Mitin, V.I. Nizhankovskii and E.P. Khlybov, 1990, Exp. Techn. Phys. **38**, 359.

Kochelaev, B.I., L. Kan, B. Elschner and S. Elschner, 1994, Phys. Rev. B **49**, 13106.

Kohn, W., and S.H. Vosko, 1960, Phys. Rev. **119**, 912.

Kojima, K., M. Kasaya and Y. Koi, 1978, J. Phys. Soc. Japan **44**, 1124.

Kontani, N., Y. Chiba, K. Sugiyama, Y. Hidaka and M. Date, 1990, J. Phys. Soc. Jpn. **59**, 3019.

Koopmann, G., K. Baberschke and S. Hüfner, 1975, Phys. Lett. A **50**, 407.

Koopmann, G., K. Baberschke and S. Hüfner, 1977a, Physica B **86–88**, 509.

Koopmann, G., K. Baberschke and S. Hüfner, 1977b, J. Phys. C **1**, 9471.

Krug von Nidda, H.-A., A. Schütz, M. Heil, B. Elschner and A. Loidl, 1997, Phys. Rev B, to be published.

Kruschel, G., 1993, Ph.D. Thesis (TH Darmstadt) unpublished.

Kübler, J., 1978, J. Phys. F **8**, 2301.

Kubo, R., and K. Tomita, 1954, J. Phys. Soc. Jpn. **9**, 888.

Kunii, S., T. Uemura, Y. Chiba, T. Kasuya and M. Date, 1985, J. Magn. & Magn. Mater. **52**, 271.

Kwapulinska, E., and K. Kaczmarska, 1990, J. Magn. & Magn. Mater. **88**, 51.

Larica, C., and B.R. Coles, 1985, Phil. Mag. **52**, 1097.

Larica, C., and A.P. Guimareas, 1976, Phys. Status Solidi B **77**, K11.

Lawrence, J.M., P.R. Riseborough and R.D. Parks, 1981, Adv. Phys. **44**, 1.

Lazuta, A.V., 1991, Physica C **181**, 127.

Lea, K.R., M.J.M. Leask and W.P. Wolf, 1962, Phys. Chem. Solids **23**, 1381.

Levin, R., D. Shaltiel and D. Davidov, 1975, Exchange interaction in the enhanced hyperfine cooling material $PrNi_5$, in: Proc. XIVth Int. Conf. on Low-Temperature Physics (LT14), Vol. 3, eds. M. Krusius and M. Vuorio (North-Holland, Amsterdam) pp. 212–215.

Levin, R., A. Grayevsky, D. Shaltiel, V. Zevin, D. Davidov, D.L. Williams and N. Kaplan, 1979a, Solid State Commun. **32**, 855.

Levin, R., A. Grayevsky, D. Shaltiel, V. Zevin and D. Davidov, 1979b, Phys. Rev. B **20**, 2624.

Levin, R., D. Davidov, D. Shaltiel and V. Zevin, 1982, J. Phys. F **12**, 1157.

Loidl, A., A. Krimmel, K. Knorr, G. Sparn, M. Lang, C. Geibel, S. Horn, A. Grauel, F. Steglich, B. Welslau, N. Grewe, H. Nakotte, F.R. de Boer and A.P. Murani, 1992, Ann. Phys. (Germany) **1**, 78.

Luft, H., and K. Baberschke, 1981, J. Appl. Phys. **52**, 2095.

Luft, H., K. Baberschke and K. Winzer, 1981, J. Appl. Phys. **52**, 2095.

Luft, H., K. Baberschke and K. Winzer, 1982, Z. Phys. B **47**, 195.

Luft, H., K. Baberschke and K. Winzer, 1983, Phys. Lett. A **95**, 186.

Mahdjour, H., C. Pappa, R. Wendler and K. Baberschke, 1986, Z. Phys. B **63**, 351.

Maki, K., 1973, Phys. Rev. B **8**, 191.

Male, S.E., and R.H. Taylor, 1975, J. Phys. F **5**, L26.

Maletta, H., and W. Felsch, 1979, Phys. Rev. B **20**, 1245.

Malik, S.K., and R. Vijayaraghavan, 1975, Phys. Rev. B **12**, 3971.

Malozemoff, A.P., and J.P. Janet, 1977, Phys. Rev. Lett. **39**, 1293.

Maple, M.B., J.W. Chen, Y. Dalichaouch, T. Kohara, C. Rossel, M.S. Torikachvili, M.W. McElfresh and J.D. Thompson, 1986, Phys. Rev. Lett. **58**, 1487.

Mason, T.E., B.D. Gaulin, J.D. Garrett, Z. Tun, W.J.C. Buyers and E.D. Isaacs, 1990, Phys. Rev. Lett. **65**, 3189.

Mason, T.E., G. Aeppli and H.A. Mook, 1992, Phys. Rev. Lett. **68**, 1414.

Matsuda, M., K. Yamada, Y. Endoh, T.R. Thurston, G. Shirane, R.J. Birgeneau, M.A. Kastner, I. Tanaka and H. Kojima, 1994, Phys. Rev. B **49**, 6958.

McLaughlin, D.E., C. Tien, W.G. Clark, M.D. Lan, Z. Fisk, J.L. Smith and H.R. Ott, 1984, Phys. Rev. Lett. **53**, 1833.

McWhan, D.B., T.M. Rice and P.H. Schmidt, 1969, Phys. Rev. B **177**, 1063.

Mehran, F., and P.W. Anderson, 1989, Solid State Commun. **71**, 29.

Mehran, F., S.E. Barnes, G.V. Chandrashekar, T.R. McGuire and M.W. Shafer, 1988a, Solid State Commun. **67**, 1187.

Mehran, F., S.E. Barnes, T.R. McGuire, T.R. Dinger, D.L. Kaiser and F. Holtzberg, 1988b, Solid State Commun. **66**, 299.

Mercurio, J.-P., S. Angelar and J. Etourneau, 1979, J. Less-Common Metals **67**, 257.

Millis, A.J., and H. Monien, 1993, Phys. Rev. Lett. **70**, 2810.

Monod, P., and Y. Berthier, 1980, J. Magn. & Magn. Mater. **15–18**, 149.

Monod, P., A. Landi, C. Blanchard, A. Deville and H. Hurdequint, 1986, J. Magn. & Magn. Mater. **59**, 132.

Moret, J.M., R. Orbach, M. Peter, D. Shaltiel, J.T. Suss, W. Zingg, R.A.B. Devine and P.H. Zimmermann, 1975, Phys. Rev. B **11**, 2002.

Moriya, T., and Y. Obata, 1958, J. Phys. Soc. Jpn. **13**, 1333.

Moto, A., A. Morimoto, M. Kumeda and T. Shimizu, 1990, Supercond. Sci. Technol. **3**, 579.

Mozurkewich, G., J.H. Elliott, M. Hardiman and R. Orbach, 1984, Phys. Rev. B **29**, 278.

Nagel, J., and K. Baberschke, 1976, EPR of Gd^{3+} in Lu and Sc single crystals, in: Int. Conf. on Crystal Field Effects in Metals and Alloys, ed. A. Furrer (Plenum Press, New York) pp. 66–70.

Nagel, J., S. Hüfner and M. Grunig, 1973, Solid State Commun. **8**, 1279.

Nagel, J., K. Baberschke and E. Tsang, 1980, J. Magn. & Magn. Mater. **15–18**, 730.

Nakamura, F., Y. Ochiai, H. Shimizu and Y. Narahara, 1990a, Phys. Rev. B **42**, 2558.

Nakamura, F., Y. Ochiai, H. Shimizu and Y. Narahara, 1990b, Physica B **165&166**, 1315.

Neukomm, H.R., and R. Hauger, 1975, Z. Physik B **20**, 323.

Ochi, M.M., and O.L.T. Menezes, 1991, Physica B **171**, 320.

Odermatt, R., M. Hardiman, S.E. Barnes, J. Pellison and M. Peter, 1979a, Helv. Phys. Acta **52**, 367.

Odermatt, R., M. Hardiman and J. van Meijel, 1979b, Solid State Commun. **32**, 1227.

Orbach, R., 1974, Phys. Lett. A **47**, 281.

Orbach, R., 1975, Dynamics of localized moments in metals, in: Proc. XIVth Int. Conf. on Low-Temperature Physics (LT14), eds M. Krusius and M. Vuorio (North-Holland, Amsterdam) pp. 375–408.

Orbach, R., 1980, J. Magn. & Magn. Mater. **15–18**, 706.

Orbach, R., M. Peter and D. Shaltiel, 1974, Arch. Sci. **27**, 141.

Oseroff, S., B.L. Gehman, S. Schultz and C. Rettori, 1975, Phys. Rev. Lett. **35**, 679.

Oseroff, S., B.L. Gehman and S. Schultz, 1977a, Phys. Rev. B **15**, 1291.

Oseroff, S., M. Passeggi, D. Wohlleben and S. Schultz, 1977b, Phys. Rev. B **15**, 1283.

Oseroff, S.B., and R. Calvo, 1978, Phys. Rev. B **18**, 3041.

Overhauser, A., 1953, Phys. Rev. **89**, 689.

Owen, J., M.E. Browne, W.D. Knight and C. Kittel, 1956, Phys. Rev. **102**, 1501.

Owen, J., M.E. Browne, V. Arp and A.F. Kip, 1957, J. Phys. Chem. Solids **2**, 85.

Palstra, T.T.M., A.A. Menovsky, J. van den Berg, A.J. Dirkmaat, P.H. Kes, G.J. Nieuwenhuys and J.A. Mydosh, 1985, Phys. Rev. Lett. **55**, 2727.

Pelegrini, F., R.W. Teale and S. Abell, 1982, J. Magn. & Magn. Mater. **29**, 105.

Peter, M., J. Dupraz and H. Cottet, 1967, Helv. Phys. Acta **40**, 301.

Plefka, T., 1973, Phys. Status Solidi B **55**, 129.

Preusse, N., W. Schäfer and B. Elschner, 1981, EPR of Gd in $Sc_{1-x}Ce_xAl_2$ intermetallic compounds, in: Valence Fluctuations in Solids, eds L.M. Falicov,

W. Hanke and M.P. Maple (North-Holland, Amsterdam) pp. 317–320.

Punnoose, A., and R.J. Singh, 1995, Int. J. Mod. Phys. B **9**, 1123.

Raizman, A., J.T. Suss, D.N. Seidman, D. Shaltiel, V. Zevin and R. Orbach, 1979, J. Appl. Phys. **50**, 7735.

Raizman, A., J.T. Suss, D.N. Seidman, D. Shaltiel and V. Zevin, 1981, Phys. Rev. Lett. **46**, 141.

Raizman, A., J.T. Suss, D.N. Seidman, D. Shaltiel and V. Zevin, 1984, EPR study of oxydation of erbium ions in a near-surface layer of a gold foil, in: Proc. XXIInd Congr. AMPERE on Magnetic Resonance and Related Phenomena, eds K.A. Müller, R. Kind and J. Roos (Zürich Ampere Commitee, University Zürich, Zürich) pp. 283–284.

Redfield, A., 1955, Phys. Rev. **98**, 1787.

Rettori, C., and D. Davidov, 1973, Phys. Rev. B **10**, 4033.

Rettori, C., D. Davidov, P. Chaikin and R. Orbach, 1973a, Phys. Rev. Lett. **30**, 473.

Rettori, C., D. Davidov, R. Orbach, E.P. Chock and B. Ricks, 1973b, Phys. Rev. B **7**, 1.

Rettori, C., H.M. Kim, E.P. Chock and D. Davidov, 1974, Phys. Rev. B **10**, 1826.

Rettori, C., D. Davidov, A. Grayevsky and W.M. Walsh, 1975a, Phys. Rev. B **11**, 4450.

Rettori, C., D. Davidov, G. Ng and E.P. Chock, 1975b, Phys. Rev. B **12**, 1298.

Rettori, C., D. Davidov, J. Suassuna, G.E. Barberis, B. Elschner and D. Born, 1978, Solid State Commun. **25**, 543.

Rettori, C., D. Rao, S.B. Oseroff, G. Amoretti, Z. Fisk, S.-W. Cheong, D. Vier, S. Schultz, M. Tovar, R.D. Zysler and J.E. Schirber, 1993, Phys. Rev. B **47**, 8156.

Rettori, G., E. Weber, J.P. Donoso, F.C.G. Gandra and G.E. Barberis, 1981, Solid State Commun. **39**, 1025.

Rigamonti, A., F. Borsa, M. Corti, T. Rega, J. Ziolo and F. Waldner, 1990, Magnetic correlations and spin dynamics in $La_{2-x}Sr_xCuO_4$ from NQR relaxation, in: Springer Series in Solid State Sciences, Vol. 90, eds J.G. Bednorz and K.A. Müller (Springer, Heidelberg) pp. 441–466.

Ritter, A.L., and R.H. Silsbee, 1978, Phys. Rev. B **17**, 2833.

Romanyukha, A.A., Yu.N. Shvachko, V.Yn. Irklin, M.I. Katsnelson, A.A. Koshta and V.V. Ustinov, 1990, Physica C **171**, 276.

Rossat-Mignod, J., L.P. Regnault, P. Bourges, P. Burlet, C. Vettier and J.Y. Henry, 1992, Neutron scattering study of the high-T_c superconducting system $YBa_2Cu_3O_{6+5}$, in: Frontiers in Solid State Sciences, Vol. 1, eds L.C. Gupta and M.S. Multani (World Scientific, Singapore) pp. 265–347.

Salamon, M.B., 1979, Solid State Commun. **31**, 781.

Salamon, M.B., and R.M. Herman, 1978, Phys. Rev. Lett. **41**, 1506.

Salomons, F.W., E. Antonides, D. Stoppels and G.A. Sawatzky, 1974, Solid State Commun **15**, 1467.

Sarkissan, D.V.B., 1979, Phil. Mag. B **39**, 413.

Sayad, H.A., and S.M. Bhagat, 1985, Phys. Rev. B **31**, 591.

Schaeffer, H., and B. Elschner, 1983, Z. Phys. B **53**, 109.

Schaeffer, H., and B. Elschner, 1985, Solid State Commun. **53**, 611.

Schäfer, W., 1971, Diploma Thesis (TH Darmstadt) unpublished.

Schäfer, W., H.K. Schmidt, B. Elschner and K.H.J. Buschow, 1972, Z. Phys. **254**, 1.

Schefzyk, R., J. Heibel, F. Steglich, R. Felten and G. Weber, 1985, Transition from Kondo to intermediate valence in $Ce_{1-x}Y_xAl_2$, in: Proc. 4th Int. Conf. on Valence Fluctuations, eds E. Müller-Hartmann, B. Roden and D. Wohlleben (North-Holland, Amsterdam) pp. 83–85.

Schlott, M., 1984, Diploma Thesis (TH Darmstadt) unpublished.

Schlott, M., 1989, Ph.D. Thesis (TH Darmstadt) unpublished.

Schlott, M., H. Schaeffer and B. Elschner, 1986, Z. Phys. B **63**, 427.

Schlott, M., B. Elschner, M. Herrmann and W. Assmus, 1988, Z. Physik B **72**, 385.

Schmidt, H.K., 1972, Z. Naturforsch. A **27**, 191.

Schmidt, H.K., W. Schäfer, G. Keller and B. Elschner, 1972, Phys. Lett. A **38**, 201.

Schrittenlacher, W., K. Baberschke, G. Koopmann and S. Hüfner, 1975, Solid State Commun. **16**, 923.

Schultz, S., M.R. Shanaburger and P.M. Platzman, 1967, Phys. Rev. Lett. **19**, 749.

Schultz, S., E.M. Gullikson, D.R. Fredkin and M. Tovar, 1980, Phys. Rev. Lett. **45**, 1508.

Schultz, S., E.M. Gullikson, D.R. Fredhin and M. Tovar, 1981, J. Appl. Phys. **52**, 1776.

Schütz, A., 1996, Diploma Thesis (TH Darmstadt) unpublished.

Searl, J.W., R.C. Smith and S.J. Wyard, 1961, Proc. Phys. Soc. (London) A **78**, 1174.

Seehra, M.S., and D.L. Huber, 1975, AIP Conference Proceedings **24**, 261.

Seipler, D., 1975, On the local susceptibilities of the conduction electrons and their exchange interaction with Gd in dilute intermetallic compounds, in: Proc. XIXth Congr. AMPERE on Magnetic Resonance and Related Phenomena, eds H. Brunner, K.H. Hausser and D. Schweitzer (Groupment Ampere, Heidelberg) pp. 297–300.

Seipler, D., and B. Elschner, 1975, Phys. Lett. A **55**, 115.

Seipler, D., and B. Elschner, 1977, Physica B **86–88**, 97.

Seipler, D., and T. Plefka, 1978, J. Phys. F **8**, 969.

Seipler, D., B. Bremiker, U. Goebel, H. Happel, H.E. Hoenig and B. Perrin, 1977, J. Phys. F 7, 599.

Shaltiel, D., J.H. Wernick, H.J. Williams and M. Peter, 1964a, Phys. Rev. A **135**, 1346.

Shaltiel, D., J.H. Wernick, H.J. Williams and M. Peter, 1964b, J. Appl. Phys. **35**, 978.

Shaltiel, D., K. Baberschke, J. Nagel and G. Koopmann, 1977, Phys. Rev. B **16**, 3262.

Shaltiel, D., S.E. Barnes, H. Bill, M. Francois, H. Hagemann, J. Jegondaz, D. Lovy, P. Monod, M. Peter, A. Revcolevschi, W. Sadowski and E. Walker, 1989a, Physica C **161**, 13.

Shaltiel, D., H. Bill, P. Fischer, M. Francois, H. Hagemann, M. Peter, Y. Ravisekhar, W. Sadowski, H.J. Scheel, G. Triscone, E. Walker and K. Ytron, 1989b, Physica C **158**, 424.

Shengelaya, A.D., J. Olejniczak and H. Drulis, 1994, Physica C **233**, 124.

Shimizu, H., 1991, J. Phys. Soc. Jpn. **60**, 3842.

Shimizu, T., K. Yoshimura, T. Nitta, T. Skakibara, T. Goto and M. Mekata, 1988, J. Phys. Soc. Jpn. **57**, 405.

Sichelschmidt, J., B. Elschner, A. Loidl and K. Fischer, 1994, Z. Phys. B **93**, 407.

Sichelschmidt, J., B. Elschner, A. Loidl and B.I. Kochelaev, 1995a, Phys. Rev. B **51**, 9199.

Sichelschmidt, J., B. Elschner, A. Loidl and B.I. Kochelaev, 1995b, Physica B **206&207**, 742.

Siebert, J.F., S.A. Dodds and R.H. Silsbee, 1974, Phys. Rev. Lett. **33**, 904.

Siebert, J.F., S.A. Dodds and R.H. Silsbee, 1976, Phys. Rev. B **14**, 4813.

Sienkiewicz, A., M.Z. Cieplak, G. Xiao and G.L. Chien, 1990, J. Less-Common Met. **164&165**, 870.

Sjöstrand, M.E., and G. Seidel, 1975, Phys. Rev. B **11**, 3292.

Skrzypek, D., K. Majewska and A. Ratuszna, 1991, Phys. Scr. **44**, 624.

Slebarski, A., K. Kaczmarska and E. Kwapulinska, 1983, J. Magn. & Magn. Mater. **38**, 51.

Spencer, H.J., and S. Doniach, 1967, Phys. Rev. Lett. **18**, 994.

Sperlich, G., and K. Jansen, 1974, Solid State Commun. **15**, 1105.

Sperlich, G., K. Jansen and G. Bang, 1973, Phys. Lett. A **45**, 423.

Spitzfaden, R., A. Loidl, J.G. Park and B.R. Coles, 1996, J. Phys.: Condens. Matter **8**, 2857.

Spörel, F., and E. Biller, 1975, Solid State Commun. **17**, 833.

Stankowski, J., W. Hilczer, J. Baszynski, B. Czyzak and L. Szczepanska, 1991, Solid State Commun. **77**, 125.

Steglich, F., J. Aarts, C.D. Bredl, W. Lieke, D. Meschede, W. Franz and H. Schäfer, 1979, Phys. Rev. Lett. **43**, 1892.

Steglich, F., B. Buschinger, P. Gegenwart, C. Geibel, R. Helfrich, P. Hellmann, M. Lang, A. Link, R. Modler, D. Jaccard and P. Link, 1995, Superconductivity and antiferromagnetism in heavy fermion metals: coexistence and competition, in: Proc. Int. Conf. on Physical Phenomena at High Magnetic Fields II, Tallahassee, eds Z. Fisk, L. Gorkov, D. Meltzer and R. Schrieffer (World Scientific, Singapore) pp. 125–136.

Stein, R.M., G.E. Barberis and C. Rettori, 1981, Solid State Commun. **39**, 1157.

Stein, R.M., J.P. Ponoso and G.E. Barberis, 1983, Phys. Lett. A **96**, 422.

Sternlieb, B.J., G. Shirane, J.M. Tranquada, M. Sato and S. Shamoto, 1993, Phys. Rev. B **47**, 5320.

Stevens, K.W.H., 1967, Rep. Progr. Phys. **30**, 189.

Stewart, G.R., Z. Fisk and M.S. Wire, 1984, Phys. Rev. B **30**, 482.

Sticht, J., M. Schlott, J. Kübler and B. Elschner, 1988, J. Magn. & Magn. Mater. **76&77**, 496.

Sturm, H., and B. Elschner, 1985, unpublished.

Sturm, H., B. Elschner and K.H. Höck, 1985, Phys. Rev. Lett. **54**, 1291.

Sugawara, K., 1977a, J. Phys. Soc. Jpn. **42**, 1154.

Sugawara, K., 1977b, J. Phys. Soc. Jpn. **42**, 1161.

Sugawara, K., and C.Y. Huang, 1975, J. Phys. Soc. Jpn. **39**, 643.

Sugawara, K., and C.Y. Huang, 1976a, J. Phys. Soc. Jpn. (Letters) **40**, 295.

Sugawara, K., and C.Y. Huang, 1976b, J. Phys. Soc. Jpn. **41**, 1534.

Sugawara, K., C.Y. Huang and B.R. Cooper, 1975, Phys. Rev. B **11**, 4455.

Sugawara, K., C.Y. Huang and D.L. Huber, 1977, J. Low Temp. Phys. **26**, 525.

Takegahara, K., H. Takahashi, A. Yanase and T. Kasuya, 1981, Solid State Commun. **39**, 857.

Takigawa, M., A.P. Reyes, P.C. Hammel, J.D. Thompson, R.H. Heffner, Z. Fisk and K.C. Ott, 1991, Phys. Rev. B **43**, 247.

Taleb, S., W.G. Clark, P. Armstrong, C. Rossel and M.B. Maple, 1988, Solid State Commun. **68**, 231.

Tao, L.J., D. Davidov, R. Orbach and E.P. Ckoch, 1971, Phys. Rev. B **4**, 5.

Tari, A., and R. Kuentzler, 1986, J. Magn. & Magn. Mater. **53**, 359.

Taylor, R.H., 1975, Adv. Phys. **24**, 681.

Taylor, R.H., and B.R. Coles, 1975, J. Phys. F **5**, 121.

Than-Trong, N., L.B. Chiu, P.R. Elliston, A.M. Stewart and K.N.R. Taylor, 1981, J. Phys. F **11**, 1123.

Title, R.S., 1965, Phys. Rev. A **138**, 631.

Todt, H., 1993, Diploma Thesis (TH Darmstadt) unpublished.

Tranquada, J.M., P.M. Gehring, G. Shirane, M. Sato and S. Shamoto, 1992, Phys. Rev. B **46**, 5561.

Troper, A., O.L.T. de Menezes and A.A. Gomes, 1979, unpublished.

Tsang, E., and K. Baberschke, 1981, J. Appl. Phys. **52**, 2208.

Uemura, T., Y. Chiba, S. Kunii, M. Kasaya, T. Kasuya and M. Date, 1986a, J. Phys. Soc. Jpn. **55**, 43.

Uemura, T., Y. Chiba, M. Hagiwara and M. Date, 1986b, J. Phys. Soc. Jpn. **55**, 3737.

Uimin, G., and J. Rossat-Mignod, 1992, Physica C **199**, 251.

Uimin, G., and V. Stepanov, 1993, Ann. Physik (Germany) **2**, 284.

Urban, P., and D. Seipler, 1977, J. Phys. F **7**, 1589.

Urban, P., B. Elschner, G. Sperlich and G. Schön, 1974a, Phys. Lett. A **49**, 418.

Urban, P., G. Sperlich and R. Neuhäusser, 1974b, Solid State Commun. **14**, 591.

Urban, P., D. Davidov, B. Elschner, T. Plefka and G. Sperlich, 1975, Phys. Rev. B **12**, 72.

Urban, P., K. Jansen, G. Sperlich and D. Davidov, 1978, J. Phys. F **8**, 977.

Van Vleck, J.H., 1948, Phys. Rev. **74**, 1168.

Varknin, D., D. Davidov, G.J. Nieuwenhuys, F.R. Hoekstra, G.E. Barberis and J.A. Mydosh, 1981, Physica B **108**, 765.

Varma, C.M., 1985, Phys. Rev. Lett. **55**, 2723.

Varma, C.M., P.B. Littlewood and S. Schmitt-Rink, 1989, Phys. Rev. Lett. **63**, 1996.

Venturini, E.L., and B. Morosin, 1977, Phys. Lett. A **61**, 326.

Vier, D.C., S.B. Oseroff, C.T. Salling, J.F. Smyth, S. Schultz, Y. Dalichaouch, B.W. Lee, M.B. Maple, Z. Fisk and J.D. Thompson, 1987, Phys. Rev. B **36**, 888.

von Molnar, S., T. Theis, A. Benoit, A. Briggs, J. Flouquet, J. Ravex and Z. Fisk, 1982, Study of the energy gap in single crystals SmB_6, in: Valence Instabilities, eds P. Wachter and H. Boppart (North-Holland, Amsterdam) pp. 389–395.

von Spalden, Y., E. Tsang, K. Baberschke and P. Schlottmann, 1983, Phys. Rev. B **28**, 20.

Walker, M.B., 1968, Phys. Rev. **176**, 432.

Walstedt, R.E., and L.R. Walker, 1975, Phys. Rev. B **11**, 3280.

Watson, R.E., S. Koide, M. Peter and A.J. Freeman, 1965, Phys. Rev. **139**, A167.

Watson, R.E., A.J. Freeman and S. Koide, 1969, Phys. Rev. **186**, 625.

Weber, C., E. Sigmund and M. Wagner, 1985, Phys. Rev. Lett. **55**, 1645.

Weber, C., E. Sigmund and M. Wagner, 1986, Phys. Status Solidi B **138**, 661.

Weber, C., E. Sigmund and M. Wagner, 1987, Phys. Status Solidi B **141**, 529.

Weissenberger, V., 1981, Diploma Thesis (TH Darmstadt) unpublished.

Weissenberger, V., B. Elschner and M.A. Continentino, 1986, Phys. Rev. B **33**, 7474.

Wienand, K.H., B. Elschner and F. Steglich, 1982, J. Magn. & Magn. Mater. **28**, 234.

Wiese, G., H. Schäffer and B. Elschner, 1990, Europhys. Lett. **11**, 791.

Wright, F., 1995, J. Phys. C **7**, 6097.

Wu, W.-Y., G. Mozurkewich and R. Orbach, 1985, Phys. Rev. B **31**, 4557.

Yafet, Y., 1963, *g*-Factors and spin-lattice relaxation of conduction electrons, in: Solid State Physics, Vol. 14, Advances in Research and Application, eds F. Seitz and D. Turnbull (Academic Press, New York) pp. 1–98.

Yang, D., B.R. Cooper, C.Y. Huang and K. Sugawara, 1979, Theory of *g*-shift and linewidth in CeP excited state EPR, in: Proc. Int. Conf. on Crystalline Electric Field and Structural Effects in f-Electron Systems, eds J.E. Crow, R.P. Guertin and T.W. Mihalisin (Plenum Press, New York) pp. 473–480.

Zevin, V., D. Shaltiel and W. Zingg, 1977a, Phys. Rev. B **16**, 1902.
Zevin, V., D. Davidov, R. Levin, D. Shaltiel and K. Baberschke, 1977b, J. Phys. F **7**, 2193.
Zimmermann, P.H., D. Davidov, R. Orbach, L.J. Tao and J. Zitkova, 1972, Phys. Rev. B **6**, 2783.
Zingg, W., H. Bill, J. Buttet and M. Peter, 1974, Phys. Rev. Lett. **32**, 1221.
Zipper, E., 1982, J. Phys. F **12**, 3123.
Zipper, E., 1983, J. Magn. & Magn. Mater. **36**, 165.
Zipper, E., K. Kaczmarska, E. Kwapulinska and J. Pichet, 1984, J. Magn. & Magn. Mater. **40**, 259.
Zomack, M., and K. Baberschke, 1981, Physica B **108**, 773.
Zomack, M., K. Baberschke and S.E. Barnes, 1983, Phys. Rev. B **27**, 4135.

Handbook on the Physics and Chemistry of Rare Earths
Vol. 24
edited by K.A. Gschneidner, Jr. and L. Eyring

Chapter 163

INTERSUBLATTICE EXCHANGE COUPLING IN THE LANTHANIDE–TRANSITION METAL INTERMETALLICS

Nguyen Huu DUC
Cryogenic Laboratory, Faculty of Physics, University of Hanoi, 90-Nguyen Trai, Thanxuân, Hanoi, Vietnam

Contents

Abbreviations

DOS	density of states	R	lanthanide
f.u.	formula unit	HR	heavy lanthanide
HFFP	high-field free-powder	LR	light lanthanide
INS	inelastic neutron scattering	RKKY	Ruderman–Kittel–Kasuya–Yosida
NMR	nuclear magnetic resonance	T	transition metal

List of symbols

A_{ij}	spin–spin coupling parameter	J	quantum number of the total angular momentum J_R for the 4f ions
A_{RR}	spin–spin coupling parameter between R spins	k_B	Boltzmann constant
A_{RT}	spin–spin coupling parameter between R and T spins	m_i	magnetic moment per ion
		m_R	magnetic moment per R ion
A_{TT}	spin–spin coupling parameter between T spins	m_T	magnetic moment per T ion
		M_i	sublattice magnetization
B	external magnetic field ($\mu_0 H$)	M_R	magnetization of the R sublattice
B^R_{mol}	effective molecular field acting on R moment in R–T compounds	M_T	magnetization of the T sublattice
		M_s	spontaneous magnetization
B^T_{mol}	effective molecular field acting on T moment in R–T compounds	$N(E_F)$	density of states at Fermi level
		N_R	number of R atoms per formula unit
$B^R_{ex,RR}$	exchange field acting on R moment due to intrasublattice (R–R) interactions	N_T	number of T atoms per formula unit
		n_{ij}	molecular-field coefficient
$B^R_{ex,RT}$	exchange field acting on R moment due to intersublattice (R–T) interactions	n_{RR}	intrasublattice molecular-field coefficient
$B^R_{mol,RR}$	molecular field acting on R moment due to intrasublattice (R–R) interactions	n_{RT}	intersublattice molecular-field coefficient
$B^R_{mol,RT}$	molecular field acting on R moment due to intersublattice (R–T) interactions	n_{TT}	intrasublattice molecular-field coefficient
$B^T_{mol,RT}$	molecular field acting on T moment due to intersublattice (R–T) interactions	p_{eff}	effective paramagnetic d-moment
$B^T_{ex,TT}$	molecular field acting on T moment due to intrasublattice (T–T) interactions	S_R	spin of the 4f ion
		S_T	spin of the 3d ion
f_R	factor describing the intra-atomic 4f–5d interaction	T_C	Curie temperature
		T_k	compensation temperature
f_{RR}	factor describing the inter-atomic 4f–4f interaction	T_R	contribution of R–R interactions to ordering temperature
f_{RT}	factor describing the inter-atomic 4f–3d interaction	T_{RT}	contribution of R–T interactions to ordering temperature
E_F	Fermi level	T_T	contribution of T–T interactions to ordering temperature
g_R	Landé factor		
G_R	de Gennes factor for R atom	Z_{ij}	number of nearest neighbours
G_T	de Gennes factor for T atom	Z_{RR}	number of R nearest neighbours of an R atom
J_R	the total angular momentum for the 4f ions		

Z_{RT}	number of T nearest neighbours of an R atom	Γ_{4f-5d}	4f–5d exchange integral
		Γ_{3d-5d}	3d–5d exchange integral
Z_{TR}	number of R nearest neighbours of a T atom	θ	polar angle
		ρ_{5d}	5d-electron density
Z_{TT}	number of T nearest neighbours of a T atom	ϕ	azimuthal angle
		χ_T	paramagnetic susceptibility of T sublattice
Z_m	magnetic valence		
Γ	exchange integral		

1. Introduction

The investigation of the lanthanide–transition-metal (R–T) intermetallic compounds has been the subject of many fundamental as well as technological studies. The lanthanide atoms exhibit an incomplete filling of the electronic 4f shell, the corresponding wave functions being well localized in the interior of the atoms. As a result, there are both spin and orbital contributions to the magnetic moments and there is a large magnetic anisotropy. On the other hand, the localized character of the wave functions yields only a weak magnetic interaction between the lanthanide atoms and therefore the Curie temperatures (T_C) of the lanthanide elements are low. In contrast, in the transition metal atoms the electrons responsible for magnetism occupy the spatially extended 3d orbitals, resulting in the strong magnetic interactions and high Curie temperatures. The intermetallic compounds of lanthanide and transition metal atoms are therefore distinguished both by large magnetic anisotropies, high magnetization and high Curie temperatures. They form an important class of materials that find applications in permanent magnets, magnetostrictive devices and magneto-optical recording.

The intrinsic properties of the lanthanide–transition-metal intermetallics can be understood in terms of exchange interactions and magnetocrystalline anisotropies. The exchange interactions take place between all unpaired spins in the 4f–3d systems. In the lanthanide–transition-metal compounds it is generally accepted there are three types of interactions, namely, the R–R interactions between the magnetic moments within the R sublattice, the T–T interactions between magnetic moments of the T sublattice and the R–T intersublattice interactions. The T–T interactions are positive and lead to the ferromagnetic coupling between the 3d moments. This interaction primarily governs the temperature dependence of the 3d magnetization and the value of the Curie temperature of a R–T compound. The R–R interaction is generally the weakest one in the R–T compounds. In the considerations of most of the lanthanide compounds with iron and cobalt, it can be ignored. The contribution of the R–T interactions to T_C is also small (in comparison with that of T–T interactions). In most cases, however, it is responsible for the internal magnetic structure and determines the thermal stability of 4f moments and the temperature dependence of the R sublattice anisotropy. In the present class of magnetic materials the magnetocrystalline anisotropy originates from both lanthanide and transition metal magnetic sublattices. At low temperatures, the lanthanide

magnetocrystalline anisotropy is strong. It is transferred by the R–T exchange interactions to the T sublattice. At high temperatures the transition metal anisotropy becomes larger than the lanthanide anisotropy. The R–T exchange interaction is responsible for the transfer to the R-sublattice. Optimal properties, thus, can be expected only when there is a sufficiently strong magnetic coupling between two sublattices.

In the last decade considerable progress has been achieved in the understanding of lanthanide–transition-metal intermetallics. This progress was possible, on the one hand, thanks to the possibility of preparing better quality samples and of applying of more powerful experimental techniques, and, on the other hand, thanks to the availability of a large number of the R–T alloys and compounds (Buschow 1980, Franse and Radwanski 1993). The latter reason is especially important, since, owing to the wide range of the intermetallics and their different stoichiometries and variable lanthanide elements, the modifications of the magnetic properties of this class of materials can be investigated systematically and the general descriptions of the physical mechanism may be found. Such a description would be very desirable as it would allow to make *a priori* predictions of the variation of the physical properties. In the same line, attempts have been carried out for the R–T intersublattice exchange interactions.

The strength of the intersublattice exchange interactions can be determined experimentally by several different methods. However, most of the experimental data available at present are served from the analysis of the ordering temperatures (Belorizky et al. 1987, Duc 1991, Duc et al. 1992a, 1993a) and of the high-field magnetization measured on free powders (Verhoef et al. 1990a,b, de Boer and Buschow 1992). On the basis of these experimental results some systematics such as the variation of the strength of the R–T interactions with lanthanide and transition metal nature, and with the lanthanide concentration have been presented in the papers by Belorizky et al. (1987), Duc (1991, 1993a), Duc et al. (1992a, 1993a) and de Boer and Buschow (1992). In accordance with the model proposed by Campbell (1972) and reinterpreted by Brooks and Johansson (1993), Duc et al. (1992a, 1993a) have proposed that the origin of the variation of the 4f–3d exchange interaction may be found in the variable degree of the 3d–5d hybridization. An approximate correlation between the value for the R–T exchange coupling and the value of the magnetic moment of the 3d ion involved in the interaction has been found: the smaller the 3d-magnetic moment the larger the exchange parameter is. In a more recent paper, Liu et al. (1994a) have added to this picture an empirical relationship between the intersublattice coupling constants and the reciprocal molar volume normalized to one R atom. They stressed the strong volume dependence of the hybridization between the 3d and 5d states. In this chapter, we discuss the important concepts and physical models used to describe the coupling between 4f and 3d spins in the lanthanide–transition metal intermetallics. The studies of the exchange interactions in the various R_mT_n and $R_mT_nX_k$ (X=B, Ti, V, ...) compounds by different theoretical and experimental methods are summarized. This contributes to the support of the general picture of the R–T exchange interactions.

This chapter is organized as follows. Section 2 presents the band description for the invariable antiparallel-coupling between the lanthanide spins and the transition metal

spins. The mechanism of the 4f–3d intersublattice exchange interactions is presented in sect. 3. In sect. 4, the notation for describing the exchange interactions is introduced. Section 5 presents methods of evaluation of the exchange coupling parameters from the analysis of Curie temperatures and from the high-field free-powder (HFFP) method. A survey of the studies of the intersublattice interactions is given in sect. 6. Section 7 presents general considerations of the 4f–3d exchange interactions derived from analyzing the ordering temperatures. These results will also be compared with data obtained from the high-field free-powder method and discussed in terms of the various effects on the 3d–5d hybridization. Concluding remarks and extensions to further detailed investigations on this topic of exchange interactions are presented in sect. 8.

2. Lanthanide–transition-metal intermetallics: a simple model for the ferrimagnetic spin ordering

In the intermetallic compounds based on lanthanides and transition metals, it is found as a rule (Campbell 1972, Buschow 1980, Franse and Radwanski 1993) that the 4f–3d spin–spin coupling is antiferromagnetic. Taking into account the coupling between the spin and orbital moments of the 4f electrons can explain the parallel and antiparallel alignments of 3d(Fe,Co,Ni) and 4f moments in the light and heavy lanthanide compounds, respectively. The exchange coupling between the R- and T-electron spins is indirect. It is thought that there is an intra-atomic, ferromagnetic exchange interaction between 4f and 5d spins of lanthanide ions and an interatomic interaction between itinerant 5d and 3d spins. The latter interaction is, in general, found to be antiparallel, which is similar to the interactions between spins of the electrons in a less than half-filled d band (R–5d electrons) and the electrons in a more than half-filled d band (T–3d electrons). However, its nature is undefined. At present, this universal picture can be understood by a simple approach of the hybridization between 5d and 3d states.

2.1. *Characteristics of band structure and 5d–3d hybridization*

In the lanthanide intermetallics, neglecting the presence of the 4f electrons, one still has to consider the R-5d, 6s and 6p (or Y-4p, 5s and 5p) valence states and the T-3d, 4s and 4p states for the electronic structure. However, since in the solid the s and p electrons form broad and rather featureless bands, these can be neglected and we can focus our attention on the 5d and 3d states. The lanthanide intermetallics, thus, were considered to be formed by the association of the relatively narrow 3d band with a wider 5d band with higher energy. The electronegativity difference between the constituents gives rise to a transfer of 5d electrons towards the unfilled 3d band. Since the screening of the nuclear potentials by the electrons is modified, the two band draw together, leading to 3d–5d hybridized states at the top of the 3d band and at the bottom of the 5d one. Such a feature of the band structure is schematically illustrated in fig. 1. The Fermi level E_F of the compounds often lies in the hybridized region where the density of state (DOS)

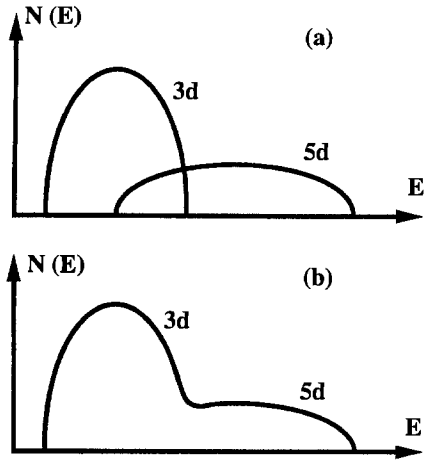

Fig. 1. Schema of the d-band structure for (a) pure metals and (b) R–Co intermetallics.

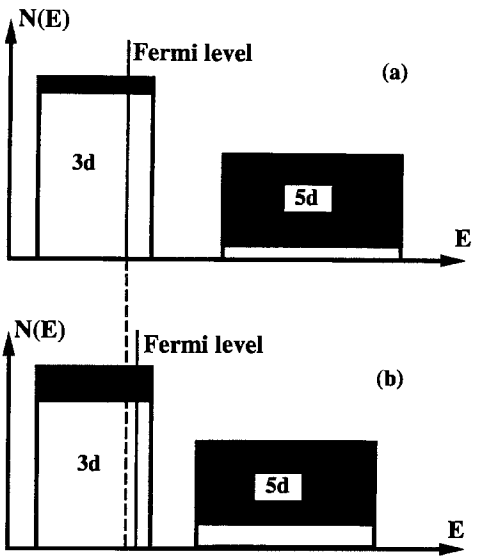

Fig. 2. Schematic DOS curves illustrating the strength of the 3d–5d hybridization and the shift of the Fermi level. The black and white areas indicate the amount of 5d and 3d states, respectively: (a) weak 3d–5d hybridization and (b) strong 3d–5d hybridization.

strongly varies, thus there are so many interesting magnetic phenomena in this class of compounds (Gignoux and Schmitt 1991).

It is a common usage to discuss the electronic structure in terms of the filling of the 3d bands in connection with the compound composed of the transition metals with less than and more than half-filled d bands. Actually, it is hard to change the R and T d-occupation numbers between the pure elements and compounds. The charge transfer leads to the modification of the energy separation between the 3d and 5d bands and changes the 3d–5d hybridization. By this way, the d-occupation numbers differ little from those of the pure metals. This trend of DOS can also be understood by the simple model of the rectangular local DOS's of 3d and 5d states. For simplicity, hereafter, we will use this simple model to describe the energy bands.

In fig. 2, two rectangles denote the schematical local DOS's of the 3d states of the transition metals and 5d states of lanthanide elements. When the energy separation between the 3d and 5d bands is large, the 3d–5d hybridization is weak as shown in fig. 2a. The difference between the atomic potentials is determined, so that the occupied states below E_F are equal to the number of the 3d and 5d electrons (Brooks and Johansson 1993, Yamada and Aoki 1993). When the number of 5d electrons increases, E_F must be brought up to a higher energy. However, if so, the number of 3d electrons also increases. To keep the number of the 3d electrons constant, the 3d–5d energy separation is reduced, so that the mixing between them becomes strong as shown in fig. 2b. Therefore, the local DOS's of the 3d and 5d states becomes low and high, respectively, in the lower energy

subband. The position of E_F shifts a little towards the higher energy. Then the number of 5d electrons increases without changing the number of 3d electrons. Such a trend has also been observed in the calculated DOS's for the RT_2 compounds by Klein et al. (1983) and Aoki and Yamada (1989).

2.2. *Ferrimagnetic spin ordering in the magnetized state of the d electrons*

2.2.1. *Effects of 3d-band splitting*

In the magnetic R–T compounds an antiparallel structure between the magnetic moment on R and T atoms exists even when R is non-magnetic Y, Lu, Sc, ... It is due to the appearance of an induced 5d-moment. In YFe_2, for instance, the observed localized moments on Y and Fe atoms are -0.67 and $1.77\mu_B$/at., respectively (Ritter 1989). YFe_2, thus, is a ferrimagnet rather than a ferromagnet. A magnetic moment of this size has also been deduced by Dumelow et al. (1986) from the pressure dependence of NMR spectra on ^{89}Y nuclei. The origin of this ferrimagnetic state is the difference between the 3d–5d(4d) mixing in the majority and minority spin bands. The schematical local DOS's of the 3d and 4d states with up (majority) and down (minority) spins are shown in fig. 3. By the exchange interactions among the 3d electrons, the DOS's of the 3d states in the up and down spin bands split and shift towards the lower and higher energy sides, respectively (see fig. 3) and a moment is developed at the T-sites. Then, the 3d–4d hybridization is reduced for the spin-up states. This lowers the occupation of 4d spin-up states. The opposite effect occurs for the spin-down states. The value of the number of the electrons with spin up and spin down, $n_{4d\uparrow}$, $n_{4d\downarrow}$, $n_{3d\downarrow}$ and $n_{3d\downarrow}$ are proportional to the areas of the respective local DOS up to E_F. As $n_{4d\downarrow}$ becomes larger than $n_{4d\uparrow}$, a negative moment m_{4d} $(=n_{4d\uparrow}-n_{4d\downarrow})$ is induced on the Y atoms. This mechanism of the appearance of the negative 4d magnetic moments has been discussed in details by Yamada and Shimizu (1985) and Brooks and Johansson (1993). From calculations, Brooks et al. (1989) obtained a value of $0.41\mu_B$ for the moment localized at a Lu site in $LuFe_2$.

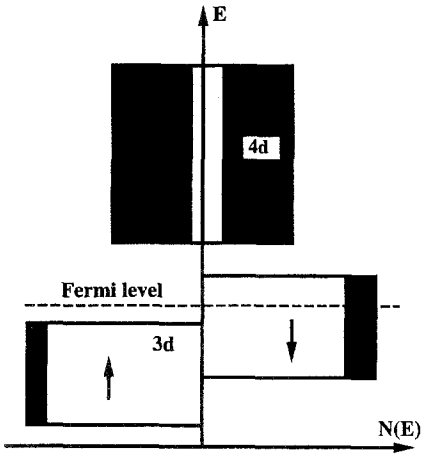

Fig. 3. Schematic local DOS curves illustrating the mechanism of the ferrimagnetic spin ordering. The black and white areas indicate the amounts of 4d and 3d states, respectively.

For the Y–Fe systems, a negative moment on Y sites that decreases with increasing Y concentration from $0.2\mu_B$ in Y_2Fe_{17} to $0.44\mu_B$ in YFe_2 was also indicated by Coehoorn (1989).

2.2.2. *Effects of external magnetic fields*

The effects of the external fields are very interesting for the R–T compounds where both R and T atoms are paramagnetic as in RCo_2 (R = Y, Lu, Sc, ...). In this case, as reported by Yamada and Shimizu (1985), the local-induced moments on Y and Co atoms in YCo_2 are also antiparallel. This fact can also be explained in the same way by hybridization between d states of the Y and Co atoms.

The schematic curves of the local DOS's in the non-magnetic state is illustrated in fig. 4a. An application of the external magnetic field to the system causes the DOS's with up and down spin to shift towards lower and higher energy sides, respectively. However, as the molecular field (intra-atomic exchange integral U_{Co}) on a Co atom is larger than that (U_Y) on an Y atom, the exchange splitting of the local DOS of Co with up and down spins is much larger than that of Y atom. Then the energy difference $\Delta\varepsilon$ between the effective atomic potentials on Co and Y atoms for up-spin becomes larger than that for the down-spin electrons. As mentioned in sect. 2.1, the strength of the hybridization will be weakened when $\Delta\varepsilon$ is large. Therefore, as shown in fig. 4b, the d states in the spin-up band mix with each other less than those in the down-spin band. As consequence, a negative magnetic moment m_Y is also induced on Y sites. Then, the molecular field created by m_Y and experienced on the Y-sublattice is in the opposite direction with respect to that on the Co-sublattice. The 4d-bands with up and down-spin shift further in opposite direction (see fig. 4c). So that the absolute value of M_{4d} becomes relatively large.

Recently, Duc et al. (1992c) have proposed a model for itinerant electron metamagnetism in which the metamagnetic transition results simply from the interplay between the magnetic and elastic energies in the simple (elliptic or rectangular) bands. However, it had already been shown that the metamagnetic behaviour is related to a peculiarity of the DOS at the Fermi level (Shimizu 1964, 1965). In the tight-binding approximation, the electronic structure of d electrons was calculated by Yamada and Shimizu (1985)

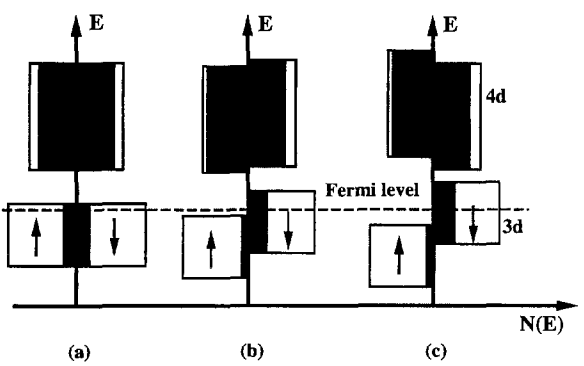

Fig. 4. Schematic curves for DOS in (a) the non-magnetic state, (b) the magnetized state by the applied field and (c) the ferromagnetic state. The black and white areas indicate the amounts of 4d and 3d states, respectively.

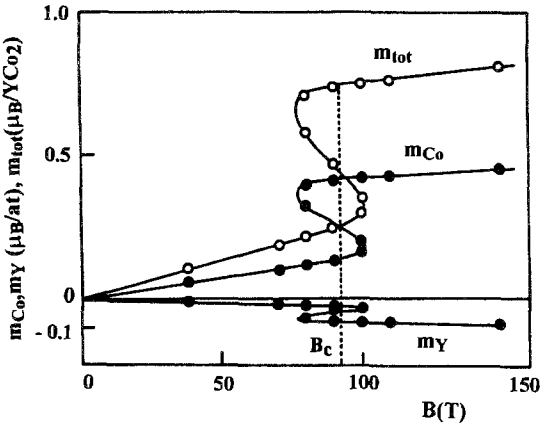

Fig. 5. The calculated partial m_{Co}, m_Y moments and total moments, m_{tot}, as a function of the applied magnetic field for YCo_2. After Yamada and Shimizu (1985).

for YCo_2. The magnetic-field dependence of the induced moment obtained at 0 K is presented in fig. 5. It shows a metamagnetic transition from the paramagnetic state to ferromagnetic state at 90 T. As can be seen from this figure, m_Y is still negative even at 150 T and a value of about $-0.1\mu_B$ is reached. In the polarized-neutron diffraction experiments, Gignoux et al. (1977c) have measured the magnetization density induced in $LuCo_2$ in an applied field of 5.72 T. They found the induced moments localized on the Co sites, and an additional diffuse density of the negative magnetic moments. But, these negative induced moments are not localized on Lu atoms. In this experiment, as above mentioned, the applied magnetic field is much lower than the critical value for the metamagnetic transition. Then, the localized Lu moment may be too small to be detected by the polarized neutrons.

2.2.3. *Effects of lanthanide (internal) molecular magnetic fields*

We continue to consider the inducement of the d magnetic moments in the enhanced Pauli 3d-subsystems by the molecular field exerted from localized 4f moments. In this case, unlike the external field, the molecular field acting on the 3d electrons is antiparallel to that acting on the 5d electrons. However, as will be shown below, once more, a rather large local moment, aligned oppositely to the R moment, can be induced on T-sites via the 5d–3d hybridization. Thus, when the T-moments are developed, the rule of the ferrimagnetic arrangement between T- and R-spins is still valid.

For most lanthanide compounds, the 4f electrons retain their atomic character in the solid. Therefore, except for some cerium compounds, the energy location of the 4f states relative to 5d and 3d state energies is not important. The localized 4f-electrons affect the magnetic character of the valence electrons through the exchange potential. This coupling, however, can take place essentially within the lanthanide atom and mainly with 5d electrons because the 4f-wave function is limited and the density and overlap between 4f and 5d states are larger than those between 4f and 6p, 6s states. The 5d electrons on the R atoms are polarized by the exchange field from the localized 4f moments.

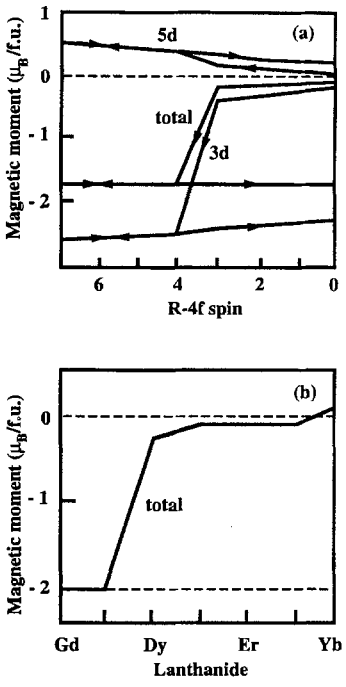

Fig. 6. (a) The calculated partial Co 3d, Gd 5d and total conduction electron moments of $GdCo_2$ as a function of 4f-spin moment. The arrows denote the direction in which the 4f spin is changed. (b) The calculated total conduction electron moments of $GdCo_2$–$YbCo_2$. After Nordström et al. (1992).

This polarization of 5d electrons would be in the same direction as that of the localized 4f moments. This is in accordance with the experimental findings that the 5d electrons do contribute a moment of $0.6\mu_B$ to the total value of $7.6\mu_B$/at. measured for Gd metal (Roeland et al. 1975) or of $0.1\mu_B$ in $GdNi_2$ (Farrell and Wallace 1966) and $GdAl_2$ (Swift and Wallace 1968). When the exchange field created by (local) 4f moments is applied to the 5d electrons, the up-spin 5d-band shifts towards the lower energy side and the down-spin 5d-band is to the higher energy side. Then, because of the difference in the relative position of the sub-bands the mixing between 5d and 3d states with up spin becomes stronger than that between the state with down spin. In the case where the Fermi level lies near the top of the 3d band, the number of 3d electrons with up spin will be smaller than that with down spin, resulting in a negative T-moment. Furthermore, the 3d subbands with the up and down spin are shifted in the opposite direction to those of 5d electrons by the molecular field of the developed T-moments. The negative 3d moment is thus stabilized. This is the mechanism of the appearance of the ferrimagnetic ordering induced by the molecular field which was observed experimentally in the magnetic lanthanide–Co_2 compounds (Yamada and Shimizu 1985). Self-consistent LMTO calculations have been made for the heavy lanthanide series of $GdCo_2$–$YbCo_2$ in which the 4f moment on the Gd was changed from zero to seven and then back again to zero by Nordström et al. (1992). The resulting computed d-electron moment is shown in fig. 6a. Increasing the 4f moment on the Gd from zero to three (corresponding to Lu–Er) the moment induced on the Co is

small but at R = Ho the d-electron moment jumps to $1.75\mu_B$/f.u. With a further increase of the 4f moment the total d-electron moment is saturated, but the 3d and 5d contributions, which are antiparallel, both increase. The results of the calculations for the real systems, i.e. with real lattice parameters, however, show a transition at R = Tb, see fig. 6b. This suggests that there is an influence of the volume effect on the 3d–5d hybridization and also on the metamagnetic behaviour in RCo_2 compounds (Duc et al. 1993b).

2.2.4. *The different effects of external and internal magnetic fields*

Gignoux et al. (1975, 1977a,b), Steiner et al. (1978) and Duc et al. (1988a, 1992b) have measured the induced moments of Co in RCo_2 and $R_xY_{1-x}Co_2$ compounds. By changing the temperature, magnetic field and concentration x, they have estimated that M_{Co} increases rapidly at an effective field of 80 to 120 T. The observed curves of M_{Co} against the external (and/or internal) fields are similar to the result observed for YCo_2 in an external high field (Goto et al. 1991), see fig. 7. However, the magnitude of M_{Co} (of about $0.55\mu_B$/Co-at. at $B = 100$ T) in YCo_2 is smaller than that in the magnetic lanthanide compounds ($0.8–1.0\mu_B$/Co-at). This difference can be explained by the different roles of the external and internal fields on the 3d–5d hybridization. In the calculations reported by Yamada and Shimizu (1985) for YCo_2 the magnetic field of 150 T applied in the same direction on Y and Co atoms yields the values of $0.454\mu_B$/Co-at. and $0.1\mu_B$/Y-at. for Co and Y atoms, respectively (see also fig. 5, sect. 2.2.3.). In order to get the values of the magnetic moments in RCo_2, the magnetic field B_Y at the Y-site was applied in the opposite direction to B_{Co} at the Co-site. Applying to $HoCo_2$, the exchange field acting on 5d electrons due to the local exchange interaction is evaluated as $B_{5d} = \sim 2400$ T (Yamada and Shimizu 1985). On the other hand, the exchange field on Co from the localized 4f moments of Ho is $B_{Co} = 156$ T (Gignoux and Givord 1979). They obtained the values of M_{Co} and M_Y equal to 0.61 and $-0.236\mu_B$/at., respectively. Subtracting the contribution of the orbital part (of $0.14\mu_B$/at.), the spin part of the observed M_{Co} becomes $0.66\mu_B$. The agreement between the calculated and observed values of M_{Co} is satisfactory. Similarly, the experimental observations of the enhancement of the Co-susceptibilities (Gignoux and Givord 1979, Duc et al. 1993b) and the magnetoresistance (Duc 1994) in the magnetic lanthanide–Co_2 compounds (in comparison to that in YCo_2), which had suggested earlier a slight variation in the d-band structure, now can be discussed in terms of the different degree of the 3d–5d mixing caused by the different effects of the external and internal magnetic fields.

2.2.5. *Effects of the combination of the local 4f-exchange and the 3d-band splitting*

The roles of the 3d-band splitting and the 4f-exchange field on the inducement of the negative 5d(4d)-moments were considered separately in sect. 2.2.1, 2.2.3 for the compounds, in which either only T- or only R-magnetic moments are present. In most of the R–T intermetallic compounds, the combination of both effects must be taken into account simultaneously. However, in the compounds where the d–d spin exchange interaction within the T sublattice is large, the T moment is developed independently.

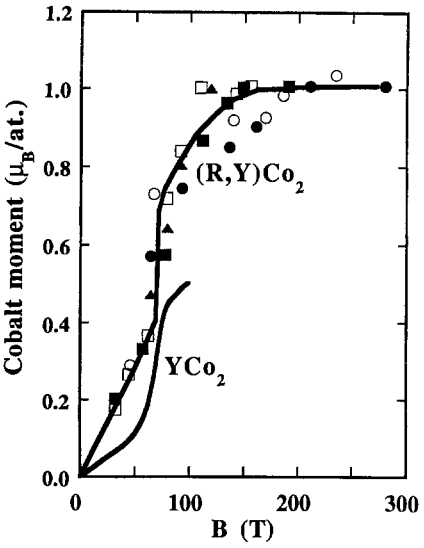

Fig. 7. Variation of Co moments as a function of molecular field (after Duc et al. 1992b) for a number of $(R_xY_{1-x})Co_2$ compounds, with R = Gd (solid circles), Tb (open circles), Dy (solid squares), Ho (open squares) and Er (triangles), and as a function of the applied field for YCo_2 (after Goto et al. 1991).

In this case, the 3d–5d hybridization produces significant negative 5d moments. The 4f moments then interact with the surrounding 5d electron spin cloud by means of the local exchange interactions, and they align parallel with the 5d-moments and, in their turn, enhance the total 5d down-spin moment. The 5d up-spin band will further be pushed away from the major 3d up-spin band and the corresponding hybridization will be decreased. This means that the local 3d up-spin moment will also increase in size. However, since we started from a saturated magnetic state, the total itinerant electron moment is fixed and only its distribution between the R and T-atoms changes. In this situation, the presence of the 4f-exchange field, thus, induces a redistribution of the spin moments between the lanthanide and transition metal sites, while the total magnetic moment remains constant (Brooks et al. 1991a–c).

3. Mechanism of the intersublattice exchange coupling in lanthanide–transition metal compounds

For the indirect exchange interactions, the RKKY interaction (Ruderman and Kittel 1954, de Gennes 1962) is naturally always a possibility. However, this theory, which was proposed for the simple metals, does not lend itself well to the treatment of the indirect exchange in the compounds. In 1972, Campbell distinguished the local 5d character of the conduction electron moment at the R-sites and postulated a 4f–5d–3d interaction path, based on the idea that due to the localized character of 4f spins their local exchange interaction with the itinerant spins can only be mediated through the local exchange interaction (mainly with exchange integral Γ_{4f-5d}) at the R-atom, with a subsequent 3d–5d interaction (Γ_{3d-5d}) of undefined nature (but similar to d–d interaction in transition

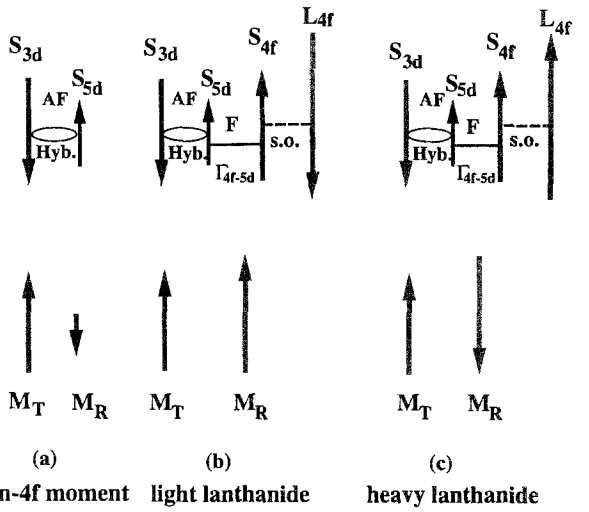

Fig. 8. Schematic description of the compositions of, and interactions between, magnetic moments in R–T intermetallics. F and AF indicate the ferromagnetic and antiferromagnetic spin couplings, respectively. The 3d–5d hybridization (hyb.), 4f–5d local exchange ($\Gamma_{4f\text{-}5d}$) and spin–orbital interactions (s.o.) are shown.

metals). Following strictly this empirical model, Li et al. (1991, 1992) have worked out the molecular field coefficient n_{RT} for the intersublattice exchange coupling which contains basically the product $\Gamma_{4f\text{-}5d} \times \Gamma_{5d\text{-}3d}$. A dramatic reinterpretation of Campbell's model, as presented in sect. 2, was given by Brooks et al. (1991a–c) and Brooks and Johansson (1993) and Yamada and Shimizu (1985). The effective exchange interactions between 4f and 3d spins involve the 4f–5d exchange ($\Gamma_{4f\text{-}5d}$), the 3d exchange energy (proportional to $\Gamma_{3d\text{-}3d}$) and the hybridization between the 3d and 5d states. In the case that $\Gamma_{3d\text{-}3d}$ is large enough to develop a moment at the T-sites, it is the 3d–5d hybridization that, firstly, produces a negative 5d moment and, secondly, is responsible for the coupling between the 5d and 3d directions and therefore the 4f and 3d directions (see sect. 2.2.1, 2.2.3). When $\Gamma_{3d\text{-}3d}$ is small, there is no 3d-band splitting. In this case, the 5d moment is induced by the exchange field from the localized 4f-moments and, then, the 3d–5d hybridization produces an enhanced 3d moment aligned antiparallel to the 5d moment (see sect. 2.2.3). Thus, the 4f–3d coupling is always mediated by the 3d–5d hybridization, independent of the way in which the 5d electrons are polarized. Following Brooks et al. (1991a–c), the importance of the 3d–5d hybridization and the true mechanism of the R–T intersublattice exchange coupling is schematized in fig. 8. It shows clearly the way how the partial moments add to the total moments, and moreover, the interactions responsible for their size and directions. For all of the three possible cases – zero 4f moment, heavy and light lanthanides – the ferrimagnetic ordering between the spins of 3d and 5d(4f) electrons is always created via the 3d–5d hybridization. This leads to a parallel moment alignment for light lanthanides and to an antiparallel moment alignment for heavy lanthanide compounds.

It follows from the calculations of Brooks et al. (1991a–c) that the exchange interaction energy between the 4f and 5d states is the quadratic form

$$E_{4f-5d} = -2\Gamma_{4f-5d} S_{4f} S_{5d}, \tag{1}$$

where the exchange integral Γ_{4f-5d} is given as

$$\Gamma_{4f-5d} = \int g\,[n(n)]\,\Psi^2_{4f}(r)\,\Psi^2_{5d}(r)\,\mathrm{d}r. \tag{2}$$

Here, $g[n]$ is a well-known (after Janak 1977, Brooks and Johansson 1983) function of the density. Γ_{4f-5d} thus depends upon the 4f–5d overlap densities and is always positive. As the 4f shell contracts, the region of overlap between the outer part of the 4f density and the inner part of the 5d density decreases. Then, a decrease of the 4f–5d exchange integrals across each series is expected. This variation of Γ_{4f-5d} can be given as (Brooks et al. 1991a–c)

$$\Gamma_{4f-5d} = \{94 - 3.4\,(x-1)\}\ \text{meV}, \tag{3}$$

where $x = 1$ for Gd, 2 for Tb, etc.

Li et al. (1991) have extended the calculation and considered also the integrals with p and s conduction electrons. They found that the values of these three integrals decrease monotonically across the lanthanide series, but the strength of Γ_{4f-6s} and Γ_{4f-6p} is much smaller than that of Γ_{4f-5d}.

In a perturbative way, the effective R–T interaction parameter A_{RT} (in the spin Hamiltonian $H_{ex} = -2\sum A_{RT} S_R S_T$, see next section) can be calculated from the energy difference ΔE between the ground sate and the reversed-spin state (Brooks et al. 1991a–c). It turns out for RFe_2 that

$$A_{RT} = \tfrac{1}{12}\,(g-1)\,\Gamma_{4f-5d}\,\frac{S_{5d}}{S_T}. \tag{4}$$

Practically, in a redistribution of the spin moments between R and T sites both S_{5d} and S_T are variable (by amounts of ΔS_{5d} and ΔS_T, respectively). However, as already mentioned in sect. 2.2.5, ΔS_{5d} and ΔS_T are almost equal. Then, because S_{5d} is much smaller than S_T, the change in the ratio S_{5d}/S_T is mainly governed by the variation of S_{5d}. The strength of the exchange-coupling parameter between the lanthanide localized moment and the transition metal itinerant moments, thus, depends above all on the properties of the 5d states induced by the hybridization with the 3d states of the neighbouring transition metal atoms and the local exchange integral Γ_{4f-5d}, but not on the product of $\Gamma_{4f-5d} \times \Gamma_{5d-3d}$ as proposed by Li et al. (1991, 1992). In this sense, the only effect of the 3d states on the R–T coupling is that they hybridize with the 5d states and thus determine the properties of the 5d states and the strength of Γ_{4f-5d}.

The band-structure calculations by Liebs et al. (1993) and Fähnle et al. (1993) pointed out that the 4f–3d exchange interactions can not be treated in a perturbative way as done by Brooks et al. (1991a–c) and Brooks and Johansson (1993) because upon the reversal of the 4f moment, the valence-electron contributions to the total moment of the R sites were found to decrease by a factor of 2–3. They stressed the importance of performing self-consistent calculations, but fully agreed that the value of the intersublattice exchange-coupling parameter A_{RT} is essentially governed by Γ_{4f-5d} and that there is no major contribution of an effective Γ_{3d-5d}.

4. Mean-field description of the exchange interactions

Although there may not be a consensus on the exact mechanism of the R–T exchange interactions, it is common usage to express this interaction as an effective exchange of the Heisenberg type:

$$H_{ex} = -2 \sum_{i,j} A_{RT}(i,j)\, S_R(i)\, S_T(j). \tag{5}$$

Here, $A_{RT}(i,j)$ is the exchange coupling between the (neighbouring) spins $S_R(i)$ of a R atom at site i and $S_T(j)$ of a T atom at site j.

Within a mean-field approach the R–T exchange interaction is described by molecular fields that are acting on the magnetic moments. In a two-sublattice model, the suitable effective molecular fields acting on the R and T moments can be written as

$$B^R_{mol} = B^R_{mol,RT} + B^R_{mol,RR} = n_{RT} M_T + n_{RR} M_R, \tag{6a}$$

$$B^T_{mol} = B^T_{mol,TT} + B^T_{mol,TR} = n_{TT} M_T + n_{TR} M_R, \tag{6b}$$

where M_T and M_R are the magnetic moment per formula unit (f.u.) of the T and R sublattices, n_{RT} is the intersublattice molecular-field coefficient, and n_{RR} and n_{TT} are the intra-sublattice molecular-field coefficients. Although the 4f moments are often larger than the moments of the 3d transition metals, the internal field acting on the lanthanide moment and originating from the T sublattice dominates that originating from the R sublattice. This is due to the much smaller value of the intra-sublattice molecular-field coefficient n_{RR} compared to that of the inter-sublattice molecular-field coefficient n_{RT}. In the analysis of most of the lanthanide compounds with iron and cobalt the contribution to the molecular field from the R–R interactions is ignored and the molecular field experienced by an R-ion is approximated by

$$B^R_{mol} = B^R_{mol,RT} = n_{RT} M_T. \tag{7}$$

The exchange energy per R-ion is

$$E^R_{exch} = -m_R B^R_{mol} = -n_{RT} m_R M_T, \tag{8}$$

where m_R is the magnetic moment of a R-ion.

In the Heisenberg representation (eq. 5), the exchange energy of an R-ion at site i can be written as

$$E^{\mathrm{R}}_{\mathrm{exch}}(i) = -2\sum_{j} A_{\mathrm{RT}}(i,j)\, S_{\mathrm{R}}(i)\, S_{\mathrm{T}}(j), \tag{9.a}$$

where the summation runs over all sites j of T-atoms.

Under the assumption, or approximation, that the moments on all T and R sites are equal, say $\langle S_{\mathrm{R}}(i)\rangle = S_{\mathrm{R}}$ for all sites i and $\langle S_{\mathrm{T}}(j)\rangle = S_{\mathrm{T}}$ for all sites j, the exchange energy is written as

$$E^{\mathrm{R}}_{\mathrm{exch}}(i) = -2S_{\mathrm{R}}S_{\mathrm{T}}\sum_{j} A_{\mathrm{RT}}(i,j). \tag{9.b}$$

In case the R sites are equivalent, the sum does not depend on the site i, and neither does $E^{\mathrm{R}}_{\mathrm{exch}}(i) \equiv E^{\mathrm{R}}_{\mathrm{exch}}$. Since $A_{\mathrm{RT}}(i,j)$ is assumed to adopt appreciable values only for RT pairs consisting of a T atom and one of its nearest R neighbours, one writes

$$\sum_{j} A_{\mathrm{RT}}(i,j) = Z_{\mathrm{RT}}A_{\mathrm{RT}}. \tag{10}$$

In this way, the characteristic exchange interaction parameter A_{RT} is defined together with the so-called "number of nearest neighbours" Z_{RT}. In case the R sites are not equivalent, analogous parameters are defined by the following expression for the average value of the exchange energy:

$$E^{\mathrm{R}}_{\mathrm{exch}} = -2Z_{\mathrm{RT}}A_{\mathrm{RT}}S_{\mathrm{R}}S_{\mathrm{T}}. \tag{11}$$

Here, the definition of $Z_{\mathrm{RT}}A_{\mathrm{RT}}$ given above is generalized to

$$Z_{\mathrm{RT}}A_{\mathrm{RT}} = \frac{1}{N_{\mathrm{R}}}\sum_{i,j} A_{\mathrm{RT}}(i,j). \tag{12}$$

Instead of applying the "nearest neighbours" criterion mentioned above, Z_{RT} is now defined as the average number of T atoms within a distance d from an R atom. Obviously, the definition of Z_{RT} defines A_{RT} simultaneously. In order to be explicit, the mathematical presentation involving a precise definition of Z_{RT} is given as

$$Z_{\mathrm{RT}} = \frac{1}{N_{\mathrm{R}}}\sum_{i,j} f_{ij}, \tag{13}$$

with $f_{ij}=1$ for $|r_i - r_j| < d$ (or any other criterion), and $f_{ij}=0$ otherwise. From eqs. (11) and (12), by interchanging the role of the T atoms and the R atoms, the

corresponding expressions involving Z_{TR} and A_{TR} can be obtained straightforwardly. For any criterion for the RT "bonds" we find the following rule to hold (Brommer 1991):

$$N_T Z_{TR} = N_R Z_{RT}. \tag{14}$$

Subsequently, we obtain $A_{RT} = A_{TR}$, as expected.

Introducing

$$S_R = (g_R - 1) J_R \tag{15}$$

one arrives at the magnetic moment of a R atom:

$$m_R = -g_R \mu_B J_R = -\frac{\mu_B S_R g_R}{g_R - 1}. \tag{16}$$

On the other hand, the magnetic M_T per f.u. of T-sublattice can be expressed as

$$M_T = N_T m_T = -g_T \mu_B N_T S_T, \tag{17}$$

with N_T the number of T atoms per f.u.

Substituting the expression derived for M_T and m_R in eq. (8), this equation can be written in terms of S_R and S_T:

$$E^R_{exch} = -\frac{g_T \mu_B^2 N_T n_{RT} S_R S_T g_R}{g_R - 1}. \tag{18}$$

Combining this relation with eqs. (9)–(10) gives, with $g_T = 2$,

$$Z_{RT} A_{RT} = -\frac{\mu_B^2 N_T n_{RT} g_R}{g_R - 1}. \tag{19}$$

Then, we can write the relation between the macroscopic intersublattice molecular-field coefficient n_{RT} and the microscopic exchange parameter A_{RT} as

$$n_{RT} = Z_{RT} A_{RT} \frac{g_R - 1}{g_R \mu_B^2 N_T}. \tag{20}$$

The corresponding expression involving n_{TR} and A_{RT} is

$$n_{TR} = Z_{TR} A_{RT} \frac{g_R - 1}{g_R \mu_B^2 N_R}. \tag{21}$$

Due to the relations $N_T Z_{TR} = N_R Z_{RT}$ and $A_{RT} = A_{TR}$, we see that the coefficients in eq. (20) (i.e. n_{RT}) and eq. (21) (i.e. n_{TR}) are equal.

Similarly, the relation between the macroscopic intra-sublattice molecular-field coefficients n_{RR}, n_{TT} and the microscopic exchange parameter A_{RR} and A_{TT} can be written as

$$n_{RR} = 2Z_{RR}A_{RR}\frac{(g_R - 1)^2}{g_R^2\mu_B^2 N_R}, \qquad n_{TT} = Z_{TT}A_{TT}\frac{1}{2\mu_B^2 N_T}, \tag{22,23}$$

where Z_{RR} is the number of R nearest neighbours of an R ion, Z_{TT} is the number of T nearest neighbours of a T ion, and other symbols have their usual meaning. In order to compare the strength of the exchange interactions within a series of isostructural compounds and between the different series of compounds, it is more appropriate to use the microscopic exchange-coupling parameters A_{ij} (i,j = R, T) rather than the macroscopic molecular field coefficients n_{ij}. Thus, A_{ij} usually appears in a more elementary discussion of the exchange interaction in lanthanide–transition metal compounds.

The exchange interaction between lanthanide and transition metal atoms can also be described as an interaction between R spins and an "exchange field" B_{exch}^R acting on the R spin:

$$2\sum_j A_{RT}S_R S_T = -2\mu_B S_R B_{exch}^R = -2(g_R - 1)\,\mu_B J_R B_{exch}^R, \tag{24}$$

which gives

$$B_{exch}^R = -\frac{Z_{RT}A_{RT}S_T}{\mu_B}. \tag{25}$$

Similarly, the "exchange field" B_{exch}^T acting on the T-spin is

$$B_{exch}^T = -\frac{Z_{TR}A_{RT}S_R}{\mu_B}. \tag{26}$$

Finally, it is interesting to derive from the comparison between eqs. (8) and (24) that

$$B_{exch}^R = B_{mol}^R\frac{g_R}{2(g_R - 1)}, \qquad B_{exch}^T = B_{mol}^T. \tag{27,28}$$

For the iron- and cobalt-rich R–T compounds, the 4f and 3d sublattice magnetic moments are strongly coupled. Values for the molecular field are typically of order of 100 T (Franse and Radwanski 1993, Liu et al. 1994a) and large applied magnetic fields are required in order to induce changes in the magnetic moment configuration of the two sublattices.

5. Evaluation of the exchange-coupling parameter

In the simplest approach, in which the two-sublattice model is used, the magnetic phenomena are still described by many parameters representing the anisotropy of

lanthanide and 3d sublattices, the sublattice moments of the two sublattices and the molecular-field coefficients n_{RR}, n_{RT} and n_{TT}. The evaluation of the exchange-coupling parameter in the R–T compounds is, thus, a complex problem. These complications force us not to restrict the estimation to one single analysis and one single compound, but to consider the trends in the evaluated parameters along the lanthanide series, for different transition metals and from various methods. As can be seen in the next section, the information of exchange interactions has been collected from the analysis of neutron-scattering data, Mössbauer and NMR experiments, thermomagnetic studies and electronic band-structure calculations. The details of these experimental and theoretical techniques have been reported by Franse and Radwanski (1993) and Brooks and Johansson (1993). Here, we present only two methods of evaluating the exchange-coupling parameter, which, in first approximation, is not disturbed by other terms of anisotropy.

5.1. *Analysis of ordering temperatures*

We consider a R–T compound. Let M_R be the magnetic 4f-moment (per mol f.u.) of the R atoms and M_T that of the (itinerant) d electrons (including all of the 3d and 5d electrons). For this system of exchange-coupled magnetic moments, placed in an external magnetic field B_o, the linearized equilibrium conditions can be written in the molecular field approximation as

$$a_T M_T M_T + n_{TR} M_R = B_o, \qquad -n_{TR} M_T + (b_R - n_{RR})\, M_R = B_o. \tag{29,30}$$

Here, a_T is the inverse susceptibility of the d-electrons, b_R is approximated by T/C_R (Duc et al. 1988a, 1992b, Brommer 1989), where C_R is the Curie constant for the R atoms.

The discriminant (determinant) D is given by

$$D = a_T (b_R - n_{RR}) - n_{RT}^2. \tag{31}$$

T_C can be determined after substituting $b_R = T/C_R$ and $1/a_T = \chi_T$ and taking $D = 0$ (Brommer 1989, Duc et al. 1993b):

$$T_C = C_R (n_{RR} + n_{RT} n_{TR} \chi_T(T_C)). \tag{32}$$

$\chi_T(T_C)$ is the susceptibility at T_C, which can be deduced from the temperature dependence of the magnetic susceptibility of the corresponding non-magnetic lanthanide compounds.

Introducing the contribution T_R to the critical temperature from the interactions between the R moments, we find

$$T_R = C_R n_{RR} = \frac{2 z_{RR} A_{RR} G_R}{3 k_B}, \tag{33}$$

where G_R is the de Gennes factor $(g_R - 1)^2 J(J+1)$ for the lanthanide atom.

The combination of eq. (32) and the relations between n_{ij} and A_{ij} (see eqs. 22–23) leads to

$$A_{RT}^2 = \frac{3k_B(T_C - T_R)}{Z_{RT}Z_{TR}G_R\chi_T(T_C)}. \tag{34}$$

By means of eq. (34), the value of the microscopic R–T exchange-coupling parameters can be deduced from the experimental values of T_C, T_R and $\chi_T(T_C)$. For all series of compounds, T_R which is representing the R–R interactions, was determined following eq. (33) under the assumption that A_{RR} has the same value as in the RNi_2 compounds (Duc et al. 1993a). There is a variety of magnetic behaviour in the paramagnetic region for the non-magnetic lanthanide compounds. YCo_2 and $LuCo_2$ are strongly enhanced Pauli paramagnets. Their susceptibilities initially increase with increasing temperature and reach a maximum at about 250 K. The evaluation of A_{RT} for the RCo_2 compounds was performed with the actual susceptibility data measured on YCo_2 or $LuCo_2$ (Belorizky et al. 1987, Duc 1991, Duc et al. 1988b, 1992a). In most Y_mT_n or Lu_mT_n compounds, in which only one type of T-magnetic moment is present, the temperature dependence of the susceptibility follows a simple Curie–Weiss law:

$$\chi_T = \frac{C_T}{T - T_T}, \tag{35}$$

where C_T is the Curie constant for the T atoms. The contribution of T atoms to the ordering temperature of each compound (with R = Tm–Pr) is evaluated by linear interpolation between the T_C in the La and Lu compounds. However, in some cases the compounds with La or Lu do not exist. Then a hypothetical ordering temperature for the compounds with non-magnetic La (or Lu) was deduced by means of extrapolation from T_C of the other considered compounds (Belorizky et al. 1987, Duc et al. 1993a). Representative T_T values for the R–T intermetallics are presented in table 1. In relation with the T–T interactions, T_T can be expressed as

$$T_T = \frac{2Z_{TT}A_{TT}G_T}{3k_B}; \tag{36}$$

G_T is the corresponding de Gennes factor for the transition metal, determined from the experimental data for the effective paramagnetic d moment:

$$G_T = S_T(S_T + 1) = \tfrac{1}{4}p_{eff}^2. \tag{37}$$

Combining eqs. (34) through (37) one arrives at

$$\left(\frac{A_{RT}}{3k_B}\right)^2 = \frac{(T_C - T_R)(T_C - T_T)}{4Z_{RT}Z_{TR}G_RG_T}. \tag{38}$$

The p_{eff}-values and other parameters used for estimating A_{RT} for the various compounds are listed in table 1.

Table 1

T-atomic magnetic moment (M_T), effective paramagnetic moment (p_{eff}), numbers of nearest neighbours of R and T atoms[a] in a number of the lanthanide–transition metal series. Values of A_{TT} deduced from the ordering temperature (T_T) for the 3d sublattice in Gd–T compounds are also listed (see eq. (36) in the text)

Compound	M_T (μ_B/at)	p_{eff} (μ_B/at)	Ref.	Z_{RR}	Z_{RT}	Ref.	Z_{TR}	Ref.	Z_{TT}	T_T (K)	A_{TT} (10^{-22} J)
RCo_2	1.0	–		4	12		6		6	–	–
RCo_3	1.3	2.8	1	6.5	14.5 (14)	6	5		6.5	300	9.6
R_2Co_7	1.5	3.0	1	–	15		4.5		–	554	–
RCo_5	1.65	3.3	1	8	18		3.5 (2)	7	9	925	17.8
R_2Co_{17}	1.65	3.3	1	4	19		2.2 (2.1)	7	10	1145	17.4
RCo_{12}	1.4	–		8	20 (20)	6	1.8		10	–	–
RCo_4B	1.0	2.35	2	8	15		2.5		8	375	12.9
$R_2Co_{14}B$	1.4	3.3	3	5	18 (16)	6	2.5		10	955	15.9
$RCo_{12}B_6$	0.43	1.9	4	–	18		1.5		6	141	8.1
RFe_2	1.5	3.4		4	12		6		6	495	11.8
RFe_3	1.75	3.5		6.5	14.5 (14)	6	5		6.5	505	10.5
R_6Fe_{23}	2.0	3.7		4	16 (16)	6	4.2		9	475	6.9
R_2Fe_{17}	2.2	4.0		4	19		2.2 (2.1)	7	10	232	2.2
RFe_4B	1.7	3.4	5	8	15		2.5		8	–	–
$R_2Fe_{14}B$	2.26	4.0	3	5	18 (16)	6	2.5 (2.1)	7	10	510	4.9
RFe_{12}	1.5	3.7	5	8	20 (20)	6	1.8		10	482	5.8
RNi_2	–	–		4	12		6		6	–	
RNi_3	0.05	0.9	1	6.5	14.5 (14)	6	5		6.5	20	0.4
R_2Ni_7	0.17	1.05	1	–	15		4.5		–	45	
RNi_5	–	–		8	18		3.6		9	–	
R_2Ni_{17}	0.3	1.5		4	19		2.2 (2.1)	7	10	150	1.4

[a] Z_{RR}, Z_{RT}, Z_{TR} and Z_{TT}, taken as average numbers over the different R and T crystallographic sites; values in parentheses taken from refs. 6 and 7.

References

(1) Kirchmayr and Poldy (1978)
(2) Pędziwiatr et al. (1987)
(3) Burzo et al. (1985)
(4) Zhou et al. (1992c)
(5) Duc (1991)
(6) Liu et al. (1994a)
(7) Franse and Radwanski (1993)

A systematic analysis of the ordering temperature was carried out in order to evaluate the R–T exchange-coupling parameter for most of the R_mT_n (T = Fe, Co, Ni; $m/n = 1/2$, 1/3, 6/23, 1/5 2/17) and $R_mT_nX_k$ (X = B, Ti, V, ..., $m/n/k = 1/4/1$, 2/14/1, 1/12/6, 1/11/1 or 1/10/2, etc.) series of compounds. The obtained results together with those derived by other methods are listed in table 2.

The method of evaluation of A_{RT} from ordering temperatures is very simple and can be applied for almost all R–T intermetallic compounds. Unfortunately, it was previously thought that this method can lead to accurate results only if the experimental error for the comparatively small differences between T_C and T_T can be kept low. As a result, this method is usually applied to estimate the intersublattice exchange-coupling constants (or intersublattice exchange fields) for the Gd compounds (Radwanski and Franse 1992, Franse and Radwanski 1993) since these compounds have the highest Curie temperatures. However, as can be seen from table 2, good agreement has been found between the present A_{RT} values and those deduced from the analysis of the high-field magnetization (Liu 1994, Liu et al. 1994a and references therein), compensation temperatures, paramagnetic susceptibilities, inelastic-neutron scattering and Mössbauer spectroscopy, etc., not only for the Gd compounds, but also for compounds with all of the other lanthanide elements.

In all of the considered compounds, it can be noted that the chosen A_{RR} is almost one order of magnitude smaller than A_{RT}. The uncertainty in R–R interactions may only lead to an small error in A_{RT}; it amounts to about 5% in the T-rich compounds such as R_2T_{17} and $R_2T_{14}B$. In the compounds where the T–T interactions are rather weak, especially in the RCo_2 compounds, the A_{RT} values derived from analyzing T_C are more sensitive to the choice of A_{RR} values. For simplicity, it was assumed that the A_{RR} values are identical to those deduced from the RNi_2 compounds. Fortunately, with this choice a rather good consistence between the present results and those derived from high-field magnetization was obtained for the RCo_2 compounds (Ballou et al. 1993a, Dubenko et al. 1995, see also table 2, entries for lanthanide–cobalt compounds). In fact, neutron measurements performed on $HoCo_2$ (Castets et al. 1980) yield the value of 0.82×10^{-23} J, which is nearly half the value of 1.8×10^{-23} J deduced for $HoNi_2$. Recently, a value of A_{RR} of almost the same magnitude has also been used to explain the difference between exchange fields derived from inelastic-neutron scattering and from the high-field free-powder (HFFP) method for $GdFe_2$ and $GdFe_{14}B$ (Liu et al. 1994a). Experiments of the high-field magnetization for free powders of $(Gd,Nd)_mNi_n$ have also indicated that A_{RR} is almost independent of the lanthanide concentration (Duc et al. 1995). In analyzing the ordering temperatures of the $RCo_{12}B_6$ compounds, the R–R interactions, however, were neglected. We will return to this problem in the next section.

5.2. *High-field free-powder (HFFP) method*

Applying Néel's multi-sublattice model (Néel 1948), the magnetization curves of a ferrimagnet and an antiferromagnet consisting of two isotropic magnetic sublattices can be considered (Tyablikov 1967). Let M_A and M_B be the magnetic moments of sublattices A and B, respectively ($M_A \neq M_B$ for a ferrimagnet and $M_A \equiv M_B$ for an antiferromagnet). If

Table 2
Curie temperature T_C (in K), compensation temperature T_k (in K) and the exchange-coupling parameter A_{RT} (10^{-23} J) for a number of lanthanide–transition-metal intermetallics

Compound	T_C	T_k	A_{RT}[a]						
			T_C	HFFP	Ref.	T_k	Ref.	Other	Ref.
Lanthanide–cobalt compounds									
$PrCo_2$	54		25.8						
$NdCo_2$	95		23.0					25.6	1
$GdCo_2$	400		18.8	19.8	2			12.5	4
$TbCo_2$	227		18.1					13.5	4
$DyCo_2$	140		18.0					12.0	4
$HoCo_2$	75		17.8					12.0	4
$ErCo_2$	32		16.0					10.5	4
								12.2	5,6
$TmCo_2$	7		17.0	14.6	3				
$PrCo_3$	350		37.0						
$NdCo_3$	395		29.8					20.0	7
$GdCo_3$	615		17.6					14.3	8
$TbCo_3$	506		15.7	17.9	9				
$DyCo_3$	450	400	15.5	19.3	9	9.0			
$HoCo_3$	408	325	14.9	20.6	9	9.6			
$ErCo_3$	380	225	15.5	17.9	9	11.1			
$TmCo_3$	355	115	15.0			12.2			
Pr_2Co_7	574		27.8						
Nd_2Co_7	609		24.9						
Sm_2Co_7	713		26.1						
Gd_2Co_7	775	428	16.6	16.6	10			12.5	11
Tb_2Co_7	717	410	16.7	15.2	10				
Dy_2Co_7	640	380	13.8	15.2	10				
Ho_2Co_7	647	230	17.1	16.6	10				
Er_2Co_7	623	140	17.9	16.6	10				
Tm_2Co_7				16.6	10				
$SmCo_5$								22.6	13,14
								16.7	15
$GdCo_5$	1020		14.9	13.8	12	10.3		12.6	16
								13.6	17
								14.1	18
$TbCo_5$	980	120	14.0	11.2	12	8.5		13.5	19
								12.9	20
$DyCo_5$	960	90	13.8	9.8	12			9.8	21
								10.8	22
								21.0	23

continued on next page

Table 2, *continued*

Compound	T_C	T_k	A_{RT} [a]						
			T_C	HFFP	Ref.	T_k	Ref.	Other	Ref.
$HoCo_5$				10.4	12				
$ErCo_5$				11.0	12			11.3	21
Pr_2Co_{17}	1160		44.6					11.5	24
Nd_2Co_{17}	1183		34.6					10.0	24
Sm_2Co_{17}								20.2	25
Gd_2Co_{17}	1240		15.1	13.2	26				
Tb_2Co_{17}	1195		14.7	11.0	26			11.2	24
Dy_2Co_{17}	1188		15.2	10.1	26			10.1	28,29
								14	23
Ho_2Co_{17}	1173		14.8	9.6	27			9.4	28,29
Er_2Co_{17}	1160		13.7	9.5	27			8.9	27
Tm_2Co_{17}				9.0	27				
Lanthanide–iron compounds									
$PrFe_2$	543		33.6					43.8	30,13
$NdFe_2$	578		26.7					36.0	30,13
$SmFe_2$	680		24.7					32.0	30,13
								20.1	31
$GdFe_2$	780		16.2	30.6	32			30.4	40
								33.7	33
								26.6	17
$TbFe_2$	713		16.3	29.0	32			29.3	30,13
								24.7	34
$DyFe_2$	640		15.0	29.0	32			28.7	30,13
$HoFe_2$	604		14.6	29.0	32			27.5	30,13
								24.7	34
$ErFe_2$	575	486	14.1	26.2	32	21.4		26.3	30,13
								24.0	35
$TmFe_2$	563	236	13.8			22.1		25.0	30,13
$SmFe_3$	650		20.6						
$GdFe_3$	728	618	12.8	19.3	32	12.2			
$TbFe_3$	648		12.5	19.3	32				
$DyFe_3$	600	546	11.3	22.1	32	11.8			
$HoFe_3$	565	393	10.9	22.9	32	11.2		11.6	36
$ErFe_3$	550	236	11.3	26.2	32	11.1			
$TmFe_3$	535		11.4						
Gd_6Fe_{23}	655		12.4						
Tb_6Fe_{23}	574	280	10.9			12.3			

continued on next page

Table 2, *continued*

Compound	T_C	T_k	A_{RT} [a]						
			T_C	HFFP	Ref.	T_k	Ref.	Other	Ref.
Dy_6Fe_{23}	545	272	10.1			12.2			
Ho_6Fe_{23}	520		10.8						
Er_6Fe_{23}	500	112	11.5	16.6	37	14.2	38		
Tm_6Fe_{23}	486		10.2					18.9	39
Pr_2Fe_{17}	283		23.3						
Nd_2Fe_{17}	227		20.2						
Sm_2Fe_{17}	385		16.9						
Gd_2Fe_{17}	460		11.2	13.8	40			13.7	17
								12.8	26,43
Tb_2Fe_{17}	408		11.6	12.4	40			9.6	43
Dy_2Fe_{17}	363		11.5	9.7	41			11.9	13
								9.5	24
								12.0	23
Ho_2Fe_{17}	325		11.1	9.7	42			11.0	13
								9.7	44
Er_2Fe_{17}	300		11.2	10.4	40			10.6	13
								8.4	24
Tm_2Fe_{17}	270		8.8						
Lanthanide–nickel compounds									
$PrNi_3$	20		6.9						
$NdNi_3$	27		7.2						
$SmNi_3$	85		18.0						
$GdNi_3$	120		8.8						
$TbNi_3$	96		10.8						
$DyNi_3$	75		10.0						
$HoNi_3$	66		11.1						
$ErNi_3$	52		10.4						
$TmNi_3$	43		11.4						
Pr_2Ni_7	85		29.6						
Nd_2Ni_7	87		20.2						
Gd_2Ni_7	120		7.0			18.9	45		
Tb_2Ni_7	100		9.1			15.2	45		
Dy_2Ni_7	80		7.3			15.2	45		
Ho_2Ni_7	70		7.2			11.0	45		
Er_2Ni_7	67		8.2			12.4	45		
Sm_2Ni_{17}	186		12.5						

continued on next page

Table 2, *continued*

Compound	T_C	T_k	A_{RT}[a]						
			T_C	HFFP	Ref.	T_k	Ref.	Other	Ref.
Gd_2Ni_{17}	205	138	8.8	8.6	46	9.7	47		
Tb_2Ni_{17}	178	130	7.1	7.9	46	7.0	47		
Dy_2Ni_{17}	170	100	6.3	6.6	46	6.2	47		
Ho_2Ni_{17}	162	73	8.2	6.2	46	5.7	47		
Er_2Ni_{17}	155	53	7.7	6.5	46	5.4	47		
Tm_2Ni_{17}	152	52	10.2	6.1	46	4.3	47		
Lanthanide–transition-metal borides									
$PrCo_4B$	455		36.3						
$NdCo_4B$	460		26.0						
$GdCo_4B$	505	410	15.5	13.8	48	12.9	49		
$TbCo_4B$	450	400	14.6	12.6	48	11.8	49		
$DyCo_4B$	425	340	14.8	11.6	48	11.7	49		
$HoCo_4B$	400	240	13.5	9.3	48	11.0	49		
$ErCo_4B$	386	163	11.5	10.4	48	11.4	49		
$Pr_2Co_{14}B$	994		37.5						
$Nd_2Co_{14}B$	1006		28.3						
$Sm_2Co_{14}B$	1030		21.5						
$Gd_2Co_{14}B$	1050		14.1	15.2	50				
$Tb_2Co_{14}B$	1030		14.3	13.4	50				
$Dy_2Co_{14}B$				13.1	50				
$Ho_2Co_{14}B$				12.6	50				
$PrCo_{12}B_6$	158		23.7						
$NdCo_{12}B_6$	159		16.1						
$SmCo_{12}B_6$	158		9.8						
$GdCo_{12}B_6$	162	51.5	6.0	7.0	51	7.0			
$TbCo_{12}B_6$	154	83.0	5.6	6.7	51	8.8			
$DyCo_{12}B_6$	148	72.2	5.1	5.6	51	7.5			
$HoCo_{12}B_6$	146	44.3	4.7	5.1	51	6.3			
$ErCo_{12}B_6$	145	25.5	5.2	5.1	51	5.5			
$TmCo_{12}B_6$	144	11.6	5.4	4.8	51	5.8			
$HoFe_4B$				13.4	52				
$ErFe_4B$				15.2	52				
$HoFe_4B$				13.4	52				
$Pr_2Fe_{14}B$	565		32.4					22.8	30,13
								23.6	33,53
$Nd_2Fe_{14}B$	592		25.7					21.0	30,13
								26.4	33,53,54

continued on next page

Table 2, *continued*

Compound	T_C	T_k	A_{RT}[a]						
			T_C	HFFP	Ref.	T_k	Ref.	Other	Ref.
$Sm_2Fe_{14}B$	621		20.2					18.2	30,13
								17.2	53
$Gd_2Fe_{14}B$	664		11.5	13.8	26			16.2	30,13
								16.4	33,53
$Tb_2Fe_{14}B$	620		11.7	15.2	55			14.5	30,13
								14.3	33,53,54
$Dy_2Fe_{14}B$	590		11.9	13.4	26			12.6	30,13
								9.8	33,53,54
$Ho_2Fe_{14}B$	570		11.4	12.4	26			13.1	30,13
								11.6	33,53,54
$Er_2Fe_{14}B$	555		11.1	12.1	55			12.2	30,13
								11.1	33,53
$Tm_2Fe_{14}B$	545		10.4	11.6	55			11.5	30,13
"RT_{12}" compounds									
$SmCo_{11}Ti$	1004	24.0							
$DyCo_{11}Ti$			13.5	56					
$HoCo_{11}Ti$			12.8	56					
$ErCo_{11}Ti$			10.9	56					
$GdCo_{10}V_2$			14.5	57					
$TbCo_{10}V_2$			13.8	57					
$DyCo_{10}V_2$			12.1	57					
$HoCo_{10}V_2$			10.9	57					
$ErCo_{10}V_2$			11.0	57					
$NdFe_{11}Ti$	527		22.3						
$SmFe_{11}Ti$	584		21.6						
$GdFe_{11}Ti$	627		12.7						
$TbFe_{11}Ti$	560		11.2						
$DyFe_{11}Ti$	534		11.2						
$HoFe_{11}Ti$	520		12.4						
$ErFe_{11}Ti$	505		11.4						
$TmFe_{11}Ti$	496		11.0						
$NdFe_{10}V_2$	570		31.7						
$SmFe_{10}V_2$	610		24.6						
$GdFe_{10}V_2$	626		12.6						
$TbFe_{10}V_2$	570		12.0						
$DyFe_{10}V_2$	540		12.2						
$HoFe_{10}V_2$	525		12.6	9.7	58				

continued on next page

Table 2, *continued*

Compound	T_C	T_k	A_{RT} [a]						
			T_C	HFFP	Ref.	T_k	Ref.	Other	Ref.
$ErFe_{10}V_2$	505		11.5	8.3	58				
$TmFe_{10}V_2$	496		11.0						

[a] T_C, data deduced from T_C (Duc et al. 1993a); HFFP, data deduced from the HFFP method (Liu 1994, Liu et al. 1994a); T_k, data deduced from T_k (Duc et al. 1993a); Other, data deduced from other experimental and theoretical methods.

References

(1) Gignoux et al. (1975)
(2) Ballou et al. (1993a)
(3) Brommer et al. (1993)
(4) Bloch and Lemaire (1970)
(5) Castets et al. (1980)
(6) Koon and Rhyne (1981)
(7) Goto et al. (1994)
(8) Kebe (1983)
(9) Li (1993)
(10) Zhou et al. (1992a)
(11) Ballou et al. (1992)
(12) Liu et al. (1991b)
(13) Liebs et al. (1993)
(14) Sankar et al. (1975)
(15) Laforest (1981)
(16) Radwanski et al. (1992a–d)
(17) Liu et al. (1994a)
(18) Ermolenko (1980)
(19) Ballou et al. (1989)
(20) Ermolenko (1985)
(21) Ermolenko (1982)
(22) Drzazga and Mydlarz (1988)
(23) Gubbens et al. (1988)
(24) Sinnema (1988)
(25) Perkins and Strassler (1977)
(26) Verhoef (1990)
(27) Liu (1994)
(28) Verhoef et al. (1990b)
(29) Franse et al. (1986)
(30) Fähnle et al. (1993)
(31) de Wijn et al. (1976)
(32) Liu et al. (1991a)
(33) Loewenhaupt et al. (1991)
(34) Koon et al. (1991)
(35) Rhyne (1987)
(36) Simmons et al. (1973)
(37) de Boer et al. (1990)
(38) Frings et al. (1983)
(39) Gubbens et al. (1984)
(40) Jacobs et al. (1992a)
(41) Jacobs et al. (1992b)
(42) Jacobs et al. (1992c)
(43) Radwanski and Franse (1992)
(44) Sinnema et al. (1987)
(45) Zhou et al. (1992b)
(46) Zhong et al. (1990a)
(47) Szewczyk et al. (1992)
(48) Liu et al. (1991a–c)
(49) Drzazga and Drzazga (1987)
(50) Radwanski et al. (1990)
(51) Zhou et al. (1992c)
(52) Buschow et al. (1990)
(53) Yamada et al. (1988)
(54) Givord et al. (1988)
(55) Verhoef et al. (1990a)
(56) Zeng (1994)
(57) Brabers et al. (1993)
(58) Zhong et al. (1990b)

both sublattices are isotropic, the magnetization curves are characterized by the transitions at the critical fields B_{c1} and B_{c2} as illustrated in fig. 9. For a ferrimagnet, in fields $B \leqslant B_{c1}$ the sublattice magnetic moments are in the antiparallel collinear structure; the resultant moment $M(=|M_A - M_B|)$ is oriented along the applied field. In intermediate fields $B_{c1} \leqslant B \leqslant B_{c2}$, the magnetic structure is non-collinear: the moments M_A and M_B do not coincide with the direction of magnetic field, but the total moment is oriented along the field. In strong fields $B \geqslant B_{c2}$, the magnetic moments are in forced ferromagnetic collinear structure and total magnetization equals $M_A + M_B$. For an antiferromagnet, the first critical field B_{c1} is zero. This model has been developed for ytterbium iron garnet and dysprosium iron garnet ferrimagnets by Clark and Callen (1968). They derived the slope of the magnetization curves in the non-collinear phase to be equal to $1/n_{AB}$ (here A = R and B = T), i.e.:

$$M = \frac{B}{n_{RT}}. \tag{39}$$

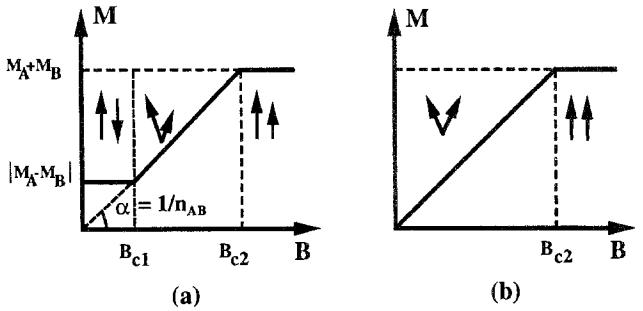

Fig. 9. Magnetization curves for (a) an isotropic ferrimagnet and (b) an isotropic antiferromagnet. The collinear ferrimagnetic, antiferromagnetic, the canted and the forced ferromagnetic moment configurations are shown.

The first and second critical fields can be determined as

$$B_{c1} = n_{RT}\,|M_R - M_T|. \qquad B_{c2} = n_{RT}\,|M_R + M_T|. \tag{40,41}$$

For the lanthanide intermetallics, this method was first applied to a monocrystalline sphere (diameter 3 mm) of the compound Ho_2Co_{17} (Franse et al. 1985). In the high-field magnetization experiments, this sphere was free to rotate in the sample holder. Around 20 T, the magnetization curve at 4.2 K was found to exhibit a kink which could be understood as a transition from the ferrimagnetic collinear to a non-collinear structure. For magnetic fields above the kink field, the magnetization of Ho_2Co_{17} is strictly linear in the field, in accordance with eq. (39). The same magnetization curve can also be obtained on powder samples with size below 40 μm. This implies that the powder particles can be considered as a collection of monocrystalline samples. Subsequently, this technique has been applied on a large number of R–T compounds and important information on the intersublattice exchange interactions has been derived. Fundamentals of this method are given in the following.

In a mean-field description, the free energy of a R–T compound consisting two magnetic sublattices with sublattice magnetic moments M_R and M_T can be represented by:

$$E = E_a^R(\Theta_R, \phi_R) + E_a^T(\Theta_R, \phi_R) + n_{RT} M_R M_T - (M_R + M_T) \cdot B. \tag{42}$$

The first two terms represent the anisotropy energies of the R and T sublattices, respectively. The third term describes the R–T exchange interaction with the intersublattice molecular-field coefficient n_{RT}. The last term represents the Zeeman energy in an external field. The equilibrium positions of M_R and M_T can be obtained by minimizing eq. (42) with respect to Θ_R, ϕ_R. However, due to the complexity of this equation, this has to be carried out numerically.

Previous investigations (see Franse and Radwanski 1993 and references therein) have shown that the anisotropy energy of the 3d sublattice at low temperatures is generally much smaller than the 4f-sublattice anisotropy. Therefore, as a first approximation, the

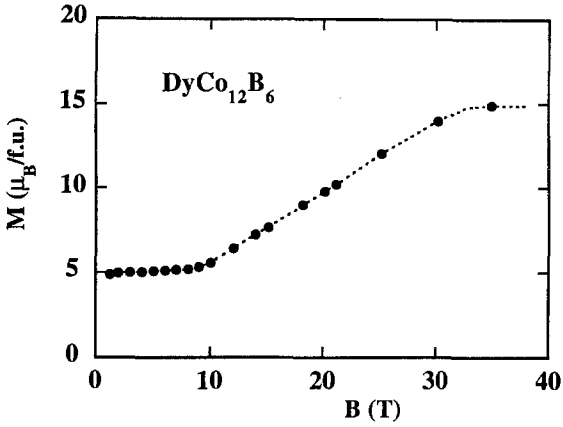

Fig. 10. High-field magnetization curve at 4.2 K of powdered $DyCo_{12}B_6$. After Zhou et al. (1992c).

former can be ignored. As a second approximation, we give samples the freedom to find, for any field value, the orientation with the lowest energy with respect to the direction of the applied magnetic field, i.e. R-sublattice magnetization can be taken parallel to the easy magnetization direction for all possible moment configurations of the two sublattices. With these two assumptions, eq. (42) reduces to

$$E = n_{RT} M_R M_T \cos\alpha - MB, \tag{43}$$

with α the angle between the two sublattice magnetizations, and the resulting magnetization M given by

$$M = \left(M_R^2 + M_T^2 + 2M_R M_T \cos\alpha\right)^{1/2}. \tag{44}$$

The equilibrium directions of M_R and M_T can now be obtained by minimizing eq. (43) with respect to any field value. In this case, the resultant magnetization curve is the same as that discussed above for the ferrimagnets. A textbook example for this type of magnetization process is the compound $DyCo_{12}B_6$, in which the full range of phenomena is observable in magnetic fields up to 40 T, see fig. 10 (Zhou et al. 1992c).

The HFFP method allows one to directly determine the strength of the R–T interactions. However, in many of the binary and ternary compounds, the difference $|M_T - M_R|$ is fairly large, so that the non-collinear sloping range is inaccessible, even with an available field strength as high as 40 T (Verhoef et al. 1990a, de Boer and Buschow 1992). For this reason, it is necessary to apply "magnetic dilution" of the larger of the two sublattice magnetizations M_T or M_R. The value of A_{RT} for "pure" R_mT_n or $R_mT_nX_k$ compounds has sometimes been derived by extrapolation from the "substituting" alloys, but, as will be discussed in sect. 7.2.4., the substitution strongly affects the electronic properties of the systems and may change the nature of the exchange coupling.

The assumption of zero anisotropy for the T sublattice is not always realistic. Especially for the Er compounds, the competition between Er and T anisotropy can even cause

the easy direction of the magnetization to be along the preferential direction of the T sublattice magnetization instead of along that of the Er sublattice. An example is the compound Er_2Fe_{17}, which shows easy-plane behaviour due to a dominant iron anisotropy even at lowest temperatures. The effects of a non-zero 3d anisotropy on the "free-powder" magnetization curves has been discussed by Hong et al. (1990) and Zhao et al. (1994). Restricting the discussion to the first anisotropy constants of the R and T sublattices, K_1^R and K_1^T, respectively, the modified expressions for the two critical fields in the free-powder magnetization curves are found as

$$B_{c1,2} = (n_{RT} \pm \Delta)\,|M_R \pm M_T|, \tag{45}$$

where Δ is given by

$$\Delta = \frac{2K_1^R K_1^T}{M_R M_T\,|K_1^R + K_1^T|}. \tag{46}$$

The linear field dependence of eq. (39) is now replaced by a more complex expression which results in a convex curve for $K_1^R K_1^T > 0$ and a concave one for $K_1^R K_1^T < 0$. However, both of these curves intersect the linear curve obtained for $K_1^T = 0$.

Finally, the determination of the numbers of nearest neighbours Z_{RT} and Z_{TR} causes some trouble in comparing the results of A_{RT} derived from the various estimations. As was discussed in sect. 4, the counting of "neighbours" must follow the rule $N_T Z_{TR} = N_R Z_{RT}$ (Brommer 1991). Practically, the nearest-neighbour numbers are determined by the crystallographic structure. In most cases, the ratio Z_{RT}/Z_{TR} for the R_mT_n compounds is fixed around the value of the ratio m/n, however, a strict value for Z_{RT} is not obvious. We list in table 1 (above) the values of Z_{RT} and Z_{TR} used by different authors (Franse and Radwanski 1993, Liu et al. 1994a and references therein). Gubbens et al. (1988), for instance, used $Z_{RT} = 19$ and $Z_{TR} = 2$ for Gd_2T_{17}. These are nearly the same as those given by Franse and Radwanski (1993), but slightly different from the numbers used in the present investigation. On the basis of a similar analysis (but with $Z_{RT} = 16$ and $Z_{TR} = 2.3$), Coey (1986) obtained a value for the exchange field of 300 T for $Gd_2Co_{14}B$, whereas the value reported by Franse and Radwanski (1993) (with $Z_{RT} = 18$ and $Z_{TR} = 2.5$) is 186 T.

6. Survey of the studies of intersublattice exchange interactions in lanthanide intermetallics

6.1. *RT_2 compounds*

The cubic Laves-phase compounds RT_2 have been studied intensively in the last decade. The simple structure with a single crystallographic site for the R and T ions makes these compounds especially suited for an extensive analysis of the basic magnetic interaction as a function of the lanthanide elements and of the 3d partner. In RCo_2, a

Table 3
R–T exchange interactions in $(R,Y)Co_2$ compounds

Compound	n_{RCo} (Tf.u./μ_B)	Ref.	A_{RCo} (10^{-23} J)	Ref.
$Gd_xY_{1-x}(Co,Al)_2$	62.0	1	19.2	1
$Tb_{0.1}Y_{0.9}(Co,Al)_2$	53.7	1	24.9	1
	36.0	2	16.7	2
$Dy_{0.88}Y_{0.12}(Co,Al)_2$	37.3	1	23.1	1
$Ho_{0.08}Y_{0.92}(Co,Al)2$	25.8	1	19.9	1
$Er_{0.14}Y_{0.86}(Co,Al)_2$	21.5	1	19.9	1
	16.5	2	15.3	2
$Tm_{0.4}Y_{0.6}(Co,Al)_2$	17.0	1	19.6	1
$Tm_xLu_{1-x}(Co,Al)_2$	13.5	1	14.6	1

References
(1) Dubenko et al. (1995) (2) Duc et al. (1997a)

Co moment is induced by the exchange interaction between the 3d and 4f spins. For the heavy R–Co_2 compounds, the value of the R–T and R–R exchange interactions was systematically determined by Bloch and Lemaire (1970) from an analysis of the paramagnetic susceptibilities. A_{RCo} turns out to be ranging from 10.2×10^{-23} J to 13.5×10^{-23} J. In a more detailed analysis, these values together with that of 25.6×10^{-23} J for $NdCo_2$ (Gignoux et al. 1975) were used to obtain the A_{RCo} values for all of the RCo_2 compounds (Duc et al. 1992b). In an analysis of the ordering temperatures, this value of A_{RCo} can be reproduced, if the contribution to T_C of the R–R interaction is given as estimated from RAl_2 compounds (Duc et al. 1993b). Neglecting the contribution of A_{RR}, the calculated A_{RCo} values can reach values of up to 20×10^{-23} J (Duc 1991, Duc et al. 1988a). We listed in table 2 the value of A_{RCo} deduced for RCo_2 with the A_{RR} values derived from RNi_2. Recently, by application of the HFFP method, A_{RCo} was shown to take the value of 19.8×10^{-23} J in $(Gd,Y)(Co,Al)_2$ (Ballou et al. 1993a) and 14.6×10^{-23} J in $(Tm,Lu)(Co,Al)_2$ (Brommer et al. 1993). A difference in A_{RCo} due to the difference between the 5d–3d and 4d–3d hybridizations has also found in the studies of Dubenko et al. (1995) for free powders of $(R,Y)(Co,Al)_2$ and $(R,Lu)(Co,Al)_2$, see table 3 (sect. 7.2.4). Inelastic neutron scattering experiments have been reported for $HoCo_2$ by Castets et al. (1980) and for $ErCo_2$ by Koon and Rhyne (1981). These authors analyzed the spectra with a set of crystal-field parameters and molecular fields $B^R_{mol}=33.4$ T and 26.4 T for $HoCo_2$ and $ErCo_2$ respectively. As a result, A_{RCo} equals 12.9×10^{-23} J and 12.2×10^{-23} J, respectively. These magnetic fields have also been used to interpret the temperature-induced spin reorientation observed in $HoCo_2$ (Aubert et al. 1978) and the specific heat in $(Er,Y)Co_2$ (Radwanski and Franse 1993). Inelastic neutron scattering studies have also been performed for RFe_2 compounds (Koon and Rhyne 1981, Rhyne 1987). INS spectra have been analyzed with a set of CEF parameters and the values for the parameter A_{RFe} given in table 2. The computations reproduced also a rather similar result

for A_{RFe} (Brooks et al. 1991a–c, Liebs et al. 1993). We noted that, in calculations of the low-temperature specific heat and of the rotation of the easy direction with temperature, a constant value of 245 T (Germano and Butera 1981) or 225 T (Atzmony and Dariel 1976) (corresponding to $A_{RFe} = 25.2 \times 10^{-23}$ J or 23.1×10^{-23} J) is reported for B_{ex}^{R}. It is worthwhile to note that, while the results deduced from the HFFP method (Liu et al. 1991a) for the (R,Y)Fe_2 compounds agree well with others, the present analysis of the ordering temperatures results in a much lower (by almost a factor of two) value for A_{RFe}. On the one hand, this may reflect the temperature dependence of the exchange interactions. On the other hand, as we will discuss in sect. 7.2.4, the exchange interaction may also be enhanced by the effect of Y substitution, so that the result derived from the HFFP method for the substituted (R,Y)Fe_2 compounds will be higher than that for the "pure" RFe_2 ones. Analogously, the above mentioned difference between the values derived from high and low temperatures for RCo_2 can be understood in the same sense.

6.2. *RT_3 compounds*

In the RFe_3 compounds, for all the heavy lanthanide elements (except R = Tm), a compensation temperature for the magnetization is observed. The values of 618 K, 512 K, 546 K, 393 K and 236 K for the Gd, Tb, Dy, Ho and Er compounds, respectively, are rather close to T_C. The estimated value of A_{RFe} from the analysis of these compensation points is in good agreement with that derived from T_C, see table 2. However, similarly to the results observed in RT_2 compounds, the A_{RT} values derived from these two methods are lower than those deduced by the HFFP method (Liu et al. 1991a). A low value of 11.6×10^{-23} J for A_{HoFe} was derived from the analysis of the paramagnetic susceptibility in $HoFe_3$ (Simmons et al. 1973). Anyway, as above mentioned for the RT_2 compounds, one should take into account the effects of the thermal variations and the effects of the Y substitution for the general consideration of the exchange coupling. Additionally, on inspection of data reported for RFe_3 from the HFFP method, the trend of A_{RFe} is found to decrease from Gd to Er.

For the RCo_3 compounds, the results obtained from T_C and HFFP are in good agreement. In these compounds, the compensation temperatures amount to 400 K, 325 K, 225 K and 115 K for Dy, Ho, Er and Tm, respectively. T_k thus is rather close to T_C (for instance, $T_k = 400$ K and $T_C = 450$ K for $DyCo_3$). From the analysis of T_C, however, we find that A_{RCo} is quite large ($A_{RT} = 15.5 \times 10^{-23}$ J), whereas a value of $A_{RT} = 9 \times 10^{-23}$ J was deduced from T_k).

In the RNi_3 compounds, the magnetic moments of the Ni ions are very small (about $0.05 \mu_B$ as reported by Gignoux et al. (1980)). An analysis of T_C, however, results in a rather large value for A_{RNi}, see table 2.

6.3. *R_2T_7 compounds*

Zhou et al. (1992a) have reported the magnetization curves at 4.2 K up to 35 T on free particles of the ferrimagnetic $(R,Y)_2Co_7$ compounds with R = Gd, Tb, Dy, Ho, Er and

Tm. An agreement between the results derived from HFFP and T_C is that the tendency for A_{RCo} to decrease for R = Gd to Tm has been found to be less pronounced. A value of about 16.5×10^{-23} J is found. However, in the high-field magnetization studies on single-crystalline Gd_2Co_7 (Ballou et al. 1992), a value of 152 T was reported for B_{ex}^{R}, which corresponds to a value for A_{RCo} of 10.2×10^{-23} J.

The highest value of T_C in the R_2Ni_7compounds is 120 K for Gd_2Ni_7, whereas $T_C = 56$ K in Y_2Ni_7. Attributing this increase to the R–T interaction, a value of 7.0×10^{-23} J is obtained for A_{RNi}. This is, however, only a half that deduced from the HFFP method (Zhou et al. 1992b) for the $(R,Y)_2Ni_7$ compounds. Once more, the influence of the 4d(Y)–5d hybridization on the R–T exchange interactions must be taken into account here. We will return to this problem in sect. 7.2.4.

6.4. *R_6T_{23} compounds*

From the slope of the magnetization curve measured for the free powder particles in the interval of 15 to 35 T by de Boer et al. (1990), a value for n_{RFe} of 1.7 T f.u/μ_B has been found for Er_6Fe_{23} and Er_5YFe_{23}. Taking $Z_{RT} = 14$, this corresponds to a value of 16.6×10^{-23} J for A_{RFe}. In an analysis of T_C, a value $Z_{RT} = 16$ has been used and the value of 11.5×10^{-23} J has been obtained. It is comparable with that of 13.5×10^{-23} J recalculated for A_{RFe} from the HFFP method with $Z_{RT} = 16$. Earlier, Frings et al. (1983) have derived from high-field magnetization measurements at 4.2 K on a polycrystalline sample a smaller value of 1.45 T f.u/μ_B. The compensation temperature in the compounds with R = Tb, Ho and Er reflects also a value of A_{RFe} of the same magnitude (Duc et al. 1993a).

6.5. *RT_5 compounds*

In the literature, the data are usually reported for non-stoichiometric compounds, such as $TbCo_{5.1}$, $DyCo_{5.2}$, $HoCo_{5.5}$ and $ErCo_{5.9}$, etc. In these compounds, T_C is of the order of 1000 K and is less sensitive to the changes of the lanthanide elements. The analysis of T_C yields values of the R–T exchange interactions that are consistent with those derived from the HFFP method (Liu et al. 1991b). With the exception of the result estimated from Mössbauer spectroscopy (Gubbens et al. 1988), the exchange-coupling parameter derived from the analysis of the compensation point, the magnetization studies and polarized neutron measurements support the above findings (see table 2). In addition, band-structure calculations have been performed for $GdCo_5$ by Liu et al. (1994a); the obtained value of 13.6×10^{-23} J for A_{RCo} is in satisfactory agreement with that of 13.8×10^{-23} J deduced from HFFP.

6.6. *R_2T_{17} compounds*

The first A_{RT} parameter reported for R_2Co_{17} was the value of 9.0×10^{-23} J taken from Clausen (1981). For the R_2Fe_{17} compounds, two sets of A_{RFe} were collected by Radwanski

et al. (1985): the first set is based on a value of 128 T for the molecular field B^{R}_{exch} acting on the Dy moments (Gubbens and Buschow 1982) and the second set on a value of 7.7×10^{-23} J for the parameter A_{RFe} deduced from the analysis of inelastic neutron scattering (Clausen 1981). High-field magnetization studies on single crystalline R_2Fe_{17} have been reviewed by Franse et al. (1992). The intersublattice exchange interaction results in the value for B^{R}_{exch} in of approximately 200 T in Gd_2Co_{17} and 290 T in Gd_2Fe_{17}. These results are in good agreement with those derived from HFFP (Verhoef 1990) and from an analysis of T_C. Recently, agreement between theory and experiment has been found in the calculations of Liebs et al. (1993) and Liu et al. (1994a).

Single crystalline samples of R_2Ni_{17} have not been reported to exist so far. For these compounds, values of the parameter A_{RNi} can be derived from T_C and T_k of bulk samples and from the high-field magnetization of free powders. The results are consistent, provided the spin moment in the paramagnetic state is taken into account in the analysis of T_C. Using the spin value $S_{Ni}=0.15$ as deduced at 4.2 K for R_2Ni_{17}, one can obtain a value of A_{RNi} which is 3 or 4 times larger than those derived from other methods (Zhong et al. 1990a).

6.7. *$R_mT_nX_k$ compounds ($X=B$, Ti, V, ...)*

In studies concerning the magnetic properties of the new class of permanent magnets, special attention is paid to the evaluation of the exchange interaction for the $R_mT_nX_k$ compounds such as $R_2T_{14}B$, RT_4B, $RT_{12}B_6$ and $RT_{12-x}T'_x$ (T' = Ti, V, Cr, ...). Different sets of A_{RT} values have been reported for a number of the heavy lanthanide compounds $R_2Fe_{14}B$, $R_2Fe_{14}C$ and $R_2Co_{14}B$, ... (see table 2). The results show that A_{RT} has the tendency to decrease from Gd to Tm; going from one series of compounds to another this parameter is, surprisingly, almost constant. In addition, the R–T exchange coupling in these $R_2T_{14}B(C)$ compounds is not much different from that reported for R_2T_{17} compounds. Calculations for the intersublattice exchange interactions for the series of $R_2Fe_{14}B$ compounds have been performed by Liebs et al. (1993). A comparison with experimental data from INS (Loewenhaupt et al. 1991) and magnetization measurements (Yamada et al. 1988, Givord et al. 1988, Radwanski et al. 1992b, Kou et al. 1992) shows only a small difference, perhaps partly caused by the fact that the different sets of crystal-field parameters were used for the data analysis. A slight deviation of A_{RFe} values arises from the fact that some studies take $Z_{RFe}=18$ (Liebs et al. 1992, Duc 1991, Duc et al. 1993a) while others use $Z_{RFe}=16$ (Liebs et al. 1993, Liu 1994). For $Gd_2Fe_{14}B$, the difference between the exchange fields derived from ISN and HFFP is also connected to the contribution of the Gd sublattice (i.e. R–R interaction) (Liu et al. 1994a).

While the data for the R–T interaction in RFe_4B only comes from the HFFP study by Buschow et al. (1990), the exchange interactions in RCo_4B and $RCo_{12}B_6$ were intensively investigated by different methods: analysis of the Curie temperatures, compensation points and HFFP (Drzazga and Drzazga 1987, Duc et al. 1992a,b, Liu et al. 1991c, Zhou et al. 1992c). These authors have derived the value of 13.8×10^{-23} J for $GdCo_4B$ (Liu et al.

1991c) whereas a smaller value is reported for $RCo_{12}B_6$ ($A_{RCo} = 7.0 \times 10^{-23}$ J for R = Gd (Zhou et al. 1992c).

The RT_{12} phase is stabilized by adding a small amount of metals like V, Cr, Mo, Ti and W according to the formula $RT_{12-x}X_x$. The $RFe_{12-x}X_x$ compounds are ferrimagnetic with T_C ranging from 627 K (Gd) to 488 K (Lu). These values of T_C are approximately 200 K higher than those of the R_2Fe_{17} compounds. For $RCo_{12-x}X_x$, T_C is a little smaller than for R_2Co_{17} compounds. The different sets of A_{RFe} parameters were collected and listed in table 2. It is worthwhile to mention here that in these systems the strength of the R–T exchange coupling depends not only on the lanthanide elements but also on the concentration of the X-component. For $HoFe_{12-x}V_x$ compounds, the HFFP data reported by Zhong et al. (1990b) show that, when x decreases from 4.0 to 3.0, A_{RFe} decreases almost linearly from 18.1×10^{-23} J to 14.0×10^{-23} J. By extrapolation, a value of 9.7×10^{-23} J can be obtained for "pure" $HoFe_{12}$ (Zhong et al. 1990b; see table 8, sect. 7.2.6).

7. General considerations

7.1. *General magnetic properties*

Various interesting properties associated with 3d magnetism are observed in lanthanide–transition metal compounds. As a general rule, the mean value of the 3d-magnetic moment decreases with respect to its value in pure metal, as a function of the amount of lanthanide alloyed (Kirchmayr and Poldy 1978). This effect is due to the transfer of lanthanide 5d and 6s conduction electrons into the transition metal band and to 5d–3d hybridization. Starting from pure iron, cobalt or nickel, the progressive introduction of lanthanides leads to a decrease of the density of the states at the Fermi level $N(E_F)$, and consequently, to a reduction in the splitting of the 3d band and to a decrease of the magnetic moment. For a given range of the concentration, the alloys are close to the condition for the Stoner criterion and magnetic instabilities can be observed. The behaviour strongly depends on the fine structure of $N(E_F)$ near E_F (Cyrot and Lavagna 1979, Yamada et al. 1984, Coehoorn 1989). The critical concentration for the disappearance of 3d magnetism occurs for cobalt at the composition RCo_2 and for nickel at RNi_5. For RNi_5 compounds, however, resurgence of 3d magnetism appears for a slightly larger R-amount and then disappears definitely as shown in fig. 11. The reappearance of 3d-Ni magnetism for higher R-content may be due to the details of the relatively complex crystal structures or may be explainable in terms of the rigid band model assuming a minimum in the density of the states. The valence electrons of R^{3+} gradually fill the 3d band. When the Fermi level is situated at a minimum or at the left-hand side of a subpeak, the Stoner criterion is not fulfilled and splitting of the 3d spin subbands disappears (RNi_5). Further filling of the 3d band then results in a reappearance of the splitting (and then the spontaneous magnetization in (Y_2Ni_7) due to the location of E_F at a subpeak of $N(E_F)$ which has some fine structure (Yamada et al. 1984). A test of this interpretation is provided by examining the

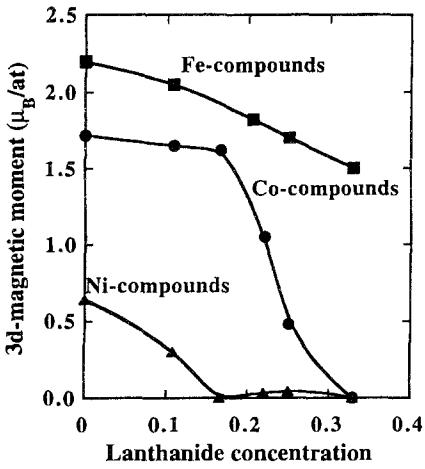

Fig. 11. The mean 3d moment in the Y–Fe, Y–Co and Y–Ni systems.

effect of the lowering of the Fermi level in YNi_3 and Y_2Ni_7 when replacing Ni by Co. Such substitutions resulted in the apparent disappearance of a 3d moment at a critical Co concentration (Poldy and Taylor 1972). Within the simple concept of a magnetic valence Z_m (Williams et al. 1983), the effects of the lanthanide concentration dependence of 3d-magnetic moments in several series of compounds have been discussed by Gavigan et al. (1988) using Friedel's interpretation (1958), that is

$$M = Z_m + 2N_{sp}^{\uparrow}, \tag{47}$$

where $2N_{sp}^{\uparrow}$ is the number of s,p electrons in the spin up state band.

Redenoting the R–T intermetallics as R_yT_{1-y} and $R_{y'}T_{1-y}X_{y''}$ ($y = y' + y''$), Z_m is then determined by the chemical values Z_T, Z_R, Z_X of the corresponding T, R and X elements, respectively, in the compounds considered and by the number $N_d^{\uparrow}$ of the d electrons in the spin-up state band in the strong ferromagnets ($N_d^{\uparrow} = 5$ per atom):

$$Z_m = 2N_d^{\uparrow}(1-y) - Z_T(1-y) - yZ_R \tag{48}$$

or

$$Z_m = 2N_d^{\uparrow}(1-y) - Z_T(1-y) - (y'Z_R + y''Z_X). \tag{49}$$

By comparing the average 3d-magnetic moment in Y–Co and Y–Fe compounds with the calculated Z_m value, Gavigan et al. (1988) concluded that a strong ferromagnetic character exists only in the compounds from pure Co to YCo_5. The observed magnetic moment per atom in the Y_2Co_7 compound and in the larger Y concentrations is lower than the calculated one. As mentioned above, strong ferromagnetism is at this point no longer stable, and the 3d-splitting is reduced and vanishes entirely in YCo_2. In Y–Fe compounds,

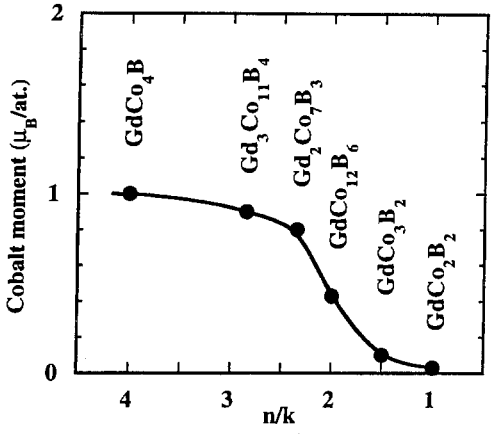

Fig. 12. The mean 3d moment in the Gd–Co–B systems.

the iron magnetic moment corresponds to a character of weak ferromagnetism. The application of the magnetic valence model was also extended to the case of the pseudo-binary and pseudo-ternary compounds (Thuy et al. 1990). An important result of this approach is that as long as strong ferromagnetism is maintained, the magnetization can be evaluated without detailed knowledge of the electron transfer and hybridization effects. Additionally, this reflects that the magnitudes and the concentration dependence of the 3d-magnetic moment can be roughly described by considering the density of both the 3d and 5d electrons or the concentration of the elements in a molar formula of R_yT_{1-y}.

In the magnetic valence approach, the lanthanide intermetallics can be considered as alloys of the transition metal T with R and X elements (X = B, Si, ...). Thus, as observed for R alloying in the R–T compounds, an increase of the concentration of the X component is also expected to lower the magnetic moment of the 3d-sublattice. As an illustration we present in fig. 12 the variation of the mean cobalt moment for the $Gd_mCo_nB_k$ compounds as a function of the relative number of cobalt atoms, n/k (Ballou et al. 1993b). In these R–Co–B systems, the cobalt moment is found to be the largest ($1.4\mu_B$) in the $Gd_2Co_{14}B$ compound and to decrease with decreasing n/k. The condition of a stable cobalt moment is fulfilled in the $GdCo_4B$, $Gd_3Co_{11}B_4$ and $Gd_2Co_7B_3$ compounds. The $GdCo_3B_2$ compound seems to be the closest to the critical region of the transition from the Pauli paramagnetic state to a state with finite cobalt moment. Thus, the critical concentration for the onset of Co magnetism in the R–Co–B takes place for $n/k \approx 1.5$–2.0.

In the application of the magnetic valence model, Z_m is determined from the chemical values $Z_{Co}(=9)$, $Z_R(=3)$ and $Z_B(=2)$ of the corresponding Co, Gd and B elements, respectively, in the alloys and by the number of d electrons in the spin-up state band ($N_d^{\uparrow}$), which is 5 per atom for a strong ferromagnet (Gavigan et al. 1988). The calculated 3d-magnetic moment in different ternary Gd–Co–B compounds is presented in fig. 13 as a function of Z_m together with that of binary Gd–Co phases. As can be seen from this figure, a good consistence between the calculated and experimental mean magnetic moment was obtained for almost of Gd–Co and Gd–Co–B compounds, except $GdCo_3B_2$

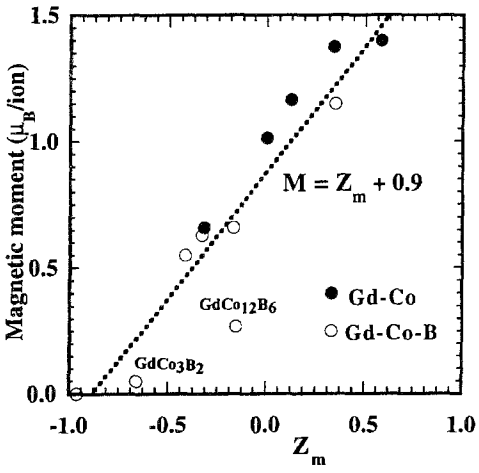

Fig. 13. Magnetic moment as a function of magnetic valence for Gd–Co and Gd–Co–B systems. After Duc and Givord (1995b).

and $GdCo_{12}B_6$. The magnetic moment per atom in $GdCo_3B_2$ and $GdCo_{12}B_6$ is much lower than calculated. This shows that weak ferromagnetism is present in these alloys. This finding, in general, stresses not only the important contribution of the 5d(Gd) electrons but also that of the p(B) electrons on the magnetic properties of the Gd–Co–B alloys. The role of the 3d–p hybridization in the variation of the R–T exchange interactions will be discussed in the next section (7.2.6).

In the compounds with magnetic lanthanides, Z_m may be changed due to the occurrence of an extra molecular field acting on the T-moment. This field is about 100 T in Gd_2Co_{17}. However, one can expect from the high-field susceptibility that the Co moment may be increased by only $0.04\mu_B$. The enhancement of the magnetic moment starts to be detectable for R_2Co_7 and is very pronounced for RCo_3 and RCo_2. The Co moment in $GdCo_3$ amounts to $1.33\mu_B$ whereas in YCo_3 it is only $0.38\mu_B$. In the RCo_4B compounds, a large high-field susceptibility of about $0.0032\mu_B$/T was observed for YCo_4B as well as for $GdCo_4B$. An increase in the Co-magnetic moment from $0.72\mu_B$/Co to $0.925\mu_B$/Co was found in (Gd,Y)Co_4B (Burzo et al. 1987). For the $RCo_{12}B_6$ compounds, however, the Co-magnetic moment is almost saturated (Zhou et al. 1992c). The variation of the 3d-magnetic moment is presented in fig. 14 for the Gd–Fe, Gd–Co and Gd–Ni systems.

In connection with the average ordered and paramagnetic moments, Burzo (1970) has summed up the results, and pointed out that a constant ratio p_{eff}/M_s is found between the 3d moment obtained from the saturation measurements in the ordered state range and the effective moment in the paramagnetic range. In the R–Fe and R–Co systems, this ratio is fixed at the value of 2, see fig. 14. For the R–Ni systems, the ratio is somewhat variable and can be as large as 5, but two types of measurement reveal the same form of the variation as a function of stoichiometry, see figs. 11 and 14. It should be pointed out here that a departure from unity is anyway to be expected since we compare (in the notation for localized moments) $g_R J$ with $g_R\sqrt{J(J+1)}$. The weaker the M_s value for a 3d moment the larger will be the discrepancy between p_{eff} and M_s, which may explain the large ratios

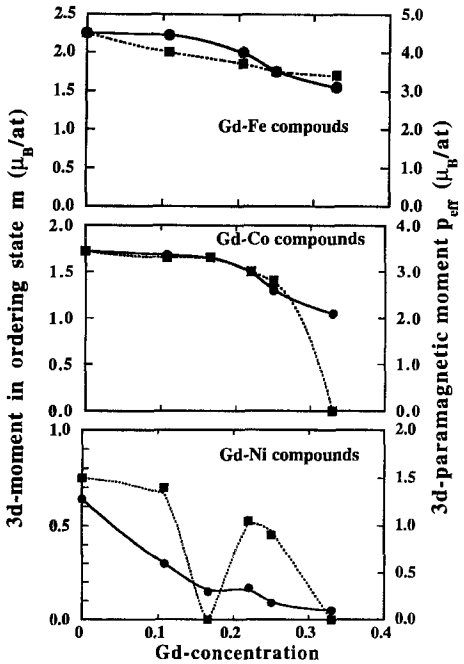

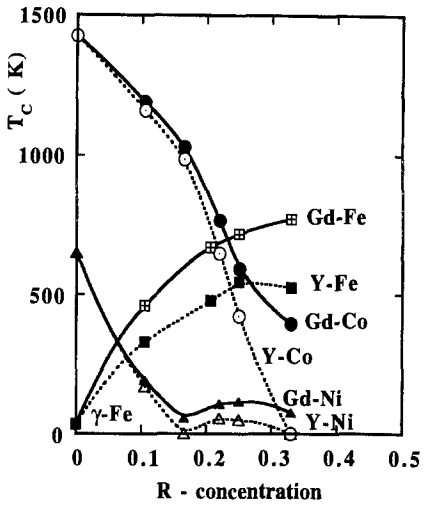

Fig. 15. The Curie temperatures of Y–T and Gd–T as a function of lanthanide concentration. In addition, the ordering temperatures of the γ-Fe, hcp-Co and fcc-Ni are shown.

Fig. 14. The deduced 3d moments from saturation measurements (circles) and from Curie constant (squares) for the Gd–Fe, Gd–Co and Gd–Ni compounds as a function of 3d concentration. The magnetic moments of the α-Fe, hcp-Co and fcc-Ni are included.

for the R–Ni compounds. Similarly, a large value of $p_{\mathrm{eff}}/M_{\mathrm{s}}$ is also found for $RCo_{12}B_6$, see table 1. We note that, in the compounds having large ratios $p_{\mathrm{eff}}/M_{\mathrm{s}}$, not only M_{s} but also T_{C} are weak. In this connection, $p_{\mathrm{eff}}/M_{\mathrm{s}}$ follows well the Rhodes–Wohlfarth plot.

In fig. 15, the T_{C} values are shown for different alloys Y–T and Gd–T. The Y–Co and Y–Ni systems show a decrease of T_{C} on introducing Y up to the composition YCo_2 and YNi_5, whereas the R–Fe (and even the Y–Fe) systems show an anomalous increase of T_{C} as the Fe concentration decreases. In these compounds, a measure of the strength of the T–T exchange interaction is given by the value of the Curie temperature of the corresponding Y–T compounds. It is an established fact that local moments are formed in the 3d itinerant electron systems and it is thus justified to write, within the molecular-field approximation, that $T_{\mathrm{C}} \propto n_{\mathrm{TT}} M_{\mathrm{T}}^2 / 3k_{\mathrm{B}}$, see eq. (36), where n_{TT} is a molecular field coefficient. For the R–Co systems, it is well known (see Lemaire 1966, Givord and Lemaire 1974) that T_{C} is approximately proportional to M_{Co}^2. For R–Fe alloys, however, n_{FeFe} decreases as the Fe-coordination number increases (Gavigan et al. 1988). The replacement of Y(Lu) by magnetic lanthanide ions raises the Curie temperature. This is due to the R–T intersublattice exchange interaction. It is interesting to mention here, before ending this section, that in contradistinction to the variation of $M_{3\mathrm{d}}$, the contribution of the R–T interaction to T_{C} [i.e. $T_{\mathrm{RT}} = T_{\mathrm{C}}(\mathrm{Gd}) - T_{\mathrm{C}}(\mathrm{Y})$] is enhanced with increasing lanthanide

concentration. Introducing this fact to the considerations for eq. (38) one can expect an increase in the strength of the R–T interaction as lanthanide concentration increases.

7.2. *General considerations of the intersublattice exchange coupling*

The 4f–3d exchange coupling parameter is of crucial importance for the description of the magnetic properties for the R–T compounds. However, a large effort on the studies of this parameter did not start until 1986 (Radwanski 1986a,b). A few years later, such a large amount of experimental results had become available that discussions could be started on the systematics of the intersublattice exchange coupling in these compounds. A first approximation is to assume that A_{RT} is a constant (Radwanski 1986a,b, Duc et al. 1990). However, Belorizky et al. (1987) have shown that in a given series of R_mT_n or RCo_2 compounds, A_{RT} increases from Tm to Pr. Such behaviour has been confirmed in other series of R–T compounds in several subsequent studies (Belorizky et al. 1988, Duc 1991, Duc et al. 1992a, 1993a). Moreover, in a systematic analysis of ordering temperatures for a number of R–T intermetallics, Duc (1991) and Duc et al. 1992a have shown that A_{RT} increases from Fe to Co alloys and that going from T-poor to T-rich compounds, both A_{RCo} and A_{RFe} decrease monotonically, following one and the same line if plotted against the 3d-moments. Later, by an analysis of the high-field magnetization data, a similar decrease of A_{RT} was shown to occur in Er_mT_n compounds (Liu et al. 1991a, de Boer and Buschow 1992). Recently, systematic considerations of 4f–3d exchange interactions were reported in several review papers by Duc (1993a) and Liu et al. (1994a). Below, we briefly review the situation with some additional extended discussion.

7.2.1. *Lanthanide concentration dependence of 4f–3d exchange interactions*

The value of A_{RT} obtained from the analysis of T_C and high-field magnetization data for various series of R–T compounds was collected and tabulated by Duc et al. (1993a) and Liu et al. (1994a). A comparison between these two sets of data and those deduced from the compensation temperature (Duc et al. 1993a) as well as by other methods has been given already in the preceding section. The results are listed in table 2. Inspection of the data shows a tendency of A_{RT} to increase with increasing R concentration. In the HFFP method the available data for A_{RT} are most complete for R = Er. Thus, the compounds with Er were selected in order to demonstrate the dependence of A_{RT} on R (Liu et al. 1991a, de Boer and Buschow 1992). In the method of the analysis of the ordering temperature, the demonstration is usually made for the Gd compounds (Duc 1991, 1993a). However, the presentation is also possible for other lanthanide elements, except for Pr–Co and Nd–Co compounds. The peculiar behaviour observed for the latter two systems can tentatively be attributed to a variable degree of intermediate-valence properties of the R elements, or to the crystal-field effect in these compounds. Here, we plot in fig. 16 all the available data for A_{RFe} as a function of the R concentration for Er–Fe compounds. It is seen that, with the exception of the large deviation for the 1/2 and 1/3 compounds (to be discussed in the next section), there is a good agreement between both sets of data. The same systematic

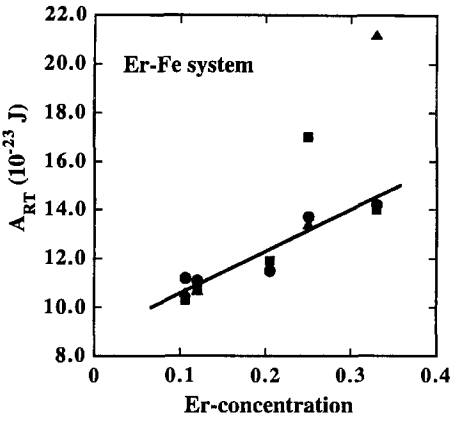

Fig. 16. A_{ErFe} deduced from T_C (circles), from HFFP (squares) and from other methods (triangles) for the Er–Fe systems. The HFFP value for $ErFe_2$ was obtained by assuming the dependence on Y concentration of A_{ErFe} in (Er, Y)Fe_2 series, see sect. 7.2.4. All data are recalculated with the same value of Z_{ErFe} used in the T_C analysis (see table 1).

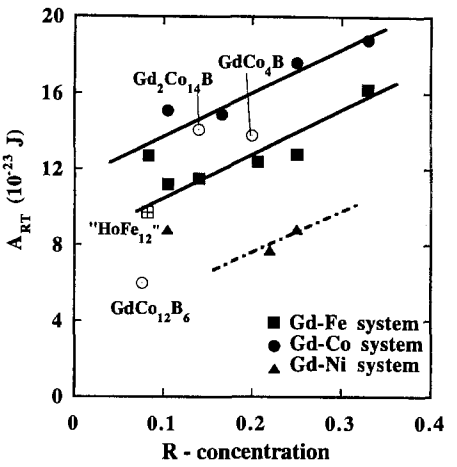

Fig. 17. A_{RT} as a function of R concentration in the Gd–Fe, Gd–Co, Gd–Ni, and Gd–Co–B compounds. The estimated A_{HoFe} value for pure "$HoFe_{12}$" is included (Zhong et al. 1990b).

tendency in the variation of A_{RCo} from one compound to another is found. Hereafter, attention will be focused on the results derived from T_C.

The results shown in fig. 16 could be ascribed to the distance dependence of the exchange interactions. This is unlikely however, since, as discussed in the preceding section, the inter-atomic 3d–5d interaction has no major contribution to the effective R–T coupling. It has been proposed by Duc et al. (1992a) that the origin of this behaviour may be found in the variable degree of 3d–5d hybridization. To illustrate this, the R-concentration dependence of A_{RT} is presented in fig. 17 for Gd–T and Gd–T–X (with T = Fe,Co, Ni and X = B, Ti, ...). The Gd-concentration dependence of the T-moments was already mentioned in sect. 7.1 (see fig. 14). Note that the A_{RT} and M_T variations are almost linear (with the exception of some R–Ni, R–T–B and $RT_{11}Ti$ compounds, which will be discussed in sect. 7.2.6), but with opposite tendencies. The decrease of M_T with increasing R concentration is usually ascribed to the increase in 3d–5d hybridization. The magnetic properties of 5d electrons and, consequently, the 4f–3d exchange interactions depend critically on this effect. In fact, it is well known from band-structure calculations for the Y–Fe compounds that the induced magnetic moment on Y atoms increases with increasing Fe concentration in spite of the decreasing Fe moment (Coehoorn 1990). Furthermore, Brooks and Johansson (1993) showed that increasing the strength of the 3d–5d hybridization usually leads to lower 3d moments but to higher A_{RT} values. The observed variation of both A_{RT} and M_T thus reflects the systematic decrease in the 3d–5d hybridization with increasing T-concentration. Then, a correlation between A_{RT} and M_T is expected for both the R–Fe and the R–Co systems. For the R–Ni system, the

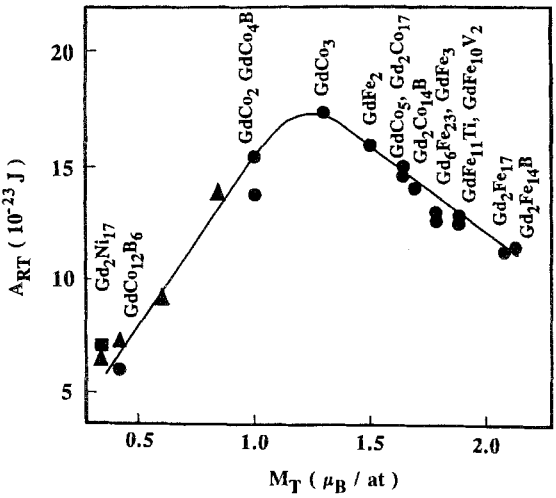

Fig. 18. A_{RT} as a function of the 3d-magnetic moment for a number of lanthanide intermetallics. Data reported for $Dy_2(Co_{1-x}Ni_x)_{17}$ (triangles) are included. After Duc (1993a).

correlation between A_{RT} and M_T is more complicated. It depends not only on the effect of the general hybridization but also on the degree of 3d–5d mixing in each subband, i.e. to the 3d-band splitting. Attempts to find a common empirical relationship between A_{RT} and the corresponding value of the 3d-magnetic moments had already been made earlier by Duc (1991) for the R–Fe and R–Co compounds. A linear relationship between both quantities was found to hold for a limited number of compounds (Duc et al. 1992a). Later, in order to investigate this relationship in a more extended way, Duc (1993a) has included the experimental data presently available as shown in fig. 18. A similar attempt has recently been done by Liu et al. (1994a). The data derived from the HFFP method for the Er compounds show the same variation of A_{RT}, however, with a considerable scatter.

For a given lanthanide, the variation of A_{RT} is thought to be determined mainly by the relation with S_{5d} (or rather the ratio of S_{5d}/S_{3d}, see eq. 4). However, due to the difficulties in the experimental determination of the value of the 5d magnetic moments, the results presented in fig. 18 are still plotted against M_T ($=M_{3d}-M_{5d}$), the total magnetic moment contributed by the 3d and 5d electrons. Experimentally, M_T is obtained from the magnetization in the compounds with non-magnetic lanthanides (R = Y, Lu) or in the Gd compounds (see table 1). It is clearly seen from this figure that A_{RT} starts to increase monotonously with increasing M_T in the compounds having small M_T-values. Then, it reaches a maximum at $M_T \approx 1.0\mu_B$/at and finally decreases with increasing M_T in almost all of the R–Fe and R–Co compounds (with $M_T > 1.0\mu_B$/at). Within the concept of the 3d–5d hybridization, these features can be understood as follows. Before hybridization, the pure 3d bands are almost filled and the pure 5d bands are almost empty. The pure 3d and 5d bands hybridize to form a mixing region at the top of the 3d bands and at the bottom of the 5d bands. When the 3d band is not split, i.e. the magnetic moment does not develop at T-sites, a 5d moment, though very small, may be induced by the exchange field from 4f moments, however, the 4f–3d interactions do not exist in this case. This is the reason

why the R–T interactions can usually be neglected in the RNi_2 compounds. Figure 17, fortunately, shows the tendency of A_{RT} to vanish at $M_T = 0$. When a moment develops at the T-sites, the energy of spin-up 3d states is lowered, reducing the 3d–5d hybridization for the spin-up states. This lowers the occupation of the 5d spin-up states. The opposite effect occurs for the spin-down states and the negative 5d moment, which is related to the 5d occupation, is induced. The 4f–5d and then the 4f–3d interactions are created. The induced 5d moment is therefore antiparallel to the 3d moment and strongly related to the 3d-band splitting. It turns out, in general, that the 3d–5d hybridization and then the strength of the 4f–5d interactions increase with increasing 3d-band splitting. For the R_2Ni_{17}, $R_2(Ni,Co)_{17}$, $RCo_{12}B_6$, RCo_4B and RCo_2 compounds, the effect of the 3d-band splitting on the increase of M_T seems to be most important, so that the increase of A_{RT} with increasing M_T is understandable.

For the compounds in which the 3d magnetism is well established (most of the R–Fe and R–Co compounds), the observed results suggests a decrease of the hybridization effects with increasing M_T. In these compounds, the 3d-band splitting can be considered to be almost saturated to its possible limit. This is evidenced by the result calculated by Trugg et al. (1992) that in $GdFe_{12}$ the value of M_T is equal to $2.12\mu_B$/Fe-at which is rather close to that observed in the pure Fe ion. Then the tendency of M_T to reach the value of the magnetic moment of pure Fe and Co metal with increasing T-concentration implies a slight decrease of M_{5d}, i.e. a reduction of the 3d–5d hybridization due to the decrease of the 5d-electron concentration contained in one formula unit of R_yT_{1-x} or $R_{y'}T_{1-y}X_{y''}$. On the other hand, the observed behaviour may indicate an increase of the energy separation between the 3d and 5d bands. Such a phenomenon can be expected to be the effect of volume, since an increase of volume will reduce the bandwidth. However, as already discussed in sect. 2 (see fig. 2), it can also be directly affected by the decreasing number of 5d electrons. Liu et al. (1994a) have recently found an interesting correlation between A_{RT} and the reciprocal value of the normalized molar volumes (V_m^{-1}) occupied by one formula unit of RT_xX_y. In this description, the number of the 5d electrons was kept constant and the exchange interactions were considered as a function of volume, i.e. as a function of the 5d electron density (ρ_{5d}). The interpretation of such behaviour is not simple since different physical parameters are involved. The first one is obviously the volume itself, as stressed by Liu et al. (1994a). Another important parameter is the number of 5d electrons shared by one R atom with all other T atoms in the surroundings. It is logical that A_{RT} be larger in R-rich alloys than in R-poor ones since it is expected that ρ_{5d} is then higher. The correlation between A_{RT} and the reciprocal value of the normalized volumes (V_m^{-1}) may be attributed to this fact as well as to volume effects since ρ_{5d} varies in the same way as V_m^{-1}. We reproduce the relation between A_{RT} and V_m^{-1} for Gd compounds in fig. 19. It may be seen from this figure that a fairly strong correlation between A_{RT} and V_m^{-1} is observed with a rather large scatter (of about 30%) of the experimental data for the compounds having low magnetic moments (for instance, such as R_2Ni_{17}, R_2Fe_7, $RCo_{12}B_6$ and RCo_4B compounds). This reflects that besides the role of the density of 5d electrons, one must bear in mind the effect of the 3d-band splitting on the 3d–5d hybridization. When the 3d-splitting is fixed, the 3d–5d hybridization will increase with decreasing normalized

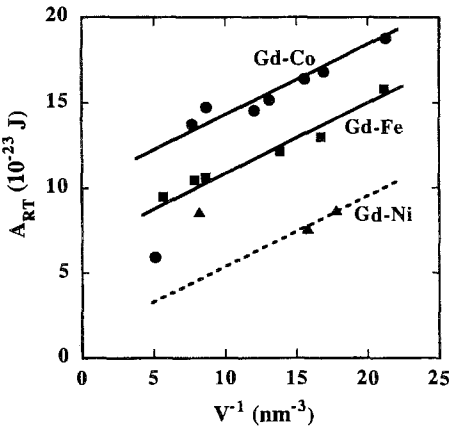

Fig. 19. A_{RT} as a function of the reciprocal values of the normalized volume per formula unit for a number of lanthanide intermetallics.

molar volume. It is the origin of the increase in A_{RT} (and decrease of M_T) with increasing R concentration in almost all of the R–Fe and R–Co intermetallics considered. However, it is worthwhile to mention here that one should not confuse this effect of the molar volume with that of the distance dependence of the R–T interactions, i.e. the volume of a crystal unit cell. It is well known that going from T-poor to T-rich compounds the R–T distance decrease (from 3.08 Å for $GdFe_2$ to 2.96 Å for Gd_2Fe_{17} and from 3.00 Å for $GdCo_2$ to 2.84 Å for Gd_2Co_{17}), although A_{RT} decreases. The 5d–3d interaction as discussed in the preceding section is distance independent and the 3d–5d interaction has no major contribution to the R–T coupling. The normalized molar volume dependence here may be related to the effect of the density of 5d states in a unit of normalized volume, but not the distance dependence. Nevertheless, this separation is important only when considering the R-concentration dependence. For a given composition of R_mT_n, the scale of the V_m and R–T distance is the same. However, even in this case the meaning of the density of 5d states is really important in a discussion of the physical mechanism of the intersublattice exchange interactions.

7.2.2. *Dependence of A_{RT} on the kind of lanthanide elements*

The values of T_C for the light lanthanide intermetallic compounds always reveal deviation from simple systematics. This deviation was taken as a characteristic feature of light lanthanide ions because of some peculiarities in the magnetic behaviour of Pr, Nd and Sm metals, which possibly are related to crystal field effects. Belorizky et al. (1987, 1988) were first to attribute this deviation to a substantial increase of the 4f–3d interaction towards the light lanthanides. However, a detailed examination of the values of the Curie temperatures in several series of lanthanide compounds reveals that this increase of the strength of the 4f–3d coupling parameter is extended across the lanthanide elements. This fact was confirmed by other methods, especially HFFP, on more than 20 series of heavy lanthanide compounds (Liu et al. 1994a). Nevertheless, in order to illustrate this trend for the complete series of lanthanides, the results derived from T_C are usually used. In fig. 20

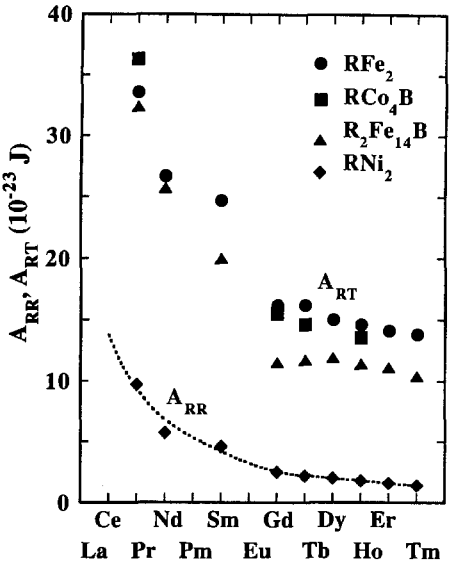

Fig. 20. A_{RT} and A_{RR} as a function of lanthanide elements for RFe_2, RCo_4B, $R_2Fe_{14}B$ and RNi_2. Data taken from Duc et al. (1993a).

we plot the R-dependence of A_{RT} for the RFe_2, $R_2Fe_{14}B$ and RCo_4B compounds. A similar trend is observed for other series. Note that the value of A_{RT} increases by a factor of about 3 (±0.2) when the component changes from Tm to Pr, whereas it increases only by a factor of about 1.2 (±0.2) from Tm to Gd. This enhancement in the exchange parameters has been quantitatively explained in terms of the distance decrease between the 4f and 5d shells from light to heavy lanthanide elements by Belorizky et al. (1987). According to Belorizky et al., the stronger decrease of the radius of the 4f-shell in comparison with the reduction of the atomic radius of the R ions leads to a smaller overlap of the 4f and 5d shells and consequently to a reduction of the 4d–3d exchange interactions. The self-consistent calculations by Brooks et al. (1991a–c) for the RFe_2 compounds show the other effect of the lanthanide contraction: it causes a substantial decrease in 5d occupation number. The decrease in lattice constant with increasing lanthanide atomic number is due to the decrease in size of the lanthanide component of the compound, which arises from the contraction of the 4f shell. The corresponding increase in the shielding of 5d states from the nucleus raises their energy and broadens the 5d energy bands. This increase of the unhybridized 5d bands reduces the 3d–5d hybridization and the charge transfer to the 5d states, i.e. reduces the 5d occupation numbers and then the R–T interactions.

In accordance with the correlation between A_{RT} and the normalized molar volume V_m, the decreasing lattice parameter alone would lead to an increase in the R–T interactions due to the enhancement of the 3d–5d hybridization. Band-structure calculations performed by Liu et al. (1994a) for hypothetical $GdFe_2$ with the lattice parameter of $ErFe_2$ (i.e. with the reduction of the cubic lattice parameter by 1.5%) shows that there is an increase in the exchange field of almost 10%. This means that within this mechanism the strength of the intersublattice exchange coupling would increase when passing through the lanthanide

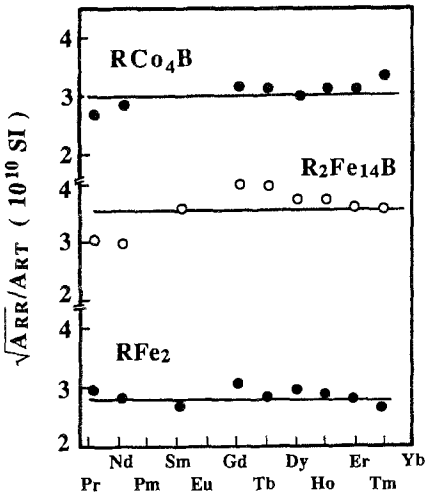

Fig. 21. Value of the ratio $r=\sqrt{A_{RR}}/A_{RT}$ (see text) for RFe_2, RCo_4B and $R_2Fe_{14}B$. After Duc et al. (1993a).

series, i.e. opposite to the effect of the 4f–5d distance. The combination of these opposite effects may be the reason that the enhancements of the 4f–3d interactions are somewhat different in the various series of the R–T compounds. As mentioned in sect. 6, the RFe_3 series may be an example where the effect of the 3d–5d mixing prevails, whereas in the R_2Co_7 series effects of the 4f–5d overlap and 5d–3d hybridization nearly cancel each other. The A_{RFe} data presented in fig. 20 for heavy lanthanide $R_2Fe_{14}B$ may be understood in the same sense.

According to Campbell's model (1972), the R–R interactions between localized 4f moments should exhibit a stronger variation, because in this interaction the 4f–5d part of the effective exchange interactions enters twice. To support this view, the ratio r (defined as $r=\sqrt{A_{RR}}/A_{RT}$) is usually considered (Belorizky et al. 1988, Duc et al. 1993a). Fortunately, r remains approximately constant going through the 4f series, see fig. 21. In particular, Duc et al. (1993b) have introduced factors $f_R=f_R(a)$, imagined to describe the intra-atomic (4f–5d) interaction, which is dependent on both the kind of lanthanide and the lattice parameter. Moreover, the inter-atomic interaction is allowed to depend on the lattice parameter by introducing a factor $f_{RR}=f_{RR}(a)$ and a factor $f_{RT}=f_{RT}(a)$ for the R–R and R–T interactions, respectively, independent of the kind of lanthanide. Then, one can write

$$A_{RR}=f_R(a)f_R(a)f_{RR}(a)A_{RR}(0), \qquad A_{RT}=f_R(a)f_{RT}(a)A_{RT}(0). \tag{50,51}$$

In order to be explicit, it was stated that $A_{RR}(0)$ and $A_{RT}(0)$ are constant (independent of the lattice parameter and kind of lanthanide). In fact they were chosen to be equal to the values for the Gd compounds. As we have discussed the variation of A_{RR} and A_{RT} over the complete series of lanthanide elements, the ratio $\sqrt{A_{RR}}/A_{RT}$ does not vary much over the series of lanthanide elements. Hence, in first approximation, one may assume f_{RR} and f_{RT},

or rather the ratio f_{RT}^2/f_{RR}, to be constant (unity). This reflects the distance independence of the inter-atomic interaction and as a result, confirms the major contribution of the 3d–5d hybridization to the strength of the R–T interactions.

7.2.3. *Dependence of A_{RT} on the nature of the 3d components*

The results presented in fig. 17 can also be used to discuss the increase of A_{RT} from Ni, Fe to Co. The fact that A_{RNi} exhibits the smallest value was to be expected, because the 3d-band splitting (and the Ni moment) is small, thus the difference of the 3d–5d hybridization between the spin subbands is small in the R–Ni compounds. In accordance with the relationship to the normalized molar volume (V_m) and the M_T (see sect. 7.2.1), the larger value of A_{RCo} in comparison with A_{RFe} is understandable, since in these two compounds both M_{Co} and $V_m(R_xCo_y)$ are smaller than the corresponding value for the compounds with Fe. As a result, one may expect that the 3d–5d hybridization decreases in the same sense, and so does A_{RT}. Nevertheless, the data derived from the HFFP method on the Er compounds show a tendency of A_{RT} to decrease in the sequence T = Fe, Co and Ni (Liu et al. 1994a). This comment, however, is not always clear, for instance, in the Er_2T_{17} system one finds $A_{RFe} = 8.8\times10^{-23}$ J, whereas $A_{RCo} = 9.5\times10^{-23}$ J (see table 2). These authors argued that going from Fe, Co to Ni the 3d electrons become more localized. For the Er-compounds, the effect of the competition between Er and Fe anisotropy can cause the easy direction of magnetization to be along the preferential direction of the 3d sublattice magnetization (Franse and de Boer 1995). This effect on the "free-powder" magnetization curves must be strict.

7.2.4. *Different effects of 3d–5d and 3d–4d hybridizations*

The HFFP method is free of any assumptions regarding the R–R interaction. However, because of the rather large difference of $|M_R - M_T|$ in almost all the lanthanide intermetallics, it can be applied for the substituted alloys only. When R is replaced by Y, the 4d electrons are introduced to the system. Thus, besides the 3d–5d hybridization, one should taken into account the influence of the 3d–4d mixing on the magnetic behaviour. For the HFFP studies, the Y substitution is applied when M_R is larger than M_T. As consequence, in the Fe, Co compounds, this "magnetic dilution" appears only in the R-rich ones, whereas it is applied to all of the R–Ni systems.

Liu et al. (1991a) have studied the R–T exchange interactions in the $(R_xY_{1-x})Fe_2$ and $(R_xY_{1-x})Fe_3$ compounds, in which $x \leqslant 0.4$ and $x \geqslant 0.45$ for the 1/2 and 1/3 compounds, respectively. Except for the $(Er,Y)Fe_2$ compounds, the value reported for A_{RFe} was deduced from the measurement on one substituted composition for almost all of the investigated series of compounds. The result, obtained for several compositions of $Er_xY_{1-x}Fe_2$, however, shows that n_{RFe} equals 31.2, 29.0, 26.7 and 28.0 T f.u./μ_B for $x = 0.25$, 0.3, 0.35 and 0.4, respectively (see table 4). Liu et al. assumed a large scatter of the n_{RFe} values, and reported a mean value of 28 T f.u./μ_B for $ErFe_2$. The result derived from the analysis of the compensation temperatures reported by Duc et al. (1988b), however, reflects a pronounced decrease of n_{RFe} with x, see also table 4. One may consider

Table 4
Molecular field coefficient n_{RFe} in the (Er,Y)Fe_2 compounds

Compound	x[a]	n_{RFe} (Tf.u./μ_B)	
		Liu et al. (1991a)	Duc et al. (1988b)
$ErFe_2$	1.0	28.8[b]	24.5
$Er_{0.8}Y_{0.2}Fe_2$	0.8		25.0
$Er_{0.6}Y_{0.4}Fe_2$	0.6		29.0
$Er_{0.40}Y_{0.60}Fe_2$	0.40	28.0	30.0
$Er_{0.35}Y_{0.65}Fe_2$	0.35	26.7	
$Er_{0.30}Y_{0.70}Fe_2$	0.30	29.0	
$Er_{0.25}Y_{0.75}Fe_2$	0.25	29.0	

[a] Formula $Er_xY_{1-x}Fe_2$.

[b] Data obtained from extrapolation (see the text).

Table 5
Exchange interaction parameter A_{RT} in a number of pseudo-binary intermetallic $(R,Y)_2Co_7$ and $(R,Y)_2Co_7B_3$ compounds

Compound	A_{RT} (10^{-23})	Reference	Compound	A_{RT} (10^{-23})	Reference
Gd_2Co_7			Dy_2Co_7		
$Gd_{1.5}Y_{0.5}Co_7$	15.5	Zhou et al. (1992a)	$Dy_{1.0}Y_{1.0}Co_7$	14.1	Zhou et al. (1992a)
$Gd_{1.4}Y_{0.6}Co_7$	16.0	Zhou et al. (1992a)	$Dy_{0.9}Y_{1.1}Co_7$	14.9	Zhou et al. (1992a)
$Gd_{1.3}Y_{0.7}Co_7$	17.5	Zhou et al. (1992a)	$Dy_{0.8}Y_{1.2}Co_7$	18.4	Zhou et al. (1992a)
Tb_2Co_7			$Er_2Co_7B_3$	9.1	Zhao (1994)
$Tb_{1.3}Y_{0.7}Co_7$	15.0	Zhou et al. (1992a)	$Er_{0.6}Y_{1.4}Co_7B_3$	27.3	Zhao et al. (1994)
$Tb_{1.2}Y_{0.8}Co_7$	14.5	Zhou et al. (1992a)	$Er_{0.5}Y_{1.5}Co_7B_3$	28.6	Zhao et al. (1994)
$Tb_{1.0}Y_{1.0}Co_7$	15.3	Zhou et al. (1992a)	$Er_{0.3}Y_{1.7}Co_7B_3$	32.8	Zhao et al. (1994)
			$Er_{0.1}Y_{1.9}Co_7B_3$	30.5	Zhao et al. (1994)

this behaviour of the R–T exchange coupling as an indication of the influence of the alloying effect, which causes the additional 3d–4d mixing. Accepting this assumption, the extrapolation of the HFFP data gives a value of about 14×10^{-23} J for A_{RFe} in $ErFe_2$. This value agrees well with that deduced from the analysis of the ordering temperature (Duc et al. 1993a, see also table 2) and allows one to explain the large difference between the data obtained from the HFFP method and the analysis of T_C. An extended model has also been applied in the analysis of the high-field magnetization for the series of $Er_2Co_7B_3$-based compounds (Zhao et al. 1994). Their set of A_{RCo} parameters also reflects the decrease of the strength of the R–T interactions as the Er concentration decreases, see table 5. A similar behaviour of A_{RT} was found in the HFFP studies on $(R,Y)_2Co_7$ by Zhou et al. (1992a). For the R–Ni compounds, the Y substitution reduces the molecular field

Table 6
Exchange interaction parameter A_{RT} in a number of pseudo-binary intermetallic $(R,Y)_2Ni_7$ and $(R,Y)_2Ni_{17}$ compounds

Compound	M_{Ni} (μ_B/f.u)	A_{RT} (10^{-23})	Reference
Gd_2Ni_7	1.2	18.0	Zhou et al. (1992b)
$Gd_{0.2}Y_{1.8}Ni_7$	0.56	21.3	Zhou et al. (1992b)
$Gd_{0.15}Y_{1.85}Ni_7$	0.69	14.9	Zhou et al. (1992b)
$Gd_{0.10}Y_{1.90}Ni_7$	0.42	15.5	Zhou et al. (1992b)
$Gd_{0.08}Y_{1.92}Co_7$	0.83	20.8	Zhou et al. (1992b)
$Gd_2Ni_{16.8}$	5.6	9.7	Zhong et al. (1990a)
$Gd_{0.8}Y_{1.2}Ni_{16.8}$	4.9	9.5	Zhong et al. (1990a)
$Gd_{0.7}Y_{1.3}Ni_{16.8}$	4.9	8.6	Zhong et al. (1990a)
$Gd_{0.6}Y_{1.4}Ni_{16.8}$	5.0	8.1	Zhong et al. (1990a)
$Gd_{0.5}Y_{1.5}Ni_{16.8}$	4.6	7.7	Zhong et al. (1990a)

acting on the 3d electrons and lowers the Ni magnetic moment. For the $(R,Y)_2Ni_7$ systems, unfortunately, the data are not clear enough to allow one to make a conclusion. The effects of the 3d-band splitting, however, seem to govern in the $(R,Y)_2Ni_{17}$ compounds (Zhong et al. 1990a; see table 6).

Recently, the different role of the 3d–5d and 3d–4d hybridizations on the R–T interactions was investigated detail by Dubenko et al. (1995) for the $(R,Lu)(Co,Al)_2$ and $(R,Y)(Co,Al)_2$ systems. The results are listed in table 3, and they show that in the Y-substituted compounds the R–T exchange interactions were strongly enhanced, whereas they are much smaller in the compounds substituted by Lu.

7.2.5. *R–T exchange interactions in the ternary R–(Fe,Co,Ni) compounds*

The ordering temperature and 3d-magnetic moment have been collected and considered systematically by Thuy et al. (1990) for the ternary Y–(Fe,Co) compounds. A characteristic feature of these compounds is that T_C and M_T vary non-linearly with the concentration. This is due to the effect of the preferential occupation and the different interactions between the 3d atoms located at different crystallographic sites (Herbst and Yelow 1986). Recently, Gavigan et al. (1988) have pointed out that in $Y_2(Co_{1-x}Fe_x)_{17}$ and $Y_2(Co_{1-x}Fe_x)_{14}B$ compounds, not only the Fe–Fe and the Co–Co interactions but also the Fe–Co ones have to be considered. The concentration dependence of the Curie temperatures can then be described by three characteristic temperatures T_{Fe}, T_{Co} and T_{Fe-Co} which are associated with the corresponding molecular field coefficients n_{FeFe}, n_{Co-Co} and n_{Co-Fe}, respectively. They found that Fe–Co interactions are not intermediate

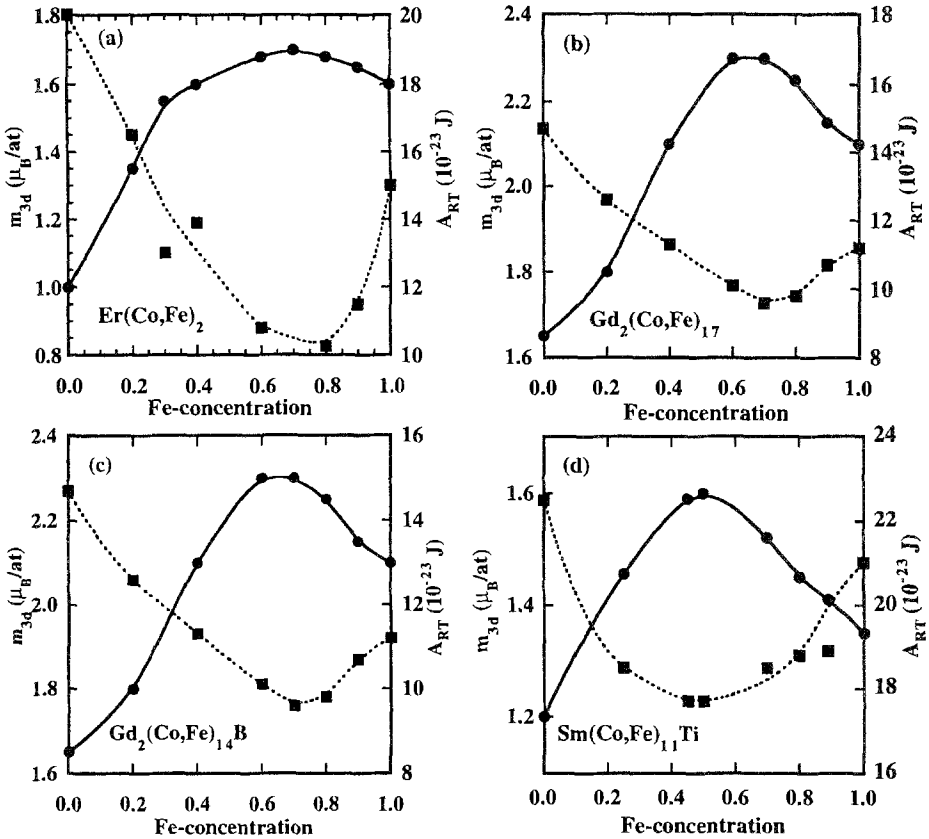

Fig. 22. The variations of mean d magnetic moments (circles) and A_{RT} (squares) as a function of Fe concentration for (a) $Er(Co,Fe)_2$, (b) $Gd_2(Co,Fe)_{17}$, (c) $Gd_2(Co,Fe)_{14}B$ and (d) $Sm(Co,Fe)_{11}Ti$. Data taken from Duc (1991).

between Fe–Fe and Co–Co interactions but are as large as Co–Co interactions. Applying the same procedure, Thuy et al. (1990) obtained as a result that T_{Fe-Co} is proportional to the product of the Fe and Co moments. In the estimation of the intersublattice exchange interaction, however, all of the 3d atoms at different sites are considered to be the same and an effective value of A_{RT} is deduced. A_{RT} data estimated from T_C were reported for $Er(Co_{1-x}Fe_x)_2$, $Gd_2(Co_{1-x}Fe_x)_{17}$, $Gd_2(Co_{1-x}Fe_x)_{14}B$ and $Sm(Co_{1-x}Fe_x)_{11}Ti$ by Duc (1991). Note that, in these systems, when going from Co-rich to Fe-rich compounds the volume increases monotonously, whereas the concentration dependence of A_{RT} in these four ternary systems shows a common complex behaviour, i.e., with increasing Fe content, A_{RT} initially decreases and then increases. Thus, $A_{RT}(x)$ shows a minimum at the composition corresponding to the maximum in the M_T curves, see fig. 22. As a result, an almost linear decrease of A_{RT} with increasing M_T is found, as plotted in

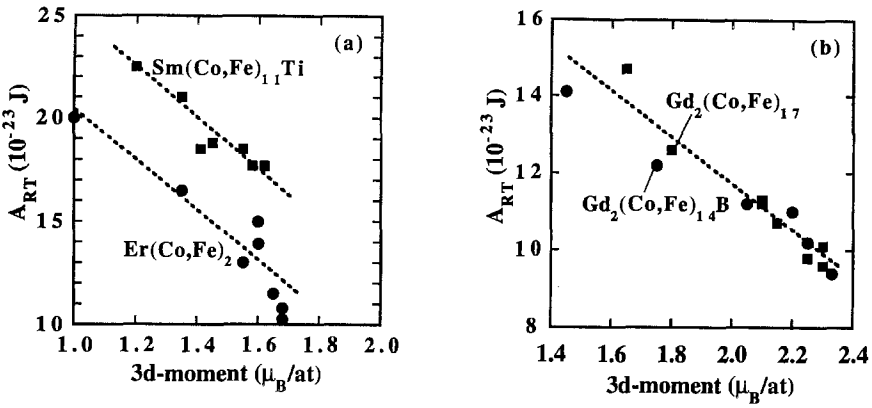

Fig. 23. Relationship between A_{RT} and d moment in (a) $Er(Co,Fe)_2$ and $Sm(Co,Fe)_{11}Ti$ compounds and (b) $Gd_2(Co,Fe)_{17}$ and $Gd_2(Co,Fe)_{14}B$ compounds. After Duc (1991).

fig. 23. A linear relationship between A_{RT} and M_T also appears with the data derived from the HFFP method for $R_2(Fe_{1-x}Al_x)_{17}$ (Jacobs et al. 1992a–c, Li 1993 and references therein), see table 7. For the R–(Co,Ni) and R–(Fe–Ni) compounds a linear relationship between A_{RT} and M_T has also been found, however, as mentioned above, with the opposite tendency. This was already illustrated in fig. 18 for $Dy_2(Co_{1-x}Ni_x)_{17}$ (Duc 1993b). We noted that another example for this can be found for $Gd(Co_{5-x}Ni_x)$ compounds, see fig. 24 (Liu et al. 1991b).

Table 7
Exchange interaction parameter A_{RT} in a number of pseudo-binary intermetallic R–(T,Al,Si,C) compounds

Compound	A_{RT} (10^{-23})	Reference	Compound	A_{RT} (10^{-23})	Reference
$DyCo_2$	18.0	Duc (1996)[a]	Er_2Fe_{17}	8.8	Sinnema (1988)
$Dy(Co_{0.95}Si_{0.05})_2$	15.1	Duc (1996)[a]	$Er_2Fe_{14}Al_3$	11.5	Li (1993)
$Dy(Co_{0.92}Si_{0.08})_2$	13.5	Duc (1996)[a]	$Er_2Fe_{13}Al_4$	10.4	Li (1993)
$Dy(Co_{0.9}Si_{0.1})_2$	12.0	Duc (1996)[a]	$Er_2Fe_{12}Al_5$	10.4	Li (1993)
Ho_2Fe_{17}	9.7	Jacobs et al. (1992a)	$Er_2Fe_{11}Al_6$	10.4	Li (1993)
$Ho_2Fe_{14}Al_3$	9.4	Jacobs et al. (1992a)	$Er_2Fe_{10}Al_7$	11.3	Jacobs et al. (1992c)
$Ho_2Fe_{13}Al_4$	10.8	Jacobs et al. (1992a)	$Er_2Fe_9Al_8$	12.7	Jacobs et al. (1992c)
$Ho_2Fe_{12}Al_5$	11.5	Jacobs et al. (1992a)	$Er_2Fe_8Al_9$	12.3	Jacobs et al. (1992c)
$Ho_2Fe_{11}Al_6$	11.3	Jacobs et al. (1992a)	$Er_2Fe_{17}C_{1.0}$	10.1	Liu et al. (1994b)
$Ho_2Fe_{10}Al_7$	12.4	Jacobs et al. (1992a)	$Er_2Fe_{17}C_{1.5}$	9.9	Liu et al. (1994b)
$Ho_2Fe_9Al_8$	11.6	Jacobs et al. (1992a)	$Er_2Fe_{17}C_{2.0}$	9.7	Liu et al. (1994b)
Ho_2Fe8Al_9	13.8	Jacobs et al. (1992a)	$Er_2Fe_{17}C_{2.5}$	9.3	Liu et al. (1994b)
$Ho_2Fe_7Al_{10}$	16.4	Jacobs et al. (1992a)	$Er_2Fe_{17}C_{3.0}$	9.1	Liu et al. (1994b)

[a] See also Duc and Oanh (1997).

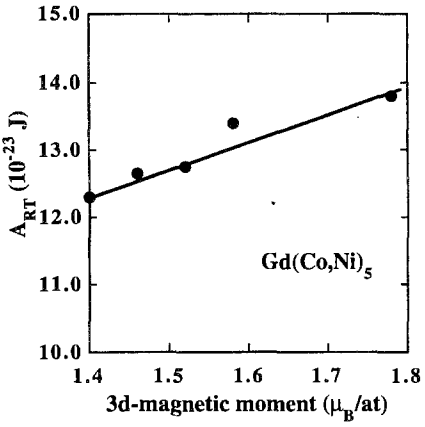

Fig. 24. A_{RT} as a function of M_T in $Gd(Co_{1-x}Ni_x)_5$. Data taken from Liu et al. (1991b).

7.2.6. *Effects of the 3d–p hybridization*

Once more, we return to the results presented in fig. 17 for the R-concentration dependence of A_{RT} with a note that the data obtained for RCo_4B compounds and even more for $RCo_{12}B_6$ do not follow those characterizing the binary compounds. In these compounds, both M_T and A_{RT} are below the expected values. This can be ascribed to the 3d–p hybridization which is important as shown by the high stability of lanthanide borides. This result suggests a decrease in the 3d–5d hybridization (Duc et al. 1993a). Electronic-structure calculations for $Y(Co,Al)_2$ and $Y(Co,Si)_2$ have been done by Aoki and Yamada (1992). It is shown that by substitution of Al or Si for Co, some 3d states of Co hybridize strongly with the 3p-states of the Al(Si) atom, which results in a modification of the electronic structure and in the lowering of the Fermi level and the 3d–5d hybridization. Experimentally, the Al substitution does not affect A_{RT} in the $R(Co,Al)_2$ compounds (Brommer et al. 1993, Ballou et al. 1993b), whereas a decrease of A_{RT} is found in the Si-substituted $R(Co,Si)_2$ compounds (Duc 1996, Duc and Oanh 1997), see table 7. On the other hand, substitution of Al for Fe in the $R_2(Fe,Al)_{17}$ enhances the R–T interactions (Jacobs et al. 1992a, Li 1993), see also table 7. The difference in effects caused by different substituents was explained by the different atomic 3p energy levels of Al and Si.

Figure 25 presents the dependence of A_{RT} on the ratio n/k for the boride alloys $R_mCo_nB_k$ (Duc and Givord 1995a, 1996). The decrease of A_{RT} with decreasing n/k is indicated. As discussed in sect. 7.1, this is due to the increasing 3d–p hybridization with increasing B concentration. The effects of the interstitial C atoms on the coupling constant were recently studied by Liu et al. (1994c). A_{RT} shows a tendency to decrease with increasing C content in the $Er_2Fe_{17}C_x$ as presented in fig. 26a (see also table 7). This was discussed in terms of a volume effects, see fig. 26b. However, the effects of the 3d–p hybridization on the intersublattice exchange coupling should also be considered here. The $R(Fe,X)_{12}$ compounds show another aspect. It is the difference in the 3d–5d hybridizations caused by the 3d transition metal with less half-filled and more half-

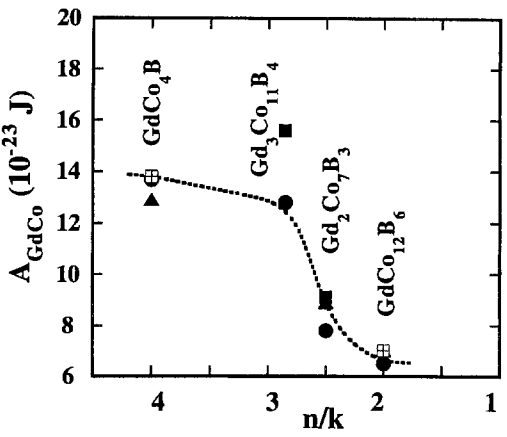

Fig. 25. A_{RT} as a function of n/k ratio in a number of $R_mCo_nB_k$ compounds. After Duc (1996).

filled bands. HFFP studies on $HoFe_{2-x}V_x$ show that the R–T exchange coupling is enhanced by V substitution (Zhong et al. 1990b, Duc et al. 1997b), see sect. 6.7 and table 8. In these systems, V atoms were found to have a small moment coupled parallel to the R spin moment (Coehoorn 1990, Jaswal et al. 1990), and this may be the reason that A_{RT} deduced for the $RFe_{12-x}M_x$ compounds is a little bit higher than the value expected for the "pure" RT_{12} compounds. Zhong et al. (1990b) have suggested that a mean-field approximation can lead to a consistent description of all the magnetic properties, if the presence of this magnetic moment is taken into account. The value of A_{RFe} for the "RFe_{12}" is then obtained by extrapolating the variation of A_{RT} as a function of V concentration. The value $A_{RFe} = 9.5 \times 10^{-23}$ J reported for "$HoFe_{12}$" fits well the tendency to decrease of intersublattice exchange coupling with increasing iron concentration, see fig. 17.

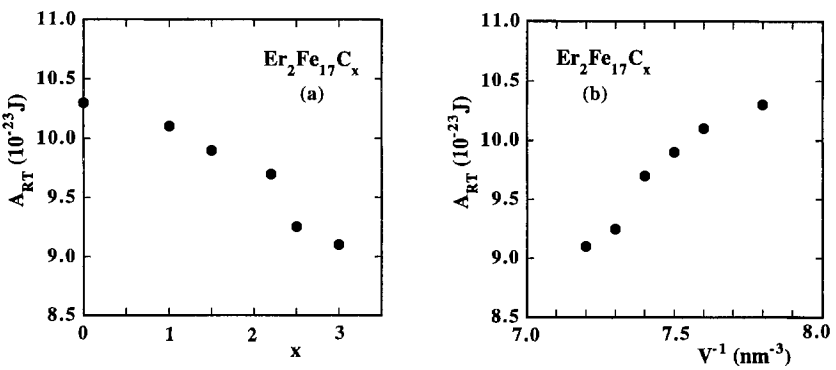

Fig. 26. Dependence of A_{RT} (a) on carbon content x and (b) on the reciprocal unit cell volume normalized to one R atom, in $Er_2Fe_{17}C_x$. After Liu (1994) and Liu et al. (1994c).

Table 8
Exchange interaction parameter A_{RT} in a number of the pseudo-binary intermetallic "RT_{12}" compounds[a]

Compound	A_{RT} (10^{-23})	Compound	A_{RT} (10^{-23})
"$HoFe_{12}$"	9.7	"$ErFe_{12}$"	8.3
$HoFe_{9.0}V_{3.0}$	14.0	$ErFe_{9.0}V_{3.0}$	11.7
$HoFe_{8.5}V_{3.5}$	16.7	$ErFe_{8.5}V_{3.5}$	13.7
$HoFe_{8.0}V_{4.0}$	18.1	$HoFe_{8.0}V_{4.0}$	17.0

[a] Data from Liu et al. (1994c).

8. Towards a better understanding of the exchange interactions in lanthanide compounds

In the last decade, enormous progress has been made in the study of the basic magnetic interactions. Experimental determination of the intersublattice coupling between the lanthanide and 3d magnetic sublattices has been carried out by means of both macroscopic and microscopic measurements. The systematic variation of the coupling parameter with the lanthanide and the 3d partner, as well as the lanthanide concentration in the intermetallics has been addressed. The detailed mechanism of exchange interactions including the role of the 3d–5d hybridization has also been provided. These findings are very interesting for discussing a unified picture of electronic and magnetic properties of lanthanide–transition-metal intermetallic compounds. The empirical correlation between the strength of the R–T exchange coupling and the magnitude of the magnetic moment of the 3d ion involved in the interaction does not mean that the origin of the exchange interactions is from the 3d-magnetic moment. This relationship confirms that not only 3d magnetism but also 4f–3d exchange coupling can be described by the same physical mechanism of the hybridization between the 3d and 5d states. An effect of the volume on the 3d–5d hybridization is expected. However, the volume effects, in the competition with the effects of the concentration of 5d electrons and of the lanthanide contraction, have not been well addressed. The separation of these effects requires experiments under high pressure. Before closing this chapter, it is worthwhile to mention that, in connection with the application of the HFFP technique, numerous extensions have been going on leading to further investigations on this topic. Recently, developments of the model to a system consisting of three magnetic sublattices have been provided by Colpa and Brabers (1994) and Brommer (1996). In this description, two or three types of exchange interactions are considered. It allows one to take into account the multiplicity of the crystallographic sites. The application was performed on the RMn_6Ge_6 system which shows antiferromagnetic coupling within the Mn sublattice. The first results for the exchange parameter A_{RMn} are in line with those for A_{RFe} and A_{RCo} (Brabers et al. 1994). This is an important starting point in considering effects of the hybridization between the 3d states in the nearly half- (or less than half-) filled d band and the 5d states on the exchange interactions. The traditional

HFFP method was described on the basis of the so-called two-(antiferromagnetically coupled) sublattice model. Until now, the application of the HFFP method, thus, has been limited to the compounds with heavy lanthanide elements. There is a possibility to extend the application of HFFP for whole lanthanide series that one can consider the compounds containing both heavy (HR) and light (LR) lanthanide elements, namely, $(HR_{1-x}LR_x)$–T compounds (Duc et al. 1995). In the case where T is non-magnetic, the $(HR_{1-x}LR_x)$–T compounds can be splitted in two subsystems of HR and LR with magnetic moments antiparallelly aligned. This is an acceptable subject to investigate the strength of the HR–LR interactions. When T is magnetic and if a three-sublattice model is available, moreover, not only the HR–LR and HR–T interactions but also the LR–T ones can be evaluated. Finally, amorphous alloys containing lanthanide metals are also of interest. They offer the possibility to study various aspects of 3d and 4f magnetism in a continuous range of lanthanide concentrations. For this class of materials, it has been found that the value for the intrinsic intersublattice exchange parameter and its variation is similar to that observed for crystalline lanthanide compounds (Radwanski and Franse 1993, Duc and Givord 1995a,b).

Acknowledgements

I would like to thank all my colleagues of the Cryogenic Laboratory for helpful discussions and comments. I am especially indebted to Professor Dr. J.J.M. Franse and Dr. D. Givord for valuable suggestions. Dr. P.E. Brommer and Dr. N.H. Luong have done a lot in order to make the manuscript readable. I have also benefited of the fruitful cooperation between the Universities of The Netherlands and Vietnam, in which Dr. F.F. Bekker and Professor Dr. T.D. Hien have played an important part. The support of the PRI-PED scheme (CNRS-France) for my stay in Grenoble has been useful for the completion of this work.

References

Aoki, M., and H. Yamada, 1989, J. Magn. & Magn. Mater. **78**, 377.

Aoki, M., and H. Yamada, 1992, Physica B **177**, 259; J. Magn. & Magn. Mater. **104–107**, 1965.

Atzmony, U., and M.B. Dariel, 1976, Phys. Rev. B **13**, 4006.

Aubert, G., D. Gignoux, F. Givord, R. Lemaire and B. Michelotti, 1978, Solid State Commun. **25**, 85.

Ballou, R., B. Gorges, H. Rakato and J.C. Ousset, 1989, Physica B **155**, 266.

Ballou, R., R.J. Radwanski, R. Lemaire and J.J.M. Franse, 1992, Physica B **177**, 262.

Ballou, R., Z.M. Gamishidze, R. Lemaire, R.Z. Levitin, A.S. Markosyan and V.V. Snegirev, 1993a, Sov. Phys. J.E.T.P. **75**, 1041.

Ballou, R., E. Burzo, A. Mincic and V. Pop, 1993b, J. Magn. & Magn. Mater. **118**, L285.

Belorizky, E., M.E. Fremy, J.P. Gavigan, D. Givord and H.S. Li, 1987, J. Appl. Phys. **61**, 3971.

Belorizky, E., J.P. Gavigan, D. Givord and H.S. Li, 1988, Europhys. Lett. **5(4)**, 349.

Bloch, D., and R. Lemaire, 1970, Phys. Rev. B **2**, 2468.

Brabers, J.H.V.J., G.F. Zhou, F.R. de Boer and K.H.J. Buschow, 1993, J. Magn. & Magn. Mater. **118**, 339.

Brabers, J.H.V.J., Q.A. Li, F.R. de Boer and K.H.J. Buschow, 1994, Trans. Magn. **30**, 1190.

Brommer, P.E., 1989, Physica B **154**, 197.

Brommer, P.E., 1991, Physica B **173**, 277.

Brommer, P.E., 1996, J. Magn. & Magn. Mater. **157/158**, 349.

Brommer, P.E., I.S. Dubenko, J.J.M. Franse, R.Z. Levitin, A.S. Markosyan, R.J. Radwanski, V.V. Snegirev and A.V. Solokov, 1993, Physica B **183**, 363.

Brooks, M.S.S., and B. Johansson, 1983, J. Phys. F **13**, L197.

Brooks, M.S.S., and B. Johansson, 1993, in: Ferromagnetic Materials, Vol. 7, ed. K.H.J. Buschow (North-Holland, Amsterdam) p. 139–230.

Brooks, M.S.S., O. Eriksson and B. Johansson, 1989, J. Phys. Condens. Matter **1**, 5861.

Brooks, M.S.S., L. Nordström and B. Johansson, 1991a, J. Phys. Condens. Matter **3**, 2357.

Brooks, M.S.S., L. Nordström and B. Johansson, 1991b, J. Phys. Condens. Matter **3**, 3393.

Brooks, M.S.S., L. Nordström and B. Johansson, 1991c, Physica B **172**, 95.

Burzo, E., 1970, C.R. Acad. Sci. Paris, Ser. B **271**, 1159.

Burzo, E., E. Oswald, M.Q. Huang, E. Boltich and W.E. Wallace, 1985, J. Appl. Phys. **57**, 4709.

Burzo, E., I. Creanga and M. Ursu, 1987, Solid State Commun. **64**, 585.

Buschow, K.H.J., 1980, in: Ferromagnetic Materials, Vol. 1, ed. E.P. Wohlfarth (North-Holland, Amsterdam) p. 297.

Buschow, K.H.J., D.B. de Mooij, X.P. Zhong and F.R. de Boer, 1990, Physica B **162**, 83.

Campbell, I.A., 1972, J. Phys. F **2**, L47.

Castets, A., D. Gignoux and B. Hennion, 1980, J. Magn. & Magn. Mater. **15–18**, 375.

Clark, A., and E. Callen, 1968, J. Appl. Phys. **39**, 5972.

Clausen, K.N., 1981, Riso National Laboratory Report, Riso R-426.

Coehoorn, R., 1989, Phys. Rev. B **39**, 13072.

Coehoorn, R., 1990, Phys. Rev. B **41**, 11790.

Coey, J.M.D., 1986, J. Less-Common Met. **126**, 21.

Colpa, J.C., and J.H.V.J. Brabers, 1994, Physica B **203**, 29.

Cyrot, M., and M. Lavagna, 1979, J. Phys. (Paris) **40**, 763.

de Boer, F.R., and K.H.J. Buschow, 1992, Physica B **177**, 199.

de Boer, F.R., X.P. Zhong, K.H.J. Buschow and J.H. Jacobs, 1990, J. Magn. & Magn. Mater. **90–91**, 25.

de Gennes, P.G., 1962, J. Phys. Radiat. **23**, 510.

de Wijn, H.W., A.M. van Diepen and K.H.J. Buschow, 1976, Phys. Status Solidi B **76**, 11.

Drzazga, Z., and M. Drzazga, 1987, J. Magn. & Magn. Mater. **65**, 21.

Drzazga, Z., and T. Mydlarz, 1988, J. Phys. (Paris) **49**, C8-515.

Dubenko, I.S., R.Z. Levitin, A.S. Markosyan and A.Yu. Sokolov, 1995, J. Magn. & Magn. Mater. **140–144**, 825.

Duc, N.H., 1991, Phys. Status Solidi B **164**, 545.

Duc, N.H., 1993a, Phys. Status Solidi B **175**, K63.

Duc, N.H., 1993b, Phys. Status Solidi B **176**, K29.

Duc, N.H., 1994, J. Magn. & Magn. Mater. **131**, 224.

Duc, N.H., 1996, J. Magn. & Magn. Mater. **152**, 219.

Duc, N.H., and D. Givord, 1995a, Proc. 2nd Int. Workshop on Materials Science, Hanoi, 10/1995, eds F.F. Bekker, N.D. Chien, J.J.M. Franse and T.D. Hien, p. 107.

Duc, N.H., and D. Givord, 1995b, J. Magn. & Magn. Mater. **151**, L13.

Duc, N.H., and D. Givord, 1996, J. Magn. & Magn. Mater. **157/158**, 169.

Duc, N.H., and T.K. Oanh, 1997, J. Phys. Condens. Matter **9**, 1585.

Duc, N.H., T.D. Hien, P.E. Brommer and J.J.M. Franse, 1988a, J. Phys. F **18**, 275.

Duc, N.H., T.D. Hien, N.H. Chau and J.J.M. Franse, 1988b, J. Phys. **49**, 509.

Duc, N.H., T.D. Hien and N.H. Chau, 1990, Acta Phys. Pol. A **78**, 471.

Duc, N.H., T.D. Hien and D. Givord, 1992a, J. Magn. & Magn. Mater. **104–107**, 1334.

Duc, N.H., T.D. Hien, P.E. Brommer and J.J.M. Franse, 1992b, J. Magn. & Magn. Mater. **104–107**, 1252.

Duc, N.H., D. Givord, C. Lacroix and C. Pinettes, 1992c, Europhys. Lett. **20**, 47.

Duc, N.H., T.D. Hien, D. Givord, J.J.M. Franse and F.R. de Boer, 1993a, J. Magn. & Magn. Mater. **124**, 305.

Duc, N.H., P.E. Brommer and J.J.M. Franse, 1993b, Physica B **191**, 239.

Duc, N.H., P.E. Brommer, F. Kayzel, C.V. Thang and J.J.M. Franse, 1995, Proc. 2nd Int. Workshop on Materials Science, Hanoi, 10/1995, eds F.F. Bekker, N.D. Chien, J.J.M. Franse and T.D. Hien, p. 137.

Duc, N.H., A.Yu. Sokolov, R.Z. Levitin and P.E. Brommer, 1997a, in preparation.

Duc, N.H., M.M. Tan, N.D. Tan, D. Givord and J. Teillet, 1997b, presented at ICM '97, J. Magn. & Magn. Mater., to be published.

Dumelow, T., P.C. Riedi, P. Mohn, K. Schwarz and Y. Yamada, 1986, J. Magn. & Magn. Mater. **54–57**, 1081.

Ermolenko, A.S., 1980, Fiz. Met. Metalloved. 50, 741 [Phys. Met. Metall. **50**, 57].

Ermolenko, A.S., 1982, in: Proc. 6th Int. Workshop on Lanthanide–Cobalt Permanent Magnets, ed. J. Fidler (Technical Univ. Viena) p. 771.

Ermolenko, A.S., 1985, Sov. Phys. Solid State **27(1)**, 148.

Fähnle, M., K. Hummler, M. Liebs and T. Beuerle, 1993, J. Appl. Phys. A **57**, 67.

Farrell, J., and W.E. Wallace, 1966, Inorg. Chem. **5**, 105.

Franse, J.J.M., and F.R. de Boer, 1995, J. Mag. & Magn. Mater. **140–144**, 789.

Franse, J.J.M., and R.J. Radwanski, 1993, in: Ferromagnetic Materials, Vol. 7, ed. K.H.P. Buschow (North-Holland, Amsterdam) p. 307.

Franse, J.J.M., F.R. de Boer, P.H. Fring, R. Gersdorf, A. Menovsky, R.J. Radwanski and S. Sinnema, 1985, Phys. Rev. B **31**, 4347.

Franse, J.J.M., R.J. Radwanski and A. Menovsky, 1986, J. Magn. & Magn. Mater. **54–57**, 1639.

Franse, J.J.M., F.E. Kayzel, C. Marquina, R.J. Radwanski and R. Verhoef, 1992, J. Alloys & Compounds **181**, 95.

Friedel, J., 1958, Nuovo Cimento Suppl. **N2**, 287.

Frings, P.H., J.J.M. Franse and G. Hilscher, 1983, J. Phys. F **13**, 175.

Gavigan, J.P., D. Givord, H.S. Li and J. Voiron, 1988, Physica B **149**, 345.

Germano, D.J., and R.A. Butera, 1981, Phys. Rev. **24**, 3912.

Gignoux, D., and F. Givord, 1979, J. Phys. F **9**, 1409.

Gignoux, D., and D. Schmitt, 1991, J. Magn. & Magn. Mater. **100**, 99.

Gignoux, D., F. Givord and R. Lemaire, 1975, Phys. Rev. B **12**, 3878.

Gignoux, D., F. Givord and W.C. Koehler, 1977a, Physica B **88–86**, 165.

Gignoux, D., F. Givord and J. Schweizer, 1977b, J. Phys. F **7**, 1823.

Gignoux, D., F. Givord, W.C. Koehler and R.M. Moon, 1977c, J. Mag. & Magn. Mater. **5**, 1972.

Gignoux, D., R. Lemaire, P. Mohlo and F. Tasset, 1980, J. Magn. & Magn. Mater. **21**, 307.

Givord, D., and R. Lemaire, 1974, IEEE Trans. Magn. **10**, 109.

Givord, D., H.S. Li, J.M. Cadogan, J.M.D. Coey, J.P. Gavigan, O. Yamada, H. Maruyama, M. Sawaga and H. Hirosawa, 1988, J. Appl. Phys. **63**, 3713.

Goto, T., T. Sakakibara, K. Mutara, H. Komatsu and K. Fukamichi, 1991, J. Magn. & Magn. Mater. **90–91**, 700.

Goto, T., K. Koui, M.I. Bartashevich, H.A. Katori, M. Yamaguchi, I. Yamoto and F. Sugaya, 1994, Tech. Rep. of ISSP A2707 (University of Tokyo).

Gubbens, P.C.M., and K.H.J. Buschow, 1982, J. Phys F **12**, 2715.

Gubbens, P.C.M., A.M. van der Kraan and K.H.J. Buschow, 1984, J. Phys. F **14**, 235.

Gubbens, P.C.V., A.M. van der Kraan and K.H.J. Buschow, 1988, J. Phys. **12**, 591.

Herbst, J.F., and W.B. Yelow, 1986, J. Appl. Phys. **60**, 4224.

Hong, N.M., N.P. Thuy and J.J.M. Franse, 1990, in: 6th Int. Symp. Magnetic Anisotropy and Coercivity in Rare Earth–Transition Metal Alloys, ed. S.G. Sankar (Carnegie Mellon University, Pittsburgh) p. 230.

Jacobs, J.H., K.H.J. Buschow, G.F. Zhou, X. Li and F.R. de Boer, 1992a, J. Magn. & Magn. Mater. **116**, 220.

Jacobs, J.H., K.H.J. Buschow, G.F. Zhou, J.P. Liu, X. Li and F.R. de Boer, 1992b, J. Magn. & Magn. Mater. **104–107**, 1275.

Jacobs, J.H., K.H.J. Buschow, G.F. Zhou and F.R. de Boer, 1992c, Physica **179**, 177.

Janak, J.F., 1977, Phys. Rev. B **16**, 255.

Jaswal, S.S., Y.G. Ren and D.J. Sellmyer, 1990, J. Appl. Phys. **67**, 4564.

Kebe, B., 1983, Thesis (Grenoble).

Kirchmayr, H., and C.A. Poldy, 1978, J. Magn. & Magn. Mater. **8**, 1.

Klein, B.M., W.E. Pickett, D.A. Paraconstantopoulos and L.L. Boyer, 1983, Phys. Rev. B **27**, 6721.

Koon, N.C., and J.J. Rhyne, 1981, Phys. Rev. B **23**, 2078.

Koon, N.C., C.M. Williams and B.N. Das, 1991, J. Magn. & Magn. Mater. **100**, 173.

Kou, C.X., T.S. Zhao, R. Grössinger, H.R. Krichmayr, X. Li and F.R. de Boer, 1992, Phys. Rev. B **46**, 11204.

Laforest, J., 1981, Thesis (Grenoble).

Lemaire, R., 1966, Cobalt **33**, 201.

Li, H.S., Y.P. Li and J.M.D. Coey, 1991, J. Phys. Condens. Matter **3**, 7227.

Li, H.S., Y.P. Li and J.M.D. Coey, 1992, J. Magn. & Magn. Mater. **104–107**, 1444.

Li, Q.A., 1993, Thesis (Institute of Physis, Beijing).
Liebs, M., K. Hummler and M. Fähnle, 1992, Phys. Rev. B **46**, 11201.
Liebs, M., K. Hummler and M. Fähnle, 1993, J. Magn. & Magn. Mater. **124**, 239.
Liu, J.P., 1994, Thesis (University of Amsterdam).
Liu, J.P., F.R. de Boer and K.H.J. Buschow, 1991a, J. Magn. & Magn. Mater. **98**, 291.
Liu, J.P., F.R. de Boer and K.H.J. Buschow, 1991b, J. Appl. Phys. **69**, 5536.
Liu, J.P., F.R. de Boer and K.H.J. Buschow, 1991c, J. Less-Common Met. **175**, 137.
Liu, J.P., F.R. de Boer, P.F. de Châtel, R. Coehoorn and K.H.J. Buschow, 1994a, J. Magn. & Magn. Mater. **134**, 159.
Liu, J.P., Z.D. Zang, D.C. Zeng, N. Tang, P.F. de Châtel, F.R. de Boer and K.H.J. Buschow, 1994b, IEEE Trans. Magn. **30**, 849.
Liu, J.P., F.R. de Boer, P.F. de Châtel and K.H.J. Buschow, 1994c, cited by Liu (1994).
Loewenhaupt, M., I. Sosnowska, A. Taylor and R. Osborn, 1991, J. Appl. Phys. **69**, 5593.
Néel, L., 1948, Ann. Phys. **3**, 137.
Nordström, L., M.S.S. Brooks and B. Johansson, 1992, J. Magn. & Magn. Mater. **104–107**, 1378.
Pędziwiatr, A.T., S.V. Jaiang, W.E. Wallace, E. Burzo and V. Pop, 1987, J. Magn. & Magn. Mater. **66**, 69.
Perkins, R.S., and S. Strassler, 1977, Phys. Rev. B **15**, 477.
Poldy, C.A., and K.N.R. Taylor, 1972, J. Phys. F **2**, L105.
Radwanski, R.J., 1986a, Phys. Status Solidi B **137**, 486.
Radwanski, R.J., 1986b, Z. Phys. B **65**, 65.
Radwanski, R.J., and J.J.M. Franse, 1992, Physica B **177**, 193.
Radwanski, R.J., and J.J.M. Franse, 1993, J. Magn. & Magn. Mater. **119**, 221.
Radwanski, R.J., J.J.M. Franse and S. Sinnema, 1985, J. Phys. F **15**, 969.
Radwanski, R.J., X.P. Zhong, F.R. de Boer and K.H.J. Buschow, 1990, Physica B **164**, 131.
Radwanski, R.J., J.J.M. Franse, P.H. Quang and F.E. Kayzel, 1992a, J. Magn. & Magn. Mater. **104–107**, 1321.
Radwanski, R.J., X.P. Zhong, F.R. de Boer, F.M. Yang, J.Y. Li, T. Kohashi, M. Ono, M. Data and A. Yamaguchi, 1992b, J. Magn. & Magn. Mater. **104–107**, 1139.
Radwanski, R.J., J.J.M. Franse, D. Gignoux, F.E. Kayzel, C. Marquina and A. Szewcyk, 1992c, Physica B **177**, 291.
Radwanski, R.J., J.J.M. Franse and R. Verhoef, 1992d, J. Magn. & Magn. Mater. **83**, 127.
Rhyne, J.J., 1987, J. Magn. & Magn. Mater. **70**, 88.
Ritter, C., 1989, J. Phys. Condens. Matter **1**, 2765.
Roeland, L.W., G.J. Cock, F.A. Muller, C.A. Moleman, K.A. McEwen, R.C. Jordan and D.W. Jones, 1975, J. Phys. F **5**, L233.
Ruderman, M.A., and C. Kittel, 1954, Phys. Rev. **96**, 99.
Sankar, S.G., V.U.S. Rao, E. Segal, W.E. Wallace, W.G.D. Frederick and H.J. Garrett, 1975, Phys. Rev. B **11**, 435.
Shimizu, M., 1964, Proc. Phys. Soc. **84**, 397.
Shimizu, M., 1965, Proc. Phys. Soc. **85**, 147.
Simmons, M., J.M. Moreau, W.J. James, F. Givord and R. Lemaire, 1973, J. Less-Common Met. **30**, 75.
Sinnema, S., 1988, Thesis (Amsterdam).
Sinnema, S., J.M.M. Franse, R.J. Radwanski, A. Menovsky and F.R. de Boer, 1987, J. Phys. F **17**, 233.
Steiner, W., E. Gratz, H. Ortbauer and H.W. Cammen, 1978, J. Phys. F **8**, 1525.
Swift, W.N., and W.E. Wallace, 1968, J. Chem. Phys. **49**, 154.
Szewczyk, A., J.R. Radwanski, J.M.M. Franse and H. Nakotte, 1992, J. Magn. & Magn. Mater. **104–107**, 1319.
Thuy, N.P., N.M. Hong, T.D. Hien and J.J.M. Franse, 1990, in: 6th Int. Symp. Magnetic Anisotropy and Coercivity in Rare Earth–Transition Metal Alloys, ed. S.G. Sankar (Carnegie Mellon University, Pittsburgh) p. 60.
Trugg, J., B. Johansson and M.S.S. Brooks, 1992, J. Magn. & Magn. Mater. **104–107**, 1447.
Tyablikov, S.V., 1967, Methods in Quantum Theory of Magnetism (Plenum Press, New York).
Verhoef, R., 1990, Thesis (University of Amsterdam).
Verhoef, R., P.H. Quang, J.J.M. Franse and R.J. Radwanski, 1990a, J. Magn. & Magn. Mater. **83**, 139.
Verhoef, R., R.J. Radwanski and J.J.M. Franse, 1990b, J. Magn. & Magn. Mater. **83**, 176.
Williams, A.R., V.L. Moruzzi, A.V. Malozemoff and K. Terakura, 1983, IEEE Trans. Magn. **19**, 1983.
Yamada, H., and M. Aoki, 1993, in: Recent Advances in Magnetism of Transition Metal Compounds, eds A. Kotani and N. Suzuki (World-Scientific, Singapore) p. 42.

Yamada, H., and M. Shimizu, 1985, J. Phys. F **15**, L180.

Yamada, H., J. Inoue, K. Terao, S. Kanda and M. Shimizu, 1984, J. Phys. F **14**, 1049.

Yamada, M., H. Kato, H. Yamamoto and Y. Nakagawa, 1988, Phys. Rev. B **38**, 620.

Zeng, D.C., 1994, Thesis (Institute of Metal Research, Shenyang).

Zhao, Z.G., 1994, Thesis (University of Amsterdam).

Zhao, Z.G., F.R. de Boer, P.F. de Châtel and K.H.J. Buschow, 1994, Physica B **193**, 45.

Zhong, X.P., F.R. de Boer, J.H. Jacobs and K.H.J. Buschow, 1990a, J. Magn. & Magn. Mater. **92**, 46.

Zhong, X.P., F.R. de Boer, D.B. de Mooij and K.H.J. Buschow, 1990b, J. Less-Common Met. **163**, 123.

Zhou, G.F., F.R. de Boer and K.H.J. Buschow, 1992a, Physica B **176**, 288.

Zhou, G.F., F.R. de Boer and K.H.J. Buschow, 1992b, J. Alloys & Compounds **187**, 299.

Zhou, G.F., X. Li, F.R. de Boer and K.H.J. Buschow, 1992c, J. Magn. & Magn. Mater. **109**, 265.

Handbook on the Physics and Chemistry of Rare Earths
Vol. 24
edited by K.A. Gschneidner, Jr. and L. Eyring

Chapter 164

STANNIDES OF RARE-EARTH AND TRANSITION METALS

R.V. SKOLOZDRA
Department of Inorganic Chemistry, Ivan Franko State University, Kyryl and Mefodiy str., 6, 290005, Lviv, Ukraine

Contents

Symbols and abbreviations

a, b, c	unit cell dimensions (in Å)
a/c	composition (or contents) in atomic percent
C	specific heat
CEC	conduction electrons concentration
C–W	Curie–Weiss law
E_F	Fermi energy
f.u.	formula unit
G	de Gennes function
G	occupation of crystallographic positions
g_J	gyromagnetic ratio
H	magnetic field strength
J	total angular momentum
k	Boltzmann constant
$\boldsymbol{k}$	propogation vector of magnetic structure (magnetic wave vector)
$\boldsymbol{k}_F$	Fermi wave vector
M	magnetization
M	metallic element (usually a transition metal)
M_s	saturation magnetization
NMR	nuclear magnetic resonance
R	rare-earth metal: Y, Sc and the lanthanides
RKKY	Ruderman–Kittel–Kasuya–Yosida exchange interaction
S	thermopower (Seebeck coefficient)
SG	space group
ST	structure type
T	temperature
T	Tesla
T_C	Curie temperature
T_c	superconducting transition temperature
TEC	thermal expansion coefficient
T_K	compensation temperature
T_m, T_t	temperature of magnetic transition
T_N	Néel temperature
V	unit cell volume
x, y	indicate variable component contents, when used as an index in the compositional formula of a compound
x/a, y/b, z/c	atom coordinates
Z	number of formula units in an unit cell
β	unit cell angle
μ	magnetic moment
ρ	electrical resistivity
χ	magnetic susceptibility
γ	electronic specific heat coefficient

χ_0	temperature independent susceptibility	μ_s	saturation magnetic moment
μ_B	Bohr magneton	θ_p	paramagnetic Curie temperature
μ_{eff}	effective magnetic moment		

1. Introduction

The discovery of new physical effects in intermetallic compounds, such as intermediate valence, heavy fermions and Kondo systems, coexistence of magnetism and superconductivity, etc., has stimulated much interest in these materials. It is also necessary to mention the powerful permanent magnets based on rare-earth intermetallides. A complex approach to the investigation of the composition, crystal structure and properties of these intermetallic compounds has been outlined and gives the possibility of solving the important problem of the determination of correlations between these characteristics.

However, there are many intermetallic compounds formed by metals and semimetals which were insufficiently studied until recently. One of these are the tin compounds with the rare earths which were started to be investigated intensively approximately 15 years ago. Results of the research on the RMn_xSn_y and RPd_2Sn stannides (some of which exhibit the coexistence of magnetism and superconductivity), and on the CeNiSn stannide which manifests semiconducting properties at low temperatures, stimulated the investigation of tin compounds with rare earths. It is also desirable to mention the semiconducting properties of the M′M″Sn compounds (M′, M″ = transition metals) with the MgAgAs structure type, even though they are formed by three metals.

In this survey the stannides containing rare earths are discussed in the following sequence: the systems investigated, the composition and crystallographic data of the compounds, and results of the research on the magnetic and transport properties. An attempt is made to find some regularities in the crystal chemistry and physical properties of the ternary stannides.

2. Binary stannides of the rare earths

2.1. *The R–Sn systems*

Phase diagrams of the binary R–Sn systems over the whole concentration range to a larger degree were investigated for the light rare earths. The following systems have been studied: Sc–Sn (in the range of 0–60 a/c Sn (Podarevskaya 1992), Y–Sn (Schmidt and McMasters 1967), La–Sn (Eremenko et al. 1988c, 1989), Ce–Sn (Borzone et al. 1982, Franceschi and Costa 1988a,b), Pr–Sn (Eremenko et al. 1987, 1988a), Nd–Sn (Eremenko et al. 1988b, Saccone et al. 1993), Sm–Sn (Percheron 1970, Borzone et al. 1982), Gd–Sn (Liu and Zheng 1984), Tb–Sn (Eremenko et al. 1991), Dy–Sn (Eremenko et al. 1992), and Yb–Sn (Palenzona and Girafici 1976, 1991). The holmium, erbium and thulium systems have been partly investigated.

Recently, Palenzona and Manfrinetti (1993) have studied the phase diagrams of the Y–Sn system and the systems of the heavy rare earths (except Yb) in the range 60–100 a/c Sn. This was a significant addition to the earlier data on these systems.

Phase diagrams of the binary R–Sn systems, the crystal structure and thermodynamic properties of binary stannides have been summarized by Bulanova and Sydorko (1994).

Some diagrams must be refined because they are not in accordance with the known crystal structure data of the binary compounds.

2.2. *Composition, crystal structure and structure types of compounds*

The most widely distributed compositions of the binary stannides are: R_5Sn_3, R_5Sn_4, $R_{11}Sn_{10}$, RSn_2, R_3Sn_7, R_2Sn_5, RSn_3. Crystallographic data of these compounds are given in table 1.

The R_3Sn compounds form only with four elements (La, Ce, Pr, Nd). Our investigations (Skolozdra 1993) showed that Ce_3Sn, Pr_3Sn and Nd_3Sn form in the alloys annealed at 870 K; for Ce_3Sn, superstructure reflections on the powder pattern are observed, which are not observed for Pr_3Sn and Nd_3Sn. We have not found the La_3Sn compound.

The R_5Sn_3 (R = La, Ce, Pr) stannides exist as two polymorphic modifications: high-temperature Mn_5Si_3 type and low-temperature W_5Si_3 type (Franceschi 1979). We have carried out an additional investigation of these systems (Skolozdra 1993). It was established that in the alloys of Ce and Pr, those that were annealed at 870 K, a compound with the W_5Si_3 type structure forms, and in unannealed alloys the compound with the Mn_5Si_3 type structure appears. These results are in accordance with Franceschi's (1979) data. But we did not find the La_5Sn_3 compound with W_5Si_3 type structure in the alloys annealed both at 870 and at 1070 K. Probably a structure transformation occurs at some temperature below 870 K. (The alloys were annealed at 670 K by Franceschi 1979.)

The R_5Sn_4 compounds crystallize in the Sm_5Ge_4 structure type which is a relative of the U_3Si_2 type and in turn of the AlB_2 structure type. There are no data on the stannides with this composition for Ho, Er, Tm; for the remaining rare earths such information has been found. Most likely this fact can be explained by the insufficient investigation of the systems with Ho, Er and Tm in this range.

Tin also forms the $Ho_{11}Ge_{10}$ type compounds almost with all lanthanides. This type is characterized by a complex structure, in which the coordination polyhedra of the small-size atoms (Ge) are deformed trigonal prisms, and tetragonal antiprisms (Gladyshevsky 1971). There are no data for the compounds with Pr, Yb and Lu.

Only three stannides of RSn composition with known structure form in the systems R–Sn. They are LaSn, EuSn (CrB structure type) and YbSn (CuAu structure type). The structure of the remaining RSn compounds (R = Pr, Nd, Tb) is unknown (table 1).

The next most frequent composition is RSn_2. It has been reported that there are other stannides between this composition and the RSn compounds (see table 1), but crystal structure were not determined except for La_3Sn_5, Ce_3Sn_5 and Pr_3Sn_5 (Pu_3Pd_5 type).

All RSn_2 compounds of the heavy rare earths have $ZrSi_2$-type structure, while the stannides $LaSn_2$, $CeSn_2$, $PrSn_2$, $NdSn_2$ and $SmSn_2$ have $NdSn_2$-type structure. The $NdSn_2$

Table 1
Crystallographic data for binary compounds of the R–Sn systems

Compound	Structure type	Space group	Lattice parameters (Å)			Reference(s)
			a	*b*	*c*	
α-Sc_5Sn_3	Mn_5Si_3	$P6_3/mcm$	8.408		6.081	Jeitschko and Parthé 1965
β-Sc_5Sn_3	unknown					Podarevskaya 1992
Sc_5Sn_4	unknown					Podarevskaya 1992
$Sc_{11}Sn_{10}$	unknown					Podarevskaya 1992
ScSn	CsCl	Pm3m	3.666			Kotur and Derkach 1994
$ScSn_2$	unknown					Bulanova and Sydorko 1994
Y_5Sn_3	Mn_5Si_3	$P6_3/mcm$	8.408		6.536	Schmidt and McMasters 1967
Y_5Sn_4	Sm_5Ge_4	Pnma	8.05	15.29	8.05	Schmidt and McMasters 1967
$Y_{11}Sn_{10}$	$Ho_{11}Ge_{10}$	I4/mmm	11.53		16.91	Schmidt and McMasters 1967
YSn_2	$ZrSi_2$	Cmcm	4.394	16.340	4.305	Schmidt and McMasters 1967
Y_2Sn_5	Y_2Sn_5	Pmmn	4.322	4.409	19.089	Palenzona and Manfrinetti 1993
YSn_3	$GdSn_3$ LT[b]		4.345	4.391	21.937	Palenzona and Manfrinetti 1993
YSn_3[a]	Cu_3Au	Pm3m	4.666			Miller and Hall 1972
La_3Sn	Cu_3Au	Pm3m	5.125			Borzone et al. 1983
La_3Sn[a]	Cu_3Au	Pm3m	4.98			Larchev and Popova 1977
La_2Sn	Ni_2In	$P6_3/mmc$	6.50		6.36	Borzone et al. 1983
β-La_5Sn_3	Mn_5Si_3	$P6_3/mcm$	9.416		6.926	Palenzona and Merlo 1966
			9.435		6.961	Franceschi 1979
α-La_5Sn_3	W_5Si_3	I4/mcm	12.749		6.343	Franceschi 1979
La_5Sn_4	Sm_5Ge_4	Pnma	8.448	16.26	8.604	Fornasini and Merlo 1971
			8.429	16.19	8.624	Eremenko et al. 1989
$La_{11}Sn_{10}$	unknown					Eremenko et al. 1989
LaSn	CrB	Cmcm	4.782	11.94	4.429	Eremenko et al. 1989
La_2Sn_3	unknown					Eremenko et al. 1989
La_3Sn_5	Pu_3Pd_5	Cmcm	10.35	8.29	10.63	Borzone et al. 1983
			10.35	8.29	10.61	Eremenko et al. 1989
$LaSn_2$	$NdSn_2$	Cmmm	4.426	15.855	4.513	Weitzer et al. 1992a
La_3Sn_7	Ce_3Sn_7	Cmmm	4.564	26.155	4.671	Weitzer et al. 1992a
La_2Sn_5	Ce_2Sn_5	Cmmm	4.623	35.742	4.681	Weitzer et al. 1992a
$LaSn_3$	Cu_3Au	Pm3m	4.7598			Harris and Raynor 1965
Ce_3Sn	Cu_3Au	Pm3m	4.929			Jeitschko et al. 1964
			4.93			Borzone et al. 1982
β-Ce_5Sn_3 HT[b]	Mn_5Si_3	$P6_3/mcm$	9.328		6.738	Jeitschko and Parthé 1967
α-Ce_5Sn_3 LT[b]	W_5Si_3	I4/mcm	12.591		6.174	Franceschi 1979
Ce_5Sn_4	Sm_5Ge_4	Pnma	8.337	16.05	8.480	Fornasini and Merlo 1971
$Ce_{11}Sn_{10}$	$Ho_{11}Ge_{10}$	I4/mmm	11.97		17.82	Borzone et al. 1982
Ce_3Sn_5	Pu_3Pd_5	Cmcm	10.255	8.225	10.58	Borzone et al. 1982
Ce_3Sn_7	Ce_3Sn_7	Cmmm	4.524	25.742	4.610	Boucherle et al. 1988

continued on next page

Table 1, *continued*

Compound	Structure type	Space group	Lattice parameters (Å)			Reference(s)
			a	*b*	*c*	
Ce_2Sn_5	Ce_2Sn_5	Cmmm	4.559	35.014	4.169	Boucherle et al. 1988
$CeSn_3$	Cu_3Au	Pm3m	4.7119			Harris and Raynor 1965
Pr_3Sn	Cu_3Au	Pm3m	4.99			Haschke et al. 1966
			4.98			Eremenko et al. 1988a
β-Pr_5Sn_3 HT[b]	Mn_5Si_3	$P6_3/mcm$	9.285		6.752	Palenzona and Merlo 1966
			9.281		6.779	Jeitschko and Parthé 1967
α-Pr_5Sn_3 LT[b]	W_5Si_3	I4/mcm	12.512		6.146	Franceschi 1979
Pr_5Sn_4	Sm_5Ge_4	Pnma	8.270	15.94	8.429	Fornasini and Merlo 1971
PrSn	unknown					Eremenko et al. 1988a
α-Pr_3Sn_5	Pu_3Pd_5	Cmcm	10.18	8.21	10.54	Eremenko et al. 1988a
β-Pr_3Sn_5	unknown					Eremenko et al. 1988a
$PrSn_2$	$NdSn_2$	Cmmm	4.482	15.897	4.590	Weitzer et al. 1992a
Pr_3Sn_7	Ce_3Sn_7	Cmmm	4.510	25.823	4.603	Weitzer et al. 1992a
Pr_2Sn_5	Ce_2Sn_5	Cmmm	4.584	35.178	4.633	Weitzer et al. 1992a
$PrSn_3$	Cu_3Au	Pm3m	4.7159			Harris and Raynor 1965
Nd_3Sn	Cu_3Au	Pm3m	5.002			Skolozdra 1993
Nd_5Sn_3	Mn_5Si_3	$P6_3/mcm$	9.200		6.717	Palenzona and Merlo 1966
			9.204		6.725	Jeitschko and Parthé 1967
Nd_5Sn_4	Sm_5Ge_4	Pnma	8.222	15.84	8.376	Fornasini and Merlo 1971
$Nd_{11}Sn_{10}$	$Ho_{11}Ge_{10}$	I4/mmm	11.87		17.59	Fornasini and Merlo 1971
NdSn	unknown					Eremenko et al. 1988b
Nd_3Sn_5	unknown					Eremenko et al. 1988b
$NdSn_2$	$NdSn_2$	Cmmm	4.440	15.913	4.562	Weitzer et al. 1992a
Nd_3Sn_7	$CeSn_7$	Cmmm	4.4990	25.778	4.5846	Weitzer et al. 1992a
Nd_2Sn_5	Ce_2Sn_5	Cmmm	4.5688	35.118	4.6139	Weitzer et al. 1992a
$NdSn_3$	Cu_3Au	Pm3m	4.6965			Harris and Raynor 1965
Sm_5Sn_3	Mn_5Si_3	$P6_3/mcm$	9.089		6.610	Palenzona and Merlo 1966
			9.106		6.651	Jeitschko and Parthé 1967
Sm_4Sn_3	Th_3P_4	$I\bar{4}3d$	9.15			Percheron 1970
Sm_5Sn_4	Sm_5Ge_4	Pnma	8.19	15.81	8.19	Percheron 1970
			8.126	15.67	8.290	Fornasini and Merlo 1971
$Sm_{11}Sn_{10}$	$Ho_{11}Ge_{10}$	I4/mmm	11.76		17.32	Fornasini and Merlo 1971
Sm_2Sn_3	tetragonal		9.10		15.40	Percheron 1970
$SmSn_2$	$NdSn_2$	Cmmm	4.420	15.839	4.505	Weitzer et al. 1992a
Sm_3Sn_7	Ce_3Sn_7	Cmmm	4.446	25.991	4.522	Weitzer et al. 1992a
Sm_2Sn_5	Ce_2Sn_5	Cmmm	4.537	34.912	5.861	Weitzer et al. 1992a
$SmSn_3$	Cu_3Au	Pm3m	4.6772			Harris and Raynor 1965
EuSn	CrB	Cmcm	4.976	11.90	4.456	Merlo and Fornasini 1967

continued on next page

Table 1, *continued*

Compound	Structure type	Space group	Lattice parameters (Å)			Reference(s)
			a	*b*	*c*	
$EuSn_3$	Cu_3Au	Pm3m	4.7349			Rossi 1934
Gd_3Sn	unknown					Liu and Zheng 1984
Gd_5Sn_3	M_5Si_3	$P6_3/mcm$	9.020		6.568	Palenzona and Merlo 1966
			9.032		6.595	Jeitschko and Parthé 1967
Gd_5Sn_4	Sm_5Ge_4	Pnma	8.046	15.53	8.193	Fornasini and Merlo 1971
Gd_8Sn_7	unknown					Liu and Zheng 1984
$Gd_{11}Sn_{10}$	$Ho_{11}Ge_{10}$	I4/mmm	11.67		17.15	Fornasini and Merlo 1971
Gd_3Sn_4	unknown					Liu and Zheng 1984
$GdSn_2$	$ZrSi_2$	Cmcm	6.410	4.428	4.322	Iandelli and Palenzona 1966
Gd_3Sn_7	Gd_3Sn_7	Cmmm	4.4591	26.523	4.3283	Skolozdra et al. 1986a
			4.375	26.476	4.452	Palenzona and Manfrinetti 1993
$GdSn_{3-x}$	$GdSn_{2.75}$	Amm2	4.355	4.404	22.044	Skolozdra et al. 1986a
$GdSn_3$ LT[b]	$GdSn_3$ LT[b]	n1[b]	4.359	4.406	22.058	Palenzona and Manfrinetti 1993
$GdSn_3$	Cu_3Au	Pm3m	4.6761			Harris and Raynor 1965
$GdSn_3$ HT[b]	Cu_3Au	Pm3m	4.678			Palenzona and Manfrinetti 1993
Tb_5Sn_3	Mn_5Si_3	$P6_3/mcm$	8.947		6.535	Palenzona and Merlo 1966
			8.951		6.535	Jeitschko and Parthé 1967
Tb_5Sn_4	Sm_5Ge_4	Pnma	8.010	15.41	8.141	Fornasini and Merlo 1971
$Tb_{11}Sn_{10}$	$Ho_{11}Ge_{10}$	I4/mmm	11.60		17.00	Fornasini and Merlo 1971
TbSn	unknown					Eremenko et al. 1991
Tb_4Sn_5	unknown					Eremenko et al. 1991
$TbSn_2$	$ZrSi_2$	Cmcm	4.404	16.301	4.307	Iandelli and Palenzona 1966
Tb_3Sn_7	Gd_3Sn_7	Cmmm	4.450	26.43	4.320	Skolozdra 1993
Tb_3Sn_7 HT[b]	Tb_3Sn_7 HT[b]	n1[b]	4.335	26.667	4.425	Palenzona and Manfrinetti 1993
Tb_3Sn_7 LT[b]	Tb_3Sn_7 LT[b]	Cmmm	4.363	26.347	4.441	Palenzona and Manfrinetti 1993
$TbSn_3$	$GdSn_{2.75}$	Amm2	4.413	4.337	21.937	Koretskaya et al. 1988a
$TbSn_3$	$GdSn_3$ LT[b]	n1[b]	4.350	4.390	21.913	Palenzona and Manfrinetti 1993
$TbSn_3$[a]	Cu_3Au	Pm3m	4.661			Miller and Hall 1972
Dy_2Sn	unknown					Chen and Zheng 1983
α-Dy_5Sn_3	Mn_5Si_3	$P6_3/mcm$	8.889		6.491	Palenzona and Merlo 1966
			8.884		6.484	Jeitschko and Parthé 1967
β-Dy_5Sn_3	unknown					Eremenko et al. 1992
Dy_5Sn_4	Sm_5Ge_4	Pnma	7.966	15.38	8.105	Fornasini and Merlo 1971
$Dy_{11}Sn_{10}$	$Ho_{11}Ge_{10}$	I4/mmm	11.503		16.88	Fornasini and Merlo 1971
DySn	unknown					Eremenko et al. 1992
Dy_4Sn_5	unknown					Eremenko et al. 1992
Dy_8Sn_9	unknown					Chen and Zheng 1983
Dy_4Sn_7	unknown					Chen and Zheng 1983

continued on next page

Table 1, *continued*

Compound	Structure type	Space group	Lattice parameters (Å)			Reference(s)
			a	*b*	*c*	
$DySn_2$	$ZrSi_2$	Cmcm	4.391	16.23	4.300	Iandelli and Palenzona 1966
Dy_3Sn_7	Gd_3Sn_7	Cmmm	4.437	26.34	4.309	Skolozdra 1993
Dy_3Sn_7 HT[b]	Tb_3Sn_7 HT[b]	nl[b]	4.328	26.566	4.416	Palenzona and Manfrinetti 1993
Dy_3Sn_7 LT[b]	Tb_3Sn_7 LT[b]	Cmmm	4.356	26.245	4.427	Palenzona and Manfrinetti 1993
$DySn_3$	$GdSn_{2.75}$	Amm2	4.387	4.336	21.804	Koretskaya et al. 1988a
$DySn_3$	$GdSn_3$ LT[b]		4.340	4.382	21.820	Palenzona and Manfrinetti 1993
$DySn_3$[a]	Cu_3Au	Pm3m	4.659			Miller and Hall 1972
$DySn_4$	unknown					Chen and Zheng 1983
Ho_5Sn_3	Mn_5Si_3	$P6_3/mcm$	8.848		6.461	Palenzona and Merlo 1966
			8.847		6.458	Jeitschko and Parthé 1967
$Ho_{11}Sn_{10}$	$Ho_{11}Ge_{10}$	I4/mmm	11.52		16.80	Fornasini and Merlo 1971
$HoSn_2$	$ZrSi_2$	Cmcm	4.377	16.185	4.292	Iandelli and Palenzona 1966
Ho_2Sn_5	Y_2Sn_5	Pmmn	4.307	4.391	18.928	Palenzona and Manfrinetti 1993
$HoSn_3$	$GdSn_{3-x}$	Amm2	4.353	4.333	21.765	Koretskaya et al. 1988a
$HoSn_3$	$GdSn_3$ LT[b]		4.335	4.373	21.757	Palenzona and Manfrinetti 1993
$HoSn_3$[a]	Cu_3Au	Pm3m	4.653			Miller and Hall 1972
Er_5Sn_3	Mn_5Si_3	$P6_3/mcm$	8.799		6.442	Palenzona and Merlo 1966
			8.810		6.442	Jeitschko and Parthé 1967
$Er_{11}Sn_{10}$	$Ho_{11}Ge_{10}$	I4/mmm	11.44		16.74	Fornasini and Merlo 1971
$ErSn_2$	$ZrSi_2$	Cmcm	4.365	16.132	4.285	Iandelli and Palenzona 1966
Er_2Sn_5	Y_2Sn_5	Pmmn	4.305	4.379	18.892	Palenzona and Manfrinetti 1993
$ErSn_3$	$GdSn_3$ LT[b]	nl[b]	4.336	4.367	21.685	Palenzona and Manfrinetti 1993
$ErSn_3$[a]	Cu_3Au	Pm3m	4.643			Miller and Hall 1972
Tm_5Sn_3	Mn_5Si_3	$P6_3/mcm$	8.776		6.411	Palenzona and Merlo 1966
			8.773		6.406	Jeitschko and Parthé 1967
$Tm_{11}Sn_{10}$	$Ho_{11}Ge_{10}$	I4/mmm	11.42		16.68	Fornasini and Merlo 1971
$TmSn_2$	$ZrSi_2$	Cmcm	4.357	16.062	4.285	Iandelli and Palenzona 1966
Tm_2Sn_5	Y_2Sn_5	Pmmn	4.299	4.372	18.835	Palenzona and Manfrinetti 1993
$TmSn_3$	$GdSn_3$ LT[b]	nl[b]	4.331	4.361	21.625	Palenzona and Manfrinetti 1993
Yb_2Sn	Ni_2In	$P6_3/mmc$	5.371		7.063	Palenzona and Girafici 1976, 1991
β-Yb_5Sn_3	Mn_5Si_3	$P6_3/mmc$	9.47		6.90	Palenzona and Girafici 1976, 1991
α-Yb_5Sn_3	Cr_5B_3	I4/mcm	7.939		14.686	Palenzona and Girafici 1976, 1991
Yb_5Sn_4	Sm_5Ge_4	Pnma	7.822	15.813	8.280	Palenzona and Girafici 1976, 1991
YbSn	CuAu	P4/mmm	4.690		4.400	Palenzona and Girafici 1976, 1991

continued on next page

Table 1, *continued*

Compound	Structure type	Space group	Lattice parameters (Å)			Reference(s)
			a	*b*	*c*	
$YbSn_3$	Cu_3Au	Pm3m	4.6721			Harris and Raynor 1965
			4.683			Palenzona and Girafici 1976
Lu_5Sn_3	Mn_5Si_3	$P6_3/mcm$	8.679		6.349	Palenzona and Merlo 1966
			8.700		6.355	Jeitschko and Parthé 1967
Lu_5Sn_4	Sm_5Ge_4	Pnma	nd[b]	nd	nd	Skolozdra and Komarovskaya 1988a
$LuSn_2$	$ZrSi_2$	Cmcm	4.343	15.997	4.273	Iandelli and Palenzona 1966
Lu_2Sn_5	Y_2Sn_5	Pmmn	4.292	4.359	18.748	Palenzona and Manfrinetti 1993

[a] Phase was obtained at high pressure.

[b] Abbreviations: HT, high temperature; LT, low temperature; nl, not listed; nd, not determined.

structure is in close correspondence with the structure type of $NdNiGa_2$ and $ZrGa_2$ (Weitzer et al. 1992a). Atomic coordinates of $NdSn_2$ are shown in table 2.

The richest tin phases are the RSn_3 compounds with the Cu_3Au structure type. With La–Gd these phases form in ordinary conditions; the phases with Y and Tb–Lu exist under high pressure.

Recently, it was established that R_3Sn_7, R_2Sn_5 and RSn_{3-x} stannides form between the RSn_2 and RSn_3 compositions. Their structures belong to the Ce_3Sn_7, Gd_3Sn_7, Ce_2Sn_5, $Tm_2Ge_{4.5}Ga_{0.5}$ and $GdSn_{2.75}$ types. Moreover, the Tb_3Sn_7 and Dy_3Sn_7 compounds have a high-temperature modification with orthorhombic lattice; however, their crystal structure has not been studied in detail (Palenzona and Manfrinetti 1993).

A single crystal of the Tb_3Sn_7 compound has been studied by Palenzona and Manfrinetti (1993). They confirmed that the structure is in close correspondence with the Gd_3Sn_7 type, determined by Skolozdra et al. (1986a), but they found additionally a partial filling of the Sn4 positions and the appearance of two other positions Sn4′ and Sn4″, corresponding to a displacement of some tin atoms with respect to the centre of the Tb2 trigonal prisms.

Structures with compositions intermediate between RSn_2 and RSn_3 can be considered, depending on the structure, as consisting of the more simple fragments of the AlB_2, Cu_3Au, CaF_2, $BaAl_4$ and α-Po types alternating with each other in a different sequence along the larger lattice parameter. Atom coordinates and occupancy factors for these structures are given in table 2.

2.3. *Properties of the compounds*

The magnetic and electrical properties of stannides have not been thoroughly studied (especially the electrical ones). The magnetic data are listed in table 3 and transport data are listed in table 4. The stannides of cerium are the most completely investigated of the

Table 2
Crystallographic data for $NdSn_2$, Ce_3Sn_7, Gd_3Sn_7, Tb_3Sn_7 (LT), Ce_2Sn_5, $Tm_2Ge_{4.5}Ga_{0.5}$ and $GdSn_{2.75}$ compounds

Atoms	Wyckoff notation	Atom coordinates			Occupation of crystallographic positions
		x/a	*y/b*	*z/c*	
$NdSn_2$: SG Cmmm; $Z=4$; $a=4.4404(8)$; $b=15.9436(44)$; $c=4.5628(8)$ Å (Palenzona and Manfrinetti 1993)					
4Nd	4(i)	0	0.180	0	1
4Sn1	4(j)	0	0.350	0.5	1
2Sn2	2(b)	0.5	0	0	1
2Sn3	2(d)	0	0	0.5	1
Ce_3Sn_7: SG Cmmm; $Z=2$; $a=4.524(1)$; $b=25.742(11)$; $c=4.610(2)$ Å (Boucherle et al. 1988)					
2Ce1	2(a)	0	0	0	1
4Ce2	4(i)	0	0.18424	0	1
2Sn1	2(c)	0.5	0	0.5	1
4Sn2	4(i)	0	0.40612	0	1
4Sn3	4(j)	0	0.09440	0.5	1
4Sn4	4(j)	0	0.28872	0.5	1
Gd_3Sn_7: SG Cmmm; $Z=2$; $a=0.4591(1)$; $b=26.523(5)$; $c=4.3823(9)$ Å (Skolozdra et al. 1986a)					
2Gd1	2(d)	0	0	0.5	1
4Gd2	4(i)	0	0.317	0	1
2Sn1	2(b)	0.5	0	0	1
4Sn2	4(i)	0	0.205	0	1
4Sn3	4(j)	0	0.403	0.5	1
4Sn4	4(j)	0	0.205	0.5	1
Tb_3Sn_7 (LT): SG Cmmm; $Z=2$; $a=4.363$; $b=26.347$; $c=4.441$ Å (Palenzona and Manfrinetti 1993)					
2Tb1	2(d)	0	0	0.5	1.00
4Tb2	4(i)	0	0.3090	0	1.00
2Sn1	2(b)	0.5	0	0	1.00
4Sn2	4(i)	0	0.1010	0	1.00
4Sn3	4(j)	0	0.4047	0.5	1.00
4Sn4	4(j)	0	0.2177	0.5	0.80
4Sn4′	4(j)	0	0.1831	0.5	0.13
4Sn4″	4(j)	0	0.245	0.5	0.07
Ce_2Sn_5: SG Cmmm; $Z=4$; $a=4.559(6)$; $b=35.014(39)$; $c=4.619(4)$ Å (Boucherle et al. 1988)					
4Ce1	4(i)	0	0.43206	0	1
4Ce2	4(i)	0	0.29764	0	1
2Sn1	2(a)	0	0	0	1
2Sn2	2(c)	0.5	0	0.5	1
4Sn3	4(i)	0	0.13661	0	1
4Sn4	4(j)	0	0.36298	0.5	1

continued on next page

Table 2, *continued*

Atoms	Wyckoff notation	Atom coordinates			Occupation of crystallographic positions
		x/a	*y/b*	*z/c*	
4Sn5	4(j)	0	0.07102	0.5	1
4Sn6	4(j)	0	0.22147	0.5	1
$Tm_2Ge_{4.5}Ga_{0.5}$ [a]: SG Pmmn; $Z=2$; $a=3.915$; $b=4.048$; $c=18.209$ Å (Gryn and Gladyshevsky 1989)					
2Tm1	2(b)	0.25	0.75	0.6920	1
2Tm2	2(a)	0.25	0.25	0.1275	1
2Ga1 [b]	2(b)	0.25	0.75	0.2626	1
2Ga2 [b]	2(b)	0.25	0.75	0.8	1
2Ga3 [b]	2(a)	0.25	0.25	0.8381	1
2Ga4 [b]	2(a)	0.25	0.25	0.5675	1
2Ga5 [b]	2(a)	0.25	0.25	0.4287	1
$GdSn_{2.75}$ ($GdSn_{3-x}$): SG Amm2; $Z=4$; $a=4.3552(4)$; $b=4.4039(6)$; $c=22.044(1)$ Å (Skolozdra et al. 1986a)					
2Gd1	2(a)	0	0	0	1.0
2Gd2	2(b)	0.5	0	0.775	1.0
2Sn1	2(a)	0	0	0.632	1.0
2Sn2	2(b)	0.5	0	0.540	0.22
2Sn3	2(a)	0	0	0.394	1.0
2Sn4	2(b)	0.5	0	0.155	1.0
2Sn5	2(a)	0	0	0.265	0.22
2Sn6	2(b)	0.5	0	0.905	0.19

[a] This type is called the Y_2Sn_5 type by Palenzona and Manfrinetti (1993).
[b] Ga = $Ge_{0.9}Ga_{0.1}$.

rare-earth compounds. This is connected with an interest in Ce compounds caused by its valence instability. These compounds are considered separately from the other stannides.

2.3.1. *Cerium stannides*

The investigation of the temperature dependences of the magnetic susceptibility and electrical resistivity of Ce_3Sn showed that this compound is a phase with a Kondo lattice (Martin 1982, Garde et al. 1989, Thompson et al. 1987, Chen et al. 1989). Its susceptibility has a high magnitude at 2 K (10^{-2} cm^3/mol) and the temperature dependence of the electrical resistivity is the same as for a Kondo system.

The properties of Ce_5Sn_3 were studied in detail by Lawrence et al. (1991). The resistivity, magnetic susceptibility and specific heat have been measured on a single crystal, which has the tetragonal structure (W_5Si_3 type). Moreover a neutron diffraction investigation was carried out on a polycrystalline specimen with the same structure. An antiferromagnetic phase transition was observed at $T_N = 17.5$ K. The obtained data showed also that Ce_5Sn_3 was a moderately heavy fermion compound. At lower temperatures the

Table 3
Magnetic properties of the R–Sn system compounds

Compound	Magnetic ordering	T_C, T_N (K)	μ (μ_B/R)	θ_p (K)	μ_{eff} (μ_B/R)	Reference(s)
Ce_3Sn				−87	2.54	Thompson et al. 1987, Chen et al. 1989
Pr_3Sn				13	3.72	Skolozdra 1993
Y_5Sn_3			Pauli paramagnet			Skolozdra 1993
La_5Sn_3			Pauli paramagnet			Skolozdra 1993
Ce_5Sn_3	A[a]	17.5		7	2.54	Lawrence et al. 1991
			1.62[b]	−19	2.54	Givord et al. 1992
			1.16[c]			
Pr_5Sn_3				96	3.53	Skolozdra 1993
Nd_5Sn_3	A[a]	40		19.1	3.57	Weitzer et al. 1992a
Gd_5Sn_3				24	8.4	Skolozdra 1993
Dy_5Sn_3				17	11.2	Skolozdra 1993
Ho_5Sn_3				10	11.1	Skolozdra 1993
Tm_5Sn_3				3	7.8	Skolozdra 1993
Lu_5Sn_3			Pauli paramagnet			Skolozdra 1993
Ce_5Sn_4	F[d]	8.2	1.14	−16	2.63	Givord et al. 1992
Nd_5Sn_4	F[d]	67	0.5	32.8	3.41	Weitzer et al. 1992a
$Nd_{11}Sn_{10}$	F[d]	75	1.5	62	3.40	Weitzer et al. 1992a
NdSn	F[d]	32	0.5	1.5	3.56	Weitzer et al. 1992a
EuSn	A[a]	10		7	8	de Vries et al. 1985
Nd_3Sn_5	A[a]	14	1.2	14.8	3.64	Weitzer et al. 1992a
$LaSn_2$			diamagnet			Weitzer et al. 1992a
$PrSn_2$	A[a]	8.4	1.6	15.2	3.1	Weitzer et al. 1992a
$NdSn_2$	A[a]	5.1		−8.9	3.69	Weitzer et al. 1992a
$SmSn_2$	A[a]	32				Weitzer et al. 1992a
La_3Sn_7			diamagnet			Weitzer et al. 1992a
Ce_3Sn_7	A[a]	5.1	1.3			Bonnet et al. 1994
Pr_3Sn_7	F[d]	11.8	1.0	16.7	3.6	Weitzer et al. 1992a
Nd_3Sn_7	F[d]	10.5	0.9	−2.0	3.65	Weitzer et al. 1992a
Sm_3Sn_7	A[a]	20				Weitzer et al. 1992a
La_2Sn_5			diamagnet			Weitzer et al. 1992a
Ce_2Sn_5				−43	2.56	Dhar et al. 1987
	A[a]	2.9	0.36			Bonnet et al. 1994
Pr_2Sn_5	A[a]	10.5	0.7	11.3	3.3	Weitzer et al. 1992a
Nd_2Sn_5	A[a]	3.8		−14.3	3.61	Weitzer et al. 1992a
$CeSn_3$		C–W (300–500 K)		−203	2.78	Sereni 1980
$PrSn_3$	A[a]	8.6	2.65	−8	3.42	Tsuchida and Wallace 1965

continued on next page

Table 3, *continued*

Compound	Magnetic ordering	T_C, T_N (K)	μ (μ_B/R)	θ_p (K)	μ_{eff} (μ_B/R)	Reference(s)
$NdSn_3$	A[a]	4.7		−22	3.6	Tsuchida and Wallace 1965
	A[a]	4.6	1.4			Lethuillier et al. 1975
	A[a]	4.9		−24.7	3.61	Weitzer et al. 1992a
$SmSn_3$	A[a]	12				Tsuchida and Wallace 1965
$EuSn_3$	A[a]	38	7.0			Tsuchida and Wallace 1965
$GdSn_3$ (cub)	A[a]	~35	7.0	−73	8.0	Tsuchida and Wallace 1965
$GdSn_{2.75}$[e]				0	7.96	Koretskaya et al. 1988a
$TbSn_3$[e]				0	9.75	Koretskaya et al. 1988a
$DySn_3$[e]				0	10.58	Koretskaya et al. 1988a
$HoSn_3$[e]				0	10.48	Koretskaya et al. 1988a
$YbSn_3$			Pauli paramagnet			Klaasse et al. 1977

[a] Antiferromagnetic ordering.
[b] For Ce in 16(k).
[c] For Ce in 4(b).
[d] Ferromagnetic ordering.
[e] $GdSn_{2.75}$ structure type.

linear coefficient of specific heat $\gamma(T)=C(T)/T$ rises to 1.6 J/(K^2 mol). A peculiarity of the entropy change was noted: a small change at the magnetic transition, and a significantly greater one was observed as a result of heavy fermion processes. The authors suppose that magnetic ordering is caused by the existence of small moments on the high symmetry Ce1 (4(b) sites), whereas the heavy fermion processes appear due to the Ce2 (16(k)) atoms in the lower symmetry site, or an even smaller moment ordering of all of the Ce sites in the form of a possible modulated structure. The other alternative is formation of the itinerant-fermion antiferromagnetism. The effects of the crystal field are powerful in the compound and as a result of this there is a great anisotropy of the magnetic susceptibility.

Givord et al. (1992) carried out magnetization measurements and a neutron diffraction investigation of the polycrystalline specimen of α-Ce_5Sn_3 (W_5Si_3 type) and determined its magnetic structure. The data of the magnetization measurements are in accordance with the results of Lawrence et al. (1991). Magnetic reflections appear at a temperature below 18 K. The propagation vector is $\boldsymbol{k}=(0,0,k_z)$ with $k_z=0.276$. The magnetic structure is a sine wave modulated structure with moments lying in the basal plane, the magnetic moments are symmetrical relative to the [1 0 0] axis. The Ce atoms are magnetic in both sites, the maximum moments of the sine waves are $1.62\mu_B$ (Ce in 16(k)) and $1.16\mu_B$ (Ce in 4(b)).

Givord et al. (1992) have also carried out magnetization measurements and a neutron investigation of the Ce_5Sn_4 compound. The phase is a ferromagnet with $T_C=8.2$ K, at temperatures above 100 K the susceptibility dependence follows the Curie–Weiss law.

Table 4
Transport properties of the R–Sn system compounds

Compound	ρ (μΩ cm)[a]		S (μV/K)		References
	78 K	300 K	80 K	300 K	
Ce_3Sn	68	75			Chen et al. 1989
at 4 K	2.5				
La_5Sn_3	112	125			Lawrence et al. 1991
at 4 K	85				
Ce_5Sn_3	92	125			Lawrence et al. 1991
at 4 K	37				
La_3Sn_7	18	70			Bonnet et al. 1994
Ce_3Sn_7	32 $\parallel X$	67 $\parallel X$			Bonnet et al. 1994
	32 $\perp Y$	59 $\perp Y$			
	38 $\parallel Z$	63 $\parallel Z$			
La_2Sn_5	9.4	35			Bonnet et al. 1994
Ce_2Sn_5	18 $\parallel X$	39 $\parallel X$			Bonnet et al. 1994
	27 $\perp Y$	76 $\perp Y$			
	39 $\parallel Z$	110 $\parallel Z$			
$LaSn_3$	6.1	20			Bonnet et al. 1994
	5.5	21			Staliński et al. 1975
			3.7[b]	4.0[b]	Kletowski 1982
$CeSn_3$	8.2	30.4			Bonnet et al. 1994
	10.3	39.8	~14	~32	Sereni 1980
at 4.2 K	0.56		~2.9		
	8.2	30			Staliński et al. 1975
			46[b]	40[b]	Kletowski 1982
$PrSn_3$			6.0[b]	4.7[b]	Kletowski 1982
$NdSn_3$			3.2[b]	4.3[b]	Kletowski 1982
$SmSn_3$	20	29			Staliński et al. 1975
at 2 K	0.2				
			10[b]	15.8[b]	Kletowski 1982
$EuSn_3$	8.3	28			Staliński et al. 1975
at 2 K	0.17				
			1.2[b]	5.6[b]	Kletowski 1982
$GdSn_{2.75}$	67	120	−1.0	−1.9	Koretskaya et al. 1988a
$GdSn_3$	9.3	24			Staliński et al. 1975
(Cu_3Au)					
at 2 K	3.5				
			0.7[b]	1.8[b]	Kletowski 1982
$HoSn_3$[c]	21	84	0.2	−0.2	Koretskaya et al. 1988a

[a] The magnitudes of resistivity and thermopower have been taken from the figures in the corresponding articles, with the exception of the data of Koretskaya et al. 1988a.
[b] In [100] direction.
[c] $GdSn_{2.75}$ structure type.

The propagation factor is $\boldsymbol{k}=(0,0,0)$. Magnetic moments of Ce1 (8(d)), Ce2 (8(d)) and Ce3 (4(c)) atoms obtained from the neutron investigations are equal to 0.77, 1.68, $0.80\mu_B$, respectively. The average atom moment of Ce is equal to $1.44\mu_B$ if all

moments are parallel and is in good accord with the value of $5\mu_B/Ce_5Sn_4$ obtained from magnetization.

Magnetic properties of Ce_3Sn_7 and Ce_2Sn_5 are similar. The dependences $\chi(T)$ indicate an antiferromagnetic phase transition at 5.1 K and 2.9 K, respectively (Boucherle et al. 1987, 1989). In accordance with these data the Ce1 atoms, which are similar to Ce atoms in $CeSn_3$, are in the state of intermediate valence, and the Ce2 atoms have the valence value equal to three. Two kinds of Ce atoms have different magnetic properties: the Ce1 atoms are nonmagnetic, and the Ce2 atoms are the carriers of the magnetic properties.

According to Dhar et al. (1987) the antiferromagnetic or ferromagnetic ordering at 3 K is characteristic of Ce_2Sn_5. With increasing applied magnetic field (>5.4 T) the peak of the specific heat disappears. At temperatures above 120 K the function $\chi(T)$ is in accordance with Curie–Weiss law. The experimental magnetic entropy is only ~42% of the one calculated theoretically for the ground state. The γ coefficient is equal to 22 mJ/(K^2 mol).

The existence of two kinds of atoms in both compounds was confirmed by neutron diffraction investigations (Givord et al. 1989). Only the Ce2 atoms have magnetic moments. In spite of similarity of crystal structure, both compounds have different magnetic structures. The Ce_2Sn_5 compounds have a modulated structure with moments of a maximum value of $1.3\mu_B$ aligned along the X axis. In the Ce_3Sn_7 stannide the moment is situated parallel to the Z axis and has the greatest value of magnetic moments $0.36\mu_B$. These moments are coupled ferromagnetically in the XZ plane, whereas the moments of the neighboring planes are antiparallel. So, the planes with parallel and antiparallel moments alternate with each other in the Y direction.

Bonnet et al. (1994) have carried out measurements of specific heat, resistivity, magnetization and inelastic neutron scattering in both compounds and presented a complete analysis of the interactions in these interesting stannides. The differences of magnetic structure of the compounds are connected with the different effects of the crystalline electric field. In both compounds a strong anisotropy of the interionic exchange coupling is displayed. For the Ce_3Sn_7 compound a negative value for the C-component of the exchange coefficient has been found. The hybridization of the cerium 4f-electron with the band electrons plays an important role in both compounds. It is suggested that the effects of hybridization are the basis of the anisotropy of the exchange interactions and of the resistivity.

A great amount of research was done on the $CeSn_3$ compound. Magnetic susceptibility of $CeSn_3$ has a maximum at 140 K, decreases below 140 K and then increases again at temperatures below 50 K. In the temperature range 300–500 K $\chi(T)$ for $CeSn_3$ follows the Curie–Weiss law with $\theta_P = -203$ K and $\mu_{eff} = 2.78\mu_B$. The dependence $S(T)$ differs from that of $LaSn_3$ and a weak maximum at ~230 K is seen (fig. 1). Anomalies have also been observed in the thermal expansion. The coefficient of the electronic specific heat is equal to 53 mJ/(K^2 mol). All these data indicate an intermediate valence behaviour for cerium in $CeSn_3$, which has been considered in detail by Sereni (1980).

Measurement of the de Haas–van Alphen effect and investigation of the Fermi surface of $CeSn_3$ (Johanson et al. 1981) showed that a hybridization occurs between

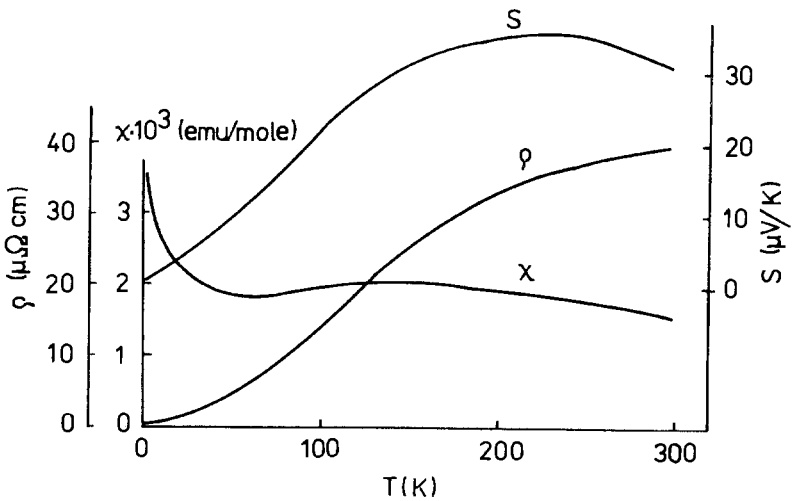

Fig. 1. Temperature dependence of the susceptibility, resistivity and thermopower of $CeSn_3$ (Sereni 1980).

the conduction electrons and localized 4f-electrons. This hybridization is confirmed by inelastic neutron scattering (Dijkman et al. 1980, Beille et al. 1977, Murani 1983). But the calculation of the band structure of $CeSn_3$ (Yanase 1983) is better described by a 4f-electron band-like character.

Ikeda and Gschneidner Jr (1982) carried out specific heat measurements on a polycrystalline sample of $CeSn_3$ under applied magnetic fields of up to 10 T. They found that the electronic specific heat coefficient is depressed with increased magnetic field while the coefficient of the T^3 term in the temperature dependence of heat capacity was raised. This has been explained by the quenching of spin fluctuations and the development of an induced magnetic field on the Ce atoms under the applied field, respectively. Later, Tsang et al. (1984) measured the specific heat in a magnetic field and the magnetic susceptibility of a single crystal in [1 1 0] and [1 0 0] directions. The temperature dependence of heat capacity is close to that which was determined by Ikeda and Gschneidner Jr (1982) but there is an anisotropy of the heat capacity of up to 5 T. Below 5 K an anisotropy appears also in magnetic susceptibility. The authors suggest that this is a result of anisotropic quenching of spin fluctuations.

The study of a $CeSn_3$ single crystal by polarised neutrons (Stassis et al. 1979) indicates an anisotropy of the form factor under an applied field of 4.3 T.

The increase of magnetic susceptibility of $CeSn_3$ at low temperatures has been associated with the presence of magnetic impurities. Tsang et al. (1984) believe that the magnetic impurities are disordered Ce atoms, i.e., face centered Ce atoms which have interchanged positions with the corner Sn atoms of the cubic Cu_3Au structure type. By means of high-field magnetization and susceptibility measurements on $CeSn_3$, Veenhuizen et al. (1986) have shown that the intrinsic susceptibility of $CeSn_3$ can be considered to

be temperature independent. The impurity content corresponds to about one percent of the Ce^{3+} ions.

Magnetic susceptibility and magnetic form factor measurements have been carried out on three single crystals of different compositions ($CeSn_{2.9}$, $CeSn_3$ and $CeSn_{3.1}$) by Boucherle et al. (1990). The authors showed that an extra 5d-contribution is added to the Ce magnetism. This contribution, revealing itself only in the compound with the stoichiometric composition, is observed at low temperatures and disappears with heating.

2.3.2. *Other binary stannides*

Only a limited number of studies have been reported for the other binary stannides of the R–Sn systems. Skolozdra (1993) measured magnetic susceptibility of the R_5Sn_3 stannides (R = Y, La, Ce, Pr, Nd, Gd, Dy, Ho, Tm, Lu) in the temperature range 78–293 K. Y_5Sn_3, La_5Sn_3, Lu_5Sn_3 are Pauli paramagnets, the reciprocal susceptibility of the remaining compounds follows the Curie–Weiss law. The paramagnetic Curie points are positive and, except for Ce_5Sn_3, decrease with increasing atomic number of R (table 3). Weitzer et al. (1992a) measured magnetic susceptibility of all stannides of La, Pr, Nd and Sm with the composition RSn_2, R_3Sn_7, R_2Sn_5 and RSn_3 (except $SmSn_3$) in the temperature range 2–600 K under an applied field of up to 6 T. The magnetic characteristics are listed in table 3. The $LaSn_2$ and La_2Sn_5 stannides are superconductors with a critical temperature of 3.6 and 5.4 K, respectively. The $PrSn_2$, Pr_2Sn_5, Nd_5Sn_3, Nd_3Sn_5 are antiferromagnets with metamagnetism, Pr_3Sn_7, Nd_5Sn_4, $Nd_{11}Sn_{10}$, Nd_3Sn_7 order ferromagnetically. $NdSn_2$, Nd_2Sn_5, $NdSn_3$, $SmSn_2$ and $SmSn_3$ are antiferromagnets at low temperatures.

The resistivity of La_3Sn_7 and La_2Sn_5 was measured by Bonnet et al. (1994). The dependences of $\rho(T)$ are of a metallic type. The value of resistivity of La_3Sn_7 at room temperature (70 μΩ cm) is two times higher than that of La_2Sn_5 (~35 μΩ cm).

For the EuSn compound the magnetic properties have been investigated by de Vries et al. (1985). Magnetic ordering is found to occur at 10 K. In the paramagnetic range the dependence $\chi(T)$ is in accordance with the Curie–Weiss law, the magnitude μ_{eff} indicates that europium is divalent.

Koretskaya et al. (1988a) have measured the magnetic susceptibility (between 78–293 K) for the stannides $GdSn_{2.75}$, $TbSn_3$, $DySn_3$, $HoSn_3$ ($GdSn_{2.75}$ type). The temperature dependence $\chi(T)$ for $GdSn_{2.75}$ follows the Curie–Weiss law; for the remaining compounds it is in accord with the Curie law. The measured resistivity and thermopower for $GdSn_{2.75}$, $HoSn_3$ are typical of the intermetallides.

The RSn_3 stannides with the Cu_3Au type crystal structure are of particular interest from the point of view of their properties. The highly symmetrical structure and the small magnitude of the lattice parameters makes it possible to calculate the kinetic parameters and electron spectrum energy. A lot of work has been devoted to the investigation of the magnetic properties of $LaSn_3$ in connection with the study on the influence of impurities on its superconductivity. Substitution of La atoms by other R atoms leads to a decrease of T_c (6.37 K for $LaSn_3$). The lowering of T_c deviates from the theory of Abrikosov and

Gor'kov on the influence of isolated magnetic impurities on T_c (Schmidt and Umlauf 1976).

Band structure of $LaSn_3$ was calculated by the self-consistent APW method (Hasegawa 1981). A small maximum is observed on the Fermi surface, which is formed mainly by the p-states of tin. Boulet et al. (1982) have measured the de Haas–van Alphen effect, the Fermi surface was constructed and the band structure was calculated. The conduction band is formed by the 5p-state of Sn and 5d-state of La. The results obtained on the single crystal by the polarized neutrons method agree with the theoretical calculation of the spin magnetic form factor. It is supposed that the Fermi level is formed mainly by the 5p-state of Sn.

The other compounds RSn_3 (R = Pr, Nd, Eu, Gd) are paramagnets with negative θ_P values (Tsuchida and Wallace 1965, Sanchez et al. 1976) and become antiferromagnets at low temperature. $YbSn_3$ is a Pauli paramagnet, while $SmSn_3$ has a complex temperature dependence $\chi(T)$ and is an antiferromagnet below 12 K.

The μ_{eff} values of Eu and Yb in $EuSn_3$ and $YbSn_3$, indicate that Eu and Yb are in the 2+ valence state, respectively.

The resistivity of the RSn_3 compounds has been studied by Staliński et al. (1973, 1975). At high temperature the dependence $\rho(T)$ is linear or almost linear, which suggests a phonon mechanism of scattering. In the vicinity of the magnetic transition a kink is observed in the curve $\rho(T)$. The results of the measurement of the specific heat and resistivity of $NdSn_2$ and $SmSn_2$ indicate the existence of an additional phase transition below the Néel point. On the basis of the thermal extension and specific heat measurements Kasaya et al. (1985) consider $SmSn_3$ as Kondo lattice. The thermopower of the RSn_3 stannides is positive, and its temperature dependence is nonlinear (Kletowski 1982). For $SmSn_3$ a maximum ($S_{max} \sim 18\,\mu V/K$) is observed at ~150 K.

3. Ternary stannides of the rare earths

3.1. *Ternary systems R–M–Sn, where M = transition metals*

The ternary systems R–M–Sn have not been studied completely. The majority of systems has been investigated by Skolozdra and co-authors (Skolozdra 1993). In other studies only individual alloys were investigated with the aim of finding new compounds. The phase diagrams are described below. One section of the review of Gladyshevsky et al. (1990) has been dedicated to the description of the ternary rare-earth–tin systems and the ternary stannides.

The compounds of R–M–Sn systems and their crystallographic data are listed in table 5.

3.1.1. *R–Mn–Sn systems*

Of all the R–Mn–Sn systems only the Nd–Mn–Sn system was studied. The isothermal sections of the phase diagram of Nd–Mn–Sn system at 1073 and 818 K were constructed

Table 5
Crystallographic data for ternary stannides

Compound	Structure type	Space group	Lattice parameters (Å)			Reference(s)
			a	*b*	*c*	
$ScCo_2Sn$	$MnCu_2Al$	Fm3m	6.187			Dwight and Kimball 1987
ScCoSn	TiNiSi	Pnma	6.773	4.402	7.339	Kotur and Kluchka 1989
$ScCo_xSn_y$	Phase *II* [a]	$I4_1/acd$	13.324			Espinosa et al. 1982
$ScNi_4Sn$	$MgCu_4Sn$	$F\bar{4}3m$	6.897			Kotur and Kluchka 1989
$ScNi_2Sn$	$MnCu_2Al$	Fm3m	6.214			Dwight and Kimball 1987
			6.228			Kotur and Kluchka 1989
Sc_2Ni_2Sn	Mo_2FeB_2	P4/mbm	7.0928		3.380	Derkach and Kotur 1994
ScNiSn	TiNiSi	Pnma	6.625	4.333	7.536	Kotur and Kluchka 1989
$ScCu_4Sn$	$MgCu_4Sn$	$F\bar{4}3m$	6.997			Kotur and Kluchka 1989
ScCuSn	$CaIn_2$	$P6_3/mmc$	4.384		6.827	Kotur and Kluchka 1989
$ScRu_xSn_y$	Phase *II* [a]	$I4_1/acd$	13.567			Espinosa et al. 1982
$ScPd_2Sn$	$MnCu_2Al$	Fm3m	6.509			Johnson and Shelton 1984
ScPdSn	ZrNiAl	$P\bar{6}2m$	7.471		3.537	Dwight et al. 1973
$ScOs_xSn_y$	Phase *III*	Fm3m	13.606			Espinosa et al. 1982
$ScIr_xSn_y$	Phase *II* [a]	$I4_1/acd$	13.575			Espinosa et al. 1982
$ScPt_2Sn$	$MnCu_2Al$	Fm3m	6.514			Dwight and Kimball 1987
ScPtSn *I*	ZrNiAl	$P\bar{6}2m$	7.41		3.62	Dwight et al. 1973
ScPtSn *II*	LiAlSi	$F\bar{4}3m$	6.997			Eberz et al. 1980
ScAuSn *I*	MgAgAs	$F\bar{4}3m$	6.422			Dwight 1976
ScAuSn *II*	LiAlSi	$F\bar{4}3m$	6.422			Eberz et al. 1980
YMn_6Sn_6	$HfFe_6Ge_6$	P6/mmm	5.512		8.984	Malaman et al. 1988
$YMnSn_2$	$TiMnSi_2$	Pbam	10.51	11.53	8.97	Venturini et al. 1989b
YFe_6Sn_6	YCo_6Ge_6	P6/mmm	5.382		4.441	Koretskaya and Skolozdra 1986
YFe_6Sn_6	YFe_6Sn_6	Cmcm	8.889	74.40	5.394	Chafik El Idrissi et al. 1991a
YCo_3Sn	$BaLi_4$	$P6_3/mmc$	8.844		7.446	Skolozdra 1993
YCo_6Sn_6	YCo_6Ge_6	P6/mmm	5.365		4.263	Skolozdra and Koretskaya 1984
YCoSn	TiNiSi	Pnma	7.208	4.499	7.503	Skolozdra et al. 1982
Y_6Co_2Sn	Ho_6Ni_2Ga	Immm	9.464	9.469	9.915	Koretskaya et al. 1988b
YCo_xSn_y	Phase *II* [a]	$I4_1/acd$	13.570			Espinosa et al. 1982
$Y_7Co_6Sn_{23}$	$Ho_7Co_6Sn_{23}$	$P\bar{3}m1$	9.653		9.873	Skolozdra et al. 1986b
$YNi_{5-x}Sn_{1+x}$	$CeCu_{4.38}In_{1.62}$	Pnnm	16.108	10.238	4.877	Skolozdra et al. 1996b
YNi_3Sn_2	$HoGa_{2.4}Ni_{2.6}$	P6/mmm	9.151		4.253	Skolozdra et al. 1988a
YNiSn	TiNiSi	Pnma	7.115	4.449	7.665	Dwight 1983
			7.121	4.427	7.649	Skolozdra et al. 1984b
$Y_9Ni_{24}Sn_{49}$	$Gd_9Ni_{24}Sn_{49}$	Im3	11.837			Komarovskaya and Skolozdra 1985
$YNiSn_2$	$LuNiSn_2$	Pnma	15.944	4.361	14.345	Komarovskaya et al. 1983a

continued on next page

Table 5, *continued*

Compound	Structure type	Space group	Lattice parameters (Å)			Reference(s)
			a	*b*	*c*	
$Y_6Cu_8Sn_8$	$Gd_6Cu_8Ge_8$	Immm	14.737	6.946	4.474	Thirion et al. 1983
YCuSn	$CaIn_2$	$P6_3/mmc$	4.505		7.286	Komarovskaya et al. 1983b
$Y_8Cu_7Sn_5$		orthorhombic	9.702	7.285	6.545	Yinghong et al. 1991
YRu_xSn_y	Phase *III*	Fm3m	13.772			Espinosa et al. 1982
YRu_xSn_y	Phase *V*		nl[b]	nl	nl	Espinosa et al. 1982
YRhSn	Fe_2P	$P\bar{6}2m$	7.54		3.77	Dwight et al. 1973
$Y_2Rh_3Sn_5$	$Y_2Rh_3Sn_5$	$Cmc2_1$	4.387	26.212	7.155	Meot-Meyer et al. 1984
YRh_xSn_y	Phase *II*[a]	$I4_1/acd$	13.771			Espinosa et al. 1982
YPd_2Sn	$MnCu_2Al$	Fm3m	6.716			Malik et al. 1985
$Y_{13}Pd_{40}Sn_{31}$	$Y_{13}Pd_{40}Sn_{13}$	P6/mmm	19.891		9.246	Cenzual and Parthé 1984
YOs_xSn_y	Phase *III*	Fm3m	13.801			Espinosa et al. 1982
YIr_xSn_y	Phase *III*	Fm3m	13.773			Espinosa et al. 1982
YPt_2Sn	$ZrPt_2Al$	$P6_3/mmc$	4.531		9.065	Dwight 1987
YPtSn	Fe_2P	$P\bar{6}2m$	7.54		3.77	Dwight et al. 1973
YAuSn	$CaIn_2$	$P6_3/mmc$	4.63		7.38	Dwight 1976
$La_6Mn_8Sn_8$	$Gd_6Cu_8Ge_8$	Immm	15.367	7.512	4.682	Weitzer et al. 1992c
$LaMn_{0.24}Sn_{1.79}$	$CeNiSi_2$	Cmcm	4.613	17.54	4.499	Skolozdra et al. 1988b
$LaMn_{0.27}Sn_2$	$CeNiSi_2$	Cmcm	4.611	17.51	4.494	François et al. 1990
$LaMn_{0.27}Sn_{1.89}$	$CeNiSi_2$	Cmcm	4.627	17.56	4.509	Weitzer et al. 1992b
$La_6Fe_{13}Sn$	$La_6Co_{11}Ga_3$	I4/mcm	8.148		24.047	Weitzer et al. 1993b
$LaFeSn_2$	$CeNiSi_2$	Cmcm	4.611	17.81	4.511	Skolozdra 1977
$LaFe_{0.34}Sn_2$	$CeNiSi_2$	Cmcm	4.610	17.23	4.490	Dörrscheidt et al. 1982
$LaFe_{0.24}Sn_{1.79}$	$CeNiSi_2$	Cmcm	4.533	17.09	4.512	Skolozdra et al. 1988b
$La_6Co_{13}Sn$	$La_6Co_{11}Ga_3$	I4/mcm	8.096		23.461	Weitzer et al. 1993b
$LaCoSn_2$	$CeNiSi_2$	Cmcm	4.529	17.86	4.529	Skolozdra 1977
$LaCo_{0.52}Sn_2$	$CeNiSi_2$	Cmcm	4.585	17.414	4.520	Dörrscheidt et al. 1982
$LaCo_{0.33}Sn_2$	$CeNiSi_2$	Cmcm	4.576	17.21	4.482	Skolozdra et al. 1988b
$LaCo_xSn_y$	Phase *I*	Pm3n	9.641			Espinosa et al. 1982
$La_6Co_8Sn_{26}$	Phase *I*	Pm3n	9.635			Skolozdra et al. 1983
$La_3Co_2Sn_7$	$La_3Co_2Sn_7$	Cmmm	4.59	27.60	4.60	Dörrscheidt and Schäfer 1980
$LaNi_5Sn$	$CeNi_5Sn$	$P6_3/mmc$	4.971		19.99	Skolozdra and Komarovskaya 1982a
$LaNi_{4-x}Sn_2$	KAu_4Sn_2	$I\bar{4}c2$	7.766		7.851	Skolozdra et al. 1988d
$LaNi_2Sn_2$ HT[b]	$CaBe_2Ge_2$	P4/nmm	4.461		10.19	Skolozdra et al. 1981b
$LaNi_2Sn_2$ LT	$LaPt_2Ge_2$	$P2_1$	4.465	4.465 $\beta=90.80°$	10.18	Skolozdra et al. 1981b

continued on next page

Table 5, *continued*

Compound	Structure type	Space group	Lattice parameters (Å)			Reference(s)
			a	*b*	*c*	
LaNiSn	TiNiSi	Pnma	7.552	4.661	7.636	Dwight 1983
			7.652	4.648	7.586	Skolozdra et al. 1984b
$La_5Ni_{1.5}Sn_{1.5}$	Cr_5B_3	I4/mcm	8.117		13.92	Skolozdra 1993
$La_9Ni_{24}Sn_{49}$	$Gd_9Ni_{24}Sn_{49}$	Im3	11.965			Komarovskaya and Skolozdra 1985
$LaNiSn_2$	$CeNiSi_2$	Cmcm	4.513	17.81	4.513	Skolozdra et al. 1988c
$LaNi_{0.74}Sn_2$	$CeNiSi_2$	Cmcm	4.526	17.79	4.510	Dörrscheidt et al. 1982
$La_3Ni_2Sn_7$	$La_3Co_2Sn_7$	Cmmm	4.584	27.51	45.87	Skolozdra et al. 1987
$La(Cu_{0.72}Sn_{0.28})_{13}$	$NaZn_{13}$	Fm3c	12.177			Komarovskaya and Skolozdra 1984
$LaCu_2Sn_2$	$CaBe_2Ge_2$	Pnma	4.485		10.523	Skolozdra and Komarovskaya 1982b
LaCuSn	AlB_2	P6/mmm	4.581		4.082	Komarovskaya et al. 1983b
$LaCu_{0.56}Sn_2$	$CeNiSi_2$	Cmcm	4.530	18.34	4.460	Dörrscheidt et al. 1982
$LaCu_{0.62}Sn_{1.83}$	$CeNiSi_2$	Cmcm	4.503	18.00	4.462	Komarovskaya et al. 1988
$LaRu_{0.56}Sn_2$	$CeNiSi_2$	Cmcm	4.658	17.13	4.596	Venturini et al. 1990
$LaRh_2Sn_4$	$NdRh_2Sn_4$	Pnma	18.692	4.536	7.259	Meot-Meyer et al. 1985
$La_2Rh_3Sn_5$	$U_2Co_3Si_5$	Ibam	10.764	12.912	6.365	Venturini et al. 1989c
$LaRh_xSn_y$	Phase *I*	Pm3n	9.745			Espinosa et al. 1982
$LaRh_xSn_y$	Phase *I'* [a]	nl [b]	9.745			Miraglia et al. 1986
LaPdSn	TiNiSn	Pnma	nl	nl	nl	Sakurai et al. 1990a
LaAgSn	$CaIn_2$	$P6_3/mmc$	4.799		7.777	Mazzone et al. 1981
$La_5Ir_4Sn_{10}$	$Sc_5Co_4Si_{10}$	P4/mbm	14.088		4.690	Venturini et al. 1982
$LaIr_xSn_y$	Phase *I*	Pm3n	9.755			Espinosa et al. 1982
$Ce_6Mn_8Sn_8$	$Gd_6Cu_8Sn_8$	Immm	15.228	7.488	4.682	Weitzer et al. 1992c
$CeMn_{0.24}Sn_{1.79}$	$CeNiSi_2$	Cmcm	4.577	17.23	4.472	Skolozdra et al. 1988b
$CeMn_{0.33}Sn_2$	$CeNiSi_2$	Cmcm	4.571	17.23	4.465	François et al. 1990
$CeMnSn_2$	$CeNiSi_2$	Cmcm	4.581	17.29	4.480	Weitzer et al. 1992b
$CeFe_{0.24}Sn_{1.79}$	$CeNiSi_2$	Cmcm	4.574	16.93	4.470	Skolozdra et al. 1988b
$CeCo_{0.33}Sn_2$	$CeNiSi_2$	Cmcm	4.560	16.97	4.478	Skolozdra et al. 1988b
$CeCo_xSn_y$	Phase *I*	Pm3n	9.598			Espinosa et al. 1982
$Ce_6Co_8Sn_{26}$	Phase *I*	Pm3n	9.594			Skolozdra et al. 1983
$CeNi_5Sn$	$CeNi_5Sn$	$P6_3/mmc$	4.9049		19.731	Skolozdra et al. 1981a
$CeNi_4Sn_2$	KAu_4Sn_2	$I\bar{4}c2$	7.753		7.869	Skolozdra et al. 1988d
Ce_2Ni_2Sn	Mo_2NiB_2	Immm	4.3936	5.7396	8.5967	Fourgeot et al. 1995
$CeNi_2Sn_2$ HT	$CaBe_2Ge_2$	P4/nmm	4.441		10.159	Pierre et al. 1994
$CeNi_2Sn_2$ LT	$LaPt_2Ge_2$	$P2_1$	4.438	4.407	10.108	Pierre et al. 1994
				$\beta=91.4°$		

continued on next page

Table 5, *continued*

Compound	Structure type	Space group	Lattice parameters (Å)			Reference(s)
			a	*b*	*c*	
CeNiSn	TiNiSi	Pnma	7.523	4.592	7.561	Skolozdra et al. 1984b
CeNiSn		$P2_1a$	7.542	4.6009	7.617	Higashi et al. 1993
$Ce_9Ni_{24}Sn_{49}$	$Gd_9Ni_{24}Sn_{49}$	Im3	11.854			Komarovskaya and Skolozdra 1985
$CeNiSn_2$	$CeNiSi_2$	Cmcm	4.485	17.74	4.485	Skolozdra et al. 1988c
$Ce_5Ni_{1.5}Sn_{1.5}$	Cr_5B_3	I4/mcm	7.975		13.59	Skolozdra 1993
$Ce_3Ni_2Sn_7$	$La_3Co_2Sn_7$	Cmmm	4.565	27.31	4.565	Skolozdra et al. 1987
$Ce(Cu_{0.72}Sn_{0.28})_{13}$	$NaZn_{13}$	Fm3c	12.153			Komarovskaya and Skolozdra 1984
$CeCu_2Sn_2$	$CaBe_2Ge_2$	P4/nmm	4.456		10.475	Skolozdra and Komarovskaya 1982b
CeCuSn	$CaIn_2$	$P6_3/mmc$	4.570		7.903	Komarovskaya et al. 1983b
$CeCu_{0.62}Sn_{1.83}$	$CeNiSi_2$	Cmcm	4.492	17.85	4.439	Komarovskaya et al. 1988
$CeRu_xSn_y$	Phase *I*	Pm3n	9.724			Espinosa et al. 1982
$CeRu_xSn_y$	Phase *V*		nl	nl	nl	Espinosa et al. 1982
CeRhSn	Fe_2P	$P\bar{6}2m$	7.55		3.97	Routsi et al. 1992b
$CeRh_2Sn_4$	$NdRh_2Sn_4$	Pnma	18.591	4.494	7.252	Meot-Meyer et al. 1985
$Ce_5Rh_4Sn_{10}$	$Sc_5Co_4Sn_{10}$	P4/mbm	14.053		4.621	Venturini et al. 1982
$CeRh_xSn_y$	Phase *I*	Pm3n	9.710			Espinosa et al. 1982
$CeRh_xSn_y$	Phase *I'* [a]	nl	9.708			Miraglia et al. 1986
CePdSn	TiNiSi	Pnma	7.541	4.705	7.984	Rossi et al. 1985
			7.526	4.742	7.931	Adroja and Malik 1992
CePdSn		$Pn2_1a$	7.5356	4.7045	7.9648	Higashi et al. 1993
CeAgSn	$CaIn_2$	$P6_3/mmc$	4.784		7.749	Mazzone et al. 1981
$Ce_5Ir_4Sn_{10}$	$Sc_5Co_4Sn_{10}$	P4/mbm	14.027		4.648	Venturini et al. 1982
$CeIr_xSn_y$	Phase *I*	Pm3n	9.720			Espinosa et al. 1982
CePtSn		$P2_1a$	7.463	4.6283	8.0159	Higashi et al. 1993
CePtSn	TiNiSi	Pnma	7.560	4.670	8.125	Kolenda et al. 1995
CeAuSn	$CaIn_2$	$P6_3/mmc$	4.73		7.71	Dwight 1976
$PrMn_6Sn_6$	$HoFe_6Sn_6$	Immm	9.0752	28.976	5.5779	Weitzer et al. 1993a
$Pr_6Mn_8Sn_8$	$Gd_6Cu_8Sn_8$	Immm	15.137	7.483	4.605	Weitzer et al. 1992c
$PrMn_{0.24}Sn_{1.79}$	$CeNiSi_2$	Cmcm	4.543	17.03	4.445	Skolozdra et al. 1988b
$PrMn_{0.29}Sn_2$	$CeNiSi_2$	Cmcm	4.550	17.06	4.449	François et al. 1990
$PrMn_{0.5}Sn_{1.83}$	$CeNiSi_2$	Cmcm	4.559	17.11	4.463	Weitzer et al. 1992b
$Pr_6Fe_{13}Sn$	$La_6Co_{11}Ga_3$	I4/mcm	8.098		23.471	Weitzer et al. 1993b
$PrFe_{0.24}Sn_{1.79}$	$CeNiSi_2$	Cmcm	4.526	16.90	4.427	Skolozdra et al. 1988b
$PrCo_{0.33}Sn_2$	$CeNiSi_2$	Cmcm	4.527	16.88	4.426	Skolozdra et al. 1988b

continued on next page

Table 5, *continued*

Compound	Structure type	Space group	Lattice parameters (Å)			Reference(s)
			a	*b*	*c*	
$PrCo_xSn_y$	Phase *I*	Pm3n	9.586			Espinosa et al. 1982
$Pr_6Co_8Sn_{26}$	Phase *I*	Pm3n	9.551			Skolozdra et al. 1983
$PrNi_5Sn$	$CeNi_5Sn$	$P6_3/mmc$	4.925		19.84	Skolozdra and Komarovskaya 1982a
$PrNi_4Sn_2$	KAu_4Sn_2	$I\bar{4}c2$	7.728		7.898	Skolozdra et al. 1988d
$PrNi_2Sn_2$	$CaBe_2Ge_2$	P4/nmm	4.429		10.13	Skolozdra et al. 1981b
PrNiSn	TiNiSi	Pnma	7.440	4.56	7.706	Dwight 1983
			7.442	4.551	7.661	Skolozdra et al. 1984b
$Pr_9Ni_{24}Sn_{49}$	$Gd_9Ni_{24}Sn_{49}$	Im3	11.903			Komarovskaya and Skolozdra 1985
$PrNiSn_2$	$CeNiSi_2$	Cmcm	4.543	17.53	4.472	Skolozdra et al. 1988c
$Pr_5Ni_{1.5}Sn_{1.5}$	Cr_5B_3	I4/mcm	7.947		13.67	Skolozdra 1993
$Pr_3Ni_2Sn_7$	$La_3Co_2Sn_7$	Cmmm	4.540	27.23	4.541	Skolozdra et al. 1987
$Pr(Cu_{0.72}Sn_{0.28})_{13}$	$NaZn_{13}$	Fm3c	12.162			Komarovskaya and Skolozdra 1984
$PrCu_2Sn_2$	$CaBe_2Ge_2$	P4/nmm	4.435		10.619	Skolozdra and Komarovskaya 1982b
PrCuSn	$CaIn_2$	$P6_3/mmc$	4.583		7.759	Komarovskaya et al. 1983b
$Pr_2Cu_4Sn_5$	$Sm_2Cu_4Sn_5$	I4mm	4.442		25.15	Komarovskaya and Skolozdra 1992
$PrCu_{0.62}Sn_{1.83}$	$CeNiSi_2$	Cmcm	4.460	17.62	4.419	Komarovskaya et al. 1988
$Pr_2Cu_{0.25}Sn_{1.25}$	AlB_2	P6/mmm	4.393		4.464	Komarovskaya et al. 1989
$PrRu_xSn_y$	Phase *I*	Pm3n	9.712			Espinosa et al. 1982
$PrRu_xSn_y$	Phase *V*		nl	nl	nl	Espinosa et al. 1982
PrRhSn	Fe_2P	$P\bar{6}2m$	7.539		3.92	Routsi et al. 1992b
$PrRh_2Sn_4$	$NdRh_2Sn_4$	Pnma	18.571	4.477	7.238	Meot-Meyer et al. 1985
$Pr_5Rh_4Sn_{10}$	$Sc_5Co_4Si_{10}$	P4/mbm	14.035		4.612	Venturini et al. 1982
$PrRh_xSn_y$	Phase *I*	Pm3n	9.693			Espinosa et al. 1982
$PrRh_xSn_y$	Phase *I'* [a]	nl	9.698			Miraglia et al. 1986
PrPdSn	TiNiSi	Pnma	7.475	4.680	7.979	Rossi et al. 1985
			7.523	4.472	7.931	Adroja and Malik 1992
PrAgSn	$CaIn_2$	$P6_3/mmc$	nl	nl	nl	Adam et al. 1990
$Pr_5Ir_4Sn_{10}$	$Sc_5Co_4Si_{10}$	P4/mbm	13.993		4.632	Venturini et al. 1982
$PrIr_xSn_y$	Phase *I*	Pm3n	9.704			Espinosa et al. 1982
$PrIr_xSn_y$	Phase *VII*		nl	nl	nl	Espinosa et al. 1982
PrPtSn	TiNiSi	Pnma	nl	nl	nl	Routsi et al. 1992a
PrAuSn	$CaIn_2$	$P6_3/mmc$	4.71		7.64	Dwight 1976

continued on next page

Table 5, *continued*

Compound	Structure type	Space group	Lattice parameters (Å)			Reference(s)
			a	*b*	*c*	
$NdMn_6Sn_6$	$HoFe_6Sn_6$	Immm	9.0666	28.9240	14.597	Weitzer et al. 1993a
$Nd_6Mn_8Sn_8$	$Gd_6Cu_8Ge_8$	Immm	12.055	7.472	4.575	Weitzer et al. 1992c
$NdMn_{0.24}Sn_{1.79}$	$CeNiSi_2$	Cmcm	4.547	16.80	4.432	Skolozdra et al. 1988b
$NdMn_{0.17}Sn_2$	$CeNiSi_2$	Cmcm	4.511	16.85	4.407	François et al. 1990
$NdMn_{0.5}Sn_{0.83}$	$CeNiSi_2$	Cmcm	4.534	16.97	4.439	Weitzer et al. 1992b
$Nd_5(Mn,Sn)_3$	W_5Si_3	I4/mcm	12.4048		6.1329	Weitzer and Rogl 1993
$Nd_6Fe_{13}Sn$	$La_6Co_{11}Ga_3$	I4/mcm	8.089		23.354	Weitzer et al. 1993b
$NdFe_{0.24}Sn_{1.79}$	$CeNiSi_2$	Cmcm	4.523	16.75	4.430	Skolozdra et al. 1988b
$NdCo_{0.33}Sn_2$	$CeNiSi_2$	Cmcm	4.497	16.84	4.436	Skolozdra et al. 1988b
$NdCo_xSn_y$	Phase *I*	Pm3n	9.563			Espinosa et al. 1982
$Nd_6Co_8Sn_{26}$	Phase *I*	Pm3n	9.553			Skolozdra et al. 1983
$NdNi_5Sn$	$CeNi_5Sn$	$P6_3/mmc$	4.923		19.73	Skolozdra and Komarovskaya 1982a
$NdNi_4Sn_2$	KAu_4Sn_2	$I\bar{4}c2$	7.753		7.869	Skolozdra et al. 1988d
$NdNi_2Sn_2$	$CaBe_2Ge_2$	P4/nmm	4.411		10.12	Skolozdra et al. 1981b
NdNiSn	CeNiSi	Pnma	7.395	4.541	7.69	Dwight 1983
			7.305	4.523	7.740	Skolozdra et al. 1984b
$Nd_9Ni_{24}Sn_{49}$	$Gd_9Ni_{24}Sn_{49}$	Im3	11.892			Komarovskaya and Skolozdra 1985
$NdNiSn_2$	$CeNiSi_2$	Cmcm	4.495	17.55	4.496	Skolozdra et al. 1988c
$Nd_5Ni_{1.5}Sn_{1.5}$	Cr_5B_3	I4/mcm	7.924		13.67	Skolozdra 1993
$Nd_3Ni_2Sn_7$	$La_3Co_2Sn_7$	Cmmm	4.524	27.10	4.524	Skolozdra et al. 1987
$Nd(Cu_{0.72}Sn_{0.28})_{13}$	$NaZn_{13}$	Fm3c	12.138			Komarovskaya and Skolozdra 1984
$NdCu_2Sn_2$	$CaBe_2Ge_2$	P4/nmm	4.432		10.264	Skolozdra and Komarovskaya 1982b
NdCuSn	$CaIn_2$	$P6_3/mmc$	4.562		7.614	Komarovskaya et al. 1983b
$NdCu_{0.62}Sn_{1.83}$	$CeNiSi_2$	Cmcm	4.470	17.41	4.398	Komarovskaya et al. 1988
$NdRu_{0.33}Sn_2$	$CeNiSi_2$	Cmcm	4.548	16.86	4.458	Venturini et al. 1990
$NdRu_xSn_y$	Phase *I*	Pm3n	9.707			Espinosa et al. 1982
$NdRu_xSn_y$	Phase *V*		nl	nl	nl	Espinosa et al. 1982
NdRhSn	Fe_2P	$P\bar{6}2m$	7.53		3.89	Routsi et al. 1992b
$NdRh_2Sn_4$	$NdRh_2Sn_4$	Pnma	18.535	4.463	7.229	Meot-Meyer et al. 1985
$NdRh_{0.42}Sn_2$	$CeNiSi_2$	Cmcm	4.538	16.91	4.460	Venturini et al. 1990
$Nd_5Rh_4Sn_{10}$	$Sc_5Co_4Sn_{10}$	P4/mbm	13.992		4.588	Venturini et al. 1982
$NdRh_xSn_y$	Phase *I*	Pm3n	9.676			Espinosa et al. 1982
$NdRh_xSn_y$	Phase *I'* [a]	nl	9.675			Miraglia et al. 1986

continued on next page

Table 5, *continued*

Compound	Structure type	Space group	Lattice parameters (Å)			Reference(s)
			a	*b*	*c*	
NdPdSn	TiNiSi	Pnma	7.424	4.665	7.951	Dwight 1983
			7.473	4.654	7.941	Adroja and Malik 1992
NdAgSn	$CaIn_2$	$P6_3/mmc$	nl	nl	nl	Adam et al. 1990
NdAgSn	LiGaGe	$P6_3mc$	nl	nl	nl	Bażela et al. 1995a
$NdIr_{0.26}Sn_2$	$CeNiSi_2$	Cmcm	4.571	16.85	4.436	Venturini et al. 1990
$NdIr_xSn_y$	Phase *I*	Pm3n	9.691			Espinosa et al. 1982
$NdIr_xSn_y$	Phase *VII*		nl	nl	nl	Espinosa et al. 1982
NdPtSn	TiNiSi	Pnma	nl	nl	nl	Routsi et al. 1992a
NdAuSn	$CaIn_2$	$P6_3/mmc$	4.70		7.59	Dwight 1976
$SmMn_6Sn_6$	$HoFe_6Sn_6$	Immm	9.0472	28.825	5.5476	Weitzer et al. 1993a
$SmMn_6Sn_6$	YCo_6Ge_6	P6/mmm	5.552		4.526	Malaman et al. 1988
$Sm_6Mn_8Sn_8$	$Gd_6Cu_8Ge_6$	Immm	14.913	7.459	4.525	Weitzer et al. 1992c
$SmMn_{0.24}Sn_{1.79}$	$CeNiSi_2$	Cmcm	4.496	16.73	4.406	Skolozdra et al. 1988b
$SmMn_{0.21}Sn_2$	$CeNiSi_2$	Cmcm	4.489	16.68	4.395	François et al. 1990
$SmMn_{0.29}Sn_{1.56}$	$CeNiSi_2$	Cmcm	4.481	16.70	4.402	Weitzer et al. 1992b
$Sm_6Fe_{13}Sn$	$La_6Co_{11}Ga_3$	I4/mcm	8.055		23.170	Weitzer et al. 1993b
$SmFe_{0.24}Sn_{1.79}$	$CeNiSi_2$	Cmcm	4.464	16.50	4.392	Skolozdra et al. 1988b
$SmCo_{0.39}Sn_{1.84}$	$CeNiSi_2$	Cmcm	4.468	16.67	4.449	Skolozdra et al. 1988b
$SmCo_xSn_y$	Phase *I*	Pm3n	9.535			Espinosa et al. 1982
$Sm_6Co_8Sn_{26}$	Phase *I*	Pm3n	9.524			Skolozdra et al. 1983
$SmNi_{5-x}Sn_{1+x}$	$CeCu_{4.38}In_{1.62}$	Pnnm	16.155	10.276	4.705	Skolozdra et al. 1996b
$SmNi_4Sn_2$	KAu_4Sn_2	$I\bar{4}c2$	7.666		7.903	Skolozdra et al. 1988d
$SmNi_3Sn_2$	$HoGa_{2.4}Ni_{2.6}$	P6/mmm	9.207		4.280	Skolozdra et al. 1988a
$SmNi_2Sn_2$	$CaBe_2Ge_2$	P4/nmm	4.391		10.09	Skolozdra et al. 1981b
SmNiSn	TiNiSi	Pnma	7.304	4.509	7.68	Dwight 1983
			7.277	4.501	7.671	Skolozdra et al. 1984b
$Sm_9Ni_{24}Sn_{49}$	$Gd_9Ni_{24}Sn_{49}$	Im3	11.871			Komarovskaya and Skolozdra 1985
$SmNi_{0.52}Sn_{1.71}$	$CeNiSi_2$	Pnma	4.469	16.59	4.378	Skolozdra et al. 1988c
$SmCu_2Sn_2$	$CaBe_2Ge_2$	P4/nmm	4.401		10.095	Skolozdra and Komarovskaya 1982b
SmCuSn	$CaIn_2$	$P6_3/mmc$	4.549		7.476	Komarovskaya et al. 1983b
$Sm_2Cu_4Sn_5$	$Sm_2Cu_4Sn_5$	I4mm	4.431		25.073	Skolozdra et al. 1991
$SmRu_xSn_y$	Phase *I*	Pm3n	9.674			Espinosa et al. 1982
$SmRu_xSn_y$	Phase *V*		nl	nl	nl	Espinosa et al. 1982
SmRhSn	Fe_2P	$P\bar{6}2m$	7.46		3.98	Dwight et al. 1973
$SmRh_2Sn_4$	$NdRh_2Sn_4$	Pnma	18.450	4.421	7.210	Meot-Meyer et al. 1985

continued on next page

Table 5, *continued*

Compound	Structure type	Space group	Lattice parameters (Å)			Reference(s)
			a	*b*	*c*	
$Sm_5Rh_4Sn_{10}$	$Sc_5Rh_4Sn_{10}$	P4/mbm	13.926		4.554	Venturini et al. 1982
$SmRh_xSn_y$	Phase *I*	Pm3n	9.657			Espinosa et al. 1982
$SmRh_xSn_y$	Phase *I'* [a]	nl	9.656			Espinosa et al. 1982
SmPdSn	TiNiSi	Pnma	7.323	4.639	7.929	Dwight 1983
			7.325	4.636	7.945	Rossi et al. 1985
			7.332	4.629	7.927	Adroja and Malik 1992
SmAgSn	$CaIn_2$	$P6_3/mmc$	4.732		7.495	Mazzone et al. 1981
$SmIr_xSn_y$	Phase *I*	Pm3n	9.668			Espinosa et al. 1982
SmPtSn	TiNiSi	Pnma	nl	nl	nl	Sakurai et al. 1995
SmAuSn	$CaIn_2$	$P6_3/mmc$	4.67		7.48	Dwight 1976
EuZnSn	$CeCu_2(KHg_2)$	Imma	4.770	7.872	8.085	Merlo et al. 1991
EuPdSn	TiNiSi	Pnma	7.498	4.682	8.039	Adroja and Malik 1992
EuCdSn	LiGaGe	$P6_3mc$	4.927		7.907	Merlo et al. 1991
$EuRh_xSn_y$	Phase *I*	Pm3n	9.749			Espinosa et al. 1982
$EuRh_xSn_y$	Phase *I'* [a]	nl	9.749			Miraglia et al. 1986
$GdMn_6Sn_6$	$HfFe_6Ge_6$	P6/mmm	5.521		9.007	Malaman et al. 1988
$GdFe_6Sn_6$	YCo_6Ge_6	P6/mmm	5.412		4.466	Koretskaya and Skolozdra 1986
$GdFe_6Sn_6$	$TbFe_6Sn_6$	Cmcm	8.933	18.66	5.384	Chafik El Idrissi et al. 1991a
$GdCo_3Sn$	$BaLi_4$	$P6_3/mmc$	8.866		7.482	Skolozdra 1993
GdCoSn	TiNiSi	Pnma	7.315	4.540	7.455	Skolozdra et al. 1982
Gd_6Co_2Sn	Ho_6Ni_2Ga	Immm	9.522	9.502	9.995	Koretskaya et al. 1988b
$GdCo_xSn_y$	Phase *I*	Pm3n	9.516			Espinosa et al. 1982
$Gd_6Co_8Sn_{26}$	Phase *I*	Pm3n	9.518			Skolozdra et al. 1983
$GdNi_{5-x}Sn_{1+x}$	$CeCu_{4.38}In_{1.62}$	Pnnm	16.152	10.276	4.892	Skolozdra et al. 1996b
$GdNi_3Sn_2$	$HoGa_{2.4}Ni_{2.6}$	P6/mmm	9.197		4.271	Skolozdra et al. 1988a
$GdNi_2Sn_2$	$CaBe_2Ge_2$	P4/nmm	4.369		9.709	Skolozdra 1993
GdNiSn	TiNiSi	Pnma	7.199	4.464	7.677	Dwight 1983
			7.198	4.469	7.627	Skolozdra et al. 1984b
$Gd_9Ni_{24}Sn_{49}$	$Gd_9Ni_{24}Sn_{49}$	Im3	11.854			Komarovskaya and Skolozdra 1985
$GdNiSn_2$	$LuNiSn_2$	Pnma	16.131	4.434	14.670	Komarovskaya et al. 1983a
Gd_6Ni_2Sn	Ho_6Ni_2Ga	Immm	9.480	9.658	10.023	Sichevich et al. 1984
$Gd_6Cu_8Sn_8$	$Gd_6Cu_8Ge_8$	Immm	14.737	6.946	4.447	Skolozdra et al. 1984a
GdCuSn	$CaIn_2$	$P6_3/mmc$	4.531		7.364	Komarovskaya et al. 1983b
$Gd_2Cu_4Sn_5$	$Sm_2Cu_4Sn_5$	I4mm	4.400		24.89	Komarovskaya and Skolozdra 1992
$GdRu_xSn_y$	Phase *III*	Fm3m	13.812			Espinosa et al. 1982

continued on next page

Table 5, *continued*

Compound	Structure type	Space group	Lattice parameters (Å)			Reference(s)
			a	*b*	*c*	
GdRhSn	Fe_2P	$P\bar{6}2m$	7.527		3.862	Dwight et al. 1973
$Gd_2Rh_3Sn_5$	$Y_2Rh_3Sn_5$	$Cmc2_1$	4.419	26.28	7.191	Meot-Meyer et al. 1984
$GdRh_xSn_y$	Phase *I*	Pm3n	9.638			Espinosa et al. 1982
$GdRh_xSn_y$	Phase *I'* [a]	nl	9.638			Miraglia et al. 1986
GdPdSn	TiNiSi	Pnma	7.254	4.618	7.912	Dwight 1983
			7.254	4.608	7.925	Rossi et al. 1985
			7.264	4.616	7.919	Adroja and Malik 1992
GdAgSn	$CaIn_2$	$P6_3/mmc$	4.712		7.435	Mazzone et al. 1981
$GdOs_xSn_y$	Phase *III*	Fm3m	13.843			Espinosa et al. 1982
$GdIr_xSn_y$	Phase *III*	Fm3m	13.811			Espinosa et al. 1982
$GdPt_2Sn$	$ZrPt_2Al$	$P6_3/mmc$	4.531		9.065	de Mooij and Buschow 1984
GdPtSn	Fe_2P	$P\bar{6}2m$	7.462		4.034	Dwight et al. 1973
$TbMn_6Sn_6$	$HfFe_6Ge_6$	P6/mmm	5.519		9.004	Malaman et al. 1988
$TbFe_6Sn_6$	YCo_6Ge_6	P6/mmm	5.397		4.477	Koretskaya and Skolozdra 1986
$TbFe_6Sn_6$	$TbFe_6Sn_6$	Cmcm	8.920	18.62	5.390	Chafik El Idrissi et al. 1991a
$TbCo_3Sn$	$BaLi_4$	$P6_3/mmc$	8.851		7.436	Skolozdra 1993
$TbCo_6Sn_6$	YCo_6Ge_6	P6/mmm	5.371		4.268	Skolozdra and Koretskaya 1984
TbCoSn	TiNiSi	Pnma	7.260	4.534	7.448	Skolozdra et al. 1982
Tb_6Co_2Sn	Ho_6Ni_2Ga	Immm	9.403	9.426	9.889	Koretskaya et al. 1988b
$TbCo_xSn_y$	Phase *I*	Pm3n	9.497			Espinosa et al. 1982
$Tb_6Co_8Sn_{26}$	Phase *I*	Pm3n	9.501			Skolozdra et al. 1983
$TbCo_xSn_y$	Phase *III*	Fm3m	17.774			Espinosa et al. 1982
$Tb_7Co_6Sn_{23}$	$Ho_7Co_6Sn_{23}$	$P\bar{3}m1$	9.655		9.878	Skolozdra et al. 1986b
$TbNi_{5-x}Sn_{1+x}$	$CeCu_{4.38}In_{1.62}$	Pnnm	16.122	10.233	4.884	Skolozdra et al. 1996b
$TbNi_3Sn_2$	$HoGa_{2.4}Ni_{2.6}$	P6/mmm	9.157		4.264	Skolozdra et al. 1988a
TbNiSn	TiNiSi	Pnma	7.146	4.448	7.661	Dwight 1983
			7.138	4.450	7.660	Skolozdra et al. 1984b
$Tb_9Ni_{24}Sn_{49}$	$Gd_9Ni_{24}Sn_{49}$	Im3	11.838			Komarovskaya and Skolozdra 1985
$TbNiSn_2$	$LuNiSn_2$	Pnma	16.062	4.425	14.603	Komarovskaya et al. 1983a
Tb_6Ni_2Sn	Ho_6Ni_2Ga	Immm	9.397	9.596	9.989	Sichevich et al. 1984
$Tb_6Cu_8Sn_8$	$Gd_6Cu_8Ge_8$	Immm	14.639	6.913	4.436	Skolozdra et al. 1984a
TbCuSn	$CaIn_2$	$P6_3/mmc$	4.509		7.291	Komarovskaya et al. 1983b
$Tb_2Cu_4Sn_5$	$Sm_2Cu_4Sn_5$	I4mm	4.392		24.80	Komarovskaya and Skolozdra 1992
$TbRu_xSn_y$	Phase *III*	Fm3m	13.784			Espinosa et al. 1982
TbRhSn	Fe_2P	$P\bar{6}2m$	7.542		3.796	Dwight et al. 1973

continued on next page

Table 5, *continued*

Compound	Structure type	Space group	Lattice parameters (Å)			Reference(s)
			a	*b*	*c*	
$Tb_2Rh_3Sn_5$	$Y_2Rh_3Sn_5$	$Cmc2_1$	4.408	26.22	7.172	Meot-Meyer et al. 1984
$TbRh_xSn_y$	Phase *III*	Fm3m	13.774			Espinosa et al. 1982
$TbRh_xSn_y$	Phase *II'*	$I4_1/acd$	13.772		27.544	Miraglia et al. 1987
TbPdSn	TiNiSi	Pnma	7.182	4.598	7.916	Dwight 1983
			7.196	4.595	7.893	Adroja and Malik 1992
$TbPd_2Sn$	$MnCu_2Al$	Fm3m	6.740			Malik et al. 1985
TbAgSn	$CaIn_2$	$P6_3/mmc$	4.695		7.372	Mazzone et al. 1981
TbAgSn	LiGaGe	$P6_3mc$	4.688		7.368	Bażela et al. 1992, 1995a
$TbOs_xSn_y$	Phase *III*	Fm3m	13.813			Espinosa et al. 1982
$TbIr_xSn_y$	Phase *III*	Fm3m	13.781			Espinosa et al. 1982
$TbIr_xSn_y$	Phase *VII*		nl	nl	nl	Espinosa et al. 1982
$TbPt_2Sn$	$ZrPt_2Al$	$P6_3/mmc$	4.522		9.021	Dwight 1987
TbPtSn	Fe_2P	$P\bar{6}2m$	7.437		4.001	Dwight et al. 1973
TbAuSn	$CaIn_2$	$P6_3/mmc$	4.64		7.39	Dwight 1976
$DyMn_6Sn_6$	$HfFe_6Ge_6$	P6/mmm	5.515		8.996	Malaman et al. 1988
$DyMnSn_2$	$TiMnSi_2$	Pbam	10.46	11.49	8.97	Venturini et al. 1989b
$DyFe_6Sn_6$	YCo_6Ge_6	P6/mmm	5.407		4.462	Koretskaya and Skolozdra 1986
$DyFe_6Sn_6$	$DyFe_6Sn_6$	Ammm	8.873	46.56	5.363	Chafik El Idrissi et al. 1991a
$DyFe_6Sn_6$	$DyFe_6Sn_6$	Cmmm	37.343	21.560	8.912	Oleksyn et al. 1995
$DyCo_3Sn$	$BaLi_4$	$P6_3/mmc$	8.836		7.419	Skolozdra 1993
$DyCo_6Sn_6$	YCo_6Ge_6	P6/mmm	5.368		4.262	Skolozdra and Koretskaya 1984
DyCoSn	TiNiSi	Pnma	7.202	4.526	7.448	Skolozdra et al. 1982
Dy_6Co_2Sn	Ho_6Ni_2Ga	Immm	9.356	9.365	9.868	Koretskaya et al. 1988b
$DyCo_xSn_y$	Phase *II* [a]	$I4_1/acd$	13.565			Espinosa et al. 1982
$DyCo_xSn_y$	Phase *VII*		nl	nl	nl	Espinosa et al. 1982
$Dy_7Co_6Sn_{23}$	$Ho_7Co_6Sn_{23}$	$P\bar{3}m1$	9.645		9.861	Skolozdra et al. 1986b
$DyNi_{5-x}Sn_{1+x}$	$CeCu_{4.38}In_{1.62}$	Pnnm	16.102	10.227	4.875	Skolozdra et al. 1996b
DyNiSn	TiNiSi	Pnma	7.112	4.439	7.656	Dwight 1983
			7.088	4.435	7.655	Skolozdra et al. 1984b
$DyNiSn_2$	$LuNiSn_2$	Pnma	16.029	4.415	14.556	Komarovskaya et al. 1983a
Dy_6Ni_2Sn	Ho_6Ni_2Sn	Immm	9.349	9.515	9.925	Sichevich et al. 1984
$Dy_6Cu_8Sn_8$	$Gd_6Cu_8Ge_8$	Immm	14.628	6.915	4.435	Skolozdra et al. 1984a
DyCuSn	$CaIn_2$	$P6_3/mmc$	4.500		7.245	Komarovskaya et al. 1983b
$DyRu_xSn_y$	Phase *II* [a]	$I4_1/acd$	13.763			Espinosa et al. 1982
DyRhSn	Fe_2P	$P\bar{6}2m$	7.529		3.771	Dwight et al. 1973
$Dy_2Rh_3Sn_5$	$Y_2Rh_3Sn_5$	$Cmc2_1$	4.394	26.18	7.142	Meot-Meyer et al. 1984
$DyRh_xSn_y$	Phase *III*	Fm3m	13.750			Espinosa et al. 1982

continued on next page

Table 5, *continued*

Compound	Structure type	Space group	Lattice parameters (Å)			Reference(s)
			a	*b*	*c*	
$DyPd_2Sn$	$MnCu_2Al$	Fm3m	6.722			Malik et al. 1985
DyPdSn	TiNiSi	Pnma	7.157	4.589	7.897	Dwight 1983
			7.158	4.591	7.900	Rossi et al. 1985
			7.160	4.587	7.895	Adroja and Malik 1992
DyAgSn	$CaIn_2$	$P6_3/mmc$	4.691		7.337	Mazzone et al. 1981
$DyOs_xSn_y$	Phase *III*	Fm3m	13.792			Espinosa et al. 1982
$DyOs_xSn_y$	Phase *II'*	$I4_1/acd$	13.775		27.550	Miraglia et al. 1987
$DyIr_xSn_y$	Phase *III*	Fm3m	13.766			Espinosa et al. 1982
$DyIr_xSn_y$	Phase *VII*		nl	nl	nl	Espinosa et al. 1982
DyPtSn	Fe_2P	$P\bar{6}2m$	7.427		3.981	Dwight et al. 1973
DyAuSn	$CaIn_2$	$P6_3/mmc$	4.63		7.36	Dwight 1976
$HoMn_6Sn_6$	$HfFe_6Ge_6$	$P6_3/mmc$	5.508		8.993	Malaman et al. 1988
$HoMnSn_2$	$TiMnSi_2$	Pbam	10.42		11.45	Venturini et al. 1989b
$HoFe_6Sn_6$	YCo_6Ge_6	P6/mmm	5.398		4.459	Koretskaya and Skolozdra 1986
$HoFe_6Sn_6$	$HoFe_6Sn_6$	Immm	8.899	27.93	5.374	Chafik El Idrissi et al. 1991a
$HoCo_3Sn$	$BaLi_4$	$P6_3/mmc$	8.841		7.377	Skolozdra 1993
$HoCo_6Sn_6$	YCo_6Ge_6	P6/mmm	5.364		4.260	Skolozdra and Koretskaya 1984
HoCoSn	TiNiSi	Pnma	7.154	4.503	7.461	Skolozdra et al. 1982
Ho_6Co_2Sn	Ho_6Ni_2Ga	Immm	9.318	9.348	9.806	Koretskaya et al. 1988b
$HoCo_xSn_y$	Phase *III*	Fm3m	13.549			Espinosa et al. 1982
$Ho_7Co_6Sn_{23}$	$Ho_7Co_6Sn_{23}$	$P\bar{3}m1$	9.628		9.846	Skolozdra et al. 1986b
$HoNi_{5-x}Sn_{1+x}$	$CeCu_{4.38}In_{1.62}$	Pnnm	16.103	10.210	4.870	Skolozdra et al. 1996b
HoNiSn	TiNiSi	Pnma	7.063	4.438	7.64	Dwight 1983
			7.050	4.422	7.622	Skolozdra et al. 1984b
Ho_2NiSn_6	Lu_2NiSn_6	Cmmm	4.305	22.421	4.387	Skolozdra et al. 1985
$HoNiSn_2$	$LuNiSn_2$	Pnma	16.000	4.404	14.503	Komarovskaya et al. 1983a
Ho_6Ni_2Sn	Ho_6Ni_2Ga	Immm	9.309	9.486	9.879	Sichevich et al. 1984
Ho_6Cu_8Sn8	$Gd_6Cu_8Sn_8$	Immm	14.544	6.901	4.412	Skolozdra et al. 1984a
HoCuSn	$CaIn_2$	$P6_3/mmc$	4.499		7.229	Komarovskaya et al. 1983b
$HoRu_xSn_y$	Phase *II*[a]	$I4_1/acd$	13.751			Espinosa et al. 1982
HoRhSn	Fe_2P	$P\bar{6}2m$	7.527		3.748	Dwight et al. 1973
$Ho_2Rh_3Sn_5$	$Y_2Rh_3Sn_5$	$Cmc2_1$	4.378	26.12	7.120	Meot-Meyer et al. 1984
$HoRh_xSn_y$	Phase *II*[a]	$I4_1/acd$	13.750			Espinosa et al. 1982
$HoRh_xSn_y$	Phase *III*	Fm3m	13.750			Espinosa et al. 1982
$HoPd_2Sn$	$MnCu_2Al$	Fm3m	6.705			Malik et al. 1985
HoPdSn	TiNiSi	Pnma	7.117	4.581	7.884	Dwight 1983
			7.111	4.577	7.881	Adroja and Malik 1992

continued on next page

Table 5, *continued*

Compound	Structure type	Space group	Lattice parameters (Å)			Reference(s)
			a	*b*	*c*	
HoPdSn	Fe_2P	$P\bar{6}2m$	7.433		3.979	Dwight et al. 1973
HoAgSn	$CaIn_2$	$P6_3/mmc$	4.672		7.319	Mazzone et al. 1981
HoAgSn	LiGaGe	$P6_3mc$	4.672		7.318	Bażela et al. 1992, 1995a
$HoOs_xSn_y$	Phase *III*	Fm3m	13.744			Espinosa et al. 1982
HoIrSn	Fe_2P	$P\bar{6}2m$	7.456		3.848	Dwight et al. 1973
$HoIr_xSn_y$	Phase *III*	Fm3m	13.750			Espinosa et al. 1982
HoPtSn	Fe_2P	$P\bar{6}2m$	7.418		3.966	Dwight et al. 1973
HoAuSn	$CaIn_2$	$P6_3/mmc$	4.62		7.35	Dwight 1976
HoAuSn	MgAgAs	$F\bar{4}3m$	6.624			Dwight 1976
$ErMn_6Sn_6$	$HfFe_6Ge_6$	P6/mmm	5.509		8.992	Malaman et al. 1988
$ErMnSn_2$	$TiMnSi_2$	Pbam	10.37	11.40	8.95	Venturini et al. 1989b
$ErFe_6Sn_6$	YCo_6Ge_6	P6/mmm	5.383		4.441	Koretskaya and Skolozdra 1986
$ErFe_6Sn_6$	$ErFe_6Sn_6$	Cmcm	8.906	37.25	5.377	Chafik El Idrissi et al. 1991a
$ErCo_3Sn$	$BaLi_4$	$P6_3/mmc$	8.801		7.421	Skolozdra 1993
$ErCo_6Sn_6$	YCo_6Ge_6	P6/mmm	5.358		4.235	Skolozdra and Koretskaya 1984
ErCoSn	TiNiSi	Pnma	7.093		4.480	Skolozdra et al. 1982
Er_6Co_2Sn	Hf_6Ni_2Ga	Immm	9.274	9.292	9.750	Koretskaya et al. 1988b
$ErCo_xSn_y$	Phase *II* [a]	$I4_1/acd$	13.524			Espinosa et al. 1982
$Er_7Co_6Sn_{23}$	$Ho_7Co_6Sn_{23}$	$P\bar{3}m1$	9.618		9.829	Skolozdra et al. 1986b
$ErNi_{5-x}Sn_{1+x}$	$CeCu_{4.38}In_{1.62}$	Pnnm	16.047	10.201	4.857	Skolozdra et al. 1996b
ErNiSn	TiNiSi	Pnma	7.016	4.425	7.629	Dwight 1983
			7.138	4.450	7.660	Skolozdra et al. 1984b
$ErNiSn_2$	$LuNiSn_2$	Pnma	15.986	4.399	14.770	Komarovskaya et al. 1983a
Er_6Ni_2Sn	Ho_6Ni_2Ga	Immm	9.245	9.417	9.819	Sichevich et al. 1984
Er_2NiSn_6	Lu_2NiSn_6	Cmmm	4.311	22.411	4.379	Skolozdra et al. 1985
$Er_6Cu_8Sn_8$	$Gd_6Cu_8Ge_8$	Immm	14.520	6.879	4.397	Skolozdra et al. 1984a
ErCuSn	$CaIn_2$	$P6_3/mmc$	4.497		7.203	Komarovskaya et al. 1983b
$ErRu_xSn_y$	Phase *II* [a]	$I4_1/acd$	13.732			Espinosa et al. 1982
ErRhSn	Fe_2P	$P\bar{6}2m$	7.519		3.730	Dwight et al. 1973
$ErRh_xSn_y$	Phase *II* [a]	$I4_1/acd$	13.698			Espinosa et al. 1982
$ErRh_xSn_y$	Phase *III*	Fm3m	13.714			Espinosa et al. 1982
$ErPd_2Sn$	$MnCu_2Al$	Fm3m	6.692			Malik et al. 1985
ErPdSn	Fe_2P	$P\bar{6}2m$	7.43		3.94	Dwight et al. 1973
ErPdSn	TiNiSi	Pnma	7.094	4.570	7.872	Adroja and Malik 1992
ErAgSn	$CaIn_2$	$P6_3/mmc$	4.661		7.291	Mazzone et al. 1981
$ErOs_xSn_y$	Phase *III*	Fm3m	13.760			Espinosa et al. 1982
ErIrSn	Fe_2P	$P\bar{6}2m$	7.452		3.822	Dwight et al. 1973

continued on next page

Table 5, *continued*

Compound	Structure type	Space group	Lattice parameters (Å)			Reference(s)
			a	*b*	*c*	
$ErIr_xSn_y$	Phase *II* [a]	$I4_1/acd$	13.713			Espinosa et al. 1982
$ErPt_2Sn$	$ZrPt_2Al$	$P6_3/mmc$	4.498		8.939	de Mooij and Buschow 1984
ErPtSn	Fe_2P	$P\bar{6}2m$	7.406		3.958	Dwight et al. 1973
ErAuSn	MgAgAs	$F\bar{4}3m$	6.606			Dwight 1976
$TmMn_6Sn_6$	$HfFe_6Ge_6$	P6/mmm	5.506		8.988	Malaman et al. 1988
$TmMnSn_2$	$TiMnSi_2$	Pbam	10.32	11.35	8.94	Venturini et al. 1989b
$TmFe_6Sn_6$	YCo_6Ge_6	P6/mmm	5.371		4.434	Koretskaya and Skolozdra 1986
$TmFe_6Sn_6$	$HfFe_6Ge_6$	P6/mmm	5.372		8.894	Chafik El Idrissi et al. 1991a
$Tm_4Fe_6Sn_{19}$	Phase *II* [a] or *II'*		13.552			Skolozdra 1993
$TmCo_3Sn$	$BaLi_4$	$P6_3/mmc$	8.781		7.468	Skolozdra 1993
$TmCo_6Sn_6$	YCo_6Ge_6	P6/mmm	5.352		4.244	Skolozdra and Koretskaya 1984
TmCoSn	TiNiSi	Pnma	7.082	4.456	7.445	Skolozdra et al. 1982
Tm_6Co_2Sn	Ho_6Ni_2Ga	Immm	9.236	9.208	9.785	Koretskaya et al. 1988b
$TmCo_xSn_y$	Phase *II* [a]	$I4_1/acd$	13.512			Espinosa et al. 1982
$TmNi_{5-x}Sn_{1+x}$	$CeCu_{4.38}In_{1.62}$	Pnnm	16.025	10.178	4.851	Skolozdra et al. 1996b
TmNiSn	TiNiSi	Pnma	7.000	4.414	7.621	Dwight 1983
			6.977	4.401	7.614	Skolozdra et al. 1984b
$TmNiSn_2$	$LuNiSn_2$	Pnma	15.979	4.382	14.409	Komarovskaya et al. 1983a
Tm_6Ni_2Sn	Ho_6Ni_2Ga	Immm	9.233	9.408	9.805	Sichevich et al. 1984
Tm_2NiSn_6	Lu_2NiSn_6	Cmmm	4.301	22.278	4.366	Skolozdra et al. 1985
$Tm_6Cu_8Sn_8$	$Gd_6Cu_8Ge_8$	Immm	14.487	6.889	4.387	Skolozdra et al. 1984a
$Tm_6Cu_8Sn_8$	$Tm_6Cu_8Sn_8$	C2/m	16.119	4.3935	6.896	Thirion et al. 1983
				$\beta = 115.88°$		
		I2/m	14.503	6.896	4.3935	Thirion et al. 1983
				$\beta = 90.55°$		
TmCuSn	$CaIn_2$	$P6_3/mmc$	4.473		7.133	Komarovskaya et al. 1983b
$TmRu_xSn_y$	Phase *II* [a]	$I4_1/acd$	13.715			Espinosa et al. 1982
TmRhSn	Fe_2P	$P\bar{6}2m$	7.534		3.690	Dwight et al. 1973
$TmRh_xSn_y$	Phase *II* [a]	$I4_1/acd$	13.679			Espinosa et al. 1982
$TmRh_xSn_y$	Phase *III*	Fm3m	13.701			Espinosa et al. 1982
$TmPd_2Sn$	$MnCu_2Al$	Fm3m	6.670			Malik et al. 1985
TmPdSm	Fe_2P	$P\bar{6}2m$	7.42		3.92	Dwight et al. 1973
TmPdSn	TiNiSi	Pnma	7.030	4.547	7.915	Adroja and Malik 1992
$TmOs_xSn_y$	Phase *III*	Fm3m	13.744			Espinosa et al. 1982
TmIrSn	Fe_2P	$P\bar{6}2m$	7.46		3.77	Dwight et al. 1973
$TmIr_xSn_y$	Phase *II* [a]	$I4_1/acd$	13.702			Espinosa et al. 1982
$TmPt_2Sn$	$ZrPt_2Al$	$P6_3/mmc$	4.493		8.916	Dwight 1987

continued on next page

Table 5, *continued*

Compound	Structure type	Space group	Lattice parameters (Å)			Reference(s)
			a	*b*	*c*	
TmPtSn	Fe_2P	$P\bar{6}2m$	7.404		3.923	Dwight et al. 1973
TmAuSn	MgAgAs	$F\bar{4}3m$	6.591			Dwight 1976
$YbCo_3Sn$	$BaLi_4$	$P6_3/mmc$	8.784		7.468	Skolozdra 1993
$YbCo_xSn_y$	Phase *I*	Pm3n	9.563			Espinosa et al. 1982
$YbNi_{5-x}Sn_{1+x}$	$CeCu_{4.38}In_{1.62}$	Pnnm	16.779	10.276	4.837	Skolozdra et al. 1996b
$YbNi_2Sn$	$MnCu_2Al$	Fm3m	6.658			Skolozdra and Komarovskaya 1983
YbNiSn	TiNiSi	Pnma	6.983	4.426	7.616	Dwight 1983
			6.960	4.396	7.597	Skolozdra et al. 1984b
Yb_5CuSn_3	Ti_5Ga_4	$P6_3/mcm$	8.892		6.518	Rieger and Parthé 1968
YbZnSn	LiGaGe	$P6_3mc$	4.649		7.476	Merlo et al. 1991
$YbRu_xSn_y$	Phase *V*		nl	nl	nl	Espinosa et al. 1982
YbRhSn	Fe_2P	$P\bar{6}2m$	7.52		3.67	Dwight et al. 1973
$YbRh_xSn_y$	Phase *I*	Pm3n	9.675			Espinosa et al. 1982
$YbRh_xSn_y$	Phase *I'* [a]	nl	9.676			Miraglia et al. 1986
$YbPd_2Sn$	$MnCu_2Al$	Fm3m	6.658			Malik et al. 1985
YbPdSn	TiNiSi	Pnma	7.154	4.586	7.885	Adroja and Malik 1992
YbAgSn	$CaIn_2$	$P6_3/mmc$	4.791		7.256	Mazzone et al. 1981
YbCdSn	ZrNiAl	$P\bar{6}2m$	7.594		4.679	Merlo et al. 1991
YbIrSn	Fe_2P	$P\bar{6}2m$	7.49		3.73	Dwight et al. 1973
$YbIr_xSn_y$	Phase *I*	Pm3n	9.709			Espinosa et al. 1982
$YbIr_xSn_y$	Phase *II* [a]	$I4_1/acd$	13.749			Espinosa et al. 1982
$YbIr_xSn_y$	Phase *III*	Fm3m	13.751			Espinosa et al. 1982
YbPtSn	Fe_2P	$P\bar{6}2m$	7.379		3.933	Dwight et al. 1973
$LuMn_6Sn_6$	$HfFe_6Ge_6$	P6/mmm	5.496		8.985	Malaman et al. 1988
$LuMnSn_2$	$TiMnSi_2$	Pbam	10.30	11.27	8.92	Venturini et al. 1989b
$LuFe_6Sn_6$	YCo_6Ge_6	P6/mmm	5.370		4.435	Koretskaya and Skolozdra 1986
$LuFe_6Sn_6$	$HfFe_6Ge_6$	P6/mmm	5.369		8.876	Chafik El Idrissi et al. 1991a
$Lu_4Fe_6Sn_{19}$	Phase *II* [a] or *II'*		13.537			Skolozdra 1993
$Lu_3Co_{7.77}Sn_4$	$Lu_3Co_{7.77}Sn_4$	$P6_3mc$	8.746		7.432	Skolozdra et al. 1996a
$LuCo_6Sn_6$	YCo_6Ge_6	P6/mmm	5.345		4.239	Skolozdra and Koretskaya 1984
LuCoSn	TiNiSi	Pnma	7.018	4.462	7.424	Skolozdra et al. 1982
Lu_6Co_2Sn	Ho_6Ni_2Sn	Immm	9.189	9.169	9.726	Koretskaya et al. 1988b
$LuCo_xSn_y$	Phase *II* [a]	$I4_1/acd$	13.480			Espinosa et al. 1982
$LuNi_4Sn$	$MgCu_4Sn$	$F\bar{4}3m$	6.981			Skolozdra and Komarovskaya 1983
$LuNi_2Sn$	$MnCu_2Al$	Fm3m	6.345			Skolozdra and Komarovskaya 1983

continued on next page

Table 5, *continued*

Compound	Structure type	Space group	Lattice parameters (Å)			Reference(s)
			a	*b*	*c*	
LuNiSn	TiNiSi	Pnma	6.93	4.401	7.601	Dwight 1983
			6.916	4.386	7.589	Skolozdra et al. 1984b
$LuNiSn_2$	$LuNiSn_2$	Pnma	15.944	4.361	14.345	Komarovskaya et al. 1983a
Lu_6Ni_2Sn	Ho_6Ni_2Ga	Immm	9.141	9.279	9.710	Sichevich et al. 1984
Lu_2NiSn_6	Lu_2NiSn_6	Cmmm	4.301	22.278	4.366	Skolozdra et al. 1985
LuCuSn	$CaIn_2$	$P6_3/mmc$	4.457		7.093	Komarovskaya et al. 1983b
$LuRu_xSn_y$	Phase *II* [a]	$I4_1/acd$	13.692			Espinosa et al. 1982
$LuRu_xSn_y$	Phase *V*		nl	nl	nl	Espinosa et al. 1982
LuRhSn	Fe_2P	$P\bar{6}2m$	7.529		3.646	Dwight et al. 1973
$LuRh_xSn_y$	Phase *II* [a]	$I4_1/acd$	13.667			Espinosa et al. 1982
$LuPd_2Sn$	$MnCu_2Al$	Fm3m	6.645			Malik et al. 1985
LuPdSn	Fe_2P	$P\bar{6}2m$	7.513		3.783	Dwight et al. 1973
$LuOs_xSn_y$	Phase *III*	Fm3m	13.720			Espinosa et al. 1982
LuIrSn	Fe_2P	$P\bar{6}2m$	7.45		3.45	Dwight et al. 1973
$LuIr_xSn_y$	Phase *II* [a]	$I4_1/acd$	13.677			Espinosa et al. 1982
LuPtSn	Fe_2P	$P\bar{6}2m$	7.382		3.902	Dwight et al. 1973
LuAuSn	MgAgAs	$F\bar{4}3m$	6.563			Dwight 1976

[a] "Cubic" lattice parameters.

[b] Abbreviations: HT, high temperature; LT, low temperature; nl, not listed.

by Weitzer and Rogl (1993). There are four ternary compounds at 1073 K: $Nd_5(Mn,Sn)_3$, $Nd_3Mn_4Sn_4$ ($Nd_6Mn_8Sn_8$), Nd_5MnSn_5 and $NdMn_{1-x}Sn_{2-y}$. The existence of two compounds was observed only at 818 K – $NdMn_6Sn_6$ and $NdMn_{1-x}Sn_{2-y}$. The structure of Nd_5MnSn_5 was not determined. Macció et al. (1993) have measured the characteristic temperatures for the ternary compounds: $NdMn_6Sn_6$ forms at 953 K by a peritectic reaction, the temperatures at the end of the crystallization process for Nd_5MnSn_5, $Nd_3Mn_3Sn_4$ and $NdMn_{0.5}Sn_{1.85}$ are 1283, 1473 and 1353 K, respectively.

3.1.2. *R–Fe–Sn systems*

The isothermal section of the Y–Fe–Sn phase diagram has been constructed (up to 30 a/c Sn at 870 K more than 30 a/c Sn at 770 K) (Skolozdra 1993). Only one compound forms in the system – YFe_6Sn_6. Iron is in equilibrium with all compounds of the Y–Sn system, except YSn_3.

The isothermal section of the phase diagrams La–Fe–Sn has been studied for the concentration from 0 to 50 a/c Sn (770 K) and from 50 to 100 a/c Sn (670 K) (Skolozdra 1993). The peculiarity of this system is the immiscibility of the ternary alloys in the range with the Sn content less than 50 a/c. In the solid state alloys in this range contain the parts of the iron, tin and other phases, marked by A and B, which apparently are

the metastable compounds. In the region rich with La there is a compound which has an approximate composition $La_{60}Fe_{15}Sn_{25}$. Unannealed alloys of this composition contain phases with unknown structures. Annealing at 870 K leads to the formation of a new structure. Strong reflections of this compound on the powder pattern are well indexed in the face-centered cubic lattice and $a = 5.66$ Å. Further annealing at 770 K leads to the decomposition of this phase and the alloy contains La_5Sn_3, α-Fe and La.

In the La–Fe–Sn system another compound with the composition $LaFeSn_2$ forms. Its composition was reported by Dörrscheidt et al. (1982) as $LaFe_{0.34}Sn_2$ for a single-crystal. As a result of a careful X-ray structure analysis of the alloys over a range of compositions, Skolozdra et al. (1988b) established that alloys annealed at 670 K form a compound with the composition $LaFe_{0.24}Sn_{1.79}$ and a defect structure of the $CeNiSi_2$ type. Powder patterns of the unannealed alloys show, that in comparison with 670 K results, the compound at higher temperatures has a wide homogeneity range between $LaFeSn_2$ and $LaFe_{0.34}Sn_2$.

A new compound $La_6Fe_{13}Sn$ has recently been found by Weitzer et al. (1993b).

In consequence of a high capacity of the alloys for oxidation and hydrolysis in air, the phase equilibria in the region La_5Sn_3–$LaFe_{0.24}Sn_{1.97}$–$LaSn_3$ have not been established.

In the Nd–Fe–Sn system the alloy with the composition $Nd_2Fe_{14}Sn$ annealed at 1273 K, was investigated by van Mens (1986). The alloy contains the binary compounds Nd_xSn_y, Nd_2Fe_{17} and Fe. Weitzer et al. (1993b) have found the $Nd_6Fe_{13}Sn$ compound.

Only one compound forms in the Gd–Fe–Sn system. Its composition is $GdFe_6Sn_6$. Phase equilibria at 870 K and 670 K (up to 55 a/c and more than 55 a/c Sn, respectively) were ascertained by Skolozdra (1993).

The Lu–Fe–Sn system is characterized by the formation of several compounds. So far three compounds are known. The isothermal sections at 870 K (0–49 a/c Sn) and 670 K (50 and more a/c Sn) have been constructed (Skolozdra 1993). The $LuFe_6Sn_6$, $Lu_4Fe_6Sn_{19}$ compounds and a phase with a high Lu content of the approximate composition $Lu_{70}Fe_{15}Sn_{15}$ form in the system.

3.1.3. *R–Co–Sn systems*

The R–Co–Sn systems, where R = Y, Ce, Sm, Gd, Lu, have been studied. The isothermal section of the phase diagram of Y–Co–Sn system has been constructed at 770 K up to 55 a/c Sn and at 670 K (more than 55 a/c Sn) (Skolozdra 1993). Nine compounds (YCo_3Sn, YCo_6Sn_6, ~YCo_2Sn_2, ~$Y_{25}Co_{30}Sn_{45}$, $Y_4Co_6Sn_{19}$, $Y_7Co_6Sn_{23}$, YCoSn, ~$Y_4Co_3Sn_3$, Y_6Co_2Sn) form in this system. The crystal structure was not determined for three compounds. A solid solution based on YSn_2 forms, with homogeneity range to 5 a/c Co.

The Ce–Co–Sn system was investigated in the range to 50 a/c at 770 K and at 670 K (more than 50 a/c Sn) (Skolozdra 1993). Five ternary compounds (~$Ce_{40}Co_{38}Sn_{22}$, ~$Ce_4Co_3Sn_3$, ~$Ce_{30}Co_{35}Sn_{35}$, $CeCo_{1-x}Sn_{2-y}$ and $Ce_6Co_8Sn_{26}$) form in the system. For the last two the crystal structure was studied. The $CeCo_{1-x}Sn_{2-y}$ phase has a variable composition. The $Ce_{40}Co_{38}Sn_{22}$ compound decomposes very quickly in air. The homogeneity range of the compounds (except for the binary compounds) is small.

The Sm–Co–Sn system has been studied at 770 K (up to 50 a/c Sn) and at 670 K (more than 50 a/c Sn) (Skolozdra 1993). Seven ternary compounds form in this system. The $SmCo_{1-x}Sn_{2-y}$ stannide has variable composition, the other compounds are characterized by the insignificant homogeneity range. The crystal structure was determined for $Sm_6Co_8Sn_{26}$, $SmCo_{1-x}Sn_{2-y}$ and Sm_6Co_2Sn, while those for ~$SmCo_3Sn$, ~$Sm_4Co_3Sn_3$, ~$SmCo_2Sn_2$, and ~$Sm_{65}Co_{25}Sm_{10}$ are unknown.

The isothermal sections of the Gd–Co–Sn phase diagram have been studied at 770 K (0–55 a/c Sn) and 670 K (more than 55 a/c Sm). In the system Gd–Co–Sn seven ternary compounds were found: $GdCo_{3-x}Sn_{1+x}$, $GdCo_6Sn_6$, ~$GdCo_2Sn_2$, $Gd_6Co_8Sn_{26}$, GdCoSn, ~$Gd_4Co_3Sn_3$ and Gd_6Co_2Sn. The structure of the $GdCo_2Sn_2$ and $Gd_4Co_3Sn_3$ have not been determined. The last one is isostructural with the analogous stannides of the Sm–Co–Sn and Y–Co–Sn system. The GdCoSn and $GdCo_6Sn_6$ compounds probably formed as a result of a peritectic or peritectoid reaction because they appear after long annealing. Only the $GdCo_{3-x}Sn_{1+x}$ ($x = 0$–0.25) compound has an appreciable homogeneity range.

The isothermal sections of the phase diagram of the Lu–Co–Sn system at 870 K (up 50 a/c Sn) and at 670 (more than 50 a/c Sn) were constructed (Skolozdra 1993). The system is characterized by the existence of eight ternary stannides: ~$Lu_{15}Co_{70}Sn_{15}$, $Lu_2Co_5Sn_3$ ($Lu_3Co_{7.7}Sn_4$), $LuCo_6Sn_6$, ~$LuCo_2Sn_2$, LuCoSn, $Lu_4Co_6Sn_{19}$, ~$Lu_{30}Co_{15}Sn_{55}$ and Lu_6Co_2Sn. The crystal structure was studied for five stannides ($Lu_3Co_{7.77}Sn_4$, $LuCo_6Sn_6$, LuCoSn, $Lu_4Co_9Sn_{19}$ and Lu_6Co_2Sn). All compounds have an inappreciable homogeneity range.

3.1.4. *R–Ni–Sn systems*

For Y, Ce, Gd and Lu the Ni-containing systems have been studied. The Y–Ni–Sn system was partly investigated (Skolozdra 1993). The alloys with a tin content up to 50 a/c were annealed at 770 K, alloys with the greater tin quantity were annealed at 670 K. In the investigated part of the system seven ternary compounds form: $YNi_{5-x}Sn_{1+x}$ ($x \approx 0.1$), ~$Y_{15}Ni_{60}Sn_{25}$, YNi_3Sn_2, YNiSn, $YNiSn_2$, $Y_9Ni_{24}Sn_{49}$ and ~$Y_{16.5}Ni_{16.5}Sn_{67}$. For the stannides $Y_{15}Ni_{60}Sn_{25}$ and $Y_{16.5}Ni_{16.5}Sn_{67}$ the structure was not studied. In the yttrium corner the Y_6Ni_2Sn stannide exists.

The isothermal section of the phase diagram of the Ce–Ni–Sn system at 600 K was constructed (fig. 2) by Skolozdra and Komarovskaya (1988a). Ten ternary compounds ($CeNi_5Sn$, $CeNi_4Sn_2$, $CeNi_2Sn_2$, $Ce_9Ni_{24}Sn_{49}$, $Ce_3Ni_2Sn_7$, $CeNi_{1-x}Sn_{2-y}$, ~Ce_2NiSn_2, CeNiSn, ~$Ce_{45}Ni_{30}Sn_{25}$, $Ce_5Ni_{1.5}Sn_{1.5}$) form in the system. The crystal structures of Ce_2NiSn_2 and $Ce_{45}Ni_{30}Sn_{25}$ were not studied. But recently the crystal structure of the Ce_2Ni_2Sn compound has been discovered (Fourgeot et al. 1995). We assumed that the $Ce_{45}Ni_{30}Sn_{25}$ compound really corresponded to Ce_2Ni_2Sn therefore the Ce_2Ni_2Sn phase was marked on the isothermal section of the Ce–Ni–Sn system at 670 K (fig. 2) instead of $Ce_{45}Ni_{30}Sn_{25}$. The $CeNi_{1-x}Sn_{2-y}$ compound has a homogeneity range. The $CeNi_2Sn_2$ stannide is characterized by polymorphism. The high temperature modification has the tetragonal $CaBe_2Ge_2$ type structure, and the low temperature modification has a monoclinic structure.

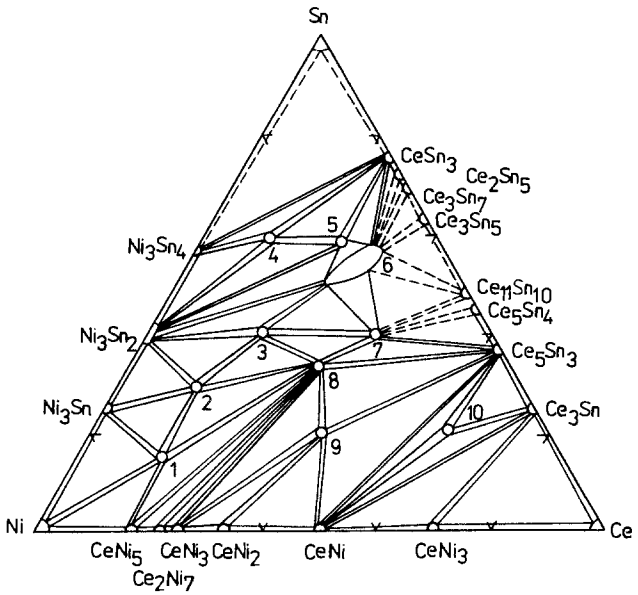

Fig. 2. Isothermal section of the Ce–Ni–Sn system at 670 K; (1) $CeNi_5Sn$; (2) $CeNi_4Sn_2$; (3) $CeNi_2Sn_2$; (4) $Ce_9Ni_{24}Sn_{49}$; (5) $Ce_3Ni_2Sn_7$; (6) $CeNi_{1-x}Sn_{2-y}$; (7) Ce_2NiSn_2; (8) CeNiSn; (9) Ce_2Ni_2Sn; (10) $Ce_5Ni_{1.5}Sn_{1.5}$ (Skolozdra and Komarovskaya 1988a).

The phase equilibria in the ternary system Gd–Ni–Sn was investigated at 770 K (up to 55 a/c Sn) and 670 K (more than 55 a/c Sn) (Skolozdra 1993). The system turned out to be rich in ternary compounds (15). For the $GdNi_3Sn_2$, $GdNi_2Sn_2$, $GdNiSn_2$, $Gd_9Ni_{24}Sn_{49}$, $GdNiSn_2$, Gd_6Ni_2Sn stannides the crystal structures are known, while those for $GdNi_{5-x}Sn_{1+x}$ ($x \approx 0.1$), ~$Gd_{15}Ni_{60}Sn_{25}$, ~$Gd_{20}Ni_{35}Sn_{45}$, ~$Gd_{25}Ni_{32}Sn_{43}$, ~$Gd_{16.5}Ni_{16.5}Sn_{67}$, ~$Gd_2NiSn_7$, ~$Gd_{45}Ni_{10}Sn_{45}$, ~$Gd_{42}Ni_{42}Sn_{16}$, ~$Gd_{62}Ni_{33}Sn_5$ stannides are unknown. The Ni solubility in $GdSn_2$ is equal to 5 a/c, the homogeneity range of the solid solution has a direction toward the $GdNiSn_2$ compound. In spite of the decrease of the tin content in the alloys, the volume of the unit cell of the solid solution increases that testifies to the formation of a solid solution formed by the insertion of nickel into the $GdSn_2$ structure. The nickel solubility in Gd_3Sn_7 and $GdSn_{2.75}$ is less than 3 a/c. The formation of the solid solution of the substitution of nickel by tin in $GdNi_5$ (5 a/c Sn) was also observed.

The Lu–Ni–Sn system has been investigated at 770 K (up to 50 a/c Sn) and 670 K (more than 50 a/c Sn) (Skolozdra and Komarovskaya 1988b). The authors have found four more compounds in the Lu–Ni binary system in addition to the known ones, and in the Lu–Sn system they have found the Lu_5Sn_4 compound.

In the ternary Lu–Ni–Sn system the existence of twelve ternary compounds was established: ~$Lu_{15}Ni_{70}Sn_{15}$, $LuNi_4Sn$, $LuNi_2Sn$, $LuNiSn$, $LuNiSn_2$, ~$Lu_{16.5}Ni_{16.5}Sn_{67}$, ~$Lu_2NiSn_7$, Lu_2NiSn_6, ~$Lu_{43}Ni_{40}Sn_{17}$, ~$Lu_{48}Ni_{40}Sn_{12}$, ~$Lu_{62}Ni_{33}Sn_5$, Lu_6Ni_2Sn. The

crystal structures have been determined for $LuNi_4Sn$, $LuNi_2Sn$, LuNiSn, $LuNiSn_2$, Lu_2NiSn_6 and Lu_6Ni_2Sn. Among binary compounds only $LuNi_4$ dissolves an appreciable quantity of the third component.

3.1.5. *R–Cu–Sn systems*

The results of the investigation of the phase equilibria in the four systems Sc–Cu–Sn, Y–Cu–Sn, Pr–Cu–Sn, Gd–Cu–Sn and Lu–Cu–Sn are given below.

The isothermal section of the phase diagram of the Sc–Cu–Sn system at 673 K was constructed (Kotur and Derkach 1994). The system is characterized by the existence of three ternary stannides: $ScCu_4Sn$, ScCuSn and Sc_6CuSn_2. The crystal structure was studied for $ScCu_4Sn$ and ScCuSn. The homogeneity range of the ternary compounds is small.

The Y–Cu–Sn system has been studied at 773 K in the range from 0 to 40 a/c Y by Yinghong et al. (1991). Three phases were found in the system: $Y_8Cu_7Sn_5$ (θ), $Y_3Cu_4Sn_3$ (β), and $Y_{19}Cu_{66}Sn_{15}$ (γ). Their structures are unknown, however, it has been established that $Y_8Cu_7Sn_5$ has an orthorhombic lattice with the parameters: $a=9.702$, $b=7.285$ and $c=6.545$ Å.

For the Pr–Cu–Sn system the isothermal section at 670 K has been determined (Komarovskaya et al. 1989). In the system there are 11 ternary compounds of the following composition: ~$Pr_{15}Cu_{70}Sn_{15}$, ~$Pr_{15}Cu_{65}Sn_{20}$, $PrCu_{9.4}Sn_{3.6}$, ~$Pr_{49}Cu_{28}Sn_{23}$, PrCuSn, $Pr_6Cu_8Sn_8$, $PrCu_2Sn_2$, $Pr_2Cu_4Sn_5$, $PrCu_{1-x}Sn_{2-y}$, ~$Pr_{35}Cu_{18}Sn_{47}$ and $PrCu_{0.25}Sn_{1.25}$. The crystal structure is unknown for the compounds $Pr_{15}Cu_{70}Sn_{15}$, $Pr_{15}Cu_{65}Sn_{20}$, $Pr_{49}Cu_{28}Sn_{33}$ and $Pr_{35}Cu_{18}Sn_{47}$. A homogeneity range has been established for the $Pr_2Cu_{1-x}Sn_{2-y}$ phase only. The solubility of the compounds in the other binary and ternary compounds is insignificant.

The isothermal section of the phase diagram of Gd–Cu–Sn system (fig. 3) has been constructed at 670 K (Skolozdra 1993). In the copper-rich range three stannides form: ~$Gd_{15}Cu_{70}Sn_{15}$, ~$Gd_{15}Cu_{65}Sn_{20}$ and ~$GdCu_7Sn_2$, the structures of which at that time were not studied. Three other compounds – GdCuSn, $Gd_6Cu_8Sn_8$ and $Gd_2Cu_4Sn_5$ – form at a copper content less than 36 a/c and have a known structure. The homogeneity range of the ternary and binary phases is insignificant.

Only three compounds form in the Lu–Cu–Sn system. The 670 K isothermal section has been determined by Komarovskaya et al. (1989). The crystal structure has been studied for LuCuSn, and the structures of $Lu_{12}Cu_{68}Sn_{20}$ and ~$Lu_6Cu_8Sn_8$ have not been determined.

3.1.6. *R–Pd–Sn systems*

The Y–Pd–Sn system has been investigated in the palladium corner by Jorda et al. (1985), where the isothermal section of the system at 1073 K has been discussed. Five phases were found: $Y_{13}Pd_{40}Sn_{31}$ (α), YPd_2Sn (β), $Y_{17}Pd_{54}Sn_{29}$ (γ), $Y_{19}Pd_{54}Sn_{27}$ (δ) and $Y_9Pd_{64}Sn_{27}$ (ε). The crystal structures have been reported for the α- and β-phases, see table 5 (above).

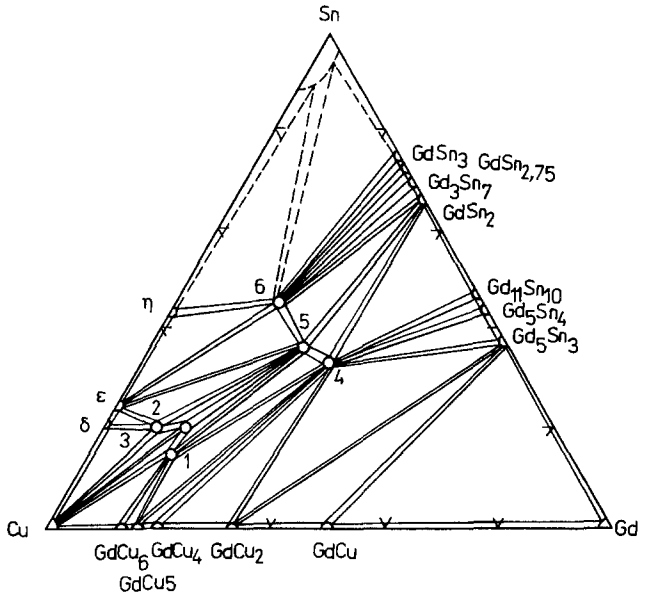

Fig. 3. Isothermal section of the Gd–Cu–Sn system at 670 K; (1) $Gd_{15}Cu_{70}Sn_{15}$; (2) $Gd_{15}Cu_{65}Sn_{20}$; (3) $GdCu_7Sn_2$; (4) GdCuSn; (5) $Gd_6Cu_8Sn_8$; (6) $Gd_2Cu_4Sn_5$ (Skolozdra 1993).

3.2. *Crystal structures of the compounds*

3.2.1. *$CeNi_5Sn$ structure type (Skolozdra et al. 1981a)*

$CeNi_5Sn$, SG $P6_3/mmc$, $Z=4$, $a=4.9049$, $c=19.371$ Å.

Atoms	Wyckoff notation	*x/a*	*y/a*	*z/c*
2Ce1	2(e)	0.333	0.667	0.25
2Ce2	2(a)	0	0	0
12Ni1	12(k)	0.831	0.662	0.1458
4Ni2	4(f)	0.333	0.667	0.5425
2Ni3	2(d)	0.333	0.667	0.75
2Ni4	2(b)	0	0	0.25
4Sn	4(f)	0.333	0.667	0.0873

The projection of the $CeNi_5Sn$ structure and coordination polyhedra of the atoms are represented in fig. 4.

The $CeNi_5Sn$ structure can be considered as one containing fragments of the $CeCu_5$ structure type and fragments of a hypothetical structure RX_7 (R and X = atoms with great

and small radii, respectively) having the following crystallographic data: SG $P6_3/mmc$, $Z=2$, $a\approx 5$ Å, $c\approx 12$ Å. From the analogous fragments the $CeCu_6$ structure can be built. The fragments are stacked in a kind of mosaic, as a parquet design. In the $CeNi_5Sn$ structure there is a simple stacking of these fragments, alternating along the Z axis. The $CaCu_5$ and RX_7 structures can be considered as a progenitor of the homologous series, the number of which are obtained by a combination of the above mentioned fragments. Cenzual and Parthé (1984) consider the $CeNi_5Sn$ structure as a hybrid, containing the fragments of the structure of the $MnCu_2Al$ and $CaCu_5$ types.

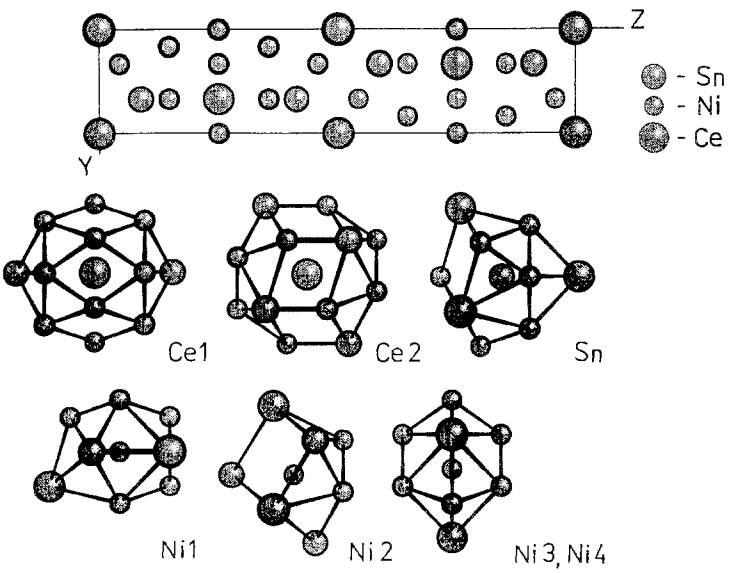

Fig. 4. Projection of the $CeNi_5Sn$ structure on the YZ plane and atom coordination polyhedra.

On the other hand, the lattice of $CeNi_5Sn$ can be considered as a structure of inserted Sn atoms into the $CaCu_5$ structure type. The unit cell of $CeNi_5Sn$ contains two unit cells of the $CaCu_5$ type, shifted from one another in the [1 1 0] direction, analogous to $CeNi_3$. In connection with such shifting of the $CaCu_5$ cells in this direction, the Ce2 atoms move forming a net which joins both cells. The Ni1 atoms shift alternatively parallel to the Z axis on both sides and that is why the net from the nickel atoms is the crimped one. As a result of above mentioned shifting the space for the insertion of Sn atoms appears and parameter c increases in comparison with the corresponding parameter of the $CaCu_5$ structure.

The structure of this type is characteristic of RNi_5Sn, where R = La, Pr and Nd.

3.2.2. *$CeCu_{4.38}In_{1.62}$ structure type (Kalychak et al. 1988)*

$HoNi_{4.9}Sn_{1.1}$, SG Pnnm, $Z=8$, $a=16.103$, $b=10.210$, $c=4.870$ Å (Skolozdra et al. 1996b).

Atoms	Wyckoff notation	*x/a*	*y/a*	*z/c*
2Ho1	2(a)	0	0	0
2Ho2	2(d)	0.5	0	0
4Ho3	4(g)	0.7540	0.3832	0
4Sn1	4(g)	0.9496	0.3084	0
4Sn2	4(g)	0.6968	0.0864	0
4Ni1 ($Ni_{0.91}Sn_{0.09}$)	4(g)	0.2208	0.301	0
4Ni2 ($Ni_{0.88}Sn_{0.12}$)	4(g)	0.5835	0.461	0
4Ni3	4(g)	0.4640	0.308	0
4Ni4	4(g)	0.352	0.148	0
4Ni5	4(g)	0.1710	0.084	0
4Ni6	4(g)	0.0996	0.462	0
8Ni7	8(h)	0.5924	0.256	0.246
8Ni8	8(h)	0.8424	0.137	0.247

The $CeCu_{4.38}In_{1.62}$ structure is a derivative of the $CeCu_6$ type (Cromer et al. 1960). It can be presented by taking two unit cells of $CeCu_6$ reflected in the plane of a sliding reflection parallel to the *YZ* plane at $x=0.5$. The unit cell of such a structure, in comparison with that of $CeCu_6$, has the parameter *a* doubled, and the parameters *b* and *c* mutually exchanged.

The $RNi_{5-x}Sn_{1+x}$ stannides, where R = Y, Sm, Gd–Yb belong to this structure type.

3.2.3. *$MgCu_4Sn$ structure type (Gladyshevsky et al. 1952)*

$LuNi_4Sn$, SG $F\bar{4}3m$, $Z=4$, $a=6.981$ Å (Skolozdra and Komarovskaya 1983).

Atoms	Wyckoff notation	*x/a*	*y/a*	*z/c*
4Lu	4(a)	0	0	0
16Ni	16(e)	0.623	0.623	0.623
4Sn	4(c)	0.25	0.25	0.25

The $MgCu_4Sn$ structure is the superstructure to the $AuBe_5$ type, which is the derivative from the $MgCu_2$ type. Only one stannide, $LuNi_4Sn$, is known to crystallize in this structure type.

3.2.4. *$NaZn_{13}$ structure type (Shoemaker et al. 1952)*

$Pr(Cu_{0.72}Sn_{0.28})_{13}$, SG Fm3c, $Z=8$, $a=12.162$ Å (Komarovskaya and Skolozdra 1984).

Atoms	Wyckoff notation	*x/a*	*y/a*	*z/c*
8Pr	8(a)	0.25	0.25	0.25
8Cu1 ($Cu_{0.72}Sn_{0.28}$)	8(b)	0	0	0
96Cu2 ($Cu_{0.72}Sn_{0.28}$)	96(i)	0	0.178	0.12

The $R(Cu_{0.72}Sn_{0.28})_{13}$ stannides, where R = La, Ce, Pr, Nd, crystallize with the $NaZn_{13}$ structure type.

3.2.5. *$La_6Co_{11}Ga_3$ structure type (Sichevich et al. 1985)*

$La_6Fe_{13}Sn$, SG I4/mcm, $Z=4$, $a=8.148$, $c=24.047$ Å (Weitzer et al. 1993b).

The coordinates of atoms have not been determined for the stannides of this structure type. The unit cell of $La_6Co_{11}Ga_3$ can be presented as a combination of the Cr_5B_3 and $U(Ni_{0.68}Si_{0.32})_{11}$ structure type fragments which are perpendicular to the *Z* axis.

The $R_6Fe_{13}Sn$ compounds, where R = La, Pr, Nd, Sm, and $La_6Co_{13}Sn$ compounds crystallize in this structure type.

3.2.6. *$BaLi_4$ structure type (Wang et al. 1965)*

YCo_3Sn, SG $P6_3/mmc$, $Z=6$, $a=8.844$, $c=7.446$ Å (Skolozdra 1993).

Atoms	Wyckoff notation	*x/a*	*y/a*	*z/c*
6Y	6(h)	0.476	0.952	0.25
12(0.5Co1+0.5Sn)	12(k)	0.166	0.332	0.572
2Co2	2(a)	0	0	0
4Co3	4(f)	0.333	0.667	0.540
6Co4	6(h)	0.097	0.194	0.25

The structure of the YCo_3Sn compound has been studied by the powder method. The RCo_3Sn phases, where R = Gd–Yb, have the same structure. As noted above (sect. 3.1.3) the $GdCo_3Sn$ compound has a homogeneity range. For the composition $GdCo_{2.8}Sn_{1.2}$ the distribution of atoms has been studied, and it differs slightly from the atom distribution in YCo_3Sn.

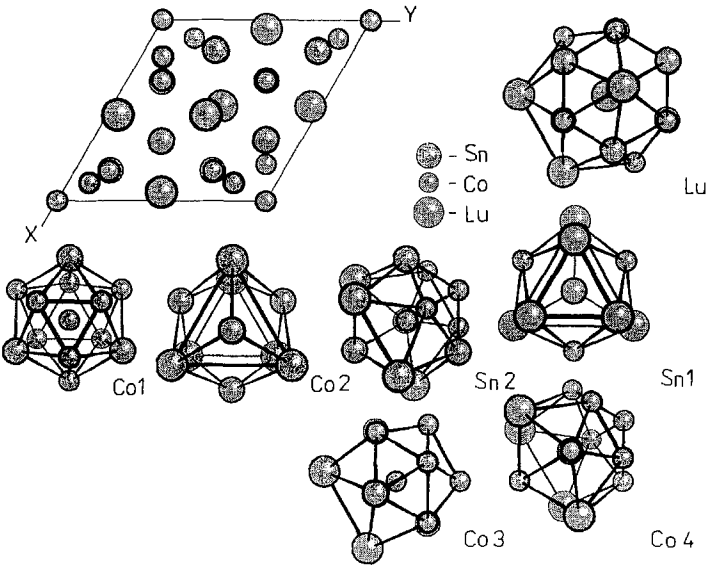

Fig. 5. Projection of the $Lu_3Co_{7.77}Sn_4$ structure on the XY plane and atom coordination polyhedra.

3.2.7. *$Lu_3Co_{7.77}Sn_4$ structure type (Skolozdra et al. 1996a)*
$Lu_3Co_{7.7}SN_4$, SG $P6_3mc$, $Z=2$, $a=8.746$, $c=7.432$ Å.

Atoms	Wyckoff notation	*x/a*	*y/a*	*z/c*
6Lu	6(c)	0.5254	−0.5254	0
2Sn1	2(b)	0.3333	0.6667	0.1987
6Sn2	6(c)	0.1720	−0.1720	0.7867
2Co1	2(a)	0	0	0.7140
1.44Co2	2(b)	0.3333	0.6667	0.850
6Co3	6(c)	0.1632	−0.1632	0.1579
6Co4	6(c)	0.1026	−0.1026	0.4686

The projection of the $Lu_3Co_{7.77}Sn_4$ structure is represented in fig. 5, this crystal structure was obtained from a single crystal study. The structure can be constructed as a deformed derivative from the $BaLi_4$ type.

The RCo_3Sn (and also $Lu_3Co_{7.77}Sn_4$) compounds are the first tin representatives of the $BaLi_4$ structure type. Owing to the smaller value of the ratio between the atom radii of R and (Co, Sn) in comparison with the ratio between atom radii of Ba and Li, a significant deformation of the structure and an increased *c/a* ratio in the RCo_3Sn phases (*c/a* in $BaLi_4$ is equal to 0.807, *c/a* in RCo_3Sn phases is equal to 0.844) was observed. Probably, shortening of interatomic distances and compression of the structure lead to the formation

of vacancies in the Co position (2(b)) for the Lu compound. In $Lu_3Co_{7.77}Sn_4$, where the tin content increases (i.e. where the sizes of the R atom and of the non-lanthanide component atom are closer to each other) a strong increase of c/a (0.855) was observed, which leads to a change of the structure.

3.2.8. *KAu_4Sn_2 structure type (Sinnen and Schuster 1978)*

$CeNi_4Sn_2$, SG $I\bar{4}c2$, $Z=4$, $a=7.753$, $c=7.869$ Å (Skolozdra et al. 1988d).

Atoms	Wyckoff notation	x/a	y/a	z/c
4Ce	4(d)	0	0.5	0
16Ni	16(i)	0.148	0.148	0.083
8Sn	8(e)	0.356	0.356	0.25

The structure of the KAu_4Sn_2 type is related to the $CuAl_2$ type (Sinnen and Schuster 1978). An analysis of the structure (Skolozdra 1993) shows, that it can be obtained from the $CuAl_2$ structure by filling the m symmetry tetrahedra in the $CuAl_2$ structure with Au atoms. In the case of a compression of the structure, a change of coordination numbers and polyhedra in comparison with the structure type $CuAl_2$ is observed.

The RNi_4Sn_2 compounds, where R = La, Nd, Pr, Sm, crystallize in this type.

3.2.9. *$MnCu_2Al$ structure type (Bradley and Rodgers 1934)*

$LuNi_2Sn$, SG Fm3m, $Z=4$, $a=6.981$ Å (Skolozdra and Komarovskaya 1983).

Atoms	Wyckoff notation	x/a	y/a	z/c
4Lu	4(b)	0.5	0.5	0.5
8Ni	8(c)	0.25	0.25	0.25
4Sn	4(a)	0	0	0

The $MnCu_2Al$ structure type is the superstructure of the BiF_3 type. The $MnCu_2Al$ structure can be considered as a derivative constructed from the close packing of Al atoms in which the octahedral vacancies are occupied by the Mn atoms and the tetrahedral vacancies by the Cu atoms.

The $ScCo_2Sn$, $ScNi_2Sn$, $YbNi_2Sn$, $LuNi_2Sn$, $ScPt_2Sn$, RPd_2Sn (R = Sc, Y, Tb–Lu) stannides belong to this type.

3.2.10. *$ZrPt_2Al$ structure type (Ferro et al. 1975)*

$GdPt_2Sn$, SG $P6_3/mmc$, $Z=2$, $a=4.531$, $c=9.065$ Å (de Mooij and Buschow 1984).

Atoms	Wyckoff notation	x/a	y/a	z/c
2Gd	2(c)	0.333	0.667	0.25
4Pt	4(f)	0.333	0.667	0.568
2Sn	2(a)	0	0	0

The $ZrPt_2Al$ structure type is a superstructure of the TiAs type, where the R atoms occupy the Ti positions. The Zr atoms form trigonal prisms, linked similarly as in the AlB_2 structure. The prisms are alternately occupied by Al atoms and pairs of Pt atoms. So the $ZrPt_2Al$ structure may be considered as a derivative of the AlB_2 structure type where in every second prism there are two atoms instead of one.

The $GdPt_2Sn$, $ErPt_2Sn$ YPt_2Sn, $TmPt_2Sn$ and $TbPt_2Sn$ compounds are characteristic of this type structure.

3.2.11. *YCo_6Ge_6 (Buchholz and Schuster 1981) and $HfFe_6Ge_6$ (Olenych et al. 1981) structure types*

$HoFe_6Sn_6$ (YCo_6Ge_6 type), SG P6/mmm, $Z=0.5$, $a=5.398$, $c=4.459$ Å (Koretskaya and Skolozdra 1986).

Atoms	Wyckoff notation	*x/a*	*y/a*	*z/c*
0.6Ho	1(a)	0	0	0
3Fe	3(g)	0.5	0	0.5
2Sn1	2(c)	0.333	0.667	0
1.3Sn2	2(e)	0	0	0.351

$GdMn_6Sn_6$ ($HfFe_6Ge_6$ type), SG P6/mmm, $Z=1$, $a=5.521$, $c=9.007$ Å (Malaman et al. 1988).

Atoms	Wyckoff notation	*x/a*	*y/a*	*z/c*
1Gd	1(b)	0	0	0
6Mn	6(i)	0.5	0	0.251
2Sn1	2(c)	0.333	0.667	0
2Sn2	2(d)	0.333	0.667	0.5
2Sn3	2(e)	0	0	0.162

In the YCo_6Ge_6 structure the Y and Ge2 atoms statistically occupy half of the positions 1(a) and 2(e), respectively, which is caused by the small value of the parameter *c*. An analogous situation is characteristic of the RM_6Sn_6 compound, but Ho and Sn2 in $HoFe_6Sn_6$ occupy little more, than half of the positions 1(a) and 2(e), respectively.

The YCo_6Ge_6 structure type is considered by Buchholz and Schuster (1981) to be a superstructure of the CoSn type, which is formed by an insertion of the R atom in the vacancies between the Co atoms, situated along the axis of the sixth order.

When an ordered placement of the atoms in the 1(a) and 2(b) positions occurs, it leads to the formation of the superstructure of the $HfFe_6Ge_6$ type and a doubling of the *c* parameter. Olenych et al. (1981) consider the $HfFe_6Ge_6$ structure as containing fragments of the $CaCu_5$ and Zr_4Al_3 structures placed along the six-fold axis or as obtained

from the $CaCu_5$ structure by the substitution of half of the Hf atoms with pairs of Ge atoms.

The RFe_6Sn_6 (R = Y, Gd–Tm, Lu) and RCo_6Sn_6 compounds crystallize in YCo_6Ge_6 type, while the RMn_6Sn_6 (R = Sc, Y, Gd–Tm, Lu) stannides crystallize in $HfFe_6Ge_6$ structure type.

Chafik El Idrissi et al. (1991a) have shown that long range ordering occurred in the RFe_6Sn_6 compounds. The $TmFe_6Sn_6$ and $LuFe_6Sn_6$ stannides are found to be isotypic with the $HfFe_6Ge_6$ type. There are few new types for other compounds: YFe_6Sn_6 – SG Cmcm, $a = 2c_h$, $b = 8\sqrt{3}a_h$, $c = a_h$; $TbFe_6Sn_6$ – SG Cmcm, $a = 2c_h$, $b = \sqrt{3}a$, $c = a_h$; $DyFe_6Sn_6$ – SG Ammm, $a = 2c_h$, $b = 5\sqrt{3}a_h$, $c = a_h$; $HoFe_6Sn_6$ – SG Immm, $a = 2c_h$, $b = 3\sqrt{3}a_h$, $c = a_h$; $ErFe_6Sn_6$ – SG Cmcm, $a = 2c_h$, $b = 4\sqrt{3}a_h$, $c = a_h$ (a_h and c_h refer to the hexagonal subcell of YCo_6Ge_6 type structure). These structural types may be described as $HfFe_6Ge_6$ blocks connected via $ScFe_6Ga_6$ type ($ThMn_{12}$ derivative) slabs (Chafik El Idrissi et al. 1991a).

The $PrMn_6Sn_6$, $NdMn_6Sn_6$ and $SmMn_6Sn_6$ are isotypic with $HoFe_6Sn_6$. A new superstructure formation has been found in an X-ray diffraction study of a $DyFe_6Sn_6$ single crystal by Oleksyn et al. (1995). The crystal structure is characterized by SG Cmmm with $a = 37.343$, $b = 21.560$ and $c = 8.912$ Å. This structure may be described as a three-dimensionally commensurate modulated structure as well.

3.2.12. *Mo_2NiB_2 (Kuzma et al. 1966) or W_2CoB_2 (Rieger et al. 1966) structure type*
Ce_2Ni_2Sn, SG Immm, $Z = 2$, $a = 4.3936$, $b = 5.7396$, $c = 8.5967$ Å (Fourgeot et al. 1995).

Atoms	Wyckoff notation	*x/a*	*y/a*	*z/c*
4Ce	4(j)	0.5	0	0.2969
4Ni	4(h)	0	0.2165	0.5
2Sn	2(a)	0	0	0

The Ce_2Ni_2Sn structure is built by a linkage of the [Ce_8] deformed double trigonal prisms. The prisms are occupied by Sn atoms or Ni–Ni pairs. The crystal structure of Ce_2Ni_2Sn can be also described by a stacking of atomic planes perpendicular to the Z axis (Fourgeot et al. 1995).

3.2.13. *$HoGa_{2.4}Ni_{2.6}$ structure type (Gryn et al. 1983)*
$GdNi_3Sn_2$, SG P6/mmm, $Z = 3$, $a = 9.207$, $c = 4.280$ Å (Skolozdra et al. 1988a).

Atoms	Wyckoff notation	*x/a*	*y/a*	*z/c*
1Gd1	1(a)	0	0	0
2Gd2	2(d)	0.333	0.667	0.50
3Ni1 ($Ni_{0.4}Sn_{0.6}$)	3(f)	0.50	0	0
6Ni2 ($Ni_{0.4}Sn_{0.6}$)	6(k)	0.272	0	0.50
6Ni3	6(c)	0.178	0.352	0

This structure type is related to the $CaCu_5$ type (Gryn et al. 1983). The $HoGa_{2.4}Ni_{2.6}$ structure differs from the $CaCu_5$ type by the placement of the bigger size atoms (Ho, Ga) relative to the Z axis. In $CaCu_5$ the Ca atoms are placed at the same height, while in $HoGa_{2.4}Ni_{2.6}$ the Ho atoms are at two heights which differ by $c/2$.

The RNi_3Sn_2 phases, where R = Y, Sm, Gd, Tb, have this type of structure.

3.2.14. *$Y_{13}Pd_{40}Sn_{31}$ structure type (Cenzual and Parthé 1984)*

$Y_{13}Pd_{40}Sn_3$, SG P6/mmm, $Z=2$, $a=19.891$, $c=9.246$ Å.

Atoms	Wyckoff notation	*x/a*	*y/a*	*z/c*
12Y1	12(n)	0.2712	0	0.2895
6Y2	6(m)	0.5761	0.1522	0.5
6Y3	6(l)	0.2433	0.4866	0
2Y4	2(e)	0	0	0.194
24Pd1	24(r)	0.1058	0.4476	0.2211
12Pd2	12(p)	0.0857	0.3209	0
12Pd3	12(o)	0.0884	0.1768	0.2419
12Pd4	12(o)	0.2603	0.5206	0.3480
6Pd5	6(m)	0.1410	0.2820	0.5
6Pd6	6(l)	0.5452	0.0904	0
6Pd7	6(k)	0.4225	0.0904	0.5
2Pd8	2(c)	0.333	0.6667	0
12Sn1	12(q)	0.1264	0.4111	0.5
12Sn2	12(o)	0.1776	0.3552	0.2333
12Sn3	12(o)	0.6073	0.2146	0.1869
6Sn4	6(k)	0.1459	0	0.5
6Sn5	6(j)	0.1621	0	0
6Sn6	6(j)	0.3862	0	0
6Sn7	6(i)	0.5	0	0.2584
2Sn8	2(d)	0.3333	0.6667	0.5

Projection of the structure is represented in fig. 6. Cenzual and Parthé (1984) consider this structure as consisting from fragments of the $CaCu_5$ and $MnCu_2Al$ structure types and columns of the prisms from the Sn and Pd atoms, which are parallel to the Z axis. No other compounds of this structure type have been reported.

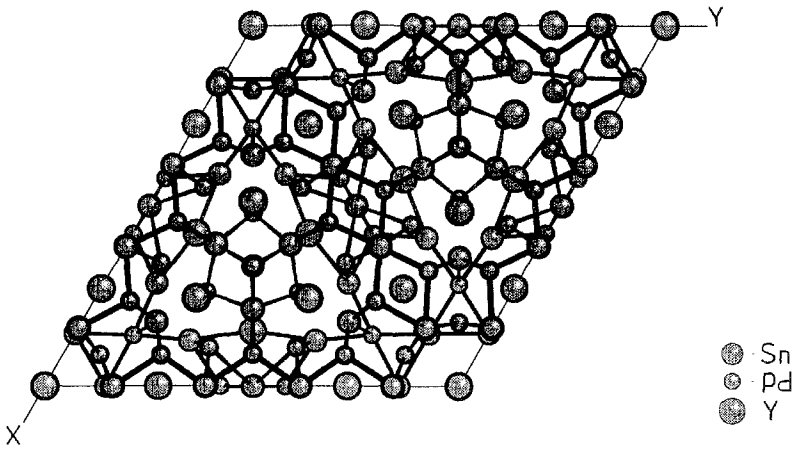

Fig. 6. Projection of the $Y_{13}Pd_{40}Sn_{31}$ structure on the *XY* plane.

3.2.15. *$CaBe_2Ge_2$ structure type (Eisenmann et al. 1972)*

$CeNi_2Sn_2$, SG P4/mmm, $Z=2$, $a=4.441$, $c=10.159$ Å (Pierre et al. 1994).

Atoms	Wyckoff notation	*x/a*	*y/a*	*z/c*
2Ce	2(c)	0	0.5	0.240
2Ni1	2(a)	0	0	0
2Ni2	2(c)	0	0.5	0.629
2Sn1	2(b)	0	0	0.5
2Sn2	2(c)	0	0.5	0.875

The $CaBe_2Ga_2$ structure is a superstructure to the $BaAl_4$ type. The RNi_2Sn_2 phases were at first thought to have the $CeAl_2Ga_2$ structure type which is also the superstructure to the $BaAl_4$ type (Skolozdra et al. 1981b). The superstructures differ from one another only by an alternation of the layers X1 (Al, Be) and X2 (Ga, Ge) atoms. In $CeAl_2Ga_2$ the layers are placed in the order X2X1X2X2X1X2, in the structure $CaBe_2Ge_2$ X1X2X1X2X1X2.

The RNi_2Sn_2 compounds (R = La–Gd) have $CaBe_2Ge_2$ structure type. But the structure appears only in unannealed or in annealed at 1073 K alloys. In the alloys annealed at lower temperatures the deformation of the tetragonal structure into a monoclinic one is observed, except for $GdNi_2Sn_2$ (Skolozdra et al. 1981b, Pierre et al. 1994).

The phases RCu_2Sn_2 also have this structure.

3.2.16. *$LaPt_2Ge_2$ structure type (Venturini et al. 1989a)*

$CeNi_2Sn_2$(LT), SG $P2_1$, $Z=2$, $a=4.432$, $b=4.407$, $c=10.108$ Å, $\beta=91.40°$ (Pierre et al. 1994).

Atoms	Wyckoff notation	*x/a*	*y/a*	*z/c*
2La	2(a)	0.276	0.25	0.241
2Ni1	2(a)	0.712	0.228	0.497
2Ni2	2(a)	0.250	0.212	0.868
2Sn1	2(a)	0.757	0.202	0.992
2Sn2	2(a)	0.230	0.188	0.617

The $CeNi_2Sn_2$ (LT) structure forms as a result of the insignificant monoclinic distortion of the $CaBe_2Ge_2$ structure type. The annealed RNi_2Sn_2 compounds (R=La, Pr, Nd, Sm) also have this structure. A neutron diffraction investigation showed that the Ce compound has a smaller than stoichiometric content of nickel ($CeNi_{1.9}Sn_2$) (Pierre et al. 1994).

3.2.17. *$Gd_6Cu_8Ge_8$ structure type (Rieger 1970)*

$Gd_6Cu_8Sn_8$, SG Immm, $Z=1$, $a=14.737$, $b=6.946$, $c=4.474$ Å (Skolozdra et al. 1984a).

Atoms	Wyckoff notation	*x/a*	*y/a*	*z/c*
2Gd1	2(d)	0.5	0	0.5
4Gd2	4(e)	0.129	0	0
8Cu	8(n)	0.327	0.186	0
4Sn1	4(f)	0.215	0.5	0
4Sn2	4(h)	0	0.201	0.5

The structure of the $Gd_6Cu_8Ge_8$ compound can be considered as consisting from the alternating fragments of the $MgCuAl_2$ and Mo_2NiB_2 structure types (fig. 7).

The $R_6Cu_8Sn_8$ stannides (R=Y, Gd–Tm) (Thirion et al. 1983, Skolozdra et al. 1984a) crystallize in this structure type. From a single crystal study it was established that $Tm_6Cu_8Sn_8$ also has a monoclinicly deformed structure which is derived from the $Gd_6Cu_8Ge_8$ type. The correspondence between the lattice parameters of monoclinic and orthorhombic phases is appreciable if the first one is considered to be in I2/m SG (see table 5).

The $R_6Mn_8Sn_8$ compounds, where R=La–Nd, Sm, also have the $Gd_6Cu_8Ge_8$ type structure.

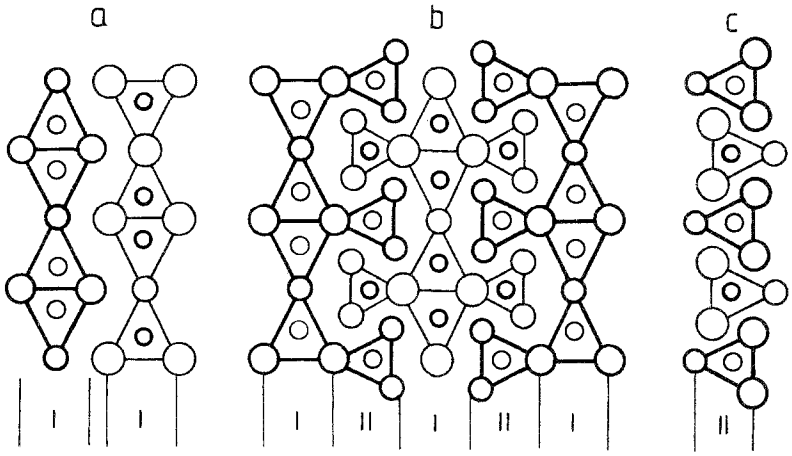

Fig. 7. The relationship between the (a) Mo_2NiB_2, (b) $Gd_6Cu_8Ge_8$ and (c) $MgCuAl_2$ structure types (Skolozdra 1993).

3.2.18. *TiNiSi structure type (Shoemaker and Shoemaker 1965)*

ErCoSn, SG Pnma, $Z=4$, $a=7.093$, $b=4.486$, $c=7.431$ Å (Skolozdra et al. 1982).

Atoms	Wyckoff notation	x/a	y/a	z/c
4Er	4(c)	0.017	0.25	0.697
4Co	4(c)	0.166	0.25	0.056
4Sn	4(c)	0.288	0.25	0.405

YNiSn, SG Pnma, $Z=4$, $a=7.126$, $b=4.439$, $c=7.674$ Å (François et al. 1985).

Atoms	Wyckoff notation	x/a	y/a	z/c
4Y	4(c)	−0.0106	0.25	0.7039
4Ni	4(c)	0.1985	0.25	0.0843
4Sn	4(c)	0.3068	0.25	0.4128

The TiNiSi structure type is a superstructure of the $PbCl_2$ type. The Ti and Ni atoms form columns of trigonal prisms inside of which there are Si atoms. The columns are linked by the Ti–Ti edges in infinite crimped slabs, placed perpendicular to the Z axis. The structure can be presented as a totality of the nets (two per unit cell) which are parallel to XY plane. In the RMSn compounds the R, Ni and Sn atoms occupy the position of Ti, Ni, Si atoms, respectively.

The structure of YNiSn has been determined by using a single-crystal X-ray method (François et al. 1985). This structure can also be described as an AlB_2 type derivative and it may be compared with the LaPtSi-type structure, which is a derivative of the $ThSi_2$ type (François et al. 1985).

The RCoSn stannides (R = Sc, Y, Gd–Tm, Lu), RNiSn (R = Sc, Y, La–Sm, Gd–Lu), RPdSn (R = La–Sm, Gd–Ho) and RPtSn (R = Ce, Pr, Sm) phases crystallize in the TiNiSi structure type.

The refinement of the CeNiSn, CePdSn and CePtSn structures has been carried out by Higashi et al. (1993). The compounds crystallize in the noncentrosymmetric space group $Pn2_1a$ with the following atomic coordinates:

Atoms	Wyckoff notation	*x/a*	*y/a*	*z/c*
4Ce	4(a)	0.48165	0.25	0.19701
4Ni	4(a)	–0.3108	0.2521	–0.4179
4Sn	4(a)	–0.18572	0.2433	–0.09076

This structure is closely related to that of TiNiSi.

3.2.19. *$CeCu_2$ structure type (Larson and Cromer 1961)*

$CeCu_2$, SG Imma, $Z = 4$, $a = 4.43$, $b = 7.05$, $c = 7.45$ Å.

The coordinates of atoms have not been determined for this type of stannide.

The $CeCu_2$ structure is an orthorhombic deformed derivative of the AlB_2 structure type, and is related to the TiNiSi structure. Only EuZnSn has this type of structure (Merlo et al. 1991).

3.2.20. *AlB_2 structure type (Hofmann and Jäniche 1936)*

LaCuSn, SG P6/mmm, $Z = 1$, $a = 4.581$, $c = 4.082$ Å (Komarovskaya et al. 1983b).

Atoms	Wyckoff notation	*x/a*	*y/a*	*z/c*
1La	1(a)	0	0	0
2Cu ($Cu_{0.5}Sn_{0.5}$)	2(d)	0.333	0.667	0.5

The $PrCu_{0.25}Sn_{1.25}$ stannide crystallizes in this structure type as well.

3.2.21. *$CaIn_2$ structure type (Iandelli 1964)*

LuCuSn, SG $P6_3/mmc$, $Z = 2$, $a = 4.457$, $c = 7.093$ Å (Komarovskaya et al. 1983b).

Atoms	Wyckoff notation	*x/a*	*y/a*	*z/c*
2Lu	2(b)	0	0	0
4Cu ($Cu_{0.5}Sn_{0.5}$)	4(f)	0.333	0.667	0.454

The RCuSn (R = Y, Ce–Tm), RAgSn (R = La, Ce, Sm–Yb), RAuSn (R = Ce–Sm, Tb–Dy) compounds crystallize in this structure type.

The AlB_2 and $CaIn_2$ types belong to the same class (with a trigonal prismatic coordination of the atoms with the smaller atom size), and to the same subgroup which is characterized by the stacking of only trigonal prisms (in accordance with the classification

of the structure types by Krypyakevich (1977)). The $CaIn_2$ structure is derived from the AlB_2 structure as a consequence of an inside deformation. The morphotrophy transition from the AlB_2 structure type to the $CaIn_2$ type in the RCuSn serie is caused by a deviation of the (Cu, Sn) atoms from the ideal positions of AlB_2 structure, that leads to a doubling of the unit cell with a symmetry change (from SG P6/mmm to SG $P6_3/mmc$). This transition is caused by the decreasing atom radii of the rare-earth atom in comparison with the La radius. This is the reason of an increase of the instability of the AlB_2 structure type and of a shortening of the distances (Cu, Sn)–(Cu, Sn).

3.2.22. *LiGaGe structure type (Bockelmann and Schuster 1974)*
YbZnSn, SG $P6_3mc$, $a=4.649$, $c=7.476$ Å (Merlo et al. 1991).

Atoms	Wyckoff notation	*x/a*	*y/a*	*z/c*
2Yb	2(a)	0	0	0.25
2Zn	2(b)	0.333	0.667	0.0619
2Sn	2(b)	0.333	0.667	0.4778

The structure is a superstructure of the $CaIn_2$ type. The YbZnSn and EuCdSn stannides crystallize in this structure type.

3.2.23. *Fe_2P structure type (Rundqvist and Jellinek 1959)*
HoPdSn, SG $P\bar{6}2m$, $Z=3$, $a=7.433$, $c=3.979$ Å (Rossi et al. 1985).

Atoms	Wyckoff notation	*x/a*	*y/a*	*z/c*
3Ho	3(g)	0.605	0	0.5
1Pd1	1(b)	0	0	0.5
2Pd2	2(c)	0.333	0.667	0
3Sn	3(f)	0.265	0	0

The RMSn (M = Rh, Pd, Ir, Pt) compounds crystallize in this structure type. These structures are characterized by an ordered distribution of R and Sn atoms. Such a distribution of different atoms in the 3(g) and 3(f) sites was observed for the first time in ZrNiAl which is a superstructure of the Fe_2P type (Krypyakevich et al. 1967). The YbCdSn stannide crystallizes in this structure type as well.

3.2.24. *MgAgAs structure type (Nowotny and Silbert 1941)*
HoAuSn, SG $F\bar{4}3m$, $Z=4$, $a=6.624$ Å (Dwight 1976).

Atoms	Wyckoff notation	*x/a*	*y/a*	*z/c*
4Ho	4(c)	0.25	0.25	0.25
4Au	4(a)	0	0	0
4Sn	4(d)	0.75	0.75	0.75

This structure type is a superstructure of the CaF_2 type. The As atoms occupy the positions of the Ca atoms; the Ag and Mg atoms regularly occupy the positions of the F atoms. The structure can also be obtained by removing one of the Cu atoms from the $MnCu_2Al$ unit cell and placing the vacancies and the copper atoms in a regular manner. The compounds which crystallize in the structure types $MnCu_2Al$ are called Heusler phases.

The RAuSn (R = Ho, Er, Tm, Lu) stannides belong to this structure type.

3.2.25. *$Sm_2Cu_4Sn_5$ structure type (Skolozdra et al. 1991)*

$Sm_2Cu_4Sn_5$, SG I4mm, $Z=2$, $a=4.431$, $c=25.073$ Å.

Atoms	Wyckoff notation	*x/a*	*y/a*	*z/c*
2Sm1	2(a)	0	0	0
2Sm2	2(a)	0	0	0.683
2Cu1	2(a)	0	0	0.539
2Cu2	2(a)	0	0	0.444
4Cu3	4(b)	0	0.5	0.596
2Sn1	2(a)	0	0	0.149
4Sn2	4(b)	0	0.5	0.901
4Sn3	4(b)	0	0.5	0.789

Projection of the $Sm_2Cu_4Sn_5$ structure is presented in fig. 8. The $Sm_2Cu_4Sn_5$ structure

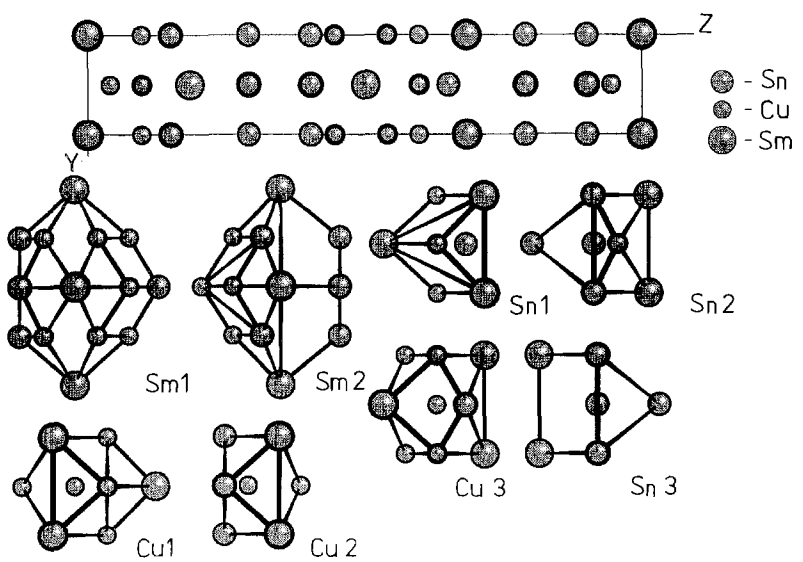

Fig. 8. Projection of the $Sm_2Cu_4Sn_5$ structure on the *YZ* plane and atom coordination polyhedra.

contains fragments of the $BaAl_4$, CaF_2 and α-Po structure types which alternate along the Z axis. Each one of two fragments of the $BaAl_4$ structure, which are in the unit cell, includes either Sm1 or Sm2 atoms and is shifted relative to the neighboring atom by $a/2$ along the X axis.

It is necessary to indicate a similarity between the $Sm_2Cu_4Sn_5$ and UNi_2Si_3 compounds (SG I4/mmm, $Z=4$, $a=3.965$, $c=24.04$ Å) (Akselrud et al. 1977a). The UNi_2Si_3 structure contains also fragments of the $BaAl_4$ and α-Po types and has the similar coordination polyhedra. The inclusion of the Sn atoms in the vacancies of the fragments of the CaF_2 type in the UNi_2Si_2 structure and the shifting of the $BaAl_4$ type fragment by $0.5a$ leads to the formation of the $Sm_2Cu_4Sn_5$ structure type. The $R_2Cu_4Sn_5$ (R = Pr, Gd, Tb) compounds crystallize in this type.

3.2.26. *$Y_2Rh_3Sn_5$ structure type (Meot-Meyer et al. 1984)*
$Y_2Rh_3Sn_5$, SG $Cmc2_1$, $Z=4$, $a=4.387$, $b=26.212$, $c=7.155$ Å.

Atoms	Wyckoff notation	*x/a*	*y/a*	*z/c*
4Y1	4(a)	0	0.1720	0.7555
4Y2	4(a)	0	0.4770	0.7374
4Rh1	4(a)	0	0.0507	0.5194
4Rh2	4(a)	0	0.7767	0.7655
4Rh3	4(a)	0	0.3934	0.4812
4Sn1	4(a)	0	0.8793	0.7347
4Sn2	4(a)	0	0.7049	0.5020
4Sn3	4(a)	0	0.5965	0.6080
4Sn4	4(a)	0	0.9527	0.4029
4Sn5	4(a)	0	0.2900	0.9761

Projection of the $Y_2Rh_3Sn_5$ structure is presented in fig. 9. The $Y_2Rh_3Sn_5$ structure according to Meot-Meyer et al. (1984) can be considered as a totality of tetrahedra composed of Rh atoms, centered by the three kinds of tin atoms (Sn1, Sn2 and Sn4). The tetrahedra form two kinds of canals in the structure: the first one has the rectangular section in which the Sn3 and Sn5 atoms are placed and the second one has triangular section in which the Y2 atoms are placed. The Y1 atoms are placed in the trigonal prisms formed by the Sn2, Sn3 and Sn5 atoms. In the structure the interatomic distances Rh1–Sn3 (2.58 Å) and Rh3–Sn2 (2.62 Å) are quite short, which is explained by the formation of covalent bonds between Rh and Sn atoms.

The $R_2Rh_3Sn_5$ (R = Gd, Tb, Dy, Ho) stannides are isostructural with $Y_2Rh_3Sn_5$.

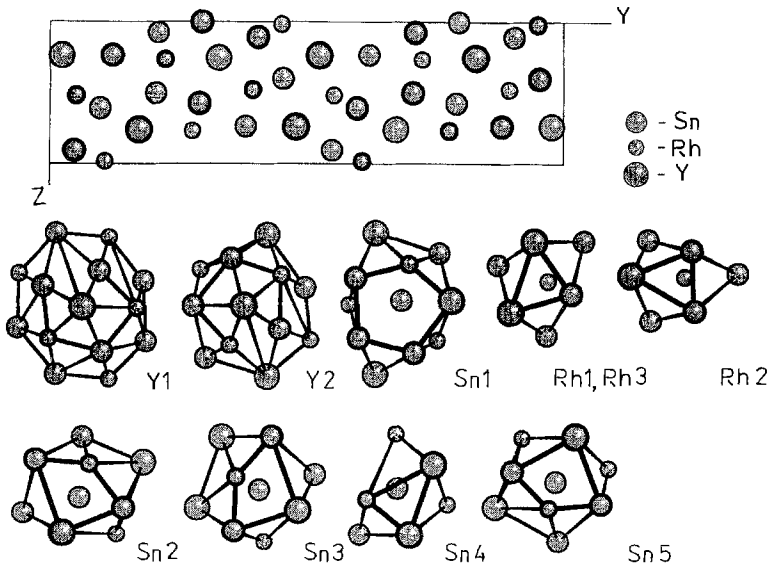

Fig. 9. Projection of the $Y_2Rh_3Sn_5$ structure on the *YZ* plane and atom coordination polyhedra.

3.2.27. *$U_2Co_3Si_5$ structure type (Akselrud et al. 1977b, Kotur et al. 1977)*

$La_2Rh_3Sn_5$, SG Ibam, $Z=4$, $a=10.764$, $b=12.912$, $c=6.365$ Å (Venturini et al. 1989c).

Atoms	Wyckoff notation	*x/a*	*y/a*	*z/c*
8La	8(j)	0.2707	0.3570	0
8Rh1	8(j)	0.1036	0.1411	0
4Rh2	4(b)	0.5	0	0.25
8Sn1	8(j)	0.3319	0.0877	0
8Sn2	8(g)	0	0.2785	0.25
4Sn3	4(a)	0	0	0.25

This structure is a derivative of the $BaAl_4$ type and can be obtained as a consequence of an orthorhombic deformation of the latter (Venturini et al. 1989c).

Only one stannide of this type is known – $La_2Rh_3Sn_5$.

3.2.28. *$Gd_9Ni_{24}Sn_{49}$ structure type (Akselrud et al. 1983)*

$Gd_9Ni_{24}Sn_{49}$, SG Im3, $Z=1$, $a=11.854$ Å.

Atoms	Wyckoff notation	*x/a*	*y/a*	*z/c*
8Gd	8(c)	0.25	0.25	0.25
2Gd ($Gd_{0.5}Sn_{0.5}$)	2(a)	0	0	0
24Ni	24(g)	0	0.156	0.324
24Sn1	24(g)	0	0.628	0.627
24Sn2	24(g)	0	0.252	0.133

Projection of the structure of the $Gd_9Ni_{24}Sn_{49}$ stannide on the *XY* plane and the coordination polyhedra of atoms are shown in fig. 10. The structure is related to the WAl_{12} structure type (Adam and Rich 1954), which belongs to the same space group (Im3) as that of $Gd_9Ni_{24}Sn_{49}$. The Al atoms are in the 24(g) site, the W atoms are in 2(a) 000, i.e. the latter ones (atoms) are placed in the top and in the centre of the unit cell. The unit cell of WAl_{12} contains 8 empty octahedra, 12 empty trigonal prisms (which are linked in pairs by their quadrangular edges), and 24 deformed square pyramids. In the $Gd_2Ni_{24}Sn_{49}$ structure the 2(a) sites are occupied by the statistical mixture from Gd and Sn atoms, the Ni atoms and two kinds of Sn atoms are in 24(g) sites, the Gd atoms are in the 8(c) sites. The compound has the formula $(Gd_{0.5}Sn_{0.5})Gd_8Ni_{24}Sn1_{24}Sn2_{24}$. A comparison

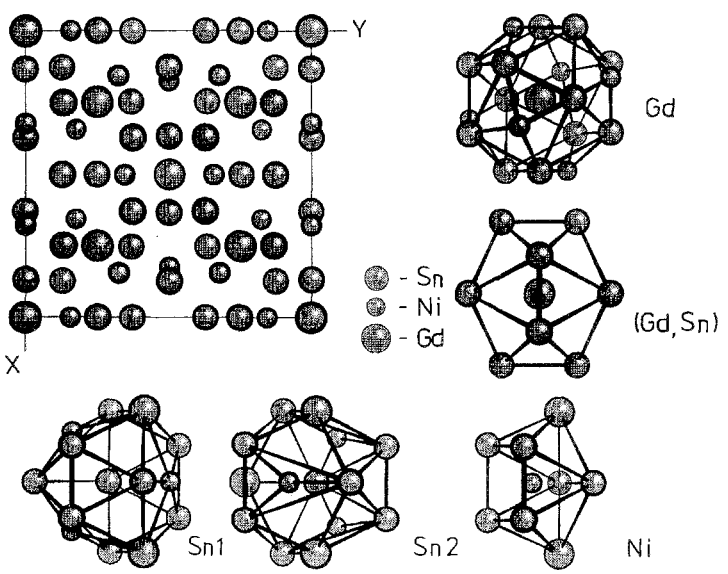

Fig. 10. Projection of the $Gd_9Ni_{24}Sn_{49}$ structure on the *XY* plane and atom coordination polyhedra.

of both structures shows that the Sn1 atoms correspond to Al atoms, the statistical mixture ($Gd_{0.5}Sn_{0.5}$) occupies the positions of the W atoms. The additional Sn2 atoms are placed in the trigonal prisms of the structure WAl_{12}. Moreover, in every prism there are two Sn2 atoms. The positions in octahedral vacancies correspond to the Gd atoms. Inclusion of the big Gd and Sn atoms leads to a shifting of the atoms and to a significant deformation of the prisms and octahedra, which causes the formation of new trigonal prisms from Sn1 and Sn2 atoms in which the Ni atoms are placed.

The compounds with Y, La–Sm, Gd, Tb also crystallize in this structure type.

3.2.29. *$NdRh_2Sn_4$ structure type (Meot-Meyer et al. 1985)*
$NdRh_2Sn_4$, SG Pnma, $Z=4$, $a=18.535$, $b=4.463$, $c=7.229$ Å.

Atoms	Wyckoff notation	*x/a*	*y/a*	*z/c*
4Nd1	4(c)	0.3574	0.25	0.5021
4Rh1	4(c)	0.4622	0.75	0.7400
4Rh2	4(c)	0.2173	0.75	0.5180
4Sn1	4(c)	0.3180	0.75	0.8043
4Sn2	4(c)	0.3062	0.75	0.2208
4Sn3	4(c)	0.4685	0.75	0.3623
4Sn4	4(c)	0.4315	0.25	0.9890

A projection of the $NdRh_2Sn_4$ structure is given in fig. 11. The $NdRh_2Sn_4$ structure

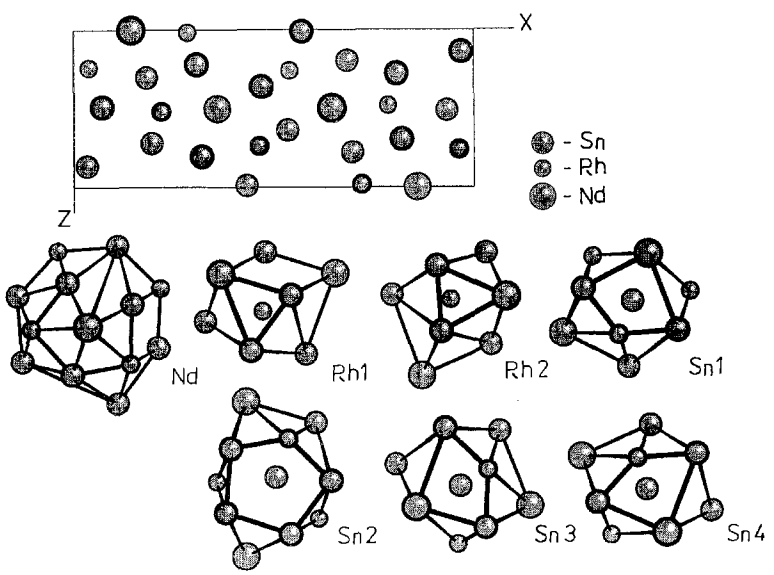

Fig. 11. Projection of the $NdRh_2Sn_4$ structure on the *XZ* plane and atom coordination polyhedra.

type is related to the $Y_2Rh_3Sn_5$ type; it is characterized by the similar motif of tetrahedra, consisting of Rh atoms.

The $NdRh_2Sn_4$ structure can also be presented as being built of isolated doubled columns of trigonal prisms. The prisms are formed by Nd and Sn atoms, and the Rh atoms are inside the prisms. The prisms are linked in double columns by ribs. The columns from the prisms are parallel to the *Y* axis and are shifted one from another by *b*/2. The space between the columns is filled with empty octahedra and half empty octahedra.

The RRh_2Sn_4 where R = La–Sm belongs to this type.

3.2.30. *$LuNiSn_2$ structure type (Komarovskaya et al. 1983a)*

$LuNiSn_2$, SG Pnma, $Z = 12$, $a = 15.944$, $b = 4.361$, $c = 14.345$ Å.

Atoms	Wyckoff notation	*x/a*	*y/a*	*z/c*
4Lu1	4(c)	0.8483	0.25	0.5267
4Lu2	4(c)	0.3743	0.25	0.2264
4Lu3	4(c)	0.1457	0.25	0.1024
4Ni1	4(c)	0.554	0.25	0.892
4Ni2	4(c)	0.807	0.25	0.7554
4Ni3	4(c)	0.301	0.25	0.456
4Sn1	4(c)	0.1833	0.25	0.3190
4Sn2	4(c)	0.4570	0.25	0.4473
4Sn3	4(c)	0.0223	0.25	0.4215
4Sn4	4(c)	0.7157	0.25	0.8931
4Sn5	4(c)	0.9693	0.25	0.7660
4Sn6	4(c)	0.6751	0.25	0.6325

A projection of the $LuNiSn_2$ structure and coordination polyhedra of the atoms are presented in fig. 12.

The $LuNiSn_2$ structure can be considered as a plane made up of a combination of the fragments of four structure types – $CuAu_3$, AlB_2, $BaAl_4$ and α-Po.

The $RNiSn_2$ compounds, where R = Y, Gd-Tm, are isostructural with this type.

3.2.31. *$TiMnSi_2$ (Venturini et al. 1982) or $ZrCrSi_2$ (Yarmoluk et al. 1982) structure type*

$YMnSn_2$, SG Pbam, $Z = 12$, $a = 10.51$, $b = 11.53$, $c = 8.97$ Å (Venturini et al. 1989b).

The coordinates of atoms have not been determined for the stannides of this structure type.

The compounds of the $TiMnSi_2$ structure type form with Mn – $RMnSn_2$, where R = Y, Dy, Ho, Er, Tm, Lu.

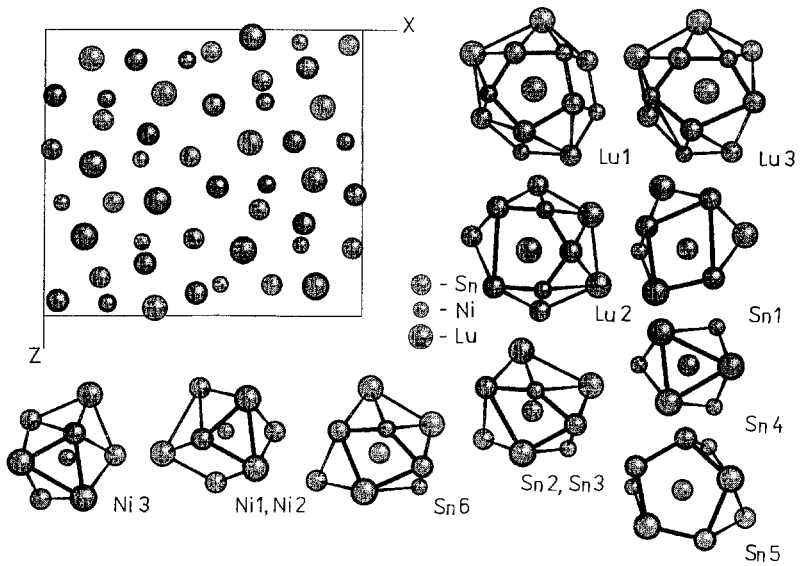

Fig. 12. Projection of the $LuNiSn_2$ structure on the *XZ* plane and atom coordination polyhedra.

3.2.32. *$CeNiSi_2$ structure type (Bodak and Gladyshevsky 1969)*
$LaNiSn_2$, SG Cmcm, $Z=4$, $a=4.513$, $b=17.81$, $c=4.513$ Å (Skolozdra 1977).

Atoms	Wyckoff notation	*x/a*	*y/a*	*z/c*
4La	4(c)	0	0.1070	0.25
4Ni	4(c)	0	0.3158	0.25
4Sn1	4(c)	0	0.4566	0.25
4Sn2	4(c)	0	0.7492	0.25

The $CeNiSi_2$ structure can be obtained by an insertion of the Ni atoms in the $ZrSi_2$ structure (Gladyshevsky and Bodak 1982). On the other hand this structure may also be considered to be formed from the fragments of the AlB_2 and $BaAl_4$ structure types.

The stannides of this structure type were studied by Skolozdra et al. (1988b), Komarovskaya et al. (1988) and Skolozdra et al. (1988c). The composition of the alloys, which have been annealed at 673 K, is presented in fig. 13.

The X-ray investigation of the R–Fe–Sn and R–Mn–Sn system showed that only the alloys with the composition $RFe_{0.33}Sn_2$ and $RMn_{0.33}Sn_2$ were homogeneous[1]. In the systems with cobalt the compounds have the homogeneous composition ranges. Their limits are dependent on the R-component. The phase with La includes the compositions 4–5, 8–12 (see fig. 13), the phases with Ce and Pr include the compositions 8–12; with Nd –

[1] Weitzer et al. (1992b) reported on the variable composition of $RMn_{1-x}Sn_{2-y}$ (R = La–Sm) at 1073 K.

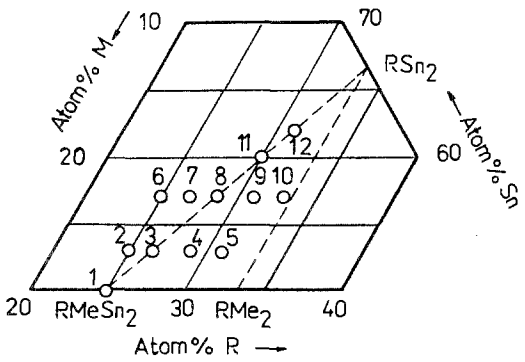

Fig. 13. The compositions of the $RM_{1-x}Sn_{2-y}$ alloys (Skolozdra et al. 1988b).

9–12; with Sm – 9–10; i. e. the homogeneity ranges are between the sections $RCoSn_2$–RSn_2 and RSn_2–RCo_2.

The homogeneity range of the nickel compounds includes the composition 1, 3–5, 8–10 for La and Ce; the homogeneity range for the compounds with Pr and Nd includes the composition 1, 3–5, 8–11, and for Sm only the alloys 5, 9–11 are homogenous.

In the systems with copper, the compounds are formed only with La (4, 5, 9, 10 compositions), Ce, Pr (3, 4, 9 compositions), Nd (3–5, 9 compositions). They do not form with Sm.

Only the compounds with nickel have the stoichiometric $RMSn_2$ composition. Moreover, these compounds have the greatest homogeneity range. A tendency towards decreasing homogeneity range was observed in the series of compounds with the same M with increasing atomic number of the R element.

The common formula for the solid solutions is $RNi_{1-x}Sn_{2-y}$. They are complex solid solutions in which the formation of the vacancies and the statistical distribution of the M and Sn atoms are combined. These solid solutions were described in more detail by Skolozdra (1993).

The calculation of the structure of the alloys with iron and manganese leads to the composition $RM_{0.24}Sn_{1.79}$ (M = Fe, Mn). The distribution and the atom sites of some $RM_{1-x}Sn_{1-y}$ compounds are as follows:

$CeMn_{0.4}Sn_{1.9}$			$NdCo_{0.9}Sn_{1.4}$			$NdCo_{0.30}Sn_{1.72}$		
Atoms	*G*	*y/b*	Atoms	*G*	*y/b*	Atoms	*G*	*y/b*
Ce	4.0(0)	0.97(3)	Nd	4.0(0)	0.075(2)	Nd	4.0(0)	0.083(1)
Mn1	1.0(5)	0.33(1)	Co1	1.3(3)	0.24(1)	Co2	1.1(3)	0.410(3)
Sn1	3.0(5)	0.445(2)	Co2	0.5(2)	0.410(3)	Co3	0.2(2)	0.724(2)
Sn2	4.0(0)	0.754(3)	Sn1	3.5(2)	0.410(3)	Sn1	2.9(2)	0.410(3)
			Sn2	4.0(0)	0.725(2)	Sn2	3.8(2)	0.724(2)

Some of the M–Sn distances are significantly shortened as a consequence of the presence of vacancies. The shortened distances (Å) are listed as follows (Skolozdra et al. 1988b):

$SmFe_{0.24}Sn_{1.79}$		$CeMn_{0.24}Sn_{1.79}$		$SmMn_{0.24}Sn_{1.79}$		$NdCo_{0.39}Sn_{1.84}$	
Fe–1Sn1	2.09	Mn–1Sn1	2.02	Mn–1Sn1	2.35	Co–2Sn2	2.26
Fe–2Sn2	2.24	Mn–2Sn2	2.61	Mn–2Sn2	2.38	Co–2Sn2	2.32
Fe–2Sn2	2.48	Mn–2Sn2	2.64	Mn–2Sn2	2.40		

The ternary tin compounds of this type also exist with Ru, Rh, Pd, Ir.

3.2.33. *Ho_6Ni_2Ga structure type (Gladyshevsky et al. 1983)*

Er_6Ni_2Sn, SG Immm, $Z=4$, $a=9.189$, $b=9.292$, $c=9.750$ Å (Sichevich et al. 1984).

Atoms	Wyckoff notation	*x/a*	*y/a*	*z/c*
8Er1	8(n)	0.197	0.208	0
8Er2	8(l)	0	0.285	0.288
8Er3	8(m)	0.208	0	0.313
4Co1	4(h)	0	0.106	0.5
4Co2	4(i)	0	0	0.146
2Sn1	2(d)	0.5	0	0.5
2Sn2	2(b)	0	0.5	0.5

In this structure the R atoms form a space framework in which there are two icosahedral, two cubooctahedral, eight tetragonal-antiprismatic and eight octahedral vacancies. The icosahedral and cubooctahedral vacancies are occupied by the larger atoms (Ga and Sn); the smaller atoms of the transition elements (Co and Ni) are placed in the tetragonal-antiprismatic vacancies. The octahedral vacancies are not occupied. The analogous framework is formed by the Al atoms in the WAl_{12} structure, where the W atoms occupy the icosahedral vacancies. The R_6M_2Sn stannides can be obtained by the insertion of 2 Sn atoms and 8 Co (Ni) atoms in the unit cell of a hypothetical $R_{12}Sn$ ($R_{24}Sn_2$) structure.

Recently, studying the phase compositions of the Er_6Ni_2Sn alloy, Gschneidner Jr et al. (1995) came to the conclusion that the correct composition of the Er_6Ni_2Sn compound is somewhat higher in tin or that this phase is formed during a solid state reaction, or both.

3.2.34. *$Sc_5Co_4Si_{10}$ structure type (Braun et al. 1980)*

$Ce_5Rh_4Sn_{10}$, SG P4/mbm, $Z=8$, $a=14.053$, $c=4.621$ Å (Venturini et al. 1982).

The coordinates of atoms have not been determined for this type of stannides.

Braun et al. (1980) consider the structure of $Sc_5Co_4Si_{10}$ as constructed from isolated columns which consist of linked pairs of trigonal prisms with Si atoms inside; the trigonal prisms are parallel to the Z axis. The mutual placing of the prisms is analogous to the position of the prisms in the U_3Si_2 structure but in the latter structure the linked pairs of trigonal prisms are not isolated but connected by ribs. The second fragment in the structure of $Sc_3Co_4Si_{10}$ is a deformed tetragonal antiprism which is placed in such a way that every free edge of the linked pairs of trigonal prism is common for both polyhedra.

The $R_5Rh_4Sn_{10}$ (R=Ce, Pr, Nd, Sm) and $R_5Ir_4Sn_{10}$ (R=La, Ce, Pr) compounds crystallize in this structure type.

3.2.35. *Cr_5B_3 structure type (Bertaut and Blum 1953, Parthé et al. 1955)*
$Ce_5Ni_{1.5}Sn_{1.5}$, SG I4/mcm, $Z=4$, $a=7.975$, $c=13.59$ Å (Skolozdra 1993).

Atoms	Wyckoff notation	*x/a*	*y/a*	*z/c*
4Ce1	4(c)	0	0	0
16Ce2	16(l)	0.171	0.5	0.141
4Ni1 ($Ni_{0.47}Sn_{0.53}$)	4(a)	0	0	0.25
8Ni2 ($Ni_{0.47}Sn_{0.53}$)	8(h)	0.365	0.865	0

The compounds of this structure type form with La, Ce and Pr. They are characteristic of the statistical distribution of the Ni and Sn atoms.

3.2.36. *Structure types of the RM_xSn_y phases (I, II, III, V, VII)*
In the R–M–Sn systems, where M=Co, Ru, Rh, Os, Ir, single crystals of the RM_xSn_y stannides have been synthesized from the melt of the tin (Cooper 1980, Espinosa 1980, Espinosa et al. 1980, 1982). The obtained compounds are very interesting because among some of them there is superconductivity and magnetic ordering. According to the X-ray data of Cooper (1980) there are five types of structures indicated as phases *I, II, III, V, VII.*

The crystal structure of the *I* phase has been investigated for $PrRh_xSn_y$ by powder method by Vandenberg (1980) and for $YbRh_xSn_y$ by single crystal method (Hodeau et al. 1980). The formula $R_6Rh_8Sn_{26}$ (i.e. $2{\cdot}SnR_3Rh_4Sn_{12}$) and the following characteristics correspond to the *I* phase.

$Yb_6Rh_8Sn_{26}$, SG Pm3n, $Z=1$, $a=9.676$ Å (Hodeau et al. 1980).

Atoms	Wyckoff notation	*x/a*	*y/a*	*z/c*
6Yb ($Yb_{0.915}Sn_{0.095}$)	6(d)	0.25	0.5	0
8Rh	8(e)	0.25	0.25	0.25
2Sn1 ($Sn_{0.943}Yb_{0.057}$)	2(a)	0	0	0
24Sn2	24(k)	0	0.30570	0.15333

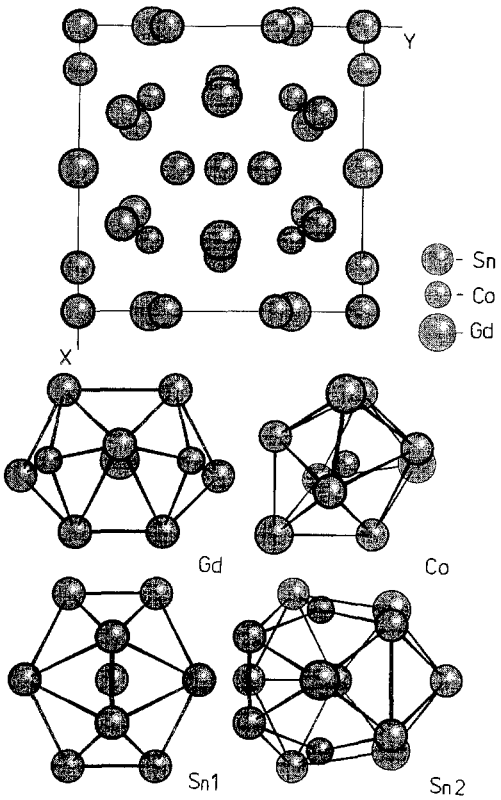

Fig. 14. Projection of the $Gd_6Co_8Sn_{26}$ structure on the *XY* plane and atom coordination polyhedra.

The structure of the *I* phase can be presented as a three-dimensional array of corner-sharing trigonal prisms which have Rh atoms in the center. Sn1 and Rh atoms occupy the icosahedral and cuboctahedral holes of this array, respectively. Yb and Sn1 atoms form a sublattice which is such as in the structure of the Cr_3Si (A15) type. Thus the structure of $SnYb_3Rh_4Sn_{12}$ is described as consisting of two substructures namely Yb_3Sn1 (motif of the Cr_3Si type) and $RhSn2_3$ (framework from the trigonal prisms) (Hodeau et al. 1980).

On the base of the analysis of the interatomic distances and the coordinations of atoms it was concluded that the Sn1, R and Rh atoms have a behaviour which is similar to cations, the Sn2 atoms have a behaviour which is similar to anions, and in the compound there is an ionic-covalent type of the bond (Hodeau et al. 1980, Miraglia et al. 1986). The authors draw a parallel between the $Sn_1R_3Rh_4Sn_{12}$ structure and the structure of the ternary oxides $A'A''B_4O_{12}$ similar to perovskite.

The $R_6Co_8Sn_{26}$ phases have been obtained by Skolozdra et al. (1983) independently from Espinosa et al. (1982). The refining of the structure carried out for the Ce and Gd compounds testifies that they have the structure of the *I* phases. The projection of the $Gd_6Co_8Sn_{26}$ structure is presented in fig. 14.

The structure of $R_6Co_8Sn_{26}$ compounds can be considered as a derivative of the $AuZn_3$ type. The $AuZn_3$ structure (SG Pm3n, $a=7.903$ Å) (Günzel and Schubert 1958) contains two kinds of Au atoms (Au1 and Au2) and one kind of Zn atoms. There are also 8 empty trigonal prisms occupying the 8(e) sites $\frac{1}{4}\frac{1}{4}\frac{1}{4}$ and 6 empty tetrahedra [6(a), $\frac{1}{2}0\frac{1}{4}$] in unit cell. The insertion of 8 atoms of cobalt in trigonal prisms and an exchange of Au1, Au2 and Zn atoms by R, Sn2 and Sn1 atoms, respectively, leads to the $R_6Co_8Sn_{26}$ structure.

As a result of the slight deformation of the *I* phase Miraglia et al. (1986) consider the *I'* phase with $a'=2a$ in cubic aspect, or $a'=2a$, $c=a$ for the tetragonal aspect. A detailed investigation of single crystals of the Rh phases shows that $R_6Rh_8Sn_{26}$ (where R = Eu, Yb, Ca, Sr, Th) has the structure of the *I* phases and the compounds with R = La–Gd really have the deformed *I'* structure. The refining of the structure showed that the larger axis of the temperature ellipsoid of the *I'* phase was on the average bigger by 0.06 Å than for the *I* phase. Such an anomaly is explained by the statistical shifting of the Sn2 atoms along the Sn1–Sn2 bond, and the deformation of the structure is manifested by a decrease of the symmetry of the $Sn1Sn2_{12}$ polyhedron.

The *II* phase is tetragonal; the structure for the first time was determined for $ErRh_xSn_y$ (Hodeau et al. 1984). The crystallographic data are as follows:

$(Sn_{1-x}Er_x)Er_4Rh_6Sn_{18}$, SG $I4_1/acd$, $Z=8$, $a=13.733$, $c=27.418$ Å (Hodeau et al. 1984).

Atoms	Wyckoff notation	*x/a*	*y/a*	*z/c*
8Er1 ($\sim Er_{0.33}Sn_{0.67}$)	8(b)	0	0.25	0.125
32Er2	32(g)	0.13343	0.13765	0.30658
16Sn1	16(f)	0.1765	0.5735	0.375
16Sn2	16(f)	0.3266	0.5766	0.125
16Sn3	16(e)	0.7111	0	0.25
32Sn4	32(g)	0.08725	0.33851	0.41909
32Sn5	32(g)	0.32578	0.25919	0.46208
32Sn6	32(g)	0.0047	0.57420	0.46223
16Rh1	16(d)	0	0.25	0.24745
32Rh2	32(g)	0.24391	0.25120	0.37501

The *II* phase is similar to the *I* phase and contains layers of trigonal prisms linked at the top. The Rh atoms are in the centers of them. But the stacking of layers is different in the two structures.

On the basis of structure analysis it was concluded that the atoms ($Sn_{1-x}Er_x$), Er2 and Rh are similar to cations, but Sn2 and Sn3 atoms are similar to anions. The Sn4 atoms take part as anions in the coordination polyhedron of the Er2 atoms, but they are not similar to the anions in the net of prisms.

The *III* phase according to the X-ray data has a cubic structure with $a = 13.7$ Å and formula $Tb_5Rh_6Sn_{18}$ (Vandenberg 1980). Gladyshevsky and Bodak (1984) showed that the structure of $Tb_5Rh_6Sn_{18}$ was a superstructure to the $Cr_{23}C_6$ type.

X-ray and electron diffraction investigations of the single crystals of the $TbRh_xSn_y$ and $DyOs_xSn_y$ (*III* phase) show that they can be considered as a disordered microtwinned *II* phase. These compounds were named as *II'* phases (Miraglia et al. 1987).

The *V* phase crystallizes in the Ir_3Sn_7 structure type and contains a small quantity of the rare earth. The *VII* phase for which the structure has not been investigated is a relative of the *V* phase but has a lower symmetry (Espinosa 1980).

3.2.37. *$Ho_7Co_6Sn_{23}$ structure type (Skolozdra et al. 1986b)*
$Ho_7Co_6Sn_{23}$, SG $P\bar{3}m1$, $Z = 1$, $a = 9.628$, $c = 9.846$ Å.

Atoms	Wyckoff notation	*x/a*	*y/a*	*z/c*
1Ho	1(a)	0	0	0
6Ho	6(i)	0.4790	0.5210	0.3064
6Co	6(i)	0.1677	0.8323	0.8015
2Sn1	2(d)	0.3333	0.6667	0.8195
6Sn2	6(i)	0.2188	0.7812	0.5451
6Sn3	6(i)	0.1179	0.8821	0.2764
1Sn4	1(b)	0	0	0.5
6Sn5	6(g)	0.3478	0	0
2Sn6	2(d)	0.3333	0.6667	0.1150

The projection of the structure and the coordination polyhedra on the *XY* plane for the $Ho_7Co_6Sn_{23}$ compound are presented in fig. 15.

The structure can be considered as related to the Mn_3Al_{10} structure type. In the Mn_3Al_{10} structure (SG $P6_3/mmc$) the Mn atoms are in the 6(h) sites, the Al0, Al1, Al2 atoms are in 2(a), 6(h), 12(k) sites, respectively (Taylor 1959). The structure is characterized by the existence of columns of empty trigonal prisms and octahedra (in the ratio 1:2), placed along the 6-fold symmetry axis (Krypyakevich 1977). The columns are linked to one another by empty octahedra. The $Ho_7Co_6Sn_{23}$ structure (fig. 16) is formed upon substitution of the Al1 atoms and half of the Al0 atoms by Ho atoms, the other half of the Al0 atoms by Sn4 atoms, the Mn atoms by Co atoms, and the Al2 atoms by Sn atoms (actually by two kinds of Sn atoms: Sn2 and Sn3), and insertion of the Sn1 atoms into the trigonal prisms, the Sn6 atoms into half of the octahedral vacancies (in such a way that the Sn1 and Sn6 atoms are divided by the octahedral vacancies), and the Sn5 atoms into the vacancies between octahedra of the second kind. This substitution and insertion of atoms leads to an increase of the *a* and *c* lattice parameters (the *c* parameter becomes approximately two times the *c* parameter in the Mn_3Al_{10} structure) and to a change of symmetry (instead of SG $P6_3/mmc$, SG $P\bar{3}m1$ appears).

The $R_7Co_6Sn_{23}$ compounds exist with R = Y, Tb–Er.

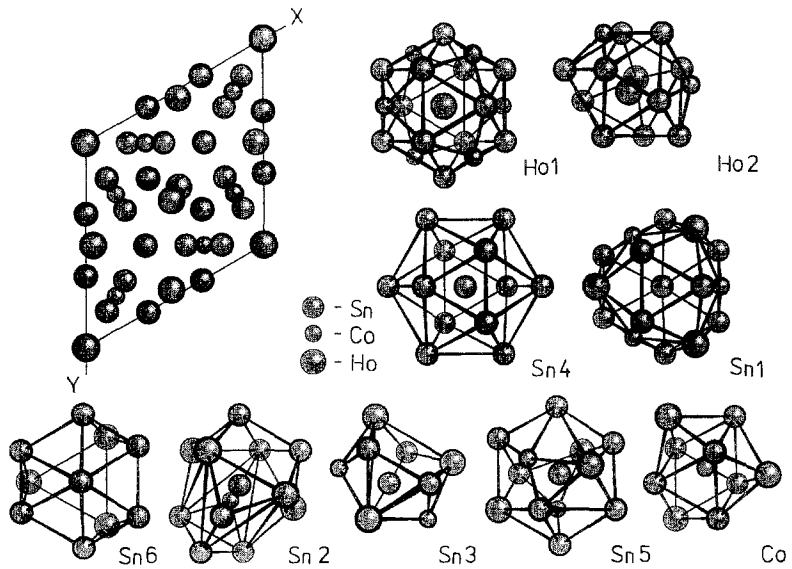

Fig. 15. Projection of the $Ho_7Co_6Sn_{23}$ structure on the XY plane and atom coordination polyhedra.

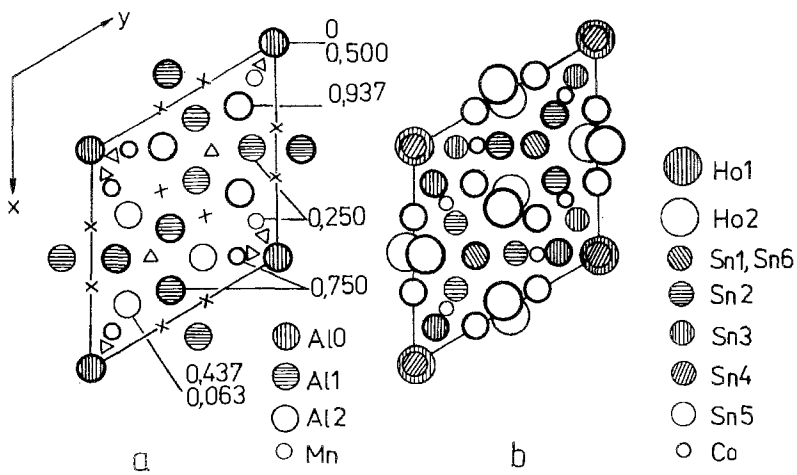

Fig. 16. Projections of the (a) Mn_3Al_{10} and (b) $Ho_7Co_6Sn_{23}$ structures on the XY plane.

3.2.38. *$La_3Co_2Sn_7$ structure type (Dörrscheidt and Schäfer 1980)*

$La_3Co_2Sn_7$, SG Cmmm, $Z=2$, $a=4.59$, $b=27.60$, $c=4.60$ Å.

Atoms	Wyckoff notation	*x/a*	*y/a*	*z/c*
2La1	2(e)	0.5	0	0.5
4La2	4(i)	0	0.1845	0
4Co	4(j)	0	0.3717	0.5
2Sn1	2(a)	0	0	0
4Sn2	4(i)	0	0.4095	0
4Sn3	4(j)	0	0.0907	0.5
4Sn4	4(j)	0	0.2822	0.5

Projections of $La_3Co_2Sn_7$ and its coordination polyhedra on the *XY* plane are presented in fig. 17.

This structure can be obtained by an insertion of the Co atoms into the vacancies of the CaF_2 fragment of the Gd_3Sn_7 structure. As a result this fragment turns into the fragment of the $BaAl_4$ type. Besides $La_3Co_2Sn_7$, the phases $R_3Ni_2Sn_7$ (R = La–Nd) also crystallize in this structure type.

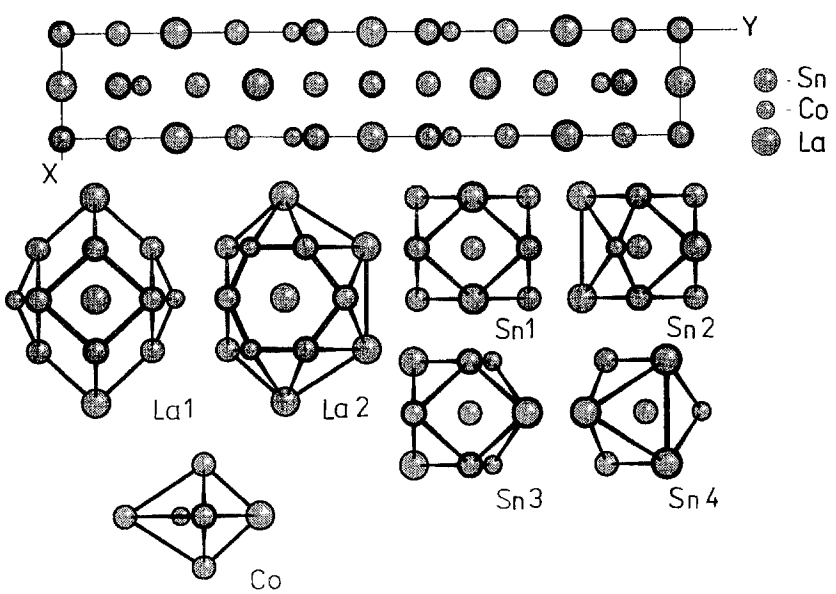

Fig. 17. Projection of the $La_3Co_2Sn_7$ structure on the *XY* plane and atom coordination polyhedra.

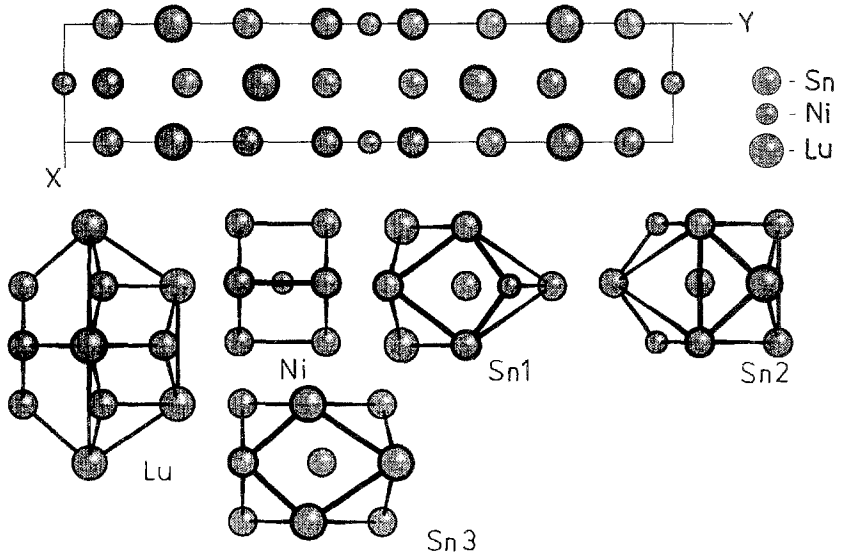

Fig. 18. Projection of the Lu_2NiSn_6 structure on the *XY* plane and atom coordination polyhedra.

3.2.39. *Lu_2NiSn_6 structure type (Skolozdra et al. 1985)*

Lu_2NiSn_6, SG Cmmm, $Z=2$, $a=4.301$, $b=22.278$, $c=4.366$ Å.

Atoms	Wyckoff notation	*x/a*	*y/a*	*z/c*
4Lu	4(i)	0	0.1781	0
2Ni	2(c)	0.5	0	0.5
4Sn1	4(i)	0	0.4291	0
4Sn2	4(j)	0	0.0709	0.5
4Sn3	4(j)	0	0.7018	0.5

Projection of the structure on the *XY* plane and the coordination polyhedra of the atoms are presented in fig. 18.

The structure is a linear combination of the fragments of the structures of the type $ZrGa_2$ and CaF_2, which alternate along the *Y* axis ($Lu_2NiSn_6 = 2LuSn_2 \times NiSn_2$). The unit cell of Lu_2NiSn_6 contains two fragments of the $ZrGa_2$ type ($2\times2LuSn_2$) and two fragments of the CaF_2 type ($2\times1NiSn_2$), the fragments of $NiSn_2$ divide the $2LuSn_2$ fragments.

The structure of this type can also be presented as a derivative of the $GdSn_{3-x}$ type, which can be obtained by the rearrangement of the Gd2 and Sn1 atoms and by shifting the Sn4 atoms in the trigonal prisms formed by the Co atoms into the cubic vacancies of the structure.

The R_2NiSn_6 (R = Ho, Er, Tm, Lu) compounds have this structure.

Table 6
Structure types of ternary stannides obtained by inserting a third component into the structure of binary compounds

Initial compounds		Atom inserted	Compounds obtained	
Composition	ST, SG		Composition	ST, SG
RNi_5	$CaCu_5$, P6/mmm	Sn	RNi_5Sn	$CeNi_5Sn$, $P6_3/mmc$
RSn[a]	NaCl, Fm3m	2Me	RNi_2Sn	$MnCu_2Al$, Fm3m
RSn_2[a]	$CuAl_2$, I4/mcm	4Ni	RNi_4Sn_2	KAu_4Sn_2, $I\bar{4}c2$
6(MSn)	CoSn, P6/mmm	R	RM_6Sn_6	YCo_6Ge_6, P6/mmm $HfFe_6Ge_6$, P6/mmm
$2(R_{0.5}Sn_{0.5})Sn_{12}$[a]	WAl_{12}, Im3	8R+24Ni+24Sn	$R_9Ni_{24}Sn_{49}$	$Gd_9Ni_{24}Sn_{49}$, Im3
$\frac{1}{2}(R_{12}Sn)$[a]	WAl_{12}, Im3	2M+1/2Sn	R_6M_2Sn	Ho_6Co_2Ga, Immm
R_6Sn_{26}[a] ($R_6Sn_2Sn_{24}$)	$AuZn_3$, Pm3n	8M	$R_6M_8Sn_{26}$ (phase *I*)	$Pr_6Rh_8Sn_{26}$, Pm3n
$2(R_{3.5}Co_3Sn_{6.5})$[a]	Mn_3Al_{10}, $P6_3/mmc$	10Sn	$R_7Co_6Sn_{23}$	$Ho_7Co_6Sn_{23}$, P3m1
R_3Sn_7	Gd_3Sn_7, Cmmm	2M	$R_3M_2Sn_7$	$La_3Co_2Sn_7$, Cmmm
$2RSn_3$	$GdSn_{2.75}$, Amm2	Ni	R_2NiSn_6	Lu_2NiSn_6, Cmmm

[a] Hypothetical compounds.

3.3. *Interconnection of the structure types of stannides with the other types*

As we have seen from the previous part, the structures of the stannides are connected in some way with the structures of other groups of compounds. Analysis shows, that the structures of the ternary stannides can be divided into three main groups. The first group contains the stannides obtained by an insertion of the third component in the structure of binary compounds. These types are presented in table 6.

The stannides with the structures of the binary compounds and their superstructures form the second group (table 7). The formation of the superstructures of the ternary stannides is connected with the change of the number of the components and ordered placement of their atoms in Wyckoff sites which are occupied in the binary compounds by one component. In most cases, M and Sn are the ordered atoms, and only in the superstructures of the TiAs type (RPt_2Sn stannides) and $Cr_{23}C_6$ (phases *III*) do the R and Sn atoms order. The structure of the RNi_2Sn ($MnCu_2Al$ type) compound can be considered as both a phase of insertion and as a superstructure.

The third group of the structure types contains structures which consist of the fragments of structures of the binary or more simple ternary compounds (table 8).

The structure of $CeNi_5Sn$, $CeNiSi_2$, $La_3Co_2Sn_7$, Lu_2NiSn_6 types are also considered as structures of insertion. In three latter types and in $Sm_2Cu_4Sn_5$ the fragments alternate along one direction (fig. 19) forming homologous series.

According to Krypyakevich's classification of the intermetallic compounds on the coordination polyhedra of the atom with the smaller size (Krypyakevich 1977), the structure types of the stannides belong to six classes: rhombododecahedral, the class with

Table 7
Structures of ternary stannides with the structures of binary compounds or their superstructures

Compound	Structure type	Space group	Superstructure type	Space group
$R(Cu,Sn)_{13}$	$NaZn_{13}$	Fm3c		
$LuNi_4Sn$	$AuBe_5$	$F\bar{4}3m$	MgCu4Sn	$F\bar{4}3m$
$RNi_{5-x}Sn_{1+x}$	$CeCu_6$	Pnma	$CeCu_{4.38}In_{1.62}$	Pnnm
RCo_3Sn	$BaLi_4$	$P6_3/mmc$		
$Lu_3Co_{7.77}Sn_4$	$BaLi_4$	$P6_3/mmc$	$Lu_3Co_{7.77}Sn_4$	$P6_3mc$
RM_2Sn	CsCl	Pm3m	$MnCu_2Al$	Fm3m
RPt_2Sn	TiAs	$P6_3/mmc$	$ZrPt_2Al$	$P6_3/mmc$
RNi_3Sn_2	$CaCu_5$	P6/mmm	$HoGa_{2.4}Ni_{2.6}$	P6/mmm
RM_2Sn_2	$BaAl_4$	I4/mmm	$CaBe_2Ge_2$	P4/nmm
	$BaAl_4$	I4/nmm	$LaPt_2Ge_2$ [a]	$P2_1$
LaCuSn	AlB_2, P6/mmm			
RCuSn	$CaIn_2$	$P6_3/mmc$		
EuZnSn	$CeCu_2$	Imma		
RMSn	$CaIn_2$	$P6_3/mmc$	LiGaGe	$P6_3/mc$
RMSn	Fe_2P	$P\bar{6}2m$	ZrNiAl	$P\bar{6}2m$
RMSn	$PbCl_2$	Pnma	TiNiSi	Pnma
RAuSn	CaF_2	Fm3m	MgAgAs	$F\bar{4}3m$
$R_5(Ni,Sn)_3$	Cr_5B_3	I4/mcm		
$La_2Rh_3Sn_5$	$BaAl_4$	I4/nmm	$U_2Co_3Si_5$ [a]	Ibam
$R_5M_6Sn_{18}$	$Cr_{23}C_6$	Fm3m	$Tb_5Rh_6Sn_{18}$	$F\bar{4}3m$

[a] The structure can be obtained as a consequence of a deformation of the corresponding structure type.

Table 8
Structure types of ternary stannides wich consist of fragments of other structures

Structure type	Fragment types	Structure type	Fragment types
$CeNi_5Sn$	$CaCu_5$, RX_7 [a]	$Gd_6Cu_8Ge_8$	$MgCuAl_2$, Mo_2NiB_2
$La_3Co_{11}Ga_3$	Cr_5B_3, $U(Ni_{0.68}Si_{0.32})_{11}$	$Sm_2Cu_4Sn_5$	α-Po, CaF_2, $BaAl_4$
$Y_{13}Pd_{40}Sn_{31}$	$CaCu_5$, $MnCu_2Al$, AlB_2	$Y_2Rh_3Sn_5$	$NdRh_2Sn_4$, TiNiSi
YFe_6Sn_6	$HfFe_6Ge_6$, $ScFe_6Ga_6$	$LuNiSn_2$	AlB_2, $BaAl_4$, $AuCu_3$, α-Fe
$TbFe_6Ge_6$	$HfFe_6Ge_6$, $ScFe_6Ga_6$	$CeNiSi_2$	AlB_2, $BaAl_4$
$DyFe_6Ge_6$	$HfFe_6Ge_6$, $ScFe_6Ga_6$	$La_3Co_2Sn_7$	AlB_2, $BaAl_4$, $AuCu_3$
$HoFe_6Ge_6$	$HfFe_6Ge_6$, $ScFe_6Ga_6$	Lu_2NiSn_6	AlB_2, CaF_2 or $ZrGa_2$, CaF_2
$ErFe_6Ge_6$	$HfFe_6Ge_6$, $ScFe_6Ga_6$		

[a] Hypothetical compound.

the defect rhombododecahedron, icosahedral, tetragonal antiprismatic, trigonal prismatic and octahedral. The smaller atoms in stannides are the transition metal atoms. But in many

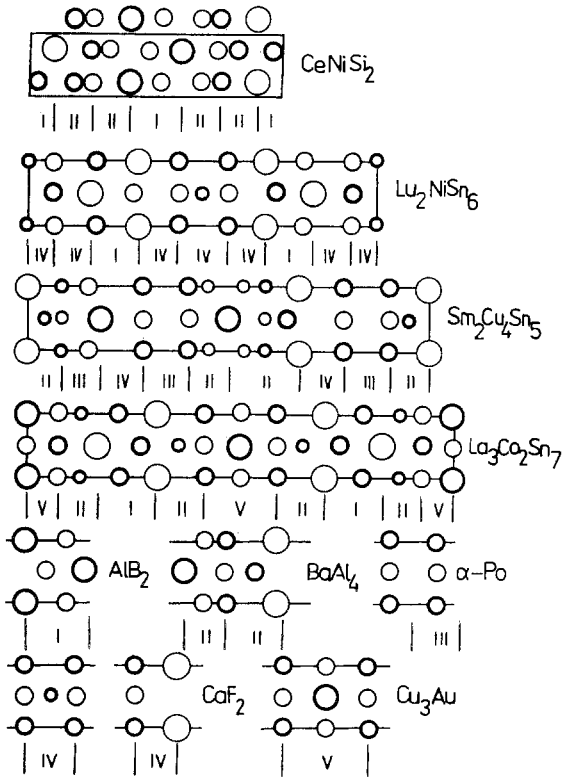

Fig. 19. Stacking of different fragments in the $CeNiSi_2$, Lu_2NiSn_6, $Sm_2Cu_4Sn_5$, and $La_3Co_2Sn_7$ structure types.

of the compounds the Sn atoms have coordination number and coordination polyhedra which are characteristic of the atoms of the smaller size. With the small content of tin and R in the compounds, tin has crystal chemistry properties which are close to the properties of the M component and are characterized by the high coordination number.

An increase of the tin concentration leads to a decrease of the coordination number for part of the Sn atoms, while the coordination number for another part of the Sn atoms remains high. Thus with increasing tin content two tendencies are revealed: to lower the coordination number (as M atoms) and to preserve the high coordination number. This and the statistical distribution of the M and Sn atoms in some stannides indicate the ability of the tin atoms to change their radius depending on the composition of the compound and its structure.

4. Properties of the ternary stannides

The magnetic and transport properties of the ternary stannides have not been investigated to any great extent. Of these, the magnetic properties have been more completely

Table 9
Magnetic and transport properties of RNi_5Sn compounds (Skolozdra and Komarovskaya 1982a, Skolozdra 1993)

Compound	θ_p (K)	μ_{eff} (μ_B)	ρ ($\mu\Omega$ cm)		S (μV/K)	
			at 78 K	at 300 K	at 90 K	at 300 K
$LaNi_5Sn$	Pauli paramagnet		41	85	−2.0	−1.3
$CeNi_5Sn$	$\chi^{-1}(T)$ not linear		30	88	5.4	4.0
$PrNi_5Sn$	−9	3.56	120	166	−3.9	−5.1
$NdNi_5Sn$	0	3.69				

investigated than the transport ones. For a majority of the compounds, the temperature range of the measurements is between 78 and 360 K.

The magnetic and transport data of the compounds are listed in tables 9–41[2].

4.1. *RNi_5Sn compounds*

The magnetic susceptibility has been measured for the RNi_5Sn compounds, where R = La, Ce, Pr, Nd, over the temperature range 80–400 K by Skolozdra and Komarovskaya (1982a). The La stannide is a Pauli paramagnet. The $\chi(T)$ function for the Pr and Nd compounds follows the modified Curie–Weiss law. The μ_{eff} values are close to the theoretical moments of the Pr^{3+} and Nd^{3+} ions (table 9).

The magnetic susceptibility of $CeNi_5Sn$ at a temperature higher than 325 K is temperature-independent ($\chi = 2.17\times10^{-6}$ cm^3/g), below 325 K χ increases with decreasing temperature and is equal to 3.21×10^{-6} cm^3/g at 78 K. The $\chi(T)$ dependence does not exhibit Curie–Weiss behaviour.

The resistivity has been measured for $LaNi_5Sn$, $CeNi_5Sn$ and $PrNi_5Sn$ (fig. 20, table 9). The function $\rho(T)$ is characterized by a negative curvature i.e., the resistivity strives towards saturation at high temperatures. In fig. 20 the thermal dependence of the thermopower measured in the range 80–400 K is presented as well. The thermopower of $CeNi_5Sn$ has a positive sign contrary to $LaNi_5Sn$ and $PrNi_5Sn$. A maximum is observed at ~120 K, which is absent for $LaNi_5Sn$ and $PrNi_5Sn$.

The Ce stannide is characterized by a significant deviation of the unit cell volume relative to its neighboring RNi_5Sn compounds (fig. 21). This, and also the dependences $\chi(T)$ and $S(T)$ suggest valence fluctuation for Ce. An investigation of the L_{III} spectra (fig. 22) shows that the Ce valence is 3.14 (Samsonova et al. 1985).

[2] The magnitudes of resistivity and thermopower listed in the tables have been taken from the figures of the corresponding articles, with the exception of the author's data.

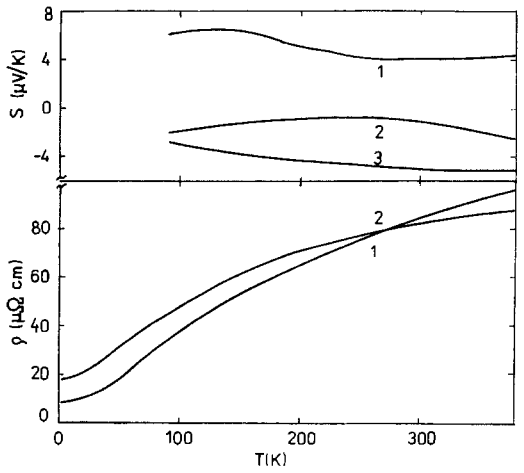

Fig. 20. Temperature dependence of the resistivity and thermopower of (1) $CeNi_5Sn$, (2) $LaNi_5Sn$ and (3) $PrNi_5Sn$ (Skolozdra 1993).

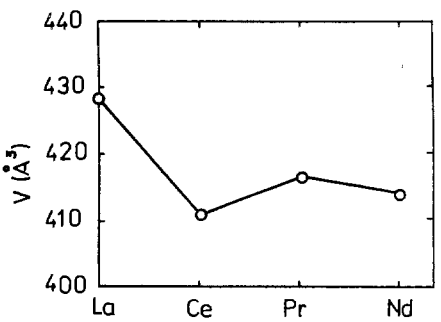

Fig. 21. Unit cell volume in the RNi_5Sn series.

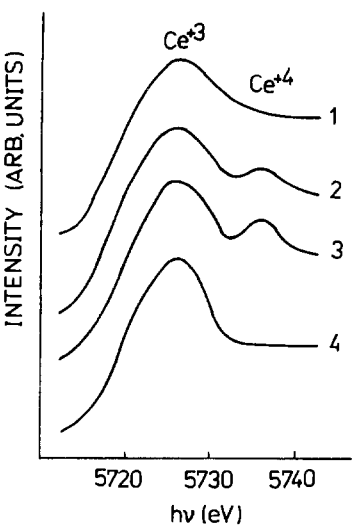

Fig. 22. The L_{III} spectra of Ce in the compounds: (1) $Ce_5Ni_{1.5}Sn_{1.5}$, (2) CeNiSn, (3) $CeNi_5Sn$ and (4) $CeNi_2Sn_2$ (Samsonova et al. 1985).

4.2. *$RNi_{5-x}Sn_{1+x}$ compounds*

The magnetization measurements of the $RNi_{5-x}Sn_{1+x}$ compounds have been carried out in the temperature range 4.5–300 K by Skolozdra et al. (1996b). The Gd, Tb, Dy, Ho, Sm compounds are magnetically ordered at low temperatures, for the Y, Er, Tm stannides no ordering is observed down to 4.5 K.

The susceptibility of $YNi_{5-x}Sn_{1+x}$ does not depend on temperature above 100 K. For the other compounds (except Sm and Yb) the susceptibility at high temperatures follows the Curie–Weiss law, at low temperatures (lower than 60–90 K for all and 140 K for

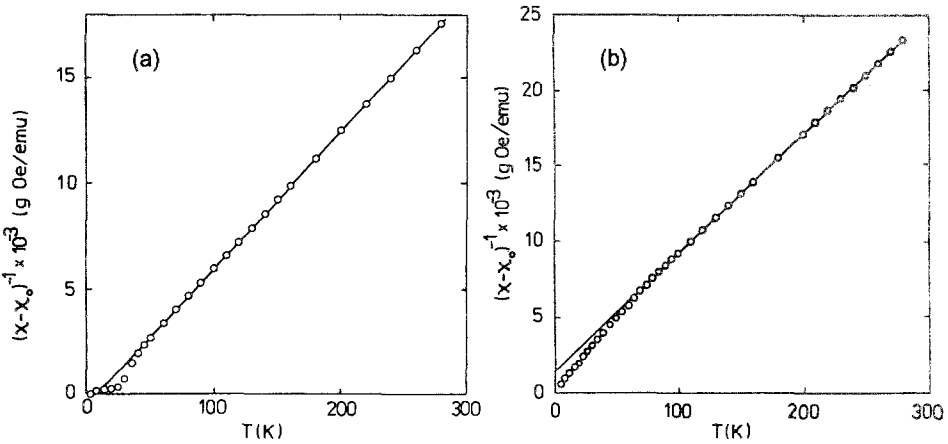

Fig. 23. Temperature dependence of the reciprocal susceptibility of (a) $GdNi_{5-x}Sn_{1+x}$ and (b) $TmNi_{5-x}Sn_{1+x}$ (Skolozdra et al. 1996b).

Dy) a deviation from the Curie–Weiss law is observed. The temperature dependence of susceptibility of $GdNi_{5-x}Sn_{1+x}$ and $TmNi_{5-x}Sn_{1+x}$ is shown in figs. 23a,b, respectively.

$YbNi_{5-x}Sn_{1+x}$ differs from the other compounds. The temperature dependence of the magnetization, $M(T)$, exhibits a sharp maximum at about 140 K. At higher temperatures (up to 300 K) $M(T)$ weakly depends on the temperature and is nonlinear which suggests the presence of an extra parasitic magnetically ordered phase. However, such a phase was not observed in the X-ray powder diffraction.

The values of the moments (table 10) indicate that the nickel atoms are nonmagnetic.

Transition to the magnetically ordered state is observed in weak applied fields. Under higher magnetic fields (3–5 T), the transition to the ordered state becomes practically invisible in the $M(T)$ dependences; and only a decrease of the susceptibility below the characteristic temperature indicates the existence of the phase transition.

Table 10
Magnetic properties of $RNi_{5-x}Sn_{1+x}$ compounds (Skolozdra et al. 1996b)

Compound	θ_p (K)	μ_{eff} (μ_B)	T_m (K)
$YNi_{5-x}Sn_{1+x}$	0.4	0.31	
$SmNi_{5-x}Sn_{1+x}$	−11	0.92	24
$GdNi_{5-x}Sn_{1+x}$	7	8.4	34
$TbNi_{5-x}Sn_{1+x}$	2	10.24	26
$DyNi_{5-x}Sn_{1+x}$	9	11.35	15
$HoNi_{5-x}Sn_{1+x}$	−3	10.78	35
$ErNi_{5-x}Sn_{1+x}$	−12	10.18	
$TmNi_{5-x}Sn_{1+x}$	−17	7.69	

4.3. *$LuNi_4Sn$ compound*

This stannide is a Pauli paramagnet (Skolozdra and Komarovskaya 1983).

4.4. *$R(Cu_{0.72}Sn_{0.28})_{13}$ compounds*

The susceptibility for La, Ce, Pr and Nd compounds has been measured between 78 and 293 K by Komarovskaya and Skolozdra (1984). The $\chi(T)$ dependence is in accord with the Curie–Weiss law (except the La stannide). The La compound is diamagnetic at 300 K ($\chi = -0.14 \times 10^{-6}$ cm^3/g) and paramagnetic at 78 K ($\chi = 0.56 \times 10^{-6}$ cm^3/g).

The resistivity of the La, Ce and Pr compounds increases with increasing temperature, and the $\rho(T)$ function is characterized by a negative curvature. The thermopower has a positive value which increases with increasing temperature (table 11).

Table 11
Magnetic and transport properties of $R(Cu_{0.72}Sn_{0.28})_{13}$ compounds (Komarovskaya and Skolozdra 1984, Skolozdra 1993)

Compound	θ_p (K)	μ_{eff} (μ_B)	ρ (μΩ cm)		S (μV/K)	
			at 78 K	at 300 K	at 90 K	at 300 K
$La(Cu_{0.72}Sn_{0.28})_{13}$	Pauli paramagnet		30	41		
$Ce(Cu_{0.72}Sn_{0.28})_{13}$	0	2.53	19	55	0.6	5.0
$Pr(Cu_{0.72}Sn_{0.28})_{13}$	10	3.54	48	96	0.3	3.8
$Nd(Cu_{0.72}Sn_{0.28})_{13}$	5	3.52				

Table 12
Magnetic properties of $R_6M_{13}Sn$ compounds (Weitzer et al. 1993b)

Compound	T_C (K)	M_s (μ_B/f.u.)	μ_s (μ_B/Co)
$La_6Co_{13}Sn$	190	14.3	1.1
$Pr_6Fe_{13}Sn$	250	2.4	
$Nd_6Fe_{13}Sn$	510	7.0	

4.5. *$R_6M_{13}Sn$ compounds*

Magnetic properties of $La_6Co_{13}Sn$, $Pr_6Fe_{13}Sn$ and $Nd_6Fe_{13}Sn$ have been measured from 5 to 600 K (Weitzer et al. 1993b). $La_6Co_{13}Sn$ exhibits ferromagnetism, and the magnetic moment of Co is equal to $1.1\mu_B$ (table 12). The temperature dependence of the magnetization curves of $Pr_6Fe_{13}Sn$ and $Nd_6Fe_{13}Sn$ suggests that an antiferromagnetic coupling of at least two magnetic sublattices is present. Some kind of antiferromagnetic

ordering within the Fe sublattice is anticipated from a Mössbauer study of the Fe compounds as well (Wiesinger et al. 1994).

4.6. *RCo_3Sn and $Lu_3Co_{7.77}Sn_4$ compounds*

The magnetic properties of the RCo_3Sn stannides were studied over the temperature range 78–1000 K under applied fields up to 1.5 T (Skolozdra 1993). The magnetization curves of $GdCo_3Sn$, $TbCo_3Sn$, $DyCo_3Sn$ and $HoCo_3Sn$ show compensation points (T_k) between 117 and 238 K (fig. 24). Perhaps, T_k of $ErCo_3Sn$ and $TmCo_3Sn$ lies below 78 K. The Curie points (T_C) are higher than 1000 K.

The magnetic moment of Co in YCo_3Sn is equal to $0.4\mu_B$ and it is smaller than μ of Co in the YCo_3, YCo_5 and Y_2Co_{17} compounds. The Yb in the $YbCo_3Sn$ compound, for which dependence $\chi(T)$ is similar to that for YCo_3Sn, is either divalent or in an intermediate valence state. There is a maximum at Yb in a plot of the unit cell volumes vs. the atomic number of the RCo_3Sn compounds which reaffirms the lower, less than 3, Yb valence.

Curves of the $M(T)$ dependence for RCo_3Sn show a ferrimagnetic ordering of the Co and R sublattices, which is characteristic of the intermetallic compounds of the heavy rare earths with Co. For $GdCo_3Sn$ the magnetic moment of Gd ($6.1\mu_B$) has been obtained by an extrapolation of the $M(T)$ curves to 0 K.

The magnetic data of the RCo_3Sn compounds are listed in table 13.

One reason for the high T_C of the RCo_3Sn phases, which have a low Co moment, can be connected with peculiarities of their structure. In the RCo_3Sn compounds a statistical mixture of (Co1, Sn), the Co2 and Co3 atoms form nets in which a fragment similar to the unit cell of the pure Co can be selected. At a particular local ordering of Co1 and Sn atoms, which statistically occupy the 12(k) position, a ferromagnetic cluster which contains only the Co atoms can appear (fig. 25). The clusters can be linked one with another along the 6-fold symmetry axis or by the Co3 atoms with the other clusters

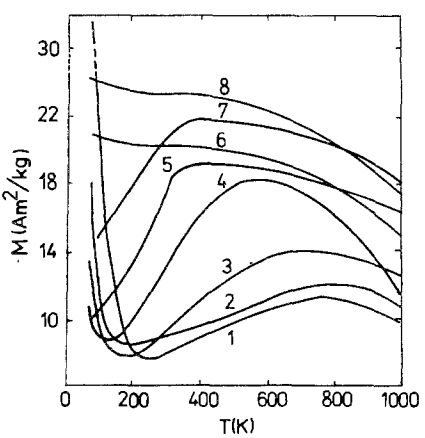

Fig. 24. Temperature dependence of the magnetization of (1) $GdCo_3Sn$, (2) $TbCo_3Sn$, (3) $DyCo_3Sn$, (4) $HoCo_3Sn$, (5) $ErCo_3Sn$, (6) YCo_3Sn, (7) $TmCo_3Sn$, (8) $YbCo_3Sn$ (Skolozdra 1993).

Table 13
Magnetic and transport properties of RCo_3Sn compounds (Skolozdra 1993)

Compound	T_k (K)	μ^a (μ_B)	ρ (μΩ cm)		S (μV/K)	
			at 78 K	at 300 K	at 90 K	at 300 K
YCo_3Sn		1.4	216	312		
$GdCo_3Sn$	238	2.5	218	258	−4.6	−10.2
$GdCo_{2.6}Sn$			140	198		
$TbCo_3Sn$	163	1.5				
$DyCo_3Sn$	163	1.0				
$HoCo_3Sn$	117	0.9	174	252		
$ErCo_3Sn$	<78	0.8				
$TmCo_3Sn$	<78	1.3				
$YbCo_3Sn$		2.0	92	126		

[a] $T = 78$ K, $H = 1.4$ T.

which are at the same height. It can be speculated that the magnetic properties of RCo_3Sn compounds are due to the presence of the ferromagnetic Co-clusters, so that the Curie temperatures are as high as in pure Co.

The resistivity of the RCo_3Sn stannides has high values and increases with increasing temperature (table 12).

For the $Lu_3Co_{7.77}Sn_4$ compound measurements of the bulk magnetization and susceptibility were carried out over the temperature range 4–300 K (Skolozdra et al. 1996a). It turns out that it is a very weak itinerant ferromagnet with $T_C = 63$ K and the Co moment of $0.19\mu_B$ at 4 K. Above 63 K $\chi(T)$ follows the Curie–Weiss law (fig. 26), and the effective

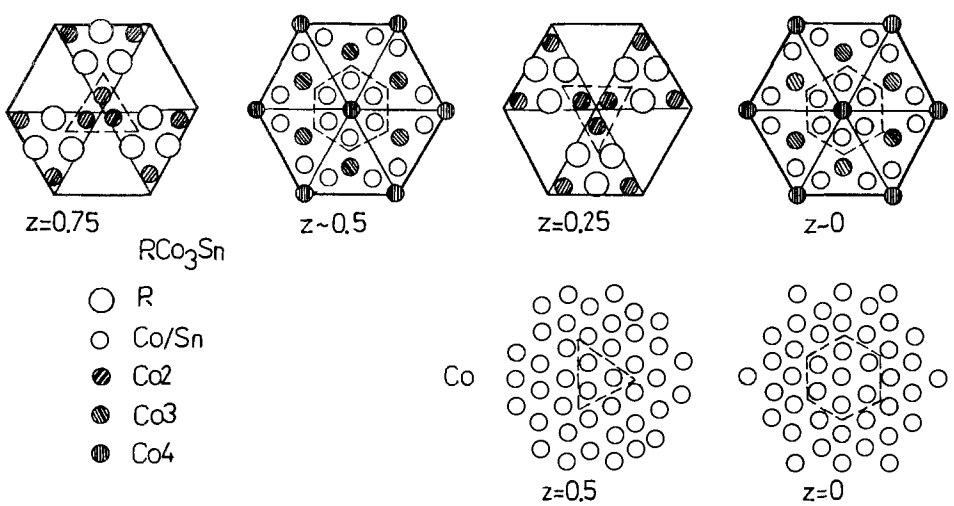

Fig. 25. The nets in the RCo_3Sn and Co structures. The outlined atoms form the clusters (Skolozdra 1993).

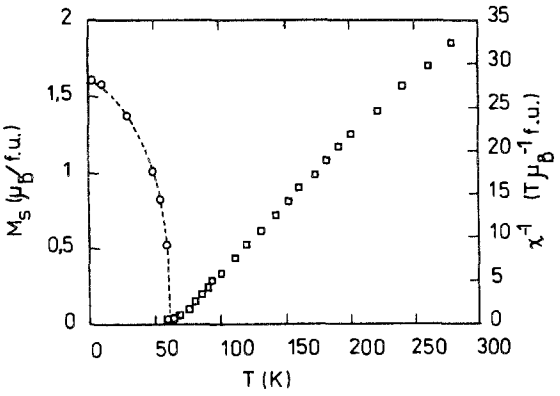

Fig. 26. Temperature dependence of the magnetization and reciprocal susceptibility of $Lu_3Co_{7.77}Sn_4$ (Skolozdra et al. 1996a).

paramagnetic moment reaches $0.67\mu_B$/Co. The $Lu_3Co_{7.77}Sn_4$ compound is similar to the YNi_3 compound in its magnetic properties. It is supposed that the magnetic moments are localized on the Co atoms with a partially filled 3d-band. This is due to the Co1 or Co4 atoms which form chains from the tetrahedra which are parallel to the Z axis with the shortened interatomic distances.

4.7. *RNi_4Sn_2 compounds*

The magnetic susceptibility of the Ce, Pr, Nd compounds exhibit Curie–Weiss behaviour between 78–293 K. $LaNi_4Sn_2$ is a Pauli paramagnet. The $\chi(T)$ function of $SmNi_4Sn_2$ weakly depends on the temperature, its susceptibility is determined by close separation between the two energy levels of the multiplets Sm^{3+} of $^6H_{5/2}$ and $^6H_{7/2}$ ($\Delta E \approx kT$) (Skolozdra et al. 1988d).

The resistivity and thermopower for $CeNi_4Sn_2$ and $LaNi_4Sn_2$ were measured. No peculiarities were observed in their temperature dependencies. It is interesting to note the high negative magnitude S of both compounds (table 14).

Table 14
Magnetic and transport properties of RNi_4Sn_2 compounds (Skolozdra et al. 1988d, Skolozdra 1993)

Compound	θ_p (K)	μ_{eff} (μ_B)	ρ (μΩ cm)		S (μV/K)	
			at 78 K	at 300 K	at 90 K	at 300 K
$LaNi_4Sn_2$	Pauli paramagnet		16	58	−12.5	−16.6
$CeNi_4Sn_2$	−17	2.27	12	33	−7.5	−15.7
$PrNi_4Sn_2$	−2	3.77				
$NdNi_4Sn_2$	14	3.76				
$SmNi_4Sn_2$	$\chi^{-1}(T)$ not linear					

4.8. *RM_2Sn compounds ($MnCu_2Al$ type)*

The $ScCo_2Sn$ stannide is ferromagnetic below 238 K. It is thought that in the temperature range 100–238 K and under weak applied fields $ScCo_2Sn$ has a helical structure, and at lower temperatures it changes to a spin glass (Lin et al. 1992). Under higher applied fields $ScCo_2Sn$ becomes ferromagnetic below T_C (238 K). $ScNi_2Sn$ is weak paramagnetic down to 1.2 K. The resistivity of $ScCo_2Sn$ and $ScNi_2Sn$ has also been measured by Lin et al. (1992). The resistivity of $ScCo_2Sn$ is higher than that of $ScNi_2Sn$ as a consequence of the magnetic contribution to the resistivity. $\chi(T)$ of $YbNi_2Sn$ is in accord with the Curie–Weiss law. $LuNi_2Sn$ is a Pauli paramagnet (Skolozdra and Komarovskaya 1983).

Magnetic properties and Mössbauer effect of the RPd_2Sn compounds (R = Tb–Yb) were investigated by Malik et al. (1985). The temperature dependence of χ follows the Curie–Weiss law, but for $TmPd_2Sn$ and $YbPd_2Sn$ the function $\chi^{-1}(T)$ deviates from linearity below 100 K, which is explained by the effects of the crystal field. From an analysis of the crystal field influence on the susceptibility it has been shown that the ground state of Tm^{3+} ion is nonmagnetic. The Yb moment is smaller than that for Yb^{3+} ion because the ground state is characterized by the Γ_6 or Γ_7 doublet which gives a lower susceptibility. $TbPd_2Sn$, $DyPd_2Sn$ and $YbPd_2Sn$ are antiferromagnetic (table 15).

Nonelastic neutron scattering experiments on $HoPd_2Sn$ and $ErPd_2Sn$ have been carried out by Li et al. (1989), and the crystal field parameters have been determined. The ground states of Ho and Er are the magnetic triplet Γ_5^1 and the magnetic quartet Γ_8^3 with magnetic moments of 5.49 and 6.31 μ_B, respectively.

Hodges and Jehanno (1988) have determined the hyperfine interaction parameters for $ErPd_2Sn$ and $YbPd_2Sn$ and the magnetic moments. The moments are equal to $5.7\mu_B$ for $ErPd_2Sn$ and $1.6\mu_B$ for $YbPd_2Sn$. It was concluded that in both cases the local environment of the R atoms is not cubic, which is explained by a partial nonordering of the crystal lattice.

The magnetic structures of the $DyPd_2Sn$ and $HoPd_2Sn$ stannides have been investigated at 1.2 and 300 K by neutron diffraction (Donaberger and Stager 1987). Both compounds are characterized by an antiferromagnetic ordering of the MnO type with the magnetic unit cell which is two times bigger than the crystallographic one. The magnetic moments are directed perpendicular to the [1 1 1] axis and lie in the (1 1 1) plane. The moments of the Dy and Ho atoms (6.7 and $4.4\mu_B$, respectively) are significantly smaller than the theoretical moments of the Dy^{3+} and Ho^{3+} ions ($10\mu_B$). Such lowering of the moments is explained by crystal field effects.

Crangle et al. (1995) indicate a complex magnetic diagram of $DyPd_2Sn$ below 10 K. The powder neutron diffraction measurements reveal an incommensurate structure. At 5.2 K this structure undergoes a transition to a commensurate magnetic phase with the moment direction confined in or close to the (1 1 1) plane.

The $ErPd_2Sn$ stannide is characterized by an antiferromagnetic structure with a double cubic magnetic lattice (Stanley et al. 1987). But there are satellites in the neutron diffraction pattern which indicate a long-range modulation of the diffraction magnetic density component.

Table 15
Magnetic properties of RM_2Sn compounds

Compound	T_C (K)	T_N (K)	μ_s (μ_B)	θ_p (K)	μ_{eff} (μ_B)	T_c (K)	Reference
$ScCo_2Sn$	270		0.55				Malik et al. 1987
	238		0.51				Lin et al. 1992
$ScNi_2Sn$	Pauli paramagnet						
$YbNi_2Sn$				−38	4.33		Skolozdra and Komarovskaya 1983
$LuNi_2Sn$	Pauli paramagnet						Skolozdra and Komarovskaya 1983
$ScPd_2Sn$						2.15	Malik et al. 1985
YPd_2Sn						4.55	Malik et al. 1985
$TbPd_2Sn$		9.0		−8.6	9.95		Malik et al. 1985
$DyPd_2Sn$		15.0		−9.3	10.83		Malik et al. 1985
		7.0	6.7		10.8		Donaberger and Stager 1987
				−4.56	10.65		Crangle et al. 1995
$HoPd_2Sn$				−6.2	10.67		Malik et al. 1985
			4.4		10.8		Donaberger and Stager 1987
			5.49				Li et al. 1989
$ErPd_2Sn$				−7.6	9.59		Malik et al. 1985
			6.31				Li et al. 1989
			5.7				Hodges and Jehanno 1988
		1.00				1.17	Shelton et al. 1986
$TmPd_2Sn$					7.4	2.82	Malik et al. 1985
$YbPd_2Sn$		0.23		−4.3	4.34	2.42	Malik et al. 1985
			1.6				Hodges and Jehanno 1988
						2.46	Kierstead et al. 1985
$LuPd_2Sn$						3.05	Malik et al. 1985
$GdPt_2Sn$	20		6.45	−10	8.22		de Mooij and Buschow 1984
$ErPt_2Sn$				19	9.79		de Mooij and Buschow 1984

The $ErPd_2Sn$ and $YbPd_2Sn$ show the coexistence of the superconductivity and magnetic order (Shelton et al. 1986, Kierstead et al. 1985) (table 15).

4.9. *RPt_2Sn compounds*

The magnetic properties of $GdPt_2Sn$ and $ErPt_2Sn$ have been studied (table 15). The Gd compound is ferromagnetic below 20 K. The Er compound does not order magnetically down to 4.2 K. The $\chi(T)$ dependence in the paramagnetic range exhibits Curie–Weiss behavior (de Mooij and Buschow 1984).

4.10. *RM_6Sn_6 compounds*

According to susceptibility measurements $ErMn_6Sn_6$, $TmMn_6Sn_6$, $LuMn_6Sn_6$, $ScMn_6Sn_6$, YMn_6Sn_6 are antiferromagnetic, and $GdMn_6Sn_6$, $TbMn_6Sn_6$, $DyMn_6Sn_6$ and $HoMn_6Sn_6$ are ferrimagnetic (Malaman et al. 1988, Venturini et al. 1991). Magnetic structures have been determined for the Tb, Dy, Ho, Er and Lu compounds (Chafik El Idrissi et al. 1991b,

Table 16
Magnetic properties of RMn_6Sn_6 compounds

Compound	T_C (K)	T_N (K)	μ (μ_B/f.u.)	μ (μ_B/Mn)	T_t (K)	θ_p (K)	μ_{eff} (μ_B/f.u.)	μ_{eff} (μ_B/Mn)	Reference
$ScMn_6Sn_6$		384				439	8.54	3.48	Venturini et al. 1991
YMn_6Sn_6		333				394	8.85	3.61	Venturini et al. 1991
$PrMn_6Sn_6$	340		12[a]			335	8.9	3.3	Weitzer et al. 1993a
$NdMn_6Sn_6$	340		4.5[a]			274	8.5	3.2	Weitzer et al. 1993a
$SmMn_6Sn_6$	380		8.0[a]			380	7.7	3.0	Weitzer et al. 1993a
$GdMn_6Sn_6$	435		4.2[b]	1.9[b]		139	12.24	3.80	Venturini et al. 1991
$TbMn_6Sn_6$	423		3.3[b]	2.1[b]	330	125	13.07	3.58	Venturini et al. 1991
			4.9[c]	2.0[c]					Chafik El Idrissi et al. 1991a
			8.6[d]	2.4[d]					Chafik El Idrissi et al. 1991a
$DyMn_6Sn_6$	393		2.7[b]	2.1[b]	33	138	14.09	3.79	Venturini et al. 1991
$HoMn_6Sn_6$	376		3.7[b]	2.3[b]	200	157	13.85	3.64	Venturini et al. 1991
			4.7[c]	2.0[c]					Chafik El Idrissi et al. 1991a
			8.4[d]	2.4[d]					Chafik El Idrissi et al. 1991a
$ErMn_6Sn_6$		352	4.2[b]	2.2[b]	75	241	12.91	3.52	Venturini et al. 1991
$TmMn_6Sn_6$		347			58	304	11.42	3.48	Venturini et al. 1991
$LuMn_6Sn_6$		353				406	8.51	3.47	Venturini et al. 1991
				1.33[c]					Venturini et al. 1993

[a] At 5 K.
[b] At 4.2 K and 2 T.
[c] At 300 K.
[d] At 2 K.

Venturini et al. 1993). The compounds with light lanthanides ($PrMn_6Sn_6$, $NdMn_6Sn_6$ and $SmMn_6Sn_6$) order ferromagnetically (Weitzer et al. 1993a). The magnetic data of RMn_6Sn_6 compounds are listed in table 16.

The study of the magnetic structure of $TbMn_6Sn_6$ and $HoMn_6Sn_6$ by neutron diffraction in the temperature range 2–300 K reveals a collinear ferrimagnetic arrangement (Chafik El Idrissi et al. 1991b). At 300 K the R and M atoms form antiferromagnetic layers with a coupling sequence Mn(+)R(−)Mn(+)Mn(+)R(−)Mn(+). At this temperature the Mn, Tb, Ho moments are equal to 2.0, 4.9 and 4.7μ_B, respectively. For $HoMn_6Sn_6$ the magnetic moments lie in the (0 0 1) plane, while in $TbMn_6Sn_6$ there is a deviation of the moment by $\varphi = 15°$ from the Z axis. As the temperature is lowered a spin rotation process is observed in both compounds such that at 2 K, the magnetic moments in $TbMn_6Sn_6$ are oriented along the Z axis and in $HoMn_6Sn_6$ they are at an angle of 50° with this axis. The moments Mn, Tb and Ho at 2 K are 2.4, 8.6 and 8.4μ_B, respectively. In the $LuMn_6Sn_6$ compound only the Mn atoms are magnetic (Venturini et al. 1993). At 300 K ferromagnetic layers of Mn atoms (Mn moments lie in the (0 0 1) plane) are ordered antiparallel to one another. Similar to the above compounds, a spin-reorientation process takes place at low temperatures, which results in the formation of an incommensurate antiferromagnetic helical arrangement.

It is reported that in the $ScMn_6Sn_6$, YMn_6Sn_6, $ErMn_6Sn_6$, $TmMn_6Sn_6$ stannides there are also complex helical magnetic structures (Venturini et al. 1993).

Table 17
Magnetic and transport properties of RFe_6Sn_6 and RCo_6Sn_6 compounds

Compound	θ_p (K)	μ_{eff} (μ_B)	ρ (μΩ cm)		S (μV/K)		Reference
			at 78 K	at 300 K	at 90 K	at 300 K	
YFe_6Sn_6			122	218	−3.9	−7.8	Skolozdra 1993
$LuFe_6Sn_6$			298	480	−6.2	−7.8	Skolozdra 1993
YCo_6Sn_6	Pauli paramagnet		63	80	−8.2	−8.6	Skolozdra and Koretskaya 1984
$TbCo_6Sn_6$	−15	9.6					Skolozdra and Koretskaya 1984
$DyCo_6Sn_6$	2	10.7					Skolozdra and Koretskaya 1984
$HoCo_6Sn_6$	−3	10.6					Skolozdra and Koretskaya 1984
$ErCo_6Sn_6$	3	9.6					Skolozdra and Koretskaya 1984
$TmCo_6Sn_6$	20	7.5					Skolozdra and Koretskaya 1984
$LuCo_6Sn_6$	Pauli paramagnet		125	179	−7.2	−7.6	Skolozdra and Koretskaya 1984, Skolozdra 1993

Dirken et al. (1991) studied ^{155}Gd Mössbauer effect in $GdMn_6Sn_6$. A comparison of these results with the results for $GdCo_3B_2$, a compound with a related structure, indicated that the V_{zz} component of the electric field gradient tensor at the Gd site was negative and its absolute value was more than 15 times smaller than that found for $GdCo_3B_2$. The second-order crystal-field parameter $A20$ has a low value compared with highly anisotropic materials. This shows the important role in anisotropic behaviour of the parameters of higher order than $A20$.

Li et al. (1995) have measured by NMR at 4.2 K the zero field hyperfine spectra of ^{159}Tb in $TbMn_6Sn_6$. The transfered hyperfine field from the transition metal sublattice is found to be approximately 24 T. The susceptibility measurements of the RFe_6Sn_6 stannides are complicated as a consequence of the presence of ferromagnetic impurities (iron stannides or iron) (Skolozdra 1993). The susceptibility was measured for two alloys – $Lu_{8.5}Fe_{44.5}Sn_{47.0}$ and $Lu_9Fe_{43}Sn_{48}$, which have slightly more Sn and lie in the two-phase region $LuFe_6Sn_6$–$Lu_4Fe_6Sn_{19}$ (the content of the later paramagnetic phase in this alloy was insignificant). The susceptibility of both alloys is nearly the same and independent of the applied field. With increasing temperature up to 240 K, the susceptibility decreases; and as the temperature increases up to 293 K it hardly changes. The obtained χ value is significantly higher than for a Pauli paramagnet. Evidently at the temperature of investigation (78–293 K) $LuFe_6Sn_6$ is a highly enhanced Pauli paramagnet.

The YCo_6Sn_6 and $YbCo_6Sn_6$ stannides are Pauli paramagnets, the temperature dependence of the susceptibility for other Co compounds follows the Curie–Weiss law (Skolozdra and Koretskaya 1984).

The resistivity has been measured for the RFe_6Sn_6 and RCo_6Sn_6 stannides (R = Y, Lu). The resistivity of the iron phases raises with increasing temperature more than that of the phases with Co. The thermopower depends slightly on the temperature (Skolozdra 1993).

The magnetic and transport data of RFe_6Sn_6 and RCo_6Sn_6 compounds are listed in table 17.

Table 18
Magnetic properties of RNi_3Sn_2 compounds (Skolozdra et al. 1988a)

Compound	θ_p (K)	μ_{eff} (μ_B)	Compound	θ_p (K)	μ_{eff} (μ_B)
YNi_3Sn_2	Pauli paramagnet		$GdNi_3Sn_2$	−9	8.0
$SmNi_3Sn_2$	$\chi^{-1}(T)$ not linear		$TbNi_3Sn_2$	−14	9.9

4.11. *RNi_3Sn_2 compounds*

In the temperature range 78–293 K the RNi_3Sn_2 compounds are paramagnetic (table 18). The Y stannide is a Pauli paramagnet, χ of $SmNi_3Sn_2$ from 200 to 300 K does not change. The susceptibility of $GdNi_3Sn_2$ and $TbNi_3Sn_2$ exhibits Curie–Weiss behaviour (Skolozdra et al. 1988a).

4.12. *RM_2Sn_2 (M = Ni, Cu, Rh, Pd, Ir, Pt) compounds*

The magnetic and transport data of the RM_2Sn_2 compounds are listed in table 19.

Among these compounds $CeNi_2Sn_2$ has been studied the most. The magnetic properties, resistivity and specific heat indicate that this stannide can be classified as a heavy fermion system.

Takabatake et al. (1990) carried out measurements of magnetic susceptibility and resistivity on a single crystal. The susceptibility is anisotropic and it can be fit to the Curie–Weiss law taking into consideration splitting of the principal state by the crystal field. The resistivity measured parallel and perpendicular to the Z axis is also anisotropic. Temperature dependences of resistivity are similar in both cases. At temperatures above 50 K the $\rho(T)$ dependence is linear; at 7 K there is a maximum in the resistivity and below 2.1 K the resistivity decreases sharply indicating an antiferromagnetic transition. The Néel temperature determined by the specific heat is 1.8 K. The γ coefficient, as it must in a heavy fermion system, has a high magnitude (650 mJ/(K^2 mol)).

In a study of powder samples Beyermann et al. (1991) have obtained a T_N value of 1.8 K. The temperature dependence $\chi(T)$ at high temperatures is in accord with the Curie–Weiss law. At low temperatures the linear dependence of $\chi(T)$ is distorted by the presence of ferromagnetic second phases.

A detailed investigation of the properties of annealed (800°C) and unannealed $CeNi_2Sn_2$ samples has been carried out by Liang et al. (1990). The observation of a small splitting of the Bragg peaks indicated that a lowering of the symmetry takes place. The $\rho(T)$ dependences for both samples are almost the same, the temperatures of minima and maxima differ: $T_{min} \approx 34.4$ K (36 K) and $T_{max} \approx 6.9$ K (8 K) for the unannealed (annealed) sample. At 2.4 K there is a kink on the $\rho(T)$ curve, which indicates an antiferromagnetic phase transition. The temperature dependence of the susceptibility of both samples follows the Curie–Weiss law, but small differences are observed in their magnetic data which are apparently caused by differences of symmetry.

Table 19
Magnetic and transport properties of RM_2Sn_2 compounds

Compound	T_N (K)	μ (μ_B)	θ_p (K)	μ_{eff} (μ_B)	ρ (μΩ cm) 78 K	ρ (μΩ cm) 300 K	S (μV/K) 90 K	S (μV/K) 300 K	Reference
$LaNi_2Sn_2$	Pauli paramagnet				21	49			Kaczmarska et al. 1993
					12[a]				
							−4.2	−12.7	Skolozdra 1993
$CeNi_2Sn_2$[b]			4.8	2.50					Liang et al. 1990
$CeNi_2Sn_2$[c]			46.4	2.58[d]					Liang et al. 1990
			6.2	2.24[e]					Liang et al. 1990
$CeNi_2Sn_2$	1.8		−58.4	2.64					Beyermann et al. 1991
	2.2	1.08[f]	−9	2.54	39	55			Kaczmarska et al. 1993
					41[a]				
$PrNi_2Sn_2$			0	3.59					Skolozdra 1993
$NdNi_2Sn_2$			0	3.73					Skolozdra 1993
$SmNi_2Sn_2$	$\chi^{-1}(T)$ not linear								Skolozdra 1993
$LaCu_2Sn_2$	Pauli paramagnet				30	49			Kaczmarska et al. 1993
					12[a]				
							−0.9	−1.8	Skolozdra 1993
$CeCu_2Sn_2$	2.1	0.95[f]	−12	2.54	47	62			Kaczmarska et al. 1993
					35[a]				
							0	−0.2	Skolozdra 1993
$PrCu_2Sn_2$			7	3.57					Skolozdra and Komarovskaya 1982b
$NdCu_2Sn_2$			4	3.63					Skolozdra and Komarovskaya 1982b
$SmCu_2Sn_2$			10	0.74					Skolozdra and Komarovskaya 1982b
$CeRh_2Sn_2$	0.47		−13.2	2.53					Beyermann et al. 1991
$CePd_2Sn_2$	0.50		−6	2.50					Beyermann et al. 1991
$CeIr_2Sn_2$	4.1								Beyermann et al. 1991
$CePt_2Sn_2$	0.88		−25.1	2.59					Beyermann et al. 1991

[a] At 4.2 K.
[b] Unannealed sample.
[c] Annealed sample at 800°C.
[d] For 180 K < T < 300 K.
[e] For 4 K < T < 60 K.
[f] At 1.5 K and 7 T.

The Ce-L_{III} absorption spectra in $CeNi_2Sn_2$ have also been investigated by Liang et al. (1990), the Ce valence value is equal to 3. Earlier, the same valence value for Ce was obtained by Samsonova et al. (1985) from an investigation of L_{III} spectra.

The tetragonal and monoclinic forms of $CeNi_2Sn_2$ have been investigated by Kaczmarska et al. (1993). For the tetragonal sample the susceptibility follows approximately the Curie–Weiss law with $\theta_p = -19$ K and $\mu_{eff} = 2.7\mu_B$. The higher value of μ_{eff} than the theoretical moment of the Ce^{3+} ion is explained by the influence of Pauli paramagnetism.

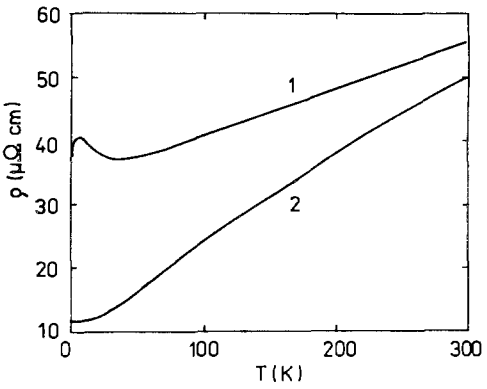

Fig. 27. Temperature dependence of the resistivity of (1) $CeNi_2Sn_2$ and (2) $LaNi_2Sn_2$ (Kaczmarska et al. 1993).

If it is subtracted then $\mu_{eff} = 2.535\mu_B$ and $\theta_p = -9$ K. The monoclinic sample contained a ferromagnetic impurity phase. After correction for this impurity term, this sample followed the Curie–Weiss behaviour with a moment close to the Ce^{3+} ionic value and $\theta_p = -7$ K. A large difference was found in comparison with the previously published magnetic data. The authors explain this difference by the existence of spurious phases in some of the annealed samples, the occurrence of a superimposed Pauli paramagnetic contribution which was not taken into account in the analysis, and a large anisotropy.

A maximum (8 K) and minimum (30 K) are observed in the temperature dependence of the resistivity; at 2.2 K a kink connected with magnetic order (fig. 27) is observed. Peculiarities in the $\rho(T)$ dependence of $CeNi_2Sn_2$ are explained by crystal field effects.

Pierre et al. (1994) determined the magnetic structure of $CeNi_2Sn_2$ at 1.4 K. As the monoclinic distortion and the displacement of Ce atoms are small, the magnetic structure is described in the parent $CaBe_2Ge_2$ cell. The magnetic structure is antiferromagnetic with a propagation vector $\boldsymbol{k} = (\frac{1}{2}, \frac{1}{2}, 0)$. The moment lies in the basal plane and is at 45° from the $\boldsymbol{k}$ vector that is along the X (or the Y) axis (fig. 28). The magnitude of the moment is $0.9\mu_B$ at 1.5 K. A peculiarity of the magnetic structure is the frustration between the Ce moments.

$LaNi_2Sn_2$ is a Pauli paramagnet, the $\chi(T)$ dependence for Pr and Nd stannides follows the Curie–Weiss law (Skolozdra et al. 1981b). The electrical resistivity for $LaNi_2Sn_2$ is shown in fig. 27.

Above 50 K the temperature dependence of the magnetic susceptibility of $CeCu_2Sn_2$ follows the Curie–Weiss law (Liang et al. 1990, Kaczmarska et al. 1993). The subtraction of the temperature-independent paramagnetism from the susceptibility leads to a value of μ_{eff} which is close to the theoretical moment of the Ce^{3+} ion. At low temperature the compound orders antiferromagnetically. The T_N value obtained from the measurement of the specific heat is equal to 1.8 K (Liang et al. 1990), and from resistivity measurements it is equal to 2.1 K (Kaczmarska et al. 1993). The resistivity of $CeCu_2Sn_2$ increases steadily with temperature, with a maximum slope at about 50 K (fig. 29). By a simple subtraction of the La compound resistivity, the magnetic contribution to the resistivity was obtained. The magnetic part of resistivity has a maximum at 75 K and then a linear decrease above

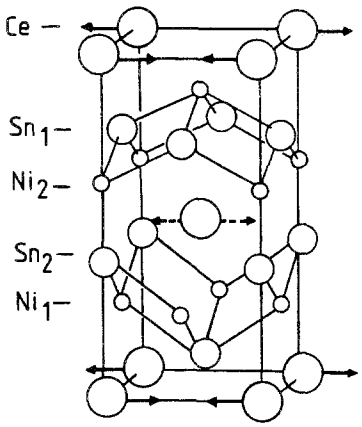

Fig. 28. Magnetic structure of $CeNi_{1.9}Sn_2$ (Pierre et al. 1994).

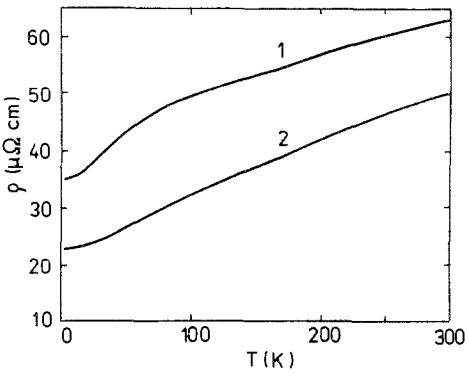

Fig. 29. Temperature dependence of the resistivity of (1) $CeCu_2Sn_2$ and (2) $LaCu_2Sn_2$ (Kaczmarska et al. 1993).

100 K when plotted vs. the logarithm of the temperature. The resistivity of $LaCu_2Sn_2$ above approximately 50 K changes linearly and at higher temperature it deviates from linearity (Kaczmarska et al. 1993).

The $LaCu_2Sn_2$ compound is a Pauli paramagnet. The magnetic susceptibility of $PrCu_2Sn_2$, $NdCu_2Sn_2$ and $SmCu_2Sn_2$ follows the modified Curie–Weiss law (Skolozdra and Komarovskaya 1982b).

Measurements of the magnetic susceptibility, resistivity and specific heat of polycrystalline samples of $CeRh_2Sn_2$, $CePd_2Sn_2$, $CeIr_2Sn_2$ and $CePt_2Sn_2$ have been carried out by Beyermann et al. (1991). These compounds undergo an antiferromagnetic phase transition at low temperatures. The $\chi(T)$ dependence of the compounds, except $CeIr_2Sn_2$, follows the Curie–Weiss law, moreover there are two ranges of the $\chi(T)$ curve: a high temperature one (above 10 K) and a low temperature one (below 10 K). The compounds have high magnitudes of the γ coefficient and are heavy fermion systems, except $CeIr_2Sn_2$, for which a Ce intermediate valence state is supposed. Maxima are observed for $\rho(T)$ dependence for $CeIr_2Sn_2$ and $CePt_2Sn_2$ in low temperature range. In the opinion of the authors the compounds are good models for the investigation of the competition between Kondo and RKKY interactions.

4.13. *Ce_2Ni_2Sn*

The magnetization and electrical resistivity reveal that Ce_2Ni_2Sn orders antiferromagnetically at $T_N = 4.7$ K (Fourgeot et al. 1995). The reciprocal susceptibility above 120 K follows the Curie–Weiss law; below 120 K the $\chi^{-1}(T)$ function deviates from linearity (fig. 30). The magnetization curve versus temperature under an applied field 0.2 T has a broad maximum around 8 K (fig. 31), followed by a sharp drop at lower temperatures, suggesting the occurrence of antiferromagnetic ordering. It is thought that the broad maximum near 8 K is caused by the spin fluctuations intensified by the Kondo effect.

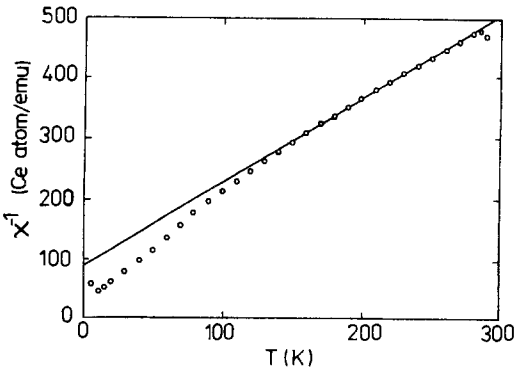

Fig. 30. Temperature dependence of the reciprocal susceptibility of Ce_2Ni_2Sn. The line follows the Curie–Weiss law (Fourgeot et al. 1995).

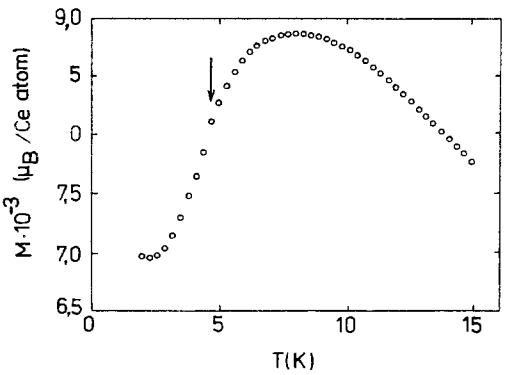

Fig. 31. Temperature dependence of the magnetization of the Ce_2Ni_2Sn compound ($H = 0.2$ T, the arrow indicates the Néel temperature) (Fourgeot et al. 1995).

The thermal dependence of the resistivity is characteristic of the magnetically ordered Kondo systems. On the curve $\rho(T)$ there is a kink at ~4.7 K as a consequence of the magnetic ordering and a broad maximum at 8 K associated with the Kondo temperature (Fourgeot et al. 1995).

4.14. *$R_6M_8Sn_8$ compounds (M = Mn, Cu)*

The magnetic data of the $R_6Mn_8Sn_8$ compounds are listed in table 20 (Weitzer et al. 1992c). The compounds with Ce, Pr, Nd and Sm undergo antiferromagnetic transitions. For $Pr_6Mn_8Sn_8$ and $Nd_6Mn_8Sn_8$ an onset of a spin-flip process is observed under a magnetic field bigger than 2.5 T. Curie–Weiss behaviour is observed at high temperatures with the exception of $Sm_6Mn_8Sn_8$. $La_6Mn_8Sn_8$ and $Ce_6Mn_8Sn_8$ show broad maxima at approximately 300 K. The Mn atoms carry a localized effective moment, as shown in table 20.

The $\chi(T)$ dependence (78–293 K) for the $R_6Cu_8Sn_8$ stannides, where R = Gd–Tm, follows the Curie–Weiss law. The paramagnetic Curie points are proportional to the de Gennes function $G = (g_J - 1)^2 J(J+1)$. Going from the Gd–Ho compounds to

Table 20
Magnetic properties of $R_6Mn_8Sn_8$ compounds (Weitzer et al. 1992c)

Compound	T_N (K)	θ_p (K)	μ_{eff} (μ_B/f.u.)	μ_{eff} (μ_B/R)	μ_{eff} (μ_B/Mn)
$La_6Mn_8Sn_8$		−475	10.9	0	5.6
$Ce_6Mn_8Sn_8$	50	−380	11.0	2.54	5.0
$Pr_6Mn_8Sn_8$	16	−24	8.6	3.58	3.0
$Nd_6Mn_8Sn_8$	45	−50	8.5	3.62	3.0
$Sm_6Mn_8Sn_8$	32				

Table 21
Magnetic and transport properties of $R_6Cu_8Sn_8$ compounds (Skolozdra et al. 1984a, Skolozdra 1993)

Compound	θ_p (K)	μ_{eff} (μ_B)	ρ (μΩ cm)		S (μV/K)	
			at 78 K	at 300 K	at 90 K	at 300 K
$Y_6Cu_8Sn_8$	Diamagnet[a]					
$Gd_6Cu_8Sn_8$	−29	8.0	18	48	0.1	−0.1
$Tb_6Cu_8Sn_8$	−18	9.7				
$Dy_6Cu_8Sn_8$	−7	10.9	40	104	−1.0	−0.1
$Ho_6Cu_8Sn_8$	−6	10.4				
$Er_6Cu_8Sn_8$	8	9.6				
$Tm_6Cu_8Sn_8$	11	7.5	32	97	0	0.6

[a] Thirion et al. 1983.

$Er_6Cu_8Sn_8$ and $Tm_6Cu_8Sn_8$ the sign of θ_p changes from positive to negative (table 21) (Skolozdra et al. 1984a).

Resistivity of $R_6Cu_8Sn_8$ in the 78–360 K temperature range changes linearly with the temperature. The magnitude of the thermopower is close to 0 and is essentially temperature independent (Skolozdra 1993).

4.15. *RCoSn compounds*

The susceptibility of the RCoSn stannides (R = Y, Gd–Tm, Lu) has been measured between 78 and 293 K by Skolozdra et al. (1982). In this temperature range χ obeys the Curie–Weiss law, except for YCoSn which is a Pauli paramagnet. The cobalt atoms are not magnetic. For LuCoSn $\chi(T)$ is in accord with a modified Curie–Weiss law with $\mu_{eff} = 0.79\mu_B$. Apparently the presence of a magnetic moment in LuCoSn is caused by the presence of other lanthanides impurities (table 22).

Görlich et al. (1994) have measured magnetization of the TbCoSn, DyCoSn, HoCoSn and ErCoSn in the temperature range 4.2–300 K. They also investigated the hyperfine interaction of ^{119}Sn by means of the Mössbauer effect between 1.9 and 300 K. The compounds order antiferromagnetically and the Mössbauer spectra suggest a complex

Table 22
Magnetic properties of RCoSn compounds

Compound	T_N (K)	μ (μ_B/f.u.)	θ_p	μ_{eff} (μ_B/R)	Reference
YCoSn	Pauli paramagnet				Skolozdra et al. 1982
TbCoSn			30	9.8	Skolozdra et al. 1982
	20.5		15	9.8	Görlich et al. 1994
DyCoSn			27	10.4	Skolozdra et al. 1982
	10.0	5.63	9	10.5	Bażela et al. 1994
	10.0		9	10.5	Görlich et al. 1994
HoCoSn			9	10.5	Skolozdra et al. 1982
	7.8	6.32	6.5	11.0	Bażela et al. 1994
	7.8		7	10.4	Görlich et al. 1994
ErCoSn			11	9.4	Skolozdra et al. 1982
	5.0	6.07	0	9.8	Bażela et al. 1994
	~4		0	9.6	Görlich et al. 1994
TmCoSn			5	7.6	Skolozdra et al. 1982
LuCoSn			3.1	0.79	Skolozdra et al. 1982

non collinear magnetic structure. A change in the type of magnetic ordering of TbCoSn has been observed at 11.6 K.

Bażela et al. (1994) and André et al. (1995a) have determined magnetic and crystal structures of the compounds with Tb, Dy, Ho and Er by neutron diffraction. They confirmed the crystal structure. Magnetization data indicate a magnetic phase transition occurring at $H = 0.26$ and 0.35 T in DyCoSn and HoCoSn, respectively. For TbCoSn two additional phase transitions at $T_t = 5.4$ K and 11.6 K are detected below T_N, whereas for HoCoSn only one is found at $T_t = 4$ K.

Neutron diffraction data indicate magnetic modulated structures for the compounds. The magnetic structure of TbCoSn in the temperature range 1.4–5 K is described by the wave vector $\boldsymbol{k}_1 = (0, \frac{1}{4}, \frac{1}{12})$. With an increase of the temperature, the wave vector changes at $T_k = 5$ K to $\boldsymbol{k}_2 = (0, \sim\frac{1}{4}, 0)$. The R moments of other compounds form a square modulated magnetic structure along the Y axis. The wave vector is $\boldsymbol{k} = (0, k_y, 0)$ with $k_y = \frac{5}{7}$ in DyCoSn, $\frac{2}{3}$ in HoCoSn and $\frac{7}{11}$ in ErCoSn.

4.16. *RNiSn compounds*

The magnetic and transport data of RNiSn compounds are listed in table 23.

Among the RNiSn compounds CeNiSn has been studied more completely. It is characterized by interesting properties at low temperatures (Aliev et al. 1988a,b, Takabatake et al. 1987). The resistivity of CeNiSn from 380 to ~300 K hardly change, then it increases and at ~50 K it has a maximum (fig. 32). As the temperature decreases a minimum is observed at ~25 K. In this temperature range the $\rho(T)$ dependence is typical

Table 23
Magnetic and transport properties of RNiSn compounds

Compound	T_N (K)	μ (μ_B)	θ_p (K)	μ_{eff} (μ_B)	ρ (μΩ cm) 78 K	ρ (μΩ cm) 300 K	S (μV/K) 90 K	S (μV/K) 300 K	Ref.
YNiSn	Pauli paramagnet								Skolozdra et al. 1984b
LaNiSn	Pauli paramagnet						−8.5	−9.5	Skolozdra 1993
					42	132			Aliev et al. 1988a
					5[a]				
CeNiSn	$\chi^{-1}(T)$ not linear				127	106	21	8.5	Aliev et al. 1988a
					180[a]		30[a]		
					27*X*[b]	24*X*	28*X*	17*X*	Takabatake et al. 1990
					27*Y*[b]	22*Y*	37*Y*	12*Y*	
					17*Z*[b]	14*Z*	19*Z*	14*Z*	
					32*X*[a]		23*X*[a]		
					26*Y*[a]		4*Y*[a]		
					28*Z*[a]		26*Z*[a]		
PrNiSn			17	3.56					Skolozdra et al. 1984b
			−10	3.67					Routsi et al. 1992b
NdNiSn			−15	3.50					Skolozdra et al. 1984b
			−4	4.2					Routsi et al. 1992b
SmNiSn	9.3	$\chi^{-1}(T)$ not linear			29	83	−3.6	−6.5	Sakurai et al. 1995
					5.6[a]		0[a]		
			−40	1.37					Routsi et al. 1992b
GdNiSn			0	8.1					Skolozdra et al. 1984b
	10.5		−3	8.8					Routsi et al. 1991
TbNiSn			−2	9.8					Skolozdra et al. 1984b
			6	11.27					Routsi et al. 1991
	18.5	8.1							Furusawa et al. 1995
		8.9							Kotsanidis et al. 1993
DyNiSn			0	10.4					Skolozdra et al. 1984b
	8.2		−1	11.06					Routsi et al. 1991
	7.3	7.2							Furusawa et al. 1995
HoNiSn			0	10.4					Skolozdra et al. 1982
	<4.2	8.5							Yakinthos et al. 1994
			−2	10.75					Routsi et al. 1991
ErNiSn			5	9.5					Skolozdra et al. 1984b
			6	9.85					Routsi et al. 1991
TmNiSn			8	7.6					Skolozdra et al. 1984b
			−4	7.65					Routsi et al. 1991
YbNiSn			−65	4.6					Skolozdra et al. 1984b
	5.5[c]	0.4	−43	4.3	269	243			Kasaya et al. 1988
					105[a]				
	5.65[c]	0.85							Bellot et al. 1992
LuNiSn	Pauli paramagnet								Skolozdra et al. 1984b

[a] At 4 K. [b] Along the *X*, *Y*, *Z* axes. [c] T_C.

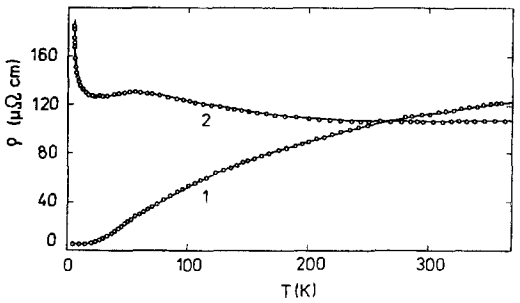

Fig. 32. Temperature dependence of the resistivity of (1) LaNiSn and (2) CeNiSn (Aliev et al. 1988a).

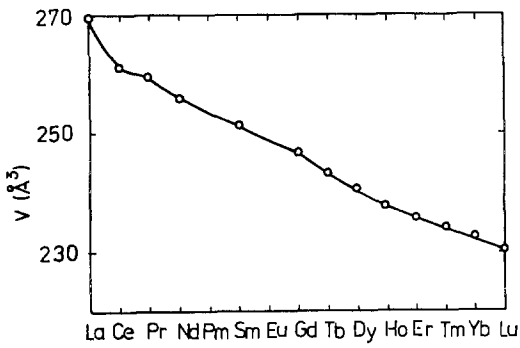

Fig. 33. Unit cell volume of the RNiSn series.

of the compounds with a Kondo lattice. The existence of a maximum in the positive thermopower at ~100 K (Skolozdra 1993); the deviation of $\chi^{-1}(T)$ from linearity at low temperature; the valence of Ce as determined from L_{III}-spectra, which is equal to 3.10 (Samsonova et al. 1985) (fig. 22); a deviation of the unit cell volume of CeNiSn compared to the RNiSn compounds (Skolozdra et al. 1984b) (fig. 33) all indicate that at middle temperatures CeNiSn is in a state of valence instability, and with decreasing temperature it transforms to a Kondo lattice state.

Below 25 K the resistivity increases and it follows the exponential law between 1.8 and 10 K with an activation energy of ~5 K, indicates the appearance of a gap in the electron spectrum at the Fermi level.

The formation of the dielectric gap leads to a sharp increase of resistivity below 10 K and to a decrease of the specific heat coefficient below 5 K. The value of γ for CeNiSn is much bigger than that of LaNiSn (265 and 25 mJ/(K^2 mol), respectively, at 5 K) (Aliev et al. 1988b).

Measurements of the susceptibility, resistivity and thermopower were carried out on a single crystal in three crystallographic directions by Takabatake et al. (1992, 1994). The anisotropy of these properties was established (fig. 34). The $\rho(T)$ (fig. 32) and $\chi(T)$ (fig. 34) curves in the direction of X axis show a peak at 12 K, but such a peak is absent in the specific heat curve. The band gap evaluated from the $\rho(T)$ dependence is 2.4, 5.5 and 5.0 K along the X, Y, Z axes, respectively. At ~3 K for $S_x(T)$ and $S_y(T)$ sharp peaks

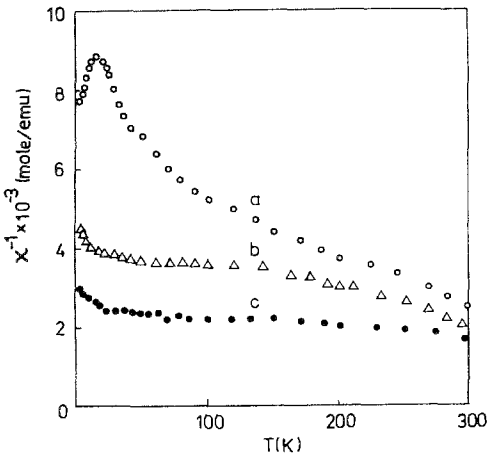

Fig. 34. Temperature dependence of the reciprocal susceptibility of the CeNiSn single crystal directed along the (a) X axis, (b) Y axis and (c) Z axis (Takabatake et al. 1992).

are observed. The magnetic contribution in specific heat divided by T shows a maximum at 6.7 K. It is thought that this indicates the development of antiferromagnetic correlations at approximately 12 K, which induce the formation of a coherent pseudogap in the narrow band of heavy particles.

It was established that the pressure leads to a violation of the coherent regime of the electron spectra and the gap disappears at the 2.4 GPa pressure (Aliev et al. 1990). Measurements of the thermal expansion coefficient (TEC) of the CeNiSn single crystal showed that the anomalies in the temperature dependence of TEC are caused by the disappearance of the gap at 0.8 GPa (Uwatoko et al. 1992). The authors suggest that the pressure decreases the density of states of the Fermi level indicating that a necessary condition for gap formation is an increase of the effective mass of electrons.

The magnetic field also influences the gap formation, with increasing applied field the resistivity decreases: at 24 T the resistivity of CeNiSn decreases by ~75% at 1.7 K (Takabatake et al. 1988). The formation of the anisotropic gap which is dependent on the applied field was studied by Hiess et al. (1994) during an investigation of the transport properties at low temperatures and under high magnetic fields. It was established that below 1 K a metallic-like behaviour appears.

The dependence of the substitution of the components on the properties of CeNiSn was reported (Aliev et al. 1990, Nishigori et al. 1993, Aliev et al. 1994). In all cases the composition change by any component leads to the disappearance of the gap.

The main cause of the gap formation in CeNiSn is not completely clear. This may be due to a development of the antiferromagnetic interactions (Takabatake et al. 1992, 1994, Adroja and Rainford 1994, Kadowaki et al. 1994) The competition between local antiferromagnetic Kondo-type correlation at temperatures about 2–8 K and long-range interactions of the Kondo-suppressed Ce magnetic moments below 0.5 K play an important role in gap formation (Aliev et al. 1994).

Magnetic properties of the rest of the RNiSn compounds at 78–300 K were reported by Skolozdra et al. (1984b). The $\chi(T)$ dependence of the RNiSn compounds, where R = Pr, Nd, Gd–Yb, follows the Curie–Weiss law. The stannides of Y, La, Lu are Pauli paramagnets.

Routsi et al. (1992b) have measured the susceptibility of the light lanthanide stannides in the temperature range 4.2–200 K. PrNiSn, NdNiSn, SmNiSn are paramagnets with a Curie–Weiss $\chi(T)$ dependence. SmNiSn orders antiferromagnetically at 9 K, PrNiSn and NdNiSn do not order down to 4.2 K. The dependence $\chi(T)$ of CeNiSn does not follow the Curie–Weiss law.

Magnetic data obtained by Routsi et al. (1992b) differ insignificantly from the data obtained by Skolozdra et al. (1984b).

Magnetic susceptibility, resistivity, thermopower from 2 to 300 K and specific heat (2–20 K) of SmNiSn were measured by Sakurai et al. (1995). The dependence $\chi^{-1}(T)$ is not linear, the $\rho(T)$ function has a negative curvature, and the thermopower has a small negative value. A kink on the $\chi^{-1}(T)$, $\rho(T)$ and $C(T)$ curves reveals an antiferromagnetic transition at 9.3 K. The second magnetic transformation is observed at 4.1 K.

The susceptibility of RNiSn phases, where R equals Y and the heavy lanthanides, has been also measured by Routsi et al. (1991) in the temperature range 4.2–200 K. The compounds are paramagnetic above 40 K, YNiSn is a Pauli paramagnet. The compounds of Gd, Tb and Dy undergo an antiferromagnetic ordering at low temperatures, the compounds with Ho, Er, Tm do not order down to 4.2 K.

Measurements of the magnetization, magnetoresistance and Hall effect have been carried out on the TbNiSn and DyNiSn single crystals under a magnetic field up to 8 T at 1.4 K by Furusawa et al. (1995). A multistep magnetization process was observed. The magnetoresistance in both compounds shows a complicated variation under magnetic field which is associated with spin fluctuations.

Magnetic structures of TbNiSn at 12 K (Kotsanidis et al. 1993) and HoNiSn at 1.4 K (Yakinthos et al. 1994) have been determined. Both compounds have antiferromagnetic incommensurate structures. The propagation vector for Tb is $\boldsymbol{k} = (0.313, 0.325, 0.0)$, and the moments are directed along the Y axis. The propagation vector for HoNiSn is equal to $\boldsymbol{k} = (\sim 0.3593, 0.3337, 0.01)$, and the direction of the moments form an angle of 75° with the Z axis.

Magnetic and electrical measurements for YbNiSn reveal that this compound is a Kondo system with a ferromagnetic transformation below 5.5 K and a small ferromagnetic moment $\sim 0.4\mu_B$ (Kasaya et al. 1988). This conclusion is confirmed by specific heat measurements (Kasaya et al. 1991). The magnetization measurements carried out on a single crystal showed the orientation of the ferromagnetic moment along the Z axis (Kasaya et al. 1991). The authors concluded that YbNiSn was a dense Kondo compound in which a weak ferromagnetic order coexisted with the heavy fermion system.

Bellot et al. (1992) have studied this compound by the ^{170}Yb Mössbauer spectroscopy method and have carried out magnetization measurements on a single crystal. It was found that the Curie point is equal to 5.65 K. There is a strong anisotropy of the magnetic properties in different crystallographic directions. The magnetic moment of Yb lies along

the Z axis and its saturated value is equal to $0.05\mu_B$. The reduced magnetic moment is attributed to a hybridization of the 4f-electrons with the conduction electrons.

4.17. *RCuSn compounds*

The magnetic properties of GdCuSn have been studied by Oesterreicher (1977). It was established that GdCuSn is an antiferromagnet with $T_N = 24$ K. The $\chi(T)$ dependence of GdCuSn and the other RCuSn compounds (R = Ce–Nd, Gd–Tm) follows the Curie–Weiss law, while SmCuSn may be described by the modified Curie–Weiss law (Komarovskaya et al. 1983b). YCuSn, LaCuSn and LuCuSn are Pauli paramagnets (table 24).

Measurements of magnetization and specific heat reveal that CeCuSn undergoes an antiferromagnetic phase transition at 8.6 K (Yang et al. 1991).

Table 24
Magnetic properties of RCuSn compounds

Compound	T_N (K)	μ (μ_B)	θ_p (K)	μ_{eff} (μ_B)	Reference
YCuSn		Pauli paramagnet			Komarovskaya et al. 1983b
LaCuSn		Pauli paramagnet			Komarovskaya et al. 1983b
CeCuSn	8.6	0.07[a]	−20	2.5	Yang et al. 1991
			−13	2.56	Komarovskaya et al. 1983b
PrCuSn			−9	3.64	Komarovskaya et al. 1983b
NdCuSn			−14	3.80	Komarovskaya et al. 1983b
SmCuSn			1	0.78	Komarovskaya et al. 1983b
GdCuSn	24		−32	8.0	Oesterreicher 1977
			−44	8.0	Komarovskaya et al. 1983b
TbCuSn			−33	9.8	Komarovskaya et al. 1983b
DyCuSn			−17	10.7	Komarovskaya et al. 1983b
HoCuSn			−6	10.7	Komarovskaya et al. 1983b
ErCuSn			−2	9.7	Komarovskaya et al. 1983b
TmCuSn			−3	7.8	Komarovskaya et al. 1983b
LuCuSn		Pauli paramagnet			Komarovskaya et al. 1983b

[a] At 1.6 K.

4.18. *RRhSn compounds*

The $\chi(T)$ temperature dependence of the RRhSn compounds (R = Y, Ce, Pr, Nd, Gd–Er) follows the Curie–Weiss law. YRhSn is a Pauli paramagnet (Routsi et al. 1992a,b). GdRhSn, TbRhSn, DyRhSn and HoRhSn order antiferromagnetically at low temperatures (table 25). The temperature dependence of χ for CeRhSn indicates it is a Kondo system or a state with valence fluctuations.

Table 25
Magnetic properties of RRhSn compounds

Compound	T_N (K)	θ_p (K)	μ_{eff} (μ_B)	Reference
YRhSn		Pauli paramagnet		Routsi et al. 1992a
CeRhSn		$\chi^{-1}(T)$ not linear		Routsi et al. 1992b
PrRhSn		10	3.83	Routsi et al. 1992b
NdRhSn		12	3.55	Routsi et al. 1992b
GdRhSn	14.8	18	8	Routsi et al. 1992a
TbRhSn	18.4	4	9.9	Routsi et al. 1992a
DyRhSn	8	−12	8	Routsi et al. 1992a
HoRhSn	1.7			Routsi et al. 1992a
		6	10.7	Routsi et al. 1992a
ErRhSn		−4	9.7	Routsi et al. 1992a

4.19. *RPdSn compounds*

The magnetic and transport data of the RPdSn compounds are listed in table 26. Magnetic and electrical properties of RPdSn, where R = La, Ce, Pr, Nd, Sm, Gd, Tb, Dy and Ho, with the TiNiSi structure type have been studied by Sakurai et al. (1990a). The compounds, except LaPdSn, are ordered antiferromagnetically, the highest T_N value is characteristic of TbPdSn (23 K). For SmPdSn and DyPdSn a second phase transition below T_N is observed. The susceptibility and resistivity of RPdSn were also measured by Adroja and Malik (1992) in the temperature range 4.2–300 K. Additionally, the properties of EuPdSn, ErPdSn (TiNiSn), TmPdSn (Fe_2P) and YbPdSn (TiNiSi) were studied. In both studies there was close agreement in the reported magnetic and transport data (table 26). EuPdSn and TmPdSn ordered antiferromagnetically. The susceptibility of YbPdSn follows the Curie–Weiss law only above 150 K. The magnitude of the EuPdSn moment indicates it is divalent. A divalent or a mixed valence state is suggested for Yb.

The $\rho(T)$ dependence of the compounds is typical of an antiferromagnet. Except CePdSn, the magnitude of thermopower of the RPdSn phases is small and is almost temperature independent.

The magnetic and electrical properties of CePdSn have been also investigated by Adroja et al. (1988) and Kasaya et al. (1988). Zygmunt and Szytuła (1995) have determined the magnetic properties of RPdSn compounds as well. The temperature dependence of the CePdSn properties indicate that it is a dense Kondo system with antiferromagnetic ordering. The magnetic structure of CePdSn has been determined by Kohgi et al. (1992) on a single crystal. CePdSn has an incommensurate magnetic structure with the propogation vector $\boldsymbol{k} = (0, 0.437, 0)$ and magnetic moment of about $1\mu_B$. The valence band photoemission spectra were studied by Nohara et al. (1993). It was established that Ce is in three valence state and the Kondo state is mainly caused by a hybridization of the Ce 4f-states with the Sn 5p-states.

Table 26
Magnetic and transport properties of RPdSn compounds

Compound	T_N (K)	μ (μ_B)	θ_p (K)	μ_{eff} (μ_B)	ρ (μΩ cm)		S (μV/K)		Reference
					4.2 K	300 K	4.2 K	300 K	
LaPdSn	Pauli paramagnet				27	290	0	−3.9	Sakurai et al. 1990a
CePdSn	7				68	457	−2.9	1.8	Sakurai et al. 1990a
	7.5		−68	2.67	180	696			Adroja and Malik 1992
		1							Kohgi et al. 1992
	6	0.2	−63	2.7					Zygmunt and Szytuła 1995
PrPdSn	3.5				75	457	−0.5	−2.1	Sakurai et al. 1990a
			−2	3.60					Adroja and Malik 1992
	4.3	1.4	−5.5	3.51					Zygmunt and Szytuła 1995
NdPdSn	3.2				17	170	0.4	−2.9	Sakurai et al. 1990a
			−8	4.93	5.5	59			Adroja and Malik 1992
	2.4	0.95	−11	3.68					Zygmunt and Szytuła 1995
SmPdSn	12				8	98	0.6	−2.1	Sakurai et al. 1990a
	11				22	194			Adroja and Malik 1992
	12.2				19	183	1.3	−2.0	Sakurai et al. 1995
EuPdSn	13		5	8.27	11	124			Adroja and Malik 1992
GdPdSn	15				11	102	0.4	−0.7	Sakurai et al. 1990a
	14.5		−27	8.16	32	175			Adroja and Malik 1992
TbPdSn	23				8.1	127	0.2	−0.1	Sakurai et al. 1990a
	23.5		−16	10.17	8.7	116			Adroja and Malik 1992
	21	7.2	−11	10.1					Gillot et al. 1995
	19	7.6							André et al. 1993
	19	2.1	−11	10.1					Zygmunt and Szytuła 1995
DyPdSn	10				8.8	90	0.1	1.5	Sakurai et al. 1990a
	11.4		−2	11.1	5.6	43			Adroja and Malik 1992
	10	4.65	−7	10.5					Zygmunt and Szytuła 1995
HoPdSn	6				2.8	47	0.4	0.1	Sakurai et al. 1990a
			−7	11.07					Adroja and Malik 1992
	3.7	6.6	−7.5	10.7					Zygmunt and Szytuła 1995
ErPdSn	5.6		−0.3	9.51	4.5	57			Adroja and Malik 1992
(TiNiSi)									
	5.2	9.0							André et al. 1995b
	5.2	9.0	3.0	9.62					Zygmunt and Szytuła 1995
TmPdSn									
(Fe_2P)			−0.1	7.98					Adroja and Malik 1992
(TiNiSi)			−1.9	7.5					Zygmunt and Szytuła 1995
YbPdSn			−5	1.45					Adroja and Malik 1992
(TiNiSi)									

Sakurai et al. (1995) have established that T_N of SmPdSn is equal to 12.2 K. At 4.2 K there is a second phase transition which is apparently connected with a change of the SmPdSn magnetic structure.

André et al. (1993) have investigated the magnetic structure of TbPdSn. Below T_N this structure is characterised by a sine wave modulated magnetic spin arrangement, which

below $T_t = 10$ K changes to a spiral cone. The magnetic structure and magnetic properties of ErPdSn has been determined by André et al. (1995b). Under applied field up to 0.2 T in the antiferromagnetic state the magnetization changes linearly, above this field a sharp jump of magnetization to the ferromagnetic state is observed. In the ordered state at 2.5 K a magnetic transition is observed. Below this temperature a modulated square structure with a propogation vector $\boldsymbol{k} = (\frac{1}{3}, \frac{1}{2}, \frac{1}{3})$ exists. Above 2.5 K a modulated sine structure with a propogation vector $\boldsymbol{k} = (k_x, k_y, k_z)$ forms.

4.20. *RAgSn compounds*

The magnetic susceptibility, resistivity, thermopower and ^{119}Sn Mössbauer absorption of RAgSn, where R = Ce, Pr, Nd, Sm, Gd–Er, have been studied by Adam et al. (1990) between 4.2–300 K. Most compounds at low temperatures are ordered antiferromagnetically (table 27). Above T_N the reciprocal susceptibility follows the Curie–Weiss law. On the $\rho(T)$ curves there are kinks corresponding to magnetic transitions. For the compounds with Ce, Pr, Sm, Gd, Td, and Ho the thermopower is positive (table 27) and changes almost linearly with increasing temperature. The thermopower of ErAgSn does not depend on the temperature. The $S(T)$ curve of NdAgSn reveals a broad minimum around 100 K. In SmAgSn below T_N (28 K) a magnetic transition is observed at 8 K.

Table 27
Magnetic and transport properties of RAgSn compounds

Compound	T_N (K)	μ (μ_B)	θ_p (K)	μ_{eff} (μ_B)	ρ (μΩ cm)		S (μV/K)		Reference
					4.2 K	300 K	4.2 K	300 K	
LaAgSn					23	48			Adam et al. 1990
CeAgSn	5.5		Curie–Weiss law[a]		58	111	0	13.5	Adam et al. 1990
					578				Sakurai et al. 1992
PrAgSn			Curie–Weiss law[a]		15	47	0.2	13.1	Adam et al. 1990
NdAgSn			Curie–Weiss law[a]		47	44	0	−2.3	Adam et al. 1990
	9	2.3							Bażela et al. 1995a
	11.5	1.6	−20	3.95					Gillot et al. 1995
SmAgSn	28		$\chi^{-1}(T)$ not linear		75	194	0.7	11.7	Adam et al. 1990
					84				Sakurai et al. 1992
GdAgSn			Curie–Weiss law[a]				0.2	6.3	Adam et al. 1990
TbAgSn			Curie–Weiss law[a]		7.8	113	0.5	8.3	Adam et al. 1990
	33	8.5							Bażela et al. 1992
	35	8.5							Bażela et al. 1995a
	35	5.0	−42	9.33					Gillot et al. 1995
DyAgSn			Curie–Weiss law[a]						Adam et al. 1990
HoAgSn	9.5		Curie–Weiss law[a]		83	151	0	4.0	Adam et al. 1990
	15	8.8							Bażela et al. 1992
	9.5	8.8							Bażela et al. 1995a
	10.5	8.3	−11	10.69	7.5				Sakurai et al. 1992
ErAgSn			Curie–Weiss law[a]		17	88	0	−0.2	Adam et al. 1990

[a] θ_p and μ_{eff} were not listed.

Bażela et al. (1992, 1995a) determined the magnetic structures of NdAgSn, TbAgSn and HoAgSn. The compounds have collinear antiferromagnetic structures with moments along the hexagonal axis. The magnetic ordering corresponds to the A_z mode. Magnetization curves under magnetic fields up to 20 T show metamagnetism.

4.21. *RPtSn compounds*

Magnetic properties of the RPtSn stannides (R = Y, Ce–Nd, Gd–Tm) have been measured over the temperature range 4.2–200 K by Routsi et al. (1992a). The YPtSn stannide is a temperature independent paramagnet, and CePtSn, TbPtSn, and DyPtSn are antiferromagnets. The reciprocal magnetic susceptibility in the paramagnetic range follows the Curie–Weiss law. The magnetic data are given in table 28. According to Sakurai et al. (1995) the Néel point of SmPtSn is 3.5 K. A second phase transition is observed at 2.1 K.

Investigations of the CePtSn properties have shown that this compound is a Kondo system with antiferromagnetic ordering (Sakurai et al. 1990b, Nishigori et al. 1993). The measurements of resistivity and thermopower have been carried out on a single crystal by Bando et al. (1994) (fig. 35). Anisotropy of the properties in three directions is

Table 28
Magnetic properties of RPtSn compounds

Compound	T_N (K)	μ (μ_B)	θ_p (K)	μ_{eff} (μ_B)	Reference
YPtSn		Pauli paramagnet			Routsi et al. 1992a
CePtSn	5.5		−28	2.5	Routsi et al. 1992a
	6.2	0.6[a]			Kadowaki et al. 1993
	T_t = 3.8	0.84[b]			
	8	0.97			Bażela et al. 1995b
PrPtSn			−8	3.78	Routsi et al. 1992a
NdPtSn			−10	4.05	Routsi et al. 1992a
SmPtSn	3.5		see text		Sakurai et al. 1995
	T_t = 2.1				
GdPtSn			32	8.9	Routsi et al. 1992a
TbPtSn	12		−6	10.2	Routsi et al. 1992a
	13.8	4.4			Bażela et al. 1995b
	T_t = 10				
DyPtSn	8		−4	10.77	Routsi et al. 1992a
HoPtSn			4	10.7	Routsi et al. 1992a
	9.2	8.5			Bażela et al. 1995b
	T_t = 3				
ErPtSn			10	10	Routsi et al. 1992a
TmPtSn			22	7.93	Routsi et al. 1992a

[a] At 4.8 K. [b] At 2 K.

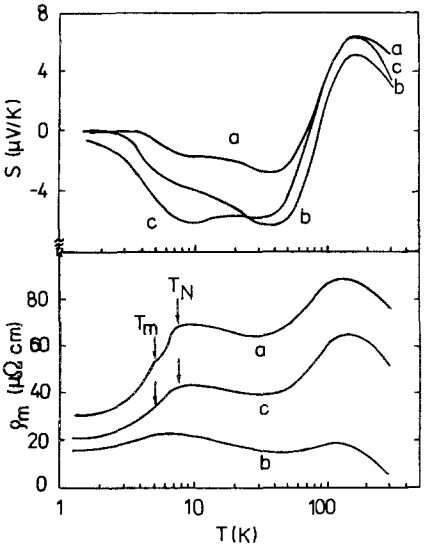

Fig. 35. Temperature dependence of the resistivity and thermopower of single crystal CePtSn directed along the (a) X axis, (b) Y axis and (c) Z axis. The arrows indicate the ordering temperatures T_N and T_m (Bando et al. 1994).

observed. There are maxima on the $\rho(T)$ and $S(T)$ curves at 150–170 K and minima at 30–40 K. Also, kinks are observed on the $\rho(T)$ curve at the magnetic transitions ($T_N = 7.5$ K and $T_t = 5.0$ K). The magnetic structure of CePtSn was determined by Kadowaki et al. (1993) using a single crystal sample. According to these data the phase transitions are at $T_N = 6.3$ K and $T_t = 3.8$ K. The magnetic structure is a single-Q-type with incommensurate modulation vectors $\boldsymbol{k} = 0.466b$ in the region between T_t and T_N.

Nohara et al. (1993) have shown that, as in CePdSn, the Kondo state in CePtSn is caused by the hybridization of the Ce 4f-states with the Sn 5p-states.

The magnetic structures of CePtSn, TbPtSn and DyPtSn were also investigated by Bażela et al. (1995b). Their data agree with the results obtained by Kadowaki et al. (1993) for CePtSn. However Bażela et al. (1995b) did not find the phase transition below T_N.

Magnetic structures of TbPtSn and HoPtSn are also sine modulated magnetic structures. The propogation vector is $\boldsymbol{k} = (0, 0.275, 0)$ and $\boldsymbol{k} = (\frac{2}{3}, \frac{2}{3}, \frac{1}{2})$ for TbPtSn and HoPtSn, respectively. In both magnetic structures there are phase transitions at $T_t = 10$ K for HoPtSn and $T_t = 3$ K for TbPtSn.

4.22. *$R_2Cu_4Sn_5$ compounds*

The susceptibility measurements of $R_2Cu_4Sn_5$ (R = Pr, Sm, Gd, Tb) have been carried out from 78 to 293 K by Komarovskaya and Skolozdra (1992). The $\chi(T)$ dependence follows the Curie–Weiss law for R = Pr, Gd and Tb. The magnetic susceptibility of Sm decreases with increasing temperature, but the law of $\chi(T)$-change for $Sm_2Cu_4Sn_5$ has not been established (table 29).

Table 29
Magnetic properties of $R_2Cu_4Sn_5$ compounds (Komarovskaya and Skolozdra 1992)

Compound	θ_p (K)	μ_{eff} (μ_B/R)	Compound	θ_p (K)	μ_{eff} (μ_B/R)
$Pr_2Cu_4Sn_5$	−3	3.78	$Gd_2Cu_4Sn_5$	−10	7.8
$Sm_2Cu_4Sn_5$	$\chi^{-1}(T)$ not linear		$Tb_2Cu_4Sn_5$	−18	9.8

Table 30
Magnetic and transport properties of $R_9Ni_{24}Sn_{49}$ compounds (Komarovskaya and Skolozdra 1985, Skolozdra 1993)

Compound	θ_p (K)	μ_{eff} (μ_B)	ρ (μΩ cm)		S (μV/K)	
			at 78 K	at 300 K	at 90 K	at 300 K
$Y_9Ni_{24}Sn_{49}$	Pauli paramagnet		44	88		
$La_9Ni_{24}Sn_{49}$	Pauli paramagnet					
$Ce_9Ni_{24}Sn_{49}$	−27	2.56	96	156	−2.0	0.8
$Pr_9Ni_{24}Sn_{49}$	−12	3.76				
$Nd_9Ni_{24}Sn_{49}$	−18	3.68				
$Sm_9Ni_{24}Sn_{49}$	$\chi^{-1}(T)$ not linear		70	120	−1.6	2.0
$Gd_9Ni_{24}Sn_{49}$	−21	7.9	82	146	−4.2	−2.8
$Tb_9Ni_{24}Sn_{49}$	−17	9.9				

4.23. *$R_9Ni_{24}Sn_{49}$ compounds*

The magnetic and transport data of $R_9Ni_{24}Sn_{49}$ compounds are listed in table 30. The $Y_9Ni_{24}Sn_{49}$ and $La_9Ni_{24}Sn_{49}$ stannides are Pauli paramagnets. The $\chi(T)$ dependence of the rest of the compounds, except Sm, follows the Curie–Weiss law (Komarovskaya and Skolozdra 1985).

The resistivity, measured for the compounds with Y, Ce, Sm, Gd in the temperature range 78–360 K, increases with increasing temperature, and $\rho(T)$ is characterized by a negative curvature. The thermopower changes insignificantly with temperature (Skolozdra 1993).

4.24. *$RNiSn_2$ compounds ($LuNiSn_2$ structure type)*

The reciprocal susceptibility for the $RNiSn_2$ compounds (R = Gd–Tm) follows the Curie–Weiss law in the temperature range 78–293 K. $YNiSn_2$ and $LuNiSn_2$ are Pauli paramagnets (Skolozdra et al. 1988a).

For some compounds the resistivity and thermopower were measured from 78 to 360 K. The Seebeck coefficient decreases with increasing temperature, while the resistivity exhibits the normal temperature dependency (table 31).

Table 31
Magnetic and transport properties of $RNiSn_2$ ($LuNiSn_2$ type) compounds (Skolozdra et al. 1988a, Skolozdra 1993)

Compound	θ_p (K)	μ_{eff} (μ_B)	ρ ($\mu\Omega$ cm)		S (μV/K)	
			at 78 K	at 300 K	at 90 K	at 300 K
$GdNiSn_2$	−44	8.0	36	70	−0.8	−0.5
$TbNiSn_2$	−15	9.7	22	53	0.2	−5.8
$DyNiSn_2$	−16	10.4				
$HoNiSn_2$	−6	10.6	21	52		
$ErNiSn_2$	−9	9.7	58	83		
$TmNiSn_2$	−5	6.9				
$LuNiSn_2$	Pauli paramagnet					

4.25. *$RMSn_2$ (M = Mn, Fe, Co, Ni, Cu) compounds ($CeNiSi_2$ structure type)*

The magnetic susceptibility has been measured for the $RM_{1-x}Sn_{2-y}$ compounds, where R = La, Ce, Pr, Nd, Sm, M = Mn, Fe, Co, Ni in the temperature range 78–293 K by Komarovskaya et al. (1988) and Skolozdra et al. (1988b,c). The samples were annealed at 770 K. Only four of the Mn and Fe alloys did not have ferromagnetic impurities ($LaMn_{0.24}Sn_{1.79}$, $CeMn_{0.24}Sn_{1.79}$, $PrMn_{0.24}Sn_{1.79}$ and $PrFe_{0.24}Sn_{1.79}$). The $\chi(T)$ dependence of these alloys follows the Curie–Weiss law. The Mn atoms possess a local magnetic moment which is equal to 4.18, 3.49 and 3.96μ_B in the La, Ce and Pr compounds, respectively (table 32). The value of the moment of $PrFe_{0.24}Sn_{1.79}$ corresponds to the theoretical moment of Pr^{3+} ion, which indicates the absence of magnetic moments on the iron atoms. All alloys of $LaM_{1-x}Sn_{2-y}$ (M = Co, Ni) compounds are Pauli paramagnets. The $LaCu_{1-x}Sn_{2-y}$ compound is diamagnetic.

The reciprocal susceptibility of the Ce, Pr, Nd compounds with Co, Ni and Cu obeys the Curie–Weiss law. The magnetic moments do not differ much from the theoretical moments of the R^{3+} ions. For the $RCo_{1-x}Sn_{2-y}$ and $RNi_{1-x}Sn_{2-y}$ alloys in the homogeneity range a wide range of θ_p values (table 31) are observed. In the alloys with a constant tin content θ_p decreases with increasing R content for the Co alloys, and for Ni alloys it rises. A change of sign at the transition from one composition to another is observed. In the $RCu_{1-x}Sn_{2-y}$ alloys θ_p changes significantly less with composition than in $RCo_{1-x}Sn_{2-y}$ and $RNi_{2-x}Sn_{2-y}$ series. Moreover, the magnitude of θ_p for $RCu_{1-x}Sn_{2-y}$ is higher than in the corresponding Ni compounds. It is also seen, that there is a tendency for θ_p to rise with an increasing number of vacancies.

The susceptibility of Sm alloys is characterized by a temperature dependence which does not follow the Curie–Weiss law.

The magnetic susceptibility of the $RMn_{1-x}Sn_{2-y}$ (R = La, Ce, Pr, Nd, Sm) alloys, annealed at 1073 K, has been measured over a large temperature range, 5–800 K, by Weitzer et al. (1992c). The authors have reaffirmed the moment of the Mn atoms (table 33). The $CeMn_{1-x}Sn_{2-y}$ compounds are ferromagnetic with $T_C = 320$ K for

Table 32
Magnetic properties of $RM_{1-x}Sn_{2-y}$ compounds (Skolozdra et al. 1988b,c, Komarovskaya et al. 1988)

Compound	θ_p (K)	μ_{eff} (μ_B)	Compound	θ_p (K)	μ_{eff} (μ_B)
$LaMn_{0.24}Sn_{1.79}$	−118	4.18[a]	$CeNi_{0.43}Sn_{1.90}$	−12	2.54
$CeMn_{0.24}Sn_{1.79}$	−36	3.28	$CeNi_{0.62}Sn_{1.83}$	−3	2.73
$PrMn_{0.24}Sn_{1.79}$	0	4.11	$CeNi_{0.34}Sn_{1.78}$	−10	2.67
$PrFe_{0.24}Sn_{1.79}$	0	3.51	$CeNi_{0.52}Sn_{1.71}$	4	2.63
$CeCo_{0.48}Sn_2$	−9	2.71	$PrNiSn_2$	−2	3.69
$CeCo_{0.33}Sn_2$	−3	2.52	$NdNiSn_2$	−3	3.73
$CeCo_{0.39}Sn_{1.8}$	−15	2.54	$LaCu_{0.62}Sn_{1.83}$	diamagnet	
$CeCo_{0.30}Sn_{1.72}$	−20	2.71	$CeCu_{0.62}Sn_{1.83}$	1	2.40
$PrCo_{0.33}Sn_2$	−2	3.52	$PrCu_{0.62}Sn_{1.83}$	10	3.62
$NdCo_{0.33}Sn_2$	−7	3.63	$NdCu_{0.74}Sn_{1.96}$	−6	3.80
$LaNiSn_2$	Pauli paramagnet		$NdCu_{0.43}Sn_{1.90}$	0	3.56
$CeNiSn_2$[b]	−2	2.45	$NdCu_{0.62}Sn_{1.83}$	−2	3.60
$CeNi_{0.51}Sn_2$	−23	2.76	$NdCu_{0.52}Sn_{1.71}$	0	3.79
$CeNi_{0.74}Sn_{1.96}$	−6	2.66			

[a] For Mn atom.
[b] T_N, 4 K; θ_p, −6.9 K; μ_{eff}, 2.56μ_B (Pecharsky et al. 1991).

Table 33
Magnetic properties of $RMn_{1-x}Sn_{2-y}$ compounds (Weitzer et al. 1992b)

Compound	T_c (K)	T_N (K)	μ_s (μ_B/f.u.)	θ_p (K)	μ_{eff} (μ_B/f.u.)	M_{eff} (μ_B/Mn)
$LaMn_{0.27}Sn_{1.89}$				−95		4.30
$CeMnSn_2$	320		0.4	117	4.03	3.12
$CeMn_{0.5}Sn_2$	520		0.55	369	3.80	4.04
$PrMn_{0.50}Sn_{0.83}$		16		−14	4.18	3.00
$PrMn_{0.33}Sn_{1.88}$		20		−5	4.16	3.63
$PrMn_{0.26}Sn_{1.88}$		16		−15	4.17	4.13
$NdMn_{0.50}Sn_{1.83}$		20		−39	4.48	3.76
$NdMn_{0.25}Sn_{1.85}$				−12	4.07	3.00

$CeMnSn_2$ and $T_C = 520$ K for $CeMn_{0.5}Sn_2$. The $\chi(T)$ dependence of the Ce compounds follow the Curie–Weiss law above the T_C points, and the $\chi(T)$ dependences of the $LaMn_{1-x}Sn_{2-y}$, $PrMn_{1-x}Sn_{2-y}$, $NdMn_{1-x}Sn_{2-y}$ and $SmMn_{1-x}Sn_{2-y}$ compounds obey the Curie–Weiss law above the liquid nitrogen temperature. The Pr, Nd and Sm compounds undergo an antiferromagnetic phase transition at low temperatures.

The magnetization versus magnetic field curves up to 3 T have been measured at 5 K. The $PrMn_{1-x}Sn_{2-y}$ compounds exhibit metamagnetic behaviour under applied field above

2.5 T. The authors assume for $RMn_{1-x}Sn_{2-y}$ the narrow band formed by the 3d-electron lies close to the Fermi level. They suggest that magnetism of these compounds preferably arises from weak R–Mn and R–R interactions, i.e. Mn atoms only couple via a RKKY mechanism.

Leithe-Jasper et al. (1994) report on the ^{119}Sn Mössbauer spectra of the $RMnSn_2$ (R = La, Ce, Pr, Nd, Sm) stannides. The compounds order magnetically close to room temperature. At the two tin sites there is a transferred hyperfine field of 3–6 T at 15 K, which depends on the rare-earth partner, especially at the Sn2 sites.

The low temperature heat capacity and magnetic properties of $CeNiSn_2$ were measured by Pecharsky et al. (1991). The susceptibility follows the Curie–Weiss law from ~40 to 300 K, at 4 K $CeNiSn_2$ undergoes an antiferromagnetic transition.

The resistivity of the $RM_{1-x}Sn_{2-y}$ alloys increases with increasing temperature. It is necessary to indicate that the $\rho(T)$ dependence of the alloys with copper is nearly linear, and the biggest deviation from this is observed for the Mn and Fe alloys. The dependence of the thermopower on the composition is not observed.

An analysis of the homogeneity ranges, magnetic and transport properties, a phenomenology model which explains the limits of homogeneity ranges and properties of the compounds $RM_{1-x}Sn_{2-y}$ was presented by Skolozdra (1993). This model proceeds from two factors – the atoms size and the structure of the energy electron spectra near the Fermi level.

4.26. *$R_5Ni_{1.5}Sn_{1.5}$ compounds*

The magnetic susceptibility has only been measured for $Ce_5Ni_{1.5}Sn_{1.5}$. The $\chi(T)$ dependence follows the Curie–Weiss law (Skolozdra 1993). The investigation of the L_{III}-spectra for $Ce_5Ni_{1.5}Sn_{1.5}$ showed that the valence of Ce in this stannide is equal to 3 (Samsonova et al. 1985) (fig. 22).

4.27. *RM_xSn_y phases*

The magnetic properties of the RM_xSn_y phases were investigated mainly at low temperature for the determination of the superconducting transition temperature (tables 34–36). The $SnEr_3Rh_4Sn_{12}$ and $(Sn_{0.58}Er_{0.42})Er_4Rh_6Sn_{18}$ compounds were studied by neutron diffraction (Bordet et al. 1986). The first compound orders antiferromagnetically below 12 K with magnetic wave vector $\boldsymbol{k} = (\frac{1}{2}, \frac{1}{2}, 0)$. In the second compound magnetic reflections are observed at 0.4 K. The magnetic moments of Er1 ($3.91\mu_B$) are oriented along the Z axis; and the moments of Er2 ($1.5\mu_B$) are aligned along the pseudoternary axis which is truncated in the cubooctahedra with Er2 atoms in the middle faces. The resistivity of the I and I' phases has been measured on single crystals.

The transport data of the RM_xSn_y compounds are listed in table 37. The temperature dependence of the resistivity of the $GdRh_{1.07}Sn_{4.21}$ compound obeys four different power laws: $\rho \approx T^{3/2}$ between 2 and 7.2 K, $\rho \approx T^2$ between 7.2 and 11.6 K, $\rho \approx T$ from 16 to 44 K, and $\rho \approx \ln T$ above 44 K (Rojek et al. 1986). These dependences are explained in

Table 34
Magnetic (T_m) and superconducting (T_c) ordering temperatures of phases *I* and *I'* (Espinosa et al. 1982)

RM_xSn_y		T_m (K)	T_c (K)	RM_xSn_y		T_m (K)	T_c (K)
R	M			R	M		
La	Co	–	8	Eu	Rh	11	–
Yb	Co	–	2.5	Gd	Rh	11.2	–
La	Ru	–	3.9	Yb	Rh	–	8.6
La	Rh	–	3.2	La	Ir	–	2.6

Table 35
Magnetic (T_m) and superconducting (T_c) ordering temperatures of phase *II* (Espinosa et al. 1982)

RM_xSn_y		T_m (K)	T_c (K)	RM_xSn_y		T_m (K)	T_c (K)
R	M			R	M		
Dy	Co	5.6	–	Dy	Rh	2.1	–
Ho	Co	2.9	–	Ho	Rh	1.7	–
Lu	Co	–	1.5	Er	Rh	0.6	1.2
Sc	Ru	3.7	–	Tm	Rh	–	2.3
Y	Ru	1.3	–	Lu	Rh	–	4.0
Sc	Rh	–	4.5	Sc	Ir	–	1.1
Y	Rh	–	3.2	Yb	Ir	–	2.2
Tb	Rh	3.8	–	Lu	Ir	–	3.2

Table 36
Magnetic (T_m) and superconducting (T_c) ordering temperatures of phases *II'* (*III*) (Espinosa et al. 1982)

RM_xSn_y		T_m (K)	T_c (K)	RM_xSn_y		T_m (K)	T_c (K)
R	M			R	M		
Y	Ru	1.3	–	Tb	Os	–	1.4
Tb	Rh	3.8	–	Ho	Os	–	1.4
Dy	Rh	2.1	–	Er	Os	0.5	1.3
Ho	Rh	1.7	–	Tm	Os	0.6	1.1
Er	Rh	0.6	1.2	Lu	Os	–	1.8
Tm	Rh	–	2.3	La	Ir	–	2.6
Sc	Os	–	1.5	Y	Ir	–	2.2
Y	Os	–	2.5				
Dy	Ir	1.55	–				

Table 37
Transport properties of RM_xSn_y compounds

Compound	ρ (μΩ cm)		S (μV/K)		Reference
	at 78 K	at 293 K	at 90 K	at 300 K	
$(Lu_{0.4}Sn_{0.6})Lu_4Fe_6Sn_{18}$	290	260	−4.2	−10.7	Skolozdra 1993
$Lu_4Fe_6Sn_{19}$	480	590			Skolozdra 1993
$Tm_4Fe_6Sn_{19}$	410	660			Skolozdra 1993
$Gd_6Co_8Sn_{26}$	80	195	−1.0	2.0	Skolozdra 1993
$Tb_6Co_8Sn_{26}$	70	170	2.0	4.0	Skolozdra 1993
$Tb_4Co_6Sn_{19}$	100	190	−3.0	−10.5	Skolozdra 1993
$Ho_4Co_6Sn_{19}$	45	145	−5.0	−14.5	Skolozdra 1993
	ρ at 10 K	ρ at 300 K			
YRh_xSn_y	28[a]	290			Remeika et al. 1980b
$PrRh_xSn_y$	5.4	114			Remeika et al. 1980b
$EuRh_{1.5}Sn_{4.2}$	16[a]	133			Rojek and Sułkowski 1987
$GdRh_{1.07}Sn_{4.21}$	842	610			Rojek et al. 1986
$HoRh_{1.2}Sn_{3.9}$	369	310			Remeika et al. 1980b
$ErRh_{1.1}Sn_{3.6}$	400	340			Remeika et al. 1980b
$ErRh_{1.1}Sn_{3.6}$	605[b]	515			Rojek and Sułkowski 1986
$TmRh_{1.3}Sn_{4.0}$	304	286			Remeika et al. 1980b
$YbRh_{1.4}Sn_{4.6}$	9.7	90			Naushad Ali et al. 1985
$LuRh_{1.2}Sn_{4.0}$	941[b]	800			Rojek and Sułkowski 1986

[a] At 4.2 K. [b] At 2 K.

terms of the coexistence of a local moment antiferromagnetism of the Gd atoms and a localized spin fluctuation or an itinerant electron ferromagnetism of the Rh atoms.

The $EuRh_{1.5}Sn_{4.2}$ and $YRh_{1.4}Sn_{4.6}$ phases have a high resistivity (Naushad Ali et al. 1985). The $\rho(T)$ curve of $EuRh_{1.5}Sn_{4.2}$ has two rectilinear ranges – from 170 to 300 K and above T_N (13 K) to 50 K. The $\rho(T)$ function of the Yb stannide below 20 K to 7.18 K is described by $\rho = \rho_0 + AT^2$. At high temperatures ρ has a tendency to saturation.

The resistivity of $ErRh_{1.1}Sn_{3.6}$ and $LuRh_{1.2}Sn_{4.0}$ decreases with rising temperature. The $\rho(T)$ function of $LuRh_{1.2}Sn_{4.0}$ is logarithmic with a broad minimum around 210 K (Rojek and Sułkowski 1986).

The $(Sn_{1-x}Lu_x)Lu_4Fe_6Sn_{18}$ and $(Sn_{1-x}Tm_x)Tm_4Fe_6Sn_{18}$ phases have a high resistivity as well (fig. 36). The substitution of a part of Sn atoms by Lu atoms [i.e. the composition $(Sn_{0.6}Lu_{0.4})Lu_4Fe_6Sn_{18}$] leads to a negative temperature coefficient of the resistivity (Skolozdra 1993).

$SmRuSn_3$ ($Sm_8Ru_8Sn_{24}$, phase *I*) is a valence fluctuating compound with antiferromagnetic ordering below 6 K (Fukuhara et al. 1992).

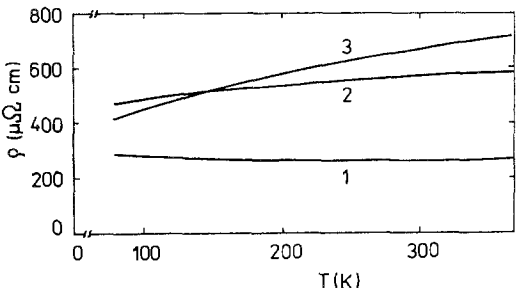

Fig. 36. Temperature dependence of the resistivity of (1) $Tm_4Fe_6Sn_{19}$, (2) $Lu_4Fe_6Sn_{18}$ and (3) $(Lu_{0.4}Sn_{0.6})Lu_4Fe_6Sn$ (Skolozdra 1993).

One of the causes of the high R values of phases *I* and *II* is the presence of a significant ion-covalent contribution to the bonding.

4.28. *R_6Co_2Sn and R_6Ni_2Sn compounds*

The temperature dependence of magnetic susceptibility has been measured for all R_6Co_2Sn compounds (Koretskaya et al. 1988b) and for some R_6Ni_2Sn compounds (Sichevich et al. 1984) in the temperature range 78–293 K (table 38). All stannides except Gd_6Co_2Sn are paramagnetic in this temperature range, the Y and Lu compounds are Pauli paramagnets. The $\chi^{-1}(T)$ function of Gd_6Co_2Sn is linear below 120 K, and above this temperature it is characterized by a negative curvature. This suggests a ferrimagnetic ordering in compound below 120 K.

Gschneidner Jr et al. (1995) have prepared and studied the Er_6Ni_2Sn compound [as well as Er_6Ni_2Pb, $Er_6Ni_2(Sn_{0.75}Ga_{0.15})$ and 50:50 Er_6Ni_2Sn/Er_3Ni]. These alloys have

Table 38
Magnetic and transport properties of R_6M_2Sn compounds (Koretskaya et al. 1988b, Sichevich et al. 1984)

Compound	θ_p (K)	μ_{eff} (μ_B)	ρ (μΩ cm)		S (μV/K)	
			at 78 K	at 300 K	at 90 K	at 300 K
Y_6Co_2Sn	Pauli paramagnet					
Gd_6Co_2Sn	$\chi^{-1}(T)$ not linear					
Tb_6Co_2Sn	38	9.4				
Dy_6Co_2Sn	15	10.6				
Ho_6Co_2Sn	10	10.5				
Er_6Co_2Sn	7	8.6				
Tm_6Co_2Sn	1	7.4	160	240	−0.4	−1.4
Lu_6Co_2Sn	Pauli paramagnet		40	180	0.3	−1.4
Tb_6Ni_2Sn	42	10.0				
Dy_6Ni_2Sn	24	10.7				
Er_6Ni_2Sn	~17[a]					
Tm_6Ni_2Sn	3	7.6				

[a] Ferrimagnetic ordering temperature (Gschneidner Jr et al. 1995).

been investigated as potential candidate materials for the lower temperature stage of Gifford–McMahon (G–M) cryocooler. The heat capacity of Er_6Ni_2Sn alloy in the as cast and annealed conditions was measured in the temperature range 1.5–40 K. The thermal dependence of heat capacity is characterised by a major peak at 17–18 K. There is also a small peak at ~2.5 K and a slightly larger one at ~8 K. These two peaks were due to transformations in additional phases because the Er_6Ni_2Sn alloy was multiphase. The peak at 17–18 K corresponds to a ferrimagnetic ordering in Er_6Ni_2Sn with $T_C \approx 17$ K.

The authors indicate that the Er_6Ni_2X phases (X = Sn, Pb) and $Er_6Ni_2(Sn_{0.75}Ga_{0.15})$ would be good cryogenic regenerator materials for a G–M cryocooler which operates down to ~10 K.

4.29. *$R_7Co_6Sn_{23}$ compounds*

For all $R_7Co_6Sn_{23}$ compounds the magnetic susceptibility between 78 and 293 K has been measured by Skolozdra et al. (1986b). The compounds with Tb, Dy, Ho, and Er are paramagnetic, their $\chi(T)$ dependence obeys the Curie–Weiss law (table 39). The $Y_7Co_6Sn_{23}$ compound is diamagnetic.

Table 39
Magnetic properties of $R_7Co_6Sn_{23}$ compounds (Skolozdra et al. 1986b)

Compound	θ_p (K)	μ_{eff} (μ_B)	Compound	θ_p (K)	μ_{eff} (μ_B)
$Y_7Co_6Sn_{23}$	diamagnet		$Ho_7Co_6Sn_{23}$	1	10.7
$Tb_7Co_6Sn_{23}$	−14	9.8	$Er_7Co_6Sn_{23}$	5	9.7
$Dy_7Co_6Sn_{23}$	−4	10.5			

4.30. *$R_3Ni_2Sn_7$ compounds*

The magnetic and transport data of $R_3Ni_2Sn_7$ compounds are listed in table 40. The $La_3Ni_2Sn_7$ stannide is diamagnetic ($\chi_{293} = -0.14 \times 10^{-6}$ cm^3/g). The $\chi(T)$ dependence of $Pr_3Ni_2Sn_7$ and $Nd_3Ni_2Sn_7$ follows the Curie–Weiss law. For $Ce_3Ni_2Sn_7$ the $\chi^{-1}(T)$ function is linear in the range 170–293 K, at lower temperature it deviates from the linear one (Skolozdra et al. 1987). The temperature dependence of the resistivity and thermopower of $Ce_3Ni_2Sn_7$ also differs from that of $La_3Ni_2Sn_7$ and $Pr_3Ni_2Sn_7$. On the basis of the $Ce_3Ni_2Sn_7$ properties an intermediate Ce valence behaviour was suggested for this compound. For $Ce_3Ni_2Sn_7$ the b lattice parameter lies below the straight line established by the other R compounds in a plot of b vs. the lanthanide atomic number.

Table 40
Magnetic and transport properties of $R_3Ni_2Sn_7$ compounds (Skolozdra et al. 1987, Skolozdra 1993)

Compound	θ_p (K)	μ_{eff} (μ_B)	ρ (μΩ cm)		S (μV/K)	
			at 78 K	at 300 K	at 90 K	at 300 K
$La_3Ni_2Sn_7$	diamagnet		66	90	−2.0	−2.0
$Ce_3Ni_2Sn_7$	39	2.47	68	140	9.2	14.0
$Pr_3Ni_2Sn_7$	−6	3.58	78	100	−1.6	−1.0
$Nd_3Ni_2Sn_7$	−5	3.73				

4.31. *R_2NiSn_6 compounds*

The temperature dependence of the magnetic susceptibility of the R_2NiSn_6 compounds (R = Ho, Er, Tm) is described by the Curie law ($\theta_p = 0$). Lu_2NiSn_6 is a Pauli paramagnet. The resistivity has a low magnitude, the $\rho(T)$ dependence is almost linear, and the thermopower is not dependent on temperature (Skolozdra et al. 1988a) (table 41).

Table 41
Magnetic and transport properties of R_2NiSn_6 compounds (Koretskaya et al. 1988a, Skolozdra 1993)

Compound	θ_p (K)	μ_{eff} (μ_B)	ρ (μΩ cm)		S (μV/K)	
			at 78 K	at 300 K	at 90 K	at 300 K
Ho_2NiSn_6	0	10.7	13	44	−0.6	0.4
Er_2NiSn_6	0	9.6				
Tm_2NiSn_6	0	7.5	18	68	−0.6	1.0
Lu_2NiSn_6	Pauli paramagnet		12	43	−0.8	0.2

4.32. *Brief discussion of the magnetic and transport properties*

Mainly the investigated ternary stannides can be divided into three groups from the point of view of their magnetic properties. The first group consists of the compounds, which contain a magnetic rare-earth atom that defines their magnetism. At high temperatures (above 50–100 K) susceptibility of the compounds of this group follows Curie–Weiss law and at low temperatures R-sublattice is ordered magnetically. The second group includes the compounds of the non-magnetic rare-earth metals (Sc, Y, La, Lu) which are Pauli paramagnets. The compounds with high magnetic ordering temperatures (near or above room temperature) caused by the ordering of the M sublattice form the third group of the stannides.

The first group contains the largest number of stannides. The effective magnetic moments of the compounds of this group are close to the theoretical moments of

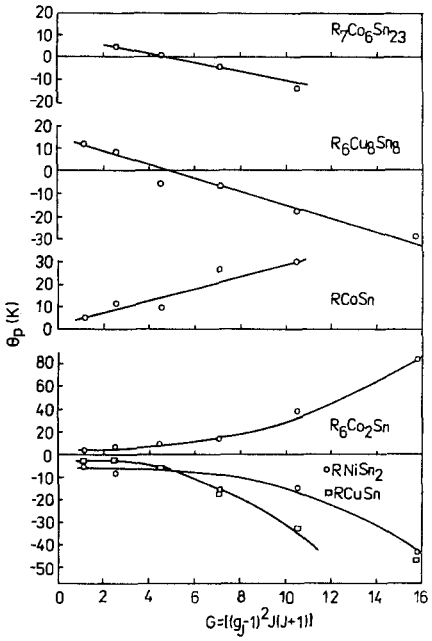

Fig. 37. The θ_p dependence of the de Gennes function of some stannides.

the corresponding R^{3+} ion, which suggests the R atoms are trivalent except for some compounds of Ce, Yb. The magnetic susceptibility of stannides with Fe, Co, Ni and Cu depends only on R, and the contribution of the transition metal atoms is insignificant. The Pauli paramagnetism of the isostructural compounds of Y, La, Lu indicates that there is little if any contribution from the transition metals to the susceptibility for these phases. In view of the fact that the Mn atoms have a local magnetic moment, the susceptibility of the Mn compounds contains two constituent parts. The paramagnet Curie points range from positive to negative values, which suggests different types of magnetic ordering.

For the compounds of the light R elements no regularity in change of the θ_p dependence on the lanthanide metal is observed as it is in the compounds of the heavy lanthanides. For the series of the isostructural RCoSn, $R_6Cu_8Sn_8$ and $R_7Co_6Sn_{23}$ compounds the θ_p magnitude is proportional to de Gennes function $G=(g_J-1)^2J(J+1)$ and there is a change in sign for θ_p for the $R_6Cu_8Sn_8$ and $R_7Co_6Sn_{23}$ compounds (see tables 21 and 39, and fig. 37).

In the frame of the RKKY theory the paramagnetic Curie point is given (Rocher 1962) as follows:

$$\Theta_p = -\frac{3\pi Z^2}{kE_F\Omega^2} J_{sf} (g_j - 1)^2 J(J+1) \sum_i F(z) \qquad (1)$$

where Ω is the atomic volume, Z is the number of conduction electrons, J_{sf} is the exchange integral between the localized lanthanide spin S and the conduction electrons spins. The function $F(z)$ is defined as

$$F(z) = (z\cos z - \sin z)\, z^{-4}, \tag{2}$$

where $z = 2\boldsymbol{k}_F r_{io}$, and r_{io} is the interatomic distance between magnetic atoms ($i = 0$) and any other atoms ($i \neq 0$).

The $F(z)$ function is an oscillating function and depends on $\boldsymbol{k}_F$. It follows from eq. (1) for a series of isostructural R compounds in the case of the RKKY exchange interaction that θ_p is proportional to the de Gennes function, while the other parameters of eq. (1), based on the similarity of the electron structure of rare earths, do not change significantly. An inversion of the θ_p sign as observed for $R_6Cu_8Sn_8$ and $R_7Co_6Sn_{23}$ can be realized only by the function $F(z)$ which changes from one sign to the opposite sign as $\boldsymbol{k}_F$ varies. An increasing or decreasing $\boldsymbol{k}_F$ can be realized by a change of the conduction electron concentration (CEC) or as a consequence of a modification of the energy band structure.

We suggest that the inversion of the θ_p sign for $R_6Cu_8Sn_8$ and $R_7Co_6Sn_{23}$ is caused by a change of the band structure because CEC in an isostructural series of the compounds does not change. Apparently in the $R_6Cu_8Sn_8$ and $R_7Co_6Sn_{23}$ compounds as the atomic number of R increases the electron energy spectrum changes with an accompanied shifting of $\boldsymbol{k}_F$. If $\boldsymbol{k}_F$ lies near the Brillouin zone, where a break of the function $E(\boldsymbol{k})$ occurs, the transformation in the electron energy spectrum can cause a deformation of the crystal structure or it can lead to the appearance of another structure. The θ_p sign inversion at the transition from $Ho_6Cu_8Sn_8$ to $Er_6Cu_8Sn_8$ and from $Dy_7Co_6Sn_{23}$ to $Ho_7Co_6Sn_{23}$ supposes such change of the electron energy spectrum. This can explain the absence of the $Yb_6Cu_8Sn_8$, $Lu_6Cu_8Sn_8$ and $Tm_7Co_6Sn_{23}$, $Yb_7Co_6Sn_{23}$, $Lu_7Co_6Sn_{23}$ compounds because a transformation in the band structure leads to the unstability of the compounds with $Gd_6Cu_8Ge_8$ and $Ho_7Co_6Sn_{23}$ type structure. The example of $Tm_6Cu_8Sn_8$ confirms this explanation, where a monoclinic deformation has been determined by single-crystal diffraction method (Thirion et al. 1983). So, on the basis of the strong change of the band electron spectrum, which is displayed in a change of the θ_p sign, it also explains a structural change in a series of compounds.

The $\theta_p(G)$ dependences of the R_6Co_2Sn, RNiSn and RCuSn compounds (fig. 37) are quite interesting. For these stannides there is a significant difference in θ_p values between neighbouring lanthanides for the beginning of the heavy lanthanides element, which becomes quite small for the second half of the series. Instead of intersecting with the G-coordinate and changing sign, the function $\theta_p(G)$ approaches the θ_p coordinate asymptotically. Apparently, in this case instead of additional transformations when one R is substituted for another R, the electron energy spectrum is stabilized, the θ_p function does not cross the G coordinate, and the compound does not change structure type, and this why isostructural compounds exist up to Lu.

The absence of a regularity of the θ_p change for many series of other compounds and also for the light lanthanides may be due to the following considerations: (1) some of

the factors which have been simplified in the RKKY theory, (2) crystal field effects, and (3) the contribution of the 5d-electrons.

The stannides of the second group are the Pauli paramagnets. Among the ternary stannides, the smallest χ values are characteristic of the Ni stannides, and the copper compounds are diamagnetic. This is due the construction of 3d-electron level of their respective atoms. With increasing Sn contents the susceptibility of the Co and Ni stannides decreases, and some of them become diamagnetic. Apparently, in the case of the complete filling of the 3d-band, the Fe, Co, and Ni compounds must be diamagnetic as for the Cu stannides. The presence of the paramagnetic susceptibility of the Co and Ni stannides, which slowly decreases with increasing tin content supposes the 3d-band is unfilled. Apparently, the state with an almost filled 3d-band is very stable, because it is clear from susceptibility that 3d-band is filled only at large tin contents. In order for the 3d-band to remain unfilled the band structure must change continuously with increase of the tin contents causing the crystal structure change.

From this point of view Skolozdra (1993) has made an explanation for the larger number of compounds in the R–Ni–Sn systems in comparison with the R–Fe–Sn and the R–Co–Sn systems.

In the copper systems a tendency for a decreasing number of compounds is observed, and is caused by another structure in the band spectrum. In this case the Fermi level lies in a region with a low density of states and an almost empty conduction band. Perhaps, at such an electronic structure of the stannides, a displacement of Fermi level is caused by a composition change and leads (with the aim of preserving the stability of the electron energy state) to the formation of a long range hybrid structure of the $CeNiSi_2$, La_3CoSn_7, Lu_2NiSn_6, and $Sm_2Cu_4Sn_5$ structure types. These structures are formed by certain fragments of more simple structures. The ternary stannides with such crystal structures have a low density of states at the Fermi level, and this is confirmed by the diamagnetism not only of the copper and nickel compounds but of the cobalt compounds as well.

The magnetic properties of the compounds of the third group in the main are determined by the transition metals i.e. the M–M interaction is stronger than the other interactions. These are the $R_6M_{13}Sn$, RCo_3Sn and RMn_6Sn_6 compounds.

The resistivities of the ternary stannides have different values and temperature dependences because of the variety of their composition and crystal structures. Skolozdra (1993) classified the stannides by their resistivity behaviours from the curvature of the $\rho(T)$ function in the range 80–360 K. A tendency that stannides with large M contents have a bigger curvature has been found. A comparison of the influence of different metals (Fe, Co, Ni, Cu) on curvature indicated that as the transition of M from iron to copper occurs, the curvature of the $\rho(T)$ function decreases and all practically studied copper stannides have a linear $\rho(T)$ dependence.

An explanation of the temperature dependence $\rho(T)$ for stannides is based on two models. According to them, the curvature of the $\rho(T)$ function is determined either by the band structure in the region of the Fermi level (Mott 1964), or it is caused by the unordering of the atoms in the crystal structure which results in the mean free path of the

electrons approaching the interatomic distances (Fisk and Webb 1976). The R atoms in the ternary stannides do not make significant contribution to the curvature from the point of view of their electronic structure. A linear $\rho(T)$ dependence above the magnetic ordering temperature of the binary compounds of the rare earth with nonmagnetic elements (Gratz and Zuckermann 1982) testifies to that. In total view point, the greater curvature for the compounds with high contents of Fe, Co in comparison with Ni, Cu is explained by the influence of the s–d scattering, which is not displayed in the copper alloys and in the alloys with high tin content. The second model explains the presence of the curvature in the $\rho(T)$ function in the compounds with statistical distribution of atoms in the crystal structure.

The temperature dependence of the thermopower for metals and alloys in the free electrons approximation is defined by the expression (Ziman 1962):

$$S = \frac{\pi^2 k^2 T}{3e} \left(\frac{\mathrm{d}\ln\sigma(E_\mathrm{F})}{\mathrm{d}E} \right)_{E=E_\mathrm{F}}, \tag{3}$$

where $\sigma(E)$ is the electrical conductivity of the electrons with an energy E_F.

It follows from eq. (3) that the thermopower must change linearly with the temperature. In most ternary stannides the dependence $S(T)$ is complex. Analysis carried out by Skolozdra (1993) shows that the deviations from linearity mainly correlate with the ones in the $\rho(T)$ dependence and are caused by the same type of mechanisms of the electron scattering. The main causes of the anomalous $S(T)$ are the peculiarities of the structure of the electron band spectrum in the region of the Fermi level, a strong electron–phonon interaction, and the presence of a statistical distribution of atoms in the crystal structure.

4.33. *Superconductivity of the ternary stannides*

From the point of view of superconductivity the RMn_xSn_y phases have been investigated to a greater degree. Many of these phases undergo a superconductive transition in the temperature range 1.1–8.6 K (see tables 34–36). The RPd_2Sn compounds (R = Sc, Y, Tm, Yb, Lu) of $MnCu_2Al$ type are also superconductors, with a T_c in the range 2–5 K (see table 15).

The $(Er_{1-x}Sn_x)Er_4Rh_6Sn_{18}$ stannide at low temperature orders ferromagnetically with the destruction of the superconductive state, i.e. it is a reentrant superconductor (Remeika et al. 1980a, Andres et al. 1981) with $T_\mathrm{c} = 1.36$ K and $T_\mathrm{C} = 0.46$ K. Measurements of susceptibility, magnetization and resistivity of a single crystal $(Er_{1-x}Sn_x)Er_4Rh_6Sn_{18}$ have shown that the superconductivity is destroyed by the onset of long-range ferromagnetic order at low temperature (Genicon et al. 1985). Studies of single crystals $(Er_{1-x}Sn_x)Er_4Rh_6Sn_{18}$ of different compositions have been carried out by Miraglia et al. (1984). The temperatures of magnetic and superconducting transitions depend on the ratio of Sn and Er atoms at the 2(a) site, i.e. on x. Single crystals are superconducting for $x \approx 0$ ($T_\mathrm{c} = 1.3$ K), are reentrant superconductors for $x \approx 0.30$ ($T_\mathrm{c} = 1.24$ K, $T_\mathrm{C} = 0.34$ K), and undergo a single magnetic transition for $x \approx 0.75$ ($T_\mathrm{C} = 0.68$ K).

With the aim of determining the mechanism of both orderings, properties of the solid solution $Er_xY_{1-x}Rh_{2.1}Sn_{3.6}$ were studied by Houwman et al. (1987). The substitution of Y by Er atoms suppresses the superconducting transition temperature from 3.13 K for $YRh_{1.1}Sn_{3.6}$ to 1.1 K for $ErRh_{1.1}Sn_{3.6}$. The reentrant superconductivity has been found for $x > 0.6$. For $x = 0.4$ the suppression of the superconductivity of the yttrium phase can be described by the Abrikosov and Gor'kov theory, considering elastic scattering of the conduction electrons by isolated spins. For the high concentration of Er T_c is reduced more than it was predicted by the Abrikosov–Gor'kov theory. This additional decreasing of T_c is attributed to an additional scattering rate, due to parallel alignment of nearest neighbour spins in coupled spin pairs, as is described fairly well by the model of Roshen and Ruvalds. The temperature of the magnetic ordering as a function of concentration is described by the model of Ogushi and Ovo model with an effective coordination number $z_{eff} = 6.1$ and an exchange constant $J = 0.30$ K (Houwman et al. 1987).

Two reentrant superconductors have been found with osmium by Fisk et al. (1982). There are the $ErOs_xSn_y$ and $TmOs_xSn_y$ compounds with $T_c = 1.3$ K, $T_C = 0.5$ K for the first stannide and with $T_c = 1.1$ K, $T_C = 0.6$ K for the second one.

The coexistence of superconductivity and magnetic order has been found in the Heusler phases $ErPd_2Sn$ and $YbPd_2Sn$. As a consequence of the measurements of the heat capacity, magnetic susceptibility, and resistivity it was established that the superconducting transition temperature in $ErPd_2Sn$ is 1.17 K (Shelton et al. 1986). A further decrease of the temperature leads to long range magnetic order at $T_C = 1.00$ K, moreover, superconductivity is not destroyed down to 40 mK (the lowest temperature to which the measurements were carried out).

Elastic and inelastic neutron scattering measurements were carried out on $ErPd_2Sn$ by Stanley et al. (1987). They have found that antiferromagnetic correlations developed below T_c with an antiferromagnetic transition occurring at ~1.0 K. The magnetic structure is of the type *II*, in which the fcc Er unit cell doubles along all three crystallographic directions. But the magnetic structure has not been determined completely because there are additional satellites indicating a modulated component of the magnetization density.

Measurements of heat capacity, resistivity and magnetic susceptibility have shown that $YbPd_2Sn$ compound undergoes a superconducting transition at 2.46 K and a magnetic transition at 0.23 K. The magnetic order does not destroy the superconductivity which coexists with the magnetic ordered phase (Kierstead et al. 1985). It is suggested that the ground state of Yb^{3+} ion is a Γ_7 magnetic doublet.

So, there are two types of compounds among the ternary stannides which are characterized by superconductivity and magnetic ordering. Compounds with a high tin content form one type – reentrant superconductors – in which long range ferromagnetic ordering destroys superconductivity. In the Heusler phases at the formation of the magnetic order superconductivity does not disappear. This can be explained by the antiferromagnetic ordering for $ErPd_2Sn$ and, apparently, for $YbPd_2Sn$ as well.

Acknowledgements

The author would like to thank Dr. L. Akselrud, Dr. L. Komarovska, Dr. T. Yanson and Mr. G. Melnyk for the interesting discussions and help in the preparation of this manuscript.

References

Adam, A., J. Sakurai, Y. Yamaguchi, H. Fujiwara, K. Mibu and T. Shinjo, 1990, J. Magn. & Magn. Mater. **90–91**, 544.

Adam, J., and J.B. Rich, 1954, Acta Crystallogr. 7, 813.

Adroja, D.T., and S.K. Malik, 1992, Phys. Rev. B **45**, 779.

Adroja, D.T., and B.D. Rainford, 1994, J. Magn. & Magn. Mater. **135**, 333.

Adroja, D.T., S.K. Malik, B.D. Padalia and R. Vijayaraghavan, 1988, Solid State Commun. **66**, 1201.

Akselrud, L.G., L.A. Lysenko, Ya.P. Yarmoluk and E.I. Gladyshevsky, 1977a, Dokl. Akad. Nauk Ukr. SSR, Ser. A **7**, 659.

Akselrud, L.G., Ya.P. Yarmoluk and E.I. Gladyshevsky, 1977b, Kristallografiya **22**, 861.

Akselrud, L.G., L.P. Komarovskaya and R.V. Skolozdra, 1983, Dokl. Akad. Nauk Ukr. SSR, Ser. B **5**, 33.

Aliev, F.G., N.B. Brandt, V.V. Moshchalkov, M.K. Zalyalyutdinov, G.I. Pak and R.V. Skolozdra, 1988a, Pis'ma Zh. Eksp. Teor. Fiz. **48**, 536.

Aliev, F.G., V.V. Moshchalkov, V.V. Kozyrkov, M.K. Zalyalyutdinov, V.V. Pryadun and R.V. Skolozdra, 1988b, J. Magn. & Magn. Mater. **76–77**, 295.

Aliev, F.G., V.V. Moshchalkov, M.K. Zalyalyutdinov, G.I. Pak, R.V. Skolozdra, P.A. Alekseev, V.N. Lazukov and I.P. Sadikov, 1990, Physica B **163**, 358.

Aliev, F.G., R. Villar, S. Vieira, R.V. Skolozdra and T. Takabatake, 1994, Physica B **199–200**, 433.

André, G., F. Bourée, A. Olés, W. Sikora, M. Kolenda and A. Szytuła, 1993, J. Magn. & Magn. Mater. **125**, 303.

André, G., W. Bażela, F. Bourée, M. Guillot, A. Oleś, W. Sikora, A. Szytuła and A. Zygmunt, 1995a, J. Alloys & Compounds **221**, 254.

André, G., F. Bourée, M. Guillot, M. Kolenda, A. Oleś, W. Sikora, A. Szytuła and A. Zygmunt, 1995b, J. Magn. & Magn. Mater. **140–144**, 879.

Andres, K., J.P. Remeika, G.P. Espinosa and A.S. Cooper, 1981, Phys. Rev. B **23**, 1179.

Bando, Y., T. Takabatake, H. Tanaka, H. Iwasaki, H. Fujii and S.K. Malik, 1994, Physica B **194–196**, 1179.

Bażela, W., J. Leciejewicz, K. Małetka and A. Szytuła, 1992, J. Magn. & Magn. Mater. **117**, L1.

Bażela, W., J. Leciewicz, N. Stuesser, A. Szytuła and A. Zygmunt, 1994, J. Magn. & Magn. Mater. **137**, 219.

Bażela, W., M. Guillot, J. Leciewicz, K. Małetka, A. Szytuła and Z. Tomkowicz, 1995a, J. Magn. & Magn. Mater. **140–144**, 1137.

Bażela, W., M. Kolenda, J. Leciejewicz, N. Stuesser, A. Szytuła and A. Zygmunt, 1995b, J. Magn. & Magn. Mater. **140–144**, 881.

Beille, J., D. Block, J. Voiron and G. Parisot, 1977, Physica B **86–88**, 231.

Bellot, P., P. Bonville, J. Hammann, J.A. Hodges, P. Imbert, G. Jehanno, L. Leylekian and L. d'Onofrio, 1992, J. Magn. & Magn. Mater. **108**, 141.

Bertaut, F., and P. Blum, 1953, C. R. Acad. Sci. Paris **236**, 1055.

Beyermann, W.P., M.F. Hundley, P.C. Canfield, J.D. Thompson, M. Latroche, C. Godart, M. Selsane, Z. Fisk and J.L. Smith, 1991, Phys. Rev. B. **43**, 13130.

Bockelmann, W., and H.U. Schuster, 1974, Z. Anorg. Allg. Chem. **410**, 233.

Bodak, O.I., and E.I. Gladyshevsky, 1969, Kristallografiya **14**, 990.

Bonnet, M., J.X. Boucherle, F. Givord, F. Lapierre, P. Lejay, J. Odin, A.P. Murani, J. Schweizer and A. Stunault, 1994, J. Magn. & Magn. Mater. **132**, 289.

Bordet, P., J.L. Hodeau, P. Wolfers, S. Miraglia, A. Benoit, M. Marezio and J.P. Remeika, 1986, Physica B **136**, 432.

Borzone, G., A. Borsese and R. Ferro, 1982, J. Less-Common Met. **85**, 195.

Borzone, G., A. Borsese and R. Ferro, 1983, Z. Anorg. Allg. Chem. **501**, 199.

Boucherle, J.X., F. Givord, P. Lejay, J. Schweizer and A. Stunault, 1987, J. Magn. & Magn. Mater. **63–64**, 575.

Boucherle, J.X., F. Givord, P. Lejay, J. Schweizer and A. Stunault, 1988, Acta Crystallogr. B **44**, 377.

Boucherle, J.X., F. Givord, P. Lejay, J. Schweizer and A. Stunault, 1989, Physica B **156–157**, 809.

Boucherle, J.X., G. Fillion, J. Flouquet, F. Givord, P. Lejay and J. Schweizer, 1990, Physica B **163**, 635.

Boulet, R.M., J.P. Jan and H.L. Skriver, 1982, J. Phys. F. **12**, 293.

Bradley, A., and J. Rodgers, 1934, Proc. Roy. Soc. A **144**, 340.

Braun, H.F., K. Yvon and R.M. Braun, 1980, Acta Crystallogr. **36**, 2397.

Buchholz, W., and H.U. Schuster, 1981, Z. Anorg. Allg. Chem. **482**, 40.

Bulanova, M.V., and P.V. Sydorko, 1994, Reports (preprint) of Institute of Material Problems (Kiev) **6**, 5.

Cenzual, K., and E. Parthé, 1984, Acta Crystallogr. C **40**, 1127.

Chafik El Idrissi, B., G. Venturini and B. Malaman, 1991a, Mater. Res. Bull. **26**, 1331.

Chafik El Idrissi, B., G. Venturini, B. Malaman and D. Fruchart, 1991b, J. Magn. & Magn. Mater. **175**, 143.

Chen, R., and F. Zheng, 1983, Acta Phys. Sin. **32**, 933.

Chen, Y.Y., J.M. Lawrence, J.D. Thompson and J.O. Willis, 1989, Phys. Rev. B **40**, 10766.

Cooper, A.S., 1980, Mater. Res. Bull. **15**, 799.

Crangle, J., K.-U. Neuman, J.G. Smith, N.K. Zayer and K.R.A. Ziebek, 1995, J. Magn. & Magn. Mater. **140–144**, 919.

Cromer, T., C. Larson and R. Roof, 1960, Acta Crystallogr. **13**, 913.

de Mooij, D.B., and K.H.J. Buschow, 1984, J. Less-Common Met. **102**, 113.

de Vries, J.W., R.C. Thiel and K.H.J. Buschow, 1985, Physica B **128**, 265.

Derkach, V.A., and B.Ya. Kotur, 1994, Izv. Akad. Nauk SSSR, Neorgan. Mater. **30**, 1001.

Dhar, S.K., K.A. Gschneidner Jr and O.D. McMasters, 1987, Phys. Rev. B **35**, 3291.

Dijkman, W.H., F.R. de Boer and P.F. de Châtel, 1980, Physica B **98**, 271.

Dirken, M.W., R.C. Thiel, J.H.V.J. Brabers, F.R. de Boer and K.H.J. Buschow, 1991, J. Alloys & Compounds **177**, L11.

Donaberger, R.L., and C.V. Stager, 1987, J. Less-Common Met. **127**, 93.

Dörrscheidt, W., and H. Schäfer, 1980, J. Less-Common Met. **70**, 1.

Dörrscheidt, W., G. Savelsberg, J. Stohr and H. Schäfer, 1982, J. Less-Common Met. **83**, 269.

Dwight, A.E., 1976, Proc. 12th Rare-Earth Res. Conf., Denver, ed. C.E. Lundin (Denver Research Institute) pp. 480–489.

Dwight, A.E., 1983, J. Less-Common Met. **93**, 411.

Dwight, A.E., 1987, Mater. Res. Bull. **22**, 201.

Dwight, A.E., and C.W. Kimball, 1987, J. Less-Common Met. **127**, 179.

Dwight, A.E., W.C. Harper and C.W. Kimball, 1973, **30**, 1.

Eberz, U., W. Seelentag and H.U. Schuster, 1980, Z. Naturforsch. **35**, 1341.

Eisenmann, B., N. May, W. Müller and H. Schäfer, 1972, Z. Naturforsch. **276**, 1155.

Eremenko, V.N., M.V. Bulanova, V.H. Batalin and V.E. Listovnichiy, 1987, Izv. Vyssh. Ucheb. Zaved. Tsvet. Met. **3**, 65.

Eremenko, V.N., M.V. Bulanova, V.E. Listovnichiy and B.M. Petyukh, 1988a, Ukr. Khim. Zh. **54**, 787.

Eremenko, V.N., M.V. Bulanova, P.S. Martsenyuk and V.E. Listovnichiy, 1988b, Ukr. Khim. Zh. **54**, 1240.

Eremenko, V.N., M.V. Bulanova, P.S. Martsenyjuk and V.E. Listovnichiy, 1988c, Dopov. Akad. Nauk Ukr. SSR, Ser. B **9**, 35.

Eremenko, V.N., M.V. Bulanova, P.S. Martsenjuk and V.E. Listovnichiy, 1989, Poroshk. Metall. **2**, 79.

Eremenko, V.N., M.V. Bulanova and P.S. Martsenyjuk, 1991, Ukr. Khim. Zh. **57**, 241.

Eremenko, V.N., M.V. Bulanova and P.S. Martsenyuk, 1992, J. Alloys & Compounds **189**, 229.

Espinosa, G.P., 1980, Mater. Res. Bull. **15**, 791.

Espinosa, G.P., A.S. Cooper, H. Barz and J.P. Remeika, 1980, Mater. Res. Bull. **15**, 1635.

Espinosa, G.P., A.S. Cooper and H. Barz, 1982, Mater. Res. Bull. **17**, 963.

Ferro, B., R. Marazza, G. Rambaldi and A. Saccone, 1975, J. Less-Common Met. **40**, 251.

Fisk, Z., and G.W. Webb, 1976, Phys. Rev. Lett. **36**, 1084.

Fisk, Z., S.E. Lambert, M.B. Maple, J.P. Remeika, G.P. Espinosa, A.S. Cooper, H. Barz and S. Oseroff, 1982, Solid State Commun. **41**, 63.

Fornasini, M.L., and F. Merlo, 1971, Atti Acad. Naz. Lincei, Cl. Sci. Fis. Mat. Nat. Rend. **50**, 186.

Fourgeot, F., B. Chevalier, P. Cravereau, L. Fournes and J. Etourneau, 1995, J. Alloys & Compounds **218**, 90.

Franceschi, E., 1979, J. Less-Common Met. **66**, 175.

Franceschi, E.E., and G.A. Costa, 1988a, J. Thermal Anal. **34**, 451.

Franceschi, E.E., and G.A. Costa, 1988b, Lanthanide & Actinide Res. **2**, 407.

François, M., B. Malaman, G. Venturini, J. Steinmetz and B. Roques, 1985, J. Less-Common Met. **108**, 45.

François, M., G. Venturini, B. Malaman and B. Roques, 1990, J. Less-Common Met. **160**, 197.

Fukuhara, T., S. Isakawa and H. Sato, 1992, J. Magn. & Magn. Mater. **104–107**, 667.

Furusawa, M., M. Kurisu, Y. Andoh, T. Takeuchi, K. Kindo and H. Hori, 1995, J. Magn. & Magn. Mater. **140–144**, 877.

Garde, C.S., J. Ray and G. Chandra, 1989, Phys. Rev. B **40**, 10116.

Genicon, J.L., J.P. Modondanon, R. Tournier, P. Caudouet, R. Fruchart, O. Peña, R. Horyn and M. Sergent, 1985, J. Appl. Phys. **57**, 3194.

Gillot, M., A. Shytuła, Z. Tomkowicz and R. Zach, 1995, J. Alloys & Compounds **226**, 131.

Givord, F., P. Lejay, E. Ressoushe, J. Schweizer and A. Stunault, 1989, Physica B **156–157**, 805.

Givord, F., P. Lejay, A. Munoz and J. Schweizer, 1992, J. Magn. & Magn. Mater. **116**, 419.

Gladyshevsky, E.I., 1971, Crystal Chemistry of Silicids and Germanids (Metallurgia, Moscou) p. 198.

Gladyshevsky, E.I., and O.I. Bodak, 1982, Crystal Chemistry of Rare Earth Intermetallic Compounds (Vyscha Shkola, Lviv) pp. 1–253.

Gladyshevsky, E.I., and O.I. Bodak, 1984, Crystal chemistry of ternary rare earth intermetallic compounds, in: Crystal Chemistry Problems (Nauka, Moscow) pp. 72–101.

Gladyshevsky, E.I., P.I. Krypiyakevich and M.Yu. Tesluk, 1952, Dokl. Akad. Nauk SSSR, Ser. Met. **85**, 81.

Gladyshevsky, E.I., Yu.N. Gryn and Ya.P. Yarmoluk, 1983, Dokl. Akad. Nauk Ukr. SSR, Ser. A **2**, 70.

Gladyshevsky, E.I., O.I. Bodak and V.K. Pecharsky, 1990, Phase equilibria and crystal chemistry in ternary earth systems with metallic elements, in: Handbook on the Physics and Chemistry of Rare Earths, Vol. 13, eds K.A. Gschneidner Jr and L. Eyring (North-Holland, Amsterdam) pp. 103–112.

Görlich, E.A., R. Kmeć, K. Latka, A. Szytuła and Z. Zygmunt, 1994, J. Phys. Condens. Matter **9**, 11127.

Gratz, E., and M.J. Zuckermann, 1982, J. Magn. & Magn. Mater. **29**, 181.

Gryn, Yu.N., and R.E. Gladyshevsky, 1989, Gallides (Mettallurgia, Moscow) p. 245.

Gryn, Yu.N., Ya.P. Yarmoluk and V.K. Pecharsky, 1983, Izv. Akad. Nauk SSSR, Met. **3**, 213.

Gschneidner Jr, K.A., V.K. Pecharsky and M. Gailloux, 1995, in: Cryocoolers, Vol. 8, ed. R.G. Ross Jr (Plenum Press, New York) p. 685.

Günzel, E., and K. Schubert, 1958, Z. Metallkd. **49**, 234.

Harris, I.R., and G.V. Raynor, 1965, J. Less-Common Met. **9**, 7.

Haschke, H., H. Nowotny and F. Benesovsky, 1966, Monatsh. Chem. **97**, 716.

Hasegawa, A., 1981, J. Phys. Soc. Jpn. **50**, 3313.

Hiess, A., C. Geibel, G. Sparn, C.D. Bredl, F. Steglich, T. Takabatake and H. Fujii, 1994, Physica B **199–200**, 437.

Higashi, I., K. Kobayashi, T. Takabatake and M. Kasaya, 1993, J. Alloys & Compounds **193**, 300.

Hodeau, J.L., J. Chenavas, M. Marezio and J.P. Remeika, 1980, Solid State Commun. **36**, 839.

Hodeau, J.L., M. Marezio and J.P. Remeika, 1984, Acta Crystallogr. B **40**, 26.

Hodges, I.A., and G. Jehanno, 1988, J. Phys. **49**, (Suppl. N1) 387.

Hofmann, W., and W. Jäniche, 1936, Z. Metallkd. **28**, 1.

Houwman, E.P., A.W.M. van de Pasch and J. Flokstra, 1987, Physica B **145**, 215.

Iandelli, A., 1964, Z. Anorg. Allg. Chem. **330**, 221.

Iandelli, A., and A. Palenzona, 1966, Atti Accad. Naz. Lincei, Cl. Sci. Fis. Mat. Nat. Rend. **40**, 623.

Ikeda, K., and K.A. Gschneidner Jr, 1982, Phys. Rev. B **25**, 4623.

Jeitschko, W., and E. Parthé, 1965, Acta Crystallogr. **19**, 275.

Jeitschko, W., and E. Parthé, 1967, Acta Crystallogr. **22**, 551.

Jeitschko, W., H. Nowotny and F. Benesovsky, 1964, Monatsh. Chem. **95**, 1040.

Johanson, W.R., G.W. Crabtree, A.S. Edelstein and O.D. McMasters, 1981, Phys. Rev. Lett. **46**, 504.

Johnson, M.L., and R.N. Shelton, 1984, Solid State Commun. **52**, 839.

Jorda, J.L., M. Ishikawa and J. Muller, 1985, J. Less-Common Met. **107**, 321.

Kaczmarska, K., J. Pierre, A. Slebarsky and R.V. Skolozdra, 1993, J. Alloys & Compounds **196**, 165.

Kadowaki, H., T. Ekino, H. Iwasaki, T. Takabatake, H. Fujii and J. Sakurai, 1993, J. Phys. Soc. Jpn. **62**, 4426.

Kadowaki, H., T. Sato, H. Yoshizawa, T. Ekino, T. Takabatake, H. Fujii, L.P. Regnault and Y. Isikawa, 1994, J. Phys. Soc. Jpn. **63**, 2074.

Kalychak, Ya.M., V.M. Baraniak, V.K. Belsky and O.D. Dmytrah, 1988, Dopov. Akad. Nauk Ukr. RSR, Ser. B **9**, 39.

Kasaya, M., B. Liu, M. Sera, T. Kasuya, D. Endoh, T. Goto and T. Fujimura, 1985, J. Magn. & Magn. Mater. **52**, 289.

Kasaya, M., T. Tani, F. Iga and T. Kasuya, 1988, J. Magn. & Magn. Mater. **76–77**, 278.

Kasaya, M., T. Tani, K. Kawate, T. Mizushima, Y. Isikawa and K. Sato, 1991, J. Phys. Soc. Jpn. **60**, 3145.

Kierstead, H.A., B.D. Dunlap, S.K. Malik, A.M. Umargji and G.K. Shenoy, 1985, Phys. Rev. B **32**, 135.

Klaasse, J.C.P., W.C.M. Mattens, F.R. de Boer and P.E. de Châtel, 1977, Physica B+C, **86–88**, 234.

Kletowski, Z., 1982, Phys. Status Solidi A **70**, K51.

Kohgi, M., K. Ohoyama, T. Osakabe and M. Kasaya, 1992, J. Magn. & Magn. Mater. **108**, 187.

Kolenda, M., J. Leciejewicz, N. Stuesser, A. Szytuła and A. Zygmunt, 1995, J. Magn. & Magn. Mater. **145**, 85.

Komarovskaya, L.P., and R.V. Skolozdra, 1984, Dokl. Akad. Nauk Ukr. SSR, Ser. B **8**, 40.

Komarovskaya, L.P., and R.V. Skolozdra, 1985, Dokl. Akad. Nauk Ukr. SSR, Ser. A **1**, 81.

Komarovskaya, L.P., and R.V. Skolozdra, 1992, Izv. Akad. Nauk SSSR, Ser. Met. **2**, 231.

Komarovskaya, L.P., L.G. Akselrud and R.V. Skolozdra, 1983a, Kristallografiya **28**, 1201.

Komarovskaya, L.P., R.V. Skolozdra and I.V. Filatova, 1983b, Dokl. Akad. Nauk Ukr. SSR, Ser. A **1**, 82.

Komarovskaya, L.P., S.A. Sadykov and R.V. Skolozdra, 1988, Ukr. Fiz. Zh. **33**, 1249.

Komarovskaya, L.P., L.A. Mykhayliv and R.V. Skolozdra, 1989, Izv. Akad. Nauk SSSR. Metal. **4**, 209.

Koretskaya, O.E., and R.V. Skolozdra, 1986, Izv. Akad. Nauk SSSR, Ser. Neorgan. Mater. **22**, 690.

Koretskaya, O.E., L.P. Komarovskaya and R.V. Skolozdra, 1988a, Izv. Akad. Nauk SSSR, Ser. Neorgan. Mater. **24**, 1299.

Koretskaya, O.E., L.A. Mykhayliv, V.A. Sadov and R.V. Skolozdra, 1988b, Vestn. Lvov. Univ. Ser. Khim. **29**, 34.

Kotsanidis, P.A., J.K. Yakintos and E. Roudaut, 1993, J. Magn. & Magn. Mater. **124**, 51.

Kotur, B.Ya., and V.A. Derkach, 1994, Visn. Lviv. Univ. Ser. Khim. **33**, 38.

Kotur, B.Ya., and I.P. Kluchka, 1989, Izv. Akad. Nauk SSSR, Ser. Neorgan. Mater. **25**, 597.

Kotur, B.Ya., O.I. Bodak and E.I. Gladyshevsky, 1977, Dokl. Akad. Nauk Ukr. SSR, Ser. A **7**, 666.

Krypyakevich, P.I., 1977, Structure Types of Intermetallic Compounds (Nauka, Moscow) pp. 1–288.

Krypyakevich, P.I., V.Ya. Markiv and E.V. Melnyk, 1967, Dokl. Akad. Nauk Ukr. SSR, Ser. A **8**, 750.

Kuzma, Yu.B., P.I. Krypyakevich and R.V. Skolozdra, 1966, Dopov. Akad Nauk Ukr. RSR. Ser. A **10**, 1290.

Larchev, V.I., and S.V. Popova, 1977, Fiz. Tverd. Tela Leningrad **19**, 1463.

Larson, A.C., and D.T. Cromer, 1961, Acta Crystallogr. **14**, 73.

Lawrence, J.M., M.F. Hundlay, J.D. Thompson, G.H. Kwei and Z. Fisk, 1991, Phys. Rev. B **43**, 11057.

Leithe-Jasper, A., F. Weitzer, P. Rogl, Qinian Qi and J.M.D. Coey, 1994, Hyperfine Interaction **94**, 2327.

Lethuillier, P., J. Pierre, K. Knorr and W. Drexel, 1975, J. Phys. **36**, 329.

Li, W.H., H.B. Stanley, T.J. Udovic, R.N. Shelton and P. Klavins, 1989, Phys. Rev. B **39**, 4119.

Li, Y., R.G. Graham, D.St.P. Bunbury, P.W. Mitchell, M.A.H. McCausland, R.S. Chaughule, L.C. Gupta, R. Vijayaraghavan and G. Godart, 1995, J. Magn. & Magn. Mater. **140–144**, 1031.

Liang, G., N. Jisrawi and M. Croft, 1990, Physica B **163**, 134.

Lin, C.L., T. Mihalisin and N. Bykovetz, 1992, J. Magn. & Magn. Mater. **116**, 335.

Liu, J.-Q., and J.-X. Zheng, 1984, Acta Phys. Sin. **33**, 1155.

Macció, D., A. Saccone and R. Ferro, 1993, J. Alloys & Compounds **201**, L13.

Malaman, B., G. Venturini and B. Roques, 1988, Mater. Res. Bull. **23**, 1629.

Malik, S.K., A.M. Umarji and G.K. Shenoy, 1985, Phys. Rev. B **31**, 6971.

Malik, S.K., A.E. Dwight, P.P. Vaishnawa and C.W. Kimball, 1987, J. Less-Common Met. **127**, 262.
Martin, R.M., 1982, Phys. Rev. Lett. **48**, 362.
Mazzone, D., D. Rossi, R. Marazza and D. Ferro, 1981, J. Less-Common Met. **80**, P17.
Meot-Meyer, M., G. Venturini, B. Malaman, J. Steinmetz and B. Roques, 1984, Mater. Res. Bull. **19**, 1181.
Meot-Meyer, M., G. Venturini, B. Malaman and B. Roques, 1985, Mater. Res. Bull. **20**, 913.
Merlo, F., and M.L. Fornasini, 1967, J. Less-Common Met. **13**, 603.
Merlo, F., M. Pani and M.L. Fornasini, 1991, J. Less-Common Met. **171**, 329.
Miller, K., and H.T. Hall, 1972, Inorg. Chem. **11**, 1188.
Miraglia, S., J.L. Hodeau, M. Marezio and H.R. Ott, 1984, Ann. Chim. Fr. **9**, 1011.
Miraglia, S., J.L. Hodeau, M. Marezio, C. Laviron, M. Ghedira and G.P. Espinosa, 1986, J. Solid State Chem. **63**, 358.
Miraglia, S., J.L. Hodeau, F. de Bergevin, M. Marezio and G.P. Espinosa, 1987, Acta Crystallogr. B **43**, 76.
Mott, N.F., 1964, Adv. Phys. **13**, 325.
Murani, A.P., 1983, Phys. Rev. B. **28**, 2308.
Naushad Ali, S.B. Woods, G. Kozłowski and A. Rojek, 1985, J. Phys. F **15**, 1547.
Nishigori, S., H. Coshima, T. Suzuki, T. Fujita, G. Nakamoto, T. Takabatake, H. Fudjii and J. Sakurai, 1993, Physica B **186–188**, 406.
Nohara, S., H. Namatame, A. Fujimori and T. Takabatake, 1993, Physica B **186–188**, 403.
Nowotny, H., and W. Silbert, 1941, Z. Metallkd. **33**, 391.
Oesterreicher, H., 1977, J. Less-Common Met. **55**, 131.
Oleksyn, O.Ya., L.G. Akselrud and H. Boehm, 1995, New superstructure formation at $DyFe_6Sn_6$ composition, in: 6th Int. Conf. on Crystal Chemistry of Intermetallic Compounds, Ukraine, Lviv, 1995 (Lviv State University, Lviv) p. 87.
Olenych, R.R., L.G. Akselrud and Ya.P. Yarmoluk, 1981, Dokl. Akad. Nauk Ukr. SSR, Ser. A **2**, 84.
Palenzona, A., and S. Girafici, 1976, J. Less-Common Met. **46**, 321.
Palenzona, A., and S. Girafici, 1991, J. Phase Equilibria **12**, 482.
Palenzona, A., and P. Manfrinetti, 1993, J. Alloys & Compounds **201**, 43.
Palenzona, A., and F. Merlo, 1966, Atti Accad. Naz. Lincei, Cl. Sci. Fis. Mat. Nat. Rend. **40**, 617.
Parthé, E., B. Lux and H. Nowotny, 1955, Monatsh. Chem. **86**, 859.
Pecharsky, V.K., K.A. Gschneidner Jr and L.L. Miller, 1991, Phys. Rev. B **43**, 10906.
Percheron, A., 1970, Colloq. Int. CNRS **180**(1), 165.
Pierre, J., B. Lambert-Andron, R.V. Skolozdra, J. Rodriguez-Carvajal and K. Kaczmarska, 1994, Physica B **202**, 143.
Podarevskaya, O.V., 1992, Thermodynamic properties of scandium, titanium and niobium, Ph.D. Chemistry thesis (Institute of Material Problems, Kiev) pp. 1–17.
Remeika, J.P., G.P. Espinosa, A.S. Cooper, H. Barz, J.M. Rowell, D.B. McWhan, J.M. Vandenberg, D.E. Moncton, Z. Fisk, L.D. Woolf, H.C. Hamaker, M.B. Maple, G. Shirane and W. Thomlinson, 1980b, Solid State Commun. **34**, 923.
Remeika, P., G.P. Espinosa, A.S. Cooper, H. Barz and J.M. Rowell, 1980a, Bull. Am. Phys. Soc. **25**, 232.
Rieger, W., 1970, Monatsh. Chem. **101**, 449.
Rieger, W., and E. Parthé, 1968, Monatsh. Chem. **99**, 291.
Rieger, W., H. Nowotny and H. Benesovski, 1966, Monatsh. Chem. **97**, 378.
Rocher, Y.A., 1962, Adv. Phys. **11**, 233.
Rojek, A., and C. Sułkowski, 1986, Phys. Status Solidi B **133**, K149.
Rojek, A., and C. Sułkowski, 1987, Phys. Status Solidi B **139**, K63.
Rojek, A., C. Sułkowski, A. Zygmunt and G. Kozłowski, 1986, Phys. Status Solidi B **134**, 125.
Rossi, A., 1934, Gazz. Chim. Ital. **64**, 832.
Rossi, D., R. Marazza and R. Ferro, 1985, J. Less-Common Met. **107**, 99.
Routsi, Ch., J.K. Yakinthos and E. Gamari-Seale, 1991, J. Magn. & Magn. Mater. **98**, 257.
Routsi, Ch.D., J.K. Yakinthos and E. Gamari-Seale, 1992a, J. Magn. & Magn. Mater. **110**, 317.
Routsi, Ch.D., J.K. Yakinthos and H. Gamari-Seale, 1992b, J. Magn. & Magn. Mater. **117**, 79.
Rundqvist, S., and F. Jellinek, 1959, Acta Chem. Scand. **13**, 425.
Saccone, A., D. Maccio and R. Ferro, 1993, J. Alloys & Compounds **201**, L9.
Sakurai, J., Y. Yamaguchi, K. Mibu and T. Shinjo, 1990a, J. Magn. & Magn. Mater. **84**, 157.
Sakurai, J., Y. Yamagushi, S. Nishigori, T. Suzuki and T. Fujita, 1990b, J. Magn. & Magn. Mater. **90–91**, 422.

Sakurai, J., S. Nakatani, A. Adam and H. Fujiwara, 1992, J. Magn. & Magn. Mater. **108**, 143.

Sakurai, J., K. Kegai, T. Kuwai, Y. Isikawa, K. Nishimura and K. Mori, 1995, J. Magn. & Magn. Mater. **140–144**, 875.

Samsonova, N.D., R.V. Skolozdra, L.D. Finkelstein and L.P. Komarovskaja, 1985, Fiz. Tverd. Tela Leningrad **27**, 2203.

Sanchez, J.P., J.M. Friedt, G.K. Shenoy, A. Percheron and J.C. Achard, 1976, J. Phys. C **9**, 2207.

Schmidt, F.A., and O.D. McMasters, 1967, J. Less-Common Met. **15**, 1.

Schmidt, W., and E. Umlauf, 1976, Commun. Phys. **1**, 67.

Sereni, J.G., 1980, J. Phys. F **10**, 2831.

Shelton, R.N., L.S. Hausermann-Berg, M.J. Johnson, P. Klavins and H.D. Yang, 1986, Phys. Rev. B. **34**, 199.

Shoemaker, C.B., and D.P. Shoemaker, 1965, Acta Crystallogr. **18**, 900.

Shoemaker, D.P., R.E. Marsh, F.J. Ewing and L. Pauling, 1952, Z. Metallkd. **49**, 234.

Sichevich, O.M., L.P. Komarovskaya, Yu.N. Gryn, Ya.P. Yarmoluk and R.V. Skolozdra, 1984, Ukr. Fiz. Zh. **29**, 1342.

Sichevich, O.M., R.V. Lapunova, A.N. Sobolev, Yu.N. Gryn and Ya.P. Yarmoluk, 1985, Kristallografiya **30**, 627.

Sinnen, H.D., and H.U. Schuster, 1978, Z. Naturfors. **33**, 1077.

Skolozdra, R.V., 1977, Vestn. Lvov. Univ. Ser. Khim. **19**, 42.

Skolozdra, R.V., 1993, Stannides of rare earth and transition metals (Svit, Lviv, Ukraine) pp. 1–200.

Skolozdra, R.V., and L.P. Komarovskaya, 1982a, Dokl. Akad. Nauk Ukr. SSR, Ser. A **6**, 83.

Skolozdra, R.V., and L.P. Komarovskaya, 1982b, Ukr. Fiz. Zh. **27**, 1834.

Skolozdra, R.V., and L.P. Komarovskaya, 1983, Ukr. Fiz. Zh. **28**, 1093.

Skolozdra, R.V., and L.P. Komarovskaya, 1988a, Izv. Akad. Nauk SSSR, Ser. Met. **2**, 214.

Skolozdra, R.V., and L.P. Komarovskaya, 1988b, Izv. Akad. Nauk SSSR, Ser. Met. **3**, 199.

Skolozdra, R.V., and O.E. Koretskaya, 1984, Ukr. Fiz. Zh. **29**, 877.

Skolozdra, R.V., V.M. Mandzyk and L.G. Akselrud, 1981a, Kristallografiya **26**, 480.

Skolozdra, R.V., V.M. Mandzyk, Yu.K. Gorelenko and V.D. Tkachuk, 1981b, Fiz. Met. Metalloved. **52**, 966.

Skolozdra, R.V., O.E. Koretskaya and Yu.K. Gorelenko, 1982, Ukr. Fiz. Zh. **27**, 263.

Skolozdra, R.V., I.V. Yasnytskaya, O.E. Koretskaya and L.G. Akselrud, 1983, Dop. Akad. Nauk Ukr. SSR, Ser. B **6**, 43.

Skolozdra, R.V., L.P. Komarovskaya and L.G. Akselrud, 1984a, Ukr. Fiz. Zh. **29**, 1395.

Skolozdra, R.V., O.E. Koretskaya and Yu.K. Gorelenko, 1984b, Izv. Akad. Nauk SSSR, Ser. Neorgan. Mater. **20**, 604.

Skolozdra, R.V., L.G. Akselrud, O.E. Koretskaya and L.P. Komarovskaya, 1985, Dokl. Akad. Nauk Ukr. SSR, Ser. B **12**, 36.

Skolozdra, R.V., L.G. Akselrud, V.K. Pecharsky and O.E. Koretskaya, 1986a, Dokl. Akad. Nauk Ukr. SSR, Ser. B **12**, 51.

Skolozdra, R.V., O.E. Koretskaya and L.G. Akselrud, 1986b, Ukr. Fiz. Zh. **31**, 1537.

Skolozdra, R.V., I.V. Yasnitskaya and L.G. Akselrud, 1987, Ukr. Fiz. Zh. **32**, 729.

Skolozdra, R.V., L.P. Komarovskaya and L.G. Akselrud, 1988a, Izv. Akad. Nauk SSSR, Ser. Neorgan. Mater. **24**, 1490.

Skolozdra, R.V., Yu.K. Gorelenko, E.E. Terletskaya and V.D. Tkachuk, 1988b, Fiz. Met. Metalloved. **66**, 864.

Skolozdra, R.V., S.A. Sadykov, L.P. Komarovskaya and O.K. Kuvandikov, 1988c, Fiz. Met. Metalloved. **65**, 527.

Skolozdra, R.V., I.V. Yasnytskaya, L.G. Akselrud and L.P. Komarovskaya, 1988d, Izv. Akad. Nauk SSSR, Ser. Neorgan. Mater. **24**, 65.

Skolozdra, R.V., L.P. Komarovskaya, O.E. Terletskaya and L.G. Akselrud, 1991, Kristallografiya **36**, 492.

Skolozdra, R.V., B. Garcia-Landa, D. Fruchart, D. Gignoux, J.L. Soubeyroux and L. Akselrud, 1996a, J. Alloys & Compounds **235**, 10.

Skolozdra, R.V., R. Szymczak, H. Szymczak, L. Romaka and M. Baran, 1996b, J. Phys. Chem. Solids **57**, 357.

Staliński, B., Z. Kletowsky and Z. Henke, 1973, Phys. Status Solidi A **19**, K165.

Staliński, B., Z. Kletowski and Z. Henke, 1975, Bull. Acad. Pol. Sci. Ser. Sci. Chim. **23**, 827.

Stanley, H.B., J.W. Lynn, R.N. Shelton and P. Klavins, 1987, J. Appl. Phys. **61**, 3371.

Stassis, C., C.K. Loong, O.D. McMasters and R.M. Moon, 1979, J. Appl. Phys. **50**, 2091.

Takabatake, M., M. Nagasawa, H. Fujii, M. Nohara, T. Suzuki, T. Fujita, G. Kido and T. Hiraoka, 1992, J. Magn. & Magn. Mater. **108**, 155.

Takabatake, T., Y. Nakazawa and M. Ishikawa, 1987, Jpn. J. Appl. Phys. **26** Suppl. 26–3, 547.

Takabatake, T., Y. Nakazawa, M. Ishikawa, T. Sakakibara, K. Koga and I. Oguro, 1988, J. Magn. & Magn. Mater. **76-77**, 87.

Takabatake, T., F. Teshima, H. Fujij, S. Nishigori, T. Suzuki, T. Fujita, Y. Yamaguchi, J. Sakurai and D. Jaccard, 1990, Phys. Rev. B **41**, 9607.

Takabatake, T., G. Nakamoto, H. Tanaka, Y. Bando, H. Fujii, S. Nishigori, H. Goshima, T. Suzuki, T. Fujita, I. Oguro, T. Hiraoka and S.K. Malik, 1994, Physica B **199–200**, 457.

Taylor, M.A., 1959, Acta Crystallogr. **12**, 393.

Thirion, F., J. Steinmetz and B. Malaman, 1983, Mat. Res. Bull. **18**, 1537.

Thompson, J.D., Z. Fisk, Y.Y. Chen and J.M. Lawrence, 1987, J. Less-Common Met. **127**, 385.

Tsang, T.W.E., K.A. Gschneidner Jr, O.D. McMasters, R.J. Stierman and S.K. Dhar, 1984, Phys. Rev. B **29**, 4185.

Tsuchida, T., and W.E. Wallace, 1965, J. Phys. Chem. **43**, 3811.

Uwatoko, Y., G. Oomi, T. Takabatake and H. Fujii, 1992, J. Magn. & Magn. Mater. **104–107**, 643.

Vandenberg, J.M., 1980, Mater. Res. Bull. **15**, 835.

van Mens, R., 1986, J. Magn. & Magn. Mater. **61**, 24.

Veenhuizen, P.A., G. van Kalkeren, J.C.P. Klaasse, A. Menovsky, A.C. Moleman, F.R. de Boer and J. Aarts, 1986, J. Magn. & Magn. Mater. **54–57**, 425.

Venturini, G., J. Steinmetz and B. Roques, 1982, J. Less-Common Met. **87**, 21.

Venturini, G., B. Malaman and B. Roques, 1989a, J. Less Common-Met. **146**, 271.

Venturini, G., B. Malaman and B. Roques, 1989b, Mater. Res. Bull. **24**, 1135.

Venturini, G., B. Malaman and B. Roques, 1989c, J. Less-Common Met. **152**, 51.

Venturini, G., M. François, B. Malaman and B. Roques, 1990, J. Less-Common Met. **160**, 215.

Venturini, G., B. Chafik El Idrissi and B. Malaman, 1991, J. Magn. & Magn. Mater. **94**, 35.

Venturini, G., R. Welter, B. Malaman and E. Ressouche, 1993, J. Alloys & Compounds **200**, 51.

Wang, F.E., F.A. Konda, C.F. Miskell and A.J. King, 1965, Acta Crystallogr. **18**, 24.

Weitzer, F., and P. Rogl, 1993, J. Phase Equilibria **14**, 676.

Weitzer, F., K. Hiebl and P. Rogl, 1992a, J. Solid State Chem. **98**, 291.

Weitzer, F., K. Hiebl and P. Rogl, 1992b, Solid State Commun. **82**, 353.

Weitzer, F., K. Hiebl, P. Rogl and H. Noël, 1992c, Ber. Bunsenges. Phys. Chem. **96**, 1715.

Weitzer, F., A. Leithe-Jasper, K. Hiebl, P. Rogl, Qinian Qi and J.M.D. Coey, 1993a, J. Appl. Phys. **73**, 8447.

Weitzer, F., A. Leithe-Jasper, P. Rogl, K. Hiebl, H. Noel, G. Wiesinger and W. Steiner, 1993b, J. Solid State Chem. **104**, 368.

Wiesinger, G., A. Rainbacher, W. Steiner, A. Leithe-Jasper, P. Rogl and F. Weitzer, 1994, Hyperfine Interactions **94**, 1915.

Yakinthos, J.K., Ch.D. Routsi and D. Roudaut, 1994, J. Magn. & Magn. Mater. **136**, 65.

Yanase, A., 1983, J. Magn. & Magn. Mater. **31–34**, 453.

Yang, F., J.P. Kuang, J. Li, E. Bruck, H. Nakotte, F.R. de Boer, X. Wu, Z. Li and Y. Wang, 1991, J. Appl. Phys. **69**, 4705.

Yarmoluk, Ya.P., M. Sikiritsa and L.G. Akselrud, 1982, Kristallografiya **27**, 1090.

Yinghong, Z., Q. Can and L. Junqin, 1991, J. Less-Common Met. **175**, 97.

Ziman, J.M., 1962, Electrons and Phonons, Chapter IX, Sect. 12 (Oxford University Press, Oxford).

Zygmunt, A., and A. Szytuła, 1995, J. Alloys & Compounds **219**, 185.

AUTHOR INDEX

SUBJECT INDEX